Proceedings of the

15th International Workshop on Deep-Inelastic Scattering and Related Subjects

DIS 2007

April 16-20, 2007
Munich, Germany

Editors:
Günter Grindhammer, Kirsten Sachs

Verlag Deutsches Elektronen-Synchrotron

Impressum

Proceedings of the 15$^{\text{th}}$ International Workshop on Deep-Inelastic Scattering and Related Subjects DIS 2007

This document is also available online at ATLANTIS Press
http://www.sciencewisepublishing.com/publications/DIS07

Conference homepage
http://www.mppmu.mpg.de/dis2007/

Slides at
http://indico.cern.ch/conferenceTimeTable.py?confId=9499

Editors: Günter Grindhammer, Kirsten Sachs
Cover Photo: ©iStockphoto.com/Björn Kindler
Photo of Participants: Daniel Greenwald (MPI for Physics, Munich)
September 2007
DESY-PROC-2007-01
ISSN 1435-8077
ISBN 978-3-935702-23-2

Published by
Deutsches Elektronen-Synchrotron, DESY
Notkestraße 85
22607 Hamburg
Germany

Content

Volume I

Summary Talks

Structure Functions and Low-x

Convenors: Alexandre Glazov, Kunihiro Nagano, Sven Moch

Structure Functions and Low-x / Electroweak Measurements (Including Top) and Beyond the Standard Model

Structure Functions and Low-x / Diffraction and Vector Mesons

Electroweak Measurements (Including Top) and Beyond the Standard Model

Convenors: Martin Wessels, James Ferrando, Thomas Nunnemann, Michael Spira

Spin Physics

Convenors: Delia Hasch, Gerhard Mallot, Daniël Boer

Volume II

Diffraction and Vector Mesons

Convenors: Laurent Favart, Uta Klein, Rolf Ent, Leszek Motyka

Diffraction and Vector Mesons / Spin Physics

Heavy Flavors

Convenors: Stephanie Menzemer, Rainer Mankel, Benno List, Michael Klasen

Heavy Flavors / Diffraction and Vector Mesons

Hadronic Final States and QCD

Convenors: Daniel Traynor, Alexandre Savin, Duncan Brown, Giulia Zanderighi

Special Session on α_s

Future of DIS

Convenors: Abhay L. Deshpande, Paul Newman, Christian Weiss

Diffraction and Vector Mesons

Convenors:
Laurent Favart,
Uta Klein,
Rolf Ent,
Leszek Motyka

On Diffraction and JIMWLK Evolution

Michael Lublinsky

State University of New York - Department of Physics and Astronomy
Stony Brook NY 11794-3800, USA

A systematic approach towards description of semi-inclusive processes at low x and with multiple rescatterings taken into account is highlighted. We discuss diffractive processes and their evolution with respect to relevant rapidity intervals.

This talk is based on Ref. [2].

• We develop a general formalism to address semi-inclusive processes at high energies and including multiple rescatterings. Part of formalism is independent of underlying high energy evolution. However, most of applications considered are within DIS framework and assume BK-JIMWLK evolution.

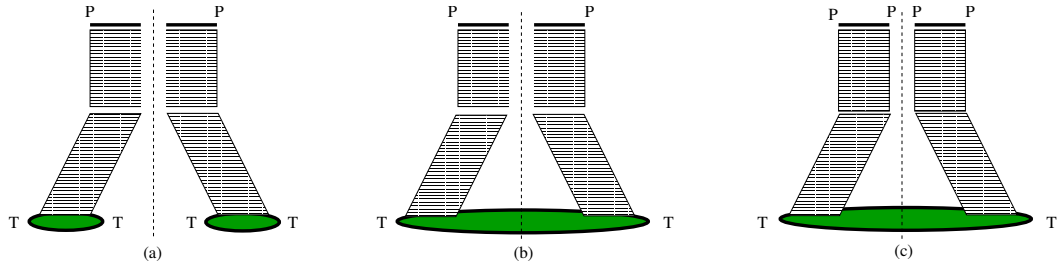

Figure 1: Diffraction and fan diagrams

• We apply our general formalism to High energy diffractive processes. We attempt to derive results not relying on the dipole (large N_c and target factorization) approximation. We reproduce and extend the result of Ref. [3] for the process of projectile diffraction with target scattered elastically. We also obtain results for projectile diffraction with target diffracting in a small rapidity interval and elastic scattering.

• We consider high energy diffraction with multiple gaps. For various diffractive processes we derive evolution equations with respect to total rapidity and gap(s).

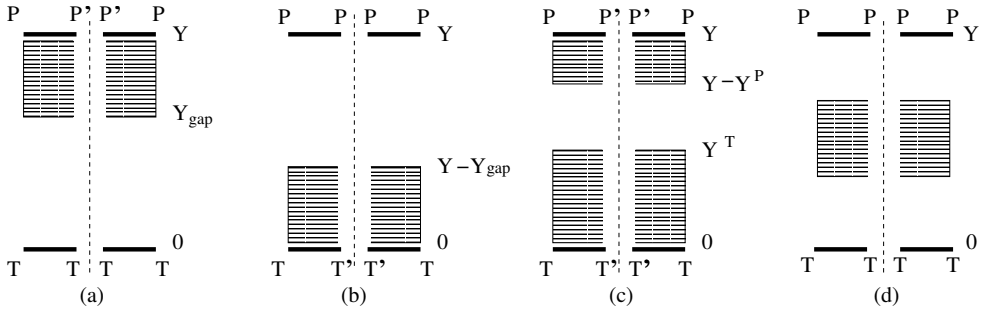

Figure 2: Various types of diffractive processes

Let me flash the formalism which is based on the evolution of hadronic wavefunction. Hadron wave function in the gluon Fock space is

$$|\Psi\rangle \;=\; \Psi[a_i^{\dagger a}(x)]|0\rangle \qquad\qquad |\Psi\rangle \;=\; |v\rangle$$

After rapidity evolution the evolved wave function becomes

$$|\Psi_{in}\rangle \;=\; \Omega_Y(\rho,\, a)\,|v\rangle\,; \qquad\qquad |v\rangle \;=\; |v\rangle \,\otimes\, |0_a\rangle$$

Here Ω is the most general evolution kernel. It is known for arbitrary dense hadron [4]. We will however concentrate on the most simple case of dilute hadron. In this limit, Ω reduces to the gluon cloud operator

$$C_Y \;\equiv\; \Omega_Y(\rho \,\to\, 0) \,=\, \mathrm{Exp}\left[i \int d^2z\, b_i^a(z) \int_\Lambda^{e^Y \Lambda} \frac{dk^+}{\pi^{1/2}|k^+|^{1/2}} \left[a_i^a(k^+,z) \,+\, a_i^{\dagger a}(k^+,z)\right)\right] .$$

with the classical WW field

$$b_i^a(z) \,=\, \frac{g}{2\pi} \int d^2x \frac{(z-x)_i}{(z-x)^2} \;\; \rho^a(x)$$

The projectile's gluon scattering of a dense target has the eikonal propagator given by the Wilson line

$$S(x) \;=\; \mathcal{P}\, \exp\left\{i \int dx^-\, T^a\, \mathbf{A}_t^a(x,x^-)\right\} .$$

with A_t characterizing the target external field. The evolution of the diagonal element of the S-matrix operator $\Sigma^P \equiv \langle \Psi_{out}|\Psi_{in}\rangle$ reads

$$\partial_Y\, \Sigma^P \;=\; -\, H^{JIMWLK}\, \Sigma^P\,; \qquad\qquad H^{JIMWLK} \;=\; \int_z \; Q_i^a(z)\; Q_i^a(z)$$

where we introduced the gluon production (and scattering) amplitude

$$Q_i^a(z) \;=\; g \int_x \; \frac{(x-z)_i}{(x-z)^2} \; \left[J_L^a(x) \,-\, S^{ab}(z)\; J_R^b(x)\right]$$

The generators of the left/right color rotations are Lie derivatives

$$J_R^a(x) \;=\; -\,\mathrm{tr}\left\{S(x)\; T^a\; \frac{\delta}{\delta S^\dagger(x)}\right\} , \qquad\qquad J_L^a(x) \;=\; -\,\mathrm{tr}\left\{T^a\; S(x)\; \frac{\delta}{\delta S^\dagger(x)}\right\}$$

This operator is visualized in Fig. 3.

Now we turn to discussion of semi-inclusive reactions. The system emerges from the collision at $t = 0$ and keeps evolving to the asymptotic time $t \to +\infty$, at which point the measurement of an observable $\hat{\mathcal{O}}$ is made

$$\langle\hat{\mathcal{O}}\rangle \;=\; \langle\, v|\, \Omega_Y^\dagger \;(1 \,-\, \hat{S}^\dagger)\, \Omega_Y \;\hat{\mathcal{O}}\; \Omega_Y^\dagger \;(1 \,-\, \hat{S})\, \Omega_Y\, |v\rangle$$

We find it convenient to introduce two targets - one for the amplitude S and another one for its conjugate $\bar{S}$. In the end of our computation we set $S = \bar{S}$.

$$\mathcal{O}_Y[S,\bar{S}] \;=\; \langle\, P_v|\, \Omega_Y^\dagger\, (1 \,-\, \hat{S}^\dagger)\, \Omega_Y \;\; \hat{\mathcal{O}} \;\; \Omega_Y^\dagger \;(1 \,-\, \hat{\bar{S}})\, \Omega_Y\, |P_v\,\rangle$$

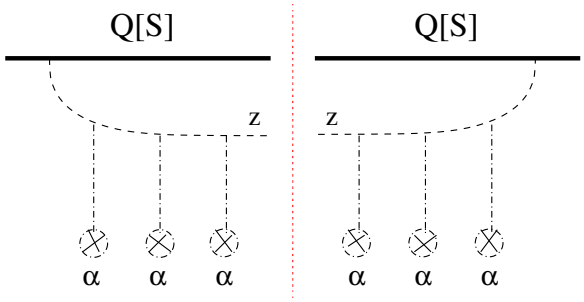

Figure 3: The operator Q

High energy evolution of the observable is given by the following equation

$$\frac{d\mathcal{O}_Y[S,\bar{S}]}{dY} \;=\; \lim_{\Delta y\to 0}\frac{\mathcal{O}_{Y+\Delta y}[S,\bar{S}] \;-\; \mathcal{O}_Y[S,\bar{S}]}{\Delta y} \;=\; -\,H_3[S,\bar{S}]\;\mathcal{O}_Y[S,\;\bar{S}]$$

Here the Hamiltonian H_3 (first introduced in [5])

$$H_3[S,\bar{S}] \;\equiv\; H_1[S] \;+\; H_1[\bar{S}] \;+\; 2\int_z Q_i^a(z,[S])\,Q_i^a(z,[\bar{S}])$$

$$H_1[S] \;\equiv\; H^{JIMWLK}[S] \;=\; \int_z Q_i^a(z,[S])\,Q_i^a(z,[S])\,, \qquad\qquad H_2[S,\bar{S}] \;\equiv\; H_1[S] + H_1[\bar{S}]$$

is illustrated in Fig. 4. The Hamiltonian H_2 appears in diffractive processes and is responsible for evolution through a rapidity gap. The Hamiltonian H_3 is presumably the answer to properly formulated question of generalization of AGK cutting rules to QCD.

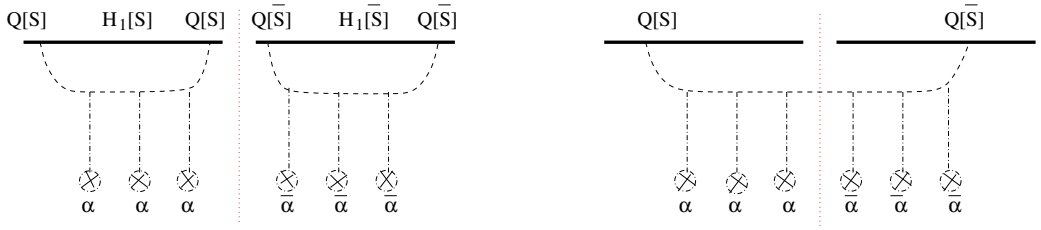

Figure 4: The Hamiltonian H_3

Having introduced the Hamiltonians we can introduce associated evolution operators:

$$U^3_{Y_1-Y_2} \;=\; Exp\,[-\,H_3\,(Y_1\;-\;Y_2)] \qquad\qquad U^2_{Y_1-Y_2} \;=\; Exp\,[-\,H_2\,(Y_1\;-\;Y_2)]$$

Thus a formal solution for inclusive diffraction with multiple gaps and multiple rescatterings (Fig. 5)

$$\sigma^{diff} \;\sim\; \int DS\,D\bar{S}\,W^t[S]\;\delta(S-\bar{S})\,U^3_{Y_0-Y_n}\;U^2_{Y_n-Y_{n-1}}\;\cdots\;U^2_{Y_1-Y_2}\,U^3_{Y-Y_1}\;\Sigma^p[S,\bar{S}]$$

This expression is quite complex and of little use. Things become less formal and more useful when passing to the dipole degrees of freedom

$$s_{x,y} \;=\; \frac{1}{N}\, tr[S_F(x)\, S_F^\dagger(y)]$$

We need to remember, however, that the factorization

$$\langle s(x,y)\, s(u,v)\rangle_T \;= \langle s(x,y)\rangle_T\, \langle s(u,v)\rangle_T$$

is not always valid. This is very important in order to include target diffractive states.

For processes involving transverse momentum transfer,a quadrupole operator is also in need

$$q_{x,y,u,v} \;=\; \frac{1}{N}\, tr[S_F(x)\, S_F^\dagger(y)\, S_F(u)\, S_F^\dagger(v)]$$

Fortunately, no other higher multiplet operators emerge, if the projectile at rest is made only out of dipoles.

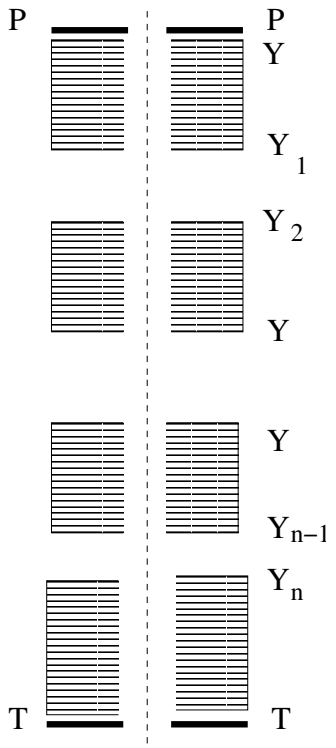

Figure 5: Diffraction with multiple gaps

Acknowledgments

Everything which is reported above has been done in collaboration with Alex Kovner. Many thanks to Alex for making hard work into a joy.

References

[1] Slides:
`http://indico.cern.ch/contributionDisplay.py?contribId=59&sessionId=7&confId=9499`

[2] A. Kovner and M. Lublinsky, JHEP **0611** 083 (2006); A. Kovner, M. Lublinsky and H. Weigert, Phys. Rev. **D74** 114023 (2006).

[3] Y. V. Kovchegov and E. Levin, Nucl. Phys. B **577** 221 (2000).

[4] A. Kovner, M. Lublinsky and U. Wiedemann, JHEP **0706** 075 (2007).

[5] M. Hentschinski, H. Weigert and A. Schafer, Phys. Rev. **D73** 051501 (2006).

Results on Inclusive Diffraction from the ZEUS Experiment by the M_X-Method

Bernd Löhr, DESY
on behalf of the ZEUS Collaboration

Diffractive deep inelastic scattering, $ep \to e'\gamma^* p \to e'XN$, has been studied at HERA with the ZEUS detector using an integrated luminosity of 52.4 pb^{-1}. The diffractive contribution to deep inelastic scattering has been determined with the M_X-method. The measurement covers a wide range in the $\gamma^* p$ c.m. energy W (45 - 220 GeV), photon virtuality Q^2 (25 - 320 GeV^2) and mass M_X (1.2 - 30 GeV). We present preliminary results on the diffractive structure function, $x_{IP}F_2^{D(3)}$. For comparison, results from our previous measurement at $Q^2 = 2.7$ - 55 GeV^2 are also included.

1 The M_X-Method

M_X is defined as the mass from all measured particles in the detector, except the scattered electron. The shape of the M_X-distribution is different for nondiffractive and diffractive events. Nondiffractive events lead to a rapidity-plateau distribution for the produced particles. Particle emission is a statistical process which may lead to a rapidity gap. The probability to find a rapidity gap Δy is given by Poisson statistics, $P(0) = e^{-\lambda \Delta y}$ where λ is the height of the plateau. This leads to the following mass distribution for nondiffractive events:

$$\frac{dN_{nondiff}}{d \ln M_X^2} = c \cdot e^{b \cdot \ln M_X^2} .$$

Diffractive events show a different M_X-distribution. For not too low and not too high values of M_X one finds experimentally [2]

$$\frac{dN_{diff}}{dM_X^2} \propto \frac{1}{M_X^2} \quad \text{from which follows} \quad \frac{dN_{diff}}{d \ln M_X^2} \approx \text{const.}$$

This can also be derived from a Triple Regge Model [3]. For the sum of nondiffractive and diffractive events one gets :

$$\frac{dN}{d \ln M_X^2} = D + c \cdot e^{b \cdot \ln M_X^2} .$$

Figure 1 shows a measured lnM_X^2-distribution. It is compared to the properly normalized distribution of the sum of MC-simulated nondiffractive and diffractive (hatched) events. Over the range $\ln M_X^2 \leq \ln W^2 - \eta_0$, which is indicated by two vertical lines, the above formula with D=const. is fitted to the measured distribution with η_0 taken from data. This gives a very good fit for the nondiffractive contribution $c \cdot e^{b \cdot \ln M_X^2}$. The fitted nondiffractive contribution is subtracted statistically from the data for each $\ln M_X^2$-bin to obtain the number of diffractive events in that bin. In the analysis only bins are used in which the diffractive part is at least 50 %. The diffractive events selected by the M_X-method contain contributions from proton-dissociative events.

This contribution was estimated in the following way. Events were selected from a kinematical region which is dominated by proton-dissociative events and show energy deposited in the detector from the proton-dissociative system M_N. A MC-simulation of proton dissociation has been tuned to describe these events. As a result, the number of proton-dissociative events with a generated mass $N_N \geq 2.3$ GeV can be well described by the MC-simulation. For each kinematical (Q^2, W, M_X)-bin the corresponding number of MC-simulated events from proton-dissociation with masses $M_N \geq 2.3$ GeV has been subtracted statistically from the diffractive data. The ZEUS inclusive diffractive data selected with the M_X-method therefore contain contributions from proton-dissociative events with $M_N < 2.3$ GeV.

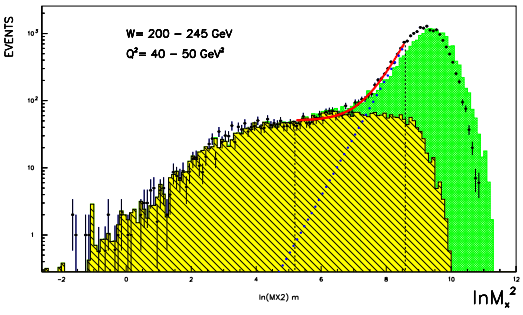

Figure 1: Measured $\ln M_x^2$ distribution. Also shown are the MC-simulated nondiffractive and diffractive (hatched) contributions. The slope of the nondiffractive contribution (dotted line) is fitted according to the formula given in the text.

2 The Diffractive Structure Function

The inclusive diffractive cross section in DIS can be expressed in terms the diffractive structure function in the same way as the inclusive DIS cross section is expressed by the DIS structure function. The inclusive diffractive process in DIS is described by the differential cross section:

$$\frac{d^3\sigma^{diff}_{\gamma^* p \to XN}}{dQ^2 d\beta dx_{IP}} = \frac{2\pi\alpha^2_{em}}{\beta Q^2}[1 + (1-y)^2] \cdot F_2^{D(3)}(\beta, x_{IP}, Q^2) \ .$$

$$\text{with} \quad x_{IP} = \frac{Q^2 + M_X^2}{Q^2 + W^2} \quad \text{and} \quad \beta = \frac{x}{x_{IP}} = \frac{Q^2}{Q^2 + M_X^2} \ .$$

The contribution from the longitudinal structure function $F_L^{D(3)}$ is small in the kinematic region of the presented analysis and is neglected.

If $F_2^{D(3)}(\beta, x_{IP}, Q^2)$ is interpreted in terms of quark densities it specifies the probability to find in a proton, which undergoes a diffractive interaction, a quark carrying the fraction $x = \beta x_{IP}$ of the proton momentum.

3 Results from the M_X-Method

In an earlier publication, ZEUS presented results [3] on inclusive diffraction obtained with the M_X-method which covered the range 2.7 GeV$^2 \leq Q^2 \leq 55$ GeV^2. In this contribution new preliminary results are presented for higher values for Q^2, namely 25 GeV$^2 \leq Q^2 \leq 320$ GeV^2. The two sets of results are called FPC I and FPC II in what follows.

In the kinematical bins $Q^2 = 25$ GeV^2 and $Q^2 = 55$ GeV^2, where results from both data sets exist, the cross sections agree within the errors. The structure function $x_{IP}F_2^{D(3)}$ as

function of x_{IP} obtained with the M_X-method is displayed in Figure 2 for the two datasets FPCI and FPC II. In all kinematic bins, a pronounced rise of $x_{IP}F_2^{D(3)}$ with decreasing x_{IP} is visible. Also shown is the result of a simultaneous fit to all the data using a modified BEKW-model [4] in a slightly modified version [3]. The BEKW-model is a dipole model which parametrizes $x_{IP}F_2^{D(3)}$ in terms contributions from: transverse photon $\rightarrow q\overline{q}$, longitudinal photon $\rightarrow q\overline{q}$, and transverse photon $\rightarrow q\overline{q}g$:

$$x_{IP}F_2^{D(3)}(\beta, x_{IP}, Q^2) = c_T \cdot F_{q\overline{q}}^T + c_L \cdot F_{q\overline{q}}^L + c_g \cdot F_{q\overline{q}g}^T.$$

The modified BEKW parametrization has five free parameters which have to be determined by a fit to the data: the normalizations of the three contributions, c_T, c_L, c_g, a coefficient, $n^{T,g}$, which determines the x_{IP}-dependence of the transverse photon and of the $q\overline{q}g$-contribution, and a coefficient, γ, which determines the β-dependence of the $q\overline{q}g$-contribution. A fit of these five parameters to the combined FPC I + II data yield $\chi^2/n_D = 0.82$ taking into account the full errors. The full line in Figure 2 shows the result of the fit. Also shown are the individual contributions. For $0.2 < \beta < 0.9$ the $(q\overline{q})_T$ contribution dominates. The gluon emission term $q\overline{q}g$ gives the largest contribution for $\beta < 0.15$. The longitudinal term $(q\overline{q})_L$ dominates for $\beta > 0.9$.

References

[1] Slides:
`http://indico.cern.ch/contributionDisplay.py?contribId=60&sessionId=7&confId=9499`

[2] K. Goulianos, Phys. Reports **101** (1983) 169; CDF Coll., F.Abe *et al.*, Phys. Rev. **D50** (1994) 5535.

[3] ZEUS Coll., S. Chekanov *et al.*, Nucl. Phys. **B 713** (2005) 3.

[4] J. Bartels *et al.*, Eur. Phys. J. **C7** (1999) 443.

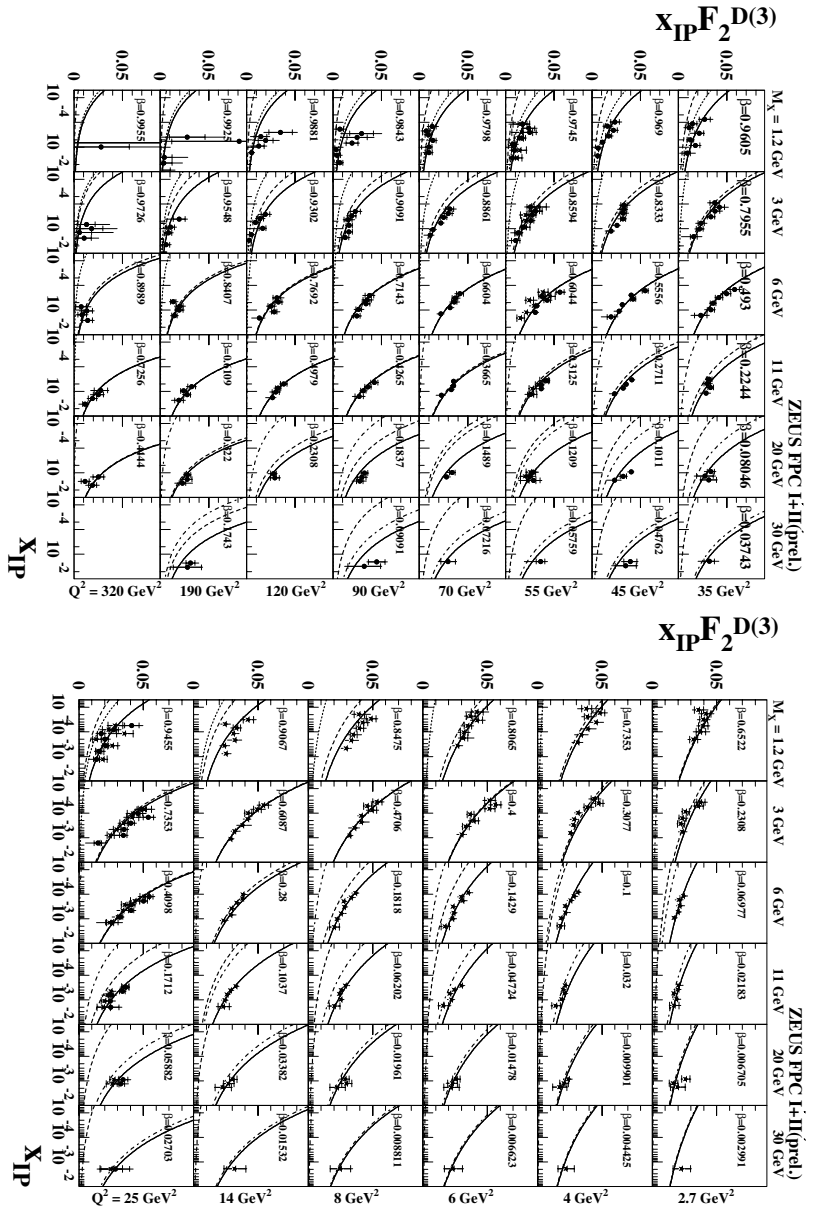

Figure 2: The diffractive structure function of the proton multiplied by x_{IP}, $x_{IP}F_2^{D(3)}$, for $\gamma^* p \to XN$, $M_N < 2.3$ GeV as a function of x_{IP} for different regions of β: FPC I and FPC II results are presented. The inner error bars show the statistical uncertainties and the full bars the statistical and systematic uncertainties added in quadrature. The curves show the results of the BEKW fit for the contributions from $(q\overline{q})$ for transverse (dashed) and longitudinal photons (dotted) and for the $(q\overline{q}g)$ contribution (dashed-dotted) together with the sum of all contributions (solid).

Measurements of diffractive structure functions with the LRG method and using the leading proton spectrometer at ZEUS

Jaroslaw Lukasik *

DESY/AGH-UST Cracow
Notkestrasse 85, D-22607 Hamburg - Germany

The ZEUS detector has been used to study dissociation of virtual photons, $\gamma^* p \to Xp$, in e^+p collisions at HERA in events with a large rapidity gap (LRG) between X and the outgoing proton, as well as in events with a measured leading proton. The data cover photon virtualities $Q^2 > 2\,\mathrm{GeV}^2$, with $M_X > 2\,\mathrm{GeV}$, where M_X is the mass of the hadronic final state X. The results are presented in terms of the diffractive structure functions, $F_2^{D(3)}$ and $F_2^{D(4)}$.

1 Introduction

The diagram of the diffractive Deep Inelastic ep Scattering (DIS) is shown in the Fig. 1. This process is characterised by the fact that p loses a small fraction of its energy and emerges from the scattering intact or dissociated into a low-mass state with a transverse momentum squared typically much smaller than $1\,\mathrm{GeV}^2$. The diffractive DIS events can be described, in addition to standard DIS variables, by the four-momentum transfer at p vertex squared t and invariant mass of $\gamma^* I\!P$ system M_X which is the mass of the system resulting from virtual photon dissociation. If also proton dissociates into higher mass state it will be denoted by N. Moreover, the diffractive structure functions are often expressed in terms of $x_{I\!P}$ and β variables. In a model with Pomeron exchange in the t channel $x_{I\!P}$ is the fraction of the proton momentum carried by the Pomeron, while β corresponds to the momentum fraction of the struck quark within the Pomeron.

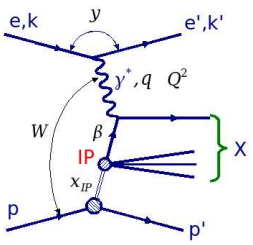

Figure 1: Diagram of the diffractive Deep Inelastic ep Scattering.

The ZEUS collaboration used two different experimental approaches to select the inclusive diffractive events:

- measurement of the final state proton by means of a Leading Proton Spectrometer (LPS method) [2],
- a large rapidity gap in the forward direction requirement (LRG method).

The preliminary results obtained with the LPS and LRG methods will be presented in the following.

The data used for this measurement were taken with the ZEUS detector at HERA ep collider in the year 2000, where HERA collided positrons of 27.6 GeV with protons of 920 GeV. The data used for the LRG and LPS analyses correspond to integrated luminosities of $45.4\,\mathrm{pb}^{-1}$ and $32.6\,\mathrm{pb}^{-1}$, respectively. The results presented here cover photon virtualities $Q^2 > 2\,\mathrm{GeV}^2$, photon-proton centre-of-mass energies $40 < W < 240\,\mathrm{GeV}$ and proton

*On behalf of the ZEUS Collaboration.

fractional momentum losses $0.0002 < x_{I\!P} < 0.02$ (LRG sample) or $0.0002 < x_{I\!P} < 0.1$ (LPS sample).

1.1 LPS method

In most of the diffractive events outgoing proton stays intact and provides a clean experimental signature. Since p_t of the outgoing proton is expected to be small (less than 1 GeV typically), it escapes through the forward beam hole. A fraction of these events can be detected by the Leading Proton Spectrometer (LPS). In the spectrum of protons measured in the LPS shown as a function of $x_L = |p_f|/|p_i|$, where p_i and p_f are the initial and final proton momenta respectively [4], a characteristic peak is observed at $x_L \simeq 1$ which corresponds to photon diffractive dissociation events. A clean sample of diffractive events is obtained by requiring $x_L > 0.97$. Measurement of the scattered proton four-momentum allows to study the t distribution in inclusive diffractive dissociation.

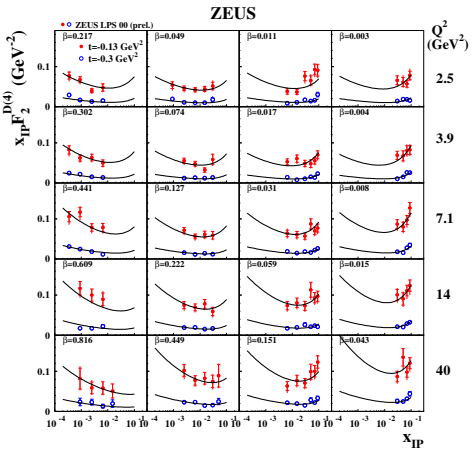

Figure 2: The diffractive structure function multiplied by $x_{I\!P}$, $x_{I\!P}F_2^{D(4)}$, in two t bins as a function of $x_{I\!P}$ for different values of Q^2 and β. The normalisation uncertainty of 10% is not shown. The continuous lines are the result of the Regge fit described in the text.

1.2 LRG method

Experimental determination of the rapidity gap rely on calculation of the pseudorapidity of the most forward going particle η_{max}, which deposits some minimum amount of energy (above noise level) in the detector. The η_{max} distribution in the DIS sample is characterised by a plateau like structure, due to diffractive events mainly, which extends to a low η_{max} values (large $\Delta\eta$). By setting an upper limit on the maximum pseudorapidity (e.g. $\eta_{max} < 3$), a diffractive sample with relatively low non-diffractive background can be selected.

2 Results

The data are presented in terms of the diffractive structure functions, $F_2^{D(3)}$ and $F_2^{D(4)}$. The results can be also presented in terms of the reduced cross section [3], $\sigma_r^{D(3)}(x_{I\!P}$, which is equal to the conventional $F_2^{D(3)}$ up to corrections due to the longitudinal structure function.

The contributions from longitudinal structure function F_L^D and Z_0 exchanges have been neglected in presented results.

2.1 Results from the LPS method

Figure 2[a] shows the measured structure function $x_{I\!P} F_2^{D(4)}$. For $x_{I\!P} < 0.01$ the structure function rises with decreasing $x_{I\!P}$. For higher values of $x_{I\!P}$ it starts to rise with increasing $x_{I\!P}$. This latter effect is attributed to the contributions from Regge trajectory exchanges reggeexch.

A sum of two contributions was fitted to the data according to

$$F_2^{D(4)} = f_{I\!P}(x_{I\!P}, t) \cdot F_2^{I\!P}(\beta, Q^2) + n_{I\!R} \cdot f_{I\!R}(x_{I\!P}, t) \cdot F_2^{I\!R}(\beta, Q^2).$$

The first term of this sum is the contribution from Pomeron exchange and the second one, from the exchanges of the Reggeon trajectories. The Reggeon structure function $F_2^{I\!R}(\beta, Q^2)$ was taken to be equal to the pion structure function as parametrised by GRV [5]. The fit was limited to $y < 0.5$ to reduce the influence of F_L^D. Result of the fit is shown in the Fig. 2.

2.2 Results from the LRG method

Inclusive diffractive data were selected with LRG method by requiring the maximum pseudorapidity to be $\eta_{max} < 3$ outside the Forward Plug Calorimeter (FPC) [7]. In addition events with energies in the FPC larger than 1 GeV were rejected.

The resulting diffractive structure function $x_{I\!P} F_2^{D(3)}$ is shown in Figures 3-5. The result of a Regge fit, performed in the same way as described previously, is shown as the continuous lines. It gives a good description of the data. No rise of $x_{I\!P} F_2^{D(3)}$ coming from Reggeexchanges can be seen because the LRG data end essentially at $x_{I\!P} = 0.01$.

The ratio of the $F_2^{D(3)}$ values obtained with the LPS method to the LRG data is shown in Fig. 6 up to $Q^2 = 40\,\mathrm{GeV}^2$. The ratio is independent of $x_{I\!P}$ and equal in each β and Q^2 bin with the average value $0.82 \pm 0.01(stat) \pm 0.03(syst)$. Since up to $x_{I\!P} = 0.01$ the LPS data contain no contribution from proton dissociation, this is an indication that the contribution from proton dissociation in the LRG data might be about 18%. However, one has to take into account the large normalisation uncertainty of about 10% of the LPS data.

3 Bibliography

References

[1] Slides: `http://indico.cern.ch/contributionDisplay.py?contribId=61&sessionId=7&confId=9499`

[2] ZEUS Coll., M. Derrick *et al.*, Z. Phys. **C73** 253 (1997).

[3] H1 Coll., A. Aktas *et al.*, hep-ex/0606004.

[4] ZEUS Coll., J. Breitweg *et al.*, Eur. Phys. J. **C1** 81 (1998).

[5] M. Glück, E. Reya and A. Vogt, Z. Phys. **C53** 127 (1992);
M. Glück, E. Reya and A. Vogt, Z. Phys. **C53** 651 (1992);
M. Glück, E. Reya and A. Vogt, Z. Phys. **C67** 433 (1995).

[6] P. D. B. Collins, *An Introduction to Regge Theory and High Energy Physics*, Cambridge University Press, Cambrige (1977).

[7] ZEUS Coll., FPC group, A. Bamberger *et al.*, Nucl. Inst. Meth. **A450** 235 (2000).

[a] From now on in each plot the inner error bars will indicate the statistical uncertainties, the outer bars the statistical and systematic uncertainties summed in quadrature.

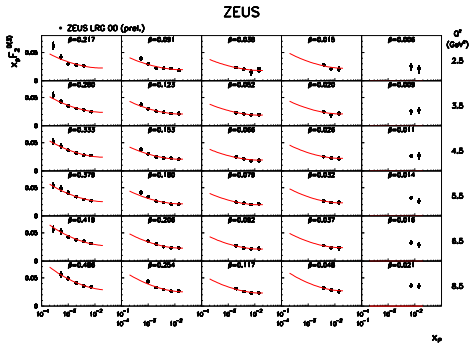

Figure 3: The diffractive structure function multiplied by $x_{I\!P}$, $x_{I\!P}F_2^{D(3)}$, obtained with the LRG method as a function of $x_{I\!P}$ for different values of Q^2 and β at low Q^2 values. The normalisation uncertainty of $\pm 2.25\%$ is not shown. The continuous lines are the result of the Regge fit described in the text.

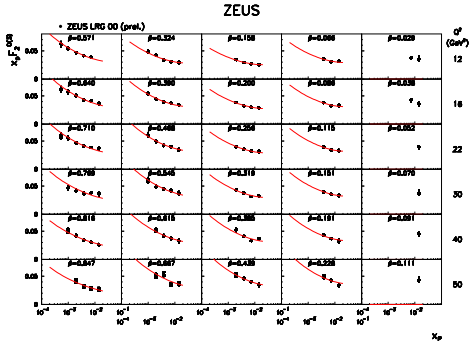

Figure 4: The diffractive structure function multiplied by $x_{I\!P}$, $x_{I\!P}F_2^{D(3)}$, obtained with the LRG method as a function of $x_{I\!P}$ for different values of Q^2 and β at intermediate Q^2 values. The normalisation uncertainty of $\pm 2.25\%$ is not shown. The continuous lines are the result of the Regge fit described in the text.

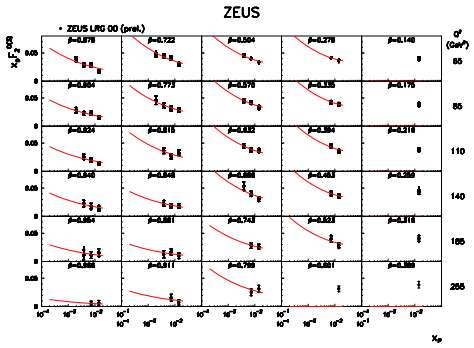

Figure 5: The diffractive structure function multiplied by $x_{I\!P}$, $x_{I\!P} F_2^{D(3)}$, obtained with the LRG method as a function of $x_{I\!P}$ for different values of Q^2 and β at high Q^2 values. The normalisation uncertainty of $\pm 2.25\%$ is not shown. The continuous lines are the result of the Regge fit described in the text.

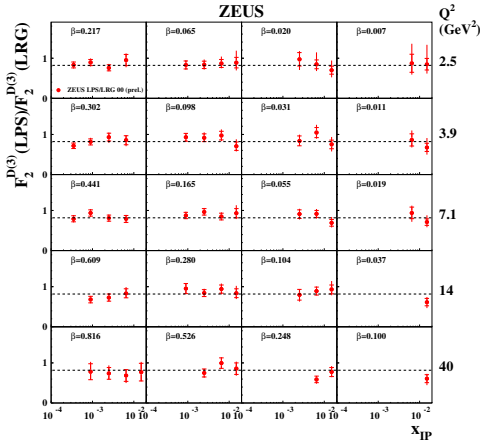

Figure 6: The ratio of the structure functions $F_2^{D(3)}$ as obtained with the LPS and LRG methods as a function of $x_{I\!P}$ for different values of Q^2 and β. The normalisation uncertainty of $^{+12}_{-10}\%$ is not shown. The lines indicate the average value of the ratio.

Diffractive Dijets in DIS and PHP

Matthias Mozer[1]

1- Vreije Universiteit Brussel - IIHE
Pleinlaan 2, 1050 Brussel - Belgium

I present measurements of dijet cross-sections in diffractive DIS and photoproduction taken with the H1 detector at the HERA accelerator. Diffractive events were identified by a rapidity gap selection. The resulting differential cross sections are compared to QCD calculations in NLO, based on parton densities extracted from inclusive diffraction. Additionally a fit of diffractive parton densities to the combined data sets of the inclusive F_2^D measurement and the dijet data was performed. This leads to reduced uncertainties for the gluon density.

1 Introduction

Theoretically it is expected that the cross sections of diffractive deep-inelastic scattering (DIS) factorises into universal diffractive parton distributions and process dependent hard scattering coefficients [2]. Diffractive parton densities have been determined from DGLAP QCD fits to inclusive diffractive HERA data [3, 4] and have been found to be dominated by the gluon distribution. Diffractive dijet production is directly sensitive to the gluon component of the diffractive exchange and has been shown - for DIS [5] - to be in decent agreement with the QCD fits to the inclusive diffractive data. In this paper, a new measurement of diffractive dijet cross sections in deep inelastic scattering is presented, based on data collected with the H1 detector at HERA. A combined NLO QCD fit is performed to the differential dijet cross sections and the inclusive diffractive structure function F_2^D in order to determine the diffractive quark and gluon distributions with higher accuracy.

However, applying this approach in LO QCD calculations to predict diffractive cross sections for dijet production in $p\bar{p}$ collisions at the Tevatron leads to an overestimation of the observed rate by approximately one order of magnitude [6]. This discrepancy has been attributed to the presence of the additional beam hadron remnant in $p\bar{p}$ collisions, which leads to secondary interactions and a breakdown of factorisation. The suppression, often characterised by a 'rapidity gap survival probability', cannot be calculated perturbatively and has been parameterised in various ways (see for example [7]).

The transition from deep-inelastic scattering to hadron-hadron scattering can be studied at HERA in a comparison of scattering processes in DIS and in photoproduction. Processes in which a real photon participates directly in the hard scattering are expected to be similar to the deep-inelastic scattering of highly virtual photons. By contrast, processes in which the photon is first resolved into partons which then initiate the hard scattering resemble hadron-hadron scattering. In this article, the final results of diffractive dijet cross sections in DIS and photoproduction are presented, based on data collected with the H1 detector at HERA.

2 Experimental Procedure

The detector setup and selection criteria for the comparison of dijet cross sections in DIS and photoproduction are described in detail in [5]. The cross scetion measurement is measured

similarly, the most notabe differences being a wider y-range (0.1-0.7) and a tighter cut on the transverse momentum of the hardest jet (5.5 GeV).

3 Rapidity Gap Survival

While diffractive dijet production in DIS shows reasonable agreement with NLO QCD calculations based on the factorisation approach, which is not the case in photoproduction. This disagreement is often interpreted as a 'rapidity gap survival probability' smaller than one due to secondary interactions of spectator partons and measured from the difference between the measured cross section and perturbative NLO QCD calculations. With this method, the uncertainty of the diffractive parton densities used for the prediction limits the accuracy of the measurement. Figure 1 shows the double ratio $\frac{((d\sigma/dW)_{data})/((d\sigma/dW)_{NLO})^{PHP}}{((d\sigma/dW)_{data})/((d\sigma/dW)_{NLO})^{DIS}}$ in which the parton density uncertainties mostly cancel. This shows that diffractive dijet production in photoproduction is significantly suppressed by a factor ~ 0.5 compared to perturbative calculations. Most surprisingly, the suppression shows no kinematic dependence.

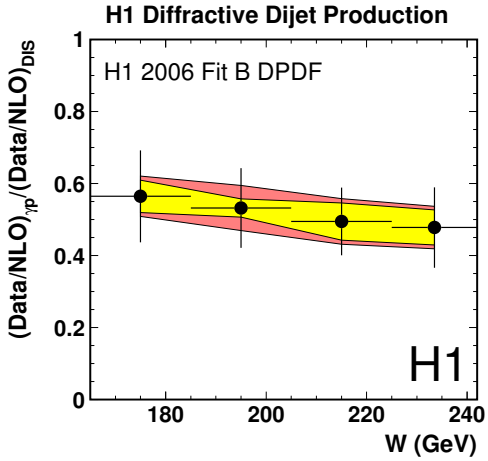

Figure 1: The double ratio $\frac{((d\sigma/dW)_{data})/((d\sigma/dW)_{NLO})^{PHP}}{((d\sigma/dW)_{data})/((d\sigma/dW)_{NLO})^{DIS}}$. The error bars on the points represent the statistical uncertainty, while the inner error band shows the experimental systematic uncertainties and the outer band represents the uncertainties connected to the NLO calculation.

4 Parton Density Fit

In DIS the differential dijet cross section in $z_{I\!P}$ is used in the fit in 4 bins of the scale variable $p_\perp^{\star 2}+Q^2$ to constrain the gluon density, where $p_\perp^\star$ is the transverse momentum of the hardest jet. These measured cross sections are shown in Figure 2 (left). Additionally the inclusive data sample of a previous H1 analysis [4] is used to constrain the quark density and the gluon density a low momentum fraction. A part of the F_2^D measurements is shown in Figure 2 (right) together with the final NLO prediction.

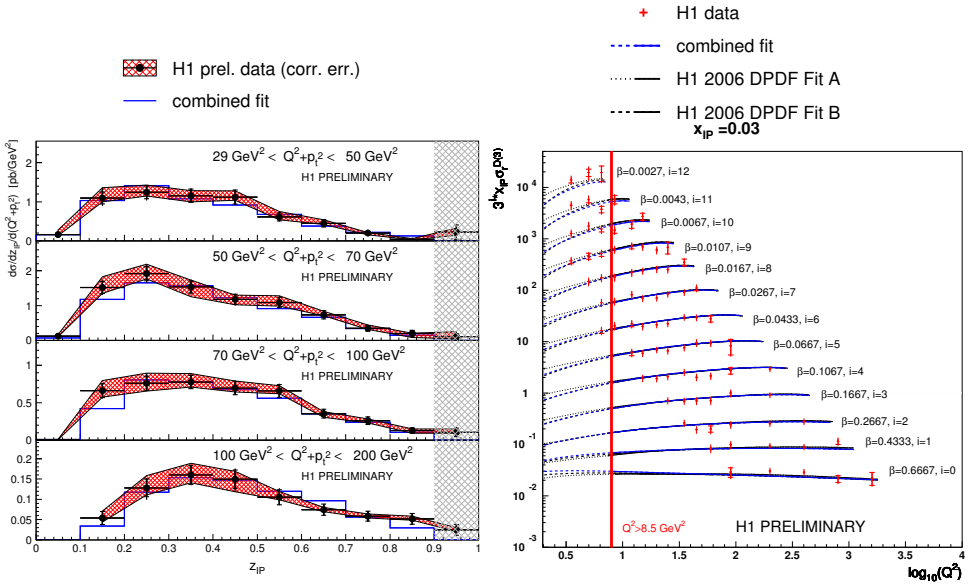

Figure 2: left: Cross section of diffractive dijets doubly differential in in $z_{I\!P}$ and the scale $\mu = Q^2 + p_\perp^{\star 2}$. The data are shown as black points with the inner and outer error-bar denoting the statistical and uncorrelated systematic uncertainties respectively. The red hatched band indicates the correlated systematic uncertainty. The blue line shows the NLO QCD prediction based on the combined fit. right: The β and Q^2 dependence of the diffractive reduced cross section $\sigma_r^{D(3)}$ multiplied by the pomeron momentum fraction $x_{I\!P}$ at $x_{I\!P} = 0.03$. The inner and outer error-bars on the data points represent the statistical and total uncertainties, respectively. The data are compared to the results of the combined fit for $E_p = 820$ GeV, which is shown as blue lines. The dashed line indicates the prediction in kinematic regions that did not enter into the fit. The two black lines indicate the predictions of the H1 2006 DPDF fit.

The parton densities are parameterised as of momentum fraction z at a starting scale Q_0^2 as $A \cdot z^B \cdot (1-z)^C$ and evolved to higher scales by the DGLAP equations in NLO. Here, A, B and C are free parameters, determined in the fit. Additionally the Regge intercept $\alpha(0)$ of the pomeron flux factor and the normalisation of the sub-leading reggeon exchange enter the fit as free parameters. From these parton densities the reduced cross section for inclusive diffractive DIS is computed in NLO as well as the dijet cross section (using the `nlojet++` program).

The fit has a high quality as shown by the overall value $\chi^2/df = 0.89$ which splits into $\chi^2/df = 27/36$ for the dijet cross sections and $\chi^2/df = 169/190$ for F_2^D. The resulting parton distributions are shown in Figure 3.

As the NLO QCD DGLAP evolution is able to describe both the shape and scaling violations of F_2^D and the dijet cross sections consistently, we conclude that QCD factorisation in DIS is valid in our kinematic region. The data has allowed for the first time to determine

both the diffractive gluon and the singlet quark distribution with good accuracy in the range $0.1 < z_{I\!P} < 0.9$.

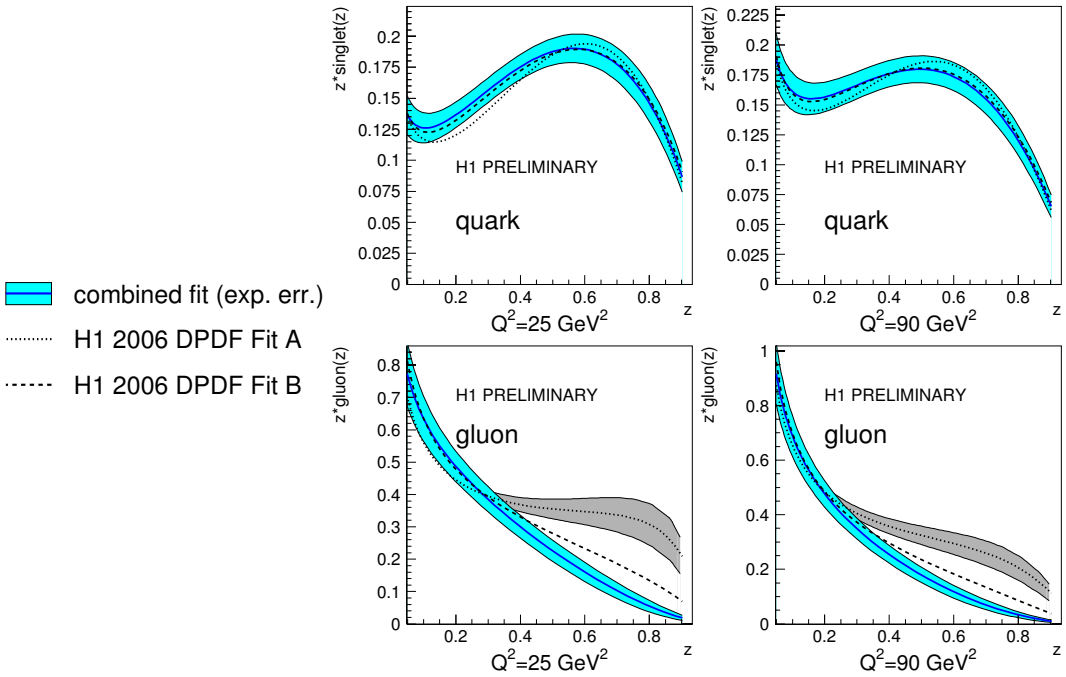

Figure 3: The diffractive singlet density (top) and diffractive gluon density (bottom) for two values of the hard scale μ: 25 GeV^2 (left) and 90 GeV^2 (right). The blue line indicates the combined fit, surrounded by the experimental uncertainty band in light blue. The two dashed lines show the two fit results from [4] for comparison.

References

[1] Slides:
`http://indico.cern.ch/contributionDisplay.py?contribId=62&sessionId=7&confId=9499`

[2] J. Collins, Phys. Rev. **D57** (1998) 3051 and erratum-ibid. **D61** (2000) 019902.

[3] C. Adloff *et al.* [H1 Collaboration], Z. Phys. **76** (1997) 613

[4] A. Aktas *et al.* [H1 Collaboration], Eur. Phys. J. C **48** (2006) 715 [hep-ex/0606004].

[5] A. Aktas *et al.* [H1 Collaboration], submitted to Eur. Phys. J. C [hep-ex/0703022].

[6] CDF Collaboration, T. Affolder *et al.*, Phys. Rev. Lett. **84** (2000) 5043.

[7] A. Kaidalov, V. Khoze, A. Martin, M. Ryskin, Phys. Lett. **B567** (2003) 61

Dijet Production in Diffractive DIS and Photoproduction at ZEUS

Yuji Yamazaki, for the ZEUS collaboration

Kobe University - Department of Physics, Graduate School of Sciences
1-1 Rokko-dai, Nada, Kobe 657-8501 - Japan

Recent ZEUS measurements on dijet production in diffractive deep-inelastic scattering and diffractive photoproduction are reviewed. The measured cross sections are compared to next-to-leading order perturbative QCD calculations using recent diffractive parton densities. For diffractive photoproduction, where the factorisation theorem is not proven, such comparison serves as a test of QCD factorisation. No clear evidence of factorisation breaking was found.

1 Introduction

Diffractive interactions studied mainly in the HERA ep collisions are so-called photon-dissociation processes, where the proton scatters with a virtual photon from the electron with the proton remaining intact and the photon dissociating into a multi-hadron state X. The exchanged state carries only a small fraction, $x_{I\!P}$, of the longitudinal momentum of the proton lost through the scatter. The scaling-violation behaviour of semi-inclusive deep-inelastic scattering (DIS) cross sections of the diffractive processes are used to extract the diffractive parton densities (dPDFs), defined as the PDFs of the proton undergoing a diffractive scattering.

Although the quark densities in dPDFs can be obtained precisely from this procedure, gluons are only loosely constrained. The dijet production, both in DIS and photoproduction, are dominated by the boson-gluon fusion process, where a hard collision of virtual photon and a gluon produces a high-p_T quark-antiquark pair. The diffractive dijet cross sections, therefore, are more directly sensitive to the gluonic content of the diffractive exchange. The dijet process also allows to reconstruct the momentum fraction, $z_{I\!P}$, of the initial parton in the diffractive exchange participating in the hard scattering, using the longitudinal momenta of jets: $z_{I\!P}^{\rm OBS} = (E_T^{\rm jet1} e^{\eta^{\rm jet1}} + E_T^{\rm jet2} e^{\eta^{\rm jet2}})/(2x_{I\!P} E_p)$, where $E_T^{\rm jet1}$ and $E_T^{\rm jet2}$ are the transverse energy of the jets with the highest and second highest $E_T^{\rm jet}$, respectively, $\eta^{\rm jet1}$ and $\eta^{\rm jet2}$ are the pseudorapidities of the corresponding jets and E_p is the energy of the incoming proton.

The QCD factorisation theorem is proven for diffractive DIS with a presence of a large photon virtuality Q^2: the dijet cross sections in diffractive DIS can also be expressed as a convolution of the dPDFs and coefficient functions. No such proof exists for diffractively photoproduced dijets. In fact, such factorisation appears to fail at the Tevatron, the highest energy $p\bar{p}$ collisions: the cross sections were suppressed with respect to the pQCD calculations. This is believed to be attributed to a class of events with more than one parton-parton scatter between the proton and the diffractive exchange, destroying the diffractive conditions and thus breaking the factorisation. A similar phenomenon could occur in photoproduction events. The photon can resolve into more than one partons and thus could also suppress the diffractive cross sections of the resolved photon processes. For dijet events, the resolved processes can be identified with an estimator, $x_\gamma^{\rm OBS}$, of the momentum fraction, x_γ, of the parton in the photon participating in the hard scattering. The estimator is reconstructed again using the longitudinal momenta of the jets: $x_\gamma^{\rm OBS} = (E_T^{\rm jet1} e^{-\eta^{\rm jet1}} + E_T^{\rm jet2} e^{-\eta^{\rm jet2}})/(2yE_e)$, where

y is the fraction of the energy of colliding photons to the incoming electron energy E_e. Events with low values of $x_\gamma^{\rm OBS}$ are dominated by resolved processes.

2 Dijets in diffractive DIS

Figure 1 shows the preliminary measurement of the differential cross sections for diffractive DIS processes by ZEUS [2]. The measurement was performed for $5 < Q^2 < 100\,\text{GeV}^2$, $100 < W < 250\,\text{GeV}$, the centre-of-mass energy of the virtual photon and the proton, $x_{I\!P} < 0.03$, $E_T^{\rm jet1} > 5\,\text{GeV}$ and $E_T^{\rm jet2} > 4\,\text{GeV}$. The jets are found in the $\gamma^* p$ frame, the centre-of-mass frame of the virtual photon and the proton, using the longitudinally-invariant k_T-algorithm. The cross sections are reasonably well described by the theoretical calculations at the next-to-leading order(NLO) by DISENT [3] using the H1 fit 2002(prel.)[4] and ZEUS LPS+charm parameterisations of dPDFs [5]. The H1 fit 2002 dPDFs was extracted from the H1 measurements of the inclusive diffraction cross sections. The ZEUS LPS+charm dPDFs utilised also the charm production cross sections for constraining the dPDFs for gluons. The good agreement shows that both dPDFs are appropriate for estimating other diffractive cross sections.

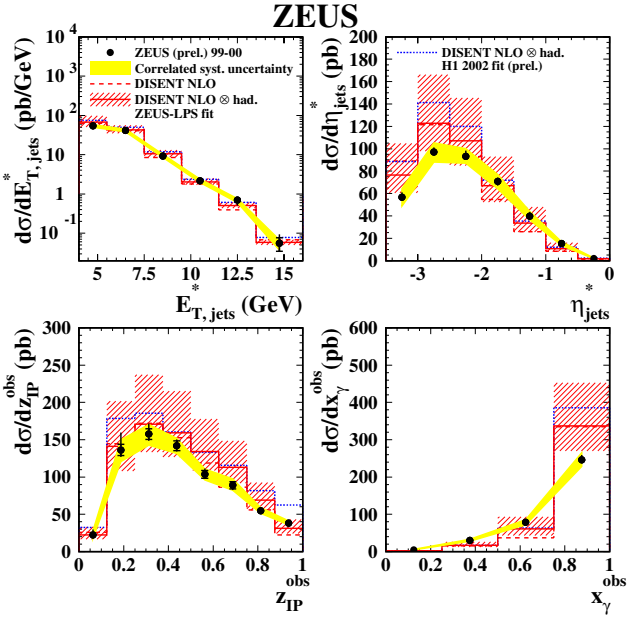

Figure 1: Differential dijet cross sections in the DIS regime for $E_T^{\rm jet}$, $\eta^{\rm jet}$, $z_{I\!P}^{\rm OBS}$ and $x_\gamma^{\rm OBS}$, compared to NLO calculations using H1 fit 2002(prel.) and ZEUS LPS+charm as dPDFs.

3 Dijets in diffractive photoproduction

The final cross section measurements of the diffractive dijet in photoproduction is presented in this workshop, with the kinematic range of $Q^2 < 1\,\text{GeV}^2$, $0.2 < y < 0.85$, $x_{I\!P} < 0.025$, $E_T^{\rm jet1} > 7.5\,\text{GeV}$ and $E_T^{\rm jet2} > 6.5\,\text{GeV}$. The jets are found using the k_T algorithm in the laboratory frame of the HERA beams, $E_e = 920\,\text{GeV}$ and $E_e = 27.5\,\text{GeV}$.

The cross sections are compared to the NLO calculations by Klasen and Kramer [7]. The calculations were originally published with the H1 fit 2002(prel.) dPDFs. The ZEUS collaboration has implemented the new dPDFs, such as the H1 fit 2006 [8], using their program. The result of the calculation, however, show about 10% difference in both shape and normalisation when compared to the calculation performed by the H1 collaboration using the program by Frixione and Ridolfi [9] in the same kinematic range of the H1 measurement.

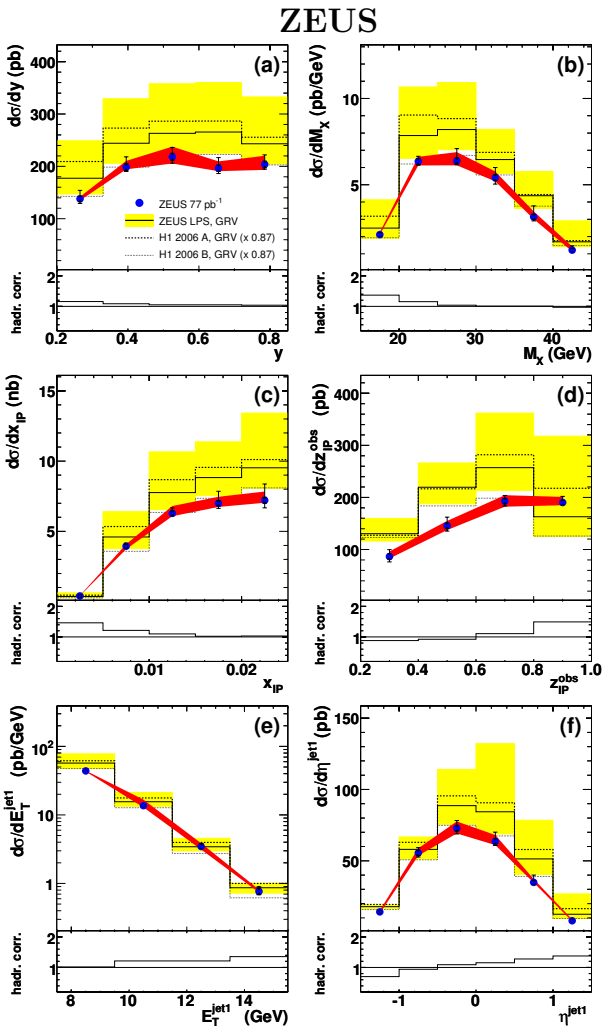

Figure 2: Differential dijet cross sections in the photoproduction regime as a function of (a) y, (b) M_X, (c) $x_{I\!P}$, (d) $z_{I\!P}^{\rm OBS}$, (e) $E_T^{\rm jet1}$ and (f) $\eta^{\rm jet1}$, compared to NLO calculations using H1 fit 2006 A and B, and ZEUS LPS+charm as dPDFs.

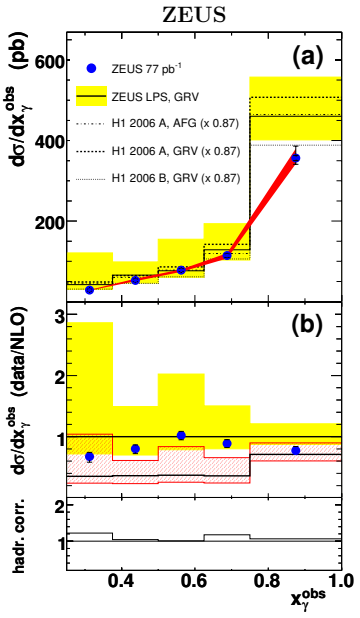

Figure 3: (a) Differential dijet cross sections in the photoproduction regime as a function of $x_\gamma^{\rm OBS}$, compared to NLO calculations using H1 2006 fitA and fitB and ZEUS LPS+charm as dPDFs. (b) The ratio of the cross sections to the prediction using the ZEUS LPS+charm dPDFs. The histogram with a hatched band shows the prediction with the resolved photon suppressed according to the prediction by Kaidalov et al. [10]: see text.

This issue is under investigation. The conclusion in this contribution, therefore, is based on the assumption that the NLO calculation is correct within about 10%.

Figure 2 shows the cross sections for the entire range of $x_\gamma^{\rm OBS}$ in comparison to the NLO calculations using the ZEUS LPS parton density as well as two variation of the H1 fit 2006 dPDFs, fitA and fitB, which use different assumption on the shape of the gluon density. The cross sections are well described by using the H1 2006 fitB. The ZEUS LPS and H1 2006

fitA give higher cross sections than the data by about 20%, but agree with the data within theoretical uncertainties.

The $x_\gamma^{\rm OBS}$ dependence of the cross sections are compared to the NLO calculations in Fig. 3. The measurement show good agreement with the calculations[a]. The model by Kaidalov et al. [10], tuned to explain the suppression of the diffractive dijet production measured by CDF [11], predicts that the resolved photon contribution is suppressed by about 1/3 at HERA. The model with such a rescaling on the resolved processes fails to describe the data. The cross sections for resolved-enriched ($x_\gamma^{\rm OBS} < 0.75$) and direct-enriched ($x_\gamma^{\rm OBS} > 0.75$) samples show also good agreement with the NLO calculations using the H1 2006 fitB parameterisation (not shown).

Summarising, no clear evidence of factorisation breaking was observed in the diffractive dijet photoproduction at HERA within the experimental and theoretical uncertainties.

4 Discussion

The negative observation of factorisation breaking in photoprduction by ZEUS appears to conflict with the conclusion from the corresponding measurement by the H1 collaboration [12]. The H1 data, however, starts from lower $E_T^{\rm jet}$: $E_T^{\rm jet1} > 5\,{\rm GeV}$ and $E_T^{\rm jet2} > 4\,{\rm GeV}$. The measurement is also extended to $x_{I\!P} < 0.03$, higher than ZEUS. For both H1 and ZEUS measurements, the $E_T^{\rm jet}$ dependence is not well reproduced by NLO: the cross sections at low $E_T^{\rm jet}$ tend to be overestimated by the calculation (see Fig. 2e). This might have lead different conclusions among measurements depending on the $E_T^{\rm jet}$ range. A more direct comparison with the same kinematic range may help to have a definitive conclusion on this issue.

References

[1] Slides:
`http://indico.cern.ch/contributionDisplay.py?contribId=63&sessionId=7&confId=9499`

[2] ZEUS Coll., Contrib. 342 for the EPS-HEP2005 Conf.(unpublished).

[3] S. Catani and M.H. Seymour, Nucl. Phys. **B485**, 291 (1997); Erratum-ibid. **B510**, 503 (1997).

[4] H1 Coll., Contrib. 980 for the ICHEP2002 Conf.(unpublished).

[5] ZEUS Coll., S. Chekanov *et al.*, Eur. Phys. J. **C38**, 43 (2004).

[6] ZEUS Coll., Contrib. 249 for the ICHEP2004 Conf.(unpublished).

[7] M. Klasen and G. Kramer, Eur. Phys. J. **C38**, 93 (2004).

[8] H1. Coll., A. Aktas et al., Eur. Phys. J. **C48**, 715 (2006).

[9] S. Frixione, Z. Kunszt and A. Signer, Nucl. Phys. **B467**, 399 (1996); S. Frixione, Nucl. Phys. **B507**, 295 (1997).

[10] A.B. Kaidalov *et al.*, Eur. Phys. J. **C21**, 521 (2001); A.B. Kaidalov *et al.*, Phys. Lett. **B567**, 61 (2003);

[11] CDF Coll., T. Affolder *et al.*, Phys. Rev. Lett. **84**, 5043 (2000).

[12] H1 Coll., A. Aktas *et al.*, DESY-07-018, Submitted to Eur. Phys. J. C.

[a] This statement is somewhat different from what was presented in the preliminary presentation by the ZEUS collaboration at the ICHEP2004 conference[6], where the cross sections as a function of $x_\gamma^{\rm OBS}$ agreed with the NLO in shape but with a normalisation factor of about 0.6. Three issues have lead the change in the relation between the measurement and the calculation: (1) the diffractive parton densities was the H1 fit 2002(prel.) parameterisation, which tend to give a higher cross section than the H1 2006 fitB; (2) the subtraction of the proton dissociation from the H1 dPDFs was necessary since the ZEUS dijet cross section is corrected to the elastic-proton photon dissociation $ep \to epX$. The H1 dPDFs are therefore scaled down by 13% in this presentation, which was missing in the ICHEP2004 contribution; (3) The ZEUS cross section measurements are revised and have changed within the quoted systematic uncertainties of the ICHEP2004 contribution.

New QCD Fits to HERA Data and Search for Exclusive Events at the Tevatron

Oldřich Kepka and Christophe Royon

DAPNIA/Service de physique des particules,
CEA/Saclay, 91191 Gif-sur-Yvette cedex, France

We describe new QCD fits to diffractive proton structure functions measured at HERA, and we use these parton densities to predict the shape of the dijet mass fraction at the Tevatron and look for the existence of exclusive events in the dijet channel.

1 QCD fits to proton diffractive structure function data from HERA

We use the most recent published data [2] on diffractive proton structure function measured by the H1 and ZEUS collaborations. Data are fitted using the following quark and gluon densities [3]:

$$\begin{aligned} zS(z,Q^2=Q_0^2) &= \left[A_S z^{B_S}(1-z)^{C_S}(1+D_S z+E_S\sqrt{z})\right]\cdot e^{\frac{0.01}{z-1}} \\ zG(z,Q^2=Q_0^2) &= \left[A_G(1-z)^{C_G}\right]\cdot e^{\frac{0.01}{z-1}}. \end{aligned}$$

In the fits, $\alpha_S(M_Z) = 0.18$ and the initial scale is taken at $Q_0^2 = 3$ GeV^2. The charm quark contribution is computed in the fixed flavour scheme using the photon-gluon fusion prescription. The pomeron intecept is found to be 0.12 using H1 data and $\chi^2/dof \sim 0.9$. With respect to the "standard" H1 approach for the QCD fits, we have more parameters for the quark and gluon densities at the starting scale which allows to fix the starting scale at 3 GeV^2 and not to fit it. We cross checked that we find the same results as H1 while making the same assumptions. Other approaches based on dipole and saturation models [4] were also tested in Ref. [3].

The gluon and quark densities are given in Fig. 1. While the quark densities are found to be relatively close for H1 and ZEUS, the gluon density differs by more than a factor 2. New preliminary data from ZEUS reduce this discrepancy. In the following, we will only use the QCD fits to the H1 data to compare with the dijet mass fractions measured in the CDF collaboration at the Tevatron. It is also worth noticing that the gluon density is poorly known at high β, where β is the momentum fraction of the pomeron carried by the interacting parton. To illustrate this, we multiply the gluon density by the factor $(1-\beta)^\nu$ and fit the parameter ν. The fit leads to $\nu = 0.0 \pm 0.6$ which demonstrates a large uncertainty of the gluon density at high β measured at HERA.

2 Search for exclusive events at the Tevatron

Exclusive events at the Tevatron or the LHC show the interesting property that the full available energy in the pomeron-pomeron system for double pomeron exchange events is used to produce the heavy mass object (dijet, diphoton...). In other words, no energy is lost in pomeron remnants. Tagging both protons scattered in the final state allow to measure precisely the kinematic properties, for instance the mass, of the produced heavy object. Exclusive events at the LHC recently captured high interest since it might be a possibility

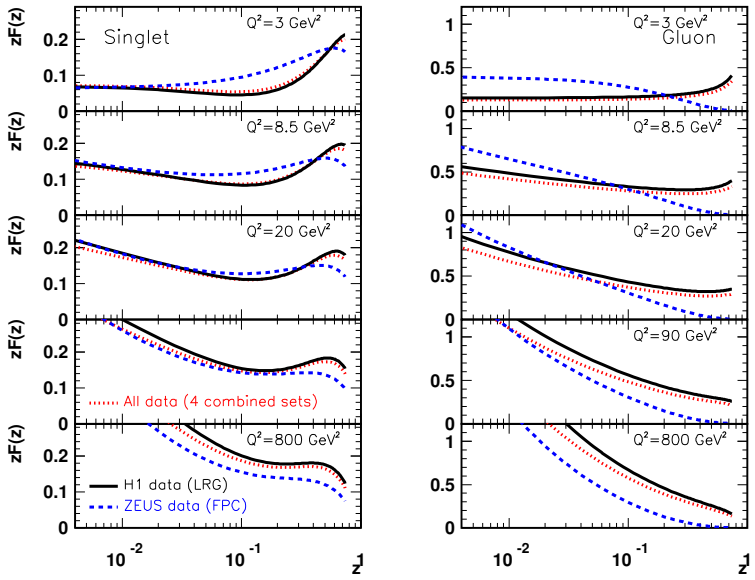

Figure 1: Gluon and quark densities in the pomeron measured using H1 and ZEUS data.

to detect the Higgs boson diffractively by tagging the diffracted protons in the final state [5].

2.1 Search for exclusive events in χ_C production

The CDF collaboration performed the search for exclusive events in the χ_C channel [6]. They obtained an upper limit of χ_C exclusive production in the $J/\Psi\gamma$ channel of $\sigma \sim 49$ pb $\pm 18 \pm 39$ pb for $y < 0.6$. In Ref. [7], we found that the contamination of inclusive events into the signal region (the tail of the inclusive distribution when little energy is taken away by the pomeron remnants) depends stronly on the assumptions on the gluon distribution in the pomeron at high β or in other words on the ν parameter. Therefore, this channel is unfortunately not conclusive concerning the existence of exclusive events.

2.2 Search for exclusive events using the dijet mass fraction at the Tevatron

One selects events with two jets only and one looks at the dijet mass fraction distribution, the ratio between the dijet mass and the total diffractive mass in the event. The CDF collaboration measured this quantity for different jet p_T cuts [8]. We compare this measurement with different models of inclusive diffraction, namely "factorised" (FM) and "Bialas Landshoff" (BL) models [10]. In the FM models, one takes the gluon and quark densities in the pomeron measured at HERA as described in the previous section and the factorisation breaking between HERA and the Tevatron only comes through the gap survival probability. The BL model is non perturbative and diffraction is obtained via the exchange of a soft pomeron, which means that the mass dependence of the exclusive cross section is quite low. The comparison between the CDF data for a jet p_T cut of 10 GeV as an example and the predictions from the FM model is given in Fig. 2. We also give in the same figure the

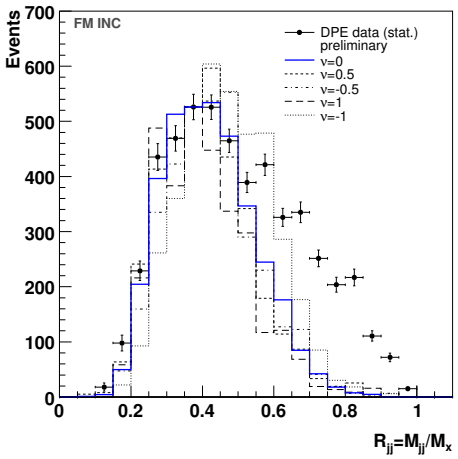

Figure 2: Dijet mass fraction measured by the CDF collaboration compared to the prediction from the "factorised model" for inclusive diffraction. The gluon density in the pomeron at high β was modified by varying the parameter ν.

effects of changing the gluon density at high β (by changing the value of the ν parameter) and we note that inclusive diffraction is not able to describe the CDF data at high dijet mass fraction, where exclusive events are expected to appear [9]. The conclusion remains unchanged when jets with $p_T > 25$ GeV are considered [9].

Adding exclusive events to the distribution of the dijet mass fraction leads to a good description of data [9] as shown in Fig. 3 where we superimpose the predictions from inclusive diffraction from the "factorised" model and exclusive one from the Durham model [10]. It is worth noticing that the exclusive "Bialas Landshoff" model [10] leads to a too small dependence of the diffractive exclusive cross section as a function of jet transverse momentum [9]. In Ref. [9], the CDF data were also compared to the soft colour interaction models [10]. While the need for exclusive events is less obvious for this model, especially at high jet p_T, the jet rapidity distribution measured by the CDF collaboration is badly reproduced. This is due to the fact that, in the SCI model, there is a large difference between requesting an intact proton in the final state and a rapidity gap [9].

2.3 Observation of exclusive events at the LHC

The exclusive contribution manifests itself as an increase in the tail of the dijet mass fraction distribution. Exclusive production slowly turns on with the increase of the jet p_T (see Ref. [9]) and with respect to the uncertainty on the gluon density this appearance is almost negligible. The exclusive production at the LHC plays a minor role for low p_T jets. Therefore, measurements e.g for $p_T < 200\,\text{GeV}$ where the inclusive production is dominant could be used to constrain the gluon density in the pomeron. The higher p_T jet region can be used to extract the exclusive contribution from the tail of the dijet mass fraction distribution. The extraction of the inclusive and exclusive jet production cross section will be of great importance at the beginning of the LHC to be able to make precise predictions on exclusive

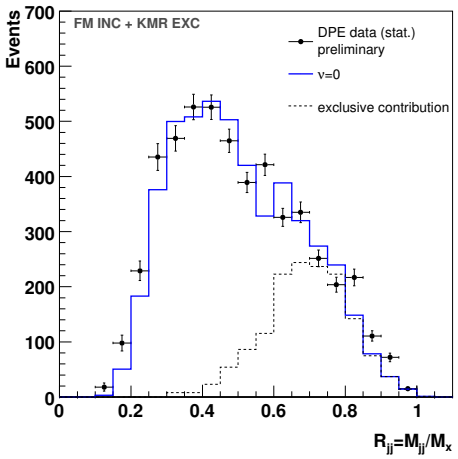

Figure 3: Dijet mass fraction measured by the CDF collaboration compared to the prediction from "factorised models" for inclusive diffraction and from the Durham model for exclusive diffraction.

Higgs production and the background later on.

References

[1] Slides: `http://indico.cern.ch/contributionDisplay.py?contribId=242&sessionId=7&confId=9499`

[2] A. Aktas *et al.* [H1 Collaboration], arXiv:hep-ex/0606004, arXiv:hep-ex/0606003; S. Chekanov *et al.* [ZEUS Collaboration], Nucl. Phys. B **713** (2005) 3.

[3] C. Royon, L. Schoeffel, R. Peschanski and E. Sauvan, Nucl. Phys. B **746** (2006) 15; C. Royon, L. Schoeffel, S. Sapeta, R. Peschanski and E. Sauvan, arXiv:hep-ph/0609291, accepted by Nucl. Phys. B.

[4] A.H.Mueller, Nucl. Phys. **B415** (1994) 373; J.Bartels, J.Ellis, H.Kowalski, M.Wuesthoff, Eur.Phys.J.C7 (1999) 443; J.Bartels, C.Royon, Mod.Phys.Lett. **A14** (1999) 1583; H.Navelet, R.Peschanski, Ch.Royon, S.Wallon, Phys. Lett. **B385** (1996) 357; A.Bialas, R.Peschanski, C.Royon, Phys. Rev. **D57** (1998) 6899; S.Munier, R.Peschanski, C.Royon, Nucl. Phys. **B534** (1998) 297

[5] M. Boonekamp, R. Peschanski and C. Royon, Phys. Lett. **B598** (2004) 243; M. Boonekamp, A. De Roeck, R. Peschanski and C. Royon, Phys. Lett. **B 550** (2002) 93; M. Boonekamp, J. Cammin, S. Lavignac, R. Peschanski and C. Royon, Phys. Rev. **D 73** (2006) 115011; V. A. Khoze, A. D. Martin and M. G. Ryskin, Eur. Phys. J. **C23** (2002) 311, Eur. Phys. J. **C24** (2002) 581.

[6] CDF Collaboration, T. Affolder *at al.*, Phys. Rev. Lett. **85**, 4215 (2000).

[7] M. Rangel, C. Royon, G. Alves, J. Barreto, R. Peschanski, hep-ph/0612297

[8] CDF Collaboration, CDF note 8493, (2006)

[9] O.Kepka, C. Royon, preprint arXiv:0704.1956

[10] M. Boonekamp, R. Peschanski, C. Royon, Phys. Rev. Lett. **87** (2001) 251806; M. Boonekamp, R. Peschanski, C. Royon, Nucl. Phys. **B669** (2003) 277; V. A. Khoze, A. D. Martin and M. G. Ryskin, Eur. Phys. J. C **48** (2006), Eur. Phys. J. **C19** (2001) 477467; A. Bialas, P. V. Landshoff, Phys. Lett. **B256** (1990) 540; R. Enberg, G. Ingelman, A. Kissavos, N. Timneanu, Phys. Rev. Lett. **89** (2002) 08180 1.

The Ratio of σ_L/σ_T in DIS at Low x

Dieter Schildknecht[1,2]

1- Fakultät für Physik, Universität Bielefeld, Universitätsstrasse 25, D-33615 Bielefeld, Germany
2- MPI für Physik, München, Föhringer Ring 6, D-80805 München, Germany

Assuming helicity independence for $q\bar{q}$ scattering in the color-dipole picture, or, equivalently proportionality of sea quark and gluon distributions, we find $R(W^2, Q^2) \cong 0.5$ at large Q^2, where $R(W^2, Q^2)$ denotes the ratio of the longitudinal and transverse photoabsorption cross sections. The forthcoming direct measurements of $R(W^2, Q^2)$ allow one to test the underlying hypotheses.

This is a brief summary of my talk at DIS 2007. We also refer to the slides of the talk, available under `http://indico.cern.ch/confAuthorIndex.py?confId=9499`. It was recently noted [2] that the dipole picture [3] of deep inelastic scattering at low $x \cong Q^2/W^2 \leq 0.1$,

$$\sigma_{\gamma^*_{L,T}p}(W^2, Q^2) = \sum_q \int d^2 r_\perp \omega^{(q)}_{L,T}(Qr_\perp, Q^2, m_q^2) \sigma_{(q\bar{q})p}(r_\perp^2, W^2), \tag{1}$$

allows one to derive an upper bound on the ratio of the cross sections induced by longitudinal and transverse photons,

$$R(W^2, Q^2) = \frac{\sigma_{\gamma^*_L p}(W^2, Q^2)}{\sigma_{\gamma^*_T p}(W^2, Q^2)} \leq \max_{r_\perp, q} \frac{\omega^{(q)}_L(Qr_\perp, Q^2, m_q^2)}{\omega^{(q)}_T(Qr_\perp, Q^2, m_q^2)} = 0.37. \tag{2}$$

Since the photon fluctuates into on-shell $q\bar{q}$ states

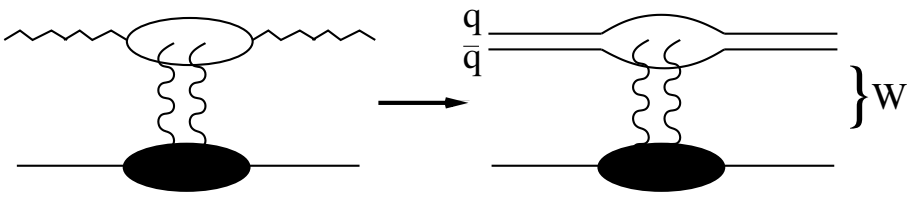

(3)

the $q\bar{q}$-scattering process entering the virtual Compton-forward-scattering amplitude is identical to the $q\bar{q}$-scattering process of on-shell $q\bar{q}$ states. Accordingly, as indicated in (1), the cross section factorizes into a Q^2-dependent probability density and a W^2-dependent (rather than x-dependent) dipole cross section. The relevance of the energy W as the dynamical variable in the low-x diffraction region may be traced back to the representation of low-x deep inelastic scattering in terms of generalized vector dominance [4] some thirty-five years ago. For the connection between the dipole picture and generalized vector dominance compare also refs. 4 and 5 and the recent review in 6. The dependence on W rather than x on the right-hand side in (1) was recently stressed by Ewerz and Nachtmann [2] in their very elaborate and explicit treatment of the foundations of the dipole picture.

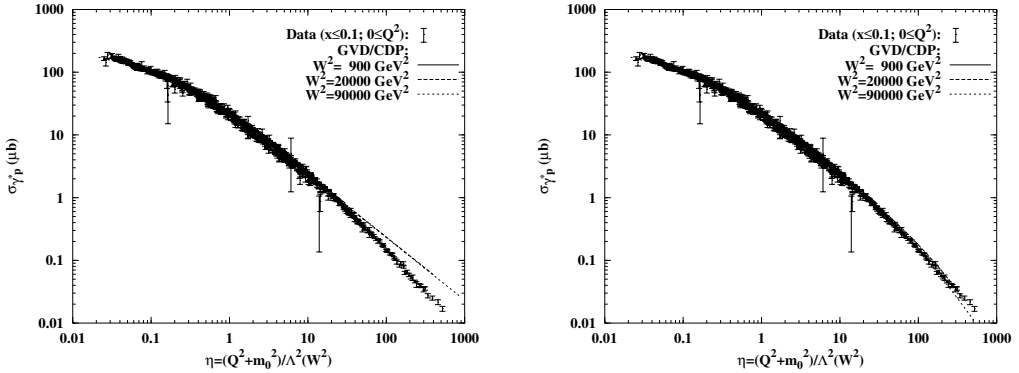

Figure 1: The total photoabsorption cross section for $m_1^2 = \infty$ and $m_1^2 = 484 GeV^2$.

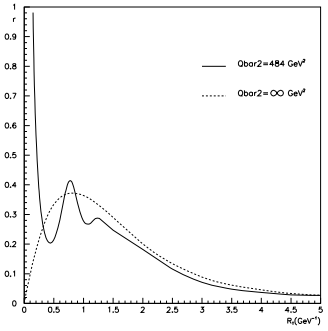

Figure 2: The ratio (7)

Since the available energy, W, is finite, the mass, $M_{q\bar{q}}$, of the contributing color dipoles must be bounded [8, 2],

$$M_{q\bar{q}}^2 = \frac{\vec{k}_\perp^{\,2}}{z(1-z)} \leq m_1^2 \equiv \bar{Q}^2 << W^2 \tag{4}$$

The bound $\bar{Q}^{\,2}$ must be identified with the upper limit of the diffractively produced masses that is expected to be substantially below the available energy. In our representation of the HERA data, we used a value of [8]

$$\bar{Q}^2 \equiv m_1^2 = (22 GeV)^2, \tag{5}$$

that was abstracted from the effective upper end of the diffractive mass spectrum observed at HERA. In Figure 1, we show that the introduction of the bound [8] (5) extends the range of validity of the representation of the cross section in terms of the scaling variable [9, 6]

$$\eta = \frac{Q^2 + m_0^2}{\Lambda_{\rm sat}^2(W^2)} \tag{6}$$

to the region of large values of η. Since $\bar{Q}^2$ is determined by the upper limit of diffractively produced masses, $\bar{Q}^2$ increases slowly with increasing energy. To adopt a constant value for the HERA energy range must be considered as an approximation.

We have analyzed[10] the effect of the restriction (4,5) on the ratio $R(W^2, Q^2)$ in (2). The probability density to find a dipole of size $r_\perp$ in the (virtual) photon now becomes dependent on $\bar{Q}^{\,2}$. The ratio of the probability densities in (2), for finite $\bar{Q}^{\,2}$ diverges in the limit of small dipoles, $r_\perp \to 0$,

$$r^{(q)}\left(Qr_\perp, \frac{Q^2}{\bar{Q}^2}\right) = \frac{\omega_L^{(q)}(Qr_\perp, Q^2, \bar{Q}^2)}{\omega_T^{(q)}(Qr_\perp, Q^2, \bar{Q}^2)} \overset{r_\perp \to 0}{\sim} \begin{cases} Q^2 r_\perp^2 \to 0 & , \text{ for } \bar{Q}^2 \to \infty \\ \frac{1}{r_\perp^2 \bar{Q}^2} \to \infty & , \text{ for } \bar{Q}^2 \text{finite} \end{cases} \tag{7}$$

and the bound (2) turns into the trivial statement

$$0 \leq R(W^2, Q^2) < \infty, \tag{8}$$

i.e. the derivation of an upper limit for $R(W^2, Q^2)$ fails, once a finite value for $\bar{Q}^2$ is adopted. Compare Figure 2 for the ratio of the probability densities, where for illustration the value (5) for $\bar{Q}^2$ is used.

Actually, the representation (1) of the dipole picture must be applied in conjunction with color transparency[3]

$$\begin{aligned} \sigma_{(q\bar{q})p}(r_\perp^2, W^2) &= \int d^2\vec{l}_\perp \, \tilde{\sigma}_{(q\bar{q})p}(\vec{l}_\perp^{\,2}, W^2)(1 - e^{-i\vec{l}_\perp \vec{r}_\perp}) \\ &\simeq \vec{r}_\perp^{\,2} \, \frac{\pi}{4} \int d\vec{l}_\perp^{\,2} \vec{l}_\perp^{\,2} \tilde{\sigma}_{(q\bar{q})p}(\vec{l}_\perp^{\,2}, W^2), \quad \text{for } \vec{r}_\perp^{\,2} \to 0. \end{aligned} \tag{9}$$

Here, $\vec{l}_\perp$ denotes the transverse momentum of the gluon absorbed by the $q\bar{q}$ pair in the forward-scattering amplitude, where two gluons of opposite transverse momentum couple to the $q\bar{q}$ pair. Since both, transitions $M_{q\bar{q}} \to M_{q\bar{q}}$ as well as $M_{q\bar{q}} \to M'_{q\bar{q}}$, occur, the restriction (4) is to be supplemented by

$$M'^2_{q\bar{q}} = \frac{(\vec{k}_\perp + \vec{l}_\perp)^2}{z(1-z)} < \bar{Q}^2. \tag{10}$$

Noting that the momentum of the gluon is entirely independent of the transverse momentum of the quarks, $k_\perp$, restrictions (4) and (10) together require

$$\vec{l}_\perp^{\,\prime 2} = \frac{\vec{l}_\perp^{\,2}}{z(1-z)} << \bar{Q}^2, \tag{11}$$

i.e. the effective change in mass of the $q\bar{q}$ state by gluon absorption must be much smaller than the upper bound $\bar{Q}^2$, where $Q^2 = m_1^2 \simeq (22GeV)^2$ at HERA.

In order to investigate the effect of the restrictions (4) and (11) on $R(W^2, Q^2)$, we appropriately start[10] with the limit of $\bar{Q}^2$ large compared with the effective value of the gluon transverse momentum, that is with the limit of $\bar{Q}^2 \to \infty$. For Q^2 large compared with the effective value of $\vec{l}_\perp^{\,\prime 2}$, i.e. $Q^2 >>< \vec{l}_\perp^{\,\prime 2} >$, where $< \vec{l}_\perp^{\,\prime 2} >$ is proportional to the "saturation scale" $\Lambda^2_{\rm sat}(W^2)$, we find

$$R(W^2, Q^2) = \underbrace{\frac{\int dy y^3 K_0^2(y)}{\int dy y^3 K_1^2(y)}}_{\frac{1}{2}} \cdot \frac{\int d\vec{l}^{\,\prime 2} \vec{l}_\perp^{\,\prime 2} \bar{\sigma}_{(q\bar{q})_L^{J=1} p}(\vec{l}_\perp^{\,\prime 2}, W^2)}{\int d\vec{l}^{\,\prime 2} \vec{l}_\perp^{\,\prime 2} \bar{\sigma}_{(q\bar{q})_T^{J=1} p}(\vec{l}_\perp^{\,\prime 2}, W^2)}. \tag{12}$$

The ratio of the integrals over modified Bessel functions in (12) yields 1/2. Note that the right-hand side in (12) depends on the ratio of the $q\bar{q}$ absorption cross sections for longitudinally and transversely polarized $(q\bar{q})^{J=1}$ (vector) states. Adopting the assumption of helicity independence[6, 8], i.e. equality of the first moment of the scattering amplitudes for longitudinal and transverse polarisation, we have from (12)

$$R(W^2, Q^2) = 0.5. \tag{13}$$

We summarize: With color transparency (two gluons coupled to $q\bar{q}$) and the hypothesis of helicity independence, we have $R(W^2, Q^2) = 0.5$ at large Q^2. A preliminary investigation[10] indicates no substantial change of this result for $\bar{Q}^2$ finite.

The hypothesis of helicity independence, at large Q^2 may be expressed in terms of a proportionality[11] of sea quark and gluon distributions. With the constant of proportionality, ρ, we then have

$$R(W^2, Q^2 >> \Lambda^2_{\rm sat}(W^2)) = \frac{1}{2\rho}, \tag{14}$$

where $\rho = 1$ corresponds to (13). Applying the evolution equation at low x, and large Q^2, one finds[11, 12] a correlation between ρ and the exponent in the W^2 dependence of the saturation scale,

$$\Lambda^2_{\rm sat}(W^2) = const. \left(\frac{W^2}{1GeV^2}\right)^{C_2} \tag{15}$$

given by

$$(2\rho + 1) C_2^{theor.} 2^{C_2^{theor.}} = 1. \tag{16}$$

Compare Table 1.

ρ	$C_2^{theor.}$	$\alpha_s \cdot$ glue	$\sigma_{\gamma^*_L}/\sigma_{\gamma^*_T}$	$F_2\left(\frac{Q^2}{x}\right)$
$\to \infty$	0	$\ll$ sea	0	$(Q^2/x)^0 = const.$
1	0.276	$\approx$ sea	$\sim \frac{1}{2}$	$(Q^2/x)^{0.276}$
0	0.65	$>$ sea	∞	$(Q^2/x)^{0.65}$

Table 1: Results for $C_2^{theor.}$ for different values of ρ

The coincidence of the theoretical value of $C_2^{theor.}$ with the fit[6] to the experimental data, $C_2^{\rm exp} = 0.27 \pm 0.1$, supports helicity independence with $\rho = 1$, i.e. $R(W^2, Q^2) = 0.5$ at large Q^2. Measurements of $R(W^2, Q^2)$ allow one to directly test the limits of the assumed proportionality of sea and gluon distributions that is equivalent to helicity independence and correlated with the rise of $F_2(W^2 = Q^2/x)$ as a function of x at fixed Q^2.

Acknowledgments

Many thanks to Kuroda-san for a fruitful collaboration.

References

[1] Slides: `http://indico.cern.ch/contributionDisplay.py?contribId=64&sessionId=7&confId=9499`
[2] C. Ewerz and O. Nachtmann, arXiv:hep-ph/0404254, hep-ph/0604087, hep-ph/0511051.
[3] N.N. Nikolaev and B.G. Zakharov, Z. Phys. **C49** 607 (1991).
[4] J.J. Sakurai and D. Schildknecht, Phys. Lett. **B40** 121 (1972); B. Gorczyca and D. Schildknecht, Phys. Lett. **B47** 71 (1973); R. Devenish and D. Schildknecht, Phys. Rev. **D19** 93 (1976).
[5] G. Cvetic, D. Schildknecht, A. Shoshi, Eur. Phys. J. **C13** 301 (2000); Acta Physica Polonica **B30** 3265 (1999).
[6] D. Schildknecht, B. Surrow, M. Tentyukov, Phys. Lett. **B499** 116 (2001); G. Cvetic, D. Schildknecht, B. Surrow, M. Tentyukov, Eur. Phys. J. **C20** 77 (2001); D. Schildknecht, B. Surrow, M. Tentyukov, Mod. Phys. Lett. **A16** 1829 (2001).
[7] D. Schildknecht, in Proc. PHOTON2005, Acta Physica Polonica B37 (2006) 595.
[8] M. Kuroda and D. Schildknecht, Phys. Rev. **D66** 094005 (2002).
[9] D. Schildknecht, in Diffraction 2000, Nucl. Phys. B (Proc. Suppl.) **99** 121 (2001); D. Schildknecht, in: G. Bruni et al. (Eds.), DIS2001, Bologna, Italy, World Scientific, Singapore, p. 798 (2002).
[10] M. Kuroda and D. Schildknecht, in preparation.
[11] M. Kuroda and D. Schildknecht, Phys. Lett. **B618** 84 (2005).
[12] D. Schildknecht, in 41st Rencontres de Moriond, March 2006, arXiV:hep-ph/0607031.

Coordinate-Space Picture and $x \to 1$ Singularities at Fixed $k_\perp$

F. Hautmann

CERN, PH-TH Division, Geneva, Switzerland and
Institut für Theoretische Physik, Universität Regensburg, Germany

This talk [1] discussed ongoing progress towards precise characterizations of parton distributions at fixed transverse momentum, focusing on matrix elements in coordinate space and the treatment of endpoint singularities.

Parton distributions unintegrated in transverse momentum are naturally defined for small x via high-energy factorization [2]. This relates off-shell matrix elements with physical cross sections at $x \to 0$, and gives a well-prescribed method to introduce unintegrated parton distributions in a gauge-invariant manner.

The question of how to characterize gauge-invariantly a $k_\perp$ distribution over the whole phase space, on the other hand, is more difficult and not yet fully answered. Its relevance was already emphasized long ago in the context of Sudakov processes [3], jet physics [4], exclusive production [5], spin physics [6]. Although a complete framework is still missing, much work is currently underway on this subject, see e.g. [7, 8, 9, 10, 11, 12, 13]. The discussion that follows focuses on aspects related to the gauge-invariant operator matrix elements and regularization methods for lightcone divergences.

To ensure gauge invariance, the approach commonly used is to generalize the matrix elements that serve to define ordinary parton distributions to the case of field operators at non-lightcone distances [6, 14]. This leads one to consider the matrix element for the quark distribution (Fig. 1)

$$\widetilde{f}(y) = \langle P|\overline{\psi}(y) V_y^\dagger(n)\gamma^+ V_0(n)\psi(0)|P\rangle \tag{1}$$

with the quark fields ψ evaluated at distance $y = (0, y^-, y_\perp)$ for arbitrary y^- and $y_\perp$, and the eikonal-line operators V given by

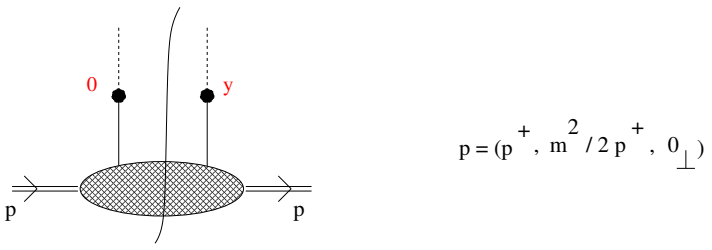

Figure 1: Quark distribution function in the target of momentum p.

$$V_y(n) = \mathcal{P}\exp\left(ig_s\int_0^\infty d\tau\ n^\mu A_\mu(y+\tau\ n)\right) \quad , \tag{2}$$

where n is the direction of the eikonal line and A is the gauge field.

However, while the use of Eq. (1) does not pose major problems at tree level, it becomes more subtle at the level of radiative corrections. Part of the subtleties are associated with incomplete KLN cancellations that come from measuring $k_\perp$ in the initial state [3, 15]. These may appear as uncancelled divergences near the endpoints for certain lightcone momentum components [16]. Another set of issues are associated with the integration over all transverse momenta, and involve the relation of unintegrated parton distributions with the ordinary ones [17, 18, 19] and the treatment of ultraviolet divergences. As observed in [20] for the case of the Sudakov form factor, the choice of a particular regularization method for the lightcone divergences also affects integrated distributions and ultraviolet subtractions.

In [11] these effects are examined by an explicit calculation at one loop using techniques for the expansion of nonlocal operators. The answer for the coordinate-space matrix element is analyzed in powers of y^2, separating logarithmic contributions from long distances and short distances,

$$\begin{aligned} \widetilde{f}_1(y) &= \frac{\alpha_s C_F}{\pi}\, p^+ \int_0^1 dv\, \frac{v}{1-v} \left\{ \left[e^{ip\cdot yv} - e^{ip\cdot y} \right] \Gamma(2-\frac{d}{2})\, (\frac{4\pi\mu^2}{\rho^2})^{2-d/2} \right. \\ &+ \left. e^{ip\cdot yv}\, \pi^{2-d/2}\, \Gamma(\frac{d}{2}-2)\, (-y^2\mu^2)^{2-d/2} + \cdots \right\} \ , \end{aligned} \tag{3}$$

where μ is the dimensional-regularization scale and ρ is an infrared mass regulator. The lightcone singularity $v \to 1$ corresponds to the exclusive phase-space boundary $x = 1$. The singularity cancels for ordinary parton distributions (first term in the right hand side of Eq. (3)) but it is present, even at $d \neq 4$ and finite ρ, in subsequent terms, which contribute to the unintegrated parton distribution [11]. This is then treated on the same footing as a physical correlation function, to be expanded in terms of the ordinary parton distributions with nontrivial, perturbatively calculable coefficient functions [17, 18].

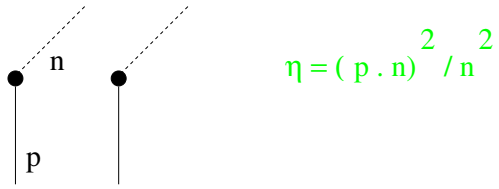

Figure 2: Cut-off regularization for the quark matrix element.

Traditionally the effect of endpoint singularities is suppressed by the use of a cut-off. This is likely the case, for instance, in existing Monte-Carlo event generators that implement unintegrated parton distributions [21, 22, 23, 24, 25]. A cut-off is also implemented in treatments [3, 13, 26] based on regularizing the parton-distribution matrix element by taking the eikonal line n to be non-lightlike (Fig. 2), combined with evolution equations in the cut-off parameter $\eta = (p\cdot n)^2/n^2$ [4, 27]. One-loop formulas in coordinate space corresponding to the regularization method of Fig. 2 are given in [11]. This method leads to a cut-off in x at fixed $k_\perp$ of order

$$1 - x \gtrsim k_\perp/\sqrt{4\eta} \ . \tag{4}$$

However, cut-off regularization is not very well-suited for applications beyond the leading order. Furthermore, as the two lightcone limits $y^2 \to 0$ and $n^2 \to 0$ do not commute, a residual dependence on the regularization parameter η is left after integrating in $k_\perp$ the distribution defined with the cut-off. The relation with the standard operator product expansion is therefore not so transparent.

An alternative approach is based on the subtractive regularization method [20, 28]. As explained in [15], in this approach the eikonal n is kept in lightlike direction but the singularities are canceled by multiplicative, gauge-invariant factors given by eikonal-line vacuum expectation values. The matrix element with subtraction factors is pictured in Fig. 3, where $\bar{y} = (0, y^-, 0_\perp)$, and u is the direction of an auxiliary (non-lightlike) eikonal that provides a gauge-invariant regulator near $x = 1$ and cancels in the matrix element at $y_\perp = 0$ [11]. The form of the counterterms is simple in coordinate space, where it can be given in terms of compact all-order expressions.

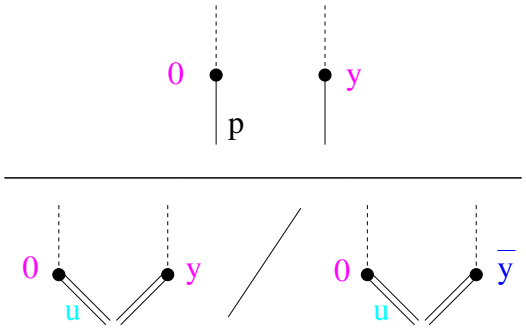

Figure 3: Matrix element with subtractive regularization.

The subtractive method is more systematic than the cut-off, and likely more suitable for using unintegrated parton distributions at subleading-log level. It can be useful for incorporating the unintegrated formulation in parton shower approaches [18, 28, 29]. Also, subleading accuracy is needed for matching large-x contributions with calculations at small x [19, 25, 30] and in the Sudakov region [31, 32].

The techniques discussed above will be instrumental to analyze factorization and evolution for $k_\perp$ parton distributions with increased precision [8, 9]. The issue of soft gluon exchanges with spectator partons is revisited in [8] for hard pp collisions. A potential breakdown of factorization at high order of perturbation theory is discussed (N^3LO correction to dihadron production, with two soft and one collinear partons), which would be of interest to verify by calculation. Also, it will be interesting to investigate how the argument of [8] is modified by the inclusion of destructive interference effects due to soft gluon coherence. A better understanding of these issues will help improve the present accuracy in current phenomenological studies of the effects of partons' transverse momentum [25, 30, 31].

References

[1] Slides:
http://indico.cern.ch/contributionDisplay.py?contribId=290&sessionId=7&confId=9499

[2] S. Catani, M. Ciafaloni and F. Hautmann, Phys. Lett. **B242** (1990) 97; Nucl. Phys. **B366** (1991) 135.

[3] J.C. Collins, in *Perturbative Quantum Chromodynamics*, ed. A.H. Mueller, World Scientific 1989, p. 573.

[4] J.C. Collins and D.E. Soper, Nucl. Phys. **B193** (1981) 381.

[5] S.J. Brodsky and G.P. Lepage, in *Perturbative Quantum Chromodynamics*, ed. A.H. Mueller, World Scientific 1989, p. 93.

[6] P. Mulders and R.D. Tangerman, Nucl. Phys. **B461** (1996) 197; D. Boer and P. Mulders, Phys. Rev. **D** 57 (1998) 5780.

[7] J.W. Qiu, W. Vogelsang and F. Yuan, arXiv:0706.1196; X. Ji, J.W. Qiu, W. Vogelsang and F. Yuan, Phys. Rev. Lett. **97** (2006) 082002.

[8] J.C. Collins and J.W. Qiu, arXiv:0705.2141.

[9] F. Ceccopieri and L. Trentadue, arXiv:0706.4242.

[10] K. Goeke, S. Meissner and A. Metz, hep-ph/0703176.

[11] F. Hautmann, hep-ph/0702196.

[12] A. Idilbi and T. Mehen, hep-ph/0702022.

[13] P. Chen, A. Idilbi and X. Ji, Nucl. Phys. **B763** (2007) 183.

[14] A.V. Belitsky, X. Ji and F. Yuan, Nucl. Phys. **B656** (2003) 165.

[15] J.C. Collins, Acta Phys. Polon. B **34** (2003) 3103.

[16] S.J. Brodsky, D.S. Hwang, B.Q. Ma and I. Schmidt, Nucl. Phys. **B593** (2001) 311.

[17] S. Catani, M. Ciafaloni and F. Hautmann, Phys. Lett. **B307** (1993) 147; S. Catani and F. Hautmann, Nucl. Phys. **B427** (1994) 475.

[18] J.C. Collins and X. Zu, JHEP **0503** (2005) 059.

[19] A.D. Martin, M.G. Ryskin and G. Watt, Eur. Phys. J. C**31** (2003) 73.

[20] J.C. Collins and F. Hautmann, Phys. Lett. B **472** (2000) 129.

[21] G. Marchesini and B.R. Webber, Nucl. Phys. **B386** (1992) 215.

[22] G. Gustafson, L. Lönnblad and G. Miu, JHEP **0209** (2002) 005; L. Lönnblad and M. Sjödahl, JHEP **0402** (2004) 042, JHEP **0505** (2005) 038.

[23] H. Jung, Mod. Phys. Lett. A19 (2004) 1.

[24] K. Golec-Biernat, S. Jadach, W. Placzek, P. Stephens and M. Skrzypek, hep-ph/0703317.

[25] S. Höche, F. Krauss and T. Teubner, arXiv:0705.4577.

[26] X. Ji, J. Ma and F. Yuan, Phys. Rev. D **71** (2005) 034005, JHEP **0507** (2005) 020.

[27] G.P. Korchemsky and G. Marchesini, Phys. Lett. B **313** (1993) 433; G.P. Korchemsky, Phys. Lett. B **220** (1989) 62.

[28] J.C. Collins and F. Hautmann, JHEP **0103** (2001) 016.

[29] C.W. Bauer and M.D. Schwartz, hep-ph/0607296.

[30] H. Jung, A.V. Kotikov, A.V. Lipatov and N.P. Zotov, arXiv:0706.3793.

[31] C.P. Yuan, talk at DIS07 Workshop, Munich, April 2007.

[32] P.M. Nadolsky, N. Kidonakis, F.I. Olness and C.P. Yuan, Phys. Rev. D **67** (2003) 074015; R. Brock, F. Landry, P.M. Nadolsky and C.P. Yuan, Phys. Rev. D **67** (2003) 073016.

Diffractive Neutral Pion Production, Chiral Symmetry and the Odderon

Carlo Ewerz[1] and Otto Nachtmann[2]

1- ECT*
Strada delle Tabarelle 286, I-38050 Villazzano (Trento), Italy

2- Institut für Theoretische Physik, Universität Heidelberg
Philosophenweg 16, D-69120 Heidelberg, Germany

We discuss the diffractive photo- and electroproduction of a single neutral pion at high energies where it can occur due to odderon exchange. We show that this process is dynamically suppressed as a consequence of chiral symmetry. Our result reconciles early theoretical expectations with the non-observation of this reaction at HERA.

1 Diffractive neutral pion production as a probe of the odderon

In this talk [1] we want to present the main results of our study [2] of diffractive production of a single neutral pion in photon-proton scattering at high energy,

$$\gamma^{(*)}(q) + p(p) \longrightarrow \pi^0(q') + X(p')\,, \tag{1}$$

where the photon can be real or virtual, and X can be any diffractively produced hadronic system. For simplicity we will in the following assume that X is a proton, but our considerations can also be applied to other states X, for example for $X = N^*$ or $X = n + \pi^+$ [2]. Since the photon and the neutral pion have opposite C-parity the object exchanged in this reaction must be odd under charge conjugation, and hence at high energy must be an odderon ($\mathbb{O}$), see Figure 1. (Note that we draw the incoming particles to the right.)

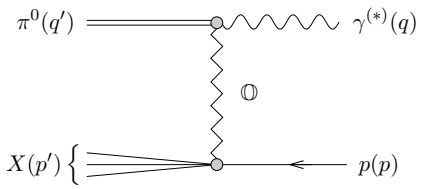

Figure 1: Diffractive photo- or electroproduction of a π^0 due to odderon exchange.

The odderon, the $C = -1$ partner of the pomeron, was introduced in [3], for a general review see [4]. It has since been studied in great detail especially from a theoretical point of view. But experimentally the odderon remains an elusive object. Some weak evidence for its existence has only been seen in elastic scattering at the ISR where the pp and $p\bar{p}$ differential cross sections show a difference at around $|t| \sim 1.3\,\mathrm{GeV}^2$ [5], for a recent discussion see [6]. There, however, the odderon is only one among many contributions and hence difficult to pin down. In recent years it has been realized that the chances to observe the odderon are better in exclusive processes in which the odderon essentially gives the only contribution. As an important example of this strategy the reaction (1) has been proposed and discussed in [7].

A detailed analysis based on a nonperturbative model of QCD dynamics performed in [8] led to the prediction

$$\sigma(\gamma p \to \pi^0 N^*) \approx 300\,\mathrm{nb}\,, \tag{2}$$

while the subsequent experimental search at HERA [9] did not find a signal and resulted in the upper bound

$$\sigma(\gamma p \to \pi^0 N^*) < 49\,\mathrm{nb}\,. \tag{3}$$

Possible causes for the failure of the prediction of [8] were discussed in [10]. Since the reaction (1) has the largest phase space of all processes in which hadrons are diffractively produced a strong dynamical suppression appeared necessary in order to provide a likely reason. In [2] we have found that the approximate chiral symmetry of QCD indeed induces a strong suppression.

2 PCAC

Let us define a quark field operator describing up and down type quarks, $\psi(x) = (u(x), d(x))^T$, and the associated triplet of axial vector currents ($a = 1, 2, 3$)

$$A^a_\mu(x) = \bar{\psi}(x)\gamma_\mu\gamma_5\frac{\tau^a}{2}\psi(x). \tag{4}$$

The well-known PCAC relation states that the divergence of this axial vector current is related to a correctly normalised pion field operator ϕ^a by

$$\partial_\lambda A^{a\lambda}(x) = \frac{f_\pi m_\pi^2}{\sqrt{2}}\,\phi^a(x)\,, \tag{5}$$

where $f_\pi \approx 130\,\mathrm{MeV}$ is the pion decay constant, see for example [11]. Let us now consider along with diffractive pion production the corresponding production of an axial vector current A^3,

$$\gamma^{(*)}(q,\nu) + p(p,s) \quad\longrightarrow\quad \pi^0(q') + p(p',s')\,, \tag{6}$$
$$\gamma^{(*)}(q,\nu) + p(p,s) \quad\longrightarrow\quad A^3(q',\mu) + p(p',s')\,, \tag{7}$$

and let us denote the corresponding amplitudes by $\mathcal{M}^\nu(\pi^0; q', p, q)$ and $\mathcal{M}^{\mu\nu}(A^3; q', p, q)$, respectively, which we consider for $q^2 \le 0$ and $q'^2 \le m_\pi^2$. Using the PCAC relation (5) we can then express the former amplitude in terms of the latter via

$$\mathcal{M}^\nu(\pi^0; q', p, q) = \frac{2\pi m_p\sqrt{2}}{f_\pi m_\pi^2}\,(-q'^2 + m_\pi^2)\,iq'_\mu\mathcal{M}^{\mu\nu}(A^3; q', p, q)\,. \tag{8}$$

3 Axial vector current production

The amplitude $\mathcal{M}^{\mu\nu}(A^3; q', p, q)$ for axial vector current production (7) can be treated with the same general nonperturbative methods that were developed for Compton scattering in [12]. We use the LSZ formula to relate the amplitude to Green's functions, and the latter can then be written as functional integrals over quark and gluon fields. Integrating out the quark degrees of freedom leads us to diagram classes characterised by their quark line skeleton. Those diagrams which contain the leading terms at high energies are shown in Figure 2, and they are exactly the odderon exchange diagrams on which we want to concentrate here. The solid lines represent full quark propagators in a given gluon field configuration, and the shaded blobs indicate the functional integral over the gluon fields.

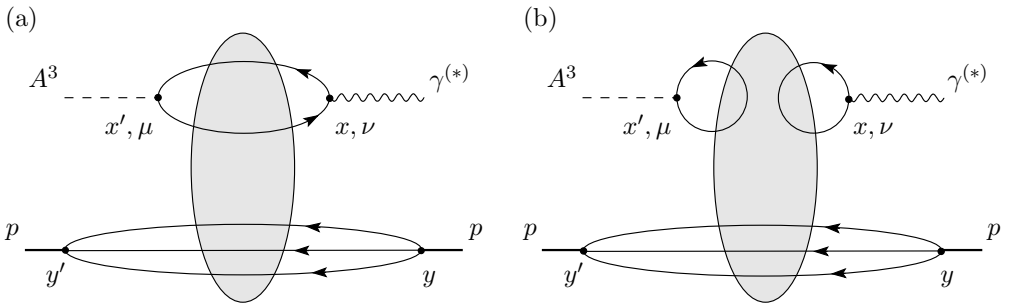

Figure 2: Leading diagrams at high energies for the reaction (7).

4 From axial vector current to pion production

We now consider the divergence of the amplitudes of Figure 2, that is we contract them with q'^{μ} or take a derivative ∂^{μ}. For the axial vector current this gives at the quark level

$$\partial^{\mu} A^3_{\mu}(x) = i[m_u \bar{u}(x)\gamma_5 u(x) - m_d \bar{d}(x)\gamma_5 d(x)]\,, \tag{9}$$

and hence there is a factor m_q of the light quark masses in the divergence amplitude. Note that the gluon anomaly does not contribute here. Such anomalous pieces are contained in the individual contribution of the quark flavours to the divergence of A^3_{μ} and would have the quark line topology of diagram (b) in Figure 2, but they cancel in $\partial^{\mu} A^3_{\mu}$.

The quark loops in the diagrams of Figure 2 which couple to the axial vector current contain a factor γ_5. As a consequence, these loops give rise to an additional factor m_q of the light quark mass. This can be shown in a more detailed analysis which makes use of Lippmann-Schwinger equations for the quark propagator, for details see [2]. Hence we find that the divergence amplitude $q'_{\mu}\mathcal{M}^{\mu\nu}(A^3; q', p, q)$ is proportional to the square of the light quark masses. More precisely,

$$q'_{\mu}\mathcal{M}^{\mu\nu}(A^3; q', p, q) = m_u^2\, \mathcal{C}^{(u)\nu}(q', p, q) - m_d^2\, \mathcal{C}^{(d)\nu}(q', p, q)\,, \tag{10}$$

where the functions $\mathcal{C}^{(q)\nu}$ have pion poles but are otherwise finite. (These poles are cancelled by the explicit factors $(-q'^2 + m_\pi^2)$ in (8) when we insert (10) there.) We know from the theory of chiral symmetry that the squared pion mass is linear in the light quark masses,

$$m_\pi^2 = B(m_u + m_d) \tag{11}$$

with

$$B = -\frac{2}{f_\pi^2}\langle 0|\bar{u}(x)u(x)|0\rangle \approx 1800\,\mathrm{MeV}\,. \tag{12}$$

Therefore we can conclude from (8) and (10) that the odderon exchange amplitude for pion production is proportional to the square of the pion mass,

$$\mathcal{M}^{\nu}(\pi^0; q', p, q) \;\sim\; \frac{1}{m_\pi^2}\,\mathcal{M}^{\mu\nu}(A^3; q', p, q) \;\sim\; \frac{1}{m_\pi^2}\, m_q^2 \;\sim\; m_\pi^2\,. \tag{13}$$

We thus find that the odderon exchange amplitude for π^0-production vanishes in the chiral limit $m_\pi^2 \to 0$. This result can be generalised to the reaction (1) with an arbitrary hadronic final state X.

5 Conclusion

We have considered the diffractive process $\gamma^{(*)}p \to \pi^0 X$ at high energies where it should be dominated by odderon exchange. As a consequence of chiral symmetry the odderon exchange amplitude for this process vanishes in the chiral limit $m_\pi^2 \to 0$. We still expect a strong dynamical suppression in the case of approximate chiral symmetry as it is realised in Nature. The cross section should be suppressed by a factor m_π^4/M^4, where M is a mass scale characterising the scattering process. In the calculation of the process $\gamma p \to \pi^0 N^*$ in [8] that effect had not been properly taken into account. A numerical estimate suggests that due to chiral symmetry the cross section found there is reduced by a factor of at least about 50 [10], changing the prediction (2) to less than about 6 nb. That reconciles the theoretical expectation with the experimental upper bound (3) of [9].

The considerations that we have outlined here can also be applied to pion production in other diffractive processes. An example that is relevant at the LHC and a future ILC is the quasidiffractive reaction $\gamma\gamma \to \pi^0\pi^0$ at high energies. Also this reaction is at high energies mediated by odderon exchange. Here an even stronger suppression due to approximate chiral symmetry is expected.

References

[1] Slides:
`http://indico.cern.ch/contributionDisplay.py?contribId=66&sessionId=7&confId=9499`

[2] C. Ewerz and O. Nachtmann, Eur. Phys. J. **C49** 685 (2007).

[3] L. Lukaszuk and B. Nicolescu, Lett. Nuovo Cim. **8** 405 (1973);
D. Joynson, E. Leader, B. Nicolescu and C. Lopez, Nuovo Cim. **A30** 345 (1975).

[4] C. Ewerz, arXiv:hep-ph/0306137 (2003).

[5] A. Breakstone *et al.*, Phys. Rev. Lett. **54** 180 (1985).

[6] H. G. Dosch, C. Ewerz and V. Schatz, Eur. Phys. J. **C24** 561 (2002).

[7] A. Schäfer, L. Mankiewicz and O. Nachtmann, in Proc. of the Workshop *Physics at HERA*, DESY Hamburg 1991, vol. 1, p. 243;
V. V. Barakhovsky, I. R. Zhitnitsky and A. N. Shelkovenko, Phys. Lett. **B267** 532 (1991);
W. Kilian and O. Nachtmann, Eur. Phys. J. **C5** 317 (1998).

[8] E. R. Berger, A. Donnachie, H. G. Dosch, W. Kilian, O. Nachtmann and M. Rueter, Eur. Phys. J. **C9** 491 (1999).

[9] C. Adloff *et al.* [H1 Collaboration], Phys. Lett. **B544** 35 (2002).

[10] A. Donnachie, H. G. Dosch and O. Nachtmann, Eur. Phys. J. **C45** 771 (2006).

[11] S. L. Adler and R. F. Dashen, *Current Algebras and Applications to Particle Physics*, W. A. Benjamin, New York (1968).

[12] C. Ewerz and O. Nachtmann, Annals Phys. **322** 1635 (2007);
C. Ewerz and O. Nachtmann, Annals Phys. **322** 1670 (2007).

Leading Neutron Production at ZEUS

W. Schmidke

Max Planck Institute for Physics
Munich, Germany

ZEUS results on leading neutron production in ep scattering are presented. Production in deep inelastic scattering and photoproduction are compared, giving indications of absorption. The data are compared to Monte Carlo, meson exchange and absorption models.

1 Introduction

Events with a neutron carrying a large fraction of the proton energy have been observed in ep scattering at HERA [1]. The dynamical mechanisms for their production are not completely understood. They may be the result of hadronization of the proton remnant, conserving baryon number in the final state. Exchange of virtual isovector mesons is also expected to contribute, predominantly the exchange of low mass π^+ mesons [2]. In this picture the proton fluctuates into a virtual n-π^+ state. The virtual π^+ scatters with the projectile lepton, leaving the fast forward neutron in the final state. Depending on the virtuality of the exchanged photon, which is a measure of how pointlike the photon is, the neutron may also rescatter with it and migrate to a region outside of the detector acceptance, leading to a depletion of neutrons in some kinematic regions [3].

The ZEUS experiment at HERA had a forward neutron calorimeter (FNC) in the proton beam direction. It measured the fraction of the beam energy carried by the neutron, x_L, and the transverse momentum transferred to the neutron, p_T. HERA machine elements along the neutron flight path limited neutron scattering angles to $\theta_n < 0.75$ mrad, restricting measurement to the kinematic region $p_T^2 < 0.476 x_L^2$ GeV^{-2}. Here we report results on leading neutron production, in both photoproduction, where the photon virtuality Q^2 is nearly zero, and in deep inelastic scattering (DIS), where Q^2 is greater than a few GeV^2. Comparisons are made to Monte Carlo models, one of which incorporate the pion exchange mechanism. Comparisons are also made to models of pion exchange incorporating rescattering, and a model including exchanges of additional mesons.

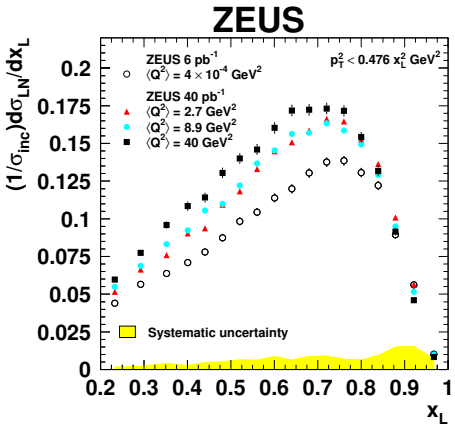

Figure 1: Neutron x_L distributions for photoproduction and three Q^2 bins of DIS.

2 Results

Leading neutron x_L distributions for photoproduction and three Q^2 bins of DIS are shown in Fig. 1. The distributions are normalized by $\sigma_{\rm inc}$, the inclusive cross section without the neutron requirement. The distributions all rise from lowest x_L due to the increase in p_T^2 space, reach a maximum near $x_L = 0.7$, and fall to zero at the kinematic limit $x_L = 1$. There is a clear increase of the relative neutron yield with Q^2. This is consistent with absorption models, where at lower Q^2 the larger photon size can result in rescattering of the neutron, where the neutron can migrate to a region outside of the detector acceptance and is lost.

For further studies the full Q^2 range of the DIS sample is taken together. The ratio of the photoproduction x_L distribution to that of the full DIS sample is shown in Fig. 2. The depletion of neutrons in the photoproduction sample increases with decreasing x_L. In pion exchange models the size of the virtual n-π^+ system is smaller at lower x_L, with increased probability of rescattering. Thus the depletion of neutrons in photoproduction is consistent with pion exchange models including absorption.

The p_T^2 distributions of neutrons in photoproduction and DIS are shown for several x_L bins in Fig. 3. They are normalized to unity at $p_T^2 = 0$. The lines are fits to exponentials in p_T^2, which give a good description of the data. The photoproduction distributions are steeper in the range $0.6 < x_L < 0.9$, with relatively fewer neutrons at high p_T^2. This is qualitatively consistent with absorption, where rescattering is more likely for the small n-π^+ separations corresponding to higher p_T^2.

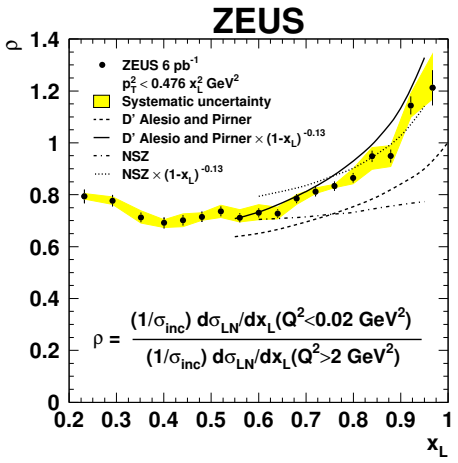

Figure 2: Ratio of neutron x_L distributions in photoproduction and DIS.

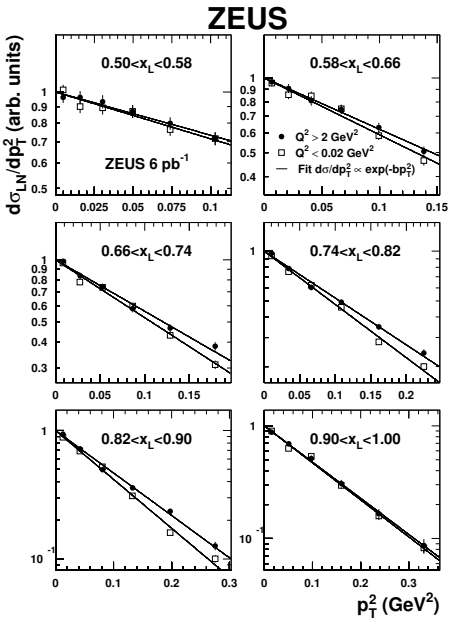

Figure 3: Neutron p_T^2 distributions for photoproduction and DIS, normalized to unity at $p_T^2 = 0$.

3 Comparison to models

The normalized neutron distributions in DIS were fit to the form

$$\frac{1}{\sigma_{\rm inc}}\frac{d\sigma_{\rm LN}}{dx_L dp_T^2} = ae^{-bp_T^2}.$$

Figure 4 shows the x_L distributions for $\theta_n < 0.75$ mrad and the intercepts a and slopes b as a function of x_L. Also on the plots are the expectations of the LEPTO [4] and RAPGAP [5] Monte Carlo models. Both were run in the configuration where neutron were produced from the fragmentation of the proton remnant [6]. LEPTO was also run implementing soft color interactions [**?**]; RAPGAP was also run including neutron production via pion exchange. Both models with only fragmentation of the proton remnant do not describe the data. They predict too few neutrons, peaked at lower x_L than the data. They do not have the broad plateau in intercepts a that the data exhibit for medium values of x_L, and they predict slopes b smaller than and without the steep x_L dependence of the data. LEPTO including soft color interactions gives an x_L distribution which better describes the peak in the data and has a slight enhancement of a at medium x_L value. RAPGAP with pion exchange gives a good description of the shapes of all distributions, although it predicts more neutrons with larger intercepts and slopes than the data.

The ratio of x_L distributions photoproduction over DIS in Fig. 2 also shows the predictions of two models of absorption [3]. The model of D' Alesio and Pirner describes the shape of the data, with increasing absorption at decreasing values of x_L, but it predicts a lower value of the ratio than the data. γp interactions have a power law dependence on the photon-proton center-of-mass energy, $\sigma \propto W^{\lambda}$, with different values of λ for DIS and photoproduction. Assuming that $\gamma\pi$ interactions have the same dependence, and recalling that $W_{\gamma\pi} = \sqrt{1-x_L} W_{\gamma p}$, the ratio of photoproduction and DIS cross sections is proportional to $(1-x_L)^{\Delta\lambda}$. After correcting the absorption factor of D' Alesio and Pirner for this differing W dependence the model give a good description of the data.

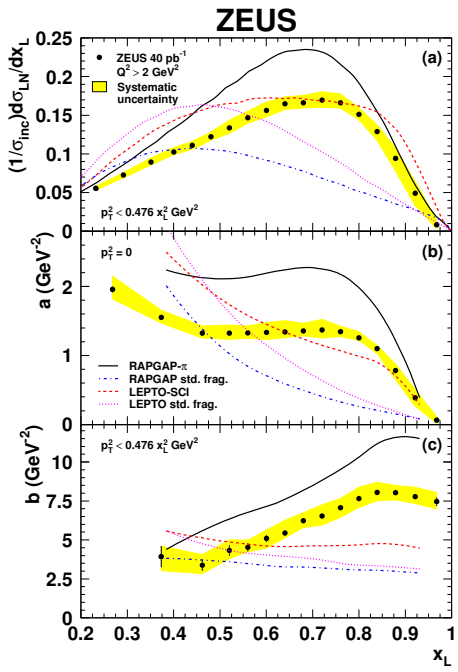

Figure 4: Leading neutron x_L distributions and intercepts and slope for DIS, compared to Monte Carlo models.

Figure 5 shows the slopes b for DIS, and the difference between slopes in photoproduction and DIS, Δb. Also shown are the predictions of a model of pion exchange incorporating neutron absorption and migration [8], and a model including in addition exchanges of ρ and a_2 mesons [9]. The model with only pion exchange predicts too high a value of the slopes, but does predicts the correct magnitude of Δb. The model including also ρ and a_2 exchanges gives a good description of the slopes, including the turnover at highest x_L. It also gives a fair prediction of the value of Δb.

4 Summary

Leading neutron energy and p_T distributions were measured in DIS and photoproduction. A decrease in neutron yield from high Q^2 DIS to very low Q^2 is indicative of absorption. Monte Carlo models incorporating only fragmentation of the proton remnant fail to describe the data. A pion exchange model gives a fair description of the energy distribution of neutron in DIS, but predicts too steep p_T^2 distributions. Addition of neutron absorption to the model describes the suppression seen in photoproduction. Adding further exchanges of ρ and a_2 mesons gives a good description also of the p_T^2 distributions.

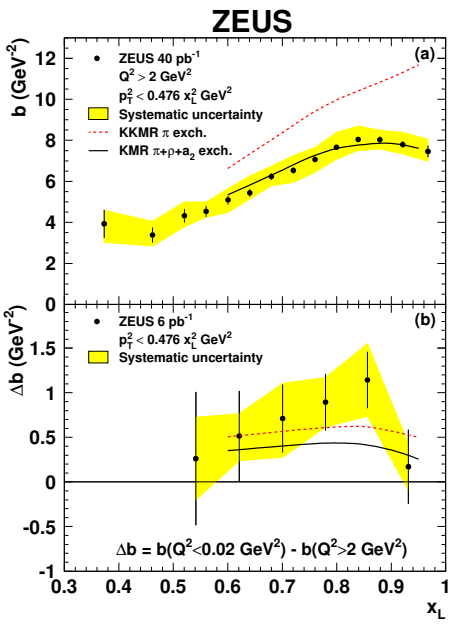

Figure 5: Neutron p_T^2 slopes in DIS (top) and difference in slopes between photoproduction and DIS (bottom). The dashed curve is a model of pion exchange including absorption; the solid curve is the model with the addition of ρ and a_2 meson exchange.

References

[1] ZEUS Coll., S. Chekanov *et al.*, Nucl. Phys. **B776** 1 (2007), and references therein.

[2] M. Bishari, Phys. Lett. **B38** 510 (1972).

[3] N.N. Nikolaev, J. Speth and B.G. Zakharov, Preprint KFA-IKP(TH)-1997-17 (hep-ph/9708290), KFA-IKP (1997);
U. D'Alesio and H.J. Pirner, Eur. Phys. J. **A7** 109 (2000).

[4] G. Ingelman, A. Edin and J. Rathsman, Comp. Phys. Comm. **101** 108 (1997).

[5] H. Jung, Comp. Phys. Comm. **86** 147 (1995).

[6] T. Sjöstrand and M. Bengtsson, Comp. Phys. Comm. **43** 367 (1987).

[7] A. Edin, G. Ingelman and J. Rathsman, Phys. Lett. **B366** 371 (1996).

[8] A.B. Kaidalov *et al.*, Eur. Phys. J. **C47** 385 (2006).

[9] V.A. Khoze, A.D. Martin and M.G. Ryskin, Preprint IPPP-06-36, DCPT-06-72 (hep-ph/0606213) 2006.

[10] Slides:
`http://indico.cern.ch/contributionDisplay.py?contribId=243&sessionId=7&confId=9499`

Recent Results on Diffraction from CDF

Christina Mesropian

The Rockefeller University
1230 York Avenue, New York NY - USA

We report recent results on diffraction and exclusive production obtained by the CDF collaboration in $p\bar{p}$ collisions at the Fermilab Tevatron collider at $\sqrt{s}$=1.96 TeV. A measurement of the Q^2 and t dependence of the diffractive structure function extracted from diffractive dijet production in the range of $10^2 < Q^2 < 10^4$ GeV^2 and $|t| < 1$ GeV^2 is presented. Results are also presented for exclusive e^+e^-, $\gamma\gamma$, and dijet production.

1 Introduction

The diffractive process in hadron-hadron colliders can be defined as a reaction in which the leading nucleon remains intact, and/or a large, non-exponentially suppressed, rapidity gap (region devoid of particles) is present. In the framework of Regge theory diffractive reactions are characterized by the exchange of a *pomeron*, a hypothetical object with vacuum quantum numbers. Diffractive reactions involving hard processes, such as production of jets, allow to study the nature of the exchanged object, the *pomeron*, in the framework of perturbative QCD (pQCD).

The CDF collaboration at the Fermilab $p\bar{p}$ collider investigated various diffractive reactions at three center of mass energies, $\sqrt{s}$=1800 GeV (Run I), $\sqrt{s}$=630 GeV (Run IC), and $\sqrt{s}$=1960 GeV (Run II). In this paper we present the latest results from Run II studies in diffractive dijet production and central exclusive e^+e^-, $\gamma\gamma$, and dijet production.

2 CDF Forward Detectors

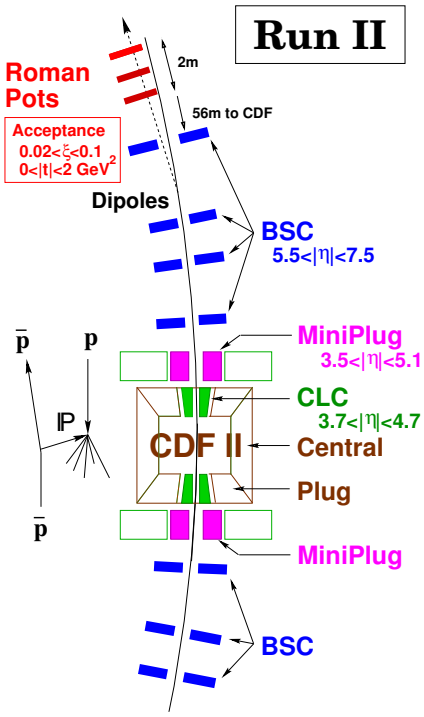

Figure 1: Layout of CDF Run II forward detectors along the beam-pipe (not to scale).

Since the identification of diffractive events requires either tagging of the leading particle or observation of a rapidity gap, the forward detectors are very important for the implementation of a diffractive program. The schematic layout of the CDF detectors in Run II is presented in Fig. 1. The Forward Detectors include the Roman Pot fiber tracker Spectrometer (RPS) to detect leading anti-protons; the Beam Shower Counters (BSCs) [2], covering the pseudorapidity range $5.5 < |\eta| < 7.5$, to detect particles from the interaction point traveling in either direction along the beam-pipe,

used to select diffractive events by identifying forward rapidity gaps, thus reducing non-diffractive background on the trigger level; the MiniPlug calorimeters (MP) [3], designed to measure energy and lateral position of both electromagnetic and hadronic showers in the pseudorapidity region of $3.5 < |\eta| < 5.1$. The ability to measure the event energy flow in the very forward rapidity region is extremely valuable for identification of diffractive events in the high luminosity environment of Run II.

3 Diffractive Dijet Production

The data sample for the study of the Single Diffractive (SD) dijet production is collected by triggering on a leading anti-proton in RPS in combination with at least one jet in the event. By comparing two samples of dijet events, diffractive and non-diffractive, the diffractive structure function is extracted. This study extends our previous results from Run I by studying the Q^2 dependence of the diffractive structure function, where Q^2 is defined as an average value of the squared mean dijet E_T. In the range of $100 < Q^2 < 10000$ GeV^2 no significant Q^2 dependence is observed, which indicates that the QCD evolution of the *pomeron* is similar to that of the proton. CDF also studied the Q^2 dependence of the four-momentum transfer squared, t, distributions in soft and hard single diffractive processes. Fig. 2 shows t distributions for different Q^2 values. The slope of the distribution at $\mid t \mid$=0 (GeV/c^2) does not show any dependence on Q^2.

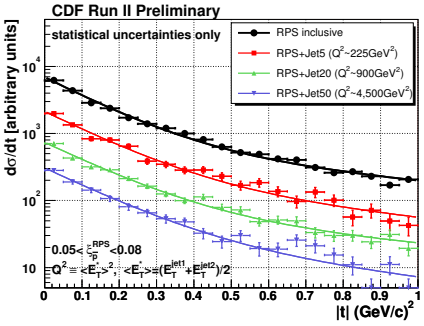

Figure 2: t distributions in soft and hard SD events for different Q^2 ranges. Data sample of 128 pb^{-1}.

4 Exclusive Dijet Production

Central exclusive production became a very interesting topic of study at CDF. In leading order QCD such exclusive processes can occur through the exchange of a color-singlet two gluon system between the nucleons, leaving large rapidity gaps in the forward regions. One of the gluons participates in a hard interaction, and an additional screening gluon is exchanged to cancel the color of the interacting gluons, and allowing the leading hadrons to stay intact. This is also a special case of dijet/diphoton production in Double *Pomeron* Exchange (DPE), $p+\bar{p} \rightarrow p+X+\bar{p}$. Central exclusive production is generally suppressed by the Sudakov form factor, however, it is a potentially useful channel to search for the light Standard Model Higgs boson, predominantly decaying to $b\bar{b}$, at the LHC, since exclusive $b\bar{b}$ production is expected to be significantly suppressed by a helicity selection ($J_Z = 0$) rule. Although the cross section for exclusive Higgs production is too small to be observed at the Tevatron, several processes mediated by the same mechanism but with the higher production rates can be studied to check theoretical predictions.

A data sample of 313 pb^{-1} for exclusive dijet production was collected with a dedicated trigger requiring a BSC gap on the proton side in the addition to a leading anti-proton in the RPS and at least one calorimeter tower with $E_T > 5$ GeV. The events in this data sample

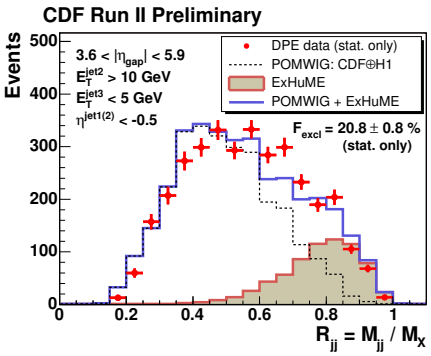

Figure 3: Dijet mass fraction R_{jj} in data (crosses) and best fit (solid line) obtained using inclusive (dashed line) and exclusive ExHuME (shaded area) MC predictions.

tower with $E_T > 5$ GeV. The events in this data sample also passed the offline requirement of an additional gap in MP on the proton-side. The observable sensitive to the amount of energy concentrated in dijet, is the dijet mass fraction $R_{jj} = M_{jj}/M_X$, where M_{jj} is the invariant mass of the two highest E_T jets, and M_X is the mass of the whole system with the exception of the leading particles. R_{jj} of exclusive dijets is expected to peak around $R_{jj} \sim 0.8$ and have a long tail toward low values due to hadronization of partons causing energy spills from the jet cones and gluon radiation in initial and final states. The exclusive signal is extracted by comparing the dijet data with inclusive DPE Monte Carlo predictions, using the POMWIG [4] event generator and detector simulation, and by looking for an excess at high R_{jj} values. The comparison of the R_{jj} distributions shows a clear excess of data at high R_{jj}. This excess is compared to different exclusive dijet production models [5, 6] implemented in ExHuME [7] and DPEMC [8] MC simulations. Fig. 3 shows the R_{jj} distribution for the data and the best fit to the data shape obtained from the inclusive POMWIG and exclusive ExHuME predictions. As can be seen from this plot, the data excess at high R_{jj} can be well described by exclusive dijet production. From the MC fits to the data, we measure the cross section of exclusive dijet production as a function of the minimum second jet E_T, see Fig. 4(left). The data prefer the ExHuME MC and pQCD calculations at LO (KMR) [5].

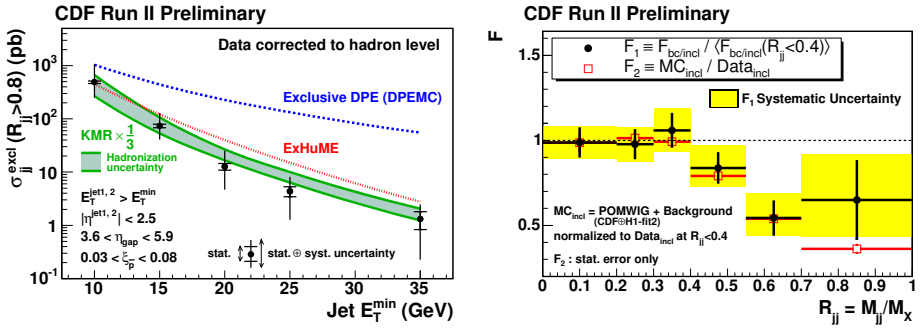

Figure 4: (left) Measured exclusive dijet cross section for R_{jj} >0.8 as a function of the minimum second jet E_T. The dashed (dotted) lines show the ExHuME (DPEMC) Monte Carlo predictions, the shaded band indicates the KMR calculations at LO parton level, scaled down by a factor 3; (right) Values of F_1 (full points) and F_2 (open squares) as a function of R_{jj}, where F_1 is the ratio of heavy flavor jets to all inclusive jets, normalized to the weighted average value in the region of $R_{jj} > 0.4$, and F_2 is the ratio of the POMWIG MC to the inclusive DPE dijet data. The systematic error is indicated by the shaded band.

Exclusive dijet production at LO is dominated by $gg \to gg$, while contributions from $gg \to q\bar{q}$ are strongly suppressed [5] by the helicity selection. Confirming this suppression will provide additional evidence to support the results obtained from MC based extraction of the exclusive dijet signal. We measure the ratio F_1 of heavy flavor quark jets to all jets as a function of R_{jj} using a data sample of 200 pb^{-1}, triggered by the presence of an anti-proton in the RPS, a forward gap on the proton side, dijets in the central region and at least one displaced vertex track with p_T >2 GeV/c. The last requirement enhances the heavy flavor content of the sample. The results, see Fig. 4(right), show the normalized ratio of heavy flavor jets to all jets as a function of R_{jj}. The trend of the F_1 ratio decreasing toward high R_{jj} values is compared with MC based results presented as F_2, where F_2 is the ratio of the inclusive MC predicted events, which are normalized to the data at R_{jj} >0.4. The two results are consistent with each other.

5 Exclusive e^+e^- and $\gamma\gamma$ Production

Here we report on the observation of exclusive e^+e^- production at hadron colliders. The data sample used for this study, corresponds to an integrated luminosity of 532 pb^{-1}, and was collected with a dedicated trigger requiring the absence of any particle signatures in the detector, except for e^+ or e^- candidates, each with transverse energy $E_T > 5$ GeV and pseudorapidity $|\eta| < 2$. With these criteria 16 events were observed compared to a background expectation of 1.9 ± 0.3 events. These events are consistent in cross section and properties with the Quantum Electro-Dynamics process $p\bar{p} \to p + e^+e^- + \bar{p}$ through two photon exchange. The measured cross section is $1.6^{+0.5}_{-0.3}$(stat) $\pm$ 0.3(syst) pb, which agrees well with the theoretical prediction of 1.71 ± 0.001 pb. This agreement is provides evidence that the cuts we make to define the central exclusive processes are correct.

The search for exclusive diphoton events, $p\bar{p} \to p+\gamma\gamma+\bar{p}$ demands the same event criteria as the exclusive e^+e^- search, and is using the same date sample. The photon candidates are defined as electromagnetic clusters with $E_T > 5$ GeV and $|\eta| < 1$ and no tracks pointing to them. Three events pass these criteria. Backgrounds to $\gamma\gamma$ production can arise from exclusive pair production of neutral mesons, ($\pi^0\pi^0$ and $\eta\eta$). These processes cannot be unambiguously distinguished from $\gamma\gamma$ production on an event by event basis. Therefore, a 95% C.L. upper limit on the exclusive $\gamma\gamma$ production cross section of 410 fb is reported, approximately a factor of 10 higher than the theoretical prediction [9].

References

[1] Slides: `http://indico.cern.ch/contributionDisplay.py?contribId=103&sessionId=7&confId=9499`

[2] M. Gallinaro, Procs. *"CDF forward detectors and diffractive structure functions at the Fermilab Tevatron* (2004) arXiv:hep-ph/0407255.

[3] K. Goulianos *et al.*, Nucl. Instrum. Methods A **518** (2004) 24 [arXiv:physics/0310156].

[4] B.E. Cox and J.R. Forshaw, Comput. Phys. Commun. **144** (2002) 104 [arXiv:hep-ph/0010303].

[5] V.A. Khoze, A.D. Martin, and M.G. Ryskin, Eur. Phys. J. C **34** (2004) 327 [arXiv:hep-ph/0401078]; A.B. Kaidalov *et al.*, Eur. Phys. J. C **33** (2004) 261 [arXiv:hep-ph/0311023].

[6] A. Bialas and P.V. Landshoff, Phys. Lett. B **256** (1991) 540.

[7] J. Monk and A. Pilkington, Comput. Phys. Commun. **175** (2006) 232 [arXiv:hep-ph/0502077].

[8] M. Boonekamp and T. Kucs, Comput. Phys. Commun. **167** (2005) 217 [arXiv:hep-ph/0312273].

[9] V.A. Khoze *et al.*, Eur. Phys. J. C **38** (2005) 475 [arXiv:hep-ph/0409037].

Recent Phenomenological Predictions for Central Exclusive Production at the LHC

B. E. Cox, F. K. Loebinger and A. D. Pilkington *

Department of Physics and Astronomy, The University of Manchester,
Manchester M13 9PL, UK.

We present the latest luminosity dependent background predictions for central exclusive processes at the LHC. The effect of these predictions on the potential observation of a Higgs boson in the MSSM is also discussed.

1 Introduction

The central exclusive process (CEP) is defined as $pp \to p + X + p$ and no other hadronic activity [2]. During the interaction, the protons remain intact, are deflected through very small angles and typically lose less than 1% of their energy. The mass of the central system can be reconstructed from just the outgoing proton momentum. Furthermore, to a very good approximation the central system, X, is produced in a 0^{++} state. Thus, by tagging the outgoing protons and measuring the momenta, the mass and quantum numbers of a resonance is known regardless of the decay products.

In this contribution, we give a brief insight into the luminosity dependent backgrounds to CEP, which have only recently been evaluated. We assume that forward proton detectors have been installed 420m from the interaction point at ATLAS (and CMS) as detailed by the FP420 proposal [3].

2 Luminosity dependent backgrounds

The luminosity dependent (or overlap) backgrounds occur due to the large number of interactions in each bunch crossing at the LHC. The largest contribution, which we denote as [p][X][p], comes from a three-fold coincidence between an inclusive hard scatter event, [X], and two single diffractive events, [p], each of which produces a proton within the acceptance of the forward detectors. The luminosity dependence of this background arises because the probability of single diffractive events occurring in a specific bunch crossing increases with the number of interactions in the bunch crossing.

The cross section, σ, can be estimated by

$$\sigma = \sigma_{[X]} \sum_{N=3}^{\infty} \frac{\lambda^N e^{-\lambda}}{N!} P_{2[p]}(N-1) \tag{1}$$

where $\sigma_{[X]}$ is the cross section of the inclusive hard scatter event and λ is the average number of interactions in a bunch crossing at the LHC. The $P_{2[p]}(n)$ factor is the probability that, given n interactions, there are at least two single diffractive events, each of which produces a proton within the acceptance of a forward detector. This probability is calculated using a trinomial distribution which utilises the fraction, f_{sd}, of events at the LHC that are single diffractive and produce an outgoing proton within the acceptance of a forward detector.

*This work was funded in the UK by PPARC/STFC.

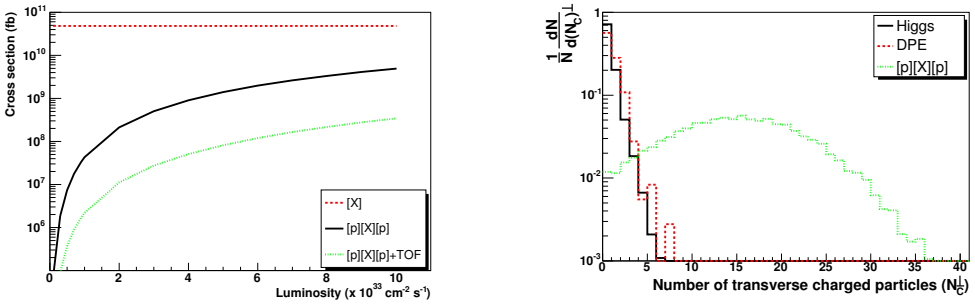

(a) (b)

Figure 1: The cross section for the overlap di-jet cross section ($E_T > 40GeV$) is shown in (a) as a function of luminosity. Figure (b) shows the number of charged particles that are perpendicular in azimuth to the leading jet.

There is a consensus between theoretical predictions and Monte Carlo event generators that $f_{sd} \sim 0.01$ for $0.002 \leq \xi \leq 0.02$, which is the approximate fractional momentum loss acceptance of FP420. Figure 1(a) shows the cross section (fb) for overlap di-jet events at the LHC after requiring that the parton has a transverse momentum of 40 GeV. The cross section dependence is approximately quadratic. The luminosity dependent background can also be reduced by using proton time-of-flight (TOF) information to construct an 'event vertex', which can be matched to the di-jet vertex (see [4]).

The overlap background is reduced further by the clean nature of the central exclusive events. Di-jets from the inclusive event will be colour connected to the proton remants and the occurance of multi-parton interactions means that there will be so-called underlying event. In figure 1(b), we compare the number of charged particles that are perpendicular in azimuth to the leading jet. The signal events are generated by the ExHuME MC [5] and the inclusive di-jet events by HERWIG [6] with JIMMY [7] used for the underlying event. To create the overlap background, the protons are added in on an event by event basis with a distribution in ξ and t given by [8]. By requiring that there are few charged particles in this region, the overlap background can be additionally reduced by a factor of ~ 100. This however, is dependent on the MC tune used to generate the inclusive events.

3 Implications for MSSM Higgs boson observation

To illustrate the effect of this luminosity dependent background, we examine the potential observation of a light MSSM Higgs boson in the $b\bar{b}$ decay channel. Within the m_h^{max} scenario, with $\tan\beta = 40$, $m_A = 120$ GeV and $\mu = 200$ GeV, the cross section of $h \to b\bar{b}$ is 17.9 fb and the Higgs boson has a mass of 119.5 GeV with a width of 3.2 GeV. The relevant backgrounds to this process are CEP $b\bar{b}$ and gg production, $b\bar{b}$ production via double pomeron exchange (DPE) and overlap. A transverse energy cut of 45 GeV is imposed on the leading jet in order to reduce the QCD backgrounds. The non-CEP backgrounds are reduced by comparing the

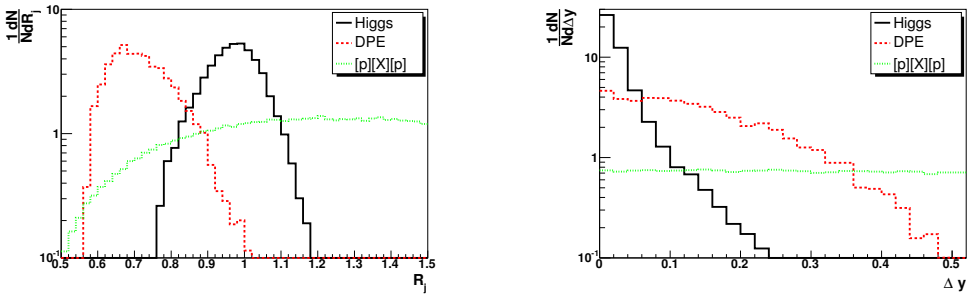

(a) (b)

Figure 2: The R_j distribution for signal, DPE and overlap backgrounds (a). The corresponding Δy distributions are shown in (b).

kinematic information from FP420 to the di-jet system.

Firstly, we use the di-jet mass fraction, which compares the mass of the di-jet system to the central mass measured by FP420. We use the R_j definition [9] for the di-jet mass fraction as it is less affected by final state radiation effects. For central exclusive backgounds, we expect that $R_j \sim 1$. Figure 2(a) compares the R_j distributions for the signal and background events after smearing the particles with the intrinsic resolution of the ATLAS detector. The DPE backgrounds, generated with the POMWIG MC [10], have a smaller R_j than CEP processes due to the presence of pomeron remnants. The overlap backgrounds typically have a large range of R_j values because the protons do not originate from the same interaction as the di-jets and the proton kinematics, in general, do not match the di-jet system. Figure 2(b) shows the equivalent plots for the Δy variable, which is the modulus of the difference between the rapidity of the central system as measured by FP420 and the average rapidity of the two jets. The CEP events are peaked at zero as expected and the backgrounds spread over a large range in Δy. An exclusive enriched sample can be obtained by requiring that $0.75 \leq R_j \leq 1.1$ and $\Delta y \leq 0.06$. After these cuts, the DPE backgrounds are negligible.

The signal cross section is 0.6 fb before trigger efficiency. The largest loss in signal is from FP420 acceptance (28%), double b-tagging efficiency (36%) and the jet E_T requirement (50%). The CEP backgrounds are reduced to 2.3 fb and the overlap background to 0.04 (5.5) fb at low (high) luminosity. However, these backgrounds are spread over the mass range 80 - 160 GeV, whereas the signal is smeared only by the FP420 mass resolution of approximately 2 GeV. To estimate the significance of a potential observation, events are selected at random for each process to create a 'data sample'. The resulting mass distribution is fitted with a null hypothesis and a background plus gaussian signal hypothesis. The significance is estimated from the $\Delta\chi^2$ of the two fits. The process is repeated for many 'samples' and an averaged significance obtained.

The limiting factor is the trigger strategy as shown in figure 3. The signal from the forward detectors arrive too late to be included in the level one trigger and the events must therefore be retained by information from the central detector. The forward proton

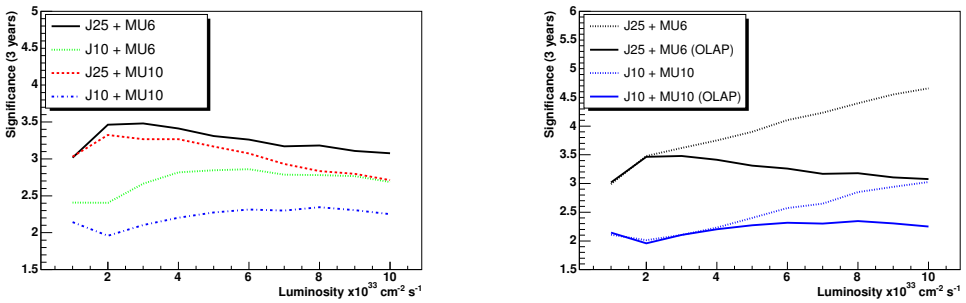

(a) (b)

Figure 3: The significance of observation as a function of luminosity (a). The different curves label different trigger strategies, i.e. J10 is a jet-rate trigger which is pre-scaled to 10 kHz and MU6 is a 6 GeV muon trigger. Fig (b) shows the effect of the overlap background.

information could then be used at level 2 to substantially reduce the rate for non-diffractive events. We define two complementary trigger strategies. The first is a low transverse momentum muon in conjunction with a jet with $E_T > 40$ GeV. The second is to have a di-jet trigger with $E_T > 40$ GeV, which is pre-scaled to a given rate. Figure 3(a) shows the significance after three years of for a combination of these triggers.

Figure 3(b) shows the effect of the overlap background at high luminosity. Without overlap, the significance can approach 5 in the best case scenario and one would expect a significance of ~ 3 for the more conservative triggers. With overlap, the significance is restricted to ~ 3 in the best case scenario. It may be possible to increase the rejection of the overlap background with improved proton time-of-flight measurements. Furthermore, the analysis presented here has not utilised forward detectors at 220m. The significance will increase when the analyses are combined.

References

[1] Slides:
`http://indico.cern.ch/contributionDisplay.py?contribId=68&sessionId=7&confId=9499`

[2] A. De Roeck, V. A. Khoze, A. D. Martin, R. Orava and M. G. Ryskin, Eur. Phys. J. C **25** (2002) 391 [arXiv:hep-ph/0207042].
J. R. Forshaw, arXiv:hep-ph/0508274.

[3] M. G. Albrow *et al.*, CERN-LHCC-2005-025.

[4] A. D. Pilkington, *Status of the FP420 project*, These proceedings.

[5] J. Monk and A. Pilkington, Comput. Phys. Commun. **175** (2006) 232 [arXiv:hep-ph/0502077].

[6] G. Corcella *et al.*, arXiv:hep-ph/0210213.

[7] J. M. Butterworth, J. R. Forshaw and M. H. Seymour, Z. Phys. C **72** (1996) 637 [arXiv:hep-ph/9601371].

[8] V. A. Khoze, A. D. Martin and M. G. Ryskin, Phys. Lett. B **643** (2006) 93 [arXiv:hep-ph/0609312].

[9] V. A. Khoze, A. D. Martin and M. G. Ryskin, Eur. Phys. J. C **48** (2006) 467 [arXiv:hep-ph/0605113].

[10] B. E. Cox and J. R. Forshaw, Comput. Phys. Commun. **144** (2002) 104 [arXiv:hep-ph/0010303].

Rapidity Gap Survival in the Black-Disk Regime

L. Frankfurt[1], C.E. Hyde[2], M. Strikman[3], C. Weiss[4] *

1- School of Physics and Astronomy, Tel Aviv University, Tel Aviv, Israel

2- Old Dominion University, Norfolk, VA 23529, USA,
and Laboratoire de Physique Corpusculaire, Université Blaise Pascal, 63177 Aubière, France

3- Department of Physics, Pennsylvania State University, University Park, PA 16802, USA

4- Theory Center, Jefferson Lab, Newport News, VA 23606, USA

We summarize how the approach to the black–disk regime (BDR) of strong interactions at TeV energies influences rapidity gap survival in exclusive hard diffraction $pp \to p + H + p$ ($H = \text{dijet}, \bar{Q}Q, \text{Higgs}$). Employing a recently developed partonic description of such processes, we discuss (a) the suppression of diffraction at small impact parameters by soft spectator interactions in the BDR; (b) further suppression by inelastic interactions of hard spectator partons in the BDR; (c) correlations between hard and soft interactions. Hard spectator interactions substantially reduce the rapidity gap survival probability at LHC energies compared to previously reported estimates.

1 Introduction

At high energies strong interactions enter a regime in which cross sections are comparable to the "geometric size" of the hadrons, and unitarity becomes an essential feature of the dynamics. By analogy with quantum–mechanical scattering from a black disk, in which particles with impact parameters $b < R_{\text{disk}}$ experience inelastic interactions with unit probability, this is known as the black–disk regime (BDR). The approach to the BDR is well–known in soft interactions, where it generally can be attributed to the "complexity" of the hadronic wave functions. It is seen *e.g.* in phenomenological parametrizations of the pp elastic scattering amplitude, whose profile function $\Gamma(b)$ approaches unity at $b = 0$ for energies $\sqrt{s} \gtrsim 2\,\text{TeV}$. More recently it was realized that the BDR is attained also in hard processes described by QCD, due to the increase of the gluon density in the proton at small x. Theoretically, this phenomenon can be studied in the scattering of a small–size color dipole ($d \sim 1/Q$) from the proton. Numerical studies show that that at TeV energies the dipole–proton interaction is close to "black" up to $Q^2 \sim$ several 10 GeV^2 [2]. This fact has numerous implications for the dynamics of pp collisions at the LHC, where multiple hard interactions are commonplace. For example, it predicts dramatic changes in the multiplicities and p_T spectra of forward particles in central pp collisions compared to extrapolations of the Tevatron data [3]. Absorption and energy loss of leading partons by inelastic interactions in the BDR can also account for the pattern of forward pion production in d–Au collisions at STAR [4].

Particularly interesting is the question what the approach to the BDR implies for exclusive hard diffractive scattering, $pp \to p + H + p$. In such processes a high–mass system ($H = \text{dijet}, \bar{Q}Q, \text{Higgs}$) is produced in a hard process involving exchange of two gluons between the protons. At the same time, the spectator systems must interact in a way such as not to produce additional particles. This restricts the set of possible trajectories in configuration space and results in a suppression of the cross section compared to non-diffractive

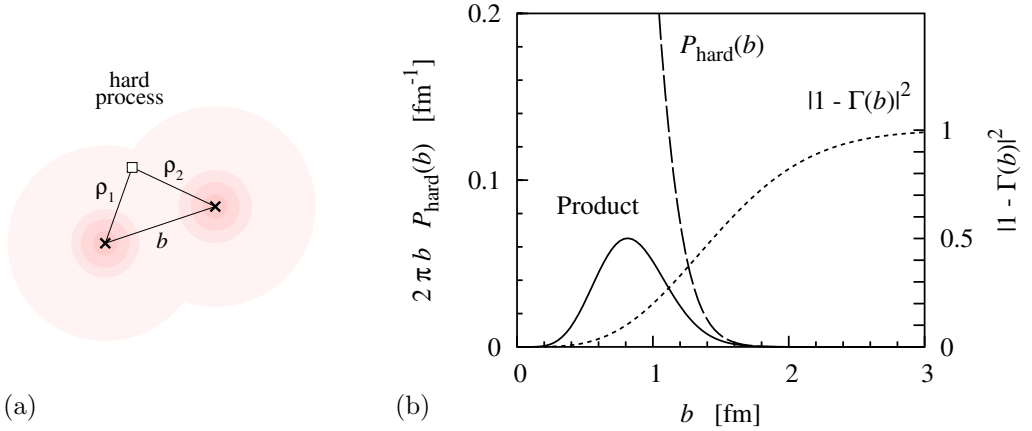

Figure 1: (a) Transverse geometry of hard diffractive pp scattering. (b) Dashed line: Probability for hard scattering process $P_{\rm hard}(\boldsymbol{b})$ as function of the pp impact parameter, b. Dotted line: Probability for no inelastic interactions between the protons, $|1-\Gamma(\boldsymbol{b})|^2$. Solid line: Product $P_{\rm hard}(\boldsymbol{b})|1-\Gamma(\boldsymbol{b})|^2$. The RGS probability (1) is given by the area under this curve. The results shown are for Higgs production at the LHC ($\sqrt{s} = 14\,\text{TeV}, M_H \sim 100\,\text{GeV}$).

events. For soft spectator interactions this suppression is measured by the so–called rapidity gap survival (RGS) probability. Important questions are (a) what role the BDR plays in traditional soft–interaction RGS; (b) how the physical picture of RGS is modified by hard spectator interactions in the BDR at LHC energies; (c) how possible correlations between hard and soft interactions affect RGS. These questions can be addressed in a recently proposed partonic description of exclusive diffraction [5], based on Gribov's parton picture of high–energy hadron–hadron scattering. This approach allows for a model–independent treatment of the interplay of hard and soft interactions, and for the consistent implementation of the BDR at high energies (for details, see Ref. [5]).

2 Black–disk regime in soft spectator interactions

A simple "geometric" picture of RGS is obtained in the approach of Ref. [5] in the approximation where hard and soft interactions are considered to be independent. The hard two–gluon exchange process can be regarded as happening locally in space–time on the typical scale of soft interactions. In the impact parameter representation (see Fig. 1a) the RGS probability can be expressed as

$$S^2 \;=\; \int d^2b\, P_{\rm hard}(\boldsymbol{b})\, |1-\Gamma(\boldsymbol{b})|^2. \qquad (1)$$

Here $P_{\rm hard}(\boldsymbol{b})$ is the probability for two hard gluons from the protons to collide in the same space–time point, given by the overlap integral of the squared transverse spatial distributions of gluons in the colliding protons, normalized to $\int d^2b\; P_{\rm hard}(\boldsymbol{b}) = 1$ (see Fig. 1b). The function $|1-\Gamma(\boldsymbol{b})|^2$ is the probability for the two protons not to interact inelastically in a collision with impact parameter b. The approach to the BDR in pp scattering at energies

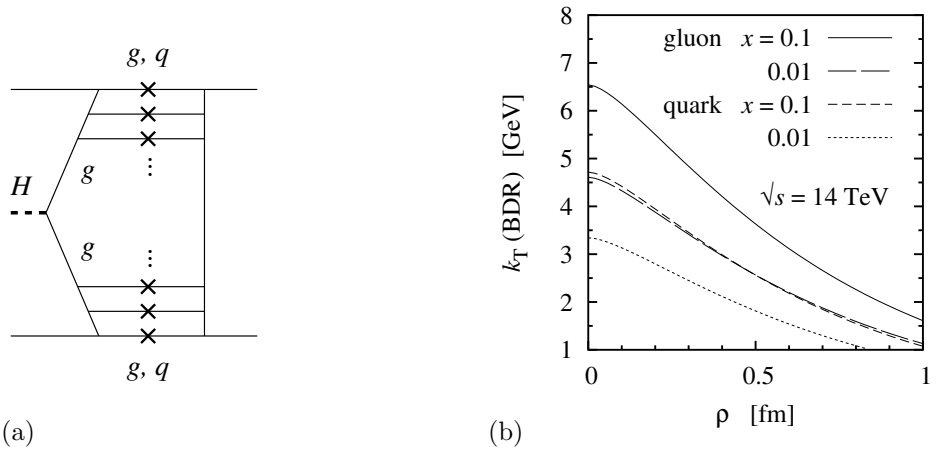

Figure 2: (a) Absorption of parent partons in the evolution by interactions in the BDR. (b) The critical transverse momentum, k_T(BDR), below which partons are absorbed with high probability ($|\Gamma^{\text{parton-proton}}| > 0.5$), as a function of the parton–proton impact parameter, ρ.

$\sqrt{s} \gtrsim 2$ TeV implies that this probability is practically zero at small impact parameters, and becomes significant only for $b \gtrsim 1$ fm (see Fig. 1b). This eliminates the contribution from small impact parameters in the integral (1) (see Fig. 1b) and determines the value of the RGS probability to be $S^2 \ll 1$. It is seen that the approach to the BDR in soft interactions plays an essential role in the physical mechanism of RGS.

3 Black–disk regime in hard spectator interactions

At LHC energies even highly virtual partons ($k^2 \sim$ few GeV^2) with $x \gtrsim 10^{-2}$ experience "black" interactions with the small–x gluons in the other proton. This new effect causes an additional suppression of diffractive scattering which is not included in the traditional RGS probability [5]. One mechanism by which this happens is the absorption of "parent" partons in the QCD evolution leading up to the hard scattering process (see Fig. 2a). Specifically, in Higgs production at the LHC the gluons producing the Higgs have momentum fractions $x_{1,2} \sim M_H/\sqrt{s} \sim 10^{-2}$; their "parent" partons in the evolution (quarks and gluons) typically have momentum fractions of the order $x \sim 10^{-1}$ and transverse momenta $k_T^2 \sim$ few GeV^2. Quantitative studies of the BDR in the dipole picture show that at the LHC energy such partons are absorbed with near–unit probability if their impact parameters with the other proton are $\rho_{1,2} \lesssim 1$ fm (see Fig. 2b). For proton–proton impact parameters $b < 1$ fm about 90% of the strength in $P_{\text{hard}}(b)$ comes from parton–proton impact parameters $\rho_{1,2} < 1$ fm (*cf.* Fig. 1a), so that this effect practically eliminates diffraction at $b < 1$ fm. Since $b < 1$ fm accounts for 2/3 of the cross section [see Eq. (1) and Fig. 1b)], and the remaining contributions at $b > 1$ fm are also reduced by absorption, we estimate that inelastic interactions of hard spectators in the BDR reduce the RGS probability at LHC energies to about 20% of its soft–interaction value. (Trajectories with no emissions, corresponding to the $\delta(1-x)$ term in the evolution kernel, are not affected by absorption; however, their contributions

are small because they effectively probe the gluon density at the soft input scale.) Since this effect "pushes" diffractive pp scattering to even larger impact parameters than allowed by soft–interaction RGS it should also manifest itself in a shift of the final–state proton transverse momentum distribution to smaller values, which could be observed in p_T–dependent measurements of diffraction at the LHC.

The estimates reported here are based on the assumption that DGLAP evolution reasonably well describes the gluon density down to $x \sim 10^{-6}$; the quantitative details (but not the basic picture) may change if small–x resummation corrections were to significantly modify the gluon density at such values of x (see Ref. [6] and references therein). The effect of hard spectator interactions described here is substantially weaker at the Tevatron energy.

4 Correlations between hard and soft interactions

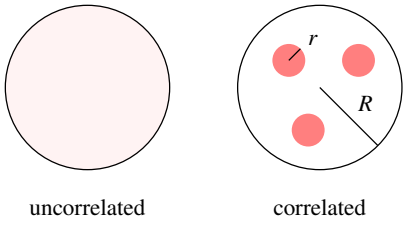

Figure 3: Transverse parton correlations.

The partonic approach to RGS of Ref. [5] also allows one to incorporate effects of correlations in the partonic wavefunction of the protons. They can lead to correlations between hard and soft interactions in diffraction, which substantially modify the picture of RGS compared to the independent interaction approximation. The CDF data on pp collisions with multiple hard processes indicate the presence of substantial transverse correlations of size $r \ll R$ between partons (see Fig. 3). A possible explanation of their origin could be the "constituent quark" structure of the proton suggested by the instanton vacuum model of chiral symmetry breaking. Such correlations modify the picture of RGS in hard diffractive pp scattering compared to the independent interaction approximation in two ways [5]. On one hand, with correlations inelastic interactions between spectators are much more likely in configurations in which two large–x partons collide in a hard process than in average configurations, reducing the RGS probability compared to the uncorrelated case. On the other hand, the "lumpiness" implies that there is generally a higher chance for the remaining spectator system not to interact inelastically compared to the mean–field approximation. A quantitative treatment of correlations in RGS, incorporating both effects, remains an outstanding problem.

References

[1] Slides:
`http://indico.cern.ch/contributionDisplay.py?contribId=67&sessionId=7&confId=9499`

[2] For a review, see: L. Frankfurt, M. Strikman and C. Weiss, Ann. Rev. Nucl. Part. Sci. **55**, 403 (2005).

[3] L. Frankfurt, M. Strikman and C. Weiss, Phys. Rev. D **69**, 114010 (2004).

[4] L. Frankfurt and M. Strikman, Phys. Lett. B **645**, 412 (2007).

[5] L. Frankfurt, C. E. Hyde-Wright, M. Strikman and C. Weiss, Phys. Rev. D **75**, 054009 (2007).

[6] M. Ciafaloni, D. Colferai, G. P. Salam and A. M. Stasto, arXiv:0707.1453 [hep-ph].

Hard Diffraction and the Color Glass Condensate

Cyrille Marquet

RIKEN BNL Research Center, Brookhaven National Laboratory, Upton, NY 11973, USA

Following the Good-and-Walker picture, hard diffraction in the high-energy/small$-x$ limit of QCD can be described in terms of eigenstates of the scattering matrix off a Color Glass Condensate. From the CGC non-linear evolution equations, it is then possible to derive the behavior of diffractive cross-sections at small x. I discuss recent results, in particular the consequences of the inclusion of Pomeron loops in the evolution.

1 Parton saturation and hard diffraction

When probing small distances inside a hadron with a fixed momentum scale $Q^2 \gg \Lambda^2_{QCD}$, one resolves its constituents quarks and gluons. As one increases the energy of the scattering process, the parton densities seen by the probe grow. At some energy much bigger than the hard scale, the gluon density has grown so large that non-linear effects become important. One enters the saturation regime of QCD, a non-linear yet weakly-coupled regime that describes the hadron as a dense system of weakly interacting partons (mainly gluons).

The transition to the saturation regime is characterized by the so-called saturation momentum $Q_s(x) = Q_0\ x^{-\lambda/2}$. This is an intrinsic scale of the high-energy hadron which increases as x decreases. $Q_0 \sim \Lambda_{QCD}$, but as the energy increases, Q_s becomes a hard scale, and the transition to saturation occurs when Q_s becomes comparable to Q. Although the saturation regime is only reached when $Q_s \sim Q$, observables are sensitive to the saturation scale already during the approach to saturation when $\Lambda_{QCD} \ll Q_s \ll Q$. This is especially true in the case of hard diffraction in deep inelastic scattering (DIS).

Both inclusive ($\gamma^* p \to X$) and diffractive ($\gamma^* p \to Xp$) DIS are processes in which a photon (of virtuality Q^2) is used as the hard probe, and at small values of $x \simeq Q^2/W^2$, parton saturation becomes relevant. The dipole picture naturally describes inclusive and diffractive events within the same theoretical framework. It expresses the scattering of the virtual photon through its fluctuation into a color singlet $q\bar{q}$ pair (or dipole) of a transverse size $r \sim 1/Q$. The dipole is then what probes the target proton, seen as a Color Glass Condensate (CGC): a dense system of gluons that interact coherently. Therefore, despite its perturbative size, the dipole cross-section is comparable to that of a pion.

The same dipole scattering amplitude $\langle T(r)\rangle_x$ enters in the formulation of the inclusive and diffractive cross-sections:

$$\begin{aligned}
&& & & r<1/Q & & 1/Q<r<1/Q_s & & r>1/Q_s \\
\frac{Q^2}{Q_s^2}\frac{d\sigma_{tot}}{d^2b} &= 4\pi\frac{Q^2}{Q_s^2}\int_0^\infty rdr\ \phi(r,Q^2)\langle T(r)\rangle_x \simeq & 1 & + & \ln\left(\frac{Q^2}{Q_s^2}\right) & + & 1 \\
\frac{Q^2}{Q_s^2}\frac{d\sigma_{diff}}{d^2b} &= 2\pi\frac{Q^2}{Q_s^2}\int_0^\infty rdr\ \phi(r,Q^2)\langle T(r)\rangle_x^2 \simeq & \frac{Q_s^2}{Q^2} & + & 1 & + & 1
\end{aligned}$$

where $\phi(r,Q^2)$ is the well-known $\gamma^* \to q\bar{q}$ wavefunction. To obtain the right-hand sides, we have decomposed the dipole-size integration into three domains: $r<1/Q$, $1/Q<r<1/Q_s$, and $r>1/Q_s$, and used the dipole amplitude $\langle T(r)\rangle_x$ discussed below. One sees that hard diffractive events ($Q^2 \gg Q_s^2$) are much more sensitive to saturation than inclusive events, as the contribution of small dipole sizes is suppressed and the dominant size is $r \sim 1/Q_s$.

2 Hard diffraction off a Color Glass Condensate

The Good-and-Walker picture of diffraction was originally meant to describe soft diffraction. They express an hadronic projectile $|P\rangle = \sum_n c_n |e_n\rangle$ in terms of hypothetic eigenstates of the interaction with the target $|e_n\rangle$, that can only scatter elastically: $\hat{S}|e_n\rangle = (1-T_n)|e_n\rangle$. The total, elastic and diffractive cross-sections are then easily obtained:

$$\sigma_{tot} = 2\sum_n c_n^2 T_n \qquad \sigma_{el} = \Big[\sum_n c_n^2 T_n\Big]^2 \qquad \sigma_{diff} = \sum_n c_n^2 T_n^2 \ . \tag{1}$$

It turns out that in the high energy limit, there exists a basis of eigenstates of the large$-N_c$ QCD $S-$matrix: sets of quark-antiquark color dipoles $|e_n\rangle = |d(r_1), \ldots, d(r_n)\rangle$ characterized by their transverse sizes r_i. In the context of deep inelastic scattering (DIS), we also know the coefficients c_n to express the virtual photon in the dipole basis. For instance, the equivalent of c_1^2 for the one-dipole state is the photon wavefunction $\phi(r, Q^2)$.

This realization of the Good-and-Walker picture allows to write down exact (within the high-energy and large$-N_c$ limits) factorization formulae for the total and diffractive cross-sections in DIS. They are expressed in terms of elastic scattering amplitudes of dipoles off the CGC $\langle T_n(\{r_i\})\rangle_Y$, where $Y = \ln(1/x)$ is the total rapidity. The average $\langle\ .\ \rangle_Y$ is an average over the CGC wavefunction that gives the energy dependence to the cross-sections.

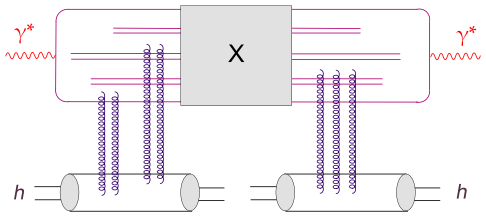

Figure 1: Representation of the factorization formula (2) for the diffractive cross-section in DIS. The virtual photon is decomposed into dipoles which interact elastically with the target hadron. The rapidity gap is Y_g and the final state X is made of particles produced over a rapidity interval $Y - Y_g$.

Formulae are similar to (1) with extra integrations over the dipoles transverse coordinates. For instance, denoting the minimal rapidity gap Y_g, the diffractive cross-section reads [2]

$$\sigma_{diff}(Y, Y_g, Q^2) = \sum_n \int dr_1 \cdots dr_n \ c_n^2(\{r_i\}, Q^2, Y - Y_g) \ \langle T_n(\{r_i\})\rangle_{Y_g}^2 \ . \tag{2}$$

This factorization is represented in Fig. 1. Besides the Q^2 dependence, the probabilities to express the virtual photon in the dipole basis c_n^2 also depend on $Y - Y_g$. Starting with the initial condition $c_n^2(\{r_i\}, Q^2, 0) = \delta_{1n}\phi(r, Q^2)$, the probabilities can be obtained from the high-energy QCD rapidity evolution. Finally, the scattering amplitude of the n-dipole state $T_n(\{r_i\})$ is given by

$$T_n(\{r_i\}) = 1 - \prod_{i=1}^{n} (1 - T(r_i))$$

where $T(r) \equiv T_1(r)$ is the scattering amplitude of the one-dipole state. The rapidity evolution of the correlators $\langle T(r_1) \ldots T(r_n)\rangle_Y$ should obtained from the CGC non-linear equations; one can then compute the diffractive cross-section.

When taking $Y_g \to Y$ in formula (2), one recovers the formula used for our previous estimates, which corresponds to restricting the diffractive final state to a $q\bar{q}$ pair. In practice the description of HERA data also requires a $q\bar{q}g$ contribution.

3 The CGC non-linear evolution equations

Within the high-energy and large$-N_c$ limits, the scattering amplitudes off the CGC are obtained from the Pomeron-loop equation [3] derived in the leading logarithmic approximation in QCD. This is a Langevin equation which exhibits the stochastic nature [4] of high-energy scattering processes in QCD. Its solution $\bar{T}$ is an event-by-event dipole scattering amplitude function of $\rho = -\ln(r^2 Q_0^2)$ and Y (Q_0 is a scale provided by the initial condition).

The solution $\bar{T}(\rho, Y)$ is characterized by a saturation scale Q_s which is a random variable whose logarithm is distributed according to a Gaussian probability law [5]. The average value is $\ln(\bar{Q}_s^2/Q_0^2) = v\bar{\alpha}Y$ and the variance is $\sigma^2 = D\bar{\alpha}Y$. The saturation exponent v determines the growth of $\bar{Q}_s$ with rapidity, and the dispersion coefficient D defines two energy regimes: the geometric scaling regime ($DY \ll 1$) and diffusive scaling regime ($DY \gg 1$).

Evolving a given initial condition yields a stochastic ensemble of solutions $\bar{T}$, from which one obtains the dipole correlators:

$$\langle T(r_1) \dots T(r_n) \rangle_Y = \left\langle \bar{T}(\rho_1, Y) \dots \bar{T}(\rho_n, Y) \right\rangle$$

where in the right-hand side, $\langle \, . \, \rangle$ is an average over the realizations of $\bar{T}$. Indeed, both quantities $\langle T \dots T \rangle_Y$ and $\left\langle \bar{T} \dots \bar{T} \right\rangle$ obey the same hierarchy of equations. One obtains the following results for the dipole scattering amplitudes [6]:

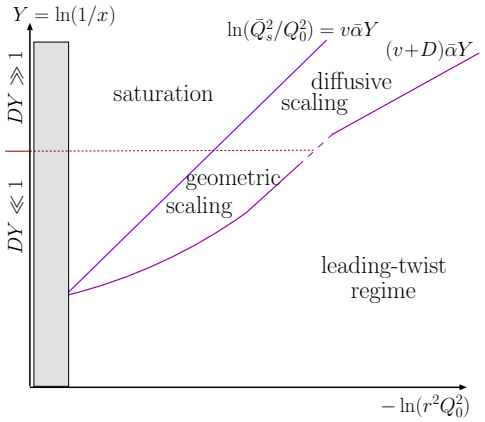

Figure 2: A diagram summarizing the high-energy QCD non-linear evolution. Shown are the average saturation line and the boundaries of the scaling regions at small values of r. With increasing Y, there is a gradual transition from geometric scaling at intermediate energies to diffusive scaling at very high energies.

$$\langle T(r_1) \dots T(r_n) \rangle_Y \overset{Y \ll 1/D}{=} \langle T(r_1) \rangle_Y \dots \langle T(r_n) \rangle_Y \ ,$$
$$\langle T(r_1) \dots T(r_n) \rangle_Y \overset{Y \gg 1/D}{=} \langle T(r_<) \rangle_Y \ , \quad r_< = \min(r_1, \dots, r_n) \ .$$

All the scattering amplitudes are expressed in terms of $\langle T(r) \rangle_Y$, the amplitude for a single dipole which features the following scaling behaviors:

$$\langle T(r) \rangle_Y \overset{Y \ll 1/D}{=} T_{gs}(r, Y) = T\left(r^2 \bar{Q}_s^2(Y)\right) \ , \tag{3}$$
$$\langle T(r) \rangle_Y \overset{Y \gg 1/D}{=} T_{ds}(r, Y) = T\left(\frac{\ln(r^2 \bar{Q}_s^2(Y))}{\sqrt{DY}}\right) \ . \tag{4}$$

In the saturation region $r\bar{Q}_s > 1$, $\langle T(r) \rangle_Y = 1$. As the dipole size r decreases, $\langle T(r) \rangle_Y$ decreases towards the weak-scattering regime following the scaling laws (3) or (4), depending on the value of DY as shown in Fig. 2. In the geometric scaling regime ($DY \ll 1$), the dispersion of the events is negligible and the averaged amplitude obeys (3). In the diffusive scaling regime ($DY \gg 1$), the dispersion of the events is important, resulting in the behavior (4). When Pomeron loops are not included in the evolution, only the geometric scaling regime appears.

4 Phenomenology

In the geometric scaling regime, instead of being a function of the two variables r and x, $T_{gs}(r,Y)$ is a function of the single variable $r\bar{Q}_s(x)$ up to inverse dipole sizes significantly larger than the saturation scale $\bar{Q}_s(x)$. This means that in the geometric scaling window in Fig. 2, $T_{gs}(r,Y)$ is constant along lines parallel to the saturation line. Physically, they are lines along which the dipole sees a constant partonic density inside the proton.

In DIS, this feature manifests itself via the so-called geometric scaling property. Instead of being a function of Q^2 and x separately, the total cross-section is only a function of $\tau = Q^2/\bar{Q}_s^2(x)$, up to large values of τ; similarly, the diffractive cross-section is only a function of $\tau_d = Q^2/\bar{Q}_s^2(x_{\mathbb{P}})$, and β :

$$\begin{aligned} \sigma_{tot}^{\gamma^* p\to X}(x,Q^2) &= \sigma_{tot}^{\gamma^* p\to X}(\tau = Q^2/\bar{Q}_s^2(x)) \ , \\ \sigma_{diff}^{\gamma^* p\to Xp}(\beta, x_{\mathbb{P}}, Q^2) &= \sigma_{diff}^{\gamma^* p\to Xp}(\beta, \tau_d = Q^2/\bar{Q}_s^2(x_{\mathbb{P}})) \ . \end{aligned}$$

Experimental measurements are compatible with those predictions [7], with the parameters $\lambda \simeq 0.25$ and $x_0 \simeq 10^{-4}$ for the average saturation scale $\bar{Q}_s(x) = (x/x_0)^{-\lambda/2}$ GeV. This determines the saturation exponent $v = \lambda/\bar{\alpha}$. HERA probes the geometric scaling regime and one could expect so of future measurements at an electron-ion collider.

The estimates of Section I (where one should now replace Q_s by $\bar{Q}_s$) are obtained in the geometric scaling regime: the total cross-section is dominated by semi-hard sizes ($1/Q < r < 1/\bar{Q}_s$) while the diffractive cross-section is dominated by dipole sizes of the order of the hardest infrared cutoff in the problem: $1/\bar{Q}_s$. In the diffusive scaling regime, up to values of Q much bigger than the average saturation scale $\bar{Q}_s$, things change drastically: both inclusive and diffractive scattering are dominated by small dipole sizes, of order $1/Q$, yet saturation plays a crucial role. Cross-sections are dominated by rare events in which the photon hits a black spot that he sees at saturation at the scale Q^2. In average the scattering is weak ($T_{ds}(r,Y) \ll 1$), but saturation is the relevant physics.

Our poor knowledge of the coefficient D prevents quantitative analysis, still the diffusive scaling regime has striking signatures. For instance the inclusive and diffractive cross-sections do not feature any Pomeron-like (power-law type) increase with the energy. It is likely out of the reach of HERA, and future studies in the context of $p-p$ collisions at the LHC are certainly of interest.

References

[1] Slides:
`http://indico.cern.ch/contributionDisplay.py?contribId=280&sessionId=7&confId=9499`

[2] Y. Hatta, E. Iancu, C. Marquet, G. Soyez and D. Triantafyllopoulos, *Nucl. Phys.* **A773** (2006) 95.

[3] A.H. Mueller, A.I. Shoshi and S.M.H. Wong, *Nucl. Phys.* **B715** (2005) 440;
E. Iancu and D.N. Triantafyllopoulos, *Phys. Lett.* **B610** (2005) 253.

[4] A.H. Mueller and A.I. Shoshi, *Nucl. Phys.* **B692** (2004) 175;
E. Iancu, A.H. Mueller and S. Munier, *Phys. Lett.* **B606** (2005) 342.

[5] E. Brunet, B. Derrida, A.H. Mueller and S. Munier, *Phys. Rev.* **E73** (2006) 056126;
C. Marquet, G. Soyez and B.-W. Xiao, *Phys. Lett.* **B639** (2006) 635.

[6] E. Iancu and D.N. Triantafyllopoulos, *Nucl. Phys.* **A756** (2005) 419;
C. Marquet, R. Peschanski and G. Soyez, *Phys. Rev.* **D73** (2006) 114005.

[7] A.M. Stasto, K. Golec-Biernat and J. Kwiecinski, *Phys. Rev. Lett.* **86** (2001) 596;
C. Marquet and L. Schoeffel, *Phys. Lett.* **B639** (2006) 471.

Exclusive ρ^0 Electroproduction

Aharon Levy[1,2] on behalf of the ZEUS collaboration

1- Raymond and Beverly Sackler Faculty of Exact Sciences, School of Physics and Astronomy, Tel Aviv University, Tel Aviv, Israel

2- DESY, Hamburg, Germany

Exclusive ρ^0 electroproduction at HERA has been studied with the ZEUS detector, using 120 pb^{-1} integrated luminosity, in the kinematic range of photon virtuality of $2 < Q^2 < 160$ GeV^2, and $\gamma^* p$ center-of-mass energy of $32 < W < 180$ GeV. The results include the Q^2 and W dependence of the $\gamma^* p \to \rho^0 p$ cross section and the distribution of the squared-four-momentum transfer to the proton, t. Also included is the ratio of longitudinal to transverse $\gamma^* p$ cross section as a function of Q^2, W and t. Finally, the effective Pomeron trajectory was extracted. The results are compared to various theoretical predictions, none of which are able to reproduce all the features of the data.

Exclusive electroproduction of light vector mesons is a particularly good process for studying the transition from the soft to the hard regime, the former being well described within the Regge phenomenology while the latter - by perturbative QCD. Among the most striking expectations in this transition is the change of the logarithmic derivative δ of the cross section σ with respect to the $\gamma^* p$ center-of-mass energy W, from a value of about 0.2 in the soft regime to 0.8 in the hard one, and the decrease of the exponential slope b of the differential cross section with respect to the squared-four-momentum transfer t, from a value of about 10 GeV^{-2} to an asymptotic value of about 5 GeV^{-2} when the virtuality Q^2 of the photon increases.

In this talk, the latest results of a high statistic measurement of the reaction $\gamma^* p \to \rho^0 p$ studied with the ZEUS detector are presented. A detailed presentation can be found in [1]. Here we present the main results.

The cross section $\sigma(\gamma^* p \to \rho^0 p)$ is presented in Fig. 1 as a function of W, for different values of Q^2. The cross section rises with W in all Q^2 bins. In order to quantify this rise, the logarithmic derivative δ of σ with respect to W is obtained by fitting the data to the expression $\sigma \sim W^\delta$ in each of the Q^2 intervals. The resulting values of δ are shown in Fig 2. Also included in this figure are values of δ from lower Q^2 measurements for the ρ^0 as well as those for ϕ, J/ψ and γ (Deeply Virtual Compton Scattering (DVCS)). In this case the results are plotted as function of $Q^2 + M^2$, where M is the mass of the vector meson. One sees a universal behaviour of the different processes, showing an increase of δ as the scale becomes larger, in agreement with the expectations mentioned above. The value at low scale is the one expected from the soft

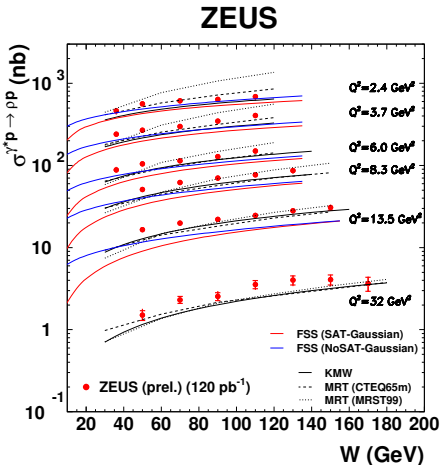

Figure 1: *W dependence of σ for different values of Q^2. The lines are the predictions of some models (see text).*

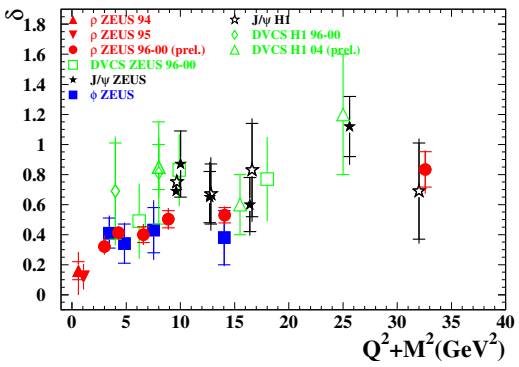

Figure 2: *δ as a function of $Q^2 + M^2$.*

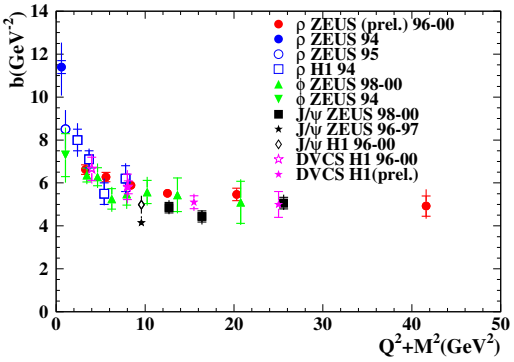

Figure 3: *b as a function of $Q^2 + M^2$.*

Pomeron intercept [2], while the one at large scale is in accordance with twice the logarithmic derivative of the gluon density with respect to W.

The differential cross section, $\mathrm{d}\sigma/\mathrm{d}t$, has been parameterised by an exponential function $e^{-b|t|}$ fitted to the data. The resulting values of b as a function of the scale $Q^2 + M^2$ are plotted in Fig. 3 together with those from other processes. As expected, b decreases to a universal value of about 5 GeV^{-2} as the scale increases. This value measures the radius of the gluon density in the proton and corresponds to a value of ~ 0.6 fm, smaller than the value of the charge density of the proton (~ 0.8 fm), indicating that the gluons are well-contained within the charge-radius of the proton.

One can study the W dependence of $\mathrm{d}\sigma/\mathrm{d}t$ for fixed t values and extract the effective Pomeron trajectory $\alpha_{IP}(t)$. This was done for two Q^2 intervals and the trajectory was fitted to a linear form to obtain the intercept $\alpha_{IP}(0)$ and the slope α'_{IP}, the values of which are tabulated in Table 1. A compilation of the effective Pomeron intercept and slope from this study together with that from other vector mesons is presented in Fig. 4. As in the other compilations, the values are plotted as a function of $Q^2 + M^2$. The value of $\alpha_{IP}(0)$ increases slightly with Q^2 while the value of α'_{IP} shows a small decrease with Q^2.

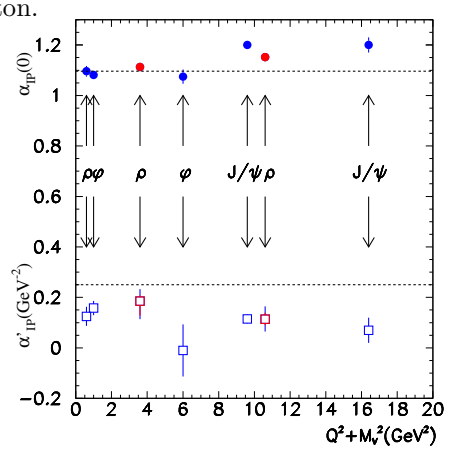

Figure 4: *A compilation of $\alpha_{IP}(0)$ and α'_{IP} for ρ, ϕ and J/ψ, as a function of $Q^2 + M^2$.*

The helicity analysis of the decay-matrix elements of the ρ^0 was used to extract the ratio R of longitudinal to transverse $\gamma^* p$ cross section, as a function of Q^2, W and t. While R is an increasing function of Q^2, as shown in Fig. 5, it is independent of W in all Q^2 intervals (Fig. 6). This unexpected behaviour indicates that the large configurations in the wave function of the transverse γ^* seem to be suppressed. This result is supported by

Q^2 (GeV^2)	$< Q^2 >$ (GeV^2)	$\alpha_{IP}(0)$	α'_{IP}(GeV^{-2}
$2-5$	3	$1.113 \pm 0.010^{+0.009}_{-0.012}$	$0.185 \pm 0.042^{+0.022}_{-0.057}$
$5-50$	10	$1.152 \pm 0.011^{+0.006}_{-0.006}$	$0.114 \pm 0.043^{+0.026}_{-0.024}$

Table 1: *The values of the Pomeron trajectory intercept $\alpha_{IP}(0)$ and slope α'_{IP}, for different Q^2 intervals.*

the independence of R on t (not shown), indicating that both polarisations of the photon fluctuate into similar size $q\bar{q}$ pairs.

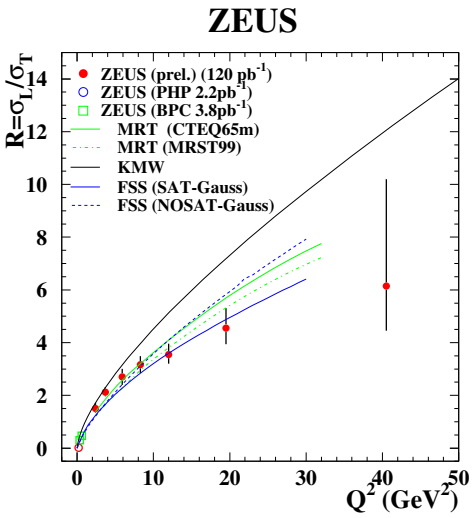

Figure 5: *R as a function of Q^2 at W=90 GeV. The lines are the prediction of models referred to in the text.*

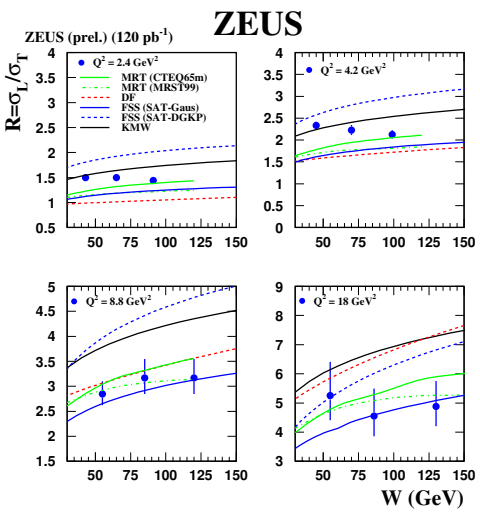

Figure 6: *The ratio R as a function of W for different Q^2 intervals. The lines are the prediction of models referred to in the text.*

The results of this study were compared to those of the H1 collaboration [3] and both measurements are in good agreement.

The results were also compared to several theoretical predictions. The predictions are a combination of perturbative and non-perturbative QCD calculations. All models use the dipole picture to describe the reaction $\gamma^* p \to \rho^0 p$. The ingredients necessary for the calculation are the virtual photon and the ρ^0 wave function and the gluon densities. Some models put their emphasis on the VM wave function [4, 5, 6, 7] while that of [8] studies the dependence on the gluon densities in the proton. Detailed comparison can be seen in [1]. Some examples are shown in Fig. 1, where the cross section values are plotted as a function of W for different Q^2 vales, in Fig. 5, where the ratio R is shown as a function of Q^2 and in Fig. 6, where R is plotted as a function of W, for different Q^2 intervals. As can be seen, none of the calculations can describe the data. The high precision of the present measurements can be most valuable to tune the different models and thus contribute to a better understanding of the ρ^0 wave function and of the gluon density in the proton.

Acknowledgments

It is a pleasure to acknowledge and thank Allen Caldwell and his local organizing committee for a superb organization of this workshop. This work was partly supported by the Israel Science Foundation (ISF).

References

[1] Slides: A. Levy, on behalf of the ZEUS Collaboration, *Exclusive ρ^0 electroproduction*, `http://indico.cern.ch/contributionDisplay.py?contribId=74&sessionId=7&confId=9499`

[2] A. Donnachie and P.L. Landshoff, *Total cross-sections*, Phys. Lett. **B 296**, 227 (1992).

[3] H1 Coll., C. Adloff et al., *Elastic electroproduction of ρ mesons at HERA*, Eur.Phys.J. **C 13**, 371 (2000).

[4] L. Frankfurt, W. Koepf and M. Strikman, *Diffractive heavy quarkonium photoproduction and electroproduction in QCD*, Phys. Rev. **D 57**, 512 (1998);
L. Frankfurt, W. Koepf and M. Strikman, *Hard diffractive electroproduction of vector mesons in QCD*, Phys. Rev. **D 54**, 3194 (1996).

[5] J.R. Forshaw, R. Sandapen and G. Shaw, *Color dipoles and ρ, ϕ electroproduction*, Phys. Rev **D 69**, 094013 (2004).

[6] H. Kowalski, L. Motyka and G. Watt, *Exclusive diffractive processes at HERA within the dipole picture*, Phys. Rev. **D 74**, 074016 (2006).

[7] H.G. Dosch and E. Ferreira, *Nonperturbative and perturbative aspects of photo- and electroproduction of vector mesons*, hep-ph/0610311 (2006).

[8] A.D. Martin, M.G. Ryskin and T. Teubner, *Q^2 dependence of diffractive vector meson electroproduction*, Phys. Rev. **D 62**, 014022 (2000).

Non-Forward Balitsky-Kovchegov Equation and Vector Mesons

Robi Peschanski[1], Cyrille Marquet[2] and Gregory Soyez[3]

1- Service de Physique Théorique - CEA/Saclay, 91191 Gif-sur-Yvette Cedex, FRANCE
2- RIKEN BNL Research Center, Brookhaven National Laboratory, Upton, NY 11973, USA
3- Physics Department, Brookhaven National Laboratory, Upton, NY 11973, USA

Considering the Balitsky-Kovchegov QCD evolution equation in full momentum space, we derive the travelling wave solutions expressing the nonlinear saturation constraints on the dipole scattering amplitude at non-zero momentum transfer. A phenomenological application to elastic vector meson production shows the compatibility of data with the QCD prediction: an *enhanced* saturation scale at intermediate momentum transfer.

1 Motivation

The saturation of parton densities at high energy has been mainly studied for the forward dipole-target scattering amplitude $\mathcal{T}(r, q = 0, Y)$, where r, q, Y are, respectively, the dipole size, the momentum transfer and the total rapidity of the process. For instance, the corresponding QCD Balitsky-Kovchegov (BK) equation [2] has been shown to provide a theoretical insight on the "geometric scaling" properties [3] of the related γ^*-proton cross-sections. Indeed, it can be related to the existence of a scaling for $\mathcal{T}(r, q = 0, Y) \sim \mathcal{T}(r^2 Q^2(Y))$ where the saturation scale is $Q^2(Y) \sim \exp cY$ and the constant c can be interpreted as the critical speed of "travelling wave" solutions of the nonlinear BK equation [4]. Our theoretical and phenomenological subjects are the extension of these properties to the non-forward amplitude $\mathcal{T}(r, q \neq 0, Y)$, which is phenomenologically relevant for the elastic production of vector mesons in deep inelastic scattering.

2 BK equation in full momentum space

In order to study the properties of $\mathcal{T}(r, q \neq 0, Y)$, one has first to deal with both conceptual and technical difficulties. It is known that the BK formalism has been originally derived in impact parameter b but then its validity especially at large b is questionable, since it leads to non physical power-law tails. Hence we start with the formulation of the BK equation in momentum q, which is more *local* but has a non-trivial nonlinear form [5]. In fact, despite this problem, the general method of travelling wave solutions can be extended in the non-forward domain [6]. It consists in 3 steps: first, one solves the equation restricted to its linear part which is related to the non-forward Balitsky Fadin Kuraev Lipatov (BFKL) equation

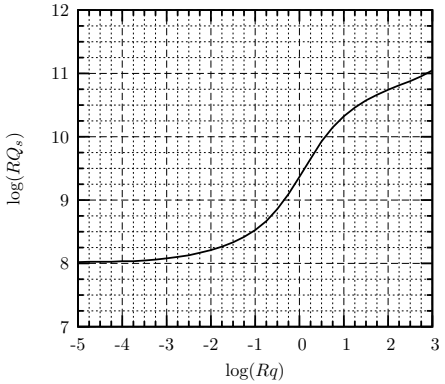

Figure 1: q^2-dependent saturation scale

[7] for the dipole-dipole amplitude *via* factorisation and whose solution takes the form of a linear superposition of waves. Second, one finds that the nonlinearities act by selecting the travelling wave with *critical* speed c, in a way which, interestingly, is independent of the specific structure of the nonlinear damping terms. Third, one obtains after enough rapidity evolution, a solution which appears independent from initial conditions ($\mathcal{T}_0 \sim r^{2\gamma_0}$) , provided these are sharper than the critical travelling wave front profile $\mathcal{T} \sim r^{2\gamma_c}$, with $\gamma_0 > \gamma_c$. Interestingly enough, QCD color transparency satisfies this criterium. Applying these gen-

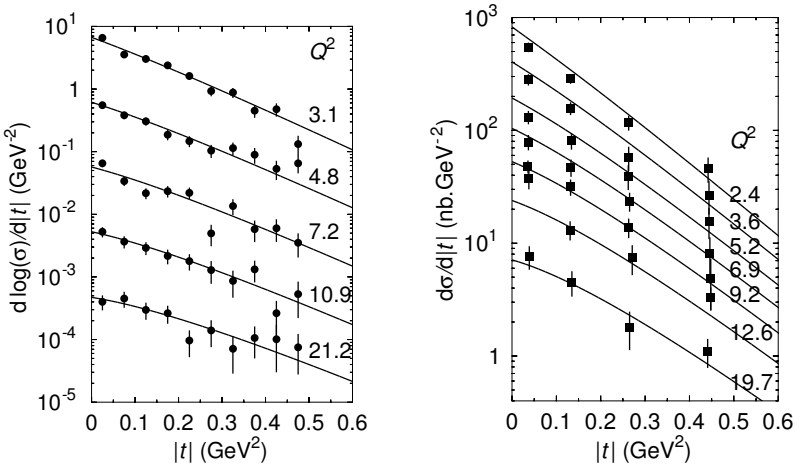

Figure 2: ρ (H1) and ϕ (ZEUS) differential cross-sections at $W = 75$ GeV

eral results on the non-forward case one finds the following QCD predictions, depending on the relative magnitude of three scales involved in the process, namely q, k_T^{-1} (the target size) and $k_P^{-1} \equiv r$ (the projectile *i.e.* dipole size).

- Near-Forward region $q \ll k_T \ll k_P$: $Q_s^2(Y) \sim k_T^2 \exp cY$
- Intermediate transfer region $k_T \ll q \ll k_P$: $Q_s^2(Y) \sim q^2 \exp cY$
- High transfer region $q \ll k_T \ll k_P$: No saturation.

Our main prediction is thus the validity of the forward travelling wave solution extended in the non-forward intermediate-transfer domain but with an *enhanced* saturation scale by the ratio q^2/k_T^2, where k_T is a typically small, nonperturbative scale. Hence we are led to predict *geometric scaling* properties with a purely perturbative initial saturation scale given by the transverse momentum. This saturation scale *enhancement* prediction is confirmed by numerical simulations of the BK solutions as shown in Fig.1.

3 QCD Saturation Model for Exclusive VM production

The differential cross-section for exclusive vector meson (VM) production at HERA, see Fig.2, can be theoretically obtained from the non-forward dipole-proton amplitude and from $\Phi_{T,L}^{\gamma^* V}$, the overlap functions between the (longitudinal and transverse) virtual photon and vector meson wave-functions [8]. For completion, we used two different VM wave-functions

of the literature, without noticeable difference in our conclusions. One writes

$$\frac{d\sigma_{T,L}^{\gamma^* p\to Vp}}{dq^2} \;=\; \frac{1}{16\pi}\left|\int d^2r\int_0^1 dz\;\Phi_{T,L}^{\gamma^* V}(z,r;Q^2,M_V^2)\;e^{-izq\cdot r}\;\mathcal{T}(r,q,Y)\right|^2 \;,$$

Following theoretical prescriptions, we consider a forward dipole-proton amplitude $\mathcal{N}_{IIM}$ satisfactorily describing the total DIS cross-sections in a saturation model [9]. We just make the saturation scale varying with q^2, following the trend shown in Fig.1 and starting from the forward model one $Q_s^2(Y)$, one writes

$$T(r,q;Y) = 2\pi R_p^2\;e^{-Bq^2}\mathcal{N}_{IIM}(r^2\;Q_s^2(Y,q))\;;\;Q_s^2(q,Y) = Q_s^2(Y)\;(1+c\;q^2)\;.$$

Cross-sections	q^2-Sat.	fixed-Sat.
$\rho,\ \sigma_{\rm el}$	1.156	1.732
$\rho,\ \frac{d\sigma}{dt}$	1.382	1.489
$\phi,\ \sigma_{\rm el}$	1.322	2.247
$\phi,\ \frac{d\sigma}{dt}$	1.076	0.931
Total	1.212	1.480

Table 1: Comparison of the χ^2/points

The factor $2\pi R_p^2\;e^{-Bq^2}$ comes from the non-perturbative proton form factor. For clarity of the analysis, we considered only B and c as free parameters of the non-forward parametrisations, the others being independently fixed by the forward analysis.

In Table 1, one displays the χ^2/point obtained by a fit of ρ (47 data points) and ϕ (34 points) total elastic production cross-sections and of ρ (50 data points) and ϕ (70 points) differential cross-sections. The Table compares the saturation fits for fixed and q^2-dependent scales, with a favour for the enhanced-scale model in the total. The model gives a comparable fit with a more conventional non-saturation model using a Q^2-dependent slope $B \propto M_V^2 + Q^2$. Some of our results for the cross-sections are displayed in the figures. In Fig.2, one shows the results of the fit for ρ-production (H1) and ϕ-production (ZEUS) differential cross-sections for a total $\gamma^* - p$ energy $W =$ 75GeV and different Q^2 values. Let us finally present our predictions for the

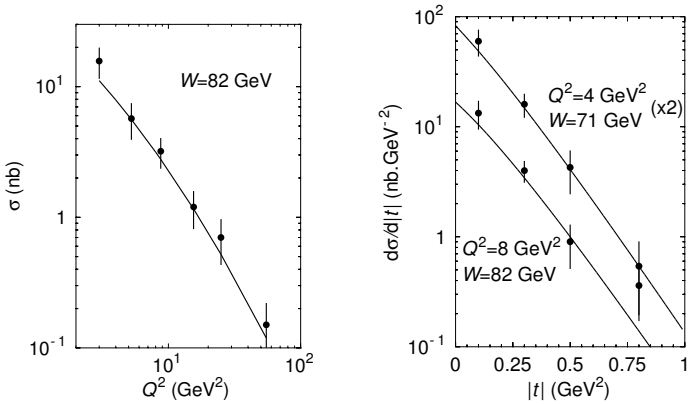

Figure 3: Predictions for the DVCS measurements. Left plot: cross-section, right plot: differential cross-section.

DVCS cross-section, which is obtained without any free parameter from our analysis. In

Fig.3, they are compared with the available data and the agreement is good in the simple chosen parametrisation.

4 Conclusions

Let us summarize our new results

• *Saturation at non-zero transfer:* The Balitsky-Kovchegov QCD evolution equation involving full momentum transfer predicts (besides the known $q = 0$ case) saturation in the *intermediate* transfer range, namely for $Q_0 < q < Q$, where Q_0 (resp. Q) is the target (resp. projectile) typical scale.

• *Characterisation of the universality class:* The universality class of the corresponding travelling-wave solutions is governed by a purely perturbative saturation scale $Q_s(Y) \equiv q^2\Omega(Y)$, where $\Omega(Y) \sim e^{cY}$ is the same rapidity evolution factor as in the forward case. Consequently the *intermediate transfer* saturation scale gets enhanced by a factor q^2/Q_0^2.

• *Phenomenology of Vector mesons:* The QCD predictions are applied in the experimentally accessible *intermediate transfer* range of vector meson production. The model uses an interpolation between the forward and non-forward saturation scale together with a parameter-frozen forward saturation model. It fits better the data on ρ (H1) and ϕ (ZEUS) cross-sections than for a non-enhanced saturation.

• *Prospects:* The next phenomenological prospect is to add charm to the discussion, both with the modification of the forward case by including the charm contribution [10] and by also considering the production of Ψ mesons. On a theoretical ground, it would be interesting to go beyond the mean-field approximation of the BK equation.

References

[1] Slides:
`http://indico.cern.ch/contributionDisplay.py?contribId=75&sessionId=7&confId=9499`

[2] I. Balitsky, *Nucl. Phys.* **B463** (1996) 99; *Phys. Lett.* **B518** (2001) 235;
Yu.V. Kovchegov, *Phys. Rev.* **D60** (1999) 034008; *Phys. Rev.* **D61** (2000) 074018.

[3] A.M. Stasto, K. Golec-Biernat and J. Kwiecinski, *Phys. Rev. Lett.* **86** (2001) 596;
C. Marquet and L. Schoeffel, *Phys. Lett.* **B639** (2006) 471.

[4] S. Munier and R. Peschanski, *Phys. Rev. Lett.* **91** (2003) 232001; *Phys. Rev.* **D69** (2004) 034008; **D70** (2004) 077503.

[5] C. Marquet and G. Soyez, *Nucl. Phys.* **A760** (2005) 208.

[6] C. Marquet, R. Peschanski and G. Soyez, *Nucl. Phys.* **A756** (2005) 399.

[7] L. N. Lipatov, Sov. Phys. JETP **63**, 904 (1986) [Zh. Eksp. Teor. Fiz. **90**, 1536 (1986)].

[8] C. Marquet, R. Peschanski and G. Soyez, *Exclusive vector meson production at HERA from QCD with saturation*, hep-ph/0702171.

[9] E. Iancu, K. Itakura and S. Munier, *Phys. Lett.* **B590** (2004) 199.

[10] K. Golec-Biernat and S. Sapeta, *Phys. Rev.* **D74** (2006) 054032;
H. Kowalski, L. Motyka and G. Watt, *Phys. Rev.* **D74** (2006) 074016;
G. Soyez, *Saturation QCD predictions with heavy quarks at HERA*, arXiv.0705.3672.

Vector Meson Production from NLL BFKL

Dmitry Yu. Ivanov[1] and Alessandro Papa[2]

1- Sobolev Institute of Mathematics
630090 Novosibirsk - Russia

2- Dipartimento di Fisica, Università della Calabria
and INFN - Gruppo Collegato di Cosenza
I-87036 Rende - Italy

The amplitude for the forward electroproduction of two light vector mesons can be written completely within perturbative QCD in the Regge limit with next-to-leading accuracy, thus providing the first example of a physical application of the BFKL approach at the next-to-leading order. We study in the case of equal photon virtualities the main systematic effects, by considering a different representation of the amplitude and different optimization methods of the perturbative series.

1 Introduction

In the BFKL approach [2], both in the leading logarithmic approximation (LLA), which means resummation of all terms $(\alpha_s \ln(s))^n$, and in the next-to-leading approximation (NLA), which means resummation of all terms $\alpha_s(\alpha_s \ln(s))^n$, the amplitude for a large-s hard collision process can be written as the convolution of the Green's function of two interacting Reggeized gluons with the impact factors of the colliding particles.

The Green's function is determined through the BFKL equation. The kernel of the BFKL equation is known now both in the forward [3] and in the non-forward [4] cases. On the other side, impact factors are known with NLA accuracy in a few cases: colliding partons [5], forward jet production [6] and forward transition from a virtual photon γ^* to a light neutral vector meson $V = \rho^0, \omega, \phi$ [7]. The most important impact factor for phenomenology, the $\gamma^* \to \gamma^*$ impact factor, is calling for a rather long calculation, which seems to be close to completion now [8, 9].

The $\gamma^* \to V$ forward impact factor can be used together with the NLA BFKL forward Green's function to build, completely within perturbative QCD and with NLA accuracy, the amplitude of the $\gamma^*\gamma^* \to VV$ reaction. This amplitude provides us with an ideal theoretical laboratory for the investigation of several open questions in the BFKL approach. Besides, this process can be studied experimentally at the future at ILC, see Refs. [10].

2 Representations of the NLA amplitude

The process under consideration is the production of two light vector mesons ($V = \rho^0, \omega, \phi$) in the collision of two virtual photons, $\gamma^*(p)\,\gamma^*(p') \to V(p_1)\,V(p_2)$. Here, neglecting the meson mass m_V, p_1 and p_2 are taken as Sudakov vectors satisfying $p_1^2 = p_2^2 = 0$ and $2(p_1p_2) = s$; the virtual photon momenta are instead $p = \alpha p_1 - Q_1^2/(\alpha s)p_2$ and $p' = \alpha' p_2 - Q_2^2/(\alpha' s)p_1$, so that the photon virtualities turn to be $p^2 = -Q_1^2$ and $(p')^2 = -Q_2^2$. We consider the kinematics when $s \gg Q_{1,2}^2 \gg \Lambda_{QCD}^2$ and $\alpha = 1 + Q_2^2/s + \mathcal{O}(s^{-2})$, $\alpha' = 1 + Q_1^2/s + \mathcal{O}(s^{-2})$. In this case vector mesons are produced by longitudinally polarized photons in the longitudinally polarized state [7]. Other helicity amplitudes are power suppressed, with a suppression factor $\sim m_V/Q_{1,2}$. We will discuss here the amplitude of the forward

scattering, i.e. when the transverse momenta of produced V mesons are zero or when the variable $t = (p_1 - p)^2$ takes its maximal value $t_0 = -Q_1^2 Q_2^2/s + \mathcal{O}(s^{-2})$.

The NLA forward amplitude can be written as a spectral decomposition on the basis of eigenfunctions of the LLA BFKL kernel:

$$\frac{\mathrm{Im}_s\left(\mathcal{A}_{exp}\right)}{D_1 D_2} = \frac{s}{(2\pi)^2} \int\limits_{-\infty}^{+\infty} d\nu \left(\frac{s}{s_0}\right)^{\bar{\alpha}_s(\mu_R)\chi(\nu) + \bar{\alpha}_s^2(\mu_R)\left(\bar{\chi}(\nu) + \frac{\beta_0}{8N_c}\chi(\nu)\left[-\chi(\nu) + \frac{10}{3}\right]\right)} \alpha_s^2(\mu_R) c_1(\nu) c_2(\nu)$$

$$\times \left[1 + \bar{\alpha}_s(\mu_R)\left(\frac{c_1^{(1)}(\nu)}{c_1(\nu)} + \frac{c_2^{(1)}(\nu)}{c_2(\nu)}\right) + \bar{\alpha}_s^2(\mu_R) \ln\left(\frac{s}{s_0}\right) \frac{\beta_0}{8N_c}\chi(\nu)\left(i\frac{d\ln(\frac{c_1(\nu)}{c_2(\nu)})}{d\nu} + 2\ln(\mu_R^2)\right)\right]. \tag{1}$$

Here the bulk of NLA kernel corrections are exponentiated, $\bar{\alpha}_s = \alpha_s N_c/\pi$ and $D_{1,2} = -4\pi e_q f_V/(N_c Q_{1,2})$, where f_V is the meson dimensional coupling constant ($f_\rho \approx 200\,\mathrm{MeV}$) and e_q should be replaced by $e/\sqrt{2}$, $e/(3\sqrt{2})$ and $-e/3$ for the case of ρ^0, ω and ϕ meson production, respectively. Two scales enter the expression (1), the renormalization scale μ_R and the scale for energy s_0.

Alternatively, the amplitude can be expressed as a series:

$$\begin{aligned} \frac{Q_1 Q_2}{D_1 D_2}\frac{\mathrm{Im}_s(\mathcal{A}_{series})}{s} &= \frac{1}{(2\pi)^2}\alpha_s(\mu_R)^2 \\ &\times \left[b_0 + \sum_{n=1}^{\infty} \bar{\alpha}_s(\mu_R)^n\, b_n \left(\ln\left(\frac{s}{s_0}\right)^n + d_n(s_0,\mu_R)\ln\left(\frac{s}{s_0}\right)^{n-1}\right)\right]. \end{aligned} \tag{2}$$

The b_n coefficients are determined by the kernel and the impact factors in LLA, while the d_n coefficients depend also on the NLA corrections to the kernel and to the impact factors. We refer to Ref. [11] for the details of the derivation and for the definition of the functions entering these expressions.

3 Numerical results

In Ref. [11] we presented some numerical results for the amplitude given in Eq. (2) for the $Q_1 = Q_2 \equiv Q$ kinematics, i.e. in the "pure" BFKL regime. We found that the d_n coefficients are negative and increasingly large in absolute values as the perturbative order increases, making evident the need of an optimization of the perturbative series. We adopted the principle of minimal sensitivity (PMS) [12], by requiring the minimal sensitivity of the predictions to the change of both the renormalization and the energy scales, μ_R and s_0. We considered the amplitude for Q^2=24 GeV^2 and $n_f = 5$ and studied its sensitivity to variation of the parameters μ_R and $Y_0 = \ln(s_0/Q^2)$. We could see that for each value of $Y = \ln(s/Q^2)$ there are quite large regions in μ_R and Y_0 where the amplitude is practically independent on μ_R and Y_0 and we got for the amplitude a smooth behaviour in Y (see the curve labeled "series - PMS" in Figs. 1 and 2). The optimal values turned out to be $\mu_R \simeq 10Q$ and $Y_0 \simeq 2$, quite far from the kinematical values $\mu_R = Q$ and $Y_0 = 0$. These "unnatural" values probably mimic large unknown NNLA corrections.

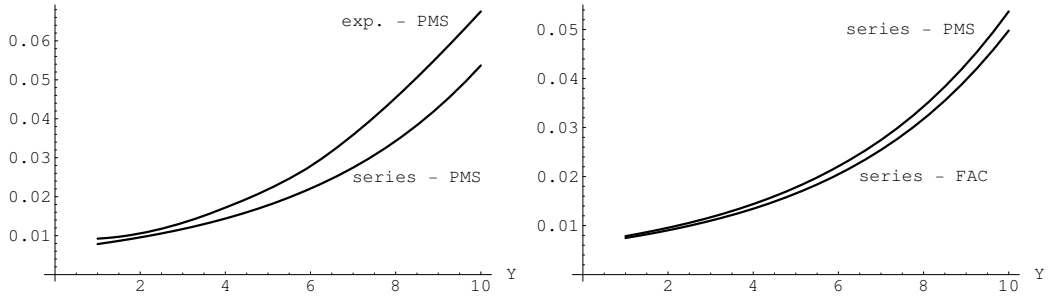

Figure 1: $\mathrm{Im}_s(\mathcal{A})Q^2/(s\,D_1 D_2)$ as a function of Y at Q^2=24 GeV^2 ($n_f = 5$): (left) series representation with PMS and "exponentiated" representation with PMS, (right) series representation with PMS and with FAC.

As an estimation of the systematic effects in our determination, we considered also the "exponentiated" representation of the amplitude, Eq. (1), and different optimization methods. For more details on the following, see Ref. [13].

At first, we compare the series and the "exponentiated" determinations using in both case the PMS method. The optimal values of μ_R and Y_0 for the "exponentiated" amplitude are quite similar to those obtained in the case of the series representation, with only a slight decrease of the optimal μ_R. Fig. 1 (left) shows that the two determinations are in good agreement at the lower energies, but deviate increasingly for large values of Y. It should be stressed, however, that the applicability domain of the BFKL approach is determined by the condition $\bar{\alpha}_s(\mu_R)Y \sim 1$ and, for Q^2=24 GeV^2 and for the typical optimal values of μ_R, one gets from this condition $Y \sim 5$. Around this value the discrepancy between the two determinations is within a few percent.

As a second check, we changed the optimization method and applied it both to the series and to the "exponentiated" representation. The method considered is the fast apparent convergence (FAC) method [14], whose strategy, when applied to a usual perturbative expansion, is to fix the renormalization scale to the value for which the highest order correction term is exactly zero. In our case, the application of the FAC method requires an adaptation, for two reasons: the first is that we have two energy parameters in the game, μ_R and Y_0, the second is that, if only strict NLA corrections are taken, the amplitude does not depend at all on these parameters. For details about the application of this method, we refer to [13]. Here, we merely show the results: the FAC method applied to the series representation (see Fig. 1 (right)) and to the exponentiated representation (see Fig. 2 (left)) gives results in nice agreement with those from the PMS method applied to the series representation, over the whole energy range considered.

Another popular optimization method is the Brodsky-Lepage-Mackenzie (BLM) one [15], which amounts to perform a finite renormalization to a physical scheme and then to choose the renormalization scale in order to remove the β_0-dependent part. We applied this method only to the series representation, Eq. (2). The result is compared with the PMS method in Fig. 2 (right) (for details, see Ref. [13]).

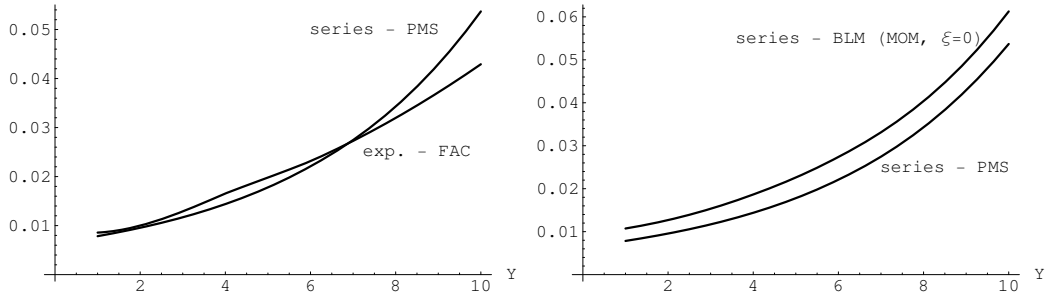

Figure 2: $\mathrm{Im}_s(\mathcal{A})Q^2/(s\,D_1 D_2)$ as a function of Y at Q^2=24 GeV^2 ($n_f = 5$): (left) series representation with PMS and "exponentiated" representation with FAC, (right) series representation with PMS and with BLM.

Acknowledgments

The work of D.I. was partially supported by grants RFBR-05-02-16211, NSh-5362.2006.2.

References

[1] Slides:
`http://indico.cern.ch/contributionDisplay.py?contribId=76&sessionId=7&confId=9499`

[2] V.S. Fadin, E.A. Kuraev, L.N. Lipatov, Phys. Lett. **B60** 50 (1975); E.A. Kuraev, L.N. Lipatov and V.S. Fadin, Zh. Eksp. Teor. Fiz. **71** 840 (1976) [Sov. Phys. JETP **44** 443 (1976)]; **72** 377 (1977) [**45** 199 (1977)]; Ya.Ya. Balitskii and L.N. Lipatov, Sov. J. Nucl. Phys. **28** 822 (1978).

[3] V.S. Fadin and L.N. Lipatov, Phys. Lett. **B429** 127 (1998); M. Ciafaloni and G. Camici, Phys. Lett. **B430** 349 (1998).

[4] V.S. Fadin and R. Fiore, Phys. Lett. **B610** 61 (2005) [*Erratum-ibid.* **B621** 61 (2005)]; Phys. Rev. **D72** 014018 (2005).

[5] V.S. Fadin, R. Fiore, M.I. Kotsky and A. Papa, Phys. Rev. **D61** 094005 (2000); Phys. Rev. **D61** 094006 (2000); M. Ciafaloni and G. Rodrigo, JHEP **0005** 042 (2000).

[6] J. Bartels, D. Colferai and G.P. Vacca, Eur. Phys. J. **C24** 83 (2002); Eur. Phys. J. **C29** 235 (2003).

[7] D.Yu. Ivanov, M.I. Kotsky and A. Papa, Eur. Phys. J. **C38** 195 (2004); Nucl. Phys. (Proc. Suppl.) **146** 117 (2005).

[8] J. Bartels, S. Gieseke and C.F. Qiao, Phys. Rev. **D63** 056014 (2001)[*Erratum-ibid.* **D65** 079902 (2002)]; J. Bartels, S. Gieseke and A. Kyrieleis, Phys. Rev. **D65** 014006 (2002); J. Bartels, D. Colferai, S. Gieseke and A. Kyrieleis, Phys. Rev. **D66** 094017 (2002); J. Bartels, Nucl. Phys. (Proc. Suppl.) 116 (2003); J. Bartels and A. Kyrieleis, Phys. Rev. **D70** 114003 (2004); V.S. Fadin, D.Yu. Ivanov and M.I. Kotsky, Phys. Atom. Nucl. **65** 1513 (2002) [Yad. Fiz. **65** 1551 (2002)]; V.S. Fadin, D.Yu. Ivanov and M.I. Kotsky, Nucl. Phys. **B658** 156 (2003).

[9] G. Chachamis and J. Bartels, "NLO Photon Impact Factor: Present Status and Outlook", PoS(DIFF2006)026.

[10] R. Enberg, B. Pire, L. Szymanowski and S. Wallon, Eur. Phys. J. **C45** 759 (2006); M. Segond, L. Szymanowski and S. Wallon, arXiv:hep-ph/0703166 (2007).

[11] D.Yu. Ivanov and A. Papa, Nucl. Phys. B **732** 183 (2006).

[12] P.M. Stevenson, Phys. Lett. **B100** 61 (1981); Phys. Rev. **D23** 2916 (1981).

[13] D.Yu. Ivanov and A. Papa, Eur. Phys. J. C **49** 947 (2007).

[14] G. Grunberg, Phys. Lett. **B95** 70 (1980) [*Erratum-ibid.* **B110** 501 (1982)]; *ibid.* **B114** 271 (1982); Phys. Rev. **D29** 2315 (1984).

[15] S.J. Brodsky, G.P. Lepage, P.B. Mackenzie, Phys. Rev. **D28** 228 (1983).

Electroproduction of Longitudinally Polarized Vector Mesons

Peter Kroll *

Universität Wuppertal, Fachbereich Physik
D-42097 Wuppertal, Germany

It is reported on an analysis of electroproduction of light vector mesons at small Bjorken-x ($x_{\rm Bj}$) within the handbag approach. The partonic subprocesses, meson electroproduction off quarks or gluons, are calculated within the modified perturbative approach (m.p.a.) in which quark transverse momenta are retained. The soft hadronic matrix elements, generalized parton distributions (GPDs), are constructed from the CTEQ6 parton distribution functions (PDFs) by means of double distributions. The cross sections for longitudinal polarized virtual photons evaluated from this approach, are in very good agreement with experiment in a wide range of kinematics.

It has been shown [1] that, at large photon virtuality Q^2, meson electroproduction factorizes in partonic subprocesses, electroproduction off gluons or quarks, $\gamma^* g(q) \to M g(q)$, and GPDs, representing soft proton matrix elements. It has also been shown that the dominant amplitude is that for transitions from longitudinally polarized virtual photons (γ^*_L) to like-wise polarized vector mesons (V_L). Other transitions are suppressed by inverse powers of Q^2. In the following it is reported on an analysis [2] of the process $\gamma^*_L p \to V_L p$, within this handbag factorization scheme carried through in the kinematical regime of low $x_{\rm Bj}$ ($\lesssim 0.2$).

The mentioned two partonic subprocesses lead to the following contributions to the amplitude $\mathcal{M}_V$ for the process $\gamma^*_L p \to V_L p$: ($x_g = 0, x_q = -1$)

$$\mathcal{M}_V^{g(q)} \;=\; e \sum_a e_a \mathcal{C}_V^a \int_{x_{g(q)}}^1 dx\, \mathcal{H}_V^{g(q)}(x,\xi,Q^2,t=0)\, H^{g(a)}(x,\xi,t)\,, \qquad (1)$$

which are to be summed coherently. The sum in (1) runs over all quark flavors while e_a denotes the corresponding quark charges in units of the positron charge e. For ρ and ϕ production the non-zero flavor weight factors $\mathcal{C}_V^a$ read $\mathcal{C}_\rho^u = -\mathcal{C}_\rho^d = 1/\sqrt{2}$ and $\mathcal{C}_\phi^s = 1$, respectively. The amplitude (1) refers to proton helicity non-flip, the flip amplitude is neglected because our interest lies in small $-t$. The functions $H^{g(a)}$ represent GPDs for gluons and quarks. They are functions of three variables - t, a momentum fraction x and skewness ξ. The latter one is kinematically fixed by $\xi \simeq x_{\rm Bj}/(2 - x_{\rm Bj})[1 + m_V^2/Q^2]$ in a small $x_{\rm Bj}$ approximation (m_V being the mass of the vector meson). To vector meson electroproduction the GPD $\widetilde{H}$ and $\widetilde{E}$ do not contribute while E can be ignored in the region of small $x_{\rm Bj}$ since it contributes $\propto \xi^2$ to the proton helicity non-flip amplitude. Thus, only the GPD H is required. In (1) only its t-dependence is considered. That of the subprocess amplitude $\mathcal{H}_V$ provides power corrections of order t/Q^2 which are neglected. In the GPDs t is scaled by a soft parameter, actually the slope of the diffraction peak.

The GPDs are constructed with the help of double distributions [3]. The chief advantage of this construction is the guaranteed polynomiality of the GPDs and the correct forward limit $\xi, t \to 0$. As is well-known at low x the PDFs behave as powers δ_i of x. These powers are determined by the intercepts of appropriate Regge trajectories. The Regge behaviour

*The author thanks Markus Diehl for presenting this talk at the DIS07 conference.

of the PDFs is transferred to the GPDs at $t = 0$ by means of the double distribution construction. It seems plausible to generate the t-dependence of the GPDs by Regge ideas, too. Assuming linear Regge trajectories $\alpha_i(t) = \alpha_i(0) + \alpha_i' t$ (i = g, sea, valence) and exponential t-dependencies of the Regge residues, one may employ the following ansatz for the double distribution ($n_g = n_{\rm sea} = 2$, $n_{\rm val} = 1$)

$$f_i(\beta,\eta,t) \,=\, {\rm e}^{b_i t}\,|\beta|^{-\alpha_i' t}\,h_i(\beta)\,\frac{\Gamma(2n_i+2)}{2^{2n_i+1}\Gamma^2(n_i+1)}\,\frac{[(1-|\beta|)^2-\eta^2]^{n_i}}{(1-|\beta|)^{2n_i+1}}\,,$$

where the function h_i represents a PDF suitably continued to negative values of x. The GPDs are then obtained by an integral over f_i

$$H^i(x,\xi,t) \,=\, \int_{-1}^{1} d\beta \int_{-1+|\beta|}^{1-|\beta|} d\eta\,\delta(\beta+\xi\eta-x)\,f_i(\beta,\eta,t)\,.$$

In Ref. [2] the Regge parameters are fixed in the following way: The integrated cross section $\sigma_L \sim \int dt |\mathcal{M}_V|^2$ behaves $\propto W^{\delta_g(Q^2)}$ at fixed Q^2 and small $x_{\rm Bj}$. Thus, δ_g can be fixed from the HERA data [4, 5, 6]. A fit provides $\delta_g = 0.10 + 0.06\ln(Q^2/4\,{\rm GeV}^2)$. For the slope of the gluon trajectory the value $\alpha_g' = 0.15\,{\rm GeV}^{-2}$ is taken. Since the sea quarks mix with the gluons under evolution, $\alpha_{\rm sea}(t) = \alpha_g(t)$ is assumed. For the valence quarks, on the other hand, a standard Regge trajectory is taken - $\alpha_{\rm val} = 0.48 + 0.90\,{\rm GeV}^{-2} t$. The slope parameter of the gluon and sea quark Regge residue is obtained from a fit to the HERA data on the differential cross section [4, 6]: $b_g \,=\, b_{\rm sea} \,=\, 2.58\,{\rm GeV}^{-2} + 0.25\,{\rm GeV}^{-2}\,\ln[m^2/(Q^2+m^2)]$ (m being the proton's mass). In the zero skewness limit the valence quark GPDs read

$$H^q_{\rm val}(x,\xi=0,t=0) \,=\, {\rm e}^{b_{\rm val} t}\,q_{\rm val}(x)\,.$$

This is very close to the ansatz advocated for in Ref. [7] in order to extract the zero-skewness GPDs from the nucleon form factor data. The comparison with that analysis reveals that one may choose $b_{\rm val} = 0$.

Working out the subprocess amplitudes from the relevant Feynman graphs in collinear approximation and to LO, one arrives at the following amplitude for ρ production

$$\mathcal{M}_\rho \,=\, e\frac{8\pi\alpha_s}{N_c Q} f_\rho\,\langle 1/\tau\rangle_\rho\,\frac{1}{\sqrt{2}}\,\Big\{\frac{1}{2\xi} I_g + \kappa_s C_F I_{\rm sea} + \frac{1}{3} C_F I^u_{\rm val} + \frac{1}{6} C_F I^d_{\rm val}\Big\}\,. \qquad (2)$$

The integral I_g reads

$$I_g = 2\int_0^1 dx \frac{\xi H^g(x,\xi,t)}{(x+\xi)(x-\xi+i\epsilon)}\,.$$

Analogous expressions hold for the other two integrals. For ϕ production the decay constant f_ρ and the $1/\tau$ moment of the ρ distribution amplitude are to be replaced by the corresponding quantities for the ϕ meson. The charge factor $1/\sqrt{2}$ is to be replaced by $-1/3$ and there is no valence quark contribution. For simplicity it is assumed that the u and d sea quark GPDs are proportional to that of the strange quark. The factor of proportionality, κ_s, is obtained from the CTEQ6 PDFs. It is about 2 at $Q^2 = 4\,{\rm GeV}^2$ and tends towards 1 for increasing Q^2. Evaluating the GPDs from the CTEQ6M PDFs [8] and adopting the asymptotic ρ meson distribution amplitude, leading to $\langle 1/\tau\rangle = 3$, one can work out the cross section σ_L for ρ production. The result, shown in Fig. 1, is evidently too large by order of magnitude at low Q^2. The deviations diminish with increasing Q^2. Note that there are large NLO corrections [9] which cancel the LO term to a large extent. Wether the inclusion of higher orders lead to agreement with experiment is unknown as yet.

As is well-known from studies of the large momentum transfer behaviour of electromagnetic form factors, the collinear approximation becomes inconsistent in the end-point regions, since the contributions from large transverse separations, **b**, of the quark and antiquark forming the meson are not sufficiently suppressed. In order to eliminate that defect the so-called m.p.a. has been invented [10] in which quark transverse degrees of freedom are retained and the accompanying gluon radiation (a Sudakov factor) is taken into account. This m.p.a. is employed in the calculation of the partonic subprocesses. Instead of distribution amplitudes rather meson wave functions have to be used in this approach. Actually, a Gaussian one $\sim \exp[-a_V^2 k_\perp^2/(\tau(1-\tau))]$ is utilized in [2]. The transverse size parameters are considered as free parameters to be adjusted to the experiment ($a_\rho = 0.75\,\mathrm{GeV}^{-1}$, $a_\phi = 0.70\,\mathrm{GeV}^{-1}$). The structure of the amplitude as given in Eq. (2) still holds if the m.p.a. is used, even the relative strength of the various contributions remain to be the same.

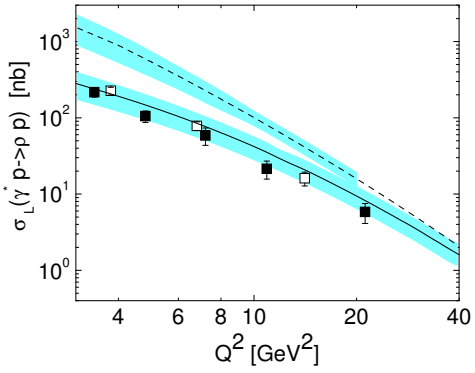

Figure 1: σ_L for ρ production at $W = 75\,\mathrm{GeV}$. Data taken from H1 [4] (solid squares) and ZEUS [5] (open squares). The solid (dashed) line represents the handbag result using the m.p.a. (collinear appr.). The error bands are due to the uncertainties of the PDFs.

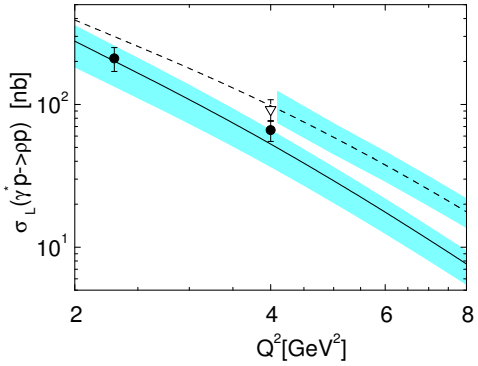

Figure 2: $\sigma_L(\rho)$ versus Q^2 at $W = 5\,\mathrm{GeV}$ (solid line) and 10 GeV (dashed line). Data taken from HERMES [11] and E665 [12].

Detailed comparison with experiment is made in Ref. [2]. Here, only a few results are presented. As one can see from Fig. 1 if the m.p.a. is used, the handbag result for $\sigma_L(\rho)$ is in fair agreement with the HERA data [4, 5] in particular if one considers the uncertainties in the theoretical results due to the errors of the PDFs. Results for σ_L at lower values of W are shown in Fig. 2. Next, in Fig. 3 the energy dependence of $\sigma_L(\rho)$ is displayed. The figure also reveals the prominent role of the gluonic contribution. The valence quark contribution is only significant below 10 GeV. Results of similar quality are obtained for ϕ production. Here, only the ratio of the cross section for ϕ and ρ production is shown in Fig. 4. For $Q^2 \to \infty$ the handbag approach predicts $\sigma_L(\phi)/\sigma_L(\rho) \longrightarrow 2/9(f_\phi/f_\rho)^2 = 0.248$. The deviations from this limit seen in Fig. 4 at finite Q^2, are generated by the breaking of flavor symmetry in the sea and, although to a lesser extent, by the meson wave function. The low value of the ratio at $W = 5\,\mathrm{GeV}$ is due to the additional valence quark contribution to the ρ cross section.

In summary - the handbag factorization scheme with the partonic subprocesses calculated within the m.p.a. and GPDs constructed from the double distributions provides reasonable results for the longitudinal cross section of ρ and ϕ electroproduction in a large range of Q^2

and W. As shown in Ref. [13] this approach can also be applied to the amplitude for transversally polarized photons. The infrared singularities occuring for that amplitude in collinear approximations are regularized in the m.p.a. by the quark transverse momenta. In Ref. [13] this amplitude has been calculated for HERA kinematics assuming that only the gluonic subprocess contributes. The inclusion of quarks for this amplitude is in progress. This analysis will provide results on σ_T and on various spin density matrix elements for the same range of Q^2 and W as for σ_L.

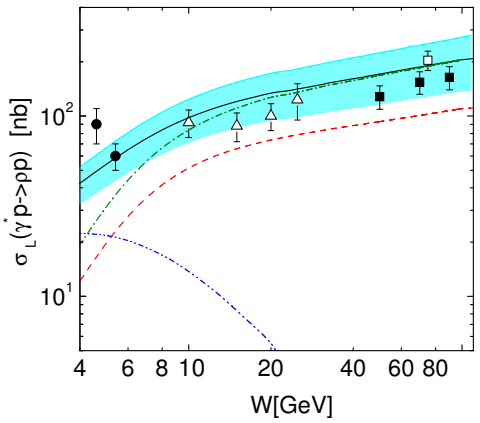

Figure 3: $\sigma_L(\rho)$ at $Q^2 = 4\,\mathrm{GeV}^2$. Data taken from H1 [4] (solid square), ZEUS [5] (open square), E665 [12] (open triangle) and HERMES [11] (solid circle). The dashed (dash-dotted, dash-dot-dotted) line represents the gluon (gluon+sea, (gluon+sea)-valence interference plus valence quark) contribution. For further notation, cf. Fig. 1.

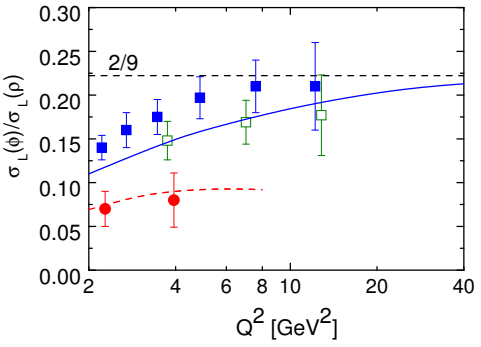

Figure 4: The ratio $\sigma_L(\phi)/\sigma_L(\rho)$. The solid (dashed) line represents the handbag result at $W = 75\,(5)\,\mathrm{GeV}$. Data are taken from H1, ZEUS and HERMES.

References

[1] A.V. Radyushkin, Phys. Lett. **B385**, 333 (1996); J.C. Collins *et al.*, Phys. Rev. D56, 2982 (1997).

[2] S. V. Goloskokov and P. Kroll, Eur. Phys. J. C **50**, 829 (2007).

[3] D. Müller *et al*, Fortschr. Phys. **42**, 101 (1994); A.V. Radyushkin, Phys. Lett. **B449**, 81 (1999).

[4] C. Adloff *et al.*, [H1 collaboration], Eur. Phys. J. **C13**, 371 (2000).

[5] J. Breitweg *et al.*, [ZEUS collaboration], Eur. Phys. J. **C6**, 603 (1999).

[6] S. Chekanov *et al.*, [ZEUS collaboration], Nucl. Phys. **718**, 3 (2005).

[7] M. Diehl, T. Feldmann, R. Jakob and P. Kroll, Eur. Phys. J. **C39**, 1 (2005).

[8] J. Pumplin *et al*, JHEP **0207**, 012 (2002).

[9] D. Y. Ivanov *et al.* JETP Lett. **80**, 226 (2004) [Pisma Zh. Eksp. Teor. Fiz. **80**, 255 (2004)], M. Diehl und W. Kugler, these proceedings.

[10] J. Botts and G. Sterman, Nucl. Phys. **B325**, 62 (1989).

[11] A. Airapetain *et al.*, [HERMES collaboration], Eur. Phys. J. **C17**, 389 (2000).

[12] M.R. Adams *et al.*, [E665 collaboration], Z. Phys. **C74**, 237 (1997).

[13] S.V. Goloskokov and P. Kroll, Eur. Phys. J. **C42** 281 (2005).

[14] Slides:
`http://indico.cern.ch/contributionDisplay.py?contribId=77&sessionId=7&confId=9499`

Deeply Virtual Compton Scattering at HERA II

Laurent Schoeffel

CEA Saclay, DAPNIA-SPP, 91191 Gif-sur-Yvette Cedex, France

A new measurement is presented of elastic deeply virtual Compton scattering (DVCS) based on data taken by the H1 detector during the complete HERA II period. The data are well described by QCD based calculations. For the first time, a beam charge asymmetry is obtained in a colliding mode, using data recorded in e^-p and e^+p. A significant non zero value is measured, related to the interference of QCD and QED processes, namely the DVCS and Bethe-Heitler reactions.

1 Introduction

The DVCS reaction, $\gamma^* p \to \gamma p$, can be interpreted as the elastic scattering of the virtual photon off the proton via a colourless exchange, producing a real photon in the final state. It has a clear experimental signature identical to that of the purely electromagnetic Bethe-Heitler (BH) process. Since these two processes have an identical final state, it follows that they can interfere. The squared photon production amplitude is then given by [2]

$$|\tau|^2 = |\tau_{BH}|^2 + |\tau_{DVCS}|^2 + \underbrace{\tau_{DVCS}\,\tau^*_{BH} + \tau^*_{DVCS}\,\tau_{BH}}_{I}, \tag{1}$$

where I denotes the interference term. For an unpolarised proton target and lepton beam, the interference term can be written quite generally as function of the azimuthal angle ϕ, the angle between the plane containing the incoming and outgoing leptons and the plane defined by the virtual and real photon [2]

$$I \propto -C\left[\cos\phi\,\mathrm{Re}\widetilde{\mathcal{M}}^{1,1} + \cos 2\phi\,\mathrm{Re}\widetilde{\mathcal{M}}^{0,1} + \cos 3\phi\,\mathrm{Re}\widetilde{\mathcal{M}}^{-1,1}\right] \tag{2}$$

where $C = \pm 1$ is the lepton beam charge and $\mathcal{M}^{i,j}$ are related to helicity amplitudes [2]. Hence, cross section measurements which are integrated over ϕ are not sensitive to the interference term but the measurement of a cross section asymmetry with respect to the beam charge is a way to single out the interference term.

A general interest of the DVCS reaction lies in the the mass difference (skewing) between the incoming virtual photon and the outgoing real photon. This skewing can be interpreted in the context of generalised parton distributions (GPDs) [3] or in the dipole model framework [4]. In the following, new DVCS cross section measurements are presented and compared to QCD based models, extending previous analyses [5, 6]. For the first time, a beam charge asymmetry is obtained in a colliding mode, using data recorded in e^-p and e^+p, during the HERA II data taking.

2 Data analysis and results

The measurements of the DVCS cross section are based on the data collected by the H1 detector during the years 2004 till 2007, with HERA running with positrons/electrons colliding protons of energy 27.6 and 920 GeV. It corresponds to an integrated luminosity of 145 pb^{-1} for each beam charge. To enhance the ratio of DVCS events w.r.t. BH ones, the

photon is required to be detected in the forward or central region of the H1 detector, with a transverse momentum $P_T > 2$ GeV, while the scattered lepton is detected in the backward region, with an energy $E > 15$ GeV. To ensure the elastic selection and reduce the proton dissociation background, the absence of activity in the forward detectors is required [5]. To extract the DVCS cross section, the BH and inelastic DVCS backgrounds are subtracted bin by bin and the data are corrected for trigger efficiency, detector acceptance and initial state photon radiation.

Results are presented in figure 1. In figure 1 (left), we notice the reasonnable agreement of all analysis samples for the dependence of the DVCS cross section as a function of the centre-of-mass energy of the $\gamma^* p$ system, W. Using the electron sample only, the typical statistical and systematical errors on cross section are 10 % and 15 % respectively. Then, we can work with this electron sample for all analyses based on cross section.

In figure 1 (right), we observe the good description of $d\sigma_{DVCS}/dt$ by a fit of the form $e^{-b|t|}$. Hence, an extraction of the t-slope parameter b is accessible for 3 values of the exchanged photon virtuality, Q^2 and W, extending the previous determinations [5]. The global value of b is found to be $5.45 \pm 0.19 \pm 0.34$ GeV^{-2} at $W = 82$ GeV and $Q^2 = 8$ GeV^2. No dependence in W is observed for b and a significant Q^2 dependence can be extracted using also previous measurements at lower Q^2 [5]. We obtain : $b(Q^2) = A\left(1 - B\log(Q^2/2)\right)$, with $A = 6.98 \pm 0.54$ GeV^{-2} and $B = 0.12 \pm 0.03$.

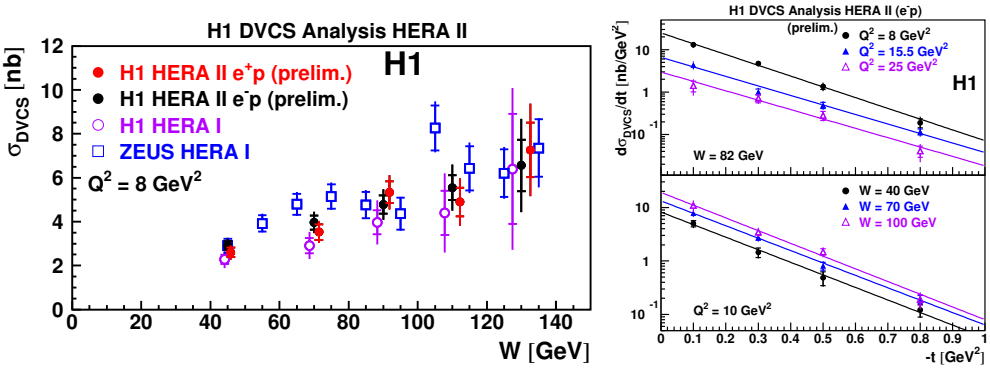

Figure 1: DVCS cross section for positrons/electrons samples as a function of W (left) and differential in t, for 3 values of Q^2 and W (right). The results of a fit of the form $e^{-b|t|}$ are also displayed.

3 QCD Interpretations

The DVCS cross section integrated over the momentum transfer can be written as

$$\sigma_{DVCS}(Q^2, W) \equiv \frac{\left[ImA\left(\gamma^* p \to \gamma p\right)_{t=0}(Q^2, W)\right]^2 (1 + \rho^2)}{16\pi\, b(Q^2, W)} \tag{3}$$

where ρ^2 is a small correction due to the real part of the amplitude and [3]. In the GPD formalism, the amplitude $ImA(\gamma^* p \to \gamma p)_{t=0}$ is directly proportional to the GPDs.

We define $S = \sqrt{\frac{\sigma_{DVCS}\ Q^4\ b(Q^2)}{(1+\rho^2)}}$, which is proportional to $|ImA\,(\gamma^* p \to \gamma p)_{t=0}(Q^2, W)|$ and therefore directly contains information on the Q^2 evolution for the GPDs. The result is shown in figure 2 (left) an compared to a GPD model [3]. A reasonable description of the weak Q^2 dependence, compatible with a logarithmic behaviour, is observed for S.

The DVCS cross section can also be interpreted within the dipole approach [4]. It expresses the scattering of the virtual photon off the proton through its fluctuation into a color singlet $q\bar{q}$ pair (or dipole) of a transverse size $r \sim 1/Q$. In the dipole approach the DVCS cross section is expected to verify the genuine property of geometric scaling [4]. This means that the cross section does not depend on both $x \simeq Q^2/W^2$ and Q^2 but obeys a scaling in a single variable $\tau = Q^2/Q_s^2$, where $Q_s(x) = Q_0(x/x_0)^{-\alpha/2}$. Using parameters $Q_0 = 1$ GeV, $\alpha = 0.25$ and $x_0 = 2.7\ 10^{-5}$ [7], we can determine the variable τ. The DVCS cross section is presented as a function of τ in figure 2 (right), which indicates that the geometric scaling property is verified within the present errors.

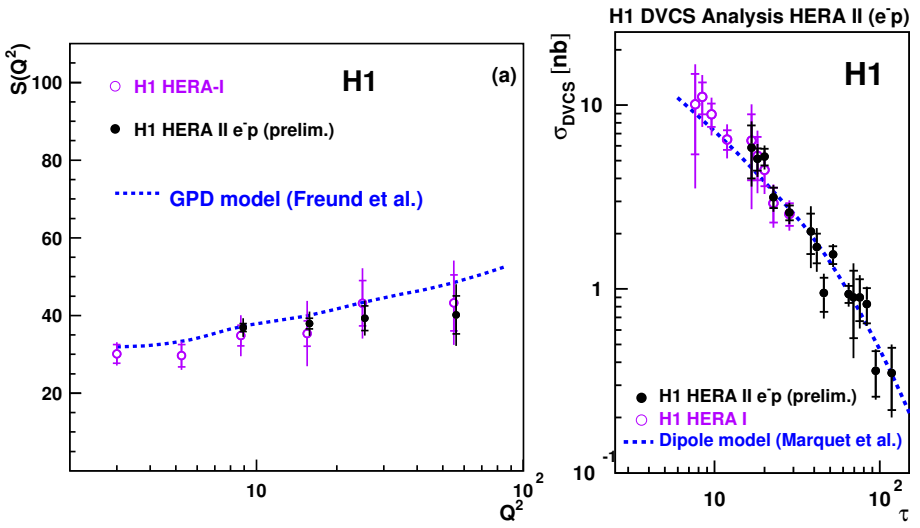

Figure 2: Observable $S = \sqrt{\frac{\sigma_{DVCS}\ Q^4\ b(Q^2)}{(1+\rho^2)}}$ with the prediction for the GPD model [3] (left). DVCS cross section measurements as a function of $\tau = Q^2/Q_s^2(x)$ with the prediction for the dipole model [4] (right).

4 Beam charge asymmetry

The determination of a cross section asymmetry with respect to the beam charge is realised by measuring the ratio $(d\sigma^+ - d\sigma^-)/(d\sigma^+ + d\sigma^-)$ as a function of ϕ. Note that ϕ is not defined when $|t| < |t|_{min} = x^2 m_p^2/(1-x)$ [2]. However, the experimental resolution in t is larger than the kinematical limit $|t|_{min}$. Therefore we can not define ϕ when $|t| < 0.05$ GeV^2 and the BCA is measured only for $|t| \geq 0.05$ GeV^2. In the expression of the BCA, $d\sigma^+$ and $d\sigma^-$ correspond to the DVCS cross section measured in positron and electron samples, over

a bin $d\phi$ [a]. Results are presented in figure 3 with a fit in $\cos\phi$, which is expected to be the first dependence in ϕ following equation (2). After applying a deconvolution method to account for the resolution on ϕ, the coefficient of the $\cos\phi$ dependence is found to be $p_1 = 0.17 \pm 0.03(stat.) \pm 0.05(sys.)$.

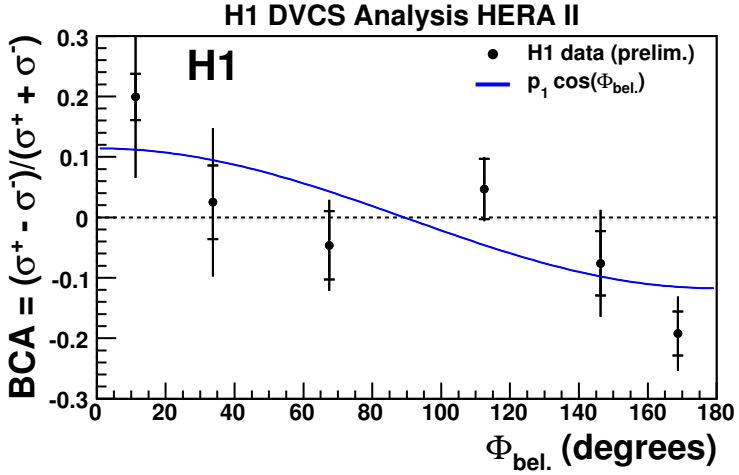

Figure 3: Beam charge asymmetry as a function of ϕ [2].

5 Conclusion

The DVCS cross section has been measured over a large kinematic domain using the complete HERA II data, extending previous analyses [5, 6]. For the first time, a beam charge asymmetry is obtained in a colliding mode, using data recorded in e^-p and e^+p. A significant non zero value is measured for $|t| \geq 0.05$ GeV^2, which is related to the interference of DVCS and BH processes.

References

[1] Slides:
`http://indico.cern.ch/contributionDisplay.py?contribId=92&sessionId=7&confId=9499`

[2] M. Diehl, T. Gousset, B. Pire and J. P. Ralston, Phys. Lett. B **411** (1997) 193 [hep-ph/9706344] ; A. V. Belitsky, D. Mueller and A. Kirchner, Nucl. Phys. B **629** (2002) 323 [hep-ph/0112108].

[3] A. Freund, Phys. Rev. D **68** (2003) 096006 [hep-ph/0306012].

[4] C. Marquet and L. Schoeffel, Phys. Lett. B **639**, 471 (2006) [hep-ph/0606079].

[5] A. Aktas *et al.* [H1 Collaboration], Eur. Phys. J. C **44**, 1 (2005) [hep-ex/0505061].

[6] S. Chekanov *et al.* [ZEUS Collaboration], Phys. Lett. B **573**, 46 (2003) [hep-ex/0305028].

[7] E. Iancu, K. Itakura and S. Munier, Phys. Lett. B **590** (2004) 199 [hep-ph/0310338].

[a] The azimuthal angle ϕ is defined according to the convention of [2].

Multi-Particle Decays of Light Mesons Measured by PHENIX at RHIC

Alexander Milov for the PHENIX Collaboration*

Brookhaven National Laboratory - Dept. of Physics,
Upton NY 11973, USA

The PHENIX experiment at RHIC measured K^0_S, η, and ω-meson production at high p_T in p+p, d+Au and Au+Au collisions at $\sqrt{s_{NN}} = 200$ GeV. Measurements performed in different hadronic decay channels give consistent results. This paper presents measured meson-to-π^0 ratios and Nuclear Modification factors in the most central d+Au and Au+Au collisions. No suppression seen in d+Au interactions is in contrast to a strong suppression of meson yields revealed in central Au+Au collisions at the same energy.

1 Analysis

The layout of the PHENIX detector [2] and the decay modes of the particles presented in this analysis are shown in Fig. 1. The reconstruction begins with pairing photons (straight lines) and selecting the π^0 candidates based on the invariant mass of the pair. The π^0 candidates are then combined between themselves, other photons or with the charged tracks and corresponding invariant mass distributions are analyzed to extract the particle yields by simultaneous fitting of the peaks and the background. The positions of the mass peaks were found to be in agreement with the particle masses measured in vacuum and the widths of the peaks, depending predominantly on the detector resolution, change from 10 MeV/c^2 for $\eta \to \pi^0\pi^+\pi^-$ to 20 MeV/c^2 for $\omega \to \pi^0\pi^+\pi^-$ and $K^0_S \to \pi^0\pi^0$ and to 30 MeV/c^2 for $\omega \to \pi^0\gamma$. The values above vary within less then 5 MeV/c^2 depending on the p_T bin which agree with the widths resulting from the detector resolution.

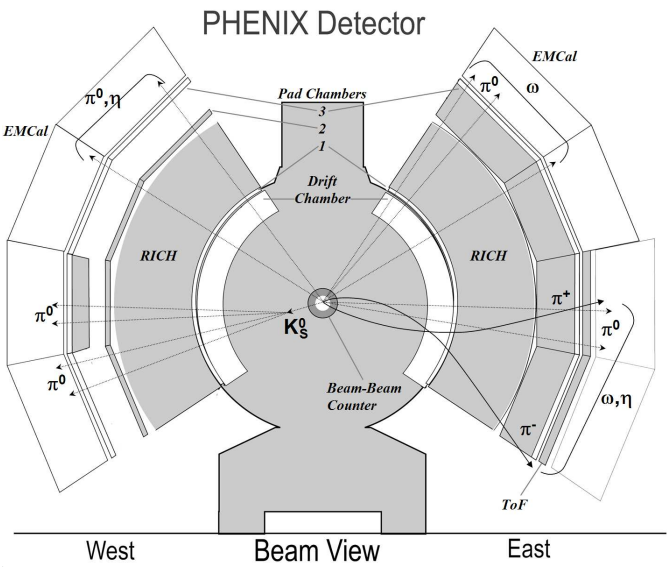

Figure 1: The PHENIX detector layout and the and the decays modes of studied particles. PHENIX subsystems not used in the analysis are shown gray.

The analysis discussed in these paper is based on the event samples accumulated during PHENIX physics Runs3,4, and 5 with integral statistics, after quality assurance selection,

*for the full list of authors see [3]

corresponding to the integrated luminosity of 1.5 nb^{-1} (p+p) 129 μb^{-1}(d+Au) and 2.5 pb^{-1} (Au+Au) in these runs respectively. The background conditions, depending on the mode of study for p_T >4-5 GeV/c, is smaller than 1:5 to 1:20 in $p+p$ and d+Au and 1:70 in Au+Au.

The raw yields have to be corrected for the limited detector acceptance, the γ-trigger efficiency, various analysis cuts, the gamma conversions in the detector preceding the calorimeter and the branching ratios of the specific decay mode. The magnitude of the corrections is calculated based on the full detector simulation and analysis of the data. The efficiencies measured in the detector configuration used during the $p+p$ data taking are shown in Fig. 2.

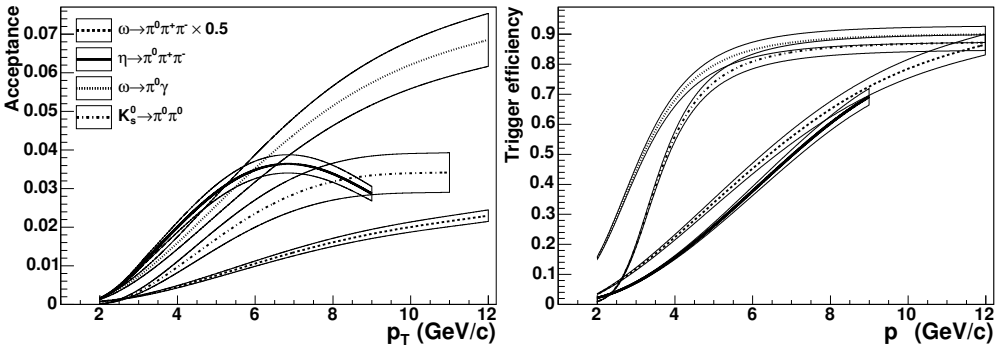

Figure 2: Shown on the left is the geometrical acceptance of the PHENIX detector for various decay modes. The right panel shows the probability that a photon coming from meson decay fires PHENIX high p_T γ-trigger. A unit corresponds to the standard "Minimum Biased" PHENIX trigger registering 23±2.2 mb.

The phase space density distribution of the true three-body decay modes $\pi^0\pi^+\pi^-$, known from the literature [6] was taken into account in the simulation. More details about this analysis can be found in [3, 4, 5]. For Au+Au events we applied an additional correction for reconstruction losses due to the detector occupancy.

The systematic errors of the measurement are listed in Tab. 1. The main source of error is the extraction of the raw yield made by fitting. The procedure is described in [3].

Source	$\omega \to \pi^0\pi^+\pi^-$		$\omega \to \pi^0\gamma$			$K^0_S \to \pi^0\pi^0$	
	$p+p$	$d+Au$	$p+p$	$d+Au$	$Au+Au$	$p+p$	$d+Au$
Acceptance	$5-10$	$9-12$	$10-20$	$8-12$	$14-16$	$10-25$	$10-20$
Trigger efficiency	$3-10$	$5-7$	$2-7$	5	-	$2-10$	5
Yield extraction	$5-25$	$10-15$	$5-15$	10	$15-35$	$7-30$	9
MB trigger	10	8	10	8	4	10	8
Total	$15-25$	$18-22$	$15-25$	$17-20$	$20-45$	$20-40$	$15-25$

Table 1: Systematic errors (in %) for different decay modes and collision systems. Values with a range indicate minimum and maximum error in the p_T range of the measurement.

2 Results

The results of the multi-particle decay measurements are presented in Fig. 3 for K-meson in the top panel, η-meson in the middle panel and ω-meson in the bottom panel.

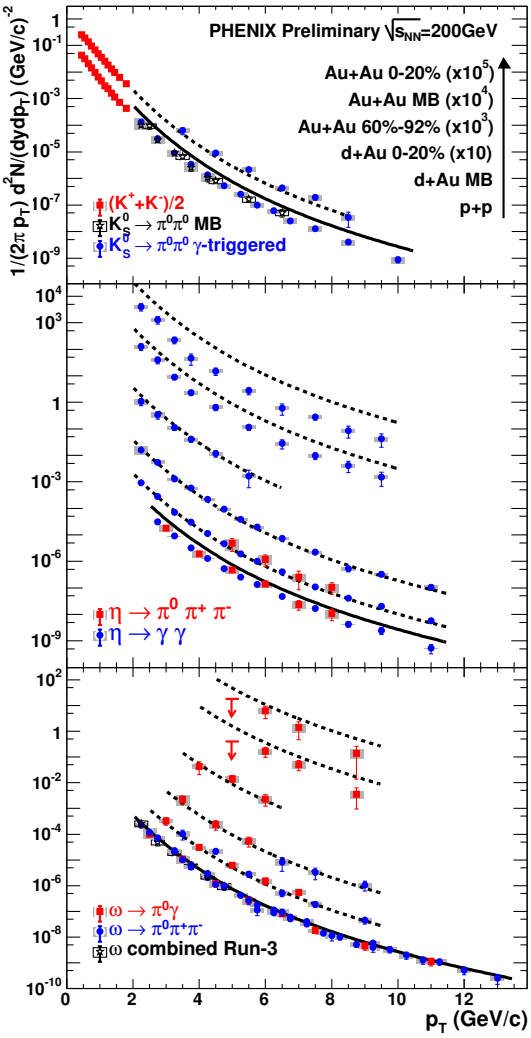

Figure 3: Invariant yields of K (top), η (middle), and ω (bottom) measured in p+p, p+Au and Au+Au collisions at $\sqrt{s_{NN}}$=200 GeV. The solid line is the parameterized π^0 spectra measured in $p+p$ [7]. The dashed lines are the π^0 spectra scaled by the meson-to-π^0 ratio in $p+p$ and the number of the binary collisions. K^+K^- data are taken from [9]

The ω-meson is measured in two decay modes, $\omega \to \pi^0\pi^+\pi^-$, $\omega \to \pi^0\gamma$ and η-meson is measured in $\eta \to \pi^0\pi^+\pi^-$, $\eta \to \gamma\gamma$. The results of the measurements for the same meson agree. The $K^0_S \to \pi^0\pi^0$ cannot be compared to $K^0_S \to \pi^+\pi^-$ from PHENIX because of the detector-induced background at the mass of the K-meson. The results are in agreement with the STAR experiment measurement in $\pi^+\pi^-$ [8]. We also see very good agreement between the results obtained in PHENIX physics Run3 and Run5 and between the results measured in triggered and Minimum Biased event samples. In the latter case the correction shown in right panels of Fig. 2 does not apply.

In the $p+p$ data the p_T range of the measurement is limited by the detector acceptance on the lower side of the range and by the available statistics on the upper side. In Run5 the ω-meson production in $p+p$ is measured out to 13 GeV/c making it the second in p_T-reach identified particle after the π^0. In the heavier collision systems the combinatorial background effectively reduces the available statistics.

The lowest data points shown in each panel of Fig. 3 are the yields measured in $p+p$ collision. Plotted above them are the Minimum Biased and 0-20% central d+Au events data. The 60%-92% peripheral, Minimum Bias and 0-20% central Au+Au collision spectra are plotted on top. For K^0_S such data are not available. All measurements are done at $\sqrt{s}, \sqrt{s_{NN}} = 200$ GeV. Central d+Au and Au+Au data are scaled by different factors for clarity.

The solid line shown in each panel is the parameterization of the invariant yield of π^0 measured in $p+p$ collisions [7]. For the η- and the K^0_S-mesons this line is above the

data points and for the ω-meson the points are much closer. Using this parameterization the non-identical meson ratios can be calculated. We find that in the $p+p$ collisions these ratios are flat above the p_T=2.5 GeV/c. Fitted by a constant the particle ratios are: ω/π^0 = 0.81±0.02±0.07, η/π^0= 0.48±0.02±0.02 and K^0/π^0 = 0.45±0.01±0.05.

Each set of points shown in Fig. 3 has a corresponding dashed line. These lines are constructed in the following way: the π^0 spectra measured in $p+p$ (solid line) is scaled with the corresponding meson-to-π^0 ratio given above. Since all ratios are found to be flat in the region of the measurement, the scaled π^0 reference corresponds to the invariant yield of the meson in the $p+p$ collisions. Those yields are further scaled by the number of binary collisions for each centrality bin in d+Au and Au+Au presented in the figure.

As one can see for all analyzed mesons the d+Au data in Minimum Bias and 0-20% most central events are very close to the dashed lines. The ratio of the two is the Nuclear Modification Factor and for the analyzed mesons it was found to be flat within the errors of the measurement. For the Minimum Bias event sample the R_{dA}'s are above unit but agree with 1 within the errors of the measurement.

In the peripheral Au+Au collisions the nuclear modification factor is not very different from 1 as the dashed line lays close to the points. This is not so in the Minimum Biased and 0-20% central Au+Au events. For ω-meson we find the R_{AA} to be 0.4±0.15. The η-meson production in central Au+Au events is suppressed by a factor of 5 compared to scaled $p+p$ reference.

3 Acknowledgments

Work of the speaker is supported by the Goldhaber Fellowship at BNL with funds provided by Brookhaven Science Associates.

References

[1] Slides:
`http://indico.cern.ch/contributionDisplay.py?contribId=93&sessionId=7&confId=9499`
[2] K. Adkox *et al.*, Nucl. Instrum. Meth. **A499** 469 (2003).
[3] S.S. Adler *et al.*, Phys. Rev. **C75** 024909 (2007).
[4] S.S. Adler *et al.*, Phys. Rev. **C75** 051902(R) (2007).
[5] V. Riabov (for the PHENIX Collaboration), nucl-ex/0702046v1.
[6] C. Alff *et al.*, Phys. Rev. Lett. **9** 325 (1962).
[7] A. Adare *et al.*, arXiv:0704.3599v1.
[8] B.I. Abelev *et al.*, Phys. Rev. **C75** 064901 (2007).
[9] S.S. Adler *et al.*, Phys.Rev. **C74** (2006) 024904.

Measurements of ϕ Mesons Reconstructed from Hadronic and Leptonic Decays by the PHENIX Experiment at RHIC

Shengli Huang (for the PHENIX Collaboration)

Vanderbilt University - Dept of Physics and Astronomy
Nashville, TN 37235

In this paper, we present the PHENIX preliminary results on the ϕ mesons mass and width, reconstructed from the K^+K^- decay in Au+Au collisions at $\sqrt{S_{NN}} = 200$ GeV. The production of ϕ mesons in 200 GeV Au+Au collisions has also been studied in both the K^+K^- and the e^+e^- decay channels. The yield and effective temperature obtained from invariant transverse mass (m_T) spectra are studied and compared as a function of centrality in both decay channels.

1 Introduction

An extremely dense and hot matter with hints of partonic properties has been generated at RHIC using ultra-heavy ion collisions [2]. The mass and width of ϕ mesons may change in this medium [3]. Since the ϕ meson is the lightest $s\bar{s}$ bound state and its mass is close to two times the kaon mass, even a small mass shift will cause a large change in the branching ratio of $\phi \rightarrow e^+e^-$ and $\phi \rightarrow K^+K^-$. Thus, comparison of the yield in these two decay channels provides a sensitive probe to study the properties of the medium. It also could provide information about the partial chiral symmetry restoration and help us understand the origin of mass. In the paper, we present the ϕ meson mass, width and their centrality dependence in 200 GeV Au+Au collisions. We also present the ϕ mesons yield obtained in the e^+e^- and the K^+K^- decay channels from the same energy and collision system.

2 Analysis Method

The PHENIX experiment [4] has two central spectrometers, which cover 90^0 in azimuth and pseudorapidity of $|\eta| < 0.35$. Each arm can measure the momentum of charged particles produced in RHIC collisions using the Drift Chamber (DC) and the first layer of the Pad Chamber (PC1). The Beam-Beam Counters (BBC) in combination with Zero Degree Calorimeters (ZDC) provide the trigger and are used to determine the z-coordinate of the collision vertex and the event centrality. PHENIX also has a 130 ps timing resolution TOF subsystem covering half of the East arm and a 500 ps timing resolution Electromagnetic Calorimeter (EMCal) covering both arms. The TOF and EMCal identify kaons within $0.3 < p(GeV/c) < 2.0$ and $0.3 < p(GeV/c) < 1.0$ respectively. Electrons are identified with the Ring Imaging Cherenkov Detector (RICH) and EMCal. To reconstruct the ϕ meson using the e^+e^- and the K^+K^- decays, we combine oppositely charged identified particles to form invariant mass distributions containing both the signal and combinatorial background. The shape of the combinatorial background is estimated by the mixed event technique, where particles are taken from different events which have similar multiplicity and collision vertex. The mixed event invariant mass distribution is normalized to $2\sqrt{N_{++}N_{--}}$, where N_{++} and N_{--} are the measured integrals of like sign yields [5].

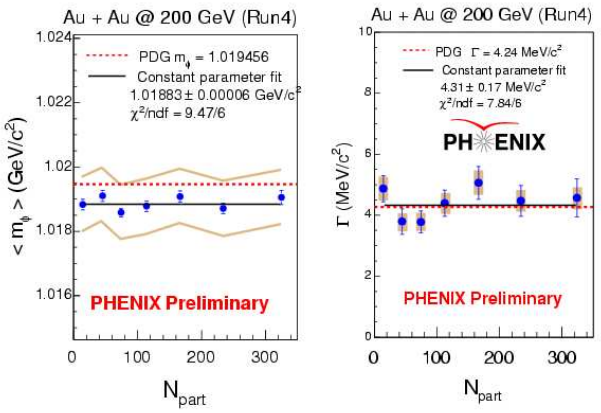

Figure 1: The centrality dependence of the ϕ meson mass and width in 200 GeV Au+Au collisions

Raw yields are counted around known particle masses after subtraction of invariant mass distributions from mixed events. To study the ϕ mesons mass and width, we use a Breit Wigner convolved with a Gaussian function to fit the ϕ meson invariant mass distribution. The Gaussian function is implemented to take into account the finite mass resolution of the detector which has been determined to be about $1.4 MeV/c^2$ by the simulation.

3 Results and Discussions

Fig.1 shows the mass and width of ϕ mesons obtained from 200 GeV Au+Au collisions in the K^+K^- decay channel. The left plot shows the mass of the ϕ mesons as a function of the number of nucleons participating in the collisions. The systematic errors are represented by two lines. The systematic errors are mainly due to the uncertainty in the magnet field. The simulation study indicates that this field uncertainty will cause about 0.9 MeV mass uncertainty. The right plot shows the mass width of the ϕ mesons as a function of the number of participants. The statistical errors are shown with blue lines and the systematic errors are shown as shadowed boxes. The systematic errors were evaluated by varying the normalization method and the fit region in the invariant mass distributions. The results shown in Fig.1 indicate that there is no centrality dependence of the ϕ mesons mass and width, and that the measurements are consistent with the PDG

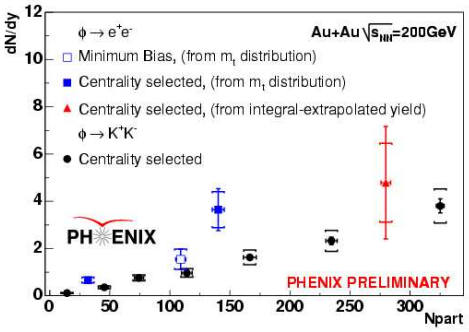

Figure 2: The centrality dependence of the ϕ meson yield measured using the e^+e^- and the K^+K^- decay channels

value.

Fig.2 shows the yield of ϕ mesons obtained at mid-rapidity from the e^+e^- and K^+K^- decays in 200 GeV Au+Au collisions. The two solid squares show the ϕ meson yield from the e^+e^- decay at centrality of $40-92\%$ and $20-40\%$. The yield is obtained by fitting the invariant transverse mass (m_T) spectra with an exponential function. The yield from the e^+e^- decays in the most central collisions is shown as triangle and the minimum bias result is shown as open square. The solid circles show the ϕ meson yield from the K^+K^- decays at different centralities. The systematic errors come primarily from the choice of the normalization method and the mass window in which the raw yield is counted. As Fig.2 shows, the yield obtained from the K^+K^- and e^+e^- decays are similar and are consistent with each other within the quoted systematic errors. No significant difference is observed. However, we note that the life time of ϕ meson is around 40 fm/c. Only low momentum (< 1 GeV/c) ϕ mesons are expected to decay inside the medium. So, a low momentum study of the mass centroid and width as well as a direct yield comparison between the two decay channels is desirable. The background in the low momentum region in the $\phi \rightarrow e^+e^-$ decay channel is prohibitively large. This measurement will become possible with the PHENIX hadron blind detector (HBD) upgrade, which will suppress the background by a factor of 30 in e^+e^- decays. After the upgrade, it will be possible to test whether the branching ratio changes in the presence of the medium. Fig.3 shows the inverse slope (effective temperature) obtained from an exponential fit to the invariant transverse mass (m_T) spectra of ϕ mesons from K^+K^- and e^+e^- decays. The solid circles are the K^+K^- decay results and the square data points are the e^+e^- decay results. The effective temperature shows little or no centrality dependence in both decay channels. The two results are consistent within errors. One may expect that the inverse slopes will differ, if the decay kaons were affected strongly by hadronic re-scattering. However within the present errors, we do not see such an effect.

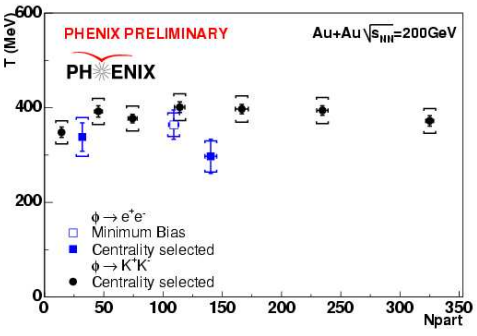

Figure 3: The centrality dependence of the effective temperature from the ϕ meson invariant m_T spectra in 200 GeV Au+Au collisions

4 Conclusions

The PHENIX experiment has measured the production of ϕ mesons using their decays into K^+K^- and e^+e^-. The mass and width of the ϕ mesons using the K^+K^- decay channel were found to be independent of the centrality of the collisions and consistent with the PDG values. The integrated yield and effective temperatures obtained from the K^+K^- and the e^+e^- decay channels are consistent with each other at different centralities within the large systematic errors. In the future, the new HBD detector will help us to refine these measurements by suppressing the large background in the e^+e^- decay channel.

5 Acknowledgments

This research is sponsored by the Division of Nuclear Physics , U.S. Department of Energy, under contract DE-FG05-92ER40712 and OJI grant DE-FG02-04ER41333. The complete list of PHENIX acknowledgments is provided in Ref [6].

References

[1] Slides:
`http://indico.cern.ch/contributionDisplay.py?contribId=94&sessionId=7&confId=9499`

[2] Phenix Collab., K. Adcox *et al.*, Nucl. Phys. A **757** (2005) 184 [arXiv:nucl-ex/0410003].

[3] G.E. Brown and M. Rho, Phys. Rev. Lett. **66** (1991) 2720; T. Hatsuda and S.H. Lee, Phys. Rev. C **46** (1992) 34; E. Oset and A. Ramos, Nucl. Phys. A **679** (2001) 616 [arXiv:nucl-th/0005046]; D. Cabrera and M.J. Vicente Vacas, Phys. Rev. C **67** (2003) 045203 [arXiv:nucl-th/0205075]; F. Klingl, T. Waas and W. Weise, Phys. Lett. B **431** (1998) 254 [arXiv:hep-ph/9709210].

[4] Phenix Collab., K. Adcox *et al.*, Nucl. Instrum. Meth. A **499** (2003) 469.

[5] Phenix Collab., A. Toia *et al.*, Nucl. Phys. A **774** (2006) 743 [arXiv:nucl-ex/0510006].

[6] Phenix Collab., A. Adare *et al.*, Phys. Rev. Lett. **97** (2006) 252002 [arXiv:hep-ex/0609010].

QCD Factorizations in $\gamma^*\gamma^* \to \rho_L^0\rho_L^0$

M.SEGOND

LPT
-Université Paris-Sud-CNRS, 91405-Orsay, France

The exclusive reaction of rho meson pair electroproduction in $\gamma^*\gamma^*$ collisions is a nice place to study various dynamics and factorization properties in the perturbative sector of QCD. At low energy (quarks dominance), this process can be considered as a way to explore QCD factorizations involving generalized distribution amplitudes (GDA) and transition distribution amplitudes (TDA), and, in the Regge limit of QCD (gluons dominance), it seems to offer a promising probe of the BFKL resummation effects which could be studied at the next international linear collider (ILC).

1 GDA/TDA factorizations at low energy

1.1 The Born order amplitude

We calculate [1] the scattering amplitude of the process $\gamma^*(q_1)\gamma^*(q_2) \to \rho_L^0(k_1)\rho_L^0(k_2)$ at Born order for both transverse and longitudinal polarizations in the forward kinematics, when quark exchanges dominate. The virtualities $Q_i^2 = -q_i^2$, supply the hard scale which justifies the perturbative computation of the amplitude M_H. The final states ρ mesons are described in the collinear factorization by their distribution amplitudes (DA) in a similar way as in the classical work of Brodsky-Lepage [2].

1.2 $\gamma_T^*\gamma_T^* \to \rho_L^0\rho_L^0$ in the generalized Bjorken limit

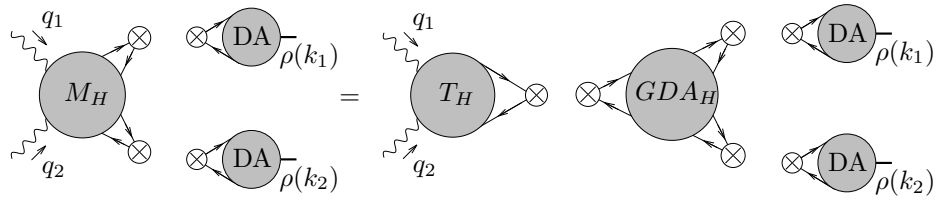

Figure 1: Factorization of the amplitude in terms of a GDA which is expressed in a perturbatively computed GDA_H convoluted with the DAs of the two ρ-mesons.

We then consider transverse photons whose scattering energy is much smaller than the typical scales of the process (close to the semi-exclusive limit in DIS when $x_{Bj} \to 1$). We obtain the same expression of the amplitude computed previously (Sec. 1.1) in a different theoretical framework which is based on the factorization property of the scattering amplitude in terms of a hard coefficient function T_H convoluted with a GDA encoding the softer part of the process, as illustrated in Fig. 1.

1.3 $\gamma_L^*\gamma_L^* \to \rho_L^0\rho_L^0$ with strong ordering of virtualities

In the regime with strong ordering of the virtualities $Q_1^2 \gg Q_2^2$, we compute the amplitude with initial longitudinally polarized photons, in a factorized formula involving a convolution of a hard coefficient function T_H and a $\gamma^* \to \rho$ TDA. This soft part is defined with the leading twist quark-antiquark non local correlator between non-diagonal matrix elements corresponding to the $\gamma \to \rho$ transition. We also obtain the same expression as in the direct calculation of the Sec. 1.1 in this kinematics.

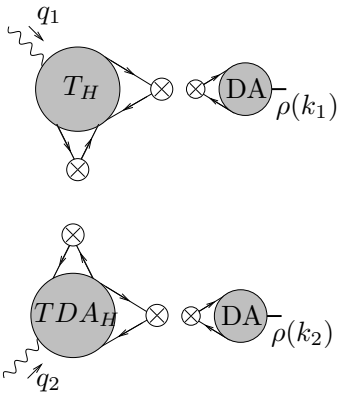

Figure 2: Factorization involving a TDA which is written as the convolution of a hard term TDA_H and a DA of the ρ-meson.

2 $k_\perp$-factorization in the Regge limit of QCD

2.1 Impact factor representation

We are focusing now on the high-energy (Regge) limit, when the cm energy $s_{\gamma^*\gamma^*}$ is much larger than all other scales of the process, in which $t-$channel gluonic exchanges dominate [3]. The highly virtual photons provides ones small transverse size objects ($q\bar{q}$ color dipoles) whose scattering is the cleanest place to study the typical Regge behaviour with $t-$channel BFKL Pomeron exchange [4], in perturbative QCD. If one selects the events with comparable photon virtualities, the BFKL resummation effects dominate with respect to the conventional partonic evolution of DGLAP [5] type. Several studies of BFKL dynamics have been performed at the level of the total cross-section [6]. At high energy, the impact factor representation of the scattering amplitude has the form of a convolution in the transverse momentum $\underline{k}$ space between the two impact factors corresponding to the transition of $\gamma^*_{L,T}(q_i) \to \rho^0_L(k_i)$ via the $t-$channel exchange of two reggeized gluons (with momenta $\underline{k}$ and $\underline{r} - \underline{k}$).

2.2 Non-forward cross-section at ILC for $e^+e^- \to e^+e^-\rho^0_L\ \rho^0_L$

Our purpose is now to evaluate at Born order and in the non-forward case the cross-section of the process $e^+e^- \to e^+e^-\rho^0_L\ \rho^0_L$ in the planned experimental conditions of the International Linear Collider (ILC). We focus on the LDC detector project and we use the potential of the very forward region accessible through the electromagnetic calorimeter BeamCal which may be installed around the beampipe at 3.65 m from the interaction point. This calorimeter allows to detect (high energetic) particles down to 4 mrad. This important technological step was not feasible a few years ago. At ILC, the foreseen cm energy is $\sqrt{s} = 500$ GeV. Moreover we impose that $s_{\gamma^*\gamma^*} > c\,Q_1\,Q_2$ (where c is an arbitrary constant). It is required by the Regge kinematics for which the impact representation is valid. We choose Q_i to be bigger than 1 GeV since it provides the hard scale of the process. $Q_{i\,max}$

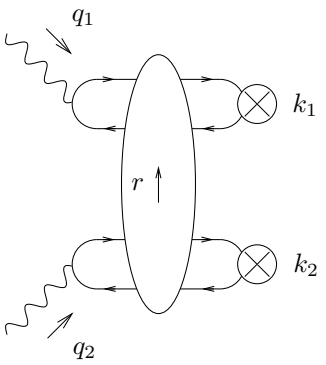

Figure 3: The amplitude of the process $\gamma^*_{L,T}(q_1)\gamma^*_{L,T}(q_2) \to \rho^0_L(k_1)\rho^0_L(k_2)$ in the impact representation.

will be fixed to 4 GeV: indeed the various amplitudes involved are completely negligible for higher values of virtualities.

We now display in Fig.4 the cross-sections as a function of the momentum transfer t for the different γ^* polarizations. For that we performed analytically the integrations over $\underline{k}$ (using conformal transformations to reduce the number of massless propagators) and numericaly the integration over the accessible phase space. We assume the QCD coupling constant to be $\alpha_s(\sqrt{Q_1 Q_2})$ running at three loops, the parameter $c = 1$ which enters in the Regge limit condition and the energy of the beam $\sqrt{s} = 500$ GeV. We see that all the differential cross-sections which involve at least one transverse photon vanish in the forward case when $t = t_{min}$, due to the s-channel helicity conservation. We finally display in the Table.1 the results for the total cross-section integrated over t for various values of c. With the foreseen nominal integrated luminosity of $125\,\mathrm{fb}^{-1}$, this will yield $4.26\,10^3$ events per year with $c = 1$.

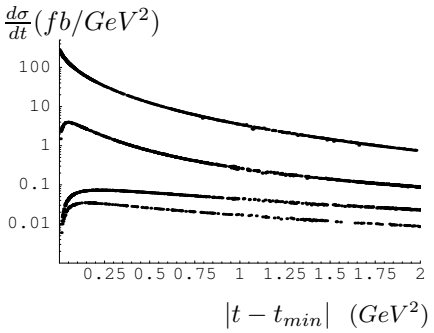

Figure 4: Cross-sections for $e^+e^- \to e^+e^-\rho_L^0 \;\; \rho_L^0$ process. Starting from above, we display the cross-sections corresponding to the $\gamma_L^*\gamma_L^*$ mode, to the $\gamma_L^*\gamma_T^*$ modes, to the $\gamma_T^*\gamma_{T'}^*$ modes with different $T \neq T'$ and finally to the $\gamma_T^*\gamma_{T'}^*$ modes with the same $T = T'$.

By looking into the upper curve in the Fig.4 related to the longitudinal polarizations, one sees that the point $t = t_{min}$ gives the maximum of the total cross-section (since the transverse polarization case vanishes at t_{min}) and then practically dictates the trend of the total cross-section which is strongly peaked in the forward direction (for the longitudinal case) and strongly decreases with t (for all polarizations). From now we only consider the forward dynamics.

c	$\sigma^{Total}\,(fb)$
1	34.1
2	29.6
10	20.3

Table 1: Total cross-section for various c.

The Fig.5 shows the cross-section (for both gluons and quarks exchanges) at t_{min} for different values of the parameter c which enters in the Regge limit condition : the increase of c leads to the suppression of quarks exchanges (studied in section 1) and we base the value of c chosen previously on the gluon exchange dominance over the quark exchange contribution.

The ILC collider is expected to run at a cm nominal energy of 500 GeV, though it might be extended in order to cover a range between 200 GeV and 1 TeV. Although the Born order cross-sections do not depend on s, the triggering effects introduce an s-dependence; note that the cross-section falls down between 500 GeV and 1 TeV. The measurability is then optimal when $\sqrt{s} = 500$ GeV. The results obtained at Born approximation can be considered as a lower limit of the cross-sections for ρ-mesons pairs production with complete BFKL evolution taken into account. We consider below only the point $t = t_{min}$ and we restrict ourselves to the leading order (LO) BFKL evolution in the saddle point approximation.

From previous studies at the level of $\gamma^*\gamma^*$ [7], the NLO contribution is expected to be between the LO and Born order cross-sections. This ordering will be preserved at the level of the e^+e^- process. The comparison of Figs.5 with Figs.6 leads to the conclusions that the BFKL evolution changes the shape of the cross-section: when increasing $\sqrt{s}$ from 500 GeV to 1 TeV, the two gluon exchange cross-section will fall down, while the cross-section with the BFKL resummation effects taken into account should more or less stay stable, with a

high number of events to be still observed for these cm energies.

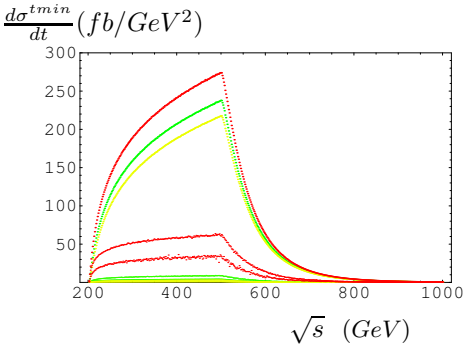

Figure 5: Cross-sections for $e^+e^- \to e^+e^-\rho_L^0\ \rho_L^0$ at $t = t_{min}$ for different values of the parameter c: the red (black) curves correspond to $c = 1$, the green (dark grey) curves to $c = 2$ and and the yellow (light grey) curves to $c = 3$. For each value of c, by decreasing order the curves correspond to gluon-exchange, quark-exchange with longitudinal virtual photons and quark-exchange with transverse virtual photons.

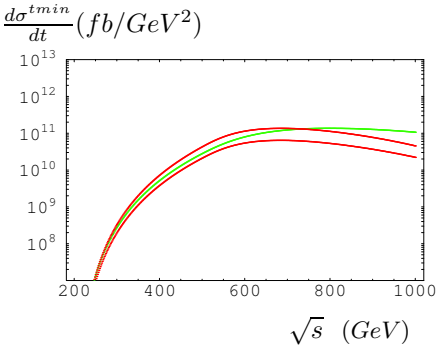

Figure 6: Cross-sections for $e^+e^- \to e^+e^-\rho_L^0\ \rho_L^0$ with LO BFKL evolution at $t = t_{min}$ for different α_s : the upper and lower red (black) curves for α_s running respectively at one and three loops and the green one for $\alpha_s = 0.46$.

3 Acknowledgments

This work was done in a collaboration with B.Pire, L.Szymanowski and S.Wallon. I am very gratefull to the DIS 2007 organizers.

4 Bibliography

Slides:
`http://indico.cern.ch/contributionDisplay.py?contribId=95&sessionId=7&confId=9499`

References

[1] B. Pire, M. Segond, L. Szymanowski and S. Wallon, Phys.Lett.B639 (2006) 642-651.

[2] S. J. Brodsky and G. P. Lepage, Phys. Lett. **B87** (1979) 359 and Phys. Rev. D **24** (1981) 1808; A.V. Efremov and A.V. Radyushkin, Phys. Lett. **B94** (1980) 245.

[3] M. Segond, L. Szymanowski and S. Wallon, hep-ph/0703166.

[4] E.A. Kuraev, L.N. Lipatov and V.S. Fadin, Phys. Lett. **B60** (1975) 50-52; Sov. Phys. JETP **44** (1976) 443-451; Sov. Phys. JETP **45** (1977) 199-204; Ya.Ya. Balitskii and L.N. Lipatov, Sov. J. Nucl. Phys. **28** (1978) 822-829.

[5] V. N. Gribov and L. N. Lipatov, Yad. Fiz. **15**, 781 (1972) [Sov. J. Nucl. Phys. **15**, 438 (1972)]; G. Altarelli and G. Parisi, Nucl. Phys. B **126**, 298 (1977); Y. L. Dokshitzer, Sov. Phys. JETP **46** (1977) 641 [Zh. Eksp. Teor. Fiz. **73** (1977) 1216].

[6] J. Bartels, A. De Roeck and H. Lotter, Phys. Lett. B **389**, 742 (1996); S. J. Brodsky, F. Hautmann and D. E. Soper, Phys. Rev. Lett. **78**, 803 (1997) [Erratum-ibid. **79**, 3544 (1997)]; J. Kwiecinski and L. Motyka, Phys. Lett. B **462**, 203 (1999); J. Bartels, C. Ewerz and R. Staritzbichler, Phys. Lett. B **492** (2000) 56; J. Kwiecinski and L. Motyka, Eur. Phys. J. C **18**, 343 (2000);M. Boonekamp, A. De Roeck, C. Royon and S. Wallon, Nucl. Phys. B **555**, 540 (1999).

[7] R. Enberg, B. Pire, L. Szymanowski and S. Wallon, Eur. Phys. J. C **45** (2006) 759; "PHOTON 2005," Warsaw, 30 Aug - 8 Sep 2005, Acta Phys. Polon. B **37** (2006) 847; D. Y. Ivanov, M. I. Kotsky and A. Papa, Eur. Phys. J. C **38** (2004) 195.

Status of the H1 Very Forward Proton Spectrometer

Laurent Favart *

I.I.H.E., Université Libre de Bruxelles, CP 230
1050 Brussels - Belgium
on behalf of the H1 Collaboration

The Very Forward Proton Spectrometer (VFPS) of the H1 experiment at HERA is collecting data since 2005. The fiber detectors in the Roman pots located at 218 and 222m downstream from the H1 interaction point, tag and measure diffractively scattered protons with a high acceptance in the $x_{I\!P}$ range [0.01, 0.025]. The experimental set up and the spectrometer tagging performance using diffractive events collected during 2006 and 2007 are discussed.

1 Introduction

In recent years considerable progress has been achieved in the partonic interpretations of diffractive processes in $e-p$ collisions (see e.g. [2]), Most of diffractive studies performed up to now at HERA have been based on the characteristic presence of a rapidity gap in the diffractive final state. The precision of this method is limited by the uncertainty related to the presence of dissociated proton background events. The only precise and unambiguous way of studying diffraction is by tagging the diffracted proton and measuring its four momentum by means of a proton spectrometer. Such devices have been used by the H1 and ZEUS Collaborations and have delivered interesting results, but their acceptances are small, with the result that the collected statistics are limited and large systematic errors affect the measurements. To fully profit from the HERA luminosity upgrade in the study of diffraction after the year 2003, a Very Forward Proton Spectrometer (VFPS) which identifies and measures the momentum of the diffracted proton with a high acceptance has therefore been installed by H1. This contribution reports the VFPS tagging performance using diffractive events collected during HERA running at high energy (27.5 GeV for the electron/positron beam and 920 GeV for the proton) in 2006 and 2007.

2 Roman Pot detectors

The VFPS [3] is a set of two "Roman pots" located at 118m and 222m downstream of the H1 interaction point. Each pot consists of an insert into the beam pipe, allowing two tracking detectors equipped with scintillating fibres to be moved very close to the proton beam.

Many aspects of the design of the Roman pots, including the stainless plunger vessel and the scintillating fiber detectors, are adaptations of the FPS proton spectrometer [4], installed and operational in H1 since 1994. Both detectors of each Roman pot consists of two planes of scintillating fibres oriented at $\pm 45^0$ w.r.t. the horizontal plane and moving perpendicularly to the beam line direction. Each detector allows to reconstruct of the position of one impact point of the scattered proton trajectory with a precision of about 100 μm. For triggering

*This work is supported by the Fonds National de la Recherche Scientifique Belge (FNRS).

purposes each detector is sandwiched between 2 scintillating planes which are connected to different PM's. A trigger signal, corresponding to a activity in at least 3 planes out of four, is delivered separately for each station at the first trigger level.

3 VFPS installation and running

The VFPS have been installed at the very end of 2003. Radiation damage of the optical readout fiber prohibited data taking during 2004. Hence data available for physics analysis started in 2005. The bulk of data were taken in 2006 and 2007, they correspond to and integrated luminosity of 140 pb^{-1}. From an operational point of view, the VFPS was into data taking position for 70% of the luminosity collected by H1.

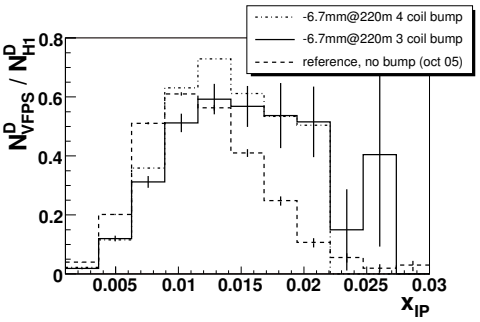

Figure 1: Ratio of events tagged by the VFPS to the diffractive events seen in H1 (see section 4) as a function of $x_{I\!P}$ for different beam optics.

The p beam orbit has been modified in April 2006 to increase the VFPS acceptance. A large fraction of protons with a energy loss above 2% w.r.t. the beam energy are hitting the beam pipe around 200m when the nominal orbit is used. The orbit has been changed moving the p outwards HERA by 6mm at about 200m from the interaction point. This procedure leads to an increase of the rate of events tagged by the VFPS at $x_{I\!P} > 0.015$ (see Fig. 1).

4 Inclusive Diffraction in DIS regime

To study the description of the beam optics and of the VFPS system by our simulation, first, VFPS tagged events, i.e. with a fired trigger, are compared to the full sample of diffractive events selected using the information from the main detector using the rapidity gap method (see e.g. [5]). The full event sample is selected asking for an electromagnetic cluster in the backward (lepton beam direction) calorimeter SpaCal of more than 10 GeV (corresponding to the scattered electron candidate), a reconstructed vertex and that the most forward particle in the main detector has pseudo-rapidity of less than 2.5 (this latest condition is equivalent to asking for a rapidity gap). Additionally the Forward Muon Detector should not have recorded a signal above the noise level. One can then look to what fraction of this sample largely dominated by diffractive events is tagged by VFPS. This selection was applied to produce the Fig. 1 discussed in the previous section. Over the 140 pb^{-1} collected, 880,000 events are tagged by the VFPS. If a kinematic cut of $Q^2 > 10$ GeV^2 is applied, 215,000 events remain.

This sample is compared to the sum of diffractive and background contributions as estimated by Monte Carlo. In Fig. 2 data corresponding to about 1 month of running in e^+p

mode with a 6mm bump applied (24 pb^{-1}) are compared to Monte Carlo predictions (see figure caption for details).

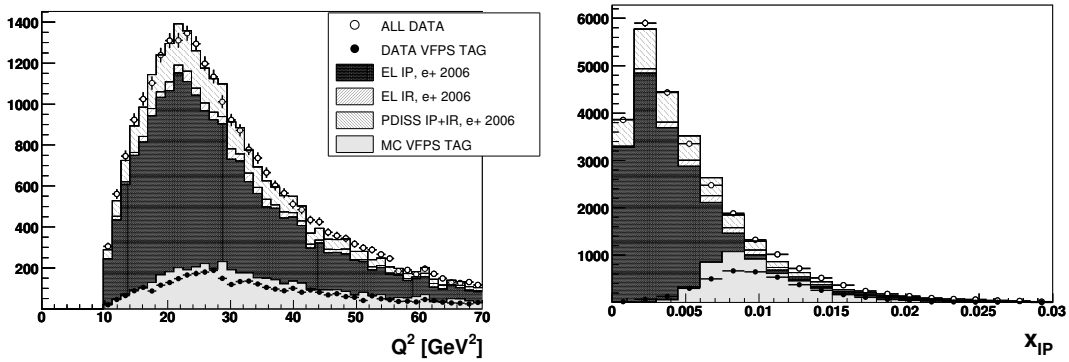

Figure 2: Diffractive events in DIS (empty points) are compared to VFPS tagged events (full points) and to Monte Carlo simulation. **Left:** as a function of Q^2. **Right:** as a function of $x_{I\!P}$. The Monte Carlo simulation contains contributions from Pomeron exchange with elastically scattered proton (EP IP), Reggeon exchange with elastically scattered proton (EP IR), Pomeron and Reggeon exchange with proton dissociation (PDISS IP+IR). Among them simulated events tagged by the VFPS are shown (MC VFPS TAG).

A good agreement is found between the full data sample and the Monte Carlo (normalized to the data luminosity). The trend in $x_{I\!P}$ of VFPS tagged sample is described by the Monte Carlo. A more precise understanding of the VFPS acceptance is needed and will lead to a better description in $x_{I\!P}$.

5 Diffractive dijets

Diffractive dijets in DIS

The analysis of diffractive dijets in DIS regime is based on $42.6e^-$ and $54.7e^+$ pb^{-1} taken in 2006. Additionally to the selection applied in the previous section, a requirement of at least two jets (using the Kt algorithm) is asked, with a minimal transverse momentum in the photon-proton frame of $p^*_{T,1} > 5.5GeV$ and $p^*_{T,2} > 4GeV$ respectively for the first and the second jet. The jets are asked to be well contained in the main detector, by requirering $\eta_{j1,j2} \in [-1, 2]$.

The $x_{I\!P}$ distribution is shown in Fig. 3a comparing the full dijet sample and VFPS tagged dijet sample. This plot illustrates the well suited acceptance of the VFPS for the dijets production in diffraction. In Fig. 3b the transverse momentum of the first jet in the laboratory frame is shown. Here again the full dijet sample is compared to the VFPS tagged dijet sample.

Diffractive dijets in photoproduction

To record with a high efficiency diffractive dijet events in photoproduction tagged by the VFPS, a special trigger has been developed. It allows to lower the threshold in jet transverse

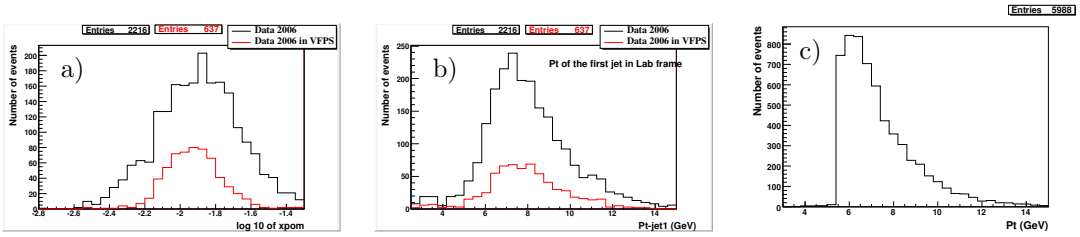

Figure 3: **a)** $x_{I\!P}$ distribution of dijet diffractive events in DIS. The highest histogram corresponds to the full dijet sample and the lowest one to the VFPS tagged dijet sample. **b)** Highest transverse momentum of jets in the laboratory frame of dijet diffractive events in DIS. The highest histogram corresponds to the full dijet sample and the lowest one to the VFPS tagged dijet sample. **c)** Highest transverse momentum of jets in the laboratory frame of dijet VFPS tagged diffractive events in photoproduction.

momentum down to 5 GeV. A luminosity of 23.7 pb^{-1} has been collected in 2006 and 2007 with that trigger corresponding to a selected sample of 6000 events. The selection criteria are the same as in the dijet DIS case except that the scattered electron escapes undetected, at small angle, in the beam pipe. Figure 3c shows the transverse momentum of the first jet in the laboratory frame (equivalent to the photon-proton frame for the transverse direction in the present photoproduction case). The distribution of VFPS tagged events cannot be compared to a full dijet sample as no trigger allowed to keep efficiently those events down to a transverse momentum of 5 GeV.

6 Conclusion

The VFPS has run successfully collecting a luminosity of 140 pb^{-1}. The observed acceptance is high (above 60%) in a region of $x_{I\!P}$ around 10^{-2}. The trend in $x_{I\!P}$ of diffractive events tagged by the VFPS is described by the Monte Carlo simulation. Important statistics have been collected (880,000 diffractive DIS events, 800 dijets diffractive DIS events and 6000 dijets diffractive events in photoproduction) for diffractive structure function measurement and QCD factorisation tests. The proton momentum reconstruction based on VFPS fiber information is still in progress.

References

[1] Slides:
`http://indico.cern.ch/contributionDisplay.py?contribId=96&sessionId=7&confId=9499`

[2] L. Favart, *Experimental review of diffractive phenomena*, in proceedings of the 10$^{\text{th}}$ International Baryons Conference (BARYONS 2004), [hep-ex/0501052].

[3] *Proposal for Installation of a Very Forward Proton Spectrometer in H1 after 2000*, **PRC-01/00**, H1 note **H1-05/00-582**, http://www-h1.desy.de/h1det/tracker/vfps/

[4] *Upgrade of the H1 Forward Spectrometer*, **PRC-96/01**

[5] J. Lukasik, these proceedings.

Status of the Forward Physics Projects in ATLAS

Stefan Ask[1]
(on behalf of the ATLAS Luminosity and Forward Physics Working Group)

1- CERN - Physics Department
CH-1211 Geneva 23 - Switzerland

The ATLAS experiment at the LHC is building several detector systems for forward physics studies and to determine the luminosity. The main forward systems consist of a Cerenkov detector called LUCID, a Zero Degree Calorimeter (ZDC) and Roman Pots which will house a scintillating fiber tracker system called ALFA. Here we report some of the forward physics activities that are foreseen in ATLAS together with the status of the related detector systems.

1 Forward detectors in ATLAS

In addition to the main ATLAS detector, also three smaller systems are built to cover the forward region [2]. These are closely connected to the luminosity determination in ATLAS, but are in addition foreseen to study forward physics. When ordered by their distance from the ATLAS interaction point (IP) the first system is a Cerenkov detector called LUCID. LUCID is the main luminosity monitor in ATLAS and is located 17 m away from the IP. The second system is the so-called *zero degree calorimeter* (ZDC) which is located at a distance of 140 m from the IP. This corresponds to the location where the LHC beam-pipe is divided into two and the ZDC is located between the beam pipes just after the split inside the so-called TAN absorber. The most remote system is the so-called ALFA system. ALFA consists of scintillating fiber trackers located inside roman pots at a distance of 240 m from the ATLAS IP. All results presented below are preliminary.

ATLAS also foresee upgrades of the roman pot program with stations at 220 m and 420 m dedicated entirely to diffractive physics, however, the status of these projects are presented by C. Royon [3] and A. Pilkington [4] at this conference.

2 The ALFA system

The ALFA (*Absolute Luminosity For ATLAS*) system consists of scintillating fiber trackers located in roman pots at a distance of 240 m on each side of the IP. The roman pots allow the detectors to approach the beam inside the LHC beam-pipe and the main purpose of ALFA is to measure elastic proton scattering at low angles. This is primarily to determine the absolute luminosity in ATLAS, but also other physics studies are foreseen such as measuring the total pp cross section, measuring elastic scattering parameters and potentially also to tag protons for diffractive studies.

For a maximum precision in the luminosity measurement, the goal is to measure elastic scattering in the Coulomb interference region, which requires a measurement of scattering angles down to about 3 μrad. In order to reach such small angles, the LHC has to run with special so-called high β^* optics, but even with this optics the detectors have to be located at a distance of only $1-2$ mm from the beam. The main requirements on the tracker are, a spatial resolution of about 30 μm, no significant non-active edge region, insensitivity to

the RF from the LHC beam and to the vacuum in the roman pot. The high β^* runs have a very low luminosity and for this reason no radiation hard technology have to be adopted.

Due to these requirements, ATLAS has chosen a scintillating fiber tracker. Prototype detectors of the ALFA tracker have been validated in beam tests at DESY [5] and CERN together with the front-end electronics and the so-called overlap detector alignment system. The tests have shown an adequate performance for the luminosity measurement and the full ALFA system is foreseen to be installed in the shutdown between 2008 and 2009.

In parallel to the detector development, the measurement of elastic scattering have been carefully simulated. The primary analysis is based on a fit of the differential cross section of elastic scattering (simplified below),

$$\frac{dN}{dt} = L \cdot \pi \left| -\frac{2\alpha}{|t|} + \frac{\sigma_{tot}}{4\pi}(i+\rho)e^{-B|t|/2} \right|^2$$

$$t = -(p \cdot \sin\theta)^2$$

to the t-distribution of the data. Figure 1 shows the reconstructed t-distribution from simulations of the ALFA measurement. As seen in the plot, the acceptance covers the interference region where the EM contribution becomes significant and give rise to the steeper slope at low t-values. Several systematic errors have been studied, for example due to beam properties, detector acceptance, alignment and background. The precision of the luminosity measurement from the fit is estimated to be $\mathcal{L} \pm 2\%(stat) \pm 2\%(syst)$. Also alternative methods to determine the luminosity are foreseen such as using the optical theorem.

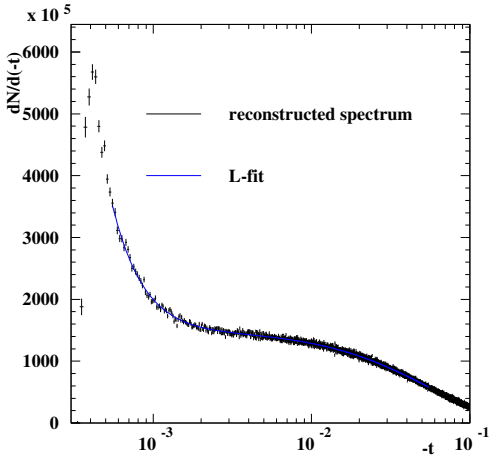

Figure 1: Simulation of the reconstructed $|t|$-distribution from the ALFA measurement.

The fit allows a measurement of the total pp cross section (σ_{tot}), the nuclear slope parameter (B) and the ratio of the real and imaginary part of the nuclear amplitude (ρ). The current results only includes statistical errors, but these indicates that the listed parameters will be possible to measure with a precision of the order of 1%, 0.5% and 4% respectivelly.

3 The LUCID system

LUCID (*LUminosity measurement using Cerenkov Integrating Detector*) is the main luminosity monitor in ATLAS. Its main purpose is to detect inelastic pp scattering in the forward direction, both in order to measure the integrated luminosity of the ATLAS runs and for on-line monitoring of the instantaneous luminosity and beam conditions. Potentially LUCID could also be used for diffractive studies, e.g. as a rapidity gap veto.

The luminosity monitoring is based on the fact that the inelastic pp rate (R_{pp}) seen by LUCID is proportional to the luminosity,

$$R_{pp} = \mu_{LUCID} \cdot f_{BC} = \sigma_{inel} \cdot \varepsilon_{LUCID} \cdot \mathcal{L}$$

Here the mean number of inelastic *pp* interactions per bunch crossing (BC) seen by LUCID, μ_{LUCID}, is related to the luminosity (L) by the inelastic cross section (σ_{inel}) and the LUCID detection efficiency (ε_{LUCID}). In this equation f_{BC} represent the bunch crossing rate. The value of μ_{LUCID} can be measured by LUCID in several ways [6],

- Zero Counting: $\mu_{LUCID} = -ln(N_{ZeroBC}/N_{TotBC})$
- Hit Counting: $\mu_{LUCID} = \langle N_{Hits/BC}\rangle / \langle N_{Hits/pp}\rangle$
- Particle Counting: $\mu_{LUCID} = \langle N_{Particles/BC}\rangle / \langle N_{Particles/pp}\rangle$.

The first method determines μ_{LUCID} from the ratio between the number of non-colliding BCs and the total number of BCs. The two following methods in principle determine μ_{LUCID} from the ratio of the mean number of particles per BC and the mean number of particles per inelastic interaction, both seen by LUCID. Hit counting normally refers to particle counting, but where the counting capability of the detector is limited by its granularity.

The main requirements of the corresponding detector system are, an acceptance to minimum bias events, sufficient time resolution to measure individual BCs and being capable of counting particles. For this purpose ATLAS has chosen the LUCID detector which consists of aluminum tubes filled with C_4F_{10} surrounding the beam-pipe and which are pointing at the ATLAS IP. The Cerenkov light emitted by a transversing particle is reflected down the tube and read-out by PMTs. The signal amplitude from the PMTs can be used to distinguish the number of particles per tube and the fast time response allows to measure individual BCs. A small scale LUCID, dedicated purely to luminosity monitoring, has been validated in testbeams and will be installed for the start up of the LHC. Based on the performance of the initial detector an optimized upgrade, including a large number of tubes, is foreseen to be installed at the same time as the upgrade of the LHC for the nominal luminosity of $\mathcal{L} = 10^{34}\ cm^{-2}s^{-1}$.

For the luminosity measurement, the general calibration strategy of LUCID is to run in parallel with an absolute measurement of the luminosity at the ATLAS IP. Initially this will most likely be obtained from the LHC machine parameters with an expected precision of about 10-15%. This will hopefully be improved in the medium term by studies of well known physics processes, like for example W or Z production as discussed in [7] at this conference. When the ALFA measurement is available this will be the main reference for calibration. In this scenario the parallel measurement of μ_{LUCID} and L will be made at optimal conditions for the absolute method (which provides L). The calibration constant, containing σ_{inel} and ε_{LUCID}, can then be determined, allowing the LUCID measurement to directly provide the luminosity at different conditions.

4 The ZDC system

The third forward system in ATLAS is the *zero degree calorimeter*, which will measure neutral particles at a 0° polar angle. The ZDC has a central role in the ATLAS heavy ion (HI) program where it is used to measure the centrality of the collisions, the luminosity as well as to provide triggers. It will, however, also be of importance both in the *pp* program as described below and for accelerator tuning where it can be used to determine the location of the IP and the beam crossing angle.

The ATLAS ZDC consists of six tungsten/quartz calorimeter modules where the light from the quartz fibers is read-out by PMTs. In addition the ZDC is equipped with horizontal quartz rods, parallel to the beam, in order to determine the location of the showers in the

plane perpendicular to the beam. The ZDC has been extensively tested and will be installed at the start up of the LHC. An upgrade is foreseen after about one year of running when additional space in the TAN absorber will become available.

In the HI runs the main purpose of the ZDC is to measure the spectator neutrons. These are remnants of the collision and provides information about both the magnitude and direction of the impact parameter. In addition, the ZDC have close to a 100% acceptance for HI collisions and together with the well known cross section of neutral particles at a zero degree angle the luminosity can be determined to a precision better than 5%. It was also shown at RHIC that neutron tagging with the ZDC was essential to design a low rate trigger for ultra-peripheral events.

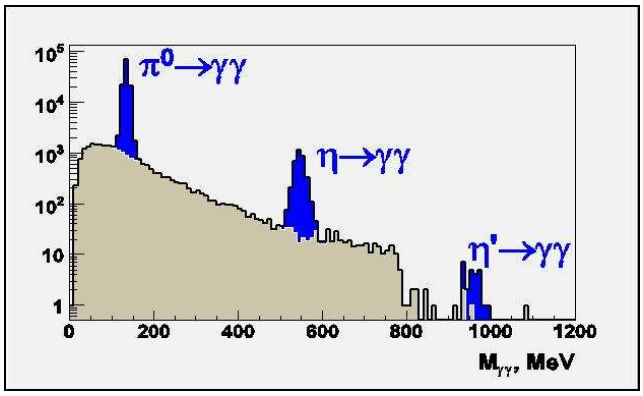

Figure 2: Simulated invariant mass spectrum as measured by the ZDC.

In the ATLAS *pp* program the ZDC will mainly be used to study forward particle production. Figure 2 shows a simulated invariant mass spectrum as measured by the ZDC. Several meson peaks are clearly visible and also other mesons and baryons can be reconstructed. The cross section measurements of particles in the forward direction at the LHC energy is of interest for several applications. For example the measurement is of large interest to the high energy cosmic ray community where the information is required to properly model air showers from high energy protons entering the atmosphere, where the proton energy at the LHC, $E_{lab} = 10^{17}\ eV$, is just below the *knee* in the cosmic ray energy spectrum. In addition the ZDC will add to the overall hermeticity of ATLAS which will be useful to suppress background in diffractive studies.

References

[1] Slides:
`http://indico.cern.ch/contributionDisplay.py?contribId=97&sessionId=7&confId=9499`

[2] *ATLAS Forward Detectors for Measurement of Elastic Scattering and Luminosity Determination*, ATLAS TDR, in preparation;
ATLAS Forward Detectors for Luminosity Measurement and Monitoring, CERN-LHCC/04-10, LHCC I-014;
Zero Degree Calorimeters for ATLAS, CERN-LHCC/07-01, LHCC I-016.

[3] *High mass diffractive physics at the LHC*, C. Royon at this conference.

[4] *Status of FP420 R&D project*, A. Pilkington at this conference.

[5] S. Ask *et al.*, Nucl. Instr. and Meth. A 568 (2006) 588-600.

[6] S. Ask, ATL-LUM-PUB-2006-001.

[7] *Precision PDF measurements at the LHC*, A. Cooper-Sarkar at this conference.

Status of Forward Physics Projects at CMS

Kerstin Borras
on behalf of the CMS Collaboration

Deutsches Elektronen-Synchrotron (DESY)
Notkestrasse 85, 22603 Hamburg - Germany

New experiments with detectors in the forward region with an unprecedented coverage of phase space are on the verge of opening a new eara for forward physics at the high energy frontier. The detector components of the CMS experiment are described as well as briefly the components of the TOTEM experiment. The physics topics achievable with these special detectors are outlined and in few cases discussed in more detail.

1 Introduction

Forward physics is one of the rare high energy physics topics with a very long tradition dating back already to the beginnings of hadron hadron scattering. The reason can be found in the large cross section for soft hadronic interactions, which leads to plenty of data. That forward physics is still a topic for intensive experimental and theoretical studies lies in its predominantly soft structure, which cannot yet be described with the methods of QCD needing a hard scale for perturbative calculations. A lot of progress in the understanding has been achieved by the analysis of semi-hard hadronic interactions, in which the processes still show the characteristic signatures of soft hadronic interactions, like diffraction, but in addition a hard scale is provided by the production of high p_T jets or D^*, being looked at with the data of the running accelerators: ep at HERA, $\bar{p}p$ at TEVATRON or pp at RHIC. In order to understand the questions opened by these data (and even older data) and to pursue the physics understanding into the new kinematic regime of the LHC, several detectors are planned to complement the coverage of the ATLAS and the CMS experiment in the forward region.

2 Detectors in the Forward Region of the CMS Interaction Point

The Interaction Point 5 is the host of the experimental setup for two collaborations as displayed in Figure 1. The CMS detector [2] covers the interaction point with tracking devices up to roughly $|\eta| < 2.5$. This is complemented by calorimetry up to $|\eta| < 3$ and is further extended by the Hadronic Forward calorimeter (HF) in the region of $3 < |\eta| < 5$, by the CASTOR calorimeter in $(5.3 < |\eta| < 6.6)$ and for neutral particles by the Zero Degree Calorimeter (ZDC) starting at about $|\eta| > 8$.

The detectors of the TOTEM experiment [3] complement this calorimetric coverage with tracking stations (T1 and T2) and with the installation of Roman Pot stations at 147m and 220m away from the interaction point.

In addition within the CMS collaboration discussions for the installation of forward proton tagging devices at 420m as proposed and studied by the FP420 Collaboration [4], a joint effort with members from CMS, ATLAS and independent physicists, are underway.

In total this results in an unprecedented coverage of the forward region at hadron colliders and a large variety of phyiscs topics which can be studied with these devices.

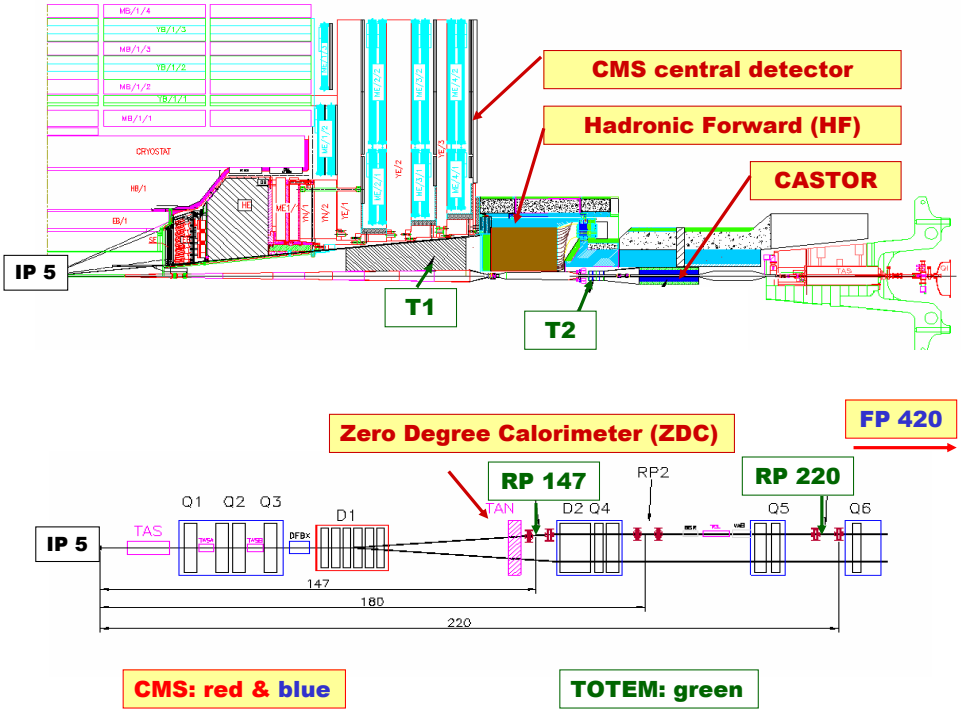

Figure 1: Region around the Interaction Point 5

3 Physics Program

The forward physics program spans a broad range of high energy physics topics from fundamental properties of QCD to new physics phenomena and the precise determination of luminosity. These aspects constitute important ingredients for the discovery of new phenomena and their interpretation, like the crucial understanding of the underlying event structure and multi-parton interactions.

Through the AGK cutting rules [5] three main areas for forward physics are closely related: diffraction, saturation at small x and multi-parton interactions. The AGK cutting rules, steming from early soft hadronic interaction analyses are now under study towards their formulation within the framework of QCD [6].

The prospects for diffractive and forward physics using the devices from the CMS and the TOTEM experiments are summarized in a common CMS and TOTEM note [8]. The experimental issues, the possible measurements and their achievable accuracy for several phyiscs analyses have been studied in more detail in this note.

The following list gives an overview on most of the possible topics of forward physics [7]:

- Diffraction:
  - soft diffraction: rapidity gap survival dynamics, multi-gap events
  - hard diffraction: prodcution of jets, $W, J/\Psi, b, t$, hard photons, study of the partonic structure of the diffractive exchange
  - double pomeron exchange events (gluon factory)
  - diffractive Higgs production
  - SUSY and other (low mass) exotics and exclusive processes.

  The different experimental observables for diffraction are the tagging of forward scattered protons and the detection of so-called rapidity gaps, areas in η devoid of particle production.
  Experimental challenges are given by the trigger thresholds and at higher luminosities by pile-up of events. Diffractive events with a hard scale constitute only a very small fraction of the total high p_T events. Therefore low trigger thresholds are desirable. For the CMS jet trigger, the typical dijet threshold is about 100 GeV per jet at luminosities around $10^{33}\mathrm{cm}^{-2}\mathrm{s}^{-1}$. These can be lowered substantially by adding a request for a track in a Roman Pot of TOTEM at 220m or in FP420. Assuming only about 1% of the total trigger bandwidth for such a dedicated forward detector stream, requiring dijets in combination with a track in the Roman Pots at 220m on one side of the interaction point would allow to lower the dijet threshold to about 40 GeV.
  For central exclusive production of a light Higgs with 120 GeV mass, this would results in a signal efficiency of approximately 10% from the jet trigger, to which another 10% efficiency can be added by triggering on one jet and one muon from the decay of one of the two b quarks. On the Higher Level Trigger, the correlation between the proton momentum loss ξ as measured by the near beam detectors at 220m or 420m, is a powerful tool to further reduce background from non–diffractive QCD dijet production.

- Low–x dynamics:
  - proton structure function, DGLAP/BFKL/CCFM evolution, parton saturation

  Special studies employ jets or Drell-Yan lepton pairs in the forward detectors.

- Multi-parton interactions and underlying event structure:
  In hadron–hadron collisions not only one hard parton–parton interaction can occur, but also additional soft interactions between the partons of the remnants of the beam particles and more hard interactions between the remaining partons. The soft interactions produce a higher energy level in the underlying event, which has to be subtracted when going back from the detector and hadron level to the parton level. The additional hard interactions can lead with standard processes to the same final state particles as looked for in new physics signatures. The final state in $pp \to W + H + X \to l + \nu\ + b\bar{b}\ + X$ can be produced with double parton interactions in one proton–proton collision with $pp \to W + X_W\ + b\bar{b} + X_b$ without any Higgs production. The contribution from multiple-parton interactions have to be understood before the new physics signal can be unfolded from the measurements.
  Predictions for the underlying event and multiple interactions vary quite a lot. In preliminary generator level studies it has been seen, that the forward region is especially sensitive in energy and mean charged particle flow to the different models for underlying event structure and multi-parton interactions [9].

- Measurements for Cosmic Ray Physics Model validation:
  At the LHC, energies corresponding to the order of 100 PeV in the fixed target frame are available and the analysis of energy and particle flow in the forward detectors will provide distinctive information for the validation of hadronic shower modeling in cosmic ray data.
- Photon-proton and photon-photon physics
- Forward physics in heavy ion (pA and AA) collisions
  - parton saturation, new phenomena (Centauro's, Strangelets...)
- Luminosity determination with QED processes ($pp \to ppee$, $pp \to pp\mu\mu$)

The study of elastic scattering and a precise measurement of the total cross section will be performed by the TOTEM collaboration.

In summary the CMS forward detectors provide the possibility for a rich program of forward physics. In conjunction with the tracking devices of TOTEM and FP420 the program comprises a large variety of physics topics for low luminosities, for example with rapidity gap selection for diffraction and underlying event structure/multi-parton interaction studies without pile-up, up to highest luminosities with discovery potential through central exclusive production of light Higgs or SUSY particles.

Acknowledgments

It is a pleasure to thank the organizers for the enjoyable conference. Special thanks are going to Monika Grothe and Hannes Jung for detailed discussions.

References

[1] Slides: `http://indico.cern.ch/contributionDisplay.py?contribId=98&sessionId=7&confId=9499`

[2] CMS Collaboration, *The CMS Physics Technical Design Report, Volume 1*, CERN-LHCC-2006-001 (2006).

[3] TOTEM Collaboration, *Technical Design Report*, CERN-LHCC-2004-002 (2004), and references therein.

[4] FP420 Collaboration, *FP420: A proposal to investigate the feasibility of installing proton tagging detectors in the 420m region of the LHC*, CERN-LHCC-2005-025 (2005).
and A. Pilkington in this conference:
`http://indico.cern.ch/contributionDisplay.py?contribId=99&sessionId=7&confId=9499`

[5] V.A. Abramowsky, V.N. Gribov, O.V. Kancheli, Sov. J. Nucl. Phys. 18 (1974), 308.

[6] J. Bartels, H. Kowalski, A. Sabio-Vera, HERA–LHC Workshop, arXiv:hep-ph/0601012/13 (2006).

[7] CMS Collaboration, Expression of Interest submitted to the LHCC Meeting in January 2004 (2004).

[8] CMS Collaboration, TOTEM Collaboration, *Prospects for Diffractive and Forward Physics at the LHC*, CERN-LHCC-2006-039/G-124 (2006), CMS Note-2007/002, TOTEM Note 06-5.

[9] K.Borras for the SMIX Initiative, HERA–LHC Workshop 2007,
`http://indico.cern.ch/materialDisplay.py?contribId=137&;sessionId=24&;materialId=slides&;confId=11784`.

Status of the FP420 Project at the LHC

Andrew D Pilkington *

Department of Physics and Astronomy, The University of Manchester,
Manchester M13 9PL, UK.

A brief motivation for the installation of forward detectors in the 420m region from the ATLAS/CMS detectors is presented and the status of the FP420 R&D project is reviewed.

1 Introduction

FP420 is an R&D collaboration that proposes to install forward detectors 420m either side of the interaction point at ATLAS and/or CMS [2]. The purpose of the detectors is to tag the protons from the central exclusive process $pp \to p + X + p$ [3], where X is a centrally produced system separated by a large rapidity gap from the outgoing protons. For central masses of approximately 120 GeV, the protons typically emerge from the beam in the large dispersion region at 420m from the interaction point. This makes FP420 a desirable upgrade for light Higgs boson searches at the LHC.

The central exclusive process is attractive for two reasons . Firstly, the protons are typically scattered through small angles and, to a good approximation, the central system is produced in a 0^{++} state. This allows the determination of the quantum numbers of any observed resonance. Secondly, because of the *exclusive* nature of the event, the mass of the central system can be reconstructed from just the outgoing proton momenta using the so-called missing mass method [4]. This allows the mass of any resonance to be determined to an accuracy of approximately 2 GeV, regardless of the decay mode of the particle.

The focus of attention in this area has been on the discovery of a Higgs boson at the LHC. The CEP Standard Model Higgs boson is predicted to be observed with 30 fb^{-1} of delivered luminosity in the WW* channel if the Higgs boson has a mass of $140 < M_h < 200$ GeV [5]. The $b\bar{b}$ decay channel of a Higgs boson has also attracted a great deal of interest because the QCD $b\bar{b}$ background is strongly suppressed by the spin-selection rules. Recently, high tanβ MSSM scenarios have been investigated with the conclusion that the $b\bar{b}$ channel will be observable up to $m_h \sim 160$ GeV. For such scenarios, the Higgs boson will be observed at the LHC (and possibly the Tevatron) in the $\tau\tau$ decay channel. However, the excellent mass resolution of FP420 would provide additional insight into the observations. Finally, the possibility of investigating the CP structure of the Higgs sector is possible at the LHC by measuring the azimuthal asymmetries of the outgoing protons [6]. Such a measurement was previously thought to possible only at a linear collider.

The proposal of FP420 has been boosted by the indication that the exclusive process is currently being observed in the CDF data. Using the Khoze, Martin and Ryskin (KMR) calculation for central exclusive production on which the majority of LHC predictions are based [7], it was predicted in [8] that an excess of events would be obervable in the DPE di-jet data at CDF. Preliminary results imply that this is in fact the case [9]. Furthermore, and significantly, CDF observe a reduction in the fraction of c and b-quark jets in the region where the excess exists. This is a direct prediction of the KMR model. CDF have also

*On behalf of FP420.

performed a search for central exclusive $\gamma\gamma$ production and observe 2 candidate events [10], which is also consistent with the KMR predictions.

2 FP420

FP420 is a magnetic spectrometer. The protons that emerge from the beam in the 420m region are tagged and the position of the proton relative to the beam depends primarily on the fractional momentum loss of the proton during the interaction. Detailed investigation has been carried out using chromaticity grids to relate the position and angle of the proton measured by FP420 to the energy and angle of the proton at the interaction point.

The first task of FP420 was to design a new 15m section to replace the interconnection cryostat in the 420m region. This interconnection cryostat, which will be present at the start-up of the LHC, is responsible for providing the continuity of the 2K beam pipes, the insulation vacuum, the electrical power, the cryogenic circuits and the thermal and radiation shielding. This continuity must be retained, whilst providing access to warm beam pipes. The re-design has been achieved mainly by using existing LHC components.

The proton position measurements will be made by two 3D silicon detector stations placed at each end of the FP420 region. 3D silicon is radiation hard and capable of withstanding the large particle fluxes that will be experienced by FP420. Furthermore, with the 3D silicon design, there is only a 5μm dead region allowing proton measurements with an almost edgeless detector. The position measurement within the silicon can be made to 10μm. The readout of the 3D silicon readout is achieved by using the standard ATLAS pixel readout chips.

The detectors will be moved closer to the beam once the beam has stabilised. The chosen movement mechanism is the Hamburg pipe, with the detectors rigidly fixed to the side of the beampipe and the pipe itself moved to place the detectors near to the beam. The standard beam pipe is replaced by a beam pipe with a pocket, to which the detector stations are attached. This allows the protons to pass through a small window of approximately 300μm, which reduces the probability of particle showering. The measurement of the detector station position relative to the beam will be made with beam positioning monitors (BPMs). It is expected that this measurement will be accurate to 50μm and benchtests are currently being performed. Investigations into the electromagnetic interaction between the beam and the re-shaped beam pipe have been completed [11]. A series of benchtests and simulations were performed, with the conclusion that the installation of FP420 will have a negligible contribution to the total impedance budget of the LHC.

The detector stations will be instrumented with quartz and gas Cherenkov timing detectors, which are capable of measuring the proton time-of-flight to an accuracy of 10ps. This enables an event vertex to be reconstructed from the difference in proton time of flight. The vertex reconstruction is necessary to remove backgrounds from events constructed from more than one proton-proton interaction. The vertex of the hard scatter can be matched to the vertex reconstructed from the proton TOF and it is expected that 95% of backgrounds from the pile-up of proton-proton interactions can be rejected by this technique.

Finally, studies into machine induced backgrounds from beam-halo, beam-gas and secondary showering have been performed. Beam-halo backgrounds from both betatron and momentum collimation have been investigated, with the conclusion that the proton rate is negligible if the detectors are approximately 5mm from the beam. The background from proton hits in FP420 from beam-gas inelastic scattering has also been found to be negligi-

ble. Secondary showering occurs due to proton transport from the interaction point. The protons interact with machine elements upstream of the detectors and produce a shower of particles (mainly neutrons and photons) in the FP420 detectors. The background rate from secondary showers is currently under investigation.

3 Summary

Instrumenting the LHC with forward detectors capable of measuring proton from central exclusive production can extend the physics potential of the ATLAS and CMS detectors. The FP420 R&D project to install such detectors is progressing well with many technical issues overcome. Studies are ongoing and those completed indicate that the search for central exclusive production is achievable at the LHC.

References

[1] Slides:
`http://indico.cern.ch/contributionDisplay.py?contribId=99&sessionId=7&confId=9499`

[2] B. E. Cox, arXiv:hep-ph/0609209.

[3] A. De Roeck, V. A. Khoze, A. D. Martin, R. Orava and M. G. Ryskin, Eur. Phys. J. C **25** (2002) 391 [arXiv:hep-ph/0207042].

[4] M. G. Albrow and A. Rostovtsev, arXiv:hep-ph/0009336.

[5] B. E. Cox *et al.*, Eur. Phys. J. C **45**, 401 (2006) [arXiv:hep-ph/0505240].

[6] J. R. Ellis, J. S. Lee and A. Pilaftsis, Phys. Rev. D **71**, 075007 (2005) [arXiv:hep-ph/0502251].

[7] J. R. Forshaw, arXiv:hep-ph/0508274.

[8] B. E. Cox and A. Pilkington, Phys. Rev. D **72**, 094024 (2005) [arXiv:hep-ph/0508249].

[9] C. Mesropian [CDF Collaboration] DIS2007, these proceedings.

[10] T. Aaltonen *et al.* [CDF Collaboration], arXiv:0707.2374 [hep-ex].

[11] Appleby, Jones and Roncarolo, *Beam coupling impedance simulations and measurements for the LHC FP420 detector*, PAC07 Conf. Proc. Albequeque, US, June 25-29 2007.

Project to Install Roman Pot Detectors at 220 m in ATLAS

Christophe Royon *

DAPNIA/Service de physique des particules,
CEA/Saclay, 91191 Gif-sur-Yvette cedex

We give a short description of the project to install roman pot detectors at 220 m from the interaction point in ATLAS. This project is dedicated to hard diffractive measurements at high luminosity.

1 Introduction

The motivation to install roman pot detectors at 220 m within ATLAS is quite clear. It extends nicely the project of measuring the total cross sections using roman pots at 240 m [2] by measuring hard diffraction at high luminosity in ATLAS in the LHC. As we will see in the following, it is also complementary to the FP420 project which aims at tagging protons at 420 m.

The physics motivation of this project corresponds to different domains of diffraction:

- A better understanding of the inclusive diffraction mechanism at the LHC by studying in detail the structure of pomeron in terms of quarks and gluons as it was done at HERA [3]. Of great importance is also the measurement of the exclusive production of diffractive events [4] and its cross section in the jet channel as a function of jet transverse momentum. Its understanding is necessary to control the background to Higgs signal.
- Looking for Higgs boson diffractive production in double pomeron exchange in the Standard Model or supersymmetric extensions of the Standard Model [5]. This is clearly a challenging topic especially at low Higgs boson masses where the Higgs boson decays in $b\bar{b}$ and the standard non-diffractive search is possible. We will detail in the following the trigger strategy.
- Sensitivity to the anomalous coupling of the photon by measuring the QED production cross section of W boson pairs. This might be the best way to access the anomalous coupling before the start of the ILC.
- Photoproduction of jets
- Other topics such as looking for stop events or measuring the top mass using the threshold scan method [6] which will depend strongly on the production cross section.

2 Roman pot design and location

We propose to install roman pots in ATLAS at 216 and 224 m on each side of the main ATLAS detectors. The project is a collaboration between the physics institutes and universities of Prague, Cracow, Stony Brook, Michigan State University, LPNHE (Paris 6), Giessen, and

*On behalf of the RP220 Collaboration

in addition the University of Chicago and the Argonne National Laboratory for the timing detectors.

The roman pot design follows as close as possible the design which is currently used by the TOTEM collaboration and the Luminosity group of the ATLAS collaboration which aims at measuring the total cross section using roman pots at 240 m. The only difference is that we only need the horizontal arms and not the vertical arms since hard diffractive protons are scattered horizontally. We will follow the TOTEM experience to build the roman pots in Vakuum Praha and to use the same technics for the step motors and the LVDT system.

Assuming one can go down to 10 (resp. 15) σ from the beam center, it is possible to measure protons with $\xi > 0.01$, and $\xi > 0.012$ on each side of ATLAS (resp. $\xi > 0.014$, $\xi > 0.016$) where ξ is the momentum fraction of the initial proton carried away by the Pomeron [7]. This can be translated in missing mass acceptance as illustrated in Fig 1. The missing mass acceptance using only the 220 m pots starts at 135 GeV, but increases slowly as a function of missing mass. It is clear that one needs both FP420 and RP220 projects, or in other words the possibility to detect scattered protons at 220 and 420 m to obtain a good acceptance on a wide range of masses since most events are asymmetric (one tag at 220 m and another one at 420 m). The precision on mass reconstruction using either two tags at 220 m or one tag at 220 m and another one at 420 m is of the order of 2-3 % on the full mass range. This shows the advantage of this measurement which allows to give a very good mass resolution on a wide range of masses, and thus to detect Higgs bosons at low masses decaying into $b\bar{b}$. The idea is to enhance the signal over background ratio by benefitting from the good resolution of the detectors and the suppression of the b jet background due to the $J_z = 0$ suppression rule for b jet exclusive production.

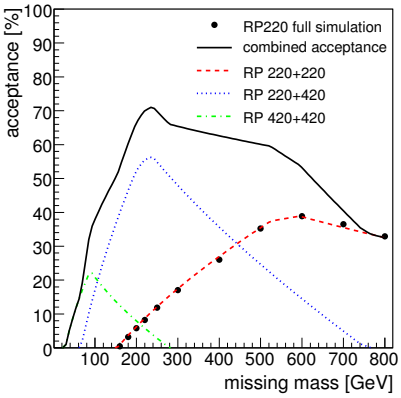

Figure 1: Roman pot detector acceptance as a function of missing mass assuming a 10σ operating positions, a dead edge for the detector of 50 μm and a thin window of 200 μm.

3 Detector inside roman pots

We propose to put inside the roman pots two kinds of detectors, namely Silicon detectors to measure precisely the position of the diffracted protons, and the mass of the produced object, such as the Higgs boson, and ξ, and precise timing detectors.

The position detectors will consist in either five layers of Silicon strips of 50 μm and two additional layers used for triggering, or 3D Silicon detectors if they are available industrially by the time we need to instal the roman pots. If the Silicon strip option is chosen, there will be four different orientations, namely X, Y, U, and V (U and V being orientated within 45 degrees with respect to X and Y). The strip size will be 50 μm and the detector size about 2 cm, which allows a measurement up to $\xi \sim 0.15$. The Silicon strip detectors will be edgeless which means that the dead edge will be of the order of 30-50 μm so that we can move the detector as close to the beam as possible without losing some acceptance due to the dead

edge. The detectors will be read out by the standard ABCNext chip being developped in Cracow for the Silicon detector of ATLAS. The latency time of the ABCNext chip is of the order of 3.5 μs which gives enough time to send back the local L1 decision from the roman pots to ATLAS (see the next paragraph about trigger for more detail), and to receive the L1 decision from ATLAS, which means a distance of about 440 m. It is also foressen to perform a slight modification of the ABCNext chip to include the trigger possibilities into the chip. The other option is to use 3D Silicon detectors using the same readout system as before (ABCNext chip). These detectors use a lateral electric field, instead of vertical in conventional planar techniques. Holes of the order of 10 μm crossing the full thickness of the detector are filled with a conductive medium in order to collect the ionisation (electrons or holes) depending on the applied bias. Both kinds of options will be tested in Prague and in Saclay using the full electronics chain (including the ABCNext chip) and a laser or a radioactive source. Beam tests at DESY or CERN are also foreseen. It is planed to install the roman pot together with the Silicon detectors during a shut down of the LHC in 2009-2010.

The timing detectors are necessary at the highest luminosity of the LHC to identify from which vertex the protons are coming from. It is expected that up to 35 interactions occur at the same bunch crossing and we need to identify from which interaction, or from which vertex the protons are coming from. A precision of the order of a few mm or 5-10 ps is required to distinguish between the different vertices and to make sure that the diffracted protons come from the hard interactions. Picosecond timing detectors are still a challenge and are developped in a collaboration between Saclay, Stony Brook, the University of Chicago and Argonne National Laboratory for medical and particle physics applications. The proton timings will be measured in a crystal of about 2.5 cm located inside the roman pots, and the signal will be read out by Micro-Channel Plates Photomultipliers developped by Photonis. The space resolution of those detectors should be of the order of a few mm since at most two protons will be detected in those detectors for one given bunch crossing at the highest luminosity. The detectors are read out with a Constant Fraction Discriminator which allows to improve the timing resolution significantly compared to usual electronics. A first version of the timing detectors is expected to be ready in 2009-2010 with a worse resolution of 40-50 ps, and the final version by 2012 with a resolution of 5-10 ps.

4 Trigger principle and rate

In this section, we would like to give the principle of the trigger using the roman pots at 220 m as well as the rates obtained using a simulation of the ATLAS detector and trigger framework.

The principle of the trigger is shown in Fig. 2 in the case of a Higgs boson decaying into $b\bar{b}$ as an example. The first level trigger comes directly from two different Silicon strip layers in each roman pot detector. It is more practical to use two dedicated planes for triggering only since it allows to use different signal thresholds for trigger and readout. The idea is to send at most five strip addresses which are hit at level 1. A local trigger is defined at the roman pot level on each side of the ATLAS experiment by combining the two trigger planes in each roman pot and the roman pots as well. If the hits are found to be compatible (not issued by noise but by real protons), the strip addresses are sent to ATLAS, which allows to compute the ξ of each proton, and the diffractive mass. This information is then combined with the information coming from the central ATLAS detector, requesting for instance two

jets above 40 GeV in the case shown in Fig. 2. At L2, the information coming from the timing detectors for each diffracted proton can be used and combined with the position of the main vertex of ATLAS to check for compatibility. Once a positive ATLAS trigger decision is taken (even without any diffracted proton), the readout informations coming from the roman pot detectors are sent to ATLAS as any subdetector.

The different trigger possibilities for the roman pots are given below:

- **Trigger on DPE events at 220 m:** This is the easiest situation since two protons can be requested at Level 1 at 220 m. Three different options are considered:
  - trigger on high mass Higgs ($M > 160$ GeV) given by ATLAS directly (decay in WW, ZZ),
  - inclusive trigger on high mass object by requesting two high p_T jets and two positive tags in roman pots,
  - trigger on jets (high p_T jets given directly by ATLAS, and low p_T jet special trigger for QCD studies highly prescaled).
  This configuration will not rise any problem concerning the L1 rate since most of the events will be triggered by ATLAS anyway, and the special diffractive triggers will be for QCD measurements and can be highly prescaled.
- **Trigger on DPE events at 220 and 420 m** This is the most delicate scenario since the information from the 420 m pots cannot be included at L1. The strategy is the following (see Table 1):
  - trigger on heavy objects (Higgs...) decaying in $b\bar{b}$ by requesting a positive tag (one side only) at 220 m with $\xi < 0.05$ (due to the 420m RP acceptance in ξ, the proton momentum fractional loss in the 220m roman pot cannot be too high if the Higgs mass is smaller than 140 GeV) , and topological cuts on jets such as the exclusiveness of the process $((E_{jet1} + E_{jet2})/E_{calo} > 0.9$, $(\eta_1 + \eta_2) \cdot \eta_{220} > 0$, where $\eta_{1,2}$ are the pseudorapidities of the two L1 jets, and η_{220} the pseudorapidity of the proton in the 220m roman pots). This trigger can hold without prescales to a luminosity up to 2.10^{33} cm^{-2}s^{-1},
  - trigger on jets (single diffraction, or double pomeron exchange) for QCD studies: can be heavily prescaled,
  - trigger on W, top... given by ATLAS with lepton triggers.
  Let us note that the rate will be of the order of 1 Hz at L2 by adding a cut on a presence of a tag in the 420 pots, on timing, and also on the compatibility of the rapidity of the central object computed using the jets or the protons in roman pots.

$\mathcal{L}$ $E_T > 40$ GeV	n_{pp} per bunch crossing	2-jet rate [kHz] [cm$^{-2} \cdot$ s^{-1}]	RP200 reduction factor	$\xi < 0.05$ reduction factor	Jet Prop.
1×10^{32}	0.35	2.6	120	300	1200
1×10^{33}	3.5	26	8.9	22	88
2×10^{33}	7	52	4.2	9.8	39.2
5×10^{33}	17.5	130	1.9	3.9	15.6
1×10^{34}	35	260	1.3	2.2	8.8

Table 1: L1 rates for 2-jet trigger with $E_T > 40$ GeV and additional reduction factors due to the requirement of triggering on diffractive proton at 220 m, and also on jet properties.

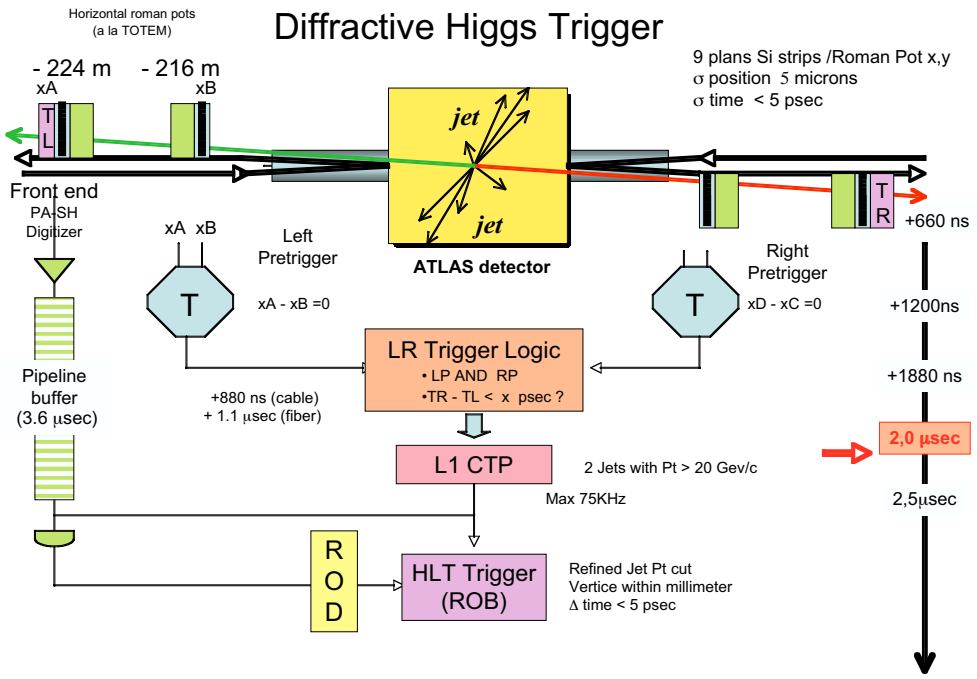

Figure 2: Principle of the L1 trigger using roman pot detectors at 220 m in the case of a Higgs boson decaying into $b\bar{b}$.

In this short report, we described the main aspects of the project to install roman pots at 220 m within ATLAS: Silicon detectors, measurement of the proton timings, and the trigger properties. This project is aimed to be proposed to ATLAS and the LHCC together with the FP420 one.

References

[1] Slides: `http://indico.cern.ch/contributionDisplay.py?contribId=100&sessionId=7&confId=9499`

[2] ATLAS luminosity project,
`http://atlas-project-lumi-fphys.web.cern.ch/atlas-project-lumi-fphys/`

[3] C. Royon, L. Schoeffel, R. Peschanski and E. Sauvan, Nucl. Phys. B **746** (2006) 15; C. Royon, L. Schoeffel, S. Sapeta, R. Peschanski and E. Sauvan, arXiv:hep-ph/0609291 and references therein.

[4] O.Kepka, C. Royon, preprint arXiv:0704.1956

[5] M. Boonekamp, R. Peschanski and C. Royon, Phys. Lett. **B598** (2004) 243; M. Boonekamp, A. De Roeck, R. Peschanski and C. Royon, Phys. Lett. **B 550** (2002) 93; V. A. Khoze, A. D. Martin and M. G. Ryskin, Eur. Phys. J. **C23** (2002) 311, Eur. Phys. J. **C24** (2002) 581.

[6] M. Boonekamp, J. Cammin, S. Lavignac, R. Peschanski and C. Royon, Phys. Rev. **D 73** (2006) 115011

[7] ATLAS note about RP220 project, to be submitted

Diffraction and Vector Mesons

Spin Physics

Exclusive Meson Production at NLO

Markus Diehl and Wolfgang Kugler

Deutsches Elektronen-Synchroton DESY
22603 Hamburg, Germany

We report on numerical studies of the NLO corrections to exclusive meson electroproduction, both in collider and fixed-target kinematics. Corrections are found to be huge at small x_B and sizeable at intermediate or large x_B.

1 Motivation and general framework

Generalized parton distributions (GPDs) are a versatile tool to quantify important aspects of hadron structure in QCD. They contain unique information on the spatial distribution of partons [1] and on the orbital angular momentum they carry in the proton [2]. The theoretically cleanest process where GPDs can be studied is deeply virtual Compton scattering (similar to inclusive DIS, which plays a dominant role in constraining the usual parton densities). Hard exclusive meson production is harder to describe quantitatively, but it provides opportunities to obtain important complementary constraints. In particular, vector meson production is more directly sensitive to the gluon distributions, which enter the Compton amplitude only at next-to-leading (NLO) order in α_s. Together with a wealth of high-quality data [3], this warrants efforts to bring meson production under theoretical control as much as possible.

In the present contribution [4] we investigate exclusive ρ production ($\gamma^* p \to \rho p$) using collinear factorization, which is applicable in the limit of large photon virtuality Q^2 at fixed Bjorken variable x_B and fixed invariant momentum transfer t to the proton [5]. In practical terms, this means that the description is restricted to sufficiently large Q^2 but can be used for both small and large x_B, thus providing a common framework for analyzing both collider and fixed-target data. The process amplitude can then be expressed in terms of GPDs for the proton, the $q\bar{q}$ distribution amplitude for the ρ, and hard-scattering kernels. The kernels are known to NLO, i.e. to order α_s^2 [6].

The requirement of "sufficiently large" Q^2 is demanding for meson production. Contributions that are formally suppressed by powers of $1/Q^2$ cannot be calculated in a completely systematic way, but the estimates [7, 8, 9] agree that for Q^2 of several GeV^2 the effect of the transverse quark momentum inside the meson cannot be neglected in the hard-scattering subprocess, as it is done in the collinear approximation. This effect can be incorporated in the modified hard-scattering picture [7, 8], in color dipole models [9], or in the MRT approach [10]. Unfortunately, the calculation of α_s corrections remains not only a technical but even a conceptual challenge in these approaches, so that the perturbative stability of their results cannot be investigated at present. One strategy in this situation is to study the NLO corrections in the collinear factorization framework, identifying kinematical regions where they are moderate or small. There one may use formulations incorporating power corrections from transverse quark momentum with greater confidence. This is the aim of the present contribution.

In the following we show results for the convolution of the unpolarized quark and gluon GPDs H^q and H^g with the corresponding hard-scattering kernels and the asymptotic form of the ρ distribution amplitude. We model the GPDs using a standard ansatz based on double

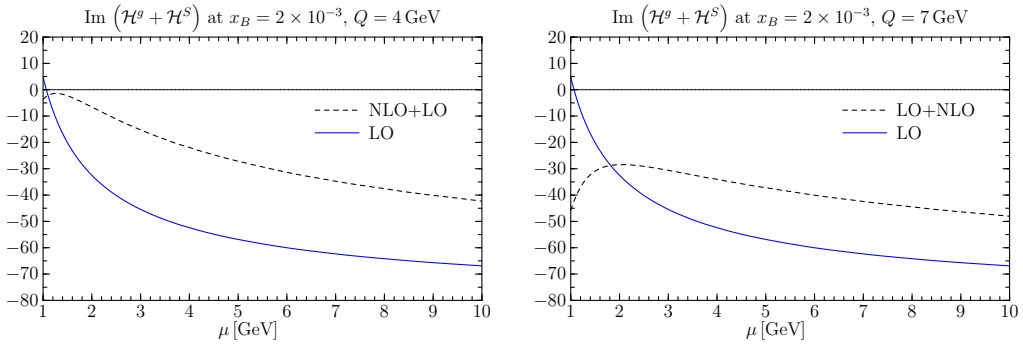

Figure 1: Imaginary part of the convolution integral for the sum of gluon and quark singlet distributions as a function of the renormalization and factorization scale μ.

distributions [11], with the CTEQ6M distributions as input. Unless indicated explicitly, we take $t = 0$ and set the factorization and renormalization scales equal, $\mu = \mu_F = \mu_R$.

2 Numerical results

In a wide kinematical range at small x_B, we find huge NLO corrections which have opposite sign to the Born term and almost cancel it. This is shown for $x_B = 2 \times 10^{-3}$ in Fig. 1, where there are indications for an onset of perturbative stability at $Q = 7\,\mathrm{GeV}$, but not yet at $Q = 4\,\mathrm{GeV}$. Taking $x_B = 2 \times 10^{-4}$ one finds no stability even at $Q = 7\,\mathrm{GeV}$, whereas for $x_B = 2 \times 10^{-2}$ the corrections are of tolerable size already at $Q = 4\,\mathrm{GeV}$.

Figure 2 shows that in kinematics relevant for HERA measurements, NLO corrections have a huge effect on the cross section and moreover lead to a flat energy behavior in conflict with experiment. Due to the strong cancellations between LO and NLO terms, the dependence on factorization and renormalization scale is not reduced when going to NLO.

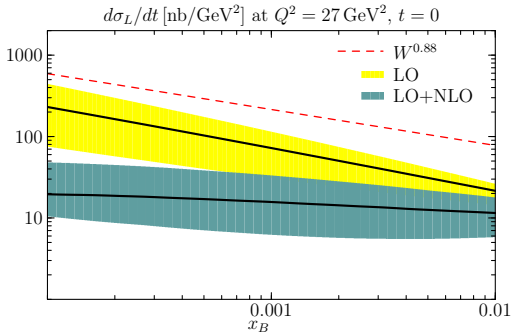

Figure 2: Cross section for $\gamma^* p \to \rho p$ with a longitudinal photon. Bands correspond to the range $Q/2 < \mu < 2Q$ and solid lines to $\mu = Q$. We also show the power-law behavior $\sigma \propto W^{0.88}$ (with arbitrary normalization) obtained from a fit to data in the range $0.001 \lesssim x_B \lesssim 0.005$ [12].

As already observed in [6] the large size of NLO corrections at small x_B can be traced back to BFKL-type logarithms appearing first at NLO for vector meson production. Such logarithms are present in many processes (including DIS) but have a rather large numerical prefactor in the present case. It is to be hoped that all-order resummation of

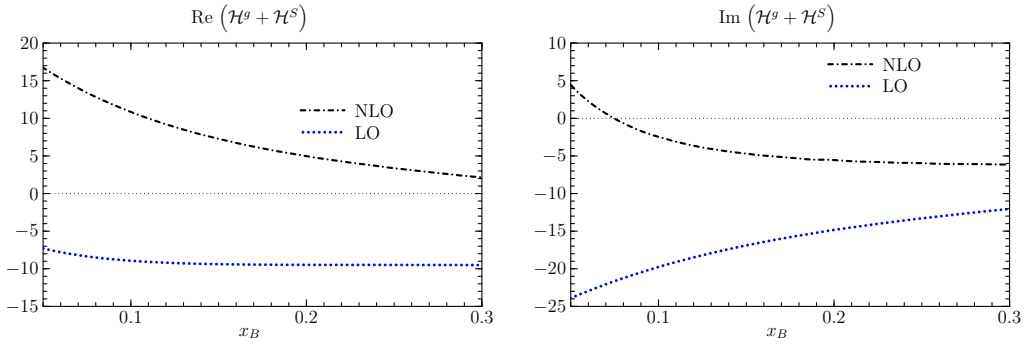

Figure 3: Real and imaginary part of the convolution integral for the sum of gluon and quark singlet distributions for $\mu_F = \mu_R = Q = 2\,\mathrm{GeV}$.

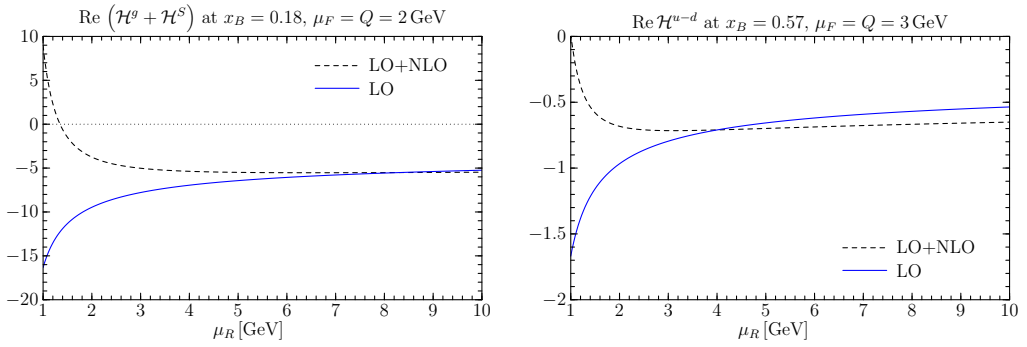

Figure 4: Renormalization scale dependence of the real part of the convolution integrals for the sum of gluon and quark singlet distributions (left) and for for the difference of u and d quark distributions (right).

these logarithms in the hard-scattering kernel will give perturbative stability at small x_B.

In the x_B range relevant for experiments at COMPASS, HERMES, and JLAB, we generally find corrections which are sizable but not huge. An exception is the real part of the gluon and quark singlet amplitudes, where corrections become large for decreasing x_B, as is seen in the left panel of Fig. 3.

In the quark nonsinglet sector there are large terms in the NLO kernel due to gluon self-energy corrections. The BLM procedure for setting the renormalization scale aims at resumming these to all orders in α_s. Applied to the process at hand, one finds however that this requires μ_R to be typically an order of magnitude smaller than Q [13, 14]. This is outside the validity of the perturbative calculation for most practically relevant Q. Numerically we find that for $\mu_R \lesssim 2\,\mathrm{GeV}$ the NLO corrections become unstable for several convolution integrals, as shown for examples in Fig. 4.

We have therefore omitted this region when estimating the scale setting error in Fig. 5, where we show the cross section in typical fixed-target kinematics. We see that NLO correc-

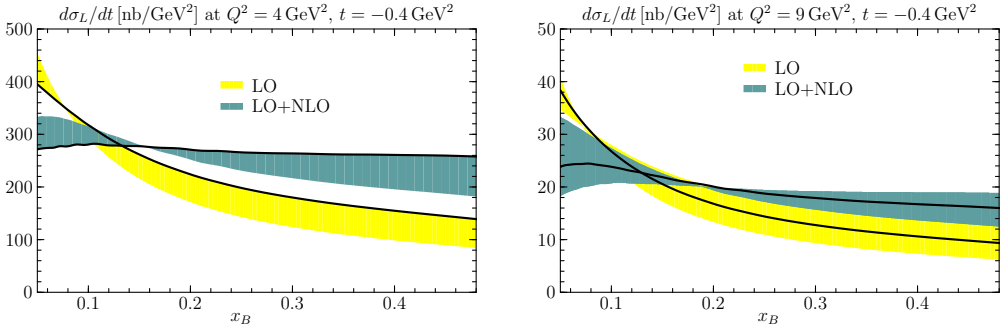

Figure 5: Cross section for $\gamma^* p \to \rho p$ with a longitudinal photon. Bands correspond to the range $2\,\mathrm{GeV} < \mu < 4\,\mathrm{GeV}$ in the left and to $2\,\mathrm{GeV} < \mu < 6\,\mathrm{GeV}$ in the right plot, and solid lines to $\mu = Q$ in both cases.

tions are quite large for $Q^2 = 4\,\mathrm{GeV}^2$, whereas for $Q^2 = 9\,\mathrm{GeV}^2$ and $x_B > 0.1$ they become moderate.

Acknowledgments

We gratefully acknowledge discussions with L. Favart, H. Fischer, D. Yu. Ivanov, A. Rostomyan and A. Schäfer. This work is supported by the Helmholtz Association, contract number VH-NG-004.

References

[1] M. Burkardt, Int. J. Mod. Phys. A **18** (2003) 173 [hep-ph/0207047].
[2] X. D. Ji, Phys. Rev. Lett. **78** (1997) 610 [hep-ph/9603249].
[3] A. Levy, these proceedings.
[4] Slides: `http://indico.cern.ch/contributionDisplay.py?contribId=83&sessionId=12&confId=9499`
[5] J. C. Collins, L. Frankfurt and M. Strikman, Phys. Rev. D **56** (1997) 2982 [hep-ph/9611433].
[6] D. Yu. Ivanov, L. Szymanowski and G. Krasnikov, JETP Lett. **80** (2004) 226 [hep-ph/0407207].
[7] S. V. Goloskokov and P. Kroll, Eur. Phys. J. C **50** (2007) 829 [hep-ph/0611290];
P. Kroll, these proceedings, arXiv:0706.2587 [hep-ph].
[8] M. Vanderhaeghen, P. A. M. Guichon and M. Guidal, Phys. Rev. D **60** (1999) 094017 [hep-ph/9905372].
[9] L. Frankfurt, W. Koepf and M. Strikman, Phys. Rev. D **54** (1996) 3194 [hep-ph/9509311].
[10] A. D. Martin, M. G. Ryskin and T. Teubner, Phys. Rev. D **55** (1997) 4329 [hep-ph/9609448];
T. Teubner, these proceedings.
[11] I. V. Musatov and A. V. Radyushkin, Phys. Rev. **D61** (2000) 074027 [hep-ph/9905376].
[12] ZEUS Collaboration, paper 594 submitted to EPS 2001, Budapest, Hungary,
`http://www-zeus.desy.de/physics/phch/conf/eps01_paper.html`
[13] A. V. Belitsky and D. Müller, Phys. Lett. B **513** (2001) 349 [hep-ph/0105046].
[14] I. V. Anikin *et al.*, Eur. Phys. J. C **42** (2005) 163 [hep-ph/0411408];
S. J. Brodsky and F. J. Llanes-Estrada, Eur. Phys. J. C **46** (2006) 751 [hep-ph/0512247].

Generalized Parton Distributions from Hadronic Observables

S. Ahmad[1], H. Honkanen[1], S. Liuti[1] and S.K. Taneja[2]

1- University of Virginia - Physics Department
382, McCormick Rd., Charlottesville, Virginia 22904 - USA

2- Ecole Polytechnique,
CPHT, F91128 Palaiseau Cedex, France

We propose a physically motivated parametrization for the unpolarized generalized parton distributions, H and E, valid at both zero and non-zero values of the skewness variable, ζ. At $\zeta = 0$, H and E are determined using constraints from simultaneous fits of experimental data on both the nucleon elastic form factors and the deep inelastic structure functions. Lattice calculations of the higher moments constrain the parametrization at $\zeta > 0$. Our method provides a step towards a model independent extraction of generalized distributions from the data that is alternative to the mathematical ansatz of double distributions.

1 Introduction

Generalized Parton Distributions (GPDs) parametrize the soft contributions in a variety of hard exclusive processes, from Deeply Virtual Compton Scattering (DVCS) to hard exclusive meson production (see [2, 3] for reviews). The conceptual idea behind their definition allows one to address a vast, previously inaccessible phenomenology, from the simultaneous description of hadronic structure in terms of transverse spatial and longitudinal momentum degrees of freedom [4], to the the access to the description of angular momentum of partons in nucleons and nuclei via Ji's sum rule [5].

At present, a central issue is the definition of a quantitative, reliable approach beyond the construction of GPDs from specific models and/or particular limiting cases, that can incorporate new incoming experimental data in a variety of ranges of the scale Q^2, and the four-momentum transfer between the incoming and outgoing protons, $\Delta \equiv (t, \zeta)$. The matching between measured quantities and Perturbative QCD (PQCD) based predictions for DVCS should proceed, owing to specific factorization theorems, similarly to the extraction of Parton Distribution Functions (PDFs) from deep inelastic scattering. A few important caveats are however present since GPDs describe *amplitudes* and are therefore more elusive observables in experimental measurements. Experiments delivering sufficiently accurate data have, in fact, just begun [6]. The comparison with experiment and the formulation of parametrizations necessarily encompasses, therefore, other strategies using additional constraints, other than from a direct comparison with the data.

We propose a strategy using a combination of experimental data on nucleon form factors, PDFs, and lattice calculations of Mellin moments with $n \geq 1$. The latter, parametrized in terms of Generalized Form Factors (GFFs), were calculated by both the QCDSF [7] and LHPC [8] collaborations for both the unpolarized and polarized cases up to $n = 3$, therefore allowing to access the skewness dependence of GPDs.

2 Generalized Parton Distributions from Lattice Moments

GPDs can be extracted most cleanly from DVCS [5]. In this contribution we concentrate on the unpolarized scattering GPDs, H, and E, from the vector (γ_μ) and tensor ($\sigma_{\mu\nu}$) interactions, respectively. We adopt the following set of kinematical variables: (ζ, X, t), where $\zeta = Q^2/2(Pq)$ is the longitudinal momentum transfer between the initial and final protons ($\zeta \approx x_{Bj}$ in the asymptotic limit, with Bjorken $x_{Bj} = Q^2/2M\nu$), $X = (kq)/(Pq)$ is the momentum fraction relative to the initial proton carried by the struck parton, $t = -\Delta^2$, is the four-momentum transfer squared. X is not directly observable, it appears in the amplitude as an integration variable [2, 3]. The need to deal with a more complicated phase space, in addition to the fact that DVCS interferes coherently with the Bethe-Heitler (BH) process, are in essence the reasons why it is more challenging to extract GPDs from experiment, wherefore guidance from phenomenologically motivated parametrizations becomes important.

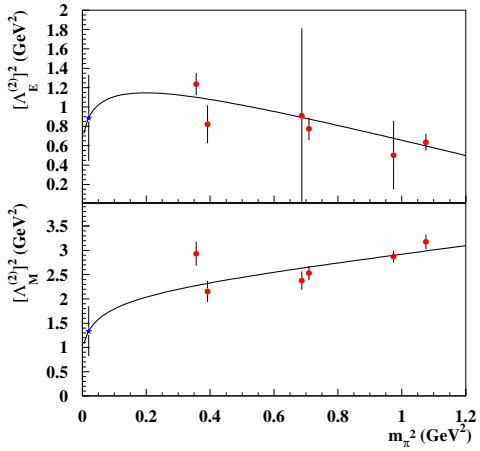

Figure 1: (color online) The dipole masses squared for $n = 2$, for the isovector magnetic (lower panel) and electric (upper panel) contributions obtained by performing fits to the lattice results of [7]. The value at the physical pion mass obtained from our fit is also shown (star).

We first present a parametrization of H and E in the flavor Non Singlet (NS) sector, valid in the $X > \zeta$ region, obtained by extending our previous zero skewness form [9], through proper kinematical shifts:

$$H(X,\zeta,t) = G^{\lambda}_{M_X}(X,\zeta,t)\, R(X,\zeta,t) \tag{1}$$

(a similar form was used for $E(X,\zeta,t)$), where $R(X,\zeta,t)$ is a Regge motivated term describing the low X and t behaviors, while $G^{\lambda}_{M_X}(X,\zeta,t)$, was obtained using a spectator model.

In order to model the $X < \zeta$ region, we observe that the higher moments of GPDs give ζ-dependent constraints, in addition to the ones from the nucleon form factors. The $n = 1, 2, 3$ moments of the NS combinations: $H^{u-d} = H^u - H^d$, and $E^{u-d} = E^u - E^d$ are available from lattice QCD [7, 8]. They can be written in terms of the isovector components as:

$$H_n^{u-d} \equiv \int dX X^{n-1}(H^u - H^d) \;=\; \frac{\tau(H_M^V)_n + (H_E^V)_n}{1+\tau} \tag{2}$$

$$E_n^{u-d} \equiv \int dX X^{n-1}(E^u - E^d) \;=\; \frac{(E_M^V)_n - (E_E^V)_n}{1+\tau}, \tag{3}$$

where the l.h.s. quantities are obtained from the lattice moments calculations, whereas $(H^V_{M(E)})_n$ and $(E^V_{M(E)})_n$ are amenable to chiral extrapolations. We used lattice calculations

for the unpolarized GFFs obtained by the QCDSF collaboration using two flavors of $\mathcal{O}(a)$-improved dynamical fermions for several values of t in the interval $0 \lesssim t \lesssim 5$ GeV^2, and covering a range of pion mass values, $m_\pi \gtrsim 500\,\mathrm{MeV}^2$. Similarly to previous evaluations [8] the GFFs for both H and E, display a dipole type behavior for all three n values, the value of the dipole mass increasing with n. We performed an extrapolation by extending to the $n = 2, 3$ moments a simple ansatz proposed in [10] for the nucleon form factors that: *i)* uses the connection between the dipole mass and the nucleons radius; *ii)* introduces a modification of the non analytic terms in the standard chiral extrapolation that suppresses the contribution of chiral loops at large m_π. Despite its simplicity, the ansatz seems to reproduce both the lattice results trend at large m_π while satisfying the main physical criteria *i)* and *ii)*. Our results for the dipole mass at $n = 2$ are shown in Fig.1.

3 Reconstruction from Bernstein Polynomials

Similarly to the PDFs case [11], with a finite number of moments in hand, one can use reconstruction methods attaining weighted averages of the GPDs, around average ranges of X. The weights are provided by the complete set of Bernstein polynomials.

In Fig.2 we show H^{u-d} reconstructed using the available lattice moments. We performed the procedure in the $X < \zeta$ region only using:

$$\overline{H}_{k,n}(\zeta,t) = \int_0^\zeta H(X,\zeta,t) b_{k,n}(X,\zeta) dX \quad k = 0, ...n, \tag{4}$$

where: $b_{k,n}(X,\zeta) = X^k\,(\zeta - X)^{n-k} / \int_0^\zeta X^k\,(\zeta - X)^{n-k}\,dX$, and we used subtracted moments, defined as:

$$(H_n)_{X<\zeta} = H_n - \int_\zeta^1 H^I(X,\zeta,t) X^n dX, \tag{5}$$

where H_n are the Mellin moments, and $H^I(X,\zeta,t)$ was obtained from Eq.(1). For $n = 2$, $k = 0, 1, 2$, the reconstruction proce-

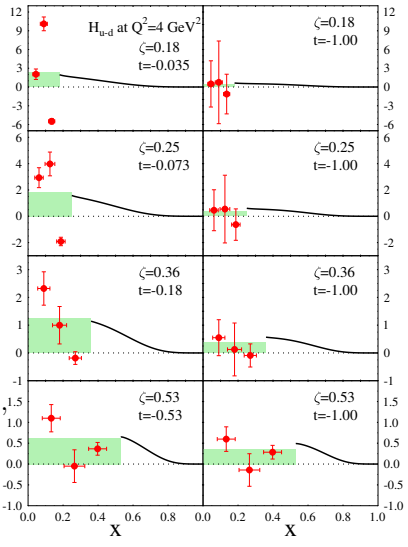

Figure 2: (color online) Comparison of H^{u-d} for different values of $\zeta$and $-t \equiv t_{min} = 0.035, 0.073, 0.18, 0.53$ GeV^2 (left panel), and $-t = -1$ GeV^2 (right panel), calculated using the procedure described in the text.

dure yields [12]:

$$\begin{aligned}
\overline{H}_{02}(\zeta X_{02}) &= \frac{1}{\zeta^3}\left\{3A_{10}^{\zeta}\,\zeta^2 - 6A_{20}^{\zeta}\,\zeta + 3\left[A_{30}^{\zeta} + \left(-\frac{2\zeta}{2-\zeta}\right)^2 A_{32}\right]\right\},\\
\overline{H}_{12}(\zeta X_{12}) &= \frac{1}{\zeta^3}\left\{6A_{20}^{\zeta}\,\zeta - 6\left[A_{30}^{\zeta} + \left(-\frac{2\zeta}{2-\zeta}\right)^2 A_{32}\right]\right\},\\
\overline{H}_{22}(\zeta X_{22}) &= \frac{1}{\zeta^3}\left\{3A_{30} + \left(-\frac{2\zeta}{2-\zeta}\right)^2 A_{32}\right\}, \qquad (6)
\end{aligned}$$

where $X_{01} = 0.25$, $X_{02} = 0.5$, $X_{03} = 0.75$, and $A_{10}, A_{20}, A_{30}, A_{32}$ are the GFFs from Ref.[7].

In conclusion, we provided a fully quantitative parametrization of the NS GPDs, valid in the region of Jefferson Lab experiments [6] that, differently from model calculations, and for the first time to our knowledge, makes use of experimental data in combination with lattice results. Given the paucity of current direct experimental measurements of GPDs, our goal is to provide more stringent, model independent predictions that will be useful both for model builders, in order to understand the dynamics of GPDs, and for the planning of future hard exclusive scattering experiments.

4 Acknowledgments

We thank Ph. Haegler, P. Kroll and G. Schierholz for useful comments. We are also grateful to J. Zanotti for providing us with the recent lattice calculations from the QCDSF collaboration. This work is supported by the U.S. Department of Energy grant no. DE-FG02-01ER41200 and NSF grant no.0426971.

References

[1] Slides: `http://indico.cern.ch/contributionDisplay.py?contribId=90&sessionId=8&confId=9499`

[2] M. Diehl, Phys. Rept. **388**, 41 (2003).

[3] A. V. Belitsky and A. V. Radyushkin, Phys. Rept. **418**, 1 (2005)

[4] M. Burkardt, Int. J. Mod. Phys. A **18**, 173 (2003); *ibid* Phys. Rev. D **62**, 071503 (2000) [Erratum-ibid. D **66**, 119903 (2002)].

[5] X. D. Ji, Phys. Rev. Lett. **78**, 610 (1997) [arXiv:hep-ph/9603249].

[6] C. Munoz Camacho *et al.* [Jefferson Lab Hall A Collaboration], Phys. Rev. Lett. **97**, 262002 (2006)

[7] M. Gockeler *et al.* [QCDSF Collaboration], Phys. Rev. D **73**, 014513 (2006), *and references therein.*

[8] R. G. Edwards *et al.* [LHPC Collaboration], PoS **LAT2005**, 056 (2006) [arXiv:hep-lat/0509185], *and references therein.*

[9] S. Ahmad, H. Honkanen, S. Liuti and S.K. Taneja, Phys. Rev. D **75**, 094003 (2007)

[10] J. D. Ashley, D. B. Leinweber, A. W. Thomas and R. D. Young, Eur. Phys. J. A **19**, 9 (2004).

[11] F.J. Yndurain, Phys. Lett. **74B** (1977) 68.

[12] S. Ahmad, H. Honkanen, S. Liuti and S.K. Taneja, *in preparation.*

Transverse Target-Spin Asymmetry of Exclusive ρ^0 Meson Production on Proton at HERMES

Armine Rostomyan[1] and Jeroen Dreschler[2]
(on behalf of the HERMES collaboration)

1- DESY
22603 Hamburg, Germany
2- NIKHEF
1009 DB Amsterdam, The Netherlands

Preliminary measurements are reported on the azimuthal single-spin asymmetry of exclusive ρ^0 mesons for a transversely polarized hydrogen target at HERMES using the 27.6 GeV HERA positron beam. Within the generalized parton distribution (GPD) formalism, this asymmetry is sensitive to the total angular momentum of quarks and gluons in the nucleon. Since the GPD formalism is only valid for mesons produced by longitudinal photons, the transverse target-spin asymmetry of longitudinal ρ^0 mesons is extracted assuming s-channel helicity conservation and compared to theoretical calculations.

1 Introduction

Hard exclusive meson production in deep inelastic lepton scattering provides access to the unknown generalized parton distributions (GPDs) of the nucleon [2]. For such reactions, it has been shown that for longitudinal virtual photons, the $\gamma^* p$ amplitude can be factorized into a hard lepton-scattering part and two soft parts which parameterize the structure of the nucleon by GPDs and the structure of the produced meson by distribution amplitude [3]. GPDs reflect the 3-dimensional structure of the nucleon and contain information about the total angular momentum carried by partons in the nucleon. Hard exclusive production of ρ^0 mesons is sensitive to the GPDs H and E which are the ones related to the total angular momenta J^q and J^g of quarks and gluons in the nucleon [4]. The GPD H is already somewhat constrained, while the GPD E is still unknown. In the case of a transversely polarized target, the interference between the GPDs H and E was shown to lead to a transverse target-spin asymmetry (TTSA) [5]. In contrast to the cross section measurements, the TTSA depends linearly on the helicity-flip distribution E with no kinematic suppression of its contribution with respect to the other GPDs. Therefore the TTSA of exclusive ρ^0 production can constrain the total angular momenta J^q and J^g.

2 TTSA of longitudinal ρ^0 mesons

For an unpolarized (U) beam and a transversely (T) polarized target the TTSA A_{UT} is defined as

$$A_{UT} = \frac{1}{P_T} \frac{d\sigma(\phi, \phi_s) - d\sigma(\phi, \phi_s + \pi)}{d\sigma(\phi, \phi_s) + d\sigma(\phi, \phi_s + \pi)}, \tag{1}$$

where the target polarization P_T is defined w.r.t. the lepton beam direction and the angles ϕ and ϕ_s are the azimuthal angles of, respectively, the produced ρ^0 meson and the target

spin vector around the virtual photon direction w.r.t. the lepton scattering plane (see Figure 1) [6].

The cross section of exclusive ρ^0 production can be factorized in terms of angular dependent and angle-independent parts:

$$\frac{d\sigma}{dx_B\, dQ^2\, dt'\, d\phi\, d\phi_s} = \frac{1}{4\pi^2}\frac{d\sigma}{dx_B\, dQ^2\, dt'} W(x_B, Q^2, t', \phi, \phi_s), \tag{2}$$

where x_B is the Bjorken scaling variable, Q^2 is the squared virtual-photon four-momentum, $t' = t - t_0$. Here $-t$ is the squared four-momentum transfer to the target and $-t_0$ represents the minimum value of $-t$.

The complete expression for the cross section of ρ^0 production is given in [7]. The angular distribution $W(\phi, \phi_s)$ can be written[a] in terms of asymmetries:

$$W(\phi, \phi_s) = \widehat{W}_{UU}(1 + A_{UU}(\phi) + P_T A_{UT}(\phi, \phi_s)), \tag{3}$$

where $A_{UU}(\phi) = W_{UU}(\phi)/\widehat{W}_{UU}$ is the unpolarized asymmetry with $\widehat{W}_{UU}$, $W_{UU}(\phi)$ being the unpolarized angular distributions and $A_{UT}(\phi, \phi_s) = W_{UT}(\phi, \phi_s)/\widehat{W}_{UU}$ is the transverse asymmetry with the transversely polarized angular distribution $W_{UT}(\phi, \phi_s)$.

Since the factorization theorem is proven for longitudinal photons only [3], the asymmetry of ρ^0 mesons induced from longitudinal photons is of theoretical interest. Under the assumption of s-channel helicity conservation (SCHC), which implies that a longitudinal vector meson originates from a longitudinal photon, the longitudinal component of the asymmetry is obtained experimentally through the decay angular distribution of ρ^0 ($\rho^0 \to \pi^+\pi^-$). Each ρ^0 helicity state (L, T) results in a characteristic dependence of the $\gamma^* p$ cross-section on the θ_π polar angle of π^+ in the ρ^0 rest frame [7]. The interference terms between different helicities of the ρ^0 production are canceled if the cross section is integrated over the φ_π azimuthal decay angle of π^+ in the ρ^0 rest frame.

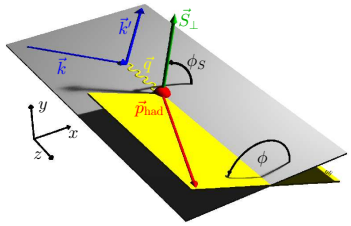

Figure 1: Definition of ϕ and ϕ_s angles.

The total angular distribution $W(\cos\theta_\pi, \phi, \phi_s)$, including the dependence on the π^+ polar angle, can be written separately for longitudinal ρ^0_L and transverse ρ^0_T mesons:

$$\begin{aligned} W(\cos\theta, \phi, \phi_s) \quad \propto \quad & \Big[\cos^2\theta_\pi\ \widehat{W}^{\rho_L}_{UU}\ \Big(1 + A^{\rho_L}_{UU}(\phi) + P_T A^{\rho_L}_{UT}(\phi, \phi_s)\Big) \\ + \quad & \sin^2\theta_\pi\ \widehat{W}^{\rho_T}_{UU}\ \Big(1 + A^{\rho_T}_{UU}(\phi) + P_T A^{\rho_T}_{UT}(\phi, \phi_s)\Big)\Big]. \end{aligned} \tag{4}$$

3 Extraction of the TTSA

The data were accumulated with the HERMES forward spectrometer during the running period 2002-2005. The 27.6 GeV positron (electron) beam was scattered off a transversely polarized hydrogen target with an average polarization of 0.72. Events with exactly one positron (electron) and two oppositely charged hadron tracks were selected. Exclusive ρ^0

[a] For simplicity hereafter x_B, Q^2 and t' are omitted.

events were identified by requiring $\Delta E = \frac{M_X^2 - M_p^2}{2M_p} < 0.6$ GeV, where M_x^2 is the missing mass squared and M_p is the proton mass. Due to the experimental resolution and limited acceptance, semi-inclusive pion production can contribute to the exclusive sample; this is the primary background. It is well reproduced by the PYTHIA simulation and is estimated to be of the order of 10%.

The TTSA asymmetry is extracted by using the unbinned maximum likelihood method where all the moments [7] of $A_{UT}(\phi, \phi_s)$, $A_{UT}^{\rho_L}(\phi, \phi_s)$ and $A_{UT}^{\rho_L}(\phi, \phi_s)$ (Eqs. 3, 4) are fitted simultaneously. In this analysis, the angular distributions $\widehat{W}_{UU}$ and the asymmetries $A_{UU}(\phi)$ of ρ^0, ρ_L^0 and ρ_T^0 meson productions are defined by unpolarized spin density matrix elements (SDMEs) [8] previously measured by HERMES [9].

4 Results

The only TTSA moment of ρ^0s produced from longitudinal photons that is related to the GPDs H and E, is the $\sin(\phi - \phi_s)$ moment. In Figure 2 the $A_{UT}^{\sin(\phi-\phi_s)}$ moment of the TTSA is presented. The panels show from left to right the integrated value and the Q^2, x_B and t' dependences of the asymmetry. For the x_B and t' dependences, Q^2 is required to be above 1 GeV^2. The upper panels represent the ρ^0 total asymmetries, while the middle and the lower panels represent the longitudinal ρ_L^0 and transverse ρ_T^0 separated asymmetries, respectively. The error bars represent the statistical uncertainties only, while the yellow bands indicate the systematic uncertainties due to the target polarization, the background subtraction procedure, the uncertainty resulting from the the unpolarized SDMEs measurement as well as the influence of the beam polarization on the final result.

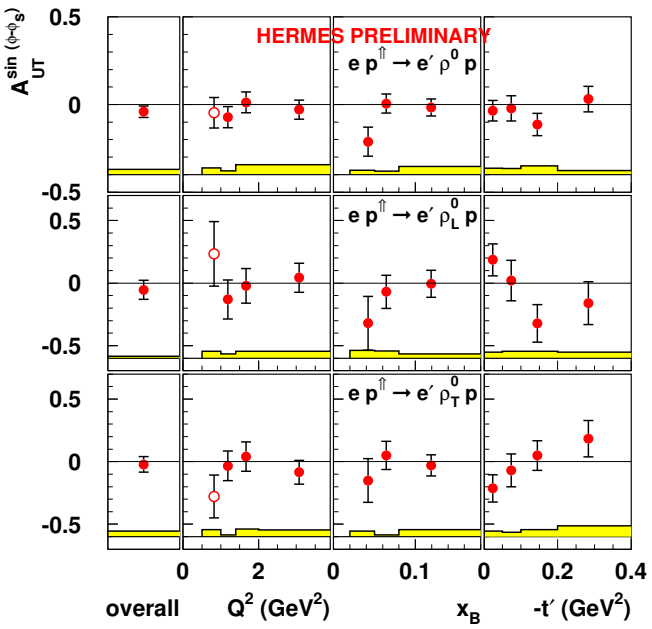

Figure 2: The integrated value, Q^2, x_B and t' dependences of the $A_{UT}^{\sin(\phi-\phi_s)}$ moment of the TTSA of exclusive ρ^0, ρ_L^0 and ρ_T^0 meson productions.

The x_B and t' dependences of the $A_{UT}^{\sin(\phi-\phi_s)}$ moment for longitudinal ρ^0 mesons are compared to the theoretical calculations [10] (see Figure 3). The longitudinal component of $A_{UT}^{\sin(\phi-\phi_s)}$ moment of the asymmetry is related to: $E/H \propto (E_q + E_g)/(H_q + H_g)$, where the E_q, H_q and E_g, H_g represent the quark and gluon GPDs, respectively. Currently no model exists for the gluon GPD E_g. In the present theoretical calculations the gluon GPD E is neglected. However, E_g is not expected to be large compared to the quark GPDs [11]. No large contribution is expected from sea quarks in our x_B range. As GPD E_q is related to

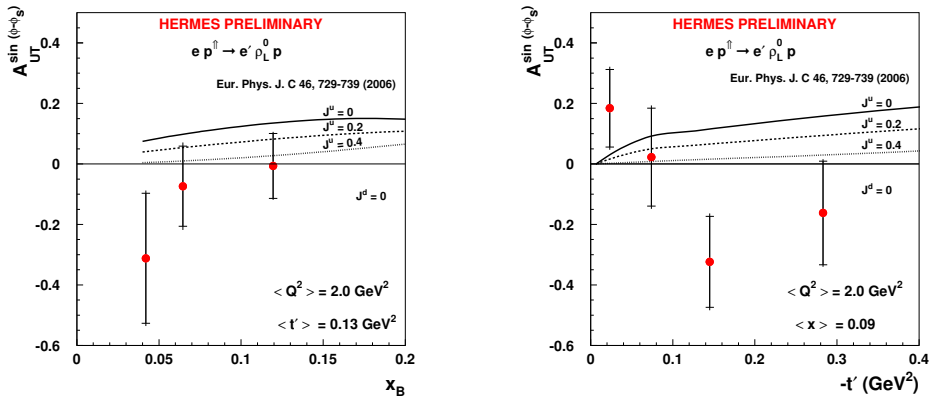

Figure 3: x_B and t' dependences of $A_{UT}^{\sin(\phi-\phi_s)}$ moment of the TTSA of exclusive production of ρ_L^0 mesons compared to the model calculations. The error bars represent the total error.

the total angular momentum J^u and J^d carried by u and d quarks, the $A_{UT}^{\sin(\phi-\phi_s)}$ moment of the asymmetry is sensitive to J^u and J^d. The various curves in Figure 3 represent those calculations for $J^u = 0$, 0.2 and 0.4 and $J^d = 0$. The $J^d = 0$ choice is motivated by the results of recent lattice calculation [12]. The comparison of x_B and t' dependences of the asymmetry with theoretical calculations indicates that the data favors positive J^u values.

5 Conclusion

The $A_{UT}^{\sin(\phi-\phi_s)}$ moment of the TTSA of exclusive ρ^0 meson production is measured on a hydrogen target. The kinematic dependences as well as the integrated value of the asymmetry are presented. In particular, the longitudinal part of the asymmetry is compared to theoretical calculations. The model suggests that the data favors positive J^u values, which is in agreement with deeply virtual Compton scattering results obtained from HERMES data [13].

References

[1] Slides: `http://indico.cern.ch/contributionDisplay.py?contribId=86&sessionId=12&confId=9499`
[2] D. Mueller et al., Fortschr. Phys. **42** (1994) 101;
A.V. Radyushkin, Phys. Rev. **D55** (1997) 7114.
[3] J. Collins, L. Frankfurt, M. Strikman, Phys. Rev. **D56** (1997) 2982.
[4] X.D. Ji, Phys. Rev. Lett. **78** (1997) 610.
[5] K. Goeke, M.V. Polyakov, M.Vanderhaeghen, Prog. Part. Nucl. Phus **47**, (2001) 401.
[6] A. Bacchetta, U. D'Alesio, M. Diehl, C.A. Miller, Phys. Rev. **D70** (2004) 117504.
[7] M. Diehl, S. Sapeta, Eur.Phys.J. **C41** (2005) 515.
[8] K. Schilling, G. Wolf, Nucl. Phys. B **61** (1973) 381.
[9] B. Marianski, DIS 2006: Proceedings of the 14th International Workshop. World Scientific (2007) 255.
[10] F. Ellinghaus, W.-D. Novak, A.V. Vinnikov, Z. Ye, Eur.Phys.J. **C46** (2006) 729.
[11] M. Diehl,Phys. Rept. **388** (2003) 41.
[12] M.Goekeler et al, Phys. Rev. Lett. **92** (2004) 042002.
[13] W.-D. Nowak, AIP Conf. Proc. 915 (2006) 603.

Are Generalized and Transverse Momentum Dependent Parton Distributions Related ?

Stephan Meißner, Andreas Metz, and Klaus Goeke

Institut für Theoretische Physik II, Ruhr-Universität Bochum,
D-44780 Bochum, Germany

The present knowledge on non-trivial relations between generalized parton distributions on the one hand and transverse momentum dependent distributions on the other is reviewed. While various relations can be found in the framework of spectator models, so far no model-independent non-trivial relations have been established.

1 Definitions and trivial relations

During the last decade a lot of effort has been devoted to study in detail generalized parton distributions (GPDs) as well as transverse momentum dependent parton distributions (TMDs). While GPDs enter the QCD description of hard exclusive reactions on the nucleon, TMDs appear in connection with various semi-inclusive processes. Recent work has suggested for the first time very interesting non-trivial relations between these two types of parton distributions [1, 2, 3, 4, 5, 6, 7]. The present short note [8] is based on Ref. [7], where the current knowledge on such relations has been reviewed and previous work on this topic has been considerably extended.

To be specific now, two leading twist quark GPDs of the nucleon are defined through

$$\begin{aligned} F^q(x,\Delta;\lambda,\lambda') &= \frac{1}{2}\int \frac{dz^-}{2\pi}\, e^{ik\cdot z}\, \langle p';\lambda'|\, \bar\psi\big(-\tfrac{1}{2}z\big)\, \gamma^+\, \mathcal{W}_{\rm GPD}\, \psi\big(\tfrac{1}{2}z\big)\, |p;\lambda\rangle \Big|_{z^+=\vec z_T=0} \\ &= \frac{1}{2P^+}\, \bar u(p',\lambda') \left(\gamma^+\, H^q(x,\xi,t) + \frac{i\sigma^{+\mu}\Delta_\mu}{2M}\, E^q(x,\xi,t)\right) u(p,\lambda)\,, \end{aligned} \tag{1}$$

with $P=(p+p')/2$ denoting the average nucleon momentum and $\Delta = p'-p$ the momentum transfer to the nucleon. The GPDs H^q and E^q depend on the variables

$$x = \frac{k^+}{P^+}\,, \qquad \xi = -\frac{\Delta^+}{2P^+}\,, \qquad t = \Delta^2\,, \tag{2}$$

where the dependence on the renormalization scale has been suppressed. Note that the Wilson line $\mathcal{W}_{\rm GPD}$ ensures the color gauge invariance of the bilocal quark operator in (1). The remaining six leading quark GPDs are obtained if one replaces the matrix γ^+ in the operator in (1) by $\gamma^+\gamma_5$ or $i\sigma^{j+}\gamma_5$ (j being a transverse index).

In a similar way, two leading twist quark TMDs are defined according to

$$\begin{aligned} \Phi^q(x,\vec k_T;S) &= \frac{1}{2}\int \frac{dz^-}{2\pi}\, \frac{d^2\vec z_T}{(2\pi)^2}\, e^{ik\cdot z}\, \langle P;S|\, \bar\psi\big(-\tfrac{1}{2}z\big)\, \gamma^+\, \mathcal{W}_{\rm TMD}\, \psi\big(\tfrac{1}{2}z\big)\, |P;S\rangle \Big|_{z^+=0} \\ &= f_1^q(x,\vec k_T^{\,2}) - \frac{\epsilon_T^{ij} k_T^i S_T^j}{M}\, f_{1T}^{\perp q}(x,\vec k_T^{\,2})\,. \end{aligned} \tag{3}$$

The TMDs depend both on the longitudinal momentum fraction x of the partons and on the transverse parton momentum $\vec k_T$. While f_1 is the familiar unpolarized quark distribution,

$f_{1T}^{\perp}$ represents the so-called Sivers function [9, 10], which appears for a transversely polarized target and is supposed to be at the origin of various observed single spin phenomena in hard semi-inclusive reactions.

There exist some trivial relations between GPDs and TMDs because of the connection between GPDs (for $\xi = t = 0$) and TMDs (integrated upon $\vec{k}_T$) on the one hand and ordinary parton distributions on the other. An example is given by

$$H^q(x,0,0) = f_1^q(x) = \int d^2\vec{k}_T\, f_1^q(x,\vec{k}_T^2)\,. \tag{4}$$

Two additional trivial relations hold on the quark sector (involving the quark helicity and transversity distribution) and also two for gluon distributions. In this note, however, we are mainly interested in non-trivial relations between GPDs and TMDs.

2 Impact parameter representation of GPDs

In Ref. [1], a non-trivial relation was proposed for the first time — a connection between the GPD E and the Sivers function $f_{1T}^{\perp}$. In that work an important role is played by the impact parameter representation of GPDs. For $\xi = 0$, GPDs in impact parameter space have a density interpretation, and are generically given by

$$\mathcal{X}(x,\vec{b}_T^2) = \int \frac{d^2\vec{\Delta}_T}{(2\pi)^2}\, e^{-i\vec{\Delta}_T\cdot\vec{b}_T}\, X(x,0,-\vec{\Delta}_T^2)\,. \tag{5}$$

Using this definition, the Fourier transform of the correlator in (1) (for $\xi = 0$) has the form

$$\mathcal{F}^q(x,\vec{b}_T;S) = \int \frac{d^2\vec{\Delta}_T}{(2\pi)^2}\, e^{-i\vec{\Delta}_T\cdot\vec{b}_T}\, F^q(x,\Delta_T;S) = \mathcal{H}^q(x,\vec{b}_T^2) + \frac{\epsilon_T^{ij} b_T^i S_T^j}{M}\left(\mathcal{E}^q(x,\vec{b}_T^2)\right)', \tag{6}$$

where the derivative of $\mathcal{E}^q$ with respect to $\vec{b}_T^2$ enters. The correlator $\mathcal{F}^q$ has the following interpretation: it describes the distribution of unpolarized quarks carrying the longitudinal momentum fraction x at a transverse position $\vec{b}_T$ inside a transversely polarized target.

If the second term on the *r.h.s.* in (6) is non-zero, $\mathcal{F}^q$ is not axially symmetric in b-space. In other words, the correlator is distorted. In fact, one can show in a model-independent way that for a nucleon target the correlator has a large distortion, where the effect for a quark flavor q is proportional to the contribution of the corresponding flavor to the anomalous magnetic moment of the nucleon [1]. One may now speculate that this large distortion should have an observable effect. Indeed in [1] it was argued that it may be related to the Sivers function. An explicit form of the relation was obtained in Ref. [3] by considering the average transverse momentum of an unpolarized quark inside a transversely polarized target,

$$\begin{aligned}\left\langle k_T^{q,i}(x)\right\rangle_{UT} &= -\int d^2\vec{k}_T\, k_T^i\, \frac{\epsilon_T^{jk} k_T^j S_T^k}{M}\, f_{1T}^{\perp q}(x,\vec{k}_T^2) \\ &= \int d^2\vec{b}_T\, \mathcal{I}^{q,i}(x,\vec{b}_T)\, \frac{\epsilon_T^{jk} b_T^j S_T^k}{M}\left(\mathcal{E}^q(x,\vec{b}_T^2)\right)'.\end{aligned} \tag{7}$$

The result in (7) represents the first quantitative non-trivial relation between a GPD and a TMD. It also provides an intuitive explanation of the Sivers effect. (In this context we refer

to [1, 2, 3] where also the meaning of the object $\mathcal{I}^q$ is discussed.) However, the relation (7) is model-dependent. It was obtained in the framework of a simple spectator model of the nucleon, treated to lowest non-trivial order in perturbation theory [3]. On the other hand, the relation (7) is quite successful from a phenomenological point of view. Therefore, it makes sense to look for additional non-trivial relations, even if they turn out to be merely model-dependent.

3 Model-independent considerations

To get some guidance for further possible non-trivial relations the structures in the GPD- and TMD-correlator can be compared [4, 7]. This procedure was first used in the case of quark distributions [4], and later on extended to the gluon sector [7]. Besides the already mentioned trivial relations (called relations of first type in [7]), one finds the following list of non-trivial analogies/relations between GPDs and TMDs [7]:

- Relations of second type

$$f_{1T}^{\perp q/g} \leftrightarrow -\Big(\mathcal{E}^{q/g}\Big)', \qquad h_1^{\perp q} \leftrightarrow -\Big(\mathcal{E}_T^q + 2\tilde{\mathcal{H}}_T^q\Big)',$$
$$\Big(h_{1T}^g + \tfrac{\vec{k}_T^2}{2M^2}\, h_{1T}^{\perp g}\Big) \leftrightarrow -2\Big(\mathcal{H}_T^g - \tfrac{\vec{b}_T^2}{M^2}\,\Delta_b \tilde{\mathcal{H}}_T^g\Big)'. \tag{8}$$

- Relations of third type

$$h_{1T}^{\perp q} \leftrightarrow 2\Big(\tilde{\mathcal{H}}_T^q\Big)'', \qquad h_1^{\perp g} \leftrightarrow 2\Big(\mathcal{E}_T^g + 2\tilde{\mathcal{H}}_T^g\Big)''. \tag{9}$$

- Relation of fourth type

$$h_{1T}^{\perp g} \leftrightarrow -4\Big(\tilde{\mathcal{H}}_T^g\Big)'''. \tag{10}$$

To the best of our knowledge Eqs. (8)–(10) contain all possible non-trivial analogies/relations between leading twist GPDs and TMDs for quarks and gluons. Moreover, the method of Refs. [4, 7] only indicates which distributions may be related, but does not provide an explicit form of a relation.

4 Model results

In Ref. [7] we have studied two spectator models in order to find explicit forms of possible non-trivial relations: first, a scalar diquark spectator model of the nucleon; second, a quark target model treated in perturbative QCD, which also allows one to study relations between gluon distributions. We found it convenient to work with GPDs in momentum rather than impact parameter representation. The relations presented in the following involve moments of GPDs and TMDs, which (also for non-integer n) are defined according to

$$X^{(n)}(x) = \frac{1}{2M^2}\int d^2\vec{\Delta}_T \left(\frac{\vec{\Delta}_T^2}{2M^2}\right)^{n-1} X(x,0,-\tfrac{\vec{\Delta}_T^2}{(1-x)^2})\,, \tag{11}$$

$$Y^{(n)}(x) = \int d^2\vec{k}_T \left(\frac{\vec{k}_T^2}{2M^2}\right)^{n} Y(x,\vec{k}_T^2)\,. \tag{12}$$

Taking as example the relation between the Sivers function and the GPD E, the relations of the second type have the form [7]

$$f_{1T}^{\perp q\,(n)}(x) = h_2(n)\,\frac{1}{1-x}\,E^{q\,(n)}(x)\,, \qquad (0 \le n \le 1)\,. \tag{13}$$

The function $h_2(n)$ is different in the two models that we considered. We note that for all relations indicated in (8) a formula corresponding to (13) holds true. Evaluating (13) for $n = 0$ and $n = 1$ one recovers results presented earlier in Refs. [6, 3]. In this context it is also worthwhile to mention that for $n = 1$ Eq. (13) is equivalent to the content of Eq. (7).

The model calculations provide the following explicit relation of third type [7],

$$h_{1T}^{\perp q\,(n)}(x) = h_3(n)\,\frac{1}{(1-x)^2}\,\tilde{H}_T^{q\,(n)}(x)\,, \qquad (0 \le n \le 1)\,, \tag{14}$$

and a corresponding formula for the gluon distributions in (9). In contrast to the previous case the function h_3 is the same in both models.

Eventually, we mention that the relation of fourth type in (10) is trivially satisfied in the quark target model, because to lowest non-trivial order in perturbation theory both the TMD $h_{1T}^{\perp g}$ and the GPD $\tilde{H}_T^g$ vanish [7].

5 Summary and discussion

This note is dealing with the question if there exist non-trivial relations between GPDs on the one hand and TMDs on the other. On the basis of model-independent considerations one can distinguish between different types of possible non-trivial relations. It turns out that so far no model-independent non-trivial relations exist and it seems even unlikely that they can ever be established. However, many relations exist in the framework of simple spectator models, treated to lowest non-trivial order in perturbation theory. Once higher order diagrams are taken into consideration some of these relations are expected to break down [7]. Nevertheless, for instance the phenomenology and the predictive power of the low-order spectator model relation between the Sivers effect and the GPD E works quite well. This is the only non-trivial relation which currently can be confronted with data. Additional input from both the experimental and theoretical side is required in order to further study all other relations between GPDs and TMDs. Future work will certainly shed more light on this interesting topic.

References

[1] M. Burkardt, Phys. Rev. D **66**, 114005 (2002).
[2] M. Burkardt, Nucl. Phys. A **735**, 185 (2004).
[3] M. Burkardt and D. S. Hwang, Phys. Rev. D **69**, 074032 (2004).
[4] M. Diehl and P. Hägler, Eur. Phys. J. C **44**, 87 (2005).
[5] M. Burkardt, Phys. Rev. D **72**, 094020 (2005).
[6] Z. Lu and I. Schmidt, Phys. Rev. D **75**, 073008 (2007).
[7] S. Meissner, A. Metz and K. Goeke, arXiv:hep-ph/0703176.
[8] Slides:
`http://indico.cern.ch/contributionDisplay.py?contribId=247&sessionId=12&confId=9499`
[9] D. W. Sivers, Phys. Rev. D **41**, 83 (1990); Phys. Rev. D **43**, 261 (1991).
[10] D. Boer and P. J. Mulders, Phys. Rev. D **57**, 5780 (1998).

A-dependence of the Beam–Spin Azimuthal Asymmetry in Deeply Virtual Compton Scattering

Hayg Guler (on behalf of the HERMES collaboration)

DESY, D-15718 Zeuthen, Germany

The nuclear-mass dependence of the beam–spin asymmetry (BSA) in deeply virtual Compton scattering has been measured at HERMES. The BSA ratios of Nuclei to Hydrogen or Deuterium have been extracted in coherent and incoherent-enriched kinematic regions separately.

1 Introduction

Lepton scattering experiments constitute an important source of information for the understanding of nucleon and nucleus structure. Until recently, this structure was described by two non-perturbative objects, form factors (FFs) and parton distribution functions (PDFs), which were measured in elastic and deep inelastic scattering (DIS) experiments, respectively. In the last decade, Generalized Parton distributions (GPDs) were recognized as a tool to give a unified description of hard exclusive processes in the Bjorken regime, i.e. for large transfers of squared four-momentum Q^2, and energy ν, of the exchanged virtual photon. The GPD formalism offers a much more complete description of nucleon structure than the well-known PDFs and FFs [2, 3]. There exist four leading-twist GPDs for each quark species in the nucleon: H, E, $\widetilde{H}$, and $\widetilde{E}$. GPDs allow to access the 3-dimensional structure of the nucleon [2]. They depend upon three kinematic quantities: the longitudinal momentum fraction of initial and final quarks, $x+\xi$ and $x-\xi$ (ξ being the longitudinal momentum asymmetry or skewness), and the reduced four-momentum squared transfer t' to the target.

2 Deeply Virtual Compton Scattering

Hard exclusive lepto-production of a real photon, deeply virtual Compton scattering (DVCS), is known to be one of the experimentally cleanest and presently the most practical way to access GPDs. This process has the same initial and final state as the Bethe-Heitler (BH) process, in which the real photon is radiated from the incoming or scattered lepton. As the two processes are experimentally indistinguishable, their amplitudes add coherently and the cross section contains an interference term I:

$$\frac{d\sigma}{dx_B\, dQ^2\, d\mid t'\mid d\phi} \propto \mid \tau_{DVCS}\mid^2 + \mid \tau_{BH}\mid^2 + I \;\;;\;\; I = \tau^*_{BH}\tau_{DVCS} + \tau^*_{DVCS}\tau_{BH} \tag{1}$$

Here $x_B = \frac{Q^2}{2M\nu}$ represents the Bjorken scaling variable. The azimuthal angle ϕ is defined as the angle between the lepton scattering plane, spanned by incoming and scattered leptons, and the photon production plane, defined by virtual and real photons. Although at HERMES energies the BH cross section dominates over that of DVCS, the DVCS amplitude can be studied via the interference term I, by measuring various azimuthal cross section asymmetries. At leading twist, the interference term can be expanded in terms of Fourier moments in ϕ [3]:

$$I \propto \pm\left(c_0^I + \sum_{n=1}^{3} c_n^I \cos(n\phi) + \lambda \sum_{n=1}^{3} s_n^I \sin(n\phi)\right), \tag{2}$$

where the $+(-)$ sign stands for a negatively (positively) charged lepton beam, and λ is its longitudinal polarization. The coefficients c_1^I and s_1^I are proportional to the real and the imaginary part of the DVCS helicity amplitude $M^{1,1}$, respectively. In the case of an unpolarized proton target, this amplitude is given by a linear combination of the complex Compton Form Factors (CFFs), $\mathcal{H}$, $\widetilde{\mathcal{H}}$ and $\mathcal{E}$, together with the known Dirac and Pauli elastic form factors F_1 and F_2:

$$M^{1,1} = F_1\,\mathcal{H} + \frac{x_B}{2-x_B}(F_1+F_2)\,\widetilde{\mathcal{H}} - \frac{t}{4M^2}F_2\,\mathcal{E} \tag{3}$$

The CFFs are convolutions of the respective twist–2 GPDs with hard scattering kernels.
Nuclear targets are studied to learn about the DVCS process in the more complicated nuclear environment. For a nuclear target there exist two distinct processes:

- the coherent process, in which the scattering occurs on the whole nucleus, which stays intact after the emission of a real photon;
- the incoherent process, where the nucleus breaks up, and the real photon is emitted by a particular proton or neutron.

3 DVCS at HERMES

HERMES is a fixed–target experiment using the 27.6 GeV longitudinally polarized electron or positron beam of the HERA collider and an internal gas target that can be filled with polarized H, D and unpolarized nuclei (N, He, Ne, Xe, Kr). The DVCS process is measured by identifying the scattered lepton and the produced real photon in the forward spectrometer [4]. As the recoil proton or nucleus can not be detected there, kinematic requirements are imposed in order to ensure the exclusivity of the reaction. In particular, the missing mass is required to be in the range $-1.5 < M_x < 1.7$ GeV, determined from Monte-Carlo simulations by comparing signal to background distributions taking into account the finite resolution of the spectrometer.

3.1 A-dependence of the Beam–Spin Asymmetry

The beam–spin asymmetry (BSA), as a function of the azimuthal angle ϕ, is calculated as

$$A_{LU}(\phi) = \frac{1}{\langle|P_l|\rangle}\frac{\overrightarrow{N}(\phi) - \overleftarrow{N}(\phi)}{\overrightarrow{N}(\phi) + \overleftarrow{N}(\phi)}, \tag{4}$$

with the luminosity normalized yields $\overrightarrow{N}$ ($\overleftarrow{N}$) using a beam with positive (negative) helicity, P_l being the beam polarization and L(U) meaning longitudinally polarized beam (unpolarized target). In leading order α_S and at leading twist, the $\sin\phi$ amplitude of the BSA, $A_{LU}^{sin\phi}$, is proportional to $Im\,M^{1,1}$. Azimuthal asymmetries with respect to the beam spin have been measured on H, D, He, N, Ne, Kr and Xe. For the three targets Deuterium [5] Neon and Krypton, preliminary BSA results integrated over the experimental acceptance are similar to that for the proton [5]. Events can be separated into coherent and incoherent-enriched samples corresponding to separate intervals in t'. Here these samples are extracted by target-dependent requirements on t' in order to provide the same value of $\langle t'\rangle$ for each target. The resulting values are:

- for the coherent-enriched sample: $\langle -t'\rangle = 0.018$ GeV^2
- for the incoherent-enriched sample: $\langle -t'\rangle = 0.2$ GeV^2.

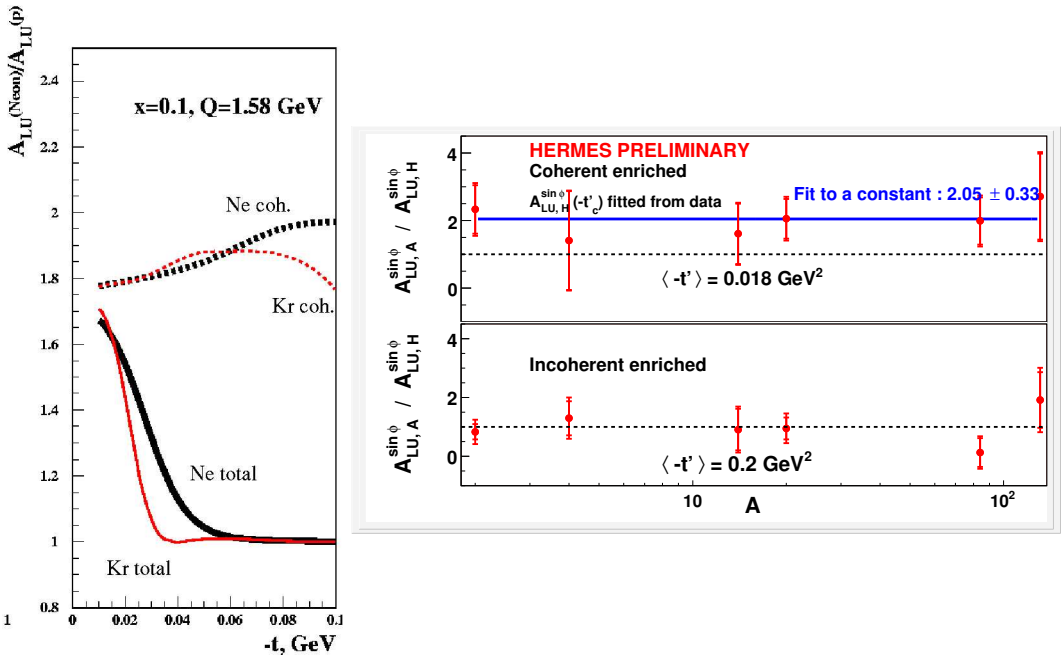

Figure 1: Left panel: model predictions for the ratio of nuclear-to-proton BSA for Neon and Krypton. Right panel: BSA ratio vs. A relative to Hydrogen data fit at $\langle -t' \rangle = 0.018$ GeV^2. The dashed line denotes unity and the solid line represents the result of a fit to a constant.

At small $\langle t' \rangle$ the Hydrogen sample has limited statistics, and hence dominates the uncertainties of the BSA ratios. The alternative is to use a fit of the hydrogen BSA anchored by $A_{LU}^{sin\phi} = 0$ at $t' = 0$, based on the theoretical expectation: $A_{LU}^{sin\phi}(t') \propto \sqrt{-t'}$ at small t'. The fit function has the form:

$$A_{LU}^{sin\phi}(t') = \frac{a \cdot \sqrt{-t'}}{1 + b \cdot \sqrt{-t'^3}} ,$$

$$\text{with the parameters : } a = -1.204\ \text{GeV}^{-1} \text{ and } b = 35\ \text{GeV}^{-3}$$

evaluated at $\langle -t' \rangle = 0.018$ GeV^2

The extracted ratios of nuclear-to-hydrogen $A_{LU}^{sin\phi}$ amplitudes for the coherent and incoherent-enriched samples are shown in the right panel of Fig. 1. The mean ratio in the coherent region deviates from unity by 2σ and is consistent with model predictions based on GPD models [8]. As shown in the left panel, they predict for Neon and Krypton a ratio to hydrogen close to 1.8 in the coherent region and consistent with unity in the incoherent one. For the incoherent-enriched sample the mean ratio is also consistent with unity as predicted by the model.

Acknowledgments

This work has been supported by the German Bundesministerium für Bildung und Forschung (BMBF) (contract nr. 06 ER 125I) and the European Community-Research Infrastructure Activity under the

FP6 ''Structuring the European Research Area" program (HadronPhysics I3, contract nr. RII3-CT-2004-506078).

References

[1] Slides:
http://indico.cern.ch/contributionDisplay.py?contribId=87&sessionId=12&confId=9499
[2] M. Burkardt, Phys. Rev. **D62** (2000) 071503; Erratum–ibid. **D 66** (2002) 119903.
[3] A.V. Belitsky and D. Müller, Nucl. Phys. **A711** (2002) 118.
[4] HERMES Coll., K. Ackerstaff et al., Nucl. Instr. and Meth. **A417** (1998) 230.
[5] F. Ellinghaus *et al.*, for the HERMES Coll., arXiv:hep–ex/0212019, AIP Conf. Proc. 675 (2002) 303, Eds. I. Y. Makdisi *et al.*.
[6] D. Müller et al., Fortschr. Phys. **42** (1994) 101.
[7] X. Ji, Phys. Rev. Lett. **78** (1997) 610, Phys. Rev. **D55** (1997) 7114.
[8] V. Guzey and M. Strikman, Phys. Rev. **C68** (2003) 015204.
[9] A.V. Radyushkin, Phys. Rev. **D56** (1997) 5524.
[10] K. Goeke et al., Prog. Part. Nucl. Phys. **47** (2001) 401.

HERMES Measurement of DVCS from p and d Targets, and Status and Prospects of the Recoil Detector

A. Mussgiller (on behalf of the HERMES collaboration)

University of Erlangen-Nuremberg - 91058 Erlangen - Germany

The Deeply Virtual Compton Scattering (DVCS) process provides the theoretically cleanest access to the unknown generalized parton distributions (GPDs). DVCS amplitudes can be measured through the interference between the Bethe-Heitler DVCS processes via the dependence of cross-section asymmetries on the azimuthal angle. The accumulated HERMES data offers access to the four GPDs in different combinations of beam charge and helicity as well as target spin. A recent highlight has been the transverse target-spin asymmetry that provides access to the total angular momentum of quarks.
In late 2005, a Recoil Detector was installed at HERMES with the purpose of greatly improving the experiment's ability to measure hard-exclusive processes during its final running period [1].

1 Introduction

The formalism of generalized parton distributions (GPDs) allows a consistent description of nucleon structure. In different limiting cases the GPDs incorporate the well-known nucleon form factors determined from elastic scattering as well as parton distributions functions (PDFs) determined from measurements of inclusive and semi-inclusive deep inelastic lepton-nucleon scattering (DIS and SIDIS respectively). Strong interest in the GPD framework has also evolved because of the fact that GPDs encode the unknown total angular momentum of quarks and gluons within the nucleon (J_q and J_g respectively). With the knowledge of the quarks' spin contribution to the spin of the nucleon, knowledge of the GPDs allows in principle also access to the orbital angular momentum of quarks (L_q) [2].
The theoretically cleanest process to constrain GPDs is Deeply-Virtual Compton Scattering (DVCS), in which a highly virtual photon (emitted by the incoming lepton beam) is absorbed by a parton of the target nucleon and produces a single real photon in the final state along with the recoiling nucleon in its ground state.

2 DVCS at HERMES

The DVCS process has the same final state as the Bethe-Heitler (BH) process, in which a real photon is radiated by either the incoming or the outgoing lepton. As this makes both processes experimentally indistinguishable, the cross section for leptoproduction of real photons is therefore given by the coherent sum of the DVCS and BH amplitudes squared:

$$d\sigma \propto |\tau_{\mathrm{DVCS}}|^2 + |\tau_{\mathrm{BH}}|^2 + \underbrace{\tau_{\mathrm{DVCS}}\tau^*_{\mathrm{BH}} + \tau^*_{\mathrm{DVCS}}\tau_{\mathrm{BH}}}_{I} \qquad (1)$$

At HERMES kinematics the BH process is the dominant contribution to the cross section. However, the DVCS amplitude can be accessed via the interference term (I) by measuring various cross section asymmetries and their dependence on the azimuthal angle ϕ, which is

defined as the angle between the lepton scattering plane and the photon production plane. The interference term can be expressed as a series of Fourier moments in the angle ϕ: [3]

$$I \propto \pm \left(c_0^I + \sum_{n=1}^{3} c_n^I \cos(n\phi) + \sum_{n=1}^{3} s_n^I \sin(n\phi) \right), \tag{2}$$

where the + or − sign is used in case of an electron or positron beam respectively and where c_0^I, c_n^I, s_n^I represent linear combinations of the Compton form factors (CFFs) which in general depend on the beam helicity and the target polarization. The GPDs themselves are convolutions of hard scattering kernels with these CFFs.

By measuring with different beam charge and helicity states and with different target polarizations (longitudinal and transverse), HERMES accesses both the real and imaginary parts of the CFFs $\mathcal{H}$, $\mathcal{E}$, $\widetilde{\mathcal{H}}$ and $\widetilde{\mathcal{H}}$ and thus the corresponding GPDs. At leading order and leading twist the expressions for the cross section differences which give rise to beam-charge (BCA), beam-spin (BSA), longitudinal target-spin (LTSA) and the transverse target-spin (TTSA) asymmetries are

$$\begin{aligned}
d\sigma(e^+,p) - d\sigma(e^-,p) &\propto \cos(\phi)\ \mathrm{Re}[F_1\mathcal{H}] \\
d\sigma(\overrightarrow{e},p) - d\sigma(\overleftarrow{e},p) &\propto \sin(\phi)\ \mathrm{Im}[F_1\mathcal{H}] \\
d\sigma(e,\overleftarrow{p}) - d\sigma(e,\overrightarrow{p}) &\propto \sin(\phi)\ \mathrm{Im}[F_1\widetilde{\mathcal{H}}] \\
d\sigma(\phi,\phi_S) - d\sigma(\phi,\phi_S+\pi) &\propto \sin(\phi-\phi_S)\cos(\phi)\ \mathrm{Im}[F_2\mathcal{H} - F_1\mathcal{E}] + \\
&\quad \cos(\phi-\phi_S)\sin(\phi)\ \mathrm{Im}[F_2\widetilde{\mathcal{H}} - F_1\xi\widetilde{\mathcal{E}}].
\end{aligned} \tag{3}$$

Here ϕ_S is the angle between the lepton scattering plane and the target polarization vector, ξ is the skewedness parameter defined as $\approx \frac{x_B}{2-x_B}$, and F_1 and F_2 are the Dirac and Pauli form factors of the proton respectively.

3 The Experiment

HERMES is a fixed target experiment that uses the 27.6 GeV electron and positron beam provided by HERA [4]. To extract the above mentioned asymmetries from the data, events were selected that contained exactly one photon and one lepton track (the latter with charge equal to the beam charge). Lepton-hadron identification is performed by a transition-radiation detector, a preshower counter and an electromagnetic calorimeter. Photons were identified by their large energy deposit in the calorimeter and preshower counter along with the absence of a corresponding track in the drift and proportional chambers. The cuts imposed on the lepton kinematics were: $Q^2 > 1$ GeV^2, $W > 3$ GeV. The angle $\theta_{\gamma^*\gamma}$ between the virtual and real photon was limited to range between 5 and 45 mrad.
For the data collected up to 2005, the recoiling proton was not detected. Exclusive DVCS events were therefore selected by applying a cut on the missing mass M_X. The exclusive region was defined as $-(1.5\ \mathrm{GeV})^2 < M_X^2 < (1.7\ \mathrm{GeV})^2$.

4 Transverse Target-Spin Asymmetry

The transverse target-spin asymmetry associated with DVCS on the proton can be measured with an unpolarized lepton beam (U) and a transversely polarized (T) hydrogen target [5].

The quark's total angular momentum J_q ($q = u, d$) can be accessed through a GPD model [6] that uses J_u and J_d as free parameters to parametrize the GPD E. Within this model the TTSA amplitude $A_{UT}^{\sin(\phi-\phi_S)\cos(\phi)}$ is found to be sensitive to J_u and J_d. Figure 1 shows the TTSA amplitudes $A_{UT}^{\sin(\phi-\phi_S)\cos(\phi)}$ and $A_{UT}^{\cos(\phi-\phi_S)\sin(\phi)}$ as a function of $-t$, x_B and Q^2 extracted from the HERMES data collected in 2002-2004. The curves in the figure represent predictions from a GPD model with different u-quark total angular momentum J_u and fixed d-quark total angular momentum $J_d = 0$ [5]. The first amplitude ($A_{UT}^{\sin(\phi-\phi_S)\cos(\phi)}$) shows the expected sensitivity to J_u and was used to obtain a first model-dependent constraint on a linear combination of J_u and J_d. The reduced χ^2 value, defined as

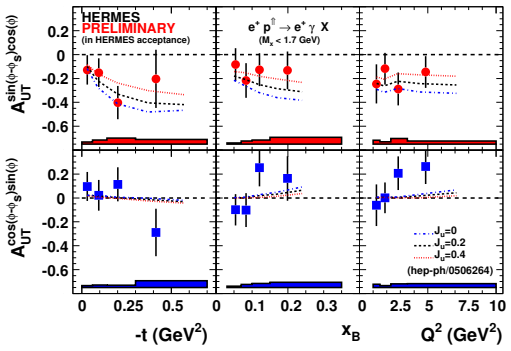

Figure 1: The TTSA amplitudes $A_{UT}^{\sin(\phi-\phi_S)\cos(\phi)}$ and $A_{UT}^{\cos(\phi-\phi_S)\sin(\phi)}$ as a function of $-t$, x_B and Q^2.

$$\Delta\chi^2 \equiv \chi^2 - \chi^2_{minimum} = \left[A^{exp} - A^{VGG}(J_u, J_d)\right]^2 / \left[\delta A^2_{stat} + \delta A^2_{sys}\right] \qquad (4)$$

is evaluated on a J_u, J_d grid. Here A^{exp} is the measured TTSA amplitude integrated over the kinematic range of the data, δA_{stat} (δA_{sys}) is the statistical (systematic) uncertainty, and A^{VGG} is the value calculated at the average kinematics of the measurement by a code [7] based on the mentioned GPD model [6]. The area in the (J_u, J_d)-plane, in which the reduced χ^2 value is not larger than one, is defined as the one-standard-deviation constraint on J_u vs. J_d and shown in Figure 2. The constraint can be parametrized as $J_u + J_d/2.9 = 0.42 \pm 0.21 \pm 0.06$, where the first uncertainty denotes the experimental uncertainty in the measured TTSA amplitude, whereas the second one is a model uncertainty from the unknown profile parameter b [6]. The D-term contribution to the GPDs H and E is set to zero, as suggested by the HERMES results on the beam charge asymmetry (BCA).

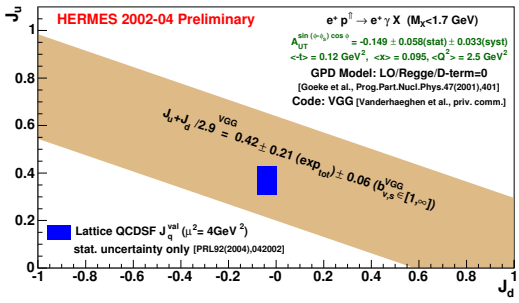

Figure 2: Model-dependent constraint on J_u and J_d. The lattice result from the QSDSF collaboration is also shown.

5 The Recoil Detector

In late 2005, a recoil detector was installed at HERMES. It allows the detection of the recoiling proton and therefore greatly reduces the background contribution in the exclusive

missing mass region. This background is due to associated BH with an intermediate Δ-resonance and to semi-inclusive processes and is reduced from about 15 % to below 1 % by the recoil detector.

The detector basically consists of three sub-detectors. The innermost is a two-layer silicon detector arranged in a diamond-like shape around the target cell inside the HERA beam vacuum at a distance of only 5 cm from the beam. It allows a precise measurement of the deposited energy and provides coordinate input for particle tracking. Outside the vacuum, two barrels with scintillating fibers provide additional input for the momentum reconstruction and measure the energy deposition of particles. The third sub-detector is a photon detector consisting of 3 layers of tungsten and scintillator. The whole detection system is enclosed in 1 T superconducting solenoid.

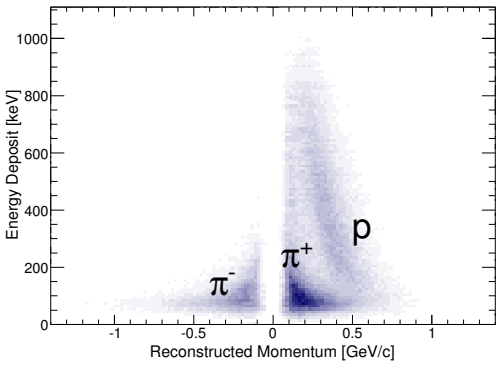

Figure 3: Energy deposit in the inner silicon detector vs. reconstructed momentum.

For low momentum particles the momentum is reconstructed by the silicon detector via the sum of the energy losses (for stopped particles) and dE/dx for particles punching through both silicon detection layers. Higher momentum particles are reconstructed via the bending in the 1 T magnetic field. The tracked particles are identified by the individual energy deposits in the silicon detectors and the fiber tracker for particle momenta below 0.6 GeV/c. Figure 3 shows the good separation between protons and positive pions. For momenta above 0.6 GeV/c the additional energy loss information from the photon detector is used. Photons from π^0 decay are identified by the photon detector in the absence of a charged track reconstructed in the recoil detector.

Acknowledgments

This work has been supported by the German Bundesministerium für Bildung und Forschung BMBF (contract nr. 06 ER 125I and 06 ER 143) and the European Community-Research Infrastructure Activity under the FP6 "Structuring the European Research Area" program (HadronPhysics I3, contract nr. RII3-CT-2004-506078).

References

[1] Slides:
`http://indico.cern.ch/contributionDisplay.py?contribId=88&sessionId=12&confId=9499`
[2] X. Ji, Phys. Rev. Lett. **78** 610 (1997); Phys. Rev. **D55** 7114 (1997).
[3] A. V. Belitsky, D. Müller and A. Kirchner, Nucl. Phys. **B269** 323 (2002)
[4] HERMES Coll., K. Ackerstaff *et al.*, Nucl. Instr. and Meth. **A417** 230 (1998)
[5] F. Ellinghaus *et al.*, Eur. Phys. J. **C46** 729 (2006)
[6] K. Goeke *et al.*, Prog. Part. Nucl. Phys. **47** 401 (2001)
[7] M. Vanderhaeghen, P. A. M. Guichon and M. Guidal, priv. comm. (2003)

Deeply Virtual Compton Scattering at JLab Hall A

Eric Voutier
for the Jefferson Lab Hall A and DVCS Collaborations

LPSC, Université Joseph Fourier, CNRS/IN2P3, INPG
53 avenue des Martyrs, F-38026 Grenoble - France

The deeply virtual Compton scattering reaction has been investigated in the Hall A of the Jefferson Laboratory by measuring longitudinally polarized $(\vec{e}, e'\gamma)$ cross sections, in the valence quark region, for protons and neutrons. In the proton channel, experimental results strongly support the factorization of the cross section at Q^2 as low as 2 GeV^2, opening the path to sytematic measurements of generalized parton distributions (GPDs). In the neutron case, preliminary data show sensitivity to the angular momentum of quarks [1].

1 Introduction

Over the ten past years, deeply virtual Compton scattering (DVCS) became the most promising process to explore the partonic structure of the nucleon [2, 3]. Similarly to the diffusion of light by a cristal, which tells about the internal structure and organization of the material, the scattering of energetic photon off the nucleon in the Bjorken regim ($Q^2 >> M^2$ and $t << Q^2$) allows to access the generalized parton distributions (GPDs) which describe the quark and gluon structure of the nucleon [4, 5]. GPDs correspond to the coherence between quantum states of different (or same) helicity, longitudinal momentum, and transverse position and can be interpreted in the impact parameter space as a distribution in the transverse plane of partons carrying longitudinal momentum fraction x [6, 7, 8]. The GPD framework provides a comprehensive picture of the nucleon structure which unifies within the same formalism form factors, structure functions, and partons angular momenta [9].

In the Jefferson Laboratory (JLab) energy range, the Bethe-Heitler (BH) process, where the real photons are emitted either by the incoming or the scattered electrons, contributes significantly to the cross section of the electro-production of photons. However, the BH process is well-known and exactly calculable from the electromagnetic form factors of the nucleon. Then, similarly to holography technique, the BH process is used as a reference amplitude which interferes with the DVCS amplitude and magnifies the underlying effects [10]. In JLab Hall A, two experimental observables have been investigated: the total $(e, e'\gamma)$ cross section

$$\frac{d^5\sigma}{dQ^2 dx_B dt d\phi_e d\varphi} = \mathcal{T}_{BH}^2 + |\mathcal{T}_{DVCS}|^2 + 2\,\mathcal{T}_{BH}\Re e\{\mathcal{T}_{DVCS}\}\ , \tag{1}$$

and the difference of polarized $(\vec{e}, e'\gamma)$ cross sections for opposite longitudinal beam helicities

$$\begin{aligned}\frac{d^5\Sigma}{dQ^2 dx_B dt d\phi_e d\varphi} &= \frac{1}{2}\left[\frac{d^5\overrightarrow{\sigma}}{dQ^2 dx_B dt d\phi_e d\varphi} - \frac{d^5\overleftarrow{\sigma}}{dQ^2 dx_B dt d\phi_e d\varphi}\right] \\ &= \mathcal{T}_{BH}\,\Im m\{\mathcal{T}_{DVCS}\} + \Re e\{\mathcal{T}_{DVCS}\}\,\Im m\{\mathcal{T}_{DVCS}\}\ .\end{aligned} \tag{2}$$

While the former gives access to the real part of the DVCS amplitude, that is the integral of a linear combination of GPDs convoluted with a quark propagator, the latter is a direct measurement of its imaginary part, which relates to a linear combination of GPDs in the

handbag dominance hypothesis [11]. A dedicated experimental program [12, 13] was set to investigate the DVCS reaction off the proton and off the neutron, with the aim to test factorization in the proton channel and to explore the sensitivity of the neutron channel to E_q, the least known and constrained GPD.

2 Experimental apparatus

A 5.75 GeV/c longitudinally polarized electron beam impinged on 15 cm liquid H_2 and D_2 cells, the latter serving as quasi-free neutron target. Scattered electrons were detected in the left High Resolution Spectrometer (HRS-L) [14] for several Q^2 and constant x_B=0.36. Real photons were detected in a PbF_2 electromagnetic calorimeter organized in an 11×12 array of 3×3×18.6 cm^3 crystals centered around the direction of the virtual photon. The calorimeter front face was 110 cm from the target center supporting the useful t acceptance -0.5 $GeV^2 < t$. Typical beam intensities of 4 μA yielded a 4×10^{37} $cm^{-2}\cdot s^{-1}$ luminosity with 76 % polarized electrons. Three independent reactions were used to calibrate and monitor the calorimeter: $H(e, e'_{\text{Calo.}} p_{\text{HRS}})$, $D(e, e'_{\text{Calo.}} \pi^-_{\text{HRS}})pp$, and $H,D(e, e'_{\text{HRS}} \pi^0_{\text{Calo.}})X$ [15]. It should be emphasized that π^-_{HRS} and $\pi^0_{\text{Calo.}}$ data are taken simultaneously with DVCS data, ensuring a continuous monitoring of the calibration and the resolution of the calorimeter.

3 Factorization in p-DVCS

The polarized cross section difference (Eq. 2) for DVCS off the proton (p-DVCS) was measured at three different Q^2 ranging from 1.5 GeV^2 to 2.3 GeV^2 [16], and was analyzed according to the harmonic structure derived in Ref. [11]. The $\sin(\phi)$ and $\sin(2\phi)$ harmonic coefficients (or moments) have been separated. In the context of this experiment, the kinematical factors entering the square of the DVCS amplitude suppress its contribution to $d^5\Sigma$ as compared to the BH·DVCS interference amplitude, leading to a direct measurement of $\Im m\{\mathcal{T}_{DVCS}\}$. The $\sin(\phi)$ moment corresponds then to the imaginary part of the linear combination $C^I(\mathcal{F})$ (Eq. 3) of the Compton form factors (CFFs) $\mathcal{H}$, $\widetilde{\mathcal{H}}$, and $\mathcal{E}$ which relate to GPDs [11]:

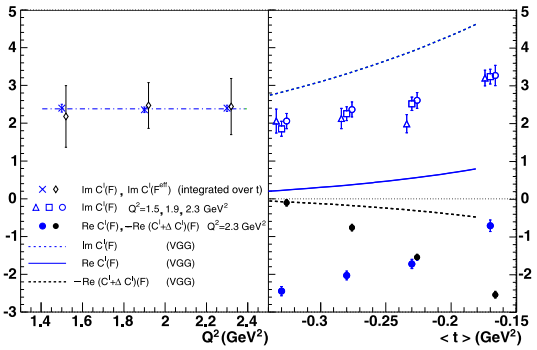

Figure 1: Q^2 and t dependences of the GPDs linear combination extracted from (un)polarized p-DVCS cross sections [16]. The different curves (right panel) are theoretical calculations from a GPD based model [19].

$$C^I(\mathcal{F}) = F_1\mathcal{H} + \xi(F_1+F_2)\widetilde{\mathcal{H}} - \frac{t}{4M^2}F_2\mathcal{E}\ . \tag{3}$$

Figure 1 shows the Q^2 dependence of the twist-2 (Eq. 3) and twist-3 ($\Im m[C^I(\mathcal{F}^{eff})]$) harmonic coefficients of $d^5\Sigma$: the observed independence on Q^2 is an indication for factorization. Furthermore, the contribution of the twist-3 terms to $d^5\Sigma$ was found to be small [16]. These features are a strong indication that factorization applies even at Q^2 as low as 2 GeV^2.

4 Importance of the DVCS amplitude

The unpolarized H$(e, e'\gamma)$p cross section was also measured at the highest Q^2 point. Neglecting the DVCS·DVCS term, the real part of the DVCS amplitude (Eq. 1) was extracted according to the harmonic structure of Ref. [11]. This leads to a $\cos(\phi)$ and $\cos(2\phi)$ dependence, the gluon contribution - which would appear as a $\cos(3\phi)$ term - being negligible in the valence quark region. Experimental data (points) are shown on Fig. 2 as a function of ϕ for the smallest $|t|$-bin. The red curve fitting the data is the sum of the different contributions to the cross section: deviations from the pure BH amplitude (blue solid curve) shows that the DVCS amplitude contributes significantly to $d^5\sigma$. This feature suggests that one should pay attention to the ϕ-dependence of the denominator when extracting GPDs from beam spin asymetries.

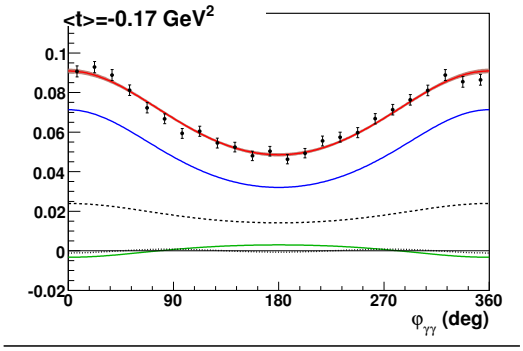

Figure 2: The ϕ-dependence of the $d^4\sigma$ differential cross section (Eq. 1 integrated over ϕ_e) in nb/GeV^4 at Q^2=2.3 GeV^2, decomposed in BH and DVCS contributions [16].

In addition to the real part of the CFFs combination of Eq. 3, the extracted harmonic coefficients give access to the combination

$$C^I(\mathcal{F}) + \Delta C^I(\mathcal{F}) = F_1\mathcal{H} - \frac{t}{4M^2}F_2\mathcal{E} - \xi^2(F_1+F_2)(\mathcal{H}+\mathcal{E}) \qquad (4)$$

which is independent of $\widetilde{\mathcal{H}}$. As for $d^5\Sigma$, the contribution of twist-3 terms to $d^5\sigma$ was found negligible, supporting again factorization [16].

5 Hunting quark angular momentum with n-DVCS

Measuring the DVCS polarized cross section difference on a neutron target (n-DVCS), one can access, similarly to the proton, the combination of Eq. 3. Because of the smallness of the Dirac form factor and the cancellation between the polarized u and d quark distributions in $\widetilde{\mathcal{H}}$, Eq. 3 is dominated by the $\mathcal{E}$ contribution. This spin-flip GPD, which cannot be constrained by deep inclusive scattering, is of particular importance in Ji's sum rule leading to the quark angular momentum [9]. The n-DVCS cross section difference $d^5\Sigma$ was deduced from the subtraction of hydrogen data to deuterium data at Q^2=1.9 GeV^2 and x_B=0.36 [17]. The remaining coherent (d-DVCS) and incoher-

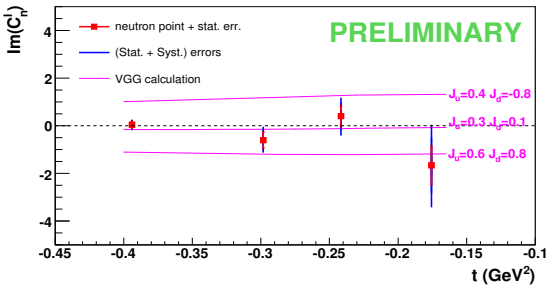

Figure 3: t-dependence of the $\sin(\phi)$ moments of the n-DVCS reaction [15]. The different curves correspond to GPD based calculations for different values of the u and d quarks contributions to the nucleon spin.

ent (n-DVCS) contributions were extracted taking advantage of their $\Delta M_X^2 = -t/2$ kinematical separation [18] in the reconstructed squared missing mass, and the twist-2 (Eq. 3) harmonic coefficient was obtained for several t values, neglecting the higher twist contributions as supported by p-DVCS data. Figure 3 [15] shows the t-dependence of the $\sin(\phi)$ moments extracted for the n-DVCS channel. They appear to be globally compatible with zero. The comparison to GPD based model calculations [19] shows the sensitivity of the present data to the contribution of the u and d quarks to the nucleon spin.

6 Conclusions

The DVCS experimental program at JLab Hall A delivered its first results: the factorization of the cross section was observed, and the power of neutron targets to reach quark angular momenta was proven. These features open unambiguously the era of systematic measurements of generalized parton distributions in DVCS processes at JLab 6 GeV, and 12 GeV in a near future.

Acknowledgments

This work was supported in part by DOE contract DOE-AC05-06OR23177 under which the Jefferson Science Associates, LLC, operates the Thomas Jefferson National Accelerator Facility, the National Science Foundation, the French Atomic Energy Commission and the National Center for Scientific Research.

References

[1] Slides:
`http://indico.cern.ch/contributionDisplay.py?contribId=89&sessionId=12&confId=9499`
[2] M. Diehl, Phys. Rep. **388** 41 (2003).
[3] A.V. Belitsky, A.V. Radyushkin, Phys. Rep. **418** 1 (2005).
[4] X. Ji, J. Osborne, Phys. Rev. **D 58** 094018 (1998).
[5] J.C. Collins, A. Freund, Phys. Rev. **D 59** 074009 (1999).
[6] M. Burkardt, Phys. Rev. **D 62** 071503 (2000).
[7] M. Diehl, Eur. Phys. Jour. **C 25** 223 (2002).
[8] A.V. Belitsky, D. Müller, Nucl. Phys. **A 711** 118c (2002).
[9] X. Ji, Phys. Rev. Lett. **78** 610 (1997).
[10] J.P. Ralston, B. Pire, Phys. Rev. **D 66** 111501 (2002).
[11] A.V. Belitsky, D. Müller, A. Kirchner, Nucl. Phys. **B 629** 323 (2002).
[12] P.Y. Bertin, C.E. Hyde-Wright, R. Ransome, F. Sabatié *et al.*, JLab Proposal **E00-110** (2000).
[13] P.Y. Bertin, C.E. Hyde-Wright, F. Sabatié, E. Voutier *et al.*, JLab Proposal **E03-106** (2003).
[14] A. Alcorn *et al.*, Nucl. Inst. Meth. **A 522** 294 (2004).
[15] M. Mazouz, Doctorat Thesis, Université Joseph Fourier, Grenoble (France), 2006.
[16] C. Muñoz Camacho *et al.*, Phys. Rev. Lett. **97** 262002 (2006).
[17] M. Mazouz *et al.*, *to be submitted to* Phys. Rev. Lett.
[18] M. Mazouz, Nucl. Phys. **A 782** 41c (2007).
[19] M. Vanderhaeghen, P.A.M. Guichon, M. Guidal, Phys. Rev. **D 60** 094017 (1999).

The Double Spin Asymmetry in Exclusive π^+ Electro-Production with CLAS

Joshua Pierce*

University of Virginia - Physics Department
382 McCormick Road, Charlottesville Virginia - United States of America

The eg1b run was conducted using CLAS at Jefferson Lab in 2000 by the CLAS collaboration. A 1.6 GeV - 5.6 GeV polarized electron beam and polarized nuclear targets (composed of NH_3 and ND_3) were used, allowing single and double spin asymmetries to be measured. This analysis deals with the double spin asymmetry $A_{||}$ in the exclusive production of positive pions from a polarized proton ($ep \rightarrow e\pi^+ n$). The double spin asymmetry was measured as a function of the four kinematic variables W, Q^2, $\cos\theta^*$, and ϕ^*. The value of this asymmetry can be used to help determine the spin structure of the resonances, due to its sensitivity to the spin dependent parts of the cross section. A brief description of the experimental setup will be given, and preliminary results for the asymmetry will be shown.

1 Introduction

Exclusive pion production is a useful tool for analyzing the nucleon resonances because of the large branching ratio of many of the resonances into the $N\pi$ channel, for example the $P_{11}(1440)$, or Roper resonance, $D_{13}(1520)$ and the $F_{15}(1680)$. This analysis is of the spin dependence of the $ep \rightarrow e\pi^+ N$ reaction using data taken with CLAS [3] during the eg1b run period at Jefferson Lab. A longitudinally polarized electron beam and a longitudinally polarized ammonia target were used in the eg1b run period.

2 Spin Dependence of the Cross-section

When both the electron and the proton are polarized, the virtual photon cross-section for exclusive π^+ production can be written in terms of the polarized response functions, R [2]. The response functions depend on W, Q^2 and $\cos\theta^*$ (the angle between the pion momentum and the momentum transfer q in the center of mass of the pion-neutron system). These equations all assume a reference frame where $\hat{z}$ is along $\vec{q}$, and $\hat{y}$ is normal to the hadronic scattering plane.

$$\begin{aligned}
\frac{d\sigma_\nu}{d\Omega_\pi} &= \frac{|\vec{q}|}{q_\gamma^{CM}}[R_T + P_y R_T^y + \epsilon_L(R_L + P_y R_L^y) \\
&+ \sqrt{2\epsilon_L(1+\epsilon)}((R_{LT} + P_y R_{LT}^y)\cos\phi^* + (P_x R_{LT}^x + P_z R_{LT}^z)\sin\phi^*) \\
&+ \epsilon((R_{TT} + P_y R_{TT}^y)\cos 2\phi^* + (P_x R_{TT}^x + P_z R_{TT}^z)\sin 2\phi^*) \\
&+ h\sqrt{2\epsilon_L(1-\epsilon)}((R_{LT'} + P_y R_{LT'}^y)\sin\phi^* + (P_x R_{LT'}^x + P_z R_{LT'}^z)\cos\phi^*) \\
&+ h\sqrt{1-\epsilon^2}(P_x R_{TT'}^x + P_z R_{TT'}^z)]
\end{aligned}$$

*For the CLAS Collaboration

The target polarization can be re-written in terms of ϕ^*, which is the angle between the hadronic and leptonic interaction planes, θ_γ, which is the production angle of the virtual photon, and P_T, the polarization as measured in the lab.

$$\begin{aligned} P_x &= P_T \sin\theta_\gamma \cos\phi^* \\ P_y &= -P_T \sin\theta_\gamma \sin\phi^* \\ P_z &= P_T \cos\theta_\gamma \end{aligned}$$

It is clear that the cross-section can be written in terms of a polarization independent part, a part that depends only on the beam polarization (h or P_B), a part that depends only on the target polarization P_T, and a part that depends on both the beam and target polarization.

$$\sigma = \sigma_0 + P_B\sigma_e + P_T\sigma_t - P_B P_T \sigma_{et} \tag{1}$$

Separating the double spin dependent part of the cross-section from each of the single spin dependent parts requires that both the beam and target polarizations be reversed.

$$A_{et} = \frac{\sigma_{et}}{\sigma_0} = \frac{(\sigma_{-+} - \sigma_{++}) + (\sigma_{+-} - \sigma_{--})}{(\sigma_{++} + \sigma_{-+}) + (\sigma_{+-} + \sigma_{--})}$$

3 Experiment

As mentioned in Sec. 1, the eg1b run used the CEBAF polarized electron beam and a polarized nuclear target [4]. The target consisted of an $^{15}NH_3$ sample, polarized using the dynamic nuclear polarization technique, which requires low temperatures and a very high magnetic field. The target was located 50 cm upstream of the center of the CLAS detector in experimental Hall B at Jefferson Lab.

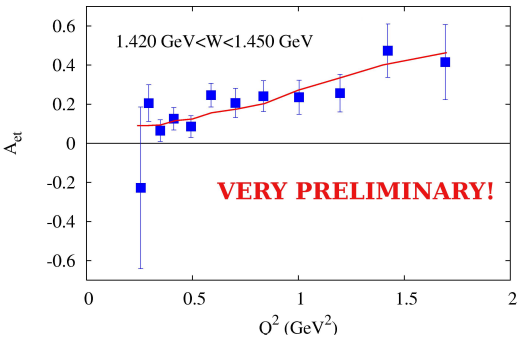

Figure 1: A_{et} as a function of Q^2 for fixed 1.420< W <1.450 GeV, averaged over $\cos\theta^*$ and ϕ^*. MAID2003 is shown for comparison

Event selection was performed by detecting the scattered electron and the produced π^+, solving for the missing mass of the undetected particle, and doing a cut on this mass about the mass of the neutron.

Equation 2 shows the relation between the double spin asymmetry and the measured counts in each helicity state. The terms N' represent the charge normalized counts for each combination of beam and target helicity. P_B is the polarization of the beam, P_T is the polarization of the target, and f_D is the dilution factor. The product of the beam and target polarizations was measured by the asymmetry for elastic scattering on the proton and comparing that to the known asymmetry. The beam polarization is known independently from runs using a Moeller polarimeter, meaning that the two can be separated.

$$A_{et} = \frac{\sigma_{et}}{\sigma_0} = \frac{1}{P_B^+ P_T^-} \frac{(N'_{-+} - N'_{++}) + r_B(N'_{+-} - N'_{--})}{(N'_{++} + N'_{-+}) + r_T(N'_{+-} + N'_{--})} \quad (2)$$

The target polarization is only reversed once per beam energy setting, and the positive and negative target polarizations are not generally equal. This requires that in addition to the counts for each helicity state being normalized to the accumulated charge on the target during that configuration, the beam and target polarizations for each given configuration must be normalized to each other. This is done in Equation 2 with the terms r_B and r_T which are the ratios of the beam and target polarization respectively for the periods when the target had negative polarization and the target had positive polarization.

Contributions from the ^{15}N and other materials, such as the liquid He surrounding the target and the target window material, are accounted for with a dilution factor f_D, which is the ratio of counts from polarizable protons to the total counts. This ratio is determined in each kinematic bin by scaling up the missing mass spectrum obtained from dedicated ^{12}C runs to approximate the unpolarized part of the $^{15}NH_3$ spectrum.

4 Results

The data have been analyzed and the double spin asymmetries have been extracted. The asymmetry was extracted as an independent function of the four kinematic variables W, Q^2, $\cos\theta^*$, and ϕ^*, as previously defined. In order to display the results, one or more kinematic variable is often averaged over. This is done by averaging the asymmetry, not simply integrating the counts. The advantage of this is that it limits the effects of acceptance on the results.

All of the results shown here are from the 4.2 GeV beam energy run. In all of the figures, comparisons are shown to MAID2003 [5]. The values for MAID2003 were generated over the same four dimensional space as the asymmetries were measured in, and then averaged together with the same weight as the asymmetry. Statistical error associated with the background subtraction and the measurement of the product of beam and target polarization are included in the statistical error bars shown, although systematic errors are not.

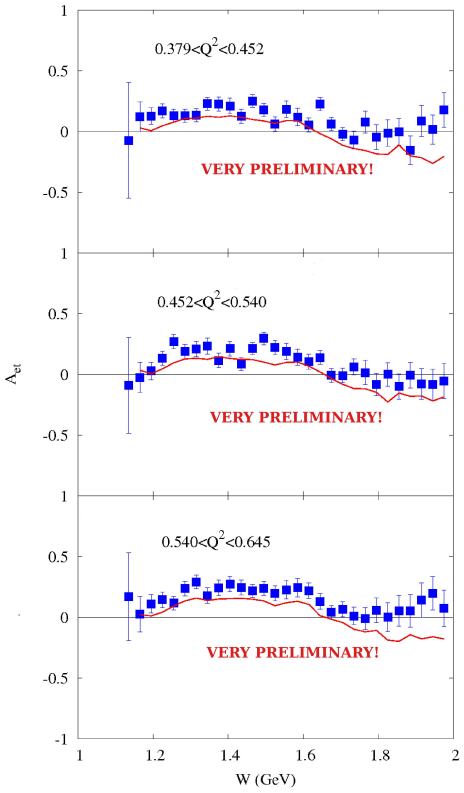

Figure 2: A_{et} as a function of W for fixed Q^2 values, averaged over $\cos\theta^*$ and ϕ^*. MAID2003 is shown for comparison

5 Conclusions and Outlook

The large amount of data collected in this experiment will enable us to significantly increase our knowledge of the spin structure of the resonances. This is already apparent from the preliminary figures shown, which have rather small error bars for fairly small bins. The addition of this data set should help in the development and enhancement of models of the multi-pole terms associated with the resonances.

Analysis of the asymmetry from the other energy settings of the experiment is proceeding, as is systematic error calculation. The additional energy settings will provide greater kinematic coverage. In addition, the single spin asymmetries are being measured. This allows access to different response functions, giving more information about the spin structure of the resonances. The high statistics and high polarizations of the eg1b run allow for the data be used for a variety of purposes. The data are being analyzed for inclusive asymmetries on both the proton and deuteron (which was the primary motivation for the run), as well as other exclusive and semi-inclusive reactions.

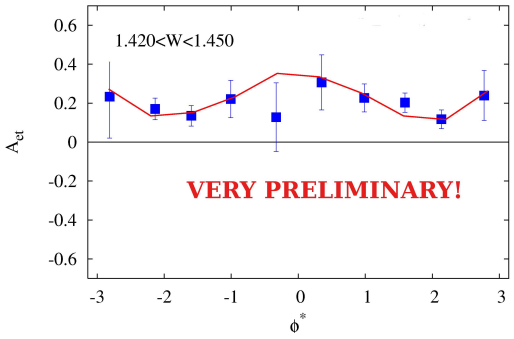

Figure 3: A_{et} as a function of ϕ^* for fixed 1.420< W <1.450 GeV, averaged over $\cos\theta^*$ and Q^2. MAID2003 is shown for comparison

References

[1] Slides:
`http://indico.cern.ch/contributionDisplay.py?contribId=84&sessionId=12&confId=9499`

[2] A. S. Raskin and T. W. Donnelly, Annals of Phys. **191** 78 (1989).

[3] B. A. Mecking *et al.*, Nucl. Instrum. Meth. **A503** 513 (2003)

[4] C. D. Keith *et al.*, Nucl. Instrum. Meth. **A501** 327 (2003)

[5] D. Drechsel *et al.*, Nucl. Phys. **A645** 145 (1999).

Heavy Flavors

Convenors:
Stephanie Menzemer,
Rainer Mankel,
Benno List,
Michael Klasen

DIS Charm Cross-Sections through D^* and D Meson Tagging by the ZEUS Detector

Hartmut Stadie
for the ZEUS Collaboration

Universität Hamburg - Institut für Experimentalphysik
Luruper Chaussee 149, D-22761 Hamburg - Germany

We summarize the results from the ZEUS experiment on D meson production in deep inelastic scattering using HERA I data and preliminary results on $D^{*\pm}$ production using HERA II data. Single differential cross sections have been measured as a function of Q^2, x, and the transverse momentum and pseudorapidity of the D meson. These measurements are compared to the prediction of next-to-leading-order QCD. Furthermore, the open charm contribution, $F_2^{c\bar{c}}$, to the proton structure function, F_2, has been extracted from the data.

1 Introduction

Charm quarks are copiously produced in deep inelastic scattering (DIS) at HERA. At sufficiently high photon virtualities, Q^2, the production of charm quarks constitutes up to 30% of the total cross section[2, 3]. The charm quark production in DIS at HERA is dominated by the interaction between the exchanged virtual photon and a gluon within the proton, the boson-gluon-fusion (BGF) mechanism. Thus, the charm cross section is directly sensitive to the gluon density in the proton.

The presented analyses were performed with data taken from 1998-2000 and 2003-2005. In these periods, HERA collided electrons or positrons with energy $E_e = 27.5$ GeV with protons of energy $E_p = 920$ GeV. The ZEUS detector is described in detail elsewhere [4]. The main components used in the presented analyzes were the compensating uranium-scintillator calorimeter, the central tracking detector and for the HERA II measurement the micro-vertex detector. The calorimeter is the major component for the reconstruction of the DIS kinematic variables.

2 D^* Cross Section Measurement using HERA II Data

HERA II data collected from 2003 to 2005 were used to measure the D^* cross section in DIS. It corresponds to an integrated luminosity of 162 pb^{-1}. The event selection of this measurement is directly comparable to previous measurements [5].

Events were required to have a reconstructed vertex within 30 cm of the nominal interaction point in z. The quantity $\delta = E - p_z = \sum_i E_i(1 - \cos\theta_i)$ was calculated using the energies, E_i, and polar angles, θ_i, and had to satisfy $30 < \delta < 60$ GeV to eliminate photoproduction events or DIS events with high-energy initial-state radiation. The photon virtuality, Q^2 and the fraction of the energy transferred to the proton in its restframe, y, were reconstructed from the energy and the angle of the scattered electron (Q^2_e,y_e) and from the hadronic system using the Jaquet-Blondel method (Q^2_{JB},y_{JB}). The kinematic region chosen for the measurement was $5 < Q^2 < 1000$ GeV^2 and $0.02 < y < 0.7$.

The selection of D^* mesons also followed the strategy used in the previous measurements [5].The D^* mesons were identified using the decay channel $D^{*+} \to D^0\pi^+$ with the subsequent decay $D^0 \to K^-\pi^+$ and the corresponding antiparticle decay. The kinematic region for the D^* candidates was $1.5 < p_T(D^*) < 15$ GeV and $|\eta(D^*)| < 1.5$. Details on the candidate reconstruction and the determination of acceptance and uncertainties can be found in a previous publication [6]. The single differential cross sections were measured as a function of Q^2, the Bjorken scaling variable, x, and the pseudorapidity and the transverse momentum of the D^* meson. The cross sections were compared to next-to-leading order (NLO) predictions from the HVQDIS program [7] using the ZEUS NLO QCD fit [8] for $m_c = 1.35$ GeV as the input parton density in the proton. As can be seen in Figure 1, the cross section $\frac{d\sigma}{dx}$ falls by about three orders of magnitude while it is still well described by the NLO calculation.

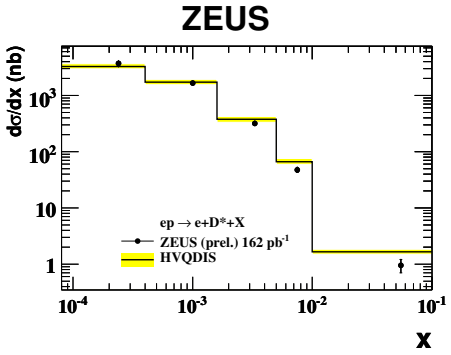

Figure 1: Differential D^* cross section as a function of the Bjorken scaling variable x. The solid points show the HERA II data while the solid line gives the NLO QCD prediction.

3 HERA I Charm Cross Section Measurements

Besides the HERA I D^* measurement [5], additional charm cross section measurements [9] were performed using an integrated luminosity of 82 pb^{-1}. Charm was tagged by reconstructing D^0, $D^\pm$ and $D_s^\pm$ charm mesons using the decay modes $D^0 \to K^-\pi+$, $D^+ \to K^-\pi^+\pi^+$, and $D_s^+ \to \phi\pi^+ \to K^+K^-\pi^+$ and their charge conjugates. The DIS kinematic region was defined by $1.5 < Q^2 < 1000$ GeV^2 and $0.02 < y < 0.7$ and charm mesons with $|\eta(D)| < 1.6$ and $p_T(D^0, D^\pm) > 3$ GeV respectively $p_T(D_s^\pm) > 2$ GeV were selected. The single differential cross sections for the different charm mesons were measured as a function of Q^2, x, $\eta(D)$, and $p_T(D)$ and agreed reasonably well with the NLO predictions [1, 9].

Furthermore, the D^* charm meson production at low Q^2 was measured with 82 pb^{-1} of HERA I data [10]. The decay $D^{*+} \to D^0\pi_s^+$ with the subsequent decay $D^0 \to K^-\pi^+$ and the corresponding an-

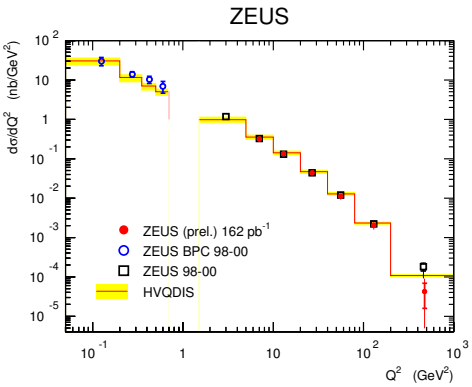

Figure 2: Differential D^* cross section as a function of the photon virtuality Q^2. The solid circles show the HERA II data while the open boxes show the results of the corresponding HERA I measurement. The open circles show the HERA I measurements using the beampipe calorimeter. The solid line gives the NLO QCD prediction with the shaded band indicating its uncertainty.

tiparticle decay were used to tag charm and the ZEUS beampipe calorimeter was used to identify the scattered electron. This allowed measurements in the kinematic region $0.05 < Q_e^2 < 0.7$ GeV and $0.02 < y < 0.7$. The D^* candidates had to satisfy $|\eta(D^*)| < 1.5$ and $1.5 < p_T(D^*) < 9.0$ GeV. This measurement combined with the other two D^* measurements allows testing of the NLO prediction over a large range of Q^2. This comparison is shown in Figure 2 and shows good agreement with the NLO QCD prediction.

4 Open Charm Contribution to the Structure Function

The extraction of the open charm contribution, $F_2^{c\bar{c}}(x,Q^2)$, to the proton structure function F_2 from the charm meson measurements was performed as described in the previous measurements [5]. $F_2^{c\bar{c}}(x,Q^2)$ can be defined in terms of the inclusive double-differential $c\bar{c}$ cross section in x and Q^2 by

$$\frac{d^2\sigma^{c\bar{c}}(x,Q^2)}{dxdQ^2} = \frac{2\pi\alpha^2}{xQ^4}\{[1+(1-y)^2]F_2^{c\bar{c}}(x,Q^2) - y^2F_L^{c\bar{c}}(x,Q^2)\}.$$

As the measured cross sections are well described in the probed kinematic region, the following relation was used to extract $F_2^{c\bar{c}}(x,Q^2)$:

$$F_{2,meas}^{c\bar{c}}(x,Q^2) = \frac{\sigma_{meas}(ep\to DX)}{\sigma_{theo}(ep\to DX)}F_{2,theo}^{c\bar{c}}(x,Q^2).$$

The cross sections in the measured charm meson region were extrapolated to the full kinematic region in $p_T(D)$ and $\eta(D)$ using HVQDIS and the $c\bar{c}$ cross section was obtained using the known fragmentation fractions. Figure 3 shows the HERA I D^* [5] and D^0,$D^\pm$,D_s [9] results and the HERA II D^* result. All measurements show good agreement with each other and the ZEUS QCD NLO fit.

5 Conclusions

The ZEUS experiment has measured the charm cross section in DIS in the photon virtuality range $0.05 < Q^2 < 1000$ GeV^2. These measurements have been compared to the prediction of leading-logarithmic Monte Carlo simulations and show good agreement. Furthermore, the open charm contribution, $F_2^{c\bar{c}}$, to the proton structure function, F_2, was extracted from the data. The different measurements show good agreement with each other and the ZEUS NLO QCD fit. Further improvements to these measurements can be expected from the additional data from the 2006 to 2007 HERA running and the HERA II $D^\pm$ analysis presented in [11].

References

[1] Slides:
`http://indico.cern.ch/contributionDisplay.py?contribId=185&sessionId=5&confId=9499`

[2] ZEUS Collab., J. Breitweg et al., Eur. Phys. J. **C 12**, 35 (2000).

[3] H1 Collab., C. Adloff et al., Phys. Lett. **B 528**, 199 (2002).

[4] ZEUS Collab., U. Holm(ed.), *The ZEUS Detector*. Status Report (unpublished), DESY (1993) available on `http://www-zeus.desy.de/bluebook/bluebook.html`.

[5] ZEUS Collab., S. Chekanov et al., Phys. Rev. **D 69**, 012004 (2004).

[6] J. Loizides, Proceedings of the XXIII International Conference on High Energy Physics (2006).

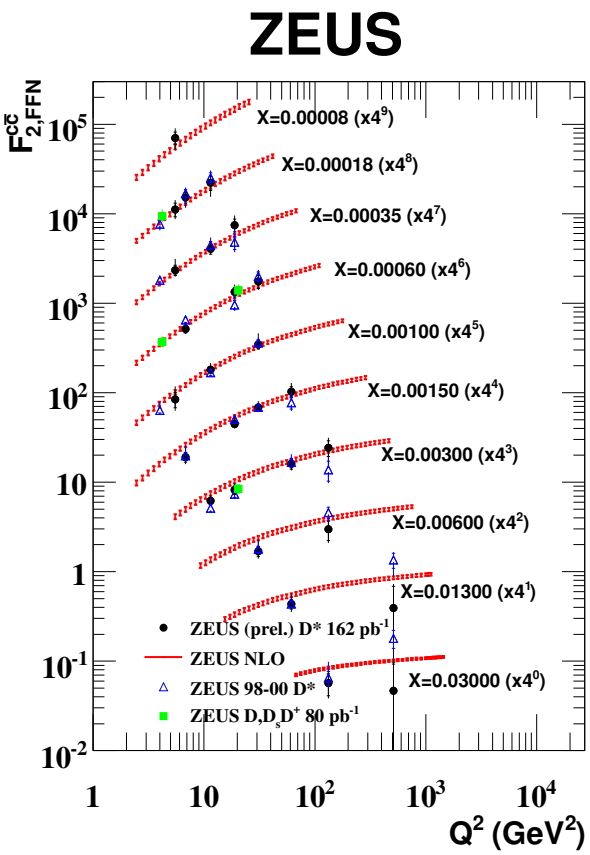

Figure 3: The measured $F_2^{c\bar{c}}$ at x values between 0.00008 and 0.03 as a function of Q^2. The circles show the HERA II D^* measurement, while the triangles show the HERA I D^* measurement. The results obtained from the HERA I measurement using D^0,$D^{\pm}$,D_s decays is shown by squares. The data are shown with statistical uncertainties (inner bars) and statistical and systematic uncertainties added in quadrature (outer bars).

[7] B. W. Harris and J. Smith, Phys. Rev. **D 57**, 2806 (1998).

[8] ZEUS Collab., S. Chekanov, Phys. Rev. **D 67**, 012007 (2003).

[9] ZEUS Collab., S. Chekanov et al., JHEP **07**, 74 (2007).

[10] ZEUS Collab., S. Chekanov et al. Phys. Lett. **B 649**, 111 (2007).

[11] D. Nicholass, these proceedings, slides:
`http://indico.cern.ch/contributionDisplay.py?contribId=191&sessionId=5&confId=9499`.

Charm Production in DIS at H1

Katerina Lipka[1] for the H1 Collaboration

University of Hamburg - Institute of Experimental Physics
Luruper Chaussee 149, 22761 Hamburg - Germany

Recent results on D^* meson production in deep inelastic scattering at HERA are presented [1]. The data were taken with the H1 detector in the years 2004 to 2006 and correspond to an integrated luminosity of 222 pb^{-1}. The analysis covers the kinematic region $5 < Q^2 < 100$ GeV^2 and $0.05 < y < 0.6$. The visible range for the D^* meson is restricted to $p_T(D^*) > 1.5$ GeV and $|\eta(D^*)| < 1.5$ where about 10,000 D^* mesons are reconstructed. Single and double differential inclusive cross sections of D^* meson production are compared to two LO Monte-Carlo simulations and a Next-to-Leading Order calculation in the massive scheme.

1 Charm production in ep scattering at HERA

In deep inelastic electron-proton scattering at HERA charm quarks are produced predominantly in the photon-gluon fusion process. The mass of the charm quark provides an additional hard scale which makes the calculations in the framework of pQCD possible. Since the gluon is always directly involved in the boson-gluon fusion process, charm production becomes an important tool for the determination of the gluon density in the proton. Recent upgrades in accelerator performance, detector hardware and event reconstruction allows high precision measurements of charm production cross sections.

Two Monte-Carlo simulations and a Next-to-Leading Order (NLO) calculation are compared to the measured cross sections. Both Monte-Carlo simulations RAPGAP [2] and CASCADE [3] are using the Leading Order Matrix element. Higher order corrections are approximated by parton showers. The parton evolution in the RAPGAP Monte-Carlo is realised in the collinear approximation according to the DGLAP [4] equations. The CASCADE Monte-Carlo uses the unintegrated gluon density and the parton evolution is done according to the CCFM [5] equations.

The NLO calculation HVQDIS [6] is realised in the fixed flavour number scheme using 3 active flavours in the proton. Charm quarks are produced dynamically and are treated as massive. The value of the charm mass is varied between 1.3 and 1.5 GeV. The parton densities CTEQ5F3 are used. Renormalisation and factorisation scales are taken to be $\mu_r = \mu_f = \mu = \sqrt{(Q^2 + 4m_c{}^2)}$ and are varied simultaneously from 0.5μ to 2μ. The charm fragmentation is performed in the lab frame according to the Peterson [7] parametrisation with the value of $\epsilon = 0.045$.

2 Charm tagging via D^* meson production at H1

In this analysis $D^{*\pm}$ mesons are used to tag the charm production in deep inelastic scattering. The D^* mesons are reconstructed using the decay chain $D^* \to D^0 + \pi_{slow} \to K + \pi + \pi_{slow}$.

The data presented here [1] were collected with the H1 detector at HERA in the years 2004-2006. During this period HERA operated with 27.5 GeV electrons[a] and 920 GeV

[a]Here and further electron is used to denote both electrons and positrons.

protons at a center-of-mass energy of $\sqrt{(s)} = 318$ GeV. The data sample used for this analysis amounts to an integrated luminosity L=222 pb^{-1}.

The detailed description of the H1 detector can be found elsewhere [8]. The scattered electron is registered in a lead-scintillating fibre calorimeter, situated in the backward region of the H1 detector. Charged particles emerging from the interaction region are measured in the central tracking detector, the major part of which consists of two cylindrical drift chambers. The analysis covers the kinematic region 5< Q^2 <100 GeV^2 and 0.05< y <0.6, where Q^2 is the four-momentum-transfer squared and y is the inelasticity. The decay products of D^* mesons are measured in the central tracking detector of H1. The range of the transverse momentum and the pseudorapidity is restricted to $1.5 < p_T(D^*) < 14$ GeV and $|\eta(D^*)| < 1.5$, with η =-ln tan(θ/2).

The signal is extracted using the mass difference distribution $\Delta m = m_{K\pi\pi} - m_{K\pi}$ of the D^* candidates and the wrong charge combinations $(K^{\pm}\pi^{\pm})\pi^{\mp}$. The wrong charge combinations provide a good description of the shape of the uncorrelated background. In Fig. 1 the Δm distribution is shown for the D^* candidates and the wrong charge background.

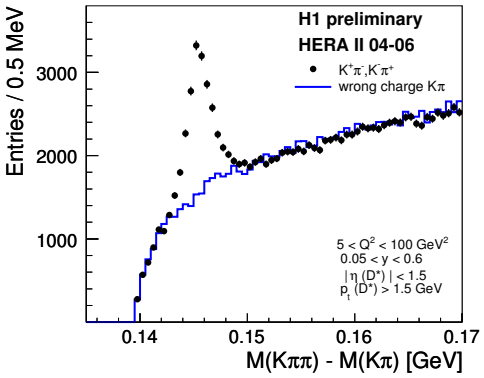

Figure 1: Mass difference distribution of D^* candidates (closed symbols) and wrong charge background (solid line)

The number of D^* mesons is determined from the simultaneous fit to the Δm distribution of the D^* candidates and the wrong charge combinations. The Crystall Ball fit function [9] is used to describe the shape of the signal. From a fit a total of 10000 D^* mesons is obtained. The contribution of reflections from the decays of D^* other than the investigated one is estimated to be 4% and is taken into account.

3 Cross section measurement

The cross section of D^* production is calculated from the number of D^* mesons using the RAPGAP Monte-Carlo simulation to correct the data for the detector acceptance and efficiency. The total D^* cross section of 4.23 nb $\pm$ 0.09$_{stat}$ $\pm$0.37$_{syst}$ is obtained. The track reconstruction efficiency contributes most into the systematic uncertainty. Single differential cross sections of D^* meson production are shown as functions of DIS kinematics in Fig. 2 in comparison to the two LO Monte-Carlo models and the NLO calculation. Both Monte-Carlo models, based on the DGLAP and the CCFM evolution equations, and the NLO calculation describe the data equally well. The cross section as a function of D^* meson kinematics is shown in Fig. 3. Both RAPGAP and CASCADE models describe the pseudorapidity distribution well, while the NLO calculation underestimates the cross section in the forward region. The D^* cross section as a function of the inelasticity of the D^* meson, which is defined as $z_D = (E(D^*) - p_z(D^*))/2yE_e$, where E_e is the electron beam energy, is shown in the right panel of Fig. 3. The inelasticity z_D represents the fraction of the photon energy carried by the D^* meson. This distribution is described poorly by the models. These features have been observed with the previous measurements [10] and become more prominent with

the higher statistics of the recent data.

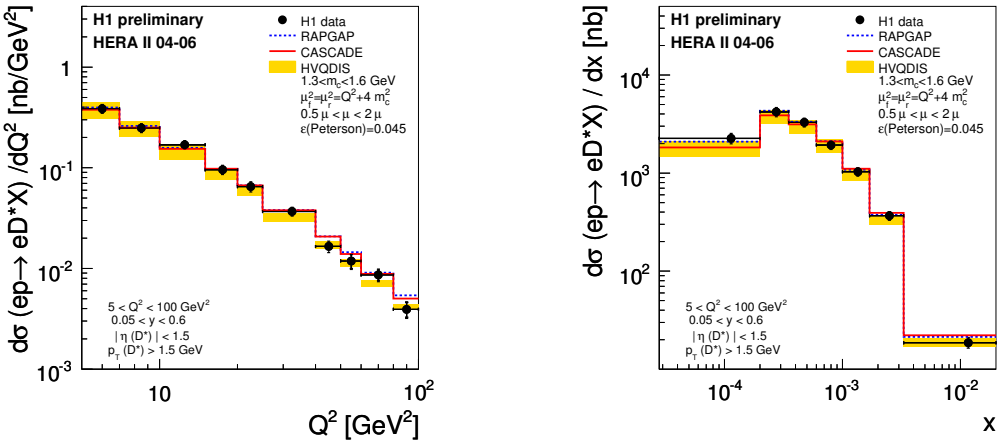

Figure 2: Differential cross section of D^* production as a function of Q^2 (left) and x(right). The data (closed symbols) are compared to the RAPGAP (dashed line) and CASCADE (solid line) Monte-Carlo simulations and the NLO calculation (shaded band).

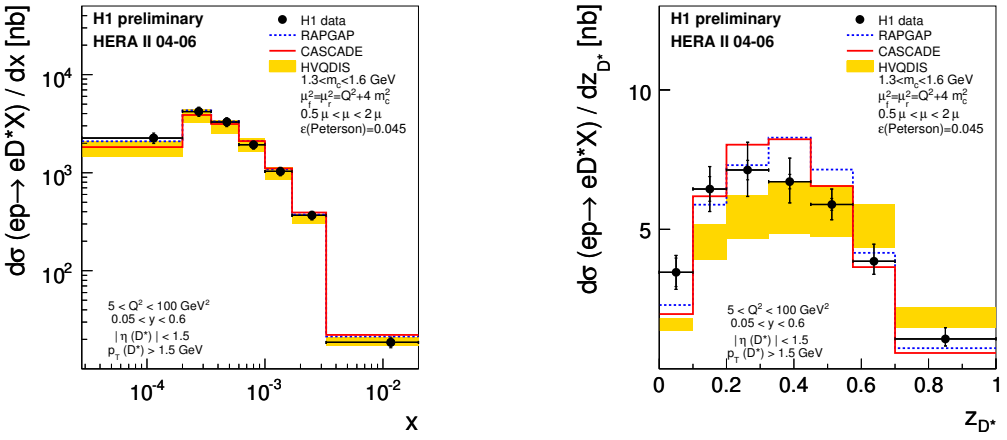

Figure 3: Differential cross section of D^* production as a function of $\eta(D^*)$ (left) and inelasticity of the D^*, z_D, (right). The data (closed symbols) are compared to the LO Monte-Carlo simulations (solid line) and the NLO calculation (shaded band).

The high statistics allows also to make more differential studies. In Fig. 4 the double-differential cross section of the D^* production are shown as a function of pseudorapidity $\eta(D^*)$ and transverse momentum $p_T(D^*)$. In general, the NLO calculation and the LO simulations are consistent with the data, however the deficits of the data description by all the models is visible. Within the theoretical uncertainties due to charm mass and scale variation

HVQDIS describes the data well, except of the lowest $p_T(D^*)$ bin. The CASCADE simulation overestimates the data at high $p_T(D^*)$, which indicates that the gluon density used in CASCADE is too large at high gluon momenta. Similar feature was observed in the previous measurement [10].

4 Conclusions and outlook

Recent H1 measurements of D^* meson production cross section are presented. About a half of the full statistics collected by H1 is analysed. The kinematical range for this analysis is given by $5 < Q^2 < 100$ GeV^2, $0.05 < y < 0.6$, and the visible D^* range is defined by $p_T(D^*) > 1.5$ GeV, $|\eta(D^*)| < 1.5$. The data is described by both the LO Monte-Carlo simulations. The NLO calculation is consistent with the data within theoretical uncertainties due to the variation of renormalisation and factorisation scales and the charm mass. With the increasing precision of the measurement the deficits of the models to describe the data become visible but still more precise data are needed to differentiate between the theoretical approaches. The whole statistics of the data collected by H1 is been analysed and both statistic and systematic precision of the data will improve significantly.

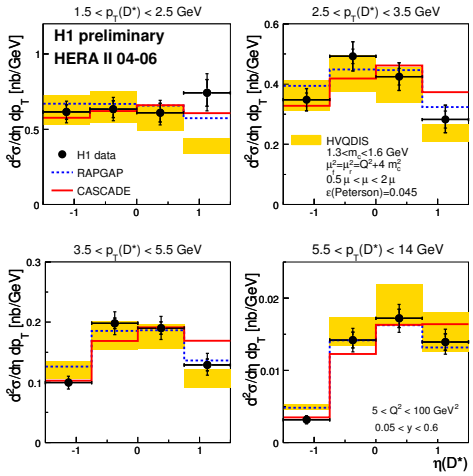

Figure 4: Double-differential cross section of D^* production as a function of $\eta(D^*)$ and $p_T(D^*)$. The data (closed symbols) are compared to the RAPGAP (dashed line) and CASCADE (solid line) Monte-Carlo simulations and the NLO calculation (shaded band).

References

[1] Slides:
`http://indico.cern.ch/contributionDisplay.py?contribId=190&sessionId=5&confId=9499`

[2] H. Jung, Comput. Phys. Commun. **86** 147 (1995).

[3] H. Jung, Comput. Phys. Commun. **143** 100 (2002).

[4] V. Gribov, L. Lipatov, Yad. Fiz. **15** 781 (1972);
G. Altarelli, G. Parsi, Nucl. Phys. B**126** 298 (1977);
Y. Dokshitzer, Zh. Eksp. Teor. Fiz. **73** 1216 (1977).

[5] M. Ciafaloni, Nucl. Phys. B.**296** 49 (1988);
S. Catani, F. Fiorani, G. Marchesini, Nucl. Phys. B**336** 18 (1990).

[6] B. Harris,J. Smith, Nucl. Phys. B**452** 109 (1995).

[7] C. Peterson *et al.* Phys.Rev. D **57** 2806 (1998)

[8] I. Abe *et al.*, Nucl. Instrum. Meth. **A 386** 310 (1997)

[9] J. E. Gaiser,*Charmonium Spectroscopy from readiative Decays of the* J/Ψ *and* $\Psi'^{\star}$, Ph. D. Thesis,Stanford University (1982)

[10] A. Aktas [H1 Collaboration] *et al.* hep-ex/0701023

Measurement of $D^{\pm}$ Meson Cross Sections in Deep Inelastic Scattering using the ZEUS Micro Vertex Detector

Dan Nicholass[1] on behalf of the ZEUS collaboration.

1- Argonne National Laboratory - University College London
Department of Physics and Astronomy, Gower Street, London - Great Britain

Measurments of charm production in deep inelastic scattering (DIS) have been carried out by the ZEUS collaboration at HERA. Results using integrated luminosities of 135 pb^{-1} of HERA II running are presented. Single differential cross sections are compared to perturbative QCD predictions. Charm cross sections are in reasonable agreement with QCD calculations. The charm contribution to the proton structure function F_2^{cc} has also been measured, and is also in reasonable agreement with QCD fits.

1 Introduction

The electron/positron-proton collider HERA at the DESY laboratory is a unique facility to test Quantum Chromo Dynamics (QCD). Charm production in deep inelastic scattering (DIS) has been extensively studied at HERA[2, 3, 4, 5, 6, 7]. These measurements are consistent with pQCD calculations indicating boson-gluon fusion (BGF) as the dominant mechanism of charm production. Charm is mainly tagged in the 'golden' decay channel of the D^* meson $D^{*+} \rightarrow K^+\pi^-\pi^-(+\text{c.c.})$. More advanced instrumentation using secondary vertex tagging have been used to measure other charm cross sections at H1[8]. ZEUS results by tagging $D^{\pm}$ mesons using the micro-vertex detector from the 2005 running phase of HERA II are reported.

2 Analysis

The measurement of $D^{\pm}$ mesons cross sections in DIS has been performed using $135\,\text{pb}^{-1}$ of e^-p data collected by the ZEUS detector in the 2005 running period.

The deep inelastic scattering regime in which the measurements were made is characterised by $Q^2 > 1\,\text{GeV}^2$, where Q^2 is the virtuality of the exchanged photon.

Tagging of the $D^{\pm}$ mesons was performed by reconstructing a candidate $D^{\pm}$ meson in its decay mode, $D^{\pm} \rightarrow K^+\pi-\pi^-$ (+c.c). Tracks in the pseudorapidity region $|\eta^{\text{track}}| < 1.6$ with transverse momentum $p_T > 0.7$ GeV for the kaon and $p_T > 0.5$ GeV for the pions were required. The $D^{\pm}$ mesons were reconstructed in the region, $3 < p_T^{D^{\pm}} < 20\,\text{GeV}$ and $|\eta^{D^{\pm}}| < 1.6$. The purity of the $D^{\pm}$ tagging was improved by utilising the precision tracking provided by the ZEUS microvertex detector (MVD).

The increased purity was achieved through the use of the signed two dimensional decay length significance (S_{DL}). This is defined to be the two dimensional distance from the secondary vertex to the primary interaction point projected onto the $D^{\pm}$ momentum vector divided by the error on this distance. Figure 1 shows the improvement in the reconstructed $D^{\pm}$ signal from using a cut on the S_{DL} variable. The uncertainty on the number of re-

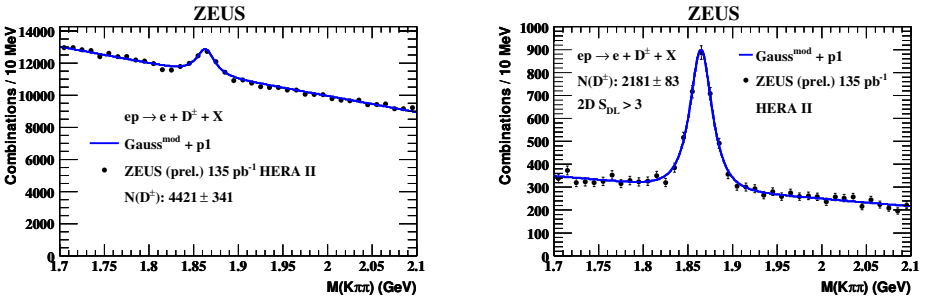

Figure 1: The effect of the $S_{\rm DL}$ cut on the precision of the reconstructed $D^{\pm}$ meson signal. The data (dots) are fitted with a modified gaussian.

constructed $D^{\pm}$ mesons is reduced from 7.7% to 3.8% by rejecting $D^{\pm}$ candidates with a $S_{DL} < 3$. After all cuts 2181 ± 83 candidates were selected.

3 Differential $D^{\pm}$ meson cross sections in DIS

Differential cross sections have been measured for the process $ep \to e + D^{\pm} + X$ as functions of Q^2, $p_T^{D^{\pm}}$, $\eta^{D^{\pm}}$ and the Bjorken scaling variable x. By definition this cross section includes contributions from beauty production though these contributions are expected to be small. The measurements are compared to the NLO QCD calculation performed in the massive scheme by Harris and Smith [9]. The $D^{\pm}$ momentum is simulated using the Peterson function for charm fragmentation. The central theoretical prediction was calculated using a charm mass of $m_c = 1.35\,\text{GeV}$ and renormalisation and factorisation scales, $\mu_R = \mu_F = \sqrt{Q^2 + 4m_c^2}$. The Peterson fragmentation function parameter (ϵ) was set to 0.035. Upper and lower bounds were estimated by independently changing the charm mass, fragmentation and renormalisation scales, Peterson ϵ parameter and the input PDFs used for the calculation [1]. The resulting deviations from the central value were then added in quadtrature to obtain the total theoretical uncertainty.

The single differential cross sections are presented in fig. 2. The beauty contribution as estimated using RAPGAP is generally small contributing most at low $p_T^{D^{\pm}}$ and small values of the scaling variable x. Previous ZEUS results from the HERA I running period are shown for comparison on the Q^2 figure, these again show the improved precision resulting from the use of the MVD. All measurements are well described by the NLO QCD prediction obtained from HVQDIS.

4 Extraction of the charm contribution to the proton structure function, F_2^{cc}.

At low values of inelasticity (y) the charm contribution to the proton structure function can be defined in terms of the double differential $c\bar{c}$ cross section in Q^2 and x.

$$\frac{d^2\sigma^{c\bar{c}}(x,Q^2)}{dxdQ^2} = \frac{2\pi\alpha^2}{xQ^4}\left\{\left[1+(1-y)^2\right]\right\} F_2^{c\bar{c}}(x,Q^2) \qquad (1)$$

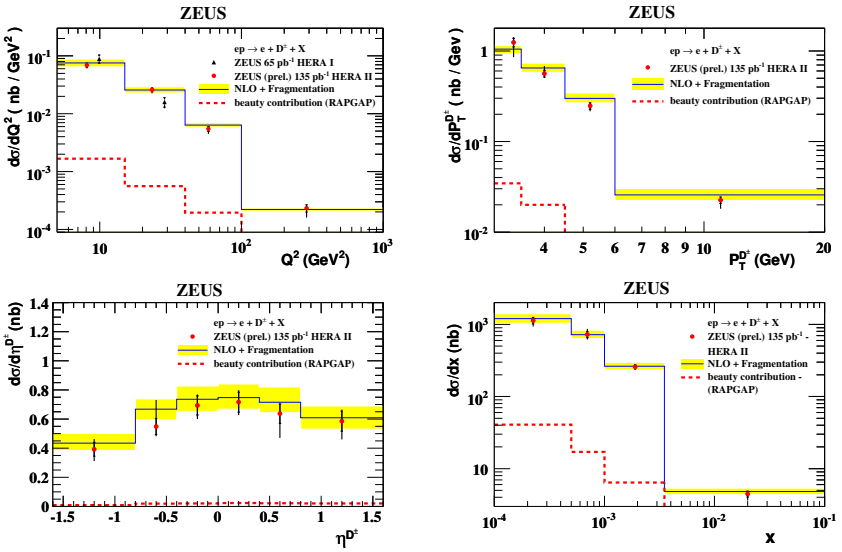

Figure 2: Single differential cross sections of the process $ep \to e + D^{\pm} + X$ as functions of Q^2, $p_T^{D^{\pm}}$, $\eta^{D^{\pm}}$ and the scaling variable x. The data (dots) are shown compared to the NLO QCD prediction with its theoretical uncertainty (yellow band). The expected beauty contribution estimated from RAPGAP (red dashed line) is also shown.

The $c\bar{c}$ cross section was obtained by measuring the $D^{\pm}$ cross section and employing the hadronisation fraction $f(c \to D^{\pm})$ to derive the total charm cross section. Since the measurement of $D^{\pm}$ mesons is only possible in a limited kinematic range a method for extrapolating to the full kinematic phase space is required. As the structure function varies only slowly it is assumed to be constant in a given Q^2 and y bin. This leads to the measured $F_2^{c\bar{c}}$ in a bin i being given by.

$$F_{2,meas}^{c\bar{c}}(x_i, Q_i^2) = \frac{\sigma_{i,\mathrm{meas}}(ep \to D^{\pm}X)}{\sigma_{i,\mathrm{theo}}(ep \to D^{\pm}X)} F_{2,\mathrm{theo}}^{c\bar{c}}(x_i, Q_i^2) \qquad (2)$$

where σ_i are the cross sections in bin i in the measured kinematic region. The value of $F_{2,\mathrm{theo}}^{c\bar{c}}$ was calculated from the NLO coefficient functions [10]. The functional form of $F_{2,\mathrm{theo}}^{c\bar{c}}$ was used to quote results for $F_2^{c\bar{c}}$ at appropriate values of Q_i^2 and x_i. In this calculation the same charm mass, parton densities and factorisation and renormalisation scales have been used as for the HVQDIS calculation of the differential cross sections. The hadronisation was performed using the Peterson fragmentation function. The beauty contribution as estimated from RAPGAP was subtracted from the data. As with the differential cross sections this contribution is small.

The measured values of $F_2^{c\bar{c}}$ are shown in fig. 3. The theoretical prediction calculated from coeeficient functions along with the prediction's uncertainty are also shown. Results from the HERA I running period are shown for comparison in the two higher Q^2 bins. It can be seen that the precision of the HERA II results is comparable even though the HERA I results are obtained by a combination of measurements of three charm mesons. This demonstrates the power of lifetime tagging techniques.

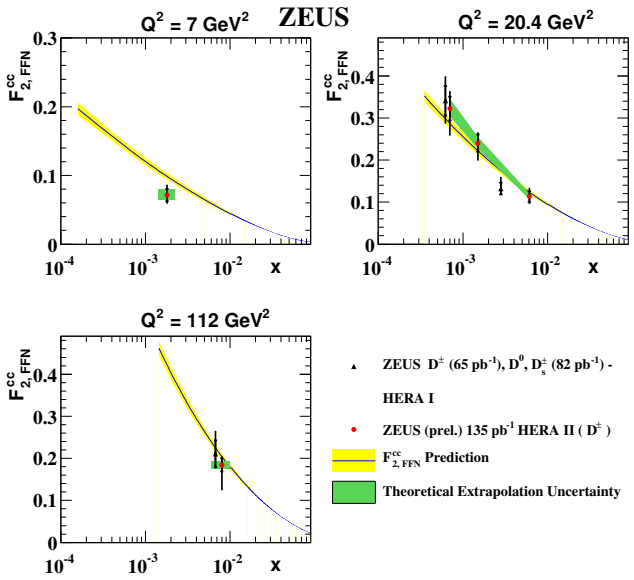

Figure 3: Measured values of the charm contribution to the proton structure function $F_2^{c\bar{c}}$ (dots) are shown along with previous ZEUS results. The uncertainty of the measurements associated with the extraction procedure is also shown (green band).

References

[1] Slides:
`http://indico.cern.ch/contributionDisplay.py?contribId=191&sessionId=5&confId=9499`

[2] ZEUS Coll., S. Chekanov et al., Phys. Rev. **D 69**, 0120004 (2004).

[3] H1 Coll., C.Adloff et al., Phys. Lett. **B 528**, 199 (2002).

[4] ZEUS Coll., J. Breitweg et al., Phys. Lett. **B 481**, 213 (2000).

[5] ZEUS Coll., J. Breitweg et al., Eur. Phys. J. **C 12**, 35 (2000).

[6] H1 Coll., C.Adloff et al., Nucl. Phys. **B 545**, 21 (1999).

[7] ZEUS Coll., J. Breitweg et al., Eur. Phys. J. **C 6**, 67 (1999).

[8] H1 Collab., A. Aktas et al., Eur. Phys. J. **C 38**, 447 (2005)

[9] Harris, B. W. and Smith, J., Phys. Rev., **D 57**, 2806 (1998)

[10] ZEUS Collaboration S. Chekanov et al., Phys. Rev. **D 67**, 012007 (2003)

Charm Production with Jets at H1

Sebastian Schmidt

Deutsches Elektronen-Synchrotron
Notkestrasse 85, 22607 Hamburg - Germany

Measurements of inclusive $D^{*\pm}$ meson production in photoproduction and deep-inelastic scattering at HERA are presented. To gain a further understanding of the production mechanism of charm, events containing jets, in addition to the $D^{*\pm}$, are selected. This allows to investigate quantities sensitive to the partons interacting in the hard subprocess such as the fractional momentum w.r.t the photon and proton, and the azimuthal angle between the jets. The data are compared with theoretical models such as NLO pQCD calculations based on the DGLAP evolution scheme or those based on CCFM evolution and k_t-unintegrated gluon distributions.

1 Introduction

Charm is produced at HERA in deep-inelastic scattering (DIS) and in photoproduction predominantly by boson-gluon-fusion between a photon originating from the positron and a gluon originating from the proton. A full understanding of this interaction is only possible if the kinematic properties of the two outgoing hard partons are completely determined. The well known tagging of charm events by $D^{*\pm}$ mesons decaying in the so called "Golden Channel" results in high precision reconstruction of the kinematic quantities, but considerably limits the available event sample due to the low branching ratios. Instead of studying events with a double tagged charm one can approximate one or both of the partons by jets and thus gain deeper insight into the production mechanism of charm at HERA.

2 Inclusive cross sections

Recently measurements of inclusive $D^{*\pm}$ meson production in DIS [2] and photoproduction [3] have been performed at HERA with the H1 detector. The results are compared with different theoretical predictions based on NLO QCD using DGLAP evolution. Predictions in the fixed flavour number scheme (FFNS) are made using the HVQDIS[4] and FNMR[7] programs for DIS and photoproduction, respectively. Predictions using the zero mass variable flavour number scheme (ZM-VFNS) [6], in which the charm mass is neglected, are available in the DIS case. Predictions using the general mass variable flavour number scheme (GM-VFNS) [8], which combines aspects of the FFNS and ZMVFNS, are available for photoproduction. In addition, the results are compared with predictions based on CCFM evolution involving the k_t-unintegrated gluon distribution in the proton calculated using the CASCADE program [5].

The kinematic range of the DIS analysis is described by restrictions on the photon virtuality $2 \leq Q^2 \leq 100\,\mathrm{GeV}^2$ and the inelasticity $0.05 \leq y \leq 0.7$. For the photoproduction sample conditions on $Q^2 < 0.01\,\mathrm{GeV}^2$ and on the photon-proton centre-of-mass energy $171 < W_{\gamma p} < 256\,\mathrm{GeV}$ are applied.

The overall description of the DIS data by the available models is reasonable. Some deviations are observed in the forward region of large pseudorapidity η which are also reflected in an excess of the data over the models in the correlated region of low inelasticity z (see Fig. 1).

The photoproduction data are described less well, especially if distributions are considered which are sensitive to the phase space of the outgoing charm quark (p_t and η). In the z distribution a similar excess of data over the models is observed as in the DIS case. In general for the photoproduction analysis — and to a lesser extent in the DIS case — the precision of the data is much higher than the accuracy of the NLO calculations, which is dominated by the uncertainty on the charm mass, the choice of factorisation and renormalisation scale and the parametrisation of the non-perturbative fragmentation.

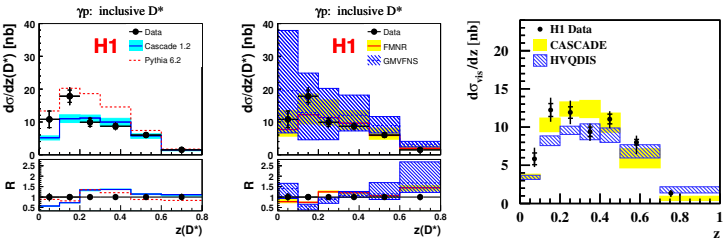

Figure 1: Differential distribution in bins of the inelasticity z for inclusive $D^{*\pm}$ meson production in photoproduction (left and middle plot) and DIS (right plot).

3 Production of $D^{*\pm}$ mesons with jets

In order to define a sample of $D^{*\pm}$ mesons with jets the $k_\perp$-cluster algorithm is applied to hadronic final state objects. For events containing a $D^{*\pm}$ meson candidate these are reconstructed from tracks and calorimeter depositions in the Breit and laboratory frame for DIS and photoproduction, respectively. The four-vector of the reconstructed $D^{*\pm}$ meson is used instead of the four-vectors of its three decay particles. The leading jet is required to have a transverse energy of $E_T > 4\,\text{GeV}$, the next-to-leading jet a transverse energy of $E_T > 3\,\text{GeV}$.

In the following a selection of interesting jet observables are discussed.

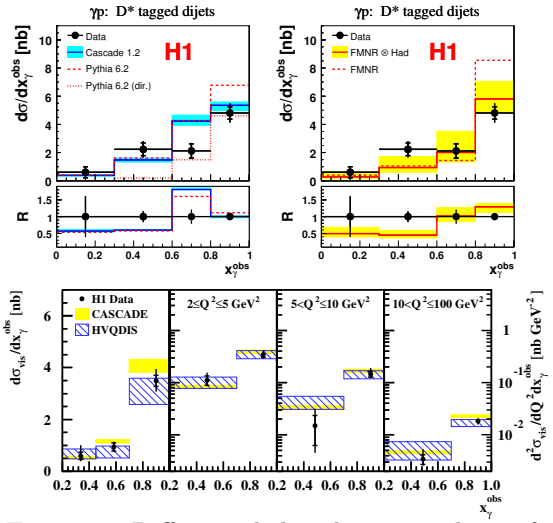

Figure 2: Differential distribution in bins of x_γ for the photoproduction case (upper plots) and the DIS case (lower plot). For DIS also double differential distributions in bins of x_γ^{obs} and Q^2 are shown.

3.1 The observables x_γ and x_g

At LO the observables x_γ^{obs} and x_g^{obs} give the observed fraction of the photon momentum carried by the parton involved in the hard subprocess and the observed fraction of the proton momentum carried by the gluon, respectively. The determination of both quantities involves the reconstruction of the 4-vectors of the partons emerging from the hard subprocess, which are approximated by the two jets.

The distribution of x_γ^{obs} (see Fig. 2) peaks for both the DIS and the photoproduction case at 1 as expected from direct processes. It has however significant contributions at lower values from so-called resolved processes. In the DIS case for HVQDIS there seems to be

no need for an additional resolved contribution beyond what is already present at NLO. CASCADE provides also a reasonable description.

For photoproduction the large cross section at small $x_\gamma^{\rm obs}$ shows that processes beyond direct photon-gluon-fusion are needed to describe the data in the collinear approach. This can be seen by comparison with the prediction for PYTHIA direct. Both PYTHIA and CASCADE give a poor description of the $x_\gamma^{\rm obs}$ distribution. All predictions underestimate the region of low $x_\gamma^{\rm obs}$ which can be seen in the normalised shape R.

Figure 3 shows differential cross sections as a function of $x_g^{\rm obs}$ integrated over Q^2 and in three regions of Q^2 for the DIS sample. Both HVQDIS and CASCADE describe the Q^2 dependence of $x_g^{\rm obs}$ with the default parton density functions (PDF) CTEQ5F3 (for HVQDIS) and A0 (for CASCADE). The sensitivity to the PDFs has been investigated by comparing with the predictions of HVQDIS using the MRST2004F3NLO parametrisation and with the predictions of CASCADE using the parametrisation J2003 set-1 for the unintegrated gluon density. The differences in the cross section are small, compared to the large theoretical and statistical uncertainties.

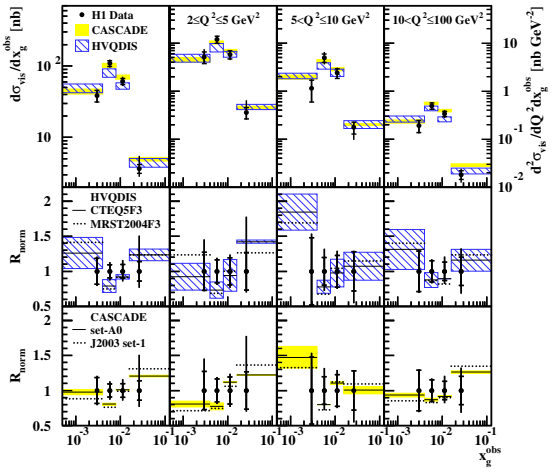

Figure 3: Differential distributions in bins of $x_g^{\rm obs}$ for DIS. In addition double differential distributions in bins of $x_g^{\rm obs}$ and Q^2 are shown. In the lower part of the plot the normalised ratio $R_{\rm norm}$ between data and the predictions is shown. Here an additional comparison between predictions using the default PDFs and alternative PDFs is performed.

3.2 The observable $\Delta\phi$

Another interesting aspect of the production process of charm at HERA is the distribution of the azimuthal angle between the two jets.[a] In leading order this distribution consists of a delta peak at 180 degrees originating from back-to-back configurations in the transverse plane. All contributions away from this value are due to higher order (and resolution) effects. As for analysies of inclusive dijets at HERA[9] disagreement between data and the theory models is observed (see Fig. 4). In both kinematic regimes for the NLO-DGLAP approach (HVQDIS) higher order contributions at small angles are lacking. However, the model based on the CCFM evolution equation using unintegrated gluon densities (CASCADE) overestimates the contributions in that region. This is most probably due to a too broad unintegrated gluon density.

[a] In the analysis of the photoproduction sample for this observable instead of the two jets representing the charm and the anti-charm quark the $D^{*\pm}$ meson and a single jet not associated with the $D^{*\pm}$ meson are studied.

4 Summary

In recent H1 analyses production cross sections of $D^{*\pm}$ mesons with jets have been studied in DIS as well as in photoproduction. They have been compared with theoretical predictions to achieve insight into the production mechanism of charm at HERA. The observable x_γ allows to separate the composition of direct and resolved processes. With the help of the observable x_g present parton density functions can be verified. The azimuthal angle between the jets[b] $\Delta\phi$ shows, depending on the model used, missing higher order contributions or a too broad k_t-unintegrated gluon density.

In general it is observed that the significance of the measurements is limited by about the same amount in the precision of the data and in the uncertainties of the theoretical calculations.

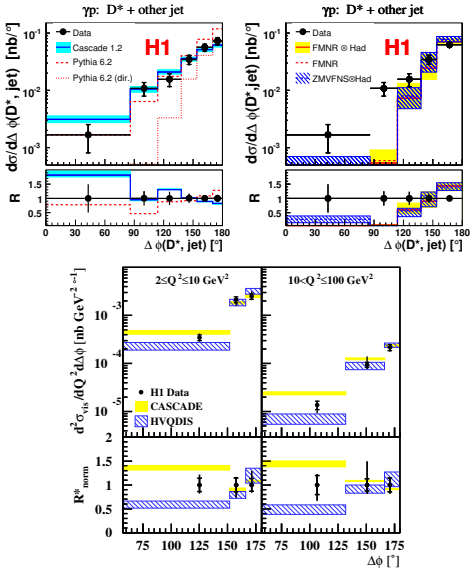

Figure 4: Differential distributions in bins of $\Delta\phi$ for photoproduction (upper plots) and in bins of Q^2 and $\Delta\phi$ for DIS (lower plot). In addition the ratios between data and the models are given, in the DIS case ($R^*_{\rm norm}$) normalised with respect to the upper two bins in $\Delta\phi$.

References

[1] Slides:
`http://indico.cern.ch/contributionDisplay.py?contribId=192&sessionId=5&confId=9499`

[2] H1 Collab., A. Aktas *et al.*, Accepted by Eur. Phys. J. C [hep-ex/0701023v1] (2007).

[3] H1 Collab., A. Aktas *et al.*, Accepted by Eur. Phys. J. C [hep-ex/0608042v1] (2006).

[4] B.W. Harris and J. Smith, Nucl. Phys. B **452** (1995) 109 [hep-ph/9503484]; B.W. Harris and J. Smith, Phys. Lett. B **353** (1995) 353 [Erratum-ibid. B **359** (1995) 423] [hep-ph/9502312].

[5] H. Jung, Comput. Phys. Commun. **143** (2002) 100 [hep-ph/0109102].

[6] B.A. Kniehl, G. Kramer and M. Maniatis, Nucl. Phys. B **771** (2005) 345; Erratum **720** (2005) 345 [hep-ph/0109102]; I. Schienbein, *Procs. of Ringberg Workshop "New Trend in HEAR Physics 2005"*, Eds. G. Grindhammer *et al.*, Ringberg Castle, Tegernsee, Germany, 2-7 Oct 2005, World Scientific Publishing Singapore 2006 [hep-ph/0601235].

[7] S. Frixione, P. Nason and G. Ridolfi, Nucl. Phys. B **454** (1995) 3 [hep-ph/9506226]; S. Frixione, M.L. Mangano, P. Nason and G. Ridolfi, Phys. Lett. B **348** (1995) 633 [hep-ph/9412348].

[8] B.A. Kniehl, G. Kramer, I. Schienbein and H. Spiesberger, Phys. Rev. D **71** (2005) 014018 [hep-ph/0410289]; B.A. Kniehl, G. Kramer, I. Schienbein and H. Spiesberger, Eur. Phys. J. C **41** (2005) 199 [hep-ph/0502194].

[9] H1 Collab., A. Aktas *et al.*, Eur. Phys. J. C **33** (2004) 477 [hep-ex/0310019].

[b] or between the $D^{*\pm}$ meson and a jet in the photoproduction case

Charm Fragmentation Function and Charm Fragmentation Fractions at ZEUS

Shuangshi Fang
(ON BEHALF OF THE ZEUS COLLABORATION)

DESY,Notkestasse 85, Hamburg 22607, Germany

Based on the data collected during 1996-2000 period at ZEUS detector, the charm fragmentation function and fragmentation fractions have been measured in photoproduction and deep inelastic scattering,respectively. The measured function is compared to different fragmentation models incorporated in leading-logarithm Monte Carlo simulations and a next-to-leading-order calculation. The shape is similar to those from e^+e^- experiments. The measured charm fractions are consistent with previous measurements.

1 Introduction

Heavy quark production offers a sensitive test of QCD predictions. In this talk[1] "heavy quark" refers to a charm(anti-charm) quark.Usually heavy quark production was divided into four steps: the production of heavy quark pairs; the development of parton showers; the transition of partons to hadrons(also known as fragmentation) and the unstable hadrons decay according to their branching fractions. The first two steps can be calculated with pQCD, while the fragmentation is a non-perturbative process. The phenomenological models[2] have been applied to study charm fragmentation and two widely used fragmentation functions are the model of Peterson *et al.*[3] and of Kartvelishvili *et al.*[4]. Since these non-perturbative models are not calculated from the first principle, experimentally study is necessary to determine the parameters of the fragmentation functions.

Experimentally, charm fragmentation functions have been studied for many years[5] in e^+e^- annihilation. It also has been studied in ep collisions by H1 collaboration[6]. The most recent published results with high precision is from Belle[7]. For a recent review of fragmentation function measurements and theory, see[8].

Meanwhile, the measured production cross sections of D^0,D^+, D^{*+} and D_s^+ charm mesons allow to extract charm fragmentation fractions which describe the probability of charm quark hadronsing into particular charm mesons. In this talk, we present the recent preliminary results for fragmentation functions and the measurement of fragmentation fractions based on HERAI data taken at ZEUS detector. The ZEUS detector is a multipurpose magnetic detector designed to study ep scattering at HERA which is described in detail in Ref.[9].

2 Charm fragmentation function

The data collected during the 1996 to 2000 running period corresponding to an integrated luminosity of 120 pb$^-$1 was used for this analysis.

The measurement was performed in the kinematic range $Q^2 < 1$ GeV^2 and $130 < W_{\gamma p} < 280$ GeV. The jets were reconstructed using the κ_T algorithm with at least one jet required to have $E_T^{jet} > 9$ GeV and $|\eta^{jet}| < 2.4$. The D^* mesons were reconstructed using

$D^* \to D^0\pi_s \to K\pi\pi_s$. The transverse momentum of D^* was required to be greater than 2 GeV and the pseudo-rapidity was required to be in the region $|\eta^{D^*}| < 1.5$. To minimise background, narrow windows were selected for the mass difference and the mass the D^0 meson: $0.1435 < \Delta M < 0.1475$ GeV and $1.83 < M(D^0) < 1.90$ GeV. Finally the D^* meson as associated with a jet by considering the closest jet in $\eta - \phi$ space and requiring R(= $\sqrt{(\eta^{jet} - \eta^{D^*})^2 + (\phi^{jet} - \phi^{D^*})^2}$)<0.6. After above selection and subtraction of the background bin-by-bin estimated from wrong-charge pairs, 1268 ± 56 D^* mesons were used for further analysis.

Since the energy of charm quark is approximated by the energy of the reconstructed D^* jet, the fragmentation observable z, the energy transferred from a charm quark to a given meson, was defined as $(E+p_\parallel)/2E_{jet}$, where the $p_\parallel$ is the longitudinal momentum of the D^* relative to the jet axis. Two Monte Carlo(MC) simulations(PYTHIA 6.1 and HERWIG 6.1) were compared with the z of the data in which PYTHIA seems to be better in describing data. The data was then corrected for detector effects using a bin-by-bin method with the PYTHIA simulation used as the central MC and the HERWIG simulation as a systematic check.

The relative cross sections were also used to extract the fragmentation parameter of Peterson function. The MC was fit to the data via a χ^2-minimisation procedure to determine the best value of ε. The result of varying ε is shown in Fig. 1 and the data is well described by the best value,$\varepsilon = 0.064 \pm 0.006^{+0.011}_{-0.008}$, of the fit(for the figures of the following fit, see[1]).

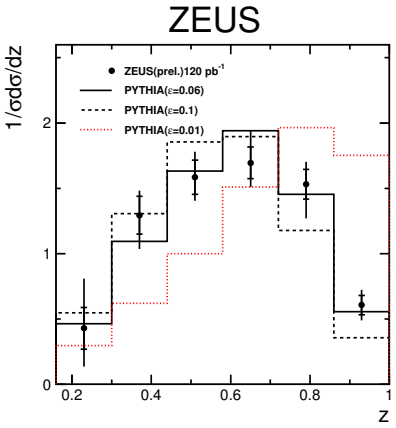

Figure 1: Relative cross section, $1/\sigma(d\sigma/dz)$, for the data(points) compared with values of parameter $\varepsilon = 1$(dashed line),$\varepsilon = 0.06$(solid line) and the $\varepsilon = 0.02$(dotted line), in the Peterson fragmentation function as as implemented in PYTHIA predictions.

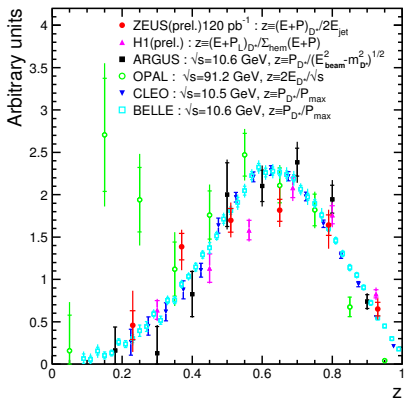

Figure 2: Fragementation function versus z for the ZEUS data compared to previous measurements. For shape comparison, the data sets were normalized to 1/(bin width) for $z > 0.3$, thus avoiding the first three bins from OPAL, which have large gluon-splitting component.

Similarly, the parameters of Peterson function and Kartvelishvili function were extracted in the next-to-leading order(NLO) framework[11], respectively. As the final state particles

in the NLO QCD calculation are partons, to enable a fair comparison with the data, the predictions were corrected for effects of hadronization. The fit to the data gives the best value of $\varepsilon = 0.0721^{+0.0139}_{-0.0123}$ and $\alpha = 2.87^{+0.33}_{-0.35}$.

The comparison of the ZEUS data with previous measurements is shown in Fig. 2. To avoid the first three bins from OPAL collaboration which have a large gluon-splitting component, the data sets were normalised to 1/(bin width) for $z > 0.3$. Although the definitions of fragmentation observable and kinematics range are different, the spectra are similar in shape.

3 Charm fragmentation fractions

Charm production in deep inelastic scattering has been measured with the ZEUS detector at HERA using an integrated luminosity of 82 pb^{-1}. Charm has been tagged by reconstructing D^*+,D^0,D^+ and $D_s^+(+c.c.)$ charm mesons. The charm hadrons were measured in the kinematic range $p_T(D^{*+}, D^0, D^+, D_s^+) > 3$ GeV for $1.5 < Q^2 < 1000$ GeV^2 and $0.02 < y < 0.7$. The production cross sections were used to extract charm fragmentation ratios and the fraction of charm quarks haronising into a particular charm meson in the kinematic range considered. The detailed description of event selection are listed in Ref.[12].

The fragmentation fractions of charm quark hadronising to a specific charm meson are listed in Table. 1. The results are compared with the values obtained in photoproduction[13], in DIS by the H1 collaboration[14] and in e^+e^- annihilations[15]. All the measurements are consistent with each other.

$f(c \to D^+)$	$0.216 \pm 0.019^{+0.002+0.008}_{-0.020-0.010}$	$R_{u/d}$	$1.22 \pm 0.11^{+0.005}_{-0.002} \pm 0.03$
$f(c \to D^0)$	$0.605 \pm 0.020^{+0.009+0.015}_{-0.052-0.023}$	γ_s	$0.225 \pm 0.030^{+0.018+0.034}_{-0.007-0.026}$
$f(c \to D_s^+)$	$0.092 \pm 0.011^{+0.007+0.012}_{-0.008-0.010}$	P_V^d	$0.617 \pm 0.038^{+0.017}_{-0.009} \pm 0.017$
$f(c \to D^{*+})$	$0.229 \pm 0.011^{+0.006+0.007}_{-0.021-0.010}$		

Table 1: The fractions of charm quarks hadronising as a particular charm meson and the results for $R_{u/d}$,γ_s and P_V^d.

In addition to charm fragmentation fractions, the fragmentation ratios shown in Table. 1 are calculated based on the measured production cross sections of charm mesons. The ratio of neutral to charged D meson production, $R_{u/d}$,is used to test the iso-spin invariance. It is consistent with 1, confirming the iso-spin invariance, which implies that u and d quarks are produced equally in charm fragmentation. The strangeness-suppression factor for charm mesons,γ_s, is given by the ratio of twice the production rate of charm-strange mesons to the production rate of non-strange charm meson. And the strange quark production is measured to be suppressed by a factor ~ 4 as shown by γ_s. The ratio of charged D mesons produced in a vector state, P_V^d, is given by the ratio of vector to the sum of vector and pseudo-scalar charm meson production cross sections. The measured P_V^d value is smaller than the naive spin counting prediction of 0.75. The ratios are in good agreement with previous measurements[13][14][15][16].

4 Summary

Charm fragmentation function has been studied in photoproduction regime with HERAI data. The parameters of Peterson and Kartvelishvili functions were extracted. The study indicates that both of the fragmentation functions provide a reasonable description of data. Comparison with previous measurements shows that the spectra are similar in shape although the fragmentation observable definitions and kinematics are different.

Charm fragmentation fractions were measured in DIS regime and the results are in good agreement with those measured in photoproduction regime and in e^+e^- annihilation. $R_{u/d}$, γ_s and P_d^V were measured which are also consistent with previou smeasurements. $R_{u/d}$ is compatible with unity which indicates the iso-spin invariance, but P_V^d was found to be smaller than the naive spin-counting prediction of 0.75.

References

[1] `http://indico.cern.ch/contributionDisplay.py?contribId=193&sessionId=5&confId=9499`

[2] P.D.B. Collins and T.P. Spiller, J. Phys. **G11**,1289(1985);
B. Andersson, G. Gustafson, and B. Söderberg, Z. Phys. C**20**,317(1983);
M.G. Bowler, Z. Phys. **C11**,169(1981).

[3] C. Peterson, D. Schlatter, I. Schmitt, and P.M. Zerwas, Phys. Rev. **D27**,105(1983).

[4] V.G. Kartvelishvili, A.K. Likhoded, and V.A. Petrov, Phys. Lett. **78B**,615(1978).

[5] ARGUS Coll., H. Albrecht *et al.*, Z. Phys. **C52**,353(1991);
OPAL Coll., R. Akers *et al.*, Z. Phys. **C67**,27(1995);
CLEO Coll., M. Artuso *et al.*, Phys. Rev. **D70**,112001(2004).

[6] H1 Coll., *Determination of the Charm Fragmentation function in Deep-Inelastic Scattering at HERA, contributed paper to XXIInd International Symposium on Lepton-Photon Interactions at High Energy, June 2005, Uppsala, Sweeden. (unpublished). 2005.*

[7] Belle Coll., R. Seuster *et al.*, Phys. Rev. **D73**,032002(2006).

[8] O. Biebel, P. Nason, and B. R. Webber, hep-ph/0109282.

[9] ZEUS Coll. M. Derrick *et al.*, Phys. Lett. **B297**,404(1992).

[10] S. Nussinov, Phys. Rev. Lett. **35**,1672(1975);
G. J. Feldman *et al.*, Phys. Rev. Lett. **38**,1313(1977).

[11] S. Frixione *et al.*, Phys. Lett. **B348**,633(1995);
S. Frixione, P. Nason and G. Ridolfi, Nucl. Phys. **B454**,3(1995).

[12] ZEUS Coll., S. Chekanov *et al.*, e-Print: **arXiv**:0705.1931 [hep-ex].

[13] ZEUS Coll., S. Chekanov *et al.*, Eur. Phys. J. **C44**,351(2005).

[14] H1 Coll., A. AKtas *et al.*, Eur. Phys. J. **C38**,447(2005).

[15] L. Gladilin, Preprint hep-ex/99120674,1999.

[16] ZEUS. Coll., J. Breitweg *et al.*, Phys. Lett. **B481**,213(2000).

Two-Loop Massive Operator Matrix Elements for Polarized and Unpolarized Deep-Inelastic Scattering

I. Bierenbaum, J. Blümlein and S. Klein *

Deutsches Elektronen-Synchrotron, DESY, Platanenallee 6, D-15738 Zeuthen, Germany

The $O(\alpha_s^2)$ massive operator matrix elements for unpolarized and polarized heavy flavor production at asymptotic values $Q^2 >> m^2$ are calculated in Mellin space without applying the integration-by-parts method. We confirm previous results given in Refs. [5, 6], however, obtain much more compact representations.

1 Introduction

The heavy-flavor corrections to deeply inelastic structure functions are very important for the range of small values of x and do contribute there on the level of 20–40%. They have to be known at the same level of accuracy as the light-flavor contributions for precision measurements of $\Lambda_{\rm QCD}$ [2] and the parton distributions. The next-to-leading order corrections were given semi-analytically in [3] for the general kinematic range. Fast and accurate implementations of these corrections in Mellin-space were given in [4]. In the region $Q^2 >> m^2$, the heavy flavor Wilson coefficients were derived analytically to $O(\alpha_s^2)$ [5, 6]. Here Q^2 denotes the virtuality of the gauge boson exchanged in deeply–inelastic scattering and m is the mass of the heavy quark. In this note we summarize the results of a first re-calculation of the operator matrix elements (OMEs) in [7,8]. The calculation is being performed in Mellin-space using harmonic sums [9, 10] without applying the integration-by-parts technique. In this way, we can significantly compactify both, the intermediary and final results. We agree with the results in [5, 6]. The unpolarized and polarized $O(\alpha_s^2)$ massive OMEs can be used to calculate the asymptotic heavy-flavor Wilson coefficients for $F_2(x, Q^2)$ and $g_1(x, Q^2)$ to $O(\alpha_s^2)$ [5–8], and for $F_L(x, Q^2)$ to $O(\alpha_s^3)$ [11].

2 The Method

In the limit $Q^2 >> m^2$ the heavy quark contributions to the twist-2 Wilson coefficients are determined by universal massive operator matrix elements $\langle i|A_l|j\rangle$ between partonic states. The process dependence is due to the corresponding massless Wilson coefficients [12]. This separation is obtained by applying the renormalization group equation(s) to the (differential) scattering cross sections, cf. [5]. In this way all logarithmic and the constant contribution in m^2/Q^2 can be determined. The operator matrix elements are calculated applying the operator insertions due to the light-cone expansion in the respective amplitudes. One obtains the following representation

$$H^{\rm S,NS}_{(2,L),i}\left(\frac{Q^2}{\mu^2}, \frac{m^2}{\mu^2}\right) = \underbrace{A^{\rm S,NS}_{k,i}\left(\frac{m^2}{\mu^2}\right)}_{\text{massive OMEs}} \otimes \underbrace{C^{\rm S,NS}_{(2,L),k}\left(\frac{Q^2}{\mu^2}\right)}_{\text{light Wilson coefficients}},$$

*This paper was supported in part by SFB-TR-9: Computergestütze Theoretische Teilchenphysik, and the Studienstiftung des Deutschen Volkes.

with $\otimes$ denoting the Mellin convolution. The OMEs contain ultraviolet and collinear divergences. The collinear singularities are absorbed into the parton distribution functions while the ultraviolet divergences are removed through renormalization. To 2–loop order, the renormalized OMEs read :

$$\begin{aligned} A_{Qg}^{(2)} &= \frac{1}{8}\left\{\widehat{P}_{qg}^{(0)} \otimes \left[P_{qq}^{(0)} - P_{gg}^{(0)} + 2\beta_0\right]\right\} \ln^2\left(\frac{m^2}{\mu^2}\right) - \frac{1}{2}\widehat{P}_{qg}^{(1)} \ln\left(\frac{m^2}{\mu^2}\right) \\ &+ \overline{a}_{Qg}^{(1)}\left[P_{qq}^{(0)} - P_{gg}^{(0)} + 2\beta_0\right] + a_{Qg}^{(2)} \,, \end{aligned}$$

and similar for the quarkonic contributions. Here, μ^2 denotes the factorization and renormalization scale, $P_{ij}^{(k-1)}$ are the kth loop splitting functions and β_0 denotes the lowest expansion coefficient of the β–function. $a_{ij}^{(k)}$ and $\bar{a}_{ij}^{(k)}$ are the $O(\varepsilon^0)$ resp. $O(\varepsilon)$-terms in the expansion of the OME, which form the main objective of the present calculation.

3 Results

We calculated the massive operator matrix elements both, for the gluon–heavy quark and light–heavy quark transitions in the flavor non-singlet and singlet cases, for unpolarized and polarized nucleon targets.

The constant contribution to the unpolarized and polarized OMEs for the transition $g \to Q$ are :

$$\begin{aligned} a_{Qg}^{(2,\rm unpol)}(N) =& 4C_F T_R \Bigg\{ \frac{N^2+N+2}{N(N+1)(N+2)} \Bigg[-\frac{1}{3}S_1^3(N-1) + \frac{4}{3}S_3(N-1) - S_1(N-1)S_2(N-1) \\ &- 2\zeta_2 S_1(N-1) \Bigg] + \frac{N^4+16N^3+15N^2-8N-4}{N^2(N+1)^2(N+2)} S_2(N-1) + \frac{3N^4+2N^3+3N^2-4N-4}{2N^2(N+1)^2(N+2)}\zeta_2 \\ &+ \frac{2}{N(N+1)} S_1^2(N-1) + \frac{N^4-N^3-16N^2+2N+4}{N^2(N+1)^2(N+2)} S_1(N-1) + \frac{P_1(N)}{2N^4(N+1)^4(N+2)} \Bigg\} \\ &+ 4C_A T_R \Bigg\{ \frac{N^2+N+2}{N(N+1)(N+2)} \Bigg[4\mathrm{M}\left[\frac{\mathrm{Li}_2(x)}{1+x}\right](N+1) + \frac{1}{3}S_1^3(N) + 3S_2(N)S_1(N) \\ &+ \frac{8}{3}S_3(N) + \beta''(N+1) - 4\beta'(N+1)S_1(N) - 4\beta(N+1)\zeta_2 + \zeta_3 \Bigg] - \frac{N^3+8N^2+11N+2}{N(N+1)^2(N+2)^2} S_1^2(N) \\ &- 2\frac{N^4-2N^3+5N^2+2N+2}{(N-1)N^2(N+1)^2(N+2)}\zeta_2 - \frac{7N^5+21N^4+13N^3+21N^2+18N+16}{(N-1)N^2(N+1)^2(N+2)^2} S_2(N) \\ &- \frac{N^6+8N^5+23N^4+54N^3+94N^2+72N+8}{N(N+1)^3(N+2)^3} S_1(N) - 4\frac{N^2-N-4}{(N+1)^2(N+2)^2}\beta'(N+1) \\ &+ \frac{P_2(N)}{(N-1)N^4(N+1)^4(N+2)^4} \Bigg\} \,. \end{aligned}$$

$$\begin{aligned} a_{Qg}^{(2,\rm pol)}(N) =& C_F T_R \Bigg\{ 4\frac{N-1}{3N(N+1)} \Big(-4S_3(N) + S_1^3(N) + 3S_1(N)S_2(N) + 6S_1(N)\zeta_2 \Big) \\ &- 4\frac{N^4+17N^3+43N^2+33N+2}{N^2(N+1)^2(N+2)} S_2(N) - 4\frac{3N^2+3N-2}{N^2(N+1)(N+2)} S_1^2(N) \\ &- 2\frac{(N-1)(3N^2+3N+2)}{N^2(N+1)^2}\zeta_2 - 4\frac{N^3-2N^2-22N-36}{N^2(N+1)(N+2)} S_1(N) - \frac{2P_3(N)}{N^4(N+1)^4(N+2)} \Bigg\} \end{aligned}$$

$$
+ C_A T_R \Biggl\{ 4 \frac{N-1}{3N(N+1)} \Bigl(12 \mathrm{M} \left[\frac{\mathrm{Li}_2(x)}{1+x} \right] (N+1) + 3\beta''(N+1) - 8 S_3(N) - S_1^3(N)
$$

$$
- 9 S_1(N) S_2(N) - 12 S_1(N) \beta'(N+1) - 12 \beta(N+1) \zeta_2 - 3 \zeta_3 \Bigr) - 16 \frac{N-1}{N(N+1)^2} \beta'(N+1)
$$

$$
+ 4 \frac{N^2+4N+5}{N(N+1)^2(N+2)} S_1^2(N) + 4 \frac{7N^3+24N^2+15N-16}{N^2(N+1)^2(N+2)} S_2(N) + 8 \frac{(N-1)(N+2)}{N^2(N+1)^2} \zeta_2
$$

$$
+ 4 \frac{N^4+4N^3-N^2-10N+2}{N(N+1)^3(N+2)} S_1(N) - \frac{4 P_4(N)}{N^4(N+1)^4(N+2)} \Biggr\} .
$$

Here $P_i(N)$ denote polynomials given in [7, 8]. The corresponding quarkonic expressions are given in [7, 8]. The integrals were performed using Mellin-Barnes techniques [13, 14] and applying generalized hypergeometric function representations. The results were further simplified using algebraic relations between harmonic sums [15]. Furthermore, structural relations for harmonic sums [16], which include half–integer relations and differentiation for the Mellin variable N, lead to the observation that the OMEs above depend only on two basic harmonic sums :

$$
S_1(N), \qquad\qquad S_{-2,1}(N) \; .
$$

We expressed $S_{-2,1}(N)$ in terms of the Mellin transform $M[\mathrm{Li}_2(x)/(1+x)](N)$ in the above. Here $\beta(N) = (1/2) \cdot [\psi((N+1)/2) - \psi(N/2)]$. Previous analyzes of various other space- and time-like 2–loop Wilson coefficients and anomalous dimensions including also the soft and virtual corrections to Bhabha-scattering [15a,16], showed that six basic functions are needed in general to express these quantities :

$$
S_1(N), \quad S_{\pm 2,1}(N), \quad S_{-3,1}(N), \quad S_{\pm 2,1,1}(N) \; .
$$

Non of the harmonic sums occurring contains an index $\{-1\}$ as observed in all other cases being analyzed.

Comparing to the results obtained in Refs. [5, 6] in x–space, there 48 functions were needed to express the final result in the unpolarized case and 24 functions in the polarized case.

To obtain expressions for the heavy flavor contributions to the structure functions in x–space, analytic continuations have to be performed to $N \, \epsilon \, \mathbf{C}$ for the basic functions given above, see [16, 18, 19]. Finally a (numeric) contour integral has to be performed around the singularities present.

4 Conclusions

We calculated the unpolarized and polarized massive operator matrix elements to $O(\alpha_s^2)$, which are needed to express the heavy flavor Wilson coefficients contributing to the deep–inelastic structure functions F_2, g_1 and F_L to $O(\alpha_s^2)$ resp. $O(\alpha_s^3)$ in the region $Q^2 >> m^2$. The calculation was performed in Mellin space without using the integration-by-parts technique, leading to nested harmonic sums. We both applied representations through Mellin–Barnes integrals and generalized hypergeometric functions. In course of the calculations, a series of new infinite sums over products of harmonic sums weighted by related functions were evaluated, cf. [7, 8]. These representations were essential to keep the complexity of the intermediary and final results as low as possible. Furthermore, we applied a series of mathematic relations for the harmonic sums to compactify the results further. We confirm the results obtained earlier in Refs. [5, 6] by other technologies.

References

[1] Slides:
http://indico.cern.ch/contributionDisplay.py?contribId=194&sessionId=5&confId=9499

[2] J. Blümlein, arXiv:0706.2430 [hep-ph], DESY 07–083;
J. Blümlein, H. Böttcher and A. Guffanti, Nucl. Phys. B **774** (2007) 182.

[3] E. Laenen, S. Riemersma, J. Smith and W. L. van Neerven, Nucl. Phys. B **392** (1993) 162;
S. Riemersma, J. Smith and W. L. van Neerven, Phys. Lett. B **347** (1995) 143.

[4] S. I. Alekhin and J. Blümlein, Phys. Lett. B **594** (2004) 299.

[5] M. Buza, Y. Matiounine, J. Smith, R. Migneron and W. L. van Neerven, Nucl. Phys. B **472** (1996) 611.

[6] M. Buza, Y. Matiounine, J. Smith and W. L. van Neerven, Nucl. Phys. B **485** (1997) 420.

[7] I. Bierenbaum, J. Blümlein and S. Klein, arXiv:hep-ph/0703285; Nucl. Phys. **B** (2007) in print.

[8] J. Blümlein and S. Klein, DESY 07–027.

[9] J. Blümlein and S. Kurth, Phys. Rev. D **60** (1999) 014018.

[10] J. A. M. Vermaseren, Int. J. Mod. Phys. A **14** (1999) 2037.

[11] J. Blümlein, A. De Freitas, W. L. van Neerven and S. Klein, Nucl. Phys. B **755** (2006) 272.

[12] E. B. Zijlstra and W. L. van Neerven, Nucl. Phys. B **383** (1992) 525; Nucl. Phys. B **417** (1994) 61 [Erratum-ibid. B **426** (1994) 245, **773** (2007) 105];
S. Moch, J. A. M. Vermaseren and A. Vogt, Phys. Lett. B **606** (2005) 123.

[13] I. Bierenbaum and S. Weinzierl, Eur. Phys. J. C **32** (2003) 67.

[14] I. Bierenbaum, J. Blümlein and S. Klein, Nucl. Phys. Proc. Suppl. **160** (2006) 85; Phys. Lett. B **648** (2007) 195.

[15] J. Blümlein, Comput. Phys. Commun. **159** (2004) 19.

[16] J. Blümlein and S. Klein, DESY 07–082, arXiv:0706.2426;
J. Blümlein, DESY 07–042.

[17] J. Blümlein and V. Ravindran, Nucl. Phys. B **716** (2005) 128; B **749** (2006) 1 ;
J. Blümlein and S. Moch, in preparation.

[18] J. Blümlein, Comput. Phys. Commun. **133** (2000) 76;
J. Blümlein and S. O. Moch, Phys. Lett. B **614** (2005) 53.

[19] A. V. Kotikov and V. N. Velizhanin, arXiv:hep-ph/0501274.

Charm at CLEO-c

Kamal K. Seth
(for the CLEO Collaboration)

Northwestern University - Department of Physics & Astronomy
Evanston, IL 60208 - USA

A minireview of the recent results from CLEO-c is presented. It includes new results in charmonium spectroscopy, charmonium-like exotics, and open-charm decays.

1 Introduction

During the last 25 years, CLEO was primarily devoted to the physics of bottomonium ($b\bar{b}$) and B–mesons. CLEO and CESR have recently morphed into CLEO-c and CESR-c to do research in the charm quark region, $\sqrt{s} = 3 - 5$ GeV to address challenging questions in charmonium spectroscopy, meson form factors, and spectroscopy of D and D_s mesons.

2 Spin–singlet states of Charmonium ($c\bar{c}$)

The spin–triplet states of charmonium ($^3S_1(J/\psi, \psi')$, $^3P_J(\chi_{c0,c1,c2})$) have been extensively studied by SLAC, Fermilab, and BES during the last 30 years. The spin–singlet states have largely defied identification and study. Neither $\eta_c' 2^1S_0)$, nor $h_c(1^1P_1)$, nor $\eta_b(1^1S_0)$ have ever been convincingly identified. This leaves us largely in the dark about the character of the all–important spin–spin hyperfine interaction between two quarks. This serious shortcoming has now been mended by the successful identification of both η_c' and h_c at CLEO.

2.1 Identification of the $\eta_c'(2^1S_0)$ state of Charmonium

The hyperfine splitting of the $1S$ state of charmonium is known to be $\Delta M_{hf}(1S) \equiv M(J/\psi) - M(\eta_c) = 116.5 \pm 1.2$ MeV. While the mass of $\psi'(2^3S_1)$ is well known, the lack of any knowledge of $\eta_c'(2^1S_0)$ has prevented us from knowing how the spin–spin interaction changes for the radially excited states. A study by Belle [2] of the decays of 45 million B mesons, $B \to K(K_S K\pi)$, gave the first hint that the η_c' mass was substantially larger than expected. In a recent measurement, CLEO has confirmed this and has successfully identified η_c' in its formation in two photon fusion, and its decay into $K_S K\pi$ [3]. Its mass spectrum, shown in Fig. 1 (left), leads to $\Delta M_{hf}(2S) = 43.1 \pm 3.4$ MeV, which is almost a factor three smaller than $\Delta M_{hf}(1S)$, and its explanation remains a challenge for the theorists.

2.2 Identification of the $h_c(1^1P_1)$ state of Charmonium

It is of great interest to determine how the hyperfine interaction changes with the orbital angular momentum between two quarks. In the generally accepted potential models, there is no long–range spin–spin component and the consequent prediction is that $\Delta M_{hf} = 0$ for all $l \neq 0$. In order to test this prediction for $l = 1$, one has to identify h_c, the singlet P state, since the triplet P states, χ_{cJ} are well known. Unfortunately, the radiative transition $\psi' \to \gamma h_c$ is forbidden by C–parity, and h_c has defied firm identification despite numerous earlier attempts. In a very challenging measurement of the isospin forbidden reaction,

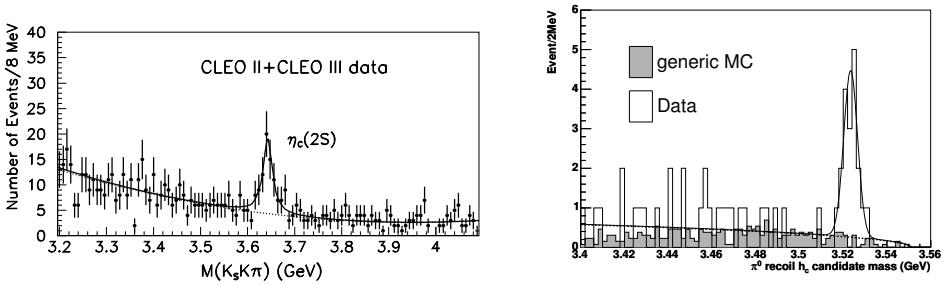

Figure 1: (left) $M(K_SK\pi)$ from CLEO showing $\eta_c(2S)$. (right) π^0 recoil mass spectrum from CLEO showing h_c in exclusive analysis of $\psi(2S) \to \pi^0 h_c,\ h_c \to \gamma\eta_c$.

$\psi' \to \pi^0 h_c$, $h_c \to \gamma\eta_c$, CLEO [4] has recently unambiguously identified h_c in both inclusive and exclusive analyses of their data for 3 million ψ'. The mass spectrum for the exclusive reaction is shown in Fig. 1 (right), where the h_c peak is clearly seen. The result is $\Delta M_{hf}(1P) = +1.0 \pm 0.6 \pm 0.4$ MeV. CLEO-c has now taken data with 24.5 million ψ', and a h_c peak with ~ 250 counts is expected, which will reduce both errors by more than a factor of two.

The determination of the ${}^3P_J$ centroid as $M(\langle {}^3P_J \rangle) = M(5\chi_{c2} + 3\chi_{c1} + \chi_{c0})$ appears to lead to $\Delta M_{hf}(1P) \approx 0$, but J.-M. Richard [5] has pointed out that a more "correct" determination of the centroid implies $\Delta M_{hf}(1P) \approx 4$ MeV.

3 Hadronic decays of χ_{cJ} states

Recently, extensive analyses of CLEO data with 3 million ψ' has been done for χ_{cJ} 2, 3, 4–body decays [6]. Analysis of our new sample of 24.5 million ψ' will greatly improve the precision of these results and increase knowledge of χ_{cJ} decays several-fold.

4 Timelike form factors of pion and kaon

Using 21 pb^{-1} of e^+e^- annihilation data taken off of the ψ' resonance, CLEO-c has made the world's first precision measurements of the timelike form factors of charged pions and kaons at $|Q|^2 = 13.48$ GeV^2 [7]. The measurements show that there is essentially no theoretical understanding of timelike form factors of mesons at present.

5 Charmonium–like states

As is well known, there has been a "renaissance" in hadron spectroscopy during the last couple of years with reports of one unexpected resonance after another by Belle and BaBar who are able to play in the game with hundreds of inverse femtobarns of luminosity. It began with X(3872), then X, Y, Z(3940), and then Y(4260). CLEO has nothing to say about X, Y, Z(3940), but it has made contributions to the study of X(3872) and Y(4260).

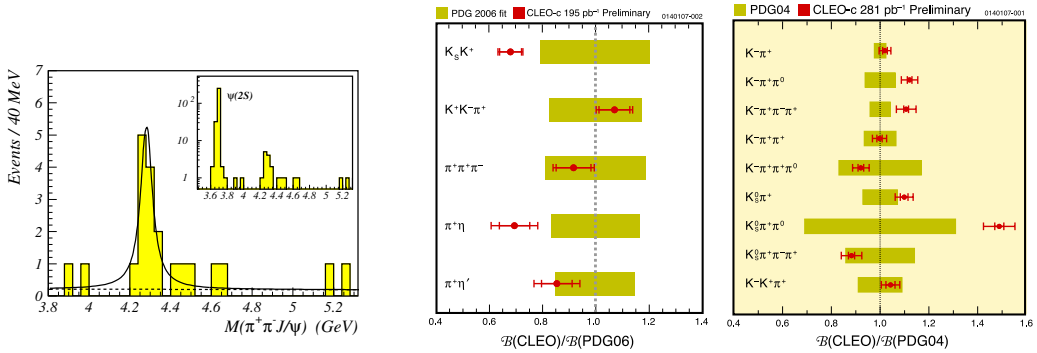

Figure 2: (left) CLEO observation of Y(4260) in two photon fusion. (middle & right) Ratios of CLEO-c results for hadronic decays of D and D_s (dots without bars) to the current PDG values (with shaded error bars).

5.1 X(3872)

Belle discovered it, and CDF and DØ have confirmed it. The state has $M(\mathrm{X}(3872))= 3871.2 \pm 0.5$ MeV, and a very narrow width, $\Gamma(\mathrm{X}(3872))< 2.3$ MeV. Numerous theoretical conjectures about the nature of this state, which prominently decays into $\pi^+\pi^- J/\psi$, have been made. The most popular among these is that it is a $D^0\overline{D^{*0}}$ molecule, inspired by the fact that its mass is very close to $M(D^0) + M(\overline{D^{*0}})$. It occured to us that for this model to survive, it is very important to know what the molecule's binding energy is. This requires an accurate measurement of the mass of D^0. At CLEO-c, we have made a precision measurement of $M(D^0)$ [8] by means of the reaction $e^+e^- \to \psi(3770) \to D^0\overline{D^0}$, $D^0 \to K_S\phi$, with the result that $M(D^0) = 1864.847 \pm 0.178$ MeV, and hence $E_B(\mathrm{X}(3872)= +0.6 \pm 0.6$ MeV. While this small binding energy allows X(3872) to be bound, it results in a prediction of its width for decay into $D^0\overline{D^0}\pi^0$ which is a factor ~ 200 smaller than that observed by Belle [9]. This could be a death–blow to the molecular model.

5.2 Y(4260)

BaBar [10] has reported observing a resonance Y(4260) with $M(\mathrm{Y}) = 4259 \pm 8^{+2}_{-6}$ MeV, $\Gamma(\mathrm{Y}) = 88 \pm 23^{+6}_{-4}$ MeV, in ISR production, $e^+e^- \to \gamma_{ISR}e^+e^- \to \gamma_{ISR}(\pi^+\pi^- J/\psi)$. At CLEO, despite a factor ~ 20 smaller luminosity, we observe (see Fig. 2(left)) a clear signal for Y(4260) with very small background [11]. The ISR observation of the resonance confirms its vector nature. This is rather bizarre because the $R \equiv \sigma(h\bar{h})/\sigma(\mu\mu)$ measurements show a deep minimum at $\sqrt{s} = 4260$ MeV, instead of a maximum expected for a vector state. The resonance is therefore rather mysterious.

6 CLEO-c as an open–charm factory

The primary motivation for CLEO to morph into CLEO-c was to become a prodigious factory for the production of open–charm hadrons, the D and D_s, and thereby enable it

	CLEO-c	Unquenched Lattice
$f(D^+)$	$222.6 \pm 16.7^{+2.8}_{-3.4}$ MeV	$201 \pm 3 \pm 17$ MeV
$f(D_s^+)$	$280.1 \pm 11.6 \pm 6.0$ MeV	$249 \pm 3 \pm 16$ MeV
$f(D_s^+)/f(D^+)$	$1.26 \pm 0.11 \pm 0.03$	$1.24 \pm 0.01 \pm 0.07$

Table 1: Measured D and D_s decay constants compared to unquenched lattice predictions.

to make important contributions to D physics, to determine form factors, CKM matrix elements, and to allow peeks into the holy–grail of *"beyond the standard model."*

CLEO-c has started this program very successfully by taking $\sim$ 540 pb^{-1} of data at $\psi(3770)$ with near threshold production of $D\overline{D}$, and $\sim$ 313 pb^{-1} at $\psi(4170)$ for near-threshold production of $D_s\overline{D_s}$. A large number of precision measurements of hadronic decays of D and D_s have already been made [12]. These are illustrated in Fig. 2(right).

Leptonic decays of D and D_s have been measured to obtain $\Gamma(D^+_{(d,s)} \to l^+\nu)$. Using the best known values of the CKM matrix elements, the decay constants $f(D^+)$and $f(D_s^+)$ have been deduced [13]. The results, listed in Table I, agree very well with the latest unquenched lattice predictions.

Semi-leptonic decays of D mesons $D^0 \to (\pi^-, K^-)e^+\nu$ and $D^+ \to (\pi^0\overline{K^0})e^+\nu$ have also been successfully measured, and using the form factors predicted by unquenched lattice calculations, the CKM matrix elements $|V_{cd}|$ and $|V_{cs}|$ have been obtained in agreement with their unitarity–based values.

7 Summary

To summarize, CLEO has made a transition to CLEO-c and is very successfully contributing to the study of the hidden flavor physics of the charmonium region and the open flavor physics of D–mesons.

References

[1] Slides: `http://indico.cern.ch/contributionDisplay.py?contribId=195&sessionId=5&confId=9499`

[2] Belle Collaboration, S. K. Choi *et al.*, Phys. Rev. Lett. **89**, 102001 (2002).

[3] CLEO Collaboration, D. M. Asner *et al.*, Phys. Rev. Lett. **92**, 142001 (2004).

[4] CLEO Collaboration, J. L. Rosner *et al.*, Phys. Rev. Lett. **95**, 102003 (2005); P. Rubin *et al.*, Phys. Rev. **D 72**, 092004 (2005).

[5] J.M. Richard, elsewhere in these proceedings.

[6] CLEO Collaboration, S. Athar *et al.*, Phys. Rev. **D 75**, 032002 (2007); G. S. Adams *et al.*, Phys. Rev. **D 75**, 071101(R) (2007).

[7] CLEO Collaboration, T. K. Pedlar *et al.*, Phys. Rev. Lett. **95**, 261803 (2005).

[8] CLEO Collaboration, C. Cawlfield *et al.*, Phys. Rev. Lett **98**, 092002 (2007).

[9] Belle Collaboration, Phys. Rev. Lett. **97**, 162002 (2006).

[10] BaBar Collaboration, Phys. Rev. Lett. **95**, 142001 (2005).

[11] CLEO Collaboration, Q. He *et al.*, Phys. Rev. **D 74**, 091104(R) (2006).

[12] CLEO Collaboration, Q. He *et al.*, Phys. Rev. Lett. **95**, 121801 (2005); S. Dytman *et al.* et al, Phys. Rev. **D 74**, 071102(R) (2006).

[13] CLEO Collaboration, M. Artuso et al., Phys. Rev. Lett. **95**, 251801 (2005); CLEO Collaboration, M. Artuso et al., arXiv:0704.0629.

Charm and Beauty Production at the Tevatron

Burkard Reisert[1] on behalf of the CDF and DØ Collaborations

1- Max-Planck-Institut für Physik
Föhringer Ring 6, 80805 München - Germany

CDF is now releasing measurements using data samples with integrated luminosities of up to $1\,\mathrm{fb}^{-1}$ enabling detailed studies of charm hadron production: Measurements of prompt charm meson pair production, spin alignment of the charmonium states J/ψ and $\psi(2S)$ and relative production of the $\chi_{c1}(P1)$ will be discussed. In addition recent measurements of the b-hadron and bottomonium production cross-section by CDF and DØ will be presented.

1 Introduction

The production and hadronization of long lived heavy quarks, c and b, in hadron hadron collisions is an active field of research in Quantum Chromo Dynamics (QCD). In the theoretical treatment of production and hadronization, the mass of the heavy quark provides a scale just at the transition between non-perturbative and perturbative regimes of QCD. Measurements of production cross-sections and polarization at production probe our understanding of QCD in this transition region.

Charm and beauty hadrons are produced in huge numbers in proton anti-proton collisions at a center-of-mass energy of $\sqrt{s} = 1.96\,\mathrm{TeV}$ at the Tevatron Collider at Fermilab. These collisions are recorded by the general purpose hadron collider detectors CDF [2] and DØ [3]. CDF's large tracking volume and precise silicon vertexing are key features in its very good performance for charm and beauty physics. Its trigger and data acquisition system, with a high bandwidth for track based triggers allows large samples to be recorded of up to several million fully reconstructed b and c hadron decays. DØ's excellent muon coverage enable measurements of b-hadrons over a wide range in rapidity y.

2 Charm meson pair production

With over $1\,\mathrm{fb}^{-1}$ of data collected by CDF, it is now possible to look for two fully reconstructed charm mesons to measure charm pair-production cross-sections in $p\bar{p}$ collisions.

For a first measurement of charm meson pair cross-sections only D^{*+} mesons, decaying to $D^0(\rightarrow K\pi)\pi$, are considered as candidates for the second charm hadron in the event, as the mass difference $\Delta m = m(K\pi\pi) - m(K\pi)$ provides a sufficient handle to suppress combinatorial background. More than 2000 signal pairs for both modes, D^0D^{*-} and D^+D^{*-} pairs, have been reconstructed.

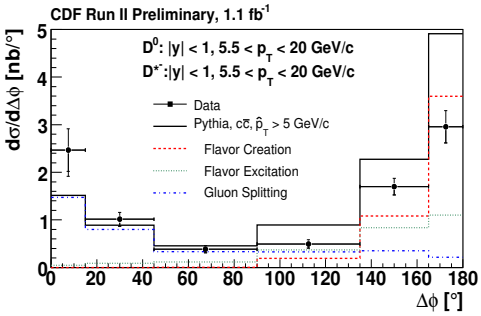

Figure 1: The D^0D^{*-} and pair cross-sections as a function of $\Delta\phi$.

Combinatorial background in the DD^{*-} sample is corrected for using a 2-dimensional sideband subtraction. The impact parameter distribution of the D^0 in the D^{*+} decay is used as a handle to extract the number of prompt pairs. The detector acceptance and reconstruction efficiencies are corrected for employing a detailed simulation of "realistic" $c\bar{c}$

events. Besides the charm mesons of interest, additional particles from fragmentation and the underlying event in the $p\bar{p}$ collision are incorporated. The simulation of pair events has been validated using large samples of inclusive D candidates from data.

Figure 1 displays the $D^0 D^{*-}$ pair cross-sections as a function of $\Delta\phi$. Collinear production is found to be as important as back-to-back production. The measurement is compared to the prediction derived from Pythia (Tune A) [4], which gives a fair estimate of the absolute pair cross-section, but underestimates (overestimates) collinear (back-to-back) production.

3 J/ψ and $\psi(2S)$ polarization

Both vector mesons are reconstructed in their decays into muon pairs, $J/\psi \to \mu^+\mu^-$ and $\psi(2S) \to \mu^+\mu^-$. The distribution of the μ^+ in the vector meson rest frame relative to the flight direction of the vector meson in the $p\bar{p}$ rest frame, measured by the polar angle θ^* depends on the polarization parameter $\alpha \in [-1, 1]$: $\frac{dN}{d\Omega} \propto 1 + \alpha \cos^2\theta^*$, where $\alpha = +1$ (-1) for transversely (longitudinally) polarized vector mesons.

The samples of prompt J/ψ and $\psi(2S)$ are purged of the secondary J/ψ and $\psi(2S)$ from B-hadron decays by cutting on the combined impact parameter significance, d_0/σ_0, of the two μ-tracks: $S = (d_0^+/\sigma_{0+})^2 + (d_0^-/\sigma_{0-})^2 \leq 8$. Conversely the samples of secondary J/ψ and $\psi(2S)$ are enriched by requiring $S \geq 16$. Residual contributions of secondary (prompt) J/ψ and $\psi(2S)$ are taken into account in the polarization fits, from which α is extracted. The polarization fit employs a template method. The templates of fully-polarized vector mesons are generated using a Monte Carlo program which has been carefully validated to correctly reproduce the kinematic distributions of J/ψ and $\psi(2S)$ mesons in the CDF data. The polarization analysis is sensitive to any unknown apparatus response that could distort the decay angle distribution. The data used for the polarization analysis were taken from June, 2004 to February, 2006. Throughout this period, the COT operation was stable and the muon trigger efficiency did not change by more than 0.2% from the plateau value of 94.1%. The integrated luminosity of this data set is 800 pb^{-1}.

The polarization of the vector mesons from B-decays, α_B, is found to be independent of its p_T. CDF measures $\alpha_B(\psi(2S)) = 0.33 \pm 0.25$ and $\alpha_B(J/\psi) = -0.066 \pm 0.050$ consistent with the more precise results from the B-factories. Figure 2 shows the polarization of prompt vector mesons as a function of their transverse momentum p_T. With increasing p_T, both the J/ψ and the $\psi(2S)$ are increasingly longitudinally polarized. The measurement for the $\psi(2S)$ is less precise due to the smaller sample size. However, thanks to the absence of

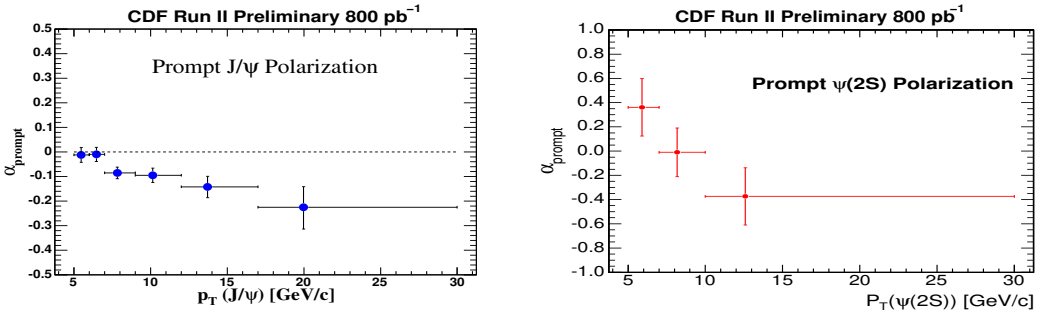

Figure 2: The polarization ($\alpha_{\rm prompt}$) of the vector meson as a function of its transverse momentum p_T, for prompt J/ψ (left) and prompt $\psi(2S)$ (right).

feed-down from χ_c states, the $\psi(2S)$ represents direct vector meson production more closely than in the case of the J/ψ.

4 Relative production of χ_{c1} and χ_{c2}

The reconstruction of the decay $\chi_{cJ} \to J/\psi(\to \mu^+\mu^-)\gamma$ is challenging, due to the need to detect low energy photons within the environment of multi-particle final states. The large integrated luminosity delivered by the Tevatron allows CDF to reconstruct the low energy photons through conversion into e^+e^- pairs in sufficient quantity. As demonstrated in Fig. 3, such a reconstruction provides the mass resolution needed to distinguish the χ_{c1} from the χ_{c2}. The effective flight distance λ_{eff} of the J/ψ provides a handle to discriminate between prompt and secondary χ_{cJ}. By applying corrections for the relative efficiencies, $\epsilon(\chi_{c1})/\epsilon(\chi_{c2})$, and branching fractions, $Br(\chi_{c1} \to J/\psi\gamma)/Br(\chi_{c2} \to J/\psi\gamma)$, the yields of prompt χ_{cJ}, obtained from a simultaneous fit to λ_{eff} and $m(J/\psi\gamma)$, are converted into the ratio of production cross-sections $\sigma_{\chi_{c2}}/\sigma_{\chi_{c1}} = 0.70 \pm 0.04(\text{stat.}) \pm 0.03(\text{syst.}) \pm 0.06(\text{br})$, with no significant p_T dependence in the measured range of $5 < p_T < 14\,\text{GeV/c}$ [5].

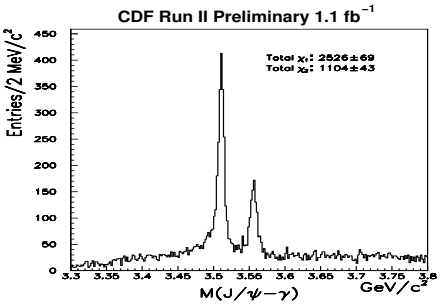

Figure 3: The $J/\psi\gamma$ invariant mass of all the χ_{cJ} candidates in the data sample.

The precision of this measurement sets a new standard. Models that predict production proportional to the number of spin states would expect this ratio to be $\frac{5}{3}$ [6]. Such models are ruled out by this measurement.

5 B-hadron production

To date, CDF has performed three measurements of the inclusive b-hadron (H_b) production cross-section in $p\bar{p}$ collisions at $\sqrt{s} = 1.96\,\text{TeV}$. The first has been the measurement using $H_b \to J/\psi X$, $J/\psi \to \mu^+\mu^-$ decays, where the displacement of the J/ψ decay vertex from the beam line served as tag of the long lived H_b. Taking advantage of the low momentum J/ψ events accessible by the CDF muon triggers, this measurement has been the first one to map out the cross-section down to $p_T(H_b) = 0\,\text{GeV/c}$ [7]. Secondly CDF has performed a measurement of the B^+ meson cross-section for $p_T(B^+) > 6\,\text{GeV/c}$. For this measurement the decay chain $B^+ \to J/\psi K^+$ with $J/\psi \to \mu^+\mu^-$ has been fully reconstructed using a dataset of $800\,\text{pb}^{-1}$. With large statistics and a very clean fully reconstructed mode, the precision of this measurement is better than 10%. The third, most recent analysis takes advantage of the distinct semileptonic $H_b \to \mu^- D^0 X$, $D^0 \to K^-\pi^+$ decay signature. This measurement is superior to previous inclusive semileptonic measurements, $H_b \to \mu X$, thanks to the clear charm tag of the fully reconstructed D^0 meson, which provides an improved purity and therefore reduced systematic uncertainties.

Figure 4 shows a compilation of differential b-hadron cross-sections. There is good agreement between these complimentary measurements and the fixed order next-to-leading log (FONLL) [8] prediction is seen to be consistent with the data.

6 Bottomonium production

Using a dataset of $159\,\mathrm{pb}^{-1}$ DØ has measured the inclusive production cross-section of the $\Upsilon(1S)$ bottomonium state using the $\Upsilon(1S) \to \mu^+\mu^-$ decay mode [9]. For the central rapidity region ($|y(\Upsilon)| < 0.6$) the cross-section times branching ratio is $732 \pm 19(\mathrm{stat}) \pm 73(\mathrm{syst.}) \pm 46(\mathrm{lumin.})\,\mathrm{pb}$. Measuring the ratios of cross-sections for the rapidity ranges $0.6 < |y(\Upsilon)| \leq 1.2$ and $1.2 < |y(\Upsilon)| \leq 1.8$ relative to the central rapidity allowed for determination of the $\Upsilon(1S)$ production cross-section in the extended rapidity ranges. As can be seen in Fig. 5 there is little variation between the rapidity regions in the shapes of the differential cross-sections, which agree reasonably well with theoretical predictions [10].

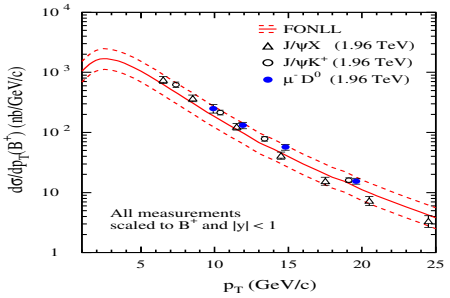

Figure 4: Differential b-hadron cross-sections compared to a FONLL [8] calculation.

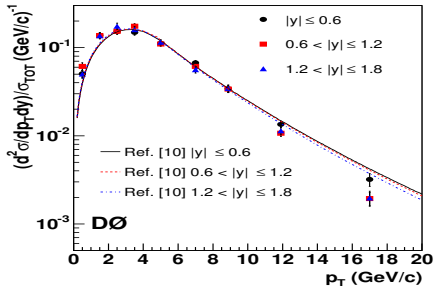

Figure 5: The normalized differential cross-section for $\Upsilon(1S)$ production.

7 Conclusion

The unprecedented integrated luminosity delivered by the Tevatron as well as the sustained excellent performance of the CDF and DØ detectors open a window of opportunity for detailed studies of the production of charm and beauty hadrons. Such studies have the potential to instigate new approaches to QCD models and calculations. The new results presented here will help improve our understanding of heavy quark production in proton (anti-)proton collisions.

References

[1] Slides:
`http://indico.cern.ch/contributionDisplay.py?contribId=238&sessionId=5&confId=9499`

[2] CDF Collaboration, D. Acosta *et al.* Phys. Rev. **D 71** 032001 (2005).

[3] DØ Collaboration, V. Abazov *et al.* Nucl. Instrum. Methods A **552** 372 (2005).

[4] R. Field and R. Craig Group, arXiv:hep-ph/0510198 (2004) and references therein.

[5] CDF Collaboration, A. Abulencia *et al.*, Phys. Rev. Lett. **98** 232001 (2007).

[6] N. Brambilla *et al.* arXiv:hep-ph/0412158 (2004). G.A. Schuler, Z. Phys. **C 71** 371 (1996).

[7] CDF Collaboration, D. Acosta *et al.*, Phys. Rev. **D 71** 032001 (2005)

[8] M. Cacciari *et al.*, JHEP **9805** 007 (1998).

[9] DØ Collaboration, V. M. Abazov *et al.*, Phys. Rev. Lett. **94** 232001 (2005)

[10] E.L. Berger *et al.*, Phys. Rev. **D 71** 034007 (2005). E.L. Berger *et al.* arXiv:hep-ph/0411026 (2004).

Heavy Quark Mass Effects in PQCD and Heavy Flavor Parton Distributions

Wu-Ki Tung[1,2], H.L. Lai[1,2,3], J. Pumplin[1], P. Nadolsky[4], and C.-P. Yuan[1].

[1] Michigan State University, East Lansing, MI - USA
[2] University of Washington, Seattle, Washington - USA
[3] Taipei Municipal University of Education, Taipei, Taiwan
[4] Argonne National Laboratory, Argonne, IL, USA

The systematic treatment of heavy quark mass effects in DIS in current CTEQ global analysis is summarized. Applications of this treatment to the comparison between theory and experimental data on DIS charm production are described. The possibility of intrinsic charm in the nucleon is studied. The issue of determining the charm mass in global analysis is discussed.

1 Introduction

Contemporary global QCD analyses of high precision Deep Inelastic Scattering (DIS) data, along with other hard processes, require a consistent treatment of heavy quark mass effects in the perturbative QCD (PQCD) framework. This review [1] summarizes key features of the formalism implemented in the current CTEQ global analysis project [3] and results on its application to heavy flavor physics in global analysis [2]. Sec. 3 presents the results of the new global fits compared to heavy flavor production data in DIS [3]. Sec. 4 addresses issues related to possible intrinsic charm in the nucleon [6]. Sec. 4 discusses the topical question: can the charm mass be reliably determined in global QCD analysis?

Due to space limitation, it is impossible to include in this short written report the figures that illustrate the results discussed in the corresponding talk, as summarized above. However, since the slides for the talk have been made available at the official conference URL [1], we shall make use of these, and refer the reader to the actual figures by the slide numbers where they appear in the posted talk [1]. The same space limitation restricts citations to only the papers and talks on which this report is directly based.

2 General PQCD framework including heavy quark masses

The key features of the general-mass PQCD framework of [3] is illustrated in slide 3 of [1].
Factorization Formula and (scheme-dependent) summation over parton flavors: Collins has established that the PQCD factorization theorem for the structure functions takes the general form $F_\lambda(x,Q^2) = \sum_a f^a \otimes \widehat{\omega}_a^\lambda$ even when the heavy quark mass effects are kept. Here, the summation is over the active parton flavor label a, $f^a(x,\mu)$ are the parton distributions at the factorization scale μ, and $\widehat{\omega}_a^\lambda(x, Q/\mu, M_i/\mu)$ are the infrared safe Wilson coefficients (or hard-scattering amplitudes) that can be calculated order-by-order in perturbation theory. The summation over "parton flavor" label a in the factorization formula is determined by the *factorization scheme* chosen to define the parton distributions $f^a(x,\mu)$. In general, we use the variable flavor number scheme.
The summation over (physical) final-state flavors: For total inclusive structure functions, the factorization formula contains an implicit summation over all possible quark flavors

in the final state: $\hat{\omega}_a = \sum_b \hat{\omega}_a^b$, where "$b$" denotes final state flavors, and $\hat{\omega}_a^b$ is the perturbatively calculable hard cross section for an incoming parton "a" to produce a final state containing flavor "b ". It is important to emphasize that "b" labels quark flavors that can be produced *physically* in the final state; it is *not* a parton label in the sense of initial-state parton flavors described in the previous subsection. In a proper implementation of the general-mass (GM) formalism, the distinction between the initial-state and final-state summations must be unambiguously and correctly observed.

Kinematic constraints and rescaling: Kinematic constraints from the phase space treatment have a significant impact on the numerical results of the calculation. In DIS, with heavy flavor produced in the final state, the most natural way to ensure the correct kinematics for both NC and CC processes is to use the *rescaling variable* $\chi = x(1 + (\Sigma_f\ M_f/Q)^2)$ in place of the usual Bjorken x in the convolution integral of the factorization formula. Here $\Sigma_f\ M_f$ is the sum of all heavy flavor masses in the final state. This is the ACOTχ prescription used in most recent literature.

Hard Scattering Amplitudes and the SACOT Scheme: The hard scattering amplitude $\widehat{\omega}_a^{\lambda}(x, Q/\mu, M_i/\mu)$ is by definition infrared safe, meaning it is free from logarithmic "mass-singularities" in the limit $M_i/Q \to 0$. Within the PQCD formalism, there is some freedom to choose how the finite mass effects are treated. The choice that makes the calculation simplest while retaining full accuracy (the SACOT scheme) can be stated as: keep the heavy quark mass dependence in the Wilson coefficients for partonic subprocesses with only light initial state partons (g, u, d, s); but use the zero-mass Wilson coefficients for subprocesses that have an initial state heavy quark (c, b). For the 4-flavor scheme to order α_s (NLO), we do the following: (a) keep the full M_c dependence of the gluon fusion subprocess; (b) for NC scattering (γ/Z exchanges), set all quark masses to zero in the quark-initiated subprocesses; and (c) for CC scattering ($W^{\pm}$ exchange), set the initial-state quark masses to zero, but keep the final-state quark masses on shell.

Choice of Factorization Scale: The total inclusive structure function F_i^{tot} is infrared safe. Consider the simple case of just one effective heavy flavor charm, $F_i^{tot} = F_i^{light} + F_i^c$ for any given flavor-number scheme. Since the right-hand side of this equation is dominated by the light-flavor term F_i^{light}, and the natural choice of scale for this term is $\mu = Q$, it is reasonable to use this choice for both terms to ensure infrared safety. On the other hand, in the case of experimentally measured semi-inclusive DIS structure functions for producing a charm particle in the final state, F_i^c is theoretically *infrared unsafe* beyond NLO. One may nonetheless perform comparison of NLO theory with experiment with the understanding that the results are intrinsically less reliable, and they can be sensitive to the choice of parameters. The most natural choice of factorization scale in this case is $\mu = \sqrt{Q^2 + M_c^2}$.

3 Results and Comparison with heavy flavor production data

Slides 4 and 5 of [1] show the size of heavy quark mass effects on the calculation of $F_2(x, Q)$ and $F_L(x, Q)$. The color coded areas (with complementary contours) indicate the fractional differences between GM and zero-mass (ZM) calculations. Understandably, the largest differences occur at low Q and low x; and the significance is much more for $F_L(x, Q)$ than for $F_2(x, Q)$, since the former vanishes at LO for the ZM case. As indicated in slide 6, the GM calculation is stable and robust. It has been used as the basis for a new round of global analysis of PDFs, using the full set of HERA Run I neutral current (NC) and charged current (CC) total cross section and heavy flavor production data, along with the usual DY

and jet data cf. [2]. Here we shall only present the comparison of the new fits to the heavy flavor production data measured at HERA.

Slide 10 shows the comparison of the ZEUS 1996-97 and 1998-2000 charm production data to the theory values obtained with the new PDF sets CTEQ6.5M (same shape for strange and non-strange seas, [3]), CTEQ6.5S0 (independent shapes for strange and non-strange seas, [5]) as well as for the older CTEQ6HQ. Plotted are ratios of $F_2^c(x,Q)$ to that of a best fit to the respective data set. The fits to data are all reasonable. The new PDFs give slightly better fits than the previous one. Slide 11 shows the comparison of the H1 charm and bottom production data to the theory values from the same PDF sets. The $F_2^c(x,Q)$ data points have more scatter around the (smooth) theory values. The overall χ^2 of these fits is however acceptable.

It is worth noting that correlated systematical errors are always taken into account in our global analysis. The data points shown on these plots have been shifted by the fitted systematic errors; hence the differences between the data points and the theory values as they appear on these plots give a faithful indication of the quality of the fits.

4 Is there intrinsic charm in the nucleon?

Many nonperturbative models of nucleon structure suggest the existence of *intrinsic charm* (IC)—a non-vanishing component of nucleon parton structure at the scale of M_c. On the other hand, practically all global analysis of the parton structure of the nucleon so far ignore this possibility and make the simplifying assumption that all heavy quark partons are radiatively generated: they only arise from perturbative QCD evolution, starting from zero at $\mu \sim M_c$. Where does the truth lie? The resolution of this dichotomy is of inherent physics interest because it concerns the fundamental structure of matter, as well as of practical interest because the cross sections for many beyond-the-standard-model (BSM) processes at hadron colliders depend on the charm parton content of the nucleon. We have addressed this problem phenomenologically by a careful global analysis based on the GM PQCD formalism that, for the first time, allows for an independent charm sector [6].

As indicated in slide 14 of [1], the following specific scenarios for the charm sea, $c(x,\mu = M_c)$, are explored within our GM global analysis framework: (i) the conventional radiatively generated charm; (ii) non-vanishing IC $c(x,M_c)$ that is *sea-like* (i.e. shaped as the light sea quarks); and (iii) IC of the kind suggested by light-cone wave function models of the nucleon (peaked at moderately large x). Within scenario (iii), we further distinguish two models: the one studied by Brodsky et al. (the BHPS model), and a meson cloud model.

Slide 15 summarizes the main results. The figure shows the goodness-of-fit for the global analysis, χ^2_{global}, as a function of the magnitude of the IC component, measured by the momentum fraction carried $\langle x\rangle_{c+\bar{c}}$, under the various scenarios. In the range $0 < \langle x\rangle_{c+\bar{c}} < 0.01$ (outlined by the horizontal oval), χ^2_{global} is largely insensitive to $\langle x\rangle_{c+\bar{c}}$, indicating that there is no strong evidence for or against IC of a magnitude in this range. However, outside this range, for $\langle x\rangle_{c+\bar{c}} > 0.01$ (outlined by the vertical oval), we see a precipitous rise of χ^2_{global} as $\langle x\rangle_{c+\bar{c}}$ increases. Thus our global analysis sets a useful upper bound on the amount of intrinsic charm that is consistent with existing data. Using a 90% confidence level (C.L.) criterion, this bound is $\langle x\rangle_{c+\bar{c}} < 0.02$.

Although models of IC generally do not predict $\langle x\rangle_{c+\bar{c}}$, typical guesstimates place it around 0.01. This is consistent with the bound we determined from the above global analysis. The presence of IC of such a magnitude can have an impact on certain BSM processes, such

as charged Higgs production in hadron collider phenomenology. Cf. slide 7 of [2], and [4, 5]. Slide 16 shows the charm distribution $c(x,\mu)$ at three energy scales $\mu = 1.3,\ 3.16,\ 85$ GeV in the BHPS scenario, for various magnitudes of the initial distribution. We see the radiatively generated component (peaked at small x) catching up with the IC component (peaked at moderate x) as μ increases. However, the latter clearly still dominates in the x region $\geqq 0.1$ even at the W/Z mass scale.

5 Can the charm mass be determined in global analysis?

In principle, heavy quark masses $M_i(\mu)$ at some renormalization scale μ are basic parameters of QCD, similar to the coupling $\alpha_s(\mu)$. Thus, just like for α_s, there has been recent interest in determining M_i, e.g. the charm mass M_c, from global QCD analysis. In particular, is it possible to perform a conventional global QCD analysis using M_c as one of the fitting parameters, and thereby determine the charm mass to be the one that gives the best fit? If so, one may further ask, is this mass the $\overline{MS}$-mass or the pole-mass?

Slides 18-20 show results of a study, following the above procedure literally: one finds that the global analysis favors a relatively small values of $M_c \sim 1.3$ GeV, and the goodness-of-fit χ^2_{global} increases with M_c. But, a closer examination of the problem immediately raises the question: what is the physical meaning of this favored value of M_c? The problem is, a chosen value of M_c affects the global QCD analysis in two distinct ways: (i) through the mass-dependent Wilson coefficients in the theoretical calculation (the pole-mass); and (ii) through the initial condition $c(x,\mu = M_c) = 0$—the implicit assumption of *radiatively generated charm* that is used in all existing global analyses. It turns out, the global fit is influenced much more by the latter than by the former. Since radiatively generated charm is only an assumption, not an integral part of the QCD theory, the value of M_c favored by global analysis is not directly related to the basic QCD charm mass parameter—it is neither the $\overline{MS}$-mass nor the pole-mass! In order to answer the original question "can the charm mass be determined in global analysis?", one needs to clearly differentiate between the two sources of dependence on M_c mentioned above. This is currently under study.

References

[1] This review is based on the talk of Wu-Ki Tung in the Heavy Flavor workgroup of DIS07: `http://indico.cern.ch/contributionDisplay.py?contribId=276&sessionId=5&confId=9499`.

[2] Slides: See Wu-Ki Tung, talk in the Structure Function workgroup in these proceedings: `http://indico.cern.ch/contributionDisplay.py?contribId=189&sessionId=8&confId=9499`.

[3] W. K. Tung, H. L. Lai, A. Belyaev, J. Pumplin, D. Stump and C. P. Yuan, JHEP **0702**, 053 (2007).

[4] See also C.-P. Yuan, talk in the Electroweak work group in these proceedings: `http://indico.cern.ch/contributionDisplay.py?contribId=120&sessionId=9&confId=9499`.

[5] H. L. Lai, P. Nadolsky, J. Pumplin, D. Stump, W. K. Tung and C. P. Yuan, JHEP **0704**, 089 (2007).

[6] J. Pumplin, H. L. Lai and W. K. Tung, Phys. Rev. D **75**, 054029 (2007).

J/ψ Suppression Measurements by the PHENIX Experiment at RHIC

Ermias T. ATOMSSA *

Laboratoire Leprince Ringuet, École Polytechnique/IN2P3
Palaiseau, 91128, France.

Suppression of the quarkonium J/ψ ($c\bar{c}$) in heavy ion collisions has long been used as a signature of deconfinement [2]. Recent measurements by the PHENIX experiment at the Relativistic Heavy Ion Collider (RHIC) show a similar anomalous suppression as the one observed by the NA50 and NA60 experiments at CERN. Data from PHENIX in various colliding system are presented. Striking features that challenge traditional views are pointed out.

1 J/ψ suppression

Heavy ion collisions provide a unique experimental way to create and characterize the Quark Gluon Plasma (QGP), a hot and dense matter that lattice QCD predicts to be produced at high temperature energy density and. Products of hard processes, which take place in the early stage of the collision, are highly sensitive probes of the evolution of the created system. Suppression of the J/ψ quarkonium, which constitutes such a probe, has been measured by the PHENIX experiment at RHIC in various interactions, as a function of impact parameter, rapidity and transverse momentum.

One convenient way to define modification in AB type heavy ion collisions (where A and B represent atomic masses of colliding nuclei) is as the ratio of the J/ψ yield in heavy ion collisions to the one expected from pQCD, as measured by the yield in p+p interactions scaled by the average number of binary nuclear collisions (N_{coll}) that take place in AB type collisions (R_{AB}).

$$R_{AB}(y, p_T) = \frac{dN_{AB}(y, p_T)/dydp_T}{< N_{coll} > dN_{pp}(y, p_T)/dydp_T}$$

Different physical effects can contribute to the experimentally observed suppression ratio. At RHIC energies, direct J/ψ's are produced mostly through gluon-gluon fusion in nucleon-nucleon scatterings early in the collision. At this level, a modification (called shadowing) of gluon PDFs in nuclei can influence the suppression measured at the end. In addition, the initial production cross section is enhanced by a feed down component from excited charmonium states that is poorly constrained by experimental measurements.

Other physical phenomena can modify the suppression ratio after J/ψ formation. One such process is the absorption by nucleons in receding collision fragments. This contribution is called nuclear absorption, and may be sensitive to the formation mechanism of J/ψ. Shadowing and nuclear absorption are known as Cold Nuclear Matter (CNM) effects. Finally there are effects that might enhance the ratio by the creation of J/ψ through the recombination of uncorrelated c and $\bar{c}$ pairs from a deconfined medium. It is thus a complicated task to disentangle all these effects and isolate the contribution from dissociation by a possible QGP.

*For the PHENIX Collaboration.

2 J/ψ measurements in PHENIX

The PHENIX detector at the Relativistic Heavy Ion Collider (RHIC) can identify and measure electrons with a pair of mid rapidity spectrometers that cover $2 \times 90°$ in azimuth and $|y| < 0.35$ in rapidity, as well as muons with a pair of forward rapidity spectrometers that cover 360° in azimuth and $1.2 < |y| < 2.2$ in rapidity. This has allowed to do J/ψ suppression ratio measurements for different colliding systems (p+p, d+Au, Au+Au and Cu+Cu) as a function of rapidity, collision centrality and transverse momentum [3, 4, 5, 6].

Event centrality characterization is done by using information from global detectors: measurements of charged multiplicity by a Beam Beam Counter and/or energy deposit by a Zero Degree Calorimeter are used to divide the total cross section into centrality classes. A Glauber model calculation in conjunction with response simulation of global detectors is used to calculate the average N_{coll} for the events in each centrality class [7].

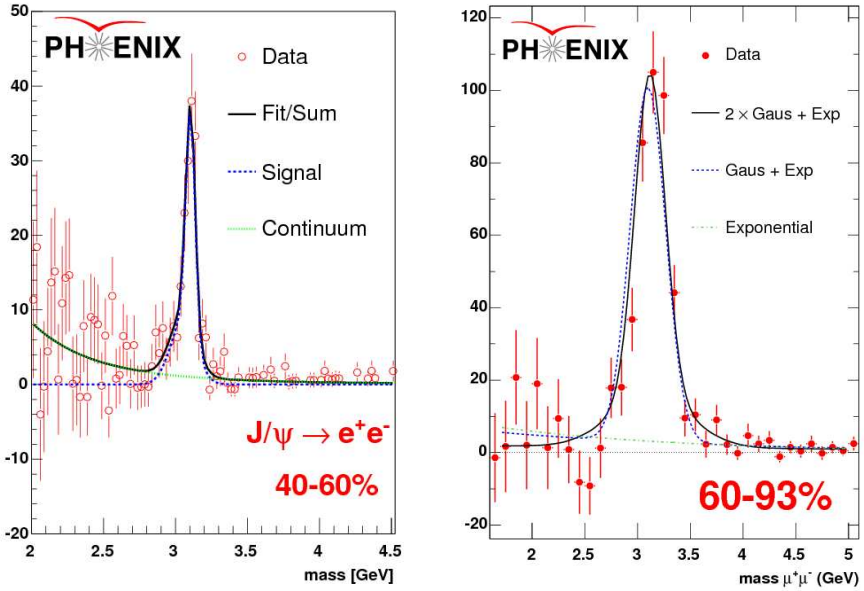

Figure 1: Left: Invariant mass spectrum of electron-positron pairs. Right: Invariant mass spectrum of muon pairs. Both plots are after subtraction of the combinatorial background.

Differential yields of J/ψ are measured through invariant mass spectra of lepton pairs (cf. Figure 1). The combinatorial background from uncorrelated unlike sign lepton pairs is estimated by mixing like sign leptons from different events. After combinatorial background subtraction, the spectra are fitted by various combinations of Gaussian and exponential functions to account respectively for J/ψ mass peak and residual backgrounds including open charm/beauty decays and Drell-Yann processes. The average value of the Gaussian integrals from the different fits is used as J/ψ yield and the dispersion is included in the systematical errors.

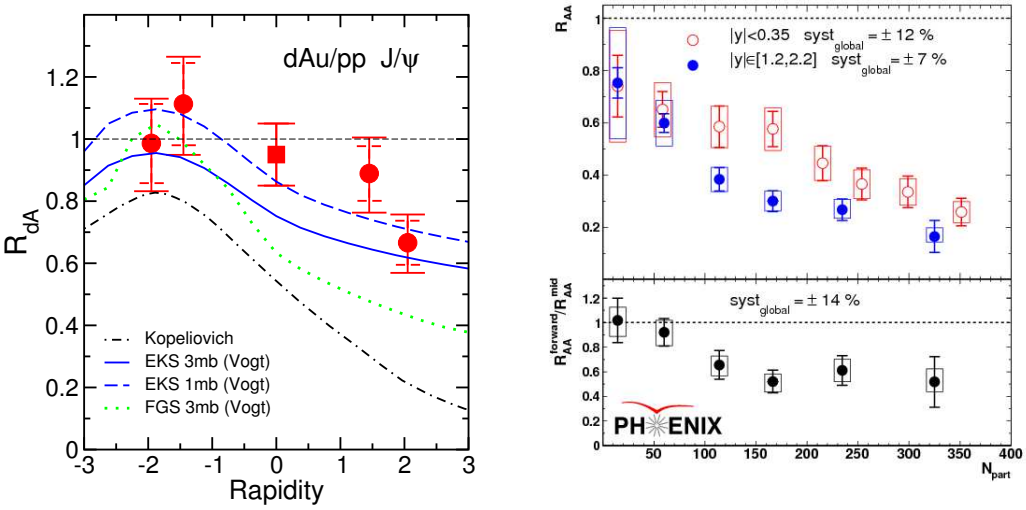

Figure 2: Left: R_{dA} as a function of rapidity for J/ψ's measured by PHENIX in d+Au collisions [4]. Right: R_{AA} for Au+Au collisions as a function of centrality for two rapidity ranges in upper panel, and the ratio between two in lower panel [5].

3 Suppression ratios from different colliding systems

On the left side, Figure 2 shows R_{dA} measurements by PHENIX from $\sim 1.5\mu b^{-1}$ worth of d+Au collisions at $\sqrt{s_{NN}} = 200$ GeV. This control experiment is intended to examine the contribution of CNM effects, because no QGP formation is expected in dA type collisions. Three models incorporating shadowing and nuclear absorption (with different cross sections) are plotted for comparison. The EKS shadowing parametrization [8] seems to reproduce the data better. Given the experimental uncertainties it is impossible to discriminate between the two absorption cross sections ($1mb$ and $3mb$).

On the right side, Figure 2 shows the J/ψ suppression ratio in Au+Au collision at $\sqrt{s_{NN}} = 200$ GeV interactions measured by PHENIX as a function of collision centrality (more central for higher N_{coll}). The Au+Au measurements are from the 2004 data set representing $\sim 160\mu b^{-1}$. Normalization is done using $\sim 3.6pb^{-1}$ of p+p collision data taken in 2005 [3]. The results are given as a function of the number of nucleons participating in inelastic collisions (N_{part}).

As expected, the modification factor approaches unity for peripheral collisions (small N_{part}). On the other hand, for very central collisions, (large N_{part}), a suppression factor of the order of five is observed at forward rapidity. Indirect comparisons [9, 10] show that this suppression ratio goes beyond what can be explained by extrapolations from d+Au measurements. Nevertheless two striking features are seen in these results:

1. The suppression ratio at mid rapidity is in very good agreement with the one measured by the NA50 and NA60 experiments at lower energy ($\sqrt{s_{NN}}$ ~17 GeV) with various ions (S+U, In+In, Pb+Pb) whereas the energy density reached is expected to be much smaller than at RHIC.

2. The suppression seen at forward rapidity is higher than the one observed at mid rapidity (cf. bottom panel of Figure 2).

These two observations, have led to the idea that the suppression seen in heavy ion collisions is not dominated by suppression mechanisms that increase with local energy density.

On the other hand models that assume suppression that grows with local density describe well the SPS data, but overestimate suppression at RHIC. They also fail to reproduce the mid to forward rapidity ratios of suppression factors.

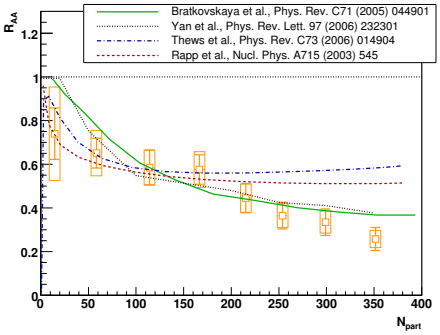

Figure 3: Predictions of various regeneration models compared to the mid rapidity result.

Although regeneration models provide an alternative, it is difficult to confirm them based only on the R_{AA} patterns due to poor constraints on their input parameters (for instance, the $c\overline{c}$ cross sections in similar conditions) to these models. To illustrate this point Figure 3 shows a few of the models [11, 12, 13, 14] that combine regeneration scenarios with suppression. Looking at distributions of other variables usually helps because recombined J/ψ tend to populate different phase space regions than J/ψ from direct pQCD processes. For instance the $< p_T^2 >$ variation as a function of centrality has already been used to this objective to some extent [15], but is again complicated by other mechanisms that contribute to the looked for effect. Another discriminating variable, is the elliptic flow (v_2) of J/ψ The current run 7 with somewhat larger statistics than previous runs and new global detectors will hopefully enable PHENIX to do these measurements.

References

[1] Slides: `http://indico.cern.ch/contributionDisplay.py?contribId=197&sessionId=5&confId=9499`

[2] T. Matsui et al. *Phys. Lett.*, B178:416, 1986.

[3] A. Adare et al. *Phys. Rev. Lett.*, 98:232002, 2007.

[4] S. S. Adler et al. *Phys. Rev. Lett.*, 96:012304, 2006.

[5] A. Adare et al. *Phys. Rev. Lett.*, 98:232301, 2007.

[6] H. Pereira Da Costa. *Nucl. Phys.*, A774:747–750, 2006.

[7] K. Adcox et al. *Phys. Rev. Lett.*, 86:3500–3505, 2001.

[8] K. J. Eskola et al. *Eur. Phys. J.*, C9:61–68, 1999.

[9] Raphael Granier de Cassagnac. hep-ph/0701222.

[10] R. Vogt. *Acta Phys. Hung.*, A25:97–103, 2006.

[11] R. L. Thews et al. *Phys. Rev.*, C73:014904, 2006.

[12] Li Yan et al. *Phys. Rev. Lett.*, 97:232301, 2006.

[13] E. L. Bratkovskaya et al. *Phys. Rev.*, C71:044901, 2005.

[14] L. Grandchamp et al. *Nucl. Phys.*, A715:545–548, 2003.

[15] R. L. Thews. *Nucl. Phys.*, A783:301–308, 2007.

Measurements of Heavy Flavor Single Leptons by PHENIX

Donald Hornback (for the PHENIX Collaboration) *

University of Tennessee - Department of Physics and Astronomy
Knoxville, TN 37996, USA

PHENIX has measured single leptons in both p+p and Au+Au collisions at $\sqrt{s_{NN}}$ = 200 GeV. Measurements in p+p collisions permit a determination of the total charm production cross section which can be compared to pQCD predictions. Heavy flavor production in Au+Au serves as a tool for studying the dense partonic matter produced in Au+Au collisions that can be interpreted through the simultaneous measurement of the azimuthal anisotropy parameter $v_2(p_T)$ and the nuclear modification factor $R_{AA}(p_T)$. In the context of existing predictions, the observed flow and energy loss of heavy quarks, in addition to that already seen for light mesons, suggests that the matter formed in Au+Au collisions at RHIC is a near-perfect fluid.

1 Studying heavy flavor production with single leptons

The measurement of single leptons at high transverse momentum ($p_T \gtrsim 1.0$ GeV/c), specifically electrons and muons which arise from the semi-leptonic decay of heavy flavor hadrons, play an important role in the study of heavy-quark production. Bottom and charm quarks are expected to have sufficient mass to permit next-to-leading order perturbative QCD (NLO pQCD) calculations to describe their production cross sections in p+p collisions at high p_T. Bottom production at the Tevatron [3] is shown to be well described by such calculations, charm production cross sections are determined to be $\approx 50\%$ higher than theory, though compatible within the experimental and theoretical uncertainties [4]. The PHENIX single electron results presented here provide improved comparisons to theoretical calculations through both extension to higher p_T and reduced experimental uncertainties. The single electron p+p measurement also serves as a baseline for the most recent single electron measurements in Au+Au collisions. Azimuthal anisotropies observed in the collective motion of charm quarks in the produced medium have interesting implications for the properties of the medium and is further discussed in section 4. PHENIX also possesses the capability to measure single muons at forward rapidity. Although such measurements are currently underway within PHENIX, the single electron measurements are well established with clear physics messages. Discussion in these proceedings are therefore restricted to single electron results.

2 PHENIX Experiment and analysis

PHENIX measures single electrons with two separate central arms, each with 90° azimuthal acceptance and pseudorapidity coverage of $|\ \eta\ | < 0.35$. Electrons are measured in the central arms using combined information from an electromagnetic calorimeter and a ring imaging Cerenkov detector. Muons are measured using two separate muon spectrometers with azimuthal coverage and covering the pseudorapidity range $1.2 < |\ \eta\ | < 2.4$. Muons are

*For the full PHENIX collaboration author list, see Ref. [2]

identified in the forward and backward directions through the use Iarocci tubes interleaved between steel absorber plates. Precise muon momentum determination is accomplished using cathode strip chambers inside a magnetic field. For more details on the PHENIX experiment, please see [5].

The identification of single electrons from heavy flavor is performed through the statistical subtraction of background sources, with the remaining lepton signal being attributed to open heavy flavor decay. This technique was first applied at the ISR at CERN, which measured single electrons from heavy flavor production in p+p collisions at $\sqrt{s}$ = 30 - 63 GeV [6]. PHENIX applies two independent background estimates, referred to as the converter and cocktail methods, which serve as experimental cross checks, allowing for a reduction in the systematic uncertainties associated with the extracted single electron production cross section [7].

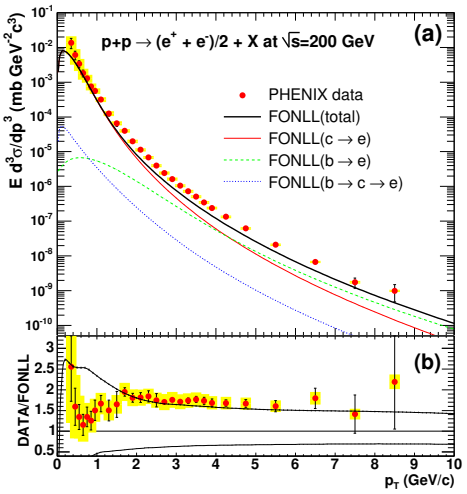

Figure 1: (a) Transverse momentum distribution of single electron production cross section compared to FONLL [8] calculation. (b) Ratio of single electron cross section to FONLL.

3 Open heavy-flavor production in p+p

At all transverse momentum the dominant source of background is from π^0 decay, directly from Dalitz decay or indirectly from photon conversion. PHENIX constrains the π^0 spectrum by direct measurement. For the convertor method a thin brass sheet (1.67% X_0) of known thickness is introduced around the beam pipe for a fraction of the total run time. This material serves to increase electrons from photon conversion by a fixed amount. Through a comparison of run periods with and without the additional conversion material, the yield of photonic electrons is accurately measured, allowing for the extraction of the heavy-flavor electron signal down to a $p_T = 0.3$ GeV/c. The "cocktail" method calculates various electron sources collectively using a Monte Carlo event generator of hadron decays. The converter method also serves to calibrate the backgrounds as estimated by the cocktail method. The

convertor method is statistically limited to low p_T due to the short run time devoted to its use. The cocktail method allows for extraction of the heavy flavor signal up to the current statistical limitations of the data, $p_T = 9.0$ GeV/c. These analysis techniques are applied to both the p+p and Au+Au measurements presented.

The production cross section of single electrons from heavy-flavor decay as measured by PHENIX is shown in Fig. 1. Figure. 1(a) shows the invariant differential cross section of single electrons compared to the central values of a Fixed Order Next to Leading Log (FONLL) [8] pQCD calculation. Relative contributions from charm and bottom are also shown, with bottom overtaking charm for $p_T > 4.0$ GeV/c. The ratio of data to FONLL is shown in Fig. 1b. The theoretical upper and lower limit band is shown. Some small p_T dependence is observed in this ratio for $p_T < 2.0$ GeV/c. Approximating this ratio as nearly constant by fitting with a line over $0.3 < p_T < 9.0$ GeV/c yields a ratio of $1.72 \pm 0.02^{stat} \pm 0.19^{sys}$. This is similar to ratios observed in charm production at the Tevatron [4]. As seen in the lower plot, the data lies along the upper theoretical uncertainty band. The total charm cross section is determined to be $\sigma_{c\bar{c}} = 567 \pm 57^{stat} \pm 224^{sys}$ μb.

4 Open heavy flavor production in Au+Au collisions

Single electrons from heavy flavor semi-leptonic decay in Au+Au collisions have also been measured by PHENIX [2]. The suppression of light hadron production at high p_T has previously been observed in Au+Au collisions at RHIC and is taken to be caused by partonic energy loss in the produced medium. Energy loss by heavy flavor quarks is expected to be less than that for light quarks due to reduced gluon radiation in the forward direction, commonly referred to as the dead-cone effect [9]. The extent of energy loss in the medium can be quantified using the nuclear modification factor, R_{AA}, which is the ratio of the yield of single electrons in Au+Au collisions for a given centrality class divided by a p+p reference scaled by the number of binary collisions for Au+Au. By construction, $R_{AA} = 1$ for processes that scale by the number of underlying nucleon-nucleon collisions.

Figure 2 shows three different plots of R_{AA} as a function of the number of participants, N_{part}. The solid circles represent the integrated heavy-flavor single electrons for $p_T > 0.3$ GeV/c, with each data point corresponding to a particular centrality class. R_{AA} does not deviate from unity for all centralities confirming the expectation that the total heavy-flavor yield follows binary scaling. The solid squares show R_{AA} for π^0 with $p_T > 4.0$ GeV/c, which exhibit the previously observed phenomena of increasing suppression with increasing centrality [10]. The open circles represent heavy-flavor single electron yield, plotted for $p_T > 3.0$ GeV/c instead of 4.0 GeV/c, since electrons from charm decay originate primarily from D mesons of $p_T > 4.0$ GeV/c. Counter to original expectations, heavy-flavor does exhibit clear high p_T suppression which increases smoothly with N_{part}, though the extent of suppression is somewhat less than that observed for the light quark π^0 meson. This suppression of heavy-flavor yields at high p_T suggests a strong coupling of heavy quarks to the partonic medium produced in Au+Au collisions [2].

This measurement has further implications when coupled with the observed elliptic flow of heavy flavor. This flow is azimuthal anisotropy characterized by the parameter v_2 which is the coefficient of the second harmonic of the Fourier expansion of the azimuthal distribution with respect to the reaction plane [11]. Figure 3 shows the PHENIX measurement of heavy-flavor single electron v_2 values (solid circles) for minimum bias Au+Au collisions. The data indicate a non-zero v_2 value for charm quarks, indicating that they participate in the

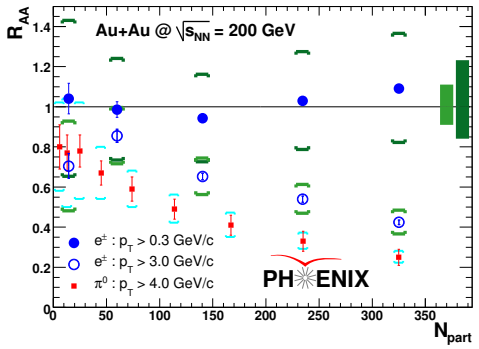

Figure 2: Nuclear modification factor, R_{AA} (defined in text) as a function of the number of participant, N_{part} for single electrons in Au+Au collisions at $\sqrt{s_{NN}} = 200$ GeV for $e^{\pm}$ and π^0.

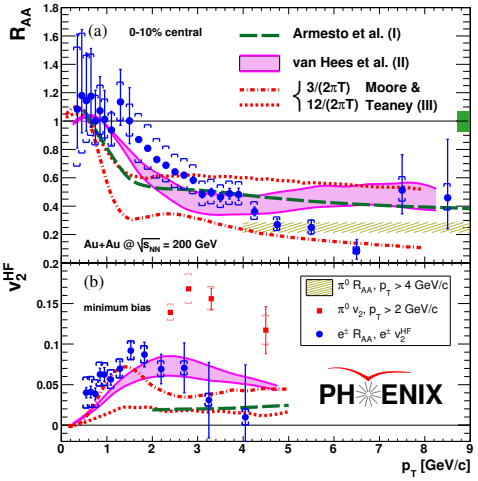

Figure 3: Comparison of measured R_{AA} and v_2 as a function of transverse momentum in Au+Au collisions with hydrodynamical models.

collective flow of the medium produced at RHIC. Most strikingly, hydrodynamical models that describe both the high p_T suppression and elliptic flow [citations] suggest that the medium's viscosity resides near the conjectured quantum lower bound, making the medium produced in Au+Au collisions at RHIC a near perfect fluid.

5 Acknowledgments

This research is sponsored by the Division of Nuclear Physics , U.S. Department of Energy, under contract DE-FG02-96ER40982 with the University of Tennessee. The complete list of PHENIX acknowledgments is provided in Ref. [7].

References

[1] Slides:
`http://indico.cern.ch/contributionDisplay.py?contribId=198&sessionId=5&confId=9499`
[2] A. Adare et al. *Phys. Rev. Lett.*, 98, 2007.
[3] Cacciari M. *hep-ph/0407187*, 2004.
[4] D. Acosta et al. *Phys. Rev. Lett.*, 91:241804, 2003.
[5] K. Adcox et al. *Nucl. Instrum. Meth. A*, 499:469–602, 2003.
[6] Perez P. *Phys. Lett.*, B112:260, 1976.
[7] A. Adare et al. *Phys. Rev. Lett.*, 97, 2006.
[8] Cacciari M. *Phys. Rev. Lett.*, 95:122001, 2005.
[9] Dokshitzer Y. and Kharzeev D. *Phys. Lett. B*, 519:199–206, 2001.
[10] A. Adare et al. *Phys. Rev. Lett.*, 96, 2006.
[11] Wong C.Y. *Phys. Lett.*, 88B:39, 1979.

Recent Heavy Flavor Results from STAR

André Mischke* for the STAR Collaboration†

Institute for Subatomic Physics, Utrecht University,
Princetonplein 5, 3584 CC Utrecht,
The Netherlands.
E-mail: a.mischke@phys.uu.nl

We report on recent heavy flavor measurements from the STAR experiment at RHIC[1]. The measured charm cross section in heavy-ion collisions scales with the number of binary collisions, which is an indication for exclusive charm production in the initial state of the collision. The observed strong suppression of non-photonic electrons at high p_{T} in Au+Au collisions together with the azimuthal correlation measurements in p+p collisions imply a suppression of B production in heavy-ion collisions. We also present recent measurements of the Υ cross section in p+p collisions.

1 Introduction

The fundamental theory of strong interactions, Quantum Chromodynamics (QCD), predicts a phase transition from hadronic matter to a system of deconfined quarks and gluons, the Quark Gluon Plasma, if the surrounding temperature exceeds a critical value. The goal of heavy-ion physics is to produce such a deconfined QCD state and to study its properties under controlled laboratory conditions. The accelerator with the current highest collision energy for atomic nuclei is the Relativistic Heavy-Ion Collider (RHIC) at Brookhaven National Laboratory. Current results from the RHIC experiments have given compelling evidences that the produced medium is indeed a plasma of quarks and gluons, but it behaves like a "perfect" fluid rather than an ideal gas [2, 3]. One of the intriguing results is the strong modification of the jet structure inside the created medium. Theoretical model calculations that attribute the jet attenuation to the energy loss of partons traversing through the medium have successfully described the present data.

The study of heavy flavor (charm, bottom) production in heavy-ion collisions provides key tests of the parton energy loss mechanisms and offers important information on the properties of the produced medium. Due to their large mass, heavy quarks are expected to be primarily produced in the early stage of the collision and, therefore, probe the complete space-time evolution of the medium. Theoretical models predicted that heavy quarks should experience smaller energy loss than light quarks while propagating through the QCD medium due to the suppression of small angle gluon radiation (dead-cone effect) [4].

2 Recent results

The charm cross section at mid-rapidity is determined from measurements of open charm mesons and from the reconstruction of heavy flavor semi-leptonic decays via muon and electron measurements. These three measurements, which are performed by the STAR Time Projection Chamber (TPC) and Time-of-Flight (ToF), cover 95% of the cross section. D^0

*The author is grateful for the support by the Nederlands Organisation for Scientific Research (NWO).
†For the full author list, see [8].

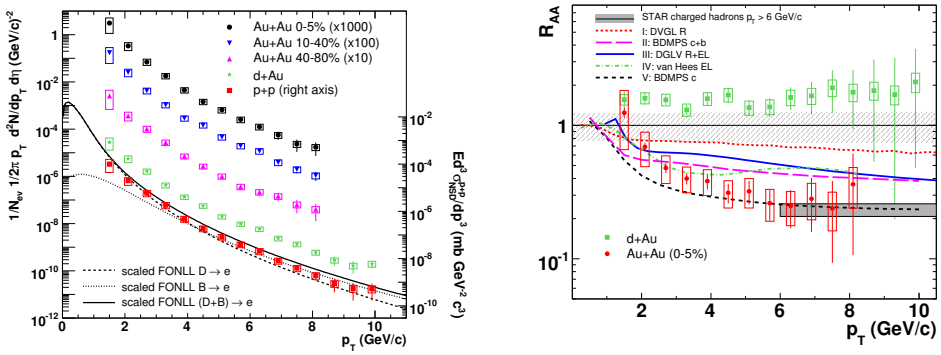

Figure 1: Left panel: Non-photonic electron spectra in p+p, d+Au and, for different centralities, in Au+Au collisions at $\sqrt{s_{\rm NN}}$= 200 GeV. The curves are pQCD predictions scaled by 5.5 for p+p collisions. The right axis gives the cross section for the p+p spectrum. The error bars (boxes) indicates the statistical (uncorrelated systematic) errors. The dashed box illustrates the overall normalization uncertainty. Right panel: Nuclear modification factor R_{AA} for d+Au and Au+Au collisions. The curves correspond to different model predictions.

mesons are reconstructed in the hadronic decay channel $D^0 \rightarrow K^-\pi^+$ by calculating the invariant mass of all oppositely charged TPC track combinations [5, 6]. The decay particles are identified using the specific energy loss (dE/dx) measured in the TPC. Muons at low $p_{\rm T}$ (< 250 MeV/c) are identified by the combination of the m^2 measurement in the ToF detector and the specific energy loss (dE/dx) measurement in the TPC. A cut on the distance of closest approach is used to separate the prompt from decay muons. The non-photonic electrons are obtained by combining the dE/dx and ToF ($|1/\beta - 1| < 0.03$) measurement. A description of the determination of the photonic electron background, the applied corrections and the procedure to calculate the charm cross section from the $p_{\rm T}$ spectra of D^0, μ and e can be found in [5]. The obtained cross section is found to be $\sigma_{cc}^{NN} = 1.40 \pm 0.11 \pm 0.39$ mb in the 12% most central Au+Au collisions. NLO calculations predict a factor of ≈ 5 smaller value for the cross section. More precise measurements are required in order to understand this discrepancy. Moreover, the cross section at mid-rapidity shows binary collision scaling which is an indication for charm production exclusive in the initial state of the collisions [7]. Hence, there is no room for thermal charm production in the medium.

Electrons at higher $p_{\rm T}$ (> 4 GeV/c) are identified by a combined measurement using the TPC and the Electromagnetic Calorimeter (EMC). The analysis details are described in [8]. Fig. 1 (left) shows the $p_{\rm T}$ spectrum of non-photonic electrons in p+p, d+Au and, for different centralities, in Au+Au collisions at $\sqrt{s_{\rm NN}}$= 200 GeV, which are measured up to 10 GeV/c. A pQCD calculation for heavy quarks production in p+p collisions [9], indicated in Fig. 1 (left) by the solid line, describes the overall shape of the $p_{\rm T}$ distribution but it has the same scaling discrepancy as observed for the charm cross section measurement. Nuclear effects are usually quantified in the nuclear modification factor R_{AA} where the yield in Au+Au is divided by the yield in p+p scaled by the number of binary collisions. The non-photonic electron yield exhibits an unexpectedly large suppression in central Au+Au collisions at high $p_{\rm T}$, suggesting substantial energy loss of heavy quarks in the produced medium (cf. Fig. 1, right). The suppression factor has a similar value as observed for light

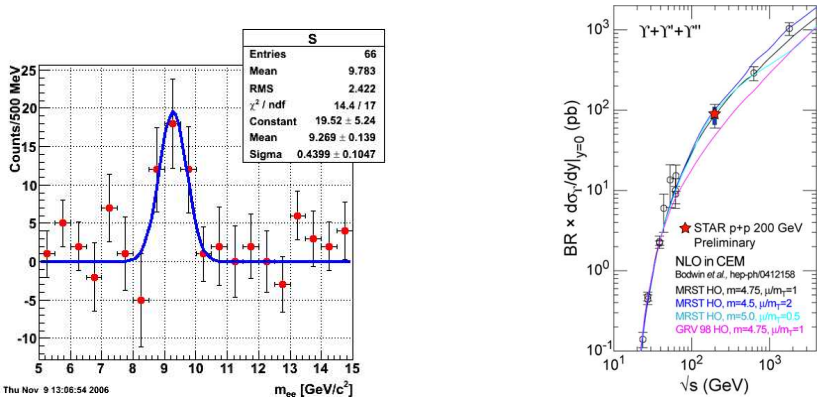

Figure 2: Left panel: Background subtracted di-electron invariant mass distribution in p+p collisions at $\sqrt{s_{\rm NN}}$= 200 GeV. The blue line indicates a Gaussian fit to the data. Right panel: Excitation function of the Υ cross section. The data is compared to previous measurments and NLO calculations. The curves of the NLO calculations are scaled by a factor of 1.44 to account for the excited states.

quark hadrons in central Au+Au collisions, indicated by the grey box in the figure. The data is compared to different energy loss models [10, 11, 12, 13] which vary essentially in the interaction processes and energy loss mechanisms taken into account. As indicated in Fig. 1 (right), all models underpredict the measured suppression factor at high $p_{\rm T}$. It has been shown that the data is described quite well if the models assume electrons from D decays only. Therefore, the observed discrepancy could indicate that the B dominance over D mesons starts at higher $p_{\rm T}$. A possible scenario for B meson suppression invokes collisional dissociation in the medium [14].

To verify the B dominance at higher $p_{\rm T}$ one has to disentangle the D and B contribution to the non-photonic electron distribution experimentally. Recent results on measurements in p+p collisions of the azimuthal angular correlations between electrons (from heavy-flavor decays) associated with charged hadrons have shown that the relative B contribution to the non-photonic electron spectrum, $B/(B+D)$, is about 40% at $p_{\rm T}$ = 5 GeV/c [15]. The measured $p_{\rm T}$ dependence of the relative B contribution can be used to verify the input parameters for most of the energy loss models. First results on a different approach show the proof of principle to disentangle the D and B contributions to the non-photonic electrons using electron-D^0 meson azimuthal correlations [16].

The suppression of heavy quarkonium states provides an essential tool to study the temperature of the medium. The large acceptance ($|\eta| < 1$ and $0 < \phi < 2\pi$) of the STAR TPC and EMC allows the measurement of Υ production at mid-rapidity. The Υ is reconstructed through the $\Upsilon \rightarrow e^+e^-$ decay channel. Both detectors have very good electron identification capabilities and allow the combined measurement of the momentum (TPC) and the energy (EMC) of the electrons. Details of the data analysis can be found in [17]. Due to the finite momentum resolution of the TPC, individual Υ states, 1S, 2S and 3S, can not be resolved. The EMC serves as a trigger for high momentum electrons utilizing two dedicated trigger settings [18]. The presented data are from the 2006 Run

where the integrated luminosity was $\mathcal{L} = 5.6$ pb^{-1}. The invariant mass distribution of unlike-sign electron pairs is shown in Fig. 2 (left). The peak width is consistent with the expected mass resolution. The corrections applied to the raw yield are discussed in [17]. The obtained production cross-section of $BR_{ee} \times \frac{d\sigma}{dy}_{y=0} = 91 \pm 28(stat.) \pm 22(sys.)$ pb follows the world data trend (cf. Fig. 2, right). Within uncertainties, the data shows very good agreement with NLO calculations. The low cross section of the Υ at RHIC energies make this a luminosity limited measurement. The upcoming measurement in heavy-ion collisions will shed more light into the expected melting of quarkonia states in the hot and dense medium and provide an estimate of the medium temperature.

3 Summary and conclusions

In this paper, we summarize recent heavy flavor results from the STAR experiment at RHIC. The charm cross-section was extracted from a combined fit to the measured spectra of open charm mesons, and electrons and muons both from semileptonic heavy flavor decays. The charm cross section in Au+Au collisions scales with the number of binary collisions supporting the assumption that charm is exclusively produced in the initial state of the collision and that there is no room for thermal production in the medium. The suppression of the nuclear modification factor of non-photonic electrons at high p_{T} in Au+Au collisions is much larger than expected. The theoretical explanations are yet inconclusive. First results on azimuthal angular correlations of non-photonic electrons and hadrons (D^0 mesons) in p+p collisions show its ability to disentangle the D and B contribution to the electron spectrum. The completion of the STAR EMC allowed the first measurement of the Υ production at mid-rapidity in p+p collisions. The Υ cross section is consistent with pQCD calculations and the world data trend. More exciting results are about to come with the STAR detector upgrades (full barrel Time-of-Flight and Heavy Flavor Tracker) which will allow direct measurements of the nuclear modification factor of D and B mesons in heavy-ion collisions.

References

[1] Slides: `http://indico.cern.ch/contributionDisplay.py?contribId=199&sessionId=5&confId=9499`
[2] B.I. Abelev *et al.* (STAR Collaboration), Nucl. Phys. **A757**, 102 (2005).
[3] P. Jacobs and X.N. Wang, Prog. Part. and Nucl. Phys. **54**, 443 (2005).
[4] Y.L. Dokshitzer and D.E. Kharzeev, Phys. Lett. **B519**, 199 (2001).
[5] J. Adams *et al.* (STAR Collaboration), Phys. Rev. Lett. **94**, 062301 (2005).
[6] H. Zhang *et al.* (STAR Collaboration), Nucl. Phys. **A774**, 701 (2006).
[7] Y. Zhang *et al.* (STAR Collaboration), J. Phys. **G32**, S529 (2006).
[8] B.I. Abelev *et al.* (STAR Collaboration), Phys. Rev. Lett. **98**, 192301 (2007).
[9] M. Cacciari, P. Nason and R. Vogt, Phys. Rev. Lett. **95**, 122001 (2005).
[10] M. Djordjevic et al., Phys. Lett. **B632**, 81 (2006).
[11] N. Armesto et al., Phys. Lett. **B637**, 362 (2006).
[12] S. Wicks et al., Nucl. Phys. **A784**, 426, (2007).
[13] H. van Hees, V. Greco and R. Rapp, Phys. Rev. **C73**, 034913 (2006).
[14] A. Adil and I. Vitev, Phys. Lett. **B649**, 139 (2007).
[15] X. Lin *et al.* (STAR Collaboration), submitted to J. Phys. **G** (arXiv: nucl-ex/0701050).
[16] A. Mischke *et al.* (STAR Collaboration), arXiv: 0705.2089.
[17] M.R. Cosentino *et al.* (STAR Collaboration), arXiv: 0706.0892.
[18] P. Djawotho *et al.* (STAR Collaboration), submitted to J. Phys. **G** (arXiv: nucl-ex/0701075).

Charmonium Singlets, Open Charm and Exotic Hadrons

Jean-Marc Richard

LPSC, CNRS-IN2P3-Ingénierie–UJF–INPG
53, avenue des Martyrs, 38026 Grenoble, France

Caution is suggested on the comparison of the spin-singlet charmonium P-state with the centre of gravity of triplet states, when the mass splitting is of the order of a few MeV. The physics of new hidden-charm states X and Y is briefly reviewed. Perspectives for producing double-charm baryons and double-charm exotic mesons are discussed.

1 Charmonium singlets

The charmonium singlet states have resisted a firm identification for many years [2], but, now the η_c, η_c' and h_c are well identified. The mass of the latter, as given by the CLEOc collaboration is [3] $m(h_c) = 3524.4 \pm 0.6 \pm 0.4\ \mathrm{MeV}/c^2$, where the first uncertainty comes from statistics and the second one from estimated systematic errors. For the previous attempts and other measurements, see, e.g., [4, 5].

It is perfectly legitimate to *define* the hyperfine splitting by $\delta = (\chi_0 + 3\chi_1 + 5\chi_2)/9 - h_c$. This leads to the experimental value [3] $\delta = 1.0 \pm 0.6 \pm 0.4\ \mathrm{MeV}/c^2$. But a superficial reading of δ could be misleading, as it suggests a very small or even vanishing effect of spin–spin forces in the 1P multiplet, while it is arguably larger, and positive, of the order of a few MeV.

In the potential models, if the spin-orbit, $V_{LS}\boldsymbol{L}.\boldsymbol{S}$ and tensor, $V_T S_{12}$ terms are treated in perturbation, the masses of triplet P-states with $J = 0$, 1 and 2 are shifted by $\{-2, -1, 1\}\langle V_{LS}\rangle$ and $\{-4, 2, -2/5\}\langle V_T\rangle$, respectively, and it is readily seen that the contributions of $\langle V_{LS}\rangle$ and $\langle V_T\rangle$ disappear in the $(2J + 1)$-weighted centre of gravity. Now the $\chi_2 - \chi_0$ splitting is of the order of 150 MeV, suggesting that at the level of 1 MeV accuracy, the calculation of the spin splittings should be pushed beyond first order. As the spin operators $\boldsymbol{L}.\boldsymbol{S}$ and $S_{12} = 3\boldsymbol{\sigma}_1.\hat{r}\,\boldsymbol{\sigma}_2.\hat{r} - \boldsymbol{\sigma}_1.\boldsymbol{\sigma}_2$ enter the Hamiltonian linearly, the ground state of the spin-triplet P-state is a concave function of the values of these operators. This means that in any potential model where the components V_{LS} and V_T are suitably regularised and inserted non-pertubatively into the wave equation, the genuine spin-orbit- and tensor-free triplet state is *above* the naive centre of gravity. As an example, if one adopts the potential of Ref. [6], which is rather conventional in the heavy-quark sector (the light-quark one is more speculative, with Goldstone-boson exchanges), the difference is about 3 MeV, which locates the experimental h_c about 4 MeV above this improved triplet benchmark.

Unfortunately, the convexity effect depends rather sensitively on the details of the regularisation of the spin-orbit and tensor terms, and many other effects have to be taken into account, for instance, the P–F orbital mixing, which pushes down the $^3\mathrm{P}_2$ state. Phenomenological potentials could also include further spin operators that are not necessary in the simplest non-relativistic reduction of one-gluon exchange, or in the Thomas precession, and, for spin triplet, cannot be reduced to spin–orbit and tensor and thus do not average out to zero in the naive centre of gravity. An example is the "quadratic spin–orbit" operator used in nuclear physics to describe the nucleon–nucleon potential.

On the theoretical side, the zero-range property of the spin-spin interaction, $V_{SS} \propto \delta^{(3)}(\boldsymbol{r})$ only holds in the simplest non-relativistic reduction à la Breit–Fermi of the Coulomb term due to one-gluon-exchange. A range of about the inverse quark mass would be reasonable, and would give a non-vanishing matrix element for P-states. Higher-order terms in perturbative QCD have been discussed in the literature, see, e.g.,[7, 8] and Refs. there. The spin–spin potential has also been estimated non-perturbatively with the lattice techniques [7], exhibiting a range that is short but finite. In some other lattice studies [7], the states χ_J and h_c are calculated directly (not à la Born–Oppenheimer through a potential), each with a specific operator adapted to its quantum numbers, as in QCD sum rules [9].

The interpretation of the mass of the η_c' also reveals the limits of simple potentials. The splitting $m(\psi') - m(\eta_c') \simeq 48$ MeV, is appreciably smaller than the predicted one in most $(c\bar{c})$ constituent models tuned to reproduce $m(\mathrm{J}/psi) - m(\eta_c) = 117$ MeV. A likely explanation is that for this 2S multiplet lying very close to the $\mathrm{D}\overline{\mathrm{D}}$ threshold, the coupling to higher Fock configurations is enhanced. The ψ' is pushed down by the very close $\mathrm{D}\overline{\mathrm{D}}$ threshold, while η_c' is less affected, since only influenced by the higher lying $\mathrm{D}^*\overline{\mathrm{D}}$ + c.c. and $\mathrm{D}^*\overline{\mathrm{D}}^*$ thresholds. This reduces the effect of the quark–antiquark spin–spin forces [10].

Hopefully, the η_b will be found shortly. Its mass can be estimated with sophisticated techniques. If one accounts for the m^{-2} factor in front of the spin-spin interaction, and the squeezing of wave-functions when the constituent masses increase, which for a logarithmic potential gives a factor $m^{3/2}$ for the squared wave function at the origin, one gets $m(\Upsilon) - m(\eta_b)$ in ratio $(m_c/m_b)^{1/2}$ to its charm analogue, i.e., about 68 MeV.

2 Single and double charm hadrons

A few years ago, several new results came in the meson sector with single charm, in particular the $\mathrm{D}_{s,J}$ states, and this stimulated an intense activity. More recently, several new baryons have been found, and nowadays, the family of charmed baryons include many states [5].

A key question in baryon spectroscopy is to find evidence for the three-body structure, i.e., states in which both $\boldsymbol{x} = \boldsymbol{r}_2 - \boldsymbol{r}_1$ and $\boldsymbol{y} \propto 2\boldsymbol{r}_3 - \boldsymbol{r}_1 - \boldsymbol{r}_2$ degrees of freedom are excited. In the harmonic-oscillator of light quarks, with flavour SU(3) symmery, this corresponds to the 20^+ multiplet, with an antisymmetric orbital wave-function $\psi(\boldsymbol{x}, \boldsymbol{y}) \propto \boldsymbol{x} \times \boldsymbol{y} \exp[-a(x^2 + y^2)/2]$ that couples to an antisymmetric spin–isospin wave function and an antisymmetric colour wave function. The lack of firm experimental candidate is perhaps due to the small cross-sections in pion- or photo-production experiments, which favour states having better overlap with the quark wave function of the target nucleon. Another picture is proposed by diquark models, in which these states do not exist, if the diquark is in its ground state.

Perhaps the first baryon with excitation in both Jacobi variables will be found in the charm sector: this state is expected to be rather narrow and to have preferentially at least one orbital excitation in its decay products.

Among ordinary hadrons, the (QQq) baryons with two heavy quarks are particularly interesting, as they combine the adiabatic motion of two heavy quarks, as in charmonium, and the relativistic motion of a light quark around a coloured source, as in D mesons.

The ground state has interesting weak-decay properties.There are huge differences among the lifetimes of D, D_s mesons and single-charm baryons. The hierarchy of the lifetimes is well understood in terms of W-exchange, or interference effects, but the differences are usually larger than estimated in calculations. In the case of hadrons with two heavy quarks, binding effects also play a role.

SELEX has serious candidates for the ground states, and more fragile evidence for the isospin partner, spin or orbital excitations [11]. However, other experiments were not able to find any double-charm baryons, in particular in e^+e^- [12]. This is a little surprising, because meanwhile the B-factories found an excess (vs. simple QCD expectations) of double charm-pair production, $e^+e^- \to (c\bar{c})(c\bar{c})$, leading to beautiful $(c\bar{c})$ spectra recoiling against the J/ψ. One would naively expect that if a $(cc\bar{c}\bar{c})$ primary system is easily produced, it sometimes rearranges into a doubly-charm diquark and a conjugate antidiquark.

When the first studies of double-charm baryons were carried out, their experimental study was out of reach. Now, with the B_c well measured, and the first indication for Ξ_{cc}, the sector of two heavy flavours seems ready for detailed spectroscopy, and one could already envisage one step beyond, i.e., triple charm. The spectrum of Ω_{ccc} was called [13] "the ultimate goal of baryon spectroscopy", the true analogue of charmonium for baryons. Here the three-quark dynamics can be tested in the static limit and confronted with theory. For instance, the level order is expected to be similar to that of charmonium, with the first excitation having a parity opposite to that of the ground-state. Remember that for light baryons, the Roper resonance, with the same positive parity as the ground-state nucleon, comes slightly lower than the first orbital excitations, and this cannot be accommodated in simple quark models.

3 Crypto-exotic and exotic hadrons

Several intriguing states have been identified in the hidden-charm sector, that are hardly compatible with genuine $(c\bar{c})$ states. The experimental situation concerning the $X(3872)$, the various X's near 3940, the $Y(4260)$, etc., is reviewed in several contributions to this conference [5].

The most popular explanation of $X(3872)$ is that of a $D\overline{D}^* + $c.c. molecule, see, e.g., [14] and Refs. there on the pioneering works by Voloshin et al., Törnqvist, Glashow et al., Ericson and Karl, Manohar et al., Braaten et al., etc. Nuclear forces acting between charmed mesons generate a nuclear potential which is weaker that the proton–neutron spin-triplet interaction, but being experienced by heavier particles, it gives comparable spectral properties, at the edge between binding and non-binding. Interesting developments have been proposed, in particular bound sates of two or several charmed or doubly-charmed baryons [15]. Also, as the D and the $\overline{D}^*$ are not strictly bound in this approach, but slightly above their threshold, one could envisage the Borromean binding of three or more heavy mesons.

There are, however, some caution in order. As stressed by Suzuki [16], due to the $D^* - D$ mass difference, the Yukawa potential in $D\overline{D}^* + $c.c. is non local, and this might weaken its efficiency. Also, the miracle in nuclear physics is the presence of a hard core, which prevents the nucleons from collapse and reinforces the role of long-range dynamics. There is no such hard core in $D\overline{D}^* + $c.c., and one should account for the direct interaction between the quarks of D and these of $\overline{D}^*$. This leads us to the alternative four-quark models.

Among these models, there is the diquark–antidiquark picture, as developed in particular by Maiani et al. [17], giving an unified picture of several new states. Notice that the diquark is an effective cluster, an approximation valid only in a given environment. If taken too seriously, some of the diquark models of X and Y, with a relatively low mass for the diquarks, could lead to predict the existence of stable triple-charm dibaryons, such as $(cccsss)$, below the $\Omega\Omega_{ccc}$ threshold.

The four-quark dynamics, and its application to $X(3872)$, is also discussed by Lipkin and Høgaasen et al. [18], among others. The chromomagnetic interaction, with a realistic treatment of flavour-symmetry breaking gives a simple explanation of the mass and decay properties of $X(3872)$ [18].

Now, a lesson from atomic physics, is that the best place for stable four-body states is not (M^+, m^+, M^-, m^-), which is slightly stable for $M = m$, but loses stability for $M/m \simeq 2.2$ [19]. However, the configurations (M^+, M^+, m^-, m^-) are more stable that these with equal masses [19]. The crucial rule is that the Coulomb interaction remains unchanged when the masses evolve from electron to muon or heavier constituents. In QCD, we have the same property, called *flavour independence*, for the spin-independent interaction. This is why states of the type $(QQ\bar{q}\bar{q})$ are predicted to exist [20], at least in the limit of large Q/q mass ratio. Their production and identification could be carried out in the experiments searching for the double-charm baryons.

A good surprise of recent high-energy experiments has been the ability of performing productively in hadron physics, and even to clarify the results claimed by dedicated low-energy experiments. Another good surprise is the ability to produce fragile and complex structures, such as antideuterium [5], bound only by 2 MeV. It is reasonable to anticipate significant progress on heavy hadrons, in particular exotic multiquarks, from the future LHC experiments, provided a small fraction of the analysis is devoted to this physics.

I thank for organisers of this beautiful DIS Conference, K. Seth of discussions there, and M. Asghar for comments on the manuscript, and J. Vijande for correspondence.

References

[1] Slides: `http://indico.cern.ch/contributionDisplay.py?contribId=200&sessionId=5&confId=9499`
[2] A. Martin and J. M. Richard, CERN Cour. **43N3** (2003) 17;T. Barnes, T. E. Browder and S. F. Tuan, arXiv:hep-ph/0408081.
[3] P. Rubin *et al.* [CLEO Collaboration], Phys. Rev. D **72** (2005) 092004.
[4] M. Andreotti *et al.*, Phys. Rev. D **72** (2005) 032001.
[5] See several contributions at this DIS Conference, in particular by K. Seth, V. Poireau, G. Pakhlova and S. Chekanov, `http://www.mppmu.mpg.de/dis2007/`.
[6] J. Vijande, F. Fernandez and A. Valcarce, J. Phys. G **31** (2005) 481.
[7] N. Brambilla *et al.* [QWG Coll.], CERN Yellow Report 2005-005 [arXiv:hep-ph/0412158].
[8] S. Recksiegel and Y. Sumino, Phys. Lett. B **578** (2004) 369.
[9] S. Narison, "QCD as a theory of hadrons", Cambridge Univ. Press, (Cambridge, U.K., 2004).
[10] A. Martin and J. M. Richard, Phys. Lett. B **115** (1982) 323; E. J. Eichten, K. Lane and C. Quigg, Phys. Rev. D **73** (2006) 014014 [Erratum-ibid. D **73** (2006) 079903]; E. Eichten, S. Godfrey, H. Mahlke and J. L. Rosner, arXiv:hep-ph/0701208; M. R. Pennington and D. J. Wilson, arXiv:0704.3384 [hep-ph].
[11] J. Engelfried [SELEX Collaboration], *In the Proceedings of International Conference on Heavy Quarks and Leptons (HQL 06), Munich, Germany, 16-20 Oct 2006, pp 003* [arXiv:hep-ex/0702001].
[12] B. Aubert *et al.* [BABAR Collaboration], Phys. Rev. D **74** (2006) 011103.
[13] B.J. Bjorken, Conf. Hadron Spectroscopy (College Park, 1985) ed. S. Oneda (AlP, New York, 1985).
[14] E. S. Swanson, Phys. Rept. **429** (2006) 243.
[15] F. Froemel, B. Julia-Diaz and D. O. Riska, Nucl. Phys. A **750** (2005) 337.
[16] M. Suzuki, Phys. Rev. D **72** (2005) 114013.
[17] L. Maiani, V. Riquer, F. Piccinini and A. D. Polosa, Phys. Rev. D **72** (2005) 031502, and refs. therein.
[18] H. Hogaasen, J. M. Richard and P. Sorba, Phys. Rev. D **73** (2006) 054013; F. Buccella et al., Eur. Phys. J. C **49** (2007) 743; H. J. Lipkin, arXiv:hep-ph/0703190.
[19] E.A.G. Armour et al., Phys. Rep. **413** (2005) 1.
[20] J. P. Ader, J. M. Richard and P. Taxil, Phys. Rev. D **25** (1982) 2370; D. M. Brink and F. Stancu, Phys. Rev. D **57** (1998) 6778; B. A. Gelman and S. Nussinov, Phys. Lett. B **551** (2003) 296; D. Janc and M. Rosina, Few Body Syst. **35** (2004) 175.

Recent Results on B Spectroscopy at the Tevatron

Martin Heck
for the CDF and D0 Collaborations

KIT - Institut für Experimentelle Kernphysik
Wolfgang-Gaede-Str. 1, 76131 Karlsruhe - Germany

The Tevatron collider at Fermilab provides a rich environment for B spectroscopy. Recently the first direct observation of the B_c meson has reduced its mass uncertainty by two orders of magnitude. A search for η_b mesons provides the best limit on its production in $p\overline{p}$ colliders. In studies on orbitally excited B_d mesons for the first time the narrow states could be separated from each other. The orbitally excited B_s mesons have been observed for the first time. With the charged $\Sigma_b^{(*)}$ a second B baryon could be established beside the Λ_b.

1 Introduction

The Tevatron is a $p\overline{p}$ collider with an energy of $\sqrt{s} = 1.96$ TeV, capable of producing all B hadron species with a cross section for $b\overline{b}$ production of about 50 μb. For each experiment, CDF and D0, an integrated luminosity of more than 2.5 fb^{-1} has been delivered, increasing faster than ever before with most parts of the detector working around 80 % of the time.
Nevertheless studies are complicated due to a 1000 times higher inelastic cross section, a high number of fragmentation tracks and mainly low transversal momentum for the b quark particles.
These disadvantages force the Tevatron experiments to use triggers, saving only events with special structures.
In each experiment a trigger based on two tracks identified as muons and consistent with the J/ψ mass for decays of $B \to J/\psi X$ is used and, specific to CDF, one based on two tracks forming a secondary vertex, using the relative longevity of B hadrons.
The studied particles can probe effective theories in a wide kinematical range, such as HQET, NRQCD, lattice calculations and others.
These proceedings first cover the ground states of B_c and η_b, then the orbitally excited states of B_d and B_s.
As baryons the Σ_b^+ and its isospin partner Σ_b^- are covered as well as their spin excited states.

2 First direct observation of B_c

Some years ago the Tevatron experiments reported the first observation of the B_c in the semileptonic decay to $J/\psi\mu/eX$ [2]. In the semileptonic decay channel it is taken advantage of the low number of leptons in an hadronic environment, but no precise mass measurement can be performed due to at least one missing neutrino.
A recent CDF study [3] in the exclusive decay channel $B_c \to J/\psi\pi^+$ finds a significant signal, shown in Fig. 1. The mass of this B_c signal is measured to be $6276.5 \pm 4.0(\text{stat}) \pm 2.7(\text{syst})\text{MeV/c}^2$. The former measurement in the semileptonic channels an uncertainty of 400MeV/c^2, which means the new measurement is two orders of magnitude better than the old one. With the new measurement, experimental uncertainties are much smaller than theoretical uncertainties.

3 Search for η_b

A CDF study [4] on the last undiscovered SM ground state meson, the η_b, is done in the decay channel $\eta_b \to J/\psi\, J/\psi$. Despite forbidden in leading order NRQCD it can be possible to see a signal in this channel, as the decay $\eta_c \to \Phi\Phi$, which is also forbidden, is seen with a branching ratio of about 1%. Scaling this by $\{\frac{m_c}{m_b}\}^4$ to account for the difference between b and c quark, one gets a prediction for the yield of η_b in a specific kinematical range. With cuts applied to enrich the signal and for a well understanding of the efficiency, 0.2 to 20 events are expected at CDF. The experimental result for the $J/\psi\, J/\psi$ mass spectrum is shown in Fig. 2. From this and the assumption, that the η_b is about 20 MeV/c^2 broad, which is a little less than the η_c, one derives a 95% confidence limit on the expected number of η_b for each η_b mass as shown in Fig. 2, too. The obtained limit is with 7.18 events for an η_b mass of 9.32 GeV/c^2 already inside the predicted range. With other measurements it can be translated to:
$\sigma(p\overline{p} \to \eta_b X;\, |\eta| < 0.6;\, \mathrm{p}_T > 3\,\mathrm{GeV/c}) \times Br(\eta_b \to J/\psi\, J/\psi) \times \{Br(J/\psi \to \mu\mu)\}^2 < 2.6\,\mathrm{pb}$,
where η is $\ln(\tan(\frac{\theta}{2}))$ with θ the angle of the η_b with respect to the beamline and p_T its transverse momentum.

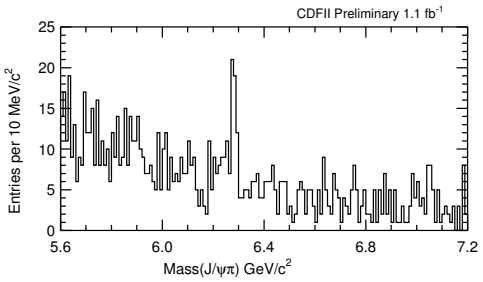

Figure 1: Mass Spectrum of $J/\psi\,\pi$ with B_c signal at about 6.3 GeV/c^2.

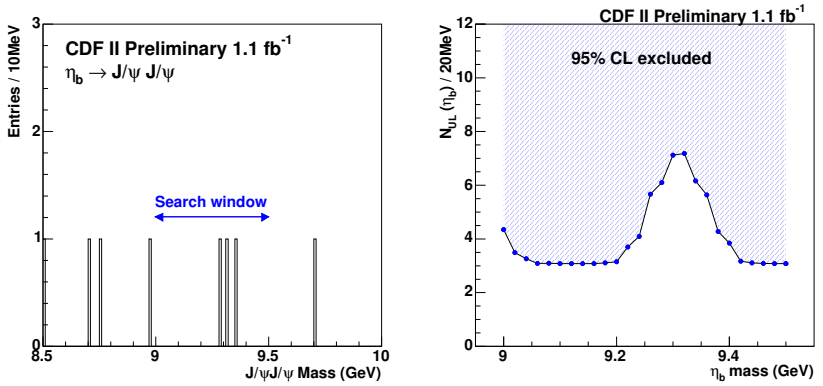

Figure 2: Mass Spectrum of $J/\psi\, J/\psi$ (left). Derived 95% confidence limit on the number of η_b (right).

4 Study of orbitally excited B_s and B_d mesons

Orbitally excited B_s and B_d mesons are studied at both Tevatron experiments [5][6]. There are four states for each meson; $B^*_{s(d)0}$ and $B_{s(d)1}$ with the orbital angular momentum (L=1)

Parameter[MeV/c^2]	D0	CDF
M(B_1)	5720.8 $\pm$ 2.5 $\pm$ 5.3	5734 $\pm$ 3 $\pm$ 2
M(B_2^*)	5746.8 $\pm$ 2.4 $\pm$ 1.7	5738 $\pm$ 5 $\pm$ 1
M(B_{s1})	-	5829.41 $\pm$ 0.21 $\pm$ 0.14 $\pm$ 0.6
M(B_{s2}^*)	5839.1 $\pm$ 1.4 $\pm$ 1.5	5839.64 $\pm$ 0.39 $\pm$ 0.14 $\pm$ 0.5

Table 1: Masses of orbital excited B and B_s mesons. The first given uncertainty is statistic, the second is systematic, and the third one, if given, is the mass uncertainty on the $B^{+(*)}$ mass.

and the spin of the light quark coupled to $\frac{1}{2}$, and $B^*_{s(d)2}$ and $B_{s(d)1}$ with an angular momentum of the light quark of $\frac{3}{2}$. The four states are commonly called $B^{**}_{s(d)}$. In HQET the strong decay $B^{**}_{s(d)} \to B^+K^-(\pi^-)$ (The decay of $B_s^{**} \to B_s\pi$ is forbidden by isospin conservation.) does not change the spin of the b quark. Therefore both states with angular momentum $\frac{3}{2}$ for the light quark are expected to decay via D-wave and to be narrow, while the other two decay via S-wave, which means they are broad. Broad states are very difficult to observe and therefore experimental studies are focused on the narrow states.

Conservation of angular momentum and parity allows for the $B_{s(d)1}$ only the decay to the spin excited B^{+*}, while $B^*_{s(d)2}$ can decay to both the ground state B^+ and B^{+*}. The studies of B_d^{**} mesons are done at D0 (CDF) on 1 fb^{-1} (370 pb^{-1}) of $p\overline{p}$ collision data, while both experiments use 1 fb^{-1} for the B_s^{**} study. In Tab. 1 the results for measured masses in these studies are shown, in Fig. 3 the B_d^{**} spectrum of D0 and in Fig. 4 the B_s^{**} spectrum of CDF are shown. The B_d^{**} masses are not in good agreement, but contain still high uncertainties. Studies with more data are ongoing.
In the B_s^{**} sector both experiments agree on the B^*_{s2}, for which LEP experiments had already evidence. CDF reports for the first time an observation of the B_{s1}, which removes the ambiguity of assigning states to the resonances.

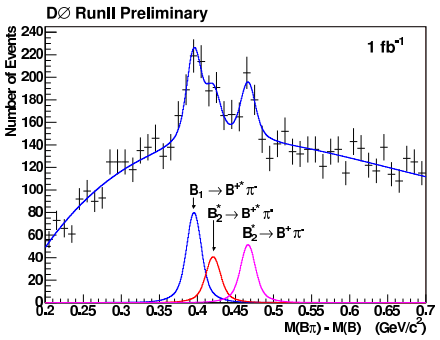

Figure 3: $B^+\pi^-$ spectrum from D0.

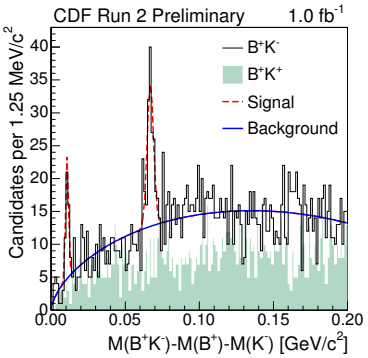

Figure 4: B^+K^- spectrum and B^+K^+ spectrum (filled area) from CDF.

5 First observation of charged $\Sigma_b^{(*)}$

Another study [7] was recently finished at CDF on Σ_b baryons. Up to now the only well established b-baryon was the Λ_b, which is an isospin singlet. The charged Σ_b baryons containing bdd or buu decaying to $\Lambda_b\pi^\pm$ form the corresponding isospin triplet together with the neutral Σ_b,

which is not studied, since neutral pions can't be detected at CDF. Based on a sample of about 3000 Λ_b's in $\Lambda_c^+\pi^-$ decay mode a blind search for charged $\Sigma_b^{(*)}$ is performed. Results for the masses of the Σ_b ground states and of the spin exited states (Σ_b^*) from a fit with widths fixed to predictions are shown in Tab 2. The obtained fit is shown in Fig. 5. The significance for all states together is higher than 5 σ and for each single state more than 3 σ except of the Σ^+, which has 1.6 σ significance.

$M(\Sigma_b^-)$	$5816^{+1.0}_{-1.0}$ MeV/c^2
$M(\Sigma_b^+)$	$5808^{+2.0}_{-2.3}$ MeV/c^2
$M(\Sigma_b^{*+})$	$5837^{+2.1}_{-1.9}$ MeV/c^2
$M(\Sigma_b^{*+})$	$5829^{+1.6}_{-1.8}$ MeV/c^2

Table 2: The masses of the studied Σ_b states with their statistical uncertainties. The systematic uncertainty is 1.7 MeV/c^2 for each state.

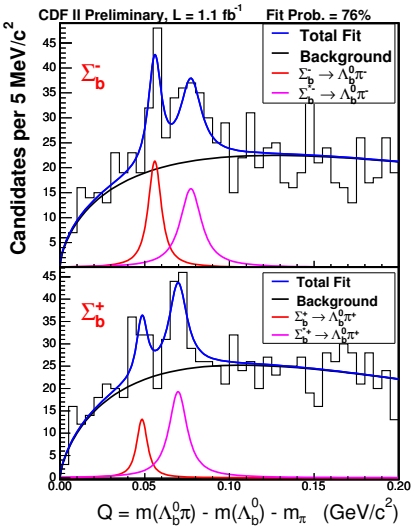

Figure 5: Mass Spectrum of $\Lambda_b\pi^\mp$. The lines show the full fit result, the background component and the signal component.

6 Summary

As seen various B states can be studied at the Tevatron on which other experiments can make only little or no contribution. We have seen the first precision measurement of the B_c mass, which seriously probes the predictions from theory. Despite η_b is not yet observed, studies cut already into its predicted parameter space. With the studies disentangling the narrow states of the B_d^{**} mesons and the first observation of B_s^{**} mesons, precise measurements are done, which can help to understand the QCD of a static color source. A contribution to this understanding is done as well by the new Σ_b baryons, which reveal a bit more of the largely unknown b-baryon sector. Since the Tevatron is running with higher luminosity than in years before, one can expect more contributions to the b-sector to come in the future.

References

[1] Slides:
`http://indico.cern.ch/contributionDisplay.py?contribId=201&sessionId=5&confId=9499`

[2] CDF Collaboration, F. Abe *et al.*, Phys. Rev. Lett. **81** 2432 (1998).

[3] CDF Collaboration, CDF note **8004**.

[4] CDF Collaboration, CDF note **8448**.

[5] DØ Collaboration, V. Abazov *et al*, arXiv:0705.3229v1 [hep-ex]; CDF Collaboration, CDF note **7938**.

[6] CDF collaboration, CDF note **8468**; DØ collaboration, DØ **note 5027**.

[7] CDF Collaboration, CDF note **8523**.

New Resonances and Meson Spectroscopy at BaBar and Belle

Vincent Poireau

Laboratoire de Physique des Particules
F-74941 Annecy-le-Vieux - France

We present a short review on the recent progresses that have been made in meson spectroscopy. We discuss the experimental discoveries made at the BaBar and Belle experiments, as well as the possible interpretations of the new resonances.

1 Introduction

Observation of a long list of new meson resonances has been recently reported by the BaBar and Belle experiments. We present here the new resonances observed in the $c\bar{s}$ and $c\bar{c}$ sectors.

Analyzes presented here were performed using data collected at the $\Upsilon(4S)$ resonance with the BaBar and Belle detectors [2], located at the PEP-II and KEKB asymmetric energy e^+e^- colliders.

2 $c\bar{s}$ mesons

Before 2003, only four $c\bar{s}$ mesons were known: two S-wave mesons, D_s ($J^P = 0^-$) and D_s^* (1^-), and two P-wave mesons, $D_{s1}(2536)$ (1^+) and $D_{s2}(2573)$ (2^+). The masses predicted by the potential model [3] were in good agreement with the measured masses. The potential model predicted also two other broad states (width of a few hundred of MeV) at masses in-between $2.4 - 2.6$ GeV/c^2.

2.1 $D_{s0}^*(2317)$ and $D_{s1}(2460)$ mesons

In 2003, two new resonances were discovered by the BaBar and CLEO experiments: the $D_{s0}^*(2317)$ and $D_{s1}(2460)$ mesons [4]. These two resonances are very narrow, and have masses well below what was predicted by the potential model. These states are very well known experimentally: masses are measured with an error below 2 MeV/c^2, 95% confidence level upper limits on widths are about 4 MeV ; J^P quantum numbers (0^+ and 1^+ for $D_{s0}^*(2317)$ and $D_{s1}(2460)$ respectively), decay modes and branching fractions are also well measured. Despite a good knowledge of these states, their theoretical interpretation is still unclear. One obvious possibility is to identify these two resonances with the 0^+ and 1^+ $c\bar{s}$ states, although it is difficult to fit these resonances within the potential model. Other interpretations have been proposed: four quark states, DK molecules or $D\pi$ atoms [5].

2.2 $D_{sJ}^*(2860)$ meson

The $D_{sJ}^*(2860)$ resonance was discovered by BaBar in 2006 [6], looking in $c\bar{c}$ continuum: $e^+e^- \to D^0K^+X$ and $e^+e^- \to D^+K_s^0X$, where X could be anything. A clear peak is observed in the DK invariant mass, with a mass of $(2856.6 \pm 1.5 \pm 5.0)$ MeV/c^2 and a width of $(47 \pm 7 \pm 10)$ MeV. Given that this resonance decays to two pseudoscalars, the J^P quantum number should be 0^+, 1^-, 2^+, etc. Different interpretations have been proposed, inside the

$c\bar{s}$ scheme: this state could be a radial excitation of the $D^*_{s0}(2317)$, but other possibilities are not ruled out [7].

2.3 $D_{sJ}(2700)$ meson

In the same analysis, BaBar reported a broad enhancement, named $X(2690)$, at a mass of $(2688 \pm 4 \pm 3)$ MeV/c^2 and a width of $(112 \pm 7 \pm 36)$ MeV. A new state, the $D_{sJ}(2700)$, was reported independently by Belle at a similar mass, looking at $B^+ \to \bar{D}^0 D^0 K^+$ events [8]. The study of the $D^0 K^+$ invariant mass reveals a clear resonance at a mass of $(2715 \pm 11^{+11}_{-14})$ MeV/c^2 with an internal width of $(115 \pm 20^{+36}_{-32})$ MeV. An helicity analysis shows that the favored J^P quantum number is 1^-. Since the $X(2690)$ and $D_{sJ}(2700)$ mesons have the same decay modes and that the mass and width are consistent with each other, it is reasonable to think that they are indeed the same state.

BaBar did a similar analysis [8], looking at events where B decays to $\bar{D}^{(*)} D^{(*)} K$. Thanks to the many final states studied, this analysis has the advantage to be able to look at four $D^0 K^+$ invariant mass distributions as well as four $D^+ K^0_s$ invariant mass distributions. Adding these final states together, a clear resonant enhancement is seen around a mass of 2700 MeV/c^2. Also, adding the four $D^{*0} K^+$ and four $D^{*+} K^0_s$ invariant mass distributions together, a similar enhancement is observed around a mass of 2700 MeV/c^2. No precise measurement was given by this preliminary analysis yet.

The potential model predicts the 2^3S_1 $c\bar{s}$ state at a mass of 2720 MeV/c^2. Also, from chiral symmetry considerations, a $1^+ - 1^-$ doublet of states has been predicted. If the 1^+ state is identified as the $D_{s1}(2536)$, the mass predicted for the 1^- state is 2721 ± 10 MeV/c^2 [9].

3 $c\bar{c}$ mesons

3.1 $X(3940)$, $Y(3940)$ and $Z(3930)$ mesons

Three new states were discovered by Belle at masses around 3940 MeV/c^2 [10]. Although their mass are very close to each other, these new states are thought to be different resonances. The $X(3940)$ state was discovered in $e^+e^- \to J/\Psi X(3940)$, looking at the recoiling mass to the J/Ψ. The parameters of this resonance are $M = (3943 \pm 6 \pm 6)$ MeV/c^2 and $\Gamma = (15.4 \pm 10.1)$ MeV. This new state was also seen decaying to DD^*, but not DD. One possible interpretation is to identify this resonance with the unobserved $c\bar{c}$ charmonium state $\eta_c(3S)[3^1S_0]$, although other interpretations have also been proposed.

A near threshold enhancement was observed by Belle in $B \to J/\Psi\omega K$, looking at the $J/\Psi\omega$ invariant mass. This resonance, called $Y(3940)$, has a mass of $(3943 \pm 11 \pm 13)$ MeV/c^2 and a width of $(87 \pm 22 \pm 26)$ MeV. This state could be interpreted as the $c\bar{c}$ state $\chi'_{c1}[2^3P_1]$.

Finally, a new resonance, the $Z(3930)$, was discovered in $\gamma\gamma \to D\bar{D}$ with a mass of $(3929 \pm 5 \pm 2)$ MeV/c^2 and a width of $(29 \pm 10 \pm 2)$ MeV. One possibility is to identify this resonance with the $c\bar{c}$ state $\chi'_{c2}[2^3P_2]$.

3.2 $X(3872)$ meson

The $X(3872)$ meson was discovered by Belle [11] in $B^\pm \to X(3872)K^\pm$ with $X(3872) \to J/\psi\pi^+\pi^-$ in 2003, and quickly confirmed by the BaBar [11], CDF and D0 experiments. Its mass is known very precisely, 3871.81 ± 0.36 MeV/c^2, and its width is less than 2.3 MeV

at 90% confidence level. This state was also observed in the final state $J/\psi\gamma$ [12], which implies that its C quantum number is equal to +1. The study of the $\pi^+\pi^-$ invariant mass distribution by Belle and an angular analysis by CDF shows that $J^{PC} = 1^{++}$ is favored (although 2^{++} is still possible). It has also to be noted that a search for a charged partner was performed by BaBar, but no signal was found [12].

The Belle experiment did a study of the channel $B \to \bar{D}^0 D^0 \pi^0 K$ and observed a clear excess in the $\bar{D}^0 D^0 \pi^0$ invariant mass [13]. The surprise came from the measure of the mass: $3875.4 \pm 0.7^{+1.2}_{-2.0}$ MeV/c^2, which is in disagreement with the mass measured in the $X(3872) \to J/\psi\pi^+\pi^-$ channel. This discrepancy was confirmed by the BaBar experiment [13], looking at the $B \to \bar{D}^0 D^{*0} K$ channel (where both decays of D^{*0}, $D^0\pi^0$ and $D^0\gamma$, are taken into account). An excess is observed in the $\bar{D}^0 D^{*0}$ invariant mass, with a mass of $3875.6 \pm 0.7^{+1.4}_{-1.5}$ MeV/c^2. The masses between Belle and BaBar are in good agreement and are 2.2σ away from the $X(3872)$ mass in the $J/\psi\pi^+\pi^-$ channel. If this excess is due to the $X(3872)$ resonance, then the quantum number $J^P = 2^+$ is disfavored.

The interpretation of the $X(3872)$ state is rather difficult [14] since there is no satisfactory $c\bar{c}$ assignment for this resonance. The coincidence between this resonance mass and the $\bar{D}^0 D^{*0}$ mass led some authors to propose that the $X(3872)$ is a bound state of the $\bar{D}^0$ and D^{*0} mesons with small binding energy. One of the prediction of this model is that $B^0 \to X(3872)K^0$ is suppressed by approximately a factor 10 compared to $B^+ \to X(3872)K^+$. Experimentally, this ratio is measured to $0.50 \pm 0.30 \pm 0.05$ in the $X(3872) \to J/\psi\pi^+\pi^-$ channel and to $2.23 \pm 0.93 \pm 0.55$ in the $B \to \bar{D}^0 D^{*0} K$ channel. It has also been proposed that the X(3872) resonance is a four quark state. In this case, the model predicts two neutral states and two charged states, with a difference of mass between the two neutral states (produced respectively in B^0 and B^+ decays) of (7 ± 2) MeV/c^2. The experimental results show a mass difference of $(2.7 \pm 1.3 \pm 0.2)$ MeV/c^2 in the $X(3872) \to J/\psi\pi^+\pi^-$ channel and (0.2 ± 1.6) MeV/c^2 in the $B \to \bar{D}^0 D^{*0} K$ channel. Other possibilities have been mentioned like glueball or hybrid state.

3.3 $Y(4260)$ meson

The $Y(4260)$ state constitutes also quite a mystery. This new state, with $J^{PC} = 1^{--}$, was discovered by BaBar in $e^+e^- \to \gamma_{ISR}(J/\psi\pi^+\pi^-)$, with a photon radiated in the initial state [15]. This resonance was confirmed by Belle [15] and CLEO, although masses disagree between experiments. BaBar measures $M = (4259 \pm 8)$ MeV/c^2 and $\Gamma = (88 \pm 23)$ MeV, Belle measures $M = (4295 \pm 10^{+10}_{-3})$ MeV/c^2 and $\Gamma = (133^{+26+13}_{-22-6})$ MeV while CLEO measures $M = (4283^{+17}_{-16} \pm 4)$ MeV/c^2. A 3σ enhancement was also reported by BaBar in $B \to Y(4260)K^-$, followed by $Y(4260) \to J/\psi\pi^+\pi^-$ [15], although this result needs confirmation by other experiments. Searches for this resonance were performed in other channels ($e^+e^- \to \gamma_{ISR}(D\bar{D})$, $e^+e^- \to \gamma_{ISR}(\Phi\pi^+\pi^-)$, $e^+e^- \to \gamma_{ISR}(p\bar{p})$, $e^+e^- \to \gamma_{ISR}(J/\psi\gamma\gamma)$), but no positive results were reported [15].

One of the surprise concerning this resonance came from the search of the $Y(4260)$ going to the decay mode $\psi(2S)\pi^+\pi^-$ in ISR production [16]. A clear signal is observed in this channel, however with a mass measurement incompatible with the previous BaBar result. The mass found in this channel is (4234 ± 24) MeV/c^2 with a width of (172 ± 33) MeV. This measurement, although incompatible with the BaBar measurement in the $J/\psi\pi^+\pi^-$ channel, is compatible with the Belle measurement. More data and experiments looking at this channel are needed to be able to conclude if this excess is due to the $Y(4260)$.

The interpretation of this state is far from obvious [17]. There is no $c\bar{c}$ assignment for a 1^{--} state of this mass. This is also probably not a glueball, since in this case we would have expected a decay to $\Phi\pi^+\pi^-$, which was not observed. Other possibilities are four quark state $[cs][\bar{c}\bar{s}]$, hybrid meson or $\omega\chi_{c1}$ molecule.

4 Conclusion

Although no new resonances were discovered in many years, BaBar and Belle gave an impressive list of new results since 1999. In the $c\bar{s}$ sector, the $D^*_{s0}(2317)$ and $D_{s1}(2460)$ mesons are now very well known experimentally, but no definite interpretation was given theoretically. The $D^*_{sJ}(2860)$ and $D_{sJ}(2700)$ mesons were discovered recently and need more experimental inputs. In the $c\bar{c}$ sector, it seems plausible to identify the $X(3940)$, $Y(3940)$ and $Z(3930)$ mesons to charmonium states, although other explanations have been proposed. The $X(3872)$ and $Y(4260)$ resonances are not charmonium states, and thus are probably the first occurrences of non standard quark content.

A lot of analyzes are still in progress with the current data set in BaBar and Belle: more decay modes for the resonances presented here are being investigated. These two experiments are taking data until the end of 2008, which is the promise of more surprises to arise.

The author is very grateful to the organizers of the DIS 2007 conference for their support and all efforts in making this venue successful.

References

[1] Slides:
`http://indico.cern.ch/contributionDisplay.py?contribId=202&sessionId=5&confId=9499`

[2] BaBar Coll., Nucl. Instrum. Meth. **A 479** 1 (2002) ; Belle Coll., Nucl. Instrum. Meth. **A 479** 117 (2002).

[3] S. Godfrey and N. Isgur, Phys. Rev. **D 32** 189 (1985).

[4] Belle Coll., Phys. Rev. Lett. **91** 262001(2003) ; BaBar Coll., Phys. Rev. **D74** 032007 (2006).

[5] H-Y Cheng and W-S Hou, Phys. Lett. **B566** 193 (2003) ; T. Barnes, F. E. Close and H. J. Lipkin, Phys. Rev. **D68** 054006 (2003) ; A. Szczepaniak, Phys. Lett. **B567** 23 (2003).

[6] BaBar Coll., Phys. Rev. Lett. **97** 222001 (2006).

[7] E. van Beveren and G. Rupp, Phys. Rev. Lett. **97** 202001 (2006) ; P. Colangelo, F. De Fazio and S. Nicotri, Phys. Lett. **B642** 48 (2006).

[8] Belle Coll., arXiv:hep-ex/0608031 (2006) ; BaBar Coll., preliminary.

[9] M. A. Nowak, M. Rho and I. Zahed, Phys.Polon. **B 35**, 2377 (2004).

[10] Belle Coll., arXiv:hep-ex/0507019 (2005) ; Belle Coll., Phys. Rev. Lett. **94** 182002 (2005) ; Belle Coll., Phys. Rev. Lett. **96** 082003 (2006).

[11] Belle Coll., Phys. Rev. Lett. **91** 262001 (2003) ; BaBar Coll., Phys. Rev. **D73** 011101 (2006).

[12] Belle Coll., arXiv:hep-ex/0505037 (2005) ; Belle Coll., arXiv:hep-ex/0505038 (2005) ; BaBar Coll., Phys. Rev. **D74** 071101 (2006).

[13] Belle Coll., Phys. Rev. Lett. **97** 162002 (2006) ; BaBar Coll., preliminary.

[14] E. Braaten and M. Kusunoki, Phys. Rev. **D71** 074005 (2005) ; L. Maiani *et al*, Phys. Rev. **D71** 014028(2005).

[15] BaBar Coll., Phys. Rev. Lett. **95** 142001(2005) ; Belle Coll., arXiv:hep-ex/0612006 (2006) ; BaBar Coll., arXiv:hep-ex/0607083 (2006) ; BaBar Coll., Phys. Rev. Letter **D73**, 011101 (2006).

[16] BaBar Coll., arXiv:hep-ex/0610057 (2006).

[17] S-L Zhu, Phys. Lett. **B625** 212 (2005) ; Phys. Rev. **D72** 031502 (2005) ; L. Maiani *et al*, Phys. Lett. **B634** 399 (2006).

B_s Mixing and Lifetime Difference Measurements

R. Kehoe (for the D0 and CDF Collaborations)

Southern Methodist University - Dept. of Physics
Dallas, TX 75275 - USA

Recent results from the Tevatron have placed important constraints on the B_s mixing and CP violation parameters. CDF has extracted a precise measure of $\Delta M_s = 17.77 \pm 0.10(\text{stat}) \pm 0.07(\text{sys})\text{ps}^{-1}$ from fully and partially reconstructed B_s decays. D0 has measured the lifetime difference in $B_s \to D_s^{(*)} D_s^{(*)}$ events to be $\Delta\Gamma_{CP} = 0.079^{+0.038}_{-0.035}(\text{stat})^{+0.031}_{-0.030}(\text{sys})$. D0 also performed a time-dependent fit to $B_s \to J/\psi\phi$ events and extracted constraints on ϕ_s and $\Delta\Gamma_s$. A four-fold ambiguity exists such that the solution $\phi_s = 0.70^{+0.47}_{-0.39}(\text{stat} + \text{sys})$ for $\Delta\Gamma_s = +0.13 \pm 0.09(\text{stat} + \text{sys})\text{ps}^{-1}$ is the closest to the standard model expectation. This paper summarizes these analyses.

1 Introduction

In the standard model, mass and weak eigenstates of fundamental fermions are related by a matrix of probabilities. For three quark generations, the corresponding CKM matrix encompasses one complex phase which provides for CP violation. One parametrization proposed by Wolfenstein organizes this matrix so that mixing and CP violation are described by two parameters, ρ and η. Neutral mesons provide an ideal laboratory in which to study CP violation because they oscillate continuously between matter and antimatter states. For the B_s system, the specific unitarity triangle constructed in the plane of the Wolfenstein parameters defines a CP phase, ϕ_s. In the absence of new effects, $\phi_s = 4.1 \pm 1.4 \times 10^{-5}$[2].

There are three primary measurements which nail down CP violation in the B_s system. The mass difference between light and heavy states is sensitive to non-standard physics from the presence of additional massive particles in loops. D0 has produced an initial constraint of $17\text{ps}^{-1} < \Delta\text{M}_\text{s} < 21\text{ps}^{-1}$ [3] in $B_s \to D_s l\nu$ decays. The lifetime difference, $\Delta\Gamma_s$, provides another important constraint on the CP violation system. Lastly, ϕ_s is an important additional test of new physics. Fourth generation models can produce a significant enhancement of $\phi_s \sim 0.5 - 0.8$[3].

This paper describes a new precision measurement of ΔM_s, as well as the first constraints on $\Delta\Gamma_s$ and ϕ_s. The measurements are performed by the CDF and D0 experiments at the Fermilab Tevatron. The accelerator has so far delivered about 2.7fb^{-1} of $p\bar{p}$ collisions, of which up to 1.2fb^{-1} are utilized in the analyses described here. The tracking and muon subsystems, and their triggers, are the primary tools used, and are described in detail elsewhere [5]. Data is taken with 2 track or single lepton plus track triggers (CDF), single muon triggers (D0) or dimuon triggers (D0 and CDF). CDF specifically exploits an impact parameter cut on tracks, D0 on the wide acceptance of its muon system.

2 Measuring the Mass Difference, ΔM_s

CDF has performed a measurement of ΔM_s in B_s semileptonic ($D_s l\nu(l \to e, \mu)$) and hadronic ($D_s\pi, D_s\pi\pi\pi, D_s\rho$) decays. Flavor is tagged with same-side and opposite-side techniques. The former involves use of a K identification likelihood and particle kinematics via an artificial neural network (ANN). The latter uses lepton, jet and K charge tagging.

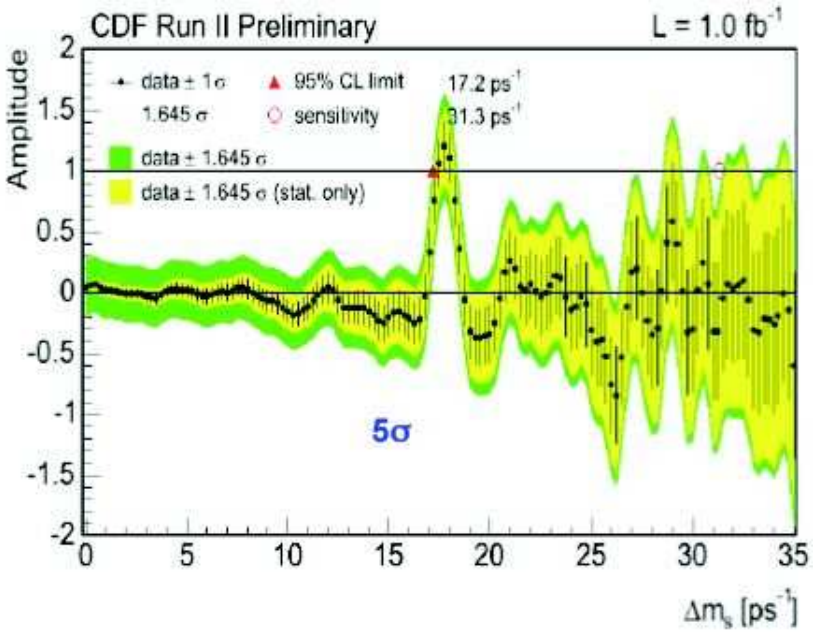

Figure 1: CDF measurement of the probability of B_s oscillations as a function of ΔM_sin ps^{-1}.

Events are selected in fully and partially reconstructed hadronic channels, and the more copious partially reconstructed semileptonic events.

The partially reconstructed events give a proper time resolution of 44.6μm. The fully reconstructed sample gives a 25.9μm resolution, which provides excellent ΔM_s sensitivity for values around $20\mathrm{ps}^{-1}$. The sensitivities are obtained channel by channel and combined in Figure 1. This illustrates essentially the Fourier transform of the proper time distribution. The resultant mass difference is $17.77 \pm 0.1(\mathrm{stat}) \pm 0.07(\mathrm{sys})\mathrm{ps}^{-1}$[6]. This can be related to the ratio of CKM elements by $\frac{\Delta M_s}{\Delta M_d} = \frac{m_{B_s}}{m_{B_d}} \left|\frac{V_{ts}}{V_{td}}\right|^2$ which gives a value of $|V_{td}/V_{ts}| = 0.2006 \pm 0.0070(\mathrm{exp})^{+0.0081}_{-0.0060}(\mathrm{theo})$.

3 Measurement of the Lifetime Difference, $\Delta\Gamma_s$

The value of $\Delta\Gamma_s$ has been extracted by D0 in $B_s \to D_s^{(*)} D_s^{(*)}$ decays. This decay is expected to be 95% CP even[7] although other estimates range as high as 30% for CP odd. The branching ratio for $D_s^{(*)} D_s^{(*)}$ can be related to the lifetime difference by the relation $2BR(B_s \to D_s^{(*)} D_s^{(*)} = \frac{\Delta\Gamma_s}{\Gamma_s}(1 + O(\frac{\Delta\Gamma_s}{\Gamma_s}))$. Signal is identified by correlated production of $D_s \to \phi\mu\nu$ and $D_s \to \phi\pi$. The decay sequence was reconstructed when $\phi \to K^+K^-$. Extra photons from D_s^* decay were ignored. A total of 13.4 events were found in the signal sample. Approximately 2 background events were estimated from data, the primary contribution coming from $B_s \to D_s\phi\mu\nu$.

In order to reduce systematics, the measurement of the branching ratio is extracted by normalizing the signal sample to a $B_s \to D_s^{(*)}\mu\nu$ sample. This sample was selected in the same way as the $B_s \to D_s^{(*)}\phi\mu\nu$ sample. The ratio of branching ratios $R = \frac{BR(B_s \to D_s D_s) BR(D_s \to \phi\mu\nu)}{BR(B_s \to \mu\nu D_s)}$ is calculable if one knows the number of μD_s events, fit from data, and the ratio of efficiencies for $B_s \to D_s^{(*)}\mu\nu$ and $B_s \to D_s^{(*)}D_s^{(*)}$, obtained from a full simulation incorporating EVTGEN[8]. The experimental value of $R = 0.015 \pm 0.007$ gives $BR(B_s \to D_s^{(*)}D_s^{(*)}) = 0.039^{+0.019}_{-0.017}(\text{stat})^{+0.015}_{-0.015}(\text{sys})$, resulting in a measurement of $\Delta\Gamma_s = 0.079^{+0.038}_{-0.035}(\text{stat})^{+0.030}_{-0.031}(\text{sys})$[9]. The constraint is reflected in Figure 2 along with other constraints including $1/\Gamma_s$ from flavor specific channels.

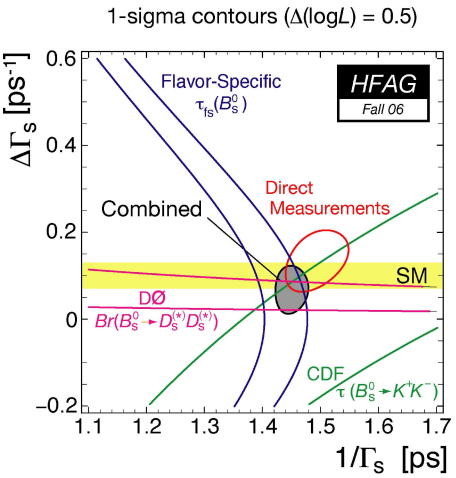

Figure 2: Constraints on $\Delta\Gamma_s$ and $1/\Gamma_s$ from several sources. The D0 measurement of $\Delta\Gamma_s$ from $B_s \to D_s^{(*)}D_s^{(*)}$ decays is shown.

4 Measurement of the CP Violating Phase, ϕ_s

D0 has pursued the extraction of ϕ_s using $B_s \to J/\psi\phi$ decays. The decay mode includes CP even and CP odd states. These states can be separated because of their different time dependent angular distributions. A large lifetime difference can allow a measurement of ϕ_s. The sample is reconstructed when $J/\psi \to \mu^+\mu^-$ and $\phi \to K^+K^-$. The reconstructed mass distribution yields an estimate of 1039 ± 45 signal events.

The time dependent fit is carried out using three angles and the proper decay time. The polar and azimuthal angles, θ and φ respectively, refer to the direction of the μ^+ in the J/ψ rest frame. In the ϕ rest frame, the K^+ has angle Ψ relative to the axis defined to point away from the J/ψ direction. Without constraining $\Delta\Gamma_s$, the fit yields solutions with a four-fold ambiguity. These are given with statistical uncertainties by $\Delta\Gamma_s = 0.17 \pm 0.09(\text{stat})$ ps and $\phi_s = \pm 0.79 \pm 0.56(\text{stat})$, or $\Delta\Gamma_s = -0.17 \pm 0.09(\text{stat})$ ps and $\phi_s = \pm 2.35 \pm 0.56(\text{stat})$ [10]. Additionally, systematic uncertainties of 0.02 ps for $\Delta\Gamma_s$ and $^{+0.14}_{-0.01}$ for ϕ_s were estimated, the latter dominated by background modeling.

These measurements were further constrained using several additional measurements. The world average of the flavor-specific lifetime of B_s mesons, $\tau_{fs} = 1.440 \pm 0.036$ ps[11], constrains the $\Delta\Gamma_s$. The semileptonic charge asymmetry induced by B_s mixing is related to the CP parameters by $A^q_{SL} = \frac{\Delta\Gamma_q}{\Delta M_q}\tan\phi_q$. By combining a previous D0 measurement of this asymmetry in $B_s \to \mu\nu D_s(D_s \to \phi\pi)$ decays [13] with a value extracted from the D0 same sign dimuon charge asymmetry[12] and the B-factory value of A^d_{sl}[11], a value of $A^s_{SL} = 0.0001 \pm 0.0090$ was obtained. The CDF ΔM_s measurement gives $\Delta\Gamma_s \tan(\phi_s) = A^s_{SL}\Delta M_s = 0.02 \pm 0.16\text{ps}^{-1}$. D0 refit the $J/\psi\phi$ data using these constraints with the result shown in Figure 3. The fourfold ambiguity remains, and the value closest to SM expectation is $\Delta\Gamma_s = 0.13 \pm 0.09(\text{stat} + \text{sys})$ ps and $\phi_s = 0.70^{+0.47}_{-0.39}(\text{stat} + \text{sys})$[14].

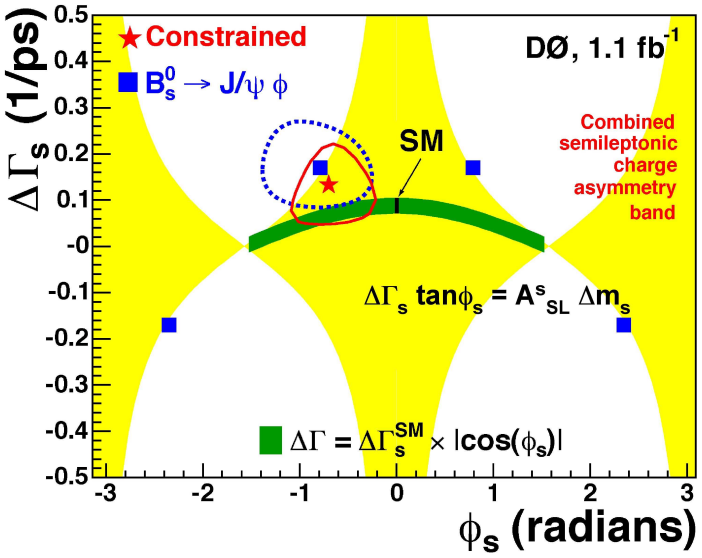

Figure 3: Projected contour limits in $\Delta\Gamma_s$ vs. ϕ_s plane from D0 final analysis of $B_s \to J/\psi\phi$ events. Other measurements of the B_s system were used to further constrain the fit.

References

[1] Slides:
`http://indico.cern.ch/contributionDisplay.py?contribId=196&sessionId=5&confId=9499`

[2] A. Lenz, U. Nierste, arXiv:hep-ph/0612167 (2006)

[3] V. Abazov et al., (D0 Collab.) Phys. Rev. Lett. **97** 021802 (2006)

[4] Hou, Nagashima and Soddu, arXiv:hep-ph/0610385 (2006)

[5] C. Hill et al., (CDF Collab.) Nucl. Instrum. Meth. Phys. Res., Sect. A **530**, 1 (2004); S. Cabrera et al., (CDF Collab.) Nucl. Instrum. Meth. Phys. Res., Sect. A **494**, 416 (2002); W. Ashmanskas et al., Nucl. Instrum. Meth. Phys. Res., Sect A **518**, 532 (2004); V. Abazov et al., (D0 Collab.) Nucl. Instrum. Meth. A **565**, 463 (2006)

[6] A. Abulencia et al., (CDF Collab.) Phys. Rev. Lett. 97 062003 (2006)

[7] R. Alexan et al., Phys. Lett. B **316**, 567 (1993)

[8] D. Lange, Nucl. Instrum. Meth. A **462**, 152 (2001)

[9] V. Abazov et al., (D0 Collab.) subm. to Phys. Rev. Lett., FERMILAB-PUB-07/047-E, hep-ex/0702049 (2007)

[10] V. Abazov et al., (D0 Collab.) subm. to Phys. Rev. Lett., FERMILAB-PUB-07/007-E, hep-ex/0701012 (2007)

[11] E. Barberio et al., (Heavy Flavor Averaging Group), in preparation

[12] V. Abazov et al., (D0 Collab.) Phys. Rev. D **94**, 092001 (2006)

[13] V. Abazov et al., (D0 Collab.), subm. to Phys. Rev. Lett., hep-ex/0701007 (2007)

[14] V. Abazov et al., (D0 Collab.), subm. to Phys. Rev. D Rapid Comm., FERMILAB-PUB-07/044-E (2007)

Review on Charmonium Production

Katja Krüger

Ruprecht-Karls-Universität Heidelberg - Kirchhoff-Institut für Physik
Im Neuenheimer Feld 227, 69120 Heidelberg - Germany

A brief overview on recent results of charmonium production in high-energy proton-proton, electron-proton and electron-positron collisions is presented. Emphasis is given to QCD dominated production mechanisms that allow a study of the interplay between perturbative and non-perturbative effects.

1 Introduction

Charmonium production in high-energy collisions [1] can be described by the perturbative production of a $c\bar{c}$ pair followed by the non-perturbative transition to the charmonium state. This transition can be modelled in different ways. An attractive approach is Non-Relativistic QCD (NRQCD) [2] which uses a factorization ansatz and takes into account all possible colour and angular momentum states for the $c\bar{c}$ pair. The transition to the charmonium state proceeds via soft gluon emission and is described by long-distance matrix elements which are universal but have to be determined from data. In the older Colour Singlet Model (CSM) [3] the $c\bar{c}$ pair has to be produced perturbatively in the same quantum state as the charmonium. For the ψ states the transition rate is determined from the leptonic decay widths. The production of P wave states cannot be predicted since it leads to divergences in the calculation [4].

Experimental results on charmonium production are dominated by J/ψ mesons due to the large cross section and the large branching fraction to leptons. The main disadvantage is the feeddown from B mesons and higher charmonium states. The feeddown is reduced for the $\psi(2s)$ meson, which is otherwise very similar. The P wave states χ_{c0}, χ_{c1} and χ_{c2} offer the possibility to study a different angular momentum state.

2 Charmonium production at the Tevatron

The prompt J/ψ and $\psi(2s)$ production cross section at the Tevatron is more than an order of magnitude larger than expected by the CSM in leading order (LO). Only recently calculations [5] in next-to-leading order (NLO) have been performed which improve the data description showing a larger cross section and a milder drop with the transverse momentum. The difference between the data and the CSM can be explained by additional colour-octet contributions in the context of NRQCD. In this approach the non-perturbative parameters can be extracted from the transverse momentum spectrum. A very decisive test of NRQCD is the measurement of the polarization of the J/ψ and $\psi(2s)$ mesons. Polarization studies have the advantage of not being sensitive to the absolute rates, but need a huge amount of statistics to provide significant results. CDF Results [6] from Tevatron Run I indicated a transverse polarization (positive α) at large transverse momenta as expected from the gluon fragmentation contribution in NRQCD calculations, while the new measurement [7] with higher statistics from Run II shows a small longitudinal polarization in this region (Fig. 1 left). Similar, but statistically less significant results are obtained for prompt $\psi(2s)$ production.

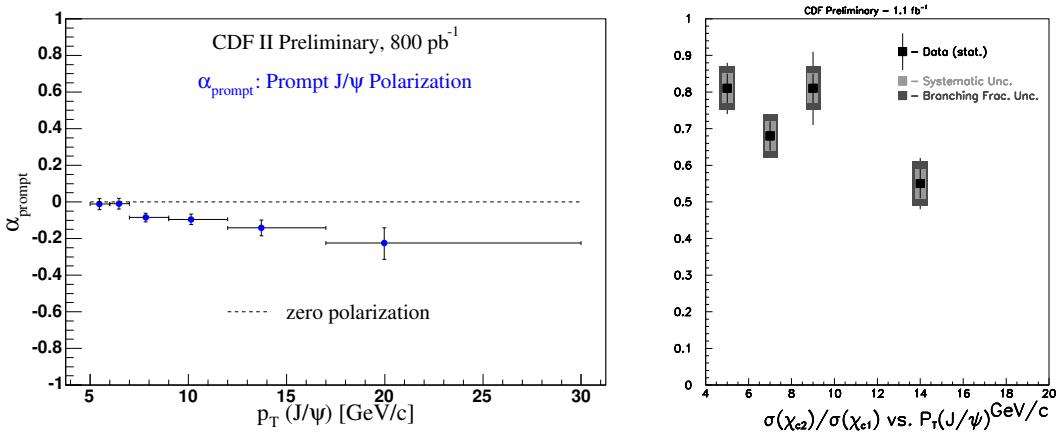

Figure 1: Charmonium production at the Tevatron: J/ψ polarization (left) and ratio of prompt production of χ_{c2} to χ_{c1} (right).

The CDF collaboration presented a measurement [8] of prompt χ_c production via their decays into $J/\psi\gamma$. The photon is reconstructed through conversion, which gives a mass resolution sufficient for resolving the different χ_c states. The result is a ratio of $\chi_{c2}/\chi_{c1} = 0.70 \pm 0.04(stat.) \pm 0.04(sys.) \pm 0.06(branching\ fraction)$ with no significant dependence on the transverse momentum (Fig. 1 right) and no signal for the χ_{c0}. This is in contradiction to the expectation from NRQCD, where the ratios should be $\chi_{c2} : \chi_{c1} : \chi_{c0} = 5 : 3 : 1$ according to simple spin counting rules.

3 Charmonium production at HERA

In electron-proton collisions two kinematic regimes are distinguished according to the virtuality Q^2 of the exchanged photon. In the photoproduction region, where $Q^2 \approx 0$, predictions for the CSM are available at next-to-leading order, while in electroproduction at larger Q^2 only leading order calculations exist. Recently new experimental results from the HERA II phase with improved statistics allow more detailed comparisons to the predictions.

3.1 Photoproduction

In general the photoproduction of J/ψ mesons at HERA [9, 10] is well described by the NLO predictions [13] in the CSM, while LO NRQCD predictions have difficulties to describe the distribution of z, the relative energy transfer from the photon to the J/ψ meson. For the J/ψ polarization [11], where only LO calculations exist, but NLO is expected to be very

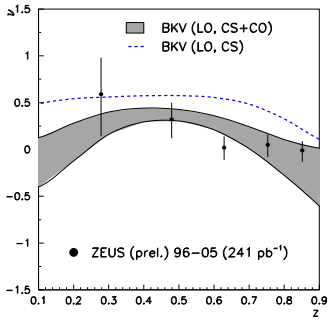

Figure 2: J/ψ polarization in photoproduction at HERA in comparison with LO CSM (dashed line) and NRQCD (grey band) calculations.

similar, some deviations of the CSM are seen at large
z, while the NRQCD calculation agrees better with the data (Fig. 2).

3.2 Electroproduction

In J/ψ electroproduction Q^2 provides an additional hard scale which should lead to a better control of the theoretical predictions. In general the LO predictions in the CSM underestimate the data by a factor $\sim 2-3$ and the transverse momentum distribution falls too steeply, while NRQCD can describe the normalization, but fails for the z distribution. For a new double differential measurement [12] in z and the transverse momentum in the photon-proton centre-of-mass frame (Fig. 3) LO CSM Monte Carlo models agree well with data in shape and show, that additional colour octet contributions must be small or very similar in shape to the colour singlet terms.

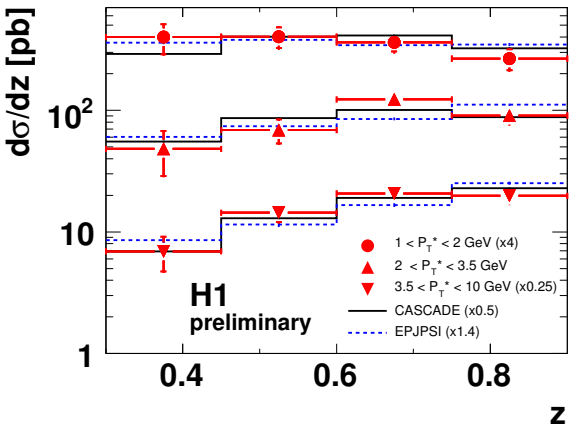

Figure 3: J/ψ electroproduction at HERA: double differential cross section compared to two LO CSM Monte Carlo predictions.

4 Charmonium production in electron-positron-annihilations

For the J/ψ production at the $\Upsilon(4S)$ resonance in electron-positron collisions the momentum spectrum in the centre-of-mass frame (Fig. 4) as measured by the BaBar [14] and Belle [15] collaborations provides a test of the production mechanism. LO NRQCD calculations predict an enhancement of the cross section at large momentum which is not observed in the data, while the CSM underestimates the cross section. Including perturbative and non-perturbative resummations in the NRQCD calculation, the data can be described in shape and normalization [16].

5 Conclusions

Charmonium production in high-energy collisions is a very active field of research. A wealth of experimental results is available and more data from the full statistics of the second running phase of the Tevatron and the HERA colliders are expected soon. All theoretical calculations fail to describe some of the measurements, so a coherent picture is still lacking.

References

[1] Slides:
http://indico.cern.ch/contributionDisplay.py?contribId=206&sessionId=5&confId=9499

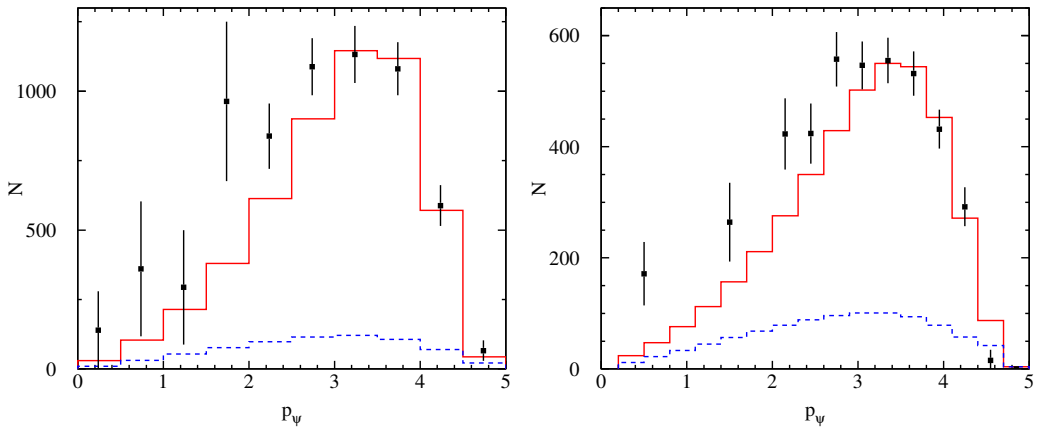

Figure 4: Momentum spectrum of J/ψ mesons produced in e^+e^--annihilations at the $\Upsilon(4S)$ measured by BaBar (left) and Belle (right) compared to predictions in the CSM (dashed line) and in NRQCD including perturbative and non-perturbative resummations (solid line).

[2] G. T. Bodwin, E. Braaten and G. P. Lepage, Phys. Rev. D **51** (1995) 1125, Erratum ibid. D **55** (1997) 5853 [arXiv:hep-ph/9407339]

[3] E. L. Berger and D. L. Jones, Phys. Rev. D **23** (1981) 1521;
R. Baier and R. Rückl, Phys. Lett. B **102** (1981) 364

[4] M. Krämer, Prog. Part. Nucl. Phys. **47**, 141 (2001) [arXiv:hep-ph/0106120]

[5] J. Campbell, F. Maltoni and F. Tramontano, arXiv:hep-ph/0703113

[6] A. A. Affolder *et al.* [CDF Collaboration], Phys. Rev. Lett. **85** (2000) 2886 [arXiv:hep-ex/0004027]

[7] CDF Collaboration, "Measurement of the J/ψ Spin Alignment in $\bar{p}p$ Collisions at $\sqrt{s} = 1.96\,\mathrm{TeV}$", CDF note 8212 (2006)

[8] A. Abulencia *et al.*, arXiv:hep-ex/0703028

[9] C. Adloff *et al.* [H1 Collaboration], Eur. Phys. J. C **25** (2002) 25 [arXiv:hep-ex/0205064]

[10] S. Chekanov *et al.* [ZEUS Collaboration], Eur. Phys. J. C **27** (2003) 173 [arXiv:hep-ex/0211011]

[11] ZEUS Collaboration, "Measurement of J/ψ helicity distributions in inelastic photoproduction at HERA", ZEUS-prel-06-015 (2006), Contributed Paper to ICHEP06

[12] H1 Collaboration, Slides:
`http://indico.cern.ch/contributionDisplay.py?contribId=78&sessionId=13&confId=9499`

[13] M. Krämer, J. Zunft, J. Steegborn and P. M. Zerwas, Phys. Lett. B **348** (1995) 657 [arXiv:hep-ph/9411372]

[14] B. Aubert *et al.* [BABAR Collaboration], Phys. Rev. Lett. **87** (2001) 162002 [arXiv:hep-ex/0106044]

[15] K. Abe *et al.* [BELLE Collaboration], Phys. Rev. Lett. **88** (2002) 052001 [arXiv:hep-ex/0110012]

[16] S. Fleming, A. K. Leibovich and T. Mehen, Phys. Rev. D **68** (2003) 094011 [arXiv:hep-ph/0306139]

B and Upsilon Cross Sections at HERA-B

Antonio Sbrizzi *

University of Bologna - Physics Department
via Irnerio 46, I-40126 Bologna - Italy

A new measurement of the $b\bar{b}$ and Υ production cross sections using HERA-B data is presented [1]. During the 2002/2003 run, HERA-B recorded approximately 150 million pA dilepton trigger events in which $150,000$ J/$\psi \to e^+e^-$ and $100,000$ J/$\psi \to \mu^+\mu^-$ decays have been reconstructed. The b events are tagged via inclusive bottom quark decays into a J/ψ, by exploiting the longitudinal separation of J/$\psi \to l^+l^-$ decay vertices from the primary pA interaction. In the dimuon channel, b events are also tagged via double semi-leptonic b decays. The Υ cross section is measured in the dimuon and dielectron decay channels.

1 Introduction

The measurement of bottom production in fixed target collisions offers the possibility to test perturbative QCD in the near threshold energy regime, where the effect of higher order processes, such as soft gluon emission, has been calculated [2, 3]. These calculations have large uncertainties due to the b quark mass and the dependence on the normalization scale.

The published experimental results are inconsistent, even though they were obtained in similar experimental conditions by searching for J/ψ [4] and semi-leptonic [5] decays of b hadrons. HERA-B recently published the most accurate result based on independent measurements of J/ψ [6] and double muonic b decays [7].

For Υ production, several measurements are available in the HERA-B energy region ($\sqrt{s} = 41.6$ GeV), but the results disagree.

2 HERA-B detector and data sample

HERA-B is a forward spectrometer installed at the 920 GeV proton storage ring of DESY. The acceptance is [15, 220] mrad in the bending plane and [15, 160] mrad in the vertical plane), which approximately corresponds to a Feynman-x (x_{F}) of $[-0.35, 0.15]$. Charged particle tracks produced in the interactions of the proton beam halo with wires of different materials (^{12}C, ^{48}Ti and ^{184}W) are tracked with a silicon microstrip detector [8] whose first station (of 8) is a few centimeters from the target system and which extends approximately 2 m further downstream. A primary vertex resolution of 500 μm along the beam and 50 μm in the perpendicular plane is achieved. Up to 13 m downstream of the target, honeycomb chambers in the outer region [9, 10] and microstrip gaseous chambers in the inner region [11] allow to track particles and to measure their momenta from the bending in a 2.13 T·m vertical magnetic field. A Cherenkov detector [12] is used for $\pi/K/p$ separation. An electromagnetic shashlik calorimeter [13] serves for e and γ identification. At the rear of the detector, muons with momenta larger than 5 GeV/c are tracked with triple stereo layers of gaseous tube chambers interleaved with hadron absorbers [14].

In the 2002/2003 run, a multilevel dilepton trigger [15] allowed to record 150 million events of pA interactions with about $250,000$ reconstructed J/$\psi \to l^+l^-$ decays (Fig. 1).

*On behalf of the HERA-B collaboration.

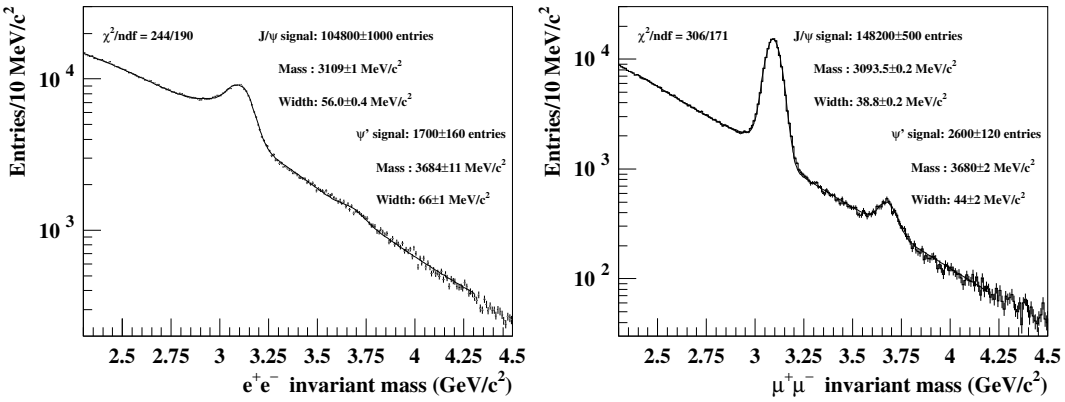

Figure 1: Invariant mass of unlike-sign dielectrons (left) and dimuons (right).

The systematic uncertainties due to the detector performance and acceptance is reduced by normalising the $b\bar{b}$ and Υ production cross sections to the prompt J/ψ cross section, as obtained from a NRQCD fit to world data ($\sigma_{J/\psi} = 502 \pm 44$ nb/nucleon [16]).

3 B production

Bottom quarks are produced in $b\bar{b}$ pairs at HERA-B. The $b\bar{b}$ cross section is extracted from data with two statistically independent measurement methods. In a first method, $b\bar{b}$ events are identified with the inclusive J/ψ decay of a b or $\bar{b}$ hadron. In a second method, $b\bar{b}$ events are tagged by searching for simultaneous semi-leptonic decays of the b and the $\bar{b}$ hadron.

3.1 Detached J/ψ analysis

In order to distinguish a prompt J/ψ from those coming from a b hadron decay, the b hadron lifetime is exploited. The typical path length of b hadrons at HERA-B is about 9 mm, well above the experimental resolution of the longitudinal primary vertex position (0.5 mm). Since there are no other long-lived particles decaying into a J/ψ, a J/ψ vertex which is detached from the primary vertex is a unique indication of a b hadron decay event.

The $b\bar{b}$ cross section can be expressed as

$$\sigma^A_{b\bar{b}} = \frac{n_{b\bar{b}}}{n_{J/\psi}} \cdot \frac{\sigma^A_{J/\psi}}{\epsilon_R \cdot \epsilon^{\Delta}_{b\bar{b}} z \cdot \mathrm{BR}(b \to J/\psi + X)} \ ,$$

where $\sigma_{J/\psi}$ is the prompt J/ψ cross section, $n_{b\bar{b}}$ and $n_{J/\psi}$ are the measured numbers of b and prompt J/ψ decay events; ϵ_R is the ratio of the J/ψ selection efficiency for b and prompt J/ψ events; $\epsilon^{\Delta}_{b\bar{b}} z$ is the efficiency of the detachment cuts. The dependency of the production cross sections on the mass number A is parameterized as $\sigma^A = \sigma_0 \cdot A^{\alpha}$, where σ_0 stands for the proton-nucleon cross section, and the parameter α stands for any possible nuclear effect. For $b\bar{b}$ production no nuclear effect is expected ($\alpha = 1$). For J/ψ production, the value measured by the E866 experiment ($\alpha = 0.96 \pm 0.01$ [17]) is used. The branching

ratio BR($b \to \mathrm{J}/\psi + X$) was measured at LEP1 from Z decays (0.0232 ± 0.0020 [18]). The efficiencies are determined through MC simulations.

A lepton track must have segments in the vertex detector and tracking systems, in addition to a set of particle identification requirements. When two opposite charge leptons are found, a vertex fit is performed. Figure 1 shows the dilepton mass distributions of reconstructed vertices, where the prompt J/ψ signal is visible.

In order to identify a detached lepton pair coming from a b decay, the longitudinal separation between the J/ψ vertex and the wire target, the lepton and J/ψ impact to the wire are exploited. The final selection procedure is obtained by a blind optimisation aiming at maximising the significance of the MC signal over the background estimated from both MC and data. Figure 2 shows the invariant mass distributions, upstream and downstream of the target, when the optimised selection criteria are applied.

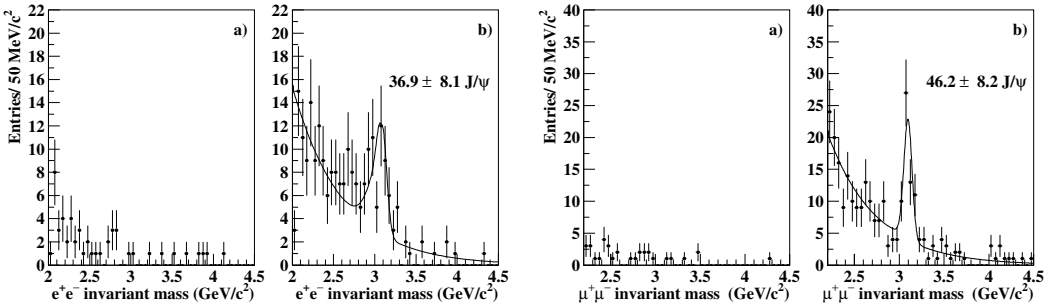

Figure 2: Dielectron (left) and dimuon (right) invariant mass distributions after vertex detachment cuts. The plots show the target upstream region (a), which is unphysical (combinatorial background) and the target downstream region (b) where $b \to \mathrm{J}/\psi + X$ decay events are visible. The solid line shows the result of a likelihood fit.

The downstream spectra in the J/ψ mass region are dominated by b decays events. Background consists of combinatorial lepton pairs (44 %) and simultaneous semi-leptonic decays of $b\bar{b}$ (43 %) and $c\bar{c}$ (13 %) pairs. Combinatorial background is estimated from the unphysical upstream events, while bottom and charm background are obtained from MC simulations.

The measured number of b decays events results from an unbinned likelihood fit of the mass spectra. The result for the combined muon and electron channels is $n_{b\bar{b}} = 83 \pm 12$ and, combined with a previous HERA-B measurement [19], it corresponds to a production cross section $\sigma_{b\bar{b}} = 14.9 \pm 2.2_{stat} \pm 2.4_{sys}$ nb/nucleon in the full x_F range.

A confirmation of the b-flavour of the tagged b events is given by the measured lifetime (1.39 ± 0.19 ps [6]) which is compatible with the expectation (1.54 ps [18]).

3.2 Double semi-leptonic b decays

After production, $b\bar{b}$ pairs hadronise and mostly decay into c hadrons. Since b and c hadrons have a large probability to decay with the emission of a muon (*semi-muonic decay*) [18], the $b\bar{b}$ production cross section is measured by searching for $b\bar{b} \to \mu^+\mu^- + X$ decay events,

in which at least two of the four heavy quarks typically produced in a $b\bar{b}$ event (b, $\bar{b}$, c, $\bar{c}$) undergo semi-muonic decays (*double muonic b decays*).

The $b\bar{b}$ cross section can be expressed as [20]

$$\sigma^A_{b\bar{b}} = \frac{n_{b\bar{b}}}{n_{\mathrm{J}/\psi}} \cdot \frac{\sigma^A_{\mathrm{J}/\psi} \cdot \mathrm{BR}(\mathrm{J}/\psi \to \mu^+\mu^-) \cdot \epsilon_{\mathrm{J}/\psi}}{\sum_j \mathrm{BR}_j(b\bar{b} \to \mu^+\mu^- + X) \cdot (1-\theta_j) \cdot \epsilon_{b\bar{b},j}} \ ,$$

where $\epsilon_{\mathrm{J}/\psi}$ is the prompt J/ψ selection efficiency and $\mathrm{BR}(\mathrm{J}/\psi) = 5.93 \pm 0.06$ % [18]. All possible decays originating from a $b\bar{b}$ pair and leading to a dimuon final state, having branching $\mathrm{BR}_j(b\bar{b} \to \mu^+\mu^- + X)$ and efficiency $\epsilon_{b\bar{b},j}$, are included. The factor θ_j accounts for the effect of neutral B meson mixing.

The $b\bar{b}$ event selection is based on a pair of oppositely charged muons not coming from the primary interaction vertex, having a large momentum transverse to the beam. The search of double semileptonic events is only performed in the muon channel due to the larger systematic uncertainty associated with the electron identification. The J/ψ mass region is excluded to be statistically independent from the result provided by the detached J/ψ analysis.

The measured number of double muonic b decay events ($n_{b\bar{b}}$) is obtained with a multiparameter likelihood fit to the data of the simulated transverse momentum (p_{T}) and impact parameter (Ip) distributions of signal and background events (Figure 3).

The background consists of double muonic decays of c hadrons and random combinations of muons from decay of low mass mesons (combinatorial background). Muons from Drell-Yan events are negligible. The result of the likelihood fit is $n_{b\bar{b}} = 83 \pm 12$, which corresponds to a production cross section of $\sigma_{b\bar{b}} = 17.5 \pm 2.6_{stat} \pm 3.3_{sys}$ nb/nucleon.

The combined result of the HERA-B measurements based on detached J/ψ and double semileptonic b decays is $\sigma_{b\bar{b}} = 15.8 \pm 1.7_{stat} \pm 1.3^{uncorr.}_{sys} \pm 2.0^{corr.}_{sys}$ nb/nucleon.

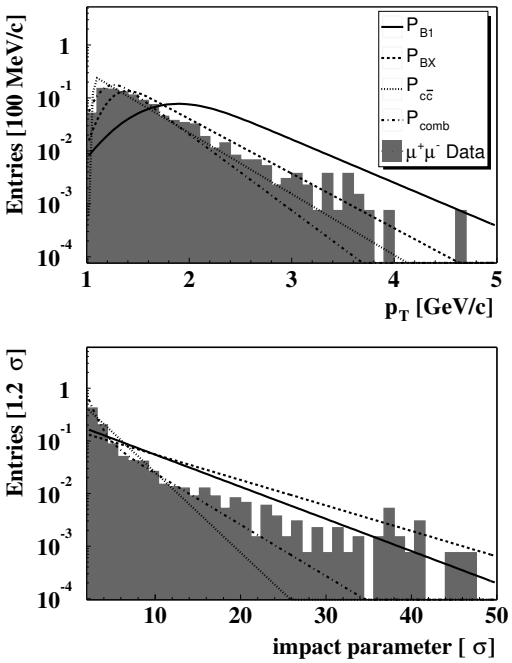

Figure 3: Simulated p_{T} (top) and Ip (bottom) distributions of double muonic b and c decays, combinatorial background and oppositely charged dimuon data.

4 Υ production

Dilepton decays are used to study Υ production. The selection criteria are similar to those applied for J/ψ identification.

Due to the broad signal and the low number of signal events over background, it is important to have a good description of the background. Combinatorial events (estimated by like-sign pairs from real data) and the Drell-Yan process (estimated from MC simulation) are the main sources of background. These two backgrounds are shown in Fig. 4, together with the Υ signals in the muon and electron channel.

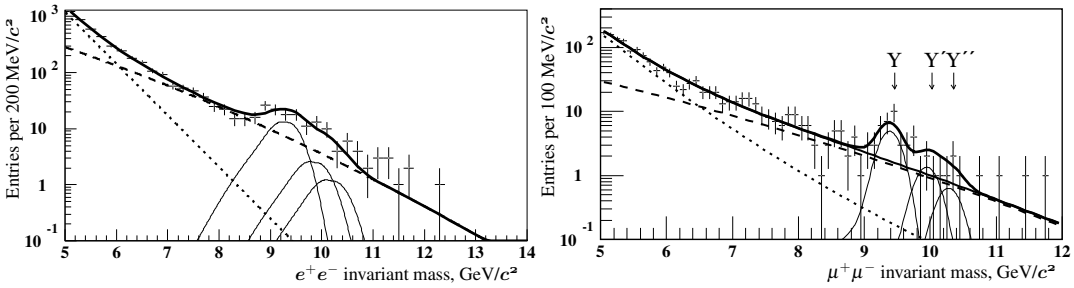

Figure 4: Dielectron (left) and dimuon (right) invariant mass spectra. Solid lines represent combinatorial and Drell-Yan background.

A good and stable fit of the signal is obtained by fixing the background shapes and the relative production ratios of $\Upsilon(1S)/\Upsilon(2S)/\Upsilon(3S)$ to the E605 results [21]. The differential cross section at central rapidity times the branching ratio can be express as

$$\mathrm{BR}(\Upsilon \to l^+l^-)\frac{d\sigma_\Upsilon}{dy}\bigg|_{y=0} = \mathrm{BR}(\mathrm{J}/\psi \to l^+l^-)\cdot\sigma_{\mathrm{J}/\psi}\cdot\frac{n_\Upsilon}{n_{\mathrm{J}/\psi}}\cdot\frac{\epsilon_{\mathrm{J}/\psi}}{\epsilon_\Upsilon}\cdot\frac{1}{\Delta y_{eff}}\ ,$$

where $\sigma_{\mathrm{J}/\psi}$ is the J/ψ production cross section, n_Υ and $n_{\mathrm{J}/\psi}$ are the numbers of observed Υ and J/ψ decays, respectively, and $\epsilon_{\mathrm{J}/\psi}$ and ϵ_Υ are the J/ψ and Υ trigger and reconstruction efficiencies. The Υ production model gives $\Delta y_{eff} = 1.068 \pm 0.002$ at $\sqrt{s} = 41.6$ GeV. The J/ψ cross section and branching ratios are the same as those used in the open $b\bar{b}$ analysis.

Combining muon and electron channels, a central rapidity production cross section of $\mathrm{BR}(\Upsilon \to l^+l^-)\frac{d\sigma_\Upsilon}{dy} = 4.5 \pm 1.1$ pb/nucleon is obtained, a value in between the E605 and E772/E771 measurements [22, 23]. The spectrum of the world available experimental data is fitted with Craigie's parameterization [24] (see Fig. 5). An additional parameter α is used for nuclear suppression and yields a result compatible with no nuclear suppression.

5 Conclusions

A $b\bar{b}$ cross section of $\sigma_{b\bar{b}} = 15.8 \pm 1.7_{stat} \pm 1.3^{uncorr.}_{sys} \pm 2.0^{corr.}_{sys}$ nb/nucleon is extracted from the largest sample of b events recorded in fixed target experiments (176 events). The result is consistent with the latest QCD predictions of Bonciani *et al.* [2] and Kidonakis *et al.* [3] (see Fig. 5). The Υ differential cross section measurement at central rapidity times the branching ratio yields a value of 4.5 ± 1.1 pb/nucleon. A global fit to the Υ data shows that the result is consistent with no nuclear suppression (see Fig. 5).

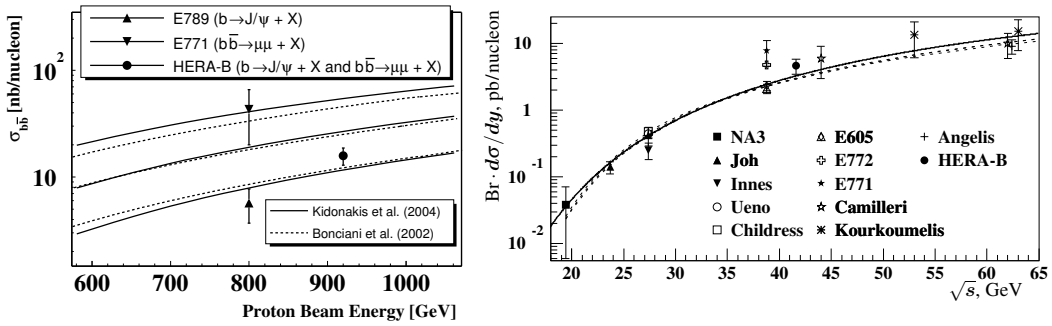

Figure 5: The left plot shows several measurements of the $b\bar{b}$ production cross section as a function of the proton energy in fixed target collisions. The theoretical predictions are superimposed. The right plot shows the Υ production cross section measured by different experiments, including HERA-B, and the modified Craigie parameterization fit.

References

[1] Slides: http://indico.cern.ch/contributiondisplay.py?contribid=237&sessionid=5&confid=9499.
[2] R. Bonciani *et al.*. *Nucl. Phys.*, B529:424, 1998.
[3] N. Kidonakis and R. Vogt. *Eur. Phys. J.*, C36:201, 2004.
[4] D. M. Jansen *et al.*. *Phys. Rev. Lett.*, 74:3118, 1995.
[5] T. Alexopoulos *et al.*. *Phys. Rev. Lett.*, 82:41, 1999.
[6] I. Abt *et al.*. *Phys. Rev.*, D73:052005, 2006.
[7] I. Abt *et al.*. *Phys. Lett.*, B650:103, 2007.
[8] C. Bauer *et al.*. *Nucl. Instrum. Meth.*, A501:39, 2003.
[9] H. Albrecht *et al.*. *Nucl. Instrum. Meth.*, A541:610, 2005.
[10] H. Albrecht *et al.*. *Nucl. Instrum. Meth.*, A555:310, 2005.
[11] Y. Bagaturia *et al.*. *Nucl. Instrum. Meth.*, A490:223, 2002.
[12] I. Ariño *et al.*. *Nucl. Instrum. Meth.*, A516:445, 2004.
[13] G. Avoni *et al.*. *Nucl. Instrum. Meth.*, A461:332, 2001.
[14] A. Arefiev *et al.*. *IEEE Trans. Nucl. Sci.*, 48:1059, 2001.
[15] V. Balagura *et al.*. *Nucl. Instrum. Meth.*, A494:526, 2002.
[16] F. Maltoni *et al.*. *Phys. Lett.*, B638:202, 2006.
[17] M. J. Leitch *et al.*. *Phys. Rev. Lett.*, 84:3256, 2000.
[18] W. M. Yao *et al.*. *J. Phys.*, G33:1, 2006.
[19] I. Abt *et al.*. *Eur. Phys. J.*, C26:345, 2003.
[20] A. Sbrizzi. PhD thesis, NIKHEF, Amsterdam, 2006.
[21] T. Yoshida *et al.*. *Phys. Rev.*, D39:3516, 1989.
[22] T. Alexopoulos *et al.*. *Phys. Lett.*, B374:271, 1996.
[23] P. L. McGaughey *et al.*. *Phys. Rev.*, D50:3038, 1994.
[24] N. S. Craigie. *Phys. Rept.*, 47:1, 1978.

Charm Physics at B Factories

Galina Pakhlova

Institute for Theoretical and Experimental Physics
Moscow - Russia

We review of the experimental status in charm mixing, charm semileptonic decays, charm baryon spectroscopy and charmonium production at Belle and BaBar.

1 Charm Mixing

After the discovery by Tevatron of $B_s^0 - \overline{B}_s^0$-oscillations D^0 and $\overline{D}^0$ remains the last flavor neutral meson system with unobserved mixing. Neutral meson mixing is characterized by parameters $x = \Delta M/\Gamma$ and $y = \Delta\Gamma/2\Gamma$, where ΔM and $\Delta\Gamma$ are the mass and width difference between the two CP eigenstates. The SM box diagram in $D^0 \leftrightarrow \overline{D}^0$ transitions is strongly GIM and CKM suppressed. However, D mixing can be enhanced by long distance effects, involving on- or off-shell $D^0 \leftrightarrow \overline{D}^0$ transitions through intermediate states accessible to both mesons, that contribute both to x and y. New Physics contribution to loops can enhance x only, and observation of $x \gg y$ would be a signal of New Physics. Observation of CP violating effects in D would be another unambiguous signature of New Physics as the SM predicts tiny CP violation beyond the present experimental sensitivity.

Experimentally one of the following techniques is exploited to search for D mixing: study of wrong-sign (WS) hadronic decays, search for WS D^0 semileptonic decays, a time-dependent Dalitz plot analysis or direct measurement of the lifetime difference between opposite CP eigenstates. The first method provides the restrictive mixing constraints, in spite of a complication due to presence of doubly-Cabibbo suppressed (DCS) contribution to the same WS final state. The interference of the mixing and DCS amplitudes results in rotation of measured $x' = x\cos\delta + y\sin\delta$ and $y' = -x\sin\delta + y\cos\delta$ by the strong phase difference δ between the mixing and DCS amplitudes. This year BaBar [2] has presented a strong evidence for D mixing in $D^0 \to K^+\pi^-$ decays. The WS decay rate is a function of proper decay-time:

$$R(t) = e^{-\Gamma t}(R_D + \sqrt{R_D}y'\Gamma t + \frac{x'^2 + y'^2}{4}(\Gamma t)^2),$$

where R_D is the DCS decay rate (Fig. 1). The mixing and DCS contributions are thus discriminated in the fit to the time-dependent rate of WS decays. The fit yields the mixing parameters to be $x'^2 = (-0.22 \pm 0.30 \pm 0.21) \cdot 10^{-3}$ and $y' = (9.7 \pm 4.4 \pm 3.3) \cdot 10^{-3}$ and a correlation between them -0.94. This result is inconsistent with the no-mixing hypothesis with a significance of 3.9σ. Belle [3] has observed an evidence for D mixing by comparing the apparent lifetime when a D^0 meson decays to the CP eigenstates K^+K^- and $\pi^+\pi^-$, and when it decays to the final state $K^-\pi^+$ (Fig. 1). They find $y_{CP} = (1.31 \pm 0.32 \pm 0.25)\%$, 3.2σ from zero. Using a time-dependent Dalitz plot analysis Belle [4] has also reported a measurement of D mixing in $D^0 \to K_s^0\pi^+\pi^-$ decays. Assuming negligible CP violation, the mixing parameters were found to be $x = (0.80 \pm 0.29^{+0.09+0.15}_{-0.07-0.14})\%$ and $y = (0.33 \pm 0.24^{+0.07+0.08}_{-0.12-0.09})\%$. Both Belle and BaBar have found no evidence for CP asymmetry in D decays.

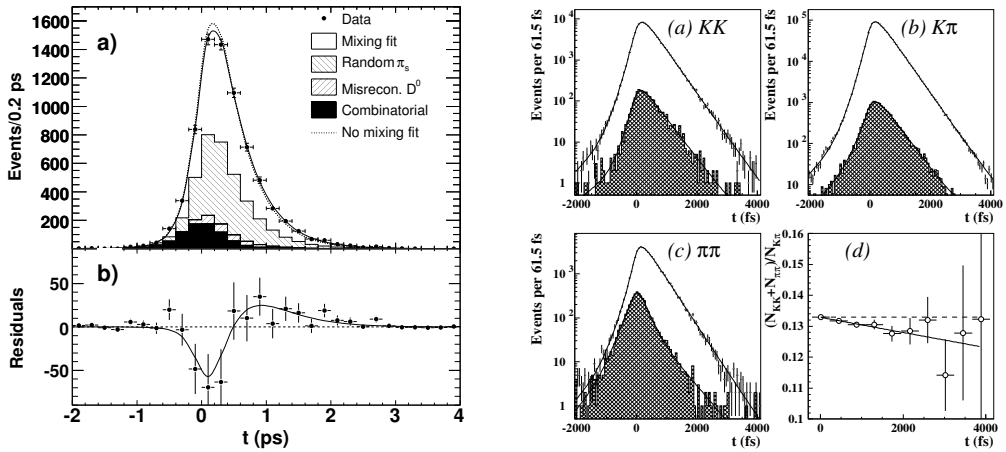

Figure 1: Left plot: (a) BaBar's the proper decay-time distribution of combined D^0 and $\overline{D}^0$ WS candidates; (b) the difference between the data and the no-mixing fit. Right plot: Belle results of the simultaneous fit to decay-time distributions of (a) $D^0 \to K^+K^-$; (b) $D^0 \to \pi^+\pi^-$; (c) $D^0 \to K^-\pi^+$ decays; (d) ratio of decay-time distributions between $D^0 \to K^+K^-/\pi^+\pi^-$ and $D^0 \to K^-\pi^+$.

2 Charm semileptonic decays

The measurements of charm semileptonic decay form factors provide a precise tests of LQCD calculations with high statistics and an important inputs for B physics. Belle [5] has measured $D^0 \to K^-\ell^+\nu$ and $D^0 \to \pi^-\ell^+\nu$ decays. The D^0 momentum was tagged through a full reconstruction of the recoiling charm meson and mesons from fragmentation in the $e^+e^- \to c\bar{c}$ events. This technique provides an excellent q^2 resolution and a low level of backgrounds though with considerably reduced statistics. Normalizing to the total number of D^0 tags, Belle has measured the absolute branching fractions to be $\mathcal{B}(D^0 \to K^-\ell^+\nu) = (3.45 \pm 0.07 \pm 0.20)\%$ and $\mathcal{B}(D^0 \to \pi^-\ell^+\nu) = (0.255 \pm 0.019 \pm 0.016)\%$ and the semileptonic form factors (within the modified pole model) $f_+^K(0) = 0.695 \pm 0.007 \pm 0.022$ and $f_+^\pi(0) = 0.624 \pm 0.020 \pm 0.030$. BaBar [6] has presented a model independent measurements of the hadronic form factor $f_+(q2)$ in the decay $D^0 \to K^-\ell^+\nu$ and the normalization of the form factor at $q^2 = 0$ determined to be $f_+(0) = 0.727 \pm 0.007 \pm 0.005 \pm 0.007$.

3 Charm baryon spectroscopy

Recently the progress in charmed-baryon spectroscopy is evident with a growing number of observed new states and decays modes. BaBar [7] has observed a new charmed baryon in the continuum events in the D^0p final state. Fig. 2 shows the D^0p invariant mass spectrum with two prominent structures: one near a mass $2880\,\mathrm{MeV}/c^2$ that is consistent with the known state $\Lambda_c(2880)$, the other at a mass of $2939.8 \pm 1.3 \pm 1.0\,\mathrm{MeV}/c^2$ and with an intrinsic width of $17.5 \pm 5.2 \pm 5.9\,\mathrm{MeV}$. As there is no evidence in the D^+p spectrum of doubly-charged partners, one can conclude that this state is excited Λ_c, temporary called $\Lambda_c(2940)$. Belle [8] reported the first observation of $\Lambda_c(2940) \to \Sigma_c(2455)\pi$ decay and measured $\Lambda_c(2880)$ and

$\Lambda_c(2940)$ parameters. An analysis of angular distributions in $\Lambda_c(2880) \to \Sigma_c(2455)\pi$ decays strongly favors a $\Lambda_c(2880)$ spin assignment of 5/2 over 3/2 or 1/2.

Belle [9] has analyzed the $\Lambda_c^+ K^-\pi^+$ final state searching for the doubly-charmed $\Xi_{cc}^+(3520)$, reported by SELEX [10]. No evidence for this state is found with the Belle data, while two new charmed strange baryons, $\Xi_{cx}^+(2980)$ and $\Xi_{cx}^+(3077)$, are clearly seen near the threshold (Fig. 2) with mass of $2978.5 \pm 2.1 \pm 2.0\,\mathrm{MeV}/c^2$ ($3076.7 \pm 0.9 \pm 0.5\,\mathrm{MeV}/c^2$) and width of $43.5 \pm 7.5 \pm 7.0\,\mathrm{MeV}$($6.2 \pm 1.2 \pm 0.8\,\mathrm{MeV}$), respectively. A significant signal at the mass of $3082.8 \pm 1.8 \pm 1.5\,\mathrm{MeV}/c^2$ for the isospin partner state decaying into $\Lambda_c^+ K_S^0\pi^-$ is also observed. Babar [11] has confirmed observation of $\Xi_{cx}^+(2980)$ and $\Xi_{cx}^+(3077)$ baryons, with the parameters consistent with the Belle measurement. The high mass of new states suggests that they can be $L = 2$ excitations, but no direct measurements of quantum numbers are made so far. Belle [12] has reported a precise measurement of masses of the $\Xi_c(2645)$ and

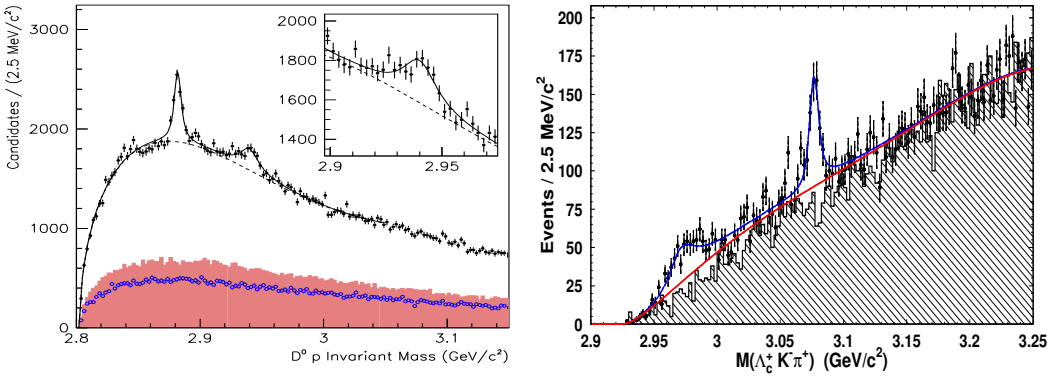

Figure 2: a) The $D^0 p$ invariant mass distribution and the contribution from false D^0 candidates estimated from D^0 mass sidebands and (open points) the mass distribution from WS $\overline{D}^0 p$ candidates. b) $\Lambda_c^+ K^-\pi^+$ invariant mass spectrum. The shaded area shows the WS combinations.

$\Xi_c(2815)$ baryons. The states $\Xi_c(2645)^{0,+}$ are observed in the $\Xi_c^{+,0}\pi^{-,+}$ decay modes, while the $\Xi_c(2815)^{0,+}$ are reconstructed in the $\Xi_c(2645)^{+,0}\pi^{-,+}$ decay modes.

Finally, the family of predicted $J^P = 3/2^+$ states was completed with the first observation by BaBar [13] of an excited singly-charmed baryon Ω_c^* (css) in the radiative decay $\Omega_c^0\gamma$. The mass difference between the Ω_c^* and the Ω_c^0 baryons has been measured to be $70.8 \pm 1.0 \pm 1.1\,\mathrm{MeV}/c^2$ in good agreement with the QCD predictions. From the momentum spectrum of the Ω_c^0 baryons in the e^+e^- center-of-mass frame Ω_c^0 production from B decays and in $e^+e^- \to c\bar{c}$ events was observed [14].

4 Measurement of the near-threshold $\sigma(e^+e^- \to D^{(*)}\overline{D}^{(*)})$ using ISR

Exclusive e^+e^- hadronic cross sections to final states with charm meson pairs are of special interest because they provide information on the spectrum of $J^{PC} = 1^{--}$ charmonium states above the open-charm threshold, which is poorly understood. To measure the e^+e^- hadronic cross section at $\sqrt{s}$ smaller than the initial e^+e^- center-of-mass (CM) energy (E_{CM}) at B-factories, initial-state radiation (ISR) can be used. ISR allows a measurement of cross

sections in a broad energy range while the high luminosity of the B-factories compensates for the suppression associated with the emission of a hard photon. BaBar [15] has performed a study of exclusive production of the $D\overline{D}$ system through ISR in a search for charmonium states, where $D = D^0$ or D^+. The $D\overline{D}$ mass spectrum shows a clear $\psi(3770)$ signal. Further structures appear in the 3.9 and 4.1 GeV/c^2 regions. No evidence is found for $Y(4260)$ decays to $D\overline{D}$, implying an upper limit $\frac{\mathcal{B}(Y(4260)\to D\bar{D})}{\mathcal{B}(Y(4260)\to J/\psi\pi^+\pi^-)} < 7.6$ (95% CL). Recently Belle [16] has reported the first measurements of exclusive $e^+e^- \to D^{*+}D^{*-}$ and $e^+e^- \to D^+D^{*-}$ cross sections at $\sqrt{s}$ around the $D^{*+}D^{*-}$ and D^+D^{*-} thresholds with ISR. A partial reconstruction technique was used to increase the efficiency and to suppress background. The shape of the $e^+e^- \to D^{*+}D^{*-}$ cross section is complicated with several local maxima and minima (Fig. 3). The minimum near 4.25 GeV/c^2 — in the $Y(4260)$ region — could be due to $D_s^*D_s^*$ (DD^{**}) threshold effects or due to destructive interference of this state with other $\psi(nS)$ states. Aside from a prominent excess near the $\psi(4040)$, the $e^+e^- \to D^+D^{*-}$ cross section is relatively featureless. The measured cross sections are compatible within errors with the $D^{(*)}\overline{D}^*$ exclusive cross section in the energy region up to 4.260 GeV measured by CLEO-c [17].

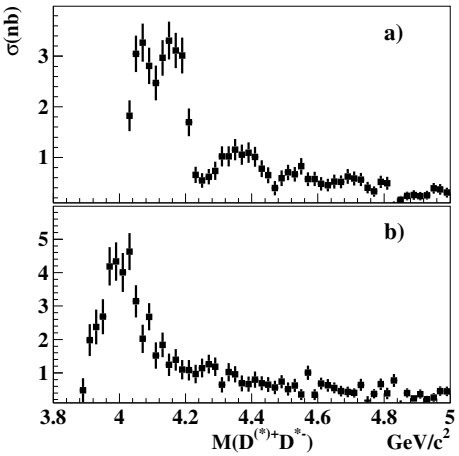

Figure 3: The exclusive cross sections for a) $e^+e^- \to D^{*+}D^{*-}$ and b) $e^+e^- \to D^+D^{*-}$.

References

[1] Slides: http://indico.cern.ch/contributionDisplay.py?contribId=208&sessionId=5&confId=9499
[2] B. Aubert *et al.* (BABAR Collab.), Phys. Rev. Lett. **98** 211802 (2007).
[3] M. Staric *et al.* (Belle Collab.), Phys. Rev. Lett. **98** 211803 (2007).
[4] K. Abe *et al.* (Belle Collab.), arXiv:0704.1000 (2007).
[5] L. Widhalm *et al.* (Belle Collab.), Phys. Rev. Lett. **97** 061804 (2006).
[6] B. Aubert *et al.* (BABAR Collab.), arXiv:0704.0020 (2007).
[7] B. Aubert *et al.* (BABAR Collab.), Phys. Rev.Lett **98** 052001 (2007).
[8] K. Abe *et al.* (Belle Collab.), arXiv:hep-ex/0608043 (2006).
[9] R. Chistov *et al.* (Belle Collab.), Phys. Rev. Lett.**97** 162001 (2006).
[10] M. Mattson *et al.* (SELEX Collab.), Phys. Rev. Lett. **89** 112001 (2002).
[11] B. Aubert *et al.* (BABAR Collab.), arXiv:hep-ex/0607042 (2006).
[12] K. Abe *et al.* (Belle Collab.), arXiv:hep-ex/0608012 (2006).
[13] B. Aubert *et al.* (BABAR Collab.), Phys. Rev. Lett.**97** 232001 (2006).
[14] B. Aubert *et al.* (BABAR Collab.), arXiv:hep-ex/0703030 (2007).
[15] B. Aubert *et al.* (BABAR Collab.), arXiv:hep-ex/0607083 (2006).
[16] G. Pakhlova *et al.* (Belle Collab.), Phys. Rev. Lett.**98** 092001 (2007).
[17] R. Poling (for CLEO Collab.), arXiv:hep-ex/0606016 (2006).

Heavy Quarkonium Decays on and off the Lattice

Alistair Hart[1] *, G.M. von Hippel[2] and R.R. Horgan[3]

1-University of Edinburgh - School of Physics
King's Buildings, Edinburgh EH9 3JZ - United Kingdom

2-University of Regina - Department of Physics
Regina, SK, S4S 0A2 - Canada

3-University of Cambridge - DAMTP
CMS, Cambridge CB3 0WA - United Kingdom

I review recent progress in understanding radiative transitions in heavy quarkonium, both on and off the lattice, and discuss our recent leptonic width matching calculation.

1 Introduction

In my conference talk (available at [1]), I reviewed papers of Dudek, Edwards and Richards [2, 3], of Lansberg and Pham [4], of Gao, Zhang and Chao [5] and of Oliveira and Coimbra [6]. As these are discussed elsewhere in these proceedings, I here concentrate on our calculation of the leptonic widths of heavy quarkonia [7].

Leptonic widths of heavy quarkonia such as the Υ or the J/ψ are an important test of electroweak Standard Model in the heavy quark sector: heavy particles should be sensitive to possible new physics at or above the electroweak scale. Leptonic decays have experimentally clean signatures. Moreover, ratios of leptonic widths can be measured to good accuracy both experimentally and on the lattice, providing a high precision test of lattice techniques.

Here we address how to improve the precision of current lattice predictions [8] to match that of experimental results [9]:

$$\frac{\Gamma_{\Upsilon(2S)\to e^+e^-} M_{2S}^2}{\Gamma_{\Upsilon(1S)\to e^+e^-} M_{1S}^2} = \begin{cases} 0.457\ (6) & \text{CLEO,} \\ 0.48\ (5) & \text{Lattice.} \end{cases}$$

2 Matching S-wave decays between NRQCD and QCD

The leptonic width of a heavy quarkonium $\bar{Q}Q$ state of mass $M_{\bar{Q}Q}$ is given by

$$\Gamma_{\bar{Q}Q\to l^+l^-} = \frac{8\pi}{3M_{\bar{Q}Q}} \left|\left\langle 0 \left| \mathbf{J}^{QCD} \right| \bar{Q}Q \right\rangle\right|^2 e_Q^2 \alpha_{em}^2$$

with nonperturbative QCD contributions coming from the matrix element $\left\langle 0 \left| \mathbf{J}^{QCD} \right| \bar{Q}Q \right\rangle$. Unfortunately, it is not possible to simulate heavy b quarks directly on a lattice (with spacing typically $a \simeq 0.1$ fm) due to their short Compton wavelengths. We must use an effective theory, such as NRQCD, and calculate the desired QCD matrix element from a set of NRQCD matrix elements which *can* be measured on the lattice:

$$\left\langle 0 \left| \mathbf{J}^{QCD} \right| \bar{Q}Q \right\rangle = \sum_i a_i \left\langle 0 \left| \mathbf{J}_i^{NRQCD} \right| \bar{Q}Q \right\rangle$$

*U.K. Royal Society University Research Fellow

In this paper we determine the matching coefficients a_i for S-wave decays, with NRQCD currents $\mathbf{J}_i^{NRQCD} = \boldsymbol{\sigma}\left(\frac{\Delta^2}{M^2}\right)^i$ (which vary as v^{2i} with the heavy quark velocity at tree level).

Discretisation removes high momentum modes, so it is reasonable to expect that we can compute the matching coefficients perturbatively, by expanding both the coefficients and the matrix elements and matching order by order in α_s:

$$a_i = \sum_n \alpha_s^n a_i^{(n)} \qquad\qquad \left\langle 0 \left| \mathbf{J} \right| \bar{Q}Q \right\rangle = \sum_n \alpha_s^n \left\langle 0 \left| \mathbf{J} \right| \bar{Q}Q \right\rangle^{(n)}$$

We calculate $a_{0,1,2}^{(0)}$ and $a_{0,1}^{(1)}$, giving an accuracy of $\mathcal{O}(\alpha_s, \alpha_s v^2, v^4)$. In the Υ system, $v^2 \sim \alpha_s \sim 10\%$ suggesting that to achieve $\sim 1\%$ accuracy, we would need to go to $\mathcal{O}(\alpha_s^2, \alpha_s v^2, v^4)$, hence requiring two-loop $a_0^{(2)}$. In matrix element ratios, however, we need only $b_{1,2} = a_{1,2}/a_0$ and such terms cancel. Our calculation thus give $\sim 1\%$ accuracy on the ratio.

We work in the Breit frame, where the decaying meson is stationary and the quark has momentum $p^\mu = (iE, 0, 0, Mv)$, use v as the non-relativistic expansion parameter (exact at the order to which we are working) and treat the quarks as being on-shell (which can also be shown to be justified). Our gauge and fermion actions are chosen to be the same as are used in current lattice simulations. The improved NRQCD action is

$$\mathcal{S}_{\mathrm{NRQCD}} = \sum_{x,t} \psi^\dagger\psi - \psi^\dagger \left(1 - \frac{a\delta H}{2}\right)\left(1 - \frac{aH_0}{2n}\right)^n U_4^\dagger \left(1 - \frac{aH_0}{2n}\right)^n \left(1 - \frac{a\delta H}{2}\right)\psi \,.$$

where n is a stability parameter for the euclidean-space Schrödinger equation, which must satisfy $n \geq 3/(Ma)$ for numerical stability. For the gauge fields, we use a Symanzik improved action with tadpole improved links.

The Feynman rules for such actions are extremely complicated, with 8000 terms in the $Q\bar{Q}g$ vertex and 70000 for the $\mathcal{O}(a)$ $Q\bar{Q}gg$. For this reason, we have developed HiPPy, a flexible, automated tool for generating Feynman rules from lattice actions [10]. It incorporates automatic differentiation techniques [11] to calculate the derivatives of the complicated Feynman diagrams. Freely available, HiPPy has also been used in a number of recent calculations [12, 13, 14].

2.1 Matching at tree level

At tree-level, the relevant matrix elements are given by

$$\begin{aligned} \left\langle 0 \left| \mathbf{J}^{QCD} \right| \bar{Q}Q \right\rangle^{(0)} &= \bar{v}(-\mathbf{p})\boldsymbol{\gamma}u(\mathbf{p}) = \chi^\dagger\boldsymbol{\sigma}\left(\frac{2}{3} + \frac{M}{3E}\right)\psi \\ \left\langle 0 \left| \mathbf{J}_i^{NRQCD} \right| \bar{Q}Q \right\rangle^{(0)} &= g_i(v)\chi^\dagger\boldsymbol{\sigma}\psi \end{aligned}$$

where

$$\begin{aligned} g_0(v) &= 1\,, \quad g_1(v) = -\frac{4}{(Ma)^2}\sin^2\left(\frac{aMv}{2}\right) = v^2 + \mathcal{O}(v^4) \\ g_2(v) &= \frac{4}{(Ma)^2}\left[4\sin^2\left(\frac{aMv}{2}\right) - \sin^2(aMv)\right] = v^4 + \mathcal{O}(v^6) \end{aligned}$$

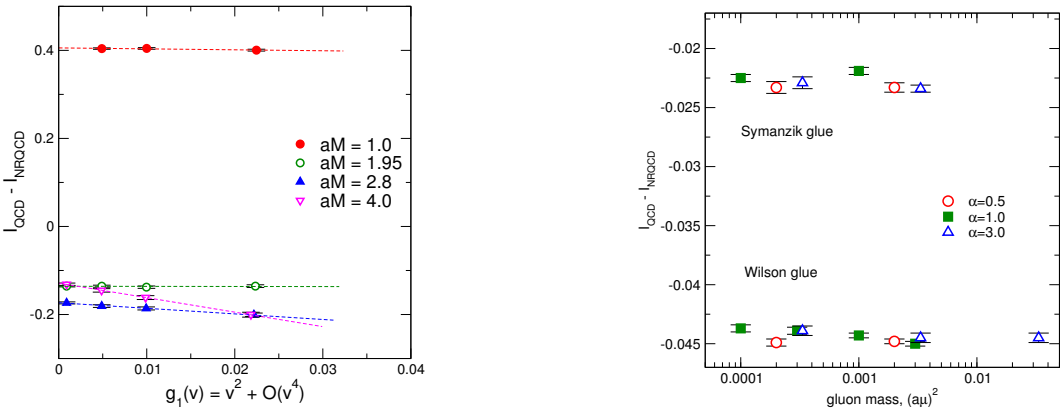

Figure 1: Left: numerical results with fits for $a^{(1)}_{0,1}$); right: results in different gauges vs. the infrared gluon mass, showing gauge and gluon mass independence.

Expanding these matrix elements in powers of v^2, we determine $a_i^{(0)}$ to match:

$$a_0^{(0)} = 1\,, \quad a_1^{(0)} = \frac{1}{6}\,, \quad a_2^{(0)} = \frac{1}{8} - \frac{(aM)^2}{72}\,.$$

2.2 Matching to one-loop order

Expanding the matching condition to first order in α_s gives

$$\sum_i \underbrace{a_i^{(1)}}_{\text{wanted}} \overbrace{\left\langle 0 \left| \mathbf{J}_i^{NRQCD} \right| \bar{Q}Q \right\rangle^{(0)}}^{\text{known functions of } v} = \overbrace{\left\langle 0 \left| \mathbf{J}^{QCD} \right| \bar{Q}Q \right\rangle^{(1)}}^{I_{QCD}} - \overbrace{\sum_i a_i^{(0)} \left\langle 0 \left| \mathbf{J}_i^{NRQCD} \right| \bar{Q}Q \right\rangle^{(1)}}^{I_{NRQCD}}$$

Both the QCD and the NRQCD matrix elements on the right-hand side contain odd powers of v coming from the Coulomb-exchange singularity; however, only even powers of v are available for matching on the left-hand side, so the odd powers must cancel exactly.

In fact, the odd powers of v are a purely infrared phenomenon, and are known exactly:

$$I_{odd} = \frac{h(v)}{12v} = -\Im\left\{ \frac{4}{3} \int \frac{d^4k}{(2\pi)^4} \frac{h(v)}{(\boldsymbol{k}^2+\mu^2)(ik_0 - \frac{\boldsymbol{k}^2+2\boldsymbol{k}\cdot\boldsymbol{p}}{2M})(ik_0 + \frac{\boldsymbol{k}^2+2\boldsymbol{k}\cdot\boldsymbol{p}}{2M})} \right\}$$

where $h(v)$ is a known even function of v. We can hence analytically subtract the odd powers from both QCD and NRQCD by rearranging the right-hand side as

$$I_{QCD} - I_{NRQCD} = (I_{QCD} - I_{odd}) - (I_{NRQCD} - I_{in}) + I_{out}$$

where we have split $I_{odd} = I_{in} + I_{out}$, inside and outside the Brillouin zone. The term $(I_{QCD} - I_{odd})$ is known analytically, while the other terms are calculated numerically using farmed VEGAS on the CCHPCF SunFire Galaxy class computer. We find the matching coefficients by fitting results for various v with $(I_{QCD} - I_{NRQCD})(v) = a_0^{(1)} - a_1^{(1)} g_1(v)$.

M_0a	n	a_0^1	a_1^1	b_1^1	b_2^0
4.0	2	-0.1288(27)	-3.32(29)	-3.30(30)	-0.0972
2.8	2	-0.1732(21)	-1.35(22)	-1.32(22)	0.0161
1.95	2	-0.1358(16)	0.26(17)	0.14(17)	0.0722
1.0	4	0.4056(20)	-0.50(17)	-0.56(17)	0.1111

Table 1: The matching coefficients, as a function of the *bare* heavy quark mass. Note that $a_0^{(0)} = 1$, $a_1^{(0)} = b_1^{(0)} = \frac{1}{6}$, and that there is *no* subtraction to prevent mixing down.

3 Results and conclusions

We have calculated matching coefficients at a number of quark masses corresponding to the bottom and charm quarks on the MILC improved staggered ensembles. We have performed extensive tests of gauge invariance, infrared regulator independence, and agreement with known results for $a_0^{(1)}$ at $v = 0$ for simpler NRQCD actions. Our results are shown in Fig. 1, as well as a plot showing the gauge and regulator independence of our results. Our final results for the matching coefficients are given in Table 1, and are currently being combined with lattice NRQCD matrix elements to predict the leptonic widths.

Acknowledgments

We thank G.P. Lepage and C.T.H. Davies for useful discussions and the Cambridge–Cranfield High Performance Computing Facility. G.M.v.H. thanks the Canadian Natural Sciences and Engineering Research Council and the Government of Saskatchewan for financial support.

References

[1] Slides: `http://indico.cern.ch/contributionDisplay.py?contribId=209&sessionId=5&confId=9499`

[2] J. J. Dudek and R. G. Edwards, Phys. Rev. Lett. **97**, 172001 (2006), [hep-ph/0607140].

[3] J. J. Dudek, R. G. Edwards and D. G. Richards, Phys. Rev. **D73**, 074507 (2006), [hep-ph/0601137].

[4] J. P. Lansberg and T. N. Pham, Phys. Rev. **D74**, 034001 (2006), [hep-ph/0603113]; Phys. Rev. **D75**, 017501 (2007), [hep-ph/0609268].

[5] Y.-J. Gao, Y.-J. Zhang and K.-T. Chao, Commun. Theor. Phys. **46**, 1017 (2006), [hep-ph/0606170]; Chin. Phys. Lett. **23**, 2376 (2006), [hep-ph/0607278]; hep-ph/0701009.

[6] O. Oliveira and R. A. Coimbra, hep-ph/0603046.

[7] A. Hart, G. M. von Hippel and R. R. Horgan, Phys. Rev. **D75**, 014008 (2007), [hep-lat/0605007]; PoS **LAT2006**, 098 (2006), [hep-lat/0609002].

[8] A. Gray *et al.*, Phys. Rev. **D72**, 094507 (2005), [hep-lat/0507013].

[9] CLEO, J. L. Rosner *et al.*, Phys. Rev. Lett. **96**, 092003 (2006), [hep-ex/0512056].

[10] A. Hart, G. M. von Hippel, R. R. Horgan and L. C. Storoni, J. Comput. Phys. **209**, 340 (2005), [hep-lat/0411026].

[11] G. M. von Hippel, Comput. Phys. Commun. **174**, 569 (2006), [physics/0506222]; arXiv:0704.0274.

[12] I. T. Drummond, A. Hart, R. R. Horgan and L. C. Storoni, Phys. Rev. **D66**, 094509 (2002), [hep-lat/0208010]; Nucl. Phys. Proc. Suppl. **119**, 470 (2003), [hep-lat/0209130]; Phys. Rev. **D68**, 057501 (2003), [hep-lat/0307010].

[13] A. Hart, R. R. Horgan and L. C. Storoni, Phys. Rev. **D70**, 034501 (2004), [hep-lat/0402033].

[14] Z. Hao, G. M. von Hippel, R. R. Horgan, Q. J. Mason and H. D. Trottier, arXiv:0705.4660.

Review of Beauty Production at HERA and Elsewhere

A.Geiser

DESY Hamburg, Germany

Experimental results on beauty production at HERA are reviewed in the context of similar measurements at other colliders. As a result of a phenomenological study of the QCD scale dependence of many different NLO and NNLO predictions, a modification of the "default" scale choice is advocated. Experimental constraints on the photon-quark coupling are also investigated. [1]

1 Introduction

Beauty production at HERA (Fig. 1) is an important tool to investigate our present understanding of the theory of Quantum Chromo-Dynamics (QCD). On one hand, the large b quark mass, taken as a hard scale, ensures that the cross sections are always perturbatively calculable. On the other hand, the simultaneous presence of competing hard scales, such as the transverse momentum (p_T) of the heavy quark, or the virtuality of the exchanged photon (Q^2), induces additional theoretical uncertainties due to terms in the perturbative expansion which depend logarithmically on the ratio of these scales. The comparison of the measured cross sections with theory predictions is therefore particularly sensitive to the way the perturbative expansion is made, and can therefore potentially discriminate how adequate a particular QCD scheme is for the decription of the cross section in question. This can also yield insights for other QCD processes at HERA, and for related processes at other colliders, including future measurements at the LHC.

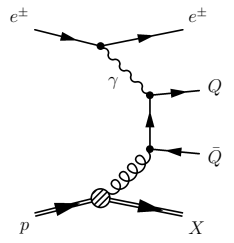

Figure 1: Feynman graph for the production of a heavy quark pair via the boson-gluon-fusion (BGF) process.

Since beauty in Deep Inelastic Scattering (DIS) is covered elsewhere [2], this contribution will concentrate on the photoproduction case ($Q^2 < 1$ GeV^2), in which the photon is quasi-real. For beauty photoproduction at HERA, possible theoretical schemes include

• The leading order plus parton shower approach, where leading order (LO) QCD matrix elements are complemented by parton showers, usually using the DGLAP [3] parton evolution equations. This approach is implemented in many Monte Carlo models, and mostly used for the purpose of acceptance corrections.

• The kt-factorization approach [4], which can alternatively be used for parton showering, combined with the use of generalized parton density functions.

• The next-to-leading order (NLO) massive approach [5]. In this approach, the heavy quark mass is fully accounted for, and heavy quarks are therefore always produced dynamically in the matrix element, as illustrated by Fig. 1. Alternative LO processes, such as flavour excitation in the photon or the proton, are treated as next-to-leading order corrections to this BGF process. Processes in which the photon acts as a hadron-like source of light quarks or gluons are also included, but make only a small contribution. This approach is expected to work best when all relevant hard scales, e.g. p_T, are of order m_b.

• For $p_T \gg m_b$, large $\log p_T/m_b$ terms could in principle spoil the reliability of the predictions. In this case, it might be preferable to switch to a so-called massless scheme, in

which the b mass is neglected kinematically. The potentially large logarithms can then be resummed to all orders (next-to leading log or NLL resummation). Since such an approach is obviously not applicable when $p_T \sim m_b$, schemes have been designed which make a continous transition between the fixed order (FO) massive, and the NLL massless scheme. This is often referred to as the FONLL scheme [6].

On the experimental side, several different methods are used to tag the beauty final state. The b quark can decay semileptonically into a muon or electron, which can be identified in the detector. The large momentum of the lepton transverse to the direction of the b-initiated jet, due to the sizeable b mass, can be used to discriminate against semileptonic charm decays or misidentified light flavour events. The finite lifetime of the B hadrons can lead to a measureable offset of the decay vertex with respect to the primary vertex of the event, which also leads to a significant impact parameter of the resulting secondary tracks. Finally, a lepton tag can e.g. be combined with a lifetime tag, with a second lepton tag, or with a D^* meson from a b decay.

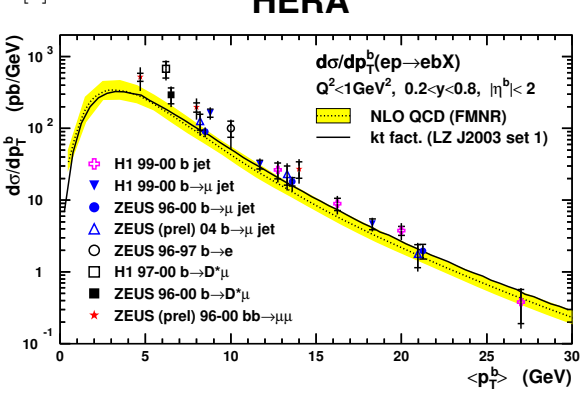

Figure 2: Beauty production cross section measurements in photoproduction at HERA as function of the transverse momentum of the b quark, compared to QCD predictions.

Fig. 2 shows a compilation of all recent HERA measurements of b photoproduction [7]. Reasonable agreement is found with both the fixed order NLO QCD prediction [5], and with a prediction based on kt factorization [8]. However, the data tend to lie somewhat above the central prediction in both cases.

A longstanding apparent discrepancy between data and theory in b production at the Tevatron was resolved by combining a more careful consideration of B fragmentation and decay parameters with an FONLL-based prediction [9]. This raises the question whether an FONLL predicton, which does not yet exist for b production at HERA, would yield an improved agreement.

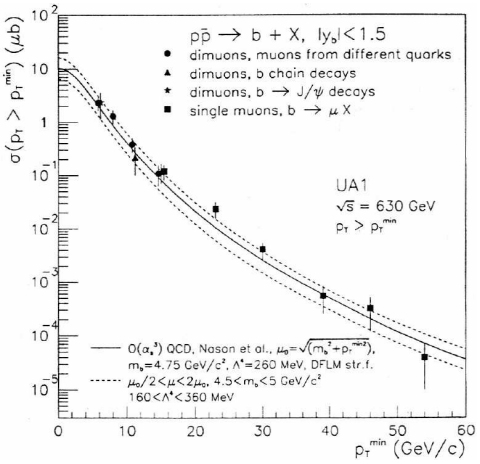

Figure 3: Integrated beauty production cross section at the $Sp\bar{p}S$ as function of the minimum p_T of the b quark, compared to NLO QCD predictions.

For this purpose, consider b production at the $Sp\bar{p}S$ collider, which had an effective parton-parton center-of-mass energy very similar to that of HERA. Fig. 3 shows the measured b quark cross section [10] compared to the original NLO calculation [11]. Good agreement was observed at a time when the Tevatron experiments were starting to claim a discrepancy. Fig. 4 shows the same original data [10] compared to the more recent FONLL calculation at b quark and B hadron level [9, 12], with identical

parameters as those used for the Tevatron. Good agreement is observed, also at muon level [12], even though NLO predictions at B hadron and muon level were not available when the measurements were made. This indicates that the B fragmentation and decay spectra, which had been studied carefully [10, 13], were treated consistently in these measurements. Furthermore, the NLO and FONLL predictions agree very well with each other, indicating that the large logs mentioned above do not yet play a significant role in this p_T range (similar to the one at HERA). This can also be seen in charm production at HERA [14] for which an FONLL prediction exists.

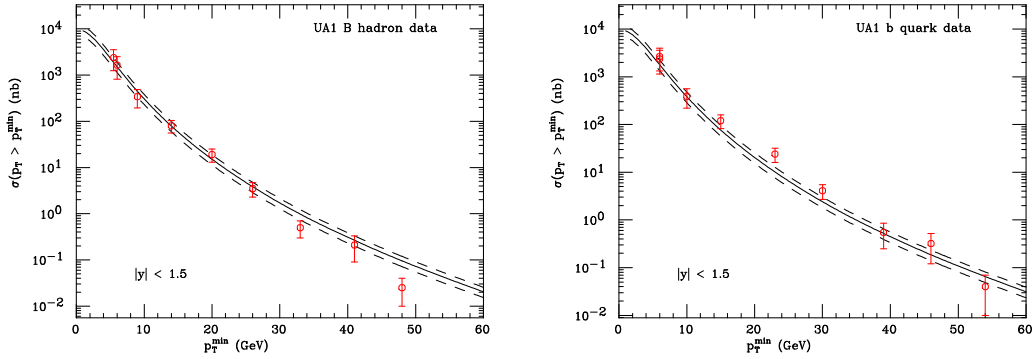

Figure 4: Integrated beauty production cross section at the $Sp\bar{p}S$ as function of the minimum p_T of the B hadron (left) and b quark (right), compared to preliminary FONLL QCD predictions [12].

In conclusion, an FONLL prediction for beauty production at HERA would be useful, but is not expected to significantly alter the data/theory comparison.

The dominant contribution to the theoretical error band of Fig. 1 is the variation of the renormalization/factorization scale by a factor 2 around the default scale $\mu_0 = \sqrt{m_b^2 + p_T^2}$. Such a variation is intended to reflect the uncertainty due to uncalculated higher orders. It might therefore be useful to reconsider this scale choice.

Ideally, in a QCD calculation to all orders, the result of the perturbatve expansion does not depend on the choice of these scales[a]. In practice, a dependence arises from the truncation of the perturbative series. Since this is an artefact of the truncation, rather than a physical effect, the optimal scale can not be "measured" from the data. It must thus be obtained phenomenologically.

Traditionally, there have been several options to choose the "optimal" scale, e.g.

• The "natural" scale of the process. This is usually taken to be the transverse energy (E_T) of the jet for jet measurements, the mass m of a heavy particle for the total production cross section of this particle, or the combination $\sqrt{m^2 + p_T^2}$ for differential cross sections of such a particle. Often, this is the only option considered. The choice of this natural scale is based on common sense, and on the hope that this will minimize the occurrance of large logs of the kind described above, for the central hard process. However, higher order subprocesses such as additional gluon radiation often occur at significantly smaller scales, such that this choice might not always be optimal.

[a] As is common practice, we will not distinguish between the factorization and renormalization scales in the following, and set both to be equal. A separate optimization of the two scales, which should be done in principle, will be left for future consideration.

• The principle of fastest apparent convergence (FAC) [15]. The only way to reliably evaluate uncalculated higher orders is to actually do the higher order calculation. Unfortunately, this is often not possible. Instead, one could hope that a scale choice which makes the leading order prediction identical to the next-to-leading order one would also minimize the NNLO corrections. Since it can not be proven, this principle, which can be found in many QCD textbooks, has not been used very much recently. However, recent actual NNLO calculations might indicate that it works phenomenologically after all (see below).
• The principle of minimal sensitivity (PMS) [16]. The idea is that when the derivative of the cross section with respect to the NLO scale variation vanishes, the NNLO crrections will presumably also be small. Again, there is no proof that this textbook principle should work, but actual NNLO calculations might indicate that it does (see below).

To illustrate these principles, consider two examples. First, the prediction for the total cross section for beauty production at HERA-B [17] (Fig. 5). The natural scale for this case is the b quark mass, $\mu_0 = m_b$, and all scales are expressed as a fraction of this reference scale. Inspecting Fig. 5, one finds that both the PMS and FAC principles, applied to the NLO prediction and to the comparison with LO (NLO stability), would yield an optimal scale of about half the natural scale. The same conclusion would be obtained by using the NLO+NLL prediction, including resummation, and comparing it to either the LO or the NLO prediction (NLO+NLL stability).

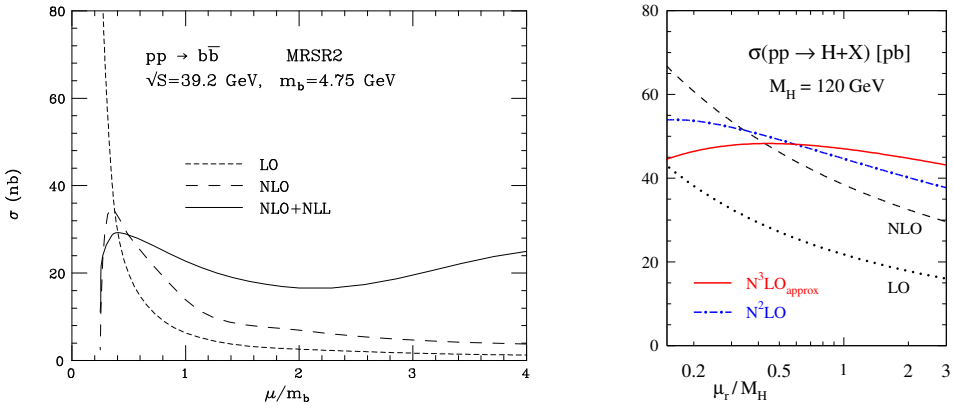

Figure 5: Scale dependence of the total cross section for beauty production at HERA-B [17] (left) and for Higgs production at LHC [18] for two different masses (right).

Second, the prediction for Higgs production at the LHC [18] (Fig. 5). The reference scale is now the Higgs mass ($\mu_0 = m_H$). However, inspecting the behaviour of the LO and NLO predictions, neither the FAC nor the PMS principle would yield a useful result in this case, since the two predictions do not cross, and the NLO prediction does not have a maximaum or minimum. This situation occurs rather frequently, and is also true for b production at HERA. Fortunately, in the case of Higgs production, the NNLO and even NNNLO predictions have actually been calculated (Fig 5). Applying the FAC and PMS prescriptions to these instead (NNLO stability), again a scale significantly lower than the default scale would be favoured. This might indicate that choosing a scale which is smaller than the default one makes sense even if the FAC and PMS principles do not yield useful values at NLO.

Beyond these examples, a more general study is needed to phenomenologically validate this approach. To avoid additional complications arising from a multiple scale problem caused by e.g. the scale Q^2 at HERA or the scale M_Z at LEP, the study was limited to cross sections for photoproduction at HERA, or hadroproduction at fixed target energies, the Tevatron, and LHC. The somewhat arbitrary selection of processes includes beauty production at the $Sp\bar{p}S$ [19, 20], the Tevatron [20], and HERA-B [17], top production at the Tevatron [17, 20], direct photon production at fixed target [21], Z [22] and Higgs [18] production at the LHC, jets at HERA [23] and at the Tevatron [24]. This selection is obviously not complete. However, it is not biased in the sense that all processes that were considered were included, and none were discarded.

In each case the natural scale as defined above was used as a reference. In addition, wherever possible, the optimal scales from both the FAC and PMS principles, evaluated at NLO (NLO stability), NLO+NLL (NLO+NLL stability), and/or NNLO/NNNLO (NNLO stability) were evaluated separately. Fig. 6 shows the result of this evaluation. Each crossing point, maximum, or minimum in Fig. 5 yields one entry into this figure, and similarly for all the other processes. The conclusion is that the FAC and PMS principles tend to favour scales which are around 25-60% of the natural scale. Amazingly, this seems to be independent of whether these principles are applied at NLO, NLO+NLL, or NNLO level. For the jet [24] or b-jet [25] cross sections at the Tevatron, it has in part already become customary to use half the natural scale as the central scale.

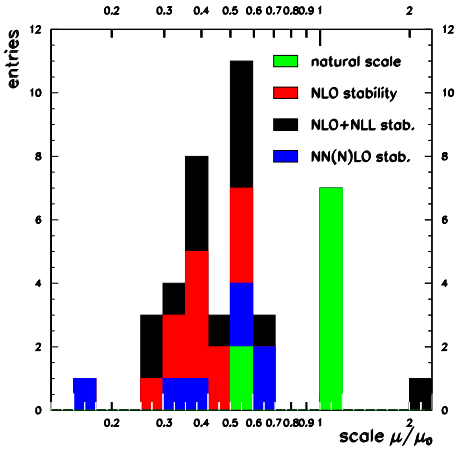

Figure 6: Summary of optimized scales derived as described in the text.

Using the natural scale as the default and varying it by a factor two, which is the choice adopted for most data/theory comparisons, covers only about half the entries, while the other half lies entirely below this range. Instead, using half the natural scale as the default and varying it by a factor two, thus still including the natural scale in the variation, covers about 95% of all the entries.

This yields the following conclusions.

• Obviously, whenever an NNLO calculation is available, it should be used.

• Whenever possible, a dedicated scale study should be made for each process for the kinematic range in question. Although there is no proof that the FAC and PMS principles should work, in practice they seem to give self-consistent and almost universal answers for processes at fixed target energies, HERA, the Tevatron, and the LHC.

• In the absence of either of the above, the default scale should be chosen to be *half* the natural scale, rather than the natural scale, in particular before claiming a discrepancy between data and theory. Empirically, this should enhance the chance that the NNLO calculation, when it becomes available, will actually lie within the quoted error band.

Now consider the application of the last proposal to actual data/theory comparisons.

Fig. 7 shows the resulting comparison for beauty production at HERA. Although before the change of the default scale the agreement was already quite reasonable, the new choice, based on theoretical/phenomenological arguments, improves the agreement. A similar statement [1] can qualitatively be made for beauty production at the $Sp\bar{p}S$ [10], the Tevatron [26], and even at RHIC [27], where a discrepancy has been claimed. The agreement with charm production at HERA [14] as well as charm [28] and top [29] production at the Tevatron also improves, or at least does not get worse. The same is true for inclusive jets at HERA, both in DIS [30] and in photoproduction [23]. In one case [31] half the scale has already been used in a published HERA result.

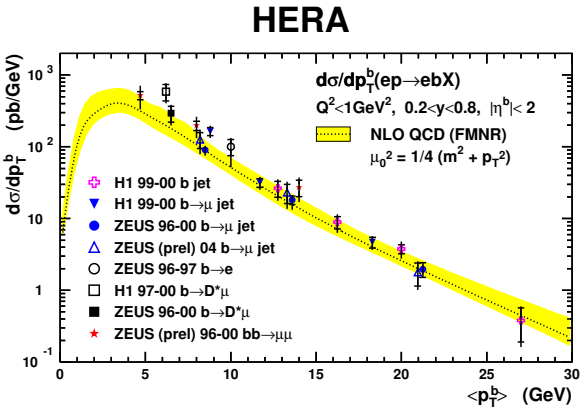

Figure 7: Beauty production cross section measurements in photoproduction at HERA as function of the transverse momentum of the b quark, compared to QCD predictions.

So far, no example is known to the author where the proposed change of default scale would result in a significant worsening of the data/theory agreement in a photo- or hadroproduction cross section. Thus, the phenomenologically motivated change seems to be supported by the data. It should therefore be considered to make it the default for future predictions at HERA, the Tevatron, and the LHC.

The investigations of the photon quark coupling are reported elsewhere [1].

References

[1] Slides:
http://indico.cern.ch/materialDisplay.py?contribId=234&sessionId=5&materialId=slides&confId=9499

[2] B. Kahle, these proceedings.

[3] V.N. Gribov and L.N. Lipatov, Yad. Fiz. **15** (1972) 781;
L.N. Lipatov, Sov. J. Nucl. Phys. **20** (1975) 94;
G.Altarelli, G. Parisi, Nucl. Phys. **B126** (1977) 298;
Y.L. Dokshitzer, Sov. Phys. JETP **46** (1977) 641.

[4] M. Ciafaloni, Nucl. Phys. **B 296** (1988) 49;
S. Catani, F. Fiorani, and G, Marchesini, Phys. Lett. **B234** (1990) 339;
S. Catani, F. Fiorani, and G. Marchesini, Nucl. Phys. **B336** (1990) 18;
G. Marchesini, Nucl. Phys. **B 445** (1995) 49.

[5] S. Frixione, P. Nason and G. Ridolfi, Nucl. Phys. B **454** (1995) 3 [hep-ph/9506226].

[6] M. Cacciari, S. Frixione and P. Nason, JHEP **0103** (2001) 006 [hep-ph/0102134].

[7] J. Breitweg *et al.* [ZEUS Collaboration], Eur. Phys. J. **C 18** (2001) 625 [hep-ex/0011081];
S. Chekanov *et al.* [ZEUS Collaboration], Phys. Rev. D **70** (2004) 012008 [hep-ex/0312057];
A. Aktas *et al.* [H1 Collaboration], Eur. Phys. J. **C 41** (2005) 453 [hep-ex/0502010];
A. Aktas *et al.* [H1 Collaboration], Phys. Lett. **B 621** (2005) 56 [hep-ex/0503038];
S. Chekanov *et al.* [ZEUS Collaboration], Eur. Phys. J. **C 50** (2007) 299 [hep-ex/0609050];
A. Aktas et al. [H1 Collaboration], Eur. Phys. J. **C 47** (2006) 597 [hep-ex/0605016];
ZEUS Collaboration, contributed paper 269, XXII International Symposium on Lepton-Photon Interactions at High Energy, Uppsala, Sweden, 2005.

[8] A.V. Lipatov, N.P. Zotov Phys. Rev. **D73** (2006) 114018 [hep-ph/0601240].

[9] M. Cacciari, P. Nason, Phys. Rev. Lett. **89** (2002) 122003 [hep-ph/0204025].

[10] C. Albajar *et al.* [UA1 Collaboration] Z. Phys. **C 61** (1994) 41;
C. Albajar *et al.* [UA1 Collaboration] Phys. Lett. **B 256** (1991) 121;
Erratum in Phys. Lett. **B 262** (1991) 497.
[11] M.L. Mangano, P. Nason, and G. Ridolfi, Nucl. Phys. **B373** (1993) 295.
[12] M. Cacciari, private communication.
[13] A. Geiser, PhD thesis, Aachen, Germany, PITHA 92/31, Oct 1992.
[14] J. Baines et al., *Heavy quarks (Working Group 3): Summary Report for the HERA-LHC Workshop Proceedings*, hep-ph/0601164.
[15] see e.g. G. Grunberg, Phys. Lett. **B 95** (1980) 70.
[16] P. M. Stevenson, Phys. Rev. **D23** (1981) 2916.
[17] R. Bonciani et al., Nucl. Phys. **B529** (1998) 424 [hep-ph/9801375].
[18] S. Moch and A. Vogt, Phys. Lett. **B 631** (2005) 48 [hep-ph/0508265].
[19] C. Albajar et al. [UA1 Collaboration], Phys. Lett. **B369**(1996) 46.
[20] S. Frixione et al., Adv. Ser. Direct. High Energy Phys. **15** (1998) 609 [hep-ph/9702287].
[21] S. Catani et al., JHEP 9903 (1999) 025 [hep-ph/9903436]
[22] C. Anastasiou et al., Phys. Rev. **D 69** (2004) 094008 [hep-ph/0312266].
[23] S. Chekanov et al. [ZEUS Collaboration], DESY-07-092 [hep-ex/0706.3809]
[24] A. Abulencia et al. [CDF Collaboration], Phys. Rev. **D75** (2007) 092006.
[25] S. Vallecorsa [CDF Collaboration], these proceedings.
[26] B. Reisert [CDF Collaboration], these proceedings.
[27] A. Mischke [STAR Collaboration], these proceedings.
[28] M. Bishai [CDF Collaboration] Phys. Rev. Lett. **91** (2003) 241804.
[29] CDF Collaboration, Preliminary Conf. Note 8148.
[30] A. Aktas et al. [H1 Collaboration], Eur. Phys. J. **C46** (2006) 27.
[31] S. Chekanov et al. [ZEUS Collaboration] Eur. Phys. J. **C44** (2005) 183 [hep-ex/0502007].

$F_2^{b\bar{b}}$ from the ZEUS HERA-II Data

Benjamin Kahle[1] on behalf of the ZEUS collaboration

1- Deutsches Elektronen-Synchrotron DESY
Hamburg, Germany

Beauty production in deep inelastic scattering with events in which a muon and a jet are observed in the final state has been measured with the ZEUS detector at HERA II using an integrated luminosity of 39 pb^{-1}. The fraction of beauty quarks in the data was determined using the distribution of the transverse momentum of the muon relative to the jet. The cross section for beauty production was measured in the kinematic range $Q^2 > 4$ GeV^2, $0.05 < y < 0.7$ and requiring a muon with $p_T^\mu > 1.5$ GeV and $\eta^\mu > -1.6$ and a jet with $E_T^{jet} > 5$ GeV and $-2 < \eta^{jet} < 2.5$. Differential cross sections in Q^2, p_T^μ, η^μ, p_T^{jet} and η^{jet} are compared to theory. Furthermore $F_2^{b\bar{b}}$, the beauty contribution to the structure function F_2, is obtained and compared to theoretical predictions.

1 Introduction

This paper reports the first ZEUS measurement at HERA II of beauty production in deep inelastic scattering (DIS), in the reaction with at least one jet and one muon in the final state: $ep \rightarrow e\ b\bar{b}\ X \rightarrow e\ jet\ \mu\ X'$. The analysis described here measures in an extended kinematic region compared to the previous ZEUS analysis of HERA I data [2] and uses a combination of multiple detector components for muon identification. This allows a lower muon transverse momentum threshold and a higher detection efficiency to investigate these regions of phase space further.
Due to the large b-quark mass, muons from semi-leptonic b-decays usually have high values of p_T^{rel}, the transverse momentum of the muon with respect to the axis of the closest jet. For muons from charm decays and in events induced by light quarks, where some of the produced hadrons are misidentified as muons, the p_T^{rel} values are lower. Therefore, the fraction of events from b-decays in the data sample can be extracted by fitting the p_T^{rel} distribution of the data to Monte Carlo (MC) simulations of the processes producing beauty, charm and light quarks. In this analysis a total visible cross section, and differential cross sections are compared to leading order (LO) plus parton shower (PS) MC predictions and next-to-leading-order (NLO) QCD calculations. Furthermore the beauty contribution to the proton structure function F_2 is measured for different Q^2 and x values and compared to theoretical predictions.

2 Data sample and selection

The data used in this measurement were collected during the 2003-2004 HERA II running period, where a proton beam of 920 GeV collided with a positron beam of 27.5 GeV, corresponding to an integrated luminosity of 39.1 pb^{-1}. A detailed description of the ZEUS detector can be found elsewhere [3].
Events were selected by requiring the presence of at least one muon and one jet in the final state. The final sample was selected in four steps: 1) inclusive DIS event selection, requiring a well reconstructed outgoing positron with energy greater than 10 GeV, $Q^2 > 4$ GeV^2 and

inelasticity $0.05 < y < 0.7$. 2) Muon finding, using different components of the ZEUS detector, yielding an efficiency of about 80% at high momentum. Cuts on $p_T^\mu > 1.5$ GeV and $\eta^\mu > -1.6$ were applied. 3) Jet finding with hadronic final-state objects, using the k_T cluster algorithm (KTCLUS) [4]. Selected events contained at least one jet with $E_T^{jet} > 5$ GeV within the detector acceptance $-2 < \eta^{jet} < 2.5$. 4) Muon-jet association, requiring a jet and a muon within a cone of $R = \sqrt{\delta\phi^2 + \delta\eta^2} < 0.7$.
The final data sample contained 4734 events. To correct the data for detector acceptance and to extract the beauty fraction, the RAPGAP 3 MC simulation [5] was used to generate signal (beauty) and background (charm) events. RAPGAP is a generator based on LO matrix elements, with higher-order QCD radiation simulated in the leading-logarithmic approximation. The hadronisation is simulated using the Lund string model as implemented in JETSET [6]. The background from light flavours was simulated using DJANGO [7]. It has been checked on a hadronic background sample of data and MC, that the DJANGO MC describes the shape of the p_T^{rel} distribution reasonably well. Some small differences are treated as a contribution to the systematic error.

3 Experimental Method

3.1 Extraction of the b-signal

The light flavour and charm quark MC samples were mixed according to their relative luminosities and the b-quark sample was added according to the beauty fraction determined from the p_T^{rel} analysis. Figure 1 shows the p_T^{rel}-distribution as measured in the ZEUS detector for the data and MC. To determine the beauty fraction in the data, the contribution from light flavour plus charm, and beauty, were allowed to vary and fitted to the data using the χ^2-method. The obtained beauty fraction is $f_{beauty} = 21 \pm 2\%(\text{stat.})$. The sum of the MC contributions shown in Fig. 1 describes the data well.
Using this method, the total visible cross section, differential cross sections in Q^2, p_T^μ, η^μ, p_T^{jet} and η^{jet} and double differential cross sections $d^2\sigma_{meas}^{b\bar{b}\to\mu}/dxdQ^2$ can be obtained.

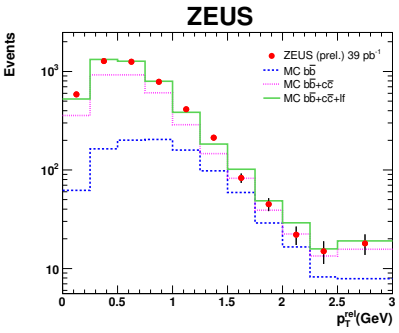

Figure 1: Measured p_T^{rel}-distribution for the data and fitted MC.

3.2 Calculation of $F_2^{b\bar{b}}$

In order to obtain $F_2^{b\bar{b}}$, the beauty contribution to F_2, cross sections in bins of Q^2 and x have been measured. The inclusive double differential cross section at low to medium Q^2 can be expressed in terms of structure functions:

$$\frac{d^2\sigma^{ep}}{dxdQ^2} = \frac{2\pi\alpha^2}{Q^4 x}\Big(\big[1+(1-y)^2\big]F_2(x,Q^2) - y^2 F_L(x,Q^2)\Big).$$

If the small contribution from F_L is neglected, the inclusive cross section is proportional to $F_2(x,Q^2)$. In complete analogy, the cross section of events containing a $b\bar{b}$-pair ($ep \to b\bar{b}X$)

is proportional to $F_2^{b\bar{b}}(x, Q^2)$.
The reduced b-cross section is defined as:

$$\tilde{\sigma}^{b\bar{b}}(x, Q^2) = \frac{d^2\sigma^{b\bar{b}}}{dxdQ^2} \frac{xQ^2}{2\pi\alpha^2(1 + (1 - y)^2)}$$

where $\tilde{\sigma}^{b\bar{b}}(x, Q^2)$ is calculated using the fixed flavour number scheme (FFNS) NLO. In terms of the measured double differential cross section, the reduced cross section is given as:

$$\tilde{\sigma}^{b\bar{b}}_{meas}(x, Q^2) = \tilde{\sigma}^{b\bar{b}}_{NLO}(x, Q^2) \frac{d^2\sigma^{b\bar{b}\to\mu}_{meas}}{dxdQ^2} \Big/ \frac{d^2\sigma^{b\bar{b}\to\mu}_{NLO}}{dxdQ^2}$$

using the ratio of measured to calculated double differential cross sections for the reaction $ep \to e\ b\bar{b}\ X \to e\ jet\ \mu\ X'$. The extrapolation factor from the measured to the full phase-space lies between 6 for low Q^2 and 3 at high Q^2. This includes the extrapolation of the p_T^b and η^b spectrum, fragmentation and decay kinematics for jet and μ and the η and p_T cuts on the muon and the jet. The branching fraction of $b\bar{b}$ to μ of 0.3924 is not included in these extrapolation factors.

4 Results

A total visible cross section of $\sigma_{b\bar{b}} = 77.1 \pm 7.8(\text{stat.}) \pm^{9.6}_{14.9}$ (syst.) pb was measured for the reaction $ep \to e\ b\bar{b}\ X \to e\ jet\ \mu\ X'$ in the kinematic region defined by: $Q^2 > 4\ \text{GeV}^2$, $0.05 < y < 0.7$, $p_T^\mu > 1.5\ \text{GeV}$, $\eta^\mu > -1.6$ and one jet with $E_T^{jet} > 5\ \text{GeV}$ and $-2 < \eta^{jet} < 2.5$ associated to the muon. The systematic uncertainty is the quadratic sum of different individual uncertainties coming from the muon-efficiency correction, p_T^{rel}-shape for light flavours, ratio of light flavours to charm, energy scale and luminosity uncertainty. This result was compared to a NLO QCD calculation from HVQDIS [8], which uses the FFNS, after folding the b-quark momentum spectrum with a Peterson fragmentation function and subsequently with a spectrum of the semi-leptonic muon momentum extracted from RAPGAP [5]. A mixture of direct ($b \to \mu$) and indirect ($b \to c \to \mu$ and $b \to \tau \to \mu$) b-hadron decays to muons has been used. The b-quark mass was set to $m_b = 4.75$ GeV and the renormalisation and factorisation scales to $\mu = \sqrt{p_T^2 + 4m_b^2}$. The CTEQ5F4 parton densities [9] have been used. The NLO QCD prediction is $\sigma_{NLO} = 32.9 \pm 3.3$ pb, where the error has been estimated by varying the scale μ by a factor of 2 and 1/2 and the mass m_b between 4.5 and 5.0 GeV. The measured total cross section is about 2σ higher than the NLO prediction. The differential cross sections were measured in the same kinematic range as the total visible cross section by repeating the fit of the p_T^{rel}-distribution in each bin. Differential cross sections as a function of Q^2, p_T^μ, η^μ, p_T^{jet} and η^{jet} are shown in [1]. In all distribution the data are

PDF	Order	Scheme	μ^2	M_b(GeV)
MRST04	α_s^2	VFNS	Q^2	4.3
MRST NNLO	α_s^3	VFNS	Q^2	4.3
CTEQ6.5	α_s^2	VFNS	$Q^2 + M^2$	4.5
HVQDIS+CTEQ5F3	α_s^2	FFNS	$p_T^2 + 4M^2$	4.75

Table 1: PDF schemes and parameters, the first three are taken from [14, 15].

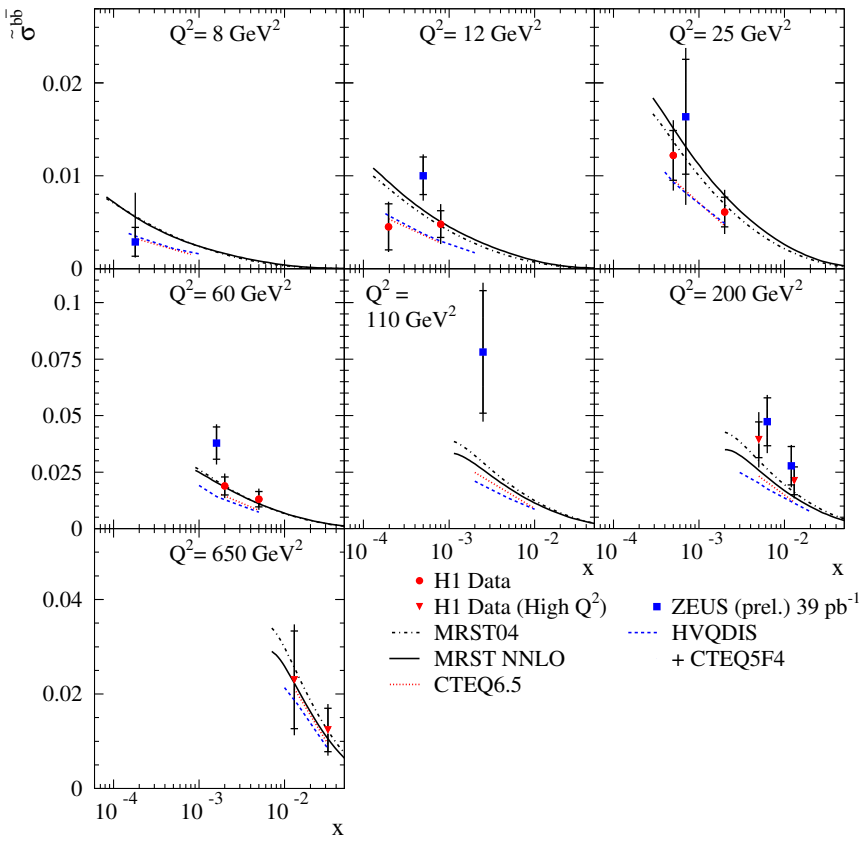

Figure 2: The measured reduced cross section shown as a function of x for different values of Q^2, together with measurements from H1 [10]. Different QCD predictions (see Tab.1) are also shown.

described in shape by the MC and by the NLO QCD calculation. The constant factor between the normalisation of the data and the NLO QCD calculations in these distributions reflects the 2σ difference seen in the total cross section. The $F_2^{b\bar{b}}$ measurements are shown in Figure 2 together with values from H1 [10]. The HVQDIS + CTEQ5F4 prediction and other predictions from NLO calculations using the variable flavour number scheme (VFNS) with different parameters (see Table 1) are shown. The ZEUS data lie above the H1 data, but are compatible within uncertainties. The large spread between the theory curves is partially caused by the use of different scales (see Tab. 1) and partially by the different treatment of the flavour threshold within VFNS between the MRST [11] and CTEQ6.5 [12, 13] predictions.

5 Conclusions

The production of beauty quarks in the deep inelastic scattering (DIS) process $ep \rightarrow e\ b\bar{b}\ X \rightarrow e\ jet\ \mu\ X'$ has been measured with the ZEUS detector at HERA II. The total visible cross section is 2σ higher than the NLO prediction. Differential cross sections $d\sigma/dQ^2$, $d\sigma/dp_T^{\mu}$, $d\sigma/d\eta^{\mu}$, $d\sigma/dp_T^{jet}$ and $d\sigma/d\eta^{jet}$ were measured. In all distributions the data are described in shape by the MC and by the NLO QCD calculation. $F_2^{b\bar{b}}$ results agree with results from H1, where a very different method was used to obtain $F_2^{b\bar{b}}$, with similar uncertainties. The measured values of $F_2^{b\bar{b}}$ are found to be described by perturbative QCD predictions within the large uncertainties.

References

[1] Slides:
`http://indico.cern.ch/contributionDisplay.py?contribId=236&sessionId=5&confId=9499`

[2] ZEUS Coll., S. Chekanov et al., Phys. Rev. **D 70**, 12008 (2004)

[3] ZEUS Coll., U. Holm (ed.), *The ZEUS Detector*. Status Report (unpublished), DESY (1993), available on `http://www-zeus.desy.de/bluebook/bluebook.html`

[4] S.D. Ellis and D.E. Soper, Phys. Rev. **D 48**, 3160 (1993)

[5] H. Jung, Comp. Phys. Comm. **86**, 147 (1995)

[6] T. Sjöstrand, Comp. Phys. Comm. **82**, 74 (1994)

[7] G.A. Schuler and H. Spiesberger, *Proc. Workshop on Physics at HERA, W. Buchmüller and G. Ingelman (eds.)*. Vol. 3, p. 1419, Hamburg, Germany, DESY (1991)

[8] B.W. Harris and J. Smith, Phys. Rev. **D 57**, 2806 (1998)

[9] CTEQ Coll., H.L. Lai *et al.*, Eur. Phys. J. **C 12**, 375 (2000)

[10] H1 Coll., Eur. Phys. J. **C 45**, 23 (2006)

[11] A.D. Martin, W.J. Stirling and R.S. Thorne, Phys. Lett. **B 636**, 259 (2006)

[12] W.K. Tung, *et al.*, Preprint hep-ph/0611254, 2006

[13] W.K. Tung. Private communication

[14] P.D. Thompson, Preprint hep-ph/0703103, 2007

[15] P.D. Thompson. Private communication

Studies of B Hadron Rare Decays and Lifetimes at the TeVatron

M. D. Corcoran
for the CDF and D0 Collaborations

Rice University - Department of Physics and Astronomy
Houston, TX 77005 - USA

The TeVatron collider at Fermilab is working well, and both the CDF and D0 experiments are collecting high-quality data at an impressive rate. The B physics program at the TeVatron is producing a wide range of new results. In this talk [1] I summarize recent results for the search for the decays $B_s(B_d) \to \mu\mu$ and B hadron lifetimes.

1 $B_s \to \mu\mu$ and $B_d \to \mu\mu$

The decays $B_s \to \mu\mu$ and $B_d \to \mu\mu$ are flavor changing neutral current decays in the Standard Model and are therefore highly suppressed. The decay $B_d \to \mu\mu$ is suppressed even more by the ratio of the CKM matrix elements V_{td}/V_{ts}. Figure 1 shows the relevant Standard Model Feynman diagrams for $B_s \to \mu\mu$. The Standard Model expectations for these modes are $BR(B_s \to \mu\mu) = 3.42 \pm 0.54 \times 10^{-9}$ and $BR(B_d \to \mu\mu) = 1.0 \pm 0.14 \times 10^{-10}$[2], still far from the current experimental limits. But many models for physics beyond the Standard Model, particularly Supersymmetry, enhance these branching ratios by orders of magnitude. Therefore observation of $B_s(B_d) \to \mu\mu$ would be evidence for new physics.

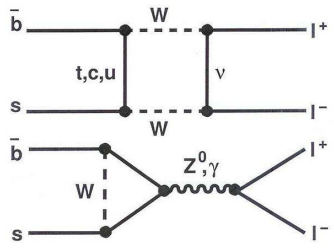

Figure 1: Standard Model diagrams for the decay $B_s \to \mu\mu$.

The new D0 limit on this decay mode, based on about 2fb^{-1} data, is the first physics result from D0 to use their L0 silicon detector. L0, inserted during the spring 2006 shutdown, provides a substantial improvement in identification and measurement of displaced vertices.

The D0 search for $B_s \to \mu\mu$ requires two muons with $p_t > 2.5$GeV and $|\eta| < 2$ which form a good vertex. A likelihood ratio (LHR) is formed using six variables: muon isolation, transverse decay length significance, B impact parameter, minimum μ impact parameter, vertex χ^2 probability, and pointing angle (the angle between the vector from the primary to the secondary vertices and the momentum of the reconstructed dimuon system). For each variable a probability density function (PDF) is determined for both signal (from Monte Carlo) and background (from $M_{\mu\mu}$ sidebands). The likelihood ratio for each event is then

$$\mathcal{L} = \frac{\prod S_i}{\prod S_i + \prod B_i}$$

where S_i is the PDF for the signal and B_i is the PDF for the background for variable i. If the variables do a good job of distinguishing signal from background, $\mathcal{L}$ is peaked near 1 for signal and near 0 for background. The left side of Figure 2 shows the LHR for signal Monte Carlo and background, with the cut indicated by the arrow. The right side of figure 2 shows the LHR vs. $M_{\mu\mu}$ plot for the RunIIa (pre-upgrade) dataset, with the final signal region in

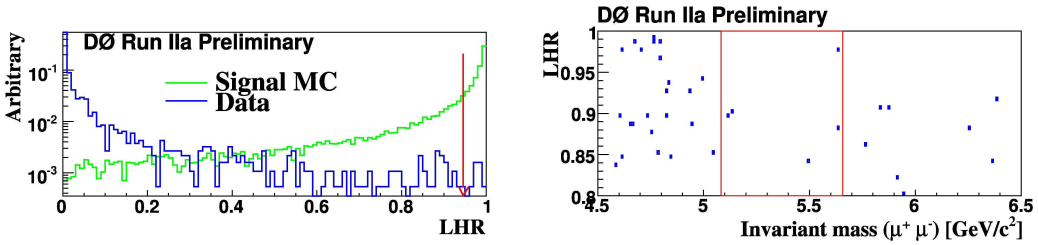

Figure 2: D0 result for the LHR for signal and background (left); the arrow indicates the value of the cut in LHR. The right plot is the LHR vs. $M_{\mu\mu}$ for the RunIIa (pre-upgrade) dataset.

dimuon mass indicated. In the RunIIa dataset, one event passes both LHR and mass cuts, while in the RunIIb dataset two events pass both cuts. The expected total background is 2.3 $\pm$ 0.36, so no excess of events over background is observed. The total flux of B_s decays for this data sample is determined from the normalization mode $B^+ \to J/\psi K^+$ with $J/\psi \to \mu\mu$. The 95% CL limit is $BR(B_s \to \mu\mu) < 9.3 \times 10^{-8}$, which is 27 times the Standard Model expectation. More information on this analysis can be found in the D0 conference note [3]

CDF has a recent result for both $B_s(B_d) \to \mu\mu$ based on 780 pb^{-1} of data.[4] Their data is divided into two subsets, one subset having both muons in their central muon detector (CMU), and the other subset allowing one muon to be in their central muon extension (CMX). For the first subset, both muons must have $p_t > 2$ GeV and $|\ \eta\ | < 0.6$. For muons in the CMX, the requirements are $p_t > 2.2$ GeV and $0.6 < |\ \eta\ | < 1.0$. The p_t of the muon pair must be greater than 4 GeV, and they must form a good vertex. In this analysis, a likelihood ratio is formed from three variables: the B isolation, the 3D pointing angle, and the probability of $c\tau$, given the known $B_s(B_d)$ lifetime. Figure 3 left shows the LHR distributions for signal and background. Figure 3 right shows the final LHR vs. dimuon mass, with the signal regions indicated. For B_s one event is observed with an expected background of 1.27 $\pm$ 0.37, and for B_d two events are observed with an expected background of 2.45 $\pm$ 0.40. Again there is no excess over the expected background. CDF has also used the normalization mode $B^+ \to J/\psi K^+$ with $J/\psi \to \mu\mu$. The resulting limits at 95% CL are $BR(B_s \to \mu\mu) < 1.0 \times 10^{-7}$ and $BR(B_d \to \mu\mu) < 2.3 \times 10^{-8}$ which are 20 and 230 times the Standard Model expectation, respectively.

We can (unofficially) combine the CDF and D0 limits to obtain a combined 95% CL limit $BR(B_s \to \mu\mu) < 5.8 \times 10^{-8}$, about 17 times the SM expectation. Both experiments have substantially more data, so this limit can be expected to improve in the near future.

2 B Hadron Lifetime Measurements

Lifetimes for B hadrons can be calculated in Heavy Quark Expansion models[5], so precision measurements of lifetimes are good tests of this model. D0 has recent measurements on Λ_b, both through the exclusive channel $\Lambda_b \to J/\Psi\Lambda$ with $J/\psi \to \mu\mu$, and through the semileptonic channel $\Lambda_b \to \Lambda_c \mu\nu X$ with $\Lambda_c \to K_s p$. CDF has a measurement in the exclusive channel only.

Figure 4 shows the CDF result [6] for the Λ_b mass and $c\tau$ distribution in the exclusive mode mentioned above. There are 532 candidate events, and a maximum likelihood fit on

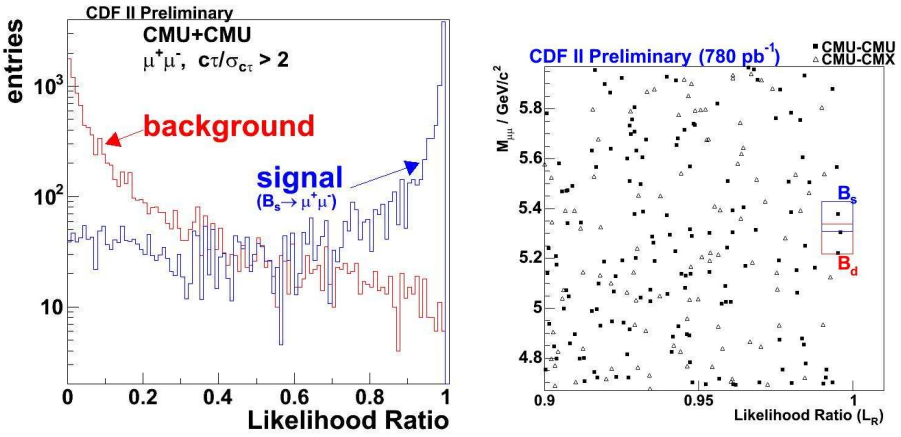

Figure 3: CDF result for the likelihood ratio for signal and background (left) and likelihood ratio vs. $M_{\mu\mu}$ (right) for the data.

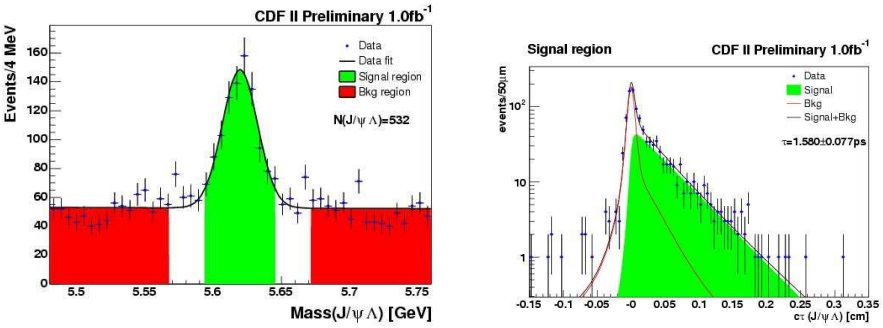

Figure 4: CDF results: Λ_b mass distribution for fully-reconstructed decays (left) and the $c\tau$ distribution for Λ_b candidates.

three variables (mass, $c\tau$ and $c\tau$ error) yields the lifetime measurement shown in figure 5.

The first D0 measurement of the Λ_b lifetime is based on 172 $\pm$ 21 events in the same exclusive mode. D0 has also measured the Λ_b lifetime in the semileptonic mode, which has much higher statistics but also much higher background. [7] The Λ_b lifetime from the semileptonic mode yields 4437 $\pm$329 events. Figure 5 shows the world data on the Λ_b lifetime. There is about a 2 standard deviation discrepancy on the Λ_b lifetime between CDF and D0. Both experiments have significantly more data, so one would expect this discrepency to be resolved soon.

CDF has also made precision measurements for $B^+ \to J/\psi K^+$, $B^0 \to J/\psi K^*$ or $J/\psi K^*$, and $B_s \to J/\psi\Phi$. All are in good agreement with previous measurements and with expectations. Figure 5 right shows the world data on the ratio of lifetimes $\tau(B^+)/\tau(B^0)$.

More information on all these measurements is available on the excellent websites of both

experiments [8].

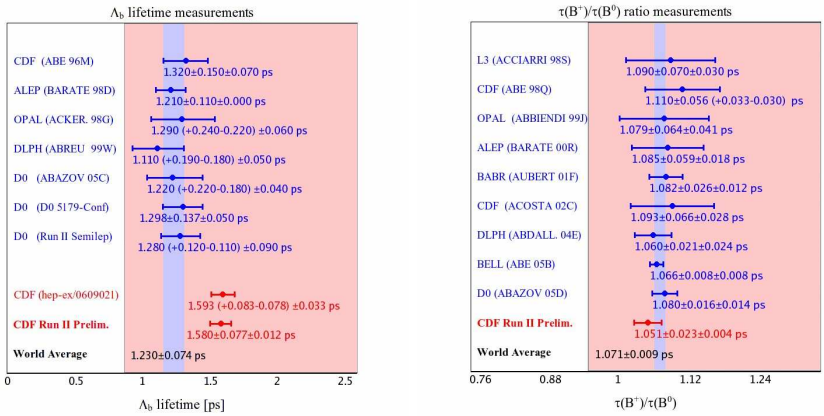

Figure 5: World results for the Λ_b lifetime (left) and for the $\tau(B^+)/\tau(B^0)$ (right).

References

[1] `http://indico.cern.ch/contributionDisplay.py?contribId=203&sessionId=5&confId=9499`

[2] A. J. Buras, Phys. Lett. **B566**, 115 (2003).

[3] D0 conference note D05344-CONF, available from the website noted below.

[4] CDF public note 8176, available from the website noted below.

[5] F. Gabbiani, Phys. Rev. **D68** 114006 (2003).

[6] CDF public note 8524.

[7] Fermilab-Pub-07/094-E (submitted to Phys. Rev. Lett.)
Fermilab-Pub-07/205-E (submitted to Phys. Rev. Lett.)

[8] http://www-cdf.fnal.gov/physics/new/bottom/bottom.html
http://www-d0.fnal.gov/Run2Physics/WWW/results.b.htm

Recent Charmonium Results form HERA-B

Martin zur Nedden *

Humboldt-Universität zu Berlin, Institut für Physik
Newtonstrasse 15, 12489 Berlin - Germany

HERA-B is a fixed-target multi-particle spectrometer experiment at the 920 GeV HERA proton beam at DESY. Approximately 150 million events were recorded with a dilepton trigger during the 2002/2003 HERA run. About 300,000 leptonic $J/\psi \to l^+l^-$ decays (170,000 in the $\mu^+\mu^-$ channel and 130,000 in the e^+e^- channel) have been reconstructed in this data sample. In addition, a huge sample of 220 million minimum biased triggered events were recorded, allowing an independent measurement of the J/ψ production cross section.

The dilepton triggered samples allow for the first time the study of charmonium production in the negative Feynman-x (x_F) region, and will provide an important input for testing the charmonium production mechanism. Results will be presented on the nuclear dependence of charmonium production, on J/ψ, χ_c and ψ' production and on their differential distributions. Furthermore, the first measurement of the nuclear suppression of charmonium production in the negative x_F region will be presented.

1 Introduction

In the data taking period of 2002/2003 HERA-B was routinely running and collected $164{\cdot}10^6$ events applying a dilepton J/ψ–trigger. HERA-B is able to reconstruct the decays of J/ψ, ψ', χ_c or Υ either in the $\mu^+\mu^-$ or in the e^+e^- decay channel. In Fig. 1 the J/ψ and ψ' peaks in the invariant mass spectra of the whole data sample are shown, corresponding to a total statistics of $N(J/\psi) \approx 300'000$ and $N(\psi') \approx 5'000$ for both decay channels. The availability of both channels is, besides the increase of statistics, crucial to cross check the results.

The target wires, close to the 920 GeV proton beam of HERA, are made of different materials (Carbon, Tungsten or Titanium) which can be used simultaneously to perform measurements of the dependence on the atomic mass number A and to control systematic effects. This enables a measurement of the nuclear dependence of the J/ψ-production by using two wires of different materials in parallel.

In order to minimize the sensitivity to systematic effects from luminosity and Monte Carlo (MC) efficiency determination, all cross section measurements are performed relative to the J/ψ production cross section. In the ratio of cross sections, the luminosity dependence and common systematic effects in the efficiency cancel out. To determine the reference value of $\sigma_{pN}(J/\psi)$ at the HERA-B energy, a global analysis has been performed on all available published J/ψ cross section measurements including the measurement of HERA-B using a sample of $2.3 \cdot 10^8$ minimum bias triggered events, which are independent from the J/ψ triggered data [2] (Fig. 1, right). The best value, obtained from a fit on $\sigma_{J/\psi}(\sqrt{s})$ with the help of a non relativistic QCD inspired model including color octet (NRQCD) [3], is for the energy of HERA–B of $\sqrt{s} = 41.6$ GeV

$$\sigma_{J/\psi} = (502 \pm 44)\,\text{nb/nucl.} \quad \text{and} \quad \sigma_{\psi'} = (65 \pm 11)\,\text{nb/nucl.} \tag{1}$$

*for the HERA-B Collaboration

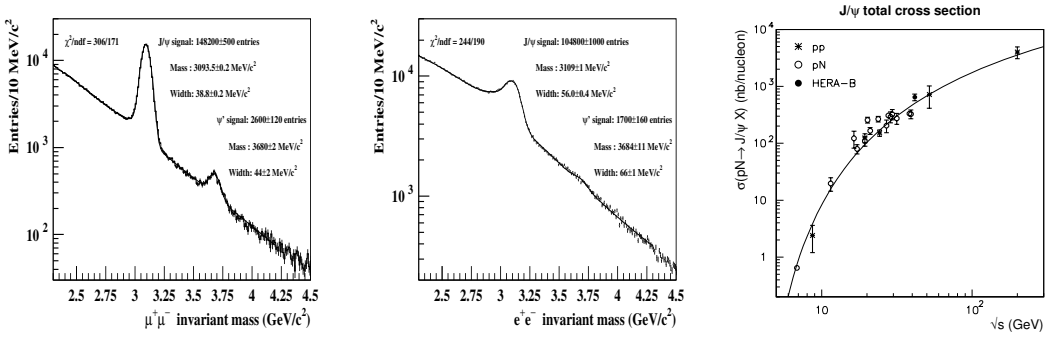

Figure 1: J/ψ production signal in the invariant mass spectra for both decay channels of triggered data and the determination of the J/ψ reference cross section using minimum biased data from HERA-B and result from other experiments.

leading to a ratio of $R_\psi = (0.130 \pm 0.019)$. The $\sigma_{J/\psi}$ value, which is in pretty good agreement to the other experiments, will be used for all further analysis as reference cross section.

2 Charmonium Production

2.1 Kinematical J/ψ Distributions

A good understanding of the kinematical distributions of J/ψ and ψ' production as a function of x_F and p_T^2 is the basis for further measurements and interpretations of all effects causing nuclear suppression or enhancement of charmonium production in nuclear interactions. With respect to the earlier experiments in that field, HERA-B is the first fixed target experiment covering the region of negative Feynmann-x ($x_F = \frac{p_L^{\rm cms}}{(p_L^{\rm cms})_{\rm max}}$) in the range of $x_F \in [-0.35, 0.15]$. The negative x_F region corresponds to small forward momenta of the produced $c\bar{c}$ pair leading to a formation of the J/ψ inside the nucleus. Since the p_T coverage of the older experiments is mostly overlapping with HERA-B, a good opportunity for cross checks is given.

Usually, the kinematical distributions are parameterized by the following interpolating shape functions provided by the Experiment E705 [4]:

$$\frac{d\,N}{d\,x_F} \propto \frac{\Big((1-x_1)\cdot(1-x_2)\Big)^C}{x_1+x_2} \quad \text{and} \quad \frac{d\,N}{d\,p_T^2} \propto A\left(1+\left(\frac{35\,\pi}{256}\cdot\frac{p_T}{\langle p_T\rangle}\right)^2\right)^{-6}$$

where $x_{1,2} = \frac{1}{2}\cdot(\sqrt{x_F^2 + \frac{4\,M^2}{s}} \pm x_F)$. The x_F parameterization is inspired by the anticipated structure function factorization of the parton fusion process for J/ψ hadro-production. The parameters C and $\langle p_T\rangle$, obtained from a fit on the corresponding kinematical distribution, give a good tool to compare the consistency of different data samples from various experiments.

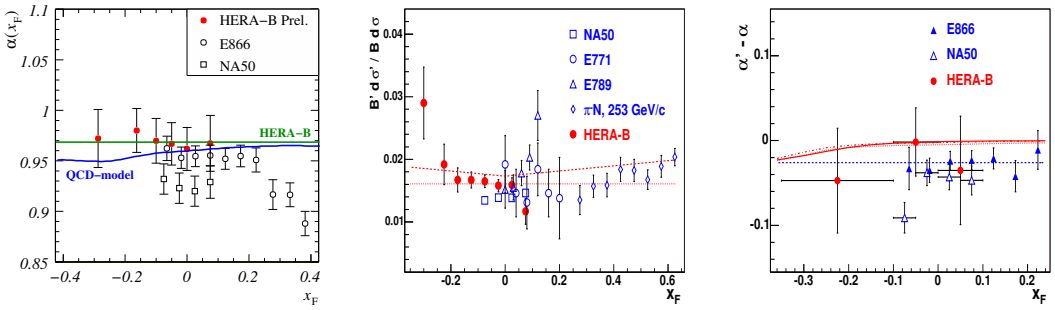

Figure 2: The Hera-B measurement of the x_F dependence of α of J/ψ production, the ψ' production ratio $R_{\psi'}$ and the difference of α for J/ψ and ψ' production $\Delta\alpha$ in comparison to E866 and NA50. The uncertainties are statistical only.

2.2 Nuclear Dependence

The nuclear dependence of the J/ψ production can be measured with low systematic uncertainty by using two different targets with different materials (carbon and tungsten) simultaneously:

$$\sigma(pA \to J/\psi X) = A^{\alpha} \cdot \sigma(pN \to J/\psi X) \;\Rightarrow\; \alpha = \frac{1}{\ln(A_{\mathrm{W}}/A_{\mathrm{C}})} \cdot \ln\left(\frac{N_{\mathrm{W}}^{J/\psi}}{N_{\mathrm{C}}^{J/\psi}} \cdot \frac{\mathcal{L}_{\mathrm{C}}}{\mathcal{L}_{\mathrm{W}}} \cdot \frac{\epsilon_{\mathrm{C}}}{\epsilon_{\mathrm{W}}}\right) \quad (2)$$

A possible suppression of the J/ψ production by nuclear effect leads to $\alpha < 1$. The measurement making use of the muon data of HERA-B is compatible with a small suppression with $\alpha = 0.969 \pm 0.003_{\mathrm{stat}} \pm 0.021_{\mathrm{sys}}$ (Fig. 2). This is in good agreement with the theoretical predictions [5] and the earlier measurements in the positive x_F region of the E866 [6] and NA50 [7] experiments. In the commonly covered $x_F$region, a good agreement is found and confirmed by the $\alpha(p_T)$ distribution.

2.3 ψ' Measurement

Beside the J/ψ, a clear peak of the ψ' state is detected at $M \approx 3.7\,\mathrm{GeV}/c^2$ (Fig. 1). The study of the ψ' to J/ψ production ratio in proton nucleus interactions is a good framework to compare the existing models of charmonium production and of charmonium absorption in nuclear matter. The ratio has been measured as [8]

$$R_{\psi'} = \frac{BR(\psi' \to l^+l^-) \cdot \sigma(\psi')}{BR(J/\psi \to l^+l^-) \cdot \sigma_{J/\psi}} = \frac{N_{\psi'}}{N_{J/\psi}} \cdot \frac{\epsilon_{J/\psi}}{\epsilon_{\psi'}} = (1.83 \pm 0.03)\,\% \quad (3)$$

Furthermore, the nuclear dependence of $R_{\psi'} \propto A^{\alpha(\psi')-\alpha J/\psi}$ has been measured according to Eq. 2. The HERA-B measurements are in well agreement with the results of the earlier experiments E866 [6] and NA50 [7] and both, $R_{\psi'}$ and $\Delta\alpha$ are compatible with no x_F dependence. The results averaged over all target materials are compared to theoretical calculations using the Color Evaporation model (CEM, [9]) for Color Singlet nuclear absorption and Non Relativistic QCD (NRQCD [10]). At the current state, the data are compatible

with both models. In addition, the parallel measurement of ψ' in the electron and muon decay channels can be used to constrain the double ratio $R_{\psi'}(\mu)/R_{\psi'}(e) = (1.00 \pm 0.08 \pm 0.04)$ as a sensitive test of lepton universality.

2.4 χ_c Measurement

A measurement of the production ratio of χ_c to the J/ψ production is an other important tool to discriminate between different models for quarkonium production. HERA-B has access to these states via the radiative decay channel $\chi_c \to J/\psi\gamma \to l^+l^-\gamma$ by selecting the χ_c based on the mass difference $\Delta M = M(l^+l^-\gamma) - M(l^+l^-)$. The background is determined by event mixing and subtracted from the spectrum. Using a signal description consisting of two Gaussians and making use of the full statistics' the two states χ_{c1} and χ_{c2} can be separated in the μ-decay channel applying a rather strong cut on the transverse photon energy of $E_T(\gamma) > 0.4$ GeV. The production ratio (Eq. 4) has been found to be $R_{\chi_c} = 0.21 \pm 0.05_{\text{stat}}$ using data from the μ-channel only. This ratio can be used to test various QCD models for charmonium formation. As can been seen in Fig. 3 the CSM (with color singlet) is disfavored with respect to the NRQCD model.

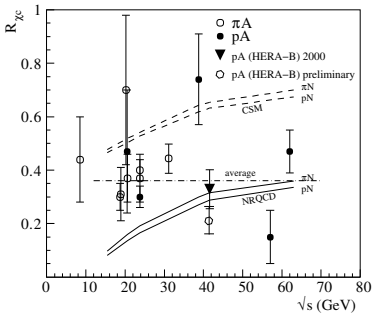

Figure 3: First measurement of $R_{\chi C}$ and the comparison of the production ratio to various models.

$$R_{\chi_c} = \frac{\sum_{i=1}^{2} \sigma(pA \to \chi_{c,i}) \cdot BR(\chi_{c,i} \to J/\psi\gamma)}{\sigma(pA \to J/\psi)} = \frac{N_{\chi_c}}{N_{J/\psi}} \cdot \frac{\epsilon_{J/\psi}}{\epsilon_{\chi_c}} \cdot \frac{1}{\epsilon_\gamma} \tag{4}$$

3 Conclusion

HERA-B stopped data taking in March 2003. Nevertheless, a rich physics program in the field of quarkonia production in nuclear matter could be realized which extends the existing measurements into the unexplored kinematical region of negative x_F.

References

[1] Slides:
`http://indico.cern.ch/contributionDisplay.py?contribId=207&sessionId=5&confId=9499`

[2] I. Abt *et al.* Phys.Lett.**B638**(2006)407.

[3] F. Maltoni, hep-ph/0003003.

[4] L. Antoniazzi *et al.* (E705 Coll.), Phys.Rev.**D46**(1992)4828.

[5] R. Vogt, Nucl.Phys. **A700**(2002)539.

[6] M.J. Leitch *et al.* (E866/NuSea Coll.), Phys.Rev.Lett.**84**(2000)3256.

[7] B. Alessandro *et al.* (NA50 Coll.), Eur.Phys.J.**C33**(2004)31.

[8] A.D. Martin *et al.*, Eur. Phys. J. **C49**(2006)545.

[9] R. Gavai *et al.* , Int.J.Mod.Phys.**A10**(1995)3043.

[10] R. Vogt, Phys.Ref.**C61**(2000)035203.

Outlook for b Physics at the LHC in ATLAS and CMS

Attila Krasznahorkay Jr.[1,2] for the ATLAS and CMS collaborations

1- University of Debrecen - Dept. of Experimental Physics
4010, Debrecen, Egyetem tér 1. - Hungary

2- CERN - PH Dept.
CH-1211, Geneva 23 - Switzerland

An overview is presented for the planned B-physics programme of the ATLAS and CMS experiments at the LHC. The physics programmes of both experiments have been prepared for the different running conditions of the accelerator. Analyses and their expected sensitivities are presented, which are planned for different luminosity configurations of the LHC.

1 Introduction

ATLAS [2] and CMS [3] are general purpose particle detectors that will run at the Large Hadron Collider (LHC) at CERN. Both of them provide good tracking, calorimetry and muon detection. They were designed mainly for high-p_T, discovery physics. B physics events on the other hand contain mostly low-p_T particles, which means that for these measurements the detectors usually have to be used in modes they were not optimised for.

The study of B-physics presents a good opportunity to check the Standard Model predictions at a high perturbative order, search for *new physics*, constrain the CKM matrix elements and to provide new information on long-distance QCD effects in matrix elements of the tensor currents.

Proton-proton collisions will happen at $\sqrt{s} = 14$ TeV at the LHC which results in a $\sigma(b\bar{b}) = 500$ μb cross section for $b\bar{b}$ pair production. This means that at low luminosity LHC running ($L = 2{\times}10^{33}$ cm^{-2}s^{-1}) $b\bar{b}$ pairs will be produced with a rate of about 10^6 Hz. Since only on the order of about 10 Hz can be written to storage for B-physics in both experiments, trigger systems with high rejection powers are needed to select the events of interest.

2 B hadron property measurements

Despite the noisy environment of the LHC, the huge B hadron production statistics will allow precise measurements of their properties. Current studies show that the first precision measurements will be possible with about 10 fb^{-1} of data, which could be gathered with one year of data taking at low luminosity.

2.1 Inclusive b cross section

Today the shape of the transverse momentum and angular distributions as well as the azimuthal angular correlations of B flavoured hadrons are reasonably well described by perturbative QCD. However the observed cross-sections at the Tevatron, HERA and LEP are larger than most[a] QCD predictions. Three mechanisms contribute to the beauty production in hadron colliders: gluon-gluon fusion and $q\bar{q}$ annihilation; flavour excitation and gluon

[a] New *mass-less* QCD calculations achieve good agreement with the measurements.

splitting. It is important to measure the B-hadron p_T spectra within large range to be able to disentangle the contributions of these mechanisms.

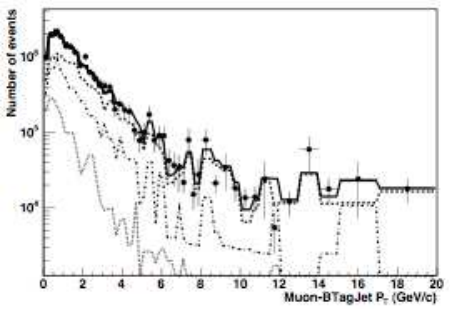

Figure 1: Fit of the muon p_T spectrum with respect to the closest b-tagged jet. The contributions of tagged muons from b events (dashed curve), c events (dot-dashed curve) and light quark events (dotted curve) as defined by the fit are shown.

CMS studied the measurement of the inclusive b cross section in the channel with a b-tagged jet and a muon in the final state [4]. The transverse momentum of the muon with respect to the b-jet axis can be used to effectively discriminate b events from the background, as is demonstrated in Figure 1. Using a maximum likelihood fit, the cross section can be extracted from this distribution.

With an integrated luminosity of 10 fb^{-1} CMS expects to study the b production cross section on a sample of 16 million b events. The current estimate shows that the measurement can reach 1.5 TeV/c as the highest measured transverse momentum for B hadrons.

2.2 B_c meson property measurements

A feasibility study was done in the CMS experiment to measure the mass and lifetime of the B_c meson [5]. They concluded that with the first fb^{-1} of data CMS will be able to reconstruct roughly 120 $B_c^+ \to J/\psi\pi^+$ with $J/\psi \to \mu^+\mu^-$ events.

A Gaussian fit of the mass distribution of these events results in a mass resolution of $22.0(stat.) \pm 14.9(syst.)$ MeV/c^2. The corresponding lifetime uncertainty is $0.044(stat.) \pm 0.010(syst.)$ ps.

3 CP violation studies

The full proper-time and angular analyses of B events allow the investigation of several parameters of physics interest. If the Standard Model expectations are correct, the weak phase (ϕ_s) will not be measured with a useful significance, but a deviation from the Standard Model could be detected. Studying the decay of heavy flavoured hadrons also presents the opportunity to measure some of the CKM matrix elements in a direct way.

3.1 Measurement of $sin(2\beta)$

ATLAS's sensitivity to measure $sin(2\beta)$ in the $B_d^0 \to J/\psi K_s$ decay was estimated on fully simulated Monte Carlo samples with a maximum likelihood method. With dedicated triggers available for the $J/\psi \to \mu^+\mu^-(e^+e^-)$ final states, ATLAS should achieve high sensitivity in this channel. The $J/\psi \to e^+e^-$ channel will mainly be used to cross-check the results from $J/\psi \to \mu^+\mu^-$, and to slightly improve on them.

It is possible to tag the flavour of the B_d^0 mesons from tagging the flavour of the b quark on the opposite side either with the jet charge or lepton flavour of that decay. Combining

all the tags, a precision of 0.01 on $sin(2\beta)$ could be achieved with 30 fb^{-1} of data at low luminosity. The systematic uncertainty on the measurement is estimated to be 0.005.

3.2 Δm_s measurement

In $B_s^0 \to D_s\pi$, $B_s^0 \to D_s a_1$ the probability to detect an initially pure B_s^0 as B_s^0 (p_+) or as $\bar{B}_s^0$ (p_-) is:

$$p_\pm(t) = e^{-\Gamma t}\left(\cosh\frac{\Delta\Gamma_s}{2}t \pm \cos\Delta m_s t\right)\frac{\Gamma^2 - \Delta\Gamma_s^2}{2\Gamma}$$

From which the Δm_s parameter can be derived. The projection of ATLAS's sensitivity to the Δm_s parameter can be seen in Figure 2. As can be seen from the plot, a 5σ limit could be obtained for CDF's recent measurement [6] already with 10 fb^{-1} of data.

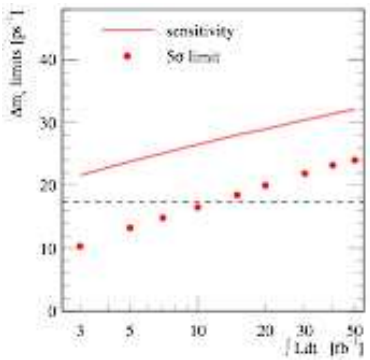

Figure 2: Δm_s measurement limits as a function of the integrated luminosity. The dashed line represents the CDF measurement.

3.3 ϕ_s measurement in $B_s^0 \to J/\psi\phi$

The $B_s^0 \to J/\psi\phi$ decay leads to three final state helicity configurations. Their linear combinations are CP eigenstates with different CP parities. The experimental observables of the $B_s^0 \to J/\psi\phi \to \mu^+\mu^- K^+K^-$ decay are three independent angles and the B_s^0 proper time. They can be used in maximum likelihood fits to extract among other parameters the weak phase (ϕ_s).

ATLAS expects to be able to select about 270k signal events from 30 fb^{-1} of data taken at low luminosity. This would allow to achieve a mass resolution on B_s^0 of 16.5 MeV and a proper life-time resolution of 83 fs. The precision for determining ϕ_s from this sample ($\sigma(\phi_s)$) is calculated to be 0.046. The fit is also expected to provide Γ_s and $\Delta\Gamma_s$ with 1% and 13% relative accuracy respectively.

In a similar analysis done by CMS [7] they found that the uncertainty on the weak phase determination with 10 fb^{-1} of data is too large to make a measurement. It has to be noted though, that CMS's sensitivity will likely largely increase by introducing flavour tagging in their analysis.

4 Rare B-decays

Flavour changing neutral current decays ($b \to d, s$) are forbidden at tree level in the Standard Model, and only occur at loop level. They are sensitive to the CKM matrix elements $|V_{td}|$, $|V_{ts}|$ and also to *new physics* beyond the Standard Model.

Each of the studied channels have two muons in their final state. This makes it possible to trigger on the events even at high LHC luminosity (L = 10^{34} cm^{-2}s^{-1}). Properly selecting di-muon signatures by the trigger and rejecting fake di-muon candidates is of high importance. A study is going on in ATLAS to evaluate the trigger's impact/bias on selecting rare B-decay

events. Preliminary results show no bias from the LVL1 2MU6 trigger on a signal sample of $B_d \to K^{0*}\mu(6)\mu(4)$ events.

4.1 $\Lambda_b \to \Lambda\mu^+\mu^-$ decays

In this process the forward-backward asymmetry (A_{FB}) is very sensitive to Supersymmetry. ATLAS's sensitivity to measure A_{FB} in this decay was measured. With 30 fb^{-1} of data 800 signal events are expected to be selected, analysing which should enable clear separation between the Standard Model and some of it's extensions.

4.2 $B_s^0 \to \mu^+\mu^-$ decays

The branching ratio of this decay is sensitive to Standard Model extensions. ATLAS showed that with 30 fb^{-1} of data it would be able to select about 21 signal- with an expected additional 60 background events. The expected event yields with 100 fb^{-1} of data at high luminosity running are about 92 signal with 900 background events.

CMS showed [8] that with 10 fb^{-1} of data they would be able to select 6.1 ± 0.6 signal events which would allow them to make a BR$(B_s^0 \to \mu^+\mu^-) < 1.4 \times 10^{-8}$ limit with a 90% confidence level.

5 Conclusion

The LHC will provide it's experiments with unprecedented statistics of heavy flavour quark production. The main physics interest in ATLAS and CMS will be to make precision measurements on B properties made possible with the large event statistics, and do measurements that can detect or constrain physics beyond the Standard Model. The B-physics program in both experiments is prepared for all luminosities of the LHC, with some analyses possible even at the highest of the planned luminosities.

References

[1] Slides:
`http://indico.cern.ch/contributionDisplay.py?contribId=240&sessionId=5&confId=9499`

[2] ATLAS detector and physics performance, Technical Design Report, CERN, Geneva, 1999.

[3] Michael Della Negra, Achille Petrilli, Alain Harvé and Lorenzo Foà, CMS Physics Technical Design Report, CERN, Geneva, 2006.

[4] V. P. Andreev, D. B. Cline and S. Otwinowski, "Measurement of open beauty production at LHC with CMS," CERN-CMS-NOTE-2006-120;

[5] X. W. Meng, J. Q. Tao and G. M. Chen, "Feasibility to study the B_c meson at CMS," CERN-CMS-NOTE-2006-118;

[6] A. Abulencia *et al.* [CDF - Run II Collaboration], Phys. Rev. Lett. **97** (2006) 062003 [AIP Conf. Proc. **870** (2006) 116] [arXiv:hep-ex/0606027].

[7] V. Ciulli, N. Magini, L. Wilke, T. Speer, K. Prokofiev, S. Shulga and T. Ilicheva, "Study of the decay $B_s^0 \to J/\psi\phi \to \mu^+\mu^-K^+K^-$," CITATION = CERN-CMS-NOTE-2006-121;

[8] U. Langenegger, "Study of $B_s \to \mu^+\mu^-$ in CMS," arXiv:hep-ex/0610039.

Heavy Flavors

Diffraction and Vector Mesons

Inelastic Electroproduction of Charmonium at HERA

M. Steder

DESY, Notkestr. 85, 22607 Hamburg, Germany

Inelastic electroproduction of J/ψ mesons is studied in ep-scattering at HERA in the range $3.6 < Q^2 < 100$ GeV^2. The data were taken with the H1 detector in the years 2004 through 2006 and correspond to an integrated luminosity of $\mathcal{L} \approx 258\text{pb}^{-1}$. Single differential and double differential cross sections are measured with increased precision compared with previous analyses.

1 Introduction

Inelastic J/ψ production in ep collisions is dominated by the process of photon–gluon fusion where a photon from the incoming electron and a gluon from the proton couple to a $c\overline{c}$ pair. The process can be calculated within non-relativistic QCD (NRQCD) where the cross section is a sum over all possible intermediate $c\overline{c}$ states, colour singlet (CS) and colour octet (CO) states. The amplitude for each $c\overline{c}$ state with definite colour and angular momentum factorises into a short distance term which can be calculated in NRQCD and a long distance matrix element (LDME) describing the transition to a J/ψ meson. The LDMEs are not calculable and have been determined from J/ψ production data in $p\overline{p}$ collisions where the CO contributions were found to be sizable. Previous HERA measurements in photoproduction showed good agreement with NLO calculations of the Colour Singlet Model (CSM), which takes only colour singlet states into account. But small colour octet contributions could not be excluded.

In this talk a measurement of single differential and double differential cross sections of inelastic J/ψ in electroproduction is presented which provides improved statistical precision in comparison to the previous measurements. The kinematic range ist restricted to $3.6 < Q^2 < 100$ GeV^2, $50 < W_{\gamma p} < 225$ GeV for medium elasticities $0.3 < z < 0.9$ and the squared transverse momentum of the J/ψ meson in the photon–proton center of mass system $p_t^{*2} > 1$ GeV^2. The systematic error has been determined to be $10 - 11\%$.

The data are compared with predictions from two Monte Carlo models generating events according to the Color Singlet model in leading order, CASCADE [3] and EPJPSI [4]. In CASCADE, higher order parton emissions based on the CCFM [5] evolution equations are matched to $\mathcal{O}(\alpha_s)$ matrix elements in which the incoming parton can be off-shell. The Monte Carlo generator EPJPSI [4] is based on the DGLAP evolution [6], assuming collinear factorization of the parton density distributions and the hard matrix elements.

2 Cross Section Measurement

Differential cross sections are determined separately for the decay channels into muons and into electrons. The cross sections are then combined by error weighted averaging. The production cross section is determined by measuring the number of events, correcting for detector efficiencies and acceptances and dividing by the integrated luminosity of 258 pb^{-1} and the corresponding branching ratio of $\mathcal{BR}(J/\psi \to ee) = (5.94 \pm 0.06)\%$ and $\mathcal{BR}(J/\psi \to \mu\mu) = (5.93 \pm 0.06)\%$, respectively [7].

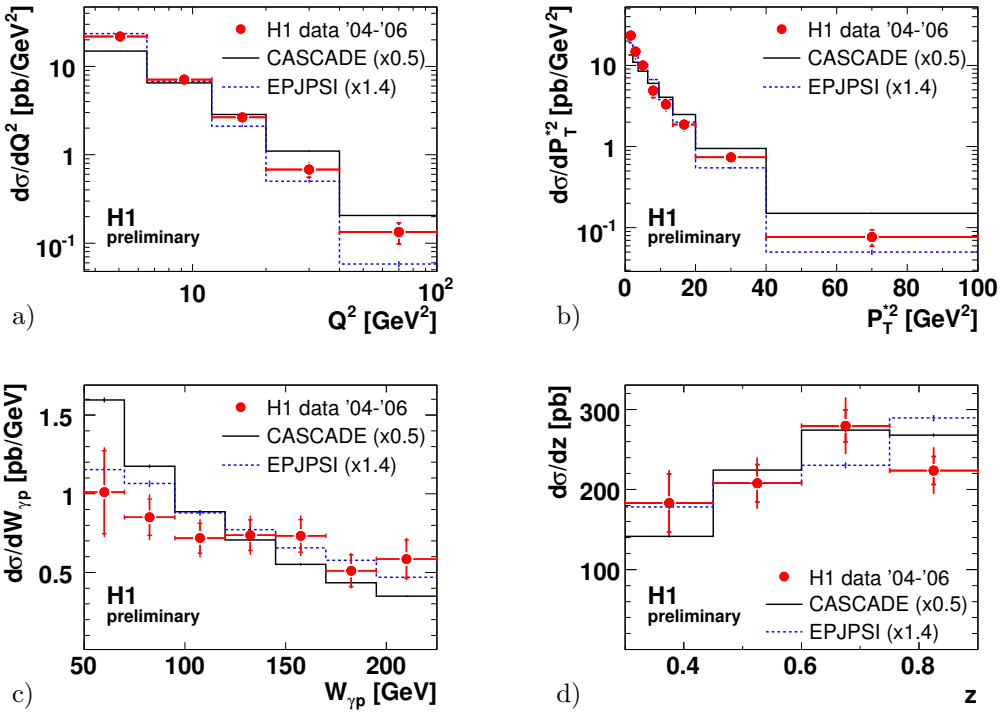

Figure 1: Differential J/ψ cross sections for the kinematic range $Q^2 > 3.6$ GeV^2, $50 < W_{\gamma p} < 225$ GeV, $0.3 < z < 0.9$ and $p^{*2}_{t,\psi} > 1$ GeV, as functions of a) Q^2, b) $p^{*2}_{t,\psi}$, c) $W_{\gamma p}$, d) z. The data are compared to the predictions from CASCADE (solid line) and EPJPSI (dashed line).

The measured cross sections are not corrected for contributions from secondary J/ψ mesons from the decays of B-Mesons, χ_c or $\psi(2S)$ mesons. The fraction of events arising from diffractive $\psi(2S)$ meson production with subsequent decay of the $\psi(2S)$ into $J/\psi + X$ is estimated to be 1.5% in the total sample and about 5% in the highest z bin. The fraction of events arising from B mesons decaying into $J/\psi + X$ is estimated to be 3.6% in the total sample and about 20% in the lowest z bin.

Differential cross sections are measured as functions of the following variables: Q^2, $W_{\gamma p}$, z, the transverse momentum squared, $p^{*2}_{t,\psi}$, of the J/ψ in the $\gamma^* p$ center of mass frame. The measured differential cross sections are shown in Figure 1. Shape comparisons of the data are performed with predictions from the CASCADE generator (solid line) and EPJPSI (dashed line), The total cross sections of the Monte Carlo simulations are normalized to the total cross section of the measurement. CASCADE shows a reasonable description of the dependence on Q^2. It has a somewhat harder distribution in $p^{*2}_{t,\psi}$ than the data. In contrast EPJPSI has a much steeper distribution in Q^2 and in $p^{*2}_{t,\psi}$. Both programs predict a somewhat flatter distribution of the cross section in z.

The distributions in $p^{*2}_{t,\psi}$ and z are further investigated in Figures 2 and 3 by dividing

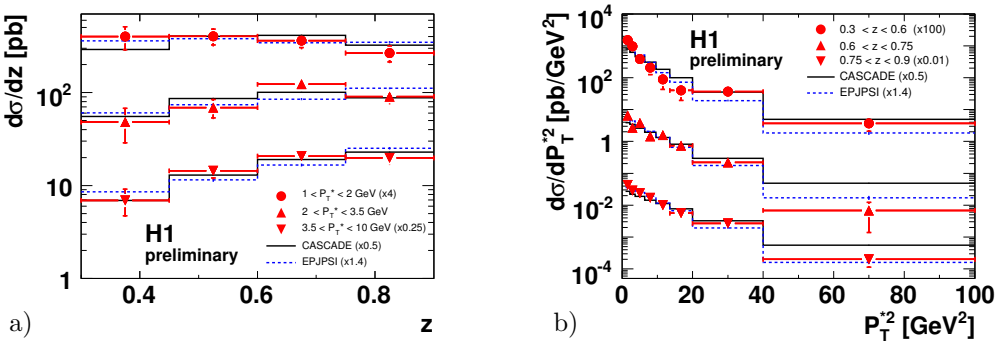

Figure 2: Differential J/ψ cross sections, $d\sigma/dz$ as a function of a) z in three bins of $p^*_{t,\psi}$ and b) $d\sigma/dp^{*2}_{t,\psi}$ as a function of $p^{*2}_{t,\psi}$ in three bins of z. The predictions from CASCADE (solid line) and EPJPSI (dashed line) are also shown.

the sample into bins of z and $p^*_{t,\psi}$, respectively. Both Monte Carlo models describe the z distribution in the largest bin of $p^*_{t,\psi}$ and the dependence on z of the slope of $p^{*2}_{t,\psi}$. At small values of z, the dependence on $p^{*2}_{t,\psi}$ is better described by CASCADE while EPJPSI agrees better at large values of z.

3 Conclusions

A measurement of inelastic J/ψ production is performed with improved statistics and systematics with respect to previous measurements. Differential and double differential cross sections are measured and compared with predictions from the MC models CASCADE and EPJPSI. Both models are not capable of describing all aspects of the data. No indications for large NRQCD contributions are seen.

References

[1] Slides:
`http://indico.cern.ch/contributionDisplay.py?contribId=78&sessionId=13&confId=9499`

[2] C. Adloff *et al.* [H1 Collaboration], Eur. Phys. J. C **25** (2002) 41 [hep-ex/0205065].

[3] H. Jung and G.P. Salam, Eur. Phys. J. C **19** (2001) 351 [hep-ph/0012143];
H. Jung, Comput. Phys. Commun. **143** (2002) 100 [hep-ph/0109102].

[4] H. Jung, in: Proc. of the Workshop on Physics at HERA, ed. W. Buchmüller and G. Ingelman, Hamburg (1992), Vol. 3, p. 1488;
H. Jung, D. Krücker, C. Greub and D. Wyler, Z. Phys. C **60** (1993) 721.

[5] M. Ciafaloni, Nucl. Phys. B **296** (1988) 49; S. Catani, F. Fiorani and G. Marchesini, Phys. Lett. B **234** (1990) 339; *idem*, Nucl. Phys. B **336** (1990) 18; G. Marchesini, Nucl. Phys. B **445** (1995) 49.

[6] V.N. Gribov and L.N. Lipatov, Yad. Fiz. **15** (1972) 781 [Sov. J. Nucl. Phys. **15** (1972) 438]; G. Altarelli and G. Parisi, Nucl. Phys. B **126** (1977) 298; Y.L. Dokshitzer, Sov. Phys. JETP **46** (1977) 641 [Zh. Eksp. Teor. Fiz. **73** (1977) 1216].

[7] W.-M. Yao *et al.* [Particle Data Group] J. Phys. G 33, 1 (2006).

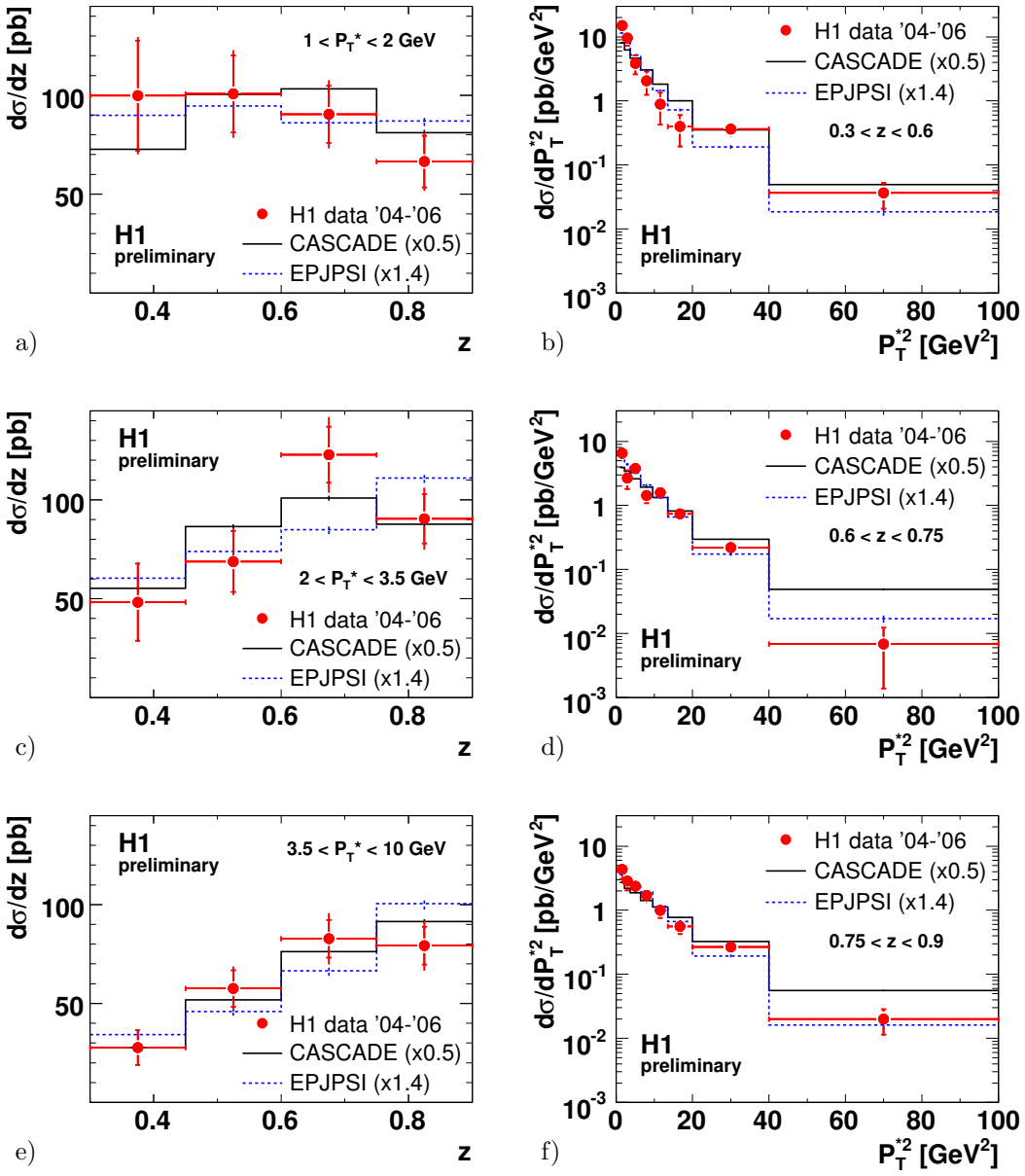

Figure 3: Differential J/ψ cross sections, $d\sigma/dz$ as a function of z in three bins of $p^*_{t,\psi}$, a) $1 < p^*_{t,\psi} < 2$ GeV, c) $2 < p^*_{t,\psi} < 3.5$ GeV, e) $3.5 < p^*_{t,\psi} < 10$ GeV and $d\sigma/dp^{*2}_{t,\psi}$ as a function of $p^{*2}_{t,\psi}$ in three bins of z, b) $0.3 < z < 0.6$, d) $0.6 < z < 0.75$ and f) $0.75 < z < 0.9$. The predictions from CASCADE (solid line) and EPJPSI (dashed line) are also shown.

Heavy Quarkonium Production in the Regge Limit of QCD

B.A. Kniehl[1], V.A. Saleev[2] and D.V. Vasin[2]

1 - II Institute of Theoretical Physics, University of Hamburg,
Luruper Chaussee 149, 22761 Hamburg - Germany

2 - Department of Physics, Samara State University,
Samara, ak. Pavlova 1, 443011 Samara - Russia

The main results of our recent articles [2, 3] are presented in this report. We study charmonium and bottomonium production at the Tevatron Collider in the framework of the Quasi-Multi-Regge-Kinematic approach and the factorization formalism of non-relativistic QCD at leading order in the strong-coupling constant α_s and the relative velocity v of the heavy quarks inside quarkonium.

1 Introduction

Heavy quarkonium production at high energies has provided a useful laboratory for testing the high-energy limit of quantum chromodynamics (QCD) as well as the interplay of perturbative and nonperturbative phenomena in QCD. The factorization formalism of nonrelativistic QCD (NRQCD) [4] is a theoretical framework for the description of heavy-quarkonium production and decay. The factorization hypothesis of NRQCD assumes the separation of the effects of long and short distances in heavy-quarkonium production. NRQCD is organized as a perturbative expansion in two small parameters, the strong-coupling constant α_s and the relative velocity v of the heavy quarks.

The phenomenology of strong interactions at high energies exhibits a dominant role of gluon interactions in quarkonium production. In the conventional parton model [5], the initial-state gluon dynamics is under the control of the Dokshitzer-Gribov-Lipatov-Altarelli-Parisi (DGLAP) evolution equations [6]. In this approach, it is assumed that $S > \mu^2 \gg \Lambda^2_{\rm QCD}$, where $\sqrt{S}$ is the invariant collision energy, μ is the typical energy scale of the hard interaction, and $\Lambda_{\rm QCD}$ is the asymptotic scale parameter. In this way, the DGLAP evolution equation takes into account only one large logarithm, namely $\ln(\mu/\Lambda_{QCD})$. In fact, the collinear approximation is used, and the transverse momenta of the initial gluons are neglected.

In the high-energy limit, the contribution from the partonic subprocesses involving t-channel gluon exchanges to the total cross section becomes dominant. The summation of the large logarithms $\ln(\sqrt{S}/\mu)$ in the evolution equation can then be more important than the one of the $\ln(\mu/\Lambda_{QCD})$ terms. In this case, the non-collinear gluon dynamics is described by the Balitsky-Fadin-Kuraev-Lipatov (BFKL) evolution equation [7]. In the region under consideration, the transverse momenta (k_T) of the incoming gluons and their off-shell properties can no longer be neglected, and we deal with *reggeized* t-channel gluons. The theoretical framework for this kind of high-energy phenomenology is the Quasi-Multi-Regge-Kinematic (QMRK) approach [8], which can be based on effective quantum field theory implemented with the non-abelian gauge-invariant action, as was suggested a few years ago [9].

2 Charmonium production at the Tevatron

During the last decade, the CDF Collaboration at the Tevatron [10, 11] collected data on charmonium production at energies $\sqrt{S} = 1.8$ TeV (run I) and $\sqrt{S} = 1.96$ TeV (run II) in the central region of pseudorapidity $|\eta| < 0.6$. The data cover a large interval in transverse momentum, namely $5 < |\mathbf{p}_T| < 20$ GeV (run I) and $|\mathbf{p}_T| < 20$ GeV (run II). The data sample of run I [10] includes transverse-momentum distributions of J/ψ mesons that were produced directly in the hard interaction, via radiative decays of χ_{cJ} mesons, via decays of ψ' mesons, and via decays of b hadrons. That of run II [11] includes transverse-momentum distributions of prompt J/ψ mesons, so far without separation into direct, χ_{cJ}-decay, and ψ'-decay contributions, and J/ψ mesons from b-hadron decays.

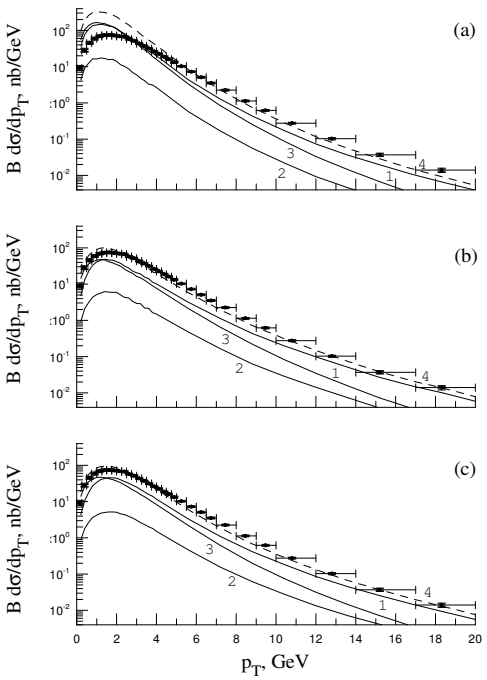

Figure 1: Prompt J/ψ production at the Tevatron with $\sqrt{S} = 1.96$ TeV [11]. The total theoretical results (4) obtained with the (a) JB, (b) JS, or (c) KMR unintegrated gluon distributions are broken down to the contributions from (1) direct production, (2) ψ' decays, and (3) χ_{cJ} decays.

In contrast to previous analyses in the collinear parton model [12] or the k_T-factorization approach [13], we perform a joint fit to the run-I and run-II CDF data [10, 11] to obtain the color-octet nonperturbative matrix elements (NMEs) for J/ψ, χ_{cJ}, and ψ' mesons. Our calculations are based on exact analytical expressions for the relevant squared amplitudes, which were previously unknown in the literature. Our fits include five experimental data sets, which come as p_T distributions of J/ψ mesons from direct production, prompt production, χ_{cJ} decays, and ψ' decays in run I, and from prompt production in run II.

In Table I of Ref. [2], we present out fit results for the relevant color-octet NMEs for three different choices of unintegrated gluon distribution function, namely JB [14], JS [15], and KMR [16]. The first one, JB, is strongly disfavoured by the charmonium data in the small p_T region, as it is shown in Fig. 1(a).

Considering the color-octet NMEs relevant for the J/ψ, ψ' and χ_{cJ} production mechanisms, we can formulate the following heuristic rule for favoured transitions from color-octet to color-singlet states: $\Delta L \simeq 0$ and $\Delta S \simeq 0$; *i.e.*, these transitions are doubly chromoelectric and preserve the orbital angular momentum and the spin of the heavy-quark bound state.

3 Bottomonium production at the Tevatron

The CDF Collaboration measured the p_T distributions of $\Upsilon(1S)$, $\Upsilon(2S)$, and $\Upsilon(3S)$ mesons in the central region of rapidity (y), $|y| < 0.4$, at $\sqrt{S} = 1.8$ TeV (run I) [17] and that of the $\Upsilon(1S)$ meson in the rapidity regions $|y| < 0.6$, $0.6 < |y| < 1.2$, and $1.2 < |y| < 1.8$ at $\sqrt{S} = 1.96$ TeV (run II) [18]. In both cases, the S-wave bottomonia were produced promptly, *i.e.*, directly or through non-forbidden decays of higher-lying S- and P-wave bottomonium states, including cascade transitions such as $\Upsilon(3S) \to \chi_{b1}(2P) \to \Upsilon(1S)$.

In contrast to previous analysis in the collinear parton model [19], we perform a joint fit to the CDF data from run I [17] and run II [18] for all p_T values, including the small-p_T region. Comparing the color-singlet and color-octet contributions, we observe that the latter is dominant in the $\Upsilon(3S)$ case and in the $\Upsilon(2S)$ case for $p_T \gtrsim 13$ GeV, while it is of minor importance in the $\Upsilon(1S)$ case in the whole p_T range considered. The fits based on the KMR, JB, and JS gluons turned out to be excellent, fair, and poor, respectively. They yielded small to vanishing values for the color-octet NMEs, see Table II of Ref. [3], especially when the estimated feed-down contributions from the as-yet unobserved $\chi_{bJ}(3P)$ states were included.

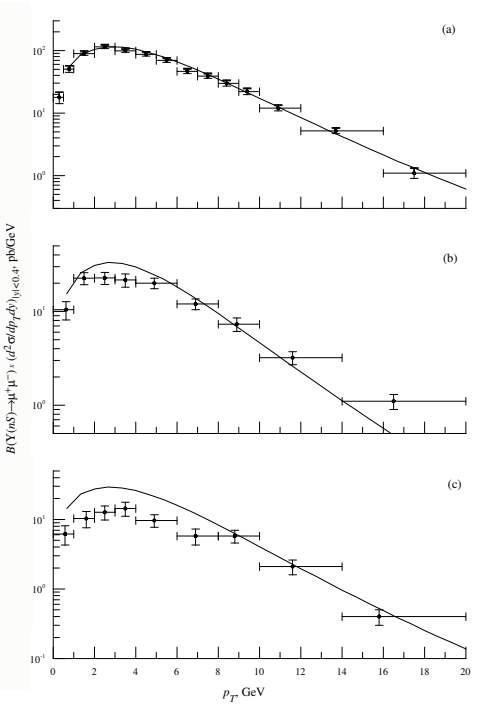

Figure 2: Prompt production of (a) $\Upsilon(1S)$, (b) $\Upsilon(2S)$, and (c) $\Upsilon(3S)$ mesons at the Tevatron with $\sqrt{S} = 1.8$ TeV [17]. The theoretical results are obtained with the KMR unintegrated gluon distribution and correspond to the color-singlet contributions, also including the estimated contribution due to the $\chi_{bJ}(3P)$ meson.

4 Conclusions

Working at LO in the QMRK approach to NRQCD, we analytically evaluated the squared amplitudes of prompt quarkonium production by reggeized gluons. We extracted the relevant color-octet NMEs, $\langle \mathcal{O}^{\mathcal{H}}[^3S_1^{(8)}] \rangle$, $\langle \mathcal{O}^{\mathcal{H}}[^1S_0^{(8)}] \rangle$, and $\langle \mathcal{O}^{\mathcal{H}}[^3P_0^{(8)}] \rangle$ for $\mathcal{H} = \psi(1S, 2S)$, $\chi_{cJ}(1P)$, $\Upsilon(1S, 2S, 3S)$, and $\chi_{bJ}(1P, 2P)$ through fits to p_T distributions measured by the CDF Collaboration in $p\bar{p}$ collisions at the Tevatron with $\sqrt{S} = 1.8$ TeV [10, 17] and 1.96 TeV [11, 18] using various unintegrated gluon distribution functions. The present analysis suggest that the color-octet NMEs of bottomonium are more strongly suppressed than those of charmonium as expected from the velocity scaling rules of NRQCD. We illustrated that the QMRK approach [9] provides a useful laboratory to describe the phenomenology of high-energy processes in the Regge limit of QCD.

Acknowledgements

V.A.S. thanks the DIS07 Local Organizing Committee for the kind hospitality during the conference and for the financial support. The work of B.A.K. was supported in part by the German Federal Ministry for Education and Research BMBF through Grant No. 05 HT6GUA and by the German Research Foundation DFG through Grant No. KN 365/6–1.

References

[1] Slides:
`http://indico.cern.ch/contributionDisplay.py?contribId=79&sessionId=13&confId=9499`

[2] B. A. Kniehl, D. V. Vasin, and V. A. Saleev, Phys. Rev. D **73**, 074022 (2006).

[3] B. A. Kniehl, V. A. Saleev, and D. V. Vasin, Phys. Rev. D **74**, 014024 (2006).

[4] G. T. Bodwin, E. Braaten, and G. P. Lepage, Phys. Rev. D **51**, 1125 (1995); **55**, 5853(E) (1997).

[5] CTEQ Collaboration, R. Brock *et al.*, Rev. Mod. Phys. **67**, 157 (1995).

[6] V. N. Gribov and L. N. Lipatov, Sov. J. Nucl. Phys. **15**, 438 (1972) [Yad. Fiz. **15**, 781 (1972)]; Yu. L. Dokshitzer, Sov. Phys. JETP **46**, 641 (1977) [Zh. Eksp. Teor. Fiz. **73**, 1216 (1977)]; G. Altarelli and G. Parisi, Nucl. Phys. B **126**, 298 (1977).

[7] E. A. Kuraev, L. N. Lipatov, and V. S. Fadin, Sov. Phys. JETP **44**, 443 (1976) [Zh. Eksp. Teor. Fiz. **71**, 840 (1976)]; I. I. Balitsky and L. N. Lipatov, Sov. J. Nucl. Phys. **28**, 822 (1978) [Yad. Fiz. **28**, 1597 (1978)].

[8] V. S. Fadin and L. N. Lipatov, Nucl. Phys. **B477**, 767 (1996).

[9] L. N. Lipatov, Nucl. Phys. B **452**, 369 (1995); E. N. Antonov, L. N. Lipatov, E. A. Kuraev, and I. O. Cherednikov, Nucl. Phys. B **721**, 111 (2005).

[10] CDF Collaboration, F. Abe *et al.*, Phys. Rev. Lett. **79**, 572 (1997); **79**, 578 (1997); CDF Collaboration, T. Affolder *et al.*, Phys. Rev. Lett. **85**, 2886 (2000).

[11] CDF Collaboration, D. Acosta *et al.*, Phys. Rev. D **71**, 032001 (2005).

[12] G. T. Bodwin, E. Braaten, and J. Lee, Phys. Rev. D **72**, 014004 (2005).

[13] Ph. Hägler, R. Kirschner, A. Schäfer, L. Szymanowski, and O. V. Teryaev, Phys. Rev. D **62**, 071502 (2000); Phys. Rev. Lett. **86**, 1446 (2001); F. Yuan and K.-T. Chao, Phys. Rev. D **63**, 034006 (2001); Phys. Rev. Lett. **87**, 022002 (2001).

[14] J. Blümlein, Report No. DESY 95-121 (1995).

[15] H. Jung and G. P. Salam, Eur. Phys. J. C **19**, 351 (2001).

[16] M. A. Kimber, A. D. Martin, and M. G. Ryskin, Phys. Rev. D **63**, 114027 (2001).

[17] CDF Collaboration, F. Abe *et al.*, Phys. Rev. Lett. **75**, 4358 (1995); CDF Collaboration, D. Acosta *et al.*, *ibid.* **88**, 161802 (2002).

[18] CDF Collaboration, V. M. Abazov *et al.*, Phys. Rev. Lett. **94**, 232001 (2005).

[19] E. Braaten, S. Fleming, and A. K. Leibovich, Phys. Rev. D **63**, 094006 (2001).

Charm Production in Diffractive DIS and PHP at ZEUS

Isabell-Alissandra Melzer-Pellmann, on behalf of the ZEUS collaboration

DESY, ZEUS group
Notkestr. 85, 22607 Hamburg, Germany

The ZEUS experiment has measured charm production in diffractive DIS and in photoproduction. The data are in agreement with perturbative QCD calculations based on various parameterisations of diffractive parton distribution functions. The results are consistent with QCD factorisation in diffractive DIS and direct photoproduction [1].

1 Introduction

In diffractive electron-proton scattering, the proton loses a small fraction of its energy and either emerges from the scattering intact, $ep \to eXp$, or dissociates into a low-mass state N, $ep \to eXN$. Hadronic states X including a $c\bar{c}$ pair are a particularly interesting component of diffractive interactions. The charm-quark mass provides a hard scale, ensuring the applicability of perturbative QCD even for small photon virtualities (photoproduction). At leading order (LO) of QCD, two types of photoproduction processes can be distinguished: direct and resolved photon processes. Charm production mainly proceeds via direct photon reactions, in which the exchanged photon participates as a point-like particle, directly interacting with a gluon from the incoming proton (photon-gluon fusion). Thus, diffractive charm production is directly sensitive to the gluon content of the diffractive exchange. In resolved photon processes, the photon behaves as a hadron-like source of partons, one of which interacts with a parton from the initial proton.

2 Diffractive D* in photoproduction

ZEUS has recently measured diffractive D^* in photoproduction [2] in the kinematic range $Q^2 < 1$ GeV^2, $130 < W < 300$ GeV, with transverse momentum $p_T(D^*) > 1.9$ GeV and pseudorapidity[a] $|\eta(D^*)| < 1.6$, using an integrated luminosity of $\mathcal{L}$ =78.6 pb^{-1}. Diffractive events were identified by a large gap in pseudorapidity between the produced hadronic state and the outgoing proton, $\eta_{\max} < 3$, reducing the fraction of proton momentum carried by the Pomeron to $x_{I\!P} < 0.035$. In addition, the energy deposited in the forward plug calorimeter (FPC), installed in the 20×20 cm^2 beam hole of the forward uranium calorimeter, was required to be consistent with zero ($E_{\mathrm{FPC}} < 1.5$ GeV). After all selections, a signal of 458 ± 30 D^* mesons was found. In order to reduce the contributions from non-diffractive background, the selection was also performed in the restriced range $x_{I\!P} < 0.01$, where 204 ± 20 D^* mesons were observed. Proton-dissociative events can also satisfy the diffractive selection requirements if the proton-dissociative system, N, has an invariant mass small enough to pass undetected through the forward beam-pipe. The fraction (f_{pd}) of these events was measured previously to be $f_{\mathrm{pd}} = 16 \pm 4(\mathrm{syst.})\%$ [3].

Cross section predictions for diffractive photoproduction of D^* mesons were calculated at the next-to-leading order (NLO) in α_s, using the fixed-flavour-number scheme, in which only

[a] The ZEUS coordinate system is a right-handed Cartesian system, with the Z axis pointing in the proton beam direction, referred to as the "forward direction", and the X axis pointing left towards the centre of HERA. The coordinate origin is at the nominal interaction point.

light flavours are active in the parton distribution functions (PDFs) and the heavy quarks are generated by the hard interaction. The calculation was performed with the FMNR code in the double-differential mode [4, 5]. The Weizsäcker-Williams approximation [6] was used to obtain the virtual photon spectrum for electroproduction with small photon virtualities. Diffractive parton distribution functions (dPDFs) were used instead of the conventional proton PDFs. The three sets of dPDFs used in the calculations were derived from NLO QCD DGLAP fits to the HERA data on diffractive deep inelastic scattering: the H1 2006 Fit A, Fit B [7] and the ZEUS LPS+charm Fit [8] dPDFs. In the ZEUS LPS+charm Fit, the diffractive DIS data were combined with the results on diffractive charm production in DIS [3] to better constrain the gluon contribution. The Reggeon contribution, which amounts to less than 2% for $x_{I\!P} = 0.01$ and grows up to $\sim 15\%$ at $x_{I\!P} = 0.035$, was not included. To account for the proton-dissociative contribution, present in the H1 2006 fits, the corresponding predictions were multiplied by the factor 0.81 [7]. The calculations were performed with $\alpha_s(M_Z) = 0.118$ GeV [9] and $m_c = 1.45$ GeV, the same values as used in the QCD fits to the HERA data. The fraction of charm quarks hadronising as D^* mesons was set to $f(c \to D^*) = 0.238$ [10]. The Peterson parameterisation [11] was used for the charm fragmentation with the Peterson parameter $\epsilon = 0.035$. The uncertainties of the calculations were estimated by varying the renormalisation and factorisation scales simultaneously with the charm mass to $\mu_R = \mu_F = 0.5 \cdot \mu$, $m_c = 1.25$ GeV and to $\mu_R = \mu_F = 2 \cdot \mu$, $m_c = 1.65$ GeV. Uncertainties on the dPDFs were not included.

The differential cross section for $ep \to eD^*X'p$ in a given variable ξ was calculated from

$$\frac{d\sigma}{d\xi} = \frac{N_{D^*} \cdot (1 - f_{\text{non-diffractive}}) \cdot (1 - f_{\text{proton-dissociation}})}{\mathcal{A} \cdot \mathcal{L} \cdot \mathcal{B} \cdot \Delta\xi} \,,$$

where N_{D^*} is the number of D^* mesons observed in a bin of size $\Delta\xi$. The overall acceptance was $\mathcal{A} = 13.9\%$. The combined $D^* \to (D^0 \to K\pi)\,\pi_s$ decay branching ratio is $\mathcal{B} = 0.0257 \pm 0.0005$ [9]. The measured cross sections are

$$\begin{aligned} \sigma_{ep\to eD^*X'p}(x_{I\!P} < 0.035) &= 1.49 \pm 0.11(\text{stat.})^{+0.11}_{-0.19}(\text{syst.}) \pm 0.07(\text{p.d.})\ \text{nb, and} \\ \sigma_{ep\to eD^*X'p}(x_{I\!P} < 0.01) &= 0.63 \pm 0.07(\text{stat.})^{+0.04}_{-0.06}(\text{syst.}) \pm 0.03(\text{p.d.})\ \text{nb.} \end{aligned}$$

The last uncertainty is due to the subtraction of the proton-dissociative background.

The differential cross section as function of $x_{I\!P}$, shown in Fig. 1, demonstrates that the NLO predictions based on the various parameterisations of dPDFs are consistent with the data, supporting the validity of diffractive QCD factorisation in diffractive direct photoproduction. Differential cross sections as function of M_X, $p_T(D^*)$, $\eta(D^*)$, $z(D^*)$ and W have also been calculated [2].

The ratio of the diffractive to the inclusive ($ep \to eD^*Y$) photoproduction cross sections for D^* mesons was also evaluated, as systematic uncertainties partly cancel in this ratio, which is defined as $\mathcal{R}_{\mathcal{D}}(D^*) = \sigma_{ep\to eD^*X'p}(x_{I\!P} < 0.035)/\sigma_{ep\to eD^*Y}$.

In the kinematic region $Q^2 < 1$ GeV^2, $130 < W < 300$ GeV ($0.17 < y < 0.89$), $p_T(D^*) > 1.9$ GeV and $|\eta(D^*)| < 1.6$, diffractive production for $x_{I\!P} < 0.035$ contributes

$$\mathcal{R}_{\mathcal{D}}(D^*) = 5.7 \pm 0.5(\text{stat.})^{+0.4}_{-0.7}(\text{syst.}) \pm 0.3(\text{p.d.})\%$$

to the inclusive D^* photoproduction cross section. The systematic uncertainty is dominated by the measurement of the diffractive cross section.

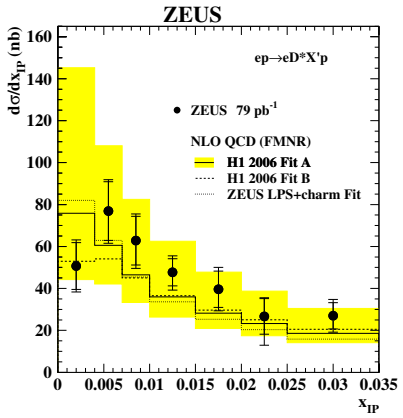

Figure 1: Differential cross section (dots) for diffractive photoproduction of D^*, measured as function of $x_{I\!P}$. The inner bars show the statistical errors; the outer bars correspond to the statistical and systematic uncertainties added in quadrature. The data are compared to the NLO QCD calculations (histograms). The shaded bands show the uncertainties coming from variations of the charm-quark mass and the factorisation and renormalisation scales.

The NLO QCD predictions for $\mathcal{R}_\mathcal{D}$ were obtained as the ratio of the diffractive cross section, calculated with the H1 2006 or ZEUS LPS+charm dPDFs, and the inclusive cross section, obtained with the CTEQ5M proton PDFs. The fraction $\mathcal{R}_\mathcal{D}$ agrees with the values measured at HERA for diffractive DIS in similar kinematic ranges [12, 3, 13]. As shown in Fig. 2, $\mathcal{R}_\mathcal{D}$ shows no dependence on Q^2 within the errors of the measurement. Differential distributions as function of $p_T(D^*)$, $\eta(D^*)$, $z(D^*)$ and W have also been calculated [2].

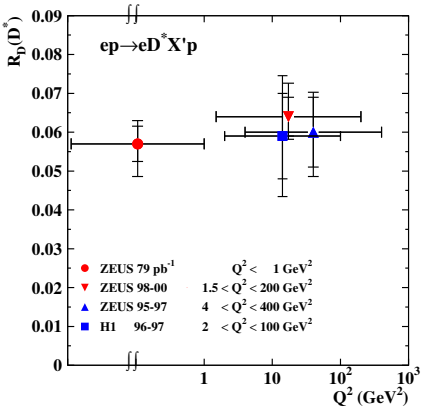

Figure 2: Fractions $\mathcal{R}_\mathcal{D}$ of D^* meson diffractive production cross sections measured at HERA in DIS [3, 13, 12] and photoproduction [2]. The inner bars show the statistical errors, the outer bars correspond to the statistical and systematic uncertainties added in quadrature.

3 Diffractive D* in DIS

Diffractive D^* in DIS has been measured by ZEUS [3] in the kinematic range $1.5 < Q^2 < 200$ GeV^2, $0.02 < y < 0.7$, $x_{I\!P} < 0.035$ and $\beta < 0.8$, where β is the fraction of the Pomeron momentum carried by the struck quark. The transverse momentum of the D^* is restricted to $p_T(D^*) > 1.5$ GeV and its pseudorapidity to $|\eta(D^*)| < 1.5$. Using an integrated luminosity of 82 pb^{-1}, 253 ± 21 D^* candidates have been found. The data have been compared to the perturbative QCD calculation program HVQDIS [14], based on a parameterisation from a gluon dominated fit to H1 and ZEUS inclusive diffractive DIS and ZEUS diffractive photoproduction data [15]. The data are in good agreement with the NLO predictions, confirming QCD factorisation in diffractive DIS as proven by Collins [16]. The ratio $\mathcal{R}_{\mathcal{D}}$ has been calculated as in the photoproduction analysis and is also shown in Fig 2.

4 Conclusions

Differential cross sections for diffractive D^* production in photoproduction and DIS have been compared to the predictions of NLO QCD calculations. The NLO predictions based on various parameterisations of diffractive PDFs are consistent with the data. The measured fraction of $D^{*\pm}$ meson photoproduction due to diffractive exchange is consistent with the measurements of $D^{*\pm}$ meson production in diffractive DIS. Within the experimental uncertainties, this fraction shows no dependence on Q^2 and W.

The results demonstrate that diffractive open-charm production is well described by the dPDF parameterisations extracted from diffractive DIS data, supporting the validity of diffractive QCD factorisation in diffractive DIS and direct photoproduction. Given the large experimental and theoretical uncertainties and the small hadron-like contribution expected by the NLO calculations, no conclusion can be drawn for the resolved photoproduction.

References

[1] Slides:
`http://indico.cern.ch/contributionDisplay.py?contribId=81&sessionId=13&confId=9499`
[2] ZEUS Collaboration, S. Chekanov *et al.*, Eur. Phys. J. **C51**, 301 (2007).
[3] ZEUS Collaboration, S. Chekanov *et al.*, Nucl. Phys. **B672**, 3 (2003).
[4] S. Frixione *et al.*, Nucl. Phys. **B412**, 225 (1994).
[5] S. Frixione *et al.*, Nucl. Phys. **B454**, 3 (1995).
[6] S. Frixione *et al.*, Phys. Lett. **B319**, 339 (1993).
[7] H1 Collaboration, A. Aktas *et al.*, Eur. Phys. J. **C48**, 71 (2006).
[8] ZEUS Collaboration, S. Chekanov *et al.*, Eur. Phys. J. **C38**, 43 (2004).
[9] W.M. Yao *et al.* (Particle Data Group), J. Phys. **G33**, 1 (2006).
[10] ZEUS Collaboration, S. Chekanov *et al.*, Eur. Phys. J. **C44**, 351 (2005).
[11] C. Peterson *et al.*, Phys. Rev. **D27**, 105 (1983).
[12] H1 Collaboration, C. Adloff *et al.*, Phys. Lett. **B 52**, 191 (2001).
[13] ZEUS Collaboration, S. Chekanov *et al.*, Phys. Lett. **B545**, 244 (2002).
[14] B.W. Harris, J. Smith, Phys. Rev. **D57**, 2806 (1998).
[15] L. Alvero et al, Phys. Rev. **D59**, 074022 (1999).
[16] J.C. Collins, Phys. Rev. **D57**, 3051 (1998).

Diffractive Open Charm Production at H1

Paul Thompson[1]

1- School of Physics - University of Birmingham
BIRMINGHAM B15 2TT - UK

Measurements are presented [1] of diffractive open charm production at HERA where two analysis techniques are used for the cross section measurements. In the first, the charm quark is tagged by the reconstruction of a $D^{*\pm}(2010)$ meson. This technique is used in deep-inelastic scattering (DIS) and photoproduction (γp). In the second, a method based on the displacement of tracks from the primary vertex is used to measure the open charm contribution to the inclusive diffractive cross section in DIS. The measurements are compared with next-to-leading order QCD predictions based on diffractive parton density functions previously obtained from a QCD analysis of the inclusive diffractive cross section at H1.

1 Introduction

In quantum chromodynamics (QCD), the theory of strong interactions, the hard scattering collinear factorization theorem [2] predicts that the cross section for diffractive deep-inelastic ep scattering (DIS) factorizes into a set of universal diffractive parton density functions (DPDFs) of the proton and process-dependent hard scattering coefficients. Next-to-leading order (NLO) DPDFs have been determined by QCD fits to the measured cross sections of inclusive diffractive scattering at HERA [3] within the factorizable Pomeron model [4] and using the DGLAP evolution equations. The DPDFs have been found to be dominated by gluons, which carry $\approx$70 % of the momentum of the diffractive exchange.

In the collinear factorization approach diffractive open charm production at HERA is expected mainly to proceed via boson gluon fusion (BGF). Thus it is directly sensitive to the gluon content of the diffractive exchange, which is only determined indirectly and for low momentum fractions $z_{I\!P}$ of the gluon in inclusive diffractive scattering via scaling violations [3]. In the BGF process a charm quark anti-quark pair ($c\bar{c}$) is produced of which one quark couples to the photon with virtuality Q^2 and the other to a gluon that emerges from the diffractive exchange.

In an alternative theoretical approach DPDFs are not introduced and diffractive scattering is explicitly modeled by the perturbative exchange of a colorless gluon state (two gluons or a gluon ladder). Formulated in the proton rest frame the "two-gluon" state of the proton can couple directly to the $c\bar{c}$ pair ($\gamma^* p \to c\bar{c}p$) or to a $c\bar{c}g$ color dipole fluctuation of the photon ($\gamma^* p \to c\bar{c}gp$) [5]. A model combining the perturbative two-gluon approach with the collinear factorization scheme, which has also been used to fit the HERA diffractive DIS cross sections, is given in [6].

This article is based on the recent paper on diffractive open charm production from H1 appearing in [7]. Two methods to identify charm production are presented. In the first method the charm quark is tagged by the reconstruction of D^* mesons. The measurement is performed in DIS and, due to the high selectivity of the trigger, extended to photoproduction (γp). The second method, which was used to measure the total inclusive charm and beauty cross sections in DIS [8, 9], is used for the first time in diffractive DIS. In this method, referred to in the following as the 'displaced track analysis', the charm quark is identified

by the reconstruction of tracks, which are displaced from the interaction vertex, that arise due to long lived charmed hadrons. This method is used in a kinematic region with high acceptance for the decay products of charmed hadrons within the silicon vertex detector of H1, which is used in the reconstruction of these tracks. With this method it is thus possible to measure the total open charm contribution to the diffractive cross section with small extrapolations from QCD calculations.

2 Results

Diffractive $D^{*\pm}$ production in DIS is studied in the kinematic range of $2 < Q^2 < 100$ GeV^2, $0.05 < y < 0.7$, $x_{I\!P} < 0.04$, $M_Y < 1.6$ GeV, $|t| < 1$ GeV^2, $p_t(D^*) > 2$ GeV, and $|\eta(D^*)| < 1.5$. In γp diffractive $D^{*\pm}$ production is studied in the kinematic range of $Q^2 < 0.01$ GeV^2, $0.3 < y < 0.65$, $x_{I\!P} < 0.04$, $M_Y < 1.6$ GeV, $|t| < 1$ GeV^2, $p_t(D^*) > 2$ GeV and $|\eta(D^*)| < 1.5$. A good agreement between the data cross sections, integrated over the kinematic ranges given above, and the NLO QCD calculations is observed.

The D^* meson cross section in DIS is also measured differentially as a function of various kinematic variables. For example, in Figure 1 the cross section as a function of $x_{I\!P}$ and an estimate of the invariant mass of the $c\bar{c}$ pair emerging from the hard scattering process $z_{I\!P}^{obs}$ is shown. The data are compared in the figure with the predictions of NLO QCD calculations based on two (Fit A and Fit B) alternative sets of diffractive parton density functions from H1 [3], which both provide a good description of the inclusive diffractive DIS data. The differences in the predictions for the two DPDFs are moderate, with $z_{I\!P}^{obs}$ showing the greatest sensitivity. However, within the present experimental errors and theoretical uncertainties these differences cannot be resolved.

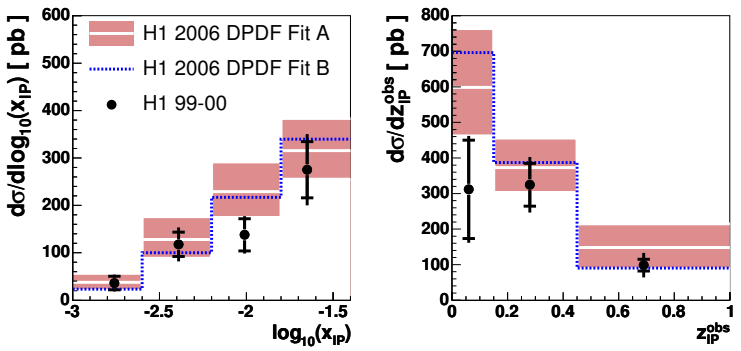

Figure 1: The diffractive D^* cross section in DIS shown as a function of $x_{I\!P}$ and $z_{I\!P}^{obs}$.

In γp the D^* cross section is also shown differentially as a function of the diffractive kinematic variables $x_{I\!P}$ and $z_{I\!P}^{obs}$ in Figure 2. The data are well described by the theoretical predictions within the larger experimental errors for γp. As in DIS the largest sensitivity to the different parameterizations of the gluon is evident in the $z_{I\!P}^{obs}$ distribution.

The good agreement of the NLO QCD predictions with the measured cross sections observed in DIS and γp, both in shape and normalization, supports the assumption that QCD factorization is applicable in both kinematic regimes. A quantity, which is less sensitive to the input of diffractive parton density functions and theoretical uncertainties is defined by $R_{\rm DIS}^{\gamma p} = \frac{\left(\sigma^{\rm meas}/\sigma^{\rm theo}\right)_{\gamma p}}{\left(\sigma^{\rm meas}/\sigma^{\rm theo}\right)_{\rm DIS}}$ where $\sigma^{\rm meas}$ and $\sigma^{\rm theo}$ denote the measured and the predicted

integrated cross section for D^* production. The ratio $R_{\rm DIS}^{\gamma p}$ is found to be $1.15 \pm 0.40(\text{stat.}) \pm 0.09(\text{syst.})$. The theoretical uncertainty on $R_{\rm DIS}^{\gamma p}$ is $\pm 7\%$. The measurement of $R_{\rm DIS}^{\gamma p}$ shows no evidence for a suppression of the γp component although the statistical error of the measurement is large.

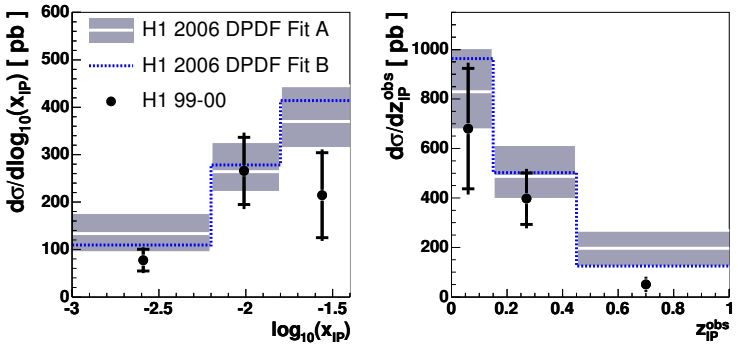

Figure 2: The diffractive D^* cross section in γp shown as a function of $x_{I\!P}$ and $z_{I\!P}^{obs}$.

An additional comparison of both the NLO QCD calculations and of the prediction from the perturbative two gluon calculation of BJKLW [5] with differential cross sections has been made in the range of validity of the model ($x_{I\!P} < 0.01$). Good agreement between the data and both the model of BJLKW and the NLO QCD calculations is observed in this kinematic range. For the two gluon calculation the $\gamma^* p \to c\bar{c}gp$ contribution is seen to dominate with the $\gamma^* p \to c\bar{c}p$ process contributing only at high values of $z_{I\!P}^{obs}$.

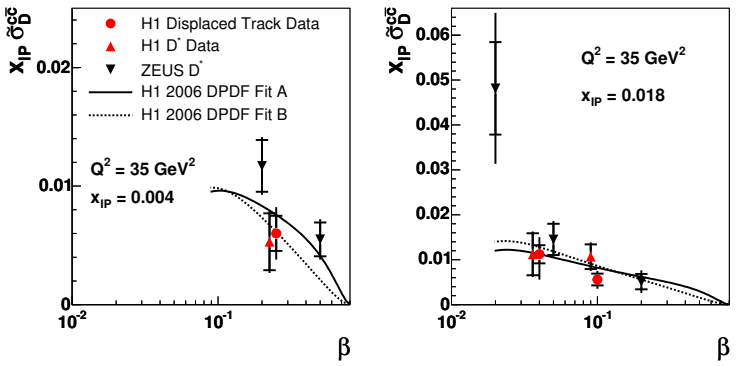

Figure 3: The reduced cross section $x_{I\!P}\tilde{\sigma}_D^{c\bar{c}}$ shown as a function of β for two different values of $x_{I\!P}$.

The measurements of the diffractive charm DIS cross sections obtained from the displaced track method are used to measure the diffractive charm reduced cross section. The reduced cross section is approximately equal to the charm contribution $F_2^{D(3)c\bar{c}}$ to the diffractive structure function $F_2^{D(3)}$. The difference is due to the contribution from the longitudinal diffractive charm cross section, which is expected to be small for the data points presented.

The measurements of $x_{I\!P}\tilde{\sigma}_D^{c\bar{c}}$ obtained from the displaced track method are shown in Figure 3 as a function of β for fixed values of Q^2 and $x_{I\!P}$. The measured points of $x_{I\!P}\tilde{\sigma}_D^{c\bar{c}}$ are compared with the results extracted from the D^* meson analysis. For this purpose the D^* cross section is measured in the same kinematic ranges as for the displaced track method. These measurements in the visible D^* kinematic range $p_t(D^*) > 2$ GeV and $|\eta(D^*)| < 1.5$

are extrapolated with the NLO calculation program HVQDIS to the full D^* kinematic phasespace in order to extract the diffractive open charm cross section. The extrapolation factors are found to be ≈ 2.5. The H1 data are also compared with D^* measurements from the ZEUS collaboration [10] which are interpolated to the same kinematic range as the H1 measurement using the NLO QCD fit and corrected with a factor of 1.23 to account for the difference in the measured range of M_Y of the experiments. The measurements for $x_{I\!P}\tilde{\sigma}_D^{c\bar{c}}$ from the displaced track analysis and the D^* extraction methods from both H1 and ZEUS are in good agreement. A comparison with the predictions of the NLO DPDFs shows a good description of the data.

The measurements have also been presented in the form of the fractional contribution of charm to the total diffractive ep cross section $f_D^{c\bar{c}}$. In the given kinematic range the value of $f_D^{c\bar{c}}$ is $\approx 20\%$ on average, which is comparable to the charm fraction in the inclusive cross section at low values of Bjorken x for similar values of Q^2 [9]. The inclusive measurements have also been compared with the predictions of the MRW model [6]. A good description of the data is observed supporting the validity of the DPDFs extracted in this model.

3 Summary

Measurements have been presented of the diffractive charm cross section in DIS and γp using two independent methods of charm reconstruction. A comparison with QCD calculations in NLO based on DPDFs obtained from inclusive diffractive scattering at H1 is in good agreement with the measurement in both kinematic regimes. No evidence is observed for a suppression in γp. At low M_X the data are found to be also well described by models based on two gluon exchange and diffractive parton densities.

4 Bibliography

References

[1] Slides:
`http://indico.cern.ch/contributionDisplay.py?contribId=82&sessionId=13&confId=9499`

[2] J. C. Collins, *Phys. Rev.* **D 57** (1998) 3051 [Erratum-ibid. **D 61** (2000) 019902] [hep-ph/9709499].

[3] H1 Collaboration, *"Measurement and QCD analysis of the diffractive deep-inelastic scattering cross section at HERA"*, DESY 06-049, accepted by *Eur. Phys. J.* **C** [hep-ex/0606004].

[4] G. Ingelman, and P. Schlein, *Phys. Lett.* **B 152** (1985) 256;
A. Donnachie and P. Landshoff, *Phys. Lett.* **B 191** (1987) 309 [Erratum-ibid. B **198** (1987) 590].

[5] J. Bartels, H. Lotter, M. Wüsthoff, *Phys. Lett.* **B 379** (1996) 239 [Erratum-ibid. B **382** (1996) 449] [hep-ph/9602363];
J. Bartels, C. Ewerz, H. Lotter, M. Wüsthoff, *Phys. Lett.* **B 386** (1996) 389 [hep-ph/9605356];
J. Bartels, H. Jung, M. Wüsthoff, *Eur. Phys. J.* **C 11** (1999) 111 [hep-ph/9903265];
J. Bartels, H. Jung, A. Kyrieleis, *Eur. Phys. J.* **C 24** (2002) 555 [hep-ph/0204269].

[6] A. D. Martin, M. G. Ryskin, G. Watt, *Eur. Phys. J.* **C 44** (2005) 69 [hep-ph/0504132];

[7] A. Aktas et al., [H1 Collaboration], *Eur. Phys. J.* **C 50** (2007) 1 [hep-ex/0610076].

[8] A. Aktas et al., [H1 Collaboration], *Eur. Phys. J.* **C 40** (2005) 349 [hep-ex/0411046].

[9] A. Aktas et al., [H1 Collaboration], *Eur. Phys. J.* **C 45** (2006) 23 [hep-ex/0507081].

[10] S. Chekanov et al., [ZEUS Collaboration], *Nucl. Phys.* **B 672** (2003) 3 [hep-ex/0307068].

Heavy Flavor Production in DGLAP Improved Saturation Model

Sebastian Sapeta[1,2]

1- M. Smoluchowski Institute of Physics, Jagellonian University,
Reymonta 4, 30-059 Cracow, Poland

2- Department of Physics, CERN, Theory Division,
CH-1211 Geneva 23, Switzerland

The saturation model with DGLAP evolution is shown to give good description of the production of the charm and beauty quarks in deep inelastic scattering. The modifications of saturation properties caused by the presence of heavy quarks are also discussed.

1 Introduction

The saturation model of Golec-Biernat and Wüsthoff (GBW) [2] has been very successful in describing both the inclusive, F_2, and diffractive, $F_2^{D(3)}$, structure functions of proton at low values of the Bjorken variable x. It incorporates the idea of parton saturation in a simple way by introducing the x-dependent saturation scale in the form $Q_s^2(x) = (x_0/x)^\lambda$ with the parameters x_0 and λ determined from the fit to F_2. The model was then improved by Bartles, Golec-Biernat and Kowalski (BGK) [3] by including the DGLAP evolution of the gluon density, whose effects are important for the small-r part of the dipole cross section. This allowed to describe the new, more precise, HERA data. However, only the three light quarks contributions to the inclusive structure function F_2 were considered by these authors.

In order to consistently describe DIS one should take into account also the contributions of the heavy quarks since, as found by H1 [5] and ZEUS [6], they may reach 30% for charm and 3% for beauty. In this short note [1] we present the results of the studies [4] of the DGLAP improved saturation model where also the charm and beauty quarks are present. The parameters of the model with the five flavors are fixed by the fit to the F_2 experimental data. Then, the contributions of the heavy quarks to the proton structure function, $F_2^{c\bar{c}}$ and $F_2^{b\bar{b}}$, as well as the longitudinal structure function F_L and the diffractive structure function $F_2^{D(3)}$ are *predicted*.

This study is related to that presented in [7] where the proton profile function is taken in a Gaussian form. In our case, however, the gluons are assumed to be evenly distributed over a certain area with a sharp boundary. Furthermore, in our approach we do not need to introduce an arbitrary mass for the light quarks as it was done in [2, 3, 7, 8, 9].

2 The DGLAP improved saturation model

The dipole picture of the photon-proton interaction at low x has been demonstrated to be a useful tool for calculating proton structure functions, both inclusive and diffractive. In this framework $\gamma^* p$ interaction is regarded as a two-stages process. Firstly, the photon with the virtuality Q^2 dissociates into a quark-antiquark par of a given flavor. This pair, referred to as a color dipole, is characterized by the fraction of the photon momentum carried by the quark (or antiquark) z and the $q\bar{q}$ transverse distance vector $\vec{r}$. The splitting is described by

the photon wave function $\Psi(\vec{r}, z, Q^2, m_f^2, e_f)$, quantity fully calculable in quantum electrodynamics (QED). In the second stage, described by the dipole cross section $\hat{\sigma}(x, \vec{r})$, the color dipole interacts with the proton and, since the non-perturbative contributions are expected to be important, modeling of $\hat{\sigma}(x, \vec{r})$ cannot be avoided. The expression for the inclusive proton structure function F_2 may be, quite generally, written as

$$F_2(x, Q^2) = \frac{Q^2}{4\pi^2\,\alpha_{\rm em}} \sum_f \sum_P \int d^2\vec{r} \int_0^1 dz\, |\Psi_P^f\,(\vec{r}, z, Q^2, m_f^2, e_f)|^2\, \hat{\sigma}\,(x, \vec{r}), \tag{1}$$

where the sums run over the quark flavors f and the polarizations of the virtual photon P.

In the BGK model the following form of the dipole cross section is used

$$\hat{\sigma}(x, r) = \sigma_0 \left\{ 1 - \exp\left(-\frac{\pi^2}{3\,\sigma_0}\, r^2\, \alpha_s(\mu^2)\, xg(x, \mu^2) \right) \right\}, \tag{2}$$

where $\mu^2 = C/r^2 + \mu_0^2$. It interpolates between the GBW cross section [2] (at large r) and the perturbative result [10] (at small r). Thus, both the feature of color transparency and gluon saturation are incorporated in this definition. The gluon distribution evolves with μ^2 according to the leading order DGLAP equation, simplified further by neglecting quarks, with the MRST inspired initial condition

$$xg(x, Q_0^2) = A_g\, x^{\lambda_g} (1 - x)^{5.6} \qquad \text{at} \qquad Q_0^2 = 1\ \text{GeV}^2. \tag{3}$$

Altogether, the model has five parameters σ_0, C, μ_0^2, A_g and λ_g, which are determined by the fit to the F_2 data. The fit with the charm and beauty contributions was performed using the recent data from H1 [11] and ZEUS [12]. The H1 data points were multiplied by 1.05 to account for slightly different normalizations between the two experiments. Since the dipole picture is expected to be valid only at sufficiently small x we restricted ourselves to $x < 0.01$. Due to the fact that the gluon density is evolved according to DGLAP equations the model is supposed to work for any value of photon virtuality. Thus, in the fit, we used the entire range of Q^2 covered by the data. This gave us 288 experimental points. The light quarks were taken massless and the typical values for the masses of the heavy quarks were used, namely $m_c = 1.3$ GeV and $m_b = 5.0$ GeV. The number of active flavors was set to 4 (for the fit with charm) or 5 (for the fit with charm and beauty), the value of $\Lambda_{\rm QCD} = 300$ MeV, and the argument in the dipole cross section was modified $x \to x\left(1 + 4m_f^2/Q^2\right)$ similarly to [2, 3].

3 Fit results and model predictions

The results of the fit with heavy quarks are summarized in Table 1, where also the light quarks fit parameters from [3] are recalled for reference. We see that the quality of the fit in terms of χ^2/ndf is good. Adding heavy quarks results in a rather dramatic change of the parameters of the model. In particular, the sign of the power λ_g alters which means that the initial gluon distribution grows with decreasing x oppose to the the case of the light quarks fit where it was valencelike.

The predictions for the heavy quark contributions to the structure function, $F_2^{c\bar{c}}$ and $F_2^{b\bar{b}}$, are presented in Fig. 1. We observe very good agreement with the data points from

	σ_0 [mb]	A_g	λ_g	C	μ_0^2	χ^2/ndf
light + c + b	22.7	1.23	- 0.080	0.35	1.60	1.16
light + c	22.4	1.35	- 0.079	0.38	1.73	1.06
light	23.8	13.71	0.41	11.10	1.00	0.97

Table 1: The results of our fits with heavy quarks to the F_2 data and the massless fit from [3].

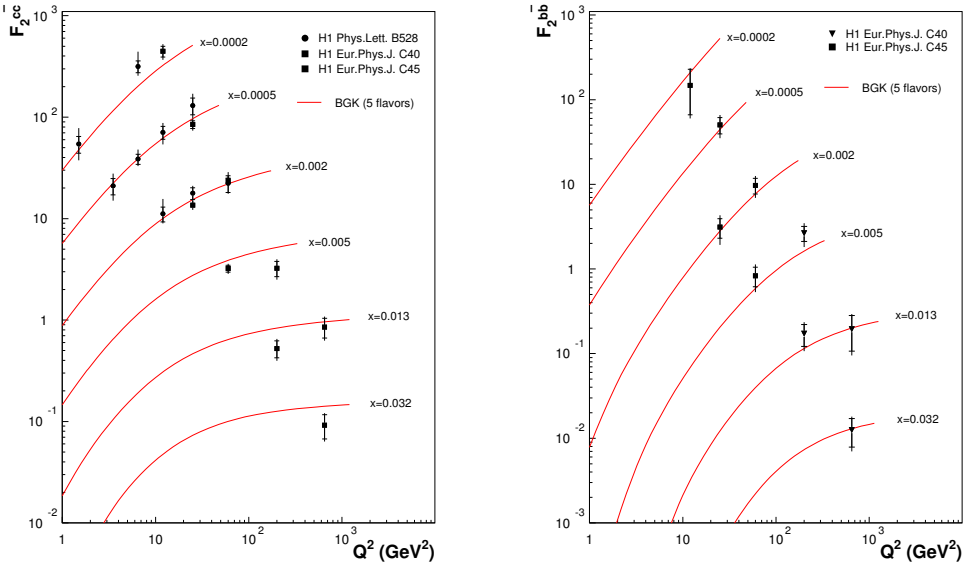

Figure 1: Predictions for the charm ($\times 4^n$) and beauty ($\times 8^n$) structure functions from the BGK model with heavy quarks compared with the H1 data [5].

H1 [5]. This persists even for $x > 0.01$ that is beyond the range used in the fit to determine the model parameters.

The diffractive structure function $F_2^{D(3)}$ was also calculated and good agreement with the H1 and ZEUS data was found. Likewise, the longitudinal structure function F_L obtained from our analysis agrees with the H1 estimations. For more details on F_L and $F_2^{D(3)}$ the reader is referred to [4].

Let us finally discuss the effect of heavy quarks on the position of the critical line. This line in (x, Q^2) plane which marks the transition to the saturation region is plotted in Fig. 2. We have checked [4] that the presence of heavy quarks shifts this line slightly towards the smaller values of Q^2 at low x. Similar behavior has been already observed in the GBW model [2]. Let us also point out that the critical line presented in Fig. 2 is very similar to that obtained by Soyez [9] in the modified Iancu, Itakura and Munier (IMM) model [8] with heavy quarks (see [4] and [9] for the precise, slightly different, definitions of the critical lines).

4 Conclusions

We have shown that the DGLAP improved saturation model with heavy quarks provides successful description of a considerable number of quantities measured in DIS. In particular, it predicts correctly the charm and beauty contributions to the proton structure function. This result is quite remarkable given the simplicity of the framework we use. This may suggest that the k_T factorization is a more efficient way of approaching DIS at small x (see also [13]) or be considered as an argument supporting the idea of saturation at HERA.

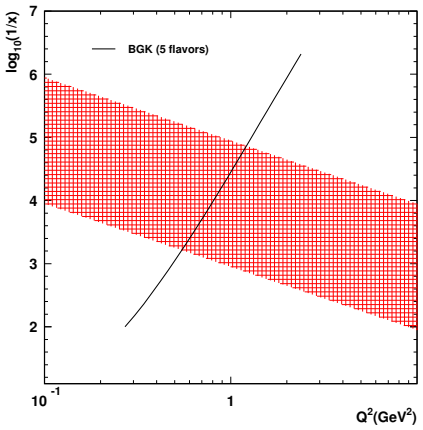

Figure 2: The critical line from our analysis together with the acceptance region of HERA.

5 Acknowledgments

I would like to express my gratitude to Krzysztof Golec-Biernat with whom this work has been done. It is also a pleasure to thank Leszek Motyka for numerous valuable discussions during this workshop. The support from Marie Curie ESRT Fellowship of the European Community's Sixth Framework Programme under contract number (MEST-CT-2005-020238) and the grant of Polish Ministry of Science N202 048 31/2647 (2006-08) are gratefully acknowledged.

References

[1] Slides:
`http://indico.cern.ch/contributionDisplay.py?contribId=80&sessionId=13&confId=9499`

[2] K. Golec-Biernat and M. Wusthoff, Phys. Rev. **D59** 014017 (1999);
K. Golec-Biernat and M. Wusthoff, Phys. Rev. **D60** 114023 (1999).

[3] J. Bartels, K. Golec-Biernat and H. Kowalski, Phys. Rev. **D66** 014001 (2002).

[4] K. Golec-Biernat and S. Sapeta, Phys. Rev. D **74** 054032 (2006).

[5] C. Adloff *et al.* [H1 Collaboration], Phys. Lett. B **528**, 199 (2002);
A. Aktas *et al.* [H1 Collaboration], Eur. Phys. J. C **40**, 349 (2005);
A. Aktas *et al.* [H1 Collaboration], Eur. Phys. J. C **45**, 23 (2006).

[6] S. Chekanov *et al.* [ZEUS Collaboration], Eur. Phys. J. C **21**, 443 (2001).

[7] H. Kowalski and D. Teaney, Phys. Rev. D **68**, 114005 (2003);
H. Kowalski, L. Motyka and G. Watt, Phys. Rev. D **74** 074016 (2006).

[8] E. Iancu, K. Itakura and S. Munier, Phys. Lett. B **590**, 199 (2004).

[9] G. Soyez, arXiv:0705.3672 [hep-ph] (2007).

[10] L. Frankfurt, A. Radyushkin and M. Strikman, Phys. Rev. **D55**, 98 (1997).

[11] C. Adloff *et al.* [H1 Collaboration], Eur. Phys. J. C **21** 33 (2001).

[12] S. Chekanov *et al.* [ZEUS Collaboration], Eur. Phys. J. C **21** 443 (2001);
J. Breitweg *et al.* [ZEUS Collaboration], Phys. Lett. B **487** 53 (2000).

[13] H. Jung, this proceedings.

Hadronic Final States and QCD

Convenors:
Daniel Traynor,
Alexandre Savin,
Duncan Brown,
Giulia Zanderighi

High Momentum Hadron and Jet Production in Photon-Photon Collisions at LEP2

Attila Krasznahorkay Jr.[1,2] for the OPAL collaboration

1- University of Debrecen - Dept. of Experimental Physics
4010, Debrecen, Egyetem tér 1. - Hungary

2- CERN - PH Dept.
CH-1211, Geneva 23 - Switzerland

The inclusive production of charged hadrons ($e^+e^- \to e^+e^- + X$) and jets ($e^+e^- \to e^+e^- + \text{jet} + X$) have been studied in collisions of quasi-real photons radiated by the LEP beams at e^+e^- centre-of-mass energies $\sqrt{s_{ee}}$ from 183 to 209 GeV. The differential cross-sections measured as a function of the transverse momentum and pseudorapidity of the hadrons and jets are compared to theoretical calculations in next-to-leading order of the strong coupling constant.

1 Introduction

We have studied the inclusive production of jets in collisions of two quasi-real photons at e^+e^- centre-of-mass energies, $\sqrt{s_{ee}}$, from 189 to 209 GeV, with a total integrated luminosity of 593 pb^{-1} [2], and the inclusive production of charged hadrons at $\sqrt{s_{ee}}$ from 183 to 209 GeV with a total integrated luminosity of 612.8 pb^{-1} [3]. The data has been collected with the OPAL [4, 5, 6] detector.

Hadronic interactions of two photons lead to the production of hadrons whose properties in Quantum Chromo Dynamics (QCD) depend on the underlying partonic processes, as well as on the way in which the partons are transformed into observable hadrons (fragmentation). In the measurement of hadron production this transformation is described by fragmentation functions obtained from fits to data. Jet observables on the other hand are constructed with the aim of minimising the difference between the observed quantity on parton and on hadron level. The remaining discrepancies (hadronisation corrections) are studied using hadronisation models as implemented in MC event generators. The studies of hadron and jet production therefore complement each other in the attempt to unveil the underlying partonic processes in the description of hadronic photon-photon interactions.

2 Analysis

For the hadron cross section measurements the tracks of the charged hadrons are reconstructed in the central tracking chamber. To select events coming from photon-photon interactions, standard cuts on reconstructed quantities are applied. Selected events have to have at least six tracks, passing tight quality cuts. Single- and double-tagged events are rejected by applying a 60 GeV cut on the total measured energy in the forward detectors. Beam-gas and beam-wall backgrounds are reduced by requiring the primary vertex to have a radial distance less than 2 cm from the beam axis and a z-distance of less than 3 cm from the interaction point.

The inclusive jet cross section analysis uses the $k_\perp$ algorithm [7, 8] to reconstruct jets from photon-photon interactions. Since high p_T inclusive jet events from photon-photon

interactions are difficult to separate from hadronic Z decays, especially at high momenta, a likelihood event selection [9] was used to separate signal and background events. The performance of the event selection is demonstrated in Figure 1.

The measured transverse momentum and pseudorapidity distributions have to be corrected for the losses due to event, track and jet selection cuts, the acceptance and the resolution of the detector. This is done using the Monte Carlo signal events which were processed by the full detector simulation and reconstruction chain. The correction factors are calculated as the bin-by-bin ratio of the generated and reconstructed Monte Carlo distributions. This method only yields reliable results if migration effects between bins due to the finite resolution of the measurements are small. The bins in the differential distributions have therefore been chosen to be significantly larger than the detector resolution, obtained from the Monte Carlo simulation.

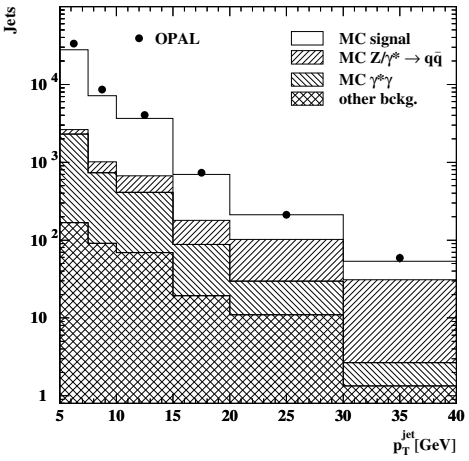

Figure 1: Number of jets in each $p_{\mathrm{T}}^{\mathrm{jet}}$ bin after event selection

NLO calculations do not take into account the possibility of an underlying event, which leads to an increased energy flow and therefore a larger cross-section above any given threshold in transverse momentum. In the inclusive jet analysis PYTHIA [10], which uses multiple parton interactions (MIA) to model this effect, was used to study either considering or leaving out multiple parton interactions for the signal MC. At the lowest transverse momenta considered, the signal MC cross-section increases by up to 20% when including MIA. This effect reduces to less than 10% for transverse momenta larger than 7 GeV.

The measured cross-sections are compared to NLO QCD calculations which describe cross-sections for partons, while the experimental cross-sections are presented for hadrons. Hadronisation corrections have also been estimated with PYTHIA. For inclusive jets the correction at $p_{\mathrm{T}}^{\mathrm{jet}} = 5$ GeV is about -15%. The correction decreases with increasing $p_{\mathrm{T}}^{\mathrm{jet}}$ and is below -5% for $p_{\mathrm{T}}^{\mathrm{jet}} > 20$ GeV.

3 Differential cross-sections

To facilitate a comparison with a recent measurement by the L3 collaboration [11], the inclusive jet cross section measurement was performed with kinematic conditions such as the ones used in the L3 analysis. Figure 2 shows the resulting inclusive jet differential cross section. It shows the total statistical and systematical uncertainties added in quadrature where larger than the marker size. The uncertainty band on the NLO calculation shows the uncertainty associated to the variation of the renormalisation scale.

Both PYTHIA 6.221 and the NLO calculation achieve a good description of the data, with the exception of the lowest bin in $p_{\mathrm{T}}^{\mathrm{jet}}$, where the NLO calculation is too low. While the L3 data points are compatible with the present measurement, they lie below the OPAL

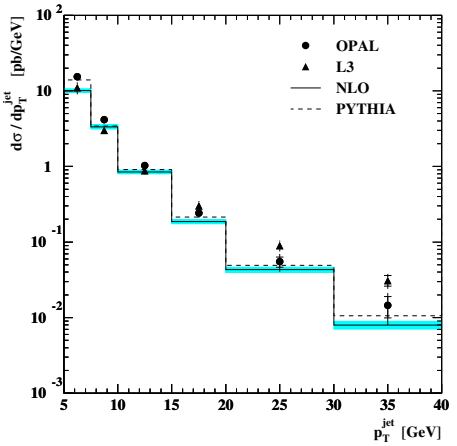

Figure 2: Inclusive jet differential cross section, $d\sigma/dp_{\mathrm{T}}^{\mathrm{jet}}$, for all jets with $|\eta^{\mathrm{jet}}| < 1.0$ compared to the results of the L3 collaboration, NLO and PYTHIA predictions.

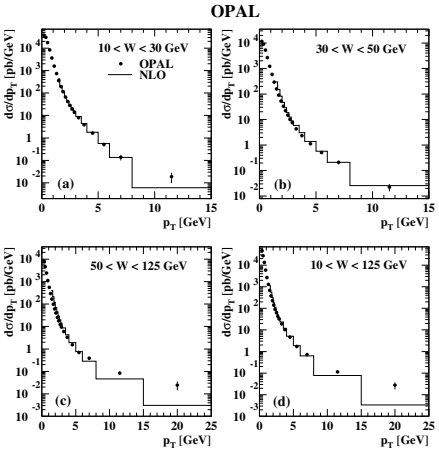

Figure 3: Differential inclusive charged hadron production cross-sections $d\sigma/dp_{\mathrm{T}}$ for $|\eta| < 1.5$ in the indicated W ranges.

data points at low $p_{\mathrm{T}}^{\mathrm{jet}}$ and above the OPAL data points at high $p_{\mathrm{T}}^{\mathrm{jet}}$, and there is a discrepancy in shape between the L3 data and the NLO calculation. This difference in shape has been reported in the L3 publication and leads to a significant disagreement between the L3 measurement and the NLO calculation at the highest $p_{\mathrm{T}}^{\mathrm{jet}}$ of up to 50 GeV studied in [11]. The OPAL analysis [2] finds the region of $p_{\mathrm{T}}^{\mathrm{jet}} > 40$ GeV to be dominated by background and hence no measurement is presented for this region.

The differential inclusive cross sections $d\sigma/dp_{\mathrm{T}}$ for charged hadrons in four ranges of the hadronic invariant mass W are shown in Figure 3. For the cross section calculation a minimum p_{T} of 1.5 GeV is required to ensure the validity of the perturbative QCD calculation. The NLO calculation achieves a good general description of the data, except for transverse momenta greater than about 10 GeV, which can be reached in the highest W range only.

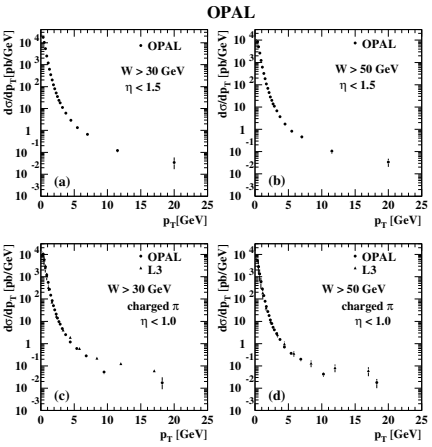

Figure 4: Differential inclusive charged hadron production cross-sections $d\sigma/dp_{\mathrm{T}}$ in the indicated η and W ranges.

Figure 4 (a) and (b) show the differential cross-section $d\sigma/dp_{\mathrm{T}}$ for charged hadrons for $W > 30$ GeV and $W > 50$ GeV. To facilitate a comparison with a recent measurement by L3 [12] of charged pions, the measure-

ment has been done in the pseudorapidity range $|\eta| < 1.0$ in (c) and (d). The OPAL data shown in Figure 4 (c) and (d) have been scaled to account for the reduced $|\eta|$ range and for the fraction of charged pions of all charged hadrons using MC simulations. From this comparison it is evident that the distributions measured by OPAL fall more rapidly towards high transverse momenta than those measured by L3, leading to a disagreement between the two experiments at high transverse momenta and a better description of the OPAL data by NLO QCD than is the case for the L3 data.

References

[1] Slides:
`http://indico.cern.ch/contributionDisplay.py?contribId=213&sessionId=6&confId=9499`

[2] G. Abbiendi *et al.* [OPAL Collaboration], "Inclusive Jet Production in Photon-Photon Collissions at $\sqrt{s_{ee}}$ from 189 to 209 GeV", Submitted to Phys. Lett. B

[3] G. Abbiendi *et al.* [OPAL Collaboration], "Inclusive Production of Charged Hadrons in Photon-Photon Collisions", Accepted by Phys. Lett. B [arXiv:hep-ex/0612045v1]

[4] K. Ahmet *et al.* [OPAL Collaboration], Nucl. Instrum. Meth. A **305** (1991) 275.

[5] G. Abbiendi *et al.* [OPAL Collaboration], Eur. Phys. J. C **14** (2000) 373 [arXiv:hep-ex/9910066].

[6] G. Abbiendi *et al.* [OPAL Collaboration], Eur. Phys. J. C **33** (2004) 173 [arXiv:hep-ex/0309053].

[7] S. Catani, Y. L. Dokshitzer, M. H. Seymour and B. R. Webber, Nucl. Phys. B **406** (1993) 187.

[8] S. D. Ellis and D. E. Soper, Phys. Rev. D **48** (1993) 3160 [arXiv:hep-ph/9305266].

[9] D. A. Karlen, Comput. Phys. **12:4** (1998) 380.

[10] T. Sjostrand, Comput. Phys. Commun. **82** (1994) 74.

[11] P. Achard *et al.* [L3 Collaboration], Phys. Lett. B **602** (2004) 157 [arXiv:hep-ex/0410012].

[12] P. Achard *et al.* [L3 Collaboration], Phys. Lett. B **554** (2003) 105 [arXiv:hep-ex/0301025].

Status of $e^+e^- \to 3$ Jets at NNLO

Aude Gehrmann

Institute for Theoretical Physics, ETH, CH-8093 Zürich, Switzerland

We present the essential ingredients of the calculation of the next-to-next-to-leading order QCD corrections to three-jet production observables in electron-positron annihilation. Infrared singularities due to double real radiation at tree level and single real radiation at one-loop are extracted using the antenna subtraction method applied at next-to-next-to-leading order. All contributions to the three-jet cross section are implemented in a parton level generator. First results obtained with this generator concerning the NNLO contribution to the thrust event shape distribution are given here.

1 Introduction

Jet production cross sections in e^+e^- annihilation processes are classical observables which can be measured very accurately. These observables can be seen as a testing ground for the applicability of perturbative QCD. Furthermore, by comparing the measured 3-jet rate with the theoretical predictions for this rate, one can determine the strong coupling constant α_s. It turns out that the current error on α_s from jet observables [2] is dominated by the theoretical uncertainty. This uncertainty is related to the renormalisation scale dependence introduced by truncating the perturbative series at a given order in α_s. So far the 3-jet rate had been calculated up to the next-to-leading order (NLO)[3]. Clearly, to improve the determination of α_s, the calculation of the NNLO corrections to the 3-jet rate becomes mandatory. This calculation is now completed. We shall here briefly report on its essential ingredients and present first phenomenologically significant results concerning the thrust distribution.

2 The $e^+e^- \to 3$ jet cross section

Three-jet production at tree-level is induced by the decay of a virtual photon (or other neutral gauge boson) into a quark-antiquark-gluon final state. At higher orders, this process receives corrections from extra real or virtual particles.The individual partonic channels that contribute through to NNLO are shown in Table 1. All of the tree-level and loop amplitudes associated with these channels are known in the literature [4, 5, 6].

Partons are combined into jets using the same jet algorithm as in experiments such that the measured jet cross sections can be directly compared with the jet cross sections predicted theoretically. For the 3-jet rate, at leading order, each parton forms a jet on its own. At NLO, up to four partons can be present in the final state, in which case two of them are combined into one jet whereas at NNLO, up to five partons can be present in the final state such that three partons are clustered in one jet. The more partons are included in the jet, the more the parton-level jets resemble the hadron level jets seen experimentally and the better the matching between theory and experiments is.

LO	$\gamma^* \to q\,\bar{q}g$	tree level
NLO	$\gamma^* \to q\,\bar{q}g$	one loop
	$\gamma^* \to q\,\bar{q}\,gg$	tree level
	$\gamma^* \to q\,\bar{q}\,q\bar{q}$	tree level

NNLO	$\gamma^* \to q\,\bar{q}g$	two loop
	$\gamma^* \to q\,\bar{q}\,gg$	one loop
	$\gamma^* \to q\,\bar{q}\,q\,\bar{q}$	one loop
	$\gamma^* \to q\,\bar{q}\,q\,\bar{q}\,g$	tree level
	$\gamma^* \to q\,\bar{q}\,g\,g\,g$	tree level

Table 1: The partonic channels contributing to $e^+e^- \to 3$ jets.

3 Infrared subtraction terms

To build 3-jet final states at a given order, a jet algorithm has to be applied separately to each partonic channel contributing at this order and all partonic channels have to be summed. However, each partonic channel contains infrared singularities which, after summation, cancel among each other. Consequently, these infrared singularities have to be extracted before the jet algorithm can be applied. While explicit infrared singularities from purely virtual contributions are obtained immediately after integration over the loop momenta, their extraction is more involved for real radiation. The singularities associated with the real emission of soft and/or collinear partons in the final state become only explicit after integrating the real radiation matrix elements over the appropriate phase space.

The infrared singularities of the real radiation contributions can be extracted using infrared subtraction terms. These terms must be constructed such that they approximate the full real radiation matrix elements in all singular limits while still being integrable analytically.

At NNLO, m-jet production is induced by final states containing up to $(m+2)$ partons, including the one-loop virtual corrections to $(m+1)$-parton final states. One introduces subtraction terms for the $(m+1)$- and $(m+2)$-parton contributions such that schematically the NNLO m-jet cross section reads,

$$\begin{aligned} \mathrm{d}\sigma^{m}_{NNLO} \;=\; & \int_{\mathrm{d}\Phi_{m+2}} \left(\mathrm{d}\sigma^{R}_{NNLO} - \mathrm{d}\sigma^{S}_{NNLO}\right) \\ & + \int_{\mathrm{d}\Phi_{m+1}} \left(\mathrm{d}\sigma^{V,1}_{NNLO} - \mathrm{d}\sigma^{VS,1}_{NNLO}\right) \\ & + \int_{\mathrm{d}\Phi_{m+2}} \mathrm{d}\sigma^{S}_{NNLO} + \int_{\mathrm{d}\Phi_{m+1}} \mathrm{d}\sigma^{VS,1}_{NNLO} + \int_{\mathrm{d}\Phi_{m}} \mathrm{d}\sigma^{V,2}_{NNLO}\,. \end{aligned} \tag{1}$$

$\mathrm{d}\sigma^{S}_{NNLO}$ denotes the real radiation subtraction term. It has the same unintegrated singular behaviour as $\mathrm{d}\sigma^{R}_{NNLO}$ in all appropriate limits. Likewise, $\mathrm{d}\sigma^{VS,1}_{NNLO}$ is the one-loop virtual subtraction term coinciding with the one-loop $(m+1)$-parton cross section $\mathrm{d}\sigma^{V,1}_{NNLO}$ in all singular limits. Finally, the two-loop correction to the m-parton cross section is denoted by $\mathrm{d}\sigma^{V,2}_{NNLO}$. Each line in the above formula is finite, free of any ϵ-poles, and can be implemented in a numerical program evaluating the jet rate.

To construct the subtraction terms, various methods exist at next-to-leading order [7] and general algorithms are available for the construction of one-particle subtraction terms [8, 9]. All of these algorithms derived in the framework of perturbative QCD are based

on the factorisation properties of matrix element and phase spaces in kinematical regions corresponding to one parton becoming soft or collinear. One of these methods is antenna subtraction [9], which derives the one-particle subtraction terms at NLO from physical three-parton matrix elements. We extended this method to NNLO level [10], deriving one- and two-particle subtraction terms from three- and four-parton matrix elements [11]. These one and two-particle subtraction terms have been integrated analytically using the results given in [12].

Using this method, to evaluate the 3-jet rate at NNLO, we obtain numerically finite contributions from five-parton and four-parton processes. Furthermore we observe an explicit analytic cancellation of infrared poles in the four-parton and three-parton contributions, thus providing us with a powerful check of our method.

4 Numerical implementation and results

The different finite contributions have been implemented in a parton-level generator evaluating the 3-jet rate. Our starting point was the generator for $e^+e^- \to 4$ jets at NLO [13]. It contained already the 4-parton and 5-parton matrix elements and was based on the NLO antenna subtraction formalism. To this generator, we added the following contributions respectively in the 5-parton, 4 parton and 3-parton channels: the NNLO subtraction terms, the 1-loop real integrated subtraction term and the 2-loop matrix element. To embed the phase space present in the subtraction terms into the full phase space we used the mappings defined in [14]. The implementation is now completed, checked and first phenomenological results will soon be available. At this conference, we presented first results concerning the thrust distribution.

At NNLO, it takes the following form: (fixing $\mu_R = Q, \alpha_S = \alpha_s(Q)$)

$$\begin{aligned}(1-T)\,\frac{1}{\sigma_{\rm had}}\,\frac{{\rm d}\sigma}{{\rm d}T} \;&=\; \left(\frac{\alpha_s}{2\pi}\right) A(T) + \left(\frac{\alpha_s}{2\pi}\right)^2 (B(T) - 2A(T)) \\ &\quad + \left(\frac{\alpha_s}{2\pi}\right)^3 (C(T) - 2\,B(T) - 1.64\,A(T))\end{aligned}$$

The fixed order contributions to the thrust distribution are given in Fig. 1. We see that the NNLO corrections are of the order of 10-15% of the total result. Although the corrections are sizeable, the perturbative expression converges for this observable.

5 Conclusions

We have discussed the essential ingredients of the calculation of the $e^+e^- \to 3$ jets at NNLO. To perform this computation, the antenna subtraction method extended up to the NNLO level was required. All contributions to the 3-jet rate were implemented into a parton-level generator and the calculation is now finalised. As a first phenomenological result, we found that the NNLO contribution to the thrust distribution yield an enhancement of $10 - 15\%$, demonstrating the perturbative stability of the fixed order approach for this observable.

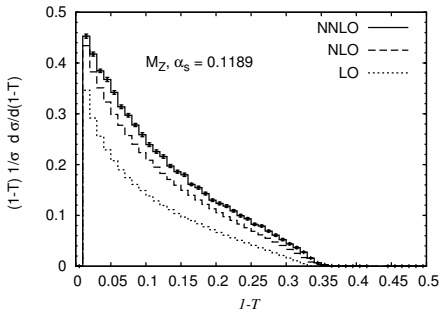

Figure 1: Thrust distribution at $\sqrt{s} = M_Z$.

References

[1] Slides:
`http://indico.cern.ch/contributionDisplay.py?contribId=171&sessionId=6&confId=9499`

[2] S. Bethke, Prog. Part. Nucl. Phys. **58** (2007) 351.

[3] R.K. Ellis, D.A. Ross and A.E. Terrano, Nucl. Phys. B **178** (1981) 421.

[4] L.W. Garland, T. Gehrmann, E.W.N. Glover, A. Koukoutsakis and E. Remiddi, Nucl. Phys. B **627** (2002) 107 and **642** (2002) 227.

[5] S. Moch, P. Uwer and S. Weinzierl, Phys. Rev. D **66** (2002) 114001.

[6] E.W.N. Glover and D.J. Miller, Phys. Lett. B **396** (1997) 257; Z. Bern, L.J. Dixon, D.A. Kosower and S. Weinzierl, Nucl. Phys. B **489** (1997) 3; J.M. Campbell, E.W.N. Glover and D.J. Miller, Phys. Lett. B **409** (1997) 503; Z. Bern, L.J. Dixon and D.A. Kosower, Nucl. Phys. B **513** (1998) 3.

[7] Z. Kunszt and D.E. Soper, Phys. Rev. D **46** (1992) 192.

[8] S. Catani and M.H. Seymour, Nucl. Phys. B **485** (1997) 291; **510** (1997) 503(E).

[9] D.A. Kosower, Phys. Rev. D **57** (1998) 5410; **71** (2005) 045016.

[10] A. Gehrmann-De Ridder, T. Gehrmann and E. W. N. Glover, JHEP **0509** (2005) 056.

[11] A. Gehrmann-De Ridder, T. Gehrmann and E.W.N. Glover, Nucl. Phys. B **691** (2004) 195; Phys. Lett. B **612** (2005) 36; **612** (2005) 49.

[12] A. Gehrmann-De Ridder, T. Gehrmann and G. Heinrich, Nucl. Phys. B **682** (2004) 265.

[13] J. Campbell, M.A. Cullen and E.W.N. Glover, Eur. Phys. J. C **9** (1999) 245.

[14] D.A. Kosower, Phys. Rev. D **67** (2003) 116003.

Measurement of Isolated Photon Production in Deep Inelastic Scattering at HERA

Katharina Müller

University of Zurich
Winterthurerstrasse 190 , CH - 8057 Zuerich - Switzerland

Results are presented on the production of isolated photons $ep \to e + \gamma + X$ in deep inelastic scattering with a four-momentum transfer squared of $4 < Q^2 < 150$ GeV^2, inelasticity $y > 0.05$ and a mass of the hadronic system $W_X > 50$ GeV. Isolated photons are selected in the range $3 < E_T^\gamma < 10$ GeV and pseudorapidity range $-1.2 < \eta^\gamma < 1.8$. The cross sections, both inclusive and for events with zero or at least one additional jet, are measured with the H1 detector at the electron-proton collider HERA. The analysis is based on a total integrated luminosity of 227 pb^{-1}. The measurements are compared to MC predictions and to a LO calculation. Both approaches underestimate the observed signal, particularly in the low Q^2 domain.

1 Introduction

Photons originating from the hard interaction in high energy collisions are a sensitive probe for precision tests of perturbative QCD and provide information on the proton structure. In contrast to measurements using hadrons, a measurement with isolated photons minimises uncertainties from parton fragmentation, hadronisation or jet identification. Furthermore, the experimental uncertainties of the energy measurement are smaller for electromagnetic showers in the calorimeter initiated by photons than for jets of hadrons. The measurement of isolated photons in deep-inelastic scattering (DIS) provides a test of QCD in a kinematic range with two hard scales, the four-momentum transfer squared Q^2 of the exchanged virtual photon and the transverse energy of the emitted photon.

Previously H1 and ZEUS [2, 3, 4] have measured prompt photon cross sections in photoproduction. An analysis of the isolated photon cross section in DIS with Q^2 larger than 35 GeV^2 has been published by ZEUS [5].

In DIS the final state photon is emitted by a quark (QQ subprocess), by wide angle radiation from the lepton (LL subprocess) or by interference (LQ subprocess). Since the photon and the scattered electron are well separated in the present analysis, low angle QED radiation is suppressed. The LL and the more interesting QQ process can not be distinguished experimentally on event basis, but only by comparison with predictions.

This paper presents the measurement of isolated photon production $e + p \to e + \gamma + X$, where X is anything. Jet production in events with isolated photons and no additional jet or with at least one jet is also investigated. The measurement range covered by this analysis significantly extends the kinematic range probed by the previous measurement [5]. The results are compared to a recent leading order, $\mathcal{O}(\alpha^3\alpha_s^0)$, calculation [6, 7] and to the predictions of the event generators PYTHIA [8], simulating the QQ process, and RAPGAP [9] for the LL process.

2 Analysis method

2.1 Event selection

The event sample used in this analysis was collected with the H1 Detector [10, 11] at HERA in the period from 1999 to 2005 at a centre-of-mass energy of 318 GeV. The corresponding integrated luminosity is 227 pb^{-1}.

DIS events are selected with the scattered electron identified by a compact electromagnetic cluster with an energy $E'_e > 10$ GeV and a polar angle $\theta_e < 177^\circ$ in the backward calorimeter (SpaCal). Q^2 is restricted to $4 < Q^2 < 150$ GeV^2 and the inelasticity to $y > 0.05$. A photon candidate is identified as a cluster in the electromagnetic section of the liquid argon (LAr) calorimeter [12, 13] with a transverse energy $3 < E_T^\gamma < 10$ GeV and pseudo-rapidity $-1.2 < \eta^\gamma < 1.8$ and no track pointing to it within 20 cm. Background from elastic Compton scattering is suppressed by a cut on the invariant mass of the hadronic system, $W_X > 50$ GeV. Jets with a transverse momentum of $P_T^{jet} > 2.5$ GeV and a pseudorapidity in the range $-2.0 < \eta^{jet} < 2.1$ are reconstructed using the k_T algorithm [14], where jets are treated as massless. The algorithm is used with a P_T-weighted recombination scheme and the separation parameter R_0 is set to one. The jet containing the photon candidate is classified as photon-jet the others as hadronic jets. Hadronic jets are restricted to the pseudorapidity range $-1.0 < \eta^{jet} < 2.1$. To ensure isolation of the photon, the fraction of the transverse energy of the photon-jet carried by the photon candidate has to be larger than 90%. The isolation criterion rejects background from photons induced by hadron decays.

2.2 Photon signal extraction

The isolated photon signal is extracted using a shower shape analysis. It is based on the fact that electromagnetic showers in the calorimeter initiated by isolated photons tend to be more narrow, symmetric and compact and tend to start off slightly deeper in the calorimeter than background showers. Six different shower shape variables are defined. The background originates mainly from neutral hadrons with subsequent decays to multi-photon states. Probability density functions are determined for the six shower shape variables, using simulated *single particles events* with photons and a mix (π^0, η, η', ρ, ω, $K^\star$, K_L^0, K_S^0, n and $\bar{n}$) of neutral hadrons, respectively. The relative contribution of any neutral hadron is taken from the RAPGAP MC. The multi-dimensional photon and background probability densities are taken as the product of the respective shower shape densities. For each measured event a discriminator is formed. It is defined as the photon probability density divided by the sum of the probability densities for photons and background. The discriminator produces generally larger values for isolated photons than for the multi-photon clusters. The contribution of photons and neutral hadrons in any analysis bin is determined by independent minimum-χ^2 fits of the signal and background discriminator distributions to the data distribution.

3 Isolated photon cross section

Differential cross sections $d\sigma/d\eta^\gamma$ and $d\sigma/dQ^2$ for the inclusive isolated photon cross section are shown in Figure 1 together with the predictions by the LO calculation. The uncertainty on the shower description gives the dominant contribution to the systematical error. The calculation is corrected to hadron level. The corrections amount to at most -30%.

The LO calculation underestimates the cross sections in average by roughly 44%, most significantly at low Q^2. The relative contribution of LL and QQ depends strongly on η^γ and Q^2. At high and medium η^γ and low Q^2, radiation by the quark dominates. The data are also compared to the MC prediction of PYTHIA for the radiation from the quark and RAPGAP for the radiation from the electron (not shown). The sum of the MC predictions gives a very similar result as the LO calculation and also underestimates the data significantly. The

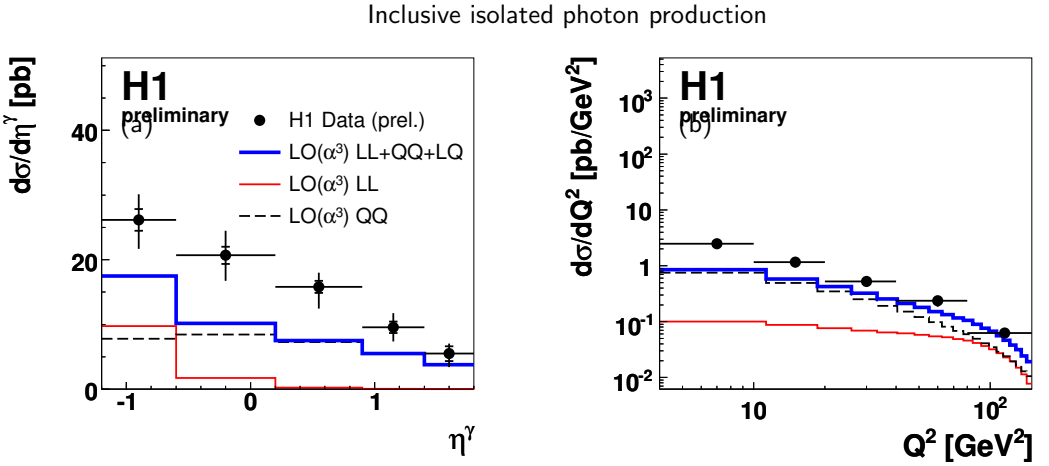

Figure 1: Inclusive differential isolated photon cross sections $d\sigma/d\eta^\gamma$ (a), $d\sigma/dQ^2$ (b) for $3 < E_T^\gamma < 10$ GeV, $-1.2 < \eta^\gamma < 1.8$, $W_X^2 > 2500$ GeV^2 and $4 < Q^2 < 150$ GeV^2. The inner error bars on the data points indicate the statistical error, the full error bars contain in addition the systematic errors added in quadrature. The cross sections are shown together with a leading order, $\alpha^3\alpha_s^0$, calculation corrected for hadronisation effects, LL corresponding to radiation from the electron and QQ to radiation from the quark.

cross section for jet production in association with isolated photons is studied using events with no or at least one hadronic jet. Figure 2 shows the differential cross sections $d\sigma/d\eta^\gamma$ for isolated photons with no-jet (a) and with jets (b). For both samples the LO calculation describes reasonably well the shape but is too low in normalisation. The LL contribution is largely suppressed for the photon plus no-jet sample due to the cut on W_X. The cross section for photon plus jets production is roughly two times higher than for the photon plus no-jets production.

4 Conclusions

The cross section for isolated photon production in deep inelastic scattering has been measured in the squared momentum transfer range $4 < Q^2 < 150$ GeV^2 and a mass of the hadronic system $W_X > 50$ GeV. A LO calculation and alternatively the PYTHIA generator for the simulation of photons radiated by the quark (QQ) together with photons radiated from the electron (LL) as predicted by RAPGAP describe the shape of the E_T^γ and η^γ distributions reasonably well, but lie below the data by 44% (LO) and 48% (MC). Both,

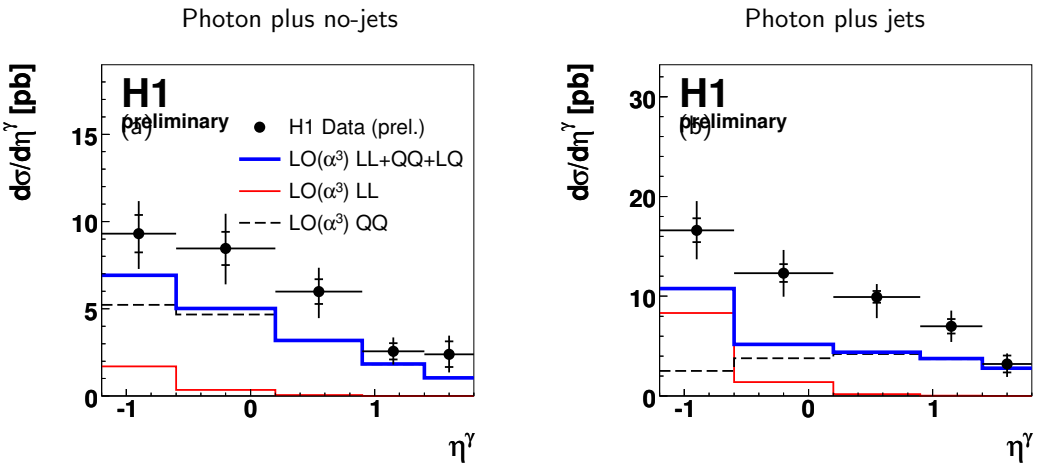

Figure 2: Differential cross sections $d\sigma/d\eta^\gamma$ for photon plus no-jets (a) and photon plus jets (b), with $P_T^{jet} > 2.5$ GeV and $-1.0 < \eta^{jet} < 2.1$. The cross sections are compared to a leading order, $\mathcal{O}(\alpha^3\alpha_s^0)$ as in Figure 1.

the LO calculation and the MC predictions are most significantly below the data at low Q^2. The cross sections for events with no or at least one hadronic jet are underestimated by the LO and MC predictions by a similar factor as in the inclusive measurement. Again the expectations are furthest below the data at low Q^2. The shapes of $d\sigma/dE_T^\gamma$ and $d\sigma/d\eta^\gamma$ are described reasonably well.

References

[1] Slides:
`http://indico.cern.ch/contributionDisplay.py?contribId=215&sessionId=6&confId=9499`

[2] J. Breitweg *et al.* [ZEUS Collaboration], Phys. Lett. B **472** (2000) 175

[3] A. Aktas *et al.* [H1 Collaboration], Eur. Phys. J. C **38** (2005) 437

[4] S. Chekanov *et al.* [ZEUS Collaboration], Eur. Phys. J. C **49** (2007) 511

[5] S. Chekanov *et al.* [ZEUS Collaboration], Phys. Lett. B **595** (2004) 86

[6] A. Gehrmann-De Ridder, T. Gehrmann and E. Poulsen, Phys. Rev. Lett. **96** (2006) 132002

[7] A. Gehrmann-De Ridder, T. Gehrmann and E. Poulsen, Eur. Phys. J. C **47** (2006) 395

[8] T. Sjöstrand *et al.*, PYTHIA 6.2 Physics and Manual (Version 6.224 is used)

[9] H. Jung, Comput. Phys. Commun. **86** (1995) 147 (Version 3.1 is used).

[10] I. Abt *et al.*, Nucl. Instr. and Meth. **A 386** (1997) 310, ibid, 348.

[11] R. D. Appuhn *et al.*, Nucl. Instrum. Meth. A **386** (1997) 397.

[12] B. Andrieu *et al.* [H1 Calorimeter Group], Nucl. Instrum. Meth. A **350** (1994) 57.

[13] B. Andrieu *et al.* [H1 Calorimeter Group], Nucl. Instrum. Meth. A **336** (1993) 499.

[14] S. D. Ellis and D. E. Soper, Phys. Rev. D **48** (1993) 3160

Prompt Photons with Associated Jets in Photoproduction at HERA

S. Chekanov

For the ZEUS Collaboration

DESY Laboratory, 22607, Hamburg, Germany.
On leave from the HEP division, Argonne National Laboratory,
9700 S.Cass Avenue, Argonne, IL 60439, USA
E-mail: chekanov@mail.desy.de

Prompt photons, together with an accompanying jet, have been studied in the photoproduction regime of ep scattering measured with the ZEUS detector at HERA. Predictions based on leading-logarithm parton-shower Monte Carlo models and next-to-leading-order (NLO) QCD underestimate the γ+jet cross sections for transverse energies of prompt photons below 7 GeV, while the k_T-factorisation QCD calculation agrees with the data in this region.

1 Theoretical calculations

Events with an isolated photon (prompt photon) are important tool to study hard interaction processes since such photons emerge without the hadronisation phase. In particular, final states with a prompt photon together with a jet are directly sensitive to the quark content of the proton through the elastic scattering of a photon by a quark, $\gamma q \to \gamma q$ (see Fig. 1). However, QCD contributions to this lowest-order process lead to a significant sensitivity to the gluon structure function. In particular, a contribution to prompt-photon events from $gq \to q\gamma$ process, in which the photon displays a hadronic structure (resolved process), is important [2–4]. Thus, prompt-photon events can constrain both proton and photon parton densities. In addition, a number of QCD predictions [2–5] can be confronted with the data.

The next-to-leading order (NLO) calculations based on the collinear factorisation and the DGLAP formalism were performed by Krawczyk and Zembrzuski (KZ) [3] and by Fontanaz, Guillet and Heinrich (FGH) [4]. No intrinsic transverse momentum of the initial-state partons in the proton was assumed. The renormalisation scale for such calculations was taken to be $\mu_R = E_T^\gamma$. In case of the KZ predictions, the GRV parameterisation of the proton, photon and fragmentation function were used [6, 7]. For the FGH calculations, MRST01 proton structure function and the AFG02 structure function for the photon were used [7]. The FGH NLO calculation takes into account high-order terms in the QCD expansion which have not been considered in the KZ approach.

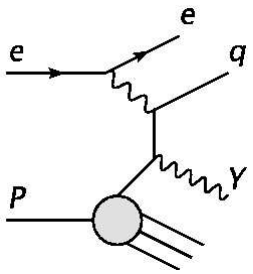

Figure 1. Lowest-order diagram (Compton scattering) for γ+jet events in ep collisions.

The QCD calculations based on the k_T-factorisation [8] approach were performed by A. Lipatov and N. Zotov (LZ) [5]. The unintegrated quark and gluon densities of the proton and photon using the Kimber-Martin-Ryskin (KMR) prescription [9] were used. As for the NLO QCD, both direct and resolved contributions are taken into account.

For all the calculations discussed above, an isolation requirement $E_T^\gamma > 0.9\, E_T^{tot}$ was used, where E_T is the transverse energy of the photon and E_T^{tot} is the total energy of the photon-candidate jet reconstructed with the longitudinally-invariant k_T algorithm in inclusive mode [10]. The γ+jet cross sections were corrected for hadronisation effects using a Monte Carlo (MC) simulation.

2 Event reconstruction

Each k_T jet, reconstructed from energy-flow objects (EFO), was classified as either a photon candidate or a hadronic jet. The photon-candidate jet was required to consist of EFOs without associated tracks and to be within the central tracking detector, $-0.74 < \eta^\gamma < 1.1$. For this jet, $E_{\rm EMC}/E_{\rm tot} > 0.9$ is required, where $E_{\rm EMC}$ is the energy reconstructed in the electromagnetic part of the CAL and $E_{\rm tot}$ is the total energy of this jet. After correction for energy losses, the cut $E_T^\gamma > 5\,$GeV was applied.

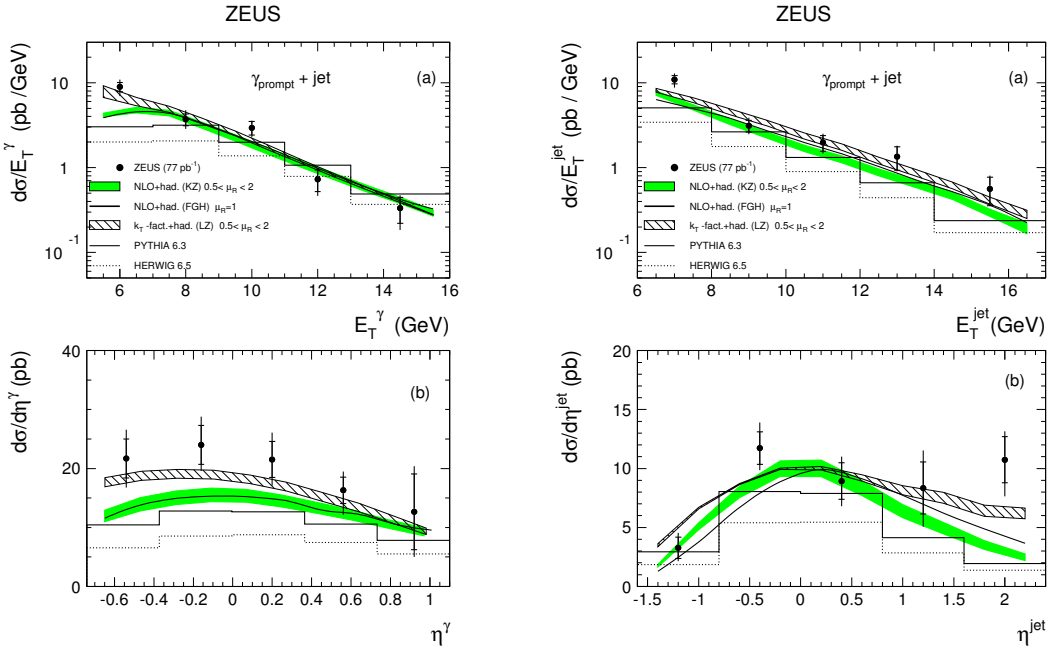

Figure 1. The differential γ+jet cross sections as functions of E_T and η for the prompt photon and the jet. The data are compared to QCD calculations and MC models. The shaded bands correspond to a typical renormalisation scale uncertainty which was obtained by changing μ_R by a factor of 0.5 and 2.

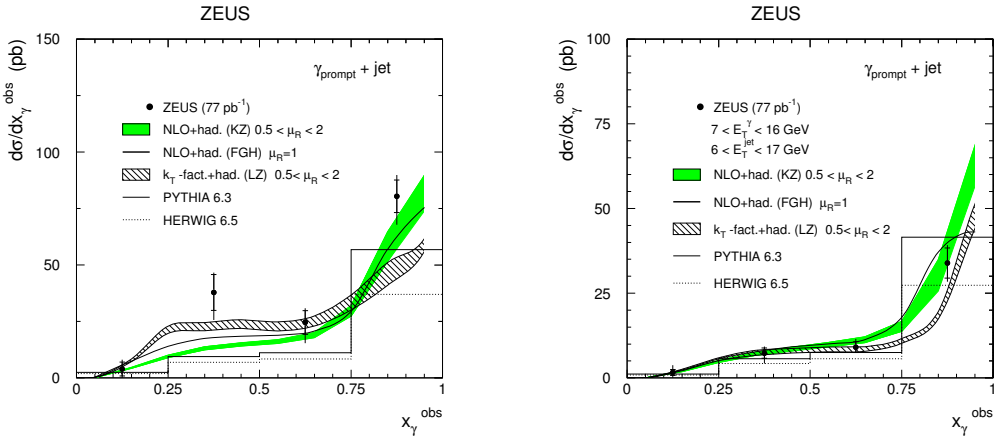

Figure 2. The $x_\gamma^{\rm obs}$ cross section for γ+jet events compared to the NLO QCD calculations and MC models for $E_T^\gamma > 5\,\text{GeV}$ (left) and $E_T^\gamma > 7\,\text{GeV}$ (right).

Hadronic jets, after correction for energy losses, were selected in the kinematic range $E_T^{\rm jet} > 6\,\text{GeV}$, $-1.6 < \eta^{\rm jet} < 2.4$. If more than one jet was found within the above kinematic cuts, the jet with the highest $E_T^{\rm jet}$ was accepted.

For the prompt-photon identification, the conversion-probability method was used [11]. In contrast to the shower-profile approach adopted in previous HERA measurements, the present approach uses the probability of conversion of photons to e^+e^- pairs in detector elements and inactive material (mainly the ZEUS superconducting coil) in front of the barrel calorimeter (BCAL). Since the conversion probability for a single photon is smaller than for multiphoton events arising from neutral meson decays (π^0, η, etc.), one can extract the γ signal by performing a statistical background subtraction.

To determine the number of charged particles in photon shower, the ZEUS barrel preshower detector (BPRE) [12] located in front of the BCAL was used. The measured output, calibrated in minimum ionising particle units (mips), is proportional to the energy loss of the incident particle after interaction with inactive material. The response of the BPRE to single isolated photons was verified using deeply virtual Compton scattering events. For the γ+jet, the BPRE signal for the γ candidates was fitted using a MC model with and without prompt photons, and the number of events associated with the photon signal was extracted.

3 Results and conclusions

The total cross section for the process $ep \to e + \gamma_{\rm prompt} + \text{jet} + X$ for $0.2 < y < 0.8$, $Q^2 < 1\,\text{GeV}^2$, $5 < E_T^\gamma < 16$ GeV, $6 < E_T^{\rm jet} < 17$ GeV, $-0.74 < \eta^\gamma < 1.1$, $-1.6 < \eta^{\rm jet} < 2.4$ and $E_T^{\gamma,(\rm true)} > 0.9\,E_T^\gamma$ was measured to be $\sigma(ep \to e + \gamma_{\rm prompt} + \text{jet} + X) = 33.1 \pm 3.0\,(\text{stat.})\,^{+4.6}_{-4.2}(\text{syst.})\,\text{pb}$.

This value agrees well with the LZ k_T-factorisation calculations ($30.7^{+3.2}_{-2.7}\,\text{pb}$), but higher than for the NLO QCD ($23.3^{+1.9}_{-1.7}\,\text{pb}$ (KZ) and $23.5^{+1.7}_{-1.6}\,\text{pb}$ (FGH)) and MC models.

The differential cross sections as functions of E_T and η for the prompt-photon candidates and for the accompanying jets are shown in Figure 1. The MC differential cross sections do

not rise as steeply at low E_T^γ as do the data. The KZ NLO prediction describes the data better. However, it underestimates the observed cross section at low E_T^γ and in the forward jet region. The FGH prediction is similar to the KZ NLO. The LZ prediction based on the k_T-factorisation approach gives the best description of the E_T and η cross sections.

Figure 2(left) shows the distribution for $x_\gamma^{\rm obs}$ defined as $\sum_{\gamma,{\rm jet}}(E_i - P_Z^i)/(2E_e y)$ (the sum runs over the photon candidate and the hadronic jet). The difference between the NLO QCD and the data is mainly concentrated in the resolved region.

It is important to verify the level of agreement with NLO when the minimum transverse energy of the detected prompt photons is increased from 5 GeV to 7 GeV. In comparison with previous measurements, such a choice may emphasize different aspect of contributions of high-order QCD radiation, since the transverse energy of the prompt-photon is larger than that of the jet.

Figure 2(right) shows the corresponding $x_\gamma^{\rm obs}$ distribution. For the $E_T^\gamma > 7$ GeV cut, both the NLO QCD and the LZ predictions agree well with the data. There is also good agreement for the E_T and η kinematic variables [11].

Acknowledgements. I thank M. Fontannaz, G. Heinrich, M. Krawczyk, A. Lipatov, N. Zotov and A. Zembrzuski for discussions and for providing the QCD calculations.

References

[1] Slides:
`http://indico.cern.ch/contributionDisplay.py?contribId=219&sessionId=6&confId=9499` .

[2] L. Gordon, W. Vogelsang, Phys. Rev. **D52**, 58 (1995).

[3] M. Krawczyk, A. Zembrzuski, Phys. Rev. **D64**, 14017 (2001).

[4] M. Fontannaz, J. P. Guillet, G. Heinrich, Eur. Phys. J. **C21**, 303 (2001).

[5] A. Lipatov, N. Zotov, Phys. Rev. **D72**, 054002 (2005).

[6] M. Glück, E. Reya, A. Vogt, Z. Phys. **C67**, 433 (1995);
M. Glück, E. Reya, A. Vogt, Phys. Rev. **D45**, 3986 (1992).

[7] A. D. Martin, et al., Eur. Phys. J. **C14**, 133 (2000);
P. Aurenche, J. P. Guillet, M. Fontannaz, Z. Phys. **C64**, 621 (1994).

[8] E. M. Levin, et al., Sov. J. Nucl. Phys. **53**, 657 (1991);
S. Catani, M. Ciafaloni, F. Hautmann, Nucl. Phys. **B366**, 135 (1991);
J. Collins, R. Ellis, Nucl. Phys. **B360**, 3 (1991).

[9] M. A. Kimber, A. D. Martin, M. G. Ryskin, Phys. Rev. **D63**, 114027 (2001);
G. Watt, A. D. Martin, M. G. Ryskin, Eur. Phys. J. **C31**, 73 (2003).

[10] S. Ellis, D. Soper, Phys. Rev. **D48**, 3160 (1993);
S. Catani, et al., Nucl. Phys. **B406**, 187 (1993).

[11] ZEUS Collaboration, S. Chekanov, et al., Eur. Phys. J. **C49**, 511 (2007).

[12] S. Magill, S. Chekanov, *Proceedings of the IX Int. Conference on Calorimetry (Annecy, Oct 9-14, 2000)*, B. Aubert, et al. (eds.), p. 625. Frascati Physics Series 21, Annecy, France (2001).

Photoproduction of Multijets and Jets with Rapidity Gaps at HERA

Alexander A. Savin *

University of Wisconsin-Madison
1150 University Ave., Madison, WI 5370-1390, USA

Three- and four-jet final states have been measured in photoproduction at HERA. Cross sections have been studied as functions of different kinematic variables and compared to predictions of leading-order models with and without mupli-parton interactions. Photoproduction of dijet events with large rapidity gap between jets shows a clear excess over the predictions of standard MC models. MC models which include a strongly interacting exchange of a color-single object are able to describe the data.

1 Three- and four-jet photoproduction

In photoproduction (PHP) at HERA, a quasi-real photon, which is emmitted by the incoming positron, interacts with a parton from the proton.

In leading order(LO) approach the photon can interact as a point-like particle, so called direct PHP, or can fluctuate into a partonic system, and subsequently transfer only a fraction of its momentum in the hard interaction, so called resolved PHP.

The hadron-like structure of the photon in resolved events gives rise to the possibility of multi-hadron interactions (MPI), where more then one pair of partons from the incoming hadrons may interact with each other.

Figure 1 presents four-jet-production cross section as a function of x_γ^{obs}, where x_γ^{obs} stays for the fraction of the photon's momentum that is exchanged in the interaction. Jets were found in the pseudorapidity region $|\eta^{jet}| \leq 2.4$ in the laboratory frame with $E_T^{jet1,2} \geq 7$ and $E_T^{jet3,4} \geq 5$ GeV. The phase space was also restricted in elasticity to $0.2 \leq y \leq 0.85$. M_{nj} measures the invariant mass of the n-jet system.

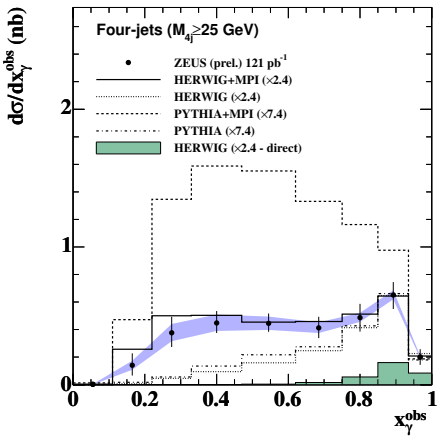

Figure 1: The four-jet-production cross section for $M_{4j} \geq 25$ GeV differential in x_γ^{obs}. HERWIG and PYTHIA predictions with and without MPI, as well as HERWIG direct component, are shown. Shaded band represents the calorimeter energy scale uncertainty.

Standard PHP MC predictions fail to describe the data. The MC underestimates the data in low-x_γ^{obs}, resolved enriched, region. Most pronounced difference is observed for the four-jet sample presented in Fig.1. The HERWIG model with MPIs, which was tuned to the three- and four-jet x_γ^{obs} and M_{nj} data presented here, describes the data well. The

*On behalf of the ZEUS collaboration

PYTHIA with MPIs tuned to generic collider data overestimates the cross sections. This problem was solved by retuning the model to the current data and new predictions will be shown in the final paper [2].

The cross sections differential in M_{nj} presented in Fig. 2 demonstrate that the three-jet sample is well described by both MC samples with and without MPI. For the four-jet sample the standard MCs describe the high tail of the M_{4j}, but significantly overestimate the cross section at low values of M_{4j}. In contrast, the MC predictions with MPI give a reasonable good description of the data over the full M_{4j} range.

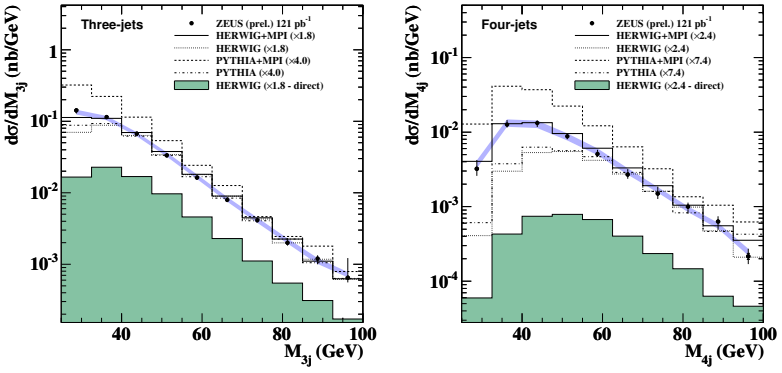

Figure 2: The three- and four-jet-production cross sections differential in M_{nj}. Other details as in Fig.1

Figure 3 shows the $d\sigma/dy$ cross section for the three-jet sample. The shape of the distribution is governed by the available phase space. Both MC models without MPI describe the shape of the distribution reasonably well. Adding the MPIs have a significant effect causing the MC predictions to deviate from the data. One of the possible explanation may be the y-dependence of the MPI, which in this case will need to be revised.

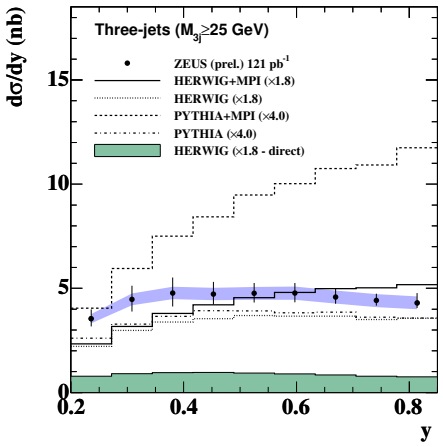

Figure 3: The three-jet-production cross section differential in y.

The three-jet measurements were also compared with predictions of $O(\alpha\alpha_S^2)$ pQCD calculations by Klasen, Kleinwort and Kramer [3]. The calculation is LO for this process. Both hadronisation and MPI corrections obtained using the average corrections taken from the two MC models were applied to the calculation. The theoretical uncertainties were found to be large. The overall magnitude and shape of the calculation largely agree with the data within large uncertainties. The description of the data was found to be much worse if the predictions were not corrected for the effects of MPIs.

2 Events with rapidity gaps between jets

The dominant mechanism for the production of jets with high transverse energy in hadronic collisions is a hard interaction between partons in the incoming hadrons via a quark or gluon propagator.

The exchange of color quantum numbers generally gives rise to jets in the final state that are color connected to each other and to the remnants of the incoming hadrons. This leads to energy flow populating the pseudorapidity region both between the jets and the hadronic remnants, and between the jets themselves. The fraction of events with little or no hadronic activity between the jets, gap fraction, is expected to be exponentially suppressed as the rapidity interval between the jets, $\Delta\eta$, increases. A non-exponentially suppressed fraction of such events would therefore be a signature of the exchange of a color-singlet object.

Events with at least two jets with $E_T^{jet1} > 6$ and $E_T^{jet2} > 5$ GeV and other cuts described in [4] were selected for this analysis. The transverse energy in the gap, E_T^{GAP}, was calculated by summing up the transverse energy of all jets, without any cut on $E_{\rm T}^{\rm jet}$, lying in the pseudorapidity region between the two highest-$E_{\rm T}^{\rm jet}$ jets.

The inclusive dijet cross section as a function of $E_{\rm T}^{\rm GAP}$ is presented in Fig. 4. At low $E_{\rm T}^{\rm GAP}$ values, where the color-singlet (CS) contribution should be most pronounced, the data demonstrate a clear excess over the non-CS (NCS) MC predictions towards small $E_{\rm T}^{\rm GAP}$ values. In order to estimate the amount of color-singlet contribution, the direct and resolved components of each MC were mixed according to their predicted MC cross sections to give the NCS MC sample. The NCS and CS MC samples were then fitted to the data according to

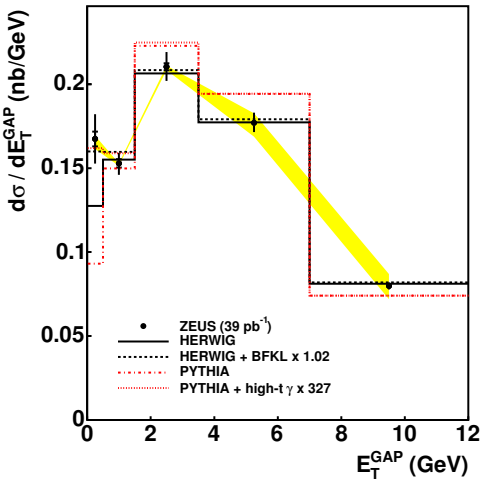

Figure 4: The inclusive dijet cross section, differential in $E_{\rm T}^{\rm GAP}$. The lines show predictions of Herwig and Pythia with and without CS exchange. The band shows the calorimeter energy-scale uncertainty.

$$\frac{d\sigma}{dE_{\rm T}^{\rm GAP}} = P_1 \frac{d\sigma^{\rm NCS}}{dE_{\rm T}^{\rm GAP}} + P_2 \frac{d\sigma^{\rm CS}}{dE_{\rm T}^{\rm GAP}},$$

where P_1 and P_2 were the free parameters of the fit. The best fit to the data resulted in $P_1 = 1.31 \pm 0.01$ and $P_2 = 327 \pm 20$ for Pythia and $P_1 = 1.93 \pm 0.01$ and $P_2 = 1.02 \pm 0.13$ for Herwig.

The large value of P_2 for Pythia reflects the very low cross section of the high-t photon exchange, which is not expected to represent the mechanism of strongly-interacting CS exchange and was only used to compare the data to an alternative CS model. In Herwig the CS exchange was implemented using the LLA BFKL model by Mueller and Tang [5].

The color-singlet contribution to the total cross section, estimated by integrating the MC predictions over the entire $E_{\rm T}^{\rm GAP}$ range, was $(2.75 \pm 0.10)\%$ for Pythia and $(2.04 \pm 0.25)\%$ for Herwig, where the errors represent only the statistical uncertainties of the fit.

Figure 5 shows the gap fraction as a function of $\Delta\eta$ for the two regions of $E_T^{\rm GAP}$. For $E_T^{\rm GAP} < 0.5$ GeV the data are consistent with a flat distribution in $\Delta\eta$. For higher $E_T^{\rm GAP}$ values the data first fall and then level out as $\Delta\eta$ increases The predictions of PYTHIA and HERWIG without color-singlet exchange lie below the data over the entire $\Delta\eta$ range. With the addition of the color-singlet contribution, both MC models describe the data well.

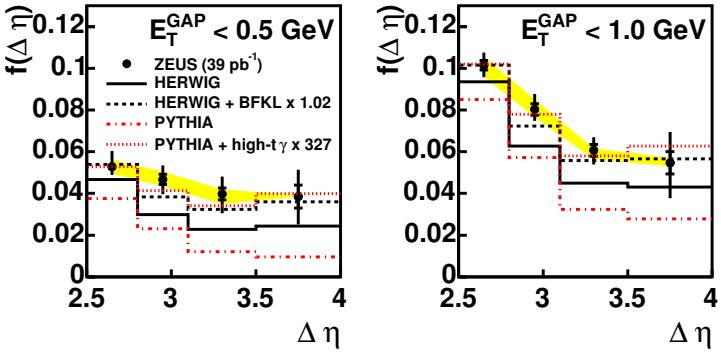

Figure 5: The gap fraction, f, as a function of $\Delta\eta$.

For comparison with other experiments and $p\bar{p}$ measurements, which are expected to be similar to the resolved-photon process, the cross sections and gap fraction were also measured as function of x_γ^{obs} (not shown). The gap fraction decreases with decreasing x_γ^{obs} and the data are reasonably described by both MC models only after including the CS contribution, especially in the resolved photon region, $x_\gamma^{obs} < 0.75$, and at low $E_T^{\rm GAP}$.

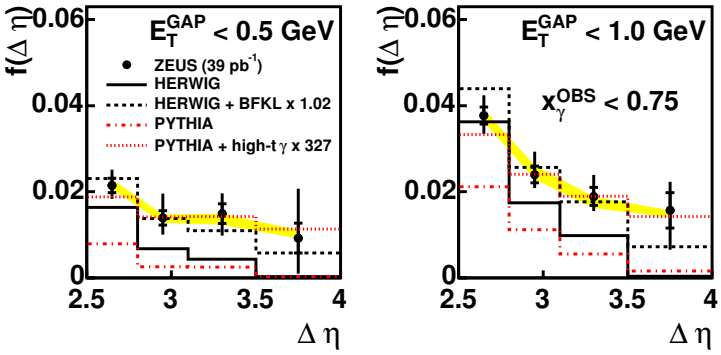

Figure 6: The gap fraction, f, as a function of $\Delta\eta$ in the resolved enriched region.

Figure 6 shows the gap fractions as a function of $\Delta\eta$ for the resolved enriched sample. For $E_T^{\rm GAP} < 0.5$ GeV and $E_T^{\rm GAP} < 1.0$ GeV, both MC models predict almost no contribution to the gap fractions from the non-color-singlet component at high values of $\Delta\eta$. Unfortunately large theoretical uncertainties and differences in the model predictions preclude a model-independent determination of the color-singlet contribution from these distributions.

References

[1] Slides: `http://indico.cern.ch/contributionDisplay.py?contribId=220&sessionId=6&confId=9499`

[2] ZEUS Coll., paper in preparation.

[3] M. Klasen, T. Kleinwort and G. Kramer, Z. Phys. Rev.-e **C1** (1998).

[4] ZEUS Coll., S. Chekanov *et al.*, Eur. Phys. J. **C50** 283 (2007)

[5] A.H. Mueller and W.K. Tang, Phys.Lett. **B310** 123 (1992)

High-E_T dijet photoproduction at HERA

Hanno Perrey *

Hamburg University - IExpPh
Luruper Chaussee 149, D-22761 Hamburg - Germany

Measurements of cross sections for high-E_T dijet production in photoproduction are presented. The data samples used were collected with the ZEUS detector at HERA and correspond to an integrated luminosity of $81.8\,\mathrm{pb}^{-1}$. The measured cross sections show sensitivity to the parton distributions in the photon and proton and to QCD effects beyond next-to-leading order. The data are therefore well-suited to further constrain the proton and photon parton distribution functions when used in global QCD fits.

1 Introduction

In photoproduction at HERA, a quasi-real photon, emitted from the incoming electron, collides with a parton from the incoming proton. The photoproduction of jets can be classified into two types of process in leading-order (LO) Quantum Chromodynamics (QCD). In direct processes, the photon participates in the hard scatter via either boson-gluon fusion or QCD Compton scattering. The second class, resolved processes, involves the photon acting as a source of quarks and gluons, with only a fraction of its momentum, x_γ^{obs}, participating in the hard scatter. Measurements of jet cross sections in photoproduction are sensitive to both the structure of the proton and photon and thus provide input to global fits of their parton densities. The objective of the measurement presented in this paper is threefold.

Firstly, the analysis was designed to provide constraints on the parton density functions (PDFs) of the photon. The effectiveness of available photon PDFs at describing HERA photoproduction data is tested by comparing the measured cross sections with next-to-leading order (NLO) predictions using different parameterizations of the photon structure, including the most up-to-date ones. The present analysis was conducted at higher transverse jet energy relative to previous publications.

Secondly, the present analysis was designed to provide constraints on the proton PDFs. A common feature of global fits to determine the proton structure is a large uncertainty in the gluon PDF for high values of x_p^{obs}, the fractional momentum at which partons inside the proton are probed. At such high values of x_p^{obs} the gluon PDF is poorly constrained and so attempts were made for the present investigation to measure cross sections which show particular sensitivity to these uncertainties. The cross sections in the following represent the best effort that can be made using HERA-I photoproduction data at high x_p .

Finally, the difference in azimuthal angle of two jets was considered. The cross sections defined in terms of this variable are directly sensitive to higher-order topologies and therefore provide a test of NLO QCD and of Monte Carlo (MC) models.

2 Data sample and event selection

The data were collected during the 1998–2000 running periods, when HERA operated with protons of energy $E_p = 920\,\mathrm{GeV}$ and electrons or positrons of energy $E_e = 27.5\,\mathrm{GeV}$. The results presented here are based on a total integrated luminosity of $81.8 \pm 1.8\,\mathrm{pb}^{-1}$.

*On behalf of the ZEUS collaboration.

The events were required to have a virtuality of the incoming photon Q^2 of less than $1\,\mathrm{GeV}^2$ and a photon-proton center-of-mass energy in the range $142 < W_{\gamma p} < 293\,\mathrm{GeV}$. Jets were reconstructed with a k_T-clustering algorithm using calorimeter information. Events were selected in which at least two jets were found with transverse jet energies of $E_T^{\mathrm{jet1}} > 20\,\mathrm{GeV}$, $E_T^{\mathrm{jet2}} > 15\,\mathrm{GeV}$ and a pseudorapidity in the range $-1 < \eta^{\mathrm{jet1,2}} < 3$, with at least one of the jets satisfying $-1 < \eta^{\mathrm{jet}} < 2.5$. This corresponds to an extension of 0.6 units in forward η direction compared to previous studies.

3 Monte Carlo models and NLO QCD calculations

The acceptance and the effects of detector response were determined using samples of simulated events. The programs Herwig 6.505 and Pythia 6.221, which implement the leading-order matrix elements, followed by parton showers and hadronization, were used. For both MC programs, the CTEQ5L and GRV-LO proton and photon PDFs, respectively, were used. The p_T^{min} for the outgoing partons from the hard scatter was set to 4 GeV. For the generation of resolved photon events, the default multi-parton interaction models were used.

For the NLO predictions, the calculation of Frixione and Ridolfi is used, which employs the subtraction method for dealing with the collinear and infra-red divergencies. The following parametrizations of the photon PDFs were used: Cornet et al. (CJK) [2], Aurenche et al. (AFG04) [3], Slominski et al. (SAL) [4], Glück et al. (GRV-HO) [5] and a previous set of PDFs from Aurenche et al. (AFG-HO) [6]. All PDFs were obtained in fits to data on the photon structure function F_2^γ from the LEP experiments, with only SAL additionally using previous dijet photoproduction data from ZEUS. The parametrization from CJK uses a more careful treatment of heavy quarks. The most striking difference between the resulting PDFs is the more rapid rise of the gluon density to low x_γ for CJK.

4 Theoretical and experimental uncertainties

The uncertainties on the pertubative QCD calculations are dominated by the effect of higher orders omitted in the pertubative expansion. These were assessed by a variation of the renormalization scale μ_R which lead to an uncertainty of $\pm$10–20% on the cross sections. Uncertainties arising from the hadronization correction and the choice of factorization scale and α_s gave much smaller contributions. All theoretical uncertainties were added in quadrature and are shown in the plots as shaded band around the central theoretical prediction.

The systematic uncertainties on the measurement are dominated by the uncertainty in the jet energy scale which is assumed to be $\pm$1%. As this uncertainty is correlated between bins, it is shown separately as shaded band in the figures. The next-largest uncertainty arises from the model dependence in the unfolding of the measured cross sections to hadron-level. Other sources of uncertainty such as variations of the cleaning cuts were also considered but are usually much smaller.

5 Dijet differential cross sections and sensitivity to photon PDFs

Dijet differential cross sections have been measured as functions of the mean transverse energy of the two leading jets $\bar{E}_T$. The measurement has been performed in two regions of

$x_\gamma^{\rm obs}$, namely a region enriched in direct photoproduction processes with $x_\gamma^{\rm obs} > 0.75$ and a resolved enriched region with $x_\gamma^{\rm obs} \leq 0.75$.

The cross sections $d\sigma/d\bar{E}_T$ are shown in Figure 1. For $x_\gamma^{\rm obs} > 0.75$, the NLO QCD predictions describe the data well, although some difference in shape is observed when using the AFG04 photon PDF. In the resolved enriched region, the prediction using CJK is much higher than the data in the first bin, but then agrees with the data for all subsequent bins. All photon PDFs have a similar shape and none can reproduce the shape of the measured distribution. In addition, apart from CJK, all are too low in the region $22.5 < \bar{E}_T < 37.5$ GeV.

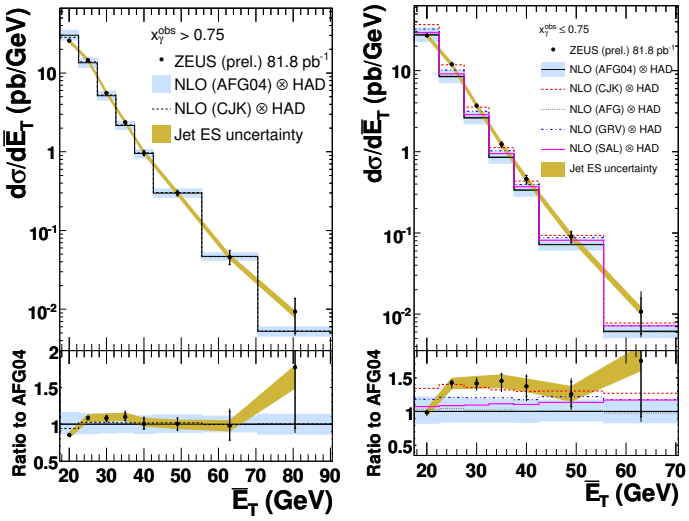

Figure 1: Cross sections $d\sigma/d\bar{E}_T$ in two regions of $x_\gamma^{\rm obs}$.

Also measured were cross sections as functions of $x_\gamma^{\rm obs}$, $x_p^{\rm obs}$, and the mean pseudorapidity of the two leading jets $\bar{\eta}$ (none shown here). For $x_\gamma^{\rm obs} > 0.75$ the data are usually well described by NLO QCD predictions, while for $x_\gamma^{\rm obs} \leq 0.75$ large deviations between predictions using different photon PDFs are observed with no PDF giving an adequate description of the data in all variables studied.

6 Measurement of $d\sigma/d|\Delta\phi|$

In LO QCD, the cross section as a function of the azimuthal difference would simply be a delta function located at π radians. However, the presence of higher-order effects results in the emission of additional partons in the final state and in values less than π radians. The cross section is therefore directly sensitive to higher-order topologies and provides a test of NLO QCD and of MC models. The cross sections measured as functions of the difference in azimuthal angle of two jets $|\Delta\phi|$ are shown in Figure 2 for $x_\gamma^{\rm obs}$ above and below 0.75.

The data are compared to predictions from NLO QCD and also the Herwig and Pythia MC programs. At high $x_\gamma^{\rm obs}$, NLO QCD agrees with the data at highest $|\Delta\phi|$, but it has a somewhat steeper fall off. The prediction from the Pythia MC program is similar to that for NLO QCD, whereas the prediction from the Herwig program describes the data well. For low $x_\gamma^{\rm obs}$, the distribution for NLO QCD is much too steep and is significantly below the data for all values of $|\Delta\phi|$ except the highest bin. The prediction from the Pythia program is less steep, but still gives a poor description. The prediction from the Herwig program is in remarkable agreement with the data.

7 Optimized cross sections

Cross-sections $d\sigma/dx_p^{\rm obs}$ optimized to be most sensitive to the uncertainty on the gluon PDF in the proton were also measured for $x_\gamma^{\rm obs}$ above and below 0.75. At high $x_\gamma^{\rm obs}$ the data are very well described by NLO QCD predictions. At low $x_\gamma^{\rm obs}$ the description by NLO QCD is less good, particularly when using the AFG04 photon PDF. Generally the predictions with CJK describe the data better. Inclusion of these data in future fits should be able to constrain the proton PDFs further, in particular that of the gluon. However, to fully exploit these data and include the cross section for low $x_\gamma^{\rm obs}$ a systematic treatment of the photon PDFs and their uncertainty is needed.

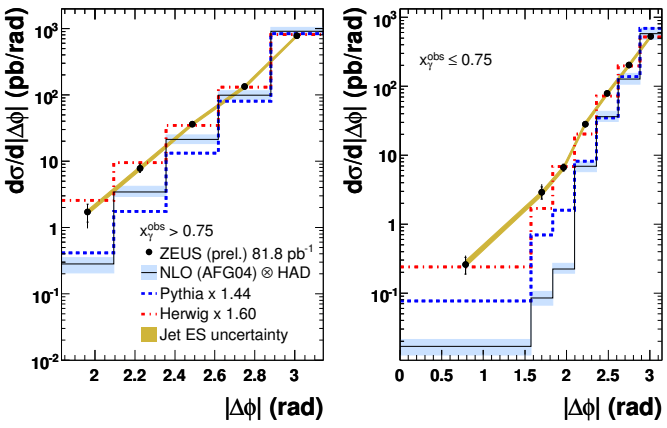

Figure 2: Cross sections $d\sigma/d|\Delta\phi|$ in two regions of $x_\gamma^{\rm obs}$.

8 Conclusions

The measured dijet cross sections in HERA 1998–2000 photoproduction data were generally found to agree well with NLO QCD predictions in the case of direct enriched cross sections with $x_\gamma^{\rm obs}$ above 0.75. For the resolved enriched cross sections at low $x_\gamma^{\rm obs} \leq 0.75$, the data are less well described by NLO. In the phase-space considered in this analysis, the different photon parameterizations give a large spread with no parton density function giving an adequate description of the data in all variables studied. Therefore the data have the potential to further constrain the PDFs in the proton and photon and should be used in future fits. The cross sections as function of $|\Delta\phi|$ are intrinsically sensitive to high-order QCD processes and are therefore a good testing ground for new calculations of higher orders or simulations thereof.

References

[1] Slides:
`http://indico.cern.ch/contributionDisplay.py?contribId=221&sessionId=6&confId=9499`

[2] F. Cornet, P. Jankowski and M. Krawczyk, Phys. Rev. D **70** (2004).

[3] P. Aurenche, R. Basu, M. Fontannaz and R. M. Godbole, Eur. Phys. J. C **34** (2004).

[4] W. Slominski, H. Abramowicz and A. Levy, Eur. Phys. J. C **45** (2006).

[5] M. Glück, E. Reya and A. Vogt, Phys. Rev. D **45**, 3986 (1992).

[6] P. Aurenche, J. P. Guillet and M. Fontannaz, Z. Phys. C **64** (1994).

Jet Production Measurements at DØ

Jochen Cammin for the DØ collaboration

University of Rochester – Department of Physics and Astronomy
Bausch & Lomb Hall, 500 Wilson Boulevard, Rochester, NY 14627-0171, USA

We report on jet production measurements with the DØ experiment in $p\bar{p}$ collisions at $\sqrt{s} = 1.96$ TeV. Measurements of the inclusive jet cross section, of the high-p_T μ-tagged cross section, and of the Z+jets cross section are presented and compared to perturbative QCD leading order and next-to-leading order predictions.

1 Introduction

Jet production processes are described using perturbative QCD. In order to test the models and constrain their parameters, most importantly the parton density functions (PDFs), measurements of jet production in various channels are performed. These measurements are also sensitive to new physics in energy regimes which are not accessible by other processes. In addition, processes with direct jet production are major backgrounds to other Standard Model processes, such as top, W/Z, or Higgs production, and a detailed understanding and accurate prediction of jet production is therefore desirable. We present measurements of jet production which utilize Run IIa datasets recorded by the DØ detector [2].

2 Jet reconstruction and energy corrections

Jets in DØ are reconstructed by combining energy deposits in the calorimeter using the DØ Run II midpoint cone algorithm [3]. The energy of the reconstructed jets needs to be corrected for resolution and energy scale effects in order to bring them to the same level as particle level jets in simulated events. Since the energy scale corrections are a major source of the total uncertainties, they are discussed briefly here. The particle level jet energy is obtained from the calorimeter jet energy by subtracting offset energy and correcting for the calorimeter response and showering: $E_{ptcl} = (E_{cal} - \text{Offset}) \,/\, (\text{Response} \times \text{Showering})$. The offset accounts for additional energy in the jet not originating from the hard process (underlying event, pile-up, calorimeter noise). The response corrects for the fraction of energy measured by the calorimeter, which is typically 60% to 80% for raw jet energies between 20 GeV and 300 GeV for a cone size of $\Delta R = 0.7$. Showering corrects for energy leaking inside and outside the jet cone. The total uncertainty on the jet energy scale (JES) corrections is about 2% for central jets with energies between 50 GeV and 150 GeV, but increases rapidly for jet energies outside this range or jets at higher rapidities.

3 Inclusive jet cross section

The measurement of the inclusive jet cross section has been updated with the final luminosity value for this dataset and is based on an integrated luminosity of 0.9 fb^{-1} [4].

A variety of single jet triggers with different prescale sets are used to cover a large transverse momentum range (Fig. 1, left). Events are selected based on run quality, jet quality criteria, and rejection of background (mostly from cosmic muons) by requiring missing $E_T < 0.7 p_T^{jet}$ and primary vertex $z < 50$ cm. The analysis is carried out for two rapidity

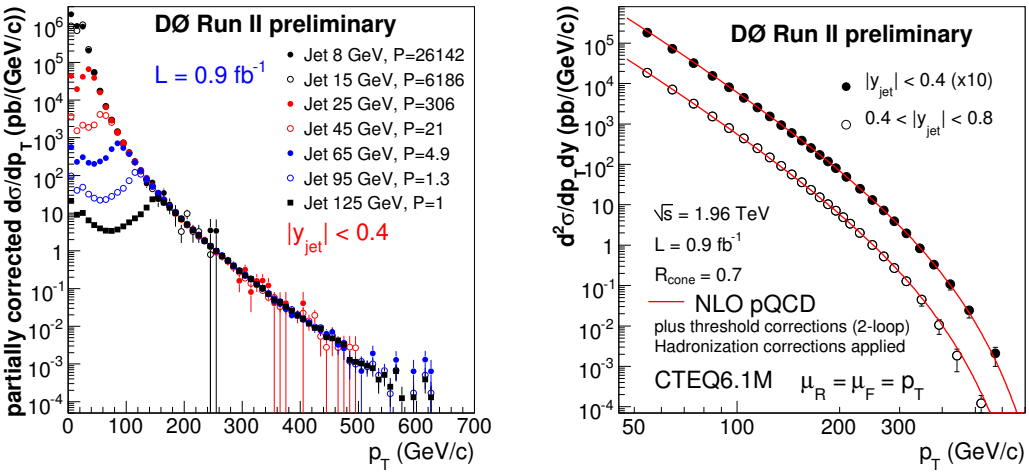

Figure 1: Left: partially corrected inclusive jet cross section for various single jet triggers and rapidity smaller than 0.4. Right: Inclusive jet cross section after resolution corrections.

ranges, $|y_{jet}| < 0.4$ and $0.4 < |y_{jet}| < 0.8$. The data are corrected for resolution and migration effects by unfolding the partially corrected cross section. The unfolding function is a convolution of an ansatz function and the jet p_T resolution measured from the p_T balance in dijet data events. The procedure is cross checked by smearing jets in simulated events with the measured resolution function, and is found to be in good agreement.

The unfolded inclusive jet cross section is shown in Fig. 1, right, and compared to a next-to-leading order prediction [5]. The prediction agrees with the data over the whole p_T range which spans eight orders of magnitude in the cross section. Figure 2, left, shows the ratio between data and prediction of the inclusive jet cross section for $|y_{jet}| < 0.4$. The prediction uses renormalization and fragmentation scales set to p_T^{jet}, CTEQ6.1M PDFs, and 2-loop threshold corrections. The shaded bands indicate the experimental uncertainties, the dashed line shows the uncertainty on the predication from the PDFs, and the dash-dotted line the prediction without 2-loop threshold corrections. The right-hand plot in Fig. 2 compares data to predictions with three different PDF sets, where the ratio is normalized to CTEQ6.1M PDFs. This set also gives the best description of the data. At high p_T the experimental uncertainties are dominated by the statistical error on the jet energy scale corrections. This error is expected to be reduced when JES corrections based on the full Run IIa dataset become available.

4 High-p_T μ-tagged cross section

Deviations in the jet production mechanism from the Standard Model prediction are more likely to show up in the third quark generation, where the quarks have non-negligible masses. A measurement of $X \to b\bar{b}$ could therefore shed light on new physics, and so a measurement of the inclusive heavy flavor cross section has been performed on 300 pb^{-1} of data. The data sample is enriched in jets from heavy flavor quarks by requiring a soft muon inside the jet

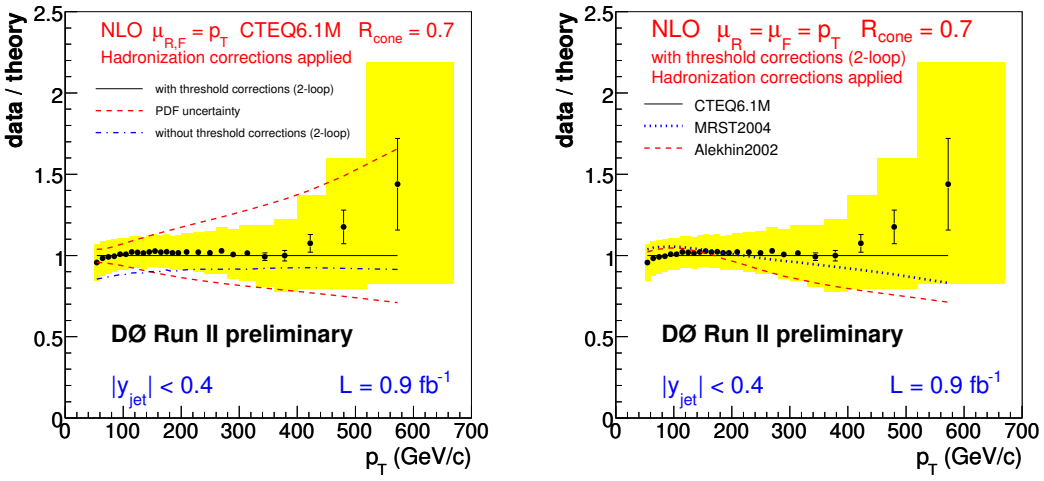

Figure 2: Left: Measured inclusive cross section, relative to a NLO prediction with CTEQ6.1M PDFs. Right: Comparison of the data to predictions from different PDFs.

cone. The μ-tag does not separate jets from b and c quarks, so the measured cross section is that of inclusive heavy flavor jets. Events are selected if at least one of the two leading jets is μ-tagged and lies within $|y_{jet}| < 0.5$. Depending on the specific trigger, a jet p_T threshold is chosen such that the trigger efficiency is at least 90%. The total event selection efficiency, including object identification efficiencies, is $31 \pm 4\%$, where the largest inefficiency stems from the muon reconstruction.

Jets matched to a muon usually originate from heavy flavor hadrons with a direct or cascade semi-leptonic decay. Since the energy of the involved neutrino cannot be measured and the muon deposits only a small fraction of its energy in the calorimeter, special energy corrections are applied to μ-tagged jets, which are derived mainly from $Z \to b\bar{b}$ Monte Carlo events. A cross check, based on the p_T imbalance of dijet data events, where one jet is μ-tagged and the other jet is not μ-tagged, shows that an additional correction is needed for μ-tagged jets in dijet events. The jet energy resolution for the unsmearing is also measured specifically for μ-tagged jets.

To calculate the μ-tagged cross section from heavy flavor hadrons, the fraction of μ-tagged jets from light flavors has to be subtracted. The heavy flavor fraction is estimated from simulated Pythia events and a full detector simulation, see left-hand plot in Fig. 3.

The right-hand plot in Fig. 3 shows the measured cross section relative to the theory prediction from Pythia with particle-level jets. Since Pythia is a leading-order Monte Carlo, the size of higher-order corrections is estimated by simply comparing the next-to-leading order cross section calculations from NLOJET++ [9] to the leading-order Pythia prediction. The data is found to lie in between these two predictions.

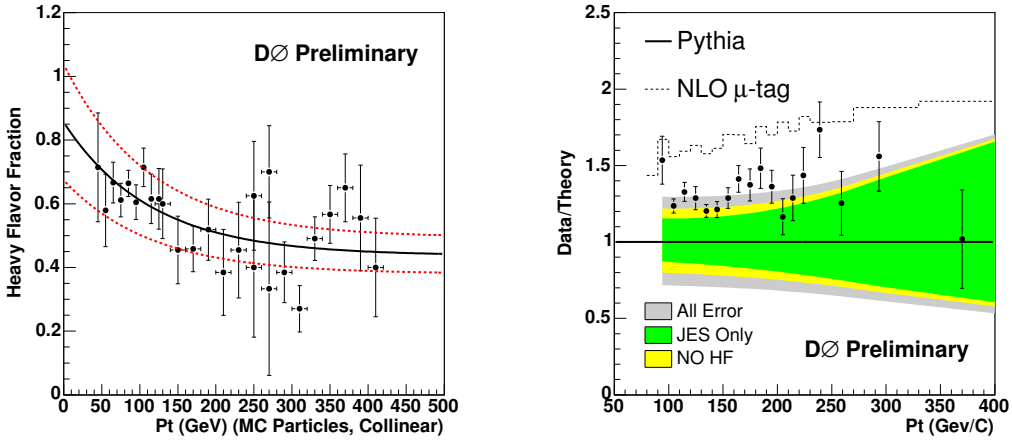

Figure 3: Left: Heavy flavor fraction in the μ-tagged sample estimated from Monte Carlo events. The dashed line indicates 20% systematic uncertainties. Right: Comparison to theory predictions. The error bands indicate the uncertainties on the measurement.

5 Z+jets cross section

The measurement of the production rates of jets accompanied by a W or Z boson which decays into leptons gives a good handle to test perturbative QCD calculations, especially the modeling of extra jet radiation. W/Z+jets events are also an important background to top and Higgs signals, and need to be understood well. It is therefore important to compare the available Monte Carlo simulation to data distributions.

The presented analysis measures the cross section of Z+jets events with $Z \rightarrow e^+e^-$ in 400 pb^{-1} of data. Events are selected if they pass certain quality criteria and have at least two reconstructed electrons with $E_T > 25$ GeV in the central region $|\eta_{det}| < 1.1$ of the detector. The invariant mass of the electron pair must be consistent with the Z boson mass, 75 GeV $< M_{ee} <$ 105 GeV. Jets are reconstructed with a cone size $R_{cone} = 0.5$. The measurements are corrected for reconstruction and acceptance efficiencies and jet energy resolution effects.

The fractional cross sections for Z+jets events in each jet multiplicity bin, compared to the inclusive Z+jets cross section, is shown in Fig. 4, left, together with predictions from Pythia [6], a leading-order matrix element calculation (Madgraph) [7] with parton showering and hadronization from Pythia (ME-PS), and from MCFM [8] for the one and two-jet bin. The matrix-element based predictions agree well with the data, whereas the Pythia prediction lacks events in the higher jet multiplicity bins as expected from a leading-order calculation. The right-hand plot in Fig. 4 shows the p_T spectra of the three highest p_T jets in data and the Madgraph predication with parton showers from Pythia. Good agreement is observed over many orders of magnitude in the cross section. The measurement is limited by systematic uncertainties with the jet energy scale as a dominant source.

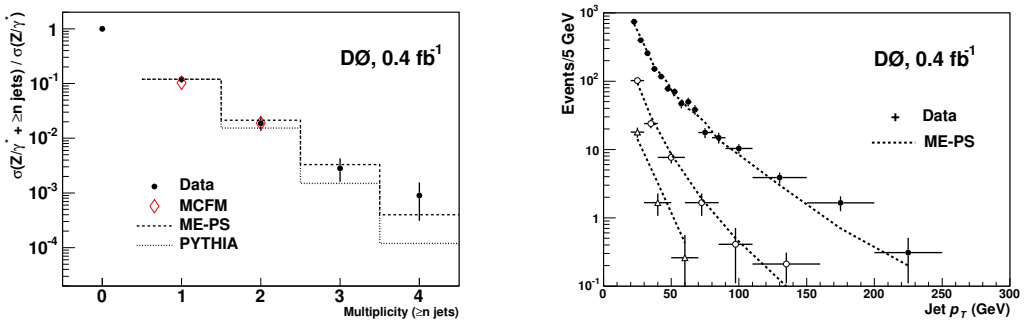

Figure 4: Left: Fractional cross section as a function of the number of reconstructed jets. The errors on the data include both statistical and systematic uncertainties. Right: spectra of the highest, second highest, and third highest p_T jet in data and the ME-PS prediction.

6 Summary

Three examples of jet production measurements utilizing data recorded with the DØ detector have been presented: the inclusive jet cross section, the high-p_T μ-tagged cross section, and the Z+jets cross section. Generally, the measurements agree well with next-to-leading order and matrix-element based predictions and help constraining theoretical models, for example for the quark and gluon PDFs. The dominant uncertainties from the jet energy scale can be improved significantly when JES corrections based on a larger data sample are available.

References

[1] Slides: `http://indico.cern.ch/contributionDisplay.py?contribId=172&sessionId=6&confId=9499`

[2] V.M. Abazov *et al.* [D0 Collaboration], Nucl. Instrum. Meth. A **565**, 463 (2006) [arXiv:physics/0507191].

[3] G.C. Blazey *et al.*, in Proceedings of the Workshop: *"QCD and Weak Boson Physics in Run II,"* edited by U. Baur, R.K. Ellis, and D. Zeppenfeld, p. 47, Fermilab-Pub-00/297 (2000).

[4] `http://www-d0.fnal.gov/Run2Physics/WWW/results/prelim/QCD/Q06/Q06.pdf`

[5] Z. Nagy, Phys. Rev. Lett. **88**, 122003 (2002),
Z. Nagy, Phys. Rev. D **68**, 094002 (2003),
T. Kluge, K. Rabbertz, M. Wobisch, publication in preparation, http://hepforge.cedar.ac.uk/fastnlo/,
N. Kidonakis, J.F. Owens, Phys. Rev. D63, 054019 (2001).

[6] T. Sjostrand, L. Lonnblad. S. Mrenna and P. Skands, arXiv:hep-ph/0308153.

[7] F. Maltoni and T. Stelzer, JHEP **0302**, 027 (2003) [arXiv:hep-ph/0208156].

[8] J. Campbell and R.K. Ellis, Phys. Rev. D **65**, 113007 (2002).

[9] Z. Nagy and Z. Trocsanyi, Phys. Rev. Lett. **87**, 082001 (2001) [arXiv:hep-ph/0104315].

[10] `http://www-d0.fnal.gov/Run2Physics/WWW/results/prelim/QCD/Q03/Q03.pdf`

[11] V.M. Abazov *et al.* [D0 Collaboration], Submitted to Phys.Rev.Lett., FERMILAB-PUB-06-283-E, arXiv:hep-ex/0608052.

[12] `http://www-d0.fnal.gov/Run2Physics/WWW/results/prelim/HIGGS/H15/H15.pdf`

Accurate Predictions for Heavy Quark Jets

Giulia Zanderighi

CERN - Theory Division, Geneve 23, CH-1211.

Heavy-flavour jets enter many of today's collider studies, yet NLO predictions for these quantities are subject to large uncertainties, larger than the corresponding experimental errors. We propose a new, infrared safe definition of heavy-quark jets which allows one to reduce theoretical uncertainties by a factor of three.

1 Introduction

When looking at the current comparison between the inclusive b-jet spectra measured by CDF and the corresponding next-to-leading order (NLO) predictions, Fig. 1 [2], one notices two striking features. Firstly, one sees a tension between data and theory: the ratio of data over NLO is around 1.2-1.5 over the whole range of accessible transverse momenta p_t of the jets. Secondly, one notices that the uncertainties associated with the theoretical predictions are embarrassingly large ($\sim 40-50\%$) for a NLO calculation and in particular they are larger than the corresponding experimental uncertainties. To understand why this happens it is useful to examine Fig. 2.

The top plots show that the large uncertainty is associated with very large K-factors. The middle plots confirm that the uncertainty is the same both with MCFM [3] and MCNLO [4]. Finally, the bottom plots illustrate the origin of the poor convergence of the perturbative expansion: when breaking down the Herwig [5] b-jet spectrum into the hard underlying channels it turns out that two NLO channels, flavour excitation, where a b-quark is kicked out of the sea-quarks, and gluon splitting, where a gluon in the final state splits into a $b\bar{b}$-pair, are larger than the leading order heavy quark production mechanism, flavour creation, when two incoming light partons produce a heavy quark pair.

The reason why supposedly higher order contributions are actually larger than the leading order channel can be clarified by counting soft and collinear logarithms associated with the splitting of gluons into $b\bar{b}$-pairs. It turns out that flavour excitation contributes with $(\alpha_s \ln p_t/m_b)^n$ and gluon splitting contributes with $(\alpha_s \ln p_t/m_b)^{2n-1}$ relative to the leading order, $\mathcal{O}(\alpha_s^2)$ process. Since $m_b \ll p_t$ these contributions are enhanced. Moreover, the

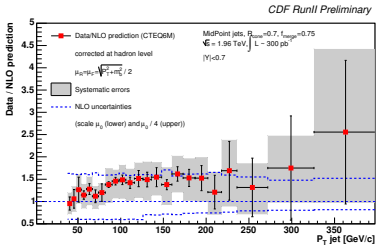

Figure 1: Ratio of the measured inclusive b-jet spectrum to the NLO prediction. The measurement is performed for jets with transverse momentum 38 GeV $< P_{T,\mathrm{jet}} <$ 400 GeV and rapidity $|y_{\mathrm{jet}}| < 0.7$.

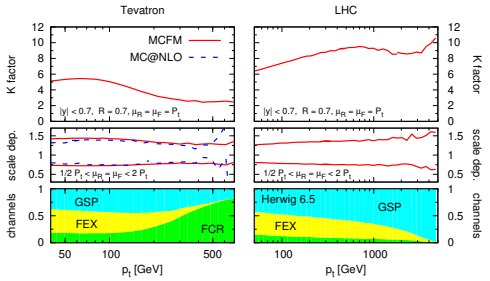

Figure 2: Top: K-factor for inclusive b-jet spectrum as computed with MCFM, clustering particles into jets using the k_t jet-algorithm with R=0.7, and selecting jets in the central rapidity region ($|y| < 0.7$). Middle: scale dependence obtained by simultaneously varying the renormalisation and factorisation scales by a factor two around p_t, the transverse momentum of the hardest jet in the event. Bottom: breakdown of the Herwig inclusive b-jet spectrum into the three major hard underlying channels contributions (for simplicity the small $bb \to bb$ is not shown).

dominant contribution to the b-jet spectrum comes from jets originated from gluon splitting, which do not correspond to one's intuitive physical idea of a b-jet, one where a hard b is produced directly in the hard scattering. [a] In the following we suggest to adopt a different jet-clustering algorithm to reconstruct b-jets. One that by making explicit use of the flavour information eliminates all higher-order logarithmic enhancements associated to gluon splittings in the b-jet spectra. This means that, after resumming initial state collinear logarithms into b-pdfs, b-jets can be computed using massless QCD calculations [6] as long as one neglects power corrections m_b^2/p_t^2 (potentially log-enhanced).

2 The heavy-quark jet algorithm

We summarize here the inclusive heavy-flavour jet algorithm for hadron-hadron collisions [7]. For any pair of final-state particles i, j define a class of distances $d_{ij}^{(F,\alpha)}$ parametrized by $0 < \alpha \leq 2$ and a jet radius R

$$d_{ij}^{(F,\alpha)} = \frac{R_{ij}^2}{R^2} \times \begin{cases} \max(k_{ti}, k_{tj})^\alpha \min(k_{ti}, k_{tj})^{2-\alpha}\,, & \text{softer of } i,j \text{ flavoured,} \\ \min(k_{ti}^2, k_{tj}^2)\,, & \text{softer of } i,j \text{ flavourless,} \end{cases} \tag{1}$$

where $R_{ij}^2 = \Delta y_{ij}^2 + \Delta\phi_{ij}^2$, $\Delta y_{ij} = y_i - y_j$, $\Delta\phi_{ij} = \phi_i - \phi_j$ and k_{ti}, y_i and ϕ_i are respectively the transverse momentum, rapidity and azimuth of particle i, with respect to the beam. For each particle i define a distance with respect to the beam B at positive rapidity,

$$d_{iB}^{(F,\alpha)} = \begin{cases} \max(k_{ti}, k_{tB}(y_i))^\alpha \min(k_{ti}, k_{tB}(y_i))^{2-\alpha}\,, & i \text{ is flavoured,} \\ \min(k_{ti}^2, k_{tB}^2(y_i))\,, & i \text{ is flavourless,} \end{cases} \tag{2}$$

with

$$k_{tB}(y) = \sum_i k_{ti} \left(\Theta(y_i - y) + \Theta(y - y_i) e^{y_i - y}\right)\,. \tag{3}$$

[a] We recall that according to the current experimental definition of a b-jets, a b-jet is any jet containing *at least* one b.

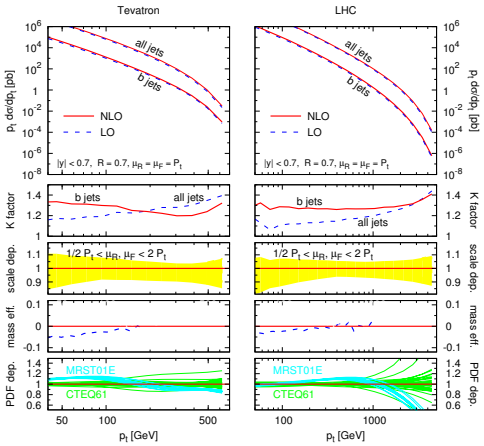

Figure 3: Inclusive jet spectrum at the Tevatron (right) and at the LHC (left). The top two panels show results for both b-jets and all-jets, while the lower three panels apply only to b-jets. See text for further details.

Similarly define a distance to the beam $\bar{B}$ at negative rapidity by replacing k_{tB} in eq. (2) with $k_{t\bar{B}}$

$$k_{t\bar{B}}(y) = \sum_i k_{ti} \left(\Theta(y - y_i) + \Theta(y_i - y)e^{y-y_i}\right) . \tag{4}$$

Identify the smallest of the distance measures. If it is a $d_{ij}^{(F,\alpha)}$, recombine i and j into a new particle, summing their flavours and 4-momenta; if it is a $d_{iB}^{(F,\alpha)}$ (or $d_{i\bar{B}}^{(F,\alpha)}$) declare i to be a jet and remove it from the list of particles. Repeat the procedure until no particles are left. We define the b-flavour or generally the heavy-flavour of a (pseudo)-particle or a jet as its net heavy flavour content, i. e. the total number of heavy quarks minus heavy anti-quarks.

The IR-safety of this algorithm was proved in [7]. Apart from allowing one to take the limit $m_Q^2 \to 0$ for the heavy quark mass (as long as collinear singularities associated with incoming heavy quarks are factorized into a heavy quark PDF), it ensures that one obtains the same results whether one considers heavy-quark flavour at parton level, or heavy-meson flavour at hadron level, modulo corrections suppressed by powers of Λ_{QCD}/p_t.

3 Results

Our results are summarized in fig. 3 [8] where we show the inclusive b-jet p_t-spectrum as obtained with the flavour algorithm specified above with $\alpha = 1$, and $R = 0.7$, the latter having been shown to limit corrections associated with the non-perturbative underlying event [9]. The left (right) column of the figure shows results for the Tevatron Run II (LHC). We have selected only those jets with rapidity $|y| < 0.7$. We also show the full inclusive jet spectrum (all jets) as obtained with a standard inclusive k_t-algorithm [10] with $R = 0.7$.

We notice the considerable reduction of K-factors, which are around 1.3 and the moderate uncertainties associated with scale variation, signaling that the perturbative expansion is now well under control. Our predictions constitute therefore the first accurate predictions for inclusive heavy quark jets.

We remark that very similar results are obtained when considering charmed jet spectra. An interesting issue there is that predictions are very sensitive to possible intrinsic charm components of the proton [11]. This means that this type of observable has a potential to set constraints on such intrinsic components.

A last remark concerns the feasibility of the experimental measurement of heavy flavour jets defined with our flavour algorithm. Our jet-clustering algorithm requires that one identify heavy-flavoured particles and that one uses a different distance measure when clustering heavy or light objects according to eq. (1). It is particularly important to identify cases when both heavy flavoured particles are in the same jet, so as to label this jet a gluon jet and eliminate it from the b-jet spectrum. Experimentally techniques for double b-tagging in the same jet already exist [12] and steady progress is to be expected in the near future [13]. However one has always a limited efficiency for single b tagging, and even more for double b-tagging in the same jet. On the other hand preliminary studies indicate that one does not necessarily need high efficiencies, but what is more crucial is that one understand those efficiencies well [8]. We look forward to further investigation in this direction.

Acknowledgments

This work is done in collaboration with Andrea Banfi and Gavin Salam.

References

[1] Slides:
`http://indico.cern.ch/contributionDisplay.py?contribId=175&sessionId=6&confId=9499`

[2] CDF Collaboration, Note 8418.

[3] http://mcfm.fnal.gov/

[4] S. Frixione and B. R. Webber, JHEP **0206** (2002) 029; S. Frixione, P. Nason and B. R. Webber, JHEP **0308** (2003) 007.

[5] G. Marchesini, B. R. Webber, G. Abbiendi, I. G. Knowles, M. H. Seymour and L. Stanco, Comput. Phys. Commun. **67** (1992) 465.

[6] Z. Nagy, Phys. Rev. Lett. **88**, 122003 (2002); Phys. Rev. D **68**, 094002 (2003).

[7] A. Banfi, G. P. Salam and G. Zanderighi, Eur. Phys. J. C **47** (2006) 113.

[8] A. Banfi, G. P. Salam and G. Zanderighi, arXiv:0704.2999 [hep-ph].

[9] A. Abulencia [CDF - Run II Collaboration], arXiv:hep-ex/0701051.

[10] S. Catani, Y. L. Dokshitzer, M. H. Seymour and B. R. Webber, Nucl. Phys. B **406**, 187 (1993); S. D. Ellis and D. E. Soper, Phys. Rev. D **48** (1993) 3160.

[11] J. Pumplin, H. L. Lai and W. K. Tung, arXiv:hep-ph/0701220.

[12] D. Acosta *et al.* [CDF Collaboration], Phys. Rev. D **71** (2005) 092001.

[13] Andrea Bocci, "Jet flavour tagging with the CMS experiment", CMS TS-2006/004 ; Christian Weiser,"A Combined Secondary Vertex Based B-Tagging Algorithm in CMS", CMS NOTE-2006/014; M. Sapinski, "Expected performance of ATLAS for measurements of jets, b-jets, tau-jets, and ETmis", SN-ATLAS-2002-012, ATL-COM-CONF-2001-006; J. Bastos, arXiv:physics/0702041.

Measurement of the $b\bar{b}$ Cross Section at CDF

Sofia Vallecorsa[1]

1- University of Geneva - Departement de physique Nucleaire e Corpuscolaire
Geneva - Switzerland

We present a $b\bar{b}$ jet cross section measurement based on about 260 pb^{-1} of data, collected by CDF Run II until September 2004. The analysis strongly relies on the CDF detector good tracking capabilities both at trigger level, as data is selected requiring two displaced tracks at Level 2, and offline, since b-tagging is performed reconstructing secondary vertices inside the jet. Jets are reconstructed using a cone algorithm and the cross section is measured in the central region ($|\eta| < 1.2$) as a function of leading jet E_T, of the $b\bar{b}$ pair invariant mass and the azimuthal angle between the two jets ($\Delta\phi$). Results are corrected to the hadron level and compared to leading order Monte Carlo (Pythia and Herwig) and NLO prediction (MC@NLO).

1 Introduction

The dominant b production mechanism at the Tevatron is believed to be pair production through the strong interaction and the study of $b\bar{b}$ correlation is useful to get a deeper insight into the effective production mechanisms and the leading order and next-to-leading order contributions [2].

For example, the lowest order QCD $b\bar{b}$ production diagrams contain only b and $\bar{b}$ quarks in the final state, for which momentum conservation requires the quarks to be produced back-to-back in azimuthal opening angle. However when higher order QCD processes are considered , the presence of additional light quarks and gluons in the final state allows the $\Delta\phi$ distribution to spread. The NLO QCD calculation of $b\bar{b}$ production includes diagrams up to $O(\alpha_s^3)$ some of which - flavor excitation and gluon splitting - provide a contribution of approximately the same magnitude as the lowest order diagrams, $O(\alpha_s^2)$.

The CDF II detector has a cylindrical symmetry around the beam-line, making it convenient to use a cylindrical coordinate system with the z axis along the proton beam direction. A detailed description can be found in [3].

2 Data Sample & Event Selection

The data sample is selected on-line using a three level trigger specifically designed to select events rich in heavy flavor making use of the Silicon Vertex Trigger (SVT, [3]) at level 2.

In the first level trigger two central calorimeter towers with E_T above 5 GeV are required together with two low resolution tracks reconstructed in the tracking chamber (p_T above 2 GeV/c); in the second level trigger, calorimeter clusters are formed around the level 1 trigger towers and events are selected to have 2 clusters with E_T greater than 15 GeV. At this level tracks are reconstructed using the SVT, which adds to the low resolution L1 tracks the information from the silicon detectors. The tracks impact parameter is measured with respect to the interaction point, with a resolution of the order of 35 μm. Events pass the level 2 selection if two SVT tracks are found which have impact parameter larger than 100 μm. In the third level trigger, jets are reconstructed using the CDF run I cone algorithm and the events are required to have at least two jets with E_T above 20 GeV. Tracks are also

reconstructed and events are selected if at least two of the $E_T > 20$ GeV jets are associated to two large impact parameter SVT tracks.

Offline events are requested to have at least one reconstructed primary vertex with z-position within 60 cm of the nominal interaction point: this preliminary requirement removes beam-related backgrounds and ensures a well-understood event-by-event jet kinematics.

Jets are reconstructed using a cone algorithm with a radius equal to 0.4 in the η-ϕ plane. Further selection requires: two jets with transverse energy greater than 35 GeV and 32 GeV respectively in the central pseudo-rapidity region ($|\eta| < 1.2$), each geometrically matched to a track reconstructed by the SVT trigger and confirmed by the silicon system and by the central tracker system; these tracks have high impact parameter, $|d_0| > 120$ μm, and $p_T > 2$ GeV/c: two such jet will be defined, in the following, as "SVT-tagged" jets. Heavy flavor jets are identified in data and Monte Carlo events via the presence of a secondary vertex (displaced with respect to the primary interaction point and originated in the decay of the long lived B hadron) using a b-tagging algorithm based on the selection of tracks with significant impact parameter in the transverse plane.

The measured jet transverse energy in the calorimeter systematically underestimates the value obtained at the hadron level (i.e. in the Monte Carlo running the same jet clustering algorithm on stable final state particles), due to energy losses in partially instrumented regions of the detector and calorimeter non linearities. This analysis makes use of the jet energy correction calculated for generic jets [4] by the collaboration.

An additional correction (of the order of 5%), specific to "SVT-tagged" jets , is calculated matching (in the η, ϕ plane) calorimeter level jets and hadronic level jets in the Monte Carlo and fitting the energy correlation $< E_{T,cal} >$ vs $< E_{T,had} >$, to a third order polynomial. The result is an average correction which is applied jet by jet to obtain the corrected transverse energy, $E_{T,corr}$ to take into account the different features of b-jets, such as a harder fragmentation or the presence of B hadron decays inside the jet cone.

Monte Carlo samples are used to measure the efficiency of the event selection and the unfolding factors to correct the cross section to the hadron level. Generated events are passed through a full detector simulation and the same reconstruction and analysis code used on data. Inclusive jet samples and $b\bar{b}$ jet samples as well as $c\bar{c}$ jet samples are generated with Pythia, using CTEQ5L Parton Distribution Functions and different parton P_T threshold. A special tuning is used to run Pythia: "Tune A", based on dedicated studies on the underlying event using Run I CDF data.

A Next-to-Leading Order prediction is calculated using MC@NLO generator [6], together with Herwig Parton Shower. The underlying event is generated using JIMMY 4.3 [5], a generator that links to Herwig and produces multi-parton interactions. Jimmy is used to generate the MC@NLO and Herwig $b\bar{b}$ samples.

2.1 Identifying b-jets using the Secondary Vertex tagging algorithm

The b-tagging algorithm reconstructs the B decay secondary vertex inside the jet. Once the vertex is found an additional cut is imposed on the two dimensional decay lenght L_{xy}, calculated as the projection on the jet axis, in the $r - \phi$ plane, of the vector pointing from the primary vertex to the secondary vertex.

The tagged jet sample includes background from charm and light quarks and gluon jets, that can be separated from the b-jet signal using the distribution of the invariant mass of the tracks associated to the secondary vertex. A full reconstruction of the invariant

mass would allow a precise separation of the b-jet sample from the background but the presence of neutral particles and the ambiguities in associating tracks to primary or secondary vertexes, limit the reconstruction of the original b mass. Nevertheless the shape of the mass distribution is different according to the flavor of the jet and mass templates are built using the Monte Carlo simulated events and they are used to fit the data distribution.

The b-tagging efficiency is defined, here, as the ratio between the number of events with 2 b-jets and 2 SVT-tagged b-jets: it is calculated using Pythia $b\bar{b}$ events requiring the two reconstructed b-jets in the central region $|\eta| < 1.2$. The result is summarized in the Fig. 1 as function of the highest energy jet E_T. The efficiency is scaled to data using a correction factor.

The b-jet purity of the double tag sample is estimated directly from data fitting the shape of the sum of the two SVT-tagged jets secondary vertex invariant masses, using template distributions from Pythia samples. A two components fit is performed using a "signal" template distribution, describing the $b\bar{b}$ case, and a "background" template, merging all the other possible contributions: $c\bar{c}$, $b\bar{c}$, $b\bar{l}$, and so on.

Figure 1), shows the fraction resulting from the fit: the 2 SVT-tagged jet sample has a very high purity (about 87%), the requirement of a SVT track matched to a b-tagged jet enhances this fraction compared to simple b-tagged jet case.

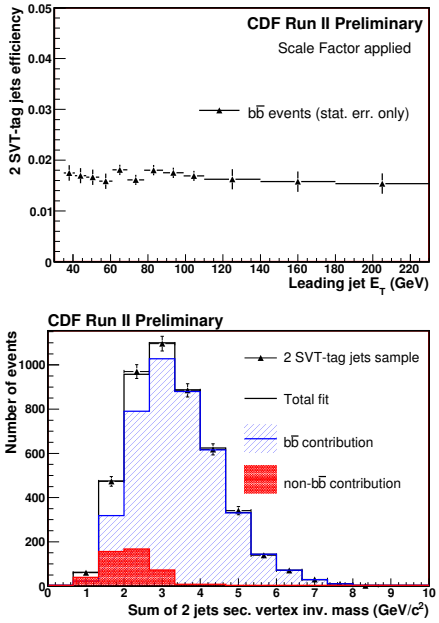

Figure 1: Efficiency for requiring two SVT-tagged jets in the event as a function of the E_T of the highest energy jet in the couple(top). Result from the fit: data is overlapped to fit prediction and Monte Carlo templates (bottom)

3 Results

The differential cross section is calculated over an integrated luminosity of about 260 pb^{-1}. It is corrected to the hadron level using "per-bin" unfolding factors, $C_i = \frac{d^2\sigma_{Had}/dE_{T,Had}}{d^2\sigma_{Cal}/dE_{T,Cal}}$, extracted from the Monte Carlo. The unfolded cross section is compared to LO Pythia and Herwig Monte Carlo and to Next-to-Leading-Order prediction, in Fig. 2 as a function of the leading jet E_T and the di-jet azimuthal difference.

The main systematic uncertainty contributions are originated by different sources: the uncertainty on the jet energy scale, which represents the main contribution (about 15-20%); the uncertainty on the luminosity (6 %); and finally the contributions related to the estimate of the tagging efficiency and the b-jet purity which are of the order of 7-8 % each.

4 Conclusion

We've presented a measurement of the $b\bar{b}$ jet cross section performed at CDF on a integrated luminosity of about 260 pb^{-1}. The events have been selected requiring two jets in the central region $|\eta| < 1.2$ with $E_T^{corr} > 35$ and $E_T > 32$ GeV, identified as b-jets using the two-dimensional Secondary Vertex algorithm and matched to two Silicon Vertex Trigger tracks with $|d_0| > 120$ μm. The differential cross section have been measured as a function of the leading jet transverse energy, the azimuthal angle between the jets and the invariant mass of the two jets. The curves have been corrected to hadron level and compared to leading order prediction by Pythia (CTEQ5L) and Herwig (CTEQ5L) and to NLO order MC@NLO events. The azimuthal angle distribution peaks at large angles, corresponding to leading order flavor creation processes, but shows a large excess at small opening angles, with respect to LO prediction (both Pythia and Herwig), suggesting the contribution from higher order processes cannot be neglected. Overall data shows a good agreement to MC@NLO prediction.

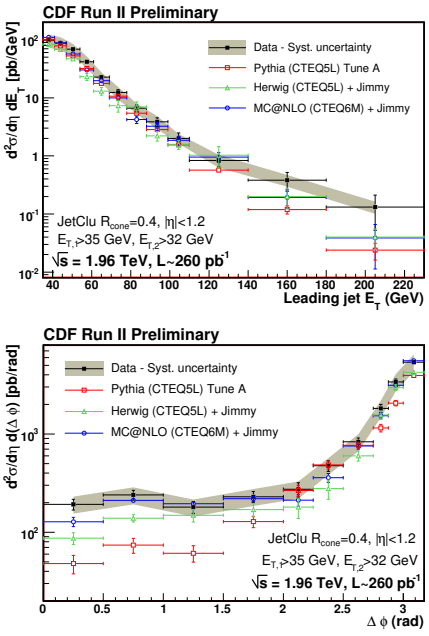

Figure 2: $b\bar{b}$ differential jet cross section as function of leading jet E_t (top) and the di-jet $\Delta\phi$ (bottom). Data is compared to hadron level cross sections obtained using: MC@NLO+JIMMY (blue), Pythia (red) and Herwig + JIMMY (green). The shaded area represents the systematic total uncertainty on the data.

5 Bibliography

References

[1] Slides:
`http://indico.cern.ch/contributionDisplay.py?contribId=222&sessionId=6&confId=9499`

[2] M. Cacciari, P. Nason, Is there a significant excess in bottom Hadroproduction at the Tevatron?, Phys. Rev. Lett. 89,122003 (2002).

[3] The CDFII Detector Technical Design Report, Fermilab-Pub-96/390-E

[4] A. Bhatti *et al.*, Determination of the Jet Energy Scale at the Collider Detector at Fermilab, Nucl. Instrum. Method A 566 (2006) 375-412

[5] J.M. Butterworth, J.R. Forshaw, M.H. Seymour, Multi-parton interactions in photo-production at HERA.

[6] S. Frixione, B.R. Webber, Matching NLO QCD computations and parton shower simulations, JHEP 0206 (2002) 029 [hep-ph/0204244].

Multi-Jet Cross Sections in Charged Current Deep Inelastic Scattering at HERA

H. Wolfe *

University of Wisconsin, Madison - Department of Physics
Madison, Wisconsin - U.S.A.

Differential jet cross sections have been measured in charged current deep inelastic ep scattering at high boson virtualities Q^2 with the ZEUS detector at HERA using an integrated luminosity of 200 pb^{-1}. Jets were identified using the $k_\top$ cluster algorithm. Polarised and unpolarised-corrected cross sections are presented for inclusive-jet production as functions of Q^2, Bjorken x, jet transverse energy and jet pseudorapidity. The dijet invariant mass cross section is also presented. Observation of three-jet events in charged-current processes is reported for the first time. The predictions of a leading-logarithm parton-shower Monte Carlo model are compared to the measurements.

1 Introduction

Jet production in charged-current (CC) deep inelastic ep scattering (DIS) provides a testing ground for QCD and for the electroweak sector of the Standard Model (SM). Up to leading order (LO) in the strong coupling constant, α_S, jet production in CC DIS proceeds via the quark-parton model ($Wq \to q$), the QCD-Compton ($Wq \to qg$) and W-gluon fusion ($Wg \to q\bar{q}$) processes. Thus, differential cross sections for jet production are sensitive to α_S and the mass of the propagator, M_W, which are fundamental parameters of the theory.

Since 2002, HERA has run with longitudinally-polarised electron or positron beams. In this paper, measurements are presented of inclusive-jet and dijet cross sections in CC e^-p DIS in the laboratory frame. Measurements of three-jet differential cross sections in CC DIS have been measured for the first time in ep collisions. A small sample of four-jet events has also been observed in the data. The measurements are presented as functions of Q^2, x, the jet transverse energy, $E_\top^{\rm jet}$, and jet pseudorapidity, $\eta^{\rm jet}$. Predictions from a leading-logarithm parton-shower Monte Carlo (MC) model are compared to the measurements. Results for negative and positive longitudinally-polarised electron beams are also presented.

2 Data selection and jet search

The data were collected during the running period 2004-2006. Samples of negatively (positively) polarised electron beams with an integrated luminosity of 105.9 (73.4) pb^{-1} and luminosity-weighted average polarisation of $P_e^{\rm neg} = -0.27$ ($P_e^{\rm pos} = +0.30$) were analysed. A detailed description of the ZEUS detector can be found elsewhere [2, 3]. The kinematic variables Q^2 and the inelasticity, y, were reconstructed using the method of Jacquet-Blondel [4], which uses the information from the hadronic energy flow of the event, and were corrected for detector effects as described elsewhere [5]. The main selection criteria rely on missing transverse momentum ($p_\top$), transverse energy ($E_\top$), Q^2 and y by requiring $p_\top > 11$ GeV, $p_\top/E_\top > 0.5$, $Q^2 > 200$ GeV^2, and $y < 0.9$.

*On behalf of the ZEUS Collaboration.

Jets were identified in the pseudorapidity (η) - azimuth (ϕ) plane of the laboratory frame using the $k_\top$ cluster algorithm [6] in the longitudinally invariant inclusive mode [7]. The jets have been reconstructed using the ZEUS calorimeter (CAL) and corrected for detector effects to yield jets of hadrons. Events with at least one jet of $-1 < \eta^{\rm jet} < 2.5$ were retained. The final inclusive-jet sample consisted of events with at least one jet of $E_\top^{\rm jet} > 14$ GeV. The dijet (three-jet) sample was selected as a subset of the inclusive sample, with the requirement of an additional jet (two jets) with $E_\top^{\rm jet} > 5$ GeV. A small number of four-jet events, with one jet of $E_\top^{\rm jet} > 14$ GeV and at least three additional jets with $E_\top^{\rm jet} > 5$ were also identified in the data.

3 Monte Carlo simulation and systematic uncertainty estimation

Samples of MC events were generated to determine the response of the detector to jets of hadrons and to evaluate the correction factors necessary to obtain the hadron-level jet cross sections. The CC DIS events were generated using the Color Dipole Model (CDM) as implemented in the ARIADNE program [8] using the CTEQ5D [9] proton parton distribution functions. Fragmentation into hadrons was performed using the Lund string model [10] as implemented in JETSET 7.4 [11].

The following sources of systematic uncertainty were considered for the measurements of the jet cross sections: absolute energy scale of the jets and CAL, $p_\top$ selection cut, photoproduction background and trigger selection. The systematic uncertainties not associated with the absolute energy scale of the jets were added in quadrature to the statistical uncertainties and are shown in the figures as error bars. The uncertainty due to the absolute energy scale of the jets is shown separately as a shaded band in each figure, due to the large bin-to-bin correlation. In addition, there was an overall normalisation uncertainty of 3.5% from the luminosity determination.

4 Results

4.1 Inclusive-jet cross sections

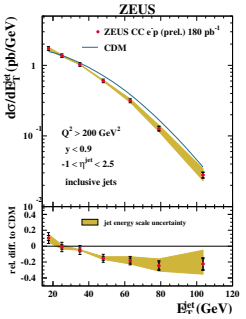

Figure 1a

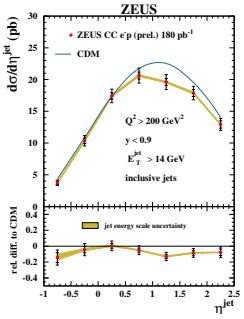

Figure 1b

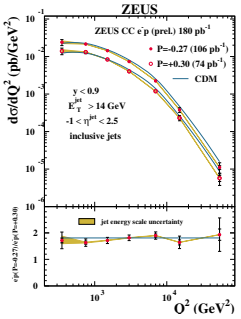

Figure 1c

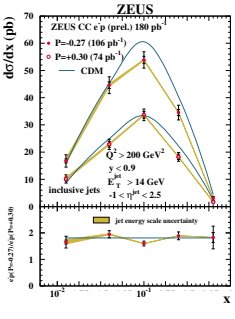

Figure 1d

Figure 1 shows the CC e^-p DIS inclusive-jet differential cross sections as functions of $E_\top^{\rm jet}$ (unpolarised-corrected), $\eta^{\rm jet}$ (unpolarised-corrected), Q^2 (polarised) and x (polarised). The

unpolarised-corrected cross section for observable A was obtained via $\frac{d\sigma}{dA} = \frac{N^{\rm unpol}_{\rm data}}{\mathcal{L}\cdot\Delta A} \cdot \frac{N^{\rm had}_{\rm MC}}{N^{\rm det}_{\rm MC}}$, where $N^{\rm unpol}_{\rm data} = \frac{N^{\rm neg}_{\rm data}}{1-P_e^{\rm neg}} + \frac{N^{\rm pos}_{\rm data}}{1-P_e^{\rm pos}}$, $\mathcal{L}$ is the total integrated luminosity and ΔA is the bin width.

Below the unpolarised-corrected differential cross sections with respect to $E_\top^{\rm jet}$ and $\eta^{\rm jet}$, the relative difference to MC is shown. Values of $E_\top^{\rm jet}$ above 100 GeV are accessible with the present statistics, and a different shape than the prediction can be seen. The measured $d\sigma/d\eta^{\rm jet}$ has a maximum at $\eta^{\rm jet} \sim 0.75$. For $200 < Q^2 \lesssim 1000$ GeV^2, the distribution displays almost no dependence on Q^2. The cross sections as functions of $E_\top^{\rm jet}$ and Q^2 show a less rapid fall-off than what is observed for the same cross sections in Neutral Current DIS processes due to the presence of the massive W propagator. The measured cross section in Fig.1d shows that the x values accessible by the data are within the range $0.013 < x < 0.63$. The measured cross sections are reasonably well described for low values of Q^2 and x; for higher values, the data lie below the predictions. In all cases, the normalisation of the prediction is in agreement with the data.

Figures 1c and 1d show the CC negatively- and positively-polarised e^-p DIS inclusive-jet differential cross sections as functions of Q^2 and x. The predictions of the leading-logarithm parton-shower MC model of CDM are compared to the data in the figure. The lower part of the figures show the ratio of the cross section for negatively- and positively-polarised electron beams, which is agreement with the predicted polarisation ratio, $(1-P_e^{\rm neg})/(1-P_e^{\rm pos}) = 1.81$.

The total inclusive-jet cross sections in the kinematic regime given by $Q^2 > 200$ GeV^2, $y < 0.9$, $E_\top^{\rm jet} > 14$ GeV and $-1 < \eta^{\rm jet} < 2.5$ are

$$\sigma_{\rm jets}(P_e = -0.27) = 64.42 \ \pm 0.96 \ \text{(stat.)} \ \pm 3.32 \ \text{(syst.)} \ ^{+0.62}_{-0.55} \ \text{(E scale) pb},$$

$$\sigma_{\rm jets}(P_e = +0.30) = 36.58 \ \pm 0.87 \ \text{(stat.)} \ \pm 1.92 \ \text{(syst.)} \ ^{+0.35}_{-0.31} \ \text{(E scale) pb},$$

which agree with SM predictions: $\sigma_{\rm jets}(P_e = -0.27) = 70$ pb and $\sigma_{\rm jets}(P_e = +0.30) = 39$ pb.

4.2 Dijet cross sections

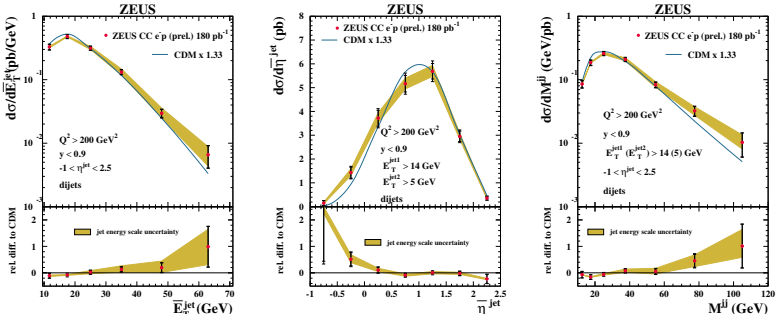

Figure 2a Figure 2b Figure 2c

Figure 2 shows the unpolarised-corrected CC e^-p DIS dijet differential cross sections as functions of mean $\eta^{\rm jet}$ ($\overline{\eta^{\rm jet}}$), mean $E_\top^{\rm jet}$ ($\overline{E_\top^{\rm jet}}$), and dijet invariant mass M^{jj}. The measured cross section as a function of $\overline{E_\top^{\rm jet}}$ exhibits a fall-off of two orders of magnitude for

$\overline{E_T^{\rm jet}} \gtrsim 20$ GeV, but displays almost no Q^2 dependence for $200 < Q^2 \lesssim 2000$ GeV^2. Figure 2c shows that values of M^{jj} above 100 GeV are accessible with the present statistics.

The predictions of the leading-logarithm parton-shower MC models of CDM are compared to the data in Figure 2. The predictions give a reasonable description of the shape of the data, but have been normalised to the total dijet measured cross section with a multiplicative factor of 1.33. For M^{jj}, the data tend to be above the MC prediction for $M^{jj} \gtrsim 70$ GeV.

4.3 Three-jet cross sections

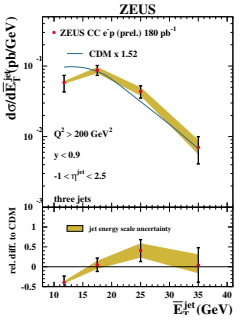

Figure 3a

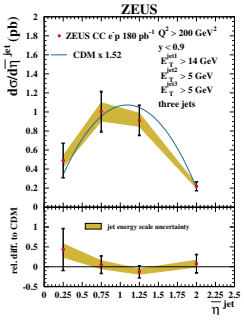

Figure 3b

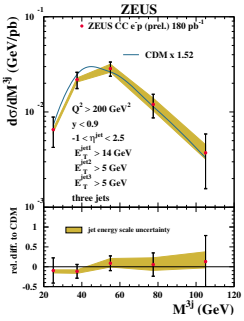

Figure 3c

Three-jet cross sections in CC DIS have been measured for the first time in ep collisions. The three-jet selected sample also contains six candidates with an extra fourth jet of $E_T^{\rm jet4} > 5$ GeV in the $\eta^{\rm jet}$ range considered.

Figure 3 shows the unpolarised-corrected CC e^-p DIS three-jet differential cross sections as functions of $\overline{E_T^{\rm jet}}$, $\overline{\eta^{\rm jet}}$, and three-jet invariant mass (M^{3j}). Values of M^{3j} above 100 GeV are accessible with the present statistics. The MC predictions give a good description of the shape of the data, but have been normalised to the total three-jet measured cross section with a multiplicative factor of 1.52.

References

[1] Slides from this presentation: `http://indico.cern.ch/contributionDisplay.py?contribId=224&sessionId=6&confId=9499`

[2] **ZEUS**, M. Derrick *et al.*, Phys. Lett. **B293**,465(1992)

[3] **ZEUS**, U.Holm(ed.), *The ZEUS Detector*. Status Report (unpublished), DESY (1993), available on `http://www-zeus.desy.de/bluebook/bluebook.html`

[4] F. Jacquet and A. Blondel, *Proc. of the Study for an ep Facility for Europe*, U. Amaldi (ed.), p.391. Hamburg, Germany (1979). Also in preprint DESY 79/48

[5] **ZEUS**, J. Breitweg *et al.*, Eur. Phys. J. **C8**,367(1999)

[6] S. Catani *et al.*, Nucl. Phys. **B406**,187(1993)

[7] S.D. Ellis and D.E. Soper, Phys. Rev. **D48**,3160(1993)

[8] L. Lönnblad, Comp. Phys. Comm. **71**,15(1992)

[9] H.L. Lai *et al.*, Eur. Phys. J. **C12**,375(2000)

[10] B. Andersson *et al.*, Phys. Rep. **97**,31(1983)

[11] T. Sjöstrand, Comp. Phys. Comm. **39**,347(1986)

Measurements of W+jet(s) and Z+jet(s) Production Cross Sections at CDF

Monica D'Onofrio[1] *

1- Institut de Fisica d'Altes Energies - IFAE
Barcelona - E08193 Spain

The Tevatron $p\bar{p}$ Collider is the highest-energy accelerator currently operational. At the beginning of 2007, the amount of collected data reached 1 fb^{-1}. In this contribution, results on W and Z boson production in association with jets are presented.

1 Introduction

Measurements on W and Z bosons production in association with highly energetic jets of hadrons are a fundamental part of the CDF physics program, since they constitute a major background for top quark physics (mainly W+jets) as well as in searches for new physics like Higgs and SuperSymmetry (*eg.* $Z \to \nu\nu$+jets irreducible background). The study of Boson+jets production provides a stringent test of perturbative QCD (pQCD) predictions, where parton-level NLO pQCD calculations are performed up to two partons in the final state. Furthermore, a significant effort is being made in the past years to build Leading Order Monte Carlo (MC) predictions for Boson+jets final states with large jet multiplicities. These predictions are based on parton-level LO Matrix Elements (ME) interfaced with Parton Showers (PS) where special prescriptions are necessary to properly match the final states and avoid double counting in the gluon radiation. Precise measurements on Boson+jet final states are necessary to validate the matching procedures.

2 Jet production in association to W bosons

The measurement of inclusive W+jets cross sections is based on an integrated luminosity of $0.32\,fb^{-1}$ carried out by CDF. W boson candidates are identified via the presence of a high P_T electron and large missing transverse energy associated to the neutrino. The definition of the measured cross section is restricted to the region of phase-space where electron P_T is above 20 GeV/c, P_T of the neutrino is above 30 GeV/c, and the transverse mass of the reconstructed W is above 20 GeV/c^2. Jets are searched for using a cone-based algorithm with cone size R = 0.4 and are required to have transverse energy $E_T^{jet} > 15$ GeV and pseudo-rapidity $|\eta^{jet}| < 2.0$. The $W \to e\nu$ candidate events are finally classified according to their jet multiplicity into four inclusive n-jet samples.

The $W(\to e\nu)$+jets data sample contains background mainly from QCD and top pair production. QCD background is described with a data-driven technique, where a genuine multi-jets event sample is extracted selecting events that pass all kinematic requirements, but which fail one or more electron identification requirements. Other background contributions from top pair production, $W \to \tau\nu$, $Z \to ee$ and dibosons are estimated using Monte Carlo samples. The total background varies from 10% at low E_T^{jet} and low jet multiplicity to 80% at high E_T^{jet} and high jet multiplicity.

*On behalf of the CDF Collaboration

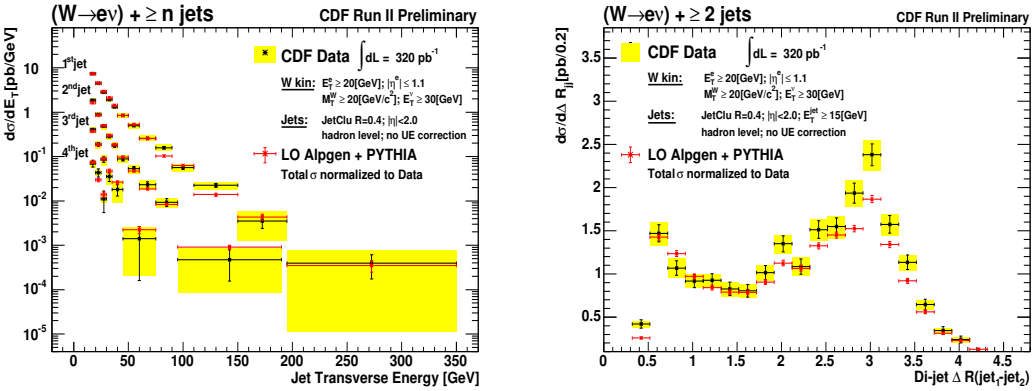

Figure 1: *Left: Differential cross section as a function of the* E_T^{jet} *of the* n^{th} *jet in inclusive* $W+\geq$ n − jet *production, compared to ME+PS predictions separately normalized to the measured inclusive cross section in each jet multiplicity sample. Right: Differential cross section as a function of* ΔR *of the 2 leading jets in* $W+\geq 2$ *jet events.*

Figure 1 (left) shows the measured differential cross section, corrected at the hadron level, as a function of the transverse energy of the n^{th} jet in inclusive $W+\geq$ n − jet production. The shaded bands are the total systematic uncertainty in each measurement and are dominated by a 3% uncertainty on the jet energy scale. The measured cross sections are compared to LO Matrix Element plus Parton Showering MC predictions as determined using ALPGEN(v2)[1]+PYTHIA. The predictions are separately normalized to the measured inclusive cross section in each jet multiplicity sample, and provide a reasonable description of the shape of the measured E_T^{jet} spectra.

Figure 1 (right) shows, for $W+\geq 2$ jet events, the measured differential cross section as a function of ΔR_{jj}, where ΔR_{jj} denotes the separation (in the η-ϕ space) between the two leading jets. ME+PS predictions normalized to the total cross section provide a reasonable description of the data.

3 Inclusive Z+jets cross section

The Z boson production cross section is 10 times smaller than the W boson cross section. However, with more than $1\,fb^{-1}$ of data, precise differential measurements on $Z(\rightarrow ee)$+jets production are also possible, with the advantage that $Z \rightarrow ee$ is a clean and almost background free signal. CDF has measured the inclusive $Z(\rightarrow ee)$+jets cross section using $1.1\,fb^{-1}$ of data. The measurement is performed in a well defined kinematic region of the jets and the Z boson decay products. Electrons must have $E_T^e > 25\,GeV$ and be in the range $66 < M_{ee} < 116\,GeV/c^2$, where one electron has to be in the central region of the calorimeter ($|\eta^e| < 1.0$) and the other can be either in the central or in the forward region ($1.2 < |\eta^e| < 2.8$). Jets are reconstructed using the MidPoint algorithm[2] with cone radius R = 0.7. The jets are required to have $p_T^{jet} > 30\,GeV/c$, $|y^{jet}| < 2.1$ and $\Delta R_{e-jet} > 0.7$, where ΔR_{e-jet} denotes the distance (y-ϕ) between the jet and each of the two electrons in

the final state.

The $Z(\rightarrow ee)$+jets data sample contains background mainly from QCD-jets and W+jets processes and it is extracted from data. Other background contributions from $t\bar{t}$, $Z(\rightarrow ee)+\gamma$, dibosons and $Z(\rightarrow \tau\tau)$+jets final states are estimated using Monte Carlo samples. The total background in inclusive $Z(\rightarrow ee)+\geq \mathrm{N_{jet}}$ production varies between 10% to 14% as N_{jet} increases.

The measured cross section is corrected to the hadron level and compared to NLO pQCD predictions. The NLO pQCD prediction is determined using MCFM[3] and includes non-pQCD contributions. Non-pQCD contributions are computed using PYTHIA Tune A MC, and the difference between PYTHIA Tune A and PYTHIA Tune DW results are quoted as systematic uncertainty. Observables that are sensitive to the MC modeling, such as jet shapes and energy flows, have been measured and a good agreement was found between data and PYTHIA Tune A and DW predictions, making both PYTHIA Tune A and DW reliable tools to extract the parton-to-hadron corrections.

In Figure 2 (left) the measured integrated jet shape – defined as the fraction of transverse momentum of the jet contained inside a cone of radius r concentric to the cone of the jet (R) in events with exactly one reconstructed primary vertex – is compared to different MC predictions with different Underlying Event (UE) settings. Both PYTHIA Tune A and PYTHIA Tune DW provide a good description of the data. Data are also compared to a PYTHIA MC sample with no interaction between proton and antiproton remnants, producing jets significantly narrower than the data. Alternatively, one can test the UE activity by looking at the energy flow in the transverse plane away from the main jet direction. Figure 2 (right) shows the measured energy flows, using calorimeter towers with $|\mathrm{y}| < 0.7$ where, event-by-event, $\phi = 0$ is defined along the direction of the momentum of the Z boson. At $|\phi| = \pi$ the measured distribution shows a prominent peak coming from the leading jet, while at $|\phi| = \pi/2$ the measured energy flow is dominated by soft UE contributions. Both PYTHIA Tune A and PYTHIA Tune DW (the latter not shown in the plot) provide a good description of the measured energy flow.

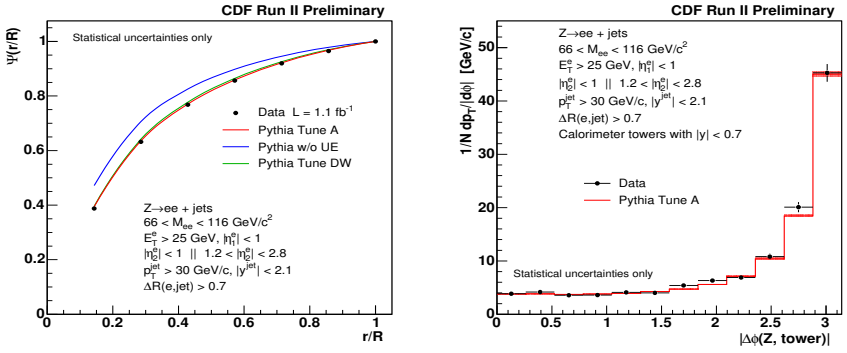

Figure 2: *Left: Integrated jet shapes in Z+jets events compared to different settings of the UE modeling. Right: Energy flow in the transverse plane in Z+jets events with respect to the Z boson direction ($\phi = 0$).*

Figure 3 shows the inclusive $Z(\rightarrow ee)$+jets cross section as a function of the transverse momentum of the jet, compared to NLO pQCD predictions. The shaded band is the total systematic uncertainty and it is dominated by a 3% uncertainty on the jet energy scale. The NLO pQCD predictions provide a good description of the measured cross section after non-pQCD corrections are included. The corrections for the non-perturbative contributions (C_{had}) are shown in the bottom part of the plot. They account for up to 25% of the cross section at low p_T^{jet}. The total cross section as a function of the inclusive jet multiplicity is shown in Fig. 4. The data are compared to LO and NLO pQCD predictions that include parton-to-hadron non-perturbative corrections. Good agreement is observed between data and NLO pQCD predictions. The plot also shows the ratio to the nominal LO prediction. An approximately constant NLO/LO k-factor is found for $N_{jet} = 1, 2$ and the data suggests a similar factor for $N_{jet} = 3$.

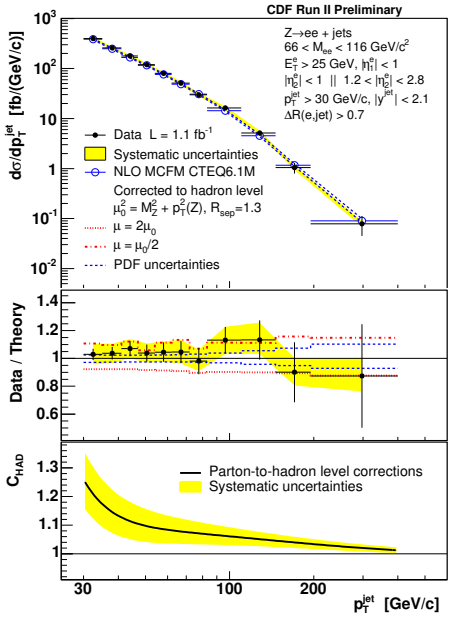

Figure 3: *Inclusive Z+jets cross section as a function of* p_T^{jet}*, compared to NLO pQCD predictions and showing the non-pQCD contributions* (C_{had}).

4 Conclusions

We have presented results on inclusive Boson+jets production in $p\bar{p}$ collisions at $\sqrt{s}$=1.96 TeV. The measurements are well described by ME+PS and NLO pQCD predictions.

5 Acknowledgments

I acknowledge the members of the CDF Collaboration for their works in achieving the results reported in this contribution.

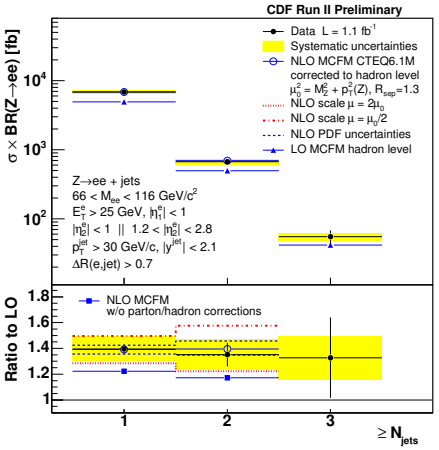

Figure 4: *Total cross section for Z(→ee)+jets production versus inclusive jet multiplicity compared to LO and NLO pQCD predictions.*

References

[1] M. Mangano *et al.* JHEP **0207**, 012 (2002).
[2] G.C. Blazey *et al*, hep-ex/0005012.
[3] J. Campbell and R.K. Ellis, Phys. Rev. D **65**, 113007 (2002).
[4] Slides:
http://indico.cern.ch/contributionDisplay.py?contribId=223&sessionId=6&confId=9499

Combining QCD and Electroweak Corrections to W-Boson Production at Hadron Colliders

G. Balossini[1], C.M. Carloni Calame [2], G. Montagna [1],
M. Moretti[3], O. Nicrosini [4], M. Treccani [3], A. Vicini [5]

1-Dipartimento di Fisica Nucleare e Teorica, Università di Pavia, and INFN, Sezione di Pavia

2-School of Physics and Astronomy, Southampton University, UK

3-Dipartimento di Fisica, Università di Ferrara, and INFN, Sezione di Ferrara, Italy

4- INFN, Sezione di Pavia, and Dipartimento di Fisica Nucleare e Teorica, Università di Pavia

5- Dipartimento di Fisica, Università di Milano, and INFN, Sezione di Milano

We review the present status of higher-order calculations for single W and Z boson production at hadron colliders, and present some preliminary results on the combination of electroweak and QCD corrections to a sample of observables of the process $p\overset{(-)}{p} \to W^{\pm} \to \mu^{\pm} + X$ at the Tevatron and at the LHC. Our phenomenological analysis shows that a high-precision knowledge of QCD and a careful combination of electroweak and strong contributions is mandatory in view of the anticipated experimental accuracy.

1 Higher-order QCD/electroweak calculations and tools

The Drell-Yan process has played a key role in the development of our understandig of QCD and electroweak (EW) interactions in hadron collider experiments, both from the experimental and theoretical point of view [2, 3]. Concerning QCD calculations and tools for EW gauge boson production at hadron colliders, the present situation reveals a quite rich structure, that includes next-to-leading-order (NLO) and next-to-next-to-leading-order (NNLO) corrections to W/Z total production rate [4, 5], NLO calculations for $W, Z + 1, 2$ jets signatures [6, 7] (available in the codes DYRAD and MCFM), resummation of leading and next-to-leading logarithms due to soft gluon radiation [8, 9] (implemented in the Monte Carlo ResBos), NLO corrections merged with QCD Parton Shower (PS) evolution [10] (in the event generator MC@NLO), NNLO corrections to W/Z production in fully differential form [11, 12, 13, 14] (available in the Monte Carlo program FEWZ), as well as leading-order multi-parton matrix elements generators matched with vetoed PS, such as, for instance, ALPGEN [15], MADEVENT [16] and SHERPA [17]. As far as complete $\mathcal{O}(\alpha)$ EW corrections to Drell-Yan processes are concerned, they have been computed independently by various authors in [18, 19, 20, 21, 22]

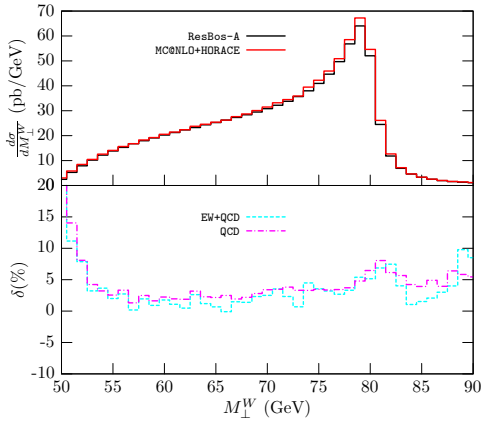

Figure 1: W transverse mass distribution at the Tevatron. Percent differences w.r.t. Resbos(-A).

for W production and in [23] for Z production. EW tools implementing exact NLO corrections to W production are DK [18], WGRAD2 [19], SANC [21] and HORACE [22], while ZGRAD2 [23] includes the full set of $\mathcal{O}(\alpha)$ EW corrections to Z production. The predictions of a subset of such calculations have been recently compared, at the level of same input parameters and cuts, in the proceedings of the Les Houches [24] and TEV4LHC [25] workshops for W production, finding a very satisfactory agreement between the various, independent calculations. The effect of the EW corrections on the determination of the W mass is large and is dominated by final-state QED radiation, enhanced by large collinear logarithms. NLO EW corrections induce a shift in the extracted value of m_W of the order of 100 MeV and higher-order effects contribute with a further shift of $\sim 10\%$ of the NLO contribution with opposite sign [26]; the latter can not be neglected, in view of the present accuracy reached at the Tevatron (see the talk by S. Malik [27]) and foreseen at the LHC ($\Delta m_W \sim 15$ MeV). In spite of this detailed knowledge of higher-order EW and QCD corrections, the combination of their effects is still at a very preliminary stage. There is only one attempt known in the literature [28], where the effects of QCD resummation are combined with NLO QED final-state corrections, leaving room for more detailed studies of the interplay between EW and QCD corrections to W/Z production at hadron colliders.

2 Combining QCD and EW corrections

The combination of QCD and EW corrections, using a factorized expression for the mixed contributions, can be cast in the following form:

$$\left[\frac{d\sigma}{d\mathcal{O}}\right]_{QCD\oplus EW} = \left\{\frac{d\sigma}{d\mathcal{O}}\right\}_{QCD} + \left\{\left[\frac{d\sigma}{d\mathcal{O}}\right]_{EW} - \left[\frac{d\sigma}{d\mathcal{O}}\right]_{Born}\right\} \qquad (1)$$

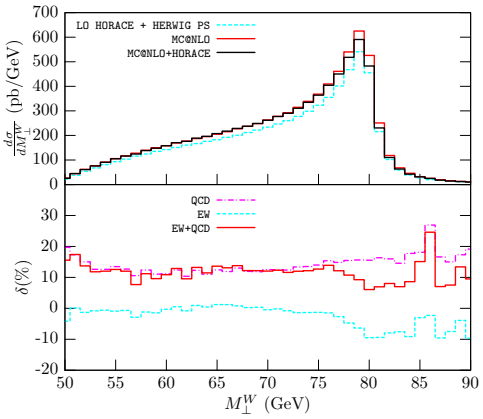

Figure 2: W transverse mass distribution at the LHC. Percent differences w.r.t. LO+PS results

where $d\sigma/d\mathcal{O}_{QCD}$ stands for the prediction of the observable $d\sigma/d\mathcal{O}$, as obtained by means of one of the state-of-the-art generators available in the literature, $d\sigma/d\mathcal{O}_{EW}$ is the HORACE prediction for the EW corrections to the $d\sigma/d\mathcal{O}$ observable, and $d\sigma/d\mathcal{O}_{Born}$ is the lowest-order result for the observable of interest. The label HERWIG PS in the second term in r.h.s. of Eq. (1) means that EW corrections are convoluted with QCD PS evolution through the HERWIG event generator, in order to (approximately) include mixed $\mathcal{O}(\alpha\alpha_s)$ corrections and to obtain a more realistic description of the observables under study. Actually, since the QCD shower evolution generates partons in the soft/collinear approximation, the results obtained for $\mathcal{O}(\alpha\alpha_s)$ corrections according to such a procedure are expected to be unreliable when hard non-collinear QCD radiation turns out to be important. However, beyond this approximation, a full two-loop calculation of $\mathcal{O}(\alpha\alpha_s)$ corrections, which is presently unavailable, would be required.

3 Numerical results

The preliminary numerical results shown in the present Section have been obtained using as standard cuts $p_\perp^l, p_\perp^{miss} > 25$ GeV for the minimum transverse momentum of the charged lepton and for the missing transverse momentum (both at the Tevatron and at the LHC) and $\eta^l_{max} < 1.2$ (2.5) at the Tevatron (LHC) for the maximum lepton pseudo-rapidity. We have also considered the case with the additional cut $M_\perp^W > 1$ TeV on the W transverse mass, cfr. Fig.3, to study the region where new heavy gauge boson could be produced. A careful tuning procedure has been carried on, to check that all the programs used in the comparison yield the same numbers under equal conditions in terms of input parameters, cuts and perturbative order. We have chosen the G_μ input scheme for the calculation of EW corrections, where, in particular, the (effective) electromagnetic coupling constant is given in the tree-level approximation by $\alpha^{\rm tree}_{G_\mu} = (\sqrt{2}/\pi) G_\mu {m_W}^2 \sin^2\vartheta_W$. However, for the coupling of external photons to charged particles needed for the evaluation of photonic corrections we use $\alpha(0) = 1/137.03599911$.

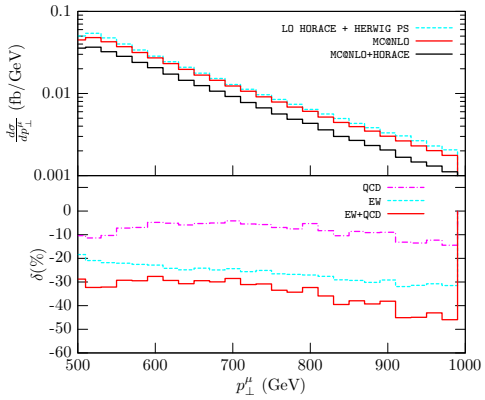

Figure 3: Large momentum tail of the lepton $p_\perp$ distribution at the LHC. Percent differences w.r.t. LO+PS results.

In Fig.1 we plot the W transverse mass distribution at the Tevatron and compare the results obtained with Resbos vs. MC@NLO (only QCD corrections) and those computed with Resbos-A vs. MC@NLO+HORACE (QCD+EW corrections). We observe an overall difference due to a different normalization of the two pure QCD codes and a clear deviation in the low transverse mass tail, which reaches the 15% level. The EW effects are dominated by QED final-state radiation; nevertheless the inclusion of exact $\mathcal{O}(\alpha)$ results and of higher-order QED terms is necessary, in view of the foreseen experimental accuracy. In Fig. 2 we plot the W transverse mass distribution at the LHC and compare the LO+PS results with the pure QCD predictions of MC@NLO and with the QCD+EW combination of MC@NLO+HORACE as in Eq.(1). The QCD corrections are large and positive and compensate the effect of the EW corrections which are negative. We observe that the peaked shape of the EW effects (cfr. Fig.4 in ref.[22]) is broadened by the convolution with the QCD parton shower. The inclusion of both EW and QCD corrections is necessary to obtain the proper descritpion of the peak region and in particular the correct shape of the transverse mass distribution, which is relevant for the extraction of the W mass. In Fig. 3 we plot the lepton transverse momentum distribution at the LHC and compare the LO+PS results with the pure QCD predictions of MC@NLO and with the QCD+EW combination of MC@NLO+HORACE. The large and negative EW corrections due to the presence of EW Sudakov logarithms sum up with large and negative effects due to the QCD corrections and reduce the distribution by -30% to -50% for $500 \le p_\perp^l \le 1000$ GeV. The large mass tail of the distribution is relevant for all the searches of physics beyond the Standard Model (SM), in particular of new heavy gauge bosons which could decay into a pair of leptons. The

accurate estimate of the SM background is very important to set reliable lower bounds on the masses of the new particles. In the last two examples we computed the relative effect of the various corrections w.r.t. the LO+PS results, having also observed the role of the QCD parton-shower in the simulation of the observables of interest.

In conclusion, we have presented the preliminary results of a study aiming at combining QCD and EW corrections, according to Eq.(1), in order to obtain an accurate description of the charged-current Drell-Yan process. The impact of the interplay between the two sets of corrections can not be neglected in data analysis, to match the accuracy foreseen e.g. in the measurement of the W boson mass.

References

[1] Slides:
`http://indico.cern.ch/contributionDisplay.py?contribId=176&sessionId=6&confId=9499`

[2] P.M. Nadolsky, AIP Conf. Proc. **753** (2005) 158

[3] U. Baur, Electroweak physics at the Tevatron and LHC: Theoretical status and perspectives, arXiv:hep-ph/0511064

[4] G. Altarelli, R. K. Ellis and G. Martinelli, Nucl. Phys. **B157** (1979) 461

[5] R. Hamberg, W. L. van Neerven and T. Matsuura, Nucl. Phys. **B359** (1991) 343 [Erratum Nucl. Phys. **B644** (2002) 403]

[6] W.T. Giele, E.W.N. Glover and D.A. Kosower, Nucl. Phys. **B403** (1993) 633

[7] J.M. Campbell and R.K. Ellis, Phys. Rev. **D65** (2002) 113007

[8] C. Balazs and C. P. Yuan, Phys. Rev. **D56** (1997) 5558

[9] F. Landry, R. Brock, P.M. Nadolsky and C.-P. Yuan, Phys. Rev. **D67** (2003) 073016

[10] S. Frixione and B. R. Webber, JHEP **0206** (2002) 029

[11] C. Anastasiou, L. J. Dixon, K. Melnikov and F. Petriello, Phys. Rev. Lett. **91** (200 3) 182002

[12] C. Anastasiou, L. J. Dixon, K. Melnikov and F. Petriello, Phys. Rev. **D69** (2004) 094008

[13] K. Melnikov and F. Petriello, Phys. Rev. Lett. **96** (2006) 231803

[14] K. Melnikov and F. Petriello, Phys. Rev. **D74** (2006) 114017

[15] M.L. Mangano, M. Moretti, F. Piccinini, R. Pittau and A.D. Polosa, JHEP **0307** (2003) 001

[16] T. Stelzer and W.F. Long, Comp. Phys. Commun. **81** (1994) 357; F. Maltoni and T. Stelzer, JHEP **02** (2003) 027

[17] T. Gleisberg, S. Höche, F. Krauss, A. Schälicke, S. Schumann and J. Winter, JHEP 0402 (2004) 056

[18] S. Dittmaier and M. Krämer, Phys. Rev. **D65** (2002) 0703007

[19] U. Baur and D. Wackeroth, Phys. Rev. **D70** (2004) 073015

[20] V. A. Zykunov, Eur. Phys. J. Direct **C3** (2001) 9; Phys. Atom. Nucl. **69** (2006) 1522

[21] A. Arbuzov, D. Bardin, S. Bondarenko, P. Christova, L. Kalinovskaya, G. Nanava and R. Sa dykov, Eur. Phys. J. **C46** (2006) 407

[22] C.M. Carloni Calame, G. Montagna, O. Nicrosini and A. Vicini, JHEP **12** (2006) 016

[23] U. Baur, O. Brein, W. Hollik, C. Schappacher and D. Wackeroth, Phys. Rev. **D65** (2002) 033007

[24] C. Buttar *et al.*, arXiv:hep-ph/0604120

[25] C. E. Gerber *et al.* [The TeV4LHC-Top and Electroweak Working Group], arXiv:0705.3251 [hep-ph].

[26] C.M. Carloni Calame, G. Montagna, O. Nicrosini and M. Treccani, Phys. Rev. **D69** (2004) 037301

[27] Slides: `http://indico.cern.ch/contributionDisplay.py?contribId=105&sessionId=9&confId=9499`

[28] Q.-H. Cao and C.-P. Yuan, Phys. Rev. Lett. **93** (2004) 042001; arXiv:hep-ph/0401171

Angular Correlations in Three-Jet Production and Jet Substructure in Neutral Current Deep Inelastic Scattering at HERA

Elias Ron, on behalf of the ZEUS collaboration

Universidad Autonoma de Madrid

Two analyses concerning jet production in *ep* collisions at a center-of-mass energy of $\sqrt{s} = 318$GeV are presented. Firstly, measurements of three-jet angular correlations between the three jets in the final state and the beam direction are investigated to separate the contributions from the different colour configurations. Secondly, measured normalised cross sections on subjet observables were used to study the pattern of parton radiation. In both analyses, jets are produced in Neutral Current (NC) deep inelastic scattering (DIS), with a required virtuality of the interaction boson $Q^2 > 125\text{GeV}^2$. A luminosity of 81.7 pb^{-1}, taken by the the ZEUS detector at HERA during the years 1998-2000, was used.

1 Angular correlations in three-jet production

1.1 Introduction

The self-coupling of the gluons is an essential feature of Quantum Chromodynamics (QCD). This is interpreted as a consequence of the SU(3), a non-Abelian group, being the underlying gauge symmetry group describing the strong interactions. The group structure is characterised in the perturbative expansion of the cross section through the colour factors, which depend on the underlying symmetry group. At leading order in the perturbative expansion, the cross section for three-jet production in *ep* scattering can be expressed as a sum of different colour configurations [2]. The partonic cross sections are:

$$\sigma_{ep\to 3\text{jets}} = C_F^2 \cdot \sigma_A + C_F C_A \cdot \sigma_B + C_F T_F \cdot \sigma_C + T_F C_A \cdot \sigma_D \tag{1}$$

In QCD, the corresponding values for the different colour configurations are $C_F = 4/3$ for the configuration that includes the $q \to qg$ vertex, $C_A = 3$ for the configuration which includes the triple-gluon vertex and $T_F = 1/2$ for the one containing the $q \to q\bar{q}$ vertex. However, for an Abelian theory like QED, $C_F = 1$, $C_A = 0$, $T_F = 3$. Thus, variables which are sensitive to contributions from different colour configurations are sensitive to the underlying symmetry group of the theory. The jet angular correlation variables used in the analysis are:

- α_{23}, defined as the angle between the two lowest transverse energy jets.
- β_{KSW}, defined as

$$cos(\beta_{KSW}) = cos\left[\frac{1}{2}(\angle[(\vec{p_1}\times\vec{p_3}),(\vec{p_2}\times\vec{p_B})] + \angle[(\vec{p_1}\times\vec{p_B}),(\vec{p_2}\times\vec{p_3})])\right], \tag{2}$$

  where $\vec{p_i}, i = 1,...,3$ is the momentum of jet i and $\vec{p_B}$ is a unit vector in the direction of the beam; the jets are ordered according to decreasing transverse energy;
- η_{max}^{jet}, the maximum pseudorapidity of the three jets with highest transverse energy.

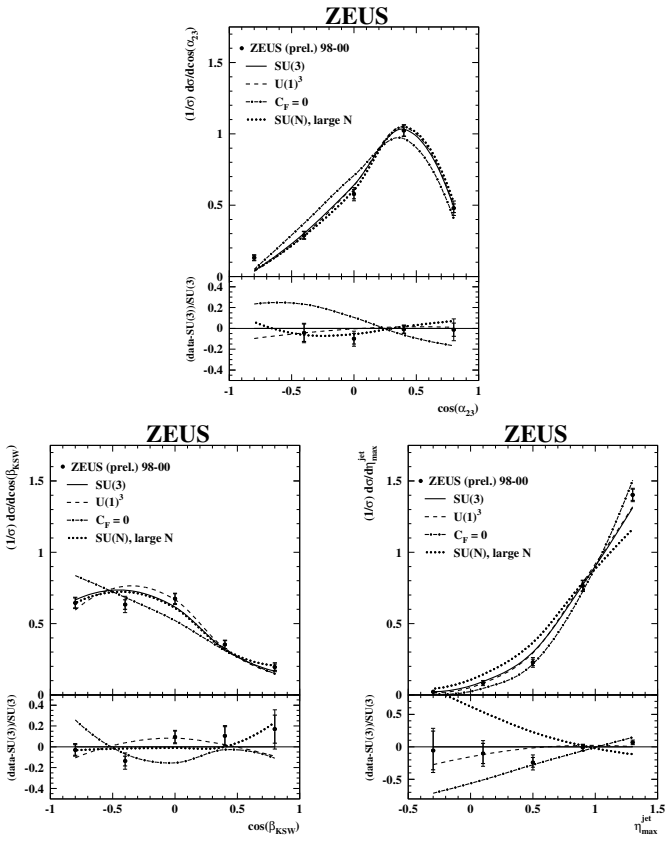

Figure 1: Measured differential cross sections as functions of the angular variables.

1.2 Results

Figure 1 shows the distribution of the normalised differential cross sections as functions of the angular variables. The data (black dots) are compared to four different predictions based on different underlying gauge symmetry groups, the non-Abelian SU(3), the Abelian group $U(1)^3$, SU(N) for large N and a situation with $C_F = 0, T_F = 1/2$ and $C_A = 3$. The inner error bar corresponds to the statistical error and the outer to the addition in quadrature of the statistical and systematical uncertainties. The theoretical predictions are obtained at leading-order (LO) with the program DISENT [3]. The calculations for each colour configuration are obtained separately and then the predictions for different underlying symmetry groups are obtained by multiplying by the corresponding colour factors. The data are found to be consistent with the admixture of colour configurations based on SU(3), as predicted by QCD. The normalised differential cross section as function of $\eta^{\rm jet}_{\rm max}$ disfavours an underlying symmetry group based on SU(N) for large N and also the situation with $C_F = 0$. This variable also provides sensitivity to distinguish the predictions based on SU(3) and the Abelian group $U(1)^3$. However, the experimental precision is not yet sufficient to do so.

2 Jet substructure

2.1 Introduction

The investigation of the internal structure of jets gives insight into the transition between a parton in a hard process and the experimentally observable jet of hadrons. At high transverse energy of the jets, $E_T^{\rm jet}$ the effects of fragmentation become negligible and the jet substructure can be calculated perturbatively. The k_T cluster algorithm [4] was used to define jets in the final state. Subjets were resolved within a jet by considering all particles associated with the jet and repeating the application of the jet finding algorithm until, for every pair of particles i and j the quantity:

$$d_{ij} = \min(E_{T,i}, E_{T,j})^2[(\eta_i - \eta_j)^2 + (\phi_i - \phi_j)^2] \tag{3}$$

was greater than $d_{\rm cut} = y_{\rm cut}(E_T^{\rm jet})^2$. The remaining clusters are called subjets. Subjet multiplicity it then defined as the number of subjets resolved within the jet, and depends on the value of the resolution parameter $d_{\rm cut}$. The jet sample in this analysis consists of those jets with exactly two subjets at a $y_{\rm cut} = 0.05$. The pattern of QCD radiation from a primary parton has been studied by measing normalised cross sections as a function of the following subjet observables: the ratio between the subjet transverse energy and that of the jet, $E_T^{\rm sbj}/E_T^{\rm jet}$, the difference between the subjet pseudorapidity (azimuth) and that of the jet, $\eta^{\rm sbj} - \eta^{\rm jet}(|\phi^{\rm sbj} - \phi^{\rm jet}|)$ and $\alpha^{\rm sbj}$, the angle, as viewed from the jet center, between the highest transverse energy subjet and the beam line in the pseudorapidity-azimuth plane. The calculations at $O(\alpha_s)$ and $O(\alpha_s^2)$ QCD calculations are used to compare with the data are based on the program DISENT.

2.2 Results

Figure shows the normalised differential cross sections as function of the variables described above. The black dots are the data, the inner error bar corresponds to the statistical uncertainty and the outer error bar to the addition in quadrature of the statistical and systematical uncertainties.
The distribution in $E_T^{\rm jet}/E^T$, which is symmetric by construction, shows that the two subjets tend to have similar transverse energies. The distribution in $\eta^{\rm sbj} - \eta^{\rm jet}$ shows an asymmetric two peak structure. The dip in the middle is a consequence of the inability to resolve subjets which are very close to each other. The distribution shows that the two subjets tend to be near to each other. The normalised differential cross section as function of $|\phi^{\rm sbj} - \phi^{\rm jet}|$ also indicates that subjets tend to be close to each other, and the dip at low values of the variable is also a consequence of resolution limitations when they are very near. As can be seen, the cross section as function of $\alpha^{\rm sbj}$ grows as $\alpha^{\rm sbj}$ grows, which indicates that the highest transverse energy subjet tends to be in the rear part of the jet. This feature, together with the fact that the highest E_T subjet tends to be closer to the jet center than the other subjet, is compatible with the asymmetry observed in the $\eta^{\rm sbj} - \eta^{\rm jet}$ distribution.

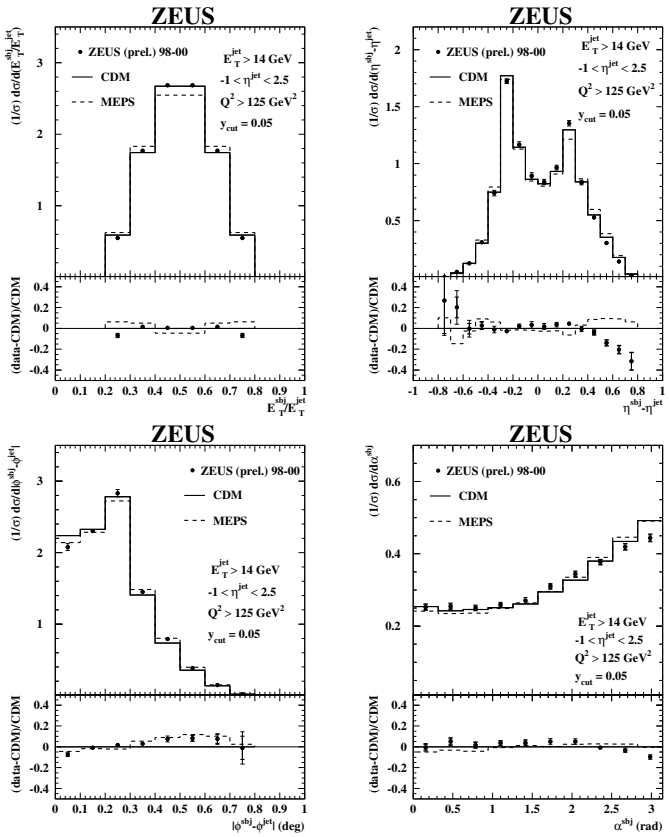

Figure 2: Measured differential cross sections as functions of a) $E_T^{\rm jet}/E^T$, b)$\eta^{\rm sbj} - \eta^{\rm jet}$, c)$|\phi^{\rm sbj} - \phi^{\rm jet}|$ and d)$\alpha^{\rm sbj}$.

References

[1] Slides:
`http://indico.cern.ch/contributionDisplay.py?contribId=225&sessionId=6&confId=9499`

[2] P. Aureche et al., Nucl. Phys. Phys. B 268, 553 (1987)

[3] S.Catani and M.H. Seymour, Nucl. Phys. B 485, 291 (1997).

[4] S.Catani et al. Nucl.Phys. B 406, 187(1993).

Dijet Azimuthal Correlations in QCD Hard Processes

Yazid Delenda *

School of Physics and Astronomy - The University of Manchester
Oxford Road, Manchester M13 9PL - U.K.

We study the azimuthal correlation distribution for dijet production in QCD hard processes. This observable is sensitive to soft and/or collinear emissions in the back-to-back region, giving rise to single and double logarithms. We provide resummed predictions to NLL accuracy for both DIS at HERA and hadronic collisions at Tevatron and perform a NLO matching to NLOJET++ results in the DIS case.

1 Introduction

Studies of soft gluon radiation and non-perturbative effects in QCD observables are of vital importance. These studies help us better understand the dynamics of QCD and enhance the accuracy of theoretical predictions for measured quantities. In several instances precision in QCD is limited not just by what powers of α_s are controlled, but also by the lack of better understanding of QCD dynamics such as the all-orders behaviour (embodied in the resummation of large logarithms) and inevitably the process of hadronisation.

Successful examples of such studies are manifested in event-shape variables at LEP and HERA. Resummed estimates for these observables, combined with NLO predictions and corrected for non-perturbative effects, have been very successful in describing the data [2, 3]. Parameters such as the strong coupling and the effective non-perturbative coupling [4] can then be consistently extracted by studying distributions and mean values of such observables (see for instance Ref. [5] for a recent review).

Going beyond the case of two hard partons is more challenging in terms of theory but is also a more stringent test of our understanding of QCD dynamics. Multi-jet event-shape variables have been studied (see Refs. [6, 7]). However for jet-defined quantities, e.g. several dijet distributions, there are currently very few resummed predictions because of the lack of theoretical insight to all orders in the presence of a jet algorithm. Many measurements are already established (see e.g. [8, 9]) and await comparison to theoretical estimates.

Effort has recently been devoted to improve the understanding of the effect of jet algorithms on QCD resummation [10, 11, 12, 13]. A clustering algorithm has an impact on the resummation of observables which are defined in a limited region of the phase-space (such as energy flow outside jets), known as "non-global" observables [14, 15]. These receive single logs which could only be resummed numerically in the large N_c limit for processes involving only two hard partons. It was shown in Ref. [10] that employing a k_t algorithm on the final-state particles reduces these logarithms in the case where only two hard partons are present. However the resummation of jet-defined quantities proved to be non-trivial [12] and the full impact of clustering algorithms on resummation has been explained more recently in Ref. [13].

With the technique of resummation using a clustering algorithm one can proceed with studying jet-defined quantities. In the present work we focus on the dijet azimuthal correlation distribution. We consider the process of production of two hard jets in DIS or hadronic

*Work done in collaboration with Andrea Banfi and Mrinal Dasgupta.

collisions. We study the azimuthal correlation defined by the azimuthal angle between the leading hard jets in the final state.

The azimuthal angle of a jet is defined by:

$$\phi_{\rm jet} = \frac{\sum_{i\in{\rm jet}} E_{t,i}\phi_i}{\sum_{i\in{\rm jet}} E_{t,i}}\,, \tag{1}$$

where the sum runs over all particles inside the jet. The observable we study has the following approximation in the soft and/or collinear regime:

$$\begin{aligned}\Delta\phi &= |\pi - \delta\phi_{\rm jets}|\,,\\ &= \left|\sum_i \frac{k_{t,i}}{p_t}\left(\sin\phi_i - \theta_{i1}\phi_i - \theta_{i2}(\pi-\phi_i)\right)\right|,\end{aligned} \tag{2}$$

where p_t is the transverse momentum of the outgoing hard partons, which we assumed to be at azimuths $\phi_1 = 0$ and $\phi_2 = \pi$. Here $\theta_{ij} = 1$ if particle i is clustered to jet j and is zero otherwise.

The above definition implies that the observable in question is global. This means that no non-global component is present and the resummed result to next-to-leading log (NLL) accuracy has no dependence on the jet algorithm. This is the recombination scheme used by the H1 collaboration at HERA to measure this observable [8]. However if one employs a recombination scheme in which the four-momentum of the jet is defined by the addition of four-momenta of particles in the jet, then our observable becomes non-global. In this case one would need to calculate the additional non-global component as well as the dependence on the jet algorithm. The DØ collaboration at Tevatron employed the latter recombination scheme to measure the observable [9, 16].

We note that in the soft and/or collinear region, i.e. close to the Born configuration in which the outgoing jets are back-to-back ($\Delta\phi \sim 0$), the distribution receives large logarithms. This region is also strongly affected by non-perturbative effects. In the present study we shall report the resummed predictions for these logarithms to NLL accuracy both in DIS and hadronic collisions and provide a matching to NLO results obtained from NLOJET++ [17] in the DIS case.

2 Resummation and matching

The resummed result for the integrated distribution for events with $\Delta\phi < \Delta$ is given by:

$$\sigma(\Delta) = \int d\mathcal{B}\frac{2}{\pi}\int_0^{+\infty}\frac{db}{b}\sin(\Delta b)\sigma_{\mathcal{B}}(b)e^{-R(b)}\,, \tag{3}$$

where we reported the result for the DIS case assuming the azimuths of the jets are recombined using Eq. (1). In Eq. (3) $\sigma_{\mathcal{B}}(b)$ is the Born cross-section for the production of two hard jets in DIS, containing parton distribution functions (pdfs) evolved to μ_f^2/b^2, with μ_f being the factorisation scale, and $d\mathcal{B}$ is the corresponding phase-space. The function $R(b)$ is the radiator which contains the resummed leading and next-to-leading logs.

The resummed result needs to be corrected to include pieces which are not captured by the resummation. Many techniques have been developed to match resummed predictions

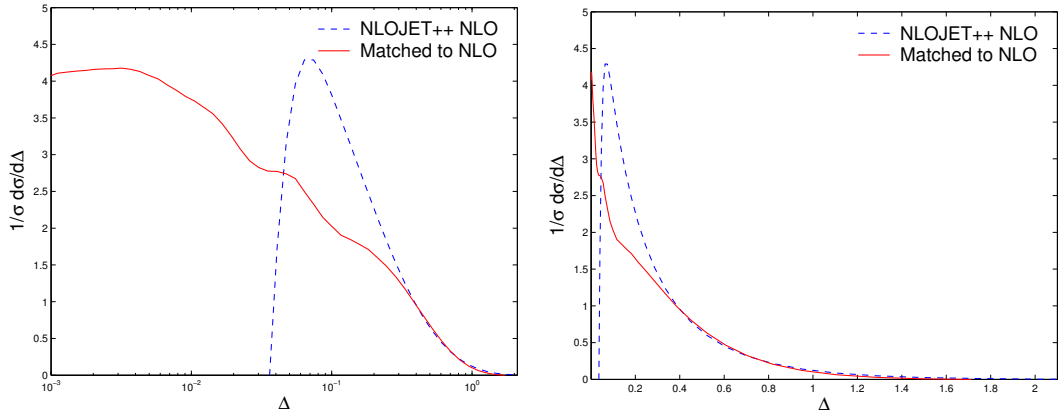

Figure 1: The Dijet azimuthal correlation distribution in DIS. A comparison between the NLO and matched results is shown. The NLO result diverges when $\Delta \to 0$, while the matched result tends to a constant. The effect of matching is to bring the distribution to NLOJET++ [17] curve at large Δ (where we expect the NLO result to hold) and to correct the resummed result at small Δ by a constant factor, not accounted for in the resummation.

with NLO results. Below we report the matching formula we use here:

$$\sigma_{\rm mat} = \sigma(\Delta)\left[1 + \left(\sigma_e^{(1)} - \sigma_r^{(1)}\right)/\sigma_0\right] + \left(\sigma_e^{(2)} - \sigma_r^{(2)}\right)\exp\left(-R_{\rm DL}\right), \tag{4}$$

where $\sigma(\Delta)$ is the resummed result, $\sigma_r^{(1)}$ and $\sigma_r^{(2)}$ are the expansion of the resummed result to $\mathcal{O}(\alpha_s)$ and $\mathcal{O}(\alpha_s^2)$ respectively and σ_0 is the Born cross section. Here σ_e denotes the integrated distributions given by NLOJET++ [17], with the superscripts indicating the order, and $R_{\rm DL}$ is the double logarithmic piece of the radiator obtained by replacing $b \to e^{-\gamma_E}/\Delta$, where γ_E is the Euler constant. We present the results in Fig. 1.

3 Hadronic collisions case

We report below the result for the dijet azimuthal correlation distribution in hadronic collisions. This has been measured at DØ using the jet recombination scheme in which the four-momentum of a jet is obtained by the sum over the four-momenta of particles in the jet. Here we only report the result which exploits Eq. (1) although similar results can be obtained for the other scheme. The resummed result is given by:

$$\sigma(\Delta) = \int d\mathcal{B}\frac{2}{\pi}\int_0^\infty \frac{db}{b}\sigma_{\mathcal{B}}(b)\sin(b\Delta)e^{-R(b)} \times S\,, \tag{5}$$

where

$$S = {\rm Tr}(He^{-SL(b)\Gamma^\dagger/2}Me^{-SL(b)\Gamma/2})/{\rm Tr}(HM)\,, \tag{6}$$

with H, Γ and M being the hard, anomalous dimension and soft matrices. These depend on the kinematics of the process and appear in various places (e.g. [18, 19, 20]). The single logarithmic function $SL(b)$ accounts for soft wide-angle emissions. Here $\sigma_{\mathcal{B}}(b)$ is the Born

cross-section for the production of two jets in hadronic collisions, which also contains pdfs from both incoming legs evolved to μ_f^2/b^2, and $d\mathcal{B}$ is the corresponding phase-space for the production of a dijet system in hadronic collisions. Note that the radiator in this case has a slightly different form than in the DIS case.

4 Future directions

Having performed an NLL resummation (and NLO matching in the DIS case) we can now compare our predictions with data and other approaches (e.g. that of Ref. [21] which implements unintegrated pdfs).

We can further our study by looking at the hadronic collisions case using the same jet definitions as those used by the DØ collaboration. The current indication is that the size of the non-global component and the impact of the jet algorithm on the "global" piece may not be significant [13, 22], particularly since these pieces contain only single logarithms while the distribution is dominated by double logarithms.

References

[1] Slides:
`http://indico.cern.ch/contributionDisplay.py?contribId=177&sessionId=6&confId=9499`

[2] M. Dasgupta and G. P. Salam, J. Phys. G **30** (2004) R143 [arXiv:hep-ph/0312283].

[3] M. Dasgupta and G. P. Salam, JHEP **0208** (2002) 032 [arXiv:hep-ph/0208073].

[4] Y. L. Dokshitzer and B. R. Webber, Phys. Lett. B **352** (1995) 451 [arXiv:hep-ph/9504219].

[5] S. Kluth, *In the Proceedings of FRIF workshop on first principles non-perturbative QCD of hadron jets, LPTHE, Paris, France, 12-14 Jan 2006, pp R002* [arXiv:hep-ex/0606046].

[6] A. Banfi, G. Marchesini, Y. L. Dokshitzer and G. Zanderighi, JHEP **0007** (2000) 002 [arXiv:hep-ph/0004027]; Phys. Lett. B **508** (2001) 269 [arXiv:hep-ph/0010267]; JHEP **0103** (2001) 007 [arXiv:hep-ph/0101205]; JHEP **0105** (2001) 040 [arXiv:hep-ph/0104162].

[7] A. Banfi, URL:
`http://indico.cern.ch/contributionDisplay.py?contribId=180&sessionId=6&confId=9499`,
Talk given at DIS 2007.

[8] M. Hansson [H1 Collaboration], DIS 2006 (Tsukuba) Proc. (2006) 539.

[9] V. M. Abazov *et al.* [DØ Collaboration], Phys. Rev. Lett. **94**, 221801 (2005) [arXiv:hep-ex/0409040].

[10] R. B. Appleby and M. H. Seymour, JHEP **0212** (2002) 063 [arXiv:hep-ph/0211426].

[11] R. B. Appleby and M. H. Seymour, JHEP **0309** (2003) 056 [arXiv:hep-ph/0308086].

[12] A. Banfi and M. Dasgupta, Phys. Lett. B **628** (2005) 49 [arXiv:hep-ph/0508159].

[13] Y. Delenda, R. Appleby, M. Dasgupta and A. Banfi, JHEP **0612** (2006) 044 [arXiv:hep-ph/0610242].

[14] M. Dasgupta and G. P. Salam, Phys. Lett. B **512** (2001) 323 [arXiv:hep-ph/0104277].

[15] M. Dasgupta and G. P. Salam, JHEP **0203** (2002) 017 [arXiv:hep-ph/0203009].

[16] M. Zielinski [DØ Collaboration], AIP Conf. Proc. **842** (2006) 265 [arXiv:hep-ex/0602019].

[17] Z. Nagy and Z. Trocsanyi, Phys. Rev. Lett. **87** (2001) 082001 [arXiv:hep-ph/0104315]; Phys. Lett. B **634** (2006) 498 [arXiv:hep-ph/0511328].

[18] J. Botts and G. Sterman, Nucl. Phys. B **325** (1989) 62.

[19] N. Kidonakis and G. Sterman, Phys. Lett. B **387** (1996) 867; Nucl. Phys. B **505** (1997) 321 [arXiv:hep-ph/9705234].

[20] N. Kidonakis, G. Oderda and G. Sterman, Nucl. Phys. B **531** (1998) 365 [arXiv:hep-ph/9803241].

[21] H. Jung, URL:
`http://indico.cern.ch/contributionDisplay.py?contribId=54&sessionId=6&confId=9499`,
Talk given at DIS 2007.

[22] A. Banfi and M. Dasgupta, JHEP **0401** (2004) 027 [arXiv:hep-ph/0312108].

Dimensional Reduction Applied to QCD at Higher Orders

Robert Harlander[1], Philipp Kant[2], Luminita Mihaila[2], Matthias Steinhauser[2] *

1- Fachbereich C - Bergische Universität Wuppertal
42097 Wuppertal - Germany

2- Theoretische Teilchenphysik - Universität Karlsruhe
76128 Karlsruhe - Germany

Recent developments in higher order calculations within the framework of Dimensional Reduction, the preferred regularization scheme for supersymmetric theories, are reported on. Special emphasis is put on the treatment of evanescent couplings, the equivalence to Dimensional Regularization, and the evaluation of $\alpha_s(M_{\rm GUT})$ from $\alpha_s(M_{\rm Z})$.

1 Dimensional Reduction

Dimensional Regularization (DREG) [2] has proven extremely successful for the evaluation of higher order corrections in quantum field theory, mostly because it preserves gauge invariance and thus does not interfere with the renormalizability of the Standard Model or QCD. Many techniques for evaluating Feynman diagrams have been developed within the framework of DREG, so perturbation theory heavily relies upon the validity of this regularization method.

Applied to SUSY theories, however, one faces the problem of explicit SUSY breaking by the need to assign different numbers of degrees of freedom to spin-1 and spin-1/2 fields. A manifestation of this SUSY breaking is that SUSY relations of couplings no longer hold at higher orders. For example, while SUSY requires equality for the quark-quark-gluon and the squark-quark-gluino couplings g and $\hat{g}$ at all energy scales, one finds that their renormalization constants differ. In fact, it is $Z_g = (1+\delta_{\hat{g}})\, Z_{\hat{g}}$, and thus

$$\hat{g} = (1+\delta_{\hat{g}})g\,, \tag{1}$$

where $\delta_{\hat{g}} = \alpha_s/(3\pi)$ [3]. In effect, the number of renormalization constants in SUSY becomes rather large when calculations are done in DREG.

As a way out, it was suggested to use Dimensional Reduction (DRED) as a regularization procedure for SUSY theories [4]. Formally, this means that space-time is compactified to $D = 4 - 2\epsilon$ dimensions ($\epsilon > 0$), while the vector fields are kept four-dimensional. As an example, consider the electron-photon vertex, which in DRED becomes

$$\bar{\psi}\gamma_\mu\psi A^\mu = \bar{\psi}\gamma_\mu\psi\hat{A}^\mu + \bar{\psi}\gamma_\mu\psi\tilde{A}^\mu = \bar{\psi}\hat{\gamma}_\mu\psi\hat{A}^\mu + \bar{\psi}\tilde{\gamma}_\mu\psi\tilde{A}^\mu\,, \tag{2}$$

where $\hat{A}^\mu$ and $\tilde{A}^\mu$ denote the D and the 2ϵ-dimensional component of the vector field A^μ. $\tilde{A}^\mu$ is also called the ϵ-scalar. Traces over the D- and 2ϵ-dimensional γ-matrices can be evaluated using

$$\{\gamma^\mu,\gamma^\nu\} = 2g_{\mu\nu} \qquad \text{and} \qquad \{\hat{\gamma}^\mu,\tilde{\gamma}^\nu\} = 0\,. \tag{3}$$

Thus, perturbative calculations in DRED require to introduce additional fields (ϵ-scalars) and an extra set of γ-matrices. Once the algebraic part of the evaluation of a Feynman amplitude is done, the tools developped for DREG can be applied without further modification.

*Work supported by the DFG through SFB/TR 9 and HA 2990/3-1.

2 Evanescent couplings

In a SUSY theory, the relation $A_\mu = \hat{A}_\mu + \tilde{A}_\mu$ is essential: it is A_μ that is part of a supermultiplet, while $\hat{A}_\mu$ and $\tilde{A}_\mu$ are introduced for purely technical reasons. Therefore, this relation must hold also at higher orders of perturbation theory.

This is not necessarily the case in a non-SUSY theory. Since $\tilde{A}_\mu$ transforms like a scalar under gauge transformations (thus the name "ϵ-scalar"), there is no symmetry to ensure that the $\tilde{A}_\mu$-couplings renormalize in the same way as the corresponding $\hat{A}_\mu$-couplings. Thus, when applying DRED to QCD, we have to introduce two different couplings for the quark-gluon vertex, for example:

$$g_s A_\mu \bar{\psi}\gamma^\mu\psi \to \hat{g}_s \hat{A}_\mu \bar{\psi}\hat{\gamma}^\mu\psi + \tilde{g}_s \tilde{A}_\mu \bar{\psi}\tilde{\gamma}^\mu\psi\,. \tag{4}$$

In order to be consistent with our journal papers [5, 6, 7][a] let us define

$$\alpha_s = \frac{\hat{g}_s^2}{4\pi}\,, \qquad \alpha_e = \frac{\tilde{g}_s^2}{4\pi}\,, \tag{5}$$

where α_e is called "evanescent coupling". Only at tree-level can one require that $\alpha_s = \alpha_e$. Higher orders lead to an energy dependece of the (minimally subtracted) couplings, governed by the RGEs[b]

$$\mu^2\frac{\mathrm{d}}{\mathrm{d}\mu^2}\alpha_s = \beta_s^{\overline{\mathrm{DR}}}(\alpha_s,\alpha_e)\,, \qquad \mu^2\frac{\mathrm{d}}{\mathrm{d}\mu^2}\alpha_e = \beta_e(\alpha_s,\alpha_e)\,. \tag{6}$$

The β-functions have been evaluated in Ref. [5] through three loops, and $\beta_s^{\overline{\mathrm{DR}}}$ is even known to four-loop order [6]. Indeed it turns out that $\beta_s^{\overline{\mathrm{DR}}} \neq \beta_e$ in standard QCD already at one-loop level. The condition $\alpha_s = \alpha_e$ can therefore be implemented only at one particular value of μ^2.

If $\overline{\mathrm{DR}}$ (i.e., DRED with minimal subtraction) is to be a viable renormalization scheme, then one should be able to transform physical results from one scheme into the other by finite shifts of the renormalized parameters. This property has been confirmed several times [8, 5, 6]. The proper conversion relation for the strong coupling between the $\overline{\mathrm{MS}}$ and the $\overline{\mathrm{DR}}$ scheme in n_f-flavor standard QCD is given at two-loop level by [5]

$$\bar{\alpha}_s = \alpha_s\left[1 - \frac{\alpha_s}{4\pi} - \frac{5}{4}\left(\frac{\alpha_s}{\pi}\right)^2 + \frac{\alpha_s\alpha_e}{12\pi^2}\,n_f + \ldots\right]\,, \tag{7}$$

where $\bar{\alpha}_s$ denotes the strong coupling in the $\overline{\mathrm{MS}}$ scheme. Three-loop corrections to this relation are known as well [6].

When evaluating physical observables in DREG, the result depends only on $\bar{\alpha}_s$, while it depends on both α_s and α_e in DRED. This ambiguity should be viewed as a freedom of the renormalization scheme: any choice of α_e determines the value of α_s by comparison to the experimental value of the physical observable at one particular scale μ_0. At any other scale μ, α_s and α_e are determined by the RGEs Eq. (6).

[a] There is a misprint in Eq. (18) of Ref. [6]: the term $-25\,n_f^2/72$ should read $-25\zeta_3/72$.

[b] In fact, there are several evanescent couplings in QCD; however, for the sake of the argument, it is sufficient to consider only α_e here.

Also, there is a unique relation between the perturbative coefficients of the $\overline{\rm DR}$ and the $\overline{\rm MS}$ expression of the physical observable, to be called R and $\bar{R}$ in what follows. For example, assume that

$$R(\alpha_s,\alpha_e)=\sum_{i,j\geq 0}\left(\frac{\alpha_s}{\pi}\right)^i\left(\frac{\alpha_e}{\pi}\right)^j r_{ij}\,,\qquad\qquad \bar{R}(\bar{\alpha}_s)=\sum_{i\geq 0}\left(\frac{\bar{\alpha}_s}{\pi}\right)^i \bar{r}_i\,. \tag{8}$$

Then, inserting Eq. (7) into Eq. (8) and requiring equality, one derives the relations

$$\begin{aligned} &r_{00}=\bar{r}_0\,,\quad r_{10}=\bar{r}_1\,,\quad r_{01}=0\,,\quad r_{20}=\bar{r}_2-\frac{\bar{r}_1}{4}\,,\quad r_{02}=0\,,\quad r_{11}=0\,,\\ &r_{30}=\bar{r}_3-\frac{\bar{r}_2}{2}-\frac{5}{4}\,\bar{r}_1\,,\quad r_{21}=\frac{n_f}{12}\,\bar{r}_1\,,\quad r_{12}=0\,,\quad r_{03}=0\,,\quad \text{etc.}\end{aligned} \tag{9}$$

3 Relation of α_s and α_e by Supersymmetry

Supersymmetry is a concept that provides solutions to some of the most pressing questions left open by the Standard Model. As already mentioned above, in a SUSY theory it is required that $\alpha_s=\alpha_e$ at all energy scales, and thus $\beta_s=\beta_e$. We can use the QCD results of Ref. [5] to test the consistency of DRED and SUSY for a SUSY Yang Mills theory at three-loop level, simply by choosing the color factors appropriately. Indeed, we find that $\beta_s=\beta_e$ through three loops in a SUSY Yang Mills theory. For a check of this relation within SUSY-QCD, one needs to include chiral fields in the fundamental representation of the gauge group, or in other words, quarks and squarks. This is work in progress.

If indeed the QCD that we observe is the low energy limit of a softly broken SUSY-QCD theory, then the freedom of choosing α_e is lost, because within this SUSY theory, we require $\alpha_e^{(\rm full)}=\alpha_s^{(\rm full)}$ at all scales. The couplings in QCD are related to those in SUSY-QCD by matching relations:

$$\alpha_s(\mu)=\zeta_s\alpha_s^{(\rm full)}(\mu)\,,\qquad \alpha_e(\mu)=\zeta_e\alpha_e^{(\rm full)}(\mu)\,, \tag{10}$$

where ζ_s and ζ_e are functions of $\alpha_s^{(\rm full)}$, the SUSY particle masses, and the "matching scale" μ (if α_s and α_e are the couplings in five-flavor QCD, then ζ_s and ζ_e depend also on the top quark mass). Note that since the dependence of $\zeta_{s,e}$ on the matching scale μ is logarithmic, one should apply Eq. (10) at a scale not too much different from the SUSY particle masses. Also, if these masses are spread over a large range, matching better be done in several steps.

ζ_s and ζ_e can be evaluated perturbatively. The two-loop expression for ζ_s has been calculated in Ref. [9], while for ζ_e only the one-loop term is known [7].

Assume now for the sake of the argument that all SUSY-QCD particle masses are identical, say $m_{\tilde{q}}=m_{\tilde{g}}=\tilde{M}\sim 1\,\text{TeV}$. If $\bar{\alpha}_s(M_Z)$ in QCD is given by experiment, then the SUSY coupling, for example at the GUT scale $\mu_{\rm GUT}$, can be determined by the following scheme:

$$\bar{\alpha}_s(M_Z)\overset{(i)}{\to}\bar{\alpha}_s(\mu_{\rm dec})\overset{(iii)}{\leftarrow}\left\{\begin{array}{c}\alpha_s(\mu_{\rm dec})\\ \alpha_e(\mu_{\rm dec})\end{array}\right\}\overset{(ii)}{\leftarrow}\alpha_s^{(\rm full)}(\mu_{\rm dec})\overset{(iv)}{\to}\alpha_s^{(\rm full)}(\mu_{\rm GUT})\,. \tag{11}$$

If the evolution is to be consistent through n-loop order, then steps (i) and (iv) need to be done through n loops, while steps (ii) and (iii) are only required through $(n-1)$ loops. Here, it is understood that one starts with a trial value α_0 for $\alpha_s^{(\rm full)}(\mu_{\rm dec})$, evaluates steps (ii) and

(*iii*), and compares the value for $\bar{\alpha}_s(\mu_{\rm dec})$ obtained in this way with the one obtained from step (*i*). If it agrees, one performs step (*iv*) with $\alpha_s^{\rm (full)}(\mu_{\rm dec}) = \alpha_0$, otherwise, one starts again with a different value for α_0.

An alternative way to proceed was applied in Ref. [7]. There, the relation between $\alpha_s(\mu_{\rm dec})$ and $\alpha_e(\mu_{\rm dec})$ was perturbatively expanded such that $\alpha_s(\mu_{\rm GUT})$ could be directly evaluated from $\bar{\alpha}_s(M_Z)$ without the need for an iterative procedure. The difference between these two approaches is formally of higher orders in α_s, but is expected to grow as the decoupling scale moves away from the SUSY masses $\tilde{M}$. At three-loop level, the two approaches are consistent with each other within each others uncertainty (derived from the experimental error on $\alpha_s(M_Z)$ [11]) over a large range of the decoupling scale. Figure 1 shows the result [7], demonstrating the numerical importance of the three-loop effects, in particular if decoupling is done at other scales than $\tilde{M}$ (quite often one finds $\mu_{\rm dec} = M_Z$, for example [10]).

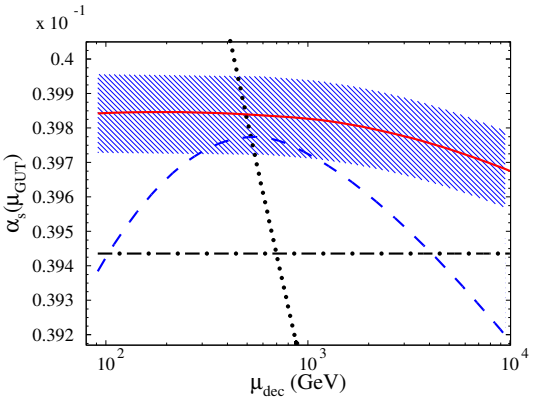

Figure 1: α_s at $\mu_{\rm GUT} \equiv 10^{16}\,$GeV derived from $\alpha_s(M_Z)$ in 1-, 2-, and 3-loop approximation (dotted, dashed, solid) as a function of the decoupling scale $\mu_{\rm dec}$. The dash-dotted curve is what results from the formula given in Ref. [10]. See Ref. [7] for details.

4 Conclusions

DRED is currently considered the appropriate regularization method for supersymmetric theories. Applied to non-SUSY theories, it leads to evanescent couplings, with their own evolution and decoupling relations. If parameters from the non-SUSY theory are to be related to SUSY parameters, the conversion relations will typically involve these evanescent couplings. Here we took these issues into account for the derivation of $\alpha_s(\mu_{\rm GUT})$ from $\alpha_s(M_Z)$ at three-loop level.

References

[1] Slides:
`http://indico.cern.ch/contributionDisplay.py?contribId=170&sessionId=6&confId=9499`

[2] G. 't Hooft and M.J. Veltman, *Nucl. Phys.* **B 44** 189 (1972).

[3] S.P. Martin and M.T. Vaughn, *Phys. Lett.* **B 318** 331 (1993).

[4] W. Siegel, *Phys. Lett.* **B 84** 193 (1979).

[5] R. Harlander, P. Kant, L. Mihaila, M. Steinhauser, *JHEP* **09** 053 (2006).

[6] R.V. Harlander, D.R.T. Jones, P. Kant, L. Mihaila, M. Steinhauser, *JHEP* **0612** 024 (2006).

[7] R.V. Harlander, L. Mihaila, M. Steinhauser, `arXiv:0706.2953 [hep-ph]`.

[8] I. Jack, D.R.T. Jones, K.L. Roberts, *Z. Phys.* **C 63** 151 (1994).

[9] R. Harlander, L. Mihaila, M. Steinhauser, *Phys. Rev.* **D 72** 095009 (2005).

[10] J.A. Aguilar-Saavedra *et al.*, *Eur. Phys. J.* **C 46** 43 (2006).

[11] S. Bethke, *Prog. Part. Nucl. Phys.* **58** 351 (2007).

Towards Precision Determination of uPDFs

Magnus Hansson[1] and Hannes Jung[2]

1- Lund University

2- DESY, FRG

The unintegrated Parton Density Function of the gluon is obtained from a fit to dijet production in DIS as measured at HERA. Reasonable descriptions of the measurements are obtained, and a first attempt to constrain the intrinsic transverse momentum distribution at small $k_\perp$ is presented [1].

1 Introduction

Unintegrated parton density functions (uPDFs) are best suited to study details of the hadronic final state in high energy ep and also in pp collisions (for a review see [2–8]). In general, the production cross section for jets, heavy quarks or gauge bosons can be written as a convolution of the uPDF $\mathcal{A}(x, k_\perp^2, \bar{q})$ with the partonic off-shell cross section $\hat{\sigma}(x_i, k_\perp^2)$, with $x_i, k_\perp$ being the longitudinal momentum fraction and the transverse momentum of the interacting parton i and $\bar{q}$ being the factorization scale. For example the cross section for $ep \to \text{jets} + X$ can be written as:

$$\frac{d\sigma^{jets}}{dE_T d\eta} = \sum_i \int\int\int dx_i \, dQ^2 d\ldots \cdot \left[dk_\perp^2 x_i \mathcal{A}(x_i, k_\perp^2, \bar{q})\right] \hat{\sigma}(x_i, k_\perp^2)$$

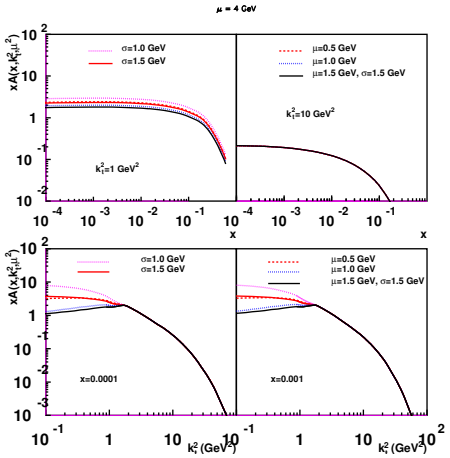

Figure 1: The unintegrated gluon distribution at a scale $\bar{q} = 4$ GeV for different values of μ and σ of the intrinsic $k_\perp$ distribution as a function of x for fixed $k_\perp$(top) and as a function of $k_\perp$ (bottom) for fixed x

At high energies, the gluon density is dominating for many processes, therefore here only the gluon uPDF is considered. It has already been shown in [9], that the predictions of the total cross section as well as differential distributions for heavy quark production at HERA and the LHC agree well in general with those coming from fixed NLO calculations. However, the details depend crucially on a precise knowledge of the uPDF. Therefore precision fits to inclusive and exclusive measurements have to be performed to determine precisely the free parameters of the uPDF: the starting distribution function at a low scale $Q_0 \sim 1$ GeV as well as parameters connected with α_s and details of the splitting functions for the perturbative evolution.

An overview and discussion of uPDFs is given in [4–6]. In a previous paper [10] the uPDF was determined from a pQCD fit using the CCFM evolution equation [11–14] to the

structure function F_2 and F_2^c with acceptable χ^2/ndf. However, the small x behavior of the uPDF obtained from F_2^c was very different compared to the one obtained from F_2.

Here also measurements of high p_t-dijet production in DIS at HERA [15–17] are investigated.

2 The method

The unintegrated gluon density is determined by a convolution of the non-perturbative starting distribution $\mathcal{A}_0(x)$ and the CCFM evolution denoted by $\tilde{\mathcal{A}}(x, k_\perp, \bar{q})$:

$$x\mathcal{A}(x, k_\perp, \bar{q}) \quad = \quad \int dx' \mathcal{A}_0(x', k_\perp) \cdot \frac{x}{x'} \tilde{\mathcal{A}} \left(\frac{x}{x'}, k_\perp, \bar{q} \right)$$

In the perturbative evolution the gluon splitting function P_{gg} including non-singular terms (as described in detail in [18, 19]) is applied.

The distribution $\mathcal{A}_0$ is parameterized at the starting scale Q_0 by:

$$x\mathcal{A}_0(x, k_\perp) \quad = \quad N x^{-B_g} \cdot (1-x)^{C_g} (1 - D_g x) \cdot \exp \left[-\frac{(\mu - k_\perp)^2}{\sigma^2} \right] \qquad (1)$$

The parameters N_g, B_g, C_g, D_g as well as μ, σ of $\mathcal{A}_0$ are free parameters which have to be constrained by measurements. It turns out, that C_g, D_g are not sensitive to the data considered here, and are therefore fixed to $C_g = 4$ and $D_g = 0$. The other parameters are determined by a fit [20] to measurements such to minimize the χ^2 defined by:

$$\chi^2 = \sum_i \left(\frac{(T - D)^2}{\sigma_i^{2\ stat} + \sigma_i^{2\ sys}} \right)$$

with T being the theory value and D the measurement with the corresponding statistical and systematic uncertainty.

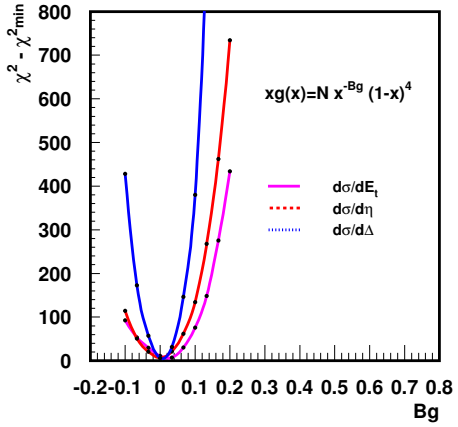

Figure 2: A scan in the parameter space of B_g for $\frac{d^3\sigma}{dQ^2 dx dE_t}$, $\frac{d^3\sigma}{dQ^2 dx d\Delta}$ and $\frac{d^3\sigma}{dQ^2 dx d\Delta\eta}$ as measured in [15].

3 The intrinsic $k_\perp$ distribution

The Gaussian form with $\mu = 0$ and a width of $\sigma \sim 1.0$ GeV of the intrinsic $k_\perp$ distribution in eq.(1) is an assumption to parameterize our ignorance about the small $k_\perp$ behavior. In the saturation model of GBW [21] the uPDF vanishes for small $k_\perp$. Such a behavior can be mimicked by a Gaussian distribution with $\mu \sim Q_0$. The effect of choosing different μ is illustrated in Fig. 1.

4 Dijets in DIS

The sensitivity of the shape in x and the intrinsic $k_\perp$ was studied for dijets in DIS [15] in the kinematic range of $5 < Q^2 < 100$ GeV^2, $10^{-4} < x < 10^{-2}$, $0.1 < y < 0.7$ and two jets with at least $E_t > 5$ GeV in the range $-1 < \eta < 2.5$. The differential cross sections $\frac{d\sigma}{dE_t}$, $\frac{d\sigma}{d\Delta\eta}$, with $\Delta\eta$ being the rapidity difference between the highest E_t jets are mainly sensitive to the x dependence of the uPDF. The same is observed for the cross section $\frac{d\sigma}{d\Delta}$ with $E_t > E_{t\,min} + \Delta$ and $E_{t\,min} = 5$ GeV. A scan over the parameter space of Bg is shown in Fig 2. With this choice of parameters the cross sections are well described, giving a reasonable χ^2/ndf. In Tab. 1 the χ^2/ndf are given for different values of Bg and the mean μ of the intrinsic $k_\perp$ distribution.

		χ^2/ndf		
Bg	μ [GeV]	$\frac{d\sigma}{dE_t}$	$\frac{d\sigma}{d\Delta\eta}$	$\frac{d\sigma}{d\Delta}$
0.025	1.5	68/37=1.8	102/35=2.3	267/89=3.0
0.25	1.5	95/37=2.5	113/35=2.5	306/89=3.4
0.025	0	63/37=1.7	93/35=2.1	284/89=3.2
0.25	0	99/37=2.7	123/35=2.7	345/89=3.9

Table 1: Quality of the description of the different differential cross sections using $Bg = 0.025$ and $Bg = 0.25$ together with $\sigma = 1.5$ GeV.

From Tab. 1 it is seen, that a value of $Bg = 0.025$ is preferred, and that the sensitivity of these measurements to the intrinsic $k_\perp$ distribution is very small.

However, the cross section as a function of $\Delta\phi$, where $\Delta\phi$ is the difference in azimuthal angle between the two leading jets in the hadronic center-of-mass frame, is directly sensitive to the transverse momentum of the incoming parton, and thus a crucial test of the uPDF.

In Fig. 3 we show a comparison of the measurement of [17] with the prediction of CASCADE using the uPDF determined before. A reasonable description of the measurement is achieved. Table 2 shows the χ^2/ndf obtained for these data and also to the azimuthal correlations from [16]. It is interesting to observe, that $\frac{d\sigma}{d\Delta\phi}$ gives also access to Bg, now with a preference to a much steeper initial gluon distribution. The measurement prefers a distribution which decreases for very small transverse momenta $k_\perp$. However it should be noted, that the form of the intrinsic $k_\perp$ distribution is not constrained.

		χ^2/ndf	
Bg	μ [GeV]	$\frac{d\sigma}{dQ^2 d\Delta\phi}$ (H1 prel)	$\frac{d\sigma}{d\Delta\phi}$ (dijets ZEUS)
0.025	1.5	163/29=5.6	332/19=17.5
0.25	1.5	128/29=4.4	234/19=12.3
0.025	0	200/29=6.9	417/19=22.0
0.25	0	237/29=8.2	338/19=17.8

Table 2: Quality of the description of $\frac{d\sigma}{d\Delta\phi}$ using $Bg = 0.025$ and $Bg = 0.25$ together with $\sigma = 1.5$ GeV by H1 [16] and ZEUS [17].

5 Conclusion

The shape of the starting gluon distribution in x and $k_\perp$ has been investigated with dijet events in DIS. Whereas the cross sections as a function of E_t prefer a soft gluon distribution ($Bg \sim 0.025$) and show little sensitivity to the intrinsic $k_\perp$ distribution, the cross sections as a function of $\Delta\phi$ prefer a much steeper gluon ($Bg \sim 0.25$) and show a clear preference to a intrinsic $k_\perp$ distribution which decreases for small $k_\perp$. The different x-slope of the initial gluon distribution, as already observed in fits to F_2 and F_2^c, is also observed in di-jet cross section measurement. Further investigations are obviously needed.

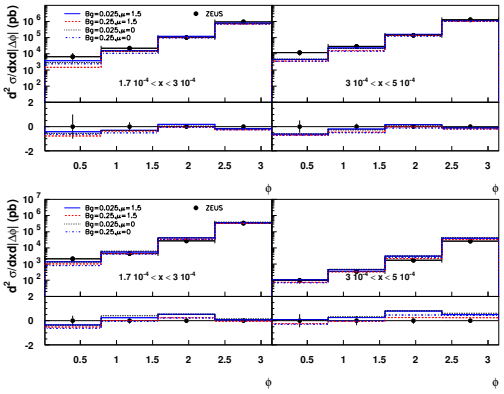

Figure 3: The cross section $\frac{d\sigma}{d\Delta\phi}$ as measured by [17] compared to predictions using CASCADE and the uPDF as in Tab. 2. The lower plots always show the ratio $R = \frac{theory-data}{data}$.

Acknowledgments

Many thanks go to the the organizers of this very interesting workshop.

References

[1] Slides:
`http://indico.cern.ch/contributionDisplay.py?contribId=54&sessionId=6&confId=9499`
[2] H. Jung, *Phys. Rev.* **D 65**, 034015 (2002). [hep-ph/0110034]
[3] H. Jung, *Mod. Phys. Lett.* **A19**, 1 (2004). [hep-ph/0311249]
[4] Small X Collaboration; B. Andersson *et al.*, *Eur. Phys. J.* **C 25**, 77 (2002). [hep-ph/0204115]
[5] Small X Collaboration, J. R. Andersen *et al.*, *Eur. Phys. J.* **C35**, 67 (2004). [hep-ph/0312333]
[6] Small X Collaboration, J. R. Andersen *et al.* (2006). [hep-ph/0604189]
[7] H. Jung. DIS 2004, Strbské Pleso, Slovakia, [hep-ph/0411287]
[8] J. Collins and H. Jung, *Need for fully unintegrated parton densities*, 2005. [hep-ph/0508280]
[9] S. Alekhin *et al.*, *Hera and the LHC - a workshop on the implications of HERA for LHC physics: Proceedings Part A and B*, 2005. [hep-ph/0601012,hep-ph/0601013], J. Baines *et al.* (2006). [hep-ph/0601164]
[10] H. Jung, A. V. Kotikov, A. V. Lipatov and N. P. Zotov, [hep-ph/0611093].
[11] M. Ciafaloni, *Nucl. Phys.* **B 296**, 49 (1988)
[12] S. Catani, F. Fiorani, and G. Marchesini, *Phys. Lett.* **B 234**, 339 (1990)
[13] S. Catani, F. Fiorani, and G. Marchesini, *Nucl. Phys.* **B 336**, 18 (1990)
[14] G. Marchesini, *Nucl. Phys.* **B 445**, 49 (1995)
[15] A. Aktas *et al.* [H1 Collaboration], Eur. Phys. J. C **33** (2004) 477 [hep-ex/0310019].
[16] M. Hansson [H1 Collaboration], "Decorrelation Of Dijets At Low X And Q**2," *Prepared for 14th International Workshop on Deep Inelastic Scattering (DIS 2006), Tsukuba, Japan, 20-24 Apr 2006*
[17] S. Chekanov *et al.* [ZEUS Collaboration], [hep-ex/0705.1931] .
[18] H. Jung, *Acta Phys. Polon.* **B33**, 2995 (2002). [hep-ph/0207239]
[19] M. Hansson and H. Jung. DIS 2003, St. Petersburg, Russia, [hep-ph/0309009]
[20] F. James and M. Roos, *Comput. Phys. Commun.* **10**, 343 (1975)
[21] K. Golec-Biernat and M. Wusthoff, Phys. Rev. D **60** (1999) 114023 [hep-ph/9903358].

Inclusive Jet Production in DIS at High Q^2 and Extraction of the Strong Coupling

Thomas Kluge *

DESY
Notkestr. 85, 22607 Hamburg - Germany

Inclusive jet production is studied in neutral current deep-inelastic positron-proton scattering at large four momentum transfer squared $Q^2 > 150\,\mathrm{GeV}^2$ with the H1 detector at HERA. The measurements are found to be well described by calculations at next-to-leading order in perturbative QCD. The running of the strong coupling is demonstrated and the value of $\alpha_s(M_Z)$ is determined.

1 Introduction and Experimental Method

Jet production in neutral current (NC) deep-inelastic scattering (DIS) at HERA provides an important testing ground for Quantum Chromodynamics (QCD). The Born contribution in DIS gives only indirect information on the strong coupling α_s via scaling violations of the proton structure functions. At leading order (LO) in α_s additional processes contribute: QCD-Compton and boson-gluon fusion.

In the Breit frame of reference [2], where the virtual boson and the proton collide head on, the Born contribution generates no transverse momenta. Partons with transverse momenta are produced in lowest order by the QCD-Compton and boson-gluon fusion processes. Jet production in the Breit frame therefore provides direct sensitivity to α_s and allows for a precision test of QCD.

In this workshop contribution new measurements of the inclusive jet cross section are presented, based on data corresponding to twice the integrated luminosity and a higher centre-of-mass energy than in the previous H1 analysis [3]. The larger data set together with improved understanding of the hadronic energy measurement significantly reduces the total uncertainty of the results. The data were collected with the H1 detector at HERA in the years 1999 and 2000. During this period HERA collided positrons of energy $E_e = 27.5\,\mathrm{GeV}$ with protons of energy $E_p = 920\,\mathrm{GeV}$ giving a centre-of-mass energy $\sqrt{s} = 319\,\mathrm{GeV}$. The data sample used in this analysis corresponds to an integrated luminosity of $65.4\,\mathrm{pb}^{-1}$.

The DIS phase space covered by this analysis is defined by $150 < Q^2 < 15000\ \mathrm{GeV}^2$, $0.2 < y < 0.7$, where y quantifies the inelasticity of the interaction. These two variables are reconstructed from the four momenta of the scattered positron and the hadronic final state particles using the electron-sigma method [4].

The jet analysis is performed in the Breit frame. The boost from the laboratory system to the Breit frame is determined by Q^2, y and the azimuthal angle of the scattered positron. Particles of the hadronic final state are clustered into jets using the inclusive k_T algorithm [5] with the p_T recombination scheme and with distance parameter $R = 1$ in the η-ϕ plane. The inclusive k_T algorithm is infrared safe and results in small hadronisation corrections [3]. Every jet with $7 < E_T < 50\,\mathrm{GeV}$ contributes to the inclusive jet cross section, regardless of the jet multiplicity in the event. In addition, the normalised inclusive jet cross section is investigated, calculated as the ratio of the number of jets to the number of selected NC

*on behalf of the H1 Collaboration

DIS events in the y range defined above. This observable equals the average jet multiplicity of NC DIS events within the given phase space. Jet cross sections and normalised jet cross sections are studied as a function of Q^2 and E_T.

The following sources of systematic uncertainty are considered: positron energy uncertainty (0.7% to 3% depending on the z-impact point of the positron in the calorimeter), positron polar angle systematic uncertainty (1 and 3 mrad), energy scale uncertainty of the reconstructed hadronic final state (2%), luminosity measurement uncertainty (1.5%). The model dependence of the data correction is below 10% in most of the bins and typically 2%. An error of 1% is estimated from QED radiative correction uncertainty. The dominant experimental uncertainties on the jet cross section arise from the model dependence of the data correction and from the LAr hadronic energy scale uncertainty. The individual contributions are added in quadrature to obtain the total systematic uncertainty. The correlations of the errors among the different bins are taken into account. For the normalised jet cross sections systematic uncertainties are reduced and the luminosity uncertainty cancels.

The theoretical prediction for the jet cross section is obtained using the NLOJET++ program [6], which performs the matrix element integration at NLO of the strong coupling, $\mathcal{O}(\alpha_s^2)$. The strong coupling is taken as $\alpha_s(M_Z) = 0.118$ and is evolved as a function of the renormalisation scale at two loop precision. The calculations are performed in the $\overline{\text{MS}}$ scheme for five massless quark flavours. The parton density functions (PDFs) of the proton are taken from the CTEQ6.5M set [7]. The factorisation scale μ_f is chosen to be Q and the renormalisation scale μ_r is chosen to be the E_T of each jet. Running of the electromagnetic coupling with Q^2 is taken into account. In order to calculate the normalised inclusive jet cross sections, the prediction of the inclusive jet cross section is divided by the prediction of the NC DIS cross section. The latter is calculated at NLO, $\mathcal{O}(\alpha_s)$, with the DISENT package [8], and the renormalisation and factorisation scales set to Q. The strong coupling is determined by repeating the perturbative calculations for many values of $\alpha_s(M_Z)$ until the best match of data and theory is found. With NLOJET++ and DISENT these calculations are prohibitively time consuming. A considerable gain in computational speed is provided by the fastNLO package [9]. All theory calculations shown in the following are obtained using fastNLO.

2 Results

The measured cross sections, corrected for detector and radiative QED effects, are presented as double differential distributions in figure 1. The data points are shown at the average value of the Q^2 or E_T in each bin. The results are compared to the perturbative QCD predictions in NLO with $\alpha_s(M_Z) = 0.118$, taking into account hadronisation effects and Z^0-exchange. The inclusive jet cross section is shown in figure 1 (left) as a function of E_T in six Q^2 bins in the range $150 < Q^2 < 15000\,\text{GeV}^2$. The data are well described by the theory over the full E_T and Q^2 ranges, with $\chi^2/\text{ndf} = 16.7/24$, taking only experimental errors into account.

For NC DIS events in the range $0.2 < y < 0.7$ and in a given Q^2 bin the normalised inclusive jet cross section is defined as the average number of jets within $-1.0 < \eta^{\text{Lab}} < 2.5$ per event. Figure 1 (right) shows the normalised inclusive jet cross section as a function of E_T in six Q^2 bins. The NLO calculation gives a good description of the data in the full E_T and Q^2 range. Compared with the inclusive jet cross section, the normalised inclusive jet cross section exhibits a smaller experimental uncertainty.

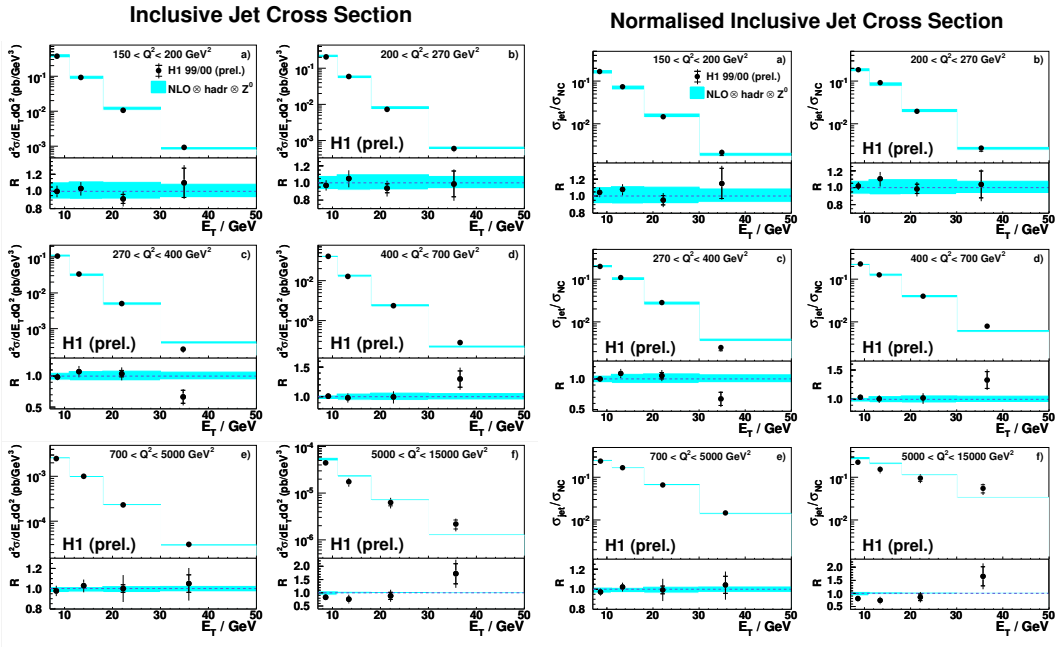

Figure 1: The double differential cross section as a function of E_T for six regions of Q^2. The data, presented with statistical errors (inner bars) and total errors (outer bars), are compared with the results of NLOJET++, corrected for hadronisation and Z^0 boson exchange.

A fit of $\alpha_s(M_Z)$ to all of the 24 measurements of the double differential inclusive jet cross sections is made, which yields $\alpha_s(M_Z) = 0.1179 \pm 0.0024\,(\text{exp.})\,^{+0.0052}_{-0.0032}\,(\text{th.}) \pm 0.0028\,(\text{pdf})$, with a fit quality: $\chi^2/\text{ndf} = 20.2/23$. To study the scale dependence of α_s, the six data points at a given E_T are used together, and four values of $\alpha_s(E_T)$ are extracted. The results are shown in figure 2a, where the running of the strong coupling is also clearly observed. In figure 2b the results using an alternative scale Q instead of E_T are shown, the four data points at a given Q^2 are used together, and six values of $\alpha_s(Q)$ are extracted. These results are larger but compatible with the values obtained at the scale E_T.

The strong coupling is also fitted to the normalised inclusive jet cross section. All 24 measurements are used in a common fit, which yields

$$\alpha_s(M_Z) = 0.1193 \pm 0.0014\,(\text{exp.})\,^{+0.0047}_{-0.0030}\,(\text{th.}) \pm 0.0016\,(\text{pdf}),$$

with a fit quality of $\chi^2/\text{ndf} = 28.7/23$. This result is compatible within errors with the value from the inclusive jet cross sections. The normalisation gives rise to cancellations of systematic effects, which lead to improved experimental and PDF uncertainties. This determination of $\alpha_s(M_Z)$ is consistent with the world average $\alpha_s(M_Z) = 0.1176 \pm 0.0020$ [10] and with the previous H1 determination from inclusive jet production measurements [3]. The dominating theory error can be reduced at the expense of a larger experimental uncertainty by restricting the phase space of the fit interval to higher values of Q^2. The smallest total uncertainty is obtained by a combined fit of the normalised inclusive jet cross section for

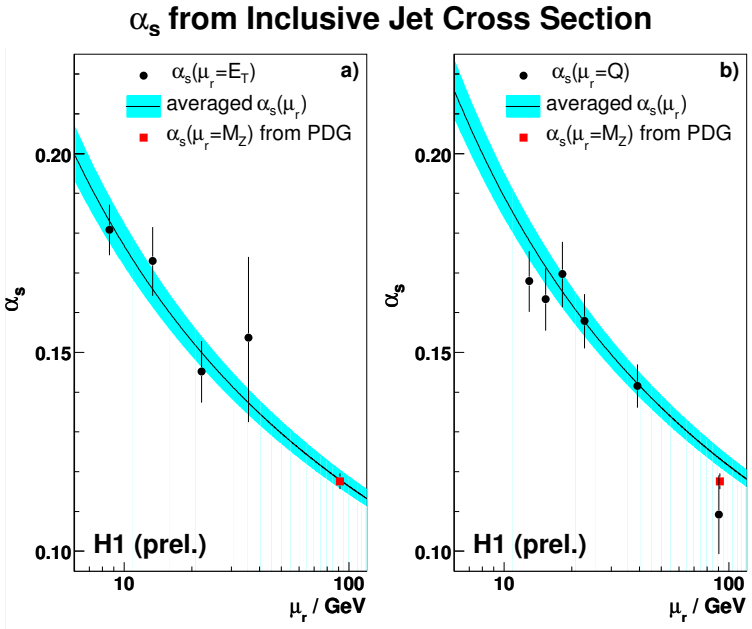

Figure 2: Results for the fitted values of a) $\alpha_s(\mu_r = E_T)$ averaged over all Q^2 regions, and b) $\alpha_s(\mu_r = Q)$ averaged over all E_T regions. The error bars denote the total experimental uncertainty for each data point. The solid curve shows the result of evolving $\alpha_s(M_Z)$ averaged from all Q^2 and E_T regions, with the band denoting the total experimental uncertainty.

$700 < Q^2 < 5000\,\mathrm{GeV}^2$: $\alpha_s(M_Z) = 0.1171 \pm 0.0023\,(\mathrm{exp.})\,^{+0.0032}_{-0.0010}\,(\mathrm{th.})\,\pm 0.0010\,(\mathrm{pdf})$, with a fit quality of $\chi^2/\mathrm{ndf} = 1.2/3$. This result shows a level of experimental precision competitive with α_s determinations from other recent jet production measurements at HERA [11] and those from e^+e^- data [12] and is in good agreement with the world average.

References

[1] Slides:
`http://indico.cern.ch/contributionDisplay.py?contribId=214&sessionId=6&confId=9499`

[2] R. P. Feynman, "Photon-Hadron Interactions", Benjamin, New York (1972).

[3] C. Adloff *et al.*, Eur. Phys. J. C **19** 289 (2001).

[4] U. Bassler and G. Bernardi, Nucl. Instrum. Meth. A **361** 197 (1995).

[5] S. D. Ellis and D. E. Soper, Phys. Rev. D **48** 3160 (1993).

[6] Z. Nagy and Z. Trocsanyi, Phys. Rev. Lett. **87** 082001 (2001).

[7] W. K. Tung *et al.*, JHEP **0702** 053 (2007).

[8] S. Catani and M. H. Seymour, Nucl. Phys. B **485** 291 (1997) [Erratum-ibid. B **510** 504 (1998)].

[9] T. Kluge, K. Rabbertz and M. Wobisch, arXiv:hep-ph/0609285 (2006).

[10] W. M. Yao *et al.*, J. Phys. G **33** 1 (2006).

[11] S. Chekanov *et al.*, Submitted to Phys. Lett. B, arXiv:hep-ex/0701039 (2007).

[12] G. Abbiendi *et al.*, Eur. Phys. J. C **47** 295 (2006).

Inclusive Jet Production in Deep-Inelastic Scattering at Low and Medium Q^2 at HERA

Artem Baghdasaryan

Yerevan Physics Institute
Alikhanyan Brothers St.2, Yerevan 375036 - Armenia

On behalf of the H1 Collaboration

Inclusive jet production is studied in deep-inelastic positron-proton scattering over a range of four momentum transfer squared $5 < Q^2 < 100$ GeV^2. The data were taken with the H1 detector at HERA in the years 1999-2000 and correspond to an integrated luminosity of 43.5 pb^{-1}. Jets are defined in the Breit frame using the inclusive k_T algorithm. Inclusive jet cross sections are measured differentially in Q^2 and E_T of the jets. Data are compared to the predictions of perturbative QCD calculations in next-to-leading order of the strong coupling α_s.

1 Introduction

Measurements of inclusive multijet cross-sections in the Breit frame at low Q^2 values ($5 < Q^2 < 100$ GeV^2) are presented. Jets are identified using the inclusive k_t algorithm applied in the Breit frame. Compared to previous H1 publications [2, 3], this measurement contains twice the statistics and has reduced systematic errors. In addition the total center of mass energy $\sqrt{s}$ is slighly higher in the new data (320 GeV compared to 300 GeV) due to higher proton beam energy. The measurements of inclusive jet production are presented in both single differential cross sections as a function of Q^2 and E_T, respectively, and in double differential cross sections in these variables.

2 Event kinematics and selection

The kinematic range of this analysis is defined by $5 < Q^2 < 100$ GeV^2 and $0.2 < y < 0.7$. The kinematic variables x, Q^2 and y are determined using the information from the scattered electron and the hadronic final state. Jets are defined using the inclusive k_t cluster algorithm in the Breit frame in which the virtual photon and the parton collide head on. In this frame the transverse energies of jets are closely related to the transverse energies of the partons emerging from the hard scattering. Jets are selected by requirung the transverse energy to be larger than 5 GeV in that frame. To ensure that jets are fully contained in the calorimeter, the pseudorapidity of jets in the laboratory frame is required to be $-1 < \eta^{Lab} < 2.5$.

The analysis use the data sample collected in positron-proton interactions during 1999-2000. The total integrated luminosity of the data sample is 43.5 pb^{-1}.

3 Monte Carlo models and correction procedure

For the the calculation of correction factors due to detector effects and the influence of initial state radiation and hadronization the RAPGAP 3.1 and DJANGOh 1.4 Monte Carlo generators are used.

The data distributions are corrected for effects of limited detector acceptance and resolution and for higher order QED effects using bin-to-bin corrections. The bin sizes were chosen as to ensure sufficient statistics and sufficiently high stability and purity in each bin. The corrections for each distribution are defined as the ratio of cross section at hadron level using the Monte Carlo sample which is generated without QED corrections to that at detector level with QED corrections included. The correction factor is taken as the average of the values obtained with DJANGOh and RAPGAP, respectively.

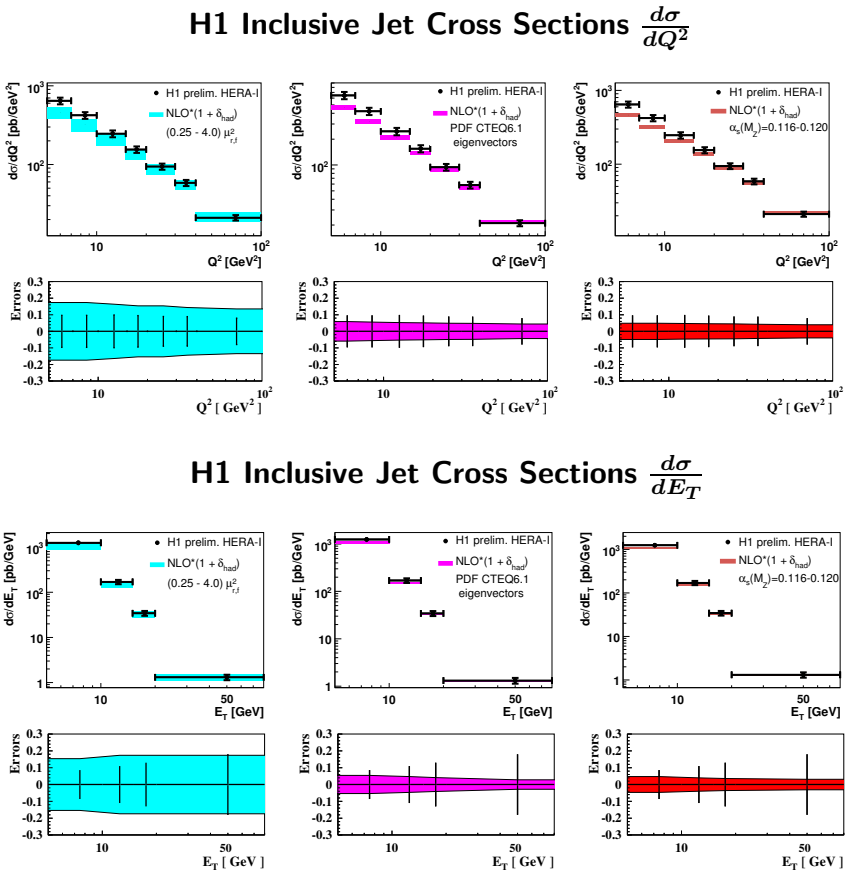

Figure 1: The inclusive cross sections vs Q^2 and E_T of the jets compared with NLO pQCD predictions, corrected for hadronization. The cross sections are shown separately for 3 different sources of theory uncertainties: the uncertainty arising from the scales (obtained by varying the renormalization and factorization scales by a factor 2 up and down), from α_s variation (varying α_s between 0.116 and 0.120) and from the proton PDFs (using 40 eigenvectors of the CTEQ6.1M proton PDF parameterization). The plots also show the relative sizes of experimental and theoretical uncertainties.

The data is compared with the NLO pQCD predictions obtained with the NLOJET++ [5] program. The parton level predictions are corrected for hadronisation effects using the Monte Carlo samples. The hadronisation correction factors are calculated as the ratios of cross sec-

tions on the parton level to that on the hadron level. The average of the corrections obtained from the two Monte Carlo programs is taken as the correction factors.

4 Results

The measured cross-sections are compared with NLO pQCD predictions obtained with the NLOJET++ [5] program. The calculations are performed in the $\overline{\text{MS}}$ scheme for five massive quark flavours, and the parton PDF of the proton taken from the CTEQ6.1M set [4]. Q^2 is used as factorization scale (μ_F), whereas the renormalization scale (μ_R) is chosen to be the E_T of the jets.

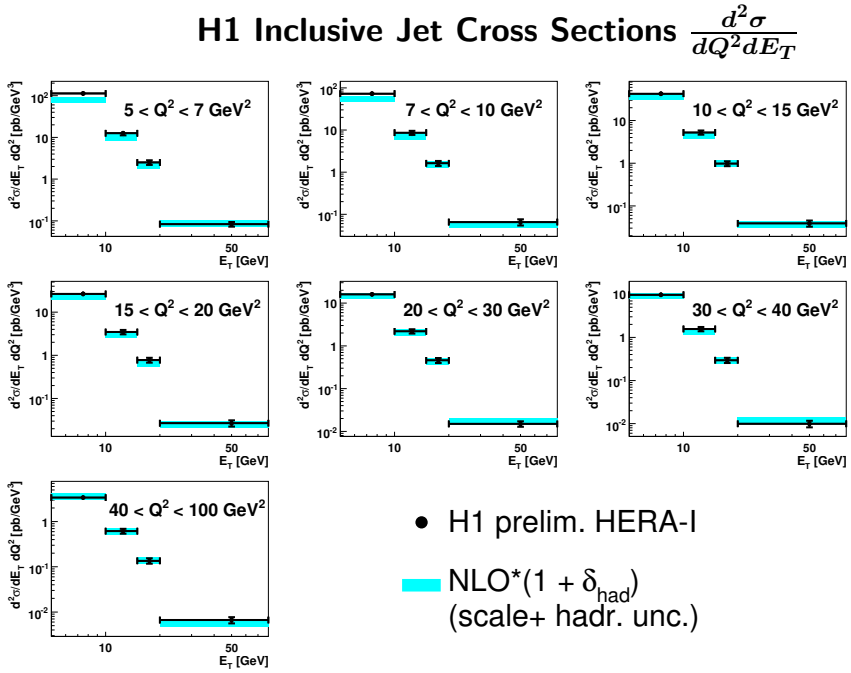

Figure 2: The inclusive double differential jet jet cross sections compared with NLO predictions corrected for hadronization. The error bands reflect the uncertainties in the NLO predictions arising from the variation of the renormalization and factorization scales by a factor 2 up and down and from the hadronization.

Figure 1 shows the inclusive cross sections as a function of Q^2 and E_T of the jets. They are compared with the NLO pQCD predictions, corrected for hadronization. The cross sections are shown separately for three different sources of theoretical uncertainties in the NLO predictions: the uncertainty arising from the scales (obtained by varying renormalization and factorization scales by a factor 2 up and down), from α_s variation (varying α_s between 0.116 and 0.120) and from the proton PDFs (using 40 eigenvectors of the CTEQ6.1M proton PDF parameterization). The scale uncertainty represents the largest theoretical uncertinty. The figure also compares the experimental and theoretical uncertainties. With the present data, a stringent test of QCD and a precise determination of the strong coupling α_s are

possible.

The double differential cross sections as a function of Q^2 and E_T of the jet are shown in Figure 2. The error band on the NLO predictions reflect the variation of the scales μ by a factor of 2 up and down using the NLOJET++. The NLO pQCD calculations corrected for hadronization provide quite reasonable description of the inclusive jet cross sections for relatively high $Q^2 \gtrsim 10\ GeV^2$ and $E_T > 10\ GeV$. At lower Q^2, the comparison indicates the need for higher order QCD corrections.

5 Summary

New measurements of the inclusive jet cross-sections at Q^2 between 5 and 100 GeV^2 performed with the H1 detector are presented. Jets are selected using the inclusive k_T algorithm in the Breit frame and are required to have a minimum transverse energy of 5 GeV. QCD calculations up to second order in the strong coupling constant α_s are compared with the data. The NLO pQCD calculations corrected for hadronization provide quite a reasonable description of the inclusive jet cross sections for relatively high $Q^2 \gtrsim 10\ GeV^2$ and E_T of the jet above 10 GeV. This constitutes a test of the perturbative QCD and opens the way to a precise determination of the strong coupling.

References

[1] Slides:
`http://indico.cern.ch/contributionDisplay.py?contribId=217&sessionId=6&confId=9499`

[2] C. Adloff *et al.* [H1 Collaboration], *Eur. Phys. J.* **C 19**, 289 (2001), [hep-ex/0010054].

[3] C. Adloff *et al.* [H1 Collaboration], *Phys. Lett.* **B 542**, 19 (2002), [hep-ex/0206029].

[4] D. Stump *et al.*, JHEP 0310:046,2003.

[5] Z. Nagy, Z. Trocsanyi, *Phys. Rev. Lett.* **87**, 082001 (2001), [hep-ph/0104315].

Jet Cross-Sections and α_S in DIS at HERA

Thomas Schörner-Sadenius *

Hamburg University - IExpPh
Luruper Chaussee 149, D-22761 Hamburg - Germany

Measurements of inclusive-jet and dijet cross-sections in high-Q^2 deep-inelastic scattering are presented together with a short overview of extractions of the strong coupling parameter α_S from jets. The data samples used were collected with the ZEUS detector at HERA-1 and HERA-2. The measured distributions are compared to QCD calculations in next-to-leading order which describe the data very well. The various determinations of α_S give a consistent picture, have competitive uncertainties and clearly demonstrate the running of the coupling predicted by QCD.

1 Introduction

Measurements of jet cross-sections in high-Q^2 deep-inelastic scattering (DIS) have traditionally been used to test the concepts of perturbative QCD (power expansion, factorisation, PDF universality). In addition, jet measurements in DIS allow precise determinations of the strong coupling α_S and are a valuable input to global fits of the PDFs (see for example [2]).

In this article measurements of jet cross-sections in high-Q^2 DIS are reported which are new in two respects: First, the first neutral-current (NC) jet measurement in a combined HERA-1+HERA-2 data sample from the ZEUS experiment is presented, showing single- and double-differential dijet cross-sections. A similar measurement of such dijet cross-sections in HERA-1 data has recently been published by the ZEUS collaboration [3]. Second, HERA-1 data have been used to measure inclusive jet cross-sections with different values of the R parameter in the inclusive k_T jet clustering algorithm [4]. This parameter defines the distance up to which two particles may be joined into a new pseudo-particle in the process of jet clustering. An investigation of the R-dependence of jet cross-sections may prove helpful for heavy flavour physics, for hadronisation studies or for physics studies at the LHC. The inclusive-jet data have in addition been used for a new determination of α_S. For this reason, this article also gives a short overview of α_S measurements from jets at ZEUS.

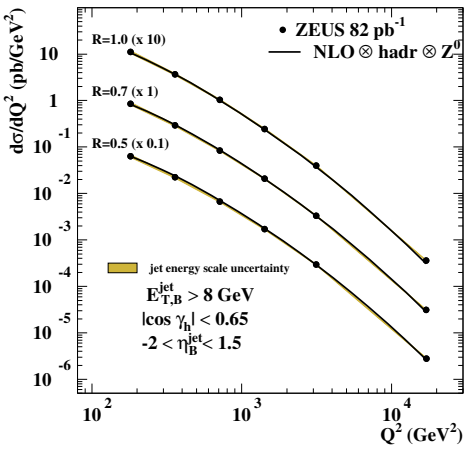

Figure 1: ZEUS inclusive-jet cross-sections $\mathrm{d}\sigma/\mathrm{d}Q^2$ for various values of R.

*On behalf of the ZEUS collaboration.

2 Data samples and selections

The inclusive-jet analysis reported on was carried out in 82 pb^{-1} of data from the years 1998-2000; the dijet analysis used in addition about 127 pb^{-1} from the electron running period in 2004/05. Together with a ZEUS jet measurement in charged-current events [5], this dijet measurement is the first jet measurement in HERA-2 data.

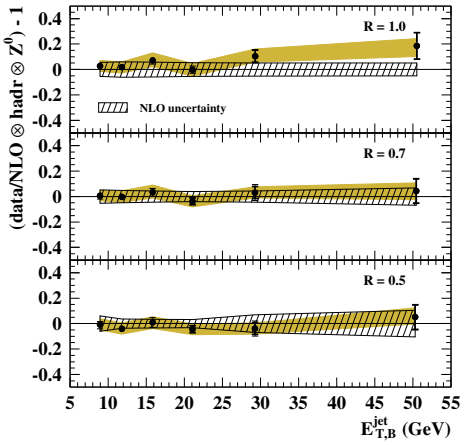

Figure 2: Ratio of data over NLO QCD for the inclusive-jet cross-sections $\mathrm{d}\sigma/\mathrm{d}E_T^{Breit}$ for various values of R.

The event selections of both the inclusive-jet and dijet measurements follow closely that described in [3] and require high values of $Q^2 > 125$ GeV^2 to ensure relatively small theoretical uncertainties. Furthermore, the requirement -0.65 $< \cos\gamma_{had} <$ 0.65 was imposed, where in lowest-order (Quark-Parton-Model) events γ_{had} corresponds to the scattering angle of the struck parton. The cut on γ_{had} helps to select phase-space regions with good acceptance and to ensure a good reconstruction of jets in the Breit reference frame.

Jets were reconstructed in the Breit frame using the longitudinally invariant k_T clustering algorithm in the inclusive mode; the Breit-frame pseudorapidities of the jets, η^{Breit}, were restricted to -2 $< \eta^{Breit} <$ 1.5, and the Breit-frame transverse energies of the jets, E_T^{Breit}, were restricted to $E_T^{Breit} > 8$ GeV. For the dijet analysis the hardest jet was in addition required to satisfy $E_T^{Breit} > 12$ GeV.

All data distributions were corrected for detector and QED radiation effects using leading-order (LO) Monte Carlo (MC) programs in a bin-to-bin fashion. The data were then compared to next-to-leading order (NLO) QCD calculations that employed either the latest PDF sets from the CTEQ group or the ZEUS-S PDFs. The NLO predictions were corrected for hadronisation effects, and in case of the inclusive-jet measurement, for Z^0 contributions.

3 Experimental and theoretical uncertainties

The experimental uncertainties are dominated by the uncertainty in the jet energy scale which is assumed to be 1-3 %, depending on the jet E_T. Resulting uncertainties on the measured cross-sections are typically 5-10 %. The next-largest uncertainty stems from the model uncertainty in the unfolding of the measured distributions to the hadron level; further sources of uncertainty like the effects of selection cut variations are typically much smaller.

On the theoretical side, the effect of higher orders not considered in the perturbative expansion and the uncertainties on the input PDFs give the largest contributions. The former is typically estimated by variations of the renormalization scale μ_R by an arbitrary, but customary amount; the effects on the cross-sections are typically in the order of 5-10 % for the inclusive jet measurements and slightly larger for the dijet measurements. The effect of the PDFs is somewhat smaller, depending on the region of phase-space considered. The

effects of the uncertainties on α_S, on the hadronization corrections and on the factorization scale are much smaller. It should be noted that in almost all experimental bins the theoretical uncertainty is significantly larger than the experimental one.

4 Inclusive-jet cross-sections

Inclusive-jet cross-sections at high Q^2 were measured as functions of the jet transverse energy in the Breit frame, E_T^{Breit} and of Q^2 for three different values of R: 0.5, 0.7, 1.0 (it turns out that for higher (lower) values of R the uncertainties due to missing higher orders (hadronisation effects) become drastically larger).

The resulting cross-section as a function of Q^2 is shown in Figure 1. The data (points) are compared to the NLO QCD prediction (lines); the description of the data by theory is good. Figure 2 shows the ratio between the measured cross-sections as functions of jet transverse energy E_T and the NLO calculations. The measurement can be seen to be dominated by the (correlated) jet energy-scale and theoretical errors (grey and hashed areas, respectively), except for the highest-E_T (and also highest-Q^2) points for which the statistical uncertainties are large (10 %). Within all errors, the data are well described by the theoretical predictions. The data have also been plotted as a function of the jet radius parameter R, integrated over all E_T and Q^2 values (not shown). A more or less linear increase of the cross-section with R can be observed, which is to be expected since with larger radii the jet algorithm picks up more and more of the jet's energy.

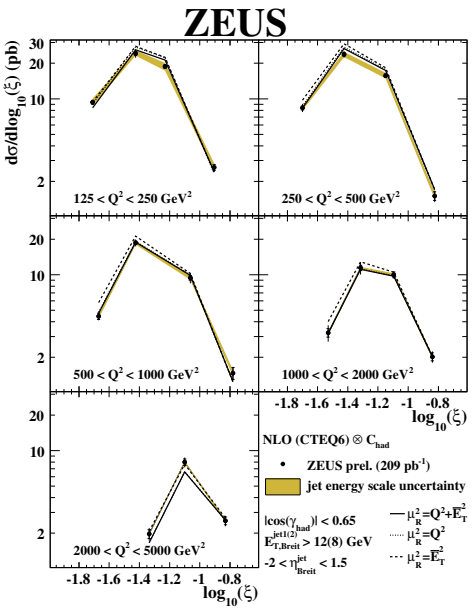

Figure 3: ZEUS dijet cross-sections $\mathrm{d}\sigma/\mathrm{dlog}\,\xi$ in different regions of Q^2.

5 Dijet cross-sections

Figure 3 shows the dijet cross-section for jets above 12 and 8 GeV, respectively, as a function of $\log_{10}\xi$ in different regions of Q^2. In leading order, the observable ξ corresponds to the momentum fraction carried away from the incoming proton by the struck parton. These cross-sections therefore depend on the two variables relevant for the PDFs, the energy scale and the momentum fraction, and thus might be useful for an improvement of the PDF precision.

The data are again compared to NLO QCD predictions, using various squared renormalization scales, namely $\mu_R^2 = Q^2 + \overline{E_T}^2$, $\mu_R^2 = Q^2$ and $\mu_R^2 = \overline{E_T}^2$. The shaded band indicates again the jet energy-scale uncertainty that is assumed to be correlated from bin to bin. Taking into account all uncertainties, the data are well described by the NLO predictions.

However, it should be noted that in different regions of phase-space different scale choices are required to achieve this good agreement: The low-Q^2 data points are better desribed using the squared scale $\mu_R^2 = Q^2 + \overline{E_T}^2$, whereas at high Q^2 $\mu_R^2 = \overline{E_T}^2$ seems more appropriate.

6 Determining α_S with jets at ZEUS

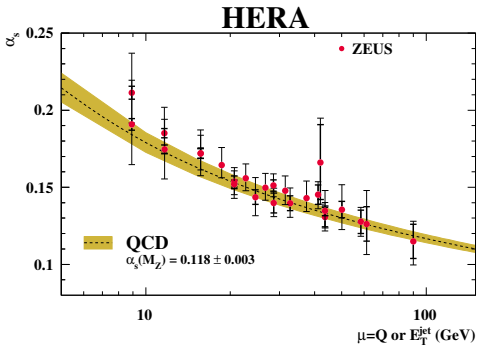

Figure 4: Comparison of various ZEUS α_S measurements from jets in DIS with the QCD prediction

The strong coupling parameter α_S has been determined from a variety of QCD measurements at ZEUS, the latest result coming from the inclusive-jet measurements described above [4]: $\alpha_S = 0.1207 \pm 0.0014(stat.) \pm^{0.0035}_{0.0033}(exp.) \pm^{0.0022}_{0.0023}(th.)$ The various measurements at different energy scales are well described by the behaviour of the coupling as expected from QCD, see Fig. 4. A combination of ZEUS and H1 α_S measurements has been carried out recently [6] and has led to a value of $\alpha_S = 0.1186 \pm 0.0011(exp.) \pm 0.0050(th.)$. The good agreement of the various measurements with each other and with the world average value indicates the high level of our present understanding of QCD. Nevertheless, it should be pointed out that the α_S measurements from jets in DIS suffer from large theoretical uncertainties which are mostly due to missing higher orders in the perturbative expansion of the presently available QCD predictions.

7 Conclusions

With the advent of HERA-2 analyses and the possibility of combined HERA-1/HERA-2 analyses, QCD studies with jets at HERA enter a new regime. In this contribution, measurements of inclusive-jet and dijet cross-sections have been discussed together with extractions of the strong coupling parameter α_S from jet and other DIS measurements. Although many jet measurements are limited by theoretical uncertainties, the impact of further jet measurements on our knowlegde of PDFs and α_S should be assessed and exploited.

References

[1] Slides:
`http://indico.cern.ch/contributionDisplay.py?contribId=218&sessionId=6&confId=9499`

[2] ZEUS Collaboration, Eur. Phys. J. **C42** (2005) 1.

[3] ZEUS Collaboration, Nucl. Phys. **B765** (2007) 1.

[4] ZEUS Collaboration, Phys. Lett. **B649** (2007) 12.

[5] H. Wolfe, these proceedings. Slides:
`http://indico.cern.ch/contributionDisplay.py?contribId=224&sessionId=6&confId=9499`

[6] C. Glasman, arXiv:hep-ex/0506035. See also presentations in this conference's session on α_S.

Mini-Jets in Deep Inelastic Scattering at HERA

S. Osman *

Lund University,
Box 118, SE 221 00, Sweden, E-mail: sakar.osman@hep.lu.se

The production of jets with low P_T, mini-jets, in deep inelastic electron-proton scattering is studied. Mini-jet multiplicities are presented as a function of the P_T of the leading jet in bins of η and Q^2. The analysis is performed for an inclusive jet sample, and for a dijet sample, where the second jet is required to have an azimuthal angle larger than 140 degrees with respect to the leading jet. The dijet sample is split into two samples which are enhanced in direct photon and resolved photon processes, respectively. The results are compared to various QCD based models. Here only the result for the inclusive jet sample will be presented.

1 Introduction

In electron-proton scattering the partonic content of the exchanged virtual photon may be resolved if the P_T of the interacting partons is larger than Q^2 and thereby the photon will behave like a hadronic object. Thus, similar to hadron-hadron scattering there will be a certain probability that collisions between the resolved photon and the proton involve more than one parton interaction, multiple interactions (MI). Previous measurement in photoproduction at HERA [2] have shown that only models with MI give a satisfactory description of the data. This analysis constitutes the first study of possible MI in DIS from measurements of low P_T jets produced in addition to the leading jet(s) of the event. The basic principle of the analysis is to define regions in phase space where contributions from the final state products originating from the primary hard interaction are expected to be small. The concept follows closely the one used by the CDF collaboration at the TEVATRON [3]

2 Analysis Method

The starting point is to define and isolate the leading jet(s) originated from the hard primary interaction and investigate the remaining regions for additional activities, which in this analysis comprise the presence of jets with low transverse momenta, mini-jets. Two different event samples are studied; *inclusive jet events* and *dijet events*, of which the latter constitutes a subsample of the inclusive sample. The analysis procedure is the following:

Inclusive jet sample: The leading jet is identified and reconstructed using the k_t-algorithm [4] in the h.c.m. rest frame. The jet with the highest transverse momentum in the h.c.m. rest frame is taken as the leading jet. The leading jet axis defines the azimuthal angle $\Delta\phi^*$=0 [a]. The region $|\Delta\phi^*| < 60^o$ is defined as the 'toward region', and is expected to contain all particles belonging to the leading jet. The angular region $|\Delta\phi^*| > 140^o$ is called the 'away region'. The transverse regions, $60^o < |\phi^*| < 120^o$ are those where contributions from the primary collision should be small and the effects from additional activities should be most visible. Event by event a 'high activity'- and 'low activity' region are defined, depending on

*On behalf of the H1 Collaboration.
[a]Observables in the h.c.m. frame are labeled with *.

which region contains the most and least transverse momentum, respectively. These four regions are shown. in Figure 2

Dijet sample: The dijet sample includes events having at least two jets, where the two reconstructed jets are required to be almost back-to-back. The leading jet is again defining $\Delta\phi^*$=0, whereas the jet axis of the jet with the second highest transverse momentum, the sub leading jet, is restricted to be inside the 'away region'. This leaves some angular space to accommodate the transverse spread of the jet within the 'away region'.

3 Event Selection

The analysis is based on data taken with the H1 detector in 1999/2000 using colliding positrons and protons at energies of 27.5 GeV and 920 GeV, respectively. The DIS events are selected by requiring a positron in the SPACAL calorimeter with $E_e^{'}$ > 9 GeV , 156° < θ_e < 175° where $E_e^{'}$ and θ_e are the energy and polar angle of the scattered positron, respectively. The photon inelasticity, y, and the virtuality, Q^2, are determined using the electron method and must fulfill $0.1 < y < 0.7$ and $5 < Q^2 < 100$ GeV^2. The invariant mass of the hadronic final state, W, is required to be higher than 200 GeV in order to enhance small x_{bj} contributions and to increase the probability of mini-jet productions.

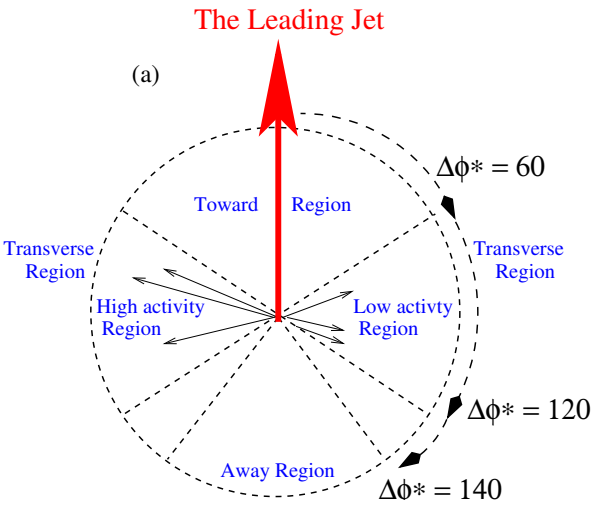

Figure 1: The transverse , toward and away regions.

The inclusive jet sample consists of events that contain at least one jet, whereas the dijet sample includes events with at least two jets. For both samples the jet with the highest transverse momentum is chosen as the leading jet and in the dijet sample the sub leading jet has to fulfill the requirement $|\Delta\phi^*_{ls}| = |\phi^*_{lj} - \phi^*_{sj}| > 140°$, where ϕ^* is the jet azimuthal angle and the labels lj and sj denotes the leading and sub leading jets, respectively. The jets are reconstructed by the inclusive k_t-algorithm [4] in its p_t weighting scheme mode, applied to combined object of tracks and calorimetric clusters in the h.c.m. rest frame. To ensure a good jet reconstruction it is required that the leading and sub leading jets must fulfill -1.7 < η^{lab} < 2.79 and $P_T^{(*)} > 5$ GeV. Here, the pseudo-rapidity is given by $\eta_j = -\ln(\tan(\theta_j/2))$, where θ_j is the polar angle of the jet in the lab frame, and P_T is the transverse energy of the jet. The pt cut are applied both in lab and h.c.m. rest frame.

Mini-jets are reconstructed with the same jet algorithm as the leading jets and within the same η^{lab} region. However, the minimum transverse momentum of a mini-jets is required to be larger than as 3 GeV both in lab and h.c.m rest frame .

Data is corrected for limited detector resolution and acceptance using a bin-by-bin procedure. Correction factors are determined using detector simulated events, generated by

the Monte Carlo programs RAPGAP [5] and DJANGO [6] with ARIADNE [7], where QED radiation has been taken into account.

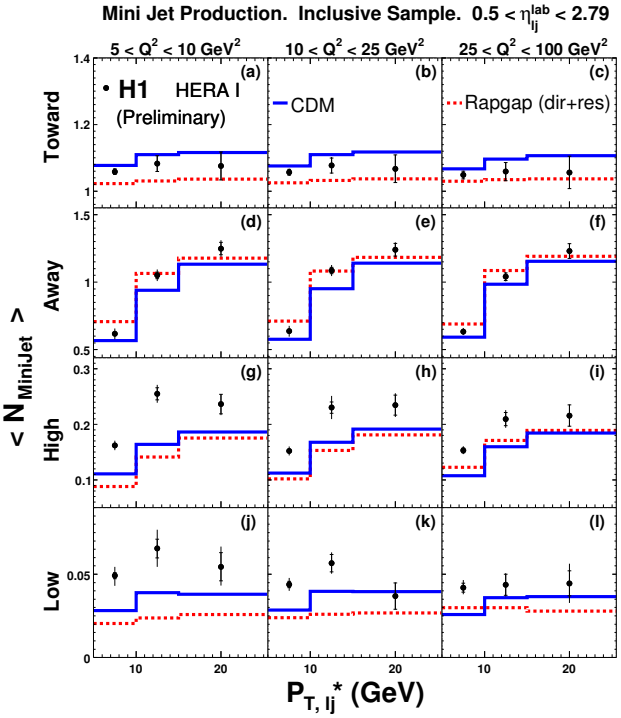

Figure 2: *The average mini-jet multiplicity at the different $\Delta\phi^*$ regions in bins of Q^2 as a function of P_T^* of the leading jet for the inclusive jet sample. The data is compared with the CDM model (solid line) and Rapgap (dashed line).*

4 Results

The average multiplicity of mini-jets, $< N_{minijet} >$, for the inclusive jet sample where the leading jet proceeds in the forward η region are shown in Figures 2 - 3 for three bins of Q^2. The data are presented as a function of P_T^* of the leading jet. Results have also been obtained for leading jets in the central region and for the dijet sample but they are not shown here, but can be found at [1]. The following can be observed:

The toward and away regions: All the different MC models, with or without MI, describe the 'toward region' well in all Q^2 bins , as expected. In the 'away region' there is an overall reasonable agreement for all models, Figures 2 - 3 (a-f).

The high activity region: The predictions of $< N_{minijet} >$ by the MC models including no MI are generally too low in all Q^2-bins, Figure 2 (g-i). PYTHIA+MI [8, 9] describes the data points fairly well in the lowest Q^2-bin and somewhat less well in the higher Q^2-bins, Figures 3 (g-i).

The low activity region: The MC models with no MI included, significantly undershoots the data, Figure 2 (j-l), in all Q^2 bins. These deviations clearly increase with decreasing Q^2-values. PYTHIA+MI gives a much, Figure 3 (j-l), better description of data, although the deviations are still large in the highest Q^2-bin.

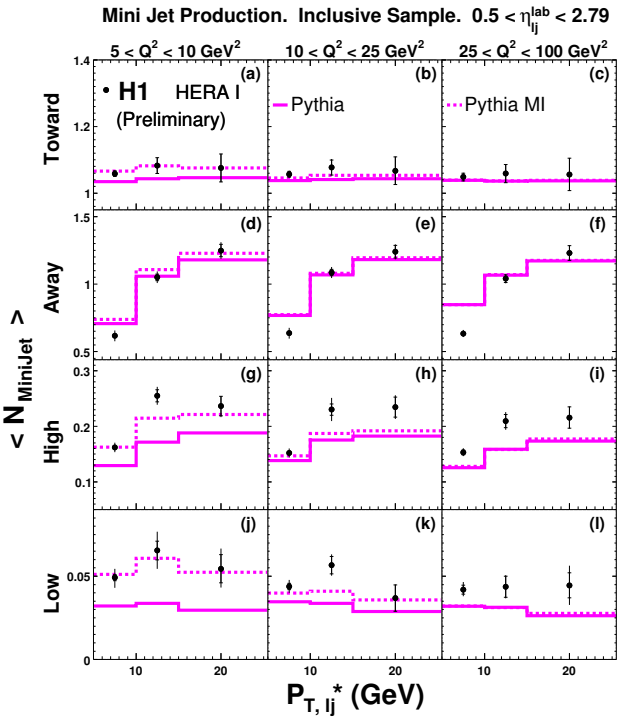

Figure 3: *The average mini-jet multiplicity at the different $\Delta\phi^*$ regions in bins of Q^2 as a function of P_T^* of the leading jet for the inclusive jet sample. The data is compared with Pythia (solid line) and Pythia with MI (dashed line).*

References

[1] Slides:
`http://indico.cern.ch/contributionDisplay.py?contribId=226&sessionId=6&confId=9499`

[2] S. Aid *et al.* [H1 Collaboration], Z. Phys. C**70** (1996) 17.

[3] D. Acosta *et al.* [CDF Collaboration], Phys. Rev. D **65** (2002) 072005.

[4] S. D. Ellis and D. E. Soper, Phys. Rev. D **48**(1993) 3160.

[5] H. Jung, Comput. Phys. Commun. **86** (1995) 147.

[6] K. Charchula, G. A. Schuler and H. Spiesberger, Comput. Phys. Commun. **81** (1994) 381.

[7] L. Lonnblad, Comput. Phys. Commun. **71** (1992) 15.

[8] T. Sjostrand, Phys. Lett. B **157** (1985) 321.

[9] T. Sjostrand, Comput. Phys. Commun. **82** (1994) 74.

Prospects for Inclusive Jet Cross-Section Measurement with Early Data at ATLAS

Dan Clements *

University of Glasgow - Department of Physics and Astronomy
Kelvin Building, Glasgow, G12 8QQ - UK

The inclusive jet cross-section was studied using the event generator NLOJET^{++} for a number of PDF sets (CTEQ6.1) in order to obtain an understanding of the uncertainties introduced by PDFs and renormalisation/factorisation scales on the theoretical cross-section. The error arising from the jet energy scale calibration was also investigated.

1 Introduction

The LHC will collide protons at a higher centre of mass energy ($\sqrt{s} = 14TeV$) and luminosity ($L = 10^{34}cm^{-2}s^{-1}$) than previously achieved, providing the opportunity to perform new physics searches (e.g SUSY) and precision tests of the Standard Model.

The inclusive jet cross-section at ATLAS is sensitive to compositeness (quark-substructure) which could be detected by comparing data with next to leading-order (NLO) QCD predictions. This process however needs to be performed carefully as poorly understood experimental and theoretical errors can lead to false signals of new physics. An understanding of these errors is hence essential in the search for physics beyond the standard model.

The inclusive jet cross-section describes the probability of obtaining a jet with a given transverse momentum. For a given event all jets within acceptance are included in the cross-section. The predicted cross-section for ATLAS using NLOJET^{++} [3] and CTEQ6.1 PDF [1] is given in Fig 1.

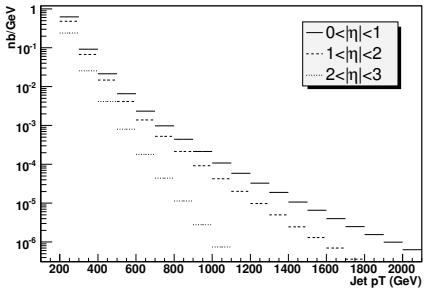

Figure 1: Inclusive jet cross-section for three pseudorapidity ranges at ATLAS,($\sqrt{s} = 14TeV$), $\mu_{r/f} = P_T/2$,(NLOJET^{++},CTEQ6.1)

2 Theoretical Errors

2.1 PDFs

PDFs are parameterised and then fit using global analyses which rely mainly on deep inelastic-scattering (DIS) data. Hence in creating a best fit PDF there is a degree of uncertainty which leads to a systematic error on cross-section predictions. The CTEQ group have attempted to quantify this uncertainty by producing a set of 40 error PDF sets along with a best fit (CTEQ6.1)[1]. The error on an observable dependent on PDFs is found by

*On behalf of the ATLAS collaboration.

calculating the observable for each PDF set and looking at its fluctuations. For inclusive jet measurements it is found that of the 40 PDF error sets, sets 29 and 30 dominate the error on the observable at high P_T and hence only these two sets need to be considered [2]. It is interesting to note that sets 29 and 30 relate to changes in the gluon distribution at high Bjorken-x which is poorly constrained from DIS data owing to the gluon being electrically neutral.

The inclusive jet-cross section was calculated using the central (best-fit) PDF and the error sets 29 and 30 over 3 regions in pseudorapidity (η). The proportional error (O(error PDF)-O(central))/O(central) was calculated in each case and is shown in Fig 2. For a jet of P_T $1TeV$ in central regions $0 < \eta < 1$ the error on the cross-section due to PDFs is $10 - 15\%$, the uncertainty in forward regions which probe the high-x region of the PDFs is considerably higher ($\sim 40\%$).

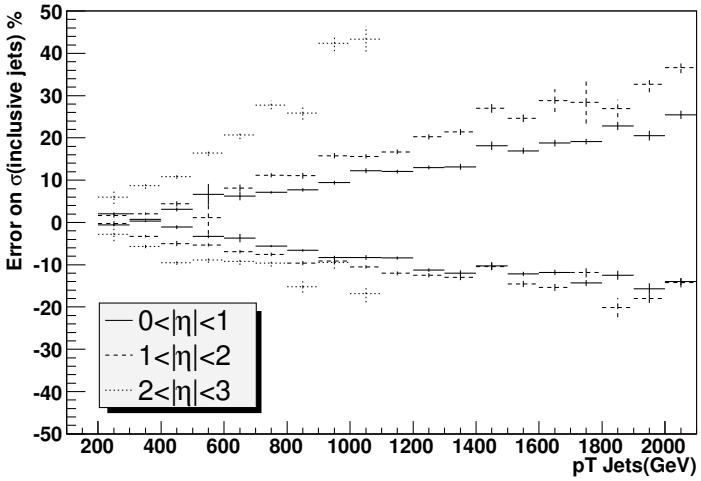

Figure 2: PDF errors on inclusive jet cross-section for three pseudorapidity regions,based on CTEQ6.1 error sets 29,30 in comparison with the best fit set. $\mu_{r/f} = P_T/2$,(NLOJET^{++},CTEQ6.1)

2.2 Renormalisation And Factorisation Scales

The renormalisation and factorisation scale (μ_r,μ_f) dependence of predictions of jet observables comes about owing to the perturbative calculation being carried out to a finite order. As an estimate of the error due to this μ_r and μ_f were varied between $P_T/2 \rightarrow 2P_T$ and the change in the predicted inclusive jet cross section recorded.

The renormalisation and factorisation scale errors were found to be fairly stable with increasing P_T of the jet at around 5-10%. This suggests that the renormalisation and factorisation scales will be important at low P_T where the PDF errors are small but will not contribute greatly to the overall error at higher P_T where PDF errors can become very large.

3 Experimental Errors

3.1 Jet Energy Scale

The energy of a jet is measured using both electromagnetic and hadronic calorimetry. This method of measurement introduces two distinct types of error to the measured jet energy. The first is a sampling error, which causes a gaussian like smearing of the jet energy around its true value. The second which will be studied here is a systematic calibration error which causes a shift of the measured peak of the jet energy (after smearing) with respect to the true jet energy.

Owing to the strong dependence of the inclusive jet cross-section on the jet energy, jet energy scale uncertainty can create significant errors. This effect was studied by introducing a systematic jet energy scale error to jets after they had been reconstructed within NLOJET^{++} and comparing the generated inclusive jet cross-section to an unshifted spectrum. This was carried out for errors on the jet energy scale of 1% ,5% and 10% the results being shown in Fig 3.

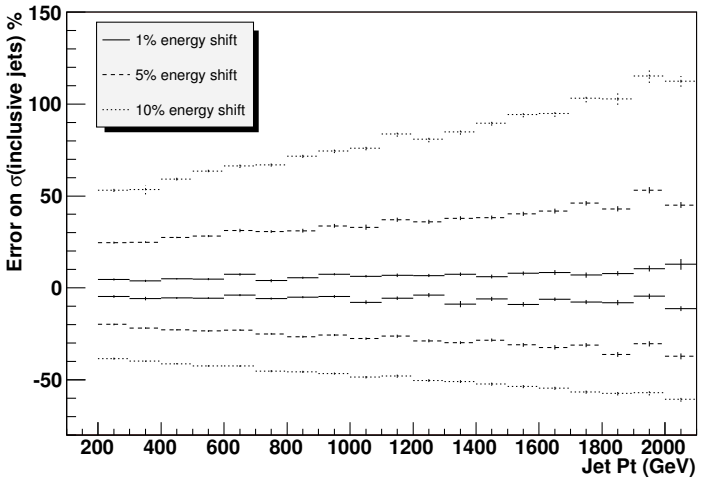

Figure 3: Jet Energy Scale errors of 1%, 5% and 10% on the inclusive jet cross-section,$\mu_{r/f} = P_T/2$,(NLOJET^{++},CTEQ6.1)

The error on the the inclusive jet cross-section is seen to grow with increasing jet energy. This is expected as a 1% error on jet energy constitues a larger absolute error on a high P_T jet than on a low P_T jet leading to an increased uncertainty in the inclusive jet cross-section. At a jet energy scale uncertainty of 1%, the error on the inclusive jet cross-section is seen to vary from 5% and 10% for jet energies between 200GeV and 2TeV. Similarly a 10% variation in jet energy scale leads to an error of between 50% and 120% over the same range.

3.2 Statistical Errors

The statistical errors on the inclusive jet cross-section at $1 fb^{-1}$ are of order 1% in the central region and 5% in the forward region for a jet of $P_T \sim 1TeV$. This suggests that at this integrated luminosity the error sources considered so far are statistically significant and will be so with early data.

4 Improving Gluon PDFs with ATLAS data

ATLAS jet data could be used in a global PDF fit in order to help constrain the high-x gluon. The recent development of integration grid-techniques such as NLOGRID [4] and FASTNLO [5] allow for a NLO cross-section to be rapidly calculated for a varying PDF. This hence allows jet data to be introduced to existing PDF global fits used by MRST and CTEQ.

A study based on pseudo-data suggests that ATLAS jet data will be able to constrain the high-x gluon if it can achieve a jet energy scale uncertainty of $\sim 1\%$. At JES uncertainties of $\sim 3\%$ the benefits of including ATLAS data into global PDF fits becomes negligible.

5 Summary

Jet data at ATLAS will provide tests of QCD and the opportunity to look for evidence of new physics. However a good control of both theoretical and experimental errors is vital in order to have confidence in any results. The theoretical uncertainty (for high pT jets) is dominated by uncertainty in the high-x gluon PDF, whilst the experimental errors are dominated by uncertainty in the jet energy scale. With early data the JES is likely to be poorly constrained ($5 - 10\%$ for jets below 1TeV), which will seriously limit the physics potential of the data. The use of in situ-calibration techniques and a growing understanding of the detector should however lead eventually to a better constrained JES 1-2% (below 1TeV) with the potential to constrain the high-x gluon.

6 Acknowledgments

The author would like to thank: C.Buttar, C.Gwenlan, T.Carli, A.Cooper-Sarkar and P.Francavilla.

7 Bibliography

References

[1] J Pumplin *et al.*, arXiv: hep-ph 0201195, (2004).
[2] D Stump *et al,*, arXiv: hep-ph 0303013, (2003).
[3] Z Nagy, Phys Rev Lett 88, 122003, (2002).
[4] T Carli *et al,*, arXiv: hep-ph 0510324 (2005).
[5] T Kluge *et al,*, arXiv: hep-ph 0609285 (2006).
[6] Slides:
`http://indico.cern.ch/contributionDisplay.py?contribId=228&sessionId=6&confId=9499`

Parton Shower Monte Carlos vs Resummed Calculations for Interjet Energy Flow Observables.

Mrinal Dasgupta *

School of Physics and Astronomy, University of Manchester
Schuster Building, Brunswick street, Manchester M13 9PL, United Kingdom.

Parton showers in Monte Carlo event generators reflect to a certain accuracy our understanding of QCD radiation at all orders. For interjet energy flow observables it has been known for some time that relevant all-order dynamics is substantially more complicated than that encoded via angular ordering in parton shower algorithms, even to leading logarithmic accuracy. Here we investigate the extent of the numerical mismatch between leading logarithmic analytical estimates (resummation) and parton showers in an effort to better understand the accuracy of parton showers for such observables.

1 Introduction

Monte Carlo (MC) event generators are the most important tools at our disposal in the search for new physics beyond the standard model. At the large hadron collider(LHC) for example, alongside the hard process where the production of hitherto unseen particles is expected to occur, there will in general be copious amounts of initial and final state QCD radiation, conversion of partons into hadrons (hadronisation), effects due to spectator interactions, multiple hard scatterings and pile-up.

In such a complex hadronic environment as good a modeling as possible of all of the above physics aspects, is of clear benefit in order to exploit the full discovery potential of the LHC. MC tools exist and are being further developed to provide a simulation of the physics described above. However of the whole range of effects mentioned above as accompanying the hard process, the only part that we understand directly from first principles of is perturbative QCD radiation. This understanding is in principle what ought to be reflected in the parton shower algorithms in various event generators.

Another source of information on QCD at all orders is provided by analytical tools such as those employed in resummation of large logarithms in QCD. This field too has seen some interesting relatively recent developments with the observation that for a large class of observables (those measuring flow of hadronic energy into limited regions of phase space and hence called non global observables) relevant all-order dynamics is much more complicated than previously imagined [2, 3]. This more complex soft gluon dynamics is not fully described by parton showers in event generators such as HERWIG and PYTHIA. The HERWIG parton shower for example is based on angular ordering of soft gluon radiation which correctly captures the leading logarithms for several observables. However for non global observables the angular ordering approximation is not formally correct at single logarithmic accuracy, which in some important cases is also leading logarithmic accuracy. In these cases the HERWIG shower cannot be a priori expected to describe even the leading logarithmic perturbative behaviour. This is even more the case for the old PYTHIA shower (before v 6.3) where angular ordering is imposed on showers pre-ordered in invariant mass,

*Work in collaboration with Andrea Banfi and Gennaro Corcella.

which leads to a poor decription of soft emissions at large angles and consequently non-global observables in particular. This is potentially worrying since non-global observables such as interjet energy flow are commonly measured experimentally and moreover they are used to improve MC models by tuning the model parameters to data on such observables e.g. hadronic activity in *toward* or *away* regions wrt the leading jet, in hadron collisions.

Given the prevalence and importance of non-global observables in QCD studies, it is worth investigating quantitatively how good a description is provided by the different parton showers e.g. those in HERWIG and PYTHIA. This can be done by comparing the parton showers to the state-of the-art analytical resummations in an effort to see what perturbative accuracy can be relied upon in the MC descriptions in such cases.

In order to get a clearer idea about what one may expect from parton showers such as those ordered in angle we first study to what extent the leading single-logarithmic behaviour can be obtained by assuming angular ordering for energy flow into a rapidity interval between hard jets. Thus we compare the full single-logarithmic resummation (possible only in the large N_c limit) with a numerical result obtained by addressing just angular ordered configurations. We then check if our conclusions are borne out by comparing the resummation to the real HERWIG parton shower. We then compare the results to the PYTHIA event generator both with the old shower and the new shower and draw some conclusions.

2 Angular ordering and non global observables

The observable we shall study is the differential E_t flow, $\frac{1}{\sigma}\frac{d\sigma}{dE_t}$ into a rapidity interval of width $\Delta\eta$ between a pair of jets. For simplicity we shall take these to be back-to–back jets produced in e^+e^- annihilation but our conclusions generalise straightforwardly to gaps between jets in any hard process. This observable involves other than the scale E_t an additional scale Q, the hard scale for the process. Typically $E_t \ll Q$ and one then has to deal with logarithms $\alpha_s^n \ln^m Q/E_t$, with $m \leq n$. We note that the leading logarithms in this case are single logarithms i.e those with $m = n$.

The resummation of the leading logarithms has been possible only in the large N_c limit [2, 3]. In this limit the complex colour algebra involved in the soft large-angle multi-gluon emission probabilities is greatly simplified and can be encoded in a dipole evolution Monte-Carlo algorithm, since the emitting ensemble reduces to a system of dipoles. Considering a dipole configuration C we can write the probability of emitting a soft gluon at scale $L' = \ln Q/\omega'$, where ω' is the gluon energy, as :

$$P'_C(L') = \alpha_s(L')\Delta_C(L', L)F_C(\theta'\phi')P_C(L), \tag{1}$$

where C' is the new configuration of dipoles after the emission of the gluon, $\Delta(L', L)$ is the no-emission probability between scales L and L' and $F_c(\theta', \phi')$ is the angular part of the dipole real emission probability. Thus explicitly we have

$$F_C(\theta_k, \phi_k) = \sum_{\text{dipoles}-\text{ij}} \frac{2C_A\,(1-\cos\theta_{ij})}{(1-\cos\theta_{ik}(1-\cos\theta_{jk})} \tag{2}$$

Then the result that contains the resummation of the leading single-logarithms is a form factor, Σ, which can be written

$$\Sigma(\alpha_s L) = \sum_{C|\Omega_{empty}} P_c(L),\ L = \ln Q/E_t. \tag{3}$$

In other words the resummed result for the probability that the transverse energy in the gap is less than some value E_t is obtained by summing over all dipole configurations such that the gap region Ω is free from emissions above that scale. In order to study the impact of angular ordering we replace F by an angular ordered (AO) approximation [a]:

$$F(\theta_k, \phi_k) \to \frac{(\cos\theta_{ik} - \cos\theta_{ij})}{(1 - \cos\theta_{ik})} + \frac{(\cos\theta_{jk} - \cos\theta_{ij})}{(1 - \cos\theta_{jk})} \tag{4}$$

such that the emission k is produced in cones around the hard legs i and j with angular size set by the opening angle of dipole ij. This angular ordering is expected to correspond to the piece included in e.g. the HERWIG shower.

In Fig. 1,we plot the resummed integrated E_t cross-section (equivalently the form factor Σ) as a function of $t \sim \frac{\alpha_s}{2\pi} \ln \frac{Q}{E_t}$ in both the AO approximation as well as the resummation in the large N_c limit, for $\Delta\eta = 1.0$. We note that angular ordering has only a modest effect and the results at say $t = 0.15$ corresponding to $Q = 100$ GeV $E_t = 1$ GeV differ by just 10 %. Also shown there ('primary' curve) is the resummation in the independent emission approximation assuming soft gluons to be emitted by just the hard partons with no correlated gluon emission other than effects included in the running coupling. The angular ordered and full results differ substantially from this stronger assumption.

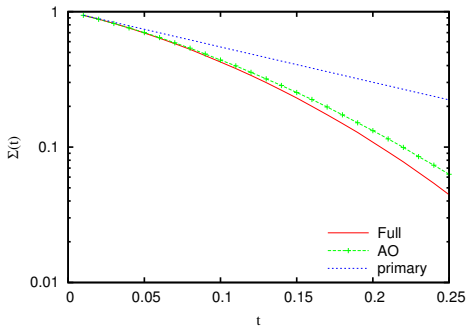

Figure 1:

3 Comparison to HERWIG and PYTHIA

We now proceed to compare to actual parton showers in HERWIG and PYTHIA. Since we are interested in the dependence on the logarithmic variable t we can in fact go to very large Q values, which helps us to kill potentially spurious subleading terms of relative order $\alpha_s(Q)$ that would be present in the MC showers. Once we draw conclusions for a given value of t , we can apply those observations to an appropriate E_t value for any Q. Given that angular ordering produces results that are in reasonable agreement with resummation we can a priori expect the HERWIG shower to also not differ substantially. This is in fact the case

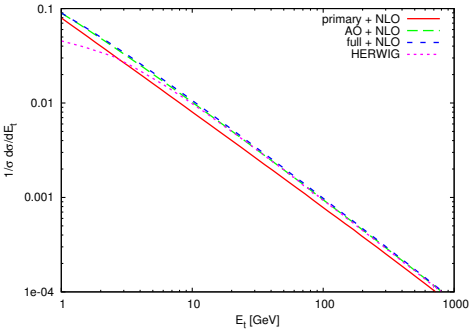

Figure 2:

[a] This replacement would be exactly correct for global observables where one could freely integrate over azimuthal angles.

as can be seen from Fig. 2 where once again for $t = 0.15$ we note just a 10 % difference between HERWIG and resummation.

For the old PYTHIA shower where angular ordering is imposed on top of ordering in invariant mass the results are significantly different. Here one notes from Fig. 3 a discrepancy of 50 % for $t = 0.15$ which may be misattributed to other (non-perturbative) physics during the procedure of tuning PYTHIA to data. Bearing in mind that the non global logarithmic effects are not universal and are absent for other (global) observables this is a potentially dangerous and inaccurate way to account for them.

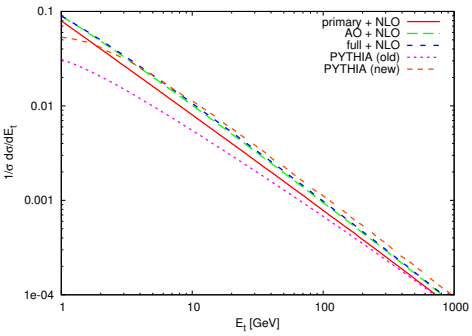

Figure 3:

For the new PYTHIA shower which implements angular ordering of soft radiation via a dipole type phase-space the results show a marked improvement and a difference of only 7.5 % is seen at $t = 0.15$. However as we increase the width of the rapidity slice in question the description from the new PYTHIA shower deteriorates and we observed that for $\Delta\eta = 3.0$ the new shower performs poorly when compared to resummation and HERWIG results.

4 Conclusions

We can conclude from our studies that while angular ordering as implemented in QCD parton showers does not formally give the correct single logarithmic behaviour for non-global observables, numerically one does not have to worry too much about the difference between angular ordered and resummed results even in this case. However ordering in other variables such as invariant mass and angle (PYTHIA old) gives rise to a poor perturbative description. This incorrect perturbative estimate may be adjusted for in other non-perturbative aspects of the MC model but this is not optimally accurate. It is imperative in our opinion, especially for observables related to energy flow between hard jets, to compare the results from HERWIG and PYTHIA both at the parton and hadron level. If large discrepancies are observed at parton level information from analytical resummed calculations where available could be exploited to better understand the uncertainty and limitations of the MC descriptions. We also observed that the new PYTHIA shower is substantially better than its earlier counterpart but noted a puzzling discrepancy at large values of the interjet rapidity interval $\Delta\eta$, which we hope can be clarified in the near future.

References

[1] Slides:
`http://indico.cern.ch/contributionDisplay.py?contribId=178&sessionId=6&confId=9499`

[2] M. Dasgupta and G.P. Salam, Phys. Lett. **B512** 323 (2001), arXiv:hep-ph/0104277 (2001).

[3] M. Dasgupta and G.P. Salam, JHEP **0203** 017 (2002), arXiv:hep-ph/0203009 (2002).

Power Corrections for Jets at Hadron Colliders

Matteo Cacciari[1], Mrinal Dasgupta[2], Lorenzo Magnea[3] and Gavin Salam[1]

1- LPTHE, CNRS UMR 7589, Université P. et M. Curie (Paris 6)
Université D. Diderot (Paris 7), 75252 Paris Cedex 05, France

2- School of Physics and Astronomy, University of Manchester
Oxford Road, Manchester M13 9PL, U.K.

3- Dipartimento di Fisica Teorica, Università di Torino, and
INFN, Sezione di Torino, Via P. Giuria, I–10125 Torino, Italy

We discuss non-perturbative QCD corrections to jet distributions in hadron collisions, focussing on hadronisation and underlying event contributions. Using soft gluon resummation and Monte-Carlo modelling we show that hadronisation dominates at small values of the jet radius R, behaving as $1/R$, while underlying event corrections grow with the jet area. This provides a handle to disentangle them and parametrize them in terms of measurable QCD parameters, which might enjoy a degree of universality.

1 Introduction

With the advent of the LHC particle physics will once again break into new territory at the high energy frontier. With 14 TeV available in the center of mass, one would naively expect that the dynamics of confinement and low-energy QCD would decouple and, thanks to factorization, have a minimal influence on high-$p_\perp$ observables (a typical figure of merit being $\Lambda/p_\perp \sim \mathcal{O}(10^{-3})$). In general, this expectation is not fulfilled. Even at very high energy, for example, no hadronic cross section can be precisely determined without a detailed knowledge of parton distributions in the colliding hadrons. Furthermore, a wide range of observables of interest for both Standard Model and BSM physics must rely upon a definition of hadronic jets and a measurement of the jet energy scale. Experience gained at the Tevatron [2] shows, for example, that a 1% uncertainty in the jet energy scale causes a 1 GeV uncertainty in the top quark mass determination, and is reflected in a 10% uncertainty in the single inclusive jet $p_\perp$ distribution at $p_\perp \sim 500$ GeV[a].

Assuming a jet has been reconstructed with an infrared and collinear safe algorithm, dependent upon a parameter R defining its size in the rapidity-azimuth plane, the energy of the jet will differ from the energy of the hard parton that originated it because of a variety of physical phenomena. Radiation from the underlying event and from pileup will spill inside the jet cone, increasing its measured energy; on the other hand, radiation produced during hadronisation will spill outside the jet cone, leading to a negative correction. It is important to realize that, while some of these corrections are definitely outside the reach of perturbative calculations (this is certainly the case for pileup, and to a certain extent for the underlying event), hadronisation corrections can be explored with perturbative methods, supplemented by soft gluon resummation and power correction technology. These methods have been successfully applied to simpler processes such as e^+e^- annihilation and DIS (for a review, see [4]), where studies of event shapes showed that power corrections to distributions can be efficiently parametrized in terms of a limited number of non-perturbative parameters, enjoying a remarkable degree of universality [5, 6]. Here we will apply for the first time these

[a]For an early study of the impact of power corrections on jet distributions, see [3].

methods to jet distributions in hadron collisions, a much more challenging environment. We consider, as an example, the single inclusive jet $p_\perp$ distribution: we show that perturbative methods lead to a prediction for the R dependence of the leading power correction, which turns out to be singular (behaving as $1/R$) for hadronisation corrections, while, as might be expected, it grows as R^2 for the underlying event. We go on to compare the analytic result to Monte Carlo models, finding broad agreement as well as some interesting differences in the details.

2 Issues in soft gluon resummation for jet distributions

Soft gluon resummation for the single-inclusive jet $p_\perp$ distribution was first performed in [7], using techniques developed in [8] and [9][b]. Since jet production in hadron collisions generically involves at least four colored partons, this is the first case in which nontrivial mixing of colour structures occurs. Formally, the structure of the resummed cross section is

$$E_J \frac{d^3\sigma}{d^3 p_J} = \frac{1}{s} \exp\left[\sum_{p=1}^{2} \mathcal{E}_{\rm IN}^{(p)} + \sum_{p=J,R} \mathcal{E}_{\rm OUT}^{(p)}\right] \cdot {\rm Tr}\left[HS\right] \ . \tag{1}$$

The factors $\mathcal{E}_{\rm IN}$ and $\mathcal{E}_{\rm OUT}$ exponentiate collinear logarithms associated with initial state radiation of the colliding partons, and with the measured and the recoil outgoing jets, respectively. At the level of power corrections, these factors are expected to generate contributions of order $(\Lambda/p_\perp)^2$, associated with jet mass effects. These corrections are negligible, and therefore we will concentrate on the contributions of soft gluons emitted at wide angles from the jet, embodied in the last factor in Eq. (1). Here the trace is taken in the space of representations of the color group that can be constructed out of the scattering hard partons, while H and S are matrices containing hard and soft gluon contributions respectively. The exponentiation of soft radiation and the structure of color mixing can be simply understood [11] by resorting to the eikonal approximation. One can show that all soft logarithms can be organized in terms of eikonal colored dipoles, given by

$$\mathcal{D}_{ij}(Q,Q_0) \equiv \int_{Q_0}^{Q} d\kappa_\perp^{(ij)} \kappa_\perp^{(ij)} \alpha_s\left(\kappa_\perp^{(ij)}\right) \int d\eta \, \frac{d\phi}{2\pi} \, \frac{p_i \cdot p_j}{p_i \cdot k \, p_j \cdot k} \, T_i \cdot T_j \ , \tag{2}$$

where the indices i, j label hard partons, T_i, T_j are the color generators in the corresponding representation, and $\kappa_\perp^{(ij)} = 2\, p_i \cdot k \, p_j \cdot k/(p_i \cdot p_j)$ is the transverse momentum with respect to the emitting dipole. For $n < 4$ hard partons, all products of color matrices can be expressed in terms of Casimir operators, and thus there is no mixing of color structures.

Before extending the discussion to power corrections, it should be noted that usage of resummations such as Eq. (1) requires great care both in the choice and in the definition of the observable. In general jet cross sections, which involve an explicit slicing of phase space, are affected by nonglobal logarithms [12]. In the present case, it turns out that the $p_\perp$ distribution is a global observable. Nonglobal logarithms will generically spoil Eq. (1) at NLL level, and might influence power correction in a way which is not currently understood. One should also note that the choice of jet algorithm may affect the results quite drastically: IR safety is a must; furthermore, we will work assuming that the jet momentum is reconstructed using four-momentum recombination.

[b] A refinement of the implementation of Ref. [7] was recently proposed in [10]

3 Radius dependence of power corrections

In order to analyze the structure of power corrections using the resummation, we consider separately each dipole in Eq. (2). For the sake of simplicity we place the measured jet at zero rapidity, which does not qualitatively affect our results. Let $\delta\xi^{\pm}(k_\perp, \eta, \phi)$ be the contribution of a soft gluon with momentum k to the observable, which we normalize as $\xi \equiv 1 - p_\perp/\sqrt{S}$. Note that the contribution is different if the gluon is recombined with the jet ($\delta\xi^+$), or is left out of it ($\delta\xi^-$). We then construct the shift in the ξ distribution due to the (ij) dipole by integrating $\delta\xi^{\pm}(k_\perp, \eta, \phi)$ over the gluon phase space, with a measure given by the eikonal dipole,

$$\Delta\xi_{ij}^{\pm}(R) \equiv \int_{\pm} d\eta \frac{d\phi}{2\pi} \int_0^{\mu_F} d\kappa_\perp^{(ij)}\, \alpha_s\left(\kappa_\perp^{(ij)}\right) k_\perp \left|\frac{\partial k_\perp}{\partial \kappa_\perp^{(ij)}}\right| \frac{p_i \cdot p_j}{p_i \cdot k\, p_j \cdot k}\, \delta\xi^{\pm}(k_\perp, \eta, \phi) \ . \qquad (3)$$

Note that $\delta\xi^+$ is integrated inside the jet cone, and $\delta\xi^-$ outside of it. The result is then a function of the jet radius R.

Different dipoles give different R dependences, with a transparent physical interpretation. The dipole constructed out of the two incoming partons has a leading power correction growing like R^2, and it is natural to interpret it as the way in which the buildup of the underlying event begins to be seen from perturbation theory. Dipoles involving the measured jet, on the other hand, behave as $1/R$ for small R. This behavior arises from gluons which are not recombined with the jet: at small R, they are allowed to be emitted very close in phase space to the radiating parton, and they begin to see the corresponding collinear singularity. All dipole integrals are expressed in terms of a low-energy moment of the strong coupling, $\mathcal{A}(\mu_F)$, which in principle could be related to the analogous quantity measured in e^+e^- annihilation. As an example, we consider the contribution of the $qq \to qq$ channel to the $p_\perp$ distribution. The dipole comprising the two incoming quarks gives

$$\Delta\xi_{\mathrm{in-in}}(R) = -\frac{4}{\sqrt{S}}\,\mathcal{A}(\mu_F)\,R\,J_1(R) = -\frac{1}{\sqrt{S}}\,\mathcal{A}(\mu_F)\,\left(2R^2 - \frac{1}{4}R^4 + \mathcal{O}\left(R^6\right)\right) \ . \qquad (4)$$

The dipole involving an incoming leg and the measured jet, on the other hand, gives

$$\Delta\xi_{\mathrm{in-J}}(R) = \frac{1}{\sqrt{S}}\,\mathcal{A}(\mu_F)\left(\frac{4}{R} - \frac{5}{4}R + \frac{23}{768}R^3 + \mathcal{O}\left(R^5\right)\right) \ . \qquad (5)$$

Notice that, as expected, this corresponds to a *negative* shift in the $p_\perp$ distribution, given the definition of ξ. We remark also that all singular contributions are essentially abelian in nature and can be directly collected into an overall shift in the physical distribution, weighed by C_F (C_A) for a quark- (gluon-) initiated jet. Terms subleading in R, however, including Eq. (4), must be recombined taking color mixing into account, and their contribution is more intricate than a simple shift.

4 Monte-Carlo analysis of hadronisation and underlying event

A powerful cross-check of the validity of the above discussion is provided by examining hadronisation corrections for a range of jet algorithms in Monte Carlo simulations. We consider dijet events from both Pythia [13] and Herwig [14] and select events whose highest-$p_\perp$ jet at parton-level has $55 < p_\perp < 70$ GeV. The selection at parton level is intended

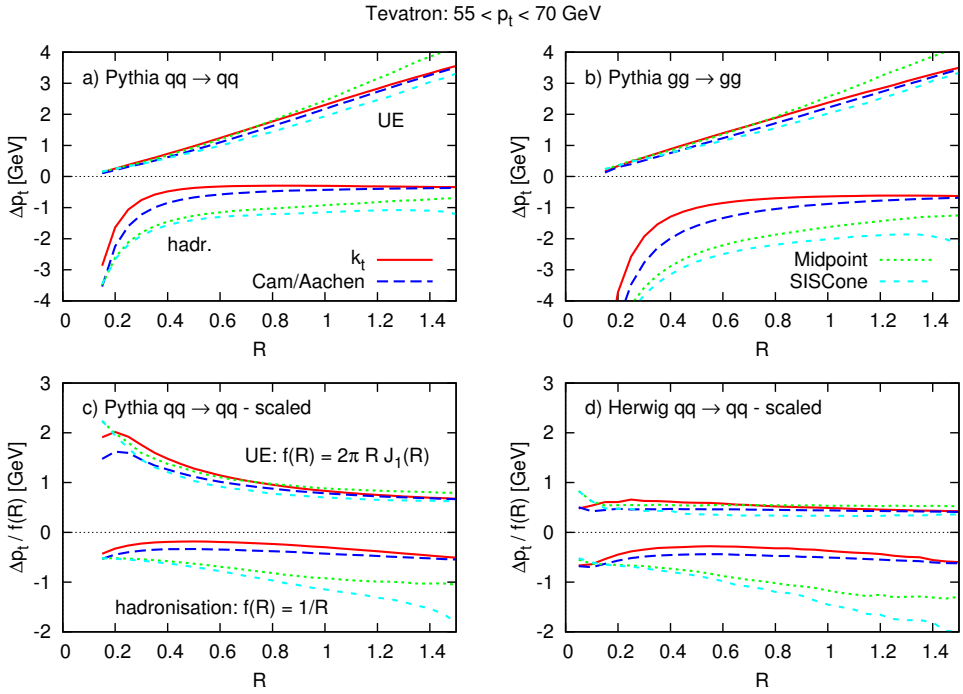

Figure 1: Shifts in p_t associated with hadronisation and underlying-event contributions for the two leading jets in Pythia 6.410 and Herwig 6.510 dijet events.

to eliminate selection bias associated with non-perturbative effects, as is appropriate for comparison with our analytical formulae. For each event we examine the average difference in p_t for the two leading jets at hadron-level as compared to parton level. This difference is separated into a hadronisation component and an underlying event contribution, the latter 'defined' as that obtained when switching on underlying event (UE) and/or multiple-interactions in each Monte Carlo program, using the default parameters of each. The UE contribution is expected to be uniform in rapidity and azimuth, scaling as πR^2 for small R, or as $2\pi R J_1(R)$ for general R with E-scheme (4-momentum) recombination.

The upper plots of Fig. 1 show the two non-perturbative components, for two hard scattering channels, as a function of R for the k_t [15], Cambridge/Aachen [16], Midpoint[c] cone [17] and SISCone [18] jet algorithms (all run through FastJet [19]). The negative result for hadronisation, divergent at small R, is consistent with Eq. (5). The rough factor of two between the hadronisation corrections for the $qq \to qq$ and $gg \to gg$ is consistent with the C_A/C_F ratio expected from Sect. 3. One notes that the cone-type algorithms have more negative corrections, differing from the sequential recombination algorithms by a term roughly independent of R whose explanation is beyond the scope of the single-gluon calculation given above. The UE event contribution to the jet $p_\perp$ is positive, as expected, and for the typical range of R studied experimentally, $0.4 < R < 0.7$, similar in magnitude to the hadronisation correction. It is largely identical for all algorithms, and roughly independent

[c]This algorithm is infrared unsafe and should be thought of as a "legacy" algorithm, shown only for historical purposes.

of the hard scattering channel.

The analytical R dependence can be studied in more depth by scaling out the expectations for hadronisation and UE, as is shown in the lower plots of Fig. 1. For recombination algorithms the result is roughly independent of R, as expected from Eq. (5). The normalisation of ~ 0.5 GeV is consistent with the magnitude of hadronisation corrections extracted at LEP. In contrast, the normalised UE correction is not constant in R. This can be shown to be a consequence of Pythia's implementation of colour-reconnections between the hard partons and the underlying event and when examining models without such reconnections, such as Herwig (and also Jimmy [20]), Fig. 1d, this effect disappears. One notes that if one extracts the UE $p_\perp$ density per unit rapidity (in the figure it is normalised per unit area) then it is ~ 6 times larger than the similarly normalised hadronisation correction, suggestive of far more violent non-perturbative dynamics.

Acknowledgements

We are grateful to Torbjorn Sjöstrand, Peter Skands and Jon Butterworth for assistance and helpful comments. Work supported in part by the EU Research and Training Network 'HEPTOOLS' under contract MRTN-CT-2006-035505 and by grant ANR-05-JCJC-0046-01 from the French Agence Nationale de la Recherche.

References

[1] Slides:
`http://indico.cern.ch/contributionDisplay.py?contribId=179&sessionId=6&confId=9499`

[2] A. Bhatti *et al.*, Nucl. Instrum. Meth. **A 566** 375 (2006), arXiv:hep-ex/0510047.

[3] M.L. Mangano, arXiv:hep-ph/9911256.

[4] M. Dasgupta and G. P. Salam, J. Phys. **G 30** R143 (2004), arXiv;hep-ph/0312283.

[5] C. F. Berger and G. Sterman, JHEP **0309** 058 (2003), arXiv:hep-ph/0307394.

[6] C.F. Berger and L. Magnea, Phys. Rev. **D 70** 094010 (2004), arXiv:hep-ph/0407024.

[7] N. Kidonakis and J. F. Owens, Phys. Rev. **D 63** 054019 (2001), arXiv:hep-ph/0007268.

[8] E. Laenen, G. Oderda and G. Sterman, Phys. Lett. **B 438** 173 (1998), arXiv:hep-ph/9806467.

[9] N. Kidonakis, G. Oderda and G. Sterman, Nucl. Phys. **B 525** 299 (1998), arXiv:hep-ph/9801268.

[10] D. de Florian and W. Vogelsang, arXiv:0704.1677 [hep-ph].

[11] Yu. L. Dokshitzer and G. Marchesini, JHEP **0601** 007 (2006), arXiv:hep-ph/0509078.

[12] M. Dasgupta and G. P. Salam, Phys. Lett. **B 512** 323 (2001), arXiv:hep-ph/0104277.

[13] T. Sjostrand *et al.*, Comp. Phys. Comm. **135** 238 (2001), arXiv:hep-ph/0010017; arXiv:hep-ph/0308153.

[14] G. Marchesini *et al.*, Comp. Phys. Comm. **67** 465 (1992); G. Corcella *et al.*, JHEP **0101** 010 (2001), arXiv:hep-ph/0011363.

[15] S. Catani *et al.*, Nucl. Phys. **B 406** 187 (1993); S.D. Ellis and D.E. Soper, Phys. Rev. **D 48** 3160 (1993), arXiv:hep-ph/9305266.

[16] Y.L. Dokshitzer *et al.*, JHEP **9708** 001 (1997), arXiv:hep-ph/9707323; M. Wobisch and T. Wengler, arXiv:hep-ph/9907280.

[17] G. C. Blazey *et al.*, arXiv:hep-ex/0005012.

[18] G.P. Salam and G. Soyez, JHEP **0705** 086 (2007), arXiv:0704.0292

[19] M. Cacciari and G. P. Salam, Phys. Lett. **B 641** 57 (2006), arXiv:hep-ph/0512210.

[20] J. M. Butterworth, J. R. Forshaw and M. H. Seymour, Z. Phys. **C 72** (1996) 637, arXiv:hep-ph/9601371.

Three-Jet Event-Shapes: First NLO+NLL+$1/Q$ Results

Andrea Banfi[1]

1- Università degli Studi di Milano-Bicocca - Dipartimento di Fisica "G. Occhialini"
Piazza della Scienza 3, 20126 Milano - Italy

Three-jet event-shape distributions can be exploited to investigate the dependence of hadronisation effects on the colour and the geometry of the underlying hard event. We present here the first comparison of data in e^+e^- annihilation and state-of-the-art theoretical predictions, including resummation of large logarithms at next-to-leading logarithmic accuracy matched to exact next-to-leading order and leading non-perturbative power corrections.

1 Power corrections to multi-jet event shapes

The remarkable success of the QCD description of two-jet event shape distributions has made these observables one of the most useful tools to test our understating of the dynamics of strong interactions, both in the perturbative (PT) and non-perturbative (NP) regime. This is because event-shape distributions span a wide range of physical scales, from the region where the event shape V is large, described well by fixed-order QCD, to the exclusive $V \to 0$ region where hadronisation effects dominate, through the intermediate region where one needs to resum large infrared and collinear logarithms. The combination of next-to-leading order (NLO) predictions and next-to-leading logarithmic (NLL) resummation, supplemented with non-perturbative (NP) hadronisation corrections provided by Monte Carlo (MC) event generators, has lead to one of the most precise determinations of the QCD coupling α_s [2].

In view of the fact that hadronisation corrections are suppressed by inverse power of the process hard scale Q, in recent years it has been attempted to describe two-jet event shape distributions at hadron level by simply adding to the NLL resummation the NP shift $\langle \delta V \rangle$ originated by leading $1/Q$ power corrections, which is a reliable approximation as long as $\langle \delta V \rangle \ll V$. The shift has a remarkably simple structure, being the product of a calculable coefficient c_V, which depends on the considered shape variable, and a genuine NP quantity $\langle k_t \rangle_{\rm NP}$, the mean transverse momentum of large-angle hadrons produced in the collision, which is variable independent (*universal*). The universality of $\langle k_t \rangle_{\rm NP}$, and hence of $1/Q$ power corrections, has been thoroughly tested both in e^+e^- annihilation and DIS, and is found to hold within 20% (see [3] for a recent review).

This universality property is based on two facts. The first is that particles responsible for leading power corrections are low transverse momentum hadrons in a central rapidity region, away from the hard jets. Any of these hadrons k contributes to a two-jet event shape V with an extra $\delta V(k) Q \simeq k_t f_V(\eta)$, with k_t and η the hadron transverse momentum and rapidity with respect to the jet axis. The second is that central hadrons are distributed uniformly in rapidity. This ensures that in the region $\langle \delta V \rangle \ll V$, where only leading power corrections are important, the dependence of $\langle \delta V \rangle$ on rapidity and transverse momentum gets factorised [4]:

$$\langle \delta V \rangle \simeq \langle k_t \rangle_{\rm NP} \, c_V, \qquad c_V = \int d\eta \, f_V(\eta) \, . \tag{1}$$

Among all models that, for two-jet events, predict a uniform rapidity distribution of central hadrons, the dispersive DMW approach [5] makes it possible to extend eq. (1) to

multi-jet event shapes, where there is no natural way to identify k_t and η. The starting point is the probability $dw(k)$ of emitting a soft dressed gluon k from a quark-antiquark pair (whose momenta are p and $\bar{p}$) in a colour singlet:

$$dw(k) = C_F \frac{dk_t^2}{k_t^2} d\eta \frac{d\phi}{2\pi} \frac{\alpha_s(k_t)}{\pi} , \qquad \eta = \frac{1}{2} \ln \frac{\bar{p}k}{pk} , \qquad k_t^2 = \frac{(2pk)(2k\bar{p})}{2p\bar{p}} , \tag{2}$$

where α_s is the physical CMW coupling [6]. The CMW coupling is then extended at low transverse momenta via a dispersion relation, and the very same probability $dw(k)$ is exploited to compute NP corrections [5]. The resulting shift $\langle \delta V \rangle$ has the same form as in eq. (1), where the c_V coefficient is identical and the NP parameter $\langle k_t \rangle_{\rm NP}$ can be expressed in terms of $\alpha_0(\mu_I)$, the average of the dispersive coupling below the merging scale μ_I, as follows [7]:

$$\langle k_t \rangle_{\rm NP} = \frac{4\mu_I}{\pi^2} C_F \mathcal{M} \left(\alpha_0(\mu_I) - \alpha_s(Q) + \mathcal{O}(\alpha_s^2) \right) , \qquad \alpha_0(\mu_I) = \int_0^{\mu_I} \frac{dk}{\mu_I} \alpha_s(k) . \tag{3}$$

Here the Milan factor $\mathcal{M}$ accounts for non-inclusiveness of event-shape variables.

One can now naturally extend the above analysis to multi-jet event shapes, where the soft dressed gluon probability is given by

$$dw(k) = \sum_{i<j} (-\vec{T}_i \cdot \vec{T}_j) \frac{d\kappa_{ij}^2}{\kappa_{ij}^2} d\eta_{ij} \frac{d\phi_{ij}}{2\pi} \frac{\alpha_s(\kappa_{ij})}{\pi} , \quad \eta_{ij} = \frac{1}{2} \ln \frac{p_j k}{p_i k} , \quad \kappa_{ij}^2 = \frac{(2p_i k)(2kp_j)}{2p_i p_j} , \tag{4}$$

with $\vec{T}_i$ the colour charge of hard parton p_i, and κ_{ij} and η_{ij} the invariant transverse momentum and rapidity with respect to the emitting dipole ij. This gives the following result for the shift:

$$\langle \delta V \rangle = \frac{4\mu_I}{\pi^2} \mathcal{M} \left(\alpha_0(\mu_I) - \alpha_s(Q) + \mathcal{O}(\alpha_s^2) \right) \sum_{i<j} (-\vec{T}_i \cdot \vec{T}_j) \, c_V^{(ij)} . \tag{5}$$

The above expression states that NP corrections to multi-jet event shapes depend on the same parameter $\alpha_0(\mu_I)$ encountered for two-jet shapes. Moreover, they depend in a non-trivial way on the colour of the underlying hard event through the correlation matrices $\vec{T}_i \cdot \vec{T}_j$ and on the event geometry (the angles between the jets) through the calculable coefficients $c_V^{(ij)}$ [8].

The simplest environment in which the validity of eq. (5) can be tested is three-jet events. Here colour conservation ensures that the colour matrices $\vec{T}_i \cdot \vec{T}_j$ are in fact proportional to the identity, thus simplifying considerably both the PT and the NP analysis.

2 Results for three-jet event shapes in e^+e^- annihilation

Two three-jet event shapes have been studied in e^+e^- annihilation, the D-parameter [9] and the thrust minor T_m [10]. Both variables are small when the three hard jets are in a near-to-planar configuration, and measure radiation outside the event plane.

We present here the first ever comparison of theoretical predictions for D and T_m differential distributions and existing data provided by the ALEPH collaboration [11]. Theoretical predictions are at the state-of-the-art level, that is NLL resummation matched to the NLO

calculation obtained with NLOJET++ [12], and leading $1/Q$ NP corrections computed with the dispersive method [9, 10]. Events with three separated jets are selected by requiring the three-jet resolution parameter y_3 in the Durham algorithm to be larger than $y_{\rm cut}$. It is then clear that different values of $y_{\rm cut}$ correspond to different event geometries.

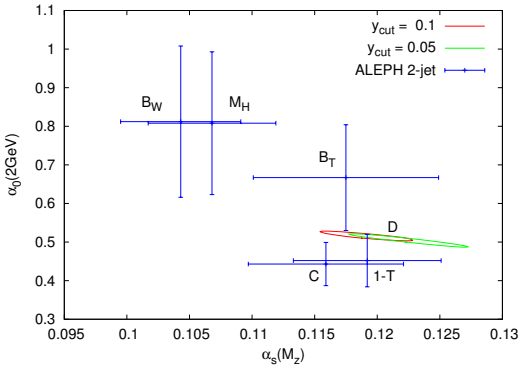

Figure 1: Contour plots in the α_s-α_0 plane for the D-parameter differential distributions corresponding to two different values of $y_{\rm cut}$.

Figure 1 shows the result of a simultaneous fit of $\alpha_s(M_Z)$ and $\alpha_0(\mu_I = 2\text{GeV})$ for the D-parameter distribution at $Q = M_Z$ corresponding to $y_{\rm cut} = 0.1$ and $y_{\rm cut} = 0.05$. The 1-σ contour plots in the α_s-α_0 plane are plotted together with results for other distributions of two-jet event shapes. There is a remarkable consistency among the various distributions, thus strongly supporting the idea that universality of $1/Q$ power corrections holds also for three-jet variables. This leads to the non-trivial implication that leading power corrections are indeed sensitive to the colour and the geometry of the hard underlying event, and moreover this dependence is the one predicted by eq. (5).

The comparison to data is less satisfactory for T_m, as can be seen from Fig. 2. There one notices a discrepancy between theory and data at large values of T_m. To track down the origin of the problem, one can look at hadronisation corrections produced by MC programs, defined as the ratio of the MC results at hadron and parton level. From the plots in [11] one can see that hadronisation corrections for the D-parameter are always larger than one, corresponding to a positive shift, consistent with our predictions. On the contrary, hadronisation corrections for T_m become smaller than one at large T_m, a feature that will never be predicted by a model based on a single dressed gluon emission from a three hard parton system. This issue is present also in the heavy-jet mass and wide-jet broadening distributions, and requires further theoretical investigation.

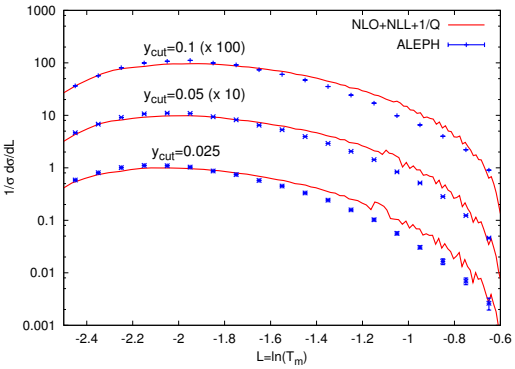

Figure 2: Theoretical predictions for T_m distribution plotted against ALEPH data for three different values of $y_{\rm cut}$.

3 Extension to other hard processes

Observables that measure the out-of-event-plane radiation in three-jet events can be introduced also in other hard processes.

In DIS two observables have been already measured. One is a variant of T_m [13], where

all momenta are in the Breit frame, and the event plane is formed by the virtual photon direction and the thrust major axis, defined as the direction that maximises the projection of transverse momenta. Differential T_m distributions have been measured both by the H1 [14] and ZEUS collaboration [15], and fits of experimental data are currently in progress. The other observable is the distribution in the transverse energy correlation $E_T E_T C(\chi)$, defined as [16]

$$E_T E_T C(\chi) = \sum_{i,j} p_{ti} p_{tj} \delta(\chi - (\pi - |\phi_i - \phi_j|)) \,. \tag{6}$$

The interesting features of the $E_T E_T C(\chi)$ distribution are that it approaches a constant for small χ and that it has fractional power corrections.

In hadron-hadron collisions one can consider for instance the production of a Z boson q in association with a hard jet $p_{\rm jet}$. The event plane is determined by the beam and the Z direction, and one can study [17]

$$T_m = \sum_i \frac{|\vec{p}_{ti} \times \vec{q}_t|}{p_{t,\rm jet} q_t} \, \Theta(\eta_0 - |\eta_i|) \,, \tag{7}$$

where the sum is extended to all hadrons not too close to the beam pipe, and the normalisation is fixed so as to cancel systematic uncertainties in the jet energy scale. In order to compare data with existing predictions, η_0 should be taken as large as is experimentally possible. The interest in this variable is that its distribution can take large corrections from the underlying event, thus making it a useful tool to tune MC models of minimum bias and multiple hard collisions. We look forward to experimental investigations in this direction.

Acknowledgements

Special thanks go to Giulia Zanderighi, for many years of fruitful collaboration on this subject. I also thank the organisers, in particular those of the Hadronic Final State session, for the pleasant and stimulating atmosphere they were able to create during the Workshop.

References

[1] Slides:
`http://indico.cern.ch/contributionDisplay.py?contribId=180&sessionId=6&confId=9499`
[2] S. Bethke, J. Phys. G **26** R27 (2000).
[3] M. Dasgupta and G. P. Salam, J. Phys. G **30** R143 (2004).
[4] B. R. Webber, arXiv:hep-ph/9411384 (1994), and references therein.
[5] Y. L. Dokshitzer, G. Marchesini and B. R. Webber, Nucl. Phys. B **469** 93 (1996).
[6] S. Catani, G. Marchesini and B. R. Webber, Nucl. Phys. B **349** 63 (1991).
[7] Y. L. Dokshitzer, A. Lucenti, G. Marchesini and G. P. Salam, JHEP **9805** 003 (1998).
[8] A. Banfi, arXiv:hep-ph/0605125 (2006).
[9] A. Banfi, Y. L. Dokshitzer, G. Marchesini and G. Zanderighi, JHEP **0105** 040 (2001).
[10] A. Banfi, Y. L. Dokshitzer, G. Marchesini and G. Zanderighi, Phys. Lett. B **508** 269 (2001).
[11] http://aleph.web.cern.ch/aleph/QCD/dat/91/lep1.html.
[12] Z. Nagy and Z. Trocsanyi, Phys. Rev. D **59** 014020 (1999) [Erratum-ibid. D **62** 099902 (2000)].
[13] A. Banfi, G. Marchesini, G. Smye and G. Zanderighi, JHEP **0111** 066 (2001).
[14] T. Kluge, Eur. Phys. J. C **33** S416 (2004); arXiv:hep-ex/0606053 (2006).
[15] S. Chekanov *et al.* [ZEUS Collaboration], Nucl. Phys. B **767** 1 (2007).
[16] A. Banfi, G. Marchesini and G. Smye, JHEP **0204** 024 (2002).
[17] A. Banfi, G. Marchesini, G. Smye and G. Zanderighi, JHEP **0108** 047 (2001).

First Observation of (Anti)Deuterons in DIS

S. Chekanov

For the ZEUS Collaboration

DESY Laboratory, 22607, Hamburg, Germany.
On leave from the HEP division, Argonne National Laboratory,
9700 S.Cass Avenue, Argonne, IL 60439, USA
E-mail: chekanov@mail.desy.de

First observation of (anti)deuterons in deep inelastic ep scattering (DIS) measured with the ZEUS detector at HERA is reported. The production rate of deuterons is higher than that of antideuterons. However, no asymmetry in the production rate of protons and antiprotons was found. The (anti)deuteron yield is approximately three orders of magnitude smaller than that of (anti)protons, which is consistent with the world measurements.

1 Introduction

Deuterons (d) are loosely bound states whose production in high energy collisions can hardly be accommodated in the standard fragmentation models. The measurements of such particles may provide an important information on the structure of fragmentation region [2] and on the formation of multiquark states [3].

In collisions involving elementary particles, several measurements have been performed in order to understand the production of $d(\bar{d})$. The cross section of $\bar{d}$ in $e^+e^- \to q\bar{q}$ collisions [4] is lower than that measured in hadronic $\Upsilon(1S)$ and $\Upsilon(2S)$ decays, and disagrees with the predictions based on the LUND string model [5]. The $(\bar{d})$ rate in $e^+e^- \to q\bar{q}$ is also lower than that in hadronic (pA [6], pp [7]) and in γp collisions at HERA [8], but higher than that in nucleus-nucleus (AA) collisions [9].

According to the coalescence model [2] developed for heavy-ion collisions, the d rate is determined by the overlap between the wave function of a proton, p, and a neutron, n, with the wave function of a d. The d cross section is the product of single-particle cross sections for p and n, with a coefficient of proportionality, B_2, reflecting the spatial size of the fragmentation region emitting the particles.

Unlike studies in AA, Ap and pp, all previous measurements in collisions involving elementary particles have been performed for $\bar{d}$, since the reconstruction of d requires a careful separation of such states from particles produced in interactions of colliding beams with residual gas in the beam pipe and secondary interactions of particles on detector material. The deep inelastic scattering (DIS) events, which are characterised by the presence of a scattered electron in the final state, provide an ideal environment for studies of d, since the background from non-ep interactions is minimal. In addition, during the 1996-2000 data taking, the ZEUS detector had a small amount of inactive material between the interaction region and the central tracking detector (CTD). This material consisted of the central beam-pipe and inner wall of the CTD, with the overall thickness of 2.9 mm of Al. This leads to a small absorption rate of $\bar{d}$, as well as to a small contribution from secondary deuterons.

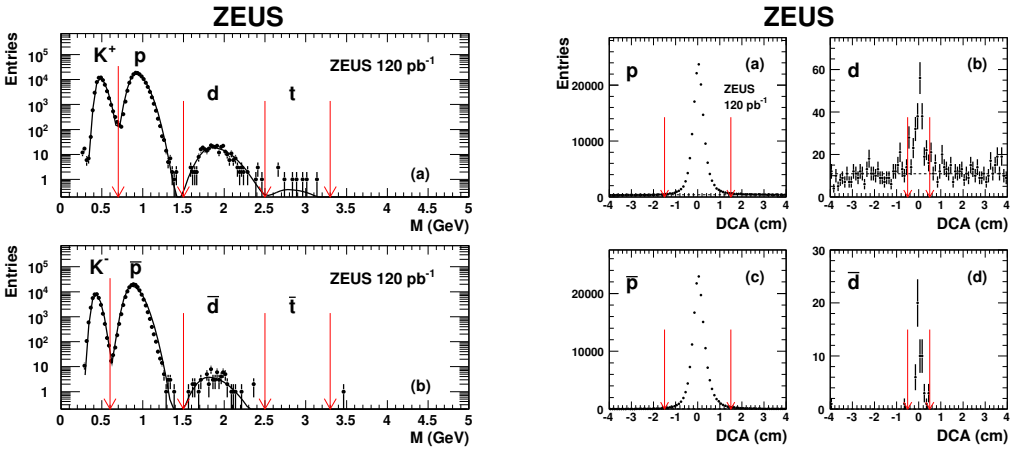

Figure 1. Left: The mass spectra reconstructed using dE/dx for positive and negative particles. Right: The DCA distributions for: (a)-(b) particles and (c)-(d) antiparticles.

The data sample used in the analysis corresponds to an integrated luminosity of 120 pb^{-1} taken between 1996 and 2000 with the ZEUS detector at HERA. After a DIS selection, the average Q^2 for the data sample was about 10 GeV^2. The particle identification was performed using the dE/dx measurement. The masses, shown in Fig. 1(left), were calculated from the measured track momentum and energy loss using the Bethe-Bloch formula.

To identify particles produced in ep collisions, the distance of closest approach (DCA) of the track to the beam spot in the transverse plane was used, since particles originating from the primary ep collisions feature small values of $|DCA|$. The DCA distribution after the mass cuts and an additional cut on the distance, ΔZ, of the Z-component of the track helix to the primary vertex, is shown in Fig. 1 (right). The number of particles produced in ep was assessed from the DCA distribution by using a side-band background subtraction. The numbers of d and $\bar{d}$ after the side-band background subtraction were 177 ± 17 and 53 ± 7, respectively. This difference was found to be unlikely related to the CTD efficiency, which usually leads to a larger number of negative tracks compared to positive ones: For example, the number of reconstructed $p(\bar{p})$ in the data after the DCA side-band background subtraction was 1.52×10^5 (1.62×10^5). Such $p - \bar{p}$ symmetry is fully accounted for by known difference in the tracking efficiency for positive and negative tracks.

Several sources of background processes for the d sample were considered [10]: events due to interactions of the incoming proton (or electron) beam with residual gas in the beam pipe (termed beam-gas interactions) and secondary interactions of particles on material between the interaction point and the central tracking detector. Extensive checks have been performed to exclude the first source. In particular, a special event selection was used for non-colliding electron and proton bunches. It was found that, after the DIS event selection, a contribution from the beam-gas events is unlikely.

Even for a clean DIS sample, d can still be produced by secondary interactions of particles on inactive material. One possible source for d is the reaction $N + N \to d + \pi^+$, where one nucleon, N, is produced by ep collisions, while the second one comes from inactive material in front of the CTD. Secondary d can also be produced in the pickup reaction $p + n \to d$ by primary nucleon interacting in the surrounding material. Checks for such sources of

background were either negative or not conclusive due to insufficient information on the production cross section of the pickup process. In particular, a check was done using the HERAII data collected with the ZEUS detector equipped with a vertex detector. For the dE/dx measurement, this additional detector increased the overall material between the interaction point and the CTD by a factor three. As expected, the production rate of d has significantly increased due to a stronger contribution from spallation processes. However, the rate of $\bar{d}$ after the DCA background subtraction was the same as for HERAI.

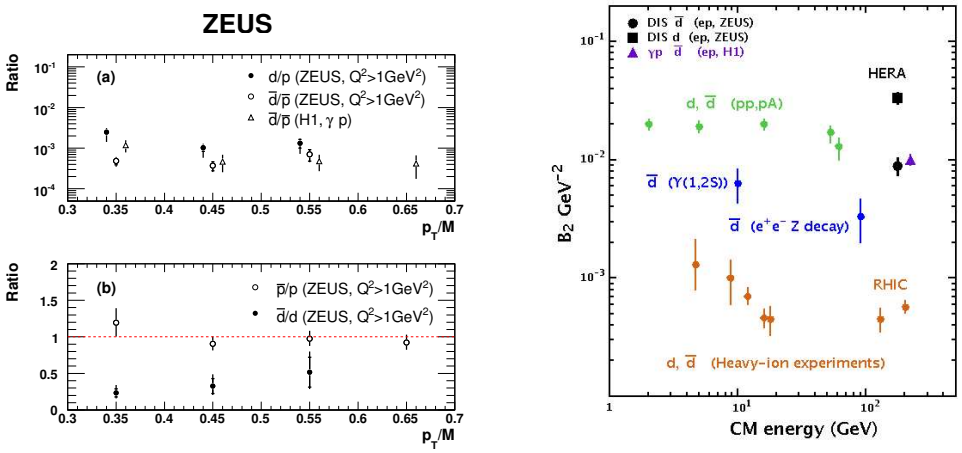

Figure 2. Left: d/p, $\bar{d}/\bar{p}$, $\bar{p}/p$ and $\bar{d}/d$ production ratios as a function of p_T/M. Right: Comparison of the B_2 values extracted from DIS with other world measurements.

The detector-corrected production ratios as a function of p_T/M are shown in Fig. 2(left). For the antiparticle ratio, there is a good agreement with the H1 published data for photoproduction [8], as well as with pp data [7]. The production rate of d is higher than that of $\bar{d}$ at low p_T. If (anti)deuterons are produced as a result of a coalescence of two (anti)nucleons, then one should expect that the $\bar{d}/d$ ratio is approximately equal to the $(\bar{p}/p)^2$ ratio for the same p_T per (anti)nucleon, assuming the same source radius for particles and antiparticles. In this case, one should expect $\bar{d}/d \simeq 1$, since the measured $\bar{p}/p$ ratio is consistent with unity. Under the assumption that secondary interactions do not produce an enhancement at $DCA = 0$ for the d case, the result would indicate that the relation between $\bar{d}/d$ and $(\bar{p}/p)^2$ expected from the coalescence model with the same B_2 for particles and antiparticles does not hold in the central fragmentation region of ep DIS collisions. In terms of the coalescence model, the d production volume in momentum space is larger than that for $\bar{d}$.

For collisions involving incoming baryon beams, there are several models [11] which predict $p-\bar{p}$ production asymmetry in the central rapidity region. The predicted asymmetry can be as high as 7% due to the presence of the incoming proton. As shown in Fig. 2(left), the experimental data for $p(\bar{p})$ are not sufficiently precise to confirm such expectations.

There are no predictions for the $d-\bar{d}$ asymmetry. It is possible that theoretical expectations for such compound states are different than those for the $p-\bar{p}$ asymmetry, since $d(\bar{d})$ are not contaminated by a large contribution from the standard baryons produced in quarks and gluon fragmentation.

The production of $d(\bar{d})$ was studied in terms of the coalescence model. The B_2 values

extracted in the region $0.3 < p_T/M < 0.7$ are shown in Figure 2(right). While the measurement of B_2 has larger experimental errors than those in the studies of the production asymmetries, it is still seen that B_2 for d tends to be higher than that for $\bar{d}$. The values of B_2 for $\bar{d}$ are in agreement with the measurements in photoproduction [8], but disagree with the B_2 measured in e^+e^- annihilation [4] at the Z resonance. In contrast to heavy-ion collisions, where B_2 strongly increases as a function of p_T due to an expanding source, the B_2 measured in ep does not strongly depend on p_T/M [10].

In summary, the first observation of (anti)deuterons in ep collisions in the DIS regime is presented. The yield of $d(\bar{d})$ is three orders of magnitude smaller than that of $p(\bar{p})$, which is in broad agreement with other experiments. The production rate of p is consistent with that of $\bar{p}$, while the production rate of d is higher than that for $\bar{d}$ for the same kinematic region.

References

[1] Slides:
`http://indico.cern.ch/contributionDisplay.py?contribId=229&sessionId=6&confId=9499` .

[2] S. Butler, C. Pearson, Phys. Rev. **129**, 836 (1963).

[3] M. Karliner, B. R. Webber, JHEP **0412**, 045 (2004).

[4] ARGUS Collaboration, H. Albrecht, et al., Phys. Lett. **B157**, 326 (1985);
ARGUS Collaboration, H. Albrecht, et al., Phys. Lett. **B236**, 102 (1990);
OPAL Collaboration, R. Akers, et al., Z. Phys. **C67**, 203 (1995);
ALEPH Collaboration, S. Schael, et al., Phys. Lett. **B639**, 16 (2006).

[5] G. Gustafson, J. Hakkinen, Z. Phys. **C61**, 683 (1994).

[6] IHEP-CERN Collaboration, F. Binon, et al., Phys. Lett. **B30**, 510 (1969);
Y. Antipov, et al., Phys. Lett. **B34**, 164 (1971);
J. Cronin, et al., Phys. Rev. **D11**, 3105 (1975).

[7] B. Alper, et al., Phys. Lett. **B46**, 265 (1973);
BRITISH-SCANDINAVIAN Collaboration, W. Gibson, et al., Nuovo Cim. Lett. **21**, 189 (1978);
V. Abramov, et al., Sov. J. Nucl. Phys. **45**, 845 (1987).

[8] H1 Collaboration, A. Aktas, et al., Eur. Phys. J. **C36**, 413 (2004).

[9] M. Aoki, et al., Phys. Rev. Lett. **69**, 2345 (1992);
NA52 (NEWMASS) Collaboration, G. Appelquist, et al., Phys. Lett. **B376**, 245 (1996);
STAR Collaboration, C. Alper, et al., Phys. Rev. Lett. **87**, 262301 (2001);
E802 Collaboration, L. Ahle, et al., Phys. Rev. **C57**, 1416 (1998);
NA44 Collaboration, I. Bearden, et al., Eur. Phys. J. **C23**, 237 (2002);
PHENIX Collaboration, S. S. Adler, et al., Phys. Rev. Lett. **94**, 122302 (2005).

[10] ZEUS Collaboration, S. Chekanov, et al., (2007). DESY-07-070, hep-ex/0705.3770.

[11] B. Kopeliovich, B. Povh, Z. Phys. **C75**, 693 (1997);
B. Kopeliovich, B. Povh, Phys. Lett. **B446**, 321 (1999);
G. Garvey, B. Z. Kopeliovich, B. Povh, Comments Mod. Phys. **A2**, 47 (2001);
S. Chekanov, Eur. Phys. J. **C44**, 367 (2005);
F. Bopp, Y. Shabelski, Phys. Atom. Nucl. **68**, 2093 (2005).

Search for Baryonic Resonances Decaying to $\Xi\pi$ in Deep-Inelastic Scattering at HERA

Marc Del Degan

ETH Zürich - Institut für Teilchenphysik
Schafmattstr. 20 - Switzerland
on behalf of the H1 Collaboration

A search for narrow baryonic resonances decaying into $\Xi^-\pi^-$ or $\Xi^-\pi^+$ and their antiparticles is carried out with the H1 detector using deep inelastic scattering events at HERA in the range of negative photon four-momentum transfer squared $2 < Q^2 < 100\,\mathrm{GeV}^2$. No signal for a new baryonic state in the mass range $1600 - 2300\,\mathrm{MeV}$ is observed in either the doubly charged or the neutral decay channels. The known baryon $\Xi(1530)^0$ is observed through its decay mode into $\Xi^-\pi^+$. Mass/dependent upper limits are given on the ratio of the production rates of new baryonic states, such as the hypothetical pentaquark states Ξ_{5q}^{--} or Ξ_{5q}^{0}, relative to the $\Xi(1530)^0$ baryon state.

1 Introduction

Various theoretical approaches [2, 3, 4] based on Quantum Chromodynamics predict the existence of exotic baryonic states composed of four valence quarks and an anti-quark, commonly known as "pentaquarks". Such states are expected to form a flavour anti-decuplet and are not explicitly forbidden within the Standard Model.

Several experiments have reported evidence for a narrow resonance with a mass around $1540\,\mathrm{MeV}$ decaying into nK^+ and pK_S^0 final states [5]. Such a state could be interpreted as an exotic strange pentaquark with a minimal quark content of $uudd\bar{s}$, lying in the apex of the spin 1/2 (or 3/2) anti-decuplet. On the other hand, a number of other experiments [5], including the H1 experiment [6], have reported non-observation of the same state.

Searches for other members of this anti-decuplet are of interest, in particular searches for the doubly strange Ξ_{5q}^{--} ($ddss\bar{u}$) and Ξ_{5q}^{+} ($uuss\bar{d}$) states, which are also manifestly exotic. The NA49 collaboration [7] at the SPS reported the observation of two baryonic resonances in fixed targed proton-proton collisions at the centre of mass energy $\sqrt{s} = 17.2\,\mathrm{GeV}$, with masses of $1862 \pm 2\,\mathrm{MeV}$ and $1864 \pm 5\,\mathrm{MeV}$, and with widths below the mass resolution of $18\,\mathrm{MeV}$. These states can be interpreted as the Ξ_{5q}^{--} ($S = -2$, $I_3 = -3/2$) and the Ξ_{5q}^{0} ($S = -2$, $I_3 = +1/2$) members of the isospin 3/2 quartet $\Xi_{3/2}$ in the anti-decuplet. These findings have not been confirmed by several other experiments (see for example [8]).

The search presented here is performed using data taken with the H1 detector at HERA. The Ξ^- particles [a] are identified through their decay into $\Lambda\pi^-$. The established baryon $\Xi(1530)^0$ [9] is observed through its decay mode $\Xi(1530)^0 \to \Xi^-\pi^+$.

2 Selection of DIS Events

The data analysed corresponding to an integrated luminosity of $\mathcal{L} = 101\,\mathrm{pb}^{-1}$ and are taken in the years 1996/1997 and 1999/2000. During this time HERA collided electrons [b]

[a] Unless explicitly mentioned, the charge conjugate states are hereafter always implicitly included.
[b] Herein, the term "electron" is used generically to refer to both electrons and positrons.

at an energy of 27.6 GeV with protons at 820 GeV ($1996/1997, 24.8\,\mathrm{pb}^{-1}$) and 920 GeV ($1999/2000, 75.7\,\mathrm{pb}^{-1}$).

The negative four momentum transfer squared Q^2 of the exchanged virtual photon and the inelasticity y as reconstructed from the scattered electron are restricted to the ranges $2 < Q^2 < 100\,\mathrm{GeV}^2$ and $0.05 < y < 0.7$.

3 Mass Spectra

The hypothetical doubly charged X^{--} and the neutral X^0 baryon states are identified by complete reconstruction of their respective decay chains through Ξ^- and Λ baryons into pions and protons, according to

$$X^{--} \rightarrow \Xi^-\pi^- \rightarrow [\Lambda\pi^-]\pi^- \rightarrow [(p\pi^-)\pi^-]\pi^- \quad (1)$$

$$X^{0} \rightarrow \Xi^-\pi^+ \rightarrow [\Lambda\pi^-]\pi^+ \rightarrow [(p\pi^-)\pi^-]\pi^+ . \quad (2)$$

In the first step, Λ baryons are identified by their charged decay mode, $\Lambda \rightarrow p\pi^-$, using pairs of oppositely charged tracks. The track with the higher momentum is assigned the proton mass. The particles are fitted to a common vertex [10] and Λ candidates are retained by applying weak kinematic selection criteria. In the second step, Ξ^- candidates are formed by fitting each of the Λ candidates with a negatively charged track assumed to be a pion to a common vertex and applying additional selection criteria. The invariant mass spectra $M(\Lambda\pi^-)$ and $M(\bar{\Lambda}\pi^+)$ of all selected Ξ^- candidates are shown in figure 1. In the last step, $X^{--/0}$ baryon candidates are formed by combining each Ξ^- candidate with one additional track, assumed to be a pion and originating at the primary vertex.

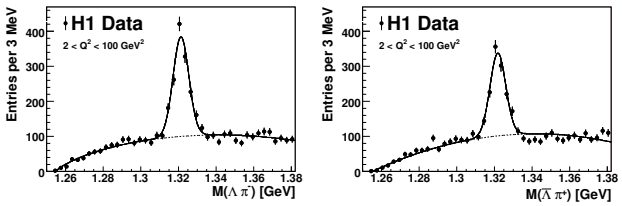

Figure 1: The invariant mass spectra for a) $\Lambda\pi^-$ and b) $\overline{\Lambda}\pi^+$ particle combinations. The solid lines show the result of a fit to the data using a Gaussian function for the Ξ^- signal and a background function as defined in equation 3 (with m_Ξ replaced accordingly by m_Λ), while the dashed lines indicate the background function only.

The resulting mass spectra for the X^0 and the X^{--} are shown in the upper part of figure 2. In the neutral spectra the signal of the well known $\Xi(1530)^0$ state is observed.

A simultaneous fit of the X^0 and the X^{--} mass spectra is performed using a function F, that contains a gaussian G for the signal $\Xi(1530)^0$ baryon and a function B for the background shape, according to

$$F = G + (1 + P_0)B; \quad B(M) = P_1(M - m_\Xi - m_\pi)^{P_2} \times (1 + P_3 M + P_4 M^2). \quad (3)$$

Here, M denotes the $\Xi\pi$ invariant mass and m_Ξ and m_π the masses of the Ξ and the π, respectively. The normalisation, the central value and the width of the Gaussian function G as well as the parameters P_i are left free in the fit. P_0 represents the relative normalisation

of the neutral to the doubly charged combinations and is set to zero for the neutral combinations. The fit yields a total of $163 \pm 24\,(stat.)$ $\Xi(1530)^0$ baryons. The reconstructed mass of $1532 \pm 2\,(stat.)$ MeV is consistent with the nominal value [9]. The measured width of $9.4 \pm 1.5(stat.)$ MeV is in agreement with the value obtained from the detector simulation.

4 Limit Calculation

No signal of a new baryonic state is observed above the $\Xi(1530)^0$ mass in either the X^0 or the X^{--} mass spectra. The resonance search can also be performed relative to the observed signal of the known $\Xi(1530)^0$ baryon, using the ratio R, which is defined as

$$R(M) = \frac{N^{res}(M,q)}{N(1530,0)} \times \frac{\epsilon(1530,0)}{\epsilon(M,q)}, \tag{4}$$

where $N(1530,0)$ represents the number of observed $\Xi(1530)^0 \rightarrow \Xi^-\pi^+$ and their antiparticle decays. $N^{res}(M,q)$, which describes the estimated number of resonance decays depending on the mass M and the charge q of the final state, is derived from the difference between the observed spectra and the expected background contribution. The mass distribution of the hypothetical signal is assumed to be a gaussian with mean M and mass-dependent width $\sigma(M)$ (obtained from Monte Carlo simulation) corresponding to the experimental mass resolution. The ratio of efficiencies in equation 4 compensates for the small difference in the reconstruction efficiencies of the $\Xi(1530)^0$ baryon and the hypothetical baryon state.

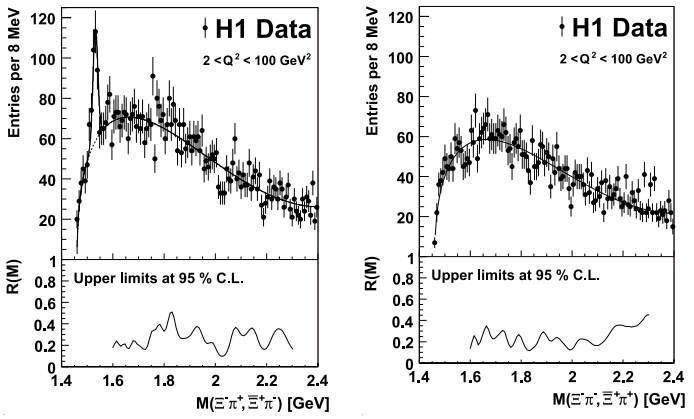

Figure 2: The invariant mass spectrum for the neutral and doubly charged combinations (upper part). The solid line shows the result of a fit to the data using the function defined in the text. The lower part shows the 95% C.L. upper limit on the ratio $R(M)$ as a function of the mass M, as defined in equation 4.

In the ratio $R(M)$ most systematic effects will cancel. This makes it insensitive to detector effects and thus provides a robust quantity for setting upper limits on the production of new narrow baryonic resonances decaying to $\Xi^-\pi^\pm$ in the mass range $1600-2300$ MeV. A mass-dependent upper limit at the 95 % confidence level (C.L.) on the ratio $R(M)$ is obtained from the observed invariant mass spectra using a modified frequentist approach based on likelihood ratios [11] analogous to the one applied in [6]. The method takes into account the statistical and systematic uncertainties in the number of signal events and background combinations.

The final results of the limit calculations are quoted for the kinematic region $2 < Q^2 < 100\,\mathrm{GeV}^2$ and $0.05 < y < 0.7$, for $p_\mathrm{T}(\Xi\pi) > 1\,\mathrm{GeV}$ and $|\eta(\Xi\pi)| < 1.5$. It is assumed that new resonances are produced by a mechanism similar to that of the known $J = 3/2$ baryons, that they decay into $\Xi\pi$ with a 100 % branching ratio, and that their natural widths are below the experimental resolution.

In the lower part of figure 2 the 95 % C.L. upper limit on the ratio $R(M)$ is presented as a function of the mass M. The non-observation of a resonance state in the mass range $1600 - 2300\,\mathrm{MeV}$ limits the production rate of a hypothetical Ξ_{5q}^{--} pentaquark to $12 - 45\,\%$ of the $\Xi(1530)^0$ production rate at the 95 % C.L., depending on the $(\Xi\pi)$-mass.

Furthermore, no signal is observed in the neutral invariant mass spectrum in the mass range $1600 - 2300\,\mathrm{MeV}$, above the $\Xi(1530)^0$ baryon, limiting the production rate of a hypothetical Ξ_{5q}^{0} pentaquark state to less than $10-50\,\%$ of that of the $\Xi(1530)^0$ baryon, depending on the $(\Xi\pi)$-mass.

5 Conclusions

A search for new narrow baryonic resonances decaying into $\Xi^-\pi^-$ and $\Xi^-\pi^+$ and their charge conjugate states is performed with the H1 detector using a DIS data sample. While there is a clear signal from the established $\Xi(1530)^0$ baryon, there are no indications of any new baryonic state decaying into $\Xi\pi$ in the mass range $1600 - 2300\,\mathrm{MeV}$. Thus H1 can not confirm the signal reported by the NA49 collaboration. Mass-dependent upper limits at the 95 % C.L. are set on the production ratio of hypothetical states, such as Ξ_{5q}^{--} and Ξ_{5q}^{0}, to the total number of observed $\Xi(1530)^0$ baryons. These limits are comparable to those measured by the ZEUS Collaboration [12].

References

[1] Slides:
`http://indico.cern.ch/contributionDisplay.py?contribId=230&sessionId=6&confId=9499`

[2] D. Diakonov, V. Petrov and M. V. Polyakov, Z. Phys. A **359** (1997) 305.

[3] R. L. Jaffe and F. Wilczek, Phys. Rev. Lett. **91** (2003) 232003 for a review on pentaquark phenomenology see R. L. Jaffe, Phys. Rept. **409** (2005) 1.

[4] M. Karliner and H. J. Lipkin, Phys. Lett. B **575** (2003) 249.

[5] For a review on the experimental search for pentaquark states, see
K. H. Hicks, Prog. Part. Nucl. Phys. **55** (2005) 647.

[6] A. Aktas *et al.* [H1 Collaboration], Phys. Lett. B **639** (2006) 202.

[7] C. Alt *et al.* [NA49 Collaboration], Phys. Rev. Lett. **92** (2004) 042003.

[8] M. I. Adamovich *et al.* [WA89 Collaboration], Phys. Rev. C **70** (2004) 022201.

[9] W. M. Yao *et al.* [Particle Data Group], J. Phys. G **33**, 1 (2006).

[10] R. Luchsinger and C. Grab, Comput. Phys. Commun. **76** (1993) 263.

[11] T. Junk, Nucl. Instrum. Meth. A **434** (1999) 435.

[12] S. Chekanov *et al.* [ZEUS Collaboration], Phys. Lett. B **610** (2005) 212.

Pentaquark Search at CLAS

Patrizia Rossi
on behalf of the CLAS Collaboration

Laboratori Nazionali di Frascati - INFN
Via Enrico Fermi 40 - 00044 Frascati (Italy)
e-mail:patrizia.rossi@lnf.infn.it

In 2004 a second-generation experimental program has been undertaken at Jefferson Laboratory (JLab), to try to find a definite answer to whether the Θ^+ and other 5-quark baryons exist. Here the results of CLAS high-statistics experiments are reported.

1 Introduction

Quantum Chromodynamics is the underlying theory of the strong interaction but its realization in hadronic physics is not completely understood. In fact, there is no explanation why the observed hadrons combine only in two colorless configurations: mesons ($q\bar{q}$) and baryons (qqq). Exotics, i.e. particles with more complex quark configurations, have been proposed since the early 70's. In 1997 an antidecuplet of 5-quarks baryons with as lowest mass member an isosinglet state, the Θ^+, with quark configuration ($uudd\bar{s}$) giving S=+1, mass $\sim$ 1.54 GeV and width $\sim$ 15 MeV was predicted [2].
Experimental evidence for the Θ^+, was reported for the first time by the LEPS Collaboration [3]. Evidence for an additional narrow exotic S=-2 state, called the Ξ^{--} with mass $\sim$ 1862 MeV was reported by the NA49 Collaboration [4]. Immediately after the LEPS announcement, several other groups analyzed old data, and found the exotic baryon Θ^+ in both pK^0 and nK^+ decay channels [5, 6, 7, 8, 9, 10, 11, 12, 13]. There were questions about some of these observations but given the weight of positive supporting evidence reported, the Particle Data Group assigned 3-star status to the Θ^+ in its 2004 edition. Nevertheless, the relatively small statistical significance of every measurement, the discrepancy in mass determination, and above all, the null results reported by a similar number of high statistics and high energy experiments [14] have driven a second-generation experimental program in different laboratories, among those JLab.

2 The CLAS program at JLab

During the year 2004-2005, new dedicated experiments have been performed in Hall B at Jefferson Laboratory (JLab) using the CLAS detector [15] with the aim of improving the statistical accuracy, by at least one order of magnitude, of the two positive published results [6, 7] on the Θ^+ pentaquark obtained from existing CLAS data, and to look for the Ξ^{--} state. Detector calibration and data quality checks have been carefully undertaken in order to achieve resolutions on the order of a few MeV for calculated invariant masses and on the order of $\sim$ 10 MeV for missing masses.

3 G10 experiment: search for pertaquarks using a deuteron target

This experiment ran using a 24 cm long liquid deuterium target and tagged photons in the energy range (0.8 - 3.59) GeV. An integrated luminosity of 50 pb^{-1} was achieved.

3.0.1 *The $\gamma d \to pK^-\Theta^+$ reaction channel*

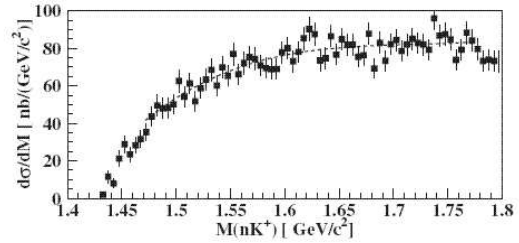

Figure 1: The cross section per mass bin of the $\gamma d \to pK^-\Theta^+$ reaction.

This reaction channel, with the Θ^+ decaying into K^+n, requires the detection of one proton, one K^+, and one K^-. The missing mass of the $\gamma d \to pK^-K^+X$ reaction was required to be within $\pm 3\sigma$ of the neutron mass and the missing momentum was required to be greater than 0.20 GeV/c in order to remove spectator neutrons. Events corresponding to ϕ-meson production were cut by requiring the K^+K^- mass to be above 1.06 GeV/c^2, and, events corresponding to the $\Lambda(1520)$ were cut by requiring 1.495 GeV/c^2 $< M(pK^-) <$ 1.545 GeV/c^2. The resulting invariant-mass spectrum of the nK^+ system, corrected for the CLAS detector acceptance and normalized by the luminosity, is shown in Fig. 1. These data show no evidence for a narrow peak near 1.54 GeV/c^2.

3.0.2 *The $\gamma d \to \Theta^+\Lambda$ reaction channel*

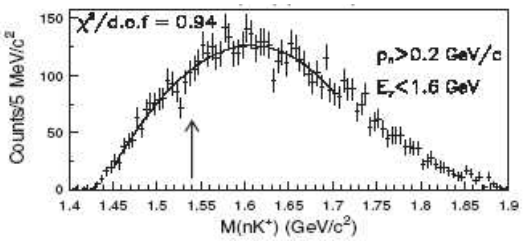

Figure 2: Invariant mass distribution of the nK^+ system for the $\gamma d \to \Lambda K^+ n$ reaction after the $E_\gamma < 1.6$ GeV and $p_n > 0.2$ GeV/c kinematical cuts were applied. The third-order polynomial fit used for the upper limit estimate is shown.

The $\gamma d \to \Theta^+\Lambda$ reaction channel has very interesting features: *i)* the strangeness content of the final state is well-defined thanks to the presence of the Λ particle which has strangeness $S = -1$; *ii)* the presence of only one K^+ and no K^- in the final state allows us to identify it without the need of cutting on competing channels ($\phi, \Lambda(1520)$), and *iii)* kinematical reflections in the NK invariant mass spectrum are excluded.
To analyze this channel, with the Θ^+ decaying into (K^+n), p, K, π were identified using momentum and time-of-flight information. After removing the background under the kaon mass peak due to p or π uncorrectly identified as K, exclusive $K^+n\pi^-p$ events were selected by computing the missing mass of the $K^+p\pi^-X$ system and choosing the events lying within $\pm 3\sigma$ around the neutron peak. The contribution of the Σ^- decaying weakly into $n\pi^-$ is removed after applying the Λ selection cut on the $p\pi^-$ invariant mass. After selecting the ΛnK^+ events, the Θ^+ signal was searched for in the invariant mass of the nK^+ system. Since the nK^+ mass spectrum did not show any evident structure, further kinematical cuts have been applied, based upon the indications in [16], in order to try to increase a possible Θ^+ signal over the non-resonant nK^+ background: *i)* non-spectator-neutron cut, and *ii)* photon-energy cut. Under these stringent kinematic conditions still no narrow peaks with statistical relevance were observed in the mass region around 1.54 GeV/c^2. The spectrum is shown in Fig. 2, where the kinematic requirements $p_n > 0.2$ GeV/c and $E_\gamma < 1.6$ GeV are applied.

3.1 G11 experiment: search for pentaquarks using a proton target

In this experiment data were taken using a 40 cm length liquid hydrogen target and photons in the energy range (1.6 - 3.8) GeV. An integrated luminosity of $\sim 70\ pb^{-1}$ was achieved.

3.1.1 The $\gamma p \to \bar{K}^0\Theta^+$ reaction channel

The exclusive reactions $\gamma p \to \bar{K}^0 K^+ n$ and $\gamma p \to \bar{K}^0 K^0 p$ were studied to look for evidence of the reaction $\gamma p \to \bar{K}^0\Theta^+$. The reactions have been isolated by detecting the K^+ and proton directly, the neutral kaon via its decay $K_s \to \pi^+\pi^-$, and the neutron or neutral kaon via the missing mass technique. Reactions involving hyperon decays which contribute to the same final states were removed in the analysis. The resulting nK^+ and pK^0 invariant mass distributions was found smooth and structureless. In particular, no evidence for a peak or an enhancement was observed at masses near 1540 MeV. For the reaction channel $\gamma p \to \bar{K}^0 K^+ n$ a comparison with the published results by the SAPHIR Collaboration [8] has been done using, in the analysis, the same cuts reported in Ref. [8]. The resulting mass distribution is shown in the inset of Fig. 3. It remains smooth and structureless.

3.1.2 The $\gamma p \to \Theta^{++} p$ reaction channel

The putative reaction $\gamma p \to K^-\Theta^{++} \to K^- p K^+$ was studied by the CLAS Collaboration in two ways: in the first case, three final state hadrons, p, K^- and K^+ were detected while in the second case only a pK^+ pair were required and the K^- was identified by missing mass reconstruction. After that, cuts were applied in the pK^- and K^+K^- mass spectra to eliminate the contribution of the $\Lambda(1520)$ and $\phi(1020)$, respectively. The pK^+ mass spectra after all cuts were applied didn't shown any evidence for any narrow structures that could be interpreted as a Θ^{++} resonance

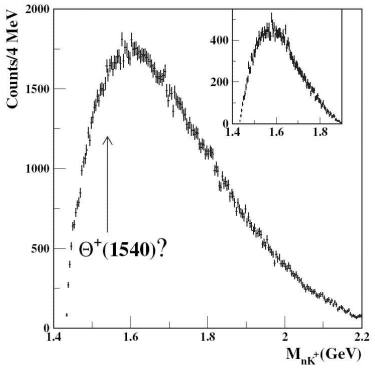

Figure 3: The nK^+ invariant mass distribution for $\gamma p \to \bar{K}^0 K^+ n$ after all cuts. The inset shows the nK^+ mass distribution with specific cuts to reproduce the SAPHIR analysis [8].

4 Cross section upper limit

Since no signal was found in any of the measured reactions, an upper limit for the Θ^+ and Θ^{++} production cross section was extracted. The NK invariant mass spectrum, acceptance corrected, was fit with the sum of a narrow Gaussian function and a polynomial that parameterize, respectively, the Θ^+ (Θ^{++}) contribution and a smooth background. The signal and background yields were then used to evaluate an upper limit at 95% confidence level using the Feldman-Cousins method [17]. For details of the followed procedure see Ref. [18, 19, 20, 21]. The final results are reported in Table 1.

5 Outlook and conclusions

In the year 2004 a comprehensive program to search for pentaquarks in high statistics and high resolution experiments has been started by the CLAS Collaboration at Jefferson Lab. No evidence for pentaquark signals has been found in the photoproduction channels studied so far. From these results, CLAS sets upper limits on photoproduction cross sections from proton and neutron targets on the order of a few nb or less. The outlook for the Θ^+ looks bleak, anyhow it seems that we have to wait a little bit more to put the last word on the pentaquark existence. In fact: *i)* the data are still contradictory (LEPS Collaboration has been able to reproduce a peak in a "repeat" measurement); *ii)* analysis, using higher statistics data, from some experiments that initially claimed the pentaquark, are still in progress (ZEUS, COSY); *iii)* some theories are able to explain the negative results obtained by CLAS [22, 23, 24]. In the meanwhile, the Particle Data Group assigned 1-star status to the Θ^+ in its 2006 edition.

Reaction	σ_{UL} (95% C.L.)
$\gamma n(p) \to pK^-\Theta^+$	< 3 nb
$\gamma d \to \Theta^+\Lambda$	< 5 nb
$\gamma p \to K^0\Theta^+$	< 1 nb
$\gamma p \to \Theta^{++}p$	< 0.15 nb

Table 1: Cross section upper limit at 95% C.L. for the measured reactions.

References

[1] Slides:
`http://indico.cern.ch/contributionDisplay.py?contribId=181&sessionId=6&confId=9499`

[2] D. Diakonv, V. Petrov, M.V. Polyakov, Z. Phys. **A359** 305 (1997).

[3] T. Nakano *et al.*, Phys. Rev. Lett. **91** 012002 (2003).

[4] C. Alt *et al.*, Phys. Rev. Lett. **92** 042003 (2004).

[5] V. Barmin *et al.*, Phys. Atom. Nucl. **66** 1715 (2003).

[6] S. Stepanyan *et al.*, Phys. Rev. Lett. **91** 252001 (2003).

[7] V. Koubarovsky *et al.*, Phys. Rev. Lett. **92** 032001 (2004).

[8] J. Barth *et al.*, Phys. Lett. **B572** 127 (2003).

[9] A. Airapetian *et al.*, Phys. Lett. **B585** 213 (2004).

[10] A.E. Asratyan, A.G. Dolgolenko, M.A. Kubantsev, Phys. Atom. Nucl. **67** 682 (2004).

[11] A. Aleev *et al.*, Phys.Atom.Nucl. **68** 974 (2005); Yad.Fiz. **68** 1012 (2005).

[12] M. Abdel-Bary *et al.*, Phys. Lett. **B595** 127 (2004).

[13] S. Chekanov *et al.*, Phys. Lett. **B591** 7 (2004).

[14] J.Z. Bai *et al.*, Phys.Rev. **D70** 012004 (2004). K.T. Knoepfle *et al.*, J.Phys. **G30** S1363 (2004); M.I. Adamovich *et al.*, Phys.Rev. **C70** 022201 (2004); C. Pinkeburg *et al.*, Eur. Phys. J. **C37** 91 (2004) ; BABAR, arXiv:hep-ex/0408064 (2004); Yu.M. Antipov *et al.*, Eur. Phys. J. **A21** 455 (2004); S. Schaet *et al.*, Phys. Lett. **B599** (2004); CDF, E690, LEP, Focus, HyperCP (QNP2004 conference presentation).

[15] B. Mecking *et al.*, Nucl. Inst. & Meth. **A503/3** 513 (2003).

[16] V. Guzey, Phys. Rev. **C69** 173 (2004).

[17] G.D. Feldman and R.D. Cousins, Phys. Rev. **D57** 3873 (2003).

[18] B. McKinnon *et al.*, Phys. Rev. Lett. **96** 212001 (2006).

[19] S. Niccolai *et al.*, Phys. Rev. Lett. **97** 032001 (2006).

[20] M. Battaglieri *et al.*, Phys. Rev. Lett. **96** 042001 (2006) ; R. De Vita *et al.*, Phys. Rev. **D74** 032001 (2006).

[21] V. Kubarovsky *et al.*, Phys. Rev. Lett. **97** 102001 (2006).

[22] S. I. Nam, A. Hosaka, H.-C. Kim, Phys. Lett. **B633** 483 (2006).

[23] V. Guzey, arXiv:hep-ph/0608129 (2006).

[24] M. Amarian, D. Diakonov, M. Poliakov, arXiv:hep-ex/0612150 (2006).

STAR Identified Particle Measurements at High Transverse Momentum in p+p $\sqrt{s} = 200$ GeV

Mark Heinz for the STAR Collaboration

Yale University, Physics Department, WNSL,
272 Whitney Ave, New Haven, CT 06520, USA

We present the STAR measurement of transverse momentum spectra at mid-rapidity for identified particles in $p+p$ collisions at $\sqrt{s} = 200$ GeV. These high statistics data are ideal for comparing to existing leading- and next-to-leading order (NLO) perturbative QCD calculations. Next-to-leading models have been successful in describing inclusive hadron production using parameterized fragmentation functions (FF) for quarks and gluons. However, in order to describe baryon spectra at NLO, knowledge of flavor separated FF is essential. Such FF have recently been parameterized using data by the OPAL experiment and allow for the first time to obtain good agreement between NLO and identified baryons from $p + p$ collisions.

1 Introduction

Perturbative QCD has proven to be successful in describing inclusive hadron production in elementary collisions. Within the theory's range of applicability, calculations at next-to-leading order (NLO) have produced accurate predictions for transverse momentum spectra of inclusive hadrons at different energy scales [2]. With the new high statistics proton-proton data at $\sqrt{s} = 200$ GeV collected by STAR, we can now extend the study to identified baryons and mesons to $p_T \sim$9 GeV/c. Perturbative QCD calculation apply the factorization ansatz to calculate hadron production and rely on three ingredients. The first part are the non-perturbative parton distribution functions (PDF) which are obtained by parameterizations of deep inelastic scattering data. They describe quantitatively how the partons share momentum within a nucleus. The second part, which is perturbatively calculable, consists of the parton cross-section amplitude evaluated to LO or NLO using Feynman diagrams. The third part consists of the non-perturbative Fragmentation functions (FF) obtained from $e^+ + e^-$ collider data using quark-tagging algorithms. These parameterized functions are sufficiently well known for fragmenting light quarks, but less well known for fragmenting gluons and heavy quarks. Recently, Kniehl, Kramer and Pötter (KKP) have shown that FF are universal between $e^+ + e^-$ and $p+p$ collisions [3]. At leading-order, we compare to string fragmentation models such as PYTHIA to investigate the dependence between hadrons and underlying parton-parton interactions [4]. In the string fragmentation approach the production of baryons is intimately related to di-quark production from strings. They then combine with a quark to produce a baryon. In NLO calculations, the accuracy of a given baryon cross-section is based on the knowledge of that specific baryon fragmentation function (FF) extracted $e^+ + e^-$ collisions.

2 Data Analysis

The present data were reconstructed using the STAR detector system which is described in more detail elsewhere [5]. The main detectors used in this analysis are the Time Projection

Chamber (TPC) and the Time of Flight detector (TOF). A total of 14 million non-singly diffractive (NSD) events were triggered with the STAR beam-beam counters (BBC) requiring two coincident charged tracks at forward rapidity ($3.3 < |\eta| < 5.0$). By simulation it was determined that the trigger measured 87% of the 30.0±3.5mb NSD cross-section. The offline primary vertex reconstruction was 76% efficient which lead to a total usable event sample of 7×10^6 events. Protons and pions in this analysis were identified using the TOF detector at p_T below 2.5 GeV/c and the TPC using the relativistic rise dE/dx at higher p_T. Details of both methods are described in [7, 8]. At $p_T \sim 3$ GeV/c the pion dE/dx is about 10-20% higher than that of kaons and protons due to the relativistic rise, resulting in a few standard deviations of seperation. The strange particles were identified from their weak decay to charged daughter particles. The following decay channels and the corresponding anti-particles were analyzed: $K^0_S \rightarrow \pi^+ + \pi^-$ (b.r. 68.6%), $\Lambda \rightarrow p + \pi^-$(b.r. 63.9%) . Particle identification of the daughters was achieved by requiring the TPC-measured dE/dx to fall within the 3σ-bands of the theoretical Bethe-Bloch parameterizations. Further background in the invariant mass was removed by applying topological cuts to the decay geometry.

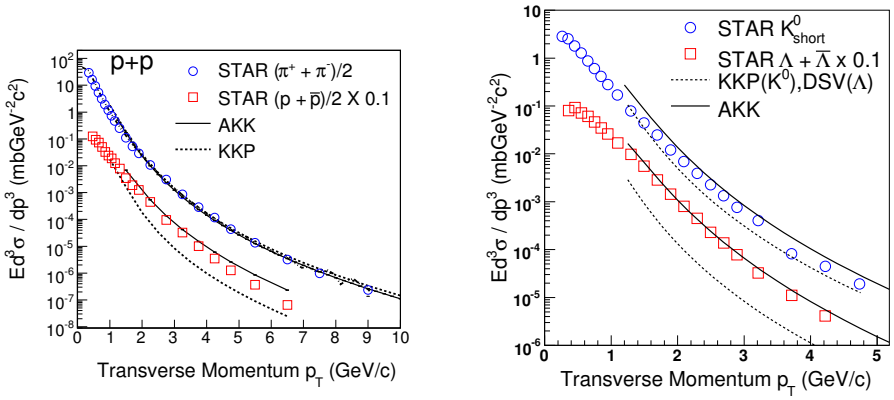

(a) (b)

Figure 1: (a)$(p + \bar{p})$ and $(\pi^+ + \pi^-)$ p_T-spectra at $|\mathbf{y}| < 0.5$ from NSD p+p at 200 GeV [9] (b) K^0_S and Λ p_T spectra at $|\mathbf{y}| < 0.5$ compared to NLO calculations using KKP, DSV and AKK fragmentation functions. [10]

3 Results

3.1 Comparison to next-to-leading order

In figure 1 we compare our transverse momentum spectra to recent next-to-leading order calculations using two different fragmentation functions (FF). The previous ones were by Kniehl-Kramer-Poetter (KKP) for pions, kaons and protons and from deFlorian-Stratmann-Vogelsang (DSV) for Λ [6, 11]. More recently Albino-Kramer-Kniehl (AKK) [12] have published FF based on the light quark-flavor tagged data from the OPAL Collaboration [13]. Clearly, these newer parameterizations improve the description of the baryon data

considerably. In order to achieve this agreement with the data, the initial gluon to Λ fragmentation function is determined by fixing it's shape to that of the proton, and then varying the normalization for the best fit. A scaling factor of 3 with respect to the proton is necessary to achieve agreement with STAR data. However, this modified FF is then tested by comparing to the Λ measurement from $p + \bar{p}$ at $\sqrt{s} = 630$ GeV and agrees well [12].

3.2 Baryon to meson ratios vs p_T

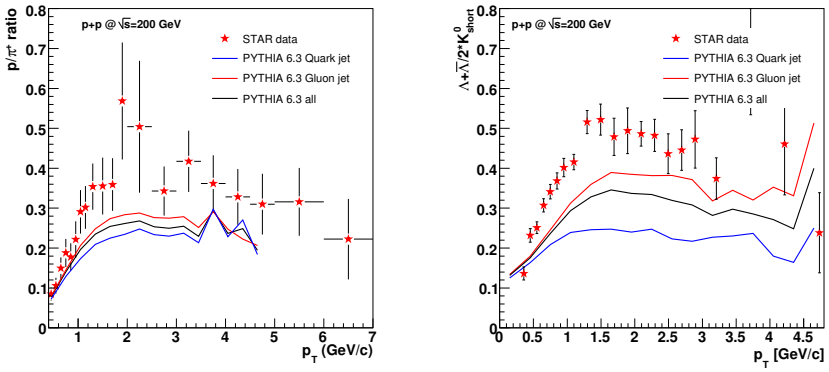

(a) (b)

Figure 2: (a) p/π ratio compared to PYTHIA for different event samples, (b) $(\Lambda + \overline{\Lambda})/2 \cdot \mathrm{K}^0_\mathrm{S}$ ratio compared to PYTHIA.

In order to further investigate the sensitivity of the baryon spectra to the fragmentation of gluons, we used a leading-order (LO) Monte Carlo simulator, PYTHIA. PYTHIA 6.3 generates events by using $2 \rightarrow 2$ LO parton processes plus additional leading-log showers and multiple interactions. We define a "Gluon-jet" event as one where the underlying partons are g-g or g-q and a "Quark-jet" event one where the underlying partons are q-q. According to the model default settings the $p + p$ events at our energy are dominated by gluon-jets (62%) with respect to quark-jets (38%). Figure 2 compares baryon-to-meson ratios to three different event types from PYTHIA. In both cases the overall ratio in the data is significantly larger at p_T ~1-3 GeV/c than the PYTHIA result. In addition, this shows that pure gluon jet events will produce a larger baryon-to-meson ratio than quark jet events.

3.3 Transverse mass (m_T) scaling

Universal transverse mass scaling of particle spectra was previously seen in $p+p$ collisions at lower ISR-energies [14]. We have compiled STAR identified particle spectra to investigate m_T-scaling. The particle spectra were arbitrarily normalized to pion spectra at $m_T = 1$ GeV. Interestingly we observe that a splitting occurs at ~2 GeV and that the meson spectra are harder than the baryon spectra. We compared this result to PYTHIA simulations scaled in the same manner. We again observe that gluon jets will fragment very differently into baryons and mesons than quark jets. For gluon jets, there is a clear shape difference between baryons and mesons consistent with the data. For quark jets, the shape difference is modified

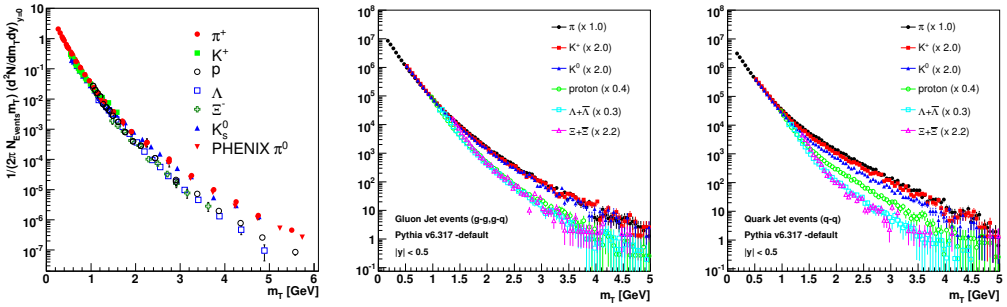

(a) (b) (c)

Figure 3: (a)Arbitrarily scaled m_T spectra for baryons and mesons from $p+p$ collisions at $\sqrt{s} = 200$ GeV. (b) Scaled m_T spectra for "Gluon-jet" events from PYTHIA. (c) Scaled m_T spectra for "Quark-jet" events from PYTHIA.

by an additional dependency on the mass of the produced particle. This may be a further indication that we observe dominance of gluon jets in $p+p$ collisions at RHIC energies.

4 Summary

We have shown that the theoretical description of identified baryons and mesons in $p+p$ collisions has recently improved thanks to new NLO calculations using light quark-flavor tagged fragmentation functions. Considerable uncertainties remain in the high-z (p_{hadron}/p_{parton}) range of the gluon FF for baryons. It appears that previous baryon-FF extracted from $e^+ + e^-$ data are inconsistent with STAR's $p+p$ data, indicating that RHIC is a valuable test of FF. Arbitrarily scaled m_T spectra for strange particles exhibit partial m_T scaling and confirm the dominance of gluon jets in $p+p$ and therefore the importance of understanding gluon fragmentation.

References

[1] Slides:
`http://indico.cern.ch/contributionDisplay.py?contribId=182&sessionId=6&confId=9499`
[2] M. van Leeuwen for the STAR Collaboration, *J. Phys. G: Nucl. Part. Phys.* **31** (2005) S881
[3] B. A. Kniehl, G. Kramer and B. Potter, *Nucl. Phys.* B **597**(2001) 337
[4] T. Sjostrand and P. Z. Skands, *Eur. Phys. J.* C **39**, (2005) 129
[5] K.H. Ackermann et al (STAR Collaboration), *Nucl. Instrum. Meth.* A**499** (2003) 624
[6] B. A. Kniehl, G. Kramer and B. Potter, *Nucl. Phys.* B **582**(2000) 514
[7] J. Adams et al. (STAR collaboration), *Phys. Lett.* B **616**, (2005) 8
[8] M. Shao (STAR collaboration), nucl-ex/0505026
[9] J. Adams et al. (STAR collaboration), *Phys. Lett.* B **637**, (2006) 161
[10] B. Abelev et al. (STAR collaboration), *Phys. Rev.* C **75**, (2007) 064901
[11] D. de Florian, M. Stratmann and W. Vogelsang, *Phys. Rev.* D **57**, (1998) 5811
[12] S. Albino et al., *Nucl. Phys.* B**734**, (2006) 50
[13] G. Abbiendi *et al.* [OPAL Collaboration], *Eur. Phys. J.* C **16**, (2000) 407
[14] G. Gatof and C.Y. Wong *Phys. Rev.* D **46**, (1992) 997

Hadronic Final States and Their Correlations in pp and Heavy Ion Collisions.

C.A. Ogilvie for the PHENIX Collaboration

Iowa State University, Ames, IA, USA

One striking observation from experiments at RHIC is the suppression of high-pt particles due to hard-scattered partons losing energy as they propagate through a dense quark-gluon plasma (QGP). The baseline information is single-particle and di-hadron distributions from p+p collisions. When measured in A+A collisions, these observables provide rich information on the QGP: how the properties of the jet are modified (fragmentation widths and yields), to how the QGP responds to a hard-parton depositing energy along its path.

1 Introduction

Heavy-ion physics has opened a rich new avenue to explore multibody QCD. By colliding two large nuclei at relativisitic speeds, sufficient energy is deposited into the central region to form a deconfined quark-gluon plasma (QGP). The plasma evolves collectively as a strongly interacting, near-thermalized fluid. These observations have led to a rich set of questions; what is the equation-of-state of a deconfined, multi-parton QCD plasma? and what are the dominant degrees-of-freedom of QGP fluid, e.g. quasi-resonances of interacting partons? ¿From a fundamental perspective the QGP is our first experimental access to the physics of multi-body non-Abelian systems. Also compared to conventional many-body systems interacting via photons, the complications due to self-interacting gluons will expand our knowledge of both general many-body physics as well as non-perturbative QCD.

We have reached a fascinating stage of our experimental endeavors: we are past the initial exploration of forming and identifying the plasma, but we are not yet at the stage where there is a certain, agreed-upon strategy as to how, for example, to determine the plasma's equation of state. The way forward is to increase our control and confidence in diagnostic probes of the plasma.

One promising probe is the passage of hard-scattered partons through the plasma just as it's being formed. As the two nuclei collide the partons within each nucleus have a well-measured, well-known probability to scatter with a high-momentum transfer, e.g. to produce two scattered partons approximately back-to-back each with a p_T above 5 GeV/c. These scattered partons travel through the nascent plasma. Hard-scattered colored partons strongly interact with the deconfined plasma and lose energy via a variety of suggested mechanisms, e.g., bremstrahlung radiation of gluons and elastic collisions with slower partons[1]. It is my goal in this talk[2] to provide an update from the PHENIX collaboration on where we stand in controling and to utilizinbg energy-loss to probe the properties of the plasma.

The PHENIX detector has been in operation since 2000 with two forward/backward muon spectrometer arms to measure quarkonia probes, and two mid-rapidity spectrometer arms to measure photons, π^0, electrons, charged hadrons, quarkonia, and other hadronic resonances. For more details on the PHENIX detector see the recent White paper summary[3].

2 Results

The spectra of high-pt hadrons from p+p collisions as measured by the experiments at RHIC have been compiled by D. d'Enterria[4]. NLO QCD calculations agree with this data very well (Fig. 1) which provides confidence that the baseline of high-pt probes is under control in p+p collisions.

The measured high-pt spectra from heavy-ion collisions is significantly reduced compared to that from p+p collisions[5], i.e. there are fewer high-pt hadrons in a heavy-ion collision. One way to plot these data is the ratio of spectra from heavy-ion collisions divided by the spectra from p+p collisions (normalized by the larger parton flux in the nuclear events). This ratio (R_{AA}) is shown in Fig. 2 for π^0, η, and direct photons. The Au+Au collisions are nearly head-on, i.e. the 10% of collisions that have the largest overlap between the incoming nuclei. Both the π^0 and the η spectra are suppressed by a factor of 5 compared to proton+proton collisions. In contrast direct-photons below 15 GeV are unsuppressed since they do not interact with the plasma. The hint of suppression at higher p_T may be due to p+n and n+n collisions in the nuclear case. The dominant feature that both π^0 and η are suppressed by the same amount supports the interpretation that high-pt partons lose energy as travel through the plasma. This is further supported by data from d+Au collisions where the hadronic spectra are not suppressed compared with p+p indicating that the suppression shown in Fig. 2 is not an initial-state effect.

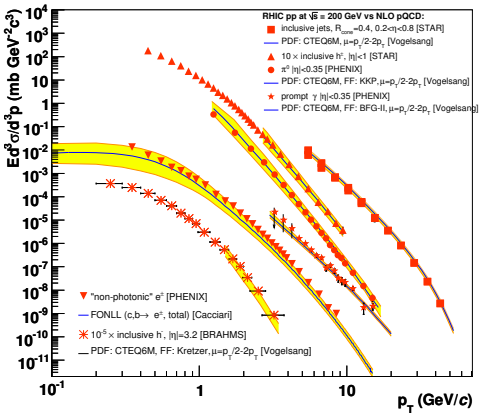

Figure 1: Compiled high-pt spectra from p+p collisions at RHIC and their comparison with NLO QCD calculations.[4]

If the energy lost by a high-momentum parton is radiated by bremstrahlung gluons then we should be able to observe the fate of this radiation. Calculations[6],[7] suggest the radiation is emitted at finite angles relative to the high-pt parton. As a baseline we have measured the yield of associated hadrons that are near in angle to a leading high-pt hadron from p+p and d+Au collisions and have extracted various jet-widths and fragmentation properties[8] [9]. We then compare this baseline to jet-structures in A+A collisions. As an example Fig. 3 shows the transverse momentum p_{out} of associated hadrons with respect to the axis defined by a high-pt π^0 for both p+p collisions and central Cu+Cu collisions. The p_{out} distibution is

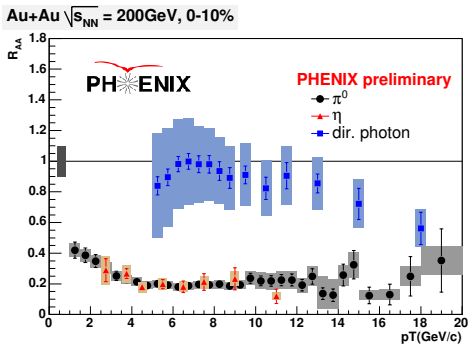

Figure 2: Ratio of the measured spectra of π^0, η, and direct photons from central Au+Au collisions divided by the spectra from p+p collisions.

broader in the heavy-ion data suggesting that the gluon radiation from the energy-loss eventually fragments and increases the yield of associated hadrons at finite angles.

The suppression of high-pt hadrons and the increased yield of associated hadrons at finite angles are two pieces of evidence that high-pt partons lose energy as they travel through the plasma. A complementary question is how does the plasma respond to the impact of a high-pt parton. To explore this we have measured the azimuthal distribution $\Delta\phi$ of associated hadrons with respect to angle defined by a leading high-pt hadron. An example is shown in Fig. 4 which contains the angular distribution of hadrons with $1 < p_T < 2.5$ GeV/c with respect to a trigger hadron between $2.5 < p_T < 4$ GeV/c[10] from central Au+Au collisions. The data shown as squares (black) are the original correlation while the data in circles (red) are after correcting for the underliying event which has an overall modulation due to the known elliptic flow. The near-side peak at $\Delta\phi \sim 0$ corresponds to hadrons from the fragmentation of the same high-pt parton. In p+p collisions the far-side peak is at $\Delta\phi \sim \pi$ which corresponds to the fragmentation of two back-to-back high-partons[8]. In striking contrast the central Au+Au data have a side peak approximately 1 radian away from the expected location of the far-side peak.

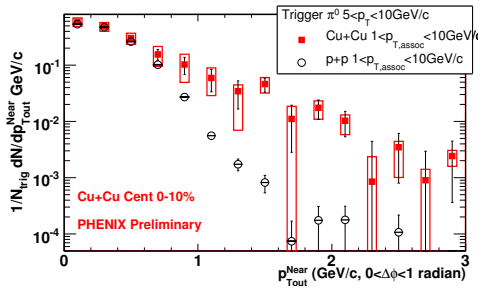

Figure 3: The p_{out} distributions from p+p and central Cu+Cu collisions.

This side-peak has been characterized in several ways: perhaps the most transparent is fitting with a gaussian displaced from π by D radians. The fitted parameter D for several centralities from both Au+Au and Cu+Cu collisions[10] smoothly increases with centrality with the results falling on a common curve from different colliding systems. This is consisent with the peak being a property of the matter that is formed during the collision, i.e. a response of the matter due to the passage of the jet. It is not yet known what this response is, though there have been predictions of a mach-cone being formed in the fluid surrounding the passage of a supersonic high-pt parton[11].

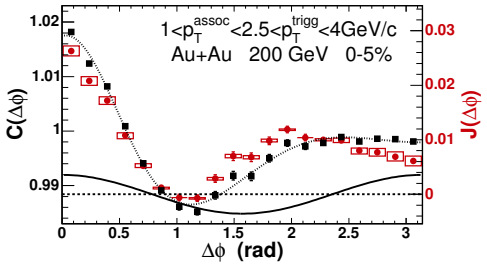

Figure 4: The azimuthal distribution of associated hadrons with respect to the axis defined by a leading trigger hadron for central Au+Au collisions. The data shown as squares (black) are the original correlation while the data in circles (red) are after correcting for the underliying event which has an overall modulation due to the known elliptic flow.

3 Next Steps

Recapping the main message of this talk: we have formed a strongly interacting QGP in experiments at RHIC and are learning how to use high-pt probes to quantify the properties of this matter. Partons traveling through this medium lose energy leading to a reduced yield

of high-pt hadrons. At the same stage an increase in the number of hadrons correlated with the leading hadron is consistent with the fragmentation of radiated, bremstrahlung gluons.

At least two key measurements are needed to increase our control and understanding of these probes. Charm and beauty quarks are predicted to lose less energy as they travel through the plasma. Calculations predict less gluon radiation due to larger gluon interference during the heavy-parton's multiple-scattering, i.e. a medium dead-cone effect. Measurements of the sum of semi-leptonic decays of charm and beauty[12] suprisingly show a high-pt suppression similar to that for pions. This is a challenge for models: if they can reproduce both light- and heavy-quark energy-loss, this will increase the confidence in how gluon radiation is modeled and increase our ability to use these probes of the QGP. Experimentally we also need to separate the spectra of charm from beauty: this required the funded upgrade of a high-precions silicon vertex detector that will be installed during 2009/10.

The second next step is to control the path-length of high-pt probes. The amount of energy-loss depends on both the density of the medium and the path-length that is traveled by the parton. How to best disentangle these two effects is an open question: work proceeds on multiple fronts; studying energy-loss versus reaction plane, centrality, and for different size colliding systems. Part of the difficulty is the strong energy-loss means that the set of partons that survive to produce high-pt hadrons, come from hard-collisions that occur predominantly near the surface of the dense matter. One possible method to alter this surface-bias is to select events that have two back-to-back high-pt hadrons. On average these partons will have traveled through similar lengths of dense matter and lost similar amounts of energy. This will shift the surface bias more towards the center of this collision.

4 Acknowledgments

The author acknowledges funding from the DOE.

References

[1] Majumder, A. nucl-th/0702066
[2] Slides:
`http://indico.cern.ch/contributionDisplay.py?contribId=231&sessionId=6&confId=9499`
[3] Adcox, K. *et al.*, Nucl. Phys. **A757** 184 (2005).
[4] d'Enterria, David, J. Phys. **G34** S53-S82 (2007).
[5] Adcox, K. *et al.*, Phys. Rev. Lett. **88** 022301 (2002).
[6] Majumder, A. and Wang, Xin-Nian, Phys. Rev. **D72** 034007 (2005).
[7] I. Vitev, Phys. Lett. **630** 78 (2005).
[8] Adler, S.S. *et al.* Phys. Rev. **D74** 072002 (2006).
[9] Adler, S.S. *et al.* Phys. Rev. **C73** 054903 (2006).
[10] Adler, S.S. *et al.* Phys. Rev. Lett. **97** 052301 (2006).
[11] J. Casalderrey-Solana, E.V. Shuryak, and D. Teaney, J. Phys. Conf. Ser. **27** 22 (2005).
[12] Adare, A. *et al.* Phys. Rev. Lett. **98** 172301 (2007).

Exclusive Hadronic Final States in e^+e^- Interactions at BABAR

Sepehr Saremi[1]

1- University of Massachusetts at Amherst - Dept of Physics
Amherst, Massachusetts - USA

The first observation of e^+e^- annihilation into states of positive C parity, $\rho^0\rho^0$ and $\phi\rho^0$ is reported. It is shown that these final states are produced through two-virtual-photon annihilation. This is based on the distributions of $cos\theta^*$, where θ^* is the center-of-mass polar angle of ϕ or ρ^0. The cross sections for the $|cos\theta^*| < 0.8$ are measured. In addition, the observation of another channel, $e^+e^- \to \phi\eta$ near $\sqrt{s} = 10.58$ GeV with a significance of 6.5σ is discussed. The cross section of the later channel for $|cos\theta^*| < 0.8$ is measured, where θ^* is the center-of-mass polar angle of ϕ meson.

1 Observation of e^+e^- annihilation into states of positive C parity, $\rho^0\rho^0$ and $\phi\rho^0$

The BABAR experiment has measured some rare, low multiplicity final states that have C= +1. These final states are produced through a two-virtual-photon annihilation (TVPA) process which is shown in Figure 1.

The channels measured by the BABAR experiment [2] are the exclusive reactions $e^+e^- \to \rho^0\rho^0$ and $e^+e^- \to \phi\rho^0$. The final state in both these channels is even under charge conjugation and cannot be produced by single-photon annihilation. The data sample used in this analysis consists of 205 fb^{-1} of data collected on the $\Upsilon(4S)$ resonance and 20 fb^{-1} collected 40 MeV below.

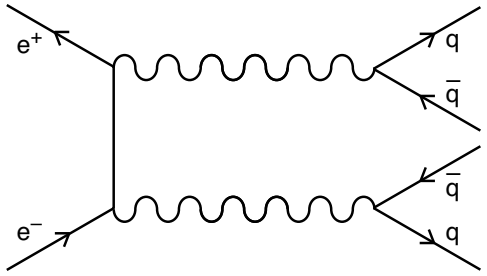

Figure 1: Two-virtual-photon annihilation diagram.

The event selection requires four well-reconstructed charged tracks with a total charge of zero. Two oppositely charged tracks must be identified as pions and the other two must be both pions or kaons.

The four tracks are fitted to a common vertex and we require the χ^2 probability to exceed 0.1%. We select events that have a reconstructed invariant mass within 170 MeV/c of the nominal c.m. energy as shown in Figure 2.

The analysis is performed using a binned maximum-likelihood fit. The fit is performed in nine rectangular regions of the two-dimensional mass distributions. The signal region is considered to be the $0.5 < m_{\pi^+\pi^-} < 1.1$ GeV/c^2 and $1.008 < m_{K^+K^-} < 1.035$ GeV/c^2 mass regions.

The number of signal events for the $\rho^0\rho^0$ and $\phi\rho^0$ channels are 1243 ± 43 and 147 ± 13 respectively with a χ^2/dof (degrees of freedom) of 6.4/4 and 2.0/3. There are a total of 1508 $\pi^+\pi^-\pi^+\pi^-$ ($\sim$ 18% background) and 163 $K^+K^-\pi^+\pi^-$ ($\sim$ 10% background) events in the signal box, respectively.

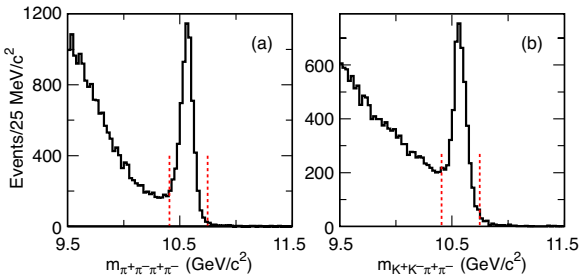

Figure 2: The invariant mass for the (a) $\pi^+\pi^-\pi^+\pi^-$ and (b) $K^+K^-\pi^+\pi^-$ final states. The dashed lines show the signal regions.

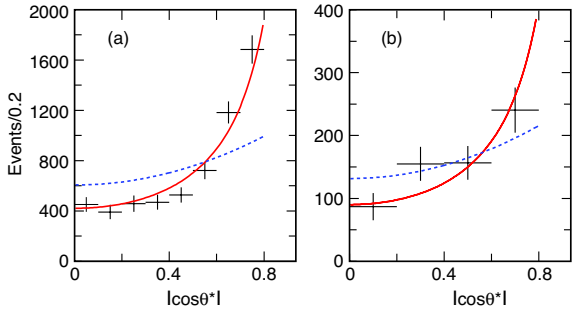

Figure 3: Distributions of the production angle for a) $\rho^0\rho^0$ and b) $\phi\rho^0$. The solid and dashed lines are the normalized $\frac{1+\cos^2\theta^*}{1-\cos^2\theta^*}$ and $1+\cos^2\theta^*$ distributions, respectively.

One can study the production mechanism by using the production angle θ^*, which is defined as the angle between the ρ^0 (ϕ) direction and the e^- beam direction in the CM frame. Figure 3 shows the $|\cos\theta^*|$ distributions after MC efficiency correction. The measurements are restricted to the fiducial region $|\cos\theta^*| < 0.8$, since the efficiency drops rapidly beyond 0.8. These forward peaking $\cos\theta^*$ distributions are consistent with the TVPA expectation [3], which can be approximated by:

$$\frac{d\sigma}{d\cos\theta^*} \propto \frac{1+\cos^2\theta^*}{1-\cos^2\theta^*}$$

in the fiducial region. The fit for TVPA hypothesis gives a χ^2/dof of 11.8/7 ($\rho^0\rho^0$) and 3.5/3 ($\phi\rho^0$). However, fitting by $1+\cos^2\theta^*$, will give a χ^2/dof of 112/7 for $\rho^0\rho^0$ and 6.3/3 for $\phi\rho^0$ respectively.

For calculating the cross section we take the branching fraction of $\phi \to K^+K^-$ to be 49.1% and that of $\rho^0 \to \pi^+\pi^-$ as 100% [4]. The TVPA cross sections within $|\cos\theta^*| < 0.8$ near $\sqrt{s} = 10.58$ GeV are:

$$\sigma_{\rm fid}(e^+e^- \to \rho^0\rho^0) = 20.7 \pm 0.7(\text{stat}) \pm 2.7(\text{syst})\ \text{fb}$$
$$\sigma_{\rm fid}(e^+e^- \to \phi\rho^0) = 5.7 \pm 0.5(\text{stat}) \pm 0.8(\text{syst})\ \text{fb}.$$

These measured cross sections are in good agreement with the calculation from a vector-dominance two-photon exchange model [3].

2 Observation of the $e^+e^- \to \phi\eta$ reaction at $\sqrt{s} = 10.58$ GeV

The most likely mechanism for the $e^+e^- \to \phi\eta$ reaction is the Feynman diagram in Figure 4. Different QCD-based models predict different s dependences for the production rates of e^+e^- annihilations to vector-pseudoscalar (VP) final states like $\phi\eta$. The CLEO experiment has measured the cross section for $e^+e^- \to \phi\eta$ at $\sqrt{s} = 3.67$ GeV [5]. Our measurement at $\sqrt{s} = 10.58$ GeV [6] provides a meaningful test of the s dependence.

Our analysis uses 204 fb^{-1} of data collected on the Υ(4S) resonance at $\sqrt{s} = 10.58$ GeV and 20 fb^{-1} collected 40 MeV below the Υ(4S) mass. To $\phi\eta$ final state is reconstructed in the $K^+K^-\gamma\gamma$ mode, by selecting two well-reconstructed oppositely charged tracks and at least two well-identified photons.

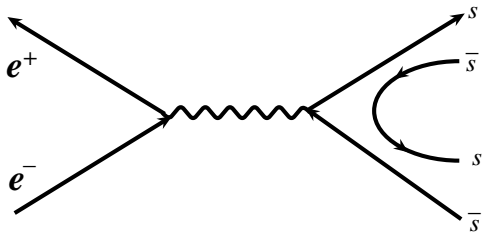

Figure 4: Two-virtual-photon annihilation diagram.

The two tracks are fitted to a common vertex with a requirement on the χ^2 probability to exceed 0.1%. The photon candidates are required to have a minimum energy of 500 MeV in the laboratory frame. We accept events with a reconstructed invariant mass of $K^+K^-\gamma\gamma$ within 230 MeV/c^{2}of the e^+e^- CM energy. In addition we require the invariant mass of K^+K^- to be close to the ϕ mass ($m_{KK} < 1.1$ GeV/c^2) and that of $\gamma\gamma$ to be near the η mass ($0.4 < m_{\gamma\gamma} < 0.8$ GeV/c^2).

The number of signal events are derived using a two-dimensional log-likelihood fit. The number of $\phi\eta$ signal events is 24 ± 5 in the ϕ mass window, where the ϕ mass window is defined as $1.008 < m_{KK} < 1.035$ GeV/c^2. This corresponds to a significance of 6.5 standard deviations. The significance is estimated by using the log-likelihood difference between signal and null hypotheses (no $\phi\eta$ signal component), $\sqrt{2ln(L_s/L_n)}$, where L_s and L_n refer to the likelihoods of the signal and null hypotheses respectively.

The cross section is calculated by taking the branching fraction of $\phi \to K^+K^-$ to be 49.1% and that of $\eta \to \gamma\gamma$ equal to 39.4% [4]. The cross section within $|\cos\theta^*| < 0.8$ near $\sqrt{s} = 10.58$ GeV is:

$$\sigma_{\rm fid}(e^+e^- \to \phi\eta) = 2.1 \pm 0.4(\text{stat}) \pm 0.1(\text{syst})\ \text{fb}.$$

There is no direct prediction for the cross section of this process at this energy. Some QCD-based models predict the $e^+e^- \to$ VP cross section to have $1/s^4$ [7, 8] dependence. Our result and that of CLEO, ($\sigma = 2.1^{+1.9}_{-1.2} \pm 0.2$ pb) at $\sqrt{s} = 3.67$ GeV (continuum) [5], favors a $1/s^3$ dependence as depicted in Figure 5.

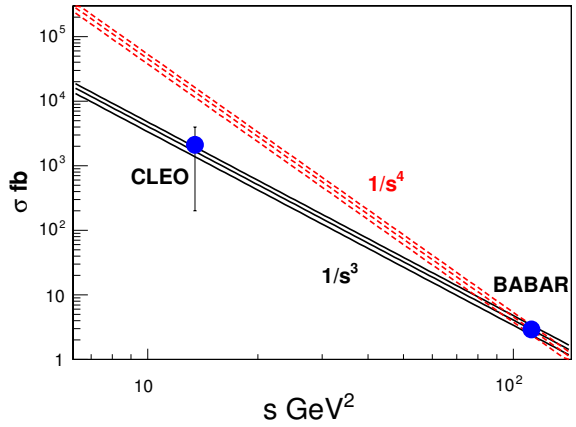

Figure 5: Extrapolations of cross sections using BABAR's measurement at $\sqrt{s} = 10.58$ GeVassuming $1/s^3$ (solid) or $1/s^4$ (dashed) energy dependence. The bands show one standard deviation uncertainties in the extrapolations. The CLEO measurement at $\sqrt{s} = 3.67$ GeV is also shown.

References

[1] Slides:
`http://indico.cern.ch/contributionDisplay.py?contribId=184&sessionId=6&confId=9499`

[2] B. Aubert *et al.* (BABAR Collaboration), Phys. Rev. Lett. **97**, 112002 (2006).

[3] M. Davier, M. Peskin, and A. Snyder, hep-ph/0606155.

[4] S. Eidelman *et al.* (Particle Data Group), Phys. Lett. B **592**, 1 (2004).

[5] G. S. Adams *et al.* (CLEO Collaboration), Phys. Rev. D **73**, 012002 (2006).

[6] B. Aubert *et al.* (BABAR Collaboration), Phys. Rev. D **74**, 111103(R) (2006).

[7] G. P. Lepage and S. J. Brodsky, Phys. Rev. D **22**, 2157 (1980); S. J. Brodsky and G. P. Lepage, Phys. Rev. D **24**, 2848 (1981).

[8] V. Chernyak, hep-ph/9906387; V. L. Chernyak and A. R. Zhitnitsky, Phys. Rept. **112**, 173 (1984).

Investigating the Onset of Color Transparency with CLAS

Maurik Holtrop[1] and the CLAS Collaboration[2] *

1- University of New Hampshire - Physics Department
Durham, NH 03824 - USA

2- Thomas Jefferson National Accelerator Facility
Newport News, VA 23606 - USA

Quantum Chromo Dynamics (QCD) predicts that point-like colorless systems will exhibit vanishingly small cross-sections and are thus expected to travel through the nucleus with little attenuation, a phenomenon known as Color Transparency (CT). An increase in nuclear transparency, T_A, for increasing momentum transfer, Q^2, would signal the onset of CT.

We present an experiment with the CLAS detector on exclusive incoherent electro-production on nuclei of the ρ^0 meson, which is a particularly sensitive reaction to study CT. Preliminary results of this experiment show a clear rise in T_A with increasing Q^2, indicating the onset of Color Transparency.[1]

1 Introduction

One of the fundamental predictions of QCD is the phenomenon of Color Transparency (CT), which was first described more than two decades ago [2, 3]. CT describes the process by which a color singlet object with a reduced transverse size has a vanishingly small interaction cross section when propagating through a nucleus. Such a Point Like Configuration (PCL) can be created in a scattering experiment at high momentum transfer (Q^2). See one of the many review articles for details [4, 5, 6].

Experimentally the onset of CT can be observed as a rise in the nuclear transparency, $T_A = \frac{\sigma_A}{A\sigma_N}$ with increasing Q^2. Many experiments have looked for a signal of CT but only a few have observed one. For an overview of the experimental status see [7].

The reaction used in this experiment is incoherent electro-production of ρ^0 mesons off nuclei, which offers many advantages. It is expected that the onset of CT occurs at a lower Q^2 for a meson $(q\bar{q})$ compared to a hadron (qqq)[8]. Also, since the ρ^0 is a vector meson, the production mechanism is well understood by the Vector Meson Dominance model (VMD) as the fluctuation of a photon (which has the same quantum numbers as a vector meson) into a $(q\bar{q})$ pair. The photon at high virtuality Q^2 is expected to produce a pair with small $\sim 1/Q^2$ transverse separation. CT then manifests itself as a vanishing absorption of this $(q\bar{q})$ pair as it propagates through the nucleus [9, 10].

The dynamical evolution of the small size $(q\bar{q})$ pair to a normal sized vector meson is controlled by the time scale called the formation time. In the rest frame of the nucleus this is given by $t_f = \frac{2\nu}{m_{V'}^2 - m_V^2}$, where V' represents the first excited state of the meson and V represents the ground state. This formation time needs to be sufficiently long to be able to observe CT.

*This work is supported in part by DOE grant #DE-FG02-88ER40410

A competing effect to CT in vector meson production is the coherence length effect, which is due to quantum coherence, the destructive interference of the amplitudes for which the interaction takes place on different bound nucleons. The coherence length effect depends on the coherence length, $l_c = \frac{2\nu}{Q^2+m_V^2}$. This effect was recently measured by the HERMES collaboration [11], see Fig. 1. Since this effect competes with the CT signal, it is important to hold the coherence length, l_c, constant. This was done in a later analysis of the same data [12], which shows a rise of T_A with increasing Q^2, but suffers from poor statistics.

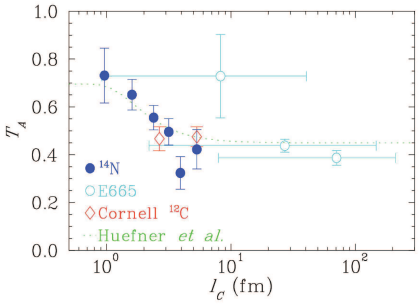

Figure 1: The Coherence Length effect measured by the HERMES collaboration [11]

2 The Experiment

Our experiment was conducted with the CLAS detector in Hall-B at Jefferson Laboratory during the EG2 run period in early 2004. The experiment used an electron beam of 5 GeV and 4 GeV on two targets simultaneously to reduce systematic errors. One of the targets was liquid deuterium and the other target was composed of a foil of either carbon, iron or lead. The targets could be clearly distinguished in the data analysis by use of a cut on the reaction vertex.

We studied the reaction $e+N \rightarrow e'+N+\rho^0 \rightarrow e'+N+\pi^+ +\pi^-$ by detecting the scattered electron and the two pions which are decay products of the ρ^0. A cut was made on $W > 2$ GeV to select the data above the resonance region. A cut on $t = (q^\mu - P_V^\mu)^2$ of $-t < 0.45$ GeV^2 selected the incoherent electro-production of the ρ^0. A further cut on the missing energy $\Delta E = \nu - E_\rho + t/M_p$ at $|\Delta E| < 0.1 GeV$ ensured proper exclusivity of the reaction. The resulting $\pi^+\pi^-$ invariant mass spectrum shows a clear signal for ρ^0 producion, see Fig. 2. The background processes to our main reaction are delta production and incoherent pion production. These background processes were modeled using the Genoa Monte Carlo generator from which we found the shapes in our spectrum. These processes were then included in the fitting procedure allowing only the relative strength to be varied. The ρ^0 signal was fit with a Breit-Wigner shape. The nuclear transparency was then computed by taking the ratio of the extracted number of counts for the nuclear target divided by the number of counts for the deuterium target and correcting

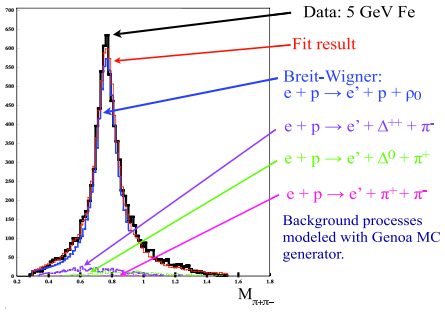

Figure 2: The $\pi^+\pi^-$ invariant mass spectrum, showing a clear signal for the ρ^0 meson. The fit result and background subtraction are indicated on the figure, see text.

for the difference in target thickness and number of nucleons, $T_A = C\frac{2N_A}{AN_D}$.

Plotting the extracted nuclear transparency, T_A versus the coherence length l_c shows that there is no significant dependence on l_c for our data, see Fig. 3. This is not too surprising since our measured l_c range is very short, less than one fermi. The l_c for this data is small due to the relatively low beam energy compared to the HERMES experiment. This means that we do not need to bin in separate bins of constant l_c for this data, since there is no competing coherence length effect.

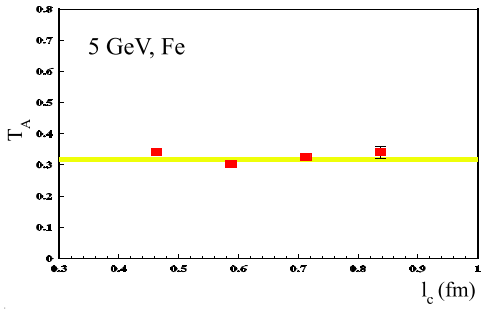

Figure 3: The nuclear transparency, T_A, plotted versus coherence length l_c for the 5 GeV iron data.

A number corrections need to be made on the T_A versus Q^2 graph. The correction for radiative effects is very small since it mostly cancels out in the ratio when computing T_A. The same is true for the corrections for the finite acceptance of the detector. A larger correction is due to pion absorption. When comparing with theoretical calculations, the decay of the ρ^0 into two pions and the subsequent absorption of of these pions in the nucleus or the target material must be taken into account. The Q^2 dependence of this process is very small, so the main effect of the pion absorption correction is to shift all the data points up by a constant amount.

3 Results

Our results are still too preliminary to be reproduced here and should not yet be cited.

The resulting T_A for the 5 GeV data with the iron target were divided into 4 bins in Q^2 ranging from a Q^2 of 0.9 GeV^2 for the central value of the lowest point to 2.5 GeV^2 for the central value of the highest point. The T_A exhibits a clear rise with increasing Q^2, rising nearly linearly over this range from approximately 0.36 to 0.46, which is far more than the statistical errors on the points. If these results withstand the final tests of our analysis, this will be a very clear indication of the onset of Color Transparency.

The data are in good agreement with the calculations by Kopeliovich [10], which almost perfectly describes the data. This model is completely parameter free after an initial fit to fix the parameters for the universal dipole cross section for a $q\bar{q}$ quark dipole with a nucleon [9]. A Glauber Model calculation by H. Lee and B. Mustapha [13] exhibits no rise over this range in Q^2 and clearly fails to describe the data, indicating that the rise in T_A cannot be explained without CT.

To complete this data analysis we will need to do a thorough study of the systematic errors. Additionally we need to continue data analysis on the 4 GeV data set and the runs with the carbon and lead targets.

4 Conclusions and Outlook

We see a clear rise of the nuclear transparency with increasing Q^2 indicating the onset of Color Transparency. These results do not have the ambiguity of the competing coherence

length effect because of the very short coherence lengths where this effect is negligible. The model predictions from Kopeliovich [10] describe the data very well.

A new experiment has been approved by the Jefferson Laboratory PAC which will extend this study to higher Q^2, up to 7.5 GeV^2, and also cover a larger range of l_c using the upgraded accelerator and upgraded CLAS detector [7]. This experiment will obtain much higher statistical precision due to the higher luminosity capabilities of the upgraded detector. This will allow us to make a much more detailed study of the Color Transparency phenomenon and the process of vector meson formation and its interaction with the nuclear medium. This will enable us to study in far more detail how the point like configuration dresses with time to form the fully complex asymptotic wave function of the hadron, which puts us at the heart of the dynamics of confinement.

References

[1] M. Holtrop. Conference slides:. http://indico.cern.ch/contributionDisplay.py?contribId=186&sessionId=6&confId=9499.

[2] Stanley J. Brodsky. Testing quantum chromodynamics. In W. Metzger E. W. Kittel and A. Stergion, editors, *XIII International Symposium on Multiparticle Dynamics, 1982*, page 963. World Scientific, Singapore, 1982.

[3] A. H. Mueller. In J. Tran Than Van, editor, *Proceedings of the XVII rencontre de Moroind, Les Arcs, France*, page 13. Editions Frontieres, Gif-sur-Yvette, 1982.

[4] L. L. Frankfurt, G. A. Miller, and M. Strikman. The geometrical color optics of coherent high-energy processes. *Ann. Rev. Nucl. Part. Sci.*, 44:501–560, 1994.

[5] Pankaj Jain, Bernard Pire, and John P. Ralston. Quantum color transparency and nuclear filtering. *Phys. Rept.*, 271:67–179, 1996.

[6] Stanley J. Brodsky, L. Frankfurt, J. F. Gunion, Alfred H. Mueller, and M. Strikman. Diffractive leptoproduction of vector mesons in qcd. *Phys. Rev.*, D50:3134–3144, 1994.

[7] K. Hafidi, M. Holtrop, and B. Mustapha. Jlab experiment **pr12-06-106**. http://www.jlab.org/exp_prog/proposals/06/PR12-06-106.pdf.

[8] B. Blaettel, G. Baym, L. L. Frankfurt, and M. Strikman. How transparent are hadrons to pions? *Phys. Rev. Lett.*, 70:896–899, 1993.

[9] B. Z. Kopeliovich, J. Nemchik, A. Schafer, and A. V. Tarasov. Color transparency versus quantum coherence in electroproduction of vector mesons off nuclei. *Phys. Rev.*, C65:035201, 2002.

[10] B. Z. Kopeliovich, J. Nemchik, and Ivan Schmidt. Color transparency at low energies: Predictions for jlab. hep-ph/0702272, 2007.

[11] K. Ackerstaff et al. Observation of a coherence length effect in exclusive ρ^0 electroproduction. *Phys. Rev. Lett.*, 82:3025–3029, 1999.

[12] A. Airapetian et al. The Q^2-dependence of nuclear transparency for exclusive ρ^0 production. *Phys. Rev. Lett.*, 90:052501, 2003.

[13] B. Mustapha and H. Lee. Private communication.

Final Results from HERMES on Hadronization in Nuclear Environment

Z. Akopov[1] *

Yerevan Physics Institute, 375036 Yerevan, Armenia

A series of semi-inclusive deep-inelastic scattering measurements on deuterium, helium, neon, krypton, and xenon targets has been performed in order to study hadronization. The data were collected with the HERMES detector at the DESY laboratory using a 27.6 GeV positron or electron beam. Hadron multiplicities on nucleus A relative to those on the deuteron, R_A^h, are presented for various hadrons (π^+, π^-, π^0, K^+, K^-, p, and $\bar{p}$) as a function of the virtual-photon energy ν, the fraction z of this energy transferred to the hadron, the photon virtuality Q^2, and the hadron transverse momentum squared p_t^2. The data reveal a systematic decrease of R_A^h with the mass number A for each hadron type h. For pions two-dimensional distributions also are presented. These indicate that the dependences of R_A^π on ν and z can largely be described as a dependence on a single variable L_c, which is a combination of ν and z. The dependence on L_c suggests in which kinematic conditions partonic and hadronic mechanisms may be dominant.

1 Introduction

Understanding the confinement of quarks and gluons in hadrons still is one of the great challenges in hadronic physics. To uncover its nature, hadronic reactions in a nuclear medium, either cold or hot, are studied. Typical examples are the measurements of hadron production on nuclear targets in semi-inclusive deep-inelastic scattering of leptons [2, 3, 4] and the jet-quenching and parton energy-loss phenomena observed in ultra-relativistic heavy-ion collisions [5]. In each case hadron yields are observed that are different from those observed in the corresponding reactions on free nucleons. The process that leads from the partons produced in the elementary interaction to the hadrons observed experimentally is commonly referred to as hadronization or fragmentation. According to theoretical estimates the hadronization process occurs over length scales varying from less than a femtometer to several tens of femtometers. At these length scales the magnitude of the strong coupling constant is such that perturbative techniques cannot be applied. Hence, hadronization is an intrinsically non-perturbative QCD process, for which only approximate theoretical approaches are presently available. Experimental data are vital for supporting these theoretical developments, since they can be used to gauge or guide the calculations.

The hadronization process in a nuclear medium can be studied by means of semi-inclusive deep-inelastic scattering (SIDIS) of electrons or positrons from nuclei. For that purpose the multiplicity ratio R_A^h is introduced, which is defined as the ratio of the number of hadrons h produced per deep-inelastic scattering (DIS) event on a nuclear target with mass number A to that for a deuterium (D) target:

$$R_A^h(\nu, Q^2, z, p_t^2) = \frac{\left(\frac{N^h(\nu,Q^2,z,p_t^2)}{N^e(\nu,Q^2)}\right)_A}{\left(\frac{N^h(\nu,Q^2,z,p_t^2)}{N^e(\nu,Q^2)}\right)_D}, \tag{1}$$

*On behalf of the HERMES Collaboration

2 Experiment and Data Analysis

The measurements were performed with the HERMES spectrometer [6] using a 27.6 GeV positron or electron beam stored in the HERA ring at DESY. Typical beam currents were 40 mA down to 5 mA. The scattered leptons and the produced hadrons were detected within

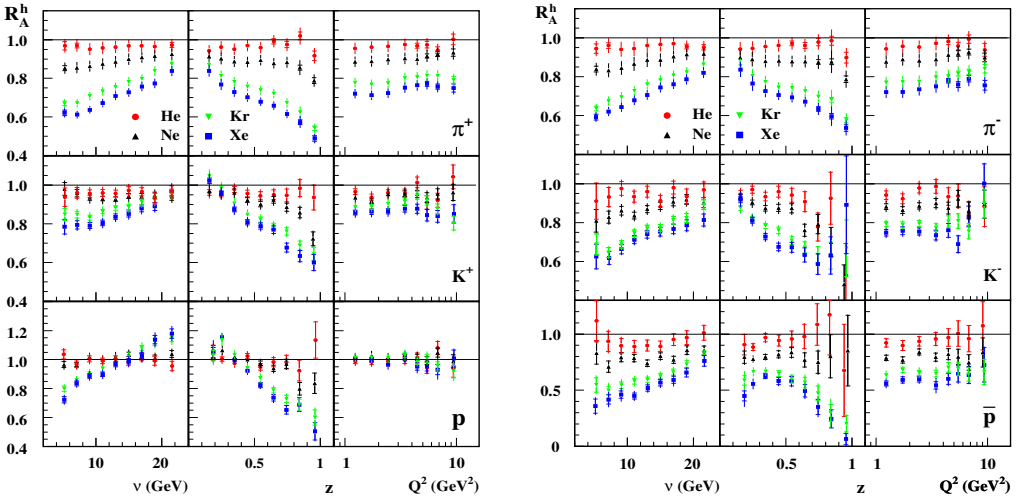

Figure 1: Values of R_A^h for positively and negatively charged hadrons as a function of ν, z, and Q^2.

an angular acceptance of ± 170 mrad horizontally and ± (40 – 140) mrad vertically. The lepton trigger was formed by a coincidence between signals from three scintillator hodoscope planes and a lead-glass calorimeter. A minimum energy deposit in the latter of 3.5 GeV (1.4 GeV) for unpolarized (polarized) target runs was required. The data were collected during the years 1999, 2000, 2004, and 2005, using unpolarized nuclear (He, Ne, Kr, Xe) and polarized or unpolarized deuterium (D) gaseous targets internal to the storage ring. The identification of charged pions, kaons, protons, and antiprotons is accomplished using the information from the Ring-Imaging Čerenkov detector (RICH) [7] The hadron multiplicity ratio R_A^h as defined in Eq. 1 was determined as a function of the leptonic (Q^2 and ν) and hadronic (z and p_t^2) variables for all identified particles and all targets. The kinematic constraints imposed on the scattered leptons were identical for all analysed data:

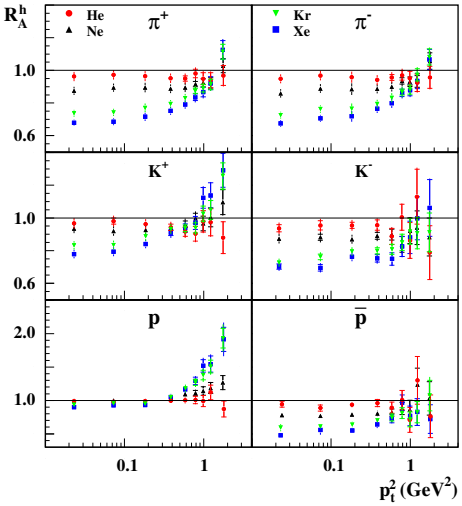

Figure 2: Values of R_A^h for positively (left panel) and negatively (right panel) charged hadrons as a function of p_t^2.

$Q^2 > 1$ GeV^2, $W = \sqrt{2M\nu + M^2 - Q^2} >$
2GeV (where M is the nucleon mass) for the invariant mass of the photon-nucleon system, and $y = \nu/E < 0.85$ for the energy fraction of the virtual photon. The constraints on W and y were applied in order to exclude nucleon resonances and to limit the magnitude of the radiative corrections to R_A^h, respectively. The resulting value of $x_{Bj} = Q^2/2M\nu$ ranged from 0.023 to 0.8.

3 Results

The experimental results are presented as dependences of the multiplicity ratios R_A^h on the various kinematic variables and the mass number A of the nucleus. The dependence of R_A^h on ν, z, Q^2, and p_t^2 for the various nuclei for all identified hadrons is shown in Figs. 1-2 The most prominent features of the data are an increased attenuation (decrease of R_A^h below unity) with increasing value of the mass number A of the nucleus and the attenuation becoming smaller (larger) with increasing values of ν (z), R_A^h dropping below 0.5 for xenon in some kinematic regions. At low values of z, especially for heavier targets and for protons and K^+ particles, a strong rise of R_A^h, even to above unity, is observed. Presumably this is due to hadronic rescattering, where a higher energy particle through nuclear reactions produces one or more lower-energy particles. By combining the data for π^+ and π^-, the dependence of R_A^π on two of the variables ν, z, Q^2, and p_t^2 together was investigated, and the results are shown in Fig. 3. The dependence on Q^2 depends weakly but noticeably

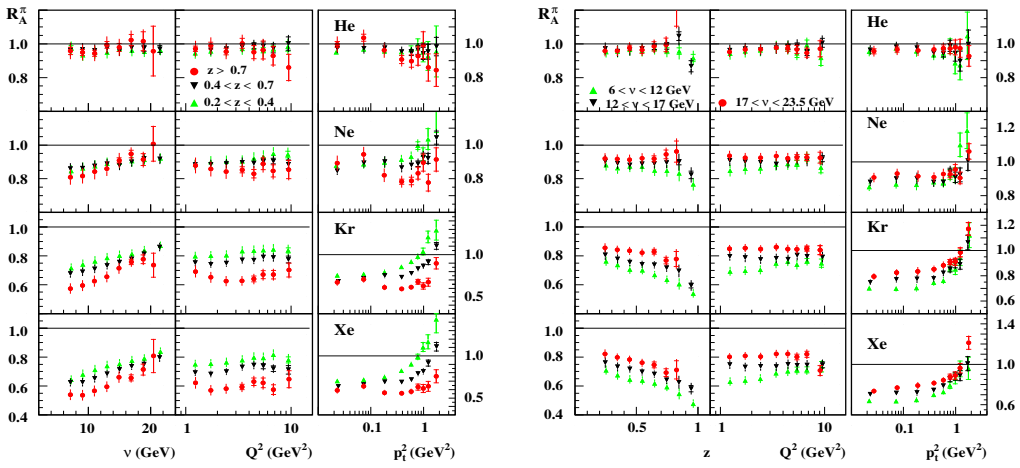

Figure 3: Values of R_A^h for charged pions for three z ranges and three ν ranges.

on the value of ν, but practically not on that of z. The dependence on p_t^2 hardly depends on ν and z, except for the disapperance of the rise at large p_t^2 at $z \to 1$ mentioned above. However, the dependences on ν and z are related. It was found that most of the dependence on ν and z can be incorporated in a dependence on the combination $L_c = z^{0.35}(1-z)\nu/\kappa$, where κ is the string tension in string models, which thus acts as a scaling variable.

Since this function is close to the one given in the Lund model for the average formation length of a particle, by inspecting the value of R_A^π vs. L_c for the four nuclei, regions can tentatively be identified, where hadronic (absorption) plus partonic mechanisms are important, and a region at higher L_c where only or mainly partonic mechanisms play a role.

In order to investigate this, values of R_A^π versus L_c for various values of ν and z are shown in Fig. 4. Here L_c is defined as:

$$L_c = f(z)\frac{\nu}{\kappa}, \qquad (2)$$

where $f(z) = z^{0.35}(1-z)$ and $\kappa = 1$ GeV/fm. This form for $f(z)$ is a convenient parametrization obeying the constraints at $z \to 0$ and $z \to 1$, and gives values for L_c as a function of z closely resembling the ones obtained with the Lund model.

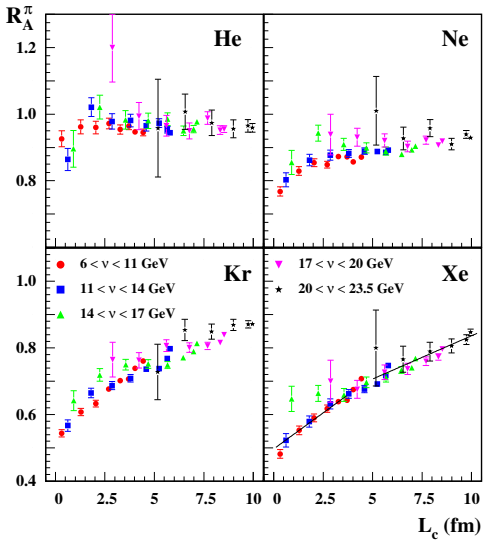

Figure 4: Values of $R_A^\pi(\nu, z)$ for He, Kr, Ne, and Xe as a function of the variable L_c, see Eq. 2. The various ν-bins are indicated by different symbols. Within the same ν bin the z bins used are $0.2-0.3-0.4-0.5-0.6-0.7-0.8-0.9-1.0$.

A clear correlation can be observed between the values of R_A^h and L_c, with only a relatively small residual spread at any fixed value of L_c. Evidently most of the dependence of R_A^h on ν or z in Fig. 3 can be described as a dependence on L_c, which thus acts as a scaling variable.

4 Conclusions

In total a very extensive data set to guide modeling hadronization in nuclear matter has been collected by the HERMES collaboration. A full theoretical description of hadronization in nuclei in one consistent framework, including partonic and hadronic (absorption plus rescattering) mechanisms is badly needed. Clearly it will be a challenge for any theoretical model that is developed to describe these data for the various hadrons and nuclei as a function of all kinematic variables, but if successful, this combination of data and theoretical interpretation will contribute essentially to the understanding of non-perturbative QCD at normal, and thence higher densities.

References

[1] Slides: `http://indico.cern.ch/contributionDisplay.py?contribId=187&sessionId=6&confId=9499`
[2] L. Osborne *et al.*, Phys. Rev. Lett. 40 (1978) 1624.
[3] A. Airapetian *et al.* [HERMES Collaboration], Eur. Phys. J. C20 (2001) 479.
[4] A. Airapetian *et al.* [HERMES Collaboration], Phys. Lett. B577 (2003) 37.
[5] J. Adams *et al.* [STAR Collaboration], Phys. Rev. Lett. 92 (2004) 112301.
[6] K. Ackerstaff *et al.* [HERMES Collaboration], Nucl. Instr. and Meth. A417 (1998) 230.
[7] N. Akopov *et al.*, Nucl. Instr. and Meth. A479 (2002) 511.

MadGraph/MadEvent at Work: From QCD to New physics

Simon de Visscher *

Universite catholique de Louvain
Centre for Particle Physics and Phenomenology
2, chemin du cyclotron, 1348 Louvain la Neuve, Belgium

The `Madgraph/MadEvent` software is a powerful user-driven matrix element based event generator. Recently, different matching schemes have been implemented which allows to generate inclusive multi-jet samples by combining parton level events with parton showers consistently. This note presents results of the Modified MLM scheme applied on $t\bar{t}$ + jets samples generated for LHC with `Madgraph/MadEvent`. First, general tools of `Madgraph/MadEvent` are briefly described. Second, the matching method as well as his impact on key observables is presented. Feasability of evaluating theoritical uncertainties of simulation chains is also illustrated.

1 `MadGraph/MadEvent` and tools: a complete chain of simulation.

One of the challenges for exploring new physics sectors at Tevatron and LHC is to extract information from processes with highly complicated final states. In hadronic colliders, the understanding of multi-jets events is probably one of the most important tasks in order to be able to extract the rare non-SM information that could be possibly produced. Therefore the correct simulation of such processes is crucial.

`MadGraph/MadEvent` [2, 3] (MG/ME) is a user-driven matrix element based event generator for high-energy collisions simulation. The whole package is accessible by the web[a] or can be downloaded and run locally on user's machine or cluster. The role of `MadGraph` is to generate all amplitudes of relevant subprocesses given by the user. The list of Feynman diagrams is also computed. Beside a very high flexibility for handling new models, processes can have many particles in the final state. Currently, models implemented are SM, MSSM, 2HDM, HEFT and UED. There are also additional possibilities for testing a new model: starting from a Lagrangian with `MadRules` or by simply adding new particles and their interactions using `UserModel`. `MadEvent` uses as input the output of MadGraph, and produces a MonteCarlo package to calculate the cross section for a given process and also generate events. The architecture of the calculation code is intrinsically parallel and is therefore convenient to use with multi-CPU clusters. Several tools are available within the MG/ME package. To perform showering and hadronization, a standard version of `Pythia` [4] is available, and a generic detector simulation can be performed using the `PGS` software [5]. Both are installed on clusters accessible by the web. In addition, two analysis packages are available: `MadAnalysis` and `ExRootAnalysis`. The output of `MadEvent` is in "Les Houches" [6] standard format, which is compliant with external tools (CMSSW, Bridge [7],...). The MG/ME package with tools therefore provides a complete chain of simulation, from the hard scale process, including signal and backgrounds in any model, down to detector simulation.

*I would like to thank Johan Alwall, Fabio Maltoni and Vincent Lemaitre for the great help they brought me all along this work.

[a] http://madgraph.phys.ucl.ac.be, http://madgraph.hep.uiuc.edu, http://madgraph.roma2.infn.it

This is therefore a natural framework to perform complete analyses in several different theoretical contexts.

2 Jet matching

Matching techniques are needed to produce inclusive samples *without double counting* between subsamples. An additional problem is to be sure that no region of the phase space is forgotten.

As shown in the figure 1, two families of matching co-exists. As main differences, reweighting of events is done using Sudakov terms and veto on parton showers in CKKW [8] matching schemes whereas MLM-based [9] schemes rejects events with jets unmatched with partons. In the CKKW case, partons are clustered in jets with the K_T algorithm [10] while the original MLM method [11] uses a cone algorithm and minimum P_T cut. The new method used here called Modified MLM matching scheme [12] can be viewed as a mixing of both families as it uses K_T clustering and reject events with jets unmatched with partons (except in highest multiplicity subsamples). The results presented here concern that scheme tested with $t\bar{t}$+ jet(s) production for LHC. W + jets inclusive production has already been tested [12] and results will be published soon.

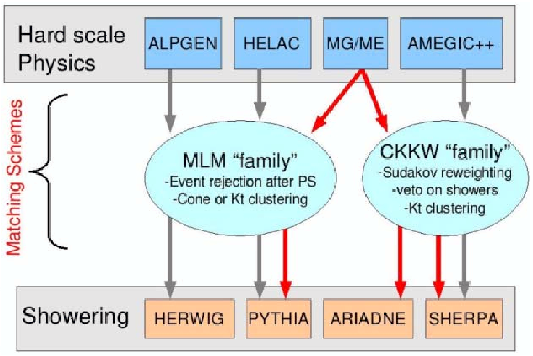

Figure 1: Flowchart of matching schemes between hard scale and showering simulators.

The modified MLM works as follows: first generate ME level events, with a minimal distance d_{cut}^{ME} in phase-space between partons [b]. The beam is also taken into account. Second perform parton showers (PS) with the appropriate algorithm (here: Pythia 6.4). PS partons are then clustered in jets with K_T, using a maximal size of jet defined by a second cutoff d_{cut}^{PS}. Finally the matching between ME partons and jets is realized. As the jet measurement is change when the showering is performed, d_{cut}^{ME} has to be smaller than d_{cut}^{PS}. A factor 1.5 between both is reasonable. If the event is not of the highest multiplicity, each parton has to be matched with one jet, and *vice versa*. On the contrary, for highest multiplicity samples, an event with additional jets can be also kept.

2.1 Differential jet rate

The differential jet rate is a key variable to check if matching works properly. The transition between the two independent regions of the phase space (below and above the cutoff) has to be smooth and invariant with respect to the cutoff used. Differential jet rates $2 \to 1$ for

[b] Distance in the phase space is defined here as

$$d^{ij} = 2\min(P_T^{(i)}, P_T^{(j)})^2[\cosh(\eta^{(i)} - \eta^{(j)}) + \cos(\phi^{(i)} - \phi^{(i)})], \quad d^{\text{ibeam}} = P_T^{(i)2}$$

$t\bar{t}$+0, 1, 2 and 3 jets is shown in the figure 2. The curves are related subsamples and their sum for different cutoffs. It appears that the transition is relatively smooth and matched shapes do not depend on the applied cut.

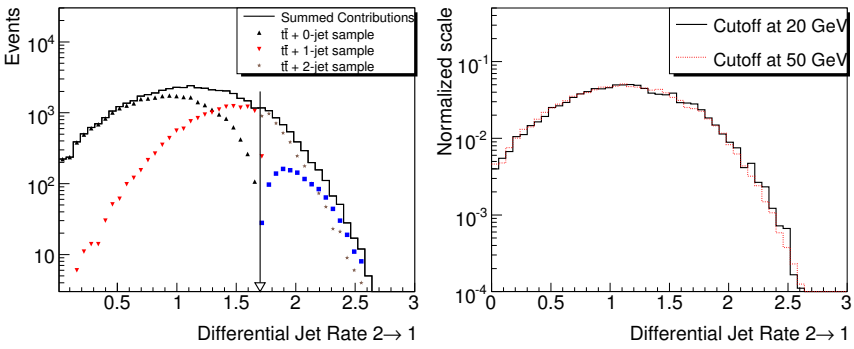

Figure 2: Differential jet rate $2 \to 1$ for $t\bar{t}$+0, 1, 2 and 3 jets for a cutoff of 50 GeV indicated by an arrow (left). Summed contributions for two different cutoffs are also shown (right).

2.2 Matching results

The impact of extra-jets on top kinematics can be revealed with (among others) $\Delta\Phi$ angle between top quarks. This is illustrated on fig. 3, where the curves are related to different subsamples as well as the sum of all contributions.

Those shapes can be compared with what as been obtained in ALPGEN (see [9]). The two matching schemes give very similar results even though the employed techniques are different.

The same holds for rapidity distributions of the leading jet as shown in the figure 4. It appears that the use of Matrix-Element generators changes radically the kinematics of jets compared to what Pythia and Herwig standalone provide, which gives a strong motivation for using the matching procedure in multi-jet process generation.

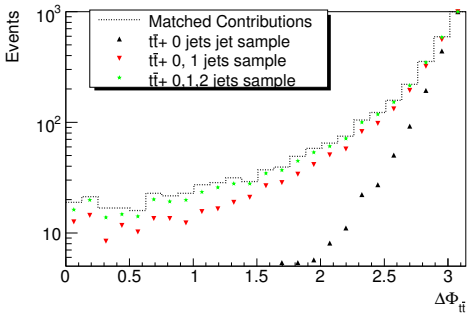

Figure 3: $\Delta\Phi(t\bar{t})$, with MG/ME + Modified MLM matching

3 Conclusion

A test of Modified MLM matching implemented in the `MadGraph/MadEvent` generator and using Pythia for showering has been done on $t\bar{t}$+ jets samples. The evaluation of differential jet rates shows that this matching scheme is a very useful tool to prevent overlapping between phase spaces described by hard-scale generator and showering software used here. Comparison has been done with the original MLM matching scheme and results are similar, which provides a strong starting point for evaluation of systematic uncertainties related to

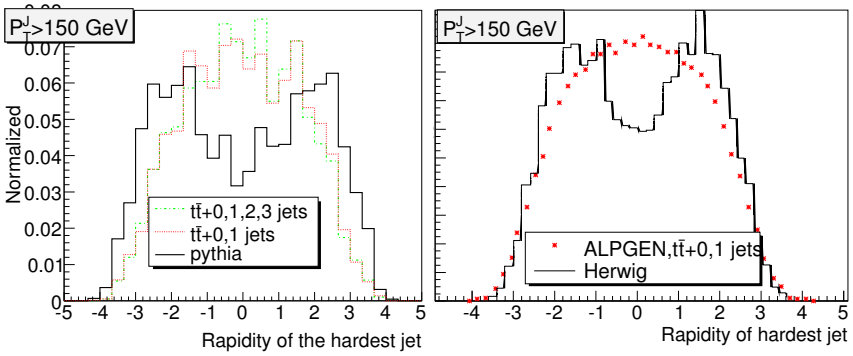

Figure 4: Rapidity of leading jet with P_T^{jet} >150 GeV obtained with MG/ME and Modified MLM matching (left) and ALPGEN and original MLM method (right). In addition distributions related to Pythia (left) and Herwig (right) standalone production are also illustrated

the simulation chain used. Moreover, this permits the generation of inclusive samples of top quark pair backgrounds at the LHC.

References

[1] Slides: `http://indico.cern.ch/contributionDisplay.py?contribId=210&sessionId=6&confId=9499`

[2] F. Maltoni and T. Stelzer. Madevent: Automatic event generation with madgraph. *JHEP*, 02:027, 2003.

[3] J. Alwall et al. Madgraph/madevent v4: The new web generation. Submitted at JHEP in June 07.

[4] T. Sjostrand et al. Pythia 6.4 physics and manual. *JHEP*, 05:026, 2006.

[5] John Conways. `http://www.physics.ucdavis.edu/~conway/research/software/pgs/pgs4-general.htm`

[6] J. Alwall et al. A standard format for les houches event files. *Comput. Phys. Commun.*, 176:300–304, 2007.

[7] Patrick Meade and Matthew Reece. Bridge: Branching ratio inquiry/decay generated events, http://www.citebase.org/abstract?id=oai:arxiv.org:hep-ph/0703031, 2007.

[8] F. Krauss. Matrix elements and parton showers in hadronic interactions. *JHEP*, 0208:015, 2002.

[9] Michelangelo L. Mangano et al. Matching matrix elements and shower evolution for top-quark production in hadronic collisions. *JHEP*, 01:013, 2007.

[10] S. Catani et al. Longitudinally invariant k(t) clustering algorithms for hadron hadron collisions. *Nucl. Phys.*, B406:187–224, 1993.

[11] Michelangelo Mangano. http://mlm.home.cern.ch/mlm/talks/lund-alpgen.pdf.

[12] J. Alwall et al. Comparative study of various algorithms for the matching of parton showers and matrix elements in hadronic collisions. to be published.

Scaled Momentum Spectra in the Current Region of the Breit Frame at HERA

Beata Brzozowska
On behalf of the ZEUS Collaboration

University of Warsaw - Institute of Experimental Physics
Hoża 69, 00-681 Warsaw - Poland

Charged particle production has been studied in deep inelastic scattering using an integrated luminosity of 0.5 fb^{-1} taken with the ZEUS detector at HERA. Scaled momentum distributions in intervals of Q^2 were investigated in the current region of the Breit frame. The fragmentation properties of the struck quark in DIS are compared with recent next-to-leading order calculations with the fragmentation functions obtained from e^+e^- experiments. Scaling violations are observed.

1 Introduction

In this paper parton fragmentation and hadronisation are studied using the inclusive charged particle spectrum in the current region of the Breit frame in deep inelastic scattering (DIS). The Breit frame [2] gives the best separation of the scattered quark fragments from the proton remnant.

The exchanged virtual boson is completely space-like and has longitudinal momentum $-Q$. The exchanged virtual photon collides elastically and head on with a quark carrying a longitudinal momentum of $Q/2$. The struck quark is scattered with equal but opposite momentum. The particles produced in the Breit frame can be assigned to one of two regions: the current region if their longitudinal momenta in the Breit frame are negative, and the target region if their longitudinal momenta are positive. The maximum momentum of a particle in the current region of this frame is $Q/2$.

In the Breit frame the scaled momentum variable x_p is defined to be equal $2p_h/Q$, where p_h is the momentum of a hadron measured in the Breit frame. This variable is transformed to $\xi_p = \ln(1/x_p)$ when comparing the data with theoretical calculations.

Recently accumulated high statistics of ep interaction permits the scaled momentum distributions to be studied as a function of Q and x in the range $0.002 < x < 0.75$ and $160 < Q^2 < 40960$ GeV^2. Together with the previous results [3] at $10 < Q^2 < 160$ GeV^2 the evolution of fragmentation functions is shown within a single experiment over a wide range of Q.

The data presented here were collected during the 1996-2007 running period at the electron-proton collider HERA using the ZEUS detector. The data of this analysis corresponded to an integrated luminosity of 0.5 fb^{-1}. A detailed description of the ZEUS detector can be found elsewhere [4].

The reconstructed tracks in the laboratory frame used in this analysis were associated with the primary event vertex and had $p_T > 150$ MeV and $|\eta| < 1.75$, where η is the pseudorapidity given by $-\ln(\tan(\theta/2))$ with θ being the polar angle of the measured track with respect to the proton direction. This was a region of high CTD acceptance, where the detector response and systematics were best understood.

Neutral current DIS events were generated using ARIADNE 4.12 [6] and LEPTO 6.5.1 [5] programs interfaced with the HERACLES [7] program for radiation correction. ARIADNE

uses the parton cascade modelled with the colour-dipole model (CDM) and for the hadronisation phase the Lund string-fragmentation model [8]. Another approach to model the parton cascade was included in LEPTO which incorporated the LO matrix element matched to parton showers (MEPS). This program also used the Lund string fragmentation model.

The distributions generated by Monte Carlo (MC) models included the products of strong and electromagnetic decays, but excluded the decay products of weakly decaying particles with lifetime greater than 3×10^{-11} s.

2 Scaled momentum spectra

The scaled momentum distributions are investigated as a function of Q and x, in the range $0.002 < x < 0.75$ and $160 < Q^2 < 40960$ GeV^2. Results are presented in Figs 1-3 together with the previous ZEUS results of $10 < Q^2 < 160$ GeV^2 [3]. Figures show the data points with statistical and systematic uncertainties.

The inclusive charged particle distributions, $1/\sigma\ d\sigma/d\xi_p$ in the current region of the Breit frame, where σ is the DIS cross section in the chosen intervals of Q^2, are shown in Fig. 1.

The scaled momentum distributions are approximately Gaussian in shape. As Q^2 increases, the multiplicity increases and, in addition, the peak of the distribution moves to larger ξ_p values. The suppression of hadron production at very small x_p or large ξ_p is a consequence of the destructive interference of soft gluons.

The MLLA predictions[9, 10] in Fig. 1 are calculated with two free energy-independent parameters adjusted to values deduced from the LEP data ($\Lambda = Q_0 = 270$ MeV for the effective energy scale and $K_h = 1.31$ for the LPHD hypothesis). The obtained limiting spectra give a reasonable description of the shape at $80 < Q^2 < 1280$ GeV^2. In the low Q^2 regions the average multiplicity is lower than predicted by MLLA which is interpreted by significant migrations of particles to the target region of the Breit frame. As Q^2 increases the peaks are shifted more than expected towards high $\ln(1/x_p)$. We conclude that the analytical MLLA QCD calculations under LPHD assumption cannot describe the data in the entire range of x_p and Q^2.

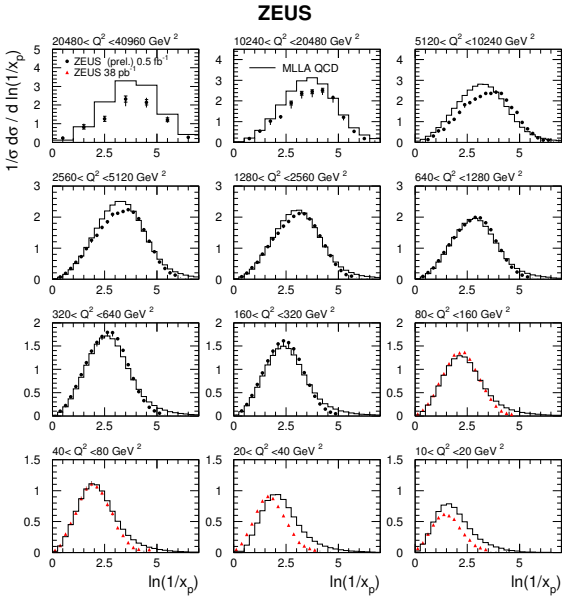

Figure 1: The charged particle distributions. The triangles points come from [3]. The full line represents the MLLA predictions.

The scaling violations can be seen more clearly if the data are plotted in bins of fixed x_p as a function of Q^2.

Figure 2 shows that the distributions rise with Q^2 at low x_p and fall-off at high x_p and high Q^2. Below $Q^2 = 80\,\mathrm{GeV}^2$ (see Fig. 1) the fall-off is due to depopulation of the current region discussed before. These regions are relatively well reproduced by ARIADNE and LEPTO predictions. At the higher Q^2 regions and higher x_p the data fall down faster than predicted by leading order MC models with parton shower included. The statistical precision of the data prevents any stronger statement to be made. No tuning of the Monte Carlo parameters has been performed to improve the agreement with the data.

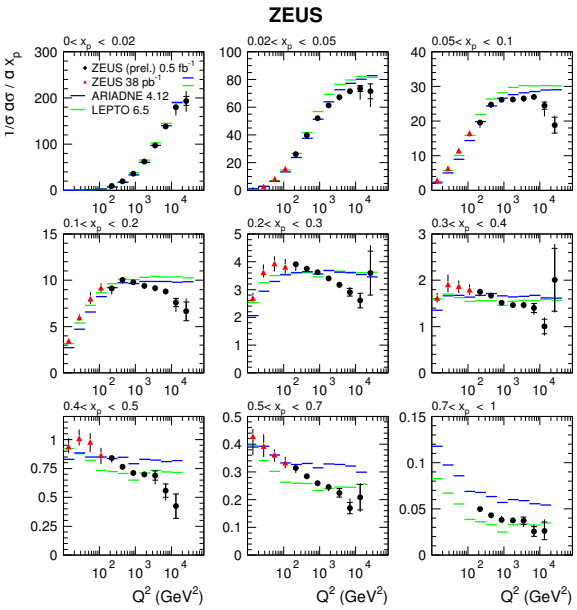

Figure 2: The inclusive charged particle distributions as a function of Q^2 in x_p bins. The triangles come from [3]. The darker (blue) lines represent the ARIADNE predictions and the lighter (green) lines represent the LEPTO predictions.

Figure 3 shows the comparisons with the NLO calculations. Generally, the calculations do not describe the data well. The data are overlaid with predictions of the available FF parametrisations [11, 12, 13] fitted from e^+e^- data. The parametrisations are calculated for $x_p > 0.1$, where the theoretical uncertainties are small and unaffected by the hadron mass effects which are not included in the fragmentation function. The logarithmic energy slope in the ep data is steeper than in all the parametrisations. At low $x_p < 0.2$ all predictions fail to describe the data. We conclude that the scaling violation in the ep data is stronger than predicted.

The observed discrepancy between data and parametrisations as well as the inconsistency with the MC models at high Q^2 may suggest that a contribution from heavy-flavor states may be different than in e^+e^- collisions.

3 Conclusions

Charged particle distributions have been measured in the current region of the Breit frame in DIS over a wide range of Q^2 values and show clear evidence in a single experiment for scaling violations in scaled momenta as a function of Q^2. They support the hypothesis of the coherent nature of QCD cascade. The data are neither well described by the MLLA calculations together with LPHD nor with NLO calculations. The leading order MC models with parton shower included need to be improved to reproduce the measured data at the highest and lowest Q^2 values.

Author thanks the DESY Directorate for the financial support and Dr. S. Albino for providing the theoretical calculations.

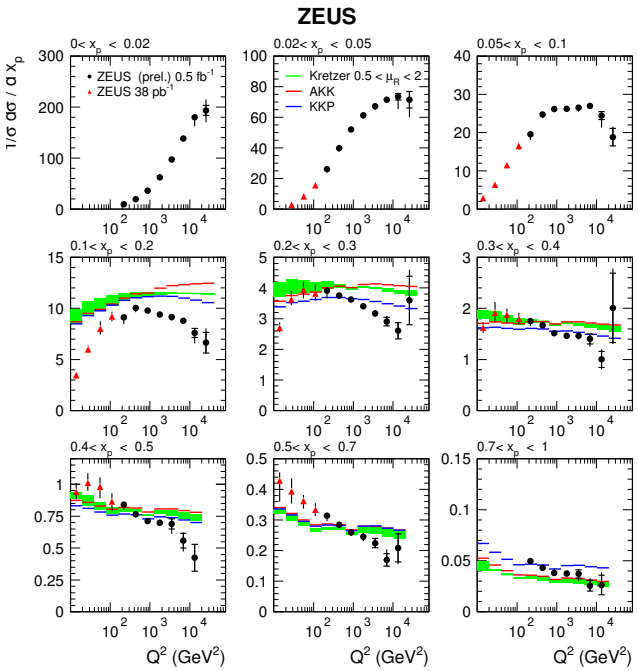

Figure 3: The inclusive charged particle distributions $1/\sigma\ d\sigma/dx_p$ as in Fig. 2. The wide (green) lines represent Kretzer's predictions, the thin and light (blue) lines represent Kniehl-Kramer-Pötter's predictions improved recently by Albino-Kniehl-Kramer and marked as the thin and dark (red) lines.

References

[1] Slides: `http://indico.cern.ch/contributionDisplay.py?contribId=232&sessionId=6&confId=9499`

[2] R.P. Feynman, *Photon Hadron Interactions* (1972).

[3] ZEUS Collaboration, M. Derrick *et al.*, Z. Phys. C **67** 93 (1995).
ZEUS Collaboration, J. Breitweg *et al.*, Phys. Lett. B **414** 428 (1997).
ZEUS Collaboration, J. Breitweg *et al.*, Eur. Phys. J. C **11** 258 (1999).

[4] ZEUS Collaboration, U. Holm *The ZEUS Detector*, Status Report (unpublished), DESY (1993), available on `http://www-zeus.desy.de/bluebook/bluebook.html`.

[5] G. Ingelman, A. Edin and J. Rathsman, Comp. Phys. Comm. **101** 108 (1997).

[6] L. Lönnblad, Comp. Phys. Comm. **71** 15 (1992).

[7] A. Kwiatkowski, H. Spiesberger and H.J. Möhring, Comp. Phys. Comm. **69** 155 (1992).

[8] B. Andersson *et al.*, Phys. Rep. **97** 31 (1983).

[9] V.A. Khoze, W. Ochs, Int. J. Mod. Phys. A **12** 2949 (1997).

[10] Y.L. Dokshitzer, V.A. Khoze, A. Mueller and S. Troyan, *Basics of Perturbative QCD*, Editions Frontiéres, Gif-sur-Yvette, France (1991).

[11] S. Kretzer, Phys. Rev. D **62** 054001 (2000).

[12] B.A. Kniehl, G. Kramer, B. Pötter, Phys. Rev. Lett. **85** 5288 (2000).

[13] S. Albino, B.A. Kniehl, G. Kramer, NUcl. Phys. B **725** 181 (2005).

Measurements of $K^{\pm}$, K^0_S, Λ and $\bar{\Lambda}$ and Bose-Einstein Correlations between Kaons at ZEUS

B.B. Levchenko *
(*On behalf of the ZEUS Collaboration)*

Moscow State University, Skobeltsyn Institute of Nuclear Physics
119991 Moscow, Russian Federation

Measurements of production of the neutral and charged strange hadrons in $e^{\pm}p$ collisions with the ZEUS detector are presented. The data on differential cross sections, baryon-to-meson ratios, baryon-antibaryon asymmetry and Bose-Einstein correlations in deep inelastic scattering and photoproduction are summarized [1].

1 Introduction

After pions, strange hadrons are most copiously produced particles in $e^{\pm}p$ collisions with a centre-of-mass energy of 318 GeV at HERA. In phenomenological models based on the Lund string scheme [2], an intensity of strange quark production is regulated by a free parameter λ_s, which has a value in the range from 0.2 to 0.4 for different processes.

The experimental results on $K^{\pm}$, K^0_S, Λ, and $\bar{\Lambda}$ production [3, 4] presented in this note are based on a data sample of $121\,\mathrm{pb}^{-1}$ collected by the ZEUS experiment at HERA. This is about 100 times larger data sample than used in previous HERA publications and extend the kinematical region of the measurements, thereby providing a tighter constraint on models.

2 Measurements of K^0_S, Λ and $\bar{\Lambda}$

Weak decaying neutral K^0_S and Λ are well reconstructed in the modes $K^0_S \to \pi^+\pi^-$, $\Lambda \to p\pi^-$, $\bar{\Lambda} \to \bar{p}\pi^+$ via displaced secondary vertices. The measurements have been performed in three different regions of Q^2: deep inelastic scattering (DIS) with $Q^2 > 25\,\mathrm{GeV}^2$; DIS with $5 < Q^2 < 25\,\mathrm{GeV}^2$; and photoproduction (PHP), $Q^2 \simeq 0\,\mathrm{GeV}^2$. In the PHP sample, two jets, each of at least 5 GeV transverse energy, were required.

Spectra of K^0_S and $\Lambda + \bar{\Lambda}$ in DIS. Measured differential cross sections are shown in Fig. 1. The cross sections are compared to the absolute predictions of ARIADNE 4.12 [5] and LEPTO 6.5 [6] MC calculations. The ARIADNE program with $\lambda_s = 0.3$ describes the $\Lambda + \bar{\Lambda}$ data reasonably well in both Q^2 samples. The description of the data on the lighter strange meson K^0_S by ARIADNE is less satisfactory. The slope of the P_T^{LAB} dependence is incorrect and in the high-Q^2 domain the data already requires $\lambda_s < 0.3$. The cross section at low x_{Bj} is underestimated for both low- and high-Q^2 samples [3]. The LEPTO MC does not describe the data well and predicts too fast grow of the cross sections with Q^2. We conclude, that in production of baryons the data requers λ_s to be approximately constant but in K^0_S production λ_s have to decrease with Q^2.

Baryon-antibaryon asymmetry in DIS and PHP. A positive asymmetry of 3.5% is predicted in DIS [7], due to the so called gluon-junction mechanism that makes it possible

*Partly supported by Russian Foundation for Basic Research grant No. 05-02-39028-NSFC-a.

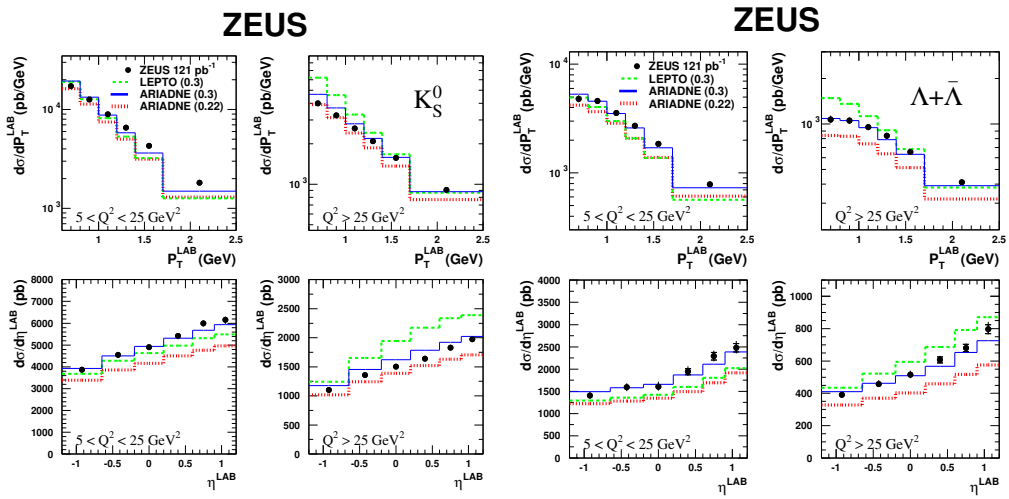

Figure 1: Differential K^0_S and $\Lambda + \bar{\Lambda}$ production cross-sections. The model predictions are at values of a strangeness suppression factor λ_s shown in parenthesis.

for the *baryon number to travel* several units of rapidity, in this case from the proton beam direction to the rapidity around 0 in the laboratory frame.

The baryon-antibaryon asymmetry $\mathcal{A} = (N(\Lambda) - N(\bar{\Lambda}))/(N(\Lambda) + N(\bar{\Lambda}))$ has been measured and compared to MC predictions from ARIADNE, LEPTO and PYTHIA [8]. The following values were obtained: $\mathcal{A} = 0.3 \pm 1.3^{+0.5}_{-0.8}\%$ at high Q^2 and have to be compared to the ARIADNE ($\lambda_s = 0.3$) prediction of $0.4 \pm 0.2\%$; in PHP $\mathcal{A} = -0.07 \pm 0.6^{+1.0}_{-1.0}\%$, compared to the PYTHIA prediction of $0.6 \pm 0.1\%$.

Figure 2 shows $\mathcal{A}$ at high-Q^2 and in PHP. In all cases, $< \mathcal{A} >$ is consistent both with no asymmetry and consistent with the very small asymmetry predicted by Monte Carlo. However, as shown in Figs 2, in DIS the baryon-antibaryon asymmetry became positive and increases in the incoming proton hemisphere ($\eta^{LAB} > 0$), as well as at P_T^{LAB} below 1 GeV.

Baryon-to-meson ratio in photoproduction. The relative yield of strange baryons and mesons was studied with the ratio $\mathcal{R} = (N(\Lambda) + N(\bar{\Lambda}))/N(K^0_S)$. Figure 3 shows $\mathcal{R}$ for the PHP sample. For the direct-enriched sample, where $x_\gamma^{\rm OBS} > 0.75$, $\mathcal{R}$ is about 0.4, the same value as in DIS at low $x_{\rm Bj}$ and low Q^2 [3]. However, $\mathcal{R}$ rises to a value of about 0.7 towards low $x_\gamma^{\rm OBS}$ (resolved-enriched sample), while it stays flat in the PYTHIA prediction.

In order to study this effect further, the PHP events were divided into two samples . In the first, called *fireball-enriched*, the jet with the highest transverse energy was required to contribute at most 30% to the total hadronic transverse energy. The other sample, containing all the other events, was called *fireball-depleted*. The measured $\mathcal{R}$ (see Fig. 3, Right:) is larger for the fireball-enriched sample, most significantly at high $P_T^{\rm LAB}$, than it is for the fireball-depleted sample. This feature is not reproduced by PYTHIA, which predicts almost the same $\mathcal{R}$ for both samples. The PYTHIA prediction reasonably describes the measured values of $\mathcal{R}$ for the fireball-depleted sample. This is not surprising as PYTHIA generates jets in events according to the multiple interaction mechanism, which makes several independent jets, like those in DIS or e^+e^- where baryons and mesons are created locally.

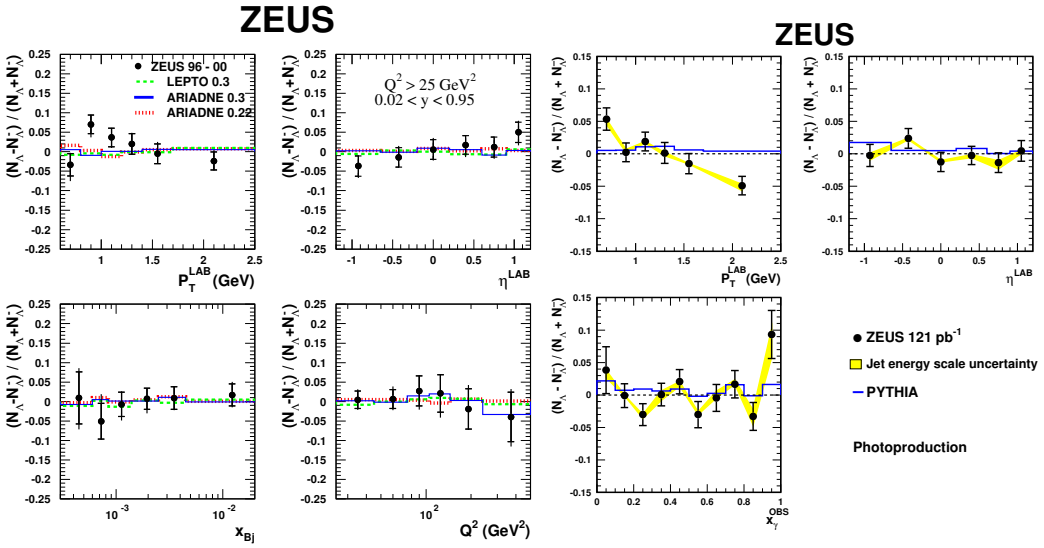

Figure 2: The baryon-antibaryon asymmetry $\mathcal{A}$ as a function of P_T^{LAB}, η^{LAB}, Q^2, $x_{\rm Bj}$ and $x_\gamma^{\rm OBS}$. Left: in the DIS high-Q^2 sample. Right: The photoproduction sample with the predictions from PYTHIA for $\lambda_s = 0.3$.

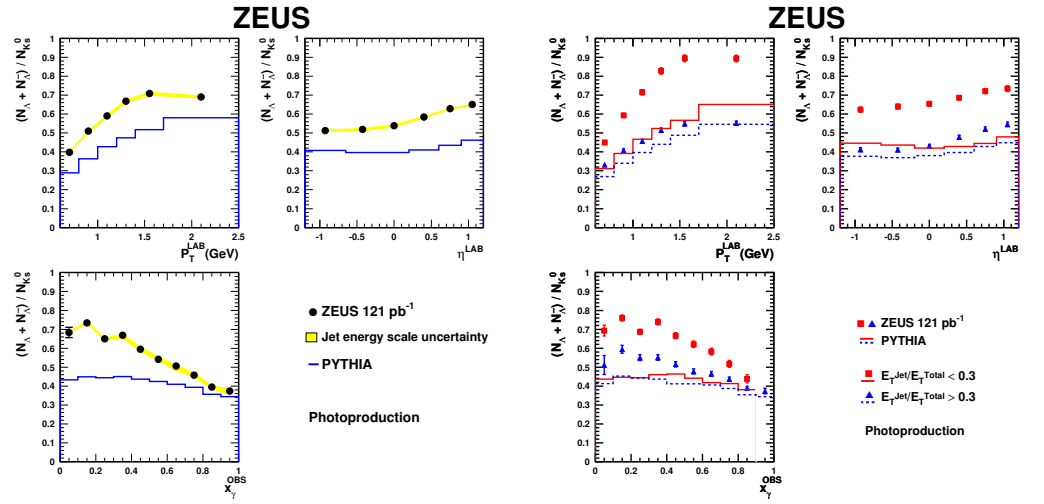

Figure 3: The ratio $\mathcal{R}$ as a function of P_T^{LAB}, η^{LAB}, and $x_\gamma^{\rm OBS}$ for the PHP events. Left: The ratio from the normal PHP sample. Right: The ratio from the fireball-enriched (squares) and the fireball-depleted (triangles) samples. The predictions from PYTHIA for $\lambda_s = 0.3$.

We note that the increase of the ratio $\mathcal{R}$ toward the proton hemisphere, reflects a rapid grow of the $\Lambda + \bar{\Lambda}$ cross section as η^{LAB} increases, as compared to the K_S^0 cross section grow [3].

3 Bose-Einstein correlations of charged and neutral kaons in DIS

Primordial quantum correlations between identical bosons, so-called Bose-Einstein correlations (BEC), so far is only the method to estimate the space-time geometry of an elementary particle emission source. The measurements of the radius of the emission source have been mostly performed with pure quantum states $\pi^{\pm}$, $K^{\pm}$, $p/\bar{p}$. For mixed quantum states, like K^0_S, the information is scare.

The results presented below were obtained with charged kaons selected using the energy-loss measurements, dE/dx. The identification of $K^{\pm}$ is possible for $p < 0.9\,\mathrm{GeV}$. The resulting data sample contained 55522 $K^{\pm}K^{\pm}$ pairs. The K^0_S mesons were identified via displaced secondary vertices. After all cuts, the selected data sample contained 18405 $K^0_S K^0_S$ pairs and 364 triples [4].

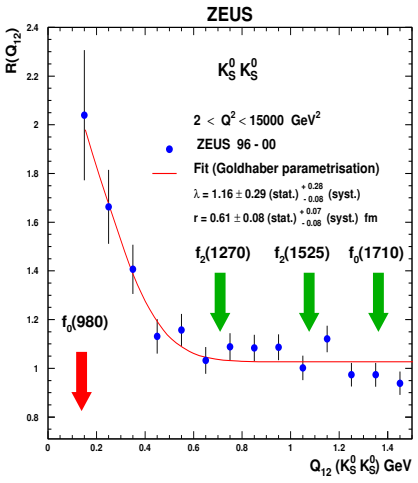

Figure 4: The two-particle correlation functions at $<Q^2>= 35\,\mathrm{GeV}^2$ for neutral kaons with fits to the Goldhaber function. Arrows indicates Q_{12} regions with contributions from resonances in the $K^0_S K^0_S$ system.

Figure 4 shows the two-particle correlation function $R(Q_{12})$ for identical kaons calculated using the double ratio method $R(Q_{12}) = R_{data}(Q_{12})/R_{MC}(Q_{12})$, where $R_{data}(Q_{12})$ is the ratio of the two-particle densities constructed from pairs of kaons coming from the same and different events. $R_{MC}(Q_{12})$ is obtained in similar way for ARIADNE MC events without BEC. Q_{12} is given by $Q_{12} = \sqrt{-(p_1 - p_2)^2}$. Assuming a Gaussian shape of emission source, $R(Q_{12})$ were fitted by the standard Goldhaber-like function $R(Q_{12}) = \alpha(1 + \lambda \exp(-Q^2_{12} r^2))$ to extract the degree of the source coherence λ and the source radius r. The measured radii for $K^{\pm}K^{\pm}$ and $K^0_S K^0_S$ are close to each other [4]. In case of $K^0_S K^0_S$, the fit (see Fig. 4) does not take into account a possible contamination from the scalar $f_0(980)$ decaying below the threshold. The most probable fraction of $f_0(980)$ which allows describe the excess of data over MC was estimated to be 4%. The results corrected for the f_0 contamination are $\lambda = 0.70 \pm 0.19^{+0.47}_{-0.53}$ and $r = 0.63 \pm 0.09^{+0.11}_{-0.08}$ fm. Thus, the $f_0(980) \to K^0_S K^0_S$ decay can significantly affect the λ parameter for $K^0_S K^0_S$ correlations. The radius values obtained in DIS agrees with e^+e^- annihilation results at LEP [4].

References

[1] B.B. Levchenko, Slides: `http://indico.cern.ch/contributionDisplay.py?contribId=233&sessionId=6&confId=9499`

[2] B. Andersson, The Lund model, in *Camb. Monogr. Part. Phys. Nucl. Phys. Cosmol.* **7** 1 (1997).

[3] ZEUS Collab., S. Chekanov *et al.*, Eur. Phys. J. **C51** 1 (2007).

[4] ZEUS Coll., S. Chekanov *et al.*, DESY-07-069 (2007), accepted by Phys. Lett. **B**.

[5] L. Lönnblad, Comp. Phys. Comm. **71**, 15 (1992).

[6] G. Ingelman, A. Edin and J. Rathsman, Comp. Phys. Comm. **101**, 108 (1997).

[7] B. Kopeliovich and B. Povh, Z. Phys. **C 75**, 693 (1997).

[8] T. Sjöstrand *et al.*, Comp. Phys. Comm. **135**, 238 (2001).

Nuclear p_t-Broadening at HERMES

Yves Van Haarlem[(1)], Anton Jgoun[(2)], Pasquale Di Nezza[(3)]
on behalf of the HERMES Collaboration

1- Department of Subatomic and Radiation Physics, University of Gent, 9000 Gent, Belgium

2- Petersburg Nuclear Physics Institute, St. Petersburg, Gatchina, 188350 Russia

3- Istituto Nazionale di Fisica Nucleare, Laboratori Nazionali di Frascati, 00044 Frascati, Italy

The first direct measurement of p_t-broadening effects in cold nuclear matter has been studied as a function of several kinematic variables for different hadron types. The data have been accumulated by the HERMES experiment at DESY, in which the HERA 27.6 GeV lepton beam scattered off several nuclear gas targets.

1 Introduction

At HERMES nuclear semi-inclusive deep-inelastic scattering (SIDIS) is used to study hadronization. In the HERMES kinematics it is very likely that hadronization takes place inside the nucleus. In this regime the nucleus acts as a nano lab providing multiple scattering centers in the form of nucleons. Effects like the EMC effect and nuclear attenuation [2] are already measured. An effect that is measured for the first time at HERMES is the modification of the transverse momentum in nuclear matter or p_t-broadening which is presented in this work. Here, p_t is the transverse momentum of the produced hadron with respect to the direction of the virtual photon. Besides the measurement of a ratio of average hadron transverse momentum (p_t-ratio): $\langle p_t^2\rangle_A^h/\langle p_t^2\rangle_D^h$ a new observable has been used: $\Delta\langle p_t^2\rangle^h$, also called p_t-broadening:

$$\Delta\langle p_t^2\rangle^h = \langle p_t^2\rangle_A^h - \langle p_t^2\rangle_D^h, \tag{1}$$

where $\langle p_t^2\rangle_A^h$ is the average transverse momentum squared obtained by a hadron of type h produced on a nuclear target with atomic mass number A, and $\langle p_t^2\rangle_D^h$ is the same but for a Deuterium target. These measurements increase our knowledge about the space-time evolution of hadronization.

Nuclear SIDIS has the advantage that there are no initial state interactions due to the fact that leptons are point-like particles that do not contain quarks which can interact before scattering of the target. This makes the interaction easier to interprete and might help to understand the more complex heavy-ion collisions.

p_t-broadening might be the most sensitive probe for the *production time* as it provides a direct measurement of the production time t_p ($\Delta\langle p_t^2\rangle \propto t_p$) in specific models, e.g. [3]. This is because the hadronizing quark only contributes at time intervals $t < t_p$ to the p_t-broadening. As soon as the pre-hadron is formed, no further broadening occurs, because inelastic interactions are suppressed for the pre-hadron (at $z > 0.5$), thus only broadening via elastic rescattering is still possible. Here, z is the energy fraction of the virtual photon carried by the produced hadron. However, the elastic cross section is so small that even for pions the mean free path in nuclear matter is about 20 fm. It is even longer for a small-size pre-hadron due to color transparency. A disappearance of the broadening effect is expected at large $z \to 1$ because of energy conservation.

2 Analysis

The data have been accumulated by the HERMES experiment at DESY, in which the HERA 27.6 GeV positron beam scattered off several nuclear gas targets [4]. Events were selected by requiring $Q^2 > 1$ GeV^2, $W^2 > 10$ GeV^2, and $\nu < 23$ GeV where W is the invariant mass of the photon-nucleon system and ν is the virtual photon energy. Pions and Kaons are identified in the momentum range $2< P <15$ GeV using the information from a ring imaging Čerenkov detector.

The p_t-broadening effects have been studied as a function of the atomic number A, Q^2, ν, and z for different hadron types produced on ^{3}He, ^{4}He, N, Ne, Kr, and Xe targets.

The pion sample was corrected for exclusive ρ^0 decay pions using a Monte Carlo simulation. This correction was only significant in the highest z bin where these decay pions contribute more than 50 %. After the correction the p_t-ratio becomes consistent with one and the p_t-broadening with zero (in the highest z-bin).

The p_t-broadening was corrected for detector smearing, acceptance effects and QED radiative effects using a PYTHIA Monte Carlo generator together with a GEANT3 simulation of the HERMES spectrometer. For p_t-broadening an unfolding method was used. For the p_t-ratio a Monte Carlo study showed that most acceptance effects cancel out except the Cahn effect which was included into the systematic uncertainty. Identified hadron samples were corrected for misidentified hadrons using an unfolding method.

The systematic uncertainty includes contributions from the correction for ρ^0 decay pions, detector smearing and acceptance, radiative effects, and hadron misidentification (if applicable). The dominant part in the systematic uncertainty of the p_t-broadening is coming from the model dependence of the acceptance correction ($\sim$ 5 %), which is estimated using the PYTHIA and the LEPTO generator, and from the Cahn effect for the p_t-ratio (4 %).

3 Results

In figure 1 (upper panel) a clear dependence of p_t-broadening on the atomic number A can be seen. It also shows that the p_t-broadening becomes consistent with zero as $z \rightarrow 1$. The latter is expected by energy conservation as the fact that a hadron with a high z value is detected means that no energy could have been lost in any kind of interaction or reaction process. In this case the final-state hadron had to be formed immediately and $t_p \rightarrow 0$. p_t-broadening increases as a function of Q^2, figure 1 (lower panel).

Figure 2 shows the $\langle p_t^2 \rangle$ ratio as a function of the atomic mass number for different momentum ranges. For $^{3,4}He$ targets the ratio is close to one for small momenta. This indicates that the size of the helium nucleus is smaller than the hadron production time. For heavier targets the ratio increases in the momentum range 2-7 GeV with a maximum around 7 GeV and then decreases. The behavior of the p_t-ratio for heavy targets at relative small momenta (below 7 GeV) can be caused by a production time that is smaller than the size of the nucleus. This could explain the increase of the p_t-ratio for increasing hadron momentum. The p_t-ratio decreases for high momentum, i.e. that the production time decreases with increasing final hadron momentum. At very large hadron momentum there are values smaller than one. In this regime z has to be close to 1 because these hadrons have the maximum possible momentum. Such behavior could point out that the intrinsic momentum of the quark in a nucleon inside the nucleus is smaller than for a quark in the free nucleon.

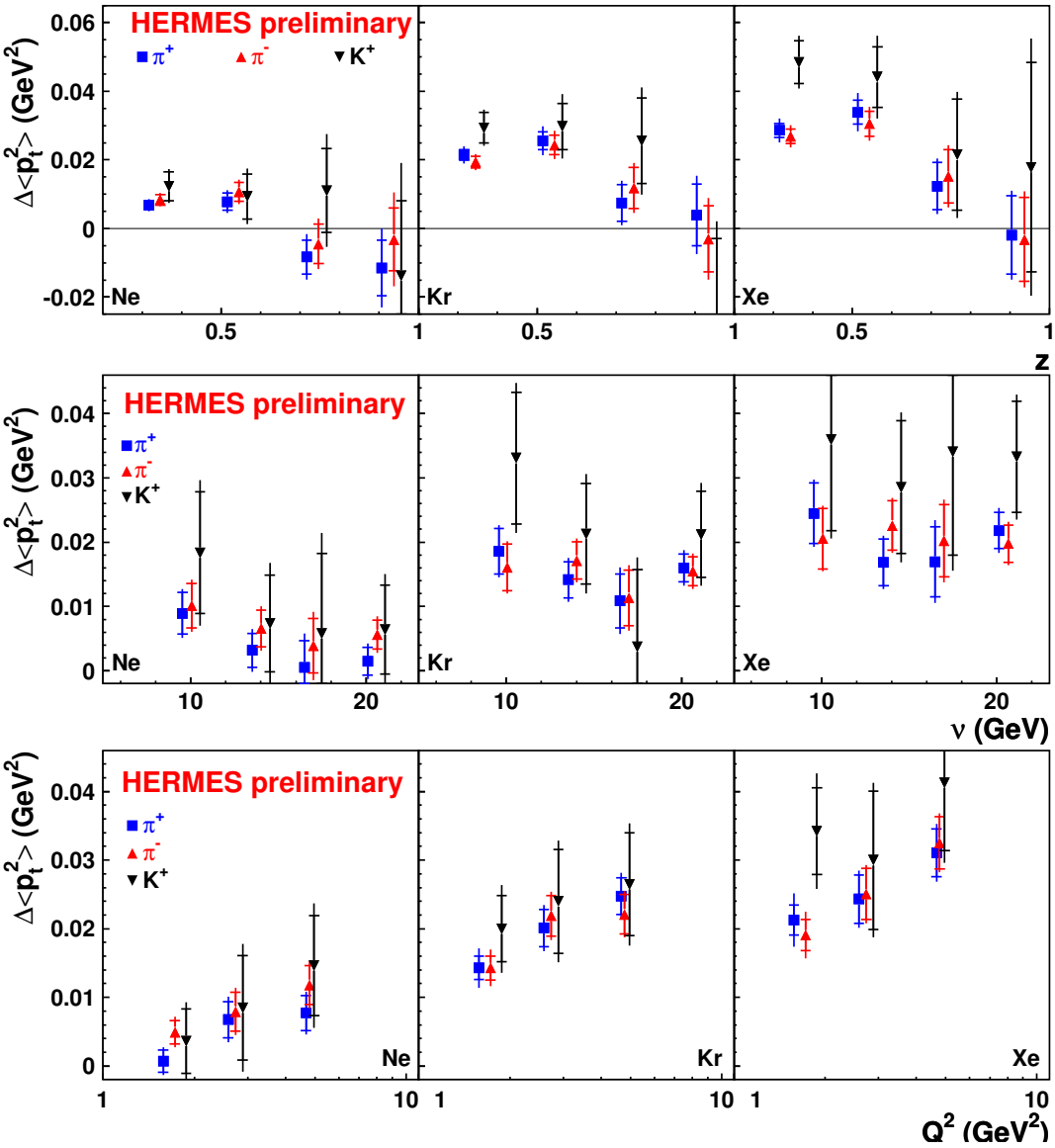

Figure 1: p_t-broadening for different hadron types produced from Ne, Kr, and Xe targets as a function of z (upper panel), ν (middle panel), and Q^2 (lower panel). The inner error bars represent the statistical error and the outer ones the quadratic sum of the statistical and systematic uncertainties.

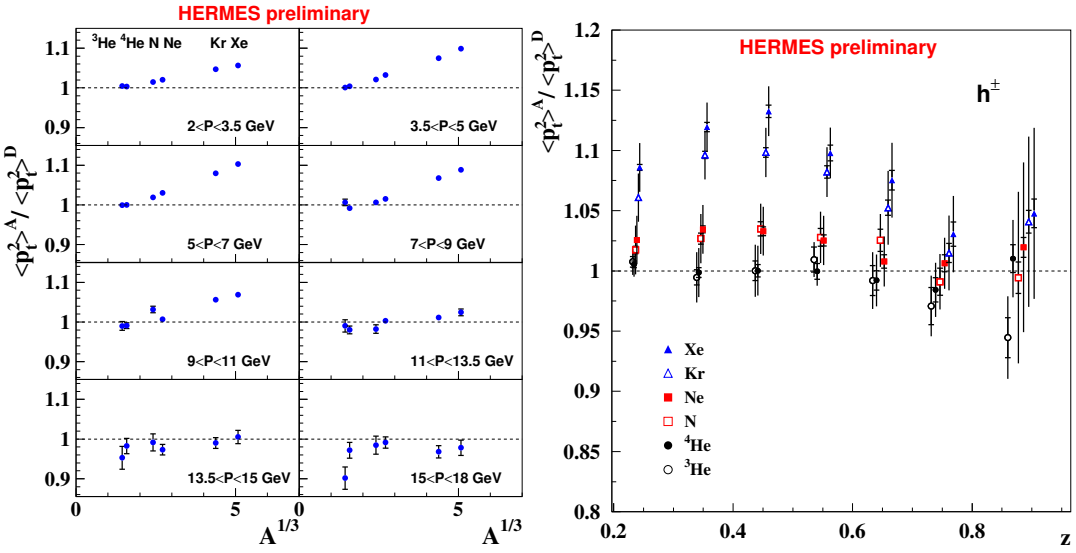

Figure 2: (Left) p_t^2-ratio versus $A^{1/3}$ for different hadron momentum regions for all charged hadrons. (Right) Charged hadron p_t-ratio versus z for several nuclear targets for all charged hadrons. The inner error bars represent the statistical error and the outer ones the quadratic sum of the statistical and systematic uncertainties.

4 Conclusions

The first measurement of p_t-broadening effects on ^{3,4}He, N, Ne, Kr, and Xe targets have been presented [7]. Results were investigated for different hadron types and as a function of several kinematic variables. A clear signal of broadening is observed and it provides very important information to this physics field were a profound interest has been expressed by theoreticians.

References

[1] Slides:
`http://indico.cern.ch/contributionDisplay.py?contribId=291&sessionId=6&confId=9499`

[2] Hermes Collaboration, A. Airapetian et al., Eur. Phys. J. **C20** (2001) 479; A. Airapetian et al., Phys. Lett. **B577** (2003) 37; A. Airapetian et al., Phys. Rev. Lett. **96** (2006) 16230; A. Airapetian et al., submitted to Nucl. Phys. **B**, arXiv:0704.3270v1 [hep-ex].

[3] B.Z. Kopeliovich, Nucl. Phys. **A740** (2004) 211.

[4] Hermes Collaboration, K. Ackerstaff et al., Nucl. Instr. Meth. **A417** (1998) 230.

[5] T. Sjöstrand et al., Comp. Phys. Comm. **135** (2001) 238.

[6] Hermes Collaboration, A. Airapetian et al., Eur. Phys. J. **C17** (2000) 3898.

[7] Hermes public plots: www-hermes.desy.de/notes/pub/trans-public-subject.html

Structural Relations between Harmonic Sums up to w=6

J. Blümlein[1] and S. Klein[1] *

Deutsches Elektronen-Synchrotron, DESY, Platanenallee 6, D-15738 Zeuthen, Germany

Multiply nested finite harmonic sums $S_{a_1 \ldots a_n}(N)$ occur in many single scale higher order calculations in Quantum Field Theory. We discuss their algebraic and structural relations to weight w=6. As an example, we consider the application of these relations to the soft and virtual corrections for Bhabha-scattering to $O(\alpha^2)$.

1 Introduction

Single scale processes in massless Quantum Field Theories [2, 3], or field theories being considered in the limit $m^2/Q^2 \to 0$ [4], both for space- and time-like processes, exhibit significant simplifications when calculated in Mellin space if compared to representations in momentum-fraction $x-$space. Here, the Wilson coefficients and splitting functions are expressed by Nielsen-type integrals

$$S_{n,p,q}(x) = \frac{(-1)^{n+p+q-1}}{\Gamma(n) p! q!} \int_0^1 \frac{dz}{z} \ln^{(n-1)}(z) \ln^p(1-zx) \ln^q(1+zx)$$

or harmonic polylogarithms [5]. The simplification is, to some extent, due to the structure of Feynman parameter integrals which possess a Mellin symmetry. The respective expressions can be expressed by finite harmonic sums $S_{a_1 \ldots a_n}(N)$ for processes to 3–loop order [6, 7], which form the appropriate language. Within the light-cone expansion, or analogous formalisms for time-like processes, the argument of the harmonic sums are even- or odd integers, depending on the process. However, one may consider mathematical generalizations, continuing the argument analytically to rational, real and complex values $N \epsilon \mathbf{Q}, \mathbf{R}, \mathbf{C}$, respectively, [6,8]. In these extensions new relations between the harmonic sums are obtained, which lead to more compact representations. Since the hard-scattering cross sections usually have to be convoluted with non-perturbative parton densities, it is convenient to widely work in Mellin space using analytic representations, also for the solution of the evolution equations. This also applies to the treatment of heavy flavor contributions in the full phase space, for which concise semi-analytic representations were derived [9]. The final $x-$space results are obtained by a single numerical Mellin–inversion performed by a contour integral around the singularities of the problem.

In this note we give a summary on the algebraic and structural relations for finite harmonic sums, occurring in hard scattering processes. As an example we consider the virtual and soft QED corrections to Bhabha-scattering to $O(\alpha^2)$ in the on-mass-shell scheme [10] to show that also this process fits to the general basis-representation being derived for various other two– and three–loop QCD processes.

*This paper was supported in part by SFB-TR-9: Computergestütze Theoretische Teilchenphysik and Studienstiftung des Deutschen Volkes.

2 Algebraic Relations

The complexity of finite harmonic sums is given by $N_{max} = 2 \cdot 3^{w-1}$, with the weight $w = \sum_{k=1}^{n} |a_k|$ growing exponentially. In the $x-$space representation of the 2–loop Wilson coefficients in QCD, which are described by $w = 4$, nearly 80 functions emerge, which corresponds to the maximum level possible, cf. [6, 11]. The algebraic relations of finite harmonic sums operate on their index set and are implied by their quasi-shuffle algebra [12]. The algebraic relations of finite harmonic sums were investigated in [13] in detail. An example for the shuffle product is

$$S_{a_1,a_2} \sqcup\!\sqcup S_{a_3,a_4} = S_{a_1,a_2,a_3,a_4}+S_{a_1,a_3,a_2,a_4}+S_{a_1,a_2,a_4,a_2}+S_{a_3,a_4,a_1,a_2}+S_{a_3,a_1,a_4,a_2}+S_{a_3,a_1,a_2,a_4} \; .$$

For a given index set the number of basic harmonic sums is counted by the number of Lyndon words and can be calculated by a Witt–formula. Investigating the type of harmonic sums emerging in physical single–scale problems up to 3–loop order, cf. [2–4], the index $\{-1\}$ never occurs. Their number is $N_{\neg -1} = [(1-\sqrt{2})^w + (1+\sqrt{2})^w]/2$ [14]. One therefore may significantly reduce the number of basic functions using $N_{\neg -1}$ in the corresponding Witt formula. The following table illustrates the corresponding complexities of combinations $\#_c$ and the number of algebraic basis elements $\#_b$ in dependence of the weight w. The initial complexity in case of the absence of indices $a_l = -1$ is lower than the number of algebraic basis elements in the complete case.

w	1	2	3	4	5	6
$\#_c$	2	8	26	80	242	728
$\#_b$	2	5	13	31	79	195
$\#_c(\neg -1)$	1	4	11	28	69	168
$\#_b(\neg -1)$	1	3	7	14	30	60

3 Structural Relations

The algebraic relations lead to a first reduction of the complexity of finite harmonic sums. They are independent of the value of these quantities. Beyond these relations, the structural relations are of a more specific type, cf. [6,15]. There are three types of these relations. The first class is implied by allowing half-integer values for N. A second class emerges through partial integration using the representations of harmonic sums through Mellin-transforms e.g. of weighted harmonic polylogarithms. The third set is implied by differentiating harmonic sums w.r.t. their argument, which requires $N \in \mathbf{R}$. To illustrate case 1 we represent

$$\frac{1}{1-x^2} = \frac{1}{2}\left[\frac{1}{1-x} + \frac{1}{1+x}\right].$$

The Mellin transform of this equation implies, that $S_{-1}(N)$ is linearly dependent of $S_1(N)$, if $N \in \mathbf{Q}$. Various relations of this type emerge at higher weight [15]. If $N \in \mathbf{R}$, one may differentiate harmonic sums and obtains

$$\frac{d}{dN} S_{a_1 \ldots a_n}(N) = \int_0^1 dx \; x^{N-1} \ln(x) f(x) \; .$$

$S_{a_1 \ldots a_n}(N)$ is given by the Mellin transform of $f(x)$. One may represent the derivative in terms of polynomials of harmonic sums and their values at $N \to \infty$. The analytic

continuation of a harmonic sum to $N \epsilon \mathbf{C}$ is a meromorphic function with poles at the non-positive integers. Up to polynomials growing $\propto S_1^m(N)$, $|N| \to \infty$, which can be separated, harmonic sums are factorial series. I.e. they obey an analytic recursion relation $F(z+1) \to F(z)$ and one may calculate their asymptotic representation for $z \to \infty$ analytically. In this way these functions are uniquely defined in the complex plane. Due to the above properties we now define equivalence classes of representations, which contain a harmonic sum and all its derivatives. We will only count these equivalence classes, since all derivatives can be easily found analytically if the respective lowest weight sum of the class is known. In the following table we summarize the functions of the basic Mellin transforms up to $w = 5$. The case $w = 6$ is still to be completed.

$w = 1$	$1/(x-1)_+$		
$w = 2$	$\ln(1+x)/(x+1)$		
$w = 3$	$\mathrm{Li}_2(x)/(x \pm 1)$		
$w = 4$	$\mathrm{Li}_3(x)/(x+1)$	$S_{1,2}(x)/(x \pm 1)$	
$w = 5$	$\mathrm{Li}_4(x)/(x \pm 1)$	$S_{1,3}(x)/(x+1)$	$S_{2,2}(x)/(x \pm 1)$
	$\mathrm{Li}_2^2(x)/(x+1)$	$[S_{2,2}(-x) - \mathrm{Li}_2^2(-x)/2]/(x \pm 1)$	
$w = 6$	$\mathrm{Li}_5(x)/(x+1)$	$S_{1,4}(x)/(x \pm 1)$	$S_{2,3}(x)/(x \pm 1)$
	$S_{3,2}(x)/(x \pm 1)$	...	

These functions emerge in the following processes : number of fct.

- $O(\alpha)$ $w \leq 2$ Wilson Coefficients/anom. dim. #1
- $O(\alpha^2)$ $w \leq 3$ Anomalous Dimensions #2
- $O(\alpha^2)$ $w \leq 4$ Wilson Coefficients $\# \leq 5$
- $O(\alpha^3)$ $w \leq 5$ Anomalous Dimensions #15
- $O(\alpha^3)$ $w \leq 6$ Wilson Coefficients #29+

4 Example: Bhabha Scattering

As an example we consider the soft- and virtual corrections to Bhabha-scattering up to $O(\alpha^2)$, $T_2(x) = \delta_0^{(2)}(x) \times (1 - x + x^2)/x^2$, [10]. The $x-$space expression simplifies in Mellin N space and depends on *three* basic functions $S_{2,1,1}, S_{2,1}$ and S_1 only aside of polynomial pre-factors :

$$
\begin{aligned}
T_2(N) \;=\; & \frac{248 + 15\,N^2 + N^4}{2(N-2)(N-1)N(N+1)(N+2)} S_{1,1,1,1}(N) - \frac{2}{(N-1)(N+1)} \mathbf{S_{2,1,1}}(N) \\
& + \frac{-340 + 120\,N + 17\,N^2 + 18\,N^3 - 31\,N^4}{2(N-2)(N-1)N(N+1)(N+2)} S_{3,1}(N) - \frac{-304 + 278N + 81N^2 - 38N^3 + 19N^4}{8(N-2)(N-1)N(N+1)(N+2)} S_4(N) \\
& + \frac{304 - 328\,N - 500\,N^2 + 330\,N^3 - 6\,N^4 + 6\,N^5 - 2\,N^6 + 4\,N^7}{(N-2)^2(N-1)^2N^2(N+1)(N+2)} \mathbf{S_{2,1}}(N) \\
& + \frac{-112 - 4\,N^2 - 4\,N^4}{(N-2)(N-1)N(N+1)(N+2)} S_{2,1}(N) \mathbf{S_1}(N) + \frac{-48 + 8\,N + 6\,N^2 + 7\,N^3}{(N-1)N(N+1)(N+2)} S_3(N) S_1(N) \\
& + \frac{-1840 + 292\,N + 5532\,N^2 + 827\,N^3 - 1978\,N^4 - 274\,N^5 + 36\,N^6 + 19\,N^7 - 22\,N^8}{4(N-2)^2(N-1)^2N^2(N+1)^2(N+2)} S_{1,1,1}(N)
\end{aligned}
$$

$$
+\frac{128 - 56\,N - 252\,N^2 + 54\,N^3 + 177\,N^4 - 91\,N^5 + 19\,N^6 + 9\,N^7}{2(N-2)(N-1)^2N^2(N+1)^2(N+2)} S_3(N)
$$

$$
+\frac{4032 - 2048\,N - 14200\,N^2 + 5036\,N^3 + 23610\,N^4 + 2521\,N^5 - 12342\,N^6}{4(N-2)^3(N-1)^3N^3(N+1)^3(N+2)} S_{1,1}(N)
$$

$$
+\frac{-3365\,N^7 + 2148\,N^8 + 903\,N^9 + 14\,N^{10} - 167\,N^{11} + 50\,N^{12}}{4(N-2)^3(N-1)^3N^3(N+1)^3(N+2)} S_{1,1}(N)
$$

$$
+\frac{-124 + 16\,N + 24\,N^2 - 4\,N^3 - 14\,N^4}{(N-2)(N-1)N(N+1)(N+2)} S_{1,1}(N)\zeta(2) + \frac{424 - 118\,N + 9\,N^2 - 2\,N^3 + 23\,N^4}{4(N-2)(N-1)N(N+1)(N+2)} S_2(N)S_{1,1}(N)
$$

$$
+\frac{224 + 144\,N - 1216\,N^2 - 56\,N^3 + 1786\,N^4 + 641\,N^5 - 406\,N^6}{4(N-2)^2(N-1)^3N^3(N+1)^3(N+2)} S_2(N)
$$

$$
+\frac{17\,N^7 - 308\,N^8 + 141\,N^9 - 56\,N^{10} + N^{11}}{4(N-2)^2(N-1)^3N^3(N+1)^3(N+2)} S_2(N) + \frac{58 + 21\,N + N^2 + 15\,N^3 + 10\,N^4}{(N-2)(N-1)N(N+1)(N+2)} S_2(N)\zeta(2)
$$

$$
+\frac{232 - 384\,N^2 - 17\,N^3 + 286\,N^4 - 128\,N^5 - 14\,N^6 + N^7}{4(N-2)(N-1)^2N^2(N+1)^2(N+2)} S_2(N)S_1(N)
$$

$$
+\frac{-560 - 26\,N - 31\,N^2 - 10\,N^3 - 33\,N^4}{8(N-2)(N-1)N(N+1)(N+2)} S_2(N)^2
$$

$$
+\frac{576 + 1088\,N - 3280\,N^2 - 5136\,N^3 + 11764\,N^4 + 20392\,N^5 - 17385\,N^6 - 30114\,N^7}{4(N-2)^3(N-1)^4N^4(N+1)^4(N+2)} S_1(N)
$$

$$
+\frac{5984\,N^8 + 17228\,N^9 - 1228\,N^{10} - 2754\,N^{11} - 112\,N^{12} - 8\,N^{13} + 33\,N^{14} - 24\,N^{15}}{4(N-2)^3(N-1)^4N^4(N+1)^4(N+2)} S_1(N)
$$

$$
+\frac{-56 + 336\,N + 522\,N^2 + 424\,N^3 - 53\,N^4 - 500\,N^5 + 60\,N^6 + 28\,N^7 - 5\,N^8}{2(N-2)^2(N-1)^2N^2(N+1)^2(N+2)} S_1(N)\zeta(2)
$$

$$
+\frac{64 + 6\,N^2 + N^3}{(N-2)(N-1)N(N+1)} S_1(N)\zeta(3) + \frac{2112 + 608\,N + 76\,N^2 - 140\,N^3 + 107\,N^4}{10(N-2)(N-1)N(N+1)(N+2)} \zeta(2)^2
$$

$$
+\frac{-224 - 136\,N + 1688\,N^2 + 1290\,N^3 - 1998\,N^4 - 1997\,N^5 + 198\,N^6}{2(N-2)^2(N-1)^3N^3(N+1)^3(N+2)} \zeta(2)
$$

$$
+\frac{405\,N^7 + 376\,N^8 - 119\,N^9 + 56\,N^{10} + 5\,N^{11}}{2(N-2)^2(N-1)^3N^3(N+1)^3(N+2)} \zeta(2)
$$

$$
+\frac{-552 + 144\,N + 1654\,N^2 - 370\,N^3 - 361\,N^4 + 19\,N^5 + 35\,N^6 - 25\,N^7}{2(N-2)^2(N-1)^2N^2(N+1)^2} \zeta(3)
$$

$$
+\frac{P_1(N)}{16(N-2)^3(N-1)^5(N+1)^5N^5(N+2)}
$$

$$
+4\frac{N^4 - N^2 + 12}{(N-2)(N-1)N(N+1)(N+2)} f_{0,2} - 2\frac{N^4 - N^2 + 12}{(N-2)(N-1)N(N+1)(N+2)} f_{0,1}^2
$$

with

$$
\begin{aligned}
P_1 \quad = \quad & 320 - 64\,N - 1920\,N^2 + 1600\,N^3 + 6524\,N^4 - 14872\,N^5 - 19036\,N^6 + 31543\,N^7 \\
& -43960\,N^8 - 13935\,N^9 + 65372\,N^{10} + 26822\,N^{11} - 44576\,N^{12} - 9558\,N^{13} \\
& +9840\,N^{14} + 339\,N^{15} + 428\,N^{16} - 371\,N^{17} + 128\,N^{18}
\end{aligned}
$$

There are no alternating sums contributing, unlike the case for other 2–loop Wilson coefficients in QCD [2, 4], where generally up to 6 functions emerge.

5 Conclusions

The single-scale quantities in Quantum Field Theories to 3 Loop Order, corresponding to $w = 6$, can be represented in a polynomial ring spanned by a few Mellin transforms of the above basic functions, which are the same for all known processes, including QED

processes, as the soft- and virtual corrections to Bhabha-scattering. This points to their general nature. The basic Mellin transforms are meromorphic functions with single poles at the non-positive integers. The total amount of harmonic sums reduces due to algebraic relations as a consequence of the index structure, and structural relations continuing the argument to N ϵ **Q**, N ϵ **R**. They can be represented in terms of factorial series up to simple "soft components". This allows an exact analytic continuation. Up to $w = 6$ physical (pseudo-) observables are free of harmonic sums with index $=\{-1\}$. To $w = 5$ all numerator functions are Nielsen integrals.

References

[1] Slides:
`http://indico.cern.ch/contributionDisplay.py?contribId=212&sessionId=6&confId=9499`

[2] J. Blümlein and V. Ravindran, Nucl. Phys. B **716** (2005) 128 [arXiv:hep-ph/0501178]; Nucl. Phys. B **749** (2006) 1 ;
J. Blümlein and S. Moch, in preparation.

[3] A. Vogt, S. Moch and J. A. M. Vermaseren, Nucl. Phys. B **691** (2004) 129; **724** (2005) 3.

[4] J. Blümlein, A. De Freitas, W. L. van Neerven and S. Klein, Nucl. Phys. B **755** (2006) 272 ;
I. Bierenbaum, J. Blümlein and S. Klein, arXiv:hep-ph/0703285; Phys. Lett. B **648** (2007) 195 ;
J. Blümlein and S. Klein, DESY 07–027.

[5] E. Remiddi and J. A. M. Vermaseren, Int. J. Mod. Phys. A **15** (2000) 725.

[6] J. Blümlein and S. Kurth, Phys. Rev. D **60** (1999) 014018.

[7] J. A. M. Vermaseren, Int. J. Mod. Phys. A **14** (1999) 2037.

[8] J. Blümlein, Comput. Phys. Commun. **133** (2000) 76;
J. Blümlein and S. O. Moch, Phys. Lett. B **614** (2005) 53.

[9] S. I. Alekhin and J. Blümlein, Phys. Lett. B **594** (2004) 299.

[10] A. A. Penin, Phys. Rev. Lett. **95** (2005) 010408 ;
T. Becher and K. Melnikov, arXiv:0704.3582 [hep-ph];
S. Actis, M. Czakon, J. Gluza and T. Riemann, arXiv:0704.2400 [hep-ph] and Refs. therein.

[11] E. B. Zijlstra and W. L. van Neerven, Nucl. Phys. B **383** (1992) 525.

[12] M. E. Hoffman, J. Algebraic Combin. **11** (2000) 49.

[13] J. Blümlein, Comput. Phys. Commun. **159** (2004) 19.

[14] M. Dittmar *et al.*, arXiv:hep-ph/0511119.

[15] J. Blümlein, Nucl. Phys. Proc. Suppl. **135** (2004) 225; DESY 07–042.

Special Session on α_s

Summary of α_s Determinations at ZEUS

Claudia Glasman *

Universidad Autónoma de Madrid, Spain
On behalf of the ZEUS Collaboration

The jet cross-section and structure-function measurements done with the ZEUS detector to extract the strong coupling constant and to test its energy-scale dependence are summarised. The values of α_s thus obtained and the HERA average are also presented.

1 Introduction

The strong coupling constant, α_s, is one of the fundamental parameters of QCD. However, its value is not predicted by the theory and has to be determined experimentally. The success of perturbative QCD (pQCD) lies on precise and consistent determinations of the coupling from many diverse phenomena such as τ decays, event shapes, Z decays, etc. At ZEUS, many precise determinations of α_s have been performed from a variety of measurements based on jet observables and on structure functions.

The procedure to determine α_s from jet observables used by ZEUS is based on the α_s dependence of the pQCD calculations and takes into account the correlation with the proton parton distribution functions (PDFs). The method consists of performing next-to-leading-order (NLO) calculations using sets of PDFs for which different values of $\alpha_s(M_Z)$ were assumed in the fits. A parameterisation of the $\alpha_s(M_Z)$ dependence of the theory for the given observable is obtained. Finally, a value for $\alpha_s(M_Z)$ is extracted from the measured cross section using such parameterisation. This procedure handles correctly the complete α_s-dependence of the NLO calculations (the explicit dependence in the partonic cross section and the implicit dependence from the PDFs) in the fit, while preserving the correlation between α_s and the PDFs.

2 Determinations of $\alpha_s(M_Z)$ at ZEUS

The exclusive dijet cross section in neutral-current (NC) deep inelastic scattering (DIS) has been measured [2] in the Breit frame in the kinematic region given by $470 < Q^2 < 20000$ GeV^2, where Q^2 is the photon virtuality. Two jets with transverse energies $E_{T,\mathrm{B}}^{\mathrm{jet1}} > 8$ and $E_{T,\mathrm{B}}^{\mathrm{jet2}} > 5$ GeV and pseudorapidity $-1 < \eta_{\mathrm{LAB}}^{\mathrm{jet}} < 2$ were selected. Figure 1a shows the ratio of the dijet cross section to the total inclusive DIS cross section as a function of Q^2. The experimental uncertainties are small, $\sim 6\%$. The theoretical uncertainties are smaller than for the individual cross sections. The measured ratio is described well by the pQCD prediction. The predictions for different values of α_s show the sensitivity of this observable to the coupling. From the measured ratio for $Q^2 > 470$ GeV^2, the value

$$\alpha_s(M_Z) = 0.1166 \pm 0.0019\ (\mathrm{stat.})\ ^{+0.0024}_{-0.0033}\ (\mathrm{exp.})\ ^{+0.0057}_{-0.0044}\ (\mathrm{th.}),$$

was extracted. In this determination, the theoretical uncertainties coming from the higher orders dominate.

*Ramón y Cajal Fellow.

Inclusive-jet cross sections in NC DIS have been measured [3] in the Breit frame in the kinematic region of $Q^2 > 125$ GeV^2. Events with at least one jet of $E_{T,\mathrm{B}}^{\mathrm{jet}} > 8$ GeV and $-2 < \eta_{\mathrm{B}}^{\mathrm{jet}} < 1.8$ were selected. There are several advantages of inclusive-jet cross sections with respect to dijet cross sections in a QCD analysis. The inclusive-jet cross sections are infrared insensitive; for dijet cross sections asymmetric $E_{T,\mathrm{B}}^{\mathrm{jet}}$ cuts are necessary to avoid the infrared-sensitive regions where the NLO programs are not reliable. This difficulty is not present in the calculations of inclusive-jet cross sections so these measurements allow tests of pQCD in a larger phase-space region than in dijet production. Furthermore, the theoretical uncertainties are smaller than in dijet cross sections. Figure 1b shows the inclusive-jet cross section as a function of Q^2 for different jet radii, R. The measured cross sections are well described by the NLO predictions. The experimental uncertainties are $\sim 5\%$. A value of α_s has been extracted from the inclusive-jet cross section with $R = 1$ for $Q^2 > 500$ GeV^2,

$$\alpha_s(M_Z) = 0.1207 \pm 0.0014\ (\mathrm{stat.})\ ^{+0.0035}_{-0.0033}\ (\mathrm{exp.})\ ^{+0.0022}_{-0.0023}\ (\mathrm{th.}).$$

The experimental uncertainties are dominated by the jet energy scale uncertainty, which amounts to $\pm 2\%$ and the theoretical uncertainties include the terms beyond NLO ($\pm 1.5\%$), the uncertainties coming from the proton PDFs ($\pm 0.7\%$) and the hadronisation corrections ($\pm 0.8\%$). This determination constitutes the most precise at HERA due to the advantages of using inclusive-jet cross sections at high Q^2, with a total theoretical uncertainty of only $\pm 1.9\%$.

The inclusive-jet cross section in photoproduction has been measured [4] as a function of E_T^{jet} (see Fig. 1c). For these processes, transverse energies of up to 95 GeV are accessible. The measured cross section shows a steep fall-off of more than five orders of magnitude within the measured range. The uncorrelated experimental uncertainties are $\sim 5\%$ at low E_T^{jet} and increase to $\sim 10\%$ at high E_T^{jet}. The theoretical uncertainty due to higher orders is $< 10\%$, and the uncertainties due to the parameterisations of the proton and photon PDFs are $< 5\%$. The hadronisation corrections are $\sim 2.5\%$ with an uncertainty of 2.5%. The LO calculation underestimates the data by $\sim 50\%$ for $E_T^{\mathrm{jet}} < 45$ GeV, whereas the NLO calculation gives a very good description of the data within the measured range. The determination of α_s from inclusive-jet cross sections in photoproduction has an additional uncertainty coming from the photon PDFs, but at the high E_T^{jet} covered by the measurements, the contribution from resolved processes is reduced and so this uncertainty is of the same order as that coming from the proton PDFs. Therefore, this determination of α_s is also one of the most precise at HERA,

$$\alpha_s(M_Z) = 0.1224 \pm 0.0001\ (\mathrm{stat.})\ ^{+0.0022}_{-0.0019}\ (\mathrm{exp.})\ ^{+0.0054}_{-0.0042}\ (\mathrm{th.}).$$

The dijet (three-jet) cross sections in NC DIS have been measured [5] as a function of Q^2 in the Breit frame for events with at least two (three) jets of $E_{T,\mathrm{B}}^{\mathrm{jet}} > 5$ GeV and $-1 < \eta_{\mathrm{LAB}}^{\mathrm{jet}} < 2.5$, in the kinematic range given by $150 < Q^2 < 15000$ GeV^2 and $0.2 < y < 0.6$, where y is the inelasticity. Events with a dijet (trijet) invariant mass $M^{\mathrm{jj}} > 25$ ($M^{\mathrm{3j}} > 25$) GeV were selected. Figure 2a shows the ratio of the trijet to the dijet cross section as a function of Q^2. The data are compared to the predictions of NLO QCD using different values of $\alpha_s(M_Z)$. This comparison shows the sensitivity of the observable to the value of α_s. The measured ratio is described well by the predictions. This ratio is well suited to determine α_s at low Q^2 since the correlated experimental and theoretical uncertainties cancel partially in the ratio. Therefore, this observable provides an accurate test of color dynamics at low Q^2,

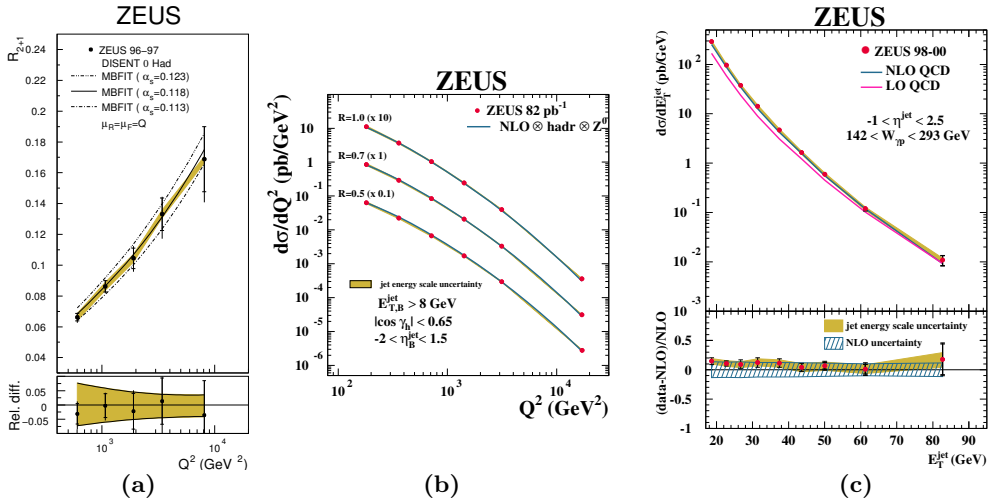

Figure 1: (a) Normalised dijet cross section as a function of Q^2 in NC DIS; (b) Inclusive-jet cross section as a function of Q^2 in NC DIS; (c) Inclusive-jet cross section as a function of $E_T^{\rm jet}$ in photoproduction.

since the theoretical uncertainty of the ratio is of the same order as at higher Q^2. From the measured ratio of trijet to dijet cross sections in the range $10 < Q^2 < 5000$ GeV^2, a value of α_s has been extracted,

$$\alpha_s(M_Z) = 0.1179 \pm 0.0013\ (\text{stat.})\ ^{+0.0028}_{-0.0046}\ (\text{exp.})\ ^{+0.0064}_{-0.0046}\ (\text{th.}),$$

with only $\sim 5\%$ uncertainty coming from higher orders at these low values of Q^2.

An independent method to extract α_s has been developed which relies on the detailed description of the internal structure of the jets by pQCD. The internal structure of jets can be studied by means of the integrated jet shape, which is defined as the average fraction of the jet transverse energy that lies inside a cone in the $\eta - \varphi$ plane of radius r concentric with the jet axis. The integrated jet shape has been measured [6] in NC DIS in the kinematic region given by $Q^2 > 125$ GeV^2 for jets of $E_T^{\rm jet} > 17$ GeV and $-1 < \eta_{\rm LAB}^{\rm jet} < 2.5$. Figure 2b shows the measurements of the mean integrated jet shape as a function of $E_T^{\rm jet}$ for a fixed value of $r = 0.5$. The measured integrated jet shape increases as $E_T^{\rm jet}$ increases. The experimental uncertainties and the corrections for detector and hadronisation effects are small for $r = 0.5$. The NLO QCD calculations give a very good description of the data and show the sensitivity of this observable to the value of $\alpha_s(M_Z)$. The extraction of α_s from the internal structure of jets gives a value with one of the smallest experimental uncertainties and negligible theoretical uncertainty coming from the PDFs, but, on the other hand, the theoretical uncertainty from the higher orders increases to about 7%. The value obtained is

$$\alpha_s(M_Z) = 0.1176 \pm 0.0009\ (\text{stat.})\ ^{+0.0009}_{-0.0026}\ (\text{exp.})\ ^{+0.0091}_{-0.0072}\ (\text{th.}).$$

A fit to inclusive DIS data, such as it is shown in Fig. 2c, and jet data has been performed [7] to extract simultaneously the proton PDFs and α_s. Conventionally, proton PDFs

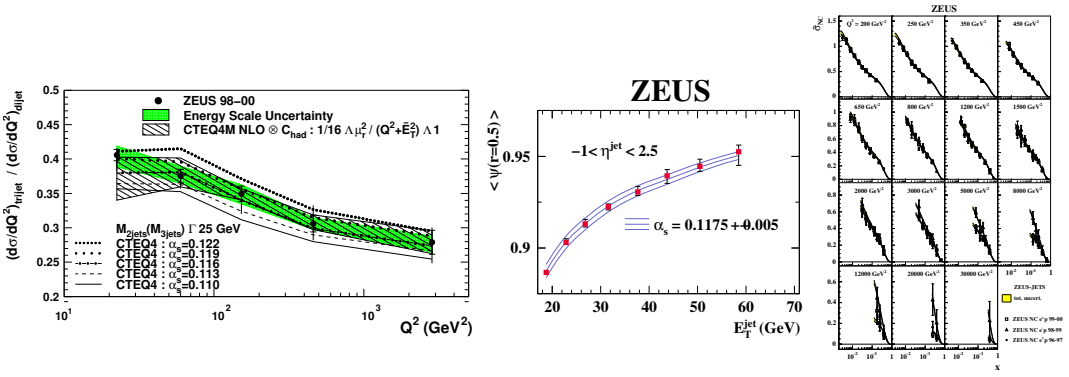

(a) **(b)** **(c)**

Figure 2: (a) Ratio of trijet to dijet cross sections as a function of Q^2 in NC DIS. (b) Mean integrated jet shape as a function of $E_T^{\rm jet}$ in NC DIS; (c) Reduced cross section as a function of x in different regions of Q^2 in NC DIS.

parameterisations are extracted by fitting inclusive DIS data, which are directly sensitive to the quark content of the proton; the gluon density is extracted via scaling violations and sum rules. On the other hand, jet cross sections are directly sensitive to both the quark and gluon densities and to $\alpha_s(M_Z)$, with the processes $\gamma^{(*)}q \to qg$ not coupled to the gluon density. Therefore, the inclusion of jet cross sections in the fit constraints significantly the gluon density and allows an extraction of $\alpha_s(M_Z)$ from structure functions which is not strongly correlated to the gluon density. The value obtained from such a fit is

$$\alpha_s(M_Z) = 0.1183 \pm 0.0028\ (\text{exp.}) \pm 0.0008\ (\text{model}) \pm 0.0050\ (\text{h.o.}),$$

which yields a very precise determination of $\alpha_s(M_Z)$ from ZEUS data alone.

Figure 3a shows a summary of the values of $\alpha_s(M_Z)$ mentioned above together with other determinations done at ZEUS. All these values are in agreement with each other and with the world average [8]. The experimental uncertainty for the determinations presented here ranges from 1.8 to 4.1%, whereas the theoretical uncertainty is between 1.9 and 7.7%. The value with the lowest theoretical uncertainty is that extracted from the inclusive-jet cross sections in NC DIS.

3 An average of $\alpha_s(M_Z)$ at HERA

To make a proper average of the determinations of $\alpha_s(M_Z)$ from the ZEUS and H1 Collaborations, the correlations among the different determinations has to be taken into account. The experimental contribution to the uncertainty due to that of the energy scale of the jets, which is the dominant source in the jet measurements, is correlated among the determinations from each experiment. On the theoretical side, the uncertainty coming from the proton PDFs is certainly correlated whereas that coming from the hadronisation corrections is only partially correlated. The uncertainty coming from terms beyond NLO is correlated up to a certain, a priori unknown, degree; since these uncertainties are dominant, special care must be taken in the treatment of these uncertainties when making an average of the determinations of $\alpha_s(M_Z)$ at HERA.

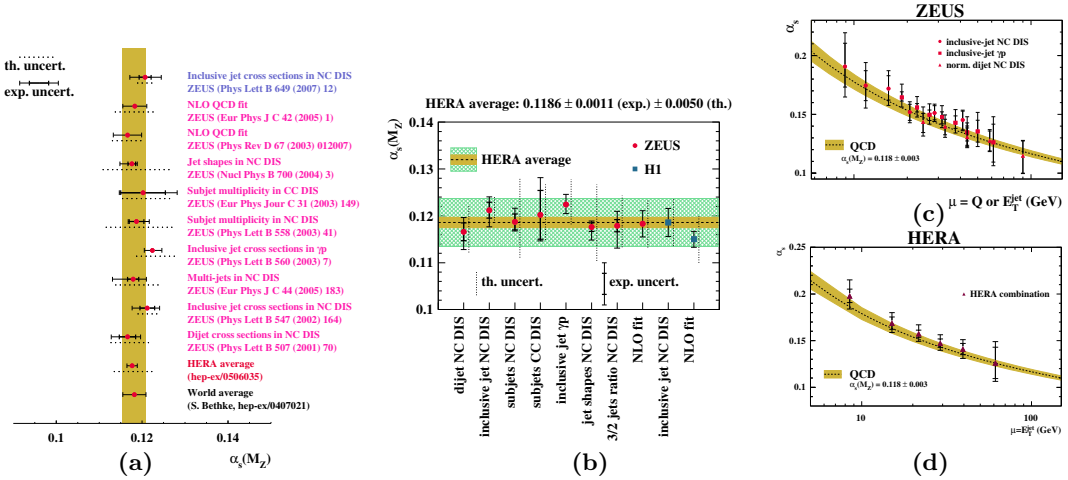

Figure 3: (a) Summary of $\alpha_s(M_Z)$ measurements at ZEUS; (b) HERA $\alpha_s(M_Z)$ average; (c) Energy-scale dependence of α_s at ZEUS; (d) HERA-combined energy-scale dependence of α_s.

A conservative approach has been used to make the average [9] in which the known correlations among the determinations of α_s coming from the same experiment were taken into account ("correlation method"). The theoretical uncertainties arising from terms beyond NLO were assumed to be (conservatively) fully correlated. Error-weighted averages were obtained separately for the ZEUS and H1 measurements. Finally, a HERA average was obtained by using the error-weighted average method on the ZEUS and H1 averages, assuming the experimental uncertainties to be uncorrelated and taking the overall theoretical uncertainty as the linear average of its contribution in each experiment. The average of the HERA measurements and its uncertainty are [9]:

$$\overline{\alpha_s(M_Z)} = 0.1186 \pm 0.0011\ (\text{exp.}) \pm 0.0050\ (\text{th.}),$$

with an experimental (theoretical) uncertainty of ~ 0.9 (4)%. This average, together with the individual values considered, is shown in Fig. 3b. It is found to be in good agreement with the world average (see Fig. 3a), which does not include any of these determinations.

4 Energy-scale dependence of α_s at ZEUS and HERA combination

The ZEUS Collaboration has tested the pQCD prediction of the energy-scale dependence of the strong coupling constant by determining α_s from the measured differential jet cross sections at different scales [2, 3, 4]. Figure 3c shows the determinations of the energy-scale dependence of α_s as a function of E_T^{jet} or Q. The determinations are consistent with the running of α_s as predicted by pQCD over a large range in the scale.

The determinations of $\alpha_s(E_T^{\text{jet}})$ from the H1 and ZEUS Collaborations at similar E_T^{jet} have been combined [9] using the correlation method explained above. The combined HERA determinations of the energy-scale dependence of α_s are shown in Fig. 3c, in which the running of α_s from HERA jet data alone is clearly observed.

References

[1] Slides:
http://indico.cern.ch/contributionDisplay.py?contribId=287&sessionId=17&confId=9499

[2] ZEUS Collaboration, J. Breitweg et al., Phys. Lett. B 507 (2001) 70.

[3] ZEUS Collaboration, S. Chekanov et al., Phys. Lett. B 649 (2007) 12.

[4] ZEUS Collaboration, S. Chekanov et al., Phys. Lett. B 560 (2003) 7.

[5] ZEUS Collaboration, S. Chekanov et al., Eur. Phys. Jour. C 44 (2005) 183.

[6] ZEUS Collaboration, S. Chekanov et al., Nucl. Phys. B 700 (2004) 3.

[7] ZEUS Collaboration, S. Chekanov et al., Eur. Phys. Jour. C 42 (2005) 1.

[8] S. Bethke, J. Phys. G 26 (2000) R27. Updated in preprint hep-ex/0407021.

[9] C. Glasman, *Proc. of the 13th International Workshop on Deep Inelastic Scattering*, S.R. Dasu and W.H. Smith (eds.), p. 689. Madison, USA (2005). Also in preprint hep-ex/0506035.

Summary of H1 Results on the Strong Coupling from Inclusive and Final States

Thomas Kluge

DESY
Notkestr. 85, 22607 Hamburg - Germany

Several determinations of the strong coupling from the H1 Collaboration are reviewed.

The following selection of results does not aim for completeness, it emphasises the diversity of α_S determinations published by the H1 Collaboration and highlights those which are the most precise and have the largest range in scale.

A simultaneous determination of the gluon distribution and of the strong coupling $\alpha_S(M_Z)$ is obtained by combining low x inclusive ep scattering data of H1 with μp scattering data of the BCDMS collaboration at high x [2]. A next-to-leading order (NLO) DGLAP QCD theory is fitted to the data. The combined result is $\alpha_S(M_Z) = 0.1150 \pm 0.0017(\text{exp.})^{+0.0009}_{-0.0005}\,(\text{model}) \pm 0.005(\text{theo.})$. The H1 data establish a strong rise of the gluon density towards low x, and consequently lead to a depletion of the gluon at high x in the fit. Hence, the fit to the BCDMS data (at high x), when complemented with the H1 data, leads to a larger value of $\alpha_S(M_Z)$ than the fit to the BCDMS data alone (fig. 1a). In the combined fit both data sets give a consistent and comparable contribution to the error on α_S (fig. 1b). The experimental error on the strong coupling is small compared to the theory error, which itself is dominated by the uncertainty of the renormalisation scale.

The probability of QCD gluon radiation in an ep scattering event is governed by the strong coupling. Hence, analyses of final states, e.g. of multi-jet events, yield constraints on α_S. In [3] jets are defined using the modified JADE algorithm in DIS. The observable is the (2+1) jet event rate, i.e. the relative fraction of 2-jet events in the sample as a function of Q^2. This measurement is corrected for hadronisation effects to the parton level and compared to a perturbative calculation at NLO. The result of a fit to the strong coupling is $\alpha_S(M_Z) = 0.117 \pm 0.003\,(\text{stat.})\,^{+0.009}_{-0.013}\,(\text{sys.}) + 0.006\,(\text{jet algorithm})$. Shown in fig. 2 is the result of the fit for four ranges in the scale Q^2, where the "running" of the strong coupling is demonstrated. The systematic error is dominated by the uncertainty of the hadronic energy scale, the renormalisation scale dependence, and the dependence on the Monte Carlo model.

Event shape variables are rather insensitive to hadronic energy scale uncertainties, since their definition uses only ratios of energies and momenta. In [5] results for five event shape variables in DIS are presented. The observables are defined in the Breit frame of reference, where the Born contribution generates no transverse momenta. Only particles in the "current" hemisphere of the Breit frame enter the definition of the event shape observables, which eliminates sensitivity to the (non-perturbative) proton remnant. Event shapes which are studied are two variants of thrust, the jet broadening, the jet mass and the C-parameter. The theory prediction relies on NLO QCD and soft gluon resummation (NLL). The rather large hadronisation effects are treated by Dokshitzer-Webber power corrections (PC). Fits to the differential distributions of the event shape variables yield an average of $\alpha_S(M_Z) = 0.1198 \pm 0.0013\,(\text{exp.})\,^{+0.0056}_{-0.0043}\,(\text{theo.})$. The errors are dominated by the renormalisation scale uncertainty, which suggests that missing higher order terms in the perturbative calculation are important. Clear evidence of the asymptotic freedom of QCD as shown in fig. 3 is found when fitting the results of individual ranges in the scale Q, and averaging over

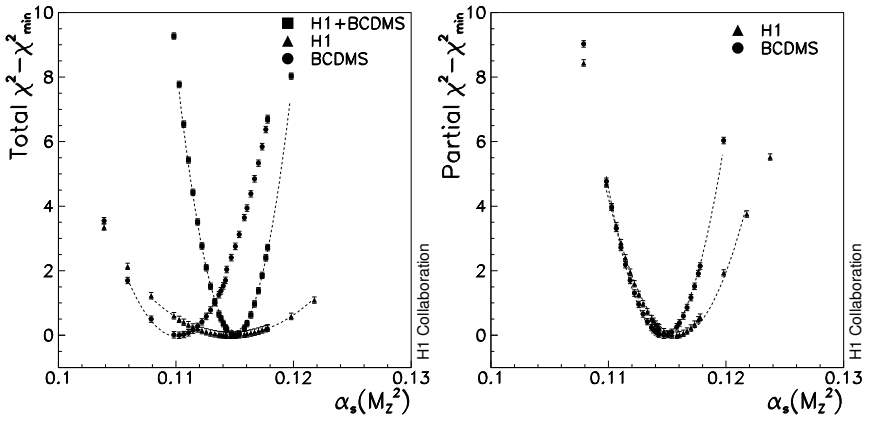

Figure 1: Determination of the strong coupling constant $\alpha_S(M_Z)$ in NLO DGLAP QCD. a) Total χ^2 for fits to the H1 *ep* and BCDMS μp data ($y_\mu > 0.3$) separately and for the fit using data of the two experiments combined. b) Partial χ^2 contributions of the H1 and BCDMS proton data in the fit to determine α_S using both experiments.

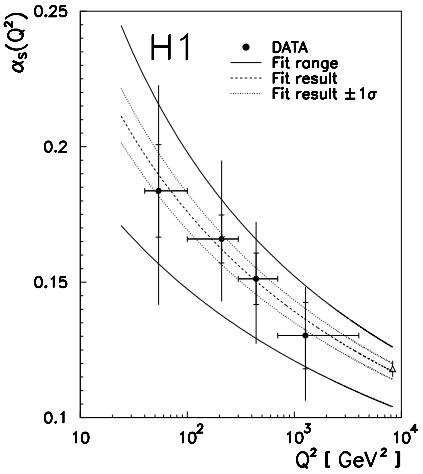

Figure 2: The α_S values derived from jet event rates as function of Q^2 with statistical errors from the data and the correction factors as inner error bars, and total errors as full error bars. The fit result (dashed line) and the 1 s.d. errors (dotted lines) are based on the individual $\alpha_S(Q^2)$ values with their statistical errors only. The solid lines represent the obtained range for $\alpha_S(M_Z)$ taking into account the systematic uncertainties. The open triangle at $Q^2 = M_Z^2$ indicates a world average $\alpha_S(M_Z) = 0.118 \pm 0.003$ [4]
.

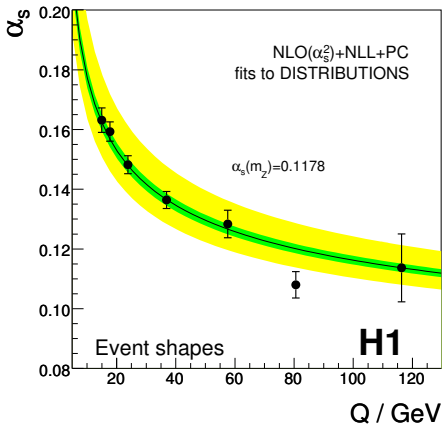

Figure 3: The strong coupling α_S as a function of the scale Q from an average of fits to differential event shape distributions. The individual results are compared with a common fit, the shaded areas represent experimental and theoretical uncertainties.

the event shapes. Note the large range in scale, from 15 GeV up to 116 GeV, i.e. beyond the Z mass, within one experiment and one analysis method.

Analyses of inclusive jet cross sections in DIS and at not too small jet transverse energies provide α_S determinations of high precision, because of only moderate higher order perturbative contributions and small hadronisation corrections. In a recent publication [6] double differential inclusive jet cross sections are presented as a function of Q^2 and of E_T of the jets in the Breit frame. The precision of QCD fits can be improved by using the *normalised* jet cross section, i.e. the ratio of the jet and the NC DIS cross section. This observable benefits from a partial cancellation of experimental and theoretical uncertainties. The measurements are found to be well described by calculations at next-to-leading order in perturbative QCD, corrected for hadronisation effects. A fit of the strong coupling yields $\alpha_S(M_Z) = 0.1193 \pm 0.0014\,(\text{exp.})\ ^{+0.0047}_{-0.0030}\,(\text{theo.}) \pm 0.0016\,(\text{pdf})$. Fig. 4 shows the results as function of E_T and Q (and using E_T and Q as renormalisation scale, respectively).

A comparison of the $\alpha_S(M_Z)$ determinations is shown on fig. 5. The results are comparable with each other and with the world averages. In the future, improvements in the precision are expected on the experimental side due to the large HERA II dataset and on the theoretical side from NNLO calculations.

References

[1] Slides:
`http://indico.cern.ch/contributionDisplay.py?contribId=288&sessionId=17&confId=9499`

[2] C. Adloff *et al.*, Eur. Phys. J. C **21** (2001) 33.

[3] C. Adloff *et al.*, Eur. Phys. J. C **6** (1999) 575.

[4] Particle Data Group, R.M. Barnett et al., Phys. Rev. **D54** (1996) 1.

[5] A. Aktas *et al.*, Eur. Phys. J. C **46** (2006) 343.

[6] A. Aktas *et al.*, Accepted by Phys.Lett.B, arXiv:0706.3722.

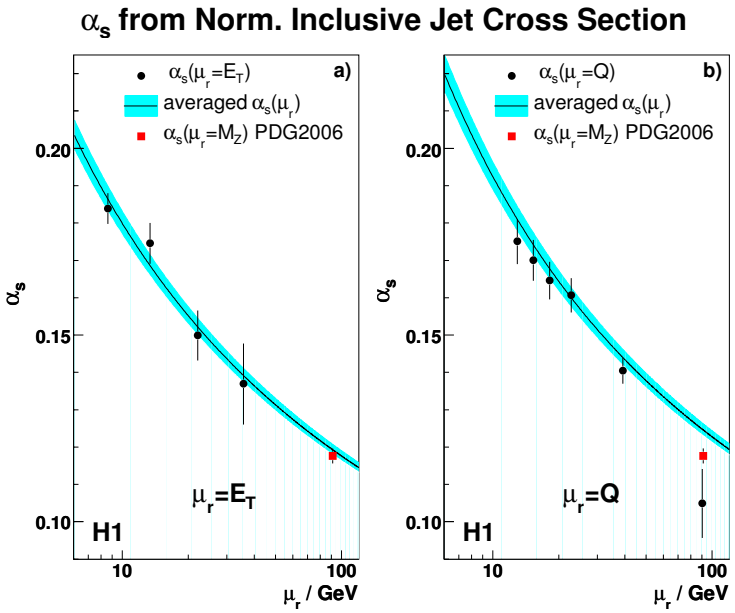

Figure 4: Determination of a) $\alpha_S(\mu_r = E_T)$ averaged over Q^2, and b) $\alpha_S(\mu_r = Q)$ averaged over E_T. The error bars denote the total experimental uncertainty for each data point. The solid curve shows the result of evolving $\alpha_S(M_Z)$ averaged from all Q^2 and E_T regions, with the band denoting the total experimental uncertainty. The world average from PDG is also shown.

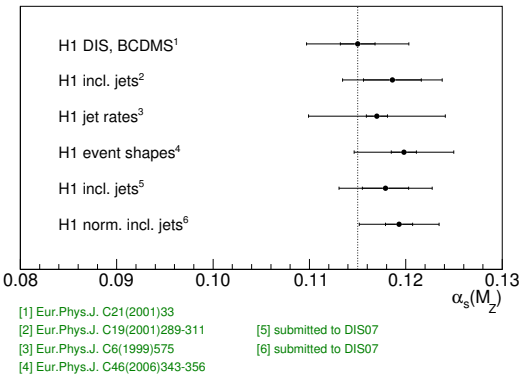

Figure 5: Selection of α_S determinations at H1, presented with experimental errors (inner error bars) and total errors (outer error bars).

$\Lambda_{\rm QCD}$ and $\alpha_s(M_Z^2)$ from DIS Structure Functions

Johannes Blümlein[1] *

Deutsches Elektronen-Synchrotron, DESY, Platanenallee 6, D-15738 Zeuthen, Germany

A brief summary is given on recent determinations of $\Lambda_{\rm QCD}$ and $\alpha_s(M_Z^2)$ from deeply inelastic structure functions.

Various QCD analyzes of the world unpolarized and polarized deep-inelastic data on charged lepton–nucleon and neutrino–nucleus scattering were performed in order to measure the QCD scale $\Lambda_{\rm QCD}$, resp. $\alpha_s(M_Z^2)$, from the scaling violations of the nucleon structure functions. In this note we give a brief overview on the status of these analyzes.[a] Most of the analyzes performed in the past were of next-to-leading order, see Table 1. Here the values of $\alpha_s(M_Z^2)$ range between 0.1171–0.1148 mainly with the exception of the old, very low BCDMS value [7] and Ref. [8] obtaining $\alpha_s(M_Z^2) = 0.112$. The typical theory error is estimated by varying the renormalization and factorization scales between $Q^2/4$ and $4 \cdot Q^2$ amounts to $\sim$5% for $\alpha_s(M_Z^2)$, a theoretical uncertainty too large to cope with the experimental uncertainty of $O(1..2\%)$ after the completion of the HERA programme. The analyzes of polarized nucleon data still yield rather large errors [10, 11] due to the present accuracy reached for polarization asymmetries. Moreover, these analyzes include data down to $Q^2 \sim 1\,{\rm GeV}^2$, which is not unproblematic w.r.t. higher twist terms, the scaling violations of which are yet unknown. The unpolarized analyzes at the present level of accuracy require rigorous cuts for potential higher twist effects, which can be achieved demanding $W^2 > 12...15\,{\rm GeV}^2$. Furthermore, we will consider only proton and deuteron data, to avoid potential interference with nuclear effects.

With the advent of the 3-loop anomalous dimensions [16] in the unpolarized case one may extend the analysis to next-to-next-to-leading order, where the remaining theory error is of $O(1\%)$ or less, see below. To cope with the present experimental errors 3–loop analyzes are mandatory. A theoretically consistent analysis can be performed at least in the non-singlet case, where the heavy flavor effects known to $O(\alpha_s^2)$, are negligibly small. 3–loop valence analyzes were performed in [8, 9]. One even may extend the non-singlet analysis to the 4–loop level [9]. A closer numerical study of the potential effect of the yet missing 4–loop anomalous dimension, performing a comparison with the recently calculated second moment in [17] shows that the overwhelming effect at 4–loops is due to the 3–loop Wilson coefficient. To see the convergence of the perturbative expansion we list the values for $\alpha_s(M_Z^2)$ obtained in the NLO, N^{2}LO, and N^{3}LO analyzes :

$$\alpha_s(M_Z^2) = 0.1148 \rightarrow 0.1134 \rightarrow 0.1142 \pm 0.0021. \tag{1}$$

The change from the N^{2}LO to the N^{3}LO value is found deeply inside the current experimental error. The N^{3}LO value corresponds to

$$\Lambda_{\rm QCD}^{\overline{\rm MS},{\rm N_f}=4} = 234 \pm 26\,{\rm MeV}\,. \tag{2}$$

A drawback of the valence analysis are small, remaining contributions of sea-quark densities in the region $x > 0.4$, the effect of which can finally only be studied in combined singlet/ non-singlet analyzes.

*This paper was supported in part by SFB-TR-9: Computergestütze Theoretische Teilchenphysik.

[a]For a recent survey on the status of deep-inelastic scattering see [2].

In the singlet case the 3–loop heavy flavor corrections are yet missing. Still analyzes may be performed to determine $\Lambda_{\rm QCD}$ under an assumption for these terms. The results are summarized in Table 1. Compared to the respective NLO analyzes, the values of $\alpha_s(M_Z^2)$ turn out to be lower by 1–2% in case comparable values are available. Three independent analyses using different codes and methods to solve the evolution equations agree [8,9,12] at the 1σ level and better. These analyzes were performed using the world structure function data for deep-inelastic charged lepton proton and deuteron scattering. The analysis in [12] is a combined singlet and non–singlet analysis and fully confirms the value of $\alpha_s(M_Z^2)$ obtained in the non–singlet analysis Ref. [9], showing that the remaining uncertainties there do not affect the value of $\Lambda_{\rm QCD}$. Alternatively to the standard $\overline{\rm MS}$-analysis one may perform factorization scheme-invariant analyzes [14], based on observables only. This method is free of shape–assumptions, in particular for the gluon density. A slightly higher value of $\alpha_s(M_Z^2)$ was found in an earlier analysis [13] using the method of Bernstein polynomials. A recent analysis [15], including also jet data from colliders, reports a much higher value of $\alpha_s(M_Z^2)$.

$\Lambda_{\rm QCD}^{\overline{\rm MS}}$ was measured also in two recent lattice simulations based on two active flavors ($N_f = 2$). These investigations paid special attention to non-perturbative renormalization and kept the systematic errors as small as possible.

$$\Lambda_{N_f=2}^{\rm latt} = 245 \pm 16 \pm 16\,{\rm MeV} \quad [17], \qquad \Lambda_{N_f=2}^{\rm latt} = 261 \pm 17 \pm 26\,{\rm MeV} \quad [18] \tag{3}$$

NLO	$\alpha_s(M_Z^2)$	expt	theory	Ref.
CTEQ6	0.1165	± 0.0065		[3]
A02	0.1171	± 0.0015	± 0.0033	[4]
ZEUS	0.1166	± 0.0049		[5]
H1	0.1150	± 0.0017	± 0.0050	[6]
BCDMS	0.110	± 0.006		[7]
GRS	0.112			[8]
BBG	0.1148	± 0.0019		[9]
BB (pol)	0.113	± 0.004	$^{+0.009}_{-0.006}$	[10]
N^{2}LO	$\alpha_s(M_Z^2)$	expt	theory	Ref.
A02m	0.1141	± 0.0014	± 0.0009	[12]
SY01(ep)	0.1166	± 0.0013		[13]
MSTW	0.1191	± 0.002	± 0.003	[15]
GRS	0.111			[8]
A06	0.1128	$+0.0015$		[12]
BBG	0.1134	$+0.0019/-0.0021$		[9]
N^{3}LO				
BBG	0.1142	$\pm$ 0.0021		[9]

Table 1: Summary of $\alpha_s(M_Z^2)$ values determined from deep-inelastic scattering.

A direct comparison with the case $N_f = 4$ in the above data analyzes is not yet possible. However, the difference between the earlier $N_f = 0$ and the present result in $\Lambda_{\rm QCD}$ amounts to $O(10\,{\rm MeV})$ only. We have to wait and see what is obtained for $N_f = 4$ in coming analyzes.

More global analyzes were performed using also semi-inclusive *ep*– and *pp*–data from jet measurement, mostly aiming on a global determination of the quark and gluon densities.

As shown in [20–23] the $\alpha_s(M_Z^2)$ values obtained in analyzing the jet data and other data sets beyond those of the structure functions differ significantly in their χ^2–profiles and fitted value for the strong coupling constant pointing to systematic differences. The jet data prefer a higher value of $\alpha_s(M_Z^2)$ than the inclusive DIS data. This effect deserves further detailed studies before one is allowed to combine these data sets for a precision determination of $\Lambda_{\rm QCD}$.

References

[1] Slides:
http://indico.cern.ch/contributionDisplay.py?contribId=289&sessionId=17&confId=9499

[2] J. Blümlein, in: Proc. of the International Conference Duality05, Frascati, eds. A. Fantoni, S. Liuti, O.A. Rondón, (World Scientific, Singapore, 2006), pp. 153; arXiv:hep-ph/0510212.

[3] J. Pumplin, D. R. Stump, J. Huston, H. L. Lai, P. Nadolsky and W. K. Tung, JHEP **0207** (2002) 012.

[4] S. Alekhin, Phys. Rev. D **68** (2003) 014002.

[5] S. Chekanov et al., ZEUS collab., Phys. Rev. **D67** (2003) 012007.

[6] C. Adloff *et al.* [H1 Collaboration], Eur. Phys. J. C **21** (2001) 33.

[7] A. C. Benvenuti *et al.* [BCDMS Collaboration], Phys. Lett. B **195** (1987) 97.

[8] M. Glück, E. Reya and C. Schuck, Nucl. Phys. B **754** (2006) 178;
M. Glück, C. Pisano and E. Reya, Eur. Phys. J. C **50** (2007) 29.

[9] J. Blümlein, H. Böttcher and A. Guffanti, Nucl. Phys. B **774** (2007) 182.

[10] J. Blümlein and H. Böttcher, Nucl. Phys. B **636** (2002) 225.

[11] G. Altarelli, R. D. Ball, S. Forte and G. Ridolfi, Acta Phys. Polon. B **29** (1998) 1145.

[12] S. Alekhin, K. Melnikov and F. Petriello, Phys. Rev. D **74** (2006) 054033.

[13] J. Santiago and F. J. Yndurain, Nucl. Phys. B **563** (1999) 45.

[14] J. Blümlein and A. Guffanti, Nucl. Phys. Proc. Suppl. **152** (2006) 87.

[15] A.D. Martin, W.J. Stirling, R.S. Thorne, and G. Watt, arXiv:0706.0459.

[16] A. Vogt, S. Moch and J. A. M. Vermaseren, Nucl. Phys. B **691** (2004) 129; **688** (2004) 101; **724** (2005) 3.

[17] P. A. Baikov and K. G. Chetyrkin, Nucl. Phys. Proc. Suppl. **160** (2006) 76.

[18] M. Della Morte, R. Frezzotti, J. Heitger, J. Rolf, R. Sommer and U. Wolff [ALPHA Collaboration], Nucl. Phys. B **713** (2005) 378.

[19] M. Göckeler, R. Horsley, A. C. Irving, D. Pleiter, P. E. L. Rakow, G. Schierholz and H. Stuben, Phys. Rev. D **73** (2006) 014513.

[20] S. Bethke, Prog. Part. Nucl. Phys. **58** (2007) 351.

[21] J. Pumplin, A. Belyaev, J. Huston, D. Stump and W. K. Tung, JHEP **0602** (2006) 032.

[22] C. Glasman, Summary of ZEUS results from inclusive and final states, these proceedings;
T. Kluge, Summary of H1 results from inclusive and final states, these proceedings.

[23] A. M. Cooper-Sarkar, arXiv:hep-ex/0511058.

Future of DIS

Convenors:
Abhay L. Deshpande,
Paul Newman,
Christian Weiss

Prospects of Future HERA Measurements

Olaf Behnke

Uni Heidelberg, Physik. Institut
Philosophenweg 12, Heidelberg 69120 - Germany

The HERA ep collider shut down on June 30, 2007, after 15 years of operation. This paper briefly discusses some of the prospects for the final measurements of H1 and ZEUS with the complete HERA data of $\sim$ 500 pb^{-1} per experiment. The focus is on the expected improvements for the proton parton densities (quarks and gluons) by measurements of inclusive structure functions, jet production and heavy flavours. Further topics like α_s determinations can be found in [1].

1 Introduction

The HERA neutral and charged current inclusive structure function data provide the basis for the most accurate proton parton density function (PDF) determinations down to low values of $x \sim 0.0001$. Figure 1 shows the current status of the published PDFs from H1 and ZEUS together with the H1 datasets that were used for the 'H1 PDF 2000' fit.

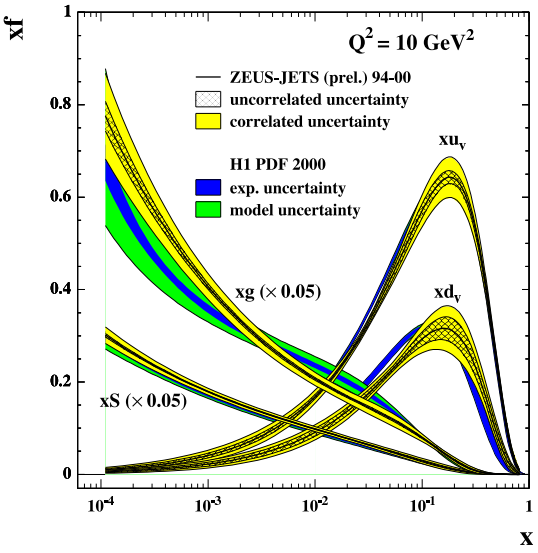

Datasets used for H1 PDF 2000	Q^2[GeV^2]	L [pb^{-1}]
NC e^+p 96/97	1.5-150	2-20
NC/CC e^+p 94-00	> 150	100
NC/CC e^-p 94-00	> 150	16
Additional datasets for final H1 PDFs	Q^2[GeV^2]	L [pb^{-1}]
NC MB99/SVX00	0.2-8.5	0.5-2
NC e^+p 00	10-150	28
NC $e^\pm p$ 03/07	$\sim 30 - 150$	300
NC/CC e^+p 03/07	> 150	~ 180
NC/CC e^-p 03/07	> 150	~ 160
DIS jets 94-07	> 150	~ 400
γp dijets 94-07	0	~ 400

Figure 1: 'H1 PDF 2000' [2] and 'ZEUS JETS PDF' [3] parton distribution functions. The H1 datasets used for the 'H1 PDF 2000' are listed in the upper half of the table, the additional H1 data available for future PDF fits are given in the lower half.

The PDFs were obtained from QCD fits to the data in Next-to-Leading-Order (NLO) perturbative QCD. HERA provides unique information, especially on the gluon density. This can be exploited for predictions of other important processes such as Higgs production in gluon gluon fusion at the LHC. The visible differences between the H1 and ZEUS gluon

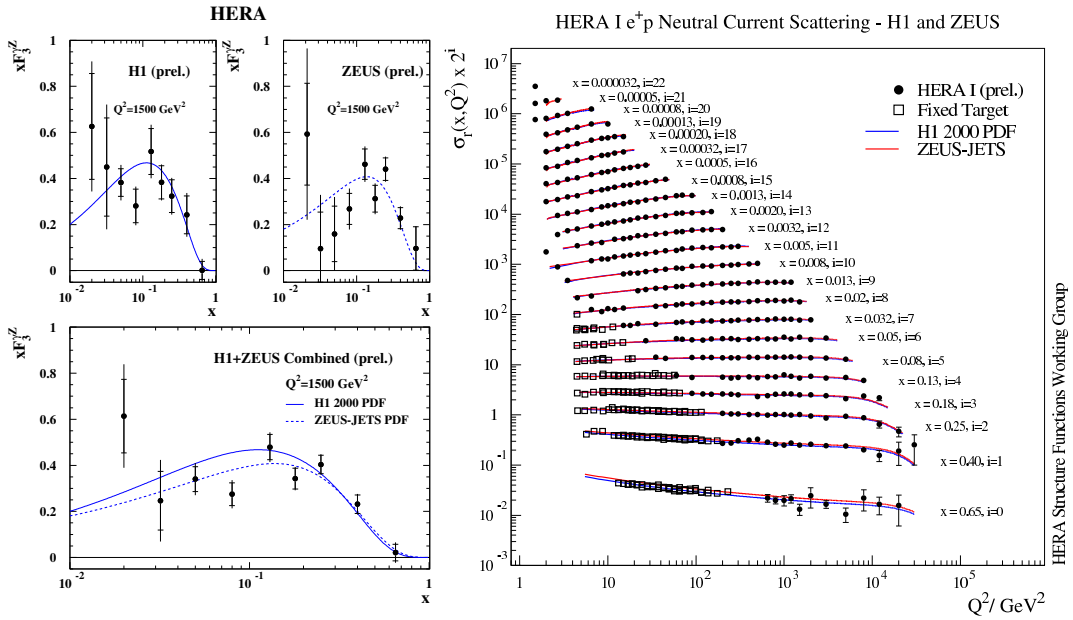

Figure 2: Combination of H1 and ZEUS measurements of the structure functions xF_3 [5] (left) and of the reduced NC cross section [6] (right).

densities (Fig. 1) indicate a seizable uncertainty which exceeds the one estimated from the error bands. One reason for this may be the different approaches used by H1 and ZEUS, e.g. for the functional form of the PDF parameterisations. In this paper we shall not investigate these or other model uncertainties but instead focus on the potential due to the inclusion of the new HERA data. The main H1 datasets available as input to improve the current PDFs are listed in the lower half of the table in Fig. 1. In some kinematic regions the statistics is improved by the new data by a factor of more than 10. This poses extreme challenges for the understanding of systematic uncertainties, especially at lower Q^2, where already the old data were mostly systematically limited. In the following some potential example improvements will be discussed that can be expected from these data. A more complete discussion can be found in [4].

1.1 Valence quarks from xF_3

Z exchange contributes to the neutral current reactions at high Q^2 at HERA. The sign of the interference term of photon and Z exchange depends on the charge of the lepton beam. This allows to access the valence quark distributions via the structure function xF_3: $xF_3 \propto \sigma_{NC}^{e^+p} - \sigma_{NC}^{e^-p} \propto 2u_v + d_v$. The results from an H1 and ZEUS combined analysis [5] are shown in Fig. 2 (left). These measurements are based on about half of the full HERA dataset. They provide unique information on valence quarks at low $x < 0.1$. The results are mostly limited by statistical errors, therefore the analysis of the complete HERA dataset will reduce the errors by approximately a factor of $\sqrt{2}$.

1.2 Sea quarks from F_2

The main information on sea quarks is provided by the structure function F_2, which is dominating the inclusive NC cross sections at low Q^2 for not so large inelasticities y. The precision of the F_2 data that have been used to obtain the PDFs shown in Fig. 1 reaches $2-3\%$ and is dominated by experimental systematic uncertainties. Improvements are at hand or can be expected due to:

- H1 and ZEUS combined [6] very recently the NC and CC inclusive cross section data which were used for their previous separate PDF determinations. The NC results are shown in Fig. 2 (right). The combination of the two datasets uses a method of weighted averaging, where parameters representing experimental systematic uncertainties (e.g. calorimeter energy scales) are also fitted. This leads to an effective cross calibration of the two experiments and finally to greatly reduced systematic errors. These H1 and ZEUS combined datasets will be used for a new PDF fit by the two collaborations.
- H1 plans to release soon the 28 pb^{-1} of low and medium Q^2 inclusive NC data ($10 < Q^2 < 150$ GeV^2) recorded in the year 2000. The main systematic errors are expected to be improved by up to a factor of two (e.g. the energy scale of the scattered electron) and thus an unprecedented precision of individual $F_2(x, Q^2)$ points of up to 1.5% is expected. The analysis of the $\sim$ 300 pb^{-1} inclusive NC data from HERA II for $Q^2 > 30$ GeV^2 needs to address the systematic errors at a new precision level and is expected to require a much longer timescale.

1.3 Gluon density determinations

At HERA the gluon density is mainly determined by the following four techniques:

- The statistically most precise determination is provided by the F_2 scaling violations, which at low x can be approximated by $dF_2/dln(Q^2) \sim \alpha_s(Q^2)xg(x, Q^2)$. The improvements of the F_2 measurements discussed above will lead to similar improvements in the determination of the scaling violations and hence also of the gluon density.
- Jet production at lower x is dominated by the the boson gluon fusion (BGF) process $\gamma^* g \rightarrow q\bar{q}$, where the photon is emitted by the beam lepton and thus provides direct access to the gluon density. ZEUS has already used high p_T jets in photoproduction and jets in high Q^2 DIS events for the 'ZEUS Jets PDF' fit to improve the determination of the gluon density considerably, especially at high proton momentum fractions $x > 0.01$. A nice feature at HERA is that the jet energy scale can be accurately calibrated via p_T balance with the scattered electron. At the highest jet p_T a scale precision of $\sim 1\%$ has already been reached by ZEUS. For the largest Q^2, x and/or p_T the HERA jet data will thus remain statistically limited in contrast to jet data at the TEVATRON. A large improvement of the gluon density precision at $x > 0.1$ of at least a factor of two can be expected from analysing the full HERA dataset and combining H1 and ZEUS measurements.
- Charm and beauty quarks are produced at HERA mainly in the BGF process $\gamma^* g \rightarrow c\bar{c}$ (or $b\bar{b}$) and thus also provide direct sensitivity to the proton gluon density. Charm events are tagged at HERA using fully reconstructed D mesons or displaced track impact parameters, the latter exploiting the long lifetime of the charm quark. Compared to jets the identification of low p_T charmed quarks provides access to gluons

which carry small proton momentum fractions $x \leq 0.01$ at not so large factorisation scales. Theoretical analyses focus on the structure function $F_2^{c\bar{c}}$, which is defined as the part of F_2 due to events with charm quarks in the final state. H1 analyses [7] of the HERA I data based on the impact parameter method resulted in precisions for $F_2^{c\bar{c}}$ of 10-30% depending on Q^2. The new HERA II data sample provides a $\sim$ four times larger dataset. At lower $Q < 60$ GeV^2 total precisions of 5% should be obtainable for $F_2^{c\bar{c}}$. Similar uncertainties can be reached with the D meson measurements. For the gluon density determination the charm data are statistically not competitive with the F_2 scaling violations. However they provide an important consistency check of the global QCD fits, especially for the highly non-trivial question of the charm quark mass treatment in the QCD analysis. Beauty production is probing the gluon density mainly at larger $x \sim 0.01$, where it is well known from the F_2 scaling violations. The $F_2^{b\bar{b}}$ measurements [7] by H1 based on displaced track impact parameters have reached a precision of 30-50% for the HERA I data. Once again, improvements of a factor of 2 or more can be expected from the HERA II data. These measurements may provide constraints for the effective beauty quark density in the proton (neglecting the beauty quark mass) which can then be used to make predictions at very large scales at the LHC for processes such as $b\bar{b} \rightarrow$ H.

- The proton structure function F_L provides another independent means to determine the gluon density. For a direct F_L determination, HERA operated in the last 3 months of its lifetime with protons of lower energies than the nominal $E_P = 920$ GeV. H1 and ZEUS have each recorded about 13 pb^{-1} and 7 pb^{-1} of data at $E_p = 460$ GeV and $E_p = 575$ GeV, respectively. These data may be used to measure F_L with sufficient precision to separate between extreme gluon density parameterisations, especially for small $x < 0.001$, where the gluon density is not so well known. These measurements cannot compete statistically with the determination from the F_2 scaling violations but provide (similarly as for charm) an important consistency test of the QCD models.

2 Conclusion

It has been demonstrated in this article that the analysis of the full HERA data sample will make significant progress in the determination of the quark and gluon densities in the proton, typically by a factor of two or more.

References

[1] Slides:
`http://indico.cern.ch/contributionDisplay.py?contribId=253&sessionId=10&confId=9499`

[2] C. Adloff *et al.* [H1 Collaboration], Eur. Phys. J. C **30** 1 (2003) [hep-ex/0304003].

[3] S. Chekanov *et al.* [ZEUS Collaboration], Eur. Phys. J. C **42** 1 (2005) [hep-ph/0503274].

[4] S. Alekhin *et al.*, see page 78 ff, hep-ph/0601012.

[5] H1 and ZEUS Collaborations, contributed paper to ICHEP2006, Moscow 2006
`http://www-h1.desy.de/h1/www/publications/htmlsplit/H1prelim-06-142.long.html`.

[6] H1 and ZEUS Collaborations, contributed paper to LP2007, Daegu 2007
`http://www-h1.desy.de/h1/www/publications/htmlsplit/H1prelim-07-141.long.html`.

[7] A. Aktas *et al.* [H1 Collaboration], Eur. Phys. J. C **45** 23 (2006) [arXiv:hep-ex/0507081].

Impact of and Constraints on PDFs at the LHC

A M Cooper-Sarkar

University of Oxford - Dept of Physics
Denys WIlkinson Building, Keble Rd, Oxford, OX1 3RH - UK

Uncertainties on parton distribution functions (PDFs) compromise discovery at the LHC for any new physics which can be described as a contact-interaction. PDF uncertainties also limit our ability to use W and Z cross-sections as anaccurate luminosity monitor. The impact of the current level of PDF uncertainty on LHC physics is reviewed and the possibility of reducing this uncertainty using LHC data is investigated.

1 Impact of PDF uncertainties on W and Z production

The kinematic plane for LHC parton kinematics is shown in Fig. 1. At leading order (LO), W and Z production occur by the process, $q\bar{q} \rightarrow W/Z$, and the momentum fractions of the partons participating in this subprocess are given by, $x_{1,2} = \frac{M}{\sqrt{s}} exp(\pm y)$, where M is the centre of mass energy of the subprocess, $M = M_W$ or M_Z, $\sqrt{s}$ is the centre of mass energy of the reaction (= 14 TeV at the LHC) and $y = \frac{1}{2} ln \frac{(E+pl)}{(E-pl)}$ gives the parton rapidity. Thus, at central rapidity, the participating partons have small momentum fractions, $x \sim 0.005$. Moving away from central rapidity sends one parton to lower x and one to higher x, but over the measurable rapidity range, $|y| < 2.5$, x values remain in the range, $5\times10^{-4} < x < 5\times10^{-2}$. Thus the scattering is happening between sea quarks. Furthermore, the high scale of the process $Q^2 = M^2 \sim 10,000\,\mathrm{GeV}^2$ ensures that the gluon is the dominant parton, see Fig. 1, so that these sea quarks have mostly been generated by the flavour blind $g \rightarrow q\bar{q}$ splitting process. Thus the precision of our knowledge of W and Z cross-sections at the LHC is crucially dependent on the uncertainty on the momentum distribution of the gluon.

The cross-sections for W/Z production have been suggested as 'standard-candle' processes for luminosity measurement, because theoretical uncertainties are well controlled, and the uncertainty from the PDFs was thought to be small (e.g. MRST01 PDFs[1] predict an impressive 2% uncertainty). However, when considering the PDF uncertainties it is necessary not only to consider the uncertainties of a particular PDF analysis but also to compare PDF analyses. Predictions for the W/Z cross-sections, decaying to the lepton decay mode, are given for modern PDF sets in Table 1.

Whereas the Z rapidity distribution can be fully reconstructed from its decay leptons, this is not possible for the W rapidity distribution, because the leptonic decay channels which we use to identify the W's have missing neutrinos. Thus we actually measure the W's decay lepton rapidity spectra rather than the W rapidity spectra. Fig. 2 compares the predictions for the lepton spectra from $W^{\pm}$ decay for the ZEUS-S [2] PDFs with those of the CTEQ6.1[3] PDFs and the MRST01 PDFs[a]. This figure is based on one million simulated, $W \rightarrow e\nu_e$, events for each of the PDF sets using HERWIG (6.505) [4]. For each of these PDF sets the eigenvector error PDF sets [5] have been simulated by PDF reweighting and k-factors have been applied to approximate an NLO generation [6]. The top part of Fig. 2, shows the $e^{\pm}$ spectra at the generator level. The events were then passed through

[a] MRST01 PDFs are used because the full error analysis is available only for this PDF set.

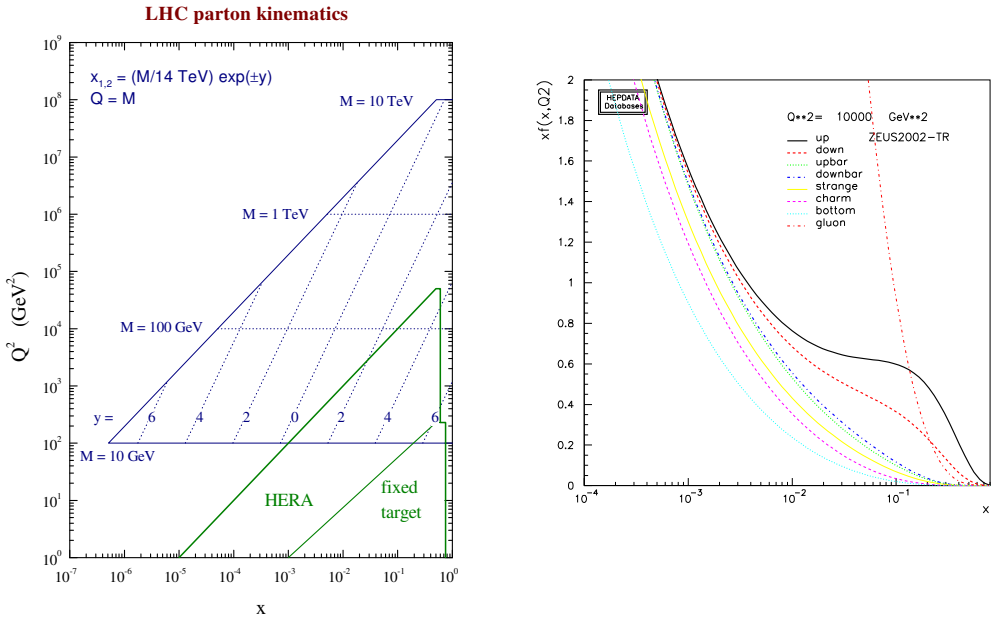

Figure 1: Left plot: The LHC kinematic plane (thanks to J Stirling). Right plot: PDF distributions at $Q^2 = 10,000$ GeV^2.

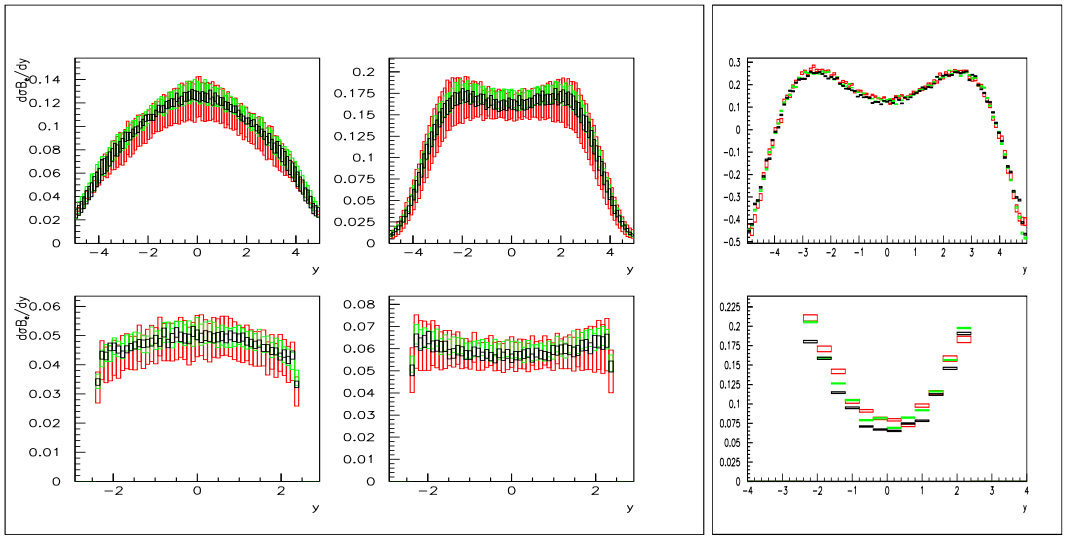

Figure 2: Top row: e^-, e^+ and A_e rapidity spectra for the lepton from the W decay, generated using HERWIG + k factors and CTEQ6.1 (red), ZEUS-S (green) and MRST2001 (black) PDF sets with full uncertainties. Bottom row: the same spectra after passing through the ATLFAST [12] detector simulation and selection cuts.(Thanks to A Tricoli)

PDF Set	$\sigma(W^+).B(W^+ \to l^+\nu_l)$	$\sigma(W^-).B(W^- \to l^-\bar{\nu}_l)$	$\sigma(Z).B(Z \to l^+l^-)$
ZEUS-JETS [7]	11.87 ± 0.45 nb	8.74 ± 0.34 nb	1.89 ± 0.07 nb
ZEUS-S [2]	12.07 ± 0.41 nb	8.76 ± 0.30 nb	1.89 ± 0.06 nb
CTEQ6.1 [3]	11.66 ± 0.56 nb	8.58 ± 0.43 nb	1.92 ± 0.08 nb
CTEQ6.5 [8]	12.44 ± 0.47 nb	9.12 ± 0.36 nb	2.04 ± 0.07 nb
MRST01 [1]	11.72 ± 0.23 nb	8.72 ± 0.16 nb	1.96 ± 0.03 nb
MRST04 [9]	11.74 ± 0.23 nb	8.71 ± 0.16 nb	1.96 ± 0.03 nb

Table 1: LHC W/Z cross-sections for decay via the lepton mode, for various PDFs

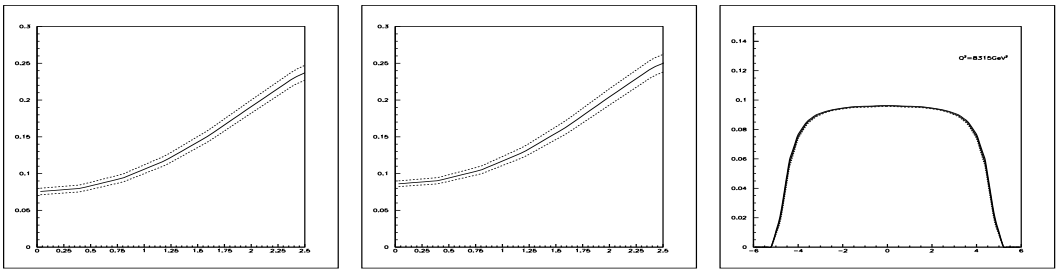

Figure 3: The lepton asymmetry, A_e, as predicted by MRST04 (left) and CTEQ6.1 (centre) PDFs. Right: the Z/W ratio, A_{ZW}, as predicted by CTEQ6.1 PDFs

the ATLFAST fast simulation of the ATLAS detector, which smears the 4-momenta of the leptons to mimic momentum dependent detector resolution. The following selection cuts are then applied: pseudorapidity, $|\eta| < 2.4$, to avoid bias at the edge of the measurable rapidity range; $p_{te} > 25$ GeV, since high p_t is necessary for electron triggering; missing $E_t > 25$ GeV, since the ν_e in a signal event will have a correspondingly large missing E_t; no reconstructed jets in the event with $p_t > 30$ GeV and recoil on the transverse plane $p_t^{recoil} < 20$ GeV, to discriminate against QCD background. The lower half of Fig. 2, shows the $e^{\pm}$ spectra at the detector level after application of cuts and smearing. Comparing the uncertainty at central rapidity, rather than the total cross-section, we see that the uncertainty estimates are rather larger: 5% for ZEUS-S; 8% for CTEQ6.1M and about 3% for MRST01. Considering both Fig. 2 and Table 1 we conclude that the spread in the predictions of these different PDF sets is larger than the uncertainty estimated by the individual analyses. Currently the overall uncertainty of these NLO predictions is $\sim 8\%$ This suggests that measurements which are accurate to $\sim 4\%$ could discriminate between PDF sets.

Since the PDF uncertainty feeding into the W^+, W^- and Z production is dominated by the gluon PDF, for all three processes, there is a strong correlation in their uncertainties, which can be removed by taking ratios. The PDF uncertainties on the W asymmetry

$$A_W = (W^+ - W^-)/(W^+ + W^-).$$

at central rapidity are dependent on the u and d valence PDFs at small x, $x \sim 0.005$. This is simply understood from LO QCD

$$A_W = (u_v - d_v)/(u_v + d_v + \bar{u} + \bar{d}).$$

We will actually measure the lepton asymmetry,

$$A_l = (l^+ - l^-)/(l^+ + l^-).$$

and predictions for A_l from MRST04 and CTEQ6.1 PDFs are shown in Fig. 3. A difference of $\sim 13\%$ at central rapidity orginates in a difference of the their valence parametrizations at low-x [10, 11] Fig. 2 also shows predictions for the lepton asymmetry, at generator and at detector level. A particular lepton rapidity can be fed from a range of W rapidities so that the contributions of partons at different x values is smeared out in the lepton spectra. The cancellation of the uncertainties due to the gluon PDF is not so perfect in the lepton asymmetry as in the W asymmetry, nevertheless the sensitivity to u and d quark valence distributions remains. Hence LHC measurements of the lepton asymmetry at central rapdity should give information on the valence distributions at small-x, $x \sim 0.005$, where there are currently no measurements.

PDF sensitivity can be removed almost completely by taking the ratio

$$A_{ZW} = Z/(W^+ + W^-)$$

as shown on the right hand side of Fig. 3. The figure has been made using CTEQ6.1 PDFs, but all modern PDF sets give an indistinguishable result. The PDF uncertainties on this quantity are as small as $\sim 1\%$. Hence this ratio can be used as a benchmarks for our understanding of Standard Model Physics at the LHC.

2 Using LHC data to improve precision on PDFs

The high cross-sections for W production at the LHC ensure that it will be the experimental systematic errors, rather than the statistical errors, which are determining. We have imposed a random 4% scatter on our samples of one million W events, generated using different PDFs, in order to investigate if measurements at this level of precision will improve PDF uncertainties at central rapidity significantly if they are input to a global PDF fit. Fig. 4 shows the e^+ rapidity spectra for events generated from the CTEQ6.1 PDFs ($|\eta| < 2.4$) and passed through the ATLFAST detector simulation and cuts. These data are then corrected back from detector level to generator level using a different PDF set- in this cases the ZEUS-S PDFs- since in practice we will not know the true PDFs. On the left hand side of the figure these data are compared to the analytic predictions from the ZEUS-S PDFs. The right hand side of the figure illustrates the result if these pseudo-data are then included in the ZEUS-S PDF fit. The central value of the fit prediction shifts, showing its sensitivity to the new data and the size of the PDF uncertainties at central rapidity decreases from 6% to 4.5%. The largest shift and improvement in uncertainty is in the PDF parameter λ_g controlling the low-x gluon at the input scale, Q_0^2: $xg(x) \sim x^{\lambda_g}$ at low-x, $\lambda_g = -0.199 \pm 0.046$, before the input of the LHC pseudo-data, compared to, $\lambda_g = -0.181 \pm 0.030$, after input. Note that whereas the relative normalisations of the e^+ and e^- spectra are predicted by the PDFs, the absolute normalisation of the data is free in the fit so that no assumptions are made on our ability to measure luminosity.

A similar study has been made for the lepton asymmetry. Whereas pseudo-data generated with CTEQ6.1 PDFs is in agreement with the ZEUS-S PDFs, pseudo-data generated with MRST04 PDFs is not, as illustrated on the left side of Fig. 5. The right side of the figure shows the result if these MRST04 pseudodata are included in the ZEUS-S PDF fit.

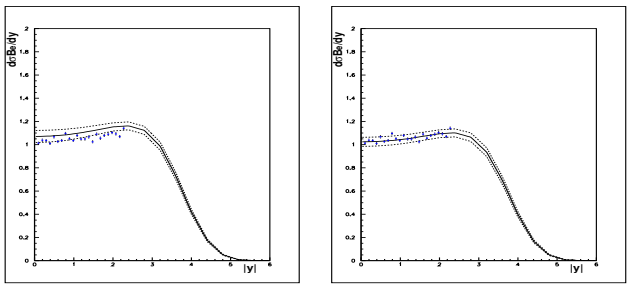

Figure 4: Left: e^+ rapidity spectrum generated from CTEQ6.1 PDFs, which have been passed through the ATLFAST detector simulation and corrected back to generator level using ZEUS-S PDFs, compared to the analytic prediction using ZEUS-S PDFs. Right: the same lepton rapidity spectrum compared to the analytic prediction AFTER including these lepton pseudo-data in the ZEUS-S PDF fit.

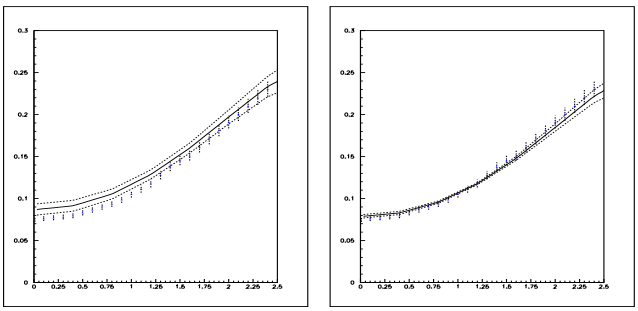

Figure 5: Left: A_l rapidity spectrum generated from MRST04 PDFs, compared to the analytic prediction using ZEUS-S PDFs. Right: the same A_l rapidity spectrum compared to the analytic prediction after including these lepton pseudo-data in the ZEUS-S PDF fit.

A good fit can only be obtained if the form of the valence parametrizations is relaxed to $xf(x) = Ax^a(1-x)^b(1+d\sqrt{x}+cx)$. The central value of the prediction shifts and the PDF uncertainties are reduced. Further information on valence distributions at larger x can be obtained by making measurements at high rapidity($y \sim 4$), see [10, 11].

3 Problems with the theoretical predictions at small-x?

However, a caveat is that the current studies have been performed using standard PDF sets which are extracted using NLO QCD in the DGLAP [13] formalism. The extension to NNLO is straightforward. However, there may be much larger uncertainties in the theoretical calculations because the kinematic region involves low-x. There may be a need to account for $ln(1/x)$ resummation (first considered in the BFKL [14] formalism) or high gluon density effects. See reference [15] for a review.

The MRST group recently produced a PDF set, MRST03 [16], which does not include any data for $x < 5 \times 10^{-3}$. The MRST03 PDF set is thus free from bias due to the

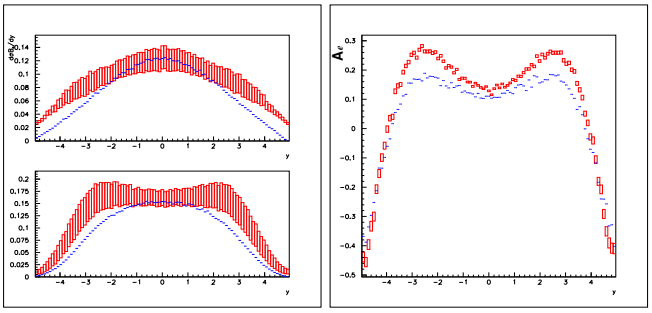

Figure 6: LHC e^+, e^-, A_e rapidity distributions for the MRST03 (blue) compared to CTEQ6.1 (red) PDFs. (Thanks to A Tricoli)

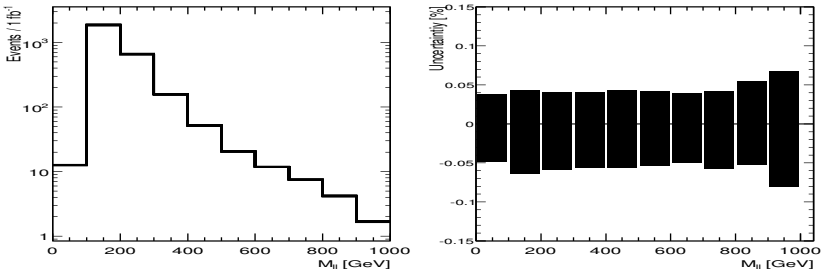

Figure 7: Left: Di-lepton mass spectrum from 50-1000 GeV Right: PDF uncertainties on this spectrum from CTEQ6.1 PDFs. (Thanks to F Heinemann)

inappropriate use of the DGLAP formalism at small-x. BUT it is also only valid to use it for $x > 5 \times 10^{-3}$. What is needed is an alternative theoretical formalism for smaller x. Nevertheless, the MRST03 PDF set may be used as a toy PDF set, to investigate the kinematic region where we might expect to see differences due to the need for an alternative formalism at small-x. Fig. 6 compares predictions using MRST03 and CTEQ6.1 PDFs. The difference in these PDFsets would become evident with data from just 6hours of running. It might be most fruitful to look for unconventional contributions to low-x physics by looking at W, Z p_t spectra rather than at the rapidity spectra. A recent calculation of the effect of a lack of p_t ordering on these spectra has shown significant differences from the conventional calculations [17], see [10].

4 Impact of PDF uncertainties on discovery physics

There are classes of discovery physics which are not much compromised by PDF uncertainties. For example, the discovery of SM Higgs as discussed in [18], see [10]. There is also recent work on PDF uncertainties on high mass di-lepton production which suggests that these uncertainties would not mask Z' production, see Fig 7.

The class of BSM physics which would be compromised by PDF uncertainties is anything which would appear in the high-E_T jet cross-sections, such as new physics which can be

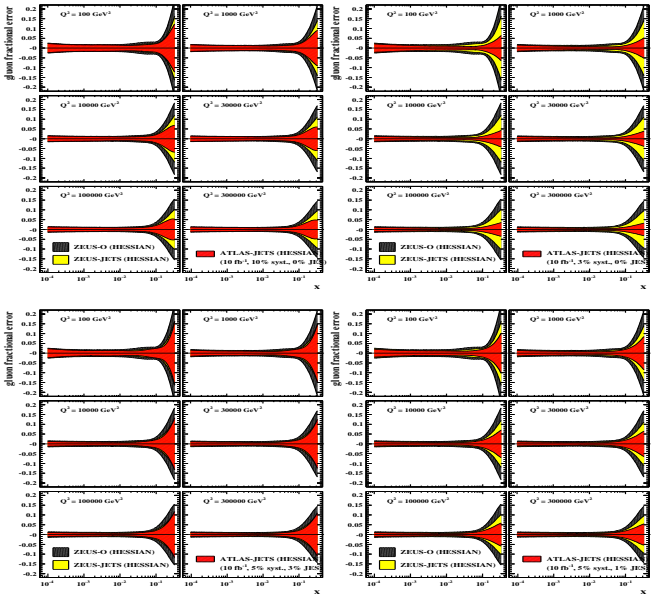

Figure 8: Fractional uncertainty on the gluon PDF at various Q^2 for the ZEUS PDF fits. ZEUS-O uses just ZEUS inclusive cross-section data, ZEUS-JETS adds ZEUS jet production data and ATLAS-JETS adds $10fb^{-1}$ of ATLAS jet pseudodata. Top left: ATLAS pseudo-data with 10% uncorrelated systematic errors. Top right: ATLAS pseudo-data with 3% uncorrelated systematic errors. Bottom left: ATLAS pseudo-data with 5% uncorrelated systematic errors and 3% correlated jet energy scale error. Bottom left: ATLAS pseudo-data with 5% uncorrelated systematic errors and 1% correlated jet energy scale error. (Thanks to C Gwenlan)

written as a contact interaction. Indeed in 1996 the high-E_T jet data at the Tevatron [19] were first taken as a signal for such new physics. However, analysis of PDF uncertainties established that these data lie well within the current level of PDF uncertainty. The main contribution to the uncertainty on the high-E_T jet cross-section comes from the high-x gluon [20]. This uncertainty also affects high-E_T jets at the scales accessible at the LHC, see for example [20] and [21] where a study is made of the possibility to distinguish compactified extra dimensions. PDF uncertainties reduce the compactification scale which can be accessed from $6TeV$ to $2TeV$.

It is clearly of interest to investigate if LHC jet measurements can themselves be used as an input to a PDF fit to decrease this level of uncertainty. Recently grid techniques have been developed to input predictions of NLO jet cross-sections to PDF fits [7, 22] and this technique can be used for LHC high-E_T jet cross-sections. Data at lower E_T and central rapidity are used, where new physics effects are not expected. The programme NLOJET was used to generate grids of parton sub-process cross-sections up to $p_T < 3GeV$, in pseudorapidity ranges $0 < \eta < 1$, $1 < \eta < 2$, $2 < \eta < 3$. These sub-process cross-sections can then be multiplied by the PDFs which are varied in the fit. LHC high-E_T jet pseudodata was generated using JETRAD and input to the ZEUS-JETS PDF fit using this technique.

In Fig 8 the results are shown for a variety of different ATLAS pseudo-data inputs. All samples assume a luminosity of $10fb^{-1}$ however, luminosity is not a restriction provided $L > 1fb^{-1}$. The top left of the figure shows the effect of using ATLAS pseudo-data with an assumed uncorrelated systematic error of 10%. This is sufficent to give an impressive decrease in uncertainty compared to current ZEUS-JETS PDFs. The top right of the figure shows the effect of using ATLAS pseudo-data with an assumed uncorrelated systematic error of 3%. The decrease in uncertainty between these two samples is striking. However, on the bottom of the figure the effect of assuming a correlated systematic uncertainty due to jet energy scale is illustrated. On the left hand side a jet energy scale of 3% is assumed and on the right hand side a jet energy scale of 1% is assumed. Even a modest 3% jet energy scale is enough to destroy the improvement we had gained. The jet energy scale would need to be as small as 1% in order to see any improvement. In view of this pessimistic conclusion it is of great interest to anticipate future improvements in our knowledge of the gluon from analysis of HERA-II inclusive cross-section and jet data [25]

References

[1] A.D. Martin et al, Eur.Phys.J **C23**,73 (2002)
[2] ZEUS Coll., S. Chekanov et al., Phys Rev D 67,012007,2003
[3] J. Pumplin et al, JHEP **0207**, 012, (2002)
[4] G. Corcella et al., JHEP **0101**, 010, (2001)
[5] M.R. Whalley, D. Bourikov, R.C. Group, hep-ph/0508110, http://hepforge.cedar.ac.uk/lhapdf/
[6] A Tricoli et al.,hep-ex/0509002, Proc. of Workshop on Implications of HERA for LHC Physics, 2005
[7] S. Chekanov et al., Eur.Phys.J **C42**,1 (2005)
[8] W.K Tung et al., JHEP **0702**, 053, (2007)
[9] A.D. Martin et al, Phys Lett **B604**, 61 (2004)
[10] Slides:
`http://indico.cern.ch/contributionDisplay.py?contribId=283&sessionId=10&confId=9499`
[11] Slides:
`http://indico.cern.ch/contributionDisplay.py?contribId=254&sessionId=8&confId=9499`
[12] http://www.hep.ucl.ac.uk/atlas/atlfast/
[13] G. Altarelli, G. Parisi, Nucl.Phys. **B126**,298 (1977);
V.N. Gribov, L.N. Lipatov, Sov.J.Nucl.Phys, **15**, 438 (1972);
L.N. Lipatov, Sov.J.Nucl.Phys, **20**, 94 (1975);
Yu.L. Dokshitzer, JETP, **46**, 641 (1977).
[14] L.N. Lipatov, Sov.J.Nucl.Phys, **23**, 338 (1976);
E.A. Kuraev, L.N. Lipatov, V.A. Fadin, JETP, **45**, 199 (1977);
Ya.Ya. Balitski, L.N. Lipatov, Sov.J.Nucl.Phys, **28**, 822 (1978);
L.N. Lipatov, Sov.J.Nucl.Phys, **63**, 904 (1980)
[15] R C E Devenish and A M Cooper-Sarkar,'Deep Inelastic Scattering', Oxford University Press,,2004
[16] A D Martin et al, Eur Phys J **C35** 325 (2004)
[17] S Berge et al., hep-ph/0508215, AIP Conf.Proc.792,722(2005)
[18] A Djouadi, S Ferrag, Phys. Lett. **B586**, 345 (2004)
[19] F Abe etal., Phys Rev Lett **77**, 438 (1996)
[20] D Stump et al, JHEP **0310**, 046, (2003)
[21] S Ferrag, hep-ph/0407303, 39th Rencontres de Moriond on QCD and High-Energy Hadronic Interactions, 2004.
[22] T Kluge et al.,hep-ph/0609285, http://projects.hepforge.org/fastnlo/
[23] S Catani et al, Nucl Phys **B485**, 291 (1997); Z Nagy, Phys Rev **D68** 094002 (2003),
`http://nagyz.web.cern.ch/nagyz/Site/NLOJET++/NLOJET++.html`
[24] W T Giele et al., Nucl Phys **B403**, 633 (1993)
[25] C. Gwenlan et al., J.Phys **G32**, 221 (2006)

Parton Distributions at the LHeC

Max Klein

University of Liverpool, Department of Physics
L69 7ZE Liverpool, United Kingdom

The LHeC provides $e^{\pm}p$ collisions at 1.4 TeV cms energy. Based on simulations of the statistics and the systematics as may be achieved with a new collider detector, the potential of the LHeC is characterised regarding DIS precision measurements as of the strong coupling constant, to per mille accuracy, and the gluon distribution. It is demonstrated that for the first time the flavour contents of the proton can be completely reconstructed. Precision measurements will be possible of the up, down, strange, charm, beauty, anti-up, anti-down and anti-strange quark distributions over a huge range in x and Q^2 hitherto not accessible. This is solely based on high precision neutral and charged current measurements, in ep and partially in eD scattering, using charm and beauty tagging for the reconstruction of the heavy quark momentum distributions.

1 Introduction

The Large Hadron Electron Collider (LHeC) project envisages deep inelastic electron and positron proton collisions using a new electron ring mounted on top of the LHC. With an electron energy E_e of typically 70 GeV in collisions with the LHC proton beam of $E_p = 7$ TeV, the LHeC achieves electron-quark collisions at a center of mass energy of up to $\sqrt{s} = 4E_eE_p = 1.4$ TeV at which new physics may be found, as the formation of resonant eq states. The design, as proposed in [1], promises to achieve luminosities of $10^{33}\,\mathrm{cm}^{-2}\mathrm{s}^{-1}$, using the standard LHC proton beam, or possibly higher if the luminosity upgrade of the LHC was realised.

A TeV energy scale ep collider is of primary importance to study new physics in the eq sector, to study the origin of mass, as is linked to the strong self-interaction of gluons, the confinement of quarks and deconfinement phase of partonic matter in nuclei, to move the deep investigation of proton structure much further, as with searches for substructure, study of parton correlations or transverse structure, to measure parton distributions in nuclei, understand the formation of the quark gluon plasma and to explore the strong interaction dynamics much deeper. In the present note it is demonstrated, based on a full simulation of systematic detector uncertainties, that the LHeC for the first time will enable the complete decomposition of proton structure into its partonic base [a]. Such a decomposition is achieved with the precise measurement of all partonic parameters, α_s, xg, u_s, u_v, $\overline{u}$, d_s, d_v, $\overline{d}$, s, $\overline{s}$, c, $\overline{c}$ and of b, $\overline{b}$, using inclusive neutral (NC) and charged current (CC) simulated data only. Low x physics and physics beyond the Standard Model with the LHeC were discussed at this workshop in [2, 3].

[a] Measurements of parton distributions in nuclei so far exist only from fixed target lN scattering experiments. The LHeC by using the LHC ion beams will extend these by four orders of magnitude in x and Q^2 and thus provide a basis for understanding phenomena as predicted in the theory of the colour-glass condensate and for interpreting data which will be taken by ALICE and the other LHC collider experiments in AA mode. Most striking phenomena are predicted in high energy eA scattering such as an increase of the relative amount of diffraction up to 50% or scaling laws of F_2 much different from Bjorken's predictions or logarithmic Q^2 variations in high energy ep scattering.

The precision measurement of parton distribution functions (pdf) in the kinematic range of the LHC, as will be provided by the LHeC, will essentially remove the otherwise neccessary assumptions on evolving measurements from the restricted HERA range into the kinematic region of the LHC. While one may hope to be able to control such an evolution in Q^2 at medium x, HERA simply has not the coverage of the small x region in which new saturation phenomena may occur. Measurements at high masses at the LHC may require a very accurate knowledge of the valence quark densities at Q^2 of order $10^{5..6}\,\mathrm{GeV}^2$. It is to be noted, however, that HERA was seriously luminosity limited to reach high $x > 0.5$. With LHC pp data some of the evolutions from HERA using perturbative QCD may be tested, as from the Drell Yan production of the weak bosons. However, these processes are also considered to allow for a precision determination of the luminosity of the LHC, and apart from a few exceptions as the $W^{\pm}$ asymmetry one hardly can determine the luminosity and simultaneously the pdf's in the kinematic range of the LHC, see also [4].

2 Simulation and Detector Requirements

To achieve maximum luminosity, for Q^2 above $100\,\mathrm{GeV}^2$, the ep interaction region at the LHeC, as considered in [1], has focusing quadrupoles placed near the vertex. This limits the forward and backward acceptance to polar angles between 10° and 170°. The region close to the beam pipe, however, is crucial for the physics at low x and for measuring the final state at large x and medium $Q^2 \sim 10^{4..5}\,\mathrm{GeV}^2$. It may be accessed with removal of these magnets at an estimated tolerable reduction of the luminosity by a factor of about 10. In this study it is assumed that tracking and calorimetry may then be extended to 1° and 179°. Thus there are two basic challenges for the LHeC detector(s) and interaction region: the accurate reconstruction of scattered electron and final state energies up to $\sim 5\,\mathrm{TeV}$ and the forward backward instrumentation close to the beam pipe to reliably access lowest and large x. The third challenge is to achieve maximum precision. This is quantified here by considering the relation of calibration and general measurement accuracy to the precision with which the strong coupling constant $\alpha_s(M_Z^2)$ can be measured. In an initial case study, here a first set of detector requirements was considered, see Table 1, roughly two times more ambitious than H1, 30 years later in modern technology developments.

Parameter	H1	LHeC
Polar angle acceptance [°]	7-177	1-179
Polar angle measurement accuracy [mrad]	0.2-1	0.1-0.5
Hadronic energy scale [%]	2	1
Electromagnetic energy scale [%]	0.2-1	0.1
Luminosity measurement accuracy [%]	1	0.5

Table 1: Acceptance and measurement accuracies typical for the H1 detector at HERA and assumed in this study for the LHeC detector. The scale uncertainties at the LHeC are chosen to achieve better than 1% cross section measurement accuracy in most of the kinematic region. They roughly match the statistical uncertainty at large x for Q^2 above $10\,000\,\mathrm{GeV}^2$ for $10\,\mathrm{fb}^{-1}$. Further studies will define this more accurately and less globally.

Simulations of NC and CC inclusive cross sections were performed for data sets of $10\,\mathrm{fb}^{-1}$ at high Q^2 and $1\,\mathrm{fb}^{-1}$ at low Q^2, for polar angles inside 10-170° and 1-179°, respec-

tively. The systematic errors were derived using electroweak Born cross section formulae from the dependence of the kinematic variables on the electron and hadron final state energies and angles with the uncertainties as given in Table 1. The numeric calculation of systematic uncertainties has been cross checked with Monte Carlo simulations for HERA. The Σ method was assumed for reconstruction and a global uncertainty of 0.5% was added to the systematic errors.

3 Strong Coupling Constant and Gluon Distribution

The strong coupling α_s is known to at best 1% accuracy, worse even than the gravitational constant. The present uncertainty of α_s limits the evaluation of grand unification of the weak, electromagnetic and strong interactions at the Planck scale. DIS is known to be a process, calculated so far to NNLO, which is best suited for a measurement of $\alpha_s(M_Z^2)$. Using NLO QCD fit programs the estimated experimental uncertainty of $\alpha_s(M_Z^2)$ is ± 0.0004 for the LHeC $e^{\pm}p$ data and ± 0.0003 when the simulated LHeC data are combined with the BCDMS μp data. Further studies are foreseen to evaluate deeper the effects of individual uncertainties and acceptance constraints in order to understand the requirements to the LHeC detector in more detail, attempting to come close to a per mille measurement accuracy. Yet, the present result already indicates the exciting potential precision DIS measurements at the LHeC have. It also poses a considerable challenge to QCD calculations since at NNLO the conventional measurement uncertainty due to the arbitrariness of the renormalisation scale is quoted to be about ± 0.001 related to the HERA range.

The gluon distribution from the present DIS data, even including di-jet cross sections, is rather inaccurately determined, in particular at low x and at large x. This is a major concern for the LHC as gg fusion processes are often the dominant production mechanism. An analysis similar to the one for $\alpha_s(M_Z^2)$ reveals that the wide range and high precision of LHeC data would allow the gluon distribution to be determined much more accurately than has been possible so far, both at low and at high x, see Figure 1.

4 Quark Distributions

With the LHeC, the light quark densities u, $\overline{u}$, d and $\overline{d}$ can be determined with very high accuracy over the full range of x from NC, CC, ep and ed data. This will resolve the long standing question on the behaviour of u/d at large x, see Figure 1, and determine the $d(x, Q^2)$ density to high accuracy. From the electroweak beam charge asymmetry a determination is obtained of high accuracy of the valence quarks, $xF_3^{\gamma Z} \propto 2u_v + d_v$, down to $x = 10^{-3}$, i.e. in a region one never could probe the valence quarks in DIS so far.

HERA has measured the density of beauty quarks in the proton for the first time, not far from threshold and to a limited accuracy of 20% for Q^2 up to a few $100\,\mathrm{GeV}^2$. It has provided more accurate measurements of the charm quark density to 5-10%. HERA has not measured the strange quark distribution.

Assuming 50% b impact parameter tagging efficiency, ϵ_b, and a charm background fraction, bg_c, of 10%, a very accurate measurement of $b(x, Q^2)$ can be done, for $x \simeq 0.00003 - 0.07$ and Q^2 from threshold to $10^5\,\mathrm{GeV}^2$. In the same range $c(x, Q^2)$ can be measured well, as is obtained with $\epsilon_c = 0.1$ and a light quark background $bg_q = 0.01$. Using the charged current reaction $W^+ s \to c$ and its charge conjugate, for the first time $s(x, Q^2)$ and $\overline{s}(x, Q^2)$ become measurable, for x between about 0.001 and 0.1 and Q^2 between 500 and $50000\,\mathrm{GeV}^2$. Such

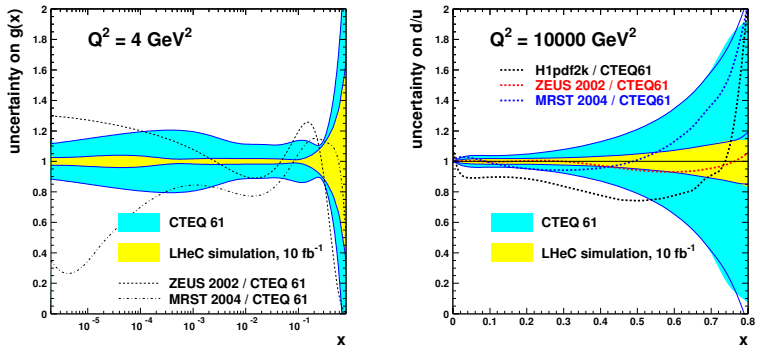

Figure 1: The gluon distribution (left) and the u/d ratio (right) as a function of $\log x$ and of x, respectively. The blue (outer) band illustrates the uncertainty of the CTEQ6.1 pdf set, the yellow (inner) band is the experimental uncertainty as determined in this analysis. The curves show by how much current QCD fits may differ, often outside the quoted uncertainty from a particular set. The present knowledge of xg is expected to be constrained better from the forthcoming final HERA data on the $\ln Q^2$ derivative of F_2 and on F_L.

measurements, simulated here with impact parameter evaluations only, will profit further from dedicated Silicon vertex detectors, extending to the forward region, and from the small beam spot size at the LHeC of $35\,\mathrm{x}\,15\,\mu\mathrm{m}^2$ only.

The measurement of parton distributions with the LHeC represents the culmination of decades of pdf measurements in lepton-nucleon DIS experiments and may turn out to be of crucial relevance for the interpretation of new physics phenomena one expects to find both in pp and also in AA collisions at the LHC. For the slides and plots of this talk see [5].

Acknowledgements

Thanks are due to T. Kluge and E. Perez for performing QCD fits on the simulated data to obtain α_s and pdf's, respectively, further to A. Mehta for guidance on the heavy quark density measurement simulation and my coauthors of [1] for much excitement and insight. Thanks to the organizers for a great workshop at Munich.

References

[1] J. Dainton et al., JINST 1 P10001 (2006) [hep-ex/0306016];
For a recent review see J. Dainton, these Proceedings.

[2] P. Newman, these Proceedings.

[3] E. Perez, these Proceedings.

[4] M. Cooper-Sarkar, these Proceedings.

[5] Slides:
`http://indico.cern.ch/contributionDisplay.py?contribId=255&sessionId=10&confId=9499`

Generalized Parton Distributions at COMPASS

F. H. Heinsius
on behalf of the COMPASS Collaboration

Ruhr-Universität Bochum, Institut für Experimentalphysik I, 44780 Bochum, Germany.

Generalized parton distributions can be probed in hard exclusive meson scattering and deeply virtual Compton scattering (DVCS). Prospects for the measurements of these processes at the COMPASS experiment at CERN will be shown. A recoil detector and additional calorimetry are planned to identify the DVCS process. Simulations for different models and a test of the recoil detector have been performed.

1 Introduction

The generalized parton distributions (GPD) make it possible to provide a coherent description of the nucleon. They can describe elastic form factors as well as helicity dependent and helicity independent parton density distributions at the same time. The angular momentum of the quarks inside the nucleon may be determined. The generalized parton distributions can be accessed by measuring deeply virtual Compton scattering and deeply virtual meson production processes at COMPASS. The GPDs are functions of 3 parameters: the longitudinal quark momentum fraction x, the longitudinal momentum transfer 2ξ with $\xi = x_{Bj}/(2 - x_{Bj})$ and the momentum transfer squared to the target nucleon t. The latter is the Fourier conjugate to the transverse impact parameter r. A three dimensional picture of the nucleon can be obtained as a function of the parameters r and x.

The COMPASS experiment at CERN is a facility to study QCD by structure and spectroscopy measurements. It is a perfect place to study generalized parton distributions. From 2002 onwards the experiment was operated with a polarized target and various aspects related to GPDs are studied: A complete analysis of ρ production is performed. Studies of exclusive ϕ and 2π production are in progress. The ratio of the GPD E/H function is investigated by the measurements on a transverse polarized target. The GPD E functions are related to the Sivers effect [2]. Sivers asymmetries are investigated at COMPASS with muons scattered off transverse polarized deuteron and proton targets [3].

In this paper the possible measurements of the generalized parton distributions in the years 2010 – 2015 are presented.

2 Possible measurements

The measurements of the generalized parton distributions will be performed with an unpolarized liquid hydrogen or liquid deuterium target surrounded by a recoil detector [4]. The CERN beamline can provide polarized muons with beam energies between 100 and 190 GeV. For the main measurements we have chosen a muon energy of 100 GeV to maximize the muon flux and the interference effects between DVCS and Bethe Heitler. Both positive and negative muons with opposite polarization of 80% and same intensities are available. For beam charge asymmetry measurements the beam charge can be changed once a day. These measurements have the advantage that not only cross sections, e.g. amplitudes squared, but also both the real and imaginary part of the DVCS amplitudes can be determined.

Measurements of the cross section difference of opposite charged and polarized muons give rise to the real part of the DVCS amplitude, while the cross section sum provides information on the imaginary part of the DVCS amplitude.

3 Simulations

Simulations of the beam charge asymmetry have been performed for the COMPASS experiment under different model assumptions on the DVCS cross section. Two models are based on double distribution parameterizations of GPDs. Model 1 assumes a dependence of $H(x,\xi,t) \propto q(x)F(t)$ [5]. Model 2 includes a correlation between x and t. It considers fast partons in the small valence core and slow partons at larger distances: $H(x,0,t) \propto q(x)e^{t<b_\perp^2>} = q(x)/x^{\alpha' t}$ with α' the slope of the Regge trajectory and $< b_\perp^2 >= \alpha' \ln 1/x$ describing the transverse extension of partons in hadronic collisions. This ansatz reproduces the chiral quark-soliton model of Ref. [6]. Two values of the α' parameter where applied to the simulations: $0.8\,(\mathrm{GeV}/c)^{-2}$ and $1.1\,(\mathrm{GeV}/c)^{-2}$.

Another way to parametrize the DVCS amplitudes is the dual parameterization, where one separates the x,ξ dependence from the ξ,t dependence. By the decomposition into Mellin moments it is straightforward to perform QCD evolution in this model. Calculations have been done by Guzey and Teckentrup [7]. Their dual parameterization with the Regge motivated t-dependence were used as model 3 in the simulations for COMPASS.

With a luminosity of $1.3 \cdot 10^{32}\,\mathrm{cm}^{-2}\mathrm{s}^{-1}$ and an efficiency of 25% it is possible to split the data in six bins in Q^2 from $1.5\,(\mathrm{GeV}/c)^2$ to $7.5\,(\mathrm{GeV}/c)^2$ and 3 bins in x_{Bj} from 0.03 to 0.27 assuming a running time of 150 days. A separation between the different models can be seen in Fig. 1. COMPASS can provide important data in the x_{Bj} region of 0.03 – 0.27 to constrain the models.

4 Experimental setup

The simulations were done for an upgraded version of the COMPASS setup at CERN. The positive and negative charged muons are scattered off a liquid hydrogen or liquid deuterium target. A 2.5 m long target has to be designed for the DVCS measurements. In addition a recoil detector to ensure the exclusivity is needed. The target will allow a minimal t of $0.06\ (\mathrm{GeV}/c)^2$. To allow for 10 bins in t a minimum time resolution of 300 ps is needed for the recoil detector. A full size prototype of the recoil detector has been tested in the fall 2006 at the COMPASS experimental area. A time resolution of 310 ps has been achieved.

The scattered muons are detected by the COMPASS trackers: scintillating fibers, silicon detectors, Micromegas, GEMs, drift chambers, straw tubes and MWPCs. The existing electromagnetic calorimeters cover an angle $\theta < 10°$. They need to be completed by additional calorimetry to cover angles up to 30 degrees to allow for efficient π^0 background rejection.

5 Outlook

Currently simulations are being performed and a proposal for GPD measurements at COMPASS is being prepared. In the years 2007 – 2009 a recoil detector, a liquid hydrogen target and an large angle electromagnetic calorimeter are planned to be constructed. Thus measurements of GPDs could be performed at the COMPASS experiment in the years 2010 – 2015. First results are expected well before possible future projects at the JLAB 12 GeV

upgrade [8] , the FAIR project [9] and at an electron ion collider [10]. A big advantage of the COMPASS experiment is that its kinematic region covers both the valence quark and the sea quark region in terms of x_{Bj}.

References

[1] Slides: `http://indico.cern.ch/contributionDisplay.py?contribId=257&sessionId=10&confId=9499`

[2] M. Burkardt and D. S. Hwan, Phys. Rev. **D69** 074032 (2004).

[3] COMPASS Collaboration, E.S. Ageev, *et al.*, Nucl. Phys. B **765** 31 (2007);
COMPASS Collaboration, V. Yu. Alexakhin, *et al.*, Phys. Rev. Lett. **94** 202002 (2005). .

[4] COMPASS Collaboration, "Outline for generalized parton distribution measurements with COMPASS at CERN", CERN report, CERN-SPSC-2005-007, Jan. 2005.

[5] Vanderhaeghen *et al.*, Phys. Rev. **D60** 094017 (1999).

[6] Goeke et al., Prog. Part. Nucl. Phys. **47**, 401 (2001).

[7] Guzey and Teckentrup, Phys. Rev. **D74** 054027 (2006).

[8] Z.-E. Meziani, "Jlab 12 GeV: Large x, Spin/Flavour and GPDs", these proceedings.

[9] B. Seitz, "PANDA at GSI: Drell-Yan, transversity, exclusive channels", these proceedings.

[10] A. Bruell, "Polarized Physics with an Electron-Ion-Collider", these proceedings.

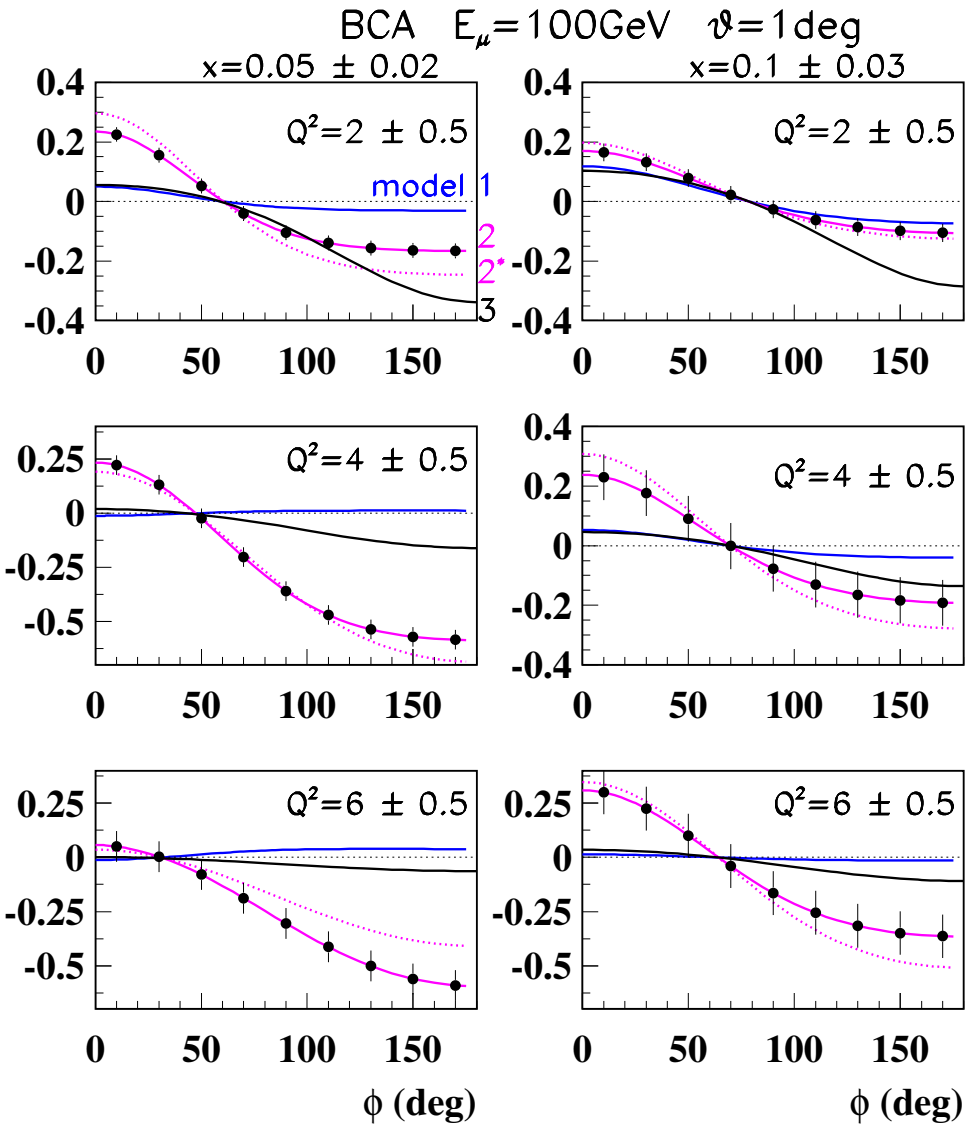

Figure 1: Azimuthal distributions of the beam charge asymmetry in 6 different x, Q^2 regions for model 1 (blue line), model 2 (line with points and error bars, $\alpha' = 0.8\,(\mathrm{GeV}/c)^{-2}$), model 2* (dotted, $\alpha' = 1.1\,(\mathrm{GeV}/c)^{-2}$), and model 3 (black line) as described in the text.

Polarized Physics with an Electron-Ion-Collider

Antje Bruell

Jefferson Lab
12000 Jefferson Avenue, Newport News, VA 23606 - USA

The perspectives of a future Electron-Ion-Collider on spin physics and nucleon structure are presented together with the present design options for such a machine.

1 Introduction

A great achievement of nuclear and particle physics has been the quantitative verification of the QCD theory in hard scattering processes, at distance scales several times smaller than the size of the proton. At these short distances, the quarks and gluons have a very clear experimental signature, and their dynamics follows the prediction of perturbative QCD calculations. Such experiments have, e.g., established that the quarks carry about 50% of the proton's momentum (the rest being carried by gluons), and - surprisingly -only 30% of the proton's spin. However, there are still glaring gaps in our knowledge of quarks and gluons inside the proton. What is the role of gluons and angular momentum in the description of the proton's spin? What is happening at very low momentum fractions where more and more gluons are expected to start overlapping each other ? How large are the correlations between quarks and gluons inside the nucleon ? And how are they distributed in transverse space ?

Recent advances in computational technology, lattice field theory algorithms, continuum model building, accelerator beam quality, and detector design have led us to the threshold of developing a true understanding of the fundamental mechanisms of QCD and the ability to solve QCD, also at a long distance scale, quantitatively. However, such an understanding requires an extensive series of precise measurements, utilizing a hard electron-quark collision not only to access deep inelastic scattering processes, but also the more selective semi-inclusive and deep exclusive processes.

This has led to the proposal of an Electron-Ion-Collider (EIC), a new machine with center-of-mass energies between 20 and 100 GeV, polarizations of both electron and proton (deuteron, ^{3}He beams) and luminosities up to 10^{35} cm^{-2}sec^{-1}. Two different approaches have been taken for the design of such a future Electron-Ion-Collider:

- One effort has focused on the utilization of the existing RHIC ion complex (eRHIC [2]). Adding either a 10 GeV linear accelerator for polarized electrons or a small 10 GeV polarized electron ring, luminosities of about $5 \cdot 10^{33}$ ($5 \cdot 10^{32}$) cm^{-2}sec^{-1} can be achieved. While the latter option uses existing accelerator technologies, a significant R&D effort is required to achieve the high intensity polarized electron current and energy recovery capability required in the design using a linear accelerator.
- In parallel, accelerator physicists at Jefferson Lab are pursuing a design which uses the CEBAF linear accelerator and requires the construction of a 30 to 225 GeV ion storage ring [3]. This represents a more ambitious design concept to realize a luminosity of up to 8x1034 cm-2s-1, using much higher collision frequencies and crab-crossing of colliding beams. In this concept, the booster rings, electron collider ring, and

ion collider ring are designed as a figure 8, a design directly aimed at spin physics opportunities.

2 The Structure of the Nucleon

Great progress in our understanding of the structure of the nucleon has been made over the last decade at the HERA collider which has established the total dominance of gluons at low values of x. However, the same data also clearly the limit of the applicability of the conventional perturbative methods: at small values of x and in the region of low Q^2, global parton distribution fitting algorithms result into gluon distributions smaller than the sea quark distributions and even turning negative. With the question still outstanding whether the gluons inside the proton can also behave as pre-existing, valence-like, constituents, or are rather the sole product of perturbative gluon Bremsstrahlung and gluon-gluon splitting processes, it is exactly this low Q^2 region where one would like to map the gluon content of the proton to study nucleon structure.

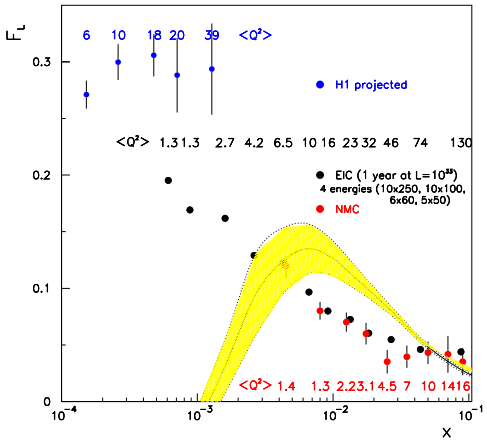

Figure 1: The longitudinal structure function F_L expected from measurements at EIC in comparison with data from NMC and the expected results from HERA.

Measurement of the longitudinal structure function F_L would directly settle these issues. F_L gives direct access to the gluon momentum distributions in the region of small x, where $F_L \approx \alpha_s(Q^2)xG(x,Q^2)$, and good access in the region of large x. The Electron-Ion Collider, with its variable energy scheme, would allow truely unprecedented measurements of F_L (see Fig. 1). For the proton, this would render a substantial decrease of the uncertainties in $G(x,Q^2)$, especially in the region of interest, i.e. at low values of x and moderate values of Q^2.

3 The Spin Structure of the Nucleon

One of the greatest successes of the Quark Parton Model is the description of the static properties of the nucleon and other baryons. Even though the naive quark parton model picture seems to perfect to account for the nucleon spin (3 valence quarks with spin 1/2 arranged to result into a proton spin of 1/2), deep inelastic scattering experiments have shown a very different picture. Over the last 20 years years the unpolarized (or spin-averaged) electron scattering measurements have been extended to precision spin-dependent measurements, rendering data on the g_1 structure function over a large range in x and about one decade in Q^2. The major surprise from these results was that quarks and anti-quarks together carry only about 30% of the nucleon's spin. To then determine how the inner constituents of the nucleons, the valence quarks and the sea of quarks and gluons, conspire to provide the spin-1/2 of the nucleon, remains a challenging key issue in nuclear physics.

Similar as in the unpolarized case, the dependence on Q^2 of the structure function g_1 has been used to constrain the gluon contribution to the proton spin. However, the precision and range in Q^2 of the existing data are far from optimal for this procedure to precisely determine the gluon spin distribution.

The proposed EIC will allow for precision measurements of the spin structure functions g_1, down to the smallest momentum fractions and over an unprecedented range of scales, as illustrated in Fig. /ref-Fig:g1q2. This will provide crucial benchmark data to better pin down our present understanding of the precise contributions to the nucleon spin of quark and anti-quark spin together. The increase range in Q^2 scales will similarly provide better constraints on the gluon contribution to the proton spin. The latter contributions can also be *directly* measured at the charm-quark mass scale with an EIC through low-Q^2 electroproduction of D° mesons. The high precision achievable in the determination of $\Delta G/G$ at EIC, using the latter method, is illustrated in Fig. 3.

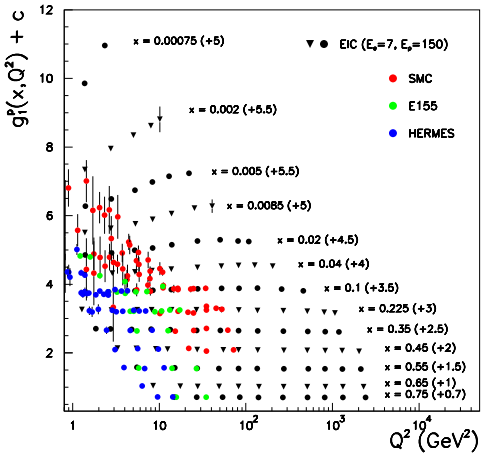

Figure 2: The expected precision on the polarized structure function $g_1(x, Q^2)$ at a future EIC in comparison with existing measurements.

With the realization that quarks and anti-quarks together only carry some 30% of the proton spin, and gluons likely not completing this picture, orbital angular momentum of quarks and gluons has become a central issue in Nuclear Physics. To determine such orbital motion within the nucleons, a completely novel area of study, has been made possible with recent major theoretical breakthroughs that introduced more complete parton distribution functions termed "*Generalized Parton Distributions*" (GPDs) and "*Transverse Momentum Dependent Parton Distributions*" (TMDs), that both both contain information not only on the longitudinal momentum but also on the transverse spatial (or momentum) distribution of quarks and gluons in a fast moving hadron. As such, they are sensitive to the orbital motion of quarks and gluons, not accessible in inclusive scattering.

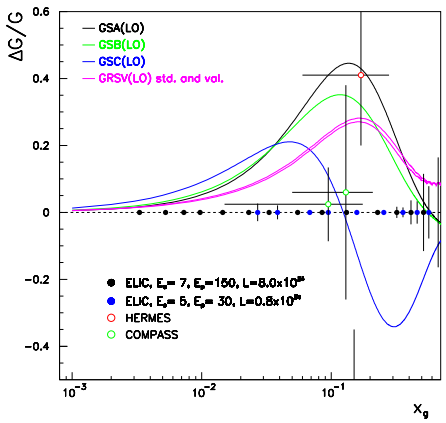

Figure 3: Measurement of the polarized gluon distribution from open charm production at the EIC in comparison with existing measurements and various models consistent with existing data.

Determination of valence quark GPDs are the flagship of the physics program at the 12-GeV Upgrade at JLab. With EIC, it will be possible to extend the surveys of GPDs

into the region where sea quarks and gluons abound. Electroproduction measurements of vector mesons, such as ρ mesons and ϕ mesons, can be used to map the transverse spatial profile of gluons. Electroproduction measurements of charged pions can be extended to reach the limit, $Q^2 > 10$ GeV^2, where one can safely believe access to GPDs is feasible for a quark-flavor separation.

Azimuthal distributions of final state hadrons in semi-inclusive deep inelastic scattering provide an independent window on the orbital motion of quarks, through the framework of TMDs. These describe transitions of nucleons with one polarization state to a quark with another polarization state. At the quark-gluon level, this probes the physics of initial and final state interactions. TMDs were introduced to explain the surprisingly large asymmetries found in hadronic reactions and , more recently, in semi-inclusive deep inelastic scattering experiments at HERMES, COMPASS, and JLab, with polarized targets.

In perturbative QCD, which applies when the transverse momentum p_T of the detected hadron is large compared to Λ_{QCD} (the scale where $\alpha_s \to \infty$), asymmetries vanish at leading twist level. The observed spin-dependent and spin-independent azimuthal asymmetries occur at p_T below 1-2 GeV, not much larger than Λ_{QCD} or the typical quark-gluon transverse momenta of order 0.5 GeV. Thus, the measured asymmetries could arise from non-colinear parton (quark-gluon) or multi-parton correlations ("higher-twist" effects, suppressed at large p_T). Presently, the intrinsic transverse momentum of partons in the nucleon is at the root of most explanations of these non-zero azimuthal asymmetries. Measurements at EIC would be crucial, as they would extend measurements planned with the 12-GeV Upgrade at JLab into a region of large p_T, sufficiently large to provide an alternative "hard" scale for precise perturbative calculations.

4 Summary

The proposed Electron-Ion-Collider is the ideal machine to extend the measurements of polarized deep-inelastic scattering into a new level of kinematic coverage and precision. This will allow a precision determination of the gluon distribution at low x and moderate Q^2, a measurement of the polarized sea quark distributions and a determination of the polarized gluon distribution over a very large range in x. Measurements of exclusive processes at sufficiently high values of Q^2 will enable to perform "gluon tomography" and thus a mapping of the transverse spatial profile of gluons. Together with measurements of transverse spin effects, these exclusive processes will determine the contribution of orbital momenta of quarks and gluons to the spin structure of the nucleon.

5 Bibliography

References

[1] Slides:
`http://indico.cern.ch/contributionDisplay.py?contribId=258&sessionId=10&confId=9499`

[2] eRHIC Zeroth Order Design Report, March 2004, edited by M. Farkhondeh and V. Ptitsyn.

[3] Zeroth-Order Design Report on Electron-Light Ion Collider at CEBAF, January 2007, edited by L. Merminga.

Using Anti-Protons to Measure Nucleon Structure – Prospects at PANDA

B. Seitz on behalf of the PANDA collaboration

University of Glasgow - Department of Physic and Astronomy
Kelvin Building, Glasgow G12 8QQ - Scotland, U.K.

Fundamental questions of hadron and nuclear physics can be addressed in interactions of anti-protons with nucleon and nuclei. Proton-antiproton annihilation is a unique tool to explore the structure of the nucleon in the time-like domain and to access quark distribution functions using Drell Yan processes or hard exclusive reactions. The planned Facility for Antiproton and Ion Research (FAIR) featuring a high energy storage ring for anti-protons will deliver a high quality beam ideally suited to access this physics with unprecedented accuracy. A universal detector system called PANDA is proposed to surround an internal target covering almost the complete solid angle.

1 Introduction

FAIR is a major upgrade planned at the existing GSI facility at Darmstadt. It covers a very broad range of modern hadronic physics. The physics program with anti-proton beams covers the investigation of hadrons and the properties of hadronic matter in the energy range up to $\sqrt{s} \approx 5.5$ GeV and at luminosities in excess of $\mathcal{L} = 10^{31} cm^{-2} s^{-1}$. The main topics to be addressed are the search for charmed hybrids and glueballs, spectroscopy of charmonium, the study of hypernuclei as well as a measurement of the properties of the proton in reaction with electromagnetic final states.

The annihilation of anti-protons with protons can be used to probe the structure of the nucleon itself by looking at electromagnetic final states, i.e. reactions with real or virtual photons as reaction products. The most prominent reactions discussed in the following are the study of parton distribution functions in the Drell Yan process and the study of the time-like behaviour of so called Generalized Distribution Amplitudes in exclusive processes and the time-like behaviour of the protons electromagnetic form factors.

The broad physics program to be addressed by this new facility poses significant challenges for the design and construction of the detector. In particular, the detector should provide:

- full angular coverage and good angular resolution for charged and neutral particles
- particle identification in a large range of particles and energies
- high resolution over the required wide range of energies
- high rate capability especially for the close-to-target and forward detectors.

The PANDA experiment thus is a multi-purpose detector system surrounding an internal target. In the following several highlights focussing on the measurement of electromagnetic final states will be briefly described, more details can be found in Ref. [2].

2 The PANDA experiment

The detector design is shown in Fig. 1. Its concept is based on a combination of a central detector (target spectrometer (TS)) within a 2 T solinoidal magnetic field covering labora-

tory angles from 5° on upwards complemented by a forward spectrometer (FS) equipped by a dipole magnet to measure particles at the most forward angles. Combining these two spectrometers allows full angular coverage and the wide range of energies to be taken into account. Both, TS and FS, will allow the detection, identification and energy/momentum reconstruction for charged and neutral particles. Particles emitted with laboratory angles

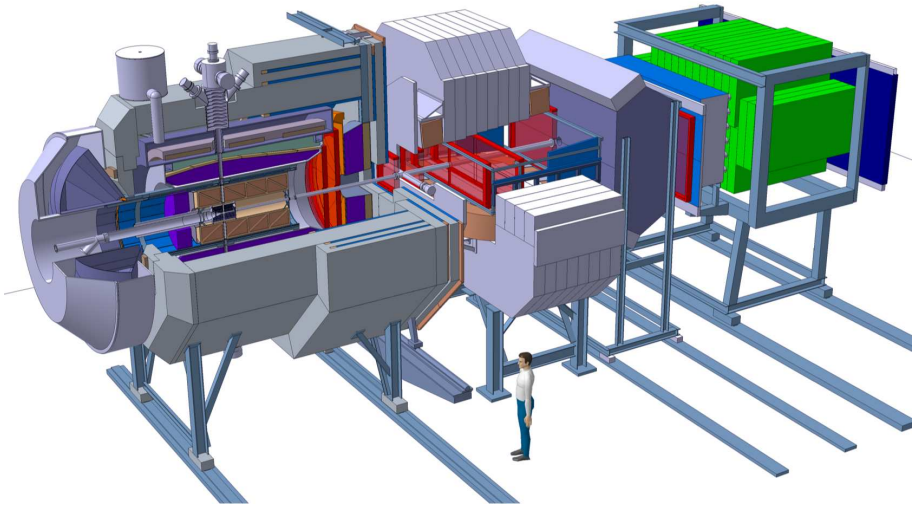

Figure 1: Sketch of the planned PANDA detector systems. The antiproton beam is entering the target spectrometer from the left. The forward spectrometer is depicted on the right.

larger than 10° are solely measured in the TS consisting of azimuthally symmetric detectors in the coils of a super-conducting magnet. Surrounding the interaction volume will be a silicon micro-vertex detector. This detector is followed by the central tracking detector, e.g a TPC. Particle identification will be realised by a variety of different techniques. The main work horse in the TS will be a DIRC-type Cherenkov counter complemented by Time-of-Flight systems and measurements of the energy deposited in the TPC and the electromagnetic calorimeter. The forward region will be covered by two sets of mini drift chambers and a flat disc DIRC. Muon–detectors will be mounted outside of the return yoke. Particles emitted with polar angles below 10° horizontally and 5° vertically are detected with the FS. It is comprised of a 1 m gap dipole and tracking detectors for momentum analysis of charged particles. Photons will be detected by a shashlyk-type calorimeter consisting of lead-scintillator sandwiches. Other neutrals and charged particles with momenta close to the beam momentum will be detected in the hadron calorimeter and muon counters. Identification of charged particles will be provided by Cherenkov and ToF counters.

3 Electromagnetic final states at PANDA

Anti-proton – proton annihilation reactions yielding electromagnetic final states probe the nucleon structure in the time-like region. They are complementary deep inelastic scattering

in probing the underlying parton distributions. Choosing a $\bar{p}$-beam allows in particular to study annihilation in the valence quark region. PANDAs excellent detector capabilities allow to separate and identify rare events with only two real photons, a real and a virtual photon (or meson) or a lepton pair in the final state offering a unique possibilities.

Drell Yan processes

The Drell Yan processes has evolved to be a standard tool for probing the partonic structure of hadrons. PANDA offers the unique opportunity to measure these processes in $\bar{p}p$ annihilation probing not only the sea-quarks, but more importantly the valence quark region. The angular dependence of the Drell Yan cross section is given by:

$$\frac{d\sigma}{d\Omega} \propto 1 + \lambda \cos^2\theta + \mu \sin 2\theta \cos\phi + \frac{\nu}{2} \sin^2\theta \cos 2\phi. \quad (1)$$

At NLO, the parameters λ and ν are related by the Lam-Tung relation $1 - \lambda = 2\nu$ [3], which was shown to be violated in pion-induced Drell Yan processes at high p_T. This violation has been explained e.g. by the existence of a chiral-odd, T-odd distribution function with an intrinsics k_T dependence [4]. This hitherto unmeasured Boer-Mulders function represents the correlation of the parton's transverse spin and k_T in an unpolarised nucleon. The Boer-Mulders function belongs to a class of functions which recently generated considerable interest, with e.g. the Collins fragmentation function, the transversity distribution and the Sivers function belonging to the same family. The latter two functions will be uniquely accessible in doubly polarised or single polarised Drell Yan processes [5]. The Sivers function is expected to change sign between measuring it in semi-inclusive DIS and in Drell Yan reactions. The observation of this sign change would be a fundamental test of QCD.

Time-like form factors

The electric and magnetic form factors G_E and G_M describing the response of the proton to time-like photons can be extracted from the cross section of the process $\bar{p}p \to e^+e^-$. Both the electric and magnetic form factors depend on the virtuality of the intermediate photon Q^2. A measurement over a large range of Q^2 is thus crucial to test the Q^2-behaviour as well as the space-like time-like equality for each value of Q^2 measured. The proton time-like form factors have been measured by various experiments near threshold and in the region of low values of Q^2. The current upper range was pioneered by E760 and E835 at Fermilab reaching up to $Q^2 \approx 15\text{GeV}^2$, while the intermediate range was recently covered by BES and BaBar [6, 7]. These experiments did not achieve the statistics required to separate $|G_E|$ and $|G_M|$ but had to work under the assumption of both being equal. A rich structure has been predicted using the scarce data in the time-like region and analytic continuation from the space-like region [8]. With PANDA running at design luminosity it will be possible to determine both form factors separately and over a large range in Q^2 reaching from threshold up to $Q^2 \approx 20$ GeV^2 or higher within a single experiment. The expected improvements in angular coverage and statistics compared to e.g. the previous experiments at Fermilab will significantly improve the existing results and allow a separation of $|G_E|$ and $|G_M|$.

Hard exclusive reactions

The recently established framework of Generalised Distribution Amplitudes (GDA) (or Transition Distribution Amplitudes (TDA)) offers a new tool in understanding the structure of the nucleon unifying diverse probes of its structure like form factors, forward parton distributions, hard exclusive production or wide angle Compton scattering. It was shown recently that the exclusive $\bar{p}p$ annihilation at large s and t can be described in terms of GDAs as well. At these kinematics, the reaction separates into a soft part parametrised by GDAs and a hard part describing the annihilation of a quasi-free $\bar{q}q$-pair into two photons.

Data from a wealth of different reactions are needed to map out this new class of functions promising a complete picture of the nucleons' structure. Most of the theoretical attention was give to the process $\bar{p}p \to \gamma\gamma$, which offers access to GDAs without additional complication like the wave-function of the mesons produces. Based on the calculation of Ref. [9] a rate of a coupled of thousand of these events will be produced per month with PANDA running at design luminosity. In addition to this, the most simple process $\bar{p}p \to \gamma\gamma$ more complicated exclusive annihilation processes with (pseudo)scalar or vector mesons as well as virtual photons in the final state will be considered as well. Interpreted in terms of TDAs, this will allow e.g. to measure the deep spatial structure of quarks inside the nucleon [10]. Taking data from hard exclusive processes in exclusive deep inelastic scattering and $p\bar{p}$ together promises for the fist time to measure the spatial location of quarks inside a nucleon.

4 Conclusion and outlook

The PANDA experiment at FAIR will be a future key experiment in understanding the nature of QCD and the structure of the nucleon. PANDA combines a unique $\bar{p}$-beam at high luminosity and precision with an innovative, complete detector set-up. This unique combination will allow precision measurement of $p\bar{p}$-annihilation into electromagnetic final states. Parton distribution functions of the nucleon like the Sivers–function and the Boer-Mulders-function are directly accessible in Drell Yan processes. The measurement of hard exclusive reactions allows access to GDAs and thus ultimately to a complete understanding of the nucleon. Last not least, measurements of time-like nucleon form factors offer exciting prospects. The PANDA experiment at FAIR will address all these issues, promising a rich harvest of physics results.

References

[1] Slides:
`http://indico.cern.ch/contributionDisplay.py?contribId=259&sessionId=10&confId=9499`

[2] PANDA Collaboration, Technical Progress Report, FAIR–ESAC/Pbar 2005.

[3] C. S. Lam, W. K. Tung, Phys. Rev. **D 21** 2712 (1980).

[4] D Boer, Phys. Rev. **D 60** 014012 (1999).

[5] P. E. Reimer, J. Phys. G: Nucl. Part. Phys. **34** S107 (2007).

[6] M. Ablikim *et al.* [BES Collaboration], Phys. Lett. B **630** 14 (2005).

[7] B. Aubert *et al.*[BaBar Collaboration], Phys. Rev. **D 73** 012005 (2006).

[8] R. Baldini *et al.*, Eur. Phys. J. **C 46** 421 (2006).

[9] A. Freund *et al.*, Phys. Rev. Lett. **90** 092001 (2003).

[10] B. Pire, L. Szymanowski, Nucl. Phys. **A 782** 9 (2007).

Physics Beyond the Standard Model at LHeC

Emmanuelle Perez

CERN, PH Department
Geneva 23 CH-1211 Switzerland

Future discoveries at the LHC may call for a future DIS programme at very high energy. This could be realised by colliding one of the LHC proton beams with a new lepton beam in the LHC tunnel. Example cases are shown where high energy *ep* data would be needed to study and fully interpret new phenomena that the LHC may discover. The consequences, for the LHC discovery potential, of our current limited knowledge of proton structure are also shortly addressed.

1 Introduction

A Large Hadron Electron Collider (LHeC), allowing *ep* or eA collisions to be performed in the LHC tunnel, is one of the possible options for the LHC upgrade. Its physics case and a possible design have been described in [1]. With a 70 GeV electron beam in collision with one of the LHC hadron beams, a centre-of-mass energy $\sqrt{s}$ of 1.4 TeV would be achieved, allowing deep-inelastic scattering (DIS) reactions to be studied for momentum transfer Q^2 up to 10^6 GeV^2 and for Bjorken x values down to 10^{-6} for $Q^2 > 1$ GeV^2. Low-x physics at LHeC is described elsewhere in these proceedings [2]. In the *ep* mode, the luminosity of this collider could reach 10^{33} cm^{-2}s^{-1} (i.e. an integrated luminosity of about 10 fb^{-1} per year) such that rare, yet unobserved, phenomena may be studied in detail, as the production of electron-quark resonances. The high luminosity would also allow for a much better determination of the proton parton distribution functions at large x as described elsewhere in these proceedings [3], which may be needed for a full interpretation of the discoveries that will, hopefully, be made at the LHC.

2 Leptoquarks and supersymmetry

An *ep* collider, providing both baryonic and leptonic quantum numbers in the initial state, is ideally suited to a study of the properties of new bosons possessing couplings to an electron-quark pair. Such particles can be squarks in supersymmetry with R-parity (R_p) violation, or first-generation leptoquark (LQ) bosons which appear naturally in various unifying theories beyond the Standard Model (SM). In *ep* collisions, they are produced as single $s-$channel resonances via the fusion of incoming electrons with quarks in the proton. They are generically referred to as "leptoquarks" in what follows.

The single LQ production cross section depends on the unknown coupling λ of the LQ to the electron-quark pair. For a coupling λ of $\mathcal{O}(0.1)$, LQ masses up to about 1 TeV could be probed at the LHeC. In *pp* interactions, such leptoquarks would be mainly pair produced and masses up to about 1.5 to 2 TeV can be probed at the LHC, independently of the coupling λ. However, the determination of the quantum numbers of this new particle in the pair-production mode is not possible (e.g. for the fermion number) or ambiguous and model-dependent (e.g. for the spin). Single LQ production is much better suited for such studies. As an example, the determination of the LQ fermion number F via single LQ production is described below.

Single LQ production at the LHC mainly proceeds via gluon-quark reactions [4]. The cross-section is however much lower than that at LHeC as shown in Fig. 1. The single production of a $F = 0$ ($|F| = 2$) LQ at the LHC, followed by the LQ decay into e^+q or $e^-\bar{q}$ (e^-q or $e^+\bar{q}$), could allow the fermion number of a first generation LQ to be determined, by comparing the signal cross-sections with an e^+ and an e^- coming from the resonant state. This comes from the fact that the parton densities for u and d at high x are much larger than those for $\bar{u}$ and $\bar{d}$. However, the asymmetry measured at the LHC may be statistically limited in a large part of the parameter space. The determination of F in ep collisions is simply obtained by comparing the cross-sections measured in e^+p and e^-p collisions. The much larger cross-section would make the determination of F possible up to the kinematic limit, for a coupling of $\mathcal{O}(0.1)$. Example asymmetries expected to be measured with 100 fb^{-1} of LHC data, and with 10 fb^{-1} of LHeC data both in e^+p and in e^-p, are shown in Fig. 2. For a coupling $\lambda = 0.1$, no information on F can be extracted from the LHC data for a LQ mass above ~ 700 GeV, while the LHeC can determine F for LQ masses up to 1 TeV.

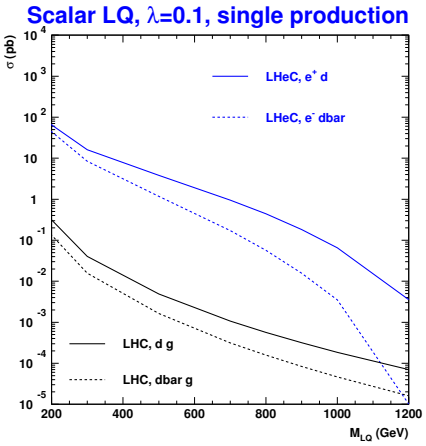

Figure 1: Cross-section for single LQ production at LHC and at LHeC. The example of a scalar LQ coupling to ed is shown here.

The LHC discovery of an ep resonance with a mass below about 1 TeV, with indications that the coupling λ is not too small, would thus be a strong motivation to pursue its study in ep collisions. The LHeC would resolve the remaining ambiguities in the determination of the LQ quantum numbers, and would provide important information on the chiral structure and on the strength of the LQ couplings.

In R_p-conserved supersymmetry, the dominant process in ep collisions consists of the associated production of a slepton and a squark. The cross-section is above 1 pb as soon as the sum of the slepton and squark masses is below 1 TeV. Hence, if squarks are discovered at the LHC with a mass not much higher than the Tevatron reach, selectrons or sneutrinos with a mass up to about 500 GeV may be observed at LHeC, slightly extending beyond the LHC reach.

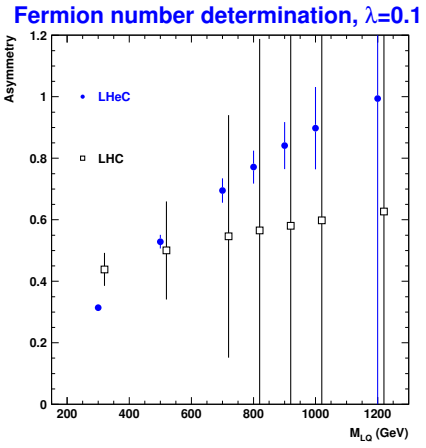

Figure 2: Asymmetries which would determine the fermion number of a LQ, the sign of the asymmetry being the relevant quantity.

3 Proton structure and the interpretation of LHC discoveries

Parton distribution functions (pdfs) are not well know yet in the high x regime, in particular for the down quark and the gluon. Although this limited knowledge would not jeopardize the discovery of a high mass new state at the LHC, as a new Z' or W' boson, it would limit the information that will come out of the LHC data. For instance, with the ultimate LHC luminosity, a W' boson could be discovered with a mass of up to about 6 TeV if its coupling to quarks is similar to that of the standard W boson. For such a high partonic centre-of-mass energy, the uncertainty of the partonic luminosity is of the order of 40%, such that only a rough estimate of the coupling of a 6 TeV W' boson to fermions will be possible. An improved knowledge of the high x parton densities, as brought by the LHeC, would be of a high value for the interpretation of the LHC discoveries. As an example, Fig. 3 shows how the uncertainties of the d and gluon densities would be decreased with 10 fb^{-1} of LHeC data.

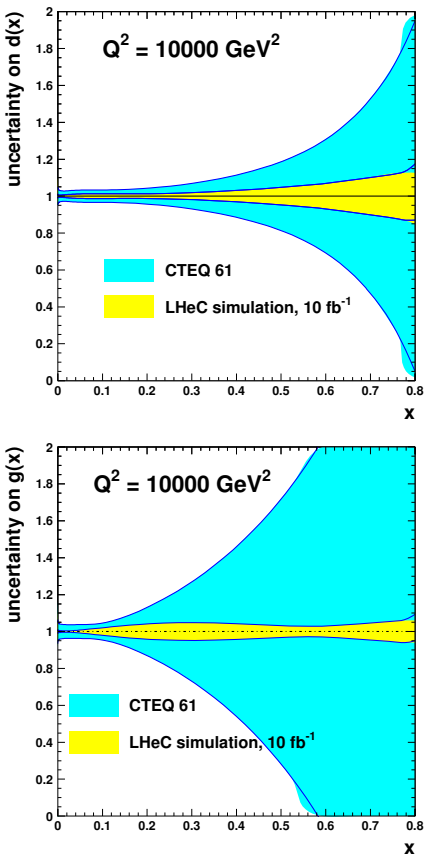

Figure 3: Uncertainty on the down quark and on the gluon densities in the proton, at a scale $Q^2 = 10^4$ GeV^2. The blue (dark-shaded) error bands show the uncertainties as obtained from the CTEQ 6.1 sets, and the yellow (light-shaded) bands show how these uncertainties would be reduced with 10 fb^{-1} of LHeC data.

In cases where new physics effects would not manifest themselves as a clear "peak" above a background, but as a smooth enhancement or decrease of the measured cross-section as compared to the SM expectation, our limited knowledge of proton pdfs may be more problematic. Such an effect could be observed e.g. in the Drell-Yan mass spectrum at the LHC, and could be due, for example, to the interference of a very heavy Z' with the SM bosons, to the exchange of a continuum of Kaluza-Klein states in the presence of large extra-dimensions, etc. Such effects in the di-electron DY spectrum can be generically studied by using an effective Lagrangian density

$$\mathcal{L}_{CI} = \sum_{i,j=L,R} \epsilon_{ij}^{eq} \frac{4\pi}{\Lambda^2} (\bar{e}_i \gamma^\mu e_i)(\bar{q}_j \gamma_\mu q_j) \qquad (1)$$

in which new physics is embedded in "contact interactions" (CI). Different models can be considered, depending on which terms are present in $\mathcal{L}_{CI}$. The parameters $\epsilon_{ij} = \pm 1$ determine whether the new amplitude(s) interfere constructively or destructively with the SM amplitudes. With 10 fb^{-1} of data, LHeC would probe scales between 25 and 45 TeV depending on the model. The sensitivity of LHC to such $eeqq$ contact interactions is similar.

Figure 4 shows how the DY cross-section would deviate from the SM value, for three examples of *eeqq* contact interactions. In the "LL" model considered here, the sum in eq. (1) only involves left-handed fermions and all amplitudes have the same phase ϵ. With only *pp* data, it will be difficult to determine simultaneously the size of the contact interaction scale Λ and the sign of the interference of the new amplitudes with respect to the SM ones: for example, for $\Lambda = 20$ TeV and $\epsilon = -1$, the decrease of the cross-section with respect to the SM prediction for di-electron masses below ~ 3 TeV, which is characteristic of a negative interference, is too small to be firmly established when pdf uncertainties are taken into account. For the same "LL" model, the sign of this interference can be unambiguously determined at LHeC from the asymmetry of σ/σ_{SM} in e^+p and e^-p data, as shown in Fig. 5.

Moreover, with a polarised lepton beam, *ep* collisions would help determine the chiral structure of the new interaction. More generally, it is very likely that both *pp* and *ep* data would be necessary to underpin the structure of new physics which would manifest itself as an *eeqq* contact interaction. Such a complementarity of *pp*, *ep* (and also *ee*) data was studied in [5] in the context of the Tevatron, HERA and LEP colliders.

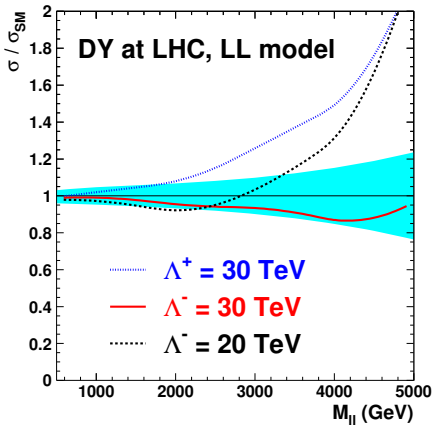

Figure 4: Example deviations, from its SM value, of the Drell-Yan cross-section at LHC as a function of the dilepton mass, in the presence of an *eeqq* contact interaction.

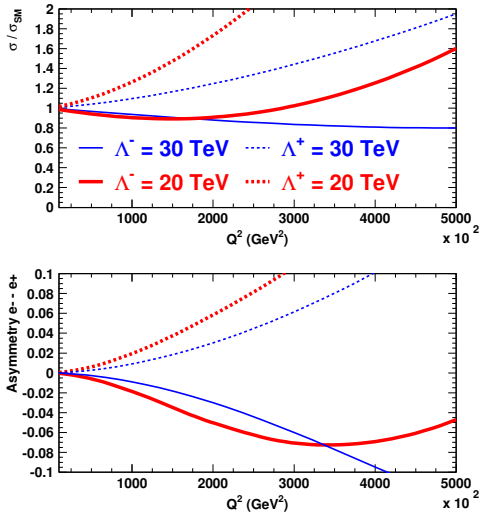

Figure 5: (top) Example deviations of the e^-p DIS cross-section at LHeC, in the presence of an *eeqq* CI. (bottom) Asymmetry of σ/σ_{SM} between e^+p and e^-p measurements.

References

[1] J.B. Dainton *et al.*, JINST **1** (2006) P10001 [hep-ex/0603016].

[2] P. Newman, these proceedings.

[3] M. Klein, these proceedings.

[4] A. Belyaev *et al.*, JHEP **09** 005 (2005) [hep-ph/0502067].

[5] A.F. Zarnecki, Eur. Phys. J. **C11** 539 (1999) [hep-ph/9904334].

[6] Slides:
`http://indico.cern.ch/contributionDisplay.py?contribId=260&sessionId=10&confId=9499`

Parity-Violating Deep Inelastic Scattering

Krishna S. Kumar[1] *

1- University of Massachusetts, Amherst - Dept of Physics
Amherst, MA 01003 - USA

We discuss the physics motivation for an experimental program of parity-violating (PV) asymmetry measurements in the deep inelastic scattering (DIS) of longitudinally polarized electrons off unpolarized fixed targets, made feasible by the intense and stable electron beam at Jefferson Laboratory especially after the planned 12 GeV upgrade. This will provide access to long standing issues in DIS physics, such as a sensitive search for charge symmetry violation at the partonic level, a clean measurement of $d(x)/u(x)$ as $x \to 1$ and a systematic study of higher-twist effects. Most importantly, it will allow a unique probe of physics at the multi-TeV scale via a precision measurement of the weak neutral current axial-vector quark coupling.

1 Introduction

Nearly 50 years ago, soon after the discovery of parity violation in beta decay, Zel'dovich speculated that there might be an analogous parity violating neutral current interaction[2]. He noted that if such an interaction existed, then parity violation would be manifested in lepton-nucleon scattering due to the interference between the weak and electromagnetic amplitudes. If one scatters longitudinally polarized electrons off unpolarized protons and flipped the sign of the beam polarization, the fractional difference in the cross-section would be proportional to the 4-momentum transfer $Q^2 \equiv -(p-p')^2$ expressed in GeV^2:

$$A_{\rm PV} \equiv \frac{\sigma_R - \sigma_L}{\sigma_R + \sigma_L} \simeq \frac{|A_Z|}{|A_\gamma|} \simeq \frac{G_F Q^2}{4\pi\alpha} \simeq 10^{-4} Q^2 \qquad (1)$$

For typical fixed target experiments, $A_{\rm PV}$ ranges from roughly 10^{-4} to as small as 10^{-7}. In the mid-seventies, parity violation in deep inelastic electron nucleon scattering was first observed by the SLAC E122 experiment[3], from which the electron-quark weak neutral current coupling could be extracted. The measurement was an important test of the SU(2)×U(1) gauge theory of electroweak interactions, and the extracted value of the electroweak mixing angle $\sin^2\theta_W$ matched the corresponding value obtained from neutral current neutrino scattering experiments.

Over the past 20 years, the experimental techniques employed to measure these tiny left-right asymmetries have been steadily refined such that statistical errors approaching 0.01 parts per million (ppm) and systematic errors of a few parts per billion (ppb) are possible[4]. Depending on the choice of target and kinematic variables, this has facilitated measurements in several important physics topics, such as many-body nuclear physics, nucleon structure and searches for physis beyond the standard model at the TeV scale.

The above mentioned physics topics have been pursued using elastic scattering on a variety of targets, with the 4-momentum transfer $Q^2 \ll 1$ GeV^2. At the higher Q^2 required to significantly improve on the E122 PVDIS measurement, neither the luminosity nor the experimental technology was available until recently. In this paper, we outline the formalism

*funded by US Department of Energy, Division of Nuclear Physics Grant DE-FG02-88R40415-A018

for the analysis of PVDIS measurements and elaborate on the rich physics program that will be enabled, especially with the 12 GeV upgrade of Jefferson Laboratory (JLab).

2 PVDIS Phenomenology

A_{PV} in DIS can be written as

$$A_{PV} = Q^2 \frac{G_F}{2\sqrt{2}\pi\alpha}\Big[a(x) + \frac{1-(1-y)^2}{1+(1-y)^2}b(x)\Big], \tag{2}$$

$$a(x) \equiv \Sigma_i f_i(x) C_{1i} q_i / \Sigma_i f_i(x) q_i^2, \tag{3}$$

$$b(x) \equiv \Sigma_i f_i(x) C_{2i} q_i / \Sigma_i f_i(x) q_i^2. \tag{4}$$

Here, $C_{1i}(C_{2i})$ are the weak vector(axial-vector) weak charges for the ith quark flavor, x is the fraction of the nucleon momentum carried by the struck quark, $f_i(x)$ are parton distribution functions and q_i are the electromagnetic charges. The $a(x)$ term arises from the product of the electron axial-vector coupling and the quark vector coupling and is typically the dominant term. For an isoscalar target such as deuterium, the dependence on structure largely cancels out in the A_{PV} ratio of the weak and electromagnetic amplitudes:

$$a(x) = \frac{6}{5}\Big[(C_{1u} - \frac{1}{2}C_{1d}) + \text{corrections}\Big]; \tag{5}$$

$$b(x) = \frac{6}{5}\Big[(C_{2u} - \frac{1}{2}C_{2d})\frac{q(x)-\bar{q}(x)}{q(x)+\bar{q}(x)} + \text{corrections}\Big], \tag{6}$$

where $q(x) = u(x) + d(x)$. For scattering off the proton,

$$a(x) = \Big[\frac{u(x) + 0.91d(x)}{u(x) + 0.25d(x)}\Big]. \tag{7}$$

In trying to make precision measurements of $A_{\rm PV}$ in PVDIS, several important issues should be taken under consideration. The $a(x)$ term is a factor of 5 to 10 larger than the $b(x)$ term because the latter involves the vector coupling of the electron, which is small in the electroweak theory. In trying to test the electroweak theory, it is important to be able to extract the value of the electroweak mixing angle $\sin^2\theta_W$ with a relative accuracy better than 1% in order to be relevant in constraining new physics at the TeV scale. Consequently, $A_{\rm PV}$ must be measured to 1% relative accuracy or better. In order to avoid uncertainties from sea-quark distributions and higher-twist effects, it is important to have $Q^2 \geq 2$ GeV^2 and $x \geq 0.35$. The DIS cross-section is steeply falling as x increases. The above factors have precluded a followup precision measurement to E122 for the past two decades.

As mentioned in the introduction, the experimental technology in $A_{\rm PV}$ has now progressed to a point where online background rejection is possible with event rates exceeding 10 MHz and normalization control at the level of 1% has been achieved [5]. Combined with the success of high current operation at Jefferson Laboratory with a beam energy approaching 6 GeV, precision PVDIS measurements become feasible for the first time. Indeed, when the beam energy is upgraded to 11 GeV in the existing experimental halls as planned, high statistics can be accumulated at high $x \sim 0.7$. As we discuss in the following, PVDIS provides access to novel aspects of nucleon structure, complementing and enhancing precision electromagnetic DIS studies.

2.1 Charge Symmetry Violation

As can be seen from Eqn. 5, $a(x) \approx 1.15$ for an isoscalar target, independent of x. This results from the assumption of charge symmetry, where the u-quark distribution in the proton is the same as the d-quark distribution in the neutron, with a similar assumption for the proton d-quark distribution: $u^p = d^n$ and $d^p = u^n$. If $a(x)$ can be measured with high precision over a range of x values, one is thus quite sensitive to charge symmetry violation (CSV). If one defines CSV parameters:

$$\delta u(x) = u^p(x) - d^n(x); \quad \delta d(x) = d^p(x) - u^n(x), \tag{8}$$

then the dependence on the parity-violating asymmetry for an isoscalar target is:

$$\frac{\delta A_{PV}}{A_{PV}} = 0.28\frac{\delta u - \delta d}{u + d} \equiv 0.28 R_{CSV}. \tag{9}$$

While R_{CSV} is known to be less than 0.01 for $x < 0.4$ from neutrino DIS measurements[6], a bag model calculation suggests that $R_{CSV} \sim 0.01$ for $x \sim 0.4$ and rising to 0.02 for $x \sim 0.6$. At high x, knowledge of $u + d$ is limited. As $x \to 1$, if $u + d$ falls off more rapidly than $\delta u - \delta d$, then R_{CSV} might rise to 0.1 at $x \sim 0.7$, which would be observable with a 1% A_{PV} measurement. Further, R_{CSV} is quite unconstrained at large x. There is the tantalizing possiblity that R_{CSV} in the moderate and high x region is a factor of 3 bigger than above-mentioned values, which would be large enough to explain the 3σ discrepancy in the neutrino-nucleon DIS measurement (NuTeV anomaly)[6].

2.2 d/u at high x

As can be seen from Eqn. 7 for PV DIS off the proton, $a(x)$ is quite sensitive to the ratio $d(x)/u(x)$. The value of d/u as $x \to 1$ is a very important parameter to pin down in DIS physics. It is required in order to properly constrain fits of parton distribution functions and impacts predictions for QCD processes at high energy colliders.

More importantly, d/u at high x provides new information on important pieces of the nucleon wave function. There is empirical evidence that the minority quark in the nucleon is suppressed at high x, an intuitive notion in terms of a hyperfine interaction. While the SU(6) wave function would predict $d/u \sim 0.5$, simple SU(6)-breaking arguments would predict $d/u \sim 0$. However, a perturbative QCD calculation predicts $d/u = 0.2$ as $x \to 1$[7].

Currently, the best estimates of d/u comes from ^{2}H DIS structure function data, but uncertainties in the ^{2}H wave-function limits the ability to discriminate between various predictions for d/u[8]. There are plans to measure d/u via the ratio of ^{3}H and ^{3}He structure functions and also via measurements of deuteron structure functions with tagged slow recoiling protons. A precise enough measurement of $a(x)$ for the proton at $x \sim 0.7$ would be able to distinguish between competing predictions for d/u as $x \to 1$. The advantage of A_{PV} measurements over other methods is that there are no nuclear corrections since the PVDIS measurement would be made on a proton target.

2.3 Weak Mixing Angle Measurement

The measurement of the PV DIS asymmetry to an accuracy of 0.5% at $Q^2 \sim 5$ GeV^2 and $x \sim 0.4$ for an isoscalar target such as deuterium, coupled with precise knowledge the

parameter $a(x)$ from other experiments, the parameter $b(x)$ can be extracted with high accuracy for the first time. This measurement would be robust only if the comprehensive PV DIS program described above is carried out. Indeed, as can be seen from Eqn. 5, $a(x)$ is independent of x and simply a function of $\sin^2\theta_W$ under the assumption of charge symmetry and assuming that higher twist effects are either directly measured or constrained. The quantity $b(x)$ is also virtually free of structure function uncertainties at high x.

This measurement would test the WNC amplitude in the lepton-quark sector, where there is currently a 3 σ discrepancy in the NuTeV result. Furthermore, combined with other measurements in elastic electron-proton scattering, precise constraints would be possible on the lesser known axial-vector quark couplings C_{2i}. This would, among other things, provide complementary constraints on various models with new heavy Z' bosons[9].

2.4 Experimental Equipment for PV DIS at high x

To comprehensively address the physics topics discussed above experimentally, a series of A_{PV} measurements in the range of 1 to 2% accuracy are required for the x range from 0.3 to 0.7, with a lever arm of a factor of 2 in Q^2 while keeping $W^2_{\rm min} > 4$ and $Q^2_{\rm min} > 1$. With the upgrade of Jlab, high luminosity with a beam energy of 11 GeV becomes possible for the first time. However, to achieve sufficient statistics at the highest possible Q^2, a spectrometer with at least 50% acceptance in the azimuth is required.

A large magnet is required to shield the detectors from target photons and to sweep out low energy charged particles. Recent studies have indicated that a solenoid would be ideal for the required geometry, mainly the long target length and the large laboratory scattering angles. Feasibility studies and detailed simulations studies have just begun, exploring the possibility to use one of the existing collider detector solenoids.

3 Summary

Parity-violating electron scattering is a mature field and addresses fundamental questions in a variety of different topics. Future measurements at Jefferson Laboratory will lead to important new insights on the structure of the nucleon and yield new and more precise measurements of the weak mixing angle.

References

[1] Slides:
`http://indico.cern.ch/contributionDisplay.py?contribId=262&sessionId=10&confId=9499`

[2] Ya.B. Zel'dovich,Ya.B., J.Exptl.Theoret.Phys. (U.S.S.R.), **36** 964 (1959).

[3] C.Y. Prescott *et al.*, Phys.Lett. **B84** 524 (1979).

[4] K.S. Kumar and P.A. Souder, Prog.Part.Nucl.Phys. **45**, S333 (2000).

[5] F.E. Maas *et al.*, Phys.Rev.Lett. **94** 152001 (2005); D.S. Armstrong *et al.*, Phys.Rev.Lett. **95** 092001 (2005); A. Acha *et al.*, Phys.Rev.Lett. **98** 032301 (2007).

[6] J.T. Londergan and A.W. Thomas, hep-ph/0407247 (2004), and references therein.

[7] G.R. Farrar and R.D. Jackson, Phys.Rev.Lett. **43** 246 (1979).

[8] W. Melnitchouk *et al.*, Phys.Rev.Lett. **84** 5455 (2000); W. Melnitchouk and A.W. Thomas, Phys.Lett. **B377** 11 (1996).

[9] M.J. Ramsey-Musolf, Phys.Rev. **C60** 015501 (1999).

Forward Physics at the LHC

David d'Enterria

CERN, PH-EP, CH-1211 Geneva 23, Switzerland

Small-angle detectors at the LHC give access to a broad physics programme within and beyond the Standard Model (SM). We review the capabilities of ALICE, ATLAS, CMS, LHCb, LHCf and TOTEM for forward physics studies in various sectors: soft and hard diffractive processes, exclusive Higgs production, low-x QCD, ultra-high-energy cosmic-rays, and electro-weak measurements [1].

Introduction

The CERN Large Hadron Collider (LHC) will provide the highest energy proton-proton and ion-ion collisions in the lab to date. The multi-TeV energy of the colliding beams opens up a phase space for particle production in an unprecedented range spanning $\Delta\eta \sim 20$ units of rapidity[a]: $y_{\rm beam} = {\rm acos}(\sqrt{s}/2) = 9.54$ for p-p at 14 TeV. As a general feature, particle production in hadronic collisions is peaked at central rapidities ($|y| \lesssim 3$ at the LHC), whereas most of the energy is emitted at very low angles (Fig. 1 left).

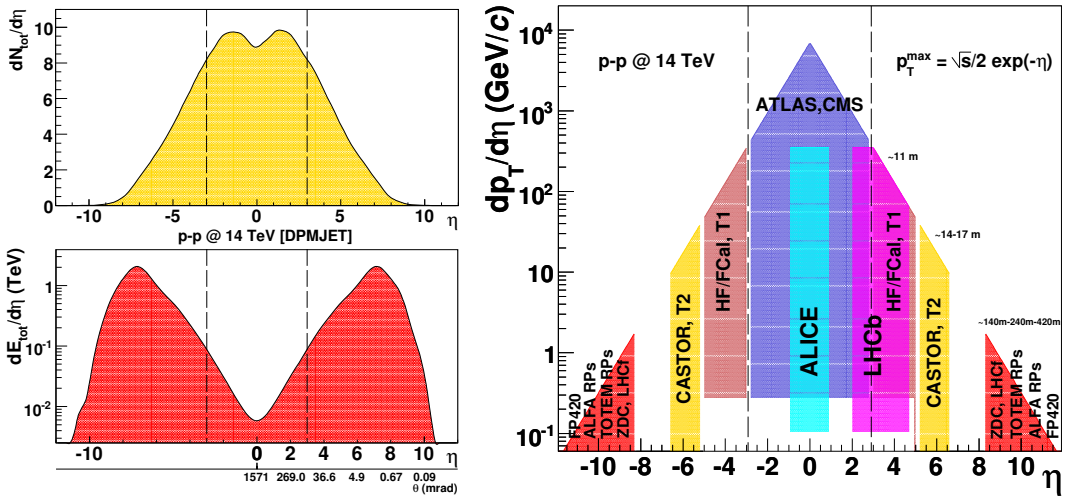

Figure 1: Left: Pseudo-rapidity distributions for the total hadron multiplicity (top) and energy (bottom) in p-p at 14 TeV as given by the DPMJET3 model [2]. Right: Approximate p_T-η coverage of current (and proposed) detectors at the LHC.

All LHC experiments feature detection capabilities at forward rapidities without parallel compared to previous colliders (Figures 1 right, and 2):

- ATLAS [4, 5] and CMS [6, 7] not only cover the largest p_T-η ranges at mid-rapidity for hadrons, electrons, photons and muons, but they feature extended instrumentation

[a]The rapidity can be thought of as the relativistically-invariant measure of longitudinal velocity. Often the *pseudorapidity* $\eta = -\ln\tan(\theta/2)$ which depends only on the polar angle wrt the beam axis, is used instead.

at distances far away from the interaction point (IP): ±11 m (ATLAS FCal and CMS HF hadronic calorimeters), ±14 m (CMS CASTOR sampling calorimeter [8]), ±140 m (Zero-Degree-Calorimeters, ZDCs [5, 9]), and ±240 m (ATLAS Roman Pots, RPs [5]).

- ALICE [10] and LHCb [11] have both forward muon spectrometers in regions, $2 \lesssim \eta \lesssim 5$, not covered by ATLAS or CMS. (In addition, ALICE has also ZDCs at ±116 m [12]).
- The TOTEM experiment [13], sharing IP5 with CMS, features two types of trackers (T1 and T2 telescopes) covering $3.1 < |\eta| < 4.7$ and $5.2 < |\eta| < 4.7$ respectively, plus proton-taggers (Roman Pots) at ±147 and ±220 m.
- The LHCf [14] tungsten-scintillator/silicon calorimeters share the location with the ATLAS ZDCs ±140 m away from IP1.
- The FP420 R&D collaboration [15, 16] aims at installing proton taggers at ±420 m from both ATLAS and CMS IPs.

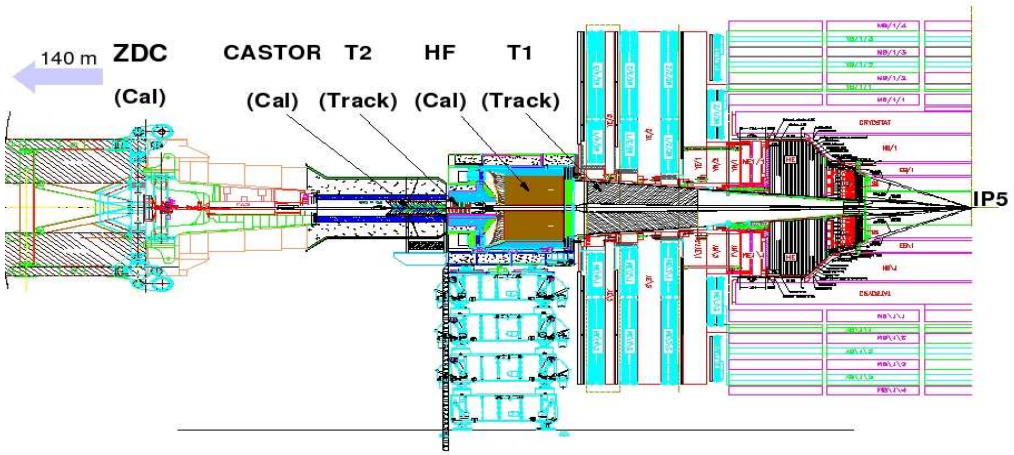

Figure 2: Layout of the detectors in the CMS/TOTEM forward region [3].

Near beam instrumentation provides access to a rich variety of physics measurements when used in three possible modes: (i) as detectors to *directly measure* a given final-state produced in the reaction (e.g. a jet in CASTOR, or a photon in LHCf/ZDC), (ii) as *tagging* devices for the (diffractively or elastically) scattered protons (in Roman Pots or other p-taggers), and/or (iii) as *vetoing* devices of final-state particles produced in the collision (e.g. requiring no hadronic activity within a large rapidity range).

The following forward physics topics will be discussed in this short review:

1. **Diffraction** (soft and hard) and **elastic** scattering [17, 18]. Measurements like the total p-p cross-section, the rapidity-gap survival probability, and hard diffraction cross-sections (heavy-Q, dijets, vector-bosons, ...) are accessible with the TOTEM and ALFA Roman Pots and/or by requiring a large enough rapidity gap in one (or both) of the forward hemispheres (e.g. HF+CASTOR in CMS).

2. **Central exclusive** production of the **Higgs** boson and other heavy (new) particles [19, 20] can be studied combining the FP420 proton-taggers with the central ATLAS and CMS detectors.
3. The phenomenology of **low-x QCD** – parton saturation, non-linear QCD evolution, small-x PDFs, multi-parton scattering [21] – can be studied via the measurement of hard QCD cross-sections in the forward direction (e.g. jets, direct-γ in HF/FCal, CASTOR, ...) or in exclusive photoproduction processes (γ-p, γ-A interactions) tagged with forward protons (neutrons) in RPs (ZDCs).
4. Models of hadronic interactions of **ultra-high-energy** (UHE) **cosmic-rays** in the upper atmosphere [22] can be effectively tuned by measuring in CASTOR, TOTEM, LHCf and ZDCs, the energy ($dE/d\eta$) and particle ($dN/d\eta$) flows in p-p, p-A, and A-A collisions.
5. **Electroweak** interactions: Ultrarelativistic protons and ions generate fluxes of (equivalent) photons which can be used for a rich programme of photoproduction studies at TeV energies [23]. Photon-induced interactions, tagged with forward protons (neutrons) in the RPs (ZDCs), allow one e.g. to measure the beam luminosity (via the pure QED process $\gamma\,\gamma \to l^+\,l^-$) or to study (anomalous) gauge boson couplings (via γ-p, γ-A $\to$ p n W, or $\gamma\,\gamma \to ZZ, WW$).

1 Total and elastic cross sections

The measurement at the LHC of the total p-p cross-section and ρ-parameter (ratio of real to imaginary part of the forward elastic scattering amplitude) provides a valuable test of fundamental quantum mechanics relations [24] like the Froissart bound $\sigma_{\rm tot} < Const \ln^2 s$, the optical theorem $\sigma_{\rm tot} \sim Im f_{el}(t=0)$, and dispersion relations $Re f_{el}(t=0) \sim Im f_{el}(t=0)$.

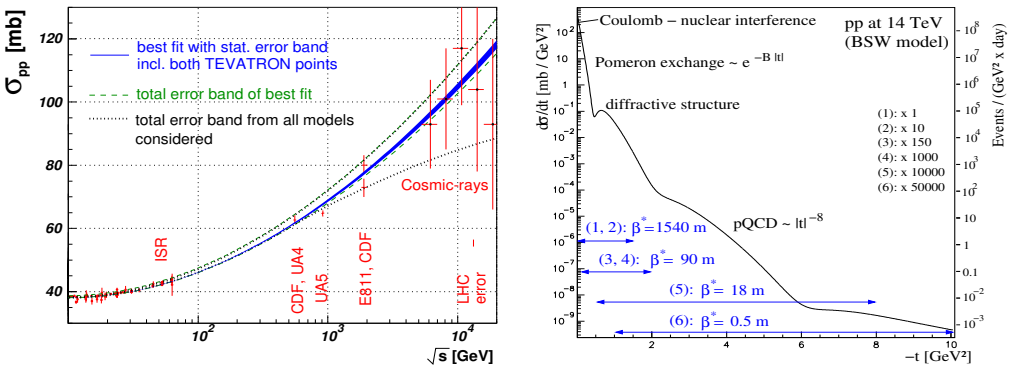

Figure 3: Left: COMPETE predictions [25] for σ_{tot} with statistical (blue solid) and total (dashed) errors (including the Tevatron ambiguity) compared to existing data. Right: Prediction for elastic p-p scattering at the LHC with various beam optics settings [26].

The main goal of TOTEM is to obtain a precise ($\sim 1\%$) measurement of the total and elastic p-p cross-section over a large range of (low) 4-momentum transfers $-t \approx p^2\theta^2$ (Fig. 3). The COMPETE [25] extrapolation values of $\sigma_{\rm tot} = 111.5$ mb and $\rho = 0.1361$ at LHC are uncertain

to within $^{+5\%}_{-8\%}$ due to a 2.6σ disagreement between the E710 and CDF measurements at Tevatron. In addition, TOTEM can also provide (via the optical theorem) the absolute p-p beam luminosity with reduced uncertainties using a low-β setting.

2 Diffractive physics

Diffractive physics covers the class of interactions that contain large rapidity gaps (LRGs, $\Delta\eta \gtrsim 4$) without hadronic production. Such event topologies imply colorless exchange, requiring two or more gluons in a color-singlet state (a *Pomeron*, $I\!P$). Depending on the number and relative separation of the LRGs, one further differentiates between single, double, or double-Pomeron-exchange (DPE) processes (Fig. 4).

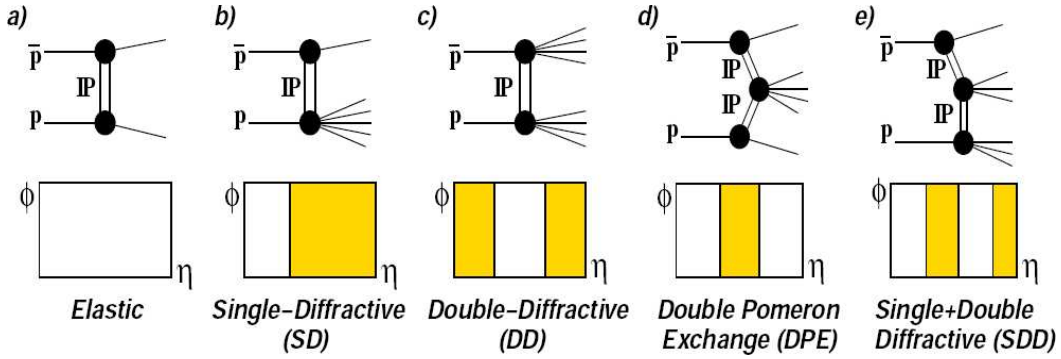

Figure 4: Event topologies in η vs azimuth ϕ for elastic and diffractive p-p interactions. Shaded (empty) areas represent particle production (rapidity gaps) regions [27].

On the one hand, soft diffraction processes are controlled by non-perturbative (Regge) dynamics and constitute a significant fraction ($\sim$20%) of the total inelastic p-p cross-section. Their characterization is thus important in order to determine the pile-up backgrounds at high luminosities. On the other, hard diffraction processes involve the production of a high-mass or large-p_T state (X = $Q\overline{Q}$, jets, W, Z ...) and are in principle calculable perturbatively by means of the factorisation theorem and diffractive (or generalised) Parton Distribution Functions, dPDFs (GPDs). The apparent breakdown of pQCD factorization in hard diffractive processes – supported by a reduced gap-survival probability in Tevatron p-$\overline{\text{p}}$ compared to e-p at HERA – has important phenomenological implications for LHC [17, 18]. Of particular interest are hard exclusive DPE processes where the centrally produced system can be a new heavy particle (see Fig. 5 and next Section).

3 Higgs (and new) physics

Central exclusive processes (CEP, Fig. 5 left) are defined as pp $\rightarrow$ p $\oplus$ X $\oplus$ p where X is a fully measured simple state such as $\chi_{c,b}$, jet-jet ($j\,j$), $l^+\,l^-$, $\gamma\,\gamma$, H, W^+W^-, ... and '$\oplus$' represents a large rap-gap ($\Delta\eta \gtrsim 4$). Central exclusive Higgs production has recently attracted lots of experimental and theoretical attention [16, 20]. First, the expected SM cross-sections are of order (3-10) fb (Fig. 5, right), but depending on $\tan\beta$ can be a factor of 10 (100) larger in minimal supersymmetric extensions of the SM (MSSM). Second, precise measurements of

the proton momenta ($dp/p \approx 10^{-4}$) allow one to measure the Higgs mass with $\sigma(m_H) \approx 2$ GeV, independent of the (central) decay mode (e.g. $b\bar{b}$, WW, ZZ). Third, spin selection rules suppress a large fraction of QCD production resulting in a very favourable 1:1 signal-to-background. Fourth, due to CEP $J^{PC} = 0^{++}$ selection rules, azimuthal correlations of the outgoing protons are likely to provide the only method at hand at the LHC to easily determine the Higgs quantum numbers. Given the currently preferred range of Higgs masses, $m_H < 200$ GeV, the optimal proton tagging acceptance is however beyond the current reach of TOTEM or ALFA RPs. The FP420 R&D collaboration proposes novel technologies (moving beam-pipe, fast 10-ps Čerenkov detectors, ...) as ATLAS and CMS upgrades for proton tagging at ±420 m.

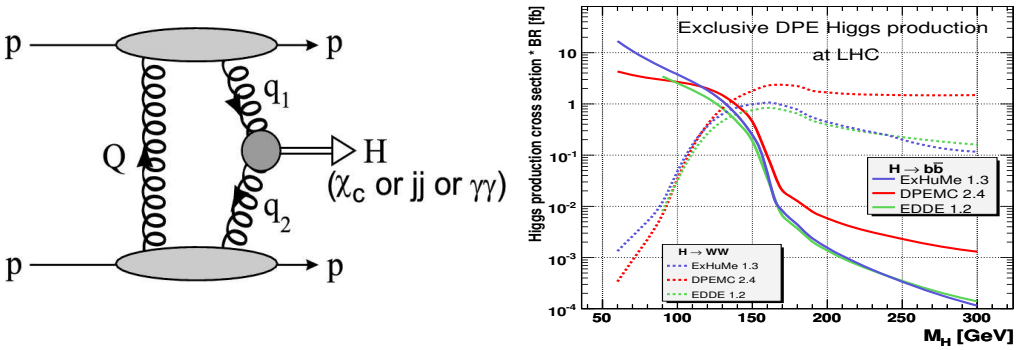

Figure 5: Left: Central exclusive Higgs production via two-gluon exchange. Right: Cross-sections for the SM Higgs ($b\bar{b}$, WW channels) from various perturbative calculations [3].

4 Low-x QCD physics

One of the main HERA observations is that the proton structure function is almost purely gluonic for values of the fractional momenta $x = p_{parton}/p_{proton} \lesssim 0.01$. Fig. 6 summarises our current knowledge of the gluon density $xG(x, Q^2)$ in the proton. In DIS, the main source of information so far on $xG(x, Q^2)$ is (indirectly) obtained from the slope of the F_2 scaling violations. Additional constraints can be obtained from F_2^{charm} [37], and diffractive photoproduction of heavy vector mesons ($J/\psi, \Upsilon$) [28]. The most direct access will come, however, from the longitudinal structure function F_L whose measurement has driven the last (lower energy) runs at HERA [29]. In hadron-hadron collisions, xG enters directly at LO in processes with prompt photons, jets, and heavy-quarks in the final state. Below $x \approx 10^{-4}$ (10^{-2}) the gluon density in the proton (nucleus) is however poorly constrained as can be seen from the right plot of Fig. 6 (Fig. 7). This is a small-x regime where one expects non-linear gluon-gluon fusion effects – not accounted for in the standard DGLAP/BFKL evolution equations – to become important and tame the rise of the parton densities [31] (Fig. 7 left). Such saturation effects are amplified in nuclear targets thanks to their increased transverse parton density.

Forward instrumentation provides an important lever arm for the measurement of the low-x structure and evolution of the parton densities. Indeed, in a $2 \to 2$ parton scattering

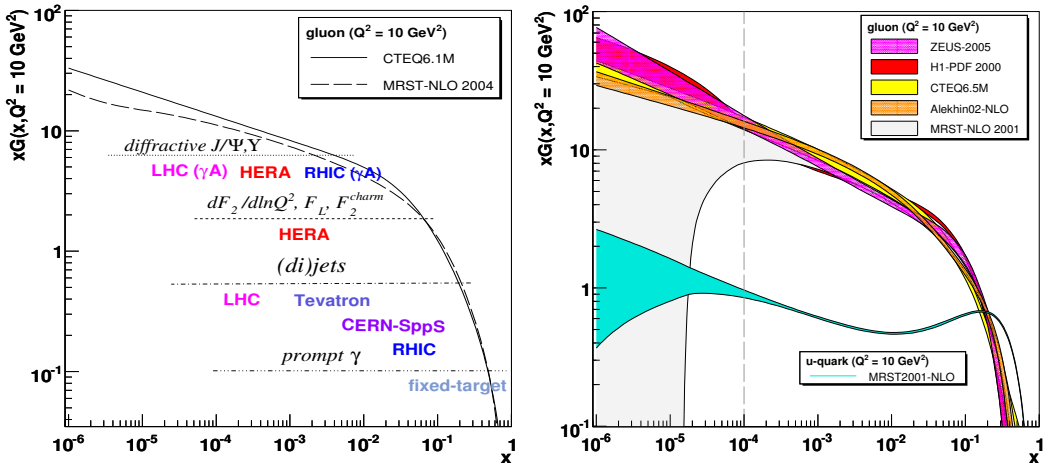

Figure 6: Left: Experimental measurements of the gluon PDF. Right: Comparison of various fits [32] of the proton $xG(x, Q^2{=}10\ \mathrm{GeV}^2)$ (the u quark PDF is also shown, for reference).

the *minimum* momentum fraction probed when a particle of momentum p_T is produced at pseudo-rapidity η is

$$x_{min} = \frac{x_T\, e^{-\eta}}{2 - x_T\, e^{\eta}} \quad \text{where} \quad x_T = 2p_T/\sqrt{s}\,, \tag{1}$$

i.e. x_{min} decreases by a factor of $\sim$10 every 2 units of rapidity. Four representative measurements of the low-x PDFs at the LHC are discussed next [21].

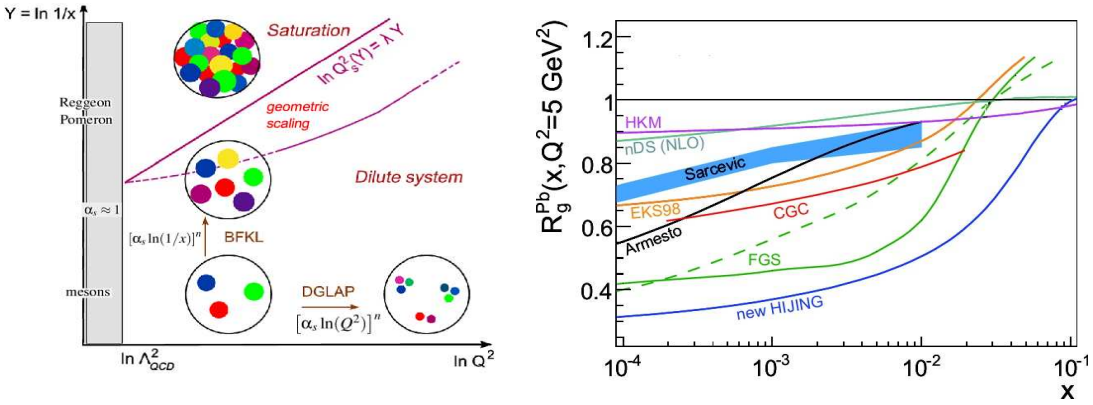

Figure 7: Left: QCD $\log(1/x)$-Q^2 plane with the different parton evolution regimes (DGLAP, BFKL, saturation). Right: Ratios of the Pb-over-proton gluon densities versus x at fixed $Q^2 = 5\ \mathrm{GeV}^2$ from various nuclear shadowing parametrizations [30].

• *Case study I: Forward (di)jets*

The measurement of (relatively soft) jets with $p_T \approx 20$ - 100 GeV/c in p-p at 14 TeV in the CASTOR forward calorimeter (5.2< $|\eta|$ <6.6) allows one to probe the PDFs at x values as low as $x \approx 10^{-6}$ (see Fig. 8 left, for jets in ATLAS FCal and CMS HF calorimeters). In addition to the single inclusive cross-sections, the production of events with two similar transverse-momentum jets emitted in each one of the forward/backward directions, the so-called "Müller-Navelet jets" (Fig. 8 right), is a particularly sensitive measure of BFKL [33] as well as non-linear [34] parton evolutions. The large rapidity interval between the jets (e.g. $\Delta\eta \approx 10$ in the extremes of HF+ and HF-) enhances large logarithms of the type $\Delta\eta \sim log(s/k_1k_2)$ which can be appropriately resummed using the BFKL equation. The phenomenological consequences expected in the BFKL regime are enhanced Müller-Navelet dijet rates and wider azimuthal decorrelations for increasing $\Delta\eta$ separations [35, 36]. Preliminary CMS analyses [3] indicate that such studies are well feasible measuring jets in each one of the hadronic forward (HF) calorimeters.

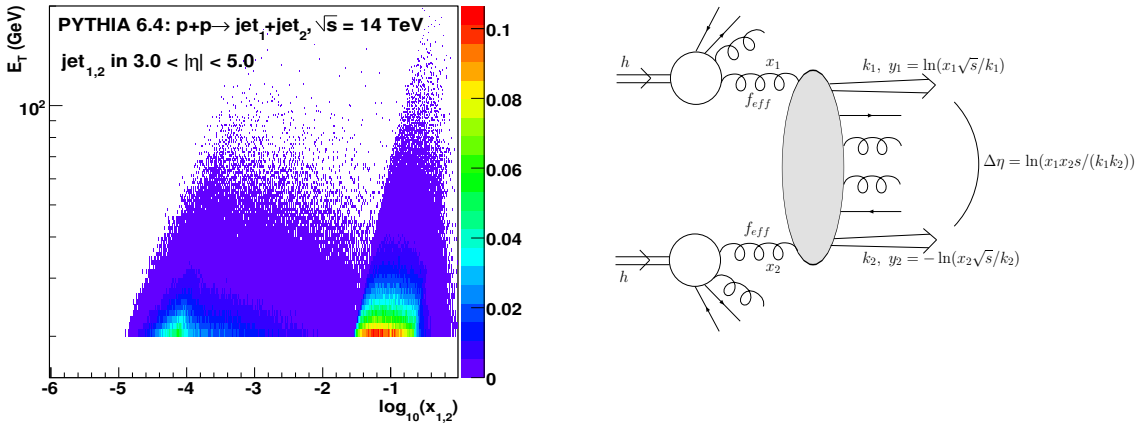

Figure 8: Left: Parton $x_{1,2}$ distributions probed in p-p collisions at $\sqrt{s} = 14$ TeV with single jet production within ATLAS/CMS forward calorimeters acceptances. Right: Müller-Navelet dijet production diagram in p-p collisions.

• *Case study II: Forward heavy-quarks*

The possibility of ALICE and LHCb (Fig. 9, left) to reconstruct heavy D and B mesons as well as quarkonia in a large forward rapidity range can also put stringent constraints on the gluon structure and evolution at low-x. Studies of small-x effects on heavy flavour production based on collinear and k_T factorization, including non-linear terms in the parton evolution, lead to varying predictions for the measured c and b cross-sections at the LHC [37]. The hadroproduction of J/ψ proceeds mainly via gluon-gluon fusion and, having a mass around the saturation scale $Q_s^{\rm LHC} \approx 3$ GeV, is also a sensitive probe of possible gluon saturation phenomena. Figure 9 right, shows the gluon x range probed in p-p collisions producing a J/ψ inside the ALICE muon arm acceptance ($2.5 \lesssim \eta \lesssim 4$). The observed differences in

the underlying PDF fits translate into variations as large as a factors of ∼2 in the finally measured cross sections [38].

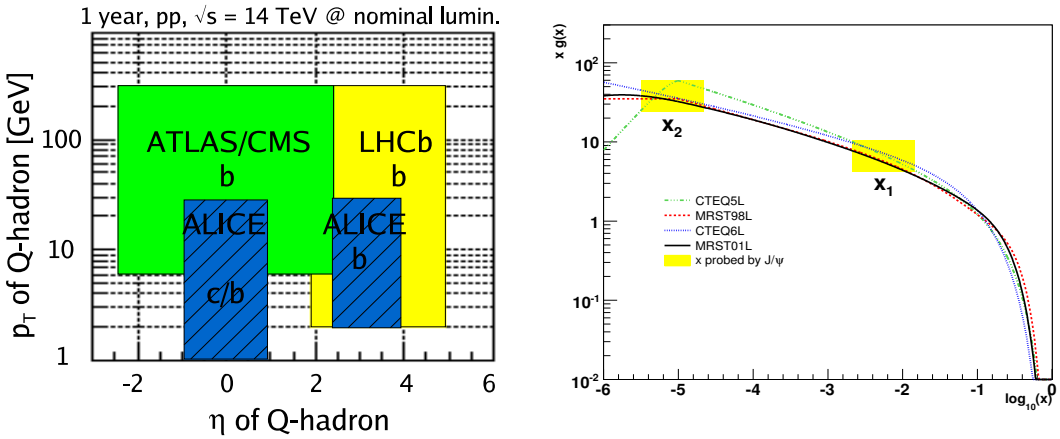

Figure 9: Left: Acceptances in (η, p_T) for open charm and bottom at the LHC [37]. Right: Sensitivity of the forward J/ψ measurement in ALICE to the gluon PDF [38].

• *Case study III: $Q\overline{Q}$ exclusive photoproduction*

Ultra-peripheral interactions (UPCs) of high-energy heavy ions generate strong electromagnetic fields which can be used to constrain the low-x behaviour of the nuclear gluon density via exclusive photoproduction of quarkonia, dijets and other hard processes [39]. Lead beams at 2.75 TeV have Lorentz factors $\gamma = 2930$ leading to maximum (equivalent) photon energies $\omega_{max} \approx \gamma/R \sim 100$ GeV, and corresponding maximum c.m. energies: $W^{max}_{\gamma\gamma} \approx 160$ GeV and $W^{max}_{\gamma\text{-A}} \approx 1$ TeV, i.e. 3–4 times higher than equivalent photoproduction studies at HERA. The x values probed in γ A→Q$\overline{\text{Q}}$ A processes (Fig. 10, left) can be as low as $x \sim 10^{-5}$ [39]. The ALICE, ATLAS and CMS experiments can measure the $J/\psi, \Upsilon \to e^+e^-, \mu^+\mu^-$ produced in electromagnetic Pb-Pb collisions tagged with neutrons detected in the ZDCs, as done at RHIC [40]. Full simulation+reconstruction analyses [41] indicate that CMS can measure a total yield of ∼500 within $|\eta| < 2.5$ for 0.5 nb^{-1} nominal Pb-Pb integrated luminosity (Fig. 10). Which such statistics, studies of the p_T and η distributions of the Υ can be carried out, helping to constrain the low-x gluon density in the Pb nucleus.

• *Case study IV: Forward Drell-Yan pairs*

High-mass Drell-Yan pair production at the very forward rapidities covered by LHCb and by the CASTOR and TOTEM T2 detectors can probe the parton densities down to $x \sim 10^{-6}$ at much higher virtualities M^2 than those accessible in other measurements discussed here. A study is currently underway in CMS [3] to combine the CASTOR electromagnetic energy measurement together with the good position resolution of T2 for charged tracks, to trigger on and reconstruct e^+e^- pairs in p-p collisions at 14 TeV, and scrutinise xg in the M^2 and x plane.

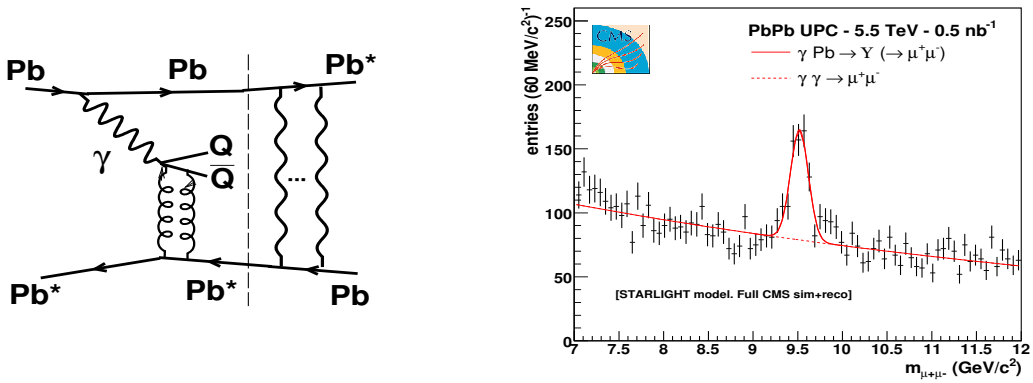

Figure 10: Left: Exclusive quarkonia photoproduction in UPCs. Right: Expected dimuon invariant mass from $\gamma\,\mathrm{Pb}\!\rightarrow \Upsilon\,\mathrm{Pb}^{\star}$ on top of $\gamma\gamma \rightarrow \mu^+\mu^-$ continuum in UPC Pb-Pb at 5.5 TeV [41].

5 Cosmic-rays physics connection

The origin of cosmic rays (CRs) with energies above 10^{15} eV is unclear, as it is the identity of the primaries. Due to their low fluxes (less than 1 particle per m^2 and year) only indirect measurements exist which use the atmosphere as a "calorimeter" (Fig. 11, left). The energy and mass of UHE cosmic rays are then obtained with the help of Monte Carlo codes which describe the shower development (dominated by forward and soft QCD interactions) in the upper atmosphere [22]. The existing MC models (Fig. 11, right) predict energy and multiplicity flows differing by factors as large as three, with significant inconsistencies in the forward region ($|\eta| > 5$). Forward measurements at LHC energies ($E_{lab} \approx 10^{17}$ eV) in p-p, p-A and A-A collisions[b] will provide strong constraints to calibrate and tune these models and make more reliable predictions for the CR energy and composition at the highest energies observed. Forward measurements at the LHC, especially in calorimeters with longitudinal segmentation like CASTOR, will in addition help to interpret exotic CR topologies like the so-called "Centauro" events [8].

6 Electroweak physics

Interesting electroweak processes in photon-photon and photon-proton,-nucleus interactions, tagged with forward instrumentation, will be also accessible for the first time at TeV energies at the LHC. Two-photon dilepton production, $\mathrm{pp} \rightarrow \mathrm{p}l^+l^-\mathrm{p}$ (Fig. 12, left) will be an excellent luminosity calibration process, with a very well known QED cross-section [42]. Experimentally, such a process can be tagged with forward protons and has a clear signature in the exclusive back-to-back dielectrons (dimuons) measured e.g. in CASTOR/T2 (in the central muon chambers). The p-p cross section calculated using LPAIR for events where both muons have $p_T > 3$ GeV/c and can, therefore, reach the CMS muon chambers is about 50 pb. About 300 events per 100 pb^{-1} are thus expected in CMS after muon trigger cuts [3]. The situation is much more favourable in the case of Pb-Pb collisions since the

[b]Note that CRs interactions in the atmosphere are mostly p,α,Fe-Air collisions.

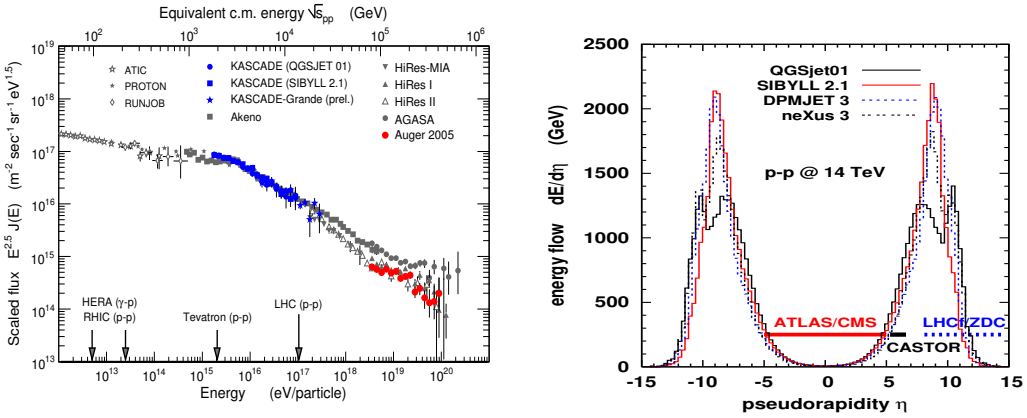

Figure 11: Left: The cosmic-ray energy distribution [22]. Right: Pseudo-rapidity energy distribution for p-p at the LHC predicted by four commonly used MC models in UHE cosmic rays physics (the acceptance of LHCf and ZDCs refers to neutral particles) [3].

dilepton continuum is much larger than in p-p (Z^4 enhancement factor, see Fig. 10 right) and the forward neutron tagging much more efficient than the forward proton one.

The couplings of gauge bosons among themselves belong to one of the least tested sectors of the electroweak theory. A process well-suited to testing the ($WW\gamma$) gauge boson self-interaction is the photoproduction of single W bosons from a nucleon (Fig. 12, right) in ultra-peripheral p-p [43], p-A and A-A [23] collisions. A large cross-section of about 1 pb is expected for large photon-proton c.m. energies, $W_{\gamma p} > 1$ TeV. In addition, the two-photon W^+W^- exclusive production probes *quartic* gauge-boson-couplings. The process has a total cross-section of more than 100 fb, and a very clear signature. Its cross-section is still about 10 fb for $W_{\gamma p} > 1$ TeV showing sensitivity to physics beyond the SM [43].

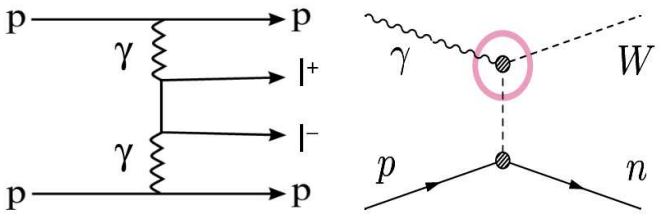

Figure 12: Photoproduction diagrams in electromagnetic proton-proton interactions: two-photon dilepton production (left), and single-W photoproduction (right). In both processes, the forward-going protons (neutrons) can be detected in RPs (ZDCs).

Acknowledgments

I would like to thank the organisers of DIS'07 – and, in particular, the conveners of the *Future of DIS* Section – for their kind invitation to such a stimulating conference. Special thanks due to Albert de Roeck, Michele Arneodo and Monika Grothe for valuable discussions. Work supported by the 6th EU Framework Programme contract MEIF-CT-2005-025073.

References

[1] Slides: `http://indico.cern.ch/contributionDisplay.py?contribId=248&sessionId=10&confId=9499`
[2] S. Roesler, R. Engel and J. Ranft, arXiv:hep-ph/0012252 (2000).
[3] M. Albrow *et al.* [CMS/TOTEM Collabs.], Prospects for diffractive and forward physics at the LHC, CERN-LHCC-2006-039 (2006).
[4] ATLAS: Detector and Physics performance TDR, CERN/LHCC-99-14 (1999).
[5] S. Ask [ATLAS Collaboration], these Proceedings, arXiv:0706.0644 [hep-ex] (2007).
[6] CMS Physics TDR, Volume I: Detector Performance and Software, CERN/LHCC-2006-001 (2006).
[7] K. Borras [CMS Collaboration], these Proceedings
[8] A. L. S. Angelis *et al.*, Nuovo Cim. **24C** 755 (2001).
[9] O. A. Grachov *et al.*, AIP Conf. Proc. **867** (2006).
[10] F. Carminati *et al.* [ALICE Collaboration], J. Phys. G **30**, 1517 (2004).
[11] LHCb, Reoptimised Detector Design and Performance TDR, CERN/LHCC 2003-030, (2003).
[12] ALICE TDR: Zero degree calorimeter (ZDC), CERN-LHCC-99-05 (1999).
[13] V. Berardi *et al.* [TOTEM Collaboration], CERN/LHCC-2004-002 (2004).
[14] Technical Design Report of the LHCf experiment, CERN-LHCC-2006-004 (2006).
[15] M. G. Albrow *et al.*, FP420 R&D proposal, CERN/LHCC-2005-025 (2005).
[16] A. Pilkington [FP420 Collaboration], these Proceedings
[17] M. Arneodo and M. Diehl, arXiv:hep-ph/0511047 (2005).
[18] K. Goulianos, arXiv:0707.1055 [hep-ex] (2007).
[19] A. De Roeck *et al.*, Eur. Phys. J. C **25** 391 (2002).
[20] V. A. Khoze, A. D. Martin and M. G. Ryskin, arXiv:0705.2314 [hep-ph], and refs. therein (2007).
[21] D. d'Enterria, Eur. Phys. J. A **31**, 816 (2007).
[22] R. Engel, Nucl. Phys. Proc. Suppl. **151** 437 (2006).
[23] A. Baltz *et al.*, arXiv:hep-ph/0702212 (2007).
[24] C. Bourrely, N. N. Khuri, A. Martin, J. Soffer and T. T. Wu, arXiv:hep-ph/0511135 (2005).
[25] J. R. Cudell *et al.* [COMPETE Collaboration], Phys. Rev. Lett. **89** 201801 (2002).
[26] G. Anelli *et al.* [TOTEM Collaboration], arXiv:hep-ex/0602025 (2006).
[27] M. E. Convery [CDF Collaboration], Acta Phys. Polon. B **36** 665 (2005).
[28] T. Teubner, these Proceedings.
[29] M. Klein, these Proceedings.
[30] N. Armesto, J. Phys. **G32**, R367 (2006)
[31] R. Venugopalan, these Proceedings.
[32] See `http://durpdg.dur.ac.uk/hepdata/pdf3.html`
[33] A. H. Müller and H. Navelet, Nucl. Phys. B **282**, 727 (1987)
[34] C. Marquet and C. Royon, Nucl. Phys. B **739**, 131 (2006)
[35] C. Royon, these Proceedings, arXiv:0706.1799 [hep-ph] (2007).
[36] A. S. Vera and F. Schwennsen, these Proceedings, arXiv:0707.0256 [hep-ph] (2007).
[37] J. Baines *et al.*, Proceeds. HERA-LHC Workshop, hep-ph/0601164 (2006).
[38] D. Stocco [ALICE Collaboration], High energy QCD ECT* Workshop, Trento (2007).
[39] K. Hencken *et al.*, J. Phys. **G** to appear, arXiv:0706.3356 (2007).
[40] D. d'Enterria, Proceeds. Quark Matter'05, nucl-ex/0601001 (2006).

[41] D. d'Enterria (ed.) *et al.*, CMS Physics TDR: High Density QCD with Heavy-Ions, J. Phys. **G** to appear.
[42] D. Bocian and K. Piotrzkowski, Acta Phys. Polon. B **35** 2417 (2004).
[43] S. Ovyn *et al.*, Proceeds. Photon'07 Int. Conf., (2007).

Low-x Physics at a Future Electron-Ion Collider (EIC) Facility

Bernd Surrow

Massachusetts Institute of Technology, Department of Physics, Laboratory for Nuclear Science
77 Massachusetts Avenue, Cambridge, MA 02139

The proposed polarized electron-ion collider (EIC) will allow for precision exploration of various novel aspects of QCD including low-x phenomena, the spin structure of the proton, and gluon saturation in heavy nuclei. As this project gains momentum, it is increasingly important for the QCD community to understand quantitatively the kinematic reach and expected sensitivities for various measurements. We briefly summarize key accelerator design parameters and then focus on expected measurement sensitivities, thus exposing how the EIC will allow an extension of the successful HERA program into exciting new regimes.

1 Introduction

QCD is a spectacularly successful theory, yet it remains an active field of research in particle physics. While it has withstood over several decades of tests, we have yet to understand fully the mechanisms by which complex and rich phenomena emerge from a theory based solely on symmetry and local gauge invariance [2]. This quest is being pursued on many fronts: hadron structure, hadron spectroscopy, high temperature phenomena and high parton density systems. There is little doubt that our current understanding of QCD, in particular the role of gluons in QCD dynamics, has been greatly advanced by using electron-proton collisions at the HERA collider, which was the first facility to probe with high luminosity deep into the regime where gluons play a dominant role in hadron structure. In the following, we discuss how a high luminosity Electron-Ion Collider (EIC) will enable similar advances in the study of strong color fields, in particular many body gluon states probed at the saturation scale. The crucial element in these studies will be the use of heavy nuclei that, when probed at small Bjorken x, amplify such novel gluon states.

2 Opportunities in low-x physics at a future EIC facility

From deep inelastic scattering (DIS) we know that gluons carry half of the momentum of the proton, and from HERA we know that gluons dominate for $x < 0.01$ [3]. However, when probed at low-x, it is predicted that the gluon distribution within a proton will saturate. There are many quantitative arguments for this, but it is rather intuitive that at sufficiently high gluon density 2→1 gluon fusion (non-linear dynamics) will begin to dominate over 1→2 gluon splitting (linear dynamics). This transition occurs at a scale commonly referred to as the saturation scale (Q_s). Geometrical considerations [4] show that, in nuclei, $Q_s \propto A^{1/3}x^{-\delta}$, where $\delta \sim 1/3$ [5]. Thus, heavy nuclei can be used to amplify the scale at which gluon saturation sets in. Figure 1 shows the saturation scale in the Q^2 versus x plane for ions ranging from protons to Au [3]. Additionally, the colored diagonal lines show the kinematic limits of the EIC for various beam energies. The shaded band illustrates the accessible saturation region for 20 GeV electrons colliding with 100 GeV Au nuclei. The saturation

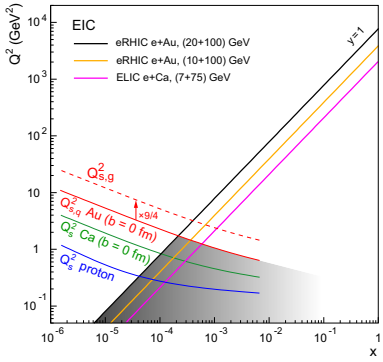

Figure 1: The kinematic plane of DIS variables x and Q^2. The straight diagonal lines represent the kinematic boundaries of the EIC under various beam configurations. Regions below the lines are accessible. The curved/dashed lines indicate the saturation scale for various ions. Color online.

scale for gluons in Au can be accessed at a factor of 10 larger x and Q^2 than Q_s for gluons in a proton. This has two significant impacts. First, by substituting heavy ions for protons, one can access the saturation regime at lower beam energies. Second, $Q^2_{s,g}(Au) > Q^2 > \Lambda^2_{QCD}$, thereby enabling use of perturbative methods for calculation. The saturation regime can be reached with reasonably modest beam energies, and it can be explored with the use of perturbative calculations.

In DIS the differential cross section $d^2\sigma/dx\ dQ^2$ can be decomposed in terms of two structure functions ($F_2(x,Q^2)$ and $F_L(x,Q^2)$), where F_2 is directly sensitive to (anti)quark distributions, and F_L is directly proportional to the gluon momentum distribution. These structure functions provide a direct means to quantitatively study saturation phenomena and we discuss them in more detail below. In the following we show the measurement prospects for various EIC configurations with a maximum center-of-mass energy of $\sqrt{s} = 14 \sim 140$ GeV/n and a maximum luminosity $L = 10^{33} \sim 10^{35}$ cm^{-2}s^{-1}, a factor of 100 higher than HERA. As the world's first electron heavy ion collider, the EIC would enable the high precision exploration of F_2 and F_L of heavy Nuclei in the saturation regime, truly *terra incognita*. As we will show, the luminosity, energy and collider kinematics will be used to differentiate competing models of low-x QCD phenomena.

One of the first measurements at the EIC will be $F_2(x,Q^2)$ for both heavy (Au) and light (d) ions. The ratio, shown versus Q^2 for four x bins, is shown in Figure 2 [3]. The points represent the anticipated statistical precision achievable with an integrated luminosity of 4/A fb^{-1}. The colored lines are predictions from competing models [3]. F_2 is directly sensitive to quark distributions, and is sensitive to gluons via scaling violations. nDS, EKS and FGS are pQCD models with differing treatment of parton shadowing, and they are compared to predictions from the Color Glass Condensate (CGC) model. Within the expected precision of the measurements, differentiation between the different models is clearly possible in the region $10^{-4} < x < 10^{-2}$.

With the ability to accelerate both light and heavy ions over a wide range of energies, the EIC will be able to make significant contributions to the understanding of the gluon distribution in the proton. At low x, $F_L(x,Q^2) \propto \alpha_s\ x\ G(x,Q^2)$, where $G(x,Q^2)$ is the

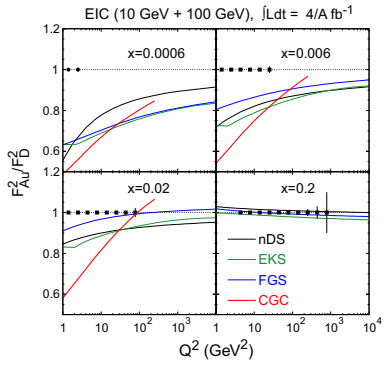

Figure 2: The ratio of $F_2(Q^2)$ in Au to that in d nuclei, for four bins in x. The symbols represent the anticipated statistical precision achievable. The curves represent models with differing treatment of low-x phenomena. Color online.

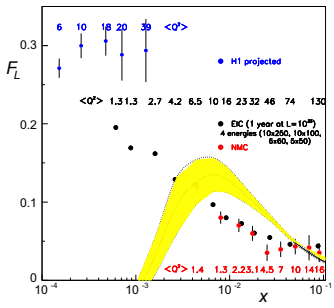

Figure 3: $F_L(x)$ for protons from fixed target (red), projected H1 (blue) and projected EIC (black). Color online.

gluon distribution. Extraction of F_L requires running at multiple beam energies, a task that highlights the flexibility of the EIC. Figure 3 shows $F_L(x)$ for a proton. The red points are from existing NMC fixed target data, and the blue H1 points show the expected precision (statistical and systematic uncertainties) achievable from the recent HERA energy scan [3]. The black points show the achievable precision from one year of running the EIC at four different energies (statistical uncertainties only) [3]. The EIC measurements will clearly compliment the HERA results, as well as bridge the region between HERA and fixed target results, contributing to a direct measurement of the gluon distribution for $10^{-4} < x < 10^{-1}$.

Finally, Figure 4 shows the ratio of gluon distributions in Pb to that in d ($R_g^{Pb} = F_L^{Pb}/F_L^d \sim G^{Pb}/G^d$) [3]. Current data on the gluon distribution at low-x in heavy nuclei is sparse. In turn, constraints on theoretical models are weak, as shown by the vast range of different theoretical predictions. The gluon distribution is critical for accurate calculations of cross sections at both RHIC and the LHC. With its high luminosity, the EIC can make significant contributions to the understanding of the gluon distribution in heavy nuclei over

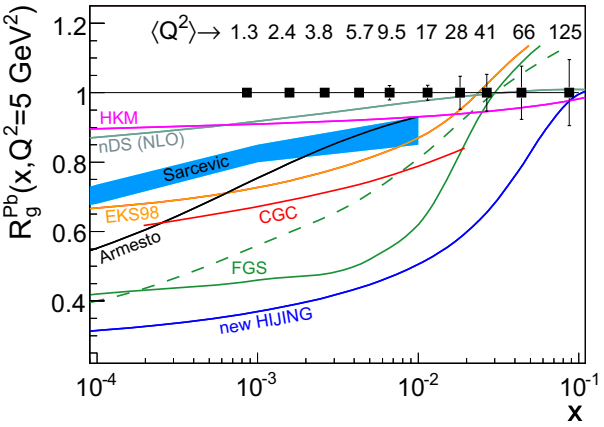

Figure 4: The ratio of F_L in Pb to that in d. The black symbols represent anticipated statistical uncertainty from 10/A fb^{-1} of EIC data, compared to the large range of model predictions over this currently unexplored kinematic range. Color online.

the relevant x range.

3 Summary

In conclusion, as the world's first high energy electron (heavy) ion collider, and with a luminosity approximately one hundred times that of HERA, the EIC will allow precision exploration of strong color fields. The use of heavy nuclei will amplify the scale at which saturation phenomena are predicted, placing it well within the accessibility of the EIC. There are many topics we have neglected to discuss, in particular diffraction, spin decomposition of the proton, and the study of partonic energy loss in cold nuclear matter. The physics program of the EIC is rich, diverse, and well targeted toward a unified understanding of strongly interacting matter. The project is gaining momentum on an international scale and will provide a continuation of the successful HERA program into exciting new regimes of QCD.

References

[1] Slides:
`http://indico.cern.ch/contributionDisplay.py?contribId=263&sessionId=10&confId=9499`

[2] F. Wilczek. *Nucl. Phys. Proc. Suppl.*, 119:3, 2003.

[3] EIC Collaboration. A high luminosity, high energy electron-ion collider, white paper prepared for the nuclear science advisory committee as input to the long-range planning 2007.

[4] K. Golec-Biernat and M. Wustoff. *Phys. Rev.*, D59:014017, 1999.

[5] C. A. Salgado N. Armesto and U. A. Wiedemann. *Phys. Rev.*, 94:0220002, 2005.

Low x Physics at the LHeC

Paul Newman

School of Physics & Astronomy, University of Birmingham, B15 2TT, UK

A first sketch is developed of the wealth of opportunity for exploring low x physics afforded by the proposed LHeC electron-nucleon (or nucleus) collider.

1 Introduction

This contribution [1] is concerned with the LHeC [2], a proposed future deep-inelastic scattering (DIS) facility at CERN, where protons or heavy ions from an existing 7 TeV LHC storage ring collide with electrons from a newly built machine (nominally 70 GeV) in the same tunnel, simultaneously with proton-proton or heavy ion collisions at the existing LHC experiments. The expected luminosity of 10^{33} cm^{-2}s^{-1} is two orders of magnitude larger than has been achieved at HERA and the centre of mass energy of 1.4 TeV is five times larger than that at HERA. Here, a first exploration is made of the rich physics potential resulting from the extension by typically a factor of 30 towards lower x at the LHeC compared with HERA (figure 1). Complementary contributions on sensitivity to parton densities and to new physics are covered in [3] and [4], respectively.

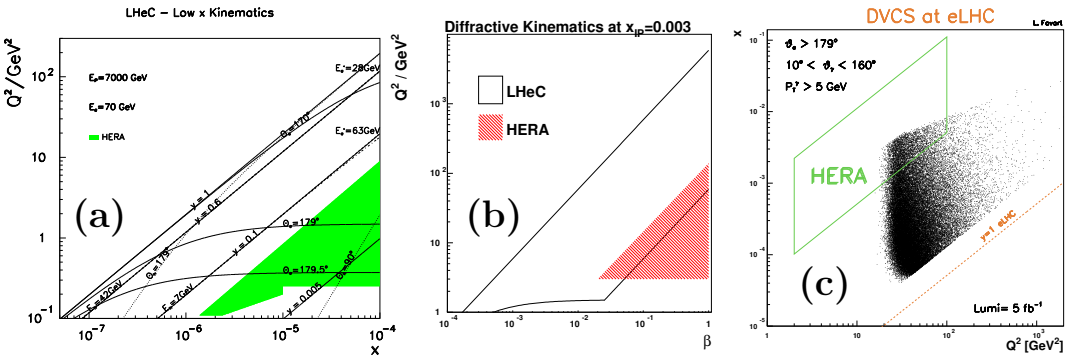

Figure 1: (a) The low x corner of the $x - Q^2$ kinematic plane at HERA and the LHeC. (b) The $\beta - Q^2$ kinematic plane for diffractive DIS at HERA and the LHeC for an example $x_{I\!P} = 0.003$. (c) Simulated DVCS events at the LHeC, illustrated in the $x - Q^2$ kinematic plane and compared with the coverage of HERA [5].

The most enduring legacy of HERA is likely to be its pioneering contribution to low x physics. Most notable among the many discoveries are the strong rise of the proton quark ($\sim F_2$) and gluon ($\sim \partial F_2/\partial \ln Q^2$) densities with decreasing x. The phenomenological consequences of the resulting high density, low coupling limit of QCD have now been explored in considerable detail. New processes such as diffractive DIS ($ep \to eXp$) and Deeply Virtual Compton Scattering (DVCS, $ep \to e\gamma p$) have been investigated for the first time. Yet many things remain rather unclear, in particular how and at which x values the increasing gluon density is tamed, as required to satisfy unitarity.

A significant problem in understanding low x physics at HERA is the kinematic correlation between the low x and low Q^2 regions (figure 1a), such that any novel low x parton

dynamics are usually entangled with effects due to the low Q^2 breakdown of perturbative QCD and the transition to the region in which quarks and gluons cease to be appropriate degrees of freedom. In order to access the very low x region where non-linear effects may be present [6], Q^2 values well below typical hadronic mass scales are therefore required at HERA, precluding a clear partonic interpretation. In contrast, it is likely to be possible[a] to observe non-linear evolution effects at the LHeC at Q^2 values for which an unambiguous partonic interpretation can be made (see section 3).

2 Low x Detector Considerations

The lower limit in accessible Q^2, and hence in x, is determined principally by the LHeC detector coverage at low electron scattering angles. The proposed beam focusing magnets [2], used to maximise the luminosity for searches and other high momentum transfer studies [4], would prevent instrumentation within 10° of the beam-pipe, resulting in little acceptance for $Q^2 < 100$ GeV^2 or $x < 5.10^{-5}$. Without these focusing magnets[b] the acceptance could extend within 1° of the beam-pipe, giving access down to $x = 5.10^{-7}$ at $Q^2 = 1$ GeV^2, whilst still collecting 1 fb^{-1} of data per year.

With the LHeC beam energies, the scattered quark direction generally lies close to central rapidity for the newly accessed lowest x range. However, the LHeC hadronic final state is boosted in the forward (outgoing proton beam) direction more strongly than is the case at HERA for the same x values. Placing detector components within 1° of the beam pipe is thus also beneficial in the forward direction. Accessing the hadronic final state over a wide rapidity range allows the inclusion of hadronic variables in the kinematic reconstruction and will be important for studies of the initial state parton cascade through forward jets, to distinguish between different parton emission models [8]. The large forward boost also has implications for studies of diffraction. A diffractive event with fractional proton longitudinal momentum loss $x_{I\!P} = 0.01$ typically deposits its most forward hadronic final state particles at pseudorapidities $\eta_{\max} \sim 5$ at the LHeC, compared with $\eta_{\max} \sim 3$ at HERA. Very forward instrumentation will therefore be required if large rapidity gap selections are to be made. Forward proton and neutron detectors should also be an integral part of any detector design.

3 Example Low x Case Studies

• **Inclusive Cross Sections and Parton Saturation:** It is expected that parton saturation effects could be conclusively established at the LHeC through the observation of deviations from expectations for one or more observable in the framework of perturbative QCD. However, in such studies at HERA, models based on colour dipole scattering [6, 9, 10] have been used in order to access the necessary very low Q^2 values.

In one example dipole study of HERA data [9], the inclusive structure function $F_2(x, Q^2)$ is subjected to fits in which the dipole cross section either does not exhibit saturation properties, or saturates as expected in two rather different models [9, 10]. All three dipole fits are able to describe the HERA data adequately in the perturbative region $Q^2 \geq 2$ GeV^2,

[a] Quantitatively, in the language of geometric scaling [7], the observed change in behaviour of the scaling curve for HERA data around $\tau = Q^2 R_0^2(x) = 1$, R_0 being the 'saturation radius' [6], is often considered as evidence for saturation. At HERA, all data with $\tau < 1$ correspond to $Q^2 \ll 1$ GeV^2. In contrast, at the LHeC, $\tau \simeq 0.15$ (0.4) is reached for $Q^2 = 1$ (2) GeV^2.

[b] Ideally the LHeC design will allow switches between configurations with and without these magnets.

whereas a clear preference for the models containing saturation effects becomes evident when data from the range $0.045 < Q^2 < 1$ GeV^2 are added [9]. Due to the non-perturbative nature of this kinematic region, there is no clear interpretation in terms of parton recombination effects. Similar conclusions are drawn when the same dipole cross sections are applied to various final state observables [11].

Figure 2 shows an extrapolation of the three dipole models [9] into the LHeC kinematic range at an example $Q^2 = 10$ GeV^2. The extrapolations are compared with a simulated LHeC measurement with 1 fb^{-1}, where statistical errors are negligible and reasonable estimates of systematic errors are at the $1-3\%$ level [3]. The LHeC data clearly distinguish between the extrapolated fits to HERA data without resorting to a region where perturbative methods are inapplicable. It remains to be shown whether this continues to be the case when the LHeC data are also included in the fits.

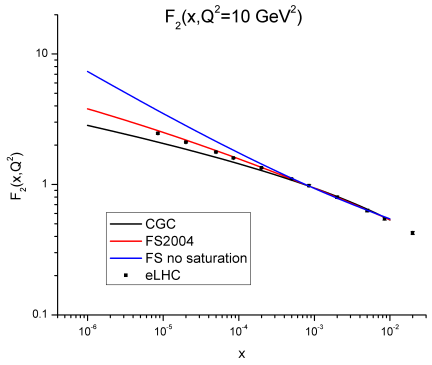

Figure 2: Example results from fits to HERA F_2 data with $10^{-4} \lesssim x < 10^{-2}$ using three different dipole models. The curves are extrapolated to lower x values [12] and compared with simulated LHeC data.

• **Diffractive DIS:** Statistical uncertainties should be insignificant for the measurement of a diffractive DIS cross section with 1 fb^{-1} at the LHeC. Systematic errors are estimated to be in the region of $5-10\%$, depending strongly on the design of the forward region of the detector. At an example $Q^2 = 10$ GeV^2, $x_{I\!P}$ values below 10^{-5} are accessible, allowing a very clean separation of the diffractive exchange from sub-leading contributions. The $\beta = x/x_{I\!P}$ and Q^2 kinematic plane at HERA and the LHeC is illustrated in figure 1b, for an example $x_{I\!P} = 0.003$. Accessing higher Q^2 at fixed β and $x_{I\!P}$ will test the factorisation properties of diffraction [13] in detail and will allow more precise constraints on diffractive parton distribution functions (DPDFs), including sensitivity to their flavour decomposition through W and Z exchange contributions. The low β region of the DPDFs will be investigated for the first time.

The tests of diffractive factorisation carried out at HERA have largely involved applying DPDFs to the prediction of diffractive jet or charm cross sections, which are sensitive to the gluon density through the boson gluon fusion process $\gamma^* g \to q\bar{q}$. This procedure is kinematically restricted to $p_\perp < M_X/2 \lesssim 15$ GeV, such that the large scale uncertainties in theoretical predictions now limit the precision of comparisons. The more favourable kinematics at the LHeC allow M_X values up to several hundred GeV to be accessed for reasonably small values of $x_{I\!P}$. This will improve the precision with which jets and charm can be used for factorisation tests and will also open up completely new topics such as diffractive beauty, W and Z production, or even the exclusive production of new 1^{--} states.

• **Deeply Virtual Compton Scattering** As at HERA, measurements of DVCS could be made at the LHeC through the inclusive selection of $ep \to ep\gamma$ events and the statistical

subtraction of the Bethe-Heitler background. A first simulation [5] assuming that final state photons with $p_\perp > 5$ GeV can be efficiently selected, leads to the simulated data shown in figure 1c. With 10 fb^{-1}, a measurement at $Q^2 = 30$ GeV^2 could be performed in seven bins of W between 150 GeV and 750 GeV, with $1 - 4\%$ statistical precision. The LHeC data are clearly complementary in coverage to their HERA counterparts and will thus give fresh information on Generalised Parton Densities.

4 Concluding Remarks

The natural next step in the further pursuit of low x physics with unpolarised hadrons is an extension of DIS studies to higher energy, equivalently, lower x. The LHeC provides a credible proposal for how this might be achieved in the framework of the LHC, whose unprecedented energy and luminosity are likely to make it the dominant high energy facility for the foreseeable future.

The studies presented here involve only a small fraction of the low x physics topics which could be addressed with the LHeC. For example, no studies have yet been performed of jet, charm, beauty, prompt photon or vectotr meson cross sections, F_L measurements or photon structure sensitivity. The possibilities with the amplified low x parton densities available when the proton beam is replaced by lead ions also remains largely unexplored to date, but must surely have a major impact on nuclear parton density, nuclear shadowing and low x saturation physics. There is thus vast scope for further study in order to fully evaluate the physics possibilities of an LHeC.

Acknowledgements

Thanks to E. Avsar, J. Dainton, L. Favart, J. Forshaw, M. Klein, L. Lonnblad, A. Mehta, E. Perez, G. Shaw and F. Willeke for their highly valued contributions to this presentation.

References

[1] Slides: `http://indico.cern.ch/contributionDisplay.py?contribId=268&sessionId=10&confId=9499`
[2] J. Dainton et al., JINST 1 (2006) P10001; J. Dainton, these proceedings.
[3] M. Klein, these proceedings.
[4] E. Perez, these proceedings.
[5] L. Favart, private communication.
[6] K. Golec-Biernat, M. Wüsthoff, Phys. Rev. D59 (1999) 014017.
[7] A. Stasto, K. Golec-Biernat, J. Kwiecinski, Phys.Rev.Lett. 86 (2001) 596.
[8] *'The THERA book: ep scattering at* $\sqrt{s} = 1$ TeV', DESY 01-123F, eds. U. Katz et al.
[9] J. Forshaw, G. Shaw, JHEP 0412 (2004) 052.
[10] E. Iancu, K. Itakura, S. Munier, Phys. Lett. B590 (2004) 199;
H. Kowalski, L. Motyka, G. Watt, Phys.Rev. D74 (2006) 074016.
[11] J. Forshaw, R. Sandapen, G. Shaw, JHEP 0611 (2006) 025.
[12] J. Forshaw, private communication.
[13] For a HERA investigation, see e.g. H1 Collbaoration, Eur. Phys. J. C48 (2006) 715, ibid 749.

Future Plans at BNL: RHIC-II and eRHIC

Samuel Aronson

Brookhaven National Laboratory
Upton, New York, USA

The development of future facilities relevant to the study of deep inelastic scattering at BNL is described.

1 Introduction

A program of high-energy nuclear physics has been carried out at BNL's Relativistic Heavy Ion Collider (RHIC) since 2000 with relativistic heavy ions and polarized protons. Figure 1 shows an aerial view of the RHIC facility; Table 1 compares the design performance parameters, the performance parameters achieved to date (which are beyond design performance in most cases) and so-called "enhanced performance", based on on-going incremental improvements to the current performance.

The scientific output of the RHIC facility and its four experiments has been outstanding. Strong evidence has been found in the final state of ultra-relativistic heavy-ion collisions of a new state of nuclear matter – a strongly coupled Quark-Gluon Plasma [2] – characterized by strong suppression of jets and particle flow in the final state. The measured properties are consistent with these characteristics arising from a partonic state characterized by very high energy density and extremely low viscosity. This striking and unexpected finding has been labeled the "Perfect Liquid" [2, 3].

In the polarized proton program at RHIC, similarly important findings are emerging. In particular, RHIC can provide collisions of longitudinally polarized protons at center of mass

Figure 1: Aerial view of RHIC.

Mode	No. of bunches	$\frac{\text{Ions}}{\text{bunch}}$ $[10^9]$	β^* [m]	Beam pol.	L^{ave}_{store} $[cm^{-2}s^{-1}]$	$A_1A_2L^{ave}_{store}$ $[cm^{-2}s^{-1}]$	$A_1A_2L^{ave}_{peak}$ $[cm^{-2}s^{-1}]$
Design values (1999)							
Au-Au	56	1.0	2		2×10^{26}	8×10^{30}	31×10^{30}
p-p	56	100	2		4×10^{30}	4×10^{30}	5×10^{30}
Achieved values							
Au-Au	103	1.1	0.8		12×10^{26}	46×10^{30}	120×10^{30}
p↑-p↑	111	130	1	65%	20×10^{30}	20×10^{30}	35×10^{30}
Enhanced design values (2009)							
Au-Au	111	1.1	0.9		8×10^{26}	31×10^{30}	155×10^{30}
p↑-p↑	111	200	0.9	70%	60×10^{30}	60×10^{30}	90×10^{30}

Table 1: RHIC design values, achieved values, and "enhanced" design values.

energies up to 500 GeV. Initial results on the double spin asymmetry, which is sensitive to the polarization of gluons in the proton wave function, are consistent with so-called "standard" predictions. If this result is upheld, it means that gluon polarization is *not* the explanation of the proton "spin crisis" [4].

These and other results, summarized elsewhere in these proceedings, point to the need for further measurements to elucidate these manifestations of QCD both at high and low temperature and density. The fundamental QCD questions now on the table are:

- How does ordinary matter get its mass, spin and other intrinsic and dynamical properties?
- How does QCD matter behave at the extraordinary temperatures attained during the first microseconds following the Big Bang?
- What is the structure of the QCD vacuum, and how is it affected by high temperature and density?
- What are the universal properties of all strongly interacting systems in the limit of high gluon density?

A key component of BNL's future plans in nuclear physics is to provide the means to extend these research programs to address these fundamental questions. The four components of this plan are as follows:

- Near-term upgrades to RHIC: Detector upgrades, Electron Beam Ion Source (EBIS, a new ion source), enhanced luminosity and polarization
- RHIC-II: Beam cooling to maintain small hadron beam emittance at top energy
- eRHIC: An electron ion collider (EIC) capable of producing e-A and polarized e-p collisions at high luminosity, plus new detectors
- Theory and computational QCD

The components of this plan are briefly described in the following sections.

2 Near-term RHIC Program

Table 2 summarizes the current planning assumptions for RHIC operations in the next three fiscal years.

The planning basis for these runs is the "enhanced performance" of RHIC shown in Table 1 above for the accelerator. The EBIS project [5] is presently under construction and will be operational in 2009/2010. At present, the experimental program is also embarked on a series of detector upgrades, based on the results to date and on the need to exploit the highest luminosities that can be made available at RHIC [6]. Several of these upgrades are currently in operation or under construction. A number of questions raised by the results to date can be addressed by the experimental program between now and 2010 [7].

Run	Species	Energy $\sqrt{s_{NN}}$ (GeV)
2008	d + Au	200
	p↑+ p↑	200
2009	Au + Au	TBD
	p↑ + p↑	TBD
2010	heavy ion	TBD
	p↑+ p↑	500

Table 2: RHIC operations in the next three fiscal years.

3 RHIC-II

A number of the most crucial questions about the structure of strongly interacting matter above the critical temperature, and about the wave function of the proton, require performance above "enhanced" levels. Below is a somewhat more specific formulation of the RHIC-relevant fundamental questions enumerated above:

- What is the mechanism of the unexpectedly fast thermal equilibration?
- What is the initial temperature and thermal evolution of the medium?
- What is the equation of state, its viscosity and other transport coefficients?
- Is there direct evidence for deconfinement? What is the screening length?
- Is chiral symmetry restored, as predicted by QCD?
- How does the new form of matter hadronize at the phase transition?
- Where is the QCD critical point?
- What is the initial state in heavy ion collisions?
- How does the nucleon get its spin?

The BNL plan, during the Near-term period described above is to develop the technology for increasing the luminosity of RHIC by a factor of 10 beyond the enhanced performance for heavy ion operation and a factor of about 3 for polarized proton operations. The detector upgrades under way during this period will enable the experiments to exploit this higher luminosity.

The luminosity-enhanced RHIC program, dubbed "RHIC-II" requires cooling of the RHIC beams at full energy, via electron-cooling [8] and other techniques. The R&D for this technology is presently under way. Figure 2 shows a schematic layout of RHIC-II.

Strong support for construction of RHIC-II is expected in the U.S. Nuclear Science Long Range Plan process. This process is under way, with a report expected to be issued during 2007.

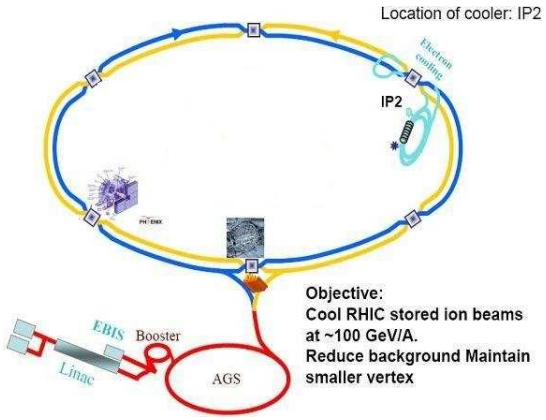

Figure 2: Schematic layout of RHIC-II.

4 eRHIC

The outstanding successes of the HERA program [9], coupled with the results from RHIC comprise major advances in understanding QCD. Moreover, it is possible to extend these accomplishments to address central questions in the role of gluons in the structure and interaction of strongly interacting matter:

- Does the self-limiting growth of color field strengths in QCD lead to universal behavior of all nuclear and hadronic matter in the vicinity of these limits?
- How does the nuclear environment affect the distribution of gluons in momentum and space?
- What is the internal landscape of a nucleon in the region dominated by sea quarks and gluons?
- How do hadronic final states form from light quarks and massless gluons in QCD?

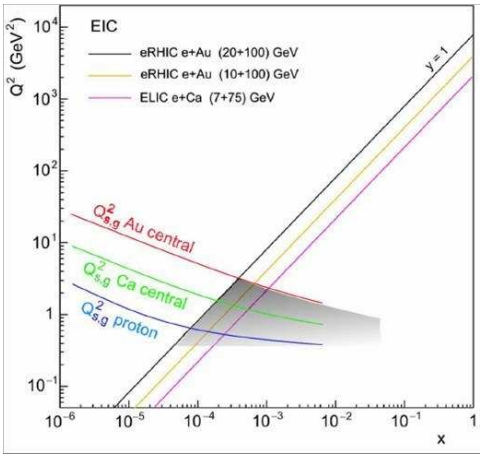

Figure 3: Kinematic reach of eRHIC and ELIC.

The physics case is further elaborated in white papers prepared for the on-going NP Long Range Plan process [10]. To address these questions requires an extension of the HERA program in the form of a new electron-ion collider (EIC) capable of exploring the x–Q^2 region relevant to gluon saturation ($x < 10^{-3}$, $Q^2 > 1$ GeV^2) with a factor 100 or so greater integrated luminosity than HERA provided in its time.

Brookhaven's plan to address this needed capability is a proposal to build eRHIC, an EIC based on the existing RHIC facility [11]. Other EIC capabilities are also being discussed at Thomas Jefferson National Laboratory (ELIC) [12] and at CERN (LHeC) [13]. Figure 3 shows the kinematic reach of eRHIC and ELIC.

The eRHIC conceptual design is fairly well-advanced and uses realistic, RHIC-based performance parameters. To achieve the desired kinematic reach, eRHIC would collide polarized electrons up to 20 GeV with either polarized protons at beam energies of 50 – 250 GeV and polarization $\geq 70\%$, or heavy ions at beam energies up to 100 GeV per nucleon. (In addition, EBIS would also allow high energy collisions of electrons with polarized ^{3}He at beam energies up to 167 GeV per nucleon.) To achieve the desired integrated luminosity in a reasonable period of time, eRHIC would provide average luminosity $\geq 10^{33}/\mathrm{cm}^2\cdot\mathrm{sec}$.

BNL envisions e-A and polarized e-p collisions at one or more intersection regions at RHIC with a high energy electron synchrotron or an energy ecovery linac (ERL). The ERL solution is currently the favored option and a schematic layout of this option is shown in Figure 4. New detectors optimized for the physics goals would be built at the intersection region or regions providing collisions with electrons. Meanwhile, the RHIC heavy ion and polarized p-p programs could continue at the existing PHENIX and STAR detectors.

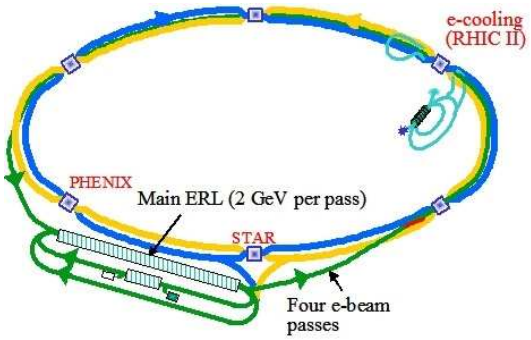

Figure 4: Schematic layout of the linac-ring option for eRHIC.

An EIC is the highest priority of the U.S. QCD community for new construction, after the completion of RHIC-II and the CEBAF energy upgrade. EIC capabilities are being considered by the broader U.S. Nuclear Physics community in the context of the NP Long Range Plan. It is expected that the Long Range Plan report will strongly endorse accelerator and detector R&D in the immediate future, with a commitment to construct such a facility to be considered in the future, probably during the next long range planning cycle (i.e., in 2012).

5 Nuclear Theory and Computational QCD

The nuclear theory effort at BNL has been a vital component of the progress made in understanding and interpreting the results coming from RHIC. In recent years the outstanding strengths of the theory group in strong interaction theory and phenomenology have been complemented by a new effort in computational lattice QCD. This has been made very effective by the presence at BNL of two "QCDOC" supercomputers [14] built by Columbia University, IBM and BNL and operated by the DOE and the RIKEN-BNL Research Center (RBRC) at BNL. These machines, each with a 20 Teraflops peak performance, are focused on lattice QCD, with the RBRC-operated machine largely devoted to finite temperature QCD. They are enabling an accelerated and more realistic study of the physics done at RHIC than has been possible to date.

BNL and Stony Brook University (SBU) have just acquired a New York State-funded 100 Teraflops BlueGene/L computer. This will be operated as the core of a center for computational science. Within a more general research program, it will provide even more capability for lattice QCD research at Brookhaven. Plans are being made for future growth of the computational capabilities available at the SBU-BNL center.

6 Summary

A key goal of BNL's plans for future research and future user facilities in nuclear science is to maintain and extend our world-class capability in the study of QCD. This is based on a proposed evolution of the highly successful RHIC program into a broader QCD laboratory, comprising high energy studies of QCD through collisions involving heavy ions, polarized or unpolarized protons and polarized electrons. The principal components of this evolution are a luminosity upgrade (RHIC-II) for nucleus-nucleus and nucleon-nucleon collisions plus an electron capability (eRHIC) for deep inelastic lepton-nucleus and lepton-nucleon collisions. These, in turn, require detector upgrades, new detectors and an increasing computational capability for lattice QCD.

7 Acknowledgements

This work was supported by the Division of Nuclear Physics of the Office of Science of the U.S. Department of Energy under contract DE-AC02-98-CH10886.

References

[1] Slides:
`http://indico.cern.ch/contributionDisplay.py?contribId=270&sessionId=10&confId=9499`

[2] I. Arsene *et al.* [BRAHMS Collaboration], Nucl. Phys. A **757** 1 (2005).
B. B. Back *et al.* [PHOBOS Collaboration], Nucl. Phys. A **757** 28 (2005).
J. Adams *et al.*, [STAR Collaboration], Nucl Phys. A **757** 102 (2005).
K. Adcox *et al.*, [PHENIX Collaboration], Nucl. Phys. A **757** 184 (2005).

[3] E. Shuryak, Prog. Part. Nucl. Phys. **53** 272 (2004).

[4] E. Leader and M. Anselmino, Z. Phys. C **41** 239 (1988).
B.I. Abelev *et al.*, [STAR Collaboration], Phys. Rev. Lett. **97** 252001 (2006).

[5] M. Wilinski, J. Alessi, E. Beebe, S. Bellavia and A. Pikin, *Electron Beam Ion Source Pre-Injector Diagnostics*, Beam Instrumentation Workshop 2006, Batavia, Illinois (2006).

[6] Mid-term plan for RHIC:
`http://www.bnl.gov/HENP/docs/RHICplanning/RHIC_Mid-termplan_print.pdf`

[7] Future Science at the Relativistic Heavy Ion Collider:
`http://www.bnl.gov/physics/rhicIIscience/`

[8] See abstracts from Particle Accelerator Conference 07, Albuquerque, New Mexico: 25 presentations on BNL's progress in implementing electron cooling.

[9] A. Deshpande, R. Milner, R. Venugopalan, and W. Vogelsang, Ann. Rev. Nucl. and Part. Sci. **55** 165 (2005).

[10] P. Jacobs *et al.*, *Phases of QCD,* Summary of the Rutgers Long Range Plan Town Meeting, New Brunswick, New Jersey (2007).
X. Ji *et al.*, *Whitepaper from DNP Town Meeting on Hadronic Physics*, New Brunswick, New Jersey (2007).
Both can be found at `http://dnp.nscl.msu.edu/`

[11] J. Beebe-Wang *et al.*, The eRHIC machine Accelerator Position Paper:
`http://www.phenix.bnl.gov/WWW/publish/abhay/Home_of_EIC/eic-info.html`

[12] ELIC: `http://casa.jlab.org/research/elic/elic.shtml`

[13] LHeC: `http://www-zeuthen.desy.de/lhec/LHeCprop.pdf`

[14] P. A. Boyle *et al.,* IBM Journal of Research and Development **49** 351 (2005).

LHeC: The Large Hadron-Electron Collider

John Dainton *

The Cockcroft Institute of Accelerator Science and Technology,
Daresbury Science and Innovation Campus, Warrington WA4 4AD, UK,
and Department of Physics, University of Liverpool, UK

Progress towards an upgrade, the LHeC, of the LHC at CERN is presented in which electron(positron)-proton (ep) physics at the TeV energy scale is realized by bringing a 70 GeV electron(positron) beam into collision with a 7 TeV hadron beam in the LHC tunnel. An ep luminosity of 10^{33} cm^{-2}s^{-1} seems feasible. An update on the physics horizon is outlined. Aspects of a first evaluation of the possibility of an e-storage ring are presented in which the aim of simultaneous pp (ion-ion AA) and ep (eA) data-taking is achieved. A putative timeline for the realization of an LHeC is mentioned.

1 Why a Universe with both Leptons and Quarks?

In 1967 our understanding of the fundamental nature and structure of matter posed a conundrum: why did matter at the femtometric scale distinguish itself as a tidy array of only two generations of "point-like", Dirac, fermions – the leptons e and μ – and a complicated spectrum of hadrons, characterized by those which could decay through the strong interaction to nucleons (non-strange hadrons) and those which couldn't (strange hadrons)?

By 1969, we had, through definitive measurements at the Stanford Linear Accelerator Collider (SLAC), clear evidence that a sub-femtometric view simplifies the hadronic spectrum to that of also of point-like, Dirac, fermions - quarks - as postulated by Gellmann and Zweig [1], and as interpreted by Bjørken and Feynman [2]. Deep-inelastic, lepton-nucleon, scattering had brought particle physics to a turning point. There followed decades of staggering progress which now culminates in today's Standard Model, and its huge impact on Cosmology and our understanding of our place in the Universe.

The definitive measurements at SLAC were of course those of the Nobel Prize-winning experiment at end-station A. There, the first measurements of deep-inelastic, lepton-nucleon, scattering were made, and the first cross sections (structure functions) obtained from the data [3]. The SLAC experiment was revolutionary not because of its centre-of-mass (CM) energy, for there were fixed target, hadron-beam, experiments at CERN, and later at Fermilab, with similar or significantly greater energy[a]. The SLAC experiment's impact was due to the combination of enough interaction energy *and* enough luminosity to populate the final state phase space where there is sensitivity to short distance structure in the nucleon: the revolutionary discoveries made were with a probe of spatial resolution of about $^1/_{10}$ fm, that is of about $^1/_{10}$th of the size of the target proton.

*Email contact with the emerging organization concerned with progressing the LHeC initiative is best made to mklein@hep.ph.liv.ac.uk or J.B.Dainton@cockcroft.ac.uk, or through the web page http://epweb2.ph.bham.ac.uk/user/newman/LHeC/LHeC.html

[a]It is worth recalling that at the time of the SLAC end-station-A discoveries in 1969 with a 20 GeV/c electron beam – 6 GeV centre-of-momentum (CM), the horizon for the energy frontier was pp physics at the CERN ISR with a CM energy of 63 GeV. Furthermore, in pp collisions hadronic jets, with a p_T dependence attributable to parton-parton scattering, were only unambiguously confirmed more than a decade later in the early 1980s at the CERN SppS collider with a CM energy of 630 GeV, a factor ∼30 larger than the original SLAC ep measurements.

Today further deep-inelastic, lepton-hadron experiments, culminating with those at HERA, have enabled us to quantify the chromodynamic picture of hadronic matter down to 1 am distance scale (about $^1/_{1000}^{th}$ of the size of stable, colour singlet, hadrons - fig.1). Furthermore, we are now able to probe the kinematic region of low Bjørken-x where proton structure is almost exclusively attributable to chromodynamic field energy. Yet despite this progress, little further understanding has emerged as to why there are three generations of point-like, Dirac, leptons, which remain distinct from three generations of point-like, Dirac, quarks. We inherit the original conundrum of the 1960s, but now in a form which has moved on to address hadronic matter at the attometric scale in terms of quarks and chromodynamics, and their relation to leptons. The question remains one of, if not the, fundamental challenges of all of physics [4].

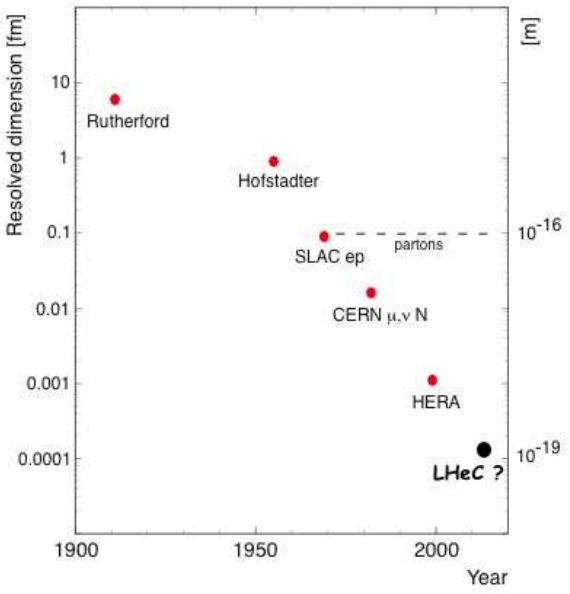

Figure 1: Resolution of lepton probe in "milestone", deep-inelastic, experiments in the 20^{th} century, including that foreseen at the LHeC in the 21^{st} century.

Our (for I am not alone [5]) purpose here is to remind you that we can now contemplate a new turning point in lepton-hadron physics of significance similar to that following the pioneering SLAC experiment in 1969. With*out* huge new investment at the soon-to-be-completed LHC, it seems feasible to contemplate an upgrade, the LHeC, for TeV, deep-inelastic, e-hadron (ep and eA) physics, while *at the same time* retaining on-going, 14 TeV, pp and AA experiments.

All that is missing is a 70 GeV (or more) electron or positron beam optimized for collisions of e-bunches with LHC p-bunches. Such an electron/positron beam at CERN, whether stored in the LHC tunnel or from a high duty cycle (CW), single pass, linac, is a feasible proposition.

We here concern ourselves primarily with an overview of the physics which must be addressed at an LHeC when electron and positron-quark (eq) collisions at TeV energy are achieved. We motivate a proposal which takes advantage of the energy and luminosity possible when the LHC hadron beams, p and A, are brought into collision with a stored electron or positron beam of realistic intensity. We demonstrate the feasibility of such a configuration as an upgrade of the LHC in which both ep and pp, or alternatively both eA and AA, physics can be pursued simultaneously. The unprecedented combination of CM energy *and* luminosity which is then achieved makes possible measurements of deep-inelastic, lepton-hadron, scattering with a spatial resolution of about $^1/_{10}$ am, that is of about $^1/_{10,000}$th of the dimension of a hadron, amounting to more than a factor 10 better than hitherto (HERA) (fig. 1).

2 Lepton-Hadron TeV Physics at the LHeC

There have been a number of considerations of how best to achieve TeV electron-proton and electron-ion[b] collisions, stemming initially from the, perhaps fanciful, idea of keeping LEP assembled and ready while installing and then operating the LHC. They stand or fall on the basis by which the pioneering SLAC experiments at end station A changed the face of physics, namely by having *both* adequate energy *and* adequate luminosity for at least an order of magnitude increase of spatial resolution (fig.1).

It is instructive to take a look at lepton-hadron experiments, both completed and contemplated, in terms of luminosity (fig. 2). Taking advantage of R&D for TeV e^+e^- physics, whenever the collision of a 250 GeV, International Linear Collider (ILC)-like, beam with a co-located TeV hadron beam, for example at HERA, is considered, luminosity has been the limiting issue (THERA, fig. 2) [6]. This is also the case when the collision of a futuristic, CLIC-technology based (few hundred GeV,or even TeV, 30 GHz), electron beam with a "super-bunched" LHC proton beam is considered (QCD Explorer, fig. 2) [7].Taking the LHC p and A beams as for pp and AA physics, an electron storage ring of energy 70 to 100 GeV in the LHC tunnel, whose design makes possible efficient bunch-crossing with the LHC beams and whose power consumption is not prohibitive (electron current 70 mA), makes possible ep collisions with a luminosity 10^{33} cm^{-2} s^{-1}. How this is done is described in section 3 below, and in much more detail in [5]. Such a luminosity exceeds that achieved at all lepton-hadron experiments so far, except those at SLAC in 1969 (fig. 2). Though yet to be evaluated, it could also be the case that a purpose-built 70 GeV, CW, e-linac in single-pass collision with LHC hadron beams could also achieve such luminosity at similar, or even lower, cost than an injection system and storage ring technology [8].

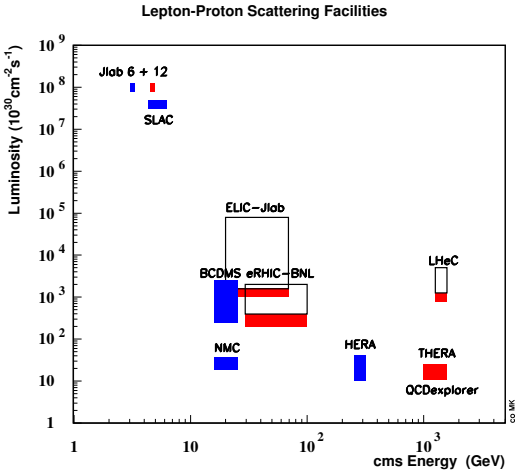

Figure 2: Luminosity achieved or foreseen at high energy, lepton-hadron, experiments; THERA and QCD-explorer are possibilities involving presently available hadron beams at HERA and the LHC which use "single-pass" linear collider electron beams; LHeC is described here; the estimated luminosity at LHeC is notable.

It is thus far from fanciful to assume that TeV ep (and eA) physics at an LHeC will be possible with *both* TeV interaction energy (70⊗7000 GeV) *and* adequate luminosity (10^{33} cm^{-2} s^{-1}) for sub-attometric eq physics.

The kinematic reach of a lepton-hadron collider is best expressed in terms of the Bjørken-x

[b]Henceforth we take it for granted that an electron linac, or an electron storage ring in the LHC tunnel, will also, like HERA, operate well as a positron linac or storage ring.

and Q^2 variables[c], that is the momentum as a fraction of the incident hadron momentum and the 4-momentum transfer squared in the interaction between the lepton and the struck parton in the hadron. Fig. 3 shows (in modest logarithmic fashion) the resulting kinematic reach of the LHeC (70⊗7000 GeV) in comparison with previous experiments. The LHeC probes the electron-quark (eq) interaction at more than 1 TeV with a spatial resolution of $^1/_{10}$ am (fig. 1). For the deepest ep interactions with $Q^2 \sim 1$ TeV^2 and with 10^{33} cm^{-2} s^{-1}, 30 events will be obtained for in a plausible data-taking year of 3 fb^{-1} at the LHeC. Furthermore, for Bjørken-x down to 10^{-7}, the LHeC probes eq physics with sub-femtometric resolution ($Q^2 \geq 1$ GeV^2) in low-x interactions where the quark is enveloped in the proton's (or ion's) immense chromodynamic field energy. For such extremely inelastic (high y) ep interactions, luminosity is only an issue if one has difficulty in the face of a huge data-rate at small angles (less than about 10^o) to the incident proton beam.

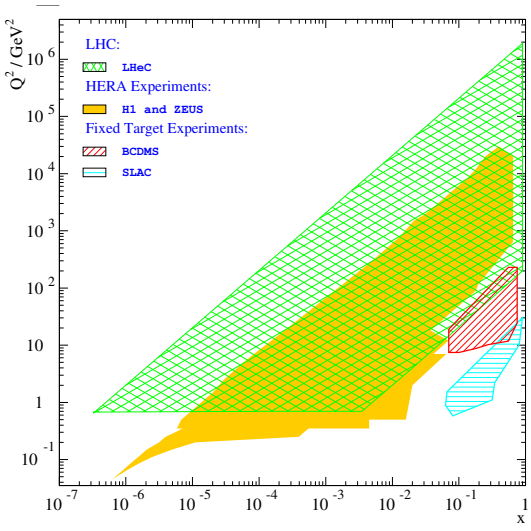

Figure 3: Kinematic reach in terms of Bjørken-x and Q^2 at lepton-proton experiments.

Attometric and sub-attometric, eq physics in an LHeC, with a purpose-built detector, is thus a powerful new probe of the Standard Model (SM), both its electroweak and its strong sectors. Experience at HERA has taught us that it is possible to make precision measurements of a swathe of eq SM processes. In contrast with collisions in a pp collider, the final state is kinematically over-constrained at the e-hadron level, and the asymmetry in colliding beam energies in the laboratory throws the important, final state, hadrons from the e-hadron interaction into the detector, whereas in the old fixed-target, lepton-hadron, experiments they dribble out through the target mass. Furthermore, and also like TeV e^+e^- physics, precision experiments are feasible in ep and eA physics at an LHeC. In neutral current SM interactions, transverse energy flow, measured with modern hadronic calorimetry is kinematically balanced against the transverse energy of the scattered lepton, which itself is measured with the precision possible using electromagnetic calorimetry. LHeC physics is truly precision physics.

It is instructive to compare the TeV physics, which is possible at the LHC in terms of the nature of the initial parton-parton interactions, with the TeV physics which is possible at the LHeC in terms of the initial e-parton interaction. For a lepton momentum of 70 GeV, ep interactions at the LHeC include final state phase space corresponding to inclusive pp at LHC for "parton-out-of-proton" inelasticity $y \leq 0.01$, that is for "parton-out-of-proton" momentum fraction $x \leq 0.01$ (Fig. 4a). Our knowledge of the parton density functions of

[c]The definitions and physical interpretation of the Lorentz covariant variables inelasticity y, Bjørken-x and Q^2 are to be found liberally distributed throughout other contributions to these proceedings!

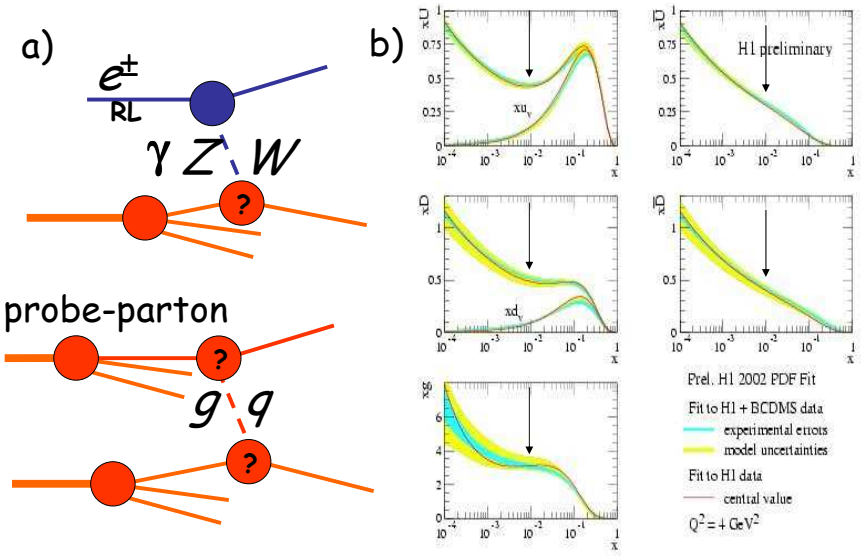

Figure 4: a) Diagrams illustrating the lepton-parton level dynamics in ep and in pp interactions at respectively the LHeC (upper) and the LHC (lower); at the LHeC the incident 70 GeV electron/positron $e^{\pm}$ (left L or right R handed, polarized, lepton) interacts electroweakly ($\gamma + Z$, W) with a parton in the 7 TeV beam; at the LHC the same phase space is covered by the inelastic interaction of a parton from one of the protons having fractional momentum Bjørken-x=0.01 with the other proton. b) Parton density functions (probability per unit ln$x$) for u and d quarks and antiquarks, and for gluons, showing the mix of quark, antiquark and gluon at x=0.01 (marked with the arrows) at LHC; at LHeC this mix is replaced by the precision electroweak probe.

the proton, which specify the latter's structure in terms of the variety of possible partons, comes right now from measurements at HERA, and is summarized in Fig. 4b). For $x \leq 0.01$, pp physics involves either a quark/antiquark or a gluon interacting with the other proton, roughly in a mix of gluon:(anti)quark of at least $\sim$ 2:1. Which of these, gluon or (anti)quark, is the probe is crucial to the interpretation of the physics, and discrimination will depend on final state jet topology and comparison with QCD and other pp-based simulation at the LHC. At LHeC the electroweak probe ($\gamma + Z$ for neutral current, W for charged current) couples in an a priori well defined, and self-verifying, manner to each distinct flavour of quark, in which the consequences are immediately manifest in the neutral and charged current inclusive cross sections and their dependence on lepton helicity. It is primarily for this reason, taken with careful experimentation, that LHeC brings precision to TeV physics at the LHC.

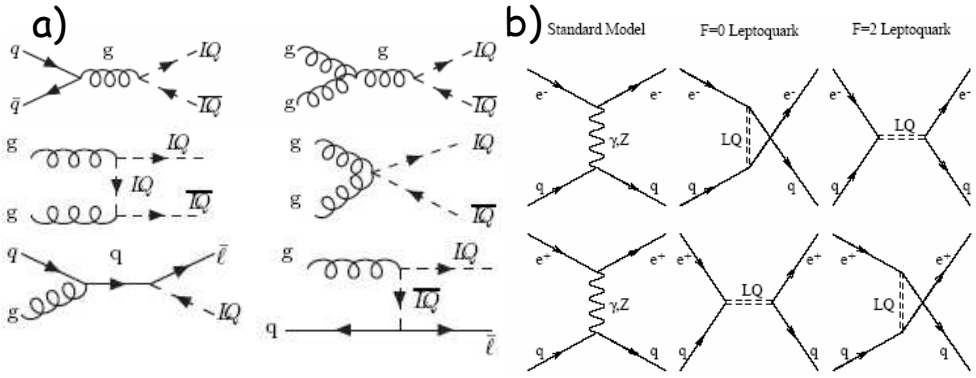

Figure 5: a) Leading order diagrammatic view of production mechanisms for new lepton-quark (lepton l, quark q, gluon g, and leptoquark tlQ) physics in parton-parton interactions, and b) for SM and similar, new, electron/positron-quark physics.

The combination of this experimental precision and of the rather clean, "SM-and-beyond", eq interaction mechanisms, means that experiments at LHeC constitute a precise, TeV-scale, discovery apparatus. Fig. 5 shows the simplest, leading order, parton-parton (a) and eq (b) processes in which new eq physics could be manifest. The new physics diagrams are displayed here in terms of "leptoquark" lines (LQ), and they can also be taken in a more generic sense given that new TeV-physics at the LHC, such as supersymmetry, could well be manifest as new lepton-quark dynamics at the LHeC. If LQ lines are interpreted as a new leptoquark spectrosocopy, most models predict that at 1 TeV the $eq \rightarrow$LQ formation cross section is 2 to 3 times larger than for similar, single, leptoquark production in parton-parton interactions.

By virtue of the electroweak nature of the deep-inelastic neutral current (NC) and charged current (CC) probes, sensitivity to signatures for new physics at LHeC is large because almost-completely-real, SM, amplitudes interfere with amplitudes for new physics (Fig. 5b). One can thus anticipate from precision analysis of the final state lepton (e or ν) and jet(s) system, including correlation with initial state lepton helicity, a detailed quantification of new phenomena. For example, measurements of decay branching ratios and even spin-parity analysis of resonant eq phenomena, both for fermion number F=0 (e^+q, i e meson) and for F=2 (e^-q I e di-fermion). The potential for such measurements was amply demonstrated at HERA, where, with hindsight but for the misfortune of the energy scale of new physics being beyond the reach of 320 GeV ep collisions, hitherto unchallengeable limits on a huge range of possibilities for new LQ physics have been obtained [9].

Of course, eq physics at the LHeC is manifest in the environment of hadrons, be they protons or heavy ions. In a sense, this of course means that the LHeC will be actually the world's most powerful and comprehensive microscope – attoscope – of matter! Many of the precision measurements which are possible will be of cross sections, in the form of for example hadronic structure functions, and new physics may well first show up as anomalies in such measurements.

To highlight the importance for discovery at the LHC of the LHeC attoscope, one only has to look at fig. 6, which illustrates the magnitude of the task, in the face of SM background,

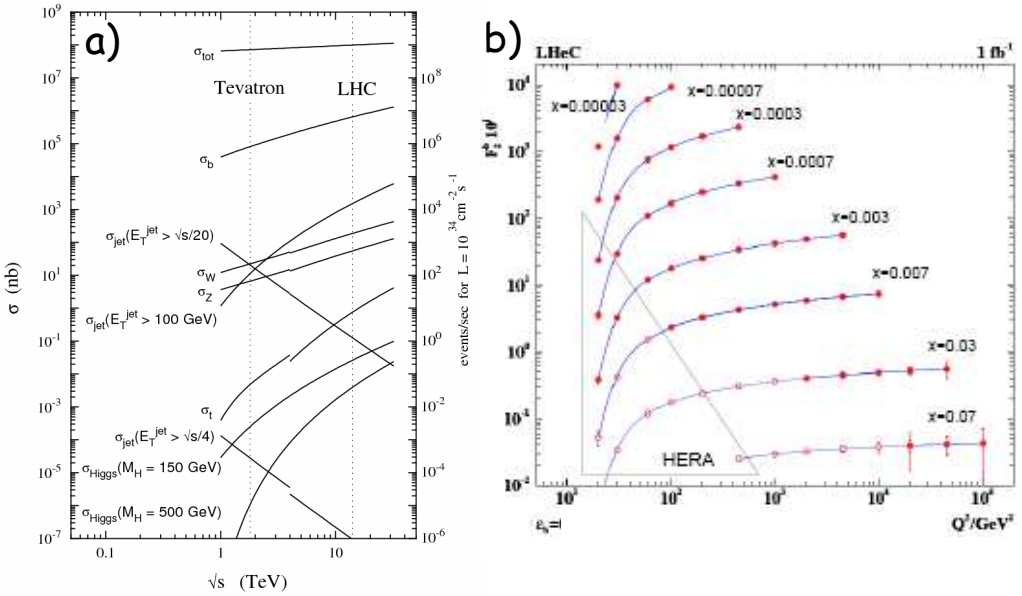

Figure 6: Total production cross sections at the LHC showing the challenge even for SM discovery; b) expectation for a measurement of F_2^bat LHeC, showing the huge increase in kinematic reach compared with HERA in Bjørken-x and Q^2, and illustrating the impracticality of relying on extrapolation from HERA to LHC energy scales to obtain accurate enough b-quark pdfs for SM background subtraction if searching for Higgs production and b-quark decay.

of discovering and identifying the Higgs at the LHC by means of its b-quark decay mode. A comprehensive, and well quantified, understanding of the contribution of b-quarks to proton structure is a pre-requisite for a conclusive outcome. Extrapolation alone, however rigorously based, of knowledge from the HERA energy scale (see [10]) to that of LHC, is no substitute for direct measurement at the LHeC (and therefore LHC!) energy scale.

At low Bjørken-x the relentless growth with decreasing x of hadronic structure functions means that kinematics, coupled with experimental acceptance, govern the reach at LHeC for eq physics (fig. 2). Luminosity only plays a role in probing rare exclusive processes at low-x. According to fig. 3, it is possible at LHeC to probe, with a precision better than a $^1/_{10}$ fm, nucleon and nuclear matter in a region in which there is enough phase space for on average up to about 5 partons to be resolved and disturbed in the chromodynamic field of the nucleon (compared with about 2 at HERA). This is an environment where the non-abelian, interaction of the chromodynamic field quanta, the gluons, plays a crucial role, and the LHeC provides the only way to probe it with precision.

Gluon-gluon, gluon-quark, gluon-antiquark, and quark-antiquark dynamics will thus be essential pieces in the jigsaw which makes up the physics programme at the LHeC. In fact HERA opened our eyes to the realization that the deep-inelastic probe at low-x constituted a completely new window on discovery and understanding of chromodynamic mechanism in both hadron structure and hadron interaction, and thereby on their inter-relationship.

For the first time it was possible to measure simultaneously *both* structure *and* dynamics in terms of partons. Just as for proton structure pre-HERA, the outcome has been seminal, showing the way towards understanding the hadron-hadron interaction cross section at high energy in terms of chromodynamics. One begins to see that the grand horizon of building a universally applicable, chromodynamic, approach to the strong interaction in hadron and nuclear physics could be possible.

The LH*e*C takes us way beyond HERA in this physics. The magnitude of gluon density in the hadronic target which is accessible at the LH*e*C may be such as to reveal new degrees of freedom in chromodynamic excitation, such as instantons. The LH*e*C is likely to put us in a regime where first gluon-gluon, and then other parton-parton, interactions are at a rate where they suppress parton densities at low-x through gluon-gluon and quark-antiquark

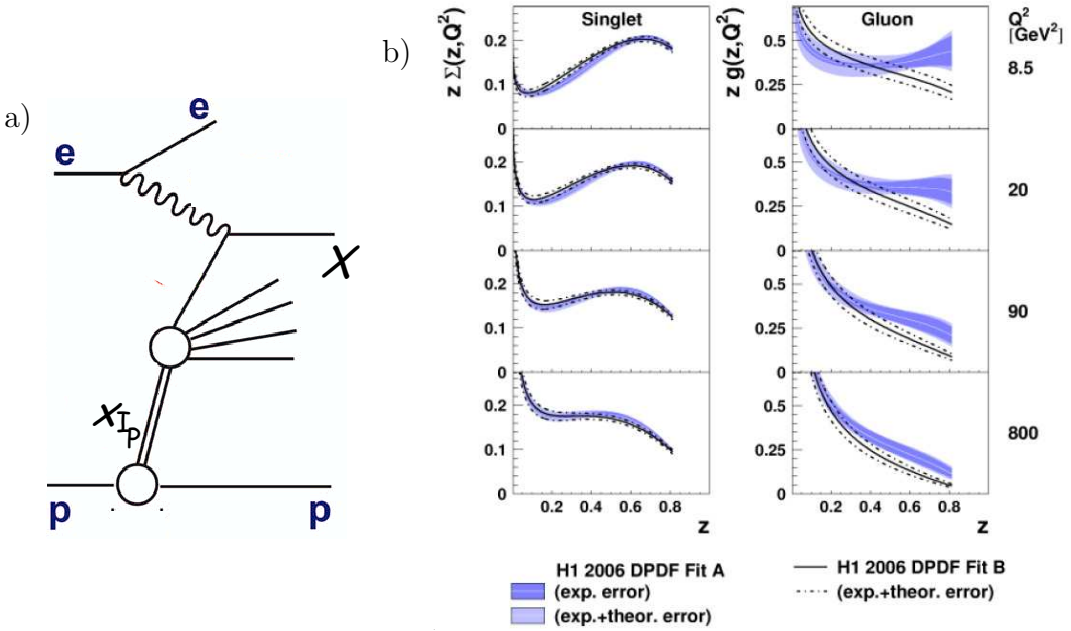

Figure 7: a) Deep-inelastic diffraction ($ep \to eXp$), in which, in low-x deep-inelastic ep scattering, the electroweak current couples to a quark and probes the diffractive interaction of a colour-singlet centre in the proton with small fractional momentum variablex_{IP}, that is in which, in the assumption of the dominance of pomeron exchange, the electroweak current probes the structure of the pomeron. b) Parton density functions for quarks (anti-quarks) and for gluons (z is the fractional momentum variable) extracted from the application of a "next-to-leading order", perturbative, QCD analysis of the structure function for deep-inelastic diffraction; this amounts to the structure function of the pomeron if diffraction at the chosenx_{IP} is taken to be dominated by this Regge trajectory with leading vacuum quantum numbers. Note the different scale of ordinate for quark and for gluon, and also note the "leading gluon" nature of diffractive structure in which the quark density resembles closely that expected from gluon splitting and in which substantial gluon density persists to larger values of z.

fusion, $gg \rightarrow g$ and $qq \rightarrow g$ ("absorption", "recombination", or "shadowing"). Therefore for the first time we may see the long awaited saturation of the relentless rise of structure functions at low-x, and we may understand it in terms of evolution between the "current" (small $Q^2 \rightarrow \infty$) and "constituent" (large $Q^2 \rightarrow 0$) pictures of hadronic structure. In terms of hadron dynamics, we will then reveal how chromodynamics causes the rise of total hadronic cross sections at high energy to level off, without which physics cannot be unitary.

It can be argued that parton recombination has already been demonstrated in the phenomena of parton hadronisation in jet physics and of colour-singlet clustering, the latter of which has been observed at HERA in the form of mesonic contributions to hadron structure at low Bjørken-x. Through the rigour of asymptotic Regge theory, these clusters can be associated with colour singlet spectroscopy and with the Regge-pole based phenomenology of "soft" hadronic interactions of the last few decades. Already HERA has revealed, through deep-inelastic measurements of diffraction (fig.7a), the short distance mechanisms at play in diffractive physics in terms of colour-singlet, gluon-gluon, dynamics ($ep \rightarrow eXp$) – it has identified the pomeron in terms of asymptotically free, chromodynamic, degrees of freedom (Fig. 7b) [11]. For quark-antiquark, colour-singlet, dynamics, it has exposed the leading meson phenomena which persist to larger x_{IP} ($ep \rightarrow eXn$) [12].

At the LHeC the reach to even lower Bjørken-x will reveal exactly how gluon-gluon and quark-antiquark dynamics underpin these colour-singlet phenomena and developments of them, such as multi-Regge dynamics and reggeon calculus [13], which are presently the remaining pieces in our present "soft" hadronic phenomenology. Put more prosaically, this amounts to probing colour-singlet clustering within, or interacting with, colour-singlet clusters, while also resolving this chromodynamic physics in terms of partonic degrees of freedom. At last a complete picture of the interplay of quarks, gluons, and hadrons within baryonic matter, including nuclei, will be possible. The results will also have immediate application to the physics of confinement in QCD.

Many new and powerful insights into hadron structure which are possible in ep physics at high energy have only recently been realised at HERA. Most notable has been the re-emergence of deep-exclusive physics, such as inelastic Compton scattering $ep \rightarrow e\gamma p$ and vector meson (VM) production $ep \rightarrow e\mathrm{VM}p$, in which the simultaneous handles of Q^2 and of the 4-momentum transfer squared t probe the full tomography of proton and nuclear structure [14]. For such proton tomography, the importance of meeting the challenge of the operation of forward proton detection in "Roman pot"-like detectors, in which both t and Feynman-x are measured, is thus further emphasized. At the LHeC one can thus foresee establishing a full picture of hadronic structure and interaction at high energy in terms both of the nature and properties of constituents, and of how these constituents are distributed within their parent structure. Sub-femtoscopic tomography may well provide the greatest sensitivity than otherwise to new, short distance, chromodynamic physics.

A sense of the impact of low-x physics at the LHeC can be gauged from the diffractive event rate as a function of inelastic diffractive mass M_X in $ep \rightarrow eXp$, to be found in fig. 8. A huge event rate (hundreds per pb^{-1} at 150 GeV) will be available. This opens the physics of 0^+ (vacuum quantum number) excitation in hadronic matter to the same scrutiny as 1^- excitation of the vacuum in LEP/ILC, e^+e^-, physics. We shall be able to measure heavy flavour dynamics in vacuum-quantum-number clusters in nucleons and nuclei. In short, the LHeC takes the physics of diffractively produced systems to the same energy scale as that of the hadronic final state at the putative ILC, and moreover extends it to chromodynamic environments beyond that of just the proton.

All of this LHeC hadronic physics, and more, is essential stuff if a full understanding of the strong interaction in terms of chromodynamics is to be achieved. Furthermore, we must have this confidence of understanding if we are to make discoveries at the TeV scale, whether at the LHC, the LHeC or elsewhere. When taken together with the ubiquity of the role of the strong sector of the SM in cosmic evolution, from the interaction and stability, or otherwise, of hadrons and of atomic nuclei and their role in nuclear synthesis, to the earliest phases of the Big Bang, such an understanding is seen to be crucial for future progress. We must continue to anticipate that the only way in which our confidence in QCD will continue to grow will be to pursue relentlessly its validity in as wide a range of phenomena as possible. HERA opened our eyes to the immense scope for testing chromodynamics in high energy ep interactions, and it has provided seminal new insight into many long-standing and unresolved issues in strong interaction physics. The LHeC is likely to provide many more answers to many more questions, and some of these answers may amount to genuinely new chromodynamic discovery.

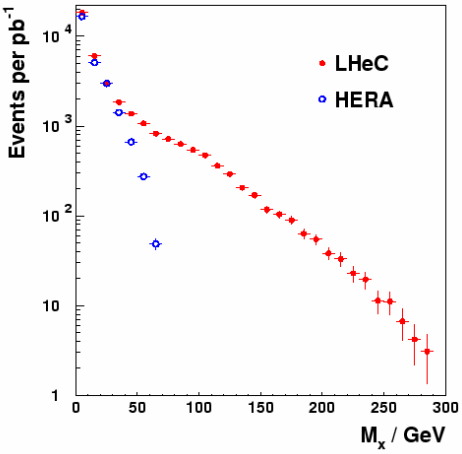

Figure 8: Event rate for deep-inelastic diffraction at the LHeC as a function of the diffractive dissociation mass M_X.

It must be clear from the few examples above that lepton-hadron interactions at the LHeC take us well into a new, TeV-energy, kinematic domain of eq physics, and that such access gives new, unique, opportunity for discovery and understanding. Put more starkly, the LHeC seems to be the *only* feasible way, both financially and technically, to make possible in a timely fashion the interaction of leptons with hadronic matter, namely quarks in various environments, at 1 TeV or more energy. The LHeC machine will thereby provide immense new insight into all sectors of the Standard Model through new discovery, and equally also through interpretation and distinction based on precision measurement.

3 LHeC - the machine

The LHeC is a pragmatic, and these days relatively modest, way to achieve a major step beyond the LHC in TeV-physics. By virtue of the unparalleled properties of the LHC hadron beams - proton and heavy ion, 7 TeV energy, a new scale of intensity – a modest 70 GeV, 70 mA, electron beam is required to achieve impressive luminosity. Here's how.

Given

- the LHC proton beam, namely bunches with 7 TeV energy, each with 1.67×10^{11} protons, of length 7.55 cm,
- the inter-bunch spacing of 25 ns,
- a normalized transverse emittance[d] ε_{pN} of 3.75 μm, and

[d] An emittance ε of a beam in a transverse dimension with Lorentz factor γ is specified as $\gamma\varepsilon_N$ where ε_N

- the experience of what really limits the current in an electron storage ring in the (once LEP) LHC tunnel, namely synchrotron radiation power loss defining the RF power consumption to be 50 MW, i.e. 28% of the CERN site load,

the well known formula for luminosity

$$L = \frac{I_e N_p \gamma_p}{4\pi e \varepsilon_{pN} \sqrt{\beta_{xp}\beta_{yp}}}$$

gives $L = 1.15{\times}10^{33}\ (\beta_{xp}\ \beta_{yp})^{-1/2}\ \mathrm{cm}^{-2}\ \mathrm{s}^{-1}$. A *more-than adequate ep* luminosity thus looks possible (at of course a *more-than-adequate* CM energy!). For a plausible set of transverse β-functions, β_{xp} and β_{yp}, of the proton beam, L is more than a factor 10 larger than that of any lepton-proton experiment since that at SLAC in the late 1960s (fig. 1).

This result relies on the feasibility of colliding the electron or positron beam with the LHC proton (and ion) beams. Cutting short (undeservedly) work [5] of substantial technical detail to its barest conclusions, it turns out to be possible to establish LHC proton bunches in collision with bunches in a plausible electron ring in the LHC interaction region (IP) IP8. Table 1 summarises the main parameters which are necessary and which result, including a luminosity of $1.04{\times}10^{33}\ \mathrm{cm}^{-2}\ \mathrm{s}^{-1}$.

Property	Unit	Leptons	Protons
Beam Energies	GeV	70	7000
Total Beam Current	mA	74	544
Number of Particles / Bunch	10^{10}	1.04	17.0
Horizontal Beam Emittance	nm	25.9	0.501
Vertical Beam Emittance	nm	5	0.501
Horizontal β-functions at IP	cm	3.77	180
Vertical β-functions at IP	cm	4.44	50
Energy loss per turn	GeV	0.676	$6 \cdot 10^{-6}$
Radiated Energy	MW	50	0.003
Bunch frequency / bunch spacing	MHz/ns	40 / 25	
Center of Mass Energy	GeV	1400	
Luminosity	$10^{33}\mathrm{cm}^{-2}\mathrm{s}^{-1}$	1.04	

Table 1: Basic LH*e*C machine parameters.

In IP8, the beams cross at 0.5 mrad in the horizontal plane, for which the electron-proton, beam-beam, interaction should not, and in this evaluation did not, in any way affect the *pp* luminosity at IP1 (ATLAS), IP2 (ALICE), and IP5 (CMS) in LHC if one anticipates simultaneous $ep(eA)$ and $pp(AA)$ physics. The other hadron beam passes through the experiment displaced a few cm vertically above the interaction region beam pipe. At each of the other three IPs, two bypass tunnels for the electron beam are necessary (2 m diameter with each section about 250 m long). Each tunnel links the main LHC tunnel to the IP survey shaft (fig. 9). In this way it seems to be possible at the LHC to have both *ep* and *pp* data-taking simultaneously (of course in different experiments!).

is the normalized emittance in that dimension. Here we have a situation in which emittance is taken to be the same in both transverse directions.

The LHeC optics at IP8 leave many metres along the beam axes for experimentation, with access for detectors down to about 9.4^o. For the low-x physics programme (see above), where luminosity is not a limitation, low-β quadrupoles could be removed to facilitate "forward" and "backward" detectors at smaller angles, down to about 1^o. The details of the optics for an interaction region for such low-x data-taking remain to be resolved.

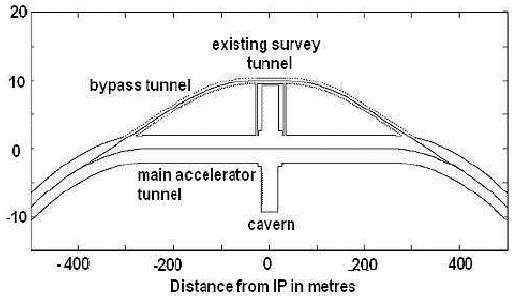

Figure 9: Schematic showing the electron bypass at IP1, IP2, and IP5, to enable simultaneous pp and ion physics; new small tunnels connect the survey tunnel to the main LHC tunnel.

Longitudinally polarized (helicity) electrons and positrons in the LHeC increase substantially sensitivity to new eq physics both in the electroweak propagators and couplings and, more generically, in unforeseen discovery and its interpretation. One of HERA's remarkable achievements was to produce substantial, useful, polarisation using the Sokolov-Ternov effect [15] and "spin-rotation". In essence the synchrotron radiation in a storage ring generates a transverse polarisation for the stored electrons or positrons during the fill (Fig. 10a). As it develops, this polarisation can be rotated to be longitudinal before the ep IP, and then back to transverse again after the IP [16]. The efficacy of the whole procedure depends largely on the alignment accuracy of the machine and the correct management of the coupling of spin motion to orbital motion such that dynamic equilibrium is achieved with minimal depolarizing effects. Already one can draw encouragement from the fact that transverse polarization could be produced in the LEP ring at 46 GeV, albeit with much patient optimization (fig. 10b). It will thus be important from the start to include the requirement of polarisation in the design of the electron ring lattice in the LHC tunnel. If, after all, a CW linac e-beam turns out to be a simpler and cheaper option than a storage ring, polarization may then be an easier issue for electrons and only slightly more of a challenge for positrons, but this has yet to be evaluated.

The first results from the evaluation which are presented above, and in more detail in [5], look extremely promising. Following completion of the details of the design and subsequent approval for construction, the realisation of an LHeC will most likely take a decade, in which the next "milestone" should be the completion of a Letter of Intent in the next two years (for 2009), and then, as soon as possible afterwards, a Technical Design Report[e].

By the time LHeC data-taking is established, meeting the challenge at the LHC of further increases in hadron beam intensity will be underway. Thus the LHeC has a unique long term potential both of luminosity growing beyond 10^{33} cm^{-2}s^{-1} and of an ep CM energy which will surely remain unsurpassed for a substantial fraction of this century.

[e]This time-line bears an uncanny resemblance to the TeVatron-HERA era, when the first HERA physics appeared in 1992 about a decade after the turn-on of the TeVatron!

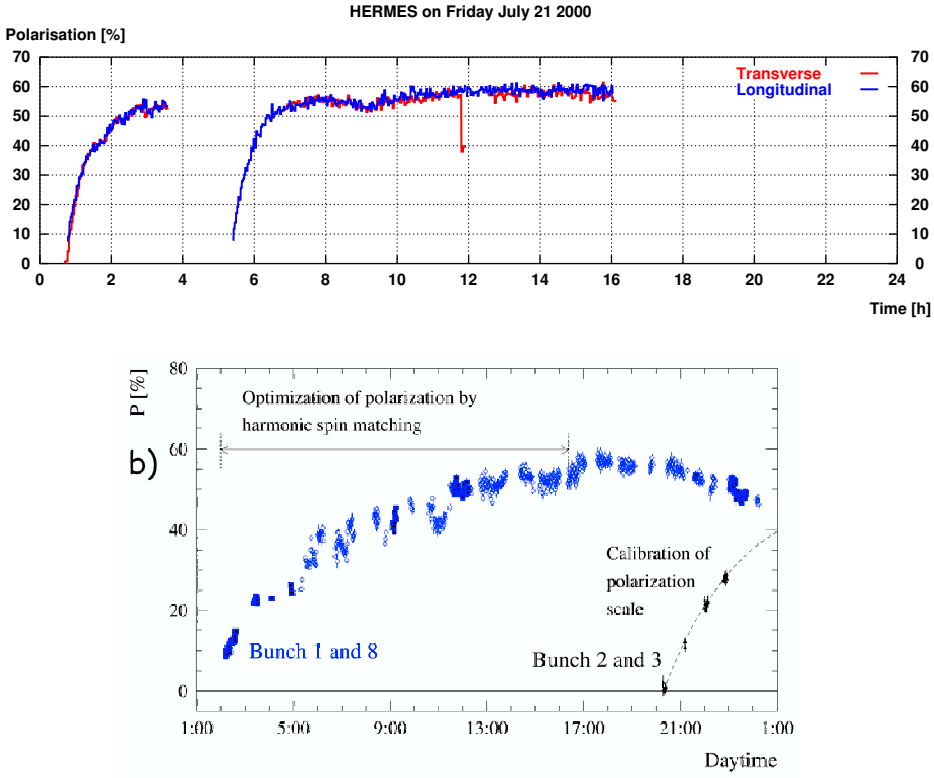

Figure 10: a) Development of transverse, and longitudinal polarization after "spin rotation", measured in the HERA ring at DESY in two positron fills; b) similar growth of transverse polarization measured in the LEP ring at CERN at 46 GeV.

4 Experimentation at the LHeC

The major feature of the LHeC (70 GeV $\otimes$ 7 TeV) kinematics is the electron-hadron beam momentum asymmetry, giving rise to the ep system moving in the proton beam direction with a Lorentz γ of about 5, compared with about 3 at HERA. This has the desirable feature that high-y (low-x) scattered electrons are boosted to larger angles, and the undesirable feature that high Q^2 physics is boosted to more forward angles.

Thus the challenge at the LHeC is detection in the "forward" (hadron beam) direction so as to resolve the expected jet structures at the TeV energy scale. For the option described in section 3 aimed at the highest luminosity, "forward" means down to about 10^o, and the challenge is to improve on instrumentation at HERA using the developments of the last 15 years in segmented track and calorimeter detectors.

For low-x physics, the challenge is to achieve multi-particle reconstruction as close to the beam pipe as possible, while maintaining as precise as possible detection at larger angles and over the appropriate range of final state lepton and jet energies. The small angle (adjacent to the beam pipe) instrumentation must also be able to resolve "rapidity gaps" in hadron

production if the wealth of colour-singlet, chromodynamic, physics is to be possible. For very forward production, one may be able to take advantage of the "Roman-pot"-like initiatives for CMS (TOTEM [18], FP420 [19]) and for ATLAS (FP420), which are now just beginning to face the reality of beam-pipe instrumentation in the full face of the LHC p-beam. Low-x eA physics poses similarly challenging, but often different, requirements for detection close to the beam-pipe.

It is not yet clear the degree to which an experiment optimized for ep physics could also be optimized for eA physics.

The timescale for completion of the LHeC machine, which is outlined in section 3 above, is also essential if thorough design, R&D, and optimization phases are to be carried out before construction of an experiment begins. Furthermore, it will be essential the specification for an experiment includes the requirement of handling the luminosity which can be foreseen throughout the lifetime of the LHC.

5 Conclusion and Summary

An LHeC, consisting of a 70 to 100 GeV electron or positron (e) beam in collision with the 7 TeV proton and ion beams at the LHC, can be built. Its energy and its luminosity, when combined with the precision and acceptance which is possible with an experiment at an ep collider, will bring *both* additional discovery *and* new understanding to future physics at the TeV energy scale.

The specifications for an electron and positron storage ring with which the necessary ep luminosity could be obtained at one LHC interaction point (IP) are realisable. They include the maintenance of pp and AA physics together with ep physics by means of an appropriate bypass for the e-beam in each of the other LHC IPs. The LHeC luminosity will increase further with improvements in the LHC hadron beam intensity.

The LHeC is therefore an upgrade of the LHC facility at CERN, and is not a new, multi-billion euro, global project. If constructed, it will stay at the "cutting-edge" for at least as long as does the LHC, taking data simultaneously with pp and heavy ion experiments.

The physics programme at the LHeC will be pivotal in the era of TeV physics at the LHC and the discoveries there which will change the face of physics in the 21^{st} century, much as lepton-proton physics has been pivotal throughout the development of the Standard Model in the 20^{th} century. There is no other way foreseen at the moment, other than with the LHeC, to investigate the direct interaction of leptons and quarks at the TeV energy scale. The LHeC is thus crucial to the pursuit of an understanding of one of the most important questions in physics, namely why are there *both* leptons *and* quarks?

Acknowledgements

I wish to thank my immediate colleagues, Des Barber, Max Klein, Paul Newman, Emmanuelle Perez, and Ferdy Willeke with whom this work has so far been completed. I hope that the opportunities, which are presented by the possibility of an LHeC, will encourage many to join in and to work with CERN with a view to the realization of an exciting new round of lepton-hadron physics at the TeV energy scale in parallel with hadron-hadron physics at the LHC.

I also wish to thank many other colleagues, too numerous to name, with whom for more than two decades I have been privileged to work at DESY. This year, 2007, HERA concludes

its data-taking phase, and DESY takes its final steps after half a century towards becoming a "light source" laboratory. It is therefore appropriate here to express my gratitude for the scientific excellence of the laboratory which has underpinned the careers of many worldwide, including myself, in Particle Physics.

Many new, and not so new, colleagues at the Cockcroft Institute and at CERN have kept my enthusiasm for LHeC from clouding the challenges which such a machine poses for accelerator physics.

Without the substantial help of the DIS07 editorial team, my contribution to these proceedings would not have been possible, for which I am also very grateful.

References

[1] M. Gell-Mann, Phys. Lett. **8** (1964) 214
G. Zweig, "An SU_3 Model for Strong Interaction Symmetry and Its Breaking", CERN Report TH-412 (Geneva 1964), and "Fractionally Charged Particles and SU_6", in Symmetries in Elementary Particle Physics (Academic Press, New York, 1965) 192.

[2] J. D. Bjørken, Phys. Rev. **179** (1969) 1547, Phys.Rev. **163** (1967) 1767
R. P. Feynman, unpublished calculations for SLAC end station A experiment (1969), and Phys. Rev. Lett. 23 (1969) 1415
M. Riordan, account of application of Feyman;s calculations to SLAC data, "The Hunting of the Quark" (Simon and Schuster 1987) 148-155

[3] R. E. Taylor, Proc. 4^{th} International Symposium on Electron and Photon Interactions at High Energies (Liverpool, England, September 14-20, 1969), 251
E. D. Bloom et al., Phys. Rev. Lett. 23 (1969) 930
M. Breidenbach, PhD Thesis, MIT Laboratory for Nuclear Science Report MIT-COO-2098-635 (1970)

[4] A. Salam, "The Unconfined Quarks and Gluons", in Proceedings, XVIII International Conference on High Energy Physics, Tbilisi, USSR, July 1976

[5] J. B. Dainton, M. Klein, P. Newman, E. Perez, F. Willeke, "Deep Inelastic Electron-Nucleon Scattering at the LHC", JINST **1** P10001, DESY-06-006, Cockcroft 06-05, `http://xxx.lanl.gov/abs/hep-ex?papernum=0603016`

[6] H. Abramowicz et al., TESLA TDR, DESY-2001-011, ECFA-2001-209 (2001); the THERA Book, DESY-LC-REV-2001-062 `http://www.ifh.de/thera/`

[7] D. Schulte and .F Zimmermann, "QCD Explorer", Proceedings of the Particle Accelerator Conference EPAC04, Lucerne, Switzerland, 2004

[8] S. Chattopadhyay, private communication

[9] H1 Collab., C. Adloff et al., Eur. Phys. J. **C11** (1999) 447

[10] H1 Collab., A. Aktas et al., Eur. Phys. J. **C45** (2006) 23
H1 Collab., A. Aktas et al., Eur. Phys. J. **C40** (2005) 349

[11] H1 Collab., A. Aktas et al., Eur. Phys. J. **C48** (2006) 715
H1 Collab., A. Aktas et al., Eur. Phys. J. **C48** (2006) 749

[12] H1 Collab., C. Adloff et al., Eur. Phys. J. **C6** (1999) 587
ZEUS Collaboration; S. Chekanov et al., Nucl. Physics **B637** (2002) 3
ZEUS Collaboration; S. Chekanov et al. Nuclear Physics **B776** (2007) 1

[13] V N Gribov, Zh. Eksp. Teor. Fiz. **53** (1967) 654
C. Edward Jones, F. E. Low, S.-H. H. Tye, G. Veneziano, J. E. Young, Phys. Rev. **D6** (1973) 1033

[14] H1 Collab., C. Adloff et al., Phys.Lett. **B517** (2001) 47
ZEUS Collaboration; S. Chekanov et al., Phys. Lett. **B573** (2003) 46-62
H1 Collab., A. Aktas et al., Eur. Phys. J. **C44** (2005) 1

[15] A. A. Sokolov, I F Ternov, Dokl. Akad. Nauk SSSR **153** (1963) 1052, [Sov. Phys. Dokl. **8** (1964) 1203]

[16] D. P. Barber et al., Phys.Lett. **B343** (1995) 436

[17] R. Assmann et al., Proc. 11th Int. Symp. on High Energy Spin Physics, Bloomington, Indiana, USA, September 1994, Eds. K. J. Heller and S.L. Smith, AIP Conf. Proc. **343** (1995) 219

[18] V. Avati et al., EPJdirect **A1** (2003) 1

[19] "FP420: an R&D Proposal to investigate the feasibility of installing proton Tagging Detectors in the 420 m Region at the LHC" http://www.fp420.com/papers/fp420_UK_2006.pdf
[20] Slides:
http://indico.cern.ch/contributionDisplay.py?contribId=271&sessionId=10&confId=9499

List of Participants

Abramowicz	Halina	DESY, Hamburg / Tel Aviv University
Abt	Iris	MPI for Physics, Munich
Akopov	Zaven	DESY, Hamburg
Alekhin	Sergey	Institute for High Energy Physics, Protvino
Antunovic	Biljana	MPI for Physics, Munich
Aronson	Samuel	Brookhaven National Laboratory, Upton
Ask	Stefan	CERN, Geneva
Atomssa	Ermias	LLR, Ecole Polytechnique, Palaiseau
Atramentov	Oleksiy	Florida State University, Tallahassee
Avsar	Emil	Lund University
Bacchetta	Alessandro	DESY, Hamburg
Baghdasaryan	Artem	Yerevan Physics Institute
Baillie	Nathan	College of William and Mary, Williamsburg
Balewski	Jan	Indiana University, Bloomington
Banfi	Andrea	Universita di Milano-Bicocca
Barlow	Nick	University of Manchester
Basso	Benjamin	Laboratoire de Physique Theorique, Orsay
Behnke	Olaf	University of Heidelberg
Bethke	Siegfried	MPI for Physics, Munich
Beuf	Guillaume	Service de physique theorique, CEA/Saclay, Gif-sur-Yvette
Bhadra	Sampa	York University, Toronto
Blümlein	Johannes	DESY, Zeuthen
Boer	Daniël	Vrije Universiteit Amsterdam
Bomhof	Cedran	Vrije Universiteit Amsterdam
Borras	Kerstin	DESY, Hamburg
Bracinik	Juraj	MPI for Physics, Munich
Brandt	Gerhard	University of Heidelberg
Bressan	Andrea	University of Trieste
Brown	Duncan	University of Virginia, Charlottesville
Bruell	Antje	Jefferson Lab, Newport News
Brzozowska	Beata	Warsaw University
Buschhorn	Gerd	MPI for Physics, Munich
Caldwell	Allen	MPI for Physics, Munich
Cammin	Jochen	University of Rochester
Caron	Sascha	University of Freiburg
Chekanov	Sergei	Argonne National Laboratory / DESY, Hamburg
Chekelian	Vladimir	MPI for Physics, Munich
Chiarelli	Giorgio	INFN Sezione di Pisa
Clements	Daniel	University of Glasgow
Cole	Philip	Idaho State University, Pocatello

Cooper-Sarkar	Amanda	Oxford University
Corcoran	Marjorie	Rice University, Houston
Corradi	Massimo	INFN Bologna
D'Alesio	Umberto	University of Cagliari and INFN, Monserrato
d'Enterria	David	CERN, Geneva
D'Onofrio	Monica	Institut de Fisica d'Altes Energies, Barcelona
Dainton	John	Cockcroft Institute and Liverpool University, Warrington
Danielson	Thomas	University of Wisconsin, Madison
Dasgupta	Mrinal	Manchester University
Daum	Karin	University of Wuppertal / DESY, Hamburg
de Boer	Ytsen	ITEP, Mocow / DESY, Hamburg
De Nardo	Lara	DESY, Hamburg / TRIUMF, Vancouver
de Visscher	Simon	Université Catholique de Louvain, Louvain La Neuve
De Wolf	Eddi	University of Antwerpen
Del Degan	Marc	ETH Zürich
Delenda	Yazid	University of Manchester
Deshpande	Abhay	SUNY, Stony Brook
Detmold	William	University of Washington, Seattle
Devenish	Robin	University of Oxford
Devgun	Prabhdip Kaur	Panjab University / MPI for Physics, Munich
Diaconu	Cristinel	CPP Marseille
Diefenthaler	Markus	Friedrich-Alexander-University, Erlangen
Diehl	Markus	DESY, Hamburg
Dokshitzer	Yuri	University Paris VI-VII and CNRS / PNPI, St. Petersburg
Dubak	Ana	University of Montenegro, Podgorica / MPI for Physics, Munich
Dubnicka	Stanislav	Inst. of Physics, Slovak Academy of Science, Bratislava
Dubnickova	Anna Zuzana	FMFI, Comenius University, Bratislava
Erdmenger	Johanna	MPI for Physics, Munich
Ermolaev	Boris	Ioffe Physico-Technical Institute, St. Petersburg
Ewerz	Carlo	ECT* Trento, Villazzano
Eyser	K. Oleg	University of California, Riverside
Fang	Shuangshi	DESY, Hamburg
Favart	Laurent	Universite Libre de Bruxelles
Feltesse	Joël	CEA and DSM/DAPNIA, Saclay, Gif-sur-Yvette
Ferrando	James	University of Oxford
Fischer	Horst	University of Freiburg
Friedrich	Jan	Technical University Munich
Gabbert	Dominik	DESY, Zeuthen
Gallo	Elisabetta	INFN Firenze
Gamberg	Leonard	Penn State University-Berks, Reading

Gehrmann	Aude	ETH Zürich
Geiser	Achim	DESY, Hamburg
Gerber	Cecilia	University of Illinois at Chicago
Glazov	Alexander	DESY, Hamburg
Gough Eschrich	Ivo	University of California, Irvine
Gousset	Thierry	Subatech-Universite de Nantes
Gouzevitch	Maxime	Ecole Polytechnique, Palaiseau
Greenshaw	Tim	Liverpool University
Grindhammer	Günter	MPI for Physics, Munich
Habib	Shiraz	University of Hamburg
Hägler	Philipp	Technical University Munich, Garching
Haisch	Ulrich	University of Zürich
Hansmann-Menzemer	Stephanie	University of Heidelberg
Harlander	Robert	University of Wuppertal
Hart	Alistair	University of Edinburgh
Hasch	Delia	INFN-Frascati
Hautmann	Francesco	University of Regensburg
Hayashii	Hisaki	Nara Womens University
Hayg	Guler	DESY, Hamburg
Heck	Martin	Karlsruhe Institute of Technology (KIT)
Heinsius	Fritz-Herbert	University of Bochum
Heinz	Mark	Yale University, New Haven
Hendlmeier	Christof	University of Regensburg
Heppelmann	Steven	Penn State University, University Park
Heuer	Rolf-Dieter	DESY, Hamburg
Hiller	Karlheinz	DESY, Zeuthen
Holtrop	Maurik	University of New Hampshire, Durham
Hornback	Donald	University of Tennessee, Knoxville
Ivanov	Dmitry	Sobolev Institute of Mathematics, Novosibirsk
Jabeen	Shabnam	Boston University
Jung	Hannes	DESY, Hamburg
Kabuss	Eva-Maria	University of Mainz
Kahle	Benjamin	DESY, Hamburg
Katzy	Judith	DESY, Hamburg
Kawamura	Hiroyuki	RIKEN, Wako
Kehoe	Robert	Southern Methodist University, Dallas
Ketzer	Bernhard	Technical University Munich, Garching
Khein	Lev	SINP, Moscow State University
Kidonakis	Nikolaos	Kennesaw State University
Kiesling	Christian	MPI for Physics, Munich
Klasen	Michael	University of Grenoble I - LPSC
Klein	Max	University of Liverpool
Klein	Uta	University of Liverpool
Kluge	Thomas	DESY, Hamburg
Kniehl	Bernd	University of Hamburg
Koblitz	Susanne	University of Mainz

Koike	Yuji	Niigata University
Kollar	Daniel	MPI for Physics, Munich
Korcsak-Gorzo	Katherine	University of Oxford
Korzenev	Alexander	Mainz University
Kotzinian	Aram	INFN Torino
Kowalski	Henri	DESY, Hamburg
Kramer	Gustav	University of Hamburg
Krasznahorkay	Attila	University of Debrecen / CERN, Geneva
Krüger	Katja	University of Heidelberg
Kuhn	Roland	Technical University Munich, Garching
Kumar	Krishna	University of Massachusetts, Amherst
Kurek	Krzysztof	Soltan Institute for Nuclear Studies, Warsaw
Königsmann	Kay	University of Freiburg
Lajoie	John	Iowa State University, Ames
Le Bihan	Anne-Catherine	CERN, Geneva
Lee	Jeong Hun	Brookhaven National Laboratory, Upton
Lendermann	Victor	University of Heidelberg
Levchenko	Boris	SINP, Moscow State University
Levy	Aharon	Tel Aviv University / DESY, Hamburg
Li	Gang	LAL, Orsay
Liebing	Patricia	RIKEN-BNL Research Center, Upton
Linden Levy	Loren	University of Illinois, Urbana
Lipatov	Lev	Petersburg Nuclear Physics Institute, St. Petersburg
Lipka	Katerina	University of Hamburg
Liptaj	Andrej	MPI for Physics, Munich
List	Benno	University of Hamburg
Liuti	Simonetta	University of Virginia, Charlottesville
Lobodzinska	Ewelina Maria	DESY, Hamburg
Löhr	Bernd	DESY, Hamburg
Loizides	John	University College London
Lublinsky	Michael	SUNY, Stony Brook
Lukasik	Jaroslaw	AGH-UST, Cracow / DESY, Hamburg
Lung	Allison	Jefferson Lab, Newport News
Magnea	Lorenzo	University of Torino
Makins	Naomi	University of Illinois at Urbana-Champaign
Malik	Sarah	University College London
Mallot	Gerhard	CERN, Geneva
Mankel	Rainer	DESY, Hamburg
Maravin	Yurii	Kansas State University, Manhattan
Marquet	Cyrille	RIKEN-BNL Research Center, Upton
Martin	John	University of Toronto
Melzer-Pellmann	Isabell-Alissandra	DESY, Hamburg
Mesropian	Christina	The Rockefeller University, New York
Metz	Andreas	Ruhr-University Bochum
Meyer	Werner	Ruhr-University Bochum

Meziani	Zein-Eddine	Temple University, Philadelphia
Miller	Andrew	TRIUMF, Vancouver
Milov	Alexander	Brookhaven National Laboratory, Upton
Mischke	Andre	Utrecht University
Moch	Sven-Olaf	DESY, Zeuthen
Motyka	Leszek	University of Hamburg / Jagellonian University, Cracow
Motylinski	Patrick	NIKHEF, Amsterdam
Mozer	Matthias	Vrije Universiteit Brussel
Müller	Katharina	University of Zürich
Mussgiller	Andreas	University of Erlangen
Nagano	Kunihiro	KEK, Tsukuba
Nagel	Thiemo	Technical University Munich, Garching
Nagy	Zoltan	CERN, Geneva
Nakamura	Isamu	KEK, Tsukuba
Naryshkin	Yuri	Petersburg Nuclear Physics Institute, St. Petersburg
Newman	Paul	University of Birmingham
Nicholass	Daniel	Argonne National Laboratory / University College London
Niebuhr	Carsten	DESY, Hamburg
Nikolaev	Nikolai	Forschungszentrum Jülich / Landau Institute, Moscow
Nowak	Grazyna	Institute of Nucelar Physics PAN, Cracow
Nunnemann	Thomas	Ludwig-Maximilians-University Munich, Garching
Ochs	Wolfgang	MPI for Physics, Munich
Ogilvie	Craig	Iowa State University, Ames
Okada	Kensuke	Riken-BNL Research Center, Upton
Olivier	Bob	MPI for Physics, Munich
Olsson	Jan	DESY, Hamburg
Osman	Sakar	Lund University
Ota	Osamu	Tokyo Metropolitan University
Pakhlova	Galina	ITEP, Moscow
Paul	Stephan	Technical University Munich, Garching
Perez	Emmanuelle	CERN, Geneva
Perrey	Hanno	University of Hamburg
Peschanski	Robi	Service de Physique Théorique, Saclay Gif-sur-Yvette
Pierce	Joshua	University of Virginia, Charlottesville
Pilkington	Andrew	University of Manchester
Pinera	Lester	University of Florida, Gainesville
Pisano	Cristian	Vrije Universiteit Amsterdam
Poireau	Vincent	LAPP, Annecy-le-Vieux
Pretz	Jörg	Bonn University
Radescu	Voica	DESY, Hamburg
Radici	Marco	INFN and University of Pavia

Raičevi	c	Nataša	University of Montenegro, Podgorica
	Raspereza	Alexei	MPI for Physics, Munich
	Rebuzzi	Daniela	INFN and University of Pavia
	Reisert	Burkard	MPI for Physics, Munich
	Richard	Jean-Marc	University of Grenoble I - LPSC
	Robson	Aidan	Glasgow University
	Rogal	Mikhail	DESY, Zeuthen
	Rojo-Chacon	Juan	LPTHE, Paris
	Ron	Elias	Universidad Autonoma de Madrid
	Roosen	Robert	Vrije Universiteit Brussels
	Rossi	Patrizia	Laboratori Nazionali di Frascati - INFN
	Rostomyan	Armine	DESY, Hamburg
	Royon	Christophe	DAPNIA-SPP, CEA Saclay, Gif-sur-Yvette
	Rurikova	Zuzana	DESY, Hamburg
	Ruspa	Marta	University of Piemonte Orientale, Novara
	Sabio Vera	Agustin	CERN, Geneva
	Saleev	Vladimir	Samara State University
	Santovetti	Emanuele	INFN - Rome II
	Sapeta	Sebastian	Jagellonian University, Cracow / CERN, Geneva
	Saremi	Sepehr	University of Massachusetts at Amherst
	Sauvan	Emmanuel	CCPM Marseille
	Savin	Alexander	University of Wisconsin, Madison
	Sbrizzi	Antonello	University of Bologna
	Schildknecht	Dieter	University of Bielefeld / MPI for Physics, Munich
	Schill	Christian	University of Freiburg
	Schilling	Frank-Peter	University of Karlsruhe
	Schlenstedt	Stefan	DESY, Zeuthen
	Schmidke	William	MPI for Physics, Munich
	Schmidt	Sebastian	DESY, Hamburg
	Schoeffel	Laurent	CEA Saclay, Gif-sur-Yvette
	Schörner-Sadenius	Thomas	University of Hamburg
	Sciulli	Frank	Columbia University, Nevis Labs., Irvington on Hudson
	Segond	Mathieu	LPT Orsay
	Seidl	Ralf	University of Illinois at Urbana-Champaign
	Seitz	Bjoern	University of Glasgow
	Seth	Kamal	Northwestern University, Evanston
	Shekhovtsova	Olga	LNF INFN, Frascati
	Shimizu	Shima	University of Tokyo
	Shoshi	Arif	Bielefeld University
	Simon	Frank	MIT, Cambridge
	Singh	Inderpal	Panjab University / MPI for Physics
	Slifer	Karl	University of Virginia, Newport News
	Specka	Arnd	Ecole Polytechnique, Palaiseau
	Spira	Michael	Paul Scherrer Institute, Villigen

Stadie	Hartmut	University of Hamburg
Stamenov	Dimitar	INRNE, Bulgarian Academy of Sciences, Sofia
Steder	Michael	DESY, Hamburg
Ströhmer	Raimund	Ludwig-Maximilians-University Munich
Stuart	David	University California, Santa Barbara
Surrow	Bernd	Massachusetts Institute of Technology, Cambridge
Szuba	Dorota	DESY, Hamburg
Tanaka	Kazuhiro	Juntendo University, Chiba
Teubner	Thomas	University of Liverpool
Thompson	Paul	University of Birmingham
Thorne	Robert	University College London
Tokushuku	Katsuo	KEK, Tsukuba
Toole	Terrence	University of Maryland, College Park
Tramontano	Francesco	Università di Napoli "Federico II"
Traynor	Daniel	Queen Mary, University of London
Trinh	Thi Nguyet	CPPM Marseille
Truöl	Peter	University of Zürich
Tseepildorj	Baatar	Institute of Physics and Technology, MAS, Ulaanbaatar
Tung	Wu-Ki	Michigan State University, East Lansing / University of Washington, Seattle
Utermann	Andre	Vrije Universiteit Amsterdam
Vallecorsa	Sofia	University of Geneva
Vallee	Claude	CPPM Marseille
Van Haarlem	Yves	University of Gent
Vargas Trevino	Andrea	DESY, Hamburg
Venugopalan	Raju	Brookhaven National Laboratory, Upton
Vicini	Alessandro	University of Milano
Vilar	Rocio	Universidad de Cantabria, Santander
Vogt	Andreas	University of Liverpool
Voutier	Eric	University of Grenoble I - LPSC
Wagner	Jeannine	University of Karlsruhe
Weiss	Christian	Jefferson Lab, Newport News
Weisz	Peter	MPI for Physics, Munich
Wessels	Martin	DESY, Hamburg
White	Chris	NIKHEF, Amsterdam
Wing	Matthew	University College London
Wolfe	Homer	University of Wisconsin, Madison
Yamazaki	Yuji	KEK, Tsukuba
Yang	Un-ki	University of Manchester
Yuan	Chien-Peng	Michigan State University, East Lansing
Zajc	William A.	Columbia University, New York
Zanderighi	Giulia	CERN, Geneva
Zotov	Nikolay	SINP, Moscow State University
zur Nedden	Martin	Humboldt-University of Berlin

List of Authors